LHCP2015

Proceedings of the Third Annual Conference on Large Hadron Collider Physics

Editors: Victor T. Kim and Dmitry E. Sosnov

ISBN: 978-5-86763-405-6

Proceedings of the Third Annual Conference on Large Hadron Collider Physics

31 August – 5 September 2015
Saint Petersburg, Russia

Editors:
Victor T. Kim and Dmitry E. Sosnov

Proceedings of

the 3rd Annual Large Hadron Collider Physics Conference

LHCP2015

Saint Petersburg, Russia
31 August – 5 September 2015

Editors:

Victor T. Kim and Dmitry E. Sosnov

B.P. Konstantinov Petersburg Nuclear Physics Institute
National Research Centre "Kurchatov Institute"

Proceedings of the 3rd Annual Large Hadron Collider Physics Conference
LHCP2015
Saint Petersburg, Russia, 31 August – 5 September 2015

Editors:
Victor T. Kim and Dmitry E. Sosnov

Photos courtesy of INNO-MIR, Dyagilev Centre,
T. Potapova, N. Sagidova and J. Richman

ISBN 978-5-86763-405-6

Printed at PNPI NRC “Kurchatov Institute”, Gatchina, Russia

PREFACE

This publication is a collection of contributions presented at the 3rd Annual Large Hadron Collider Physics Conference (LHCP2015), which was held at Saint Petersburg, Russia, from August 31 to September 5 2015.

The LHCP2015 conference is the major international conference of the collaborations at the Large Hadron Collider (LHC) at the European Organization for Nuclear Research (CERN), Geneva. This conference is a result of a recent merger of two international conferences: "Physics at Large Hadron Collider" and "Hadron Collider Physics Symposium". The first LHCP conferences were held in Barcelona, May 2013 (LHCP2013) and in New York City, June 2014 (LHCP2014).

The LHCP2015 was a special conference, where fresh results from the LHC Run 2 were presented for the first time. The program was devoted to a review of the latest experimental and theoretical results on hadron collider physics, and to discussions on the outlook for the coming years. During the plenary talks and the parallel and poster sessions, there were lively discussions between experimentalists and theorists on various topics such as the Standard Model Physics and Beyond, the Higgs Boson, the Supersymmetry and the Heavy Ion Physics, as well as planning for the high luminosity Upgrades.

More details and the genuine talk's slides can be found on the LHCP2015 web-page:
https://indico.cern.ch/event/389531/timetable/

The conference was attended by about 350 participants from 30 countries, who delivered 142 talks and presented 58 posters. The conference website was visited more than 20 thousand times from 102 countries.

The LHCP2015 was jointly organized by the National Research Centre "Kurchatov Institute" (NRC KI, Moscow), the B.P. Konstantinov Petersburg Nuclear Physics Institute of NRC KI (PNPI NRC KI, Gatchina), the Institute of High Energy Physics Institute of NRC KI (IHEP NRC KI, Protvino), the A.I. Alikhanov Institute of Theoretical and Experimental Physics of NRC KI (ITEP NRC KI, Moscow), the Joint Institute for Nuclear Research (JINR, Dubna), the Saint Petersburg State University (SPbSU), the Saint Petersburg Polytechnic University (SPbPU) and the European Organization for Nuclear Research (CERN) with support and partnership of the Saint Petersburg Scientific Center of the Russian Academy of Sciences (SPbSC RAS), the Russian Foundation for Basic Research (RFBR), INNO-MIR and the Yandex School of Data and Analysis (YSDA).

During the conference, there were various social events. In particular, a piano concert by Polina Ossetinskaya and an exhibition "Arts@CMS" at SPbPU. The LHCP2015 press-conference for national and local media was held at SPbSU. There were also two satellite events: the YSDA School with about 50 participants, and the LHCP2015 Outreach Event at SPbPU, where about 250 school students and school teachers were presented.

The Editors: Victor T. Kim (PNPI NRC KI, Gatchina & SPbPU, St. Petersburg)
Dmitry E. Sosnov (PNPI NRC KI, Gatchina)

ORGANIZERS

National Research Centre “Kurchatov Institute” (NRC KI, Moscow)

B.P. Konstantinov Petersburg Nuclear Physics Institute of NRC KI (PNPI NRC KI, Gatchina)

Institute of High Energy Physics Institute of NRC KI (IHEP NRC KI, Protvino)

A.I. Alikhanov Institute of Theoretical and Experimental Physics of NRC KI (ITEP NRC KI, Moscow)

Joint Institute for Nuclear Research (JINR, Dubna)

Saint Petersburg State University (SPbSU)

Saint Petersburg Polytechnic University (SPbPU)

European Organization for Nuclear Research (CERN)

PARTNERS AND SPONSORS

Saint Petersburg Scientific Center of the Russian Academy of Sciences (SPbSC RAS)

Russian Foundation for Basic Research (RFBR)

INNO-MIR Ltd.

Yandex School of Data and Analysis (YSDA)

International Advisory Committee

Tiziano Camporesi (CERN, Geneva)
Marcela Carena (FNAL, Batavia)
Dave Charlton (Univ. of Birmingham)
Daniel Denegri (CEA, Saclay)
Paolo Giubellino (CERN & INFN, Torino)
Andrei Golutvin (IC, London)
Paul Grannis (Stony Brook Univ.)
Peter Jenni (CERN & Univ. of Freiburg)
Mikhail Kovalchuk (NRC KI, Moscow)
Lev Lipatov (PNPI, Gatchina & SPbSU, St. Petersburg)
Mario Martinez (ICREA & IFAE, Barcelona)
Victor Matveev (JINR, Dubna)
Srini Rajagopalan (BNL, Upton)
Valery Rubakov (INR RAS, Moscow)
Karel Safarik (CERN, Geneva)
Katsuo Tokushuku (KEK, Tsukuba)
Mike Tuts (Columbia Univ.)
Guy Wilkinson (Univ. of Oxford)

National Organizing Committee

Sergey Afonin (SPbSU, St. Petersburg) – NOC Co-Chair
Yaroslav Berdnikov (SPbPU, St. Petersburg) – NOC Co-Chair
Alexandre Bondar (BINP SDRAS, Novosibirsk)
Igor Dremin (LPI RAS, Moscow)
Victor Egorychev (ITEP NRC KI, Moscow)
Oleg Fedin (PNPI NRC KI, Gatchina) – NOC Co-Chair
Grigory Feofilov (SPbSU, St. Petersburg)
Igor Golutvin (JINR, Dubna)
Gennady Kozlov (JINR, Dubna)
Vladimir Petrov (IHEP NRC KI, Protvino)
Nikolai Rusakovich (JINR, Dubna)
Victor Sarantsev (PNPI NRC KI, Gatchina)
Victor Savrin (SINP MSU, Moscow)

Conference Chairs

Gregorio Bernardi (LPNHE & Univ. of Paris VI & VII)
Guenakh Mitselmakher (Univ. of Florida)
Alexey Vorobyev (PNPI NRC KI, Gatchina)
Alexandre Zaitsev (IHEP NRC KI, Protvino)

Conference Scientific Secretary

Victor Kim (PNPI NRC KI, Gatchina & SPbPU, St. Petersburg)

Program Committee

Alexander Andrianov (SPbSU, St. Petersburg)
Federico Antinori (INFN, Padova)
Vadim Bednyakov (JINR, Dubna)
Eduard Boos (SINP MSU, Moscow)
Sally Dawson (BNL, Upton)
Vladimir Gavrilov (ITEP NRC KI, Moscow)
Tim Gershon (Univ. of Warwick, Coventry)
Christophe Grojean (Univ. of Barcelona)
Dmitri Kazakov (JINR, Dubna)
Patrick Koppenburg (NIKHEF, Amsterdam)
Frank Krauss (IPPP, Durham)
Stephanie Majewski (Univ. of Oregon, Eugene)
Luca Malgeri (CERN, Geneva) – PC Co-Chair
Vladislav Manko (NRC KI, Moscow)
Bill Murray (Univ. of Warwick, Coventry & STFC) – PC Co-Chair
Alexandre Nikitenko (IC, London & ITEP NRC KI, Moscow)
Vladimir Obraztsov (IHEP NRC KI, Protvino)
Jim Olsen (Princeton Univ.)
Juan Rojo (Univ. of Oxford)
Mikhail Ryskin (PNPI NRC KI, Gatchina)
Vladimir Shevchenko (NRC KI, Moscow)
Matt Strassler (Rutgers Univ.)
Tim Tait (Univ. of California, Irvine)
David Toback (Texas A&M Univ., College Station)
Rick van Kooten (Indiana Univ., Bloomington)
Ermanno Vercellin (Univ. of Torino & INFN, Torino)

Technical Secretariat

Kirsti Aspola (CERN, Geneva)
Alina Belova (CERN, Geneva)
Natalia Nikitina (PNPI NRC KI, Gatchina)
Alina Petukhova (INNO-MIR, St. Petersburg)
Rimma Zheronkina (PNPI NRC KI, Gatchina)

Contents

Heavy Flavour physics: parallel talks

Heavy Ion physics: parallel talks

Performance: parallel talks

Upgrade: parallel talks

Future Colliders: parallel talks

Closing plenary talks

Poster presentations

Opening plenary talks

Proceedings of the LHCP2015 Conference, St. Petersburg, Russia, August 31 - September 5, 2015

Editors: V.T. Kim and D.E. Sosnov

First Look at the LHC 13 TeV Data With The CMS Detector

PAOLO SPAGNOLO

INFN sez. di Pisa, Italy

paolo.spagnolo@cern.ch

On behalf of the CMS Collaboration

Abstract. First results with the data collected in CMS detector after two months of Run II collisions at $\sqrt{s} = 13$ TeV, corresponding to few tens of inverse pb of luminsity, are presented in these proceedings. Data analyses are focused on the Physics commissioning and the first results and plots of Standard Model studies, b, top and Electroweak Physics. Some new results on searches for Physics beyond the Standard Model, Exotica and Susy, are also shown, with a particular emphasis on a dielectron event recently collected with an unexpected high invariant mass of 2.9 TeV.

INTRODUCTION

After the recent starting of Run II at a collision energy of 13 TeV, the CMS Collaboration is working in three directions:

1. The Run I analyses that are still on-going with new precision results.
2. The Run II at 13 TeV with detector and Physics commissioning and first results from data collected.
3. The preparation for the future detector upgrades.

After a brief flash on the 8 TeV Run I analyses status, this presentation is mainly dedicated to the second item, the first look at the 13 TeV data. At the startup of the new Run of LHC, a problem with the cryogenic supply of the CMS magnet occurred. This caused a relevant amount of data, corresponding to the 35% of Luminosity collected so far, was taken without magnetic B field on. However recent data have been collected efficiently with the field on and the strategy is to wait for the winter shut down in order to investigate and fix this issue of the cold box system.

RUN I LEGACY

So far CMS published more than 450 papers on the Run I data analyses, corresponding about to 20 fb^{-1} collected at 8 TeV and 5 fb^{-1} collected at 7 TeV. 2015 is still a very active year on this point of view, with many new precision analyses on the Standard Model, Electro-weak, top and B Physics recently submitted for a publication. An extensive study of the Higgs properties was performed and unfortunately no deviation from the Standard Models couplings was observed [2], as shown in Fig. 1. No evidence or hint of new Physics, Susy or Exotica in the 8 TeV data was observed. This made the 13 TeV data LHC Run II even more exiting since it will be a unique opportunity at CERN and in the whole world Particle Physics programs for the future years to open a window on the unknown and probe new Physics scenarios.

Among the many different analyses of Run I, in this proceeding I report as golden example, the new Vector Boson Fusion Higgs to $b\bar{b}$ measurement recently performed in CMS [3]. It is the first time at LHC this very difficult analysis is implemented, because of the huge QCD background rate. This measurement, considered as impossible only few years ago, was made with the help of the new sophisticated neural network techniques, such the color-reconnection and the quark-gluon separation, that helped to reduce the unfavored background rate to a decent ratio. Thanks to this new analysis that was included in a global fit with VH and ttH Higgs production channels, the Hbb coupling in CMS is now measured with a sensitivity of 2.6 σ and its value is in total agreement with the Standard Model Higgs. Figure 2 shows the likelihood combination for this measurement.

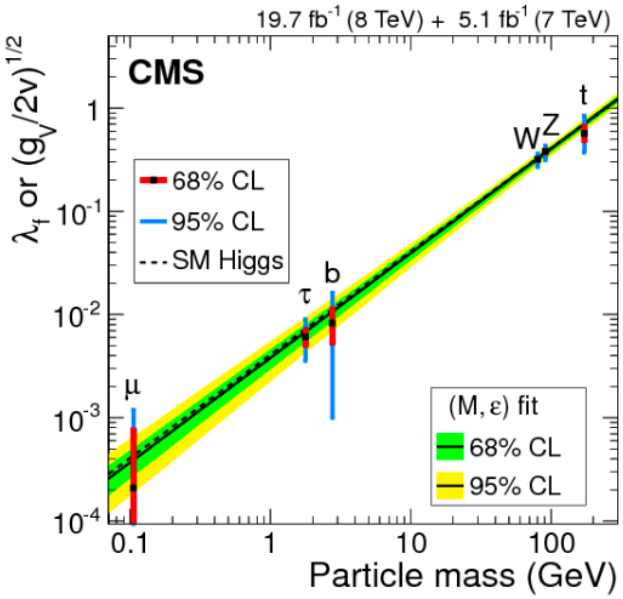

FIGURE 1. Higgs coupling to fermions measured by CMS in the Run I data

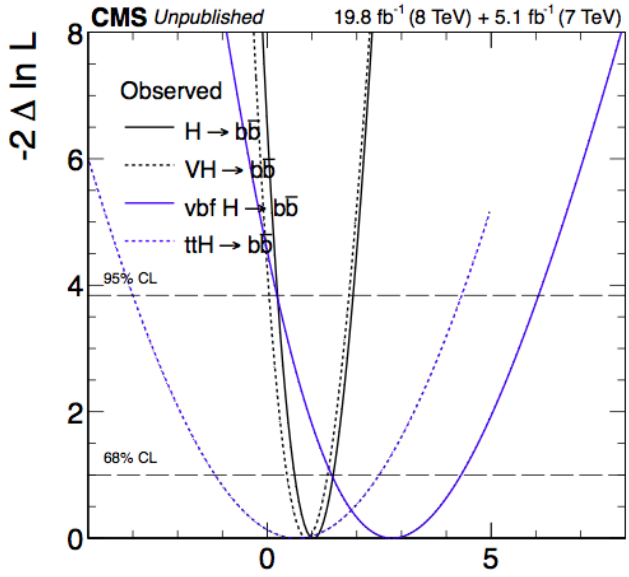

FIGURE 2. Signal strength relative to the Standard Model fit of the Higgs to bb decay channel with the combination of different production mode

RUN II FEATURES and DETECTOR PREPARATION

The Run II at 13 TeV of collision energy has important new key points for the LHC Physics. For the first time this energy will be probe in a collider, opening possible scenarios of new Physics beyond the limits of Run I. Besides, thanks to the increased parton luminosity, the effective cross-section for the Standard Model and new Physics processes is dramatically increased leading to supersede the actual limits of Run I searches for new particles after few fb^{-1}. This will be a unique and exciting opportunity for new discovery in Particle Physics.

The CMS detector is described here [1]. CMS prepared to this new Run with an upgrade of some parts of its sub-detectors implemented during the recent Long Shut-down (LS1). A new thinner beam pipe has been positioned in the interaction center to allow the next installation of a new inner Tracker layer. The pixel part of the Tracker is now operating by design with the $-20°$ C temperature to decrease the noise and improve the radiation hardness of the subdetector. New luminosity telescopes have been added in the forward region to improve luminosity measurements. A 4th muon station was installed in the end-caps as foreseen by design and new HCAL photosensors improved the hadronic calorimetry systems. Other minor recovery interventions and adjustments during LS1 allowed to have a optimal Run II start-up with all sub-detector operating with active channel fraction higher than Run I and always between 96 and 100%. Improved DAQ, Computing and Software will also allow to have a faster event reconstruction, new data format with compact high level data object and move to multi-threading with multi-core queues at CERN and Tier-1. On the Trigger side, L1 calorimeter trigger has been updated and further L1 upgrades are planned for 2016. Besides significant efforts on algorithm improvements with emphasis on pile-up mitigation have been implemented.

FIRST COLLISIONS and PHYSICS COMMISSIONING

The first collision at 13 TeV in CMS was recorded in early morning on May 21st, 2015: a new hera in Particle Physics just started. Few weeks after, the first CMS paper, entitled *Pseudorapidity distribution of charged hadrons in proton-proton collisions at* $\sqrt{s} = 13$ *TeV* , was submitted to a publication [4]. This measurement, showed in Fig. 3, performed in CMS in a special early run at 13 TeV taken with B = 0 T, gives an handle on the relative weight of soft and hard scattering contribution, testing also the compatibility between data and simulations.

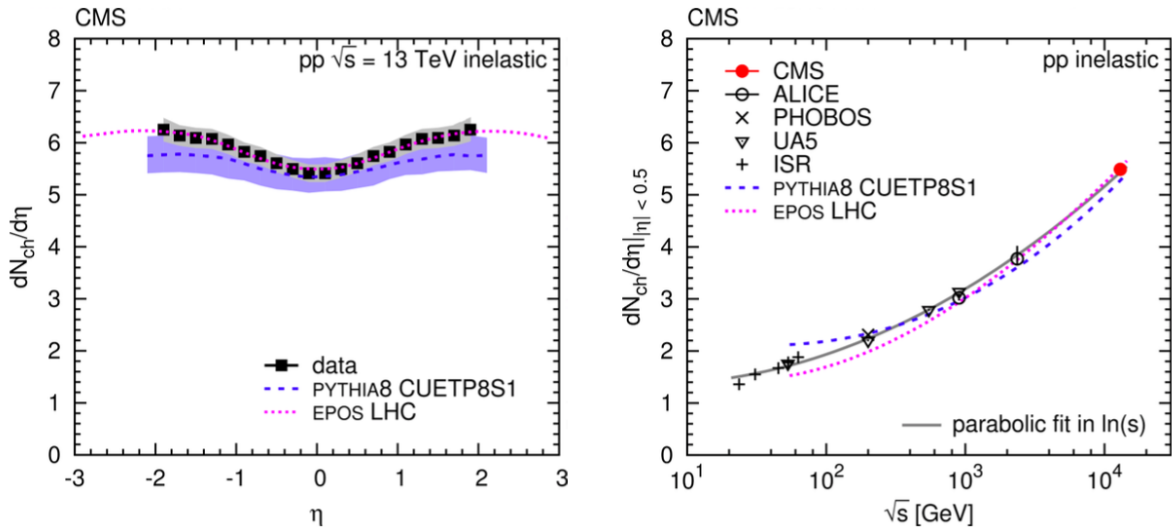

FIGURE 3. Pseudorapidity distribution of charged hadrons (left) and integrated cross-section in function of collision energy (right)

Then alignment was performed, first with Cosmics and after with collisions data, with nuclear interactions used as detector radiography to verify and map the Tracker inner layers position. A detailed dimuon spectroscopy allowed to "re-discover" all the Standard Model candles, from strange and charmed resonances, B Physics up to Z, as plotted in Fig. 4. Dielectron and ditau resonances were also measured.

The restart of the CMS magnet after LS1 was more complicated than anticipated due to a problem with the cryogenic system in providing liquid Helium. Inefficiencies of the oil separation system of the compressors for the warm

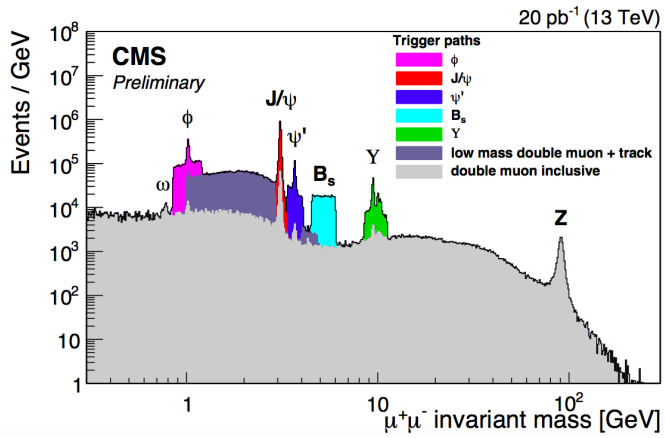

FIGURE 4. Muon spectroscopy for different trigger paths

Helium required several interventions and delayed the start of routine operation of the cryogenic system. The data delivered during the first two weeks of LHC re-commissioning with beams at low luminosity have been collected without magnetic field. Currently the magnet can be operated, but the continuous up-time is still limited by the performance of the cryogenic system requiring more frequent maintenance than usual. A comprehensive program to re-establish its nominal performance is underway. These recovery activities for the cryogenic system will be synchronized with the accelerator schedule in order to run for adequately long periods. Consolidation and repair program is ongoing during the technical stop while a full cleanup of the Cold Box is foreseen for the long Technical Stop at the end of the year

EARLY ANALYSES RESULTS

Top Physics is one of the first topics expected to be covered by CMS Run II program. The top pair production cross-section, is considerably large to be measured with few tens of pb^{-1} of luminosity collected in the very first data analyzed. The top pair cross-section is measured both in the dilepton and in the lepton+jet final states. The first measurement is obtained through the study of hadronic jets for events containing one isolated muon and one isolated electron forming an invariant mass greater than 50 GeV, the second allow to reconstruct hadronic top quark candidate mass for events containing one isolated muon and four jets candidates out of which two pass a tight b-tagging threshold. At the time of this presentation, the top pair inclusive cross-section was measured in dilepton final states [5] with 42 pb^{-1} to be:

$$\sigma_{tt}(13TeV) = 772 \pm 60(sta) \pm 62(sys) \pm 93(lum)pb$$

This result, compared to the Run I ones, is in a perfect agreement with the theoretical curves as shown in Fig. 5. With the same analysis, also differential cross-section respect to all the typical kinematic variables were measured [5]. Besides, new Run I results have been recently published, and an updated measurement of the top pole mass from NNPDF30 pdf was extracted:

$$M_{top,pole} = 173.6^{+1.7}_{-1.8}\, GeV$$

The analyses searching for Supersymmetry need more statistics to be implemented. Nevertheless, key observables shape in data were checked with Montecarlo simulation, Trigger efficiencies measured and background estimation methods tested. Examples of this exercise are plotted in Fig 6.

Early searches for new Physics started in dijet, diphoton, dilepton and lepton+missing transverse energy (MET). Dijet analysis with the current integrated luminosity of 42 pb^{-1} is expect to exceed the sensitivity of the 8 TeV Run I analyses for narrow resonances with masses greater than about 5 TeV. Figure 7 shows the invariant mass dijet spectrum: above 3.5 TeV about 5 background events are expected from the fit to data and 4 are observed, with a highest mass of 5.4 TeV.

In Fig. 8 the observed limits at 95% CL on the cross-sections of qq, qg, gg resonances are plotted: limits get worse when there are gluons in the final state because radiation increases and resolution degrades. Limits are reported

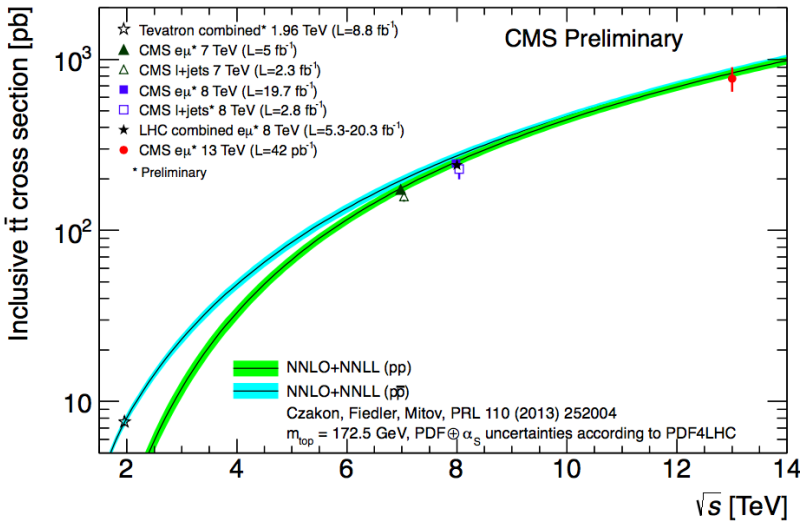

FIGURE 5. Inclusive cross-section of top pair production at the hadron colliders

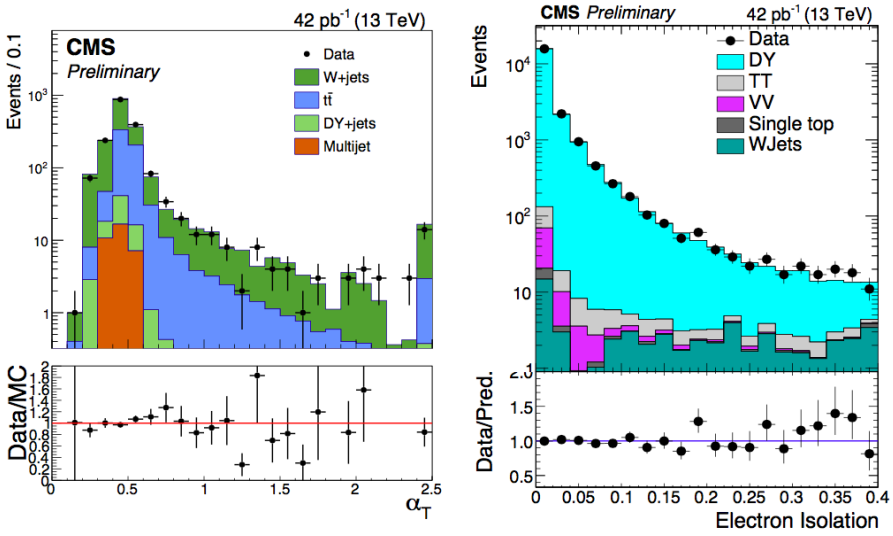

FIGURE 6. Comparison data vs simulations for two variables, α_T and electron isolation, commonly used in the SUSY search analyses

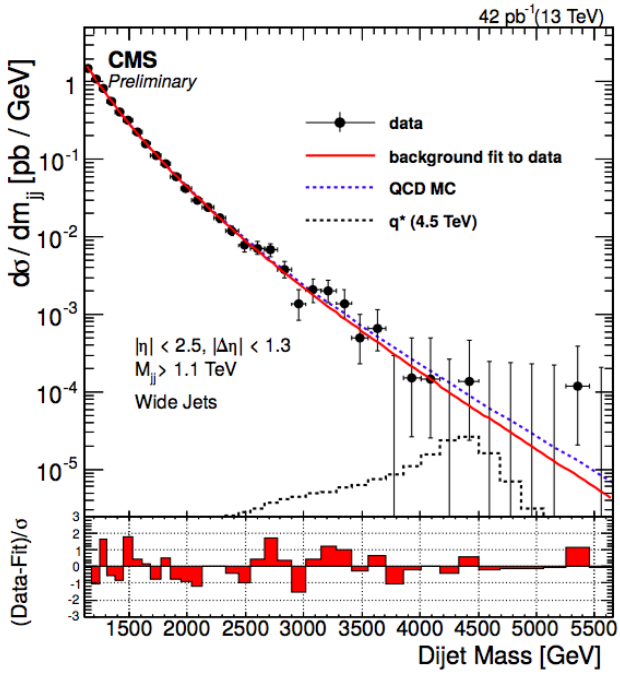

FIGURE 7. Dijet invariant mass

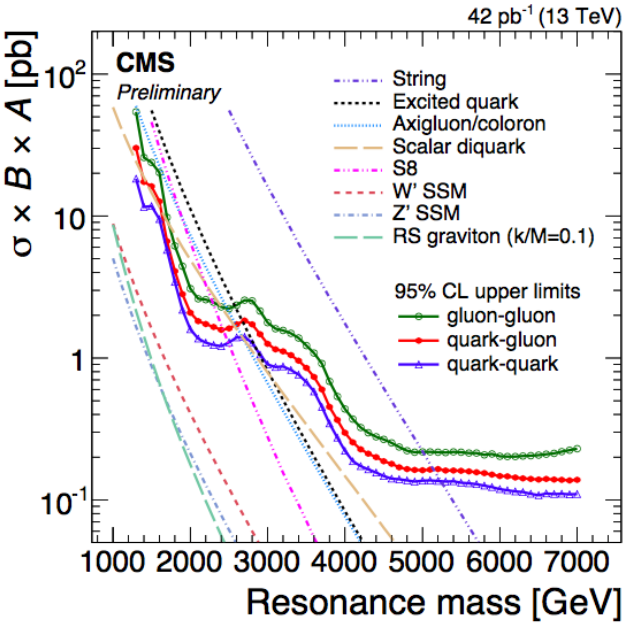

FIGURE 8. Limits for searches in dijet events

Model	Mass Limits (TeV)			
	Run 1 (20 fb^{-1})		Run 2 (42 pb^{-1})	
	Observed	Expected	Observed	Expected
String Resonance (S)	5.0	4.9	5.1	5.2
Excited Quark (q*)	3.5	3.7	2.7	2.9
Axigluon (A) / Coloron (C)	3.7	3.9	2.7	2.9
Scalar Diquark (D)	4.7	4.7	2.7	3.3
Color Octet Scalar (S8)	2.7	2.6	2.3	2.0

FIGURE 9. Limits for searches in dijet events

in Fig. 9 with the comparison of the Run I results and confirmRun the Run II is already more sensitive than Run I for masses greater than 5 TeV[6].

Diphoton analysis recorded first high mass events, requiring a minimum transverse momentum of 100 GeV for each photon and a pseudorapidity lower than 2.5 with at least one photon candidate in the ECAL Barrel. Figure 10 displays the event with highest mass, namely 730 GeV.

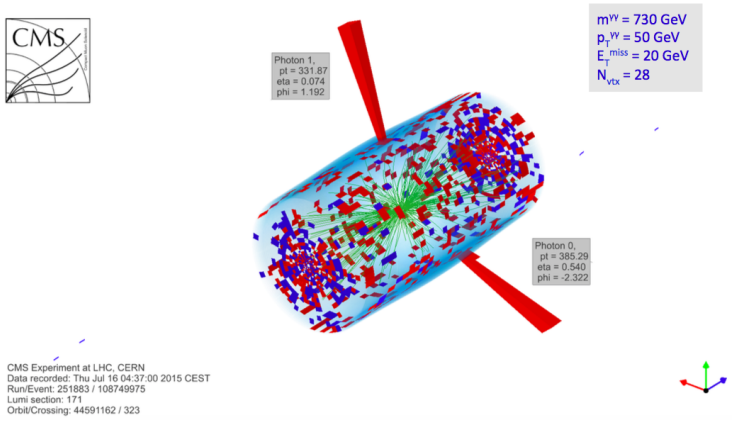

FIGURE 10. Event display for the highest mass diphoton event

The high momentum muons reconstruction still suffers for the early alignment used in data, nevertheless both dimuon and single muon with missing transverse energy (muon+MET) analyses gave first results on the search for Z' and W' respectively [8], [7]. Figure 11 and 12 show the dimuon invariant mass spectrum and the muon+MET transverse mass. In the dimuon analysis two isolated muons with transverse momentum greater than 48 GeV and pseudorapidity lower than 2.4 are required in the event. Highest mass dimuon event was observed at 920 GeV. For the muon+MET, a good-quality isolated high momentum muon, with transverse momentum greater than 55 GeV and pseudorapidity lower than 2.4, is selected when accompanied by a large missing transverse energy. In both cases the mass spectra in the data are compatible with the Montecarlo expectation from Standard Model and no excess is observed at high mass.

Also the dielectron search for a high mass resonance has been performed [8], requiring two electrons in ECAL with transverse energy greater than 35 GeV and at least one electron in the ECAL barrel. The invariant mass spectrum, showed in Fig. 13, with events up to 1 TeV, seemed to be in perfect agreement with simulations up to few days before this presentation when an extraordinary high mass event of 2.9 was observed in the data. The event display of this high mass event is showed in Fig. 14: the event consists in two perfectly balanced electrons and no other significant activity, with a negative Collins-Soper angle while Drell Yang background is peaked toward positive values. Previous highest mass event from Run Run II was 1.8 TeV (1.9 TeV for muons) and Run I limits for Z' Search do not exclude one Z' event at this mass with this luminosity. Background is very low but not negligible, about 0.002 events for mass greater

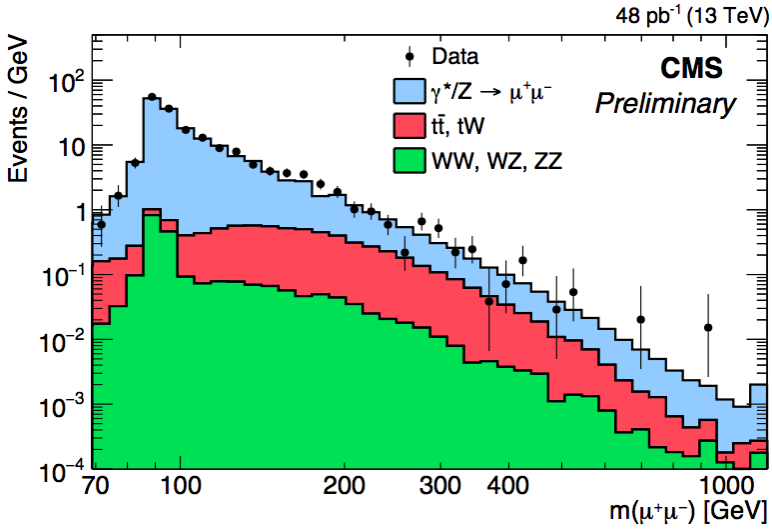

FIGURE 11. Invariant mass spectrum for dimuon events

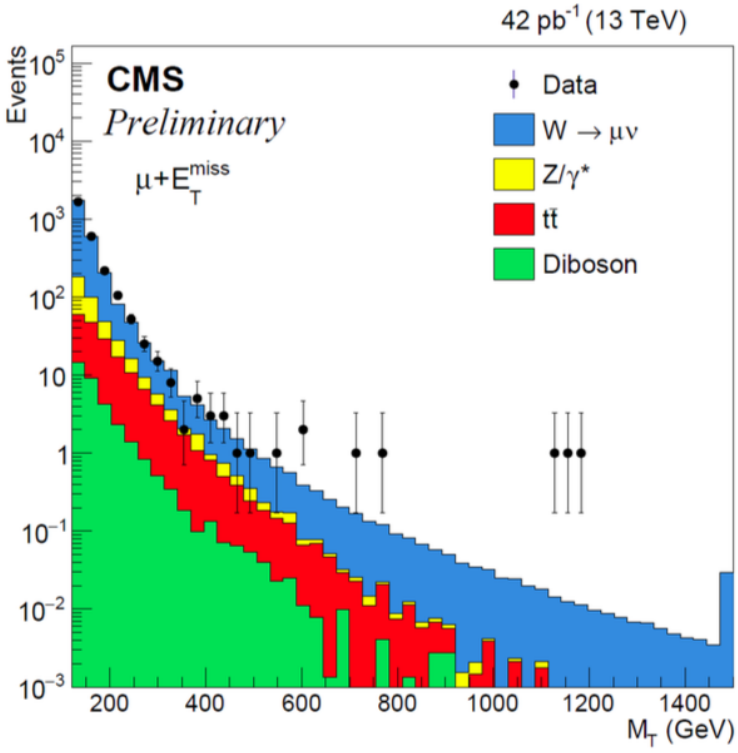

FIGURE 12. Transverse mass for muon+MET events

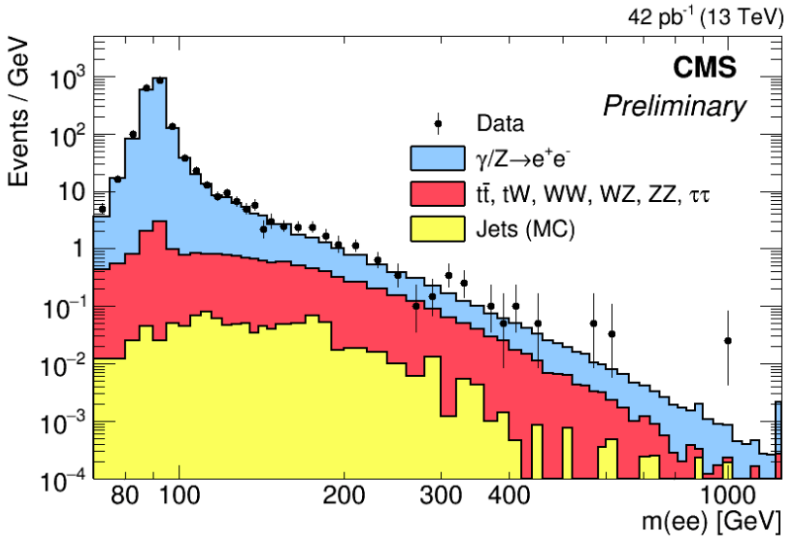

FIGURE 13. Invariant mass spectrum for dielectron events

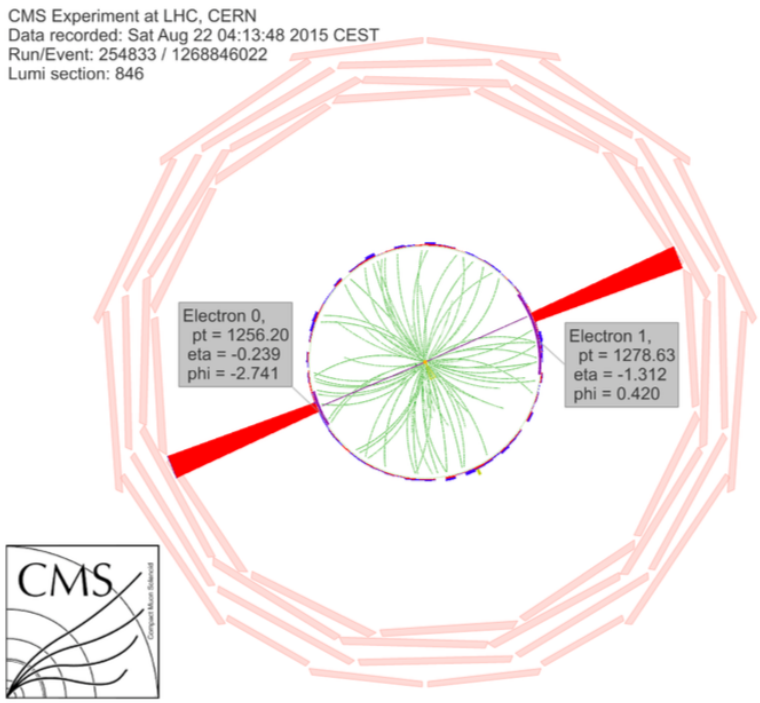

FIGURE 14. Event display for the dielectron event with invariant mass of 2.9 TeV

than 2.5 TeV, leading to a probability of a few per mille to observe this event from a fluctuation of the background. Nevertheless, this event can be a rare background fluctuation and we are waiting for new data, to understand if it is the case.

CONCLUSIONS

A new challenging time just started with the LHC Run II at 13 TeV while Run I analyses of 8 TeV data are still on-going with new precision results. All the CMS sub-detectors are in an optimal shape and reconstruction algorithms optimized for higher pile up. First exciting events and results from 13 TeV are already public with a luminosity of about 50 pb^{-1} while we are expecting to surpass the Run I search sensitivity for many New Physics signatures after a luminosity of few fb^{-1} that will be collected in the next months. Interesting time are expected ahead of us.

ACKNOWLEDGMENTS

I want to congratulate all the CMS members involved in the detector set up for Run II and in the analyses presented here for their contributions to the success of the CMS effort. These results presented on behalf of the CMS collaboration, were produced thanks to the work of our colleagues in the CERN accelerator departments.

REFERENCES

[1] S. Chatrchyan *et al.* [CMS Collaboration], "The CMS experiment at the CERN LHC," JINST **3**, S08004 (2008). doi:10.1088/1748-0221/3/08/S08004

[2] CMS Collaboration [CMS Collaboration], "Measurements of the Higgs boson production and decay rates and constraints on its couplings from a combined ATLAS and CMS analysis of the LHC pp collision data at sqrt s = 7 and 8 TeV," CMS-PAS-HIG-15-002.

[3] V. Khachatryan *et al.* [CMS Collaboration], "Search for the standard model Higgs boson produced through vector boson fusion and decaying to $b\bar{b}$," Phys. Rev. D **92** (2015) 3, 032008 doi:10.1103/PhysRevD.92.032008 [arXiv:1506.01010 [hep-ex]].

[4] V. Khachatryan *et al.* [CMS Collaboration], "Pseudorapidity distribution of charged hadrons in proton-proton collisions at $\sqrt{s}$ = 13 TeV," Phys. Lett. B **751**, 143 (2015) doi:10.1016/j.physletb.2015.10.004 [arXiv:1507.05915 [hep-ex]].

[5] CMS Collaboration [CMS Collaboration], "Measurement of the top quark pair production cross section in proton-proton collisions at $\sqrt{s}$=13 TeV with the CMS detector," CMS-PAS-TOP-15-003.

[6] CMS Collaboration [CMS Collaboration], "Search for Narrow Resonances using the Dijet Mass Spectrum with 40 pb^{-1} of pp Collisions at $\sqrt{s}$=13 TeV," CMS-PAS-EXO-15-001.

[7] CMS Collaboration [CMS Collaboration], "Search for SSM W' production, in the lepton+MET final state at a center-of-mass energy of 13 TeV," CMS-PAS-EXO-15-006.

[8] CMS Collaboration [CMS Collaboration], "Search for a Narrow Resonance Produced in 13 TeV pp Collisions Decaying to Electron Pair or Muon Pair Final States," CMS-PAS-EXO-15-005.

Proceedings of the LHCP2015 Conference, St. Petersburg, Russia, August 31 - September 5, 2015

Editors: V.T. Kim and D.E. Sosnov

First Look at 13 TeV Data and Highlights from the Most Recent Analyses

ANTON POLUEKTOV[1,2]

[1]*The University of Warwick, Coventry CV4 7AL, UK*
[2]*Budker Institute of Nuclear Physics, Lavrentieva 11, Novosibirsk, 630090, Russia*

Anton.Poluektov@cern.ch

On behalf of the LHCb Collaboration

Abstract. In these proceedings, I will report the first results of LHCb collaboration using 13 TeV proton-proton collision data collected in the summer of 2015, and will highlight one important result based on 3 fb^{-1} data taken in 2011-2012, the observation of pentaquark-like states in the decay $\Lambda_b^0 \to J/\psi\, pK^-$.

INTRODUCTION

The LHCb experiment is primarily aimed at studies of processes involving beauty and charm decays in proton-proton collisions at the LHC [1]. It is designed as a single-arm spectrometer to cover the pseudorapidity range $2 < \eta < 5$ corresponding to the maximum of $b\bar{b}$ production in pp collisions at the LHC design energy of 14 TeV. The detector provides excellent vertex resolution to allow, in particular, measurement of fast oscillations in the B_s^0 system, and rejection of the large combinatorial background arising from tracks coming from the primary pp interaction vertex. It offers good identification of charged final state particles (pions, kaons, protons, muons, electrons) in a wide momentum range; this is necessary to tag the initial flavour of B mesons and to suppress misidentification backgrounds. The high-resolution tracker provides good mass and momentum resolution, while the calorimeter system allows to measure decays with neutral particles (π^0 or γ) in the final state. The detector features an efficient trigger system which allows to select, in particular, fully-hadronic final states.

During the LHC Run 1, LHCb has collected 1 fb^{-1} in 2011 (at the center-of-mass energy of pp collisions of 7 TeV) and 2 fb^{-1} in 2012 (at 8 TeV). This data sample was used to produce more than 250 publications, and this number will increase since many analyses using this data sample are still ongoing.

Here, I will cover the first analyses using 13 TeV collisions delivered in 2015 (Run 2), and will highlight the recent observation of pentaquark-like states performed using Run 1 data.

LHCB IN LHC RUN 2

In the LHC Run 2, which started in 2015, LHCb had taken around 20 pb^{-1} by September 2015[1] at the center-of-mass energy of 13 TeV. This sample has been used in early measurements of beauty and charm production which will be covered here.

The most significant changes of the detector compared to Run 1 are in the trigger. The LHCb software trigger (High-level trigger, HLT) has undergone several levels of modifications since the start of data taking. In 2011 and early 2012, the trigger has been operated in a configuration corresponding to the original design [2], however, with an increased output rate of 5 kHz to accommodate charm decays. In 2012, the *deferred trigger* configuration was

[1]This was the situation by the time of the LHCP2015 conference presentation. The full pp dataset accumulated in 2015 is 320 pb^{-1}.

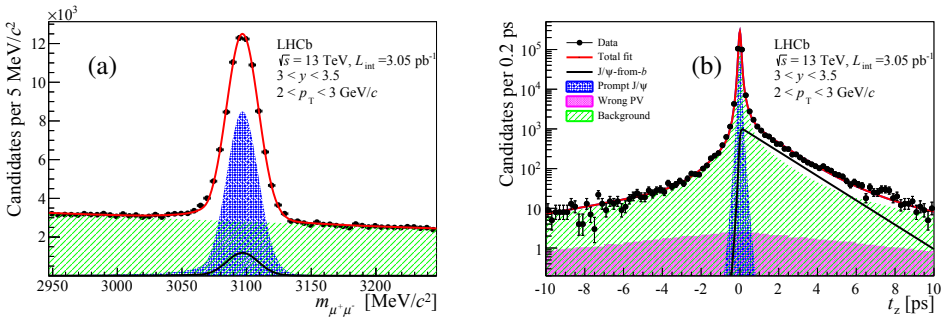

FIGURE 1. (a) Invariant mass of $\mu^+\mu^-$ combinations with the $J/\psi \to \mu^+\mu^-$ signal. (b) Decay time distribution for $J/\psi \to \mu^+\mu^-$ candidates [4].

introduced [3]: 20% of the output rate after the hardware (L0) stage has been deferred to disk and processed during periods of operation without physics beams.

For Run 2, the *split trigger* has been introduced in which the full output of the first stage of the software trigger (HLT1) is stored on disks of the trigger computing farm. This output is immediately used for the online calibration and alignment, such that the second stage (HLT2) of the trigger uses high-quality calibration (in particular, of particle identification). This modification also enables to use the candidates created by the exclusive selections of the trigger directly in the physics analysis. These candidates are stored in a so-called `Turbo` stream that takes up 5 kHz of the total 12.5 kHz output rate. Since the underlying event is not stored for the events of this stream, the size of these events is much smaller and it allows one to select high-yield signals, such as prompt charm or charmonium, which otherwise would need to be prescaled. The 13 TeV measurements presented here have been analysed using the `Turbo` stream.

FIRST MEASUREMENTS WITH 13 TEV DATA

The first measurement LHCb has performed using the 13 TeV sample is the production of J/ψ meson in pp collisions [4]. The measurement of this cross-section as a function of p_T and rapidity tests QCD calculations in both the perturbative (that is achieved in the production of $c\bar{c}$ in pp collisions) and non-perturbative (in the hadronisation of $c\bar{c}$ pair into a J/ψ meson) regimes. Additionally, by studying the production of secondary J/ψ which come from the decays of beauty hadrons, one can measure the cross-section of $b\bar{b}$ production at 13 TeV which is crucial to reliably estimate the prospects of B physics measurements in Run 2.

The J/ψ candidates are reconstructed from pairs of muons, and their yield is obtained from the fit of the $\mu^+\mu^-$ invariant mass (Fig 1(a)). The prompt and secondary J/ψ are distinguished by fitting the distribution of decay time projection onto beam axis t_z (Fig. 1(b)). Around 10^6 J/ψ candidates are reconstructed in the $3.05 \pm 0.12\,\text{pb}^{-1}$ data sample used for the analysis.

The cross-sections of J/ψ production obtained in the LHCb acceptance ($p_T(J/\psi) < 14$ GeV, rapidity $2.0 < y < 4.5$) are $15.30 \pm 0.03 \pm 0.86$ μb for prompt J/ψ and $2.34 \pm 0.01 \pm 0.13$ μb for J/ψ from B decays. The latter can be used to obtain the total cross-section of $b\bar{b}$ production in pp collisions that equals $515 \pm 2 \pm 53$ μb. Comparison with the previous measurements of J/ψ production cross-section at 2.76, 7 and 8 TeV shows a linear rise for both the prompt and secondary components (Fig. 2). It is interesting to note that the value of $b\bar{b}$ production cross-section is very close to the value used in early LHCb performance studies (500 μb at 14 TeV [5]). The differential cross-sections of J/ψ production are also measured as functions of p_T and rapidity (see the paper [4] for the complete set of results) and compared to various theoretical models.

Another measurement with early 13 TeV data is the production of charm mesons, D^0, D^+, D_s^+ and D^{*+} [6]. This measurement is performed using $4.98 \pm 0.19\,\text{pb}^{-1}$ of data. The charm mesons are reconstructed in the channels $D^0 \to K^-\pi^+$, $D^+ \to K^-\pi^+\pi^+$, $D_s^+ \to \phi\pi^+$ and $D^{*+} \to D^0\pi^+$. The signal yields are obtained by fitting the invariant mass distribution of the candidates (see Fig. 3(a) for the invariant mass distribution of $D^0 \to K^-\pi^+$). The prompt component is separated from D mesons produced in decays of beauty hadrons using the distribution of the impact parameter χ^2 of the charm meson candidates (see Fig. 3(b)).

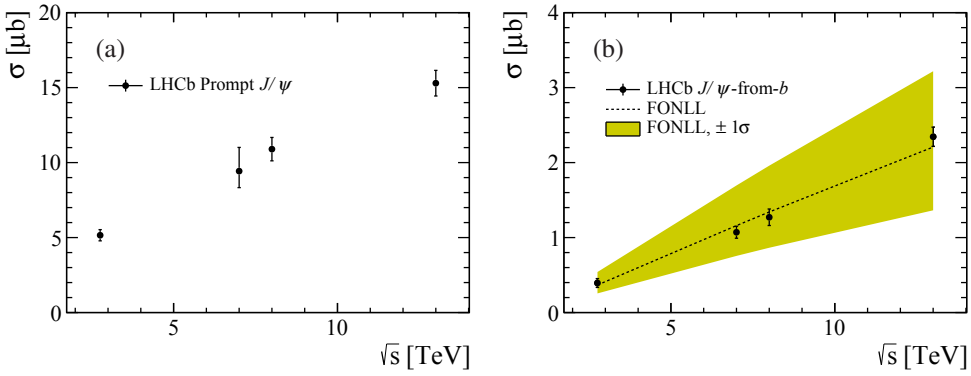

FIGURE 2. Production cross section as a function of beam energy for (a) prompt J/ψ and (b) J/ψ from B decays [4].

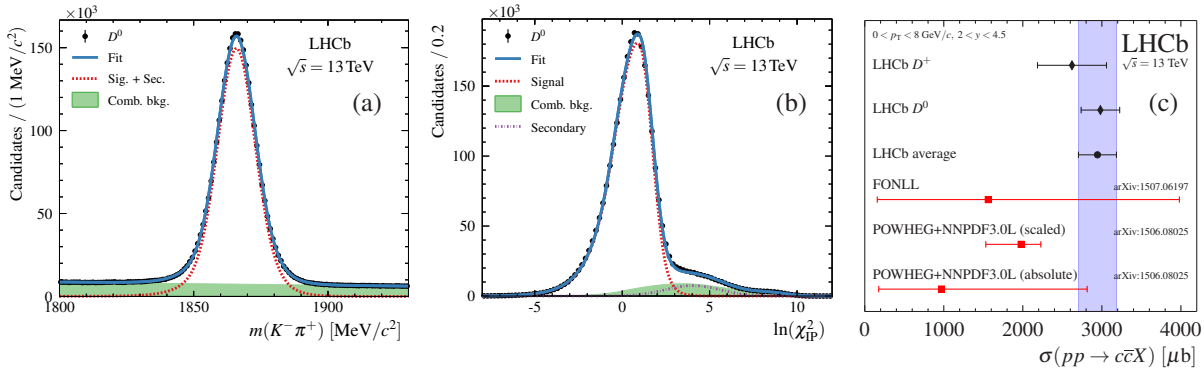

FIGURE 3. (a) Invariant mass and (b) impact parameter χ^2 distribution of $D^0 \to K^-\pi^+$ candidates, and (c) total cross-section of $c\bar{c}$ production in 13 TeV pp collisions [6]

The two highest-yield modes, $D^0 \to K^-\pi^+$ and $D^+ \to K^-\pi^+\pi^+$, are used to obtain the full $c\bar{c}$ production cross-section in the analysis acceptance $p_{\rm T}(D) < 8\,{\rm GeV}$, $2.0 < y < 4.5$. This calculation uses the fragmentation fractions of $c\bar{c}$ to the D meson of each kind obtained from e^+e^- data [7] and provides two independent measurements of this quantity. The calculated $c\bar{c}$ cross sections agree very well (see Fig. 3), and are somewhat higher than the theoretical predictions. The total cross-section value obtained from the combination of $D^0 \to K^-\pi^+$ and $D^+ \to K^-\pi^+\pi^+$ modes is $\sigma(pp \to c\bar{c}) = 2940 \pm 3 \pm 180 \pm 160\,\mu{\rm b}$, where the first uncertainty is statistical, the second systematic and the third is due to fragmentation fractions used. As in the case of J/ψ production analysis, the paper [6] presents differential cross sections for the mesons of each kind as functions of p_T and rapidity, and compares them with the theoretical expectations.

OBSERVATION OF PENTAQUARK-LIKE STATES

One of the most significant highlights of the Run 1 operation of LHCb is the observation of pentaquark-like states. While the existence of exotic mesons has recently been claimed in many analyses, searches for baryons beyond the conventional three-quark structure have so far been unsuccessful (for a comprehensive review of pentaquark searches, see *e.g.* [8]). Now LHCb presents the first conclusive observation of the exotic pentaquark-like structure [9].

The exotic structure is observed in the $\Lambda_b^0 \to J/\psi\, pK^-$ decay, where conventional resonances are only expected in the pK^- spectrum. The full Run 1 sample of 3 fb^{-1} offers a high yield of this decay (about 26000 decays) with low background of only 5.4%. Investigation of the Dalitz plot distribution (Fig. 4) shows a clear peak in the $J/\psi\, p$ spectrum with mass of about 4450 MeV which should correspond to the exotic state with the minimal quark content

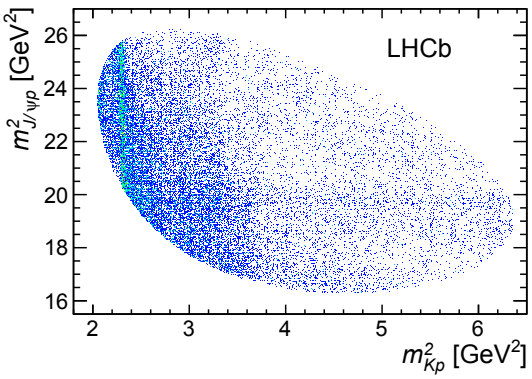

FIGURE 4. Dalitz plot of $\Lambda_b^0 \to J/\psi\, pK^-$ decay [9].

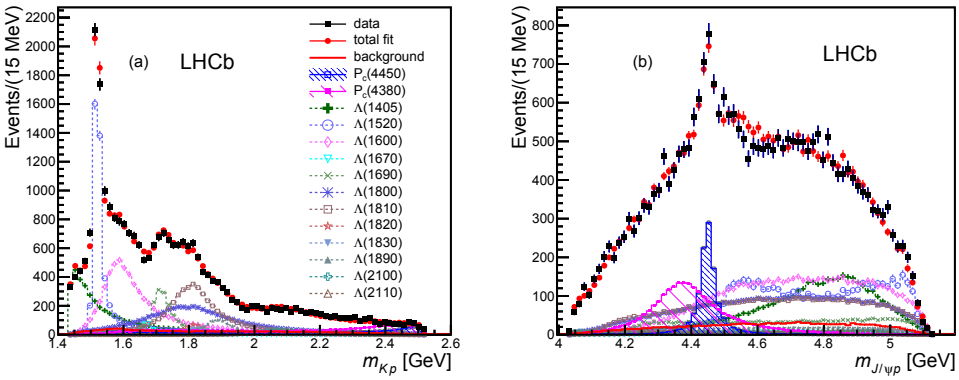

FIGURE 5. (a) $m(pK^-)$ and (b) $m(J/\psi\, p)$ projections of the $\Lambda_b^0 \to J/\psi\, pK^-$ decay density and its fit result [9].

$uudc\bar{c}$ (hidden charm pentaquark, denoted as P_c).

To study the nature of the $J/\psi\, p$ structure, a full amplitude analysis of the $\Lambda_b^0 \to J/\psi\, pK^-$ decay has been performed. The fit uses the five decay angles of the $J/\psi\, pK^-$ system as well as the invariant mass of the pK^- combination as variables of the six-dimensional phase space. An amplitude model which includes only the known 14 resonances in the pK^- channel does not give satisfactory description. Inclusion of a resonant state with spin-parity $J^P = 5/2^+$ in $J/\psi\, p$ channel significantly improves the fit, but is still not sufficient. Finally, introduction of a second, wider, $J/\psi\, p$ state results in a satisfactory fit. The fit prefers the two states to have spins $3/2$ and $5/2$ and opposite parity. Projections of the data and the fit result onto $m(pK^-)$ and $m(J/\psi\, p)$ invariant masses are shown in Fig. 5.

While from looking at the $m(J/\psi\, p)$ projection the need for the second wider resonance may not be obvious, investigation of the slices of $m(J/\psi\, p)$ distribution for various ranges of pK^- mass and helicity angles makes the need for interference between two states of opposite parities apparent. The parameters of the two states obtained from the amplitude fit are as follows: $M = 4380 \pm 8 \pm 29\,\text{MeV}$, $\Gamma = 205 \pm 18 \pm 86\,\text{MeV}$ for $P_c(4380)$, and $M = 4449.8 \pm 1.7 \pm 2.5\,\text{MeV}$, $\Gamma = 39 \pm 5 \pm 19\,\text{MeV}$ for $P_c(4450)$. The significances of the lower and higher mass states (including statistical and systematic effects) are 9 and 12 standard deviations, respectively.

Moreover, a model-independent study of the behaviour of the $J/\psi\, p$ amplitude as a function of invariant mass is performed with fits where both the real and imaginary parts of the complex amplitude are floated in bins of invariant mass. In this case, interference with other structures of the $\Lambda_b^0 \to J/\psi\, pK^-$ amplitude allows one to extract the amplitudes in each bin and test whether the rotation of phase is consistent with what should be expected from a resonance. As can be seen from the fit result (Fig. 6), the $3/2^-$ amplitude around 4450 MeV clearly has resonant behaviour, while for the $5/2^+$ amplitude in the vicinity of the proposed $P_c(4380)$ state more data is needed for a completely model-independent conclusion.

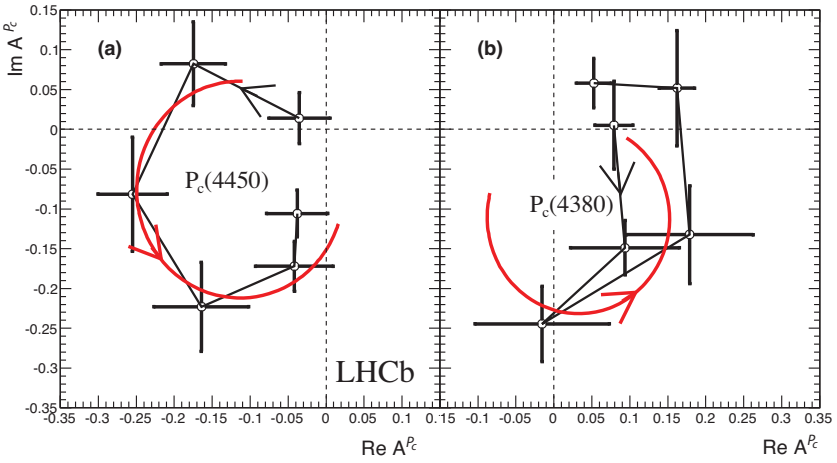

FIGURE 6. Argand plots for the $J/\psi\, p$ amplitude in the invariant mass regions around (a) 4450 and (b) 4380 MeV [9].

CONCLUSION

In 2015, LHCb has successfully started data taking with pp collisions at the center-of-mass energy of 13 TeV. The new split trigger configuration and `Turbo` stream allowed the collaboration to complete the first analyses with these data on a very short time scale. Two such analyses are reported here: measurements of prompt and secondary J/ψ production (which, in particular, leads to the measurement of $b\bar{b}$ cross-section in 13 TeV pp collisions) and prompt charm production with 13 TeV.

The most recent highlight using the data taken in Run 1 is the observation of pentaquark-like states. The amplitude of the $\Lambda_b^0 \to J/\psi\, pK^-$ decay features exotic contributions in the $J/\psi\, p$ channel with minimum quark content $c\bar{c}uud$. The resonant behaviour of these states has been shown in a model-independent way by measuring the phase rotation as a function of invariant mass.

ACKNOWLEDGMENTS

I am grateful to the organisers of the LHCP2015 conference in St. Petersburg (Russia) where these results have been presented for excellent organisation and hospitality. I would like to acknowledge support by the Science and Technology Facilities Council (United Kingdom), and by the Russian Foundation for Basic Research grant 14-02-00569 A.

REFERENCES

[1] A. A. Alves Jr *et al.* (LHCb collaboration), JINST **3**, p. S08005 (2008).
[2] R. Aaij *et al.*, JINST **8**, p. P04022 (2013), arXiv:1211.3055 [hep-ex] .
[3] J. Albrecht, V. V. Gligorov, G. Raven, and S. Tolk (LHCb HLT project), *Proceedings, 20th International Conference on Computing in High Energy and Nuclear Physics (CHEP 2013)*, J. Phys. Conf. Ser. **513**, p. 012001 (2014), arXiv:1310.8544 [hep-ex] .
[4] R. Aaij *et al.* (LHCb), (2015), arXiv:1509.00771 [hep-ex] .
[5] H. Dijkstra, H. J. Hilke, T. Nakada, and T. Ypsilantis, "LHCb Letter of Intent, LHCb Collaboration," Tech. Rep. LHCb-95-001 (CERN, Geneva, 1995).
[6] R. Aaij *et al.* (LHCb), (2015), arXiv:1510.01707 [hep-ex] .
[7] C. Amsler *et al.* (Particle Data Group), Phys. Lett. **B667**, 1–1340 (2008).
[8] R. A. Schumacher, *Particles and nuclei : Seventeenth International Conference on Particles and Nuclei, Santa Fe, New Mexico, 23-30 October 2005*, AIP Conf. Proc. **842**, 409–417 (2006), [,409(2005)], arXiv:nucl-ex/0512042 [nucl-ex] .
[9] R. Aaij *et al.* (LHCb), Phys. Rev. Lett. **115**, p. 072001 (2015), arXiv:1507.03414 [hep-ex] .

Higgs boson physics: plenary talks

Proceedings of the LHCP2015 Conference, St. Petersburg, Russia, August 31 - September 5, 2015

Editors: V.T. Kim and D.E. Sosnov

Higgs Differential Cross Sections, Spin/CP Measurements, and Rare Channels at the LHC and Tevatron

KERSTIN TACKMANN

DESY, Hamburg, Germany

kerstin.tackmann@cern.ch

On behalf of the ATLAS, CMS, CDF and D0 Collaborations

Abstract. These proceedings report on a collection of Higgs boson property studies based on the LHC Run 1 dataset, consisting of about 25 fb^{-1} pp collision data collected at a center-of-mass energy of 7 and 8 TeV by the ATLAS and CMS experiments at the Large Hadron Collider, as well as a study from the CDF and D0 experiments, based on about 10 fb^{-1} $p\bar{p}$ collision data taken at a center-of-mass energy of 1.96 TeV at the Tevatron collider. The results of total, fiducial and differential cross section measurements are reported, and studies of the spin and parity are described. No significant deviation from the Standard Model predictions has been found. Searches for rare decay channels, including $H \to Z\gamma$, $H \to \mu\mu$, $H \to J/\psi\gamma$ and $H \to \gamma^*\gamma \to \ell\ell\gamma$ do not show any evidence for signal and upper limits on their branching fractions are set.

INTRODUCTION

In summer 2012, the ATLAS [1] and CMS [2] collaborations announced the discovery of a new particle in the Standard Model (SM) Higgs boson searches [3, 4] at the Large Hadron Collider (LHC) at CERN. Since then, the ATLAS and CMS experiments at the LHC, and the CDF and D0 experiments at the Tevatron have carried out studies of the new particle's properties and confirmed its identity as a Higgs boson. The studies now aim at determining whether it is the Higgs boson as predicted by the SM, or if an extended model is needed. For this purpose, its decays, production modes and couplings have been studied, and its spin and parity properties have been tested.

In the SM, Higgs boson production is expected to take place predominantly through gluon fusion with a cross section of about 19.5 pb for pp collisions at a center-of-mass energy of 8 TeV and for a Higgs boson with mass of 125 GeV. Vector-boson fusion has a much smaller cross section of about 1.6 pb, but has a very distinct signature with two forward jets with little hadronic activity in between. Associated production with a vector boson has a similarly distinct topology, the W or Z boson can be reconstructed in leptonic decays, and a similar cross section of 1.1 pb. Associated production with a $t\bar{t}$ pair has a much smaller cross section of 0.1 pb, but its signal topology with the decay products of two top quarks makes it a promising channel to study. The main Higgs boson decay channels are into pairs of fermions, $b\bar{b}$ (with a predicted branching fraction of 57.7%) and $\tau\tau$ (6.3%), and into pairs of bosons, WW^* (21.5%), ZZ^* (2.6%) and $\gamma\gamma$ (0.23%).

These proceedings discuss fiducial and differential cross section measurements, spin and parity studies, including a study from the CDF and D0 collaborations, as well as searches for rare decay modes. The measurement of the Higgs boson mass and studies of the production modes and couplings are described in [5]. Many of the results presented here are based on significantly improved detector calibration, reconstruction and analysis techniques, when compared to earlier results based on a partial or the same dataset.

CROSS SECTION MEASUREMENTS

Fiducial and differential cross section measurements, optimized to minimize the model dependence of their results, are complementary to the more model-dependent coupling measurements (see [6] and references therein), as well as for

example the spin and parity studies described below. Thanks to their excellent invariant mass resolution, which allows for a robust subtraction of the non-Higgs background, the final states of Higgs boson decays to two photons and to four leptons are well-suited for cross section measurements. The fiducial regions, also used for the differential measurements, are defined to minimize the needed acceptance corrections for the final state particles. In the $H \to ZZ^* \to 4\ell$ measurements the fiducial region is defined by requirements on the leptons' transverse momenta and pseudorapidities as well as the event topology. In the $H \to \gamma\gamma$ measurements it is defined by the photons' transverse momenta and pseudorapidities. Details can be found in [7, 8, 9, 10]. In some of the analyses isolation requirements have been used in the fiducial region definition for the photons or leptons to reduce the model dependence as the isolation efficiency in $t\bar{t}H$ production differs significantly from the isolation efficiency in the other production processes which result in fewer hadronic jets in the final state.

Fiducial and total cross sections

The fiducial cross sections measured with about 20 fb^{-1} of pp collision data taken at a center-of-mass energy of $\sqrt{s}$ =8 TeV by the ATLAS and CMS experiments are shown in Table 1. With the present dataset, the measurements have limited statistical precision. For this reason, a more precise measurement (by 25-30%) of the total cross section can be obtained by combining different decay channels, at the expense of a slightly larger model dependence. For the combination, the measurements from $H \to ZZ^* \to 4\ell$ and $H \to \gamma\gamma$ are extrapolated to the full phase space. The extrapolations include corrections for the fiducial acceptances, which are $(47 \pm 1)\%$ and $(60 \pm 1)\%$ for $H \to ZZ^* \to 4\ell$ and $H \to \gamma\gamma$, respectively, and the branching fractions, for which the SM predictions are used. The separate and combined total cross sections are shown in Figure 1(a), together with several theoretical predictions. Figure 1(b) shows the $\sqrt{s}$ dependence of the fiducial cross section measured in $H \to ZZ^* \to 4\ell$ compared to the theoretical prediction, using in addition about 5 fb^{-1} of 7 TeV pp collision data.

TABLE 1. Measured fiducial cross sections in $H \to ZZ^* \to 4\ell$ and $H \to \gamma\gamma$ decays by the ATLAS and CMS experiments at $\sqrt{s}$ =8 TeV [7, 8, 9, 10] and SM predictions.

	ATLAS	**CMS**
$H \to 4\ell$ (meas.)	$\sigma = 2.11^{+0.53}_{-0.47}(\text{stat})^{+0.08}_{-0.08}(\text{syst})$ fb	$\sigma = 1.11^{+0.41}_{-0.35}(\text{stat})^{+0.14}_{-0.10}(\text{syst})^{+0.08}_{-0.02}(\text{model})$ fb
$H \to 4\ell$ (pred.)	$\sigma^{\text{SM}} = 1.30^{+0.13}_{-0.13}$ fb	$\sigma^{\text{SM}} = 1.15^{+0.12}_{-0.13}$ fb
$H \to \gamma\gamma$ (meas.)	$\sigma = 43.2 \pm 9.4(\text{stat})^{+3.2}_{-2.9}(\text{syst}) \pm 1.2(\text{lumi})$ fb	$\sigma = 32 \pm 10(\text{stat}) \pm 3(\text{syst})$ fb
$H \to \gamma\gamma$ (pred.)	$\sigma^{\text{SM}} = 30.5 \pm 3.3$ fb	$\sigma^{\text{SM}} = 31^{+4}_{-3}$ fb

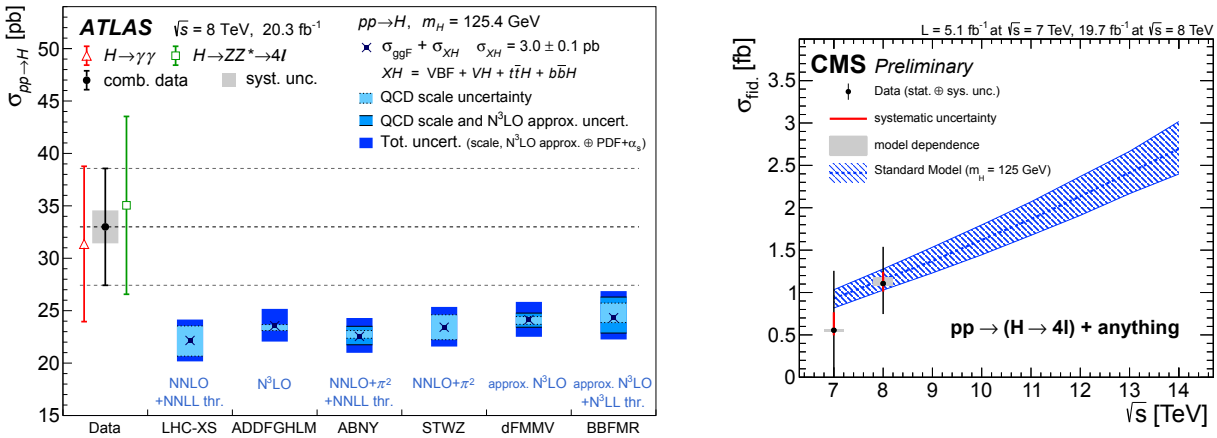

FIGURE 1. (a) Total cross section for $pp \to H$ measured in $H \to ZZ^* \to 4\ell$ and $H \to \gamma\gamma$ decays compared to several theoretical predictions [11]. (b) Fiducial cross section in the $H \to ZZ^* \to 4\ell$ measured by CMS at $\sqrt{s}$ = 7 and 8 TeV [8], compared with the SM prediction.

In general, there is decent agreement between the measurements and the SM predictions. The cross sections measured by ATLAS tend to be a bit larger than the predictions. The p-values quantifying the agreement between the measured total cross section and the cross section prediction following the recommendations of the LHC Higgs Cross Section Working Group [12] (the preliminary fixed-order N^{3}LO prediction [13]) is 5.5% (9%), using bifurcated Gaussian distributions to model asymmetric theoretical uncertainties.

Differential cross sections

Differential cross section measurements have been carried out for a variety of observables with about 20 fb^{-1} of $\sqrt{s}$ =8 TeV pp collision data. Several measurements probe the kinematics of Higgs boson production and are sensitive to the relative contributions of the different production modes and QCD effects, such as the Higgs boson transverse momentum (p_{T}), while others are sensitive to PDFs, such as the Higgs boson rapidity. Measurements of the number

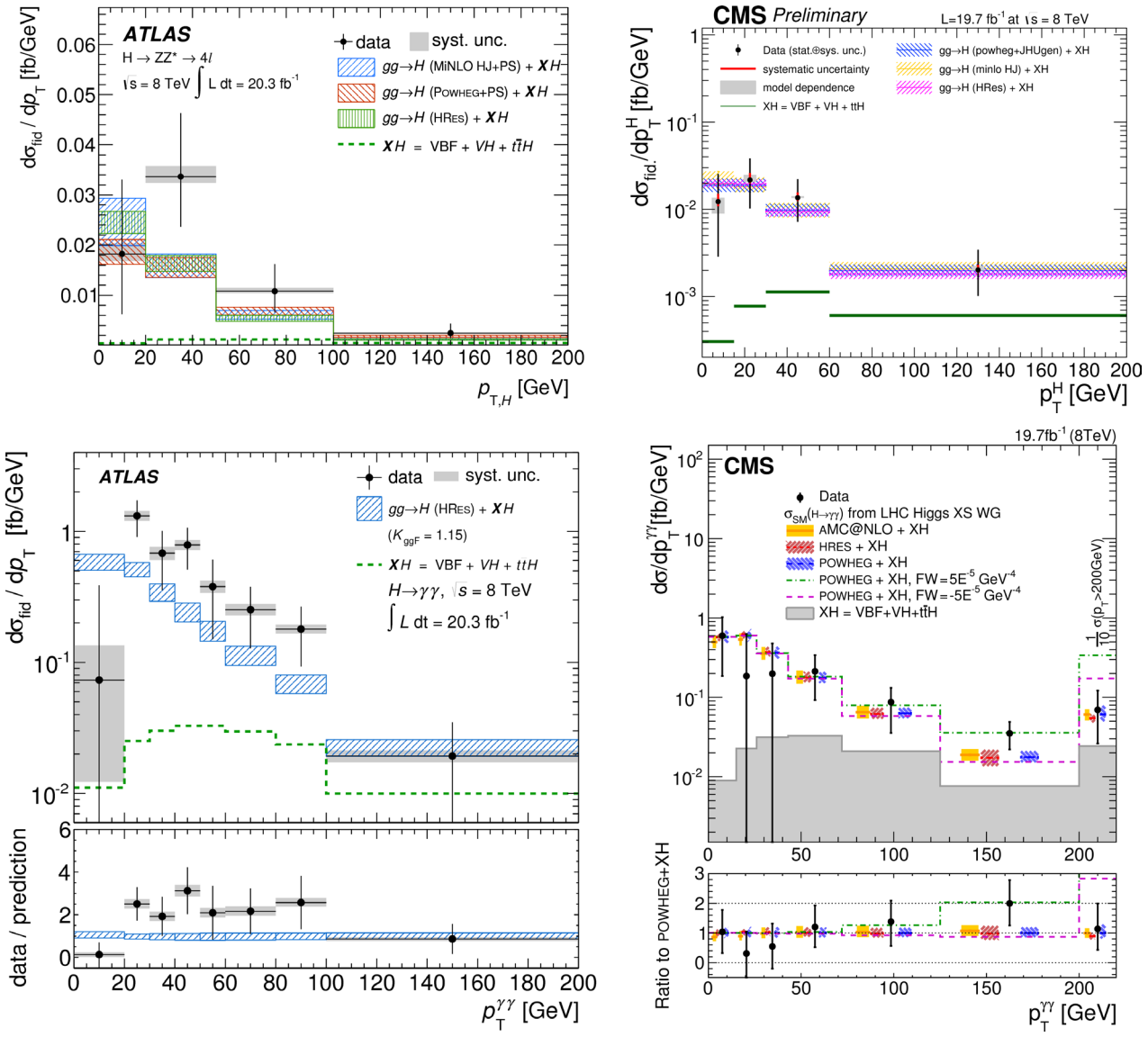

FIGURE 2. Higgs boson transverse momentum spectra measured in $H \to ZZ^* \to 4\ell$ by (a) ATLAS [7] and (b) CMS [8], and Higgs boson transverse momentum spectra measured in $H \to \gamma\gamma$ by (c) ATLAS [9] and (d) CMS [10].

of the jets and their transverse momentum and rapidity spectra test the theoretical description of QCD radiation in gluon fusion and the relative contributions of the different production modes. Distributions like the invariant mass of the two highest-p_{T} jets and their azimuthal difference in events with at least two jets have characteristic shapes for vector-boson fusion and are sensitive to the contribution of this production mode. Angular distributions of the photons and leptons are sensitive to the spin and parity of the Higgs boson.

As example, Figure 2 shows the Higgs boson transverse momentum distribution measured in $H \to ZZ^* \to 4\ell$ and $H \to \gamma\gamma$ decays compared to several SM predictions. The measurements were unfolded for resolution, efficiency and residual acceptance effects.

Despite the fairly large statistical uncertainties, the measurements allow for interesting comparisons with the simulation predictions used for other Higgs boson property measurements as well as the best available analytic predictions.

Interpretation of $H \to \gamma\gamma$ differential cross sections in terms of effective operators

The Higgs boson transverse momentum distribution, the distribution of the number of jets produced in addition to the Higgs boson, the invariant mass of the two highest-p_{T} jets and their azimuthal separation in events with at least two jets, as well as the transverse momentum distribution of the highest-p_{T} jet in events with at least one jet are used in a combined analysis [14], taking into account the statistical correlations between the five distributions. In this analysis, the SM Lagrangian is augmented with dimension six CP-even and CP-odd operators sensitive to Higgs boson interactions with gauge bosons. The effective Lagrangian is [15, 16]

$$\mathcal{L}_{\mathrm{eff}} = \mathcal{L}_{\mathrm{SM}} + \quad \bar{c}_\gamma O_\gamma + \bar{c}_g O_g + \bar{c}_{HW} O_{HW} + \bar{c}_{HB} O_{HB} + \tilde{c}_\gamma \tilde{O}_\gamma + \tilde{c}_g \tilde{O}_g + \tilde{c}_{HW} \tilde{O}_{HW} + \tilde{c}_{HB} \tilde{O}_{HB},$$

where the O_i and $\tilde{O}_i$ are the dimension-six operators and $\bar{c}_i$ and $\tilde{c}_i$ are Wilson coefficients. The operators O_γ and $\tilde{O}_\gamma$ (O_g and $\tilde{O}_g$) introduce new interactions between the Higgs boson and two photons (gluons). O_{HW} and $\tilde{O}_{HW}$ give rise to new HWW, HZZ and $HZ\gamma$ interactions, and O_{HB} and $\tilde{O}_{HB}$ contribute to HZZ and $HZ\gamma$ interactions. The analysis is sensitive to these operators through vector-boson fusion and associated production with vector bosons. For gluon fusion, vector-boson fusion and production in association with a vector boson, predictions from leading-order matrix elements are used, with up to two additional partons in the final state for gluon fusion. Leading-order predictions obtained using MADGRAPH5 [17] are then reweighted to account for higher-order QCD and electroweak corrections to the SM processes, assuming that these corrections factorize from the effects of effective operators.

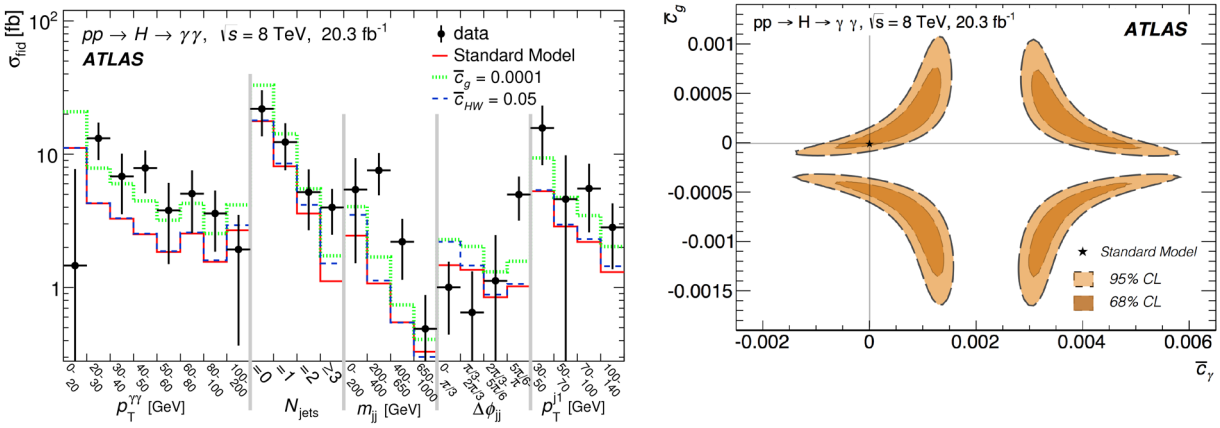

FIGURE 3. (a) The five differential distributions used for the combined analysis, compared to SM predictions and to predictions with non-SM contributions. (b) Confidence regions for a two-dimensional scan of $\bar{c}_\gamma$ and $\bar{c}_g$, when the other Wilson coefficients are set to zero [14].

Figure 3(a) shows the distributions used in the combined analysis, a SM prediction, as well as the effect that certain non-SM contributions would have on the distributions. Figure 3(b) shows the two-dimensional confidence region for two of the Wilson coefficients, $\bar{c}_\gamma$ and $\bar{c}_g$. Similarly, limits are derived on other combinations of Wilson

coefficients. The confidence regions for $\bar{c}_{HW}$ and $\tilde{c}_{HW}$ can be translated to the same basis used for the ATLAS results for non-SM CP-even and CP-odd HVV interactions using angular analyses of $H \to WW^* \to \ell\nu\ell\nu$ and $H \to ZZ^* \to 4\ell$ decays discussed below. The limits obtained from the $H \to \gamma\gamma$ analysis are $-0.08 < \tilde{\kappa}_{HVV}/\kappa_{\rm SM} < 0.09$ and $-0.22 < \tan\alpha\tilde{\kappa}_{AVV}/\kappa_{\rm SM} < 0.22$. They are about a factor seven stronger than the constraints from the CP analysis due to increased sensitivity to the contributions from the different Higgs boson production modes from the use of rate and jet kinematic information in this analysis.

SPIN AND PARITY STUDIES AT THE LHC

As the SM makes the clear prediction that the Higgs boson has spin zero and an even CP value ($J^{PC} = 0^{++}$), any observed deviation would be a clear sign of non-SM physics. The observation of the decay to two photons excludes $J = 1$ by the Landau-Yang theorem [18, 19]. The observation of the $H \to WW^*$ and $H \to ZZ^*$ decays with roughly the branching fractions predicted by the SM favors an even CP value, as a CP-odd boson would decay to these final states only through loops, resulting in much smaller branching fractions. Nevertheless, various spin and parity models are studied directly, and exclusion limits for alternative models are set [20, 21].

Spin and parity tests use the angular and kinematic distributions in decays to dibosons. The four-body decays $H \to ZZ^* \to 4\ell$ and $H \to WW^* \to \ell\nu\ell\nu$ probe all possible J^P, while the two-body $H \to \gamma\gamma$ decay cannot probe alternative $J = 0$ hypotheses. The studies are based purely on shape information and do not take into account the measured rates (the total rate as well as the contributions from the different production modes) to minimize the model dependence of the results.

The analyses in the different decay channels are based on various techniques and kinematic variables and use about 25 fb^{-1} collected at $\sqrt{s}$ =7 and 8 TeV.

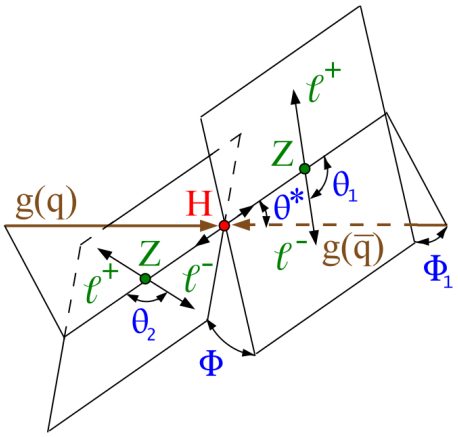

FIGURE 4. Illustration of the production and decay kinematic variables in the process $gg(q\bar{q}) \to H \to ZZ^* \to 4\ell$. The production angles θ^* and Φ_1 are shown in the H rest frame and the decay angles θ_1, θ_2 and Φ are taken in the Z rest frames [21].

In $H \to ZZ^* \to 4\ell$ decays, the complete kinematic information can be reconstructed with high precision. Figure 4 illustrates the production and decay angles. In addition, the invariant masses of the Z candidates and the four-lepton system are used in the analyses. Some of the studies performed do not use the production angles Φ_1 and $\cos\theta^*$ to remove production model dependence for $J = 1, 2$, or since the differential distributions for $J = 0$ are independent of the production angles, respectively.

The CMS studies of the $H \to WW^* \to \ell\nu\ell\nu$ decay are based on the dilepton invariant mass distribution and the transverse mass of the final state objects, given by $m_{\rm T}^2 = 2p_{\rm T}^{\ell\ell}E_{\rm T}^{\rm miss}(1 - \cos\Delta\phi(\ell\ell, \vec{E}_{\rm T}^{\rm miss}))$, where $p_{\rm T}^{\ell\ell}$ is the dilepton transverse momentum, $\vec{E}_{\rm T}^{\rm miss}$ is the missing transverse momentum and $\Delta\phi(\ell\ell, \vec{E}_{\rm T}^{\rm miss})$ is the azimuthal angle between the dilepton pair and the missing transverse momentum. The ATLAS study uses in addition $p_{\rm T}^{\ell\ell}$ and $\Delta\phi_{\ell\ell}$.

Spin studies in the $H \to \gamma\gamma$ decay make use of the production angle of the two photons measured in the Collins-Soper frame $\cos(\theta^*)$ and the transverse momentum of the diphoton pair.

Alternative spin and parity models

The specific models and also the formalism in which the tested models are formulated are not the same for the ATLAS and the CMS studies. While the ATLAS studies are formulated in terms of effective Lagrangians based on [22], the CMS studies are formulated in terms of anomalous couplings based on [23, 24]. A brief overview of the models and their formulations is given here for the spin-0 and spin-2 cases. For the results presented here, the spin-1 case is only tested by CMS, and the decay amplitude is written in terms of a vector and a pseudovector contribution.

Spin 0

The ATLAS studies are based on the following Lagrangian for a spin-0 particle H_0,

$$\begin{aligned}\mathcal{L}_0 &= \cos(\alpha)\kappa_{\rm SM}\left[\tfrac{1}{2}g_{HZZ}Z_\mu Z^\mu + g_{HWW}W^+_\mu W^{-\mu}\right]H_0 \\ &\quad -\tfrac{1}{4}\tfrac{1}{\Lambda}\left[\cos(\alpha)\kappa_{\rm HZZ}Z_{\mu\nu}Z^{\mu\nu} + \sin(\alpha)\kappa_{\rm AZZ}Z_{\mu\nu}\tilde{Z}^{\mu\nu}\right]H_0 \\ &\quad -\tfrac{1}{2}\tfrac{1}{\Lambda}\left[\cos(\alpha)\kappa_{\rm HWW}W^+_{\mu\nu}W^{-\mu\nu} + \cos(\alpha)\kappa_{\rm AWW}W^+_{\mu\nu}\tilde{W}^{-\mu\nu}\right]H_0,\end{aligned}$$

where V^μ are the vector fields ($V = W, Z$), $V^{\mu\nu}$ are the reduced field tensors and $\tilde{V}^{\mu\nu}$ their duals. The couplings of the SM CP-even, BSM CP-even and CP-odd interactions are given by $\kappa_{\rm SM}$, κ_{HVV} and κ_{AVV}, and α allows for mixing between the different states.

The CMS studies are based on the amplitude

$$A(HVV) \sim \left[a_1^{VV} + \frac{\kappa_1^{VV}q^2_{V1} + \kappa_2^{VV}q^2_{V2}}{(\Lambda_1^{VV})^2}\right]m^2_{V1}\epsilon^*_{V1}\epsilon^*_{V2} + a_2^{VV}f^{*(1)}_{\mu\nu}f^{*(2)\mu\nu} + a_3^{VV}f^{*(1)}_{\mu\nu}\tilde{f}^{*(2),\mu\nu},$$

where $V_{1,2}$ are the $Z_{1,2}$ and $W_{1,2}$ with four-momenta $q_{V1,2}$ and polarization vectors $\epsilon_{V1,2}$, and $f^{(1,2)\mu\nu} = \epsilon^\mu_{V1,2}q^\nu_{V1,2} - \epsilon^\nu_{V1,2}q^\mu_{V1,2}$ is the field strength tensor and $\tilde{f}^{(1,2)}_{\mu\mu}$ its dual. At tree-level, the a_1^{VV}-term is the SM contribution, the a_3^{VV}-term is the CP-odd contribution, while the other terms are non-SM CP-even contributions. Non-tree-level-a_1^{VV} terms have a negligible effect in the SM and can therefore be interpreted as non-SM contributions if found to be sizable.

Spin 2

The interaction of a spin-2 particle H with fermions and vector bosons can be described by

$$\mathcal{L}_2 = -\frac{1}{\Lambda}\left(\sum_V \kappa_V H^{\mu\nu}T^V_{\mu\nu} + \sum_f \kappa_f H^{\mu\nu}T^f_{\mu\nu}\right),$$

where $H^{\mu\nu}$ is the spin-2 field and $T^{V,f}_{\mu\nu}$ are the energy-momentum tensors of the vector bosons and fermions, respectively. The strength of the interactions is given by the couplings $\kappa_{V,f}$. The couplings can be taken to be equal for all particles, referred to as universal couplings scenario (UC), while scenarios with different couplings to the different particles are referred to as non-universal couplings scenarios (non-UC).

A number of models are tested by ATLAS and CMS, with different emphases. ATLAS considers UC and non-UC scenarios, and takes into account processes where additional particles are produced together with the Higgs boson. As the branching fractions predicted by UC models (about 5% for $H \to \gamma\gamma$ and negligible branching fractions for $H \to ZZ^*$ and $H \to WW^*$) are disfavored, $\kappa_{\gamma,Z,W}$ are not constrained to be equal to the other couplings, and the (non-)universality in the following refers to the couplings to quarks and gluons, $\kappa_{q,g}$ to be equal or not. Non-UC models predict an enhancement of the H transverse momentum spectrum at large transverse momentum. As the effective field theory (EFT) description is only valid up to a certain energy scale Λ, the analyses for non-UC scenarios require $p_{\rm T}^H$ <300 GeV and < 125 GeV in a tighter selection. Three scenarios are explored: $\kappa_q = \kappa_g$ (UC), $\kappa_q = 0$ and $\kappa_q = 2\kappa_g$. CMS considers models with various higher-order operators compared to the Lagrangian above, but with no additional particles in the final state.

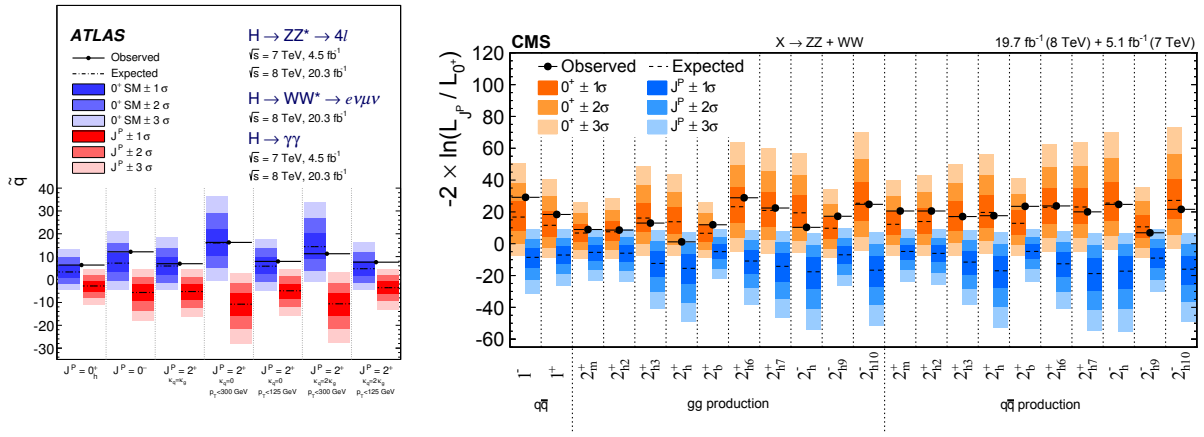

FIGURE 5. Distribution of the test statistics for the SM Higgs boson and alternative models from (a) ATLAS [20] and (b) CMS [21]. The expected distributions for the SM and the alternative models are shown as colored bands (note that blue shows the SM in the ATLAS figure and the alternative model in the CMS figure), while the observed values are shown as data points.

Fixed hypotheses tests

As a first step, non-SM hypotheses for $J^P = 0^\pm, 1^\pm$ and $2^\pm$, not considering possible mixing between different CP states, are tested against the SM $J^P = 0^+$ hypothesis. The ratio of profiled likelihoods for the SM and the alternative hypothesis serves as the test statistics, and its distributions for the SM and alternative hypothesis is evaluated on pseudo-experiments. The CL_s method is used to determine the level of exclusion of the alternative model. The analyses combine the information from $H \to ZZ^* \to 4\ell$ and $H \to WW^* \to \ell\nu\ell\nu$, and in the case of the ATLAS experiment, also $H \to \gamma\gamma$.

The various tested models and their agreement with the SM and the alternative hypothesis is shown in Figure 5. The alternative non-SM models with $J^P = 0^\pm, 1^\pm$ and $2^\pm$ are typically excluded at more than 99% confidence level.

CP mixing studies

Assuming spin-0, the coupling structure of the HVV couplings can be studied, allowing for mixing between SM CP-even, BSM CP-even and CP-odd contributions.

The ATLAS analysis presents the results in terms of ratios of couplings $(\tilde{\kappa}_{AVV}/\kappa_{\mathrm{SM}}) \cdot \tan\alpha$ and $\kappa_{HVV}/\kappa_{\mathrm{SM}}$, where only one of the ratios was considered at a time, and the other one assumed to be zero. Here,

$$\tilde{\kappa}_{AVV} = \frac{1}{4}\frac{v}{\Lambda}\kappa_{AVV} \text{ and } \tilde{\kappa}_{HVV} = \frac{1}{4}\frac{v}{\Lambda}\kappa_{HVV},$$

and v is the vaccum expectation value of the SM Higgs field. The combination of $H \to ZZ^* \to 4\ell$ and $H \to WW^* \to \ell\nu\ell\nu$ is performed under the assumption of the same non-SM admixture in the two decay channels.

The likelihood scans for $\kappa_{HVV}/\kappa_{\mathrm{SM}}$, and $(\tilde{\kappa}_{AVV}/\kappa_{\mathrm{SM}}) \cdot \tan\alpha$ are shown in Figure 6. No significant admixture of non-SM CP states is observed.

The CMS analysis uses a parametrization in terms of effective fractional cross sections f_{ai} and their phases ϕ_{ai} with respect to the SM tree-level couplings $a_1 = a_1^{ZZ}$ and a_1^{WW} given by

$$f_{a2,3} = \frac{|a_{2,3}|^2\sigma_{2,3}}{|a_1|^2\sigma_1 + |a_2|^2\sigma_2 + |a_3|^2\sigma_3 + \bar{\sigma}_{\Lambda 1}/\Lambda_1^4 + \ldots}, \quad \phi_{a2,3} = \arg\frac{a_1}{a_{2,3}},$$

with σ_i the cross section of the process corresponding to $a_i = 1$, $a_{j\neq i} = 0$ and $\bar{\sigma}_{\Lambda 1}$ the effective cross section of the process corresponding to Λ_1 =1 TeV, and where the VV-subscripts have been suppressed. $f_{\Lambda 1}$ with phase $\phi_{\Lambda 1}$ is defined analogously. For the combination of $H \to ZZ^* \to 4\ell$ and $H \to WW^* \to \ell\nu\ell\nu$, the results are expressed as f_{ai}

for the ZZ coupling and the ratio of the couplings in the two channels

$$r_{ai} = \frac{a_i^{WW}/a_1^{WW}}{a_i/a_1}, \text{ or } R_{ai} = \frac{r_{ai}|r_{ai}|}{1+r_{ai}^2}.$$

Confidence intervals are obtained for $f_{a2,3}\cos(\phi_{a2,3})$ and $f_{\Lambda 1}\cos(\phi_{\Lambda 1})$, and no deviation from the SM predictions is found. The observed likelihood scans for $f_{a2,3}\cos(\phi_{a2,3})$ are shown in Figure 7.

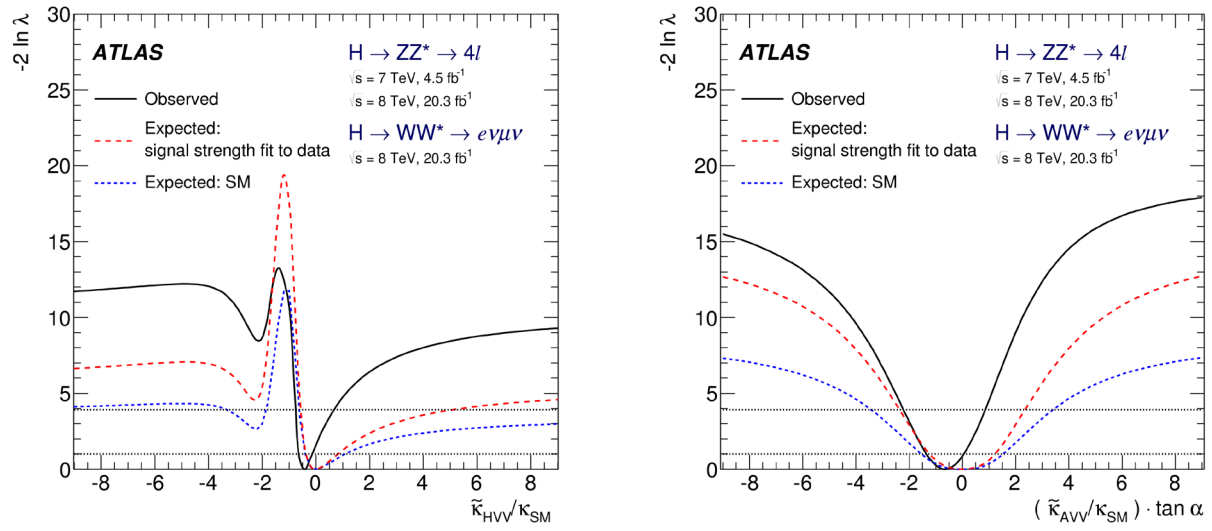

FIGURE 6. Likelihood scans for (a) $\kappa_{HVV}/\kappa_{\rm SM}$ and (b) $(\tilde{\kappa}_{AVV}/\kappa_{\rm SM})\cdot\tan\alpha$ [20].

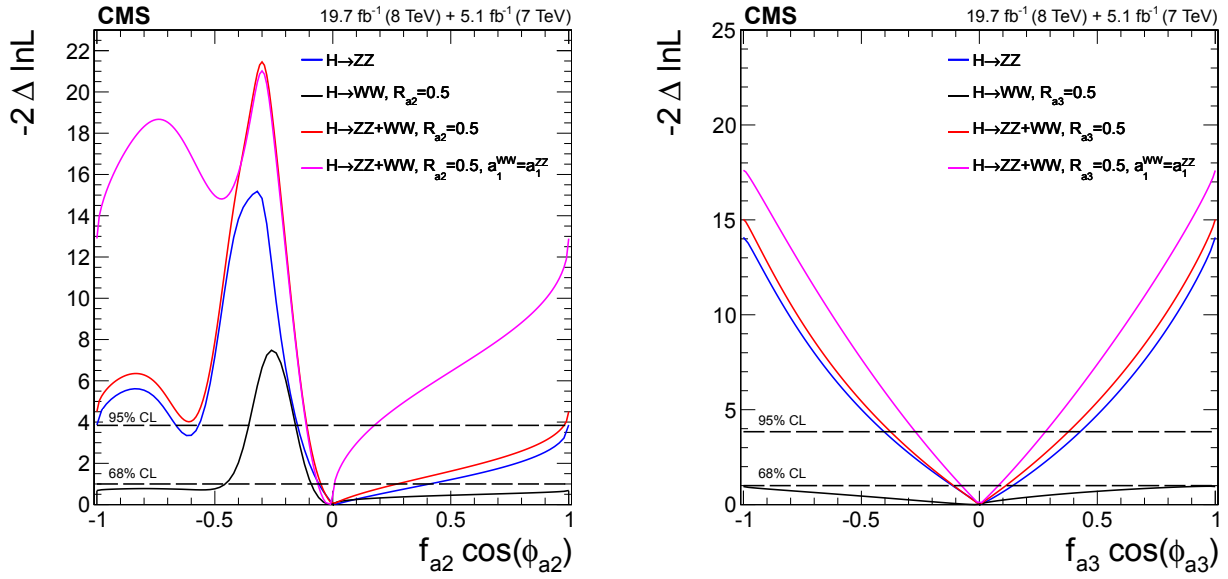

FIGURE 7. Likelihood scans for (a) $f_{a2}\cos(\phi_{a2})$ and (b) $f_{a3}\cos(\phi_{a3})$ separately and combined for $H \to ZZ^* \to 4\ell$ and $H \to WW^* \to \ell\nu\ell\nu$ with and without the assumption of the constraint of $a_1^{WW} = a_1$ [21].

SPIN AND PARITY STUDIES AT TEVATRON

The CDF and D0 experiments have performed spin and parity studies using Higgs bosons production in association with vector bosons and decays into the $b\bar{b}$ final state [25]. The studies are based on about 10 fb^{-1} of $p\bar{p}$ collisions with $\sqrt{s}$ =1.96 TeV recorded by the CDF and D0 experiments at the Fermilab Tevatron. Two specific models are tested, a $J^P = 0^-$ and a $J^P = 2^+$ model [26], which do not predict the production cross sections or decay branching fractions. The study makes use of the behavior of the production rate near threshold in β, where $\beta = 2p/\sqrt{\hat{s}}$ with p the momentum of the Higgs boson in the VH rest frame, and $\sqrt{\hat{s}}$ the total energy of the VH system in its rest frame. For a SM Higgs boson, the production rate at threshold is linear in β, while the tested $J^P = 0^-$ and $J^P = 2^+$ models tested exhibit a β^3 and β^5 dependence, respectively. Due to the different threshold behavior, also the distribution of the VH invariant mass significantly is different. The analyses are based on the m_{VH} distribution (D0) and a MVA discriminant (CDF). Figure 8(a) shows the distribution of $\log_{10}(s/b)$ using bins of the final discriminants for all search channels in the CDF and D0 analyses from the $J^P = 0^-$ analysis.

The analysis uses scaling factors $\mu_{\rm SM}$ and $\mu_{\rm exotic}$, providing the normalization of the signal with respect to the SM production cross section times branching fraction. The presence of a $J^P = 0^-$ or $J^P = 2^+$ signal is tested both in addition to and instead of the SM Higgs boson. No evidence is seen for a $J^P = 0^-$ or $J^P = 2^+$ exotic Higgs boson, neither produced in admixture nor instead of a SM Higgs boson. For $\mu_{\rm SM} = 0$, a $J = 0^-$ or $J = 2^+$ signal is excluded with a significance of 5σ and 4.9σ assuming the SM Higgs boson production cross sections times branching fraction to $b\bar{b}$. The strong exclusion can be obtained thanks to the enhanced production at threshold and the hard m_{VH} spectrum predicted by the $J^P = 0^-$ and 2^+ models.

The best simultaneous fit for $\mu_{\rm SM}$ and $\mu_{\rm exotic}$ is consistent with a SM Higgs boson without exotic admixture. Figure 8(b) shows upper limits on the fraction of exotic admixture ($f_{JP} = \mu_{\rm exotic}/(\mu_{\rm SM} + \mu_{\rm exotic})$) as a function of $\mu = \mu_{\rm SM} + \mu_{\rm exotic}$.

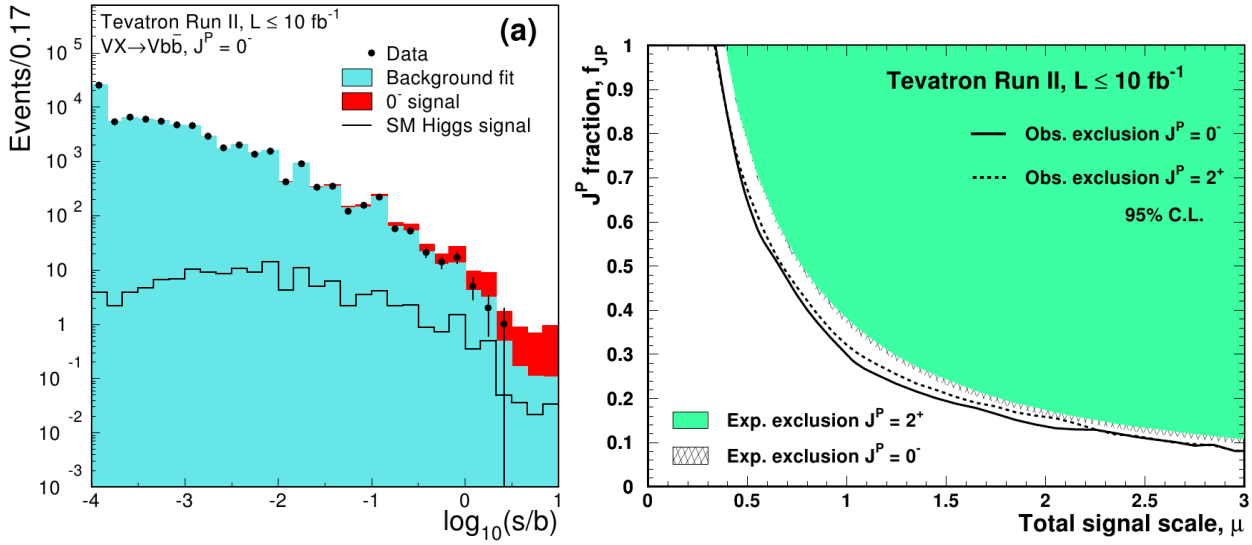

FIGURE 8. (a) Distribution of $\log_{10}(s/b)$ from all search channels from CDF and D0 for the $J^P = 0^-$ search. The exotic signal is shown with $\mu_{\rm exotic} = 1$. The exotic Higgs boson is denoted as X in the plot. (b) Expected and observed upper limits at 95% CL on the fraction of exotic admixture with $J^P = 0^-$ and 2^+ [25].

RARE DECAY CHANNELS

The SM predicts very small branching fractions for many Higgs boson decay channels, much below what could be expected to be observed with the $\sqrt{s}$ =7 and 8 TeV dataset. An observation of such a rare decay would be a clear sign of physics beyond the SM. Setting limits on their branching fractions provides constraints on models beyond the SM.

Search for the $H \to Z\gamma$ decay

The $H \to Z\gamma$ decay proceeds through a loop, and as such is sensitive to potential new particles that could contribute to the loop. In reality, a careful tuning of parameters is needed in many models to enhance the $H \to Z\gamma$ decay rate by more than a factor of two compared to the SM, but larger enhancements are possible in some models.

In the SM, the branching fraction of $H \to Z\gamma$ is predicted to be 0.16%, only somewhat smaller than the $H \to \gamma\gamma$ branching fraction. Reconstructing the Z boson in its decays to two leptons (electrons or muons) results in a good $m_{Z\gamma}$ invariant mass resolution of about 1-3% and a much higher signal-to-background ratio than other possible Z decay channels, but reduces the number of expected signal events due to the $Z \to \ell\ell$ branching fraction of about 6.7%.

The analyses [27, 28], based on about 25 fb^{-1} of pp collisions at $\sqrt{s}$ =7 and 8 TeV, require two same-flavor opposite-sign leptons (electrons or muons) with p_{T} above 10-20 GeV and an invariant mass compatible with the Z boson mass, as well as an isolated photon with p_{T} greater than 15 GeV. The events are categorized based on the Z and γ kinematics, assuming a SM-like Higgs boson. As one example, the difference in pseudorapidity between the Z and the photon candidate in signal and background simulation and in data is shown in Figure 9(a). The CMS analysis also uses a dijet category with requirements to enhance the contribution from vector boson fusion production. The event categorization splits events into classes of different expected invariant mass resolution and signal-to-background ratio and improves the sensitivity of the analysis by 20-40%.

The analyses perform a signal-plus-background fit to the three-body invariant mass distribution, parametrizing the shape of the background by an analytical function. Due to the large backgrounds from non-Higgs $Z\gamma$ production and Z+jets production where a jet is misidentified as photon, the expected signal-to-background ratio is only about 0.3%.

Figure 9(b) shows the invariant mass spectrum measured by CMS, together with the fitted background and the expected signal enhanced by a factor of 75. At a Higgs mass of 125.5 GeV (125 GeV), the ATLAS (CMS) experiment sets a limit at 11 (9.5) times the SM expectation at a confidence level of 95%. The expected limit is 9 (10) times the SM expectation.

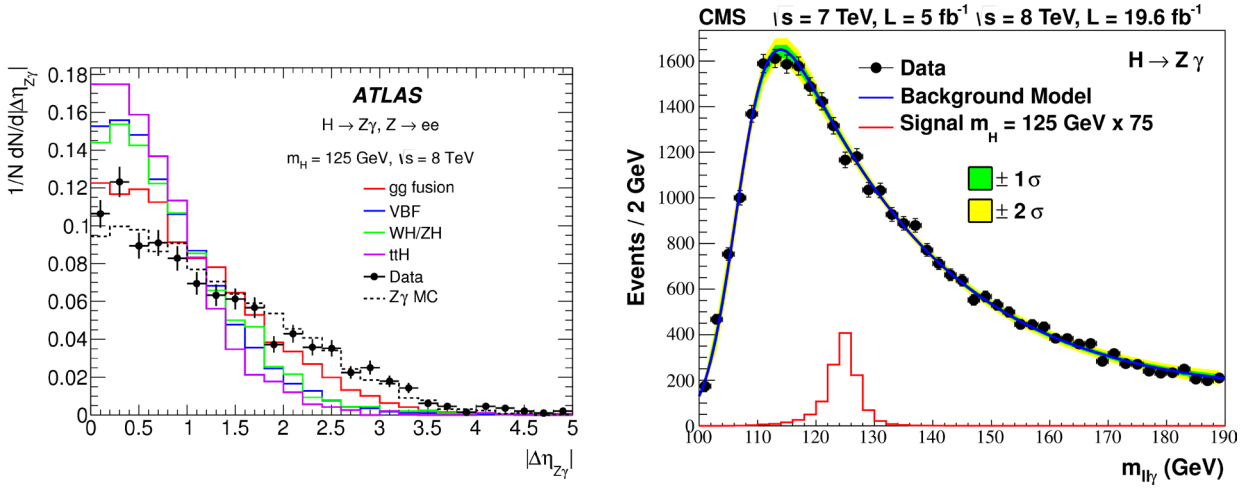

FIGURE 9. (a) Normalized distributions of the pseudorapidity difference of the Z boson and the photon candidate for the different SM Higgs boson production modes, non-Higgs $Z\gamma$ background and in data [27]. Three-body invariant mass spectrum observed in data, background fit and expected signal enhanced by a factor of 75 [28].

Search for the $H \to \mu\mu$ decay

The $H \to \mu\mu$ decay channels offers a clean probe of Higgs boson couplings to the second generation fermions. In the SM, the branching fraction to the two-muon final state is predicted to be only 0.02%.

The analyses [29, 30], based on about 25 fb^{-1} of pp collisions at $\sqrt{s}$ =7 and 8 TeV, require two opposite-sign isolated muons with transverse momentum greater than 25 and 15 GeV. They benefit from the very good dimuon mass resolution of 1.5-2.5%. Figure 10(a) shows the dimuon invariant mass distribution in data and its expected

composition from simulation. The largest background comes from $Z/\gamma^* \to \mu\mu$ events and smaller contributions are from $t\bar{t}$, WW production and other processes. The expected signal-to-background ratio is about 0.4%. Events are categorized, assuming a SM-like Higgs boson, by splitting the events into classes of different expected invariant mass resolution and signal-to-background ratio. The categorization is based on the pseudorapidity of the muons and the transverse momentum of the dimuon system, and introduces one or several dijet categories in the ATLAS and CMS analysis, respectively.

The analyses perform a signal-plus-background fit to the dimuon invariant mass distribution parametrizing the shape of the background by an analytical function. Figure 10(b) shows the dimuon invariant mass spectrum measured by CMS overlaid with the fitted background shape. At a Higgs mass of 125 GeV (125.5 GeV), the CMS (ATLAS) experiment sets a limit at 7.4 (7) times the SM expectation at a confidence level of 95%. The expected limit is 6.5 (7.2) times the SM expectation. The observed limit translates into an limit at 95% confidence level on the branching fraction into two muons of 1.6×10^{-3} and 1.5×10^{-3}, respectively.

CMS carries out a similar search for $H \to ee$ using the 8 TeV dataset and sets an upper limit at 95% confidence level at 1.9×10^{-3} for the branching fraction into an electron-positron pair, which corresponds to about 3.7×10^{5} times the SM expectation.

With the observation of the $H \to \tau\tau$ decay [6], not seeing evidence of the $H \to \mu\mu$ and the $H \to ee$ decay confirms that the Higgs couplings are not flavor universal.

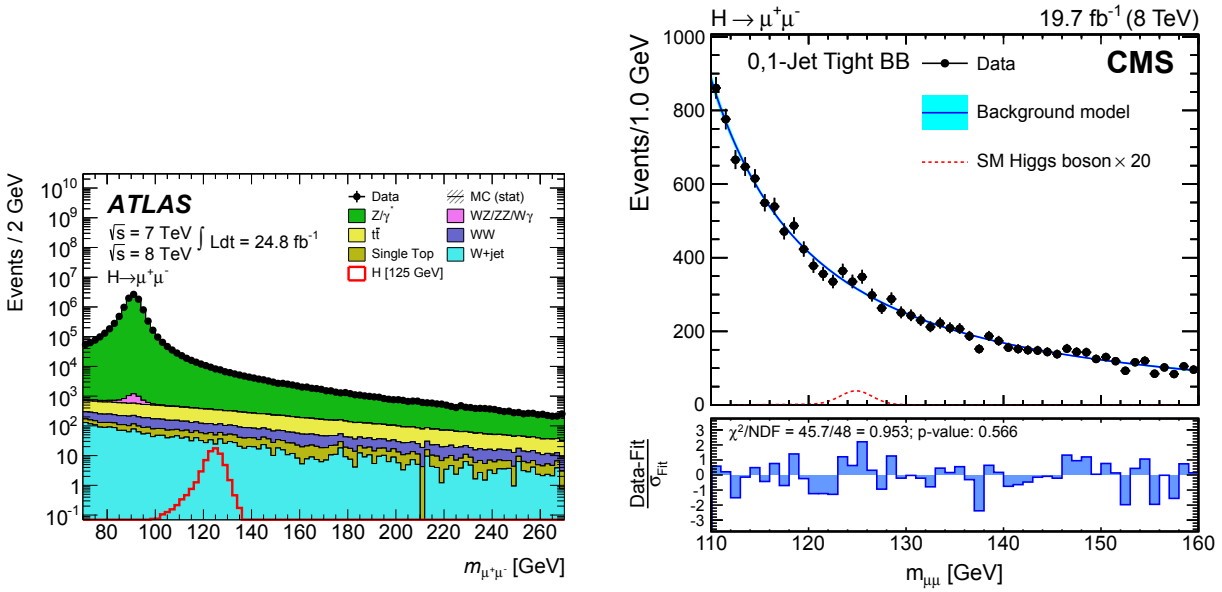

FIGURE 10. (a) Dimuon invariant mass distribution in data and its composition as expected from the simulation, together with the expected $H \to \mu\mu$ signal [29]. (b) Dimuon invariant mass spectrum, the fitted background and the expected signal enlarged by a factor of 20 [30].

Search for the $H \to J/\psi\gamma$ and $H \to \Upsilon(nS)\gamma$ decays

Rare decays to a J/ψ and a photon could provide sensitivity to the size and sign of the Higgs Yukawa coupling to c quarks [31, 32]. The sensitivity to the sign of the coupling is provided through the interference of the smaller direct production, where the Higgs boson couplings directly to the charm quark, and the larger indirect production, without direct coupling of the Higgs boson to the charm quark. In the SM, the branching fraction to $J/\psi\gamma$ can be predicted quite accurately. The expected branching fractions are $(2.8\pm0.2)\times10^{-6}$ for the $H \to J/\psi\gamma$ decay and $(6.1^{+17.4}_{-6.1}, 2.0^{+1.9}_{-1.3}, 2.4^{+1.8}_{-1.3})\times10^{-10}$ for the $H \to \Upsilon(1,2,3S)\gamma$ decays [33].

The analysis is based on 20.3 fb^{-1} of pp collision data taken at $\sqrt{s}$ =8 TeV by the ATLAS detector [34]. The analysis requires two opposite-sign isolated muons, and the higher-p_{T} muon is required to have a transerve momentum greater than 20 GeV. Dimuon candidates with a mass within 0.2 GeV of the J/ψ mass are retained as J/ψ candidates

and dimuon candidates with an invariant mass between 8 and 12 GeV are retained as $\Upsilon(nS)$ candidates. The dimuon system is required to have a momentum greater than 36 GeV. Backgrounds from b-hadron decays are suppressed by a requirement on the transverse flight length significance. The photon candidate is required to be isolated and have a transverse momentum greater than 36 GeV. Events are categorized according to the pseudorapidity of the muons and whether the photon is reconstructed as converted or unconverted photon.

The three-body invariant mass $m_{\mu\mu\gamma}$ distribution is shown in Figure 11(a) for the $H \to J/\psi\gamma$ search. The main background is inclusive quarkonium production where a jet in the event is misidentified as photon. This background is modeled with a nonparametric data-driven approach in the signal-plus-background fits, which are performed simultaneously in $m_{\mu\mu\gamma}$ and $p_{\mathrm{T}}^{\mu\mu\gamma}$ for the $H \to J/\psi\gamma$ search and in $m_{\mu\mu\gamma}$, $p_{\mathrm{T}}^{\mu\mu\gamma}$ and $m_{\mu\mu}$ for the $H \to \Upsilon(nS)\gamma$ search.

Limits on the $H \to J/\psi\gamma$ and $H \to \Upsilon(nS)\gamma$ branching fractions are set using the CL_s formalism. The observed limit at 95% confidence level is 1.5×10^{-3} (expected $1.2^{+0.6}_{-0.3}\times10^{-3}$) for the $H \to J/\psi\gamma$ decay, which corresponds to about 540 times the SM branching fraction. For the $H \to \Upsilon(1,2,3S)\gamma$ branching fractions, the observed limits are $(1.3, 1.9, 1.3)\times10^{-3}$ (expected $(1.8^{+0.9}_{-0.5}, 2.1^{+1.1}_{-0.6}, 1.8^{+0.9}_{-0.5})\times10^{-3}$).

The CMS experiment also sets a limit on the $H \to J/\psi\gamma$ branching fraction in the context of the $H \to \gamma^*\gamma \to \ell\ell\gamma$ analysis described below. For this result, the selection is modified: The dimuon and the photon transverse momenta are required to be greater than 40 GeV, and the dimuon invariant mass is required to be around the J/ψ mass, 2.9 GeV$< m_{\mu\mu} <$3.3 GeV. The observed limit on the $H \to J/\psi\gamma$ branching fraction is 1.5×10^{-3} at 95% confidence level.

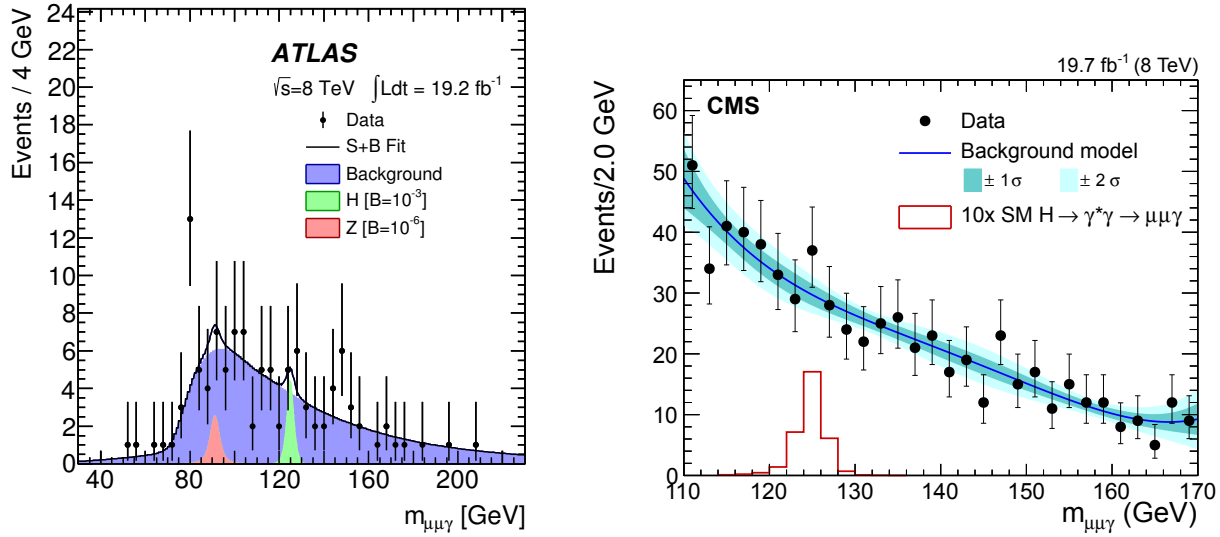

FIGURE 11. (a) Three-body invariant mass distribution measured in data and the signal and background contributions. The $H \to J/\psi\gamma$ and $Z \to J/\psi\gamma$ contributions are shown as expected for branching fractions of 10^{-3} and 10^{-6}, respectively [34]. (b) Three-body invariant mass distributions measured in data and fitted background. The expected signal is shown enlarged by a factor of 10 [35].

Search for the $H \to \gamma^*\gamma \to \ell\ell\gamma$ decay

The Higgs boson decay into $\ell\ell\gamma$ where the dilepton pair has a low invariant mass has contributions from $H \to \gamma^*\gamma$ and $H \to Z\gamma$ decays, from $H \to \ell\ell$ decays with final state radiation, from higher-order processes (known as box diagrams), which have a negligible contribution, and from $H \to J/\psi\gamma$ and $H \to \Upsilon(nS)\gamma$ decays. Once the decay to $\ell\ell\gamma$ is observed, non-trivial angular distributions and forward-backward asymmetries will allow for Higgs boson property studies.

The analysis is based on 19.7 fb^{-1} of pp collision data taken at $\sqrt{s}$ =8 TeV by the CMS detector [35]. The analysis requires two opposite-sign same-flavor leptons. Muons are required to have a transverse momentum larger than 23 (4) GeV for the leading (subleading) muon, and the dimuon invariant mass is required to be smaller than 20 GeV to suppress the $H \to Z\gamma$ contribution, rejecting the regions 2.9 GeV$< m_{\mu\mu} <$3.3 GeV and 9.3 GeV$< m_{\mu\mu} <$9.7 GeV to suppress $H \to J/\psi\gamma$ and $H \to \Upsilon(nS)\gamma$ contributions. In the electron channel, the energy deposits of the electron and

positron merge in the calorimeter and the pair is therefore reconstructed from one energy cluster with energy greater than 30 GeV, and with two matching tracks. The invariant mass reconstructed from the tracks is required to be smaller than 1.5 GeV. The photon and the dilepton transverse momenta must satisfy $p_{\mathrm{T}} > 0.3 m_{\ell\ell\gamma}$.

The three-body invariant mass distribution in the muon channel is shown in Figure 11(b). The background is modeled with an analytic function that is fitted to the data. The analysis sets a limit on the branching fraction for $H \to \gamma^*\gamma \to \ell\ell\gamma$ at 7.7 times the SM expectation at 95% confidence level. The expected limit is at 6.4 times the SM expectation.

CONCLUSIONS

The LHC Run 1 dataset, about 25 fb^{-1} pp collisions taken at $\sqrt{s}$ =7 and 8 TeV, as well as the Tevatron dataset of about 10 fb^{-1} $p\bar{p}$ collisions taken at $\sqrt{s}$ =1.96 TeV, have allowed quite detailed property studies of the Higgs boson discovered in summer 2012. All measured and studied Higgs boson properties are consistent with the expectations from the SM within the currently still sizable uncertainties.

Fiducial and differential cross section measurements have been carried out in the $H \to \gamma\gamma$ and $H \to ZZ^* \to 4\ell$ decays. As almost model-independent results, they complement the other property measurements. Explicit studies of the quantum numbers favor a SM $J^P = 0^+$ interpretation. All other tested spin and pure CP hypotheses, including $J^P = 0^\pm, 1^\pm$ and $2^\pm$ models, are strongly disfavored. Limits are set on the admixture of $J^P = 0^-$ or a non-SM $J^P = 0^+$ component to a SM-like $J^P = 0^+$ by the LHC experiments and on the admixture of a $J^P = 0^-$ or $J^P = 2^+$ component to a SM-like $J^P = 0^+$ by the Tevatron experiments. Searches for rare decays offer the possibility to find a sign of physics beyond the SM, in the case that a signal is observed, and otherwise constrain the parameter space of beyond the SM models. The non-observation of $H \to \mu\mu$ also provides evidence of the Higgs boson couplings to fermions not being flavor universal.

The expected dataset from LHC Run 2, taken at $\sqrt{s}$ =13 and maybe 14 TeV, will offer an exciting Higgs physics program for the next years.

REFERENCES

[1] ATLAS Collaboration, JINST **3**, p. S08003 (2008).
[2] CMS Collaboration, JINST **3**, p. S08004 (2008).
[3] ATLAS Collaboration, Phys. Lett. B **716**, 1–29 (2012), arXiv:1207.7214 [hep-ex] .
[4] CMS Collaboration, Phys. Lett. B **716**, 30–61 (2012), arXiv:1207.7235 [hep-ex] .
[5] M. Pieri, these proceedings (2015).
[6] ATLAS and CMS Collaborations, ATLAS-CONF-2015-044, CMS-PAS-HIG-15-002 (2015), https://cds.cern.ch/record/2052552.
[7] ATLAS Collaboration, Phys. Lett. B **738**, 234–253 (2014), arXiv:1408.3226 [hep-ex] .
[8] CMS Collaboration, CMS-PAS-HIG-14-028 (2015), https://cds.cern.ch/record/2040210.
[9] ATLAS Collaboration, JHEP **09**, p. 112 (2014), arXiv:1407.4222 [hep-ex] .
[10] CMS Collaboration, Accepted by Eur. Phys. J. C (2015), arXiv:1508.07819 [hep-ex] .
[11] ATLAS Collaboration, Phys. Rev. Lett. **115**, p. 091801 (2015), arXiv:1504.05833 [hep-ex] .
[12] S. Dittmaier *et al.* (LHC Higgs Cross Section Working Group), CERN-2011-002 (2011), arXiv:1101.0593 [hep-ph] .
[13] C. Anastasiou, C. Duhr, F. Dulat, F. Herzog, and B. Mistlberger, Phys. Rev. Lett. **114**, p. 212001 (2015), arXiv:1503.06056 [hep-ph] .
[14] ATLAS Collaboration, Accepted by Phys. Lett. B (2015), arXiv:1508.02507 [hep-ex] .
[15] G. F. Giudice, C. Grojean, A. Pomarol, and R. Rattazzi, JHEP **06**, p. 045 (2007), arXiv:hep-ph/0703164 [hep-ph] .
[16] R. Contino, M. Ghezzi, C. Grojean, M. Muhlleitner, and M. Spira, JHEP **07**, p. 035 (2013), arXiv:1303.3876 [hep-ph] .
[17] J. Alwall, M. Herquet, F. Maltoni, O. Mattelaer, and T. Stelzer, JHEP **06**, p. 128 (2011), arXiv:1106.0522 [hep-ph] .
[18] L. Landau, Dokl.Akad.Nauk Ser.Fiz. **60**, 207–209 (1948).
[19] C.-N. Yang, Phys.Rev. **77**, 242–245 (1950).
[20] ATLAS Collaboration, Eur. Phys. J. C **75**, p. 476 (2015), arXiv:1506.05669 [hep-ex] .

[21] CMS Collaboration, Phys. Rev. D **92**, p. 012004 (2015), arXiv:1411.3441 [hep-ex] .
[22] P. Artoisenet *et al.*, JHEP **11**, p. 043 (2013), arXiv:1306.6464 [hep-ph] .
[23] Y. Gao, A. V. Gritsan, Z. Guo, K. Melnikov, M. Schulze, and N. V. Tran, Phys. Rev. D **81**, p. 075022 (2010), arXiv:1001.3396 [hep-ph] .
[24] S. Bolognesi, Y. Gao, A. V. Gritsan, K. Melnikov, M. Schulze, N. V. Tran, and A. Whitbeck, Phys. Rev. D **86**, p. 095031 (2012), arXiv:1208.4018 [hep-ph] .
[25] T. Aaltonen *et al.* (CDF, D0), Phys. Rev. Lett. **114**, p. 151802 (2015), arXiv:1502.00967 [hep-ex] .
[26] D. J. Miller, S. Y. Choi, B. Eberle, M. M. Muhlleitner, and P. M. Zerwas, Phys. Lett. B **505**, 149–154 (2001), arXiv:hep-ph/0102023 [hep-ph] .
[27] ATLAS Collaboration, Phys. Lett. B **732**, 8–27 (2014), arXiv:1402.3051 [hep-ex] .
[28] CMS Collaboration, Phys. Lett. B **726**, 587–609 (2013), arXiv:1307.5515 [hep-ex] .
[29] ATLAS Collaboration, Phys. Lett. B **738**, 68–86 (2014), arXiv:1406.7663 [hep-ex] .
[30] CMS Collaboration, Phys. Lett. B **744**, 184–207 (2015), arXiv:1410.6679 [hep-ex] .
[31] G. T. Bodwin, F. Petriello, S. Stoynev, and M. Velasco, Phys. Rev. D **88**, p. 053003 (2013), arXiv:1306.5770 [hep-ph] .
[32] A. L. Kagan, G. Perez, F. Petriello, Y. Soreq, S. Stoynev, and J. Zupan, Phys. Rev. Lett. **114**, p. 101802 (2015), arXiv:1406.1722 [hep-ph] .
[33] G. T. Bodwin, H. S. Chung, J.-H. Ee, J. Lee, and F. Petriello, Phys. Rev. D **90**, p. 113010 (2014), arXiv:1407.6695 [hep-ph] .
[34] ATLAS Collaboration, Phys. Rev. Lett. **114**, p. 121801 (2015), arXiv:1501.03276 [hep-ex] .
[35] CMS Collaboration, Accepted by Phys. Lett. B (2015), arXiv:1507.03031 [hep-ex] .

Proceedings of the LHCP2015 Conference, St. Petersburg, Russia, August 31 - September 5, 2015

Editors: V.T. Kim and D.E. Sosnov

Measurements of the Higgs boson production and decay rates and constraints on its couplings at the LHC

MARCO PIERI

UC San Diego, United States

Marco.Pieri@cern.ch

On behalf of the ATLAS and CMS Collaborations

Abstract. ATLAS and CMS Higgs boson analyses have been combined to precisely measure the Higgs boson mass. The result is $m_H = 125.09 \pm 0.24$ GeV. Combined measurements of the Higgs boson production and decay rates, and constraints on its couplings to other particles have been obtained. The results are based on the proton-proton collision data collected at the LHC with the ATLAS and CMS detectors in 2011 and 2012, corresponding to integrated luminosities per experiment of approximately 5 fb^{-1} at $\sqrt{s} = 7$ TeV and 20 fb^{-1} at $\sqrt{s} = 8$ TeV. The combined signal yield relative to the standard model prediction is 1.09 ± 0.11. Many other measurements have been carried out in more or less constrained assumptions and all measurement are consistent with the standard model. The increased sensitivity coming from the combination of the two experiments allows to obtain a significance of 5.4σ for the VBF production process and of 5.5σ for Higgs boson decays into τ-lepton pairs.

INTRODUCTION

After the Higgs boson discovery in 2012 [1, 2], ATLAS [3] and CMS [4] have carried out a detailed research program to measure the Higgs boson properties [5–14]. To date none of the measured Higgs boson properties [15, 16] shows significant deviations from the predictions of the standard model [17–20] (SM). The Higgs boson is produced at the LHC in five main production processes: gluon fusion (ggF) that is the dominant one, vector boson fusion (VBF), where the Higgs boson is produced in association with two jets with a large gap in rapidity, associated production with Z (ZH) or W (WH) vector bosons (collectively referred as VH), and associated production with a pair of top quarks (ttH). The Feynman diagrams corresponding to these processes are shown in Figure 1. Other production processes with lower cross sections are also predicted, such as Higgs production processes in association with a single top quark and a W boson or a quark (tH). These processes have a negligible cross section in the SM but they can be enhanced in other models and typically in the case of opposite sign between boson and fermion couplings.

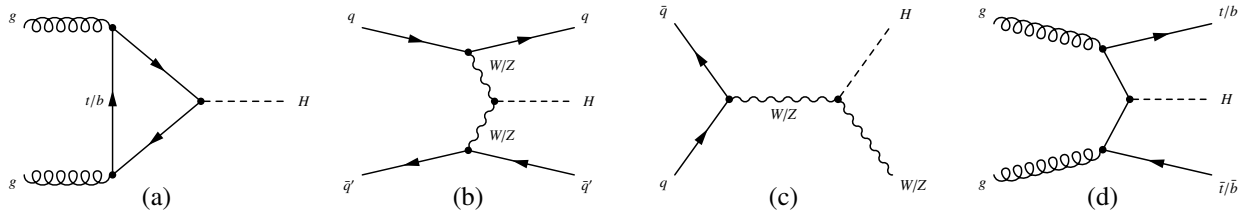

FIGURE 1. Leading-order Feynman diagrams for Higgs boson production through the (a) ggF, (b) VBF, (c) VH, and (d) ttH production processes.

The Higgs boson decays into fermion pairs with a Yukawa coupling proportional to the fermion mass, into vector boson with a gauge coupling proportional to the square of the W or Z mass, and to gluon and photon pairs through fermion and boson loops. The production cross sections and the branching fractions (BR) as function of the mass are displayed in Figure 2. Production cross sections and decay BRs are taken from [21–24]. The production cross sections

have uncertainties of about 10% fer the ggF and ttH processes, and 2-3% for VBF and VH; the BR uncertainties lie in the range 2-5% for the most easily measurable decay modes at the LHC. The specific values employed in this analysis are reported in Ref. [25].

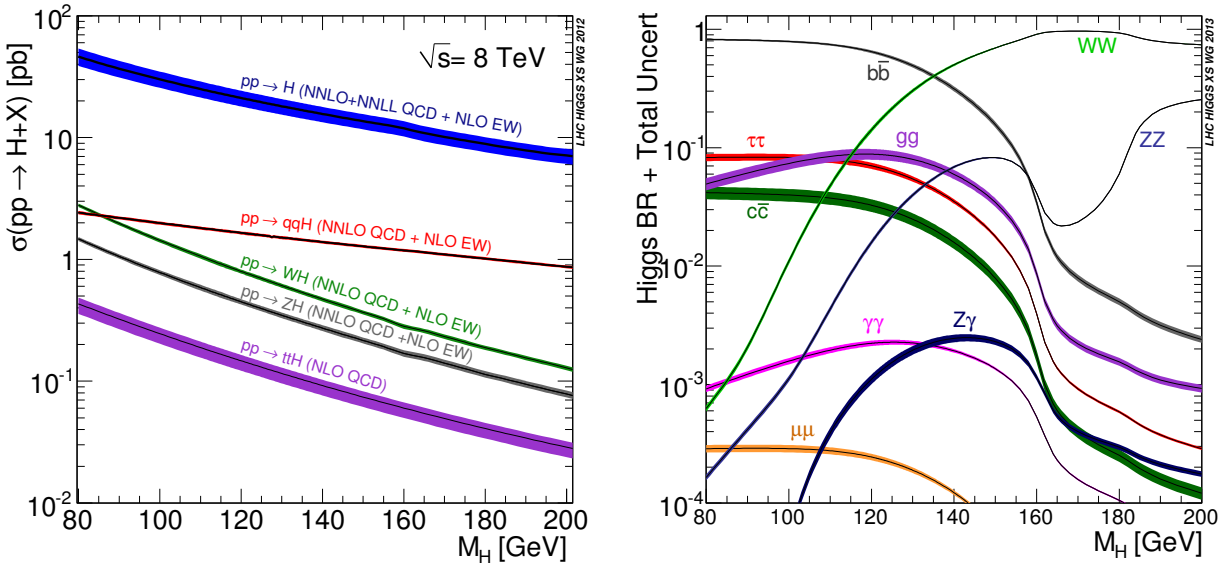

FIGURE 2. Left: production cross sections [21] and right: decay branching fractions [24], as function of the Higgs boson mass.

MASS MEASUREMENT

The Higgs boson mass is a free parameter of the SM and once specified, production cross sections and BRs are all predicted by the theory. The measurement of the mass is therefore needed to compare cross section and BR measurement with the SM predictions. The mass is measured at the LHC using the two high resolution channels $H \to \gamma\gamma$ and $H \to ZZ \to 4\ell$. ATLAS and CMS results have been combined [5, 16] and yield a measurement $m_H = 125.09 \pm 0.24 = 125.09 \pm 0.21(\text{stat.}) \pm 0.11(\text{syst.})$ GeV, where the uncertainty is still dominated by the statistical component. While the combined measurements in the $H \to \gamma\gamma$ and $H \to ZZ \to 4\ell$ channels are in very good agreement, there is a small tension between the four individual measurements that gives a p-value of compatibility with a common mass hypothesis of 10%. The individual results in each channel, together with the combined results, are shown in Figure 3.

PRODUCTION, DECAYS AND COUPLINGS

ATLAS and CMS results are combined for the measurement of the Higgs boson production and decay rates and for tests of its couplings [25]. With the combination, given that the uncertainty of almost all measurements is statistically dominated, the increase in sensitivity is approximately $\sqrt{2}$, corresponding to almost doubling the integrated luminosity. All analyses from ATLAS and CMS that were combined in both individual experiment combinations [6, 7] are included in this combination. Namely those addressing the five main production channels indicated above in the five main decays into $\gamma\gamma$, ZZ, WW, $\tau\tau$ and bb with the exception of the ggF and VBF production channels in the bb decay mode. Even if not at the same level of sensitivity, also the inclusive and VBF production of the $H \to \mu\mu$ decay channel have been combined in specific cases. For each analysis in each decay channel, events are classified into categories with different sensitivity to the different production processes. A total of about 300 categories for each experiment are combined and provide sensitivity to most of the production and decay channels. The other less important production processes, such as tH are selected by analyses addressing other similar modes that provide some sensitivity. An underlying assumption for all these analyses is that the Higgs boson is SM-like. The other important assumption

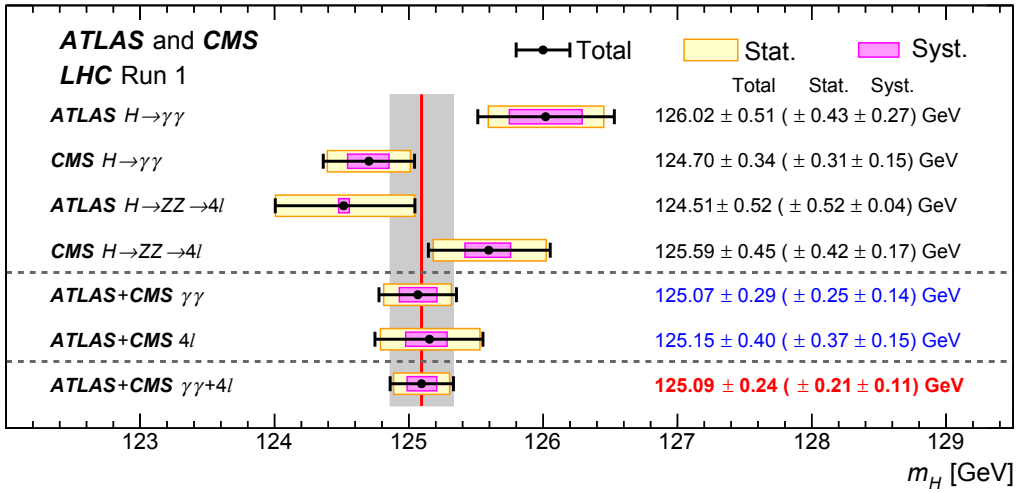

FIGURE 3. Summary of the individual and combined Higgs boson mass measurements [5].

is that the Higgs boson width, predicted to be approximately 4 MeV in the SM, is small such that the narrow width approximation holds and that production and decay can be factorized:

$$\sigma_i \cdot \mathrm{BR}^f = \frac{\sigma_i(\vec{\kappa}) \cdot \Gamma^f(\vec{\kappa})}{\Gamma_H}. \tag{1}$$

Results are rigorously valid only for small deviations from these assumptions. However larger deviations would also be detected by the different analyses. To date, all studies from ATLAS and CMS are consistent with these hypotheses [15].

The statistical method employed for the combination is a profile likelihood asymptotic method that is the the same used in all ATLAS and CMS Higgs-related publications and is described in [26]. For each value of the parameters of interest, all systematic uncertainties (nuisance parameters) are varied to maximize the likelihood function (profiled). The total number of nuisance parameters in the fits is approximately 4200, of which a large fraction is related to statistical uncertainties due to the finite size of the MC data samples. Most experimental uncertainties are assumed uncorrelated between the two experiments and many tests have been carried out to check the possible impact of neglected correlations, that was found negligible. For this combination all SM cross section values have been synchronized between the ATLAS and CMS analyses. The main correlated systematic uncertainties between ATLAS and CMS are the theory systematic uncertainties in cross sections and BRs.

Measurement of signal strengths

The signal strengths μ_i^f are defined as the ratios of cross sections and branching fractions to the corresponding SM predictions such that:

$$\mu_i^f = \frac{\sigma_i \cdot \mathrm{BR}^f}{(\sigma_i)_{\mathrm{SM}} \cdot (\mathrm{BR}^f)_{\mathrm{SM}}} = \mu_i \times \mu^f, \tag{2}$$

where the subscript i and superscript f indicate the production mode and decay channel, respectively. By definition all μ_i^f are equal to 1 for the SM Higgs boson.

The most constrained possible parameterisation is obtained introducing a global signal strength μ that corresponds to a single multiplier that scales all cross section times BR products. A combined fit for the global μ, also assuming that its value is the same at 7 and 8 TeV CM energies, gives:

$$\mu = 1.09^{+0.11}_{-0.10} = 1.09^{+0.07}_{-0.07}\ (\mathrm{stat})\ ^{+0.04}_{-0.04}\ (\mathrm{expt})\ ^{+0.03}_{-0.03}\ (\mathrm{thbgd})^{+0.07}_{-0.06}\ (\mathrm{thsig}).$$

The expected and observed combined measurement as well as the results from the individual experiments are reported in Table 1 with the uncertainty decomposed into four components: statistical, theoretical (signal and background),

TABLE 1. Combined observed and expected global signal strengths μ and observed individual ATLAS and CMS measurements. The uncertainties are decomposed into four independent components. These results are derived assuming that the ratios between the different Higgs boson production cross sections and different branching fractions are the same as in the SM.

	Best-fit μ	Uncertainty				
		Total	Stat	Expt	Thbgd	Thsig
ATLAS and CMS (meas.)	1.09	$^{+0.11}_{-0.10}$	$^{+0.07}_{-0.07}$	$^{+0.04}_{-0.04}$	$^{+0.03}_{-0.03}$	$^{+0.07}_{-0.06}$
ATLAS and CMS (exp.)	–	$^{+0.11}_{-0.10}$	$^{+0.07}_{-0.07}$	$^{+0.04}_{-0.04}$	$^{+0.03}_{-0.03}$	$^{+0.06}_{-0.06}$
ATLAS (meas.)	1.20	$^{+0.15}_{-0.14}$	$^{+0.10}_{-0.10}$	$^{+0.06}_{-0.06}$	$^{+0.04}_{-0.04}$	$^{+0.08}_{-0.07}$
CMS (meas.)	0.98	$^{+0.14}_{-0.13}$	$^{+0.10}_{-0.09}$	$^{+0.06}_{-0.05}$	$^{+0.04}_{-0.04}$	$^{+0.08}_{-0.07}$

and other experimental. For the combined measurement all components are comparable and it becomes apparent how future improvements of this measurement need contributions both from the experimental and theoretical side. The signal theory uncertainty due to QCD scale variations and PDF are currently as large as the statistical uncertainty. Currently theory uncertainties are being considerably reduced from the theory side [27]. On the other hand, this is the most constrained and precise measurement related to the Higgs couplings and all other measurement that will be shown are still dominated by statistical uncertainties.

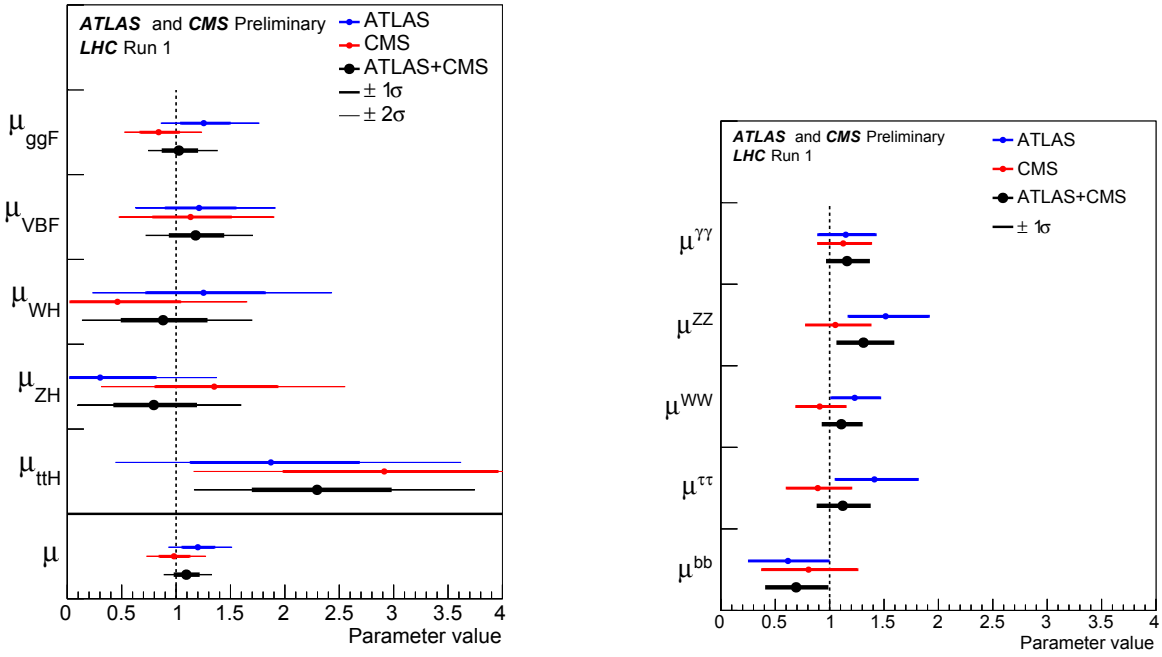

FIGURE 4. Left: results for the production signal strengths for ATLAS, CMS and their combination. The error bars indicate the 1σ (thick lines) and 2σ (thin lines) confidence intervals. The measurements of the global signal strength μ are also shown [25]. Right: corresponding results for the decay signal strengths [25].

Production modes and decay BRs can be tested in the μ-framework by alternatively constraining decays and production rates to the SM. Figure 4 shows the corresponding results for the five production modes and five decay channels. Also, the global μ is reported for reference and the SM prediction at $\mu = 1$ is shown. The measurement that shows the largest deviation from the SM, a 2.3σ excess, is ttH where the excess mainly comes from the multi-lepton analysis and more specifically from the CMS same-sign $\mu\mu$X category. The overall probability for the different mea-

surements of the production signal strengths to be compatible with the SM is 25% and does not show any significant deviation from the theory predictions. From the same likelihood scans evaluated at $\mu = 0$, it is also possible to derive

TABLE 2. Measured and expected significances for the observation of Higgs boson production processes and decay channels from the combination of ATLAS and CMS. All results are obtained alternatively constraining the decays or the production to their SM values.

Production process	Measured significance (σ)	Expected significance (σ)
VBF	5.4	4.7
WH	2.4	2.7
ZH	2.3	2.9
VH	3.5	4.2
ttH	4.4	2.0
Decay channel		
$H \to \tau\tau$	5.5	5.0
$H \to bb$	2.6	3.7

the significance of the observation of the different production and decay processes. This is shown for those that have not yet been unambiguously established by the individual experiments in Table 2. Thanks to the large increase in sensitivity achieved through the combination, the VBF process and the $H \to \tau\tau$ decay are now also established with a significance larger than 5σ, and VH with a significance larger than 3σ. Also ttH is detected with a significance of 4.4σ (2.0σ expected) while for $H \to bb$ the observed significance does not yet reach 3σ.

An additional test is performed from a combined fit using as free parameters, for each decay channel f, different signal strengths for the production processes sensitive to Higgs boson couplings to fermions (ggF and ttH) and to vector bosons (VBF and VH), indicated with $\mu_F^f = \mu_{ggF+ttH}^f$ and $\mu_V^f = \mu_{VBF+VH}^f$, respectively. Figure 5 shows the 2D confidence level (CL) regions of a 10-parameter fit of the fermion and boson signal strength for each of the five main decay channels. For all of them the SM prediction lies within the 1σ region. Given that the decay BRs cancel for each pair μ_F^f, μ_V^f, it is also possible to perform a fit for the ratio μ_V/μ_F, profiling the individual fermion related signal strengths μ_F^f. It gives $\mu_V/\mu_F = 1.06^{+0.35}_{-0.27}$ that also agrees with the SM predictions.

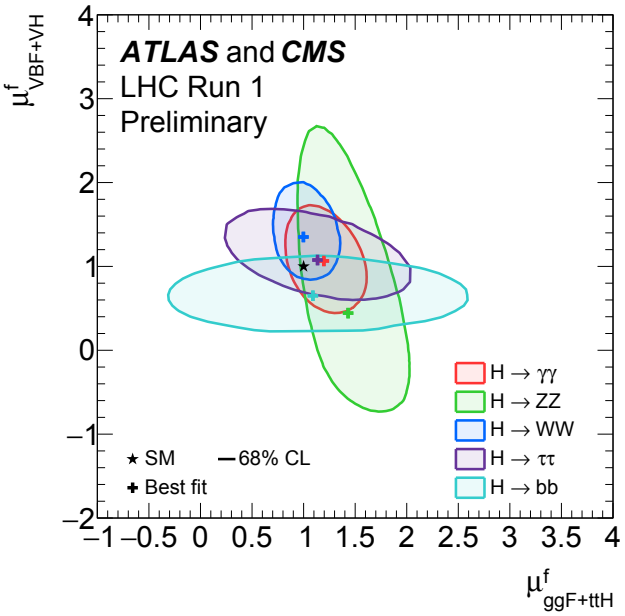

FIGURE 5. Likelihood contours in the $(\mu_{ggF+ttH}^f, \mu_{VBF+VH}^f)$ plane for the combination of ATLAS and CMS for the five main decay channels. The 68% CL regions, and the best-fit values are shown [25].

Coupling modifiers and κ-framework

The so-called κ-framework has been developed within the LHC Higgs cross section working group [24]. Within that framework he Higgs boson couplings are scaled by coupling modifiers $\vec{\kappa}$ such that:

$$\kappa_j^2 = \sigma_j/\sigma_j^{\rm SM} \quad \text{or} \quad \kappa_j^2 = \Gamma^j/\Gamma^j_{\rm SM}, \tag{3}$$

when the cross section times BR of a given channel is indicated as:

$$\sigma_i \cdot {\rm BR}^f = \frac{\sigma_i(\vec{\kappa}) \cdot \Gamma^f(\vec{\kappa})}{\Gamma_H}, \tag{4}$$

where Γ_H is the total width of the Higgs boson and Γ^f is the partial width of the Higgs boson decay to the final state f.

The Higgs boson width is parameterised as: $\kappa_H^2 = \sum_j {\rm BR}^j_{\rm SM}\kappa_j^2$. The relation $\kappa_H^2 = \Gamma_H/\Gamma_H^{\rm SM}$ is valid if only SM decays are possible, though their BRs may differ from the SM predictions, and the assumptions on the non-measured ones indicated below are valid). If BSM decays are allowed it becomes:

$$\Gamma_H = \frac{\kappa_H^2 \cdot \Gamma_H^{\rm SM}}{1 - {\rm BR}_{\rm BSM}}, \tag{5}$$

where ${\rm BR}_{\rm BSM}$ represents the total branching fraction into BSM decays that includes both decays that are not allowed in the SM and modifications of the SM decays that are not directly probed in the searches, such as for example decays into cc and into gg.

From these definitions and taking into account the latest calculations, it is possible to parameterise all cross sections and partial widths as function of $\vec{\kappa}$ as indicated in Table 3. The couplings modifiers that cannot be constrained with sufficient sensitivity by the current analyses are assumed to be the same as similar ones, for example $\kappa_c = \kappa_t$, $\kappa_s = \kappa_b$, and so on. Each of the coupling modifiers $\vec{\kappa}$ is 1 in the SM and deviations from this value could be caused by various BSM effects.

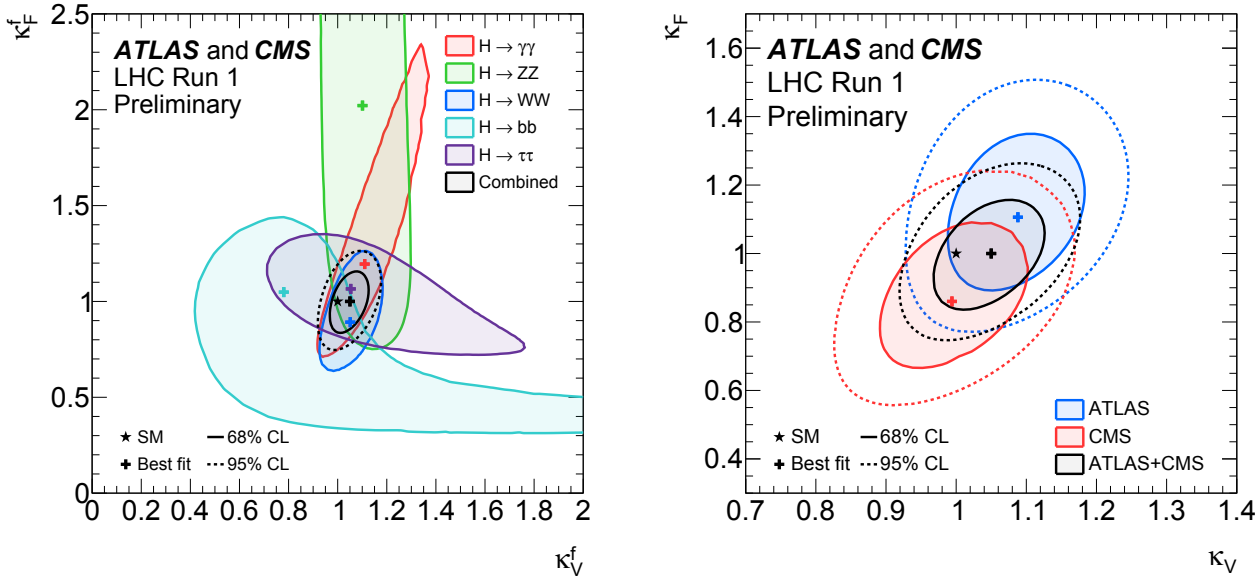

FIGURE 6. Left: negative log-likelihood contours of κ_F^f versus κ_V^f for the combination of ATLAS and CMS and for the individual decay channels as well as for their global combination (κ_F versus κ_V shown in black), assuming that all coupling modifiers are positive [25]; right: negative log-likelihood contours of κ_F versus κ_V for ATLAS, CMS and their combination [25].

Two scenarios are considered: one when loops are resolved in terms of the loop content structure predicted in the SM, the other when the gluon fusion and the photon decay loops are described by the effective couplings κ_g and κ_γ.

TABLE 3. Higgs boson production cross sections σ_i, partial decay widths Γ^f and total decay width (assuming no BSM decays) parameterised as a function of the $\vec{\kappa}$ coupling modifiers. The approximate numerical values are given for $\sqrt{s} = 8$ TeV and $m_H = 125.09$ GeV. The ggF and $H \to \gamma\gamma$ decay loops can also be parameterised with effective couplings κ_g and κ_γ.

Production	Loops	Interference	Multiplicative factor	
$\sigma(gg\text{F})$	✓	$b-t$	$\kappa_g^2 \sim$	$1.06 \cdot \kappa_t^2 + 0.01 \cdot \kappa_b^2 - 0.07 \cdot \kappa_t\kappa_b$
$\sigma(V\text{BF})$	–	–	$\sim$	$0.74 \cdot \kappa_W^2 + 0.26 \cdot \kappa_Z^2$
$\sigma(WH)$	–	–	$\sim$	κ_W^2
$\sigma(qq/qg \to ZH)$	–	–	$\sim$	κ_Z^2
$\sigma(gg \to ZH)$	✓	$Z-t$	$\sim$	$2.27 \cdot \kappa_Z^2 + 0.37 \cdot \kappa_t^2 - 1.64 \cdot \kappa_Z\kappa_t$
$\sigma(ttH)$	–	–	$\sim$	κ_t^2
$\sigma(gb \to WtH)$	–	$W-t$	$\sim$	$1.84 \cdot \kappa_t^2 + 1.57 \cdot \kappa_W^2 - 2.41 \cdot \kappa_t\kappa_W$
$\sigma(qb \to tHq)$	–	$W-t$	$\sim$	$3.4 \cdot \kappa_t^2 + 3.56 \cdot \kappa_W^2 - 5.96 \cdot \kappa_t\kappa_W$
$\sigma(bbH)$	–	–	$\sim$	κ_b^2
Partial decay width				
Γ^{ZZ}	–	–	$\sim$	κ_Z^2
Γ^{WW}	–	–	$\sim$	κ_W^2
$\Gamma^{\gamma\gamma}$	✓	$W-t$	$\kappa_\gamma^2 \sim$	$1.59 \cdot \kappa_W^2 + 0.07 \cdot \kappa_t^2 - 0.66 \cdot \kappa_W\kappa_t$
$\Gamma^{\tau\tau}$	–	–	$\sim$	κ_τ^2
Γ^{bb}	–	–	$\sim$	κ_b^2
$\Gamma^{\mu\mu}$	–	–	$\sim$	κ_μ^2
Total width for $\text{BR}_{\text{BSM}} = 0$				
Γ_H	✓	–	$\kappa_H^2 \sim$	$0.57 \cdot \kappa_b^2 + 0.22 \cdot \kappa_W^2 + 0.09 \cdot \kappa_g^2 +$ $+ 0.06 \cdot \kappa_t^2 + 0.03 \cdot \kappa_Z^2 + 0.03 \cdot \kappa_c^2 +$ $+ 0.0023 \cdot \kappa_\gamma^2 + 0.0016 \cdot \kappa_{(Z\gamma)}^2 +$ $+ 0.0001 \cdot \kappa_s^2 + 0.00022 \cdot \kappa_\mu^2$

Possible deviations from the SM could appear in two different ways: if new physics manifests itself with the presence of particles with mass smaller than $m_H/2$, additional decays could be present and BR_{BSM} would be affected; if instead new physics introduces particles with higher masses, the loop structure would be modified and the effective couplings would be affected. The parameterisations considered in the following address both these scenarios.

The most constrained k-parameterisation consists in assuming the same coupling modifiers for all Higgs boson couplings to vector bosons and to fermions, indicated with κ_V and κ_F respectively. A complementary fit, that disentangles the contribution of the different decay channels, is performed using different κ_V^f and κ_F^f for each of the five final states and carrying out a 10-parameter fit. The results in terms of 2D 68% confidence level regions are shown in Figure 7 and they are consistent with the SM prediction $\kappa_V^f = \kappa_F^f = \kappa_V = \kappa_F = 1$.

The above fit is performed assuming that all coupling modifiers are positive. If this assumption is relaxed, given that all cross sections and BRs only depend on the sign of the ratio of κ_F and κ_V, the phase space can be limited, without any loss of generality to the positive values of κ_V. The result is shown in Figure 7. Some of the channels provide some minor sensitivity to the sign of the coupling ratio through sub-dominant loop production processes (mainly tH and $gg \to ZH$) for which the negative relative couplings change the sign of the interference effect. Nevertheless the main sensitivity comes from the difference in the prediction for positive and negative κ_V/κ_F in the $H \to \gamma\gamma$ channel, due to the large interference between the top quark and W loops. From the fit of all channels and assuming global κ_V and κ_F, a negative κ_V/κ_F ratio is excluded almost at the 5σ level.

The next parameterisation studied in order of complexity is one that assumes that all loops are resolved in terms of the SM vertices and that there are no BSM decays. In this case also $H \to \mu\mu$ analyses are included and six coupling modifiers (κ_W, κ_Z, κ_t, κ_b, κ_τ, and κ_μ) are assumed to be positive and are simultaneously determined from a fit to the

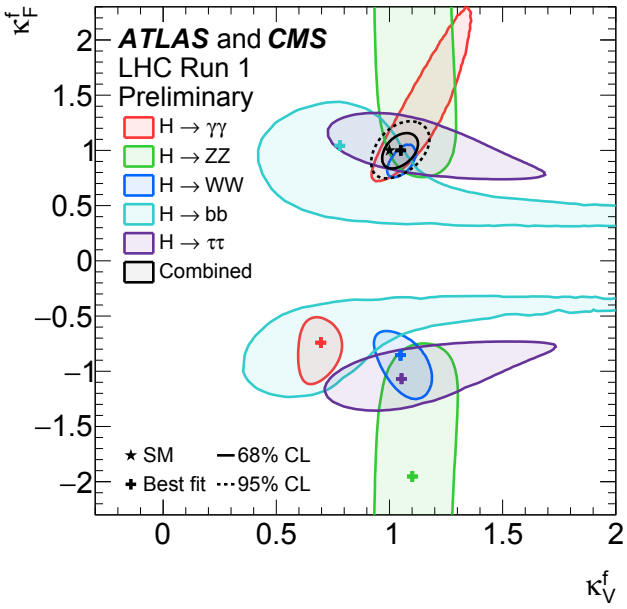

FIGURE 7. Negative log-likelihood contours of κ_F^f versus κ_V^f for the combination of ATLAS and CMS and for the individual decay channels, as well as for their global combination (κ_F versus κ_V shown in black), without any assumptions on the relative sign of the coupling modifiers [25].

data. The results are shown in Figure 8 left. The same results are shown in Figure 8 right in terms of the reduced couplings modifiers

$$\sqrt{\kappa_{V,i}\frac{g_{V,i}}{2v}} = \sqrt{\kappa_{V,i}}\frac{m_{V,i}}{v}, \tag{6}$$

for the vector bosons, and

$$\kappa_{F,i}\frac{y_{F,i}}{\sqrt{2}} = \kappa_{F,i}\frac{m_{F,i}}{v}, \tag{7}$$

for the fermions. Here g and y are the absolute gauge and Yukawa coupling strengths, respectively, v is the vacuum expectation value of the Higgs field, the subscripts V and F indicate vector bosons and fermions, and the subscript i refers to the different particles coupling to the Higgs boson. The reduced coupling modifiers scale linearly with the particle masses as expected for the SM Higgs boson and provide a pictorial qualitative indication of the consistency of the results with the SM prediction that is indicated by the diagonal line.

To test the possible presence of additional particles running in the loops, the assumption that the structure of the two main loops entering the analysis, gluon fusion and $H \to \gamma\gamma$ loop is described by the SM is relaxed and effective couplings are introduced. In this case, as only $\sigma\times$BR can be measured, it is not possible to derive constraints on the total Higgs boson width Γ_H. Two fits are performed: one not allowing additional BSM decays, with BSM physics only contributing to the loops, and the other imposing the constraint $\kappa_Z,\ \kappa_W \leq 1$. The latter relation is implied in many BSM models and is able to provide an upper limit to the total width and, consequently, to the partial width of BSM decays, described by the branching fraction into BSM particles, invisible or undetected, and modifications of the standard decays that are not directly tested in the analysis such as into cc, gg and $\mu\mu$ for example. The results of the two fits for all the coupling modifiers are shown in Figure 9 left while Figure 9 right shows the likelihood scan of the parameter $\mathrm{BR}_{\mathrm{BSM}}$ that gives a 95% CL upper limit $\mathrm{BR}_{\mathrm{BSM}} < 0.34$. From these results constraints on various BSM models can be derived. The limits on the BSM partial width can be re-interpreted as limits on the total width that can be compared with those obtained by ATLAS and CMS in different ways [28, 29].

Assuming that BSM physics only enters through the loops, as for example if additional heavy fermions were present, all other coupling modifiers are constrained to their SM predictions. The results of a fit for the two effective coupling modifiers κ_g and κ_γ is shown in Figure 10 and again shows no deviations from the SM.

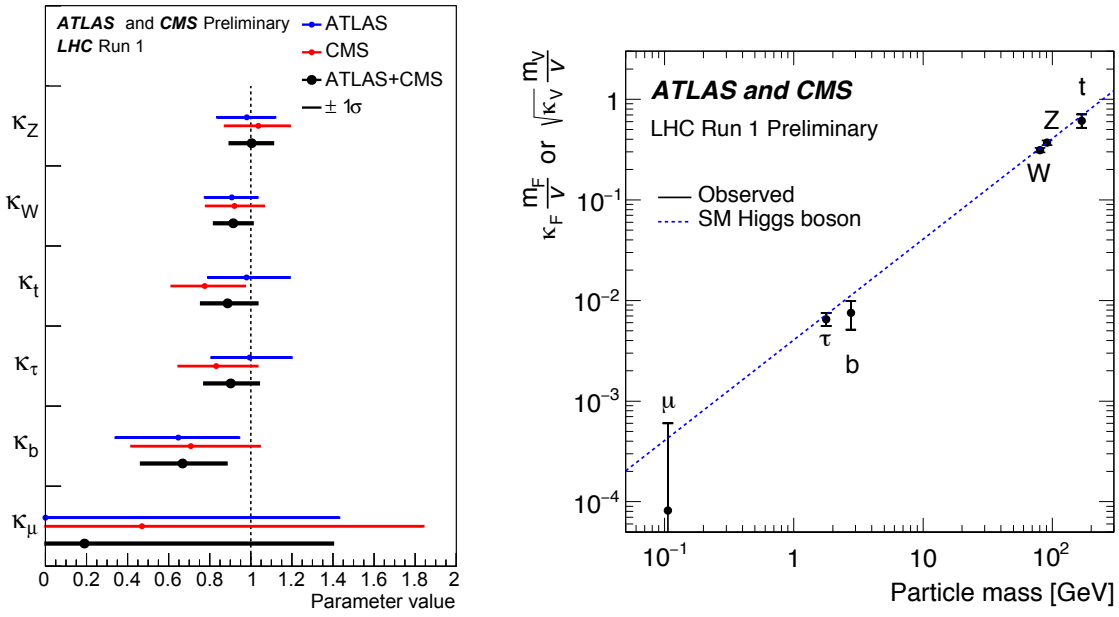

FIGURE 8. Left: best-fit values of parameters for the combination of ATLAS and CMS and separately for each experiment, for the parameterisation with all loops resolved, $\mathrm{BR}_{\mathrm{BSM}} = 0$, and $\kappa_j \geq 0$ [25]; right: fit results for the combination of ATLAS and CMS in terms of reduced coupling modifiers $\sqrt{\kappa_{V,i}\frac{g_{V,i}}{2v}} = \sqrt{\kappa_{V,i}}\frac{m_{V,i}}{v}$ for the weak vector bosons, and $\kappa_{F,i}\frac{y_{F,i}}{\sqrt{2}} = \kappa_{F,i}\frac{m_{F,i}}{v}$ for the fermions, as a function of the particle mass. The dashed line indicates the SM prediction [25].

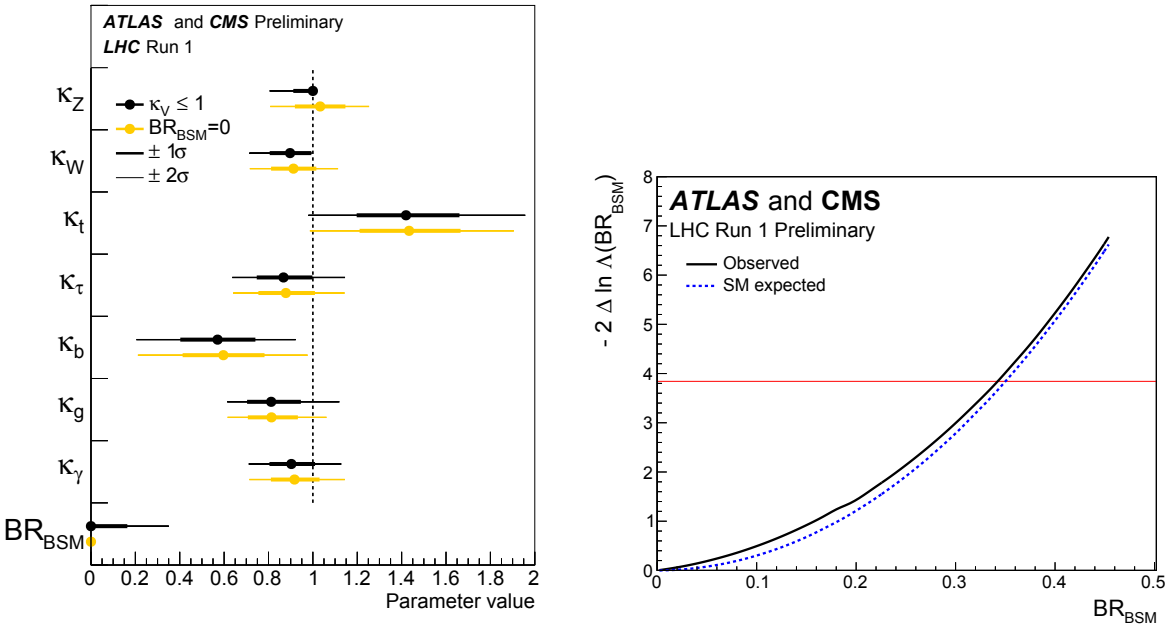

FIGURE 9. Left: fit results for the two parameterisations allowing BSM loop couplings, with $\kappa_V \leq 1$, or without additional BSM contributions to the Higgs boson width, i.e. $\mathrm{BR}_{\mathrm{BSM}} = 0$. The error bars indicate the 1σ (thick lines) and 2σ (thin lines) CL intervals [25]. Right: Observed and expected negative log-likelihood scan of $\mathrm{BR}_{\mathrm{BSM}}$, shown for the combination of ATLAS and CMS for the parameterisation with the constraint $\kappa_V \leq 1$ [25].

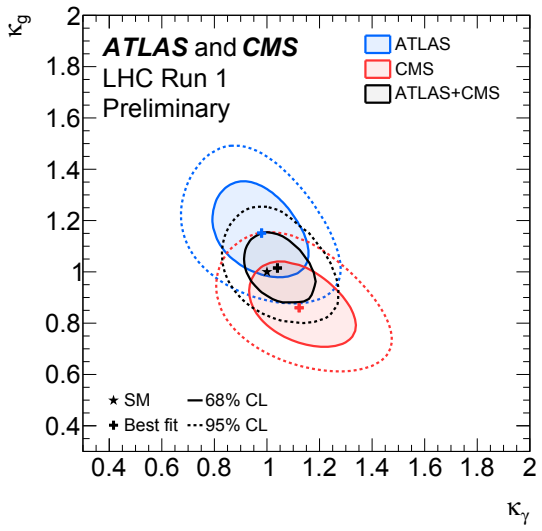

FIGURE 10. Combined and individual negative log-likelihood contours at 68% and 95% CL of κ_γ versus κ_g for the parameterisation constraining all the other coupling modifiers to their SM values and assuming $\mathrm{BR}_{\mathrm{BSM}} = 0$ [25].

TABLE 4. Summary of the results of the two parameterisations probing the ratios of coupling modifiers for up-type versus down-type fermions and for leptons versus quarks. Combined observed and expected confidence intervals are indicated at 68% CL.

Parameter	ATLAS+CMS	
	Measured	Expected uncertainty
λ_{du}	$0.91^{+0.12}_{-0.11}$	$[-1.21, -0.92] \cup [0.87, 1.14]$
λ_{Vu}	$0.99^{+0.13}_{-0.12}$	$^{+0.20}_{-0.12}$
κ_{uu}	$1.09^{+0.22}_{-0.19}$	$^{+0.20}_{-0.27}$
$\lvert\lambda_{lq}\rvert$	$1.06^{+0.15}_{-0.14}$	$^{+0.16}_{-0.14}$
λ_{Vq}	$1.09^{+0.14}_{-0.13}$	$^{+0.13}_{-0.11}$
κ_{qq}	$0.94^{+0.17}_{-0.15}$	$^{+0.18}_{-0.16}$

In the fermion sector the symmetry between up and down fermions and between quarks and leptons, that could deviate from the SM for example in two Higgs doublet models, is tested by allowing to vary: $\lambda_{du} = \kappa_d/\kappa_u$ and $\lambda_{lq} = \kappa_l/\kappa_q$ for the two different tests and also $\lambda_{Vu} = \kappa_V/\kappa_u$ and $\kappa_{uu} = \kappa_u \cdot \kappa_u/\kappa_H$ in both of them. The relation $\kappa_W = \kappa_Z = \kappa_V$ is assumed in this test and the total width is allowed to vary. The results are reported in Table 4 and are once again all consistent with the SM.

Generic parameterisations based on ratios

In all measurements of rates it is not possible to disentangle between production cross sections and decay branching fractions without additional assumptions. However it is possible to perform a measurement of ratios of production cross sections and of branching fractions. All these ratios are normalized to a single cross section times BR product that can is chosen to be $\sigma(gg \to H \to ZZ)$. The production times decay $i \to H \to f$ can be expressed using ratios as:

$$\sigma_i \cdot \mathrm{BR}^f = \sigma(gg \to H \to ZZ) \times \left(\frac{\sigma_i}{\sigma_{gg\mathrm{F}}}\right) \times \left(\frac{\mathrm{BR}^f}{\mathrm{BR}^{ZZ}}\right). \quad (8)$$

TABLE 5. Parameters of interest in the two generic parameterisations of ratios of cross sections and branching fractions, and of ratios of coupling modifiers. For both parameterisations, the $gg \to H \to ZZ$ channel, indicated in the first row, is chosen as the reference. There are two more parameters of interest in the case of the first parameterisation, because the three independent ratios of production cross sections $\sigma_{VBF}/\sigma_{ggF}$, σ_{WH}/σ_{ggF}, and σ_{ZH}/σ_{ggF}, and the ratio of branching fractions, BR^{WW}/BR^{ZZ}, can all be expressed as functions of two parameters, λ_{WZ} and λ_{Zg}, in the coupling parameterisation.

σ and BR ratio model	Coupling-strength ratio model
$\sigma(gg \to H \to ZZ)$	$\kappa_{gZ} = \kappa_g \cdot \kappa_Z/\kappa_H$
$\sigma_{VBF}/\sigma_{ggF}$	
σ_{WH}/σ_{ggF}	
σ_{ZH}/σ_{ggF}	$\lambda_{Zg} = \kappa_Z/\kappa_g$
$\sigma_{ttH}/\sigma_{ggF}$	$\lambda_{tg} = \kappa_t/\kappa_g$
BR^{WW}/BR^{ZZ}	$\lambda_{WZ} = \kappa_W/\kappa_Z$
$BR^{\gamma\gamma}/BR^{ZZ}$	$\lambda_{\gamma Z} = \kappa_{\gamma g}/\kappa_Z$
$BR^{\tau\tau}/BR^{ZZ}$	$\lambda_{tZ} = \kappa_\tau/\kappa_Z$
BR^{bb}/BR^{ZZ}	$\lambda_{bZ} = \kappa_b/\kappa_Z$

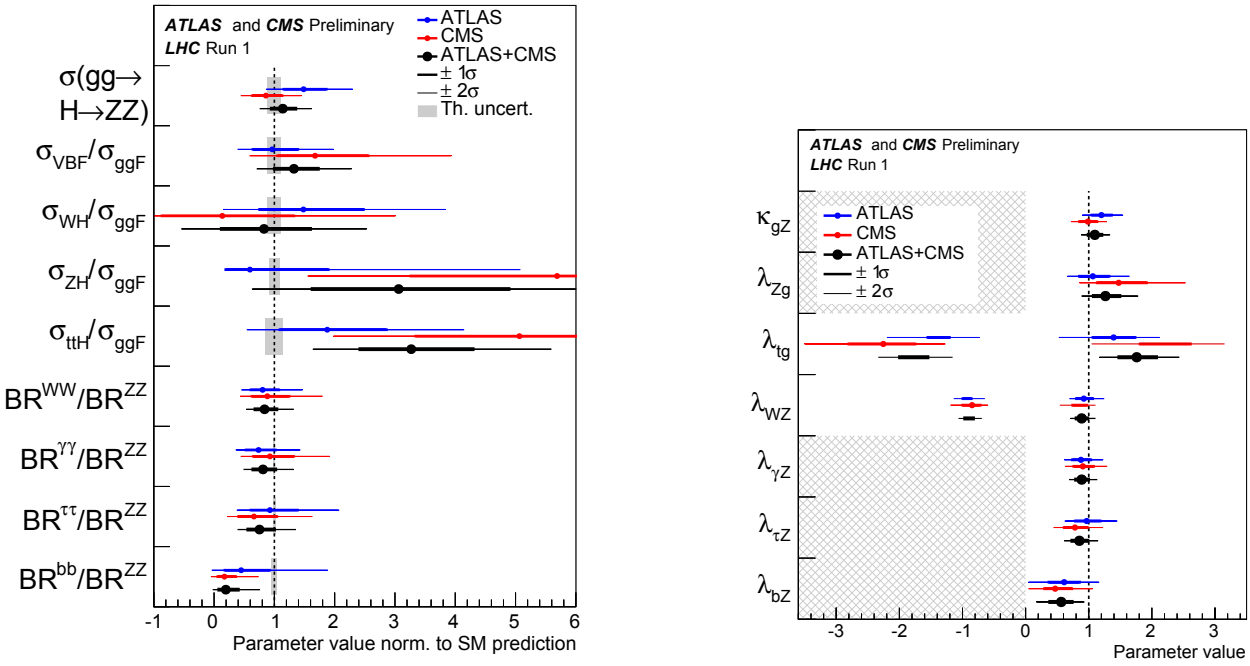

FIGURE 11. Left: best-fit values of the $\sigma(gg \to H \to ZZ)$ cross section and of ratios of cross sections and branching fractions for the combination of ATLAS and CMS measurements as well as for the individual ATLAS and CMS experiments. All results are normalized to the SM predictions whose uncertainties are indicated by the shaded bands [25]. Right: results of the ratios of Higgs boson coupling modifiers, as obtained from the generic parameterisation described in the text for the combination of ATLAS and CMS measurements as well as for the individual ATLAS and CMS experiments. Also shown for completeness are the results for each experiment. The hatched areas indicate the parameters which are assumed to be positive without loss of generality [25].

The parameters of interest in this parameterisation are: the reference, chosen to be $\sigma(gg \to H \to ZZ)$, the four ratios of cross sections σ_i/σ_{ggF}, and four ratios of branching fractions $BR^f BR^{ZZ}$, for a total of 9 independent parameters. All parameters are indicated in the first column of Table 5. This approach has the advantage that the main

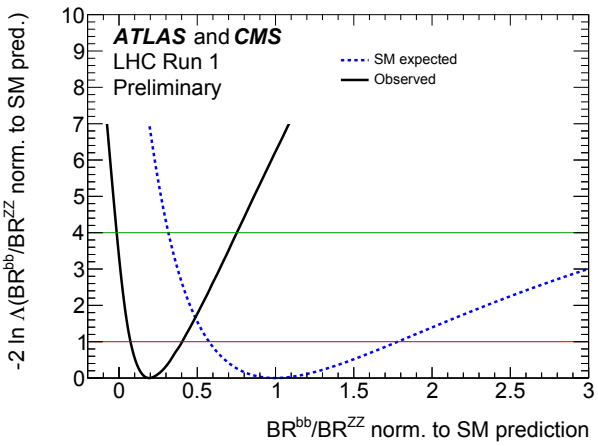

FIGURE 12. Observed (solid line) and expected (dashed line) negative log-likelihood scan of the $\mathrm{BR}^{bb}/\mathrm{BR}^{ZZ}$ parameter. The two horizontal lines at value of 1 and 4 indicate the value of the profile likelihood ratio corresponding to a 1σ and 2σ confidence interval respectively [25].

theory signal uncertainties, namely those in the inclusive production cross sections, do not enter in the measurements, and also that the results do not change if the corresponding theory predictions are updated. The results are shown in Figure 11 left. The overall probability for the different measurements to be compatible with the SM hypothesis is 16% and the largest discrepancies arise from the measurements of $\sigma_{ttH}/\sigma_{ggF}$ and $\mathrm{BR}^{bb}/\mathrm{BR}^{ZZ}$. The former is driven by the excess in ttH discussed in the context of the μ-framework. The latter comes from the measurement $\mathrm{BR}^{bb}/\mathrm{BR}^{ZZ} = 0.19^{+0.21}_{-0.12}$ that is on the low side mainly because of the low measured values of the ZH and ttH cross sections, coupled with a relatively low yield measured in the VH, $H \to bb$ channel. On the other hand, the discrepancy is 2.5σ, smaller than it could appear from the uncertainties of the measurement, because the likelihood scan presents a highly asymmetric behaviour as shown in Fig. 12.

The parameterisation in terms of ratios of coupling modifiers differs from the one based on cross sections and branching fractions mainly because the three independent ratios of production cross sections $\sigma_{VBF}/\sigma_{ggF}$, σ_{WH}/σ_{ggF}, and σ_{ZH}/σ_{ggF}, and the ratio of branching fractions, $\mathrm{BR}^{WW}/\mathrm{BR}^{ZZ}$, only depend on the two parameters λ_{WZ} and λ_{Zg}, and therefore this parameterisation has two parameters less than the other. The seven independent parameters are indicated in the second column of Table 5. The results of this parameterisation are reported in Figure 11 right. Again the largest discrepancies from the SM, still at a level of approximately 2σ, are observed on the parameters λ_{tg} and λ_{bZ}, related to the large ttH measured cross section and small measured $H \to bb$ branching fraction, respectively.

CONCLUSIONS

ATLAS and CMS Higgs boson results on the mass and the couplings have been combined and the sensitivity improves by almost a factor $\sqrt{2}$, corresponding to doubling the integrated luminosity by adding the data collected by the two experiments. ATLAS and CMS Higgs boson analyses have been combined to precisely measure the Higgs boson mass. The result is $m_H = 125.09 \pm 0.24$ GeV. Combined measurements of the Higgs boson production and decay rates, and constraints on its couplings to other particles have been obtained. The results are based on the proton-proton collision data collected at the LHC with the ATLAS and CMS detectors in 2011 and 2012, corresponding to integrated luminosities per experiment of approximately 5 fb^{-1} at $\sqrt{s} = 7$ TeV and 20 fb^{-1} at $\sqrt{s} = 8$ TeV. The combined signal yield relative to the SM prediction is 1.09 ± 0.11. Many other measurements have been carried out in more or less constrained assumptions and all measurement are consistent with the standard model. The increased sensitivity coming from the combination of the two experiments allows to obtain a significance of 5.4σ for the VBF production process and of 5.5σ for Higgs boson decays into τ-lepton pairs. LHC Run-2 has started at 13 TeV and the precision of all these measurements will be improved during the coming years thanks to higher energy, larger integrated luminosity and progress in the theory predictions.

REFERENCES

[1] ATLAS Collaboration, Phys. Lett. B **716** (2012) 1, arXiv:1207.7214 [hep-ex].
[2] CMS Collaboration, Phys. Lett. B **716** (2012) 30, arXiv:1207.7235 [hep-ex].
[3] ATLAS Collaboration, JINST **3** (2008) S08003.
[4] CMS Collaboration, JINST **3** (2008) S08004.
[5] ATLAS and CMS Collaborations, Phys. Rev. Lett. **114** (2015) 191803, arXiv:1503.07589 [hep-ex].
[6] ATLAS Collaboration, arXiv:1507.04548 [hep-ex], submitted for publication in *Eur. Phys. J. C*.
[7] CMS Collaboration, Eur. Phys. J. C **75** (2015) 212, arXiv:1412.8662 [hep-ex].
[8] CMS Collaboration, Phys. Rev. Lett. **110** no. 8, (2013) 081803, arXiv:1212.6639 [hep-ex].
[9] ATLAS Collaboration, Phys. Lett. B **726** (2013) 120, arXiv:1307.1432 [hep-ex].
[10] CMS Collaboration, Phys. Rev. D **92**, 012004 (2015), arXiv:1411.3441 [hep-ex].
[11] ATLAS Collaboration, JHEP **1409** (2014) 112, arXiv:1407.4222 [hep-ex].
[12] ATLAS Collaboration, Phys. Lett. B **738** (2014) 234, arXiv:1408.3226 [hep-ex].
[13] CMS Collaboration, arXiv:1508.07819 [hep-ex], submitted for publication in *Eur. Phys. J. C*.
[14] CMS Collaboration, CMS Physics Analysis Summary CMS-PAS-HIG-14-028, 2015.
[15] K. Tackmann, these proceedings.
[16] M. Venturi, these proceedings.
[17] F. Englert and R. Brout, Phys. Rev. Lett. **13** (1964) 321.
[18] P. W. Higgs, Phys. Lett. **12** (1964) 132.
[19] P. W. Higgs, Phys. Rev. Lett. **13** (1964) 508.
[20] G. S. Guralnik, C. R. Hagen, and T. W. B. Kibble, Phys. Rev. Lett. **13** (1964) 585.
[21] LHC Higgs Cross Section Working Group, https://twiki.cern.ch/twiki/bin/view/LHCPhysics/LHCHXSWG.
[22] S. Dittmaier et al., arXiv:1101.0593 [hep-ph].
[23] S. Dittmaier et al., arXiv:1201.3084 [hep-ph].
[24] S. Heinemeyer et al., arXiv:1307.1347 [hep-ph].
[25] ATLAS and CMS Collaborations, ATLAS-CONF-2015-044, CMS-PAS-HIG-15-002, 2015.
[26] ATLAS and CMS Collaborations, ATL-PHYS-PUB-2011-011, CERN-CMS-NOTE-2011-005 (2011).
[27] A. Vicini, these proceedings.
[28] ATLAS Collaboration, Eur. Phys. J. C **75** (2015) 335, arXiv:1503.01060 [hep-ex].
[29] CMS Collaboration, Phys. Lett. B **736** (2014) 64, arXiv:1405.3455 [hep-ex].

Proceedings of the LHCP2015 Conference, St. Petersburg, Russia, August 31 - September 5, 2015

Editors: V.T. Kim and D.E. Sosnov

Calculating Higgs boson properties in the Standard Model

KIRILL MELNIKOV

Institute for Theoretical Particle Physics, Karlsruhe Institute of Technology, Karlsruhe, Germany

kirill.melnikov@kit.edu

Abstract. In this talk, I describe the highlights of the recent theoretical work in precision Higgs physics, focusing on the Standard Model aspects.

INTRODUCTION

Discovery of the Higgs boson completed the construction of the Standard Model. For the first time in the history of particle physics, we have a theory that allows us to describe many, if not all, phenomena at particle colliders and elsewhere. The existence of this "complete" theory has important implications for the Higgs boson physics since the properties of the Higgs boson in the Standard Model are completely determined once its mass is measured. Indeed, in the Standard Model

- the Higgs boson is a spin-zero, neutral particle;
- its couplings to fermions are proportional to fermion masses;
- its couplings to massive gauge bosons are proportional to masses of gauge bosons squared;
- its self-coupling is proportional to the Higgs boson mass squared;
- its coupling to massless gauge bosons appears only at one loop and is proportional to the trace of the energy-momentum tensor of the corresponding gauge boson field.

This picture of the Higgs boson, c.f. Fig. 1, is consistent with available experimental data which strongly suggests that the Higgs boson is indeed the spin-zero, CP-even particle. This information is extracted by analyzing shapes of certain kinematic distributions of Higgs decay products, that are sensitive to the Higgs spin and CP-properties. We note that the shapes of the most sensitive distributions often follow from general principles, such as the angular momentum conservation, and are not affected by QCD effects. Verification of the Higgs couplings is a more complicated matter. Indeed, to extract couplings, we use theoretical predictions for cross sections and those predictions are affected by large radiative corrections. Currently, the Higgs couplings are known experimentally with the precision of about twenty percent. It is however, well-known that the radiative corrections increase the Higgs production cross section in gluon fusion by about a factor two. Hence, already with the current data and with the current level of precision, we are quite sensitive to radiative corrections. In the future the importance of accurate theory predictions for Higgs boson production cross sections and kinematic distributions will only increase as more and more data will become available.

To obtain those high-precision predictions for Higgs boson production at colliders, we use the general QCD factorization framework, extensively studied and verified at the Tevatron and the LHC. In this framework, the Higgs production cross sections are written as

$$\sigma_H = \int \mathrm{d}x_1 \mathrm{d}x_2 f_j(x_1) f_i(x_2) \sigma_{ij}(x_1, x_2) F_J \left(1 + O(\Lambda_{\rm QCD}/Q)\right). \qquad (1)$$

Therefore, description of any *hard* Higgs-related process requires parton distribution functions, partonic cross sections and well-defined infra-red- safe selection criteria F_J. The non-perturbative corrections shown in Eq.(1) are expected to be suppressed by powers of $\Lambda_{\rm QCD}$ over the hard scale although it is worth remembering that the theory of these power corrections does not exist. For realistic Higgs masses and sufficiently inclusive cuts, we should expect factorization

$J = 0$

Mass $m = 125.7 \pm 0.4$ GeV

H^0 Signal Strengths in Different Channels

Combined Final States $= 1.17 \pm 0.17$ (S = 1.2)
$WW^* = 0.87^{+0.24}_{-0.22}$
$ZZ^* = 1.11^{+0.34}_{-0.28}$ (S = 1.3)
$\gamma\gamma = 1.58^{+0.27}_{-0.23}$
$b\bar{b} = 1.1 \pm 0.5$
$\tau^+\tau^- = 0.4 \pm 0.6$
$Z\gamma < 9.5$, CL = 95%

FIGURE 1. Having officially made it to the Particle Data Group booklet, the Higgs boson is a recognized particle.

violations to be within a few percent although this statement will require further clarifications and studies. On the contrary, until very recently, the accuracy of theoretical predictions for partonic production cross sections was typically worse than ten percent; a similar error was associated with the imprecise knowledge of parton distribution functions. For this reason, the focus of theorists involved in Higgs phenomenology in recent years was on improving perturbative predictions for partonic cross sections and on making sure that uncertainties of parton distributions and other input parameters are under control.

Perturbative computation of partonic cross sections is an important and very active field of research. The level of sophistication that has been reached in connection with precise predictions for Higgs-related processes at the LHC is truly without a precedent. Indeed, all major Higgs production and decay channels are currently known through NLO QCD (many are known through NNLO QCD) and NLO electroweak. Many associated Higgs production channels with high jet multiplicity are also known at least through NLO QCD. Matching and merging of NLO QCD results with parton showers is available thanks to automated programs such as MC@NLO, Powheg, Sherpa and others. The available theoretical description of the Higgs boson production cross sections at the LHC is therefore of the highest quality.

Although NLO QCD and EW computations, as well as matching and merging, are very important topics, they are also relatively well-established by now and, as such, can be dealt with in a relatively straightforward way. For this reason, I will not discuss them. Instead, I want to present and discuss three recent results that, in my opinion, have a potential to significantly affect the way we think about precision Higgs physics at hadron colliders. These results include

1. the NNNLO QCD computation of the inclusive Higgs boson production cross section in gluon fusion [1];
2. the NNLO QCD computation of the fiducial cross section for the production of the Higgs boson and a jet at the LHC [2, 3];
3. the NNLO QCD calculation of the Higgs production cross section in weak boson fusion at the LHC [4].

These three results are important since they give us a new perspective on the ultimate precision achievable on the theory side in the exploration of Higgs boson physics at the LHC. Another important lesson that these results seem to teach us is that, beyond a certain level of precision, the fixed order computations are indispensable and can not be substituted by the results of the approximate methods, such as the resummations. In what follows, I will describe the three computations and the lessons we can learn from them, and then conclude.

INCLUSIVE HIGGS BOSON PRODUCTION IN GLUON FUSION

Gluon fusion is the dominant Higgs boson production mechanism at the LHC. The production rate is known to be affected by large $O(100\%)$ QCD corrections. These corrections have been recently calculated to an astounding three-loop order in the infinite top quark mass limit [1]. This is an extremely non-trivial computation whose success is

σ/pb	2 TeV	7 TeV	8 TeV	13 TeV	14 TeV
$\mu = \frac{m_H}{2}$	$0.99^{+0.43\%}_{-4.65\%}$	$15.31^{+0.31\%}_{-3.08\%}$	$19.47^{+0.32\%}_{-2.99\%}$	$44.31^{+0.31\%}_{-2.64\%}$	$49.87^{+0.32\%}_{-2.61\%}$
$\mu = m_H$	$0.94^{+4.87\%}_{-7.35\%}$	$14.84^{+3.18\%}_{-5.27\%}$	$18.90^{+3.08\%}_{-5.02\%}$	$43.14^{+2.71\%}_{-4.45\%}$	$48.57^{+2.68\%}_{-4.24\%}$

FIGURE 2. Results for the NNNLO Higgs production cross section in gluon fusion, from Ref.[1].

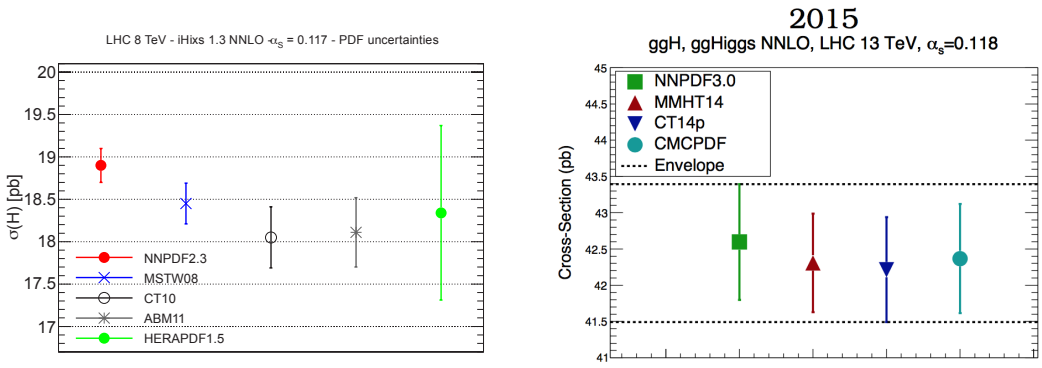

FIGURE 3. The recent evolution of predictions for Higgs boson production cross section caused by changes in parton distribution functions.

determined by the ingenuity of its authors, powerful computational technologies that appeared in recent years and capabilities of the modern hardware.

There are many interesting points about this calculation but I would like to emphasize just a few. First, the perturbative series apparently *do converge*. This sounds like a trivial matter but it is no small feat as the corrections start at almost 100% at NLO, are still $O(20\%)$ at NNLO but decrease to just $O(4\%)$ at NNNLO; all quoted numbers refer to a situation where the factorization and renormalization scales are set to the mass of the Higgs boson. As the consequence of the three-loop calculation, the residual scale uncertainty, defined in a conventional way by changing the scale by a factor two around the central value, is at the level of just three percent.

Having reached this level of perturbative precision, it is interesting to ask if we can claim now that it is possible, at least on the theory side, to imagine measuring the Higgs boson couplings at hadron colliders to similar perturbative accuracy. The answer to this question is negative, since at this level of precision, many other effects become relevant and need to be re-considered. They include uncertainties of parton distribution functions, effects of top and bottom masses, electroweak corrections and non-perturbative effects. However, there is no doubt that the very existence of the NNNLO computation will provide enough motivation to further improve our understanding of these effects in the near future.

As an example, I will briefly discuss the issue of parton distribution functions. The question that I would like to address is whether or not our knowledge of parton distribution functions is sufficient for studying the Higgs boson production cross section in gluon fusion with a few percent precision. There are two points that I want to make in this respect. First, it is useful to access the quality of our knowledge of parton distribution functions by comparing parton distribution functions determined by different groups. If we do so, we recognize that the situation is very dynamical; in fact the agreement between different groups on gluon luminosities for producing a 125 GeV particle at 13 TeV collider has improved compared to the situation that existed until very recently. Although the current situation (right plot) indicates a variation of less than a per cent and for this reason is much better than it was in the summer (left plot), there is no guarantee that a "stable equilibrium" is reached. In fact, as the gluon luminosities for 125 GeV become closer, some unexpected differences in other luminosities are known to appear for larger invariant masses.

The second point is the following. Strictly speaking, the NNNLO QCD calculation requires NNNLO PDFs which are not (and probably will never be) available. There is an argument [5] that for a Higgs boson with the mass of 125 GeV produced at the 8 TeV LHC one does not need NNNLO PDFs. The argument is based on an observation that the dependence on the "perturbative order" of the PDFs at this "point" is weak. On the other hand, for objects

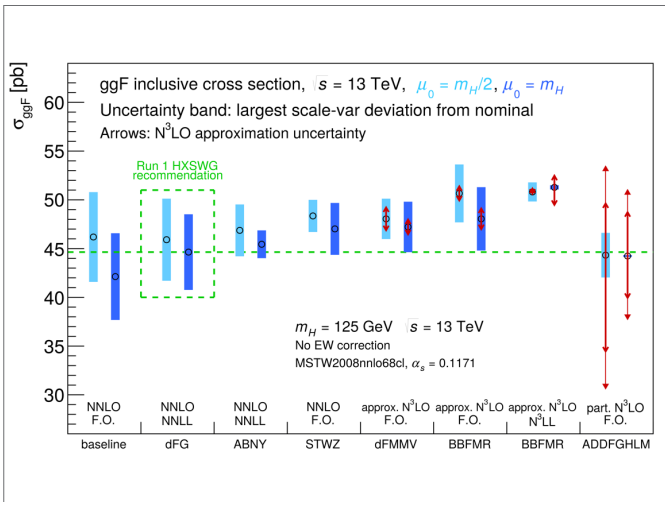

FIGURE 4. A comparison of exact and approximate NNNLO QCD predictions for Higgs boson production in gluon fusion. Source: the Higgs cross section working group.

with larger invariant masses – for example for top quark pairs -the dependence on the "perturbative order" is stronger and *cannot be neglected* [5]. Note also that these are just empirical observations and, as far as I know, there is no deep understanding of these facts. So in my opinion this means that without convincing estimate of NNNLO PDF effects it will be impossible to claim that we can predict the Higgs boson production cross section in gluon fusion to a precision better than a few percent (whatever few means), even on the theory side. Imagine that a few percent discrepancy is discovered in Higgs-to-gluon coupling. It will be very difficult to take this discrepancy seriously given the fact that NNNLO PDFs are not available.

Another important point in connection with the NNNLO QCD computation is that, for the first time in hadron collider physics, we can compare the result of the exact computation with approximate estimates of three-loop radiative corrections. The estimates are based on the observation that the Higgs boson production in gluon fusion receives dominant corrections from the emission of soft gluons and/or from "large numbers" such as e.g. π^2 appearing because of the time-like kinematics of the production process. In my opinion, it is very important to understand if these approximate results withstand the check of an explicit computation. Apart from the Higgs physics, where the exact result exists and, as such, clearly supersedes the approximate ones, such understanding is important in general since for, approximate calculations to be valid, one needs, roughly, the color flow in the event, the energy scale of the collision and the color charges of colliding partons. If we can check how approximate computations work for the Higgs production in gluon fusion, we can definitely be more certain about the validity of higher-order estimates for other processes.

The Higgs cross section working group assembled predictions from different sources and came up with a plot shown in Fig. 4 which is supposed to clarify this issue but which definitely leaves more questions than answers. Let me make a few comments. First, the NNLO and NNNLO predictions are clearly in good agreement and the error bars of the NNNLO results are obviously smaller; no surprises here. Second, it is not always easy to reconcile this plot with statements that are made in the original papers. For example, the authors of the dFMMV result [6] claim *exactly* the same difference between their approximate NNNLO and exact NNLO cross sections as the exact NNNLO computation seems to show, yet, by looking at the plot we can not say that these results actually agree. Finally, it is important to understand why the BBFMR result [7] is so much higher than everything else and why the claimed precision of this approximate computation is so high. This point is especially important since the BBFMR group claims the most advanced and sophisticated approximation to Higgs production in gluon fusion that utilizes constraints from different kinematic regimes, including both the threshold (soft gluon emissions) and the high-energy (BFKL). Let me emphasize again that the reason I discuss this plot is that I think it attempts to answer a very important question but, to my mind, it does not convey a clear and unambiguous message. It is very important to do this exercise right and get to the correct conclusion since this should affect the way we think about estimates of higher-order radiative corrections for other LHC processes.

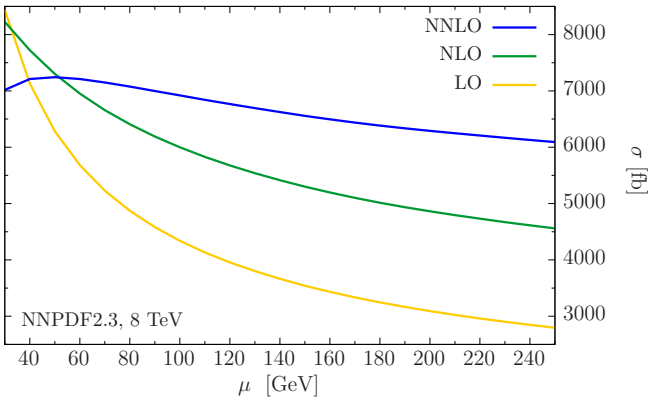

FIGURE 5. Scale dependence for $H + j$ cross section at the 8 TeV LHC in various orders of perturbative QCD [2]. See text for details.

LHC 13 TeV	$\epsilon^{\mathrm{N^3LO+NNLL+LL_R}}$	$\Sigma_{\text{0-jet}}^{\mathrm{N^3LO+NNLL+LL_R}}$ [pb]	$\Sigma_{\text{0-jet}}^{\mathrm{N^3LO}}$	$\Sigma_{\text{0-jet}}^{\mathrm{NNLO+NNLL}}$
$p_{\mathrm{t,veto}} = 25\,\mathrm{GeV}$	$0.539^{+0.017}_{-0.008}$	$24.7^{+0.8}_{-1.0}$	$24.3^{+0.5}_{-1.0}$	$24.6^{+2.6}_{-3.8}$
$p_{\mathrm{t,veto}} = 30\,\mathrm{GeV}$	$0.608^{+0.016}_{-0.007}$	$27.9^{+0.7}_{-1.1}$	$27.5^{+0.5}_{-1.1}$	$27.7^{+2.9}_{-4.0}$

FIGURE 6. Efficiencies ϵ and integrated cross sections Σ for the two values of the jet transverse momenta [10]. See details in the text.

HIGGS BOSON PRODUCTION IN ASSOCIATION WITH JET

In the previous Section we discussed the inclusive production of the Higgs boson. Yet, the realities of the experimental analysis force us to understand fiducial cross sections and finer details of QCD radiation that accompanies the production of the Higgs boson. The simplest process that goes beyond the inclusive production is the production of the Higgs boson in association with a jet. A better understanding of this process is important for improving various phenomenological analyses, including the transverse momentum distribution of the Higgs boson and the refined understanding of the production cross section for producing the Higgs boson without detectable QCD radiation.

The production of the Higgs boson in association with jet was recently computed through NNLO in perturbative QCD in the infinite top mass limit [2, 3] (see [8, 9] for earlier work). The results for the total cross section at 8 TeV LHC obtained with the anti-k_t algorithm and a jet transverse momentum cut of 30 GeV are shown in Fig. 5. The NNLO QCD corrections computed for the renormalization and factorization scales set to the Higgs boson mass are close to twenty percent; the scale uncertainty is reduced to about 9 percent. One can use these results, together with the NNNLO QCD computation [1] of the inclusive cross section $pp \to H$, discussed earlier, to obtain refined predictions for the number of Higgs bosons produced at the LHC without detectable hard QCD radiation.

The events in that category belong to the so-called zero-jet bin and the separation of events with the Higgs boson into zero-jet, one-jet etc. bins is important since events with different number of jets are affected by very different background processes. We can find the zero-jet cross section by subtracting the $H + j$ cross section from the inclusive Higgs production cross section in matching orders of perturbative QCD. Until very recently, this "matching order" was NNLO for the inclusive and NLO for the H+jet cross sections but since both of these cross sections are now computed to one higher perturbative order, new result for the zero-jet cross section can be obtained. This was recently done in Ref.[10].

Similar to the discussion of the inclusive Higgs boson production and the many approximate calculations that pre-dated it, the Higgs zero-jet cross section was also estimated using approximate results for higher order corrections, obtained by resumming various enhanced terms that contribute to exclusive cross sections. With NNNLO QCD result for the Higgs production and the NNLO result for the H+jet production, we are now in position to compare approximate and exact results. This is done in Fig. 6. There we show the results for 13 TeV obtained with NNPDF2.3. Jets are defined with an anti-k_t algorithm with the jet radius $R = 0.5$. The renormalization, factorization and resummation

$$\text{anti}-\text{k}_t, \quad \Delta R = 0.4, \quad p_{j\perp} = 30 \text{ GeV}, \text{abs}(y_j) < 4.4$$
$$p_{\perp,\gamma_1} > 43.75 \text{ GeV}, \quad p_{\perp,\gamma_2} = 31.25 \text{ GeV}, \quad \Delta R_{\gamma j} > 0.4$$

FIGURE 7. Kinematic selection cuts for fiducial volume cross section for $H + j$ process by ATLAS collaboration [11].

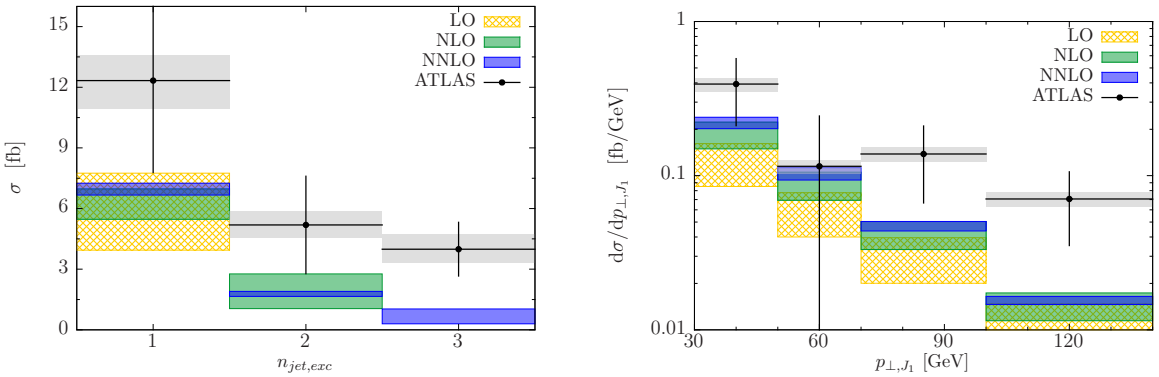

FIGURE 8. Inclusive cross sections with definite number of jets (right) and the transverse momentum distribution of the leading jet. Results of the ATLAS collaboration [11] are compared to the theory predictions [12].

scales are all set to $m_H/2$ and the effects of bottom and top quark masses are accounted for in an approximate way. The results are given for zero-jet efficiencies and one-jet cross sections and are computed either at fixed orders in perturbation theory or including the resummations on top of it. We immediately observe several things. First, there is absolutely no breakdown of perturbation theory for the jet $p_\perp$ cut as low as 25 GeV. Second, theoretical uncertainties from scale variation of lower order calculations are reliable. Third, the difference between resummed and fixed order results is so insignificant that it is impossible to claim that resummed results improve on fixed order predictions. Of course, the above remarks do not imply that the resummations are useless but they do imply that the theory remains perturbative all the way down to $p_\perp \sim 25$ GeV, in contrast to many claims to the contrary. It would be very interesting to actually *observe* a clear breakdown of perturbation theory by decreasing the cut on the jet transverse momentum; so far, this has not been done.

Although we do get very useful physics insights from these computations, they are still not completely satisfactory. Indeed, the main drawback is that they can not describe fiducial volume cross sections since decays of the Higgs boson are not included. This, however, is easy to do, at least in principle, since the Higgs boson is a scalar particle and no spin correlations are involved. What makes the calculation of the fiducial volume cross sections even more interesting is that there are measurements of the fiducial volume cross section by ATLAS and CMS collaborations, so that theoretical fiducial volume cross sections can be directly compared with experimental measurements.

The ATLAS selection criteria [11] for photons and jets used to define the fiducial volume cross section are shown in Fig. 7. ATLAS measures the following cross section

$$\sigma^{\text{fid,ATLAS}}_{H+j} = 21.5 \pm 5.3(\text{stat}) \pm 2.3(\text{sys}) \pm 0.6(\text{lumi}) \text{ fb}, \tag{2}$$

where statistical, systematic and luminosity uncertainty are displayed. For comparison, the NNLO QCD theoretical prediction is [12]

$$\sigma^{\text{fid,NNLO}}_{H+J} = 9.46^{+0.56}_{-0.84} \text{ fb}. \tag{3}$$

We note that the QCD corrections increase the leading order fiducial $H + j$ cross section by a factor 1.74 but even this increase is not sufficient to get the central value in agreement with the ATLAS measurement. It is interesting to point out that the theory prediction is about a factor of ten(!) more precise than the ATLAS measurement; this, of course is mostly caused by still relatively low statistics. If we compare the fiducial result for the ATLAS cross section with the NNLO prediction, we find that the ATLAS results is higher by approximately two standard deviations. However, it is striking that the ratio of the central values of the two cross section is larger than two and, therefore, the agreement between theory and experiment is worse than in the inclusive $gg \to H \to \gamma\gamma$ measurement.

Of course, once the Higgs boson decays are included on the theory side, any fiducial cross section or distribution can be obtained and compared to the experimental results. A few examples of such a comparison are shown in Fig. 8.

	$\sigma^{\rm nocuts}$[pb]	$\sigma^{\rm VBF\ cuts}$[pb]
LO	$4.032^{+0.057}_{-0.069}$	$0.957^{+0.066}_{-0.059}$
NLO	$3.929^{+0.024}_{-0.023}$	$0.876^{+0.008}_{-0.018}$
NNLO	$3.888^{+0.016}_{-0.012}$	$0.826^{+0.013}_{-0.014}$

FIGURE 9. Weak boson fusion cross sections in different orders in perturbation theory at the 13 TeV LHC [10].

In the left pane of Fig. 8 we show the comparison of the inclusive cross sections for the production of the Higgs boson with definite number of jets; in the right pane – the transverse momentum distribution of the leading jet. It is clear that data is always higher than the theory prediction and that shapes of theoretical and experimental jet transverse momentum distributions are quite different. Although these discrepancies are not statistically significant, they are peculiar and call for a refined analysis. The existence of precise theory prediction should provide enough motivation to do this as soon as possible during the Run II of the LHC.

HIGGS BOSON IN WEAK BOSON FUSION

.

The next topic I would like to discuss is the production of the Higgs boson in weak boson fusion. This is an interesting process for a variety of reasons, including direct access to the Higgs boson couplings to electroweak gauge bosons which, according to the Standard Model, are completely fixed by the Higgs boson quantum numbers.

Due to color conservation, computations of NLO QCD corrections are simple - the upper and lower quark lines receive QCD corrections but the two blocks do not talk to each other. As the consequence, one can view the whole process – and the QCD corrections to it – as the "deep inelastic scattering squared" and use DIS building blocks – the structure functions – to compute the QCD corrections. For NLO QCD this observation is not essential since the calculation can be easily done anyhow but for the NNLO it becomes useful since the NNLO QCD results for the structure functions are available.

The QCD corrections obtained in this approach were calculated earlier [13] and found to be small. Note that this result refers to the inclusive cross section, rather than the cross section subject to WBF cuts, but it was always assumed that the size of the QCD corrections to the inclusive cross section is indicative of the size of QCD corrections to cross sections with WBF cuts. Interestingly, the recent computation [4] shows that this assumption is incorrect and that, in fact, one can get larger corrections for fiducial volume cross sections. The comparison of radiative corrections to inclusive and fiducial WBF cross sections is shown in Fig. 9.

What is also interesting is that in many cases shapes of NNLO QCD corrections to kinematic distributions seem to be rather different from what one could expect based on existing NLO computations and/or parton shower results. This is quite surprising since it is not quite clear why NNLO QCD corrections should affect the kinematics so much even accounting for the fact that the WBF cuts are quite aggressive. If these results hold, the message – again – will be that approximate results may indicate the magnitude of the expected effects but not more than that and that studies of production cross sections and distributions at the $O(5-10)$ percent precision level will require NNLO QCD calculations.

Conclusions

Our ability to study the Higgs boson physics at the LHC is intimately related to the availability of precise theoretical predictions for the Higgs boson production and decay. In the past year, we have seen a very impressive progress in this field that includes NNNLO QCD prediction for the inclusive Higgs boson production cross section in gluon fusion, the fiducial volume results for Higgs plus jet and the Higgs boson production in weak boson fusion. These results will definitely contribute to enabling much more precise extraction of the Higgs boson couplings than was previously anticipated.

As the increased precision of fixed order computations becomes available, fixed order results are compared to the results of various approximate computations that aim at estimating higher order corrections from lower order results. From the comparisons that we have so far, it appears that approximate methods often do not provide satisfactory

results although, I think, the jury is still out. It is nevertheless very important to clarify this issue since its resolution will affect the way we think about reliability of such approximate computations for other LHC processes.

The impressive progress with fixed order computations, as well as with merging processes with different jet multiplicities and matching them to parton shower, should enable us to verify or disprove the Standard Model nature of the Higgs boson at the LHC in a convincing and reliable way. We look forward to application of these results to Higgs physics during the Run II at the LHC.

ACKNOWLEDGMENTS

I would like to thank the organizers of the LHCP2015 conference for the invitation to give this talk and for creating an inspiring atmosphere during the meeting.

REFERENCES

[1] C. Anastasiou, C. Duhr, F. Dulat, F. Herzog and B. Mistlberger, Phys. Rev. Lett **114** (2015), 212001.
[2] R. Boughezal, F. Caola, K. Melnikov, F. Petriello and M. Schulze, Phys. Rev. Lett. **115**, no. 8, 082003 (2015)
[3] R. Boughezal, C. Focke, W. Giele, X. Liu and F. Petriello, Phys. Lett. B **748**, 5 (2015).
[4] M. Cacciari, F. A. Dreyer, A. Karlberg, G. P. Salam and G. Zanderighi, Phys. Rev. Lett. **115**, no. 8, 082002 (2015)
[5] S. Forte, A. Isgr and G. Vita, Phys. Lett. B **731**, 136 (2014).
[6] D. de Florian, J. Mazzitelli, S. Moch and A. Vogt, JHEP **1410**, 176 (2014).
[7] R. D. Ball, M. Bonvini, S. Forte, S. Marzani and G. Ridolfi, Nucl. Phys. B **874**, 746 (2013).
[8] R. Boughezal, F. Caola, K. Melnikov, F. Petriello and M. Schulze, JHEP **1306**, 072 (2013).
[9] X. Chen, T. Gehrmann, E.W.N. Glover and M. Jaquier, Phys. Lett. B**740**, 147 (2015).
[10] A. Banfi, F. Caola, F. A. Dreyer, P. F. Monni, G. P. Salam, G. Zanderighi and F. Dulat, arXiv:1511.02886 [hep-ph].
[11] G. Aad *et al.* (ATLAS collaboration), JHEP 1409 (2014), 112.
[12] F. Caola, K. Melnikov and M. Schulze, Phys. Rev. D **92**, no. 7, 074032 (2015) doi:10.1103/PhysRevD.92.074032 [arXiv:1508.02684 [hep-ph]].
[13] P. Bolzoni, F. Maltoni, S. O. Moch and M. Zaro, Phys. Rev. Lett. **105**, 011801 (2010) doi:10.1103/PhysRevLett.105.011801 [arXiv:1003.4451 [hep-ph]].

Higgs boson physics: parallel talks

Proceedings of the LHCP2015 Conference, St. Petersburg, Russia, August 31 - September 5, 2015

Editors: V.T. Kim and D.E. Sosnov

Extending the Higgs sector: an extra singlet.

M. I. VYSOTSKY

Institute for Theoretical and Experimental Physics, Moscow, 117218, Russia

vysotsky@itep.ru

Abstract. Bounds on singlet admixture in 125 GeV h boson from electroweak radiative corrections and data on h production and decays are obtained. Possibility of double h production enhancement at 14 TeV LHC due to heavy higgs contribution is considered.

Introduction

This talk is based on the paper [1].

After the discovery of the Higgs (BEH) boson [2, 3], all fundamental particles of the Standard Model (SM) are finally found, and now even passionate adepts of the SM should look for physics beyond it. The pattern of particles we have is rather asymmetric: there are twelve vector bosons, many leptons and quarks with spin $1/2$ and only one scalar particle h with mass 125 GeV. That is why it is quite probable that there are other still undiscovered fundamental scalar particles in Nature. The purpose of the present paper is to consider the simplest extension of the SM by adding one real scalar field to it. We will study the degree of enhancement of double higgs production at LHC due to an extra singlet. To do this we should analyze bounds on the mass of the additional scalar particle and its mixing with isodoublet state.

An enhancement of hh production occurs due to the mixing of the SM isodoublet with additional scalar field which is proportional to the vacuum expectation value (vev) of this field. Thus isosinglet is singled out: its vev does not violate custodial symmetry and can be large. For higher representations special care is needed; see paper [4] where an introduction of isotriplet(s) in the SM is discussed.

The model

Adding to the SM a real field X, we take the scalar fields potential in the following form:

$$V(\Phi, X) = -\frac{m_\Phi^2}{2}\Phi^\dagger\Phi + \frac{m_X^2}{2}X^2 + \frac{\lambda}{2}(\Phi^\dagger\Phi)^2 + \mu\Phi^\dagger\Phi X, \tag{1}$$

where Φ is an isodoublet. Two combinations of the parameters entering (1) are known experimentally: it is the mass of one of the two scalar states, h, which equals 125 GeV and the isodoublet expectation value $v_\Phi = 246$ GeV. The two remaining combinations are determined by the mass of the second scalar, H (we take $m_H > m_h$, though this is not obligatory), and the angle α which describes singlet-doublet admixture:

$$\begin{cases} h = \phi\cos\alpha + \chi\sin\alpha, \\ H = -\phi\sin\alpha + \chi\cos\alpha, \end{cases} \qquad \begin{cases} \phi = h\cos\alpha - H\sin\alpha, \\ \chi = h\sin\alpha + H\cos\alpha. \end{cases} \tag{2}$$

Substituting in (1)

$$\Phi = \begin{pmatrix} \phi^+ \\ \frac{1}{\sqrt{2}}(v_\Phi + \phi + i\eta) \end{pmatrix}, \qquad X = v_X + \chi, \tag{3}$$

at the minimum of the potential we get:

$$\begin{cases} \lambda v_\Phi^2 + 2\mu v_X = m_\Phi^2, \\ 2m_X^2 v_X + \mu v_\Phi^2 = 0, \end{cases} \tag{4}$$

so μ is negative. For the mass matrix using (4) we get:

$$M = \begin{pmatrix} V_{\phi\phi} & V_{\phi\chi} \\ V_{\phi\chi} & V_{\chi\chi} \end{pmatrix} = \begin{pmatrix} \lambda v_\Phi^2 & \mu v_\Phi \\ \mu v_\Phi & m_X^2 \end{pmatrix}, \tag{5}$$

where $V_{\phi\chi} \equiv \frac{\partial^2 V}{\partial\phi\partial\chi}, \ldots$ Eigenvalues of (5) determine masses of scalar particles:

$$m_{h,H}^2 = \frac{1}{2}\lambda v_\Phi^2 + \frac{1}{2}m_X^2 \mp \sqrt{\left(\frac{1}{2}\lambda v_\Phi^2 - \frac{1}{2}m_X^2\right)^2 + \mu^2 v_\Phi^2}, \tag{6}$$

where "–" corresponds to m_h and "+"—to m_H. Eigenfunctions are determined by the mixing angle α:

$$\sin 2\alpha = \frac{-2\mu v_\Phi}{m_H^2 - m_h^2}, \quad \tan\alpha = \frac{m_h^2 - \lambda v_\Phi^2}{\mu v_\Phi}. \tag{7}$$

Equations (7) determine μ and λ for the given mixing angle α, while equations (6) determine m_X for given α as well. Finally, equations (4) determine the values of m_Φ and v_X.

Bounds from h production at LHC and electroweak precision observables

ATLAS and CMS collaborations had detected h production and decays in the reactions

$$pp \to h \to f_i, \tag{8}$$

where $f_i, i = 1, 2, \ldots, 5$ designate the so-called "Big five" final state channels: WW^*, ZZ^*, $\gamma\gamma$, $\tau\bar{\tau}$, $b\bar{b}$. Cross sections of reactions (8) are equal to the higgs production cross section times branching ratio of the corresponding decay channel. Quantities μ_i are introduced according to the following definition:

$$\mu_i \equiv \frac{\sigma_{pp\to h} \cdot \Gamma_{h\to f_i}/\Gamma_h}{(\sigma_{pp\to h} \cdot \Gamma_{h\to f_i}/\Gamma_h)_{\mathrm{SM}}}. \tag{9}$$

According to ATLAS and CMS results, all μ_i are compatible with one within experimental and theoretical accuracy. It means that no New Physics are up to now observed in h production and decays.

In the model with an extra isosinglet, production and decay probabilities of h equal that in the SM multiplied by a factor $\cos^2\alpha$, that is why we have:

$$\mu_i = \cos^2\alpha, \tag{10}$$

and existing bounds on μ_i are translated into bounds on the mixing angle α. Taking into account all measured production and decay channels, for the average values experimentalists obtain [5, 6]:

$$\text{ATLAS:} \qquad \mu = 1.30^{+0.18}_{-0.17}, \tag{11}$$

$$\text{CMS:} \qquad \mu = 1.00^{+0.14}_{-0.13}\left[\pm 0.09(\text{stat.})^{+0.08}_{-0.07}(\text{theor.}) \pm 0.07(\text{syst.})\right] \tag{12}$$

Let us stress that the theoretical uncertainty in the calculation of $pp \to h$ production cross section at LHC does not allow to reduce substantially the uncertainty in the value of μ. Bounds from electroweak precision observables (EWPO) are not affected by this particular uncertainty.

We fit experimental data with the help of LEPTOP program [7] using $m_h = 125.14$ GeV. The result of the SM fit which accounts the h mass measurement is shown in Table 1. Quality of the fit is characterised by the χ^2 value

$$\chi^2/n_{\text{d.o.f.}} = 19.6/13. \tag{13}$$

TABLE 1: EWPO fit of the Standard Model

Observable	Experimental value	Standard Model	Pull
Γ_Z, GeV	2.4952(23)	2.4966(14)	−0.5895
σ_h, nb	41.541(37)	41.475(14)	1.7746
R_l	20.771(25)	20.744(18)	1.0831
$A_{\rm FB}^l$	0.0171(10)	0.0165(2)	0.6572
A_τ	0.1439(43)	0.1484(7)	−1.0452
R_b	0.2163(7)	0.2158(0)	0.7699
R_c	0.1721(30)	0.1722(0)	−0.0277
$A_{\rm FB}^b$	0.0992(16)	0.1040(5)	−3.0303
$A_{\rm FB}^c$	0.0707(35)	0.0744(4)	−1.0565
$s_l^2\ (Q_{\rm FB})$	0.2324(12)	0.2313(1)	0.8771
$A_{\rm LR}$	0.1514(22)	0.1484(7)	1.3822
A_b	0.923(20)	0.9349(1)	−0.5941
A_c	0.670(27)	0.6685(3)	0.0567
M_W, GeV	80.3846(146)	80.3725(67)	0.8322
m_t, GeV	173.24(95)	174.32(89)	−1.1370
$1/\bar{\alpha}$	128.954(48)	129.023(37)	−1.4378

Higgs boson contributions to electroweak observables at one loop are described in LEPTOP by functions $H_i(h) = H_i(m_h^2/m_Z^2)$. In the case of an extra singlet the following substitution should be performed:

$$H_i(h) \to \cos^2\alpha\ H_i(h) + \sin^2\alpha\ H_i(H),\ H = m_H^2/m_Z^2. \tag{14}$$

The same substitution should be made for the functions $\delta_4 V_i(t,h)$, $t = m_t^2/m_Z^2$, which describe two loops radiative corrections enhanced as m_t^4. In two loops quadratic dependence on higgs mass appears which is described by functions $\delta_5 V_i$. Calculations of these corrections in the case of an extra singlet higgs is not easy. An approximate upper bound has been estimated by assuming that

$$\delta_5 V_i(H) < \delta_5 V_i((1000\ \text{GeV})^2/m_Z^2) \approx 100\ \delta_5 V_i(h) \text{ for } m_H < 1000\ \text{GeV}. \tag{15}$$

Comparison of two calculations, one with $\delta_5 V_i(h) = \cos^2\alpha\ \delta_5 V_i(h)$, and the other with

$$\delta_5 V_i(h) = \cos^2\alpha\ \delta_5 V_i(h) + 100 \cdot \sin^2\alpha\ \delta_5 V_i(h), \tag{16}$$

showed that the correction to the values of $\sin\alpha$ in Fig. 1 is less than 10^{-3}.

Bounds from EWPO on the singlet model parameters are presented in Fig. (a). χ^2 minimum is reached at $\sin\alpha = 0$, $m_H = 150$ GeV, which is the minimum value allowed for m_H in the fit. Experimental data are avoiding heavy higgs. The value of χ^2 at the minimum coincides with the SM result (13). Lines of constant χ^2 correpospond to $\Delta\chi^2 = 1, 4, 9, \ldots$. Probabilities that $(\sin\alpha, m_H)$ values are below these lines are 39%, 86%, 98.9%, ...

Bounds accounting for both EWPO and direct h production data (11), (12) are shown in Fig. (b). We see that for heavy H bounds from EWPO dominate, while for light H measurement of μ is more important.

h, H and hh production at LHC

The main purpose of this section is to find what enhancement of double higgs production cross section is possible with enlarged higgs sector. Let us remind that in the SM double h production cross section is very small. According

to the recent result [9], at $\sqrt{s} = 14$ TeV $\sigma^{\rm NNLO}(pp \to hh) = 40$ fb with a $10 \div 15\%$ accuracy. We will demonstrate that enlarged higgs sector allows to strongly enhance double h production.

The cross section of H production at LHC equals that for the SM higgs production (for $(m_h)_{\rm SM} = m_H$) multiplied by $\sin^2\alpha$. Cross section of the SM higgs production at NNLO we take from Table 3 of [8]. In order to obtain cross section of resonant hh production in H decays we should multiply cross section of H production by ${\rm Br}(H \to hh)$.

Let us consider H decays. Decays to hh, W^+W^-, ZZ and $t\bar{t}$ dominate. For the Hhh coupling we obtain:

$$\begin{aligned}\Delta\mathcal{L}_{Hhh} &= \left[\frac{3}{2}\lambda v_\Phi \cos^2\alpha \sin\alpha - \frac{\mu}{2}\cos\alpha(1-3\sin^2\alpha)\right] Hh^2 \\ &= \frac{2m_h^2 + m_H^2}{2v_\Phi}\sin\alpha\cos^2\alpha\ Hh^2 \\ &\equiv g_{Hhh} Hh^2,\end{aligned} \tag{17}$$

thus

$$\Gamma_{H\to hh} = \frac{g_{Hhh}^2}{8\pi m_H}\sqrt{1-\left(\frac{2m_h}{m_H}\right)^2}. \tag{18}$$

Decays to W^+W^-, ZZ, $t\bar{t}$ occur through isodoublet admixture in H:

$$\begin{aligned}\Delta\mathcal{L} &= \frac{2m_W^2}{v_\Phi}\sin\alpha\ HW^+W^- + \frac{m_Z^2}{v_\Phi}\sin\alpha\ HZ^2 + \frac{m_t}{v_\Phi}\sin\alpha\ Ht\bar{t} \\ &\equiv g_{HWW} HW^+W^- + \frac{1}{2}g_{HZZ} HZ^2 + g_{Ht\bar{t}} Ht\bar{t},\end{aligned} \tag{19}$$

thus

$$\Gamma_{H\to W^+W^-} = \frac{g_{HWW}^2 m_H^3}{64\pi m_W^4}\left[1 - 4\frac{m_W^2}{m_H^2} + 12\frac{m_W^4}{m_H^4}\right]\sqrt{1-\left(\frac{2m_W}{m_H}\right)^2}, \tag{20}$$

$$\Gamma_{H\to ZZ} = \frac{g_{HZZ}^2 m_H^3}{128\pi m_Z^4}\left[1 - 4\frac{m_Z^2}{m_H^2} + 12\frac{m_Z^4}{m_H^4}\right]\sqrt{1-\left(\frac{2m_Z}{m_H}\right)^2}, \tag{21}$$

$$\Gamma_{H\to t\bar{t}} = \frac{3g_{Ht\bar{t}}^2 m_H}{8\pi}\left[1-\left(\frac{2m_t}{m_H}\right)^2\right]^{\frac{3}{2}}. \tag{22}$$

The dependence of the widths and branching ratios of H decays on mixing angle α for $m_H = 300$ GeV are shown in Figure 2.

For the cross section of the reaction $pp \to H \to hh$ we have:

$$\sigma(pp \to H \to hh) = \sigma(pp \to h)_{\rm SM} \cdot \sin^2\alpha \cdot {\rm Br}(H \to hh), \tag{23}$$

the lines of constant cross section are shown in Fig. 3. $H \to ZZ$ decay can be used in order to find H; its cross section divided by that for the SM higgs boson with $(m_h)_{\rm SM} = m_H$ is

$$R \equiv \frac{\sigma(pp \to H)\cdot{\rm Br}(H \to ZZ)}{(\sigma(pp \to h)\cdot{\rm Br}(h \to ZZ))_{\rm SM}} = \frac{\sin^4\alpha}{\sin^2\alpha + \frac{\Gamma(H\to hh)}{\Gamma_{\rm SM}}}. \tag{24}$$

Contour plot of R is presented in Fig. 4. Let us note that R does not depend on $\sqrt{s}$.

Conclusions

In the models with extended higgs sector strong resonant enhancement of double higgs production is possible which makes the search of $pp \to hh$ reaction at Run 2 LHC especially interesting. According to Fig. 3 cross section of $pp \to H \to hh$ reaction can be as large as 0.5 pb, ten times larger than the SM value.

The search for H boson can also go in the same way as it was for the heavy SM boson h. Probability of H observation diminishes compared to that of h because of a) suppression of H production cross section by the factor $\sin^2\alpha \leq 0.2$; b) suppression of $\mathrm{Br}(H \to ZZ)$ because of additional $H \to hh$ decay mode. Taking these two factors into account, we get about factor 10 suppression of $pp \to H \to ZZ$ process probability compared to that for the SM higgs boson (see Fig. 4).

Results for the search of higgs-like boson in ZZ decay mode can be found in [10], Figure 5. Comparing it with our Fig. 4, we observe that experimental data start to be sensitive to the singlet model expectation for maximally allowed values of the mixing angle α.

I am grateful to the organizers of the LHCP 2015 Conference for the hospitality in Saint Petersburg.

REFERENCES

[1] S. Godunov, A. Rozanov, M. Vysotsky, E. Zhemchugov, arXiv:1503.01618.
[2] The ATLAS collaboration, Phys. Lett. **B716** 1 (2012).
[3] The CMS collaboration, Phys. Lett. **B716** 30 (2012).
[4] S. Godunov, M. Vysotsky, E. Zhemchugov, JETP Vol. 147 (3) (2015), arXiv:1408.0184.
[5] The ATLAS collaboration, ATLAS-CONF-2014-009 (2014).
[6] The CMS collaboration, CERN-PH-EP-2014-288, CMS-HIG-14-009, arXiv:1412.8662, (2014).
[7] V. A. Novikov, L. B. Okun, A. N. Rozanov, M. I. Vysotsky, CPPM-95-1, arXiv:hep-ph/9503308.
[8] S. Dittmaier, C. Mariotti, G. Passarino et al., CERN-2011-002, arXiv:1101.0593.
[9] D. de Florian and J. Mazzitelli, PoS LL2014 (2014) 029, DESY 14-080 / LPN 14-073, arXiv:1405.4704.
[10] The CMS collaboration, CMS PAS HIG-13-002 (2013).

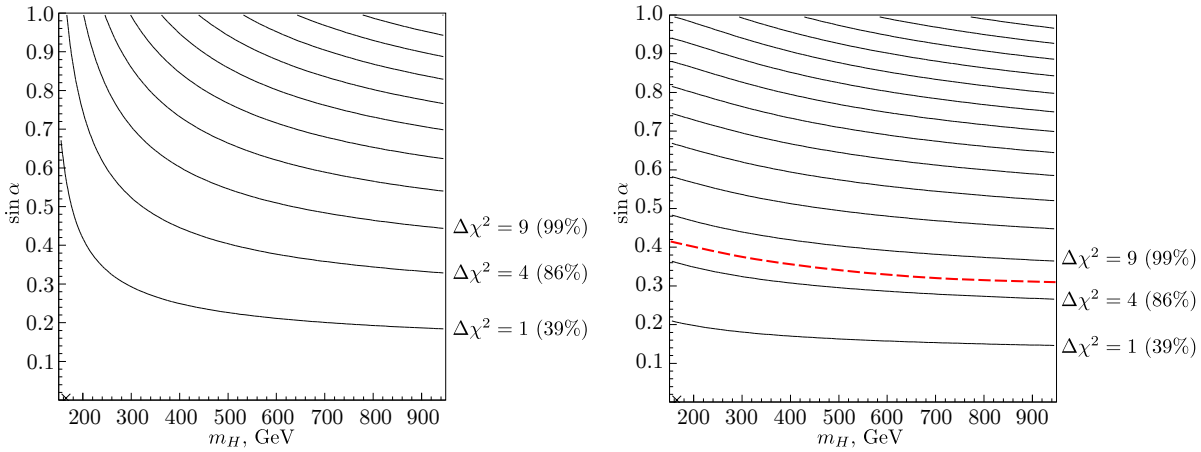

(a) Bounds from electroweak precision observables.

(b) Bounds from both electroweak precision observables and signal strength measurements (11), (12). The dashed line corresponds to $\Delta\chi^2 = 5.99$; the probability that numerical values of $(m_H, \sin\alpha)$ are below it equals 95%.

FIGURE 1: Bounds on the singlet model parameters.

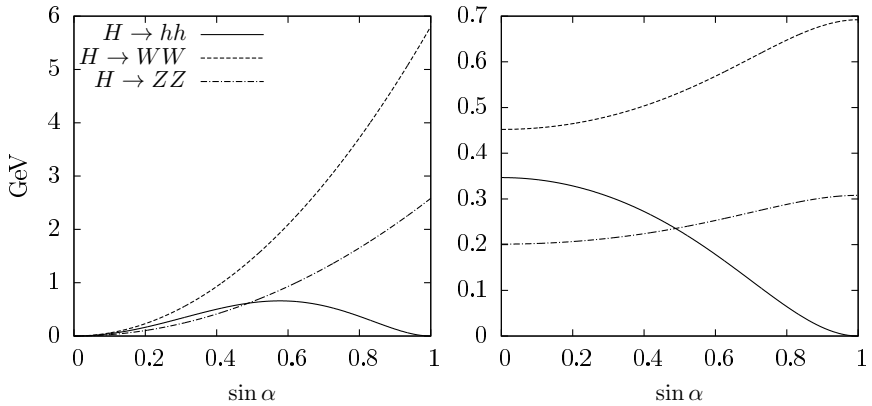

(a) Decay widths.

(b) Branching ratios.

FIGURE 2: Decay widths and branching ratios of the heavy higgs boson for $m_H = 300$ GeV.

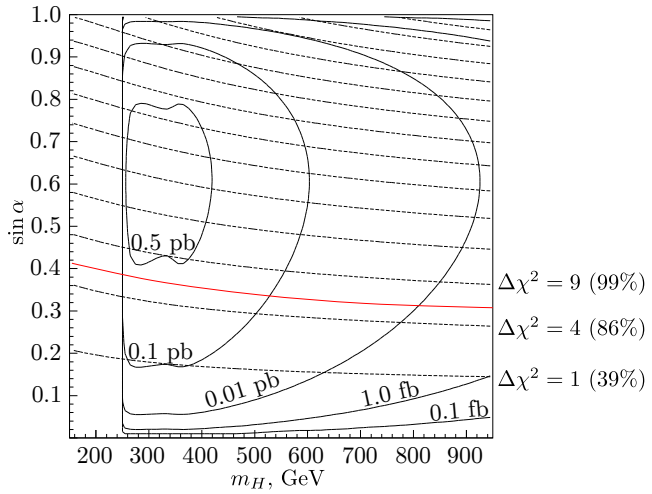

FIGURE 3: Contour plot of $\sigma(pp \to H \to hh)$ for $\sqrt{s} = 14$ TeV. In this figure we neglect small effects of $H \to hh^*$.

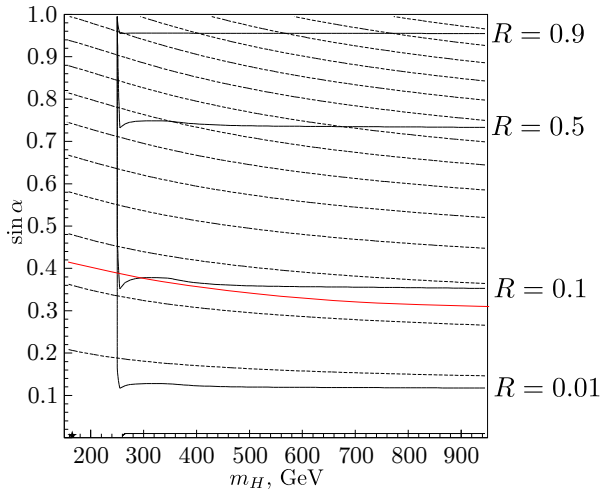

FIGURE 4: Contour plot of $R \equiv \frac{\sigma(pp\to H)\mathrm{Br}(H\to ZZ)}{(\sigma(pp\to h)\mathrm{Br}(h\to ZZ))_{\mathrm{SM}}}$. In the calculation of R we assume $m_H > 2m_h$.

Proceedings of the LHCP2015 Conference, St. Petersburg, Russia, August 31 - September 5, 2015

Editors: V.T. Kim and D.E. Sosnov

Double Higgs Boson Production in See-Saw Type II and the Georgi-Machacek Model

S.I. GODUNOV[1,2]

[1]*Institute for Theoretical and Experimental Physics, Moscow, 117218, Russia*
[2]*Novosibirsk State University, Novosibirsk, 630090, Russia*

[a)]sgodunov@itep.ru

Abstract. The enhancement of double Higgs boson production in the extensions of the Standard Model with extra isotriplets is studied. In the see-saw type II model decays of new heavy scalar H can contribute to the double Higgs production cross section as much as Standard Model channels. In the model with two isotriplets (the Georgi–Machacek model) the custodial symmetry is preserved and the strongest bound on triplet parameters is removed so the production cross section can be much larger. The $H \to ZZ$ decay mode is usually considered as one of the most promising ways to discover new heavy neutral scalar H. We show that in the Georgi–Machacek model it is possible to get large enhancement of double SM-like Higgs boson production due to H decays while ZZ and WW decay channels could be highly suppressed.

INTRODUCTION

After the discovery of the Higgs boson h at the LHC [1] the next steps to check the Standard Model (SM) are the measurement of the coupling constants of the h boson to other SM particles with better accuracy and the measurement of the h self-coupling which determines the shape of the potential. In the SM the triple and quartic couplings are predicted in terms of the known h mass and vacuum expectation value. Deviations from these predictions would mean the existence of New Physics in the h potential. The triple coupling can be measured at the LHC in double h production, in which the gluon fusion dominates: $gg \to hh$. However, the $2h$ production cross section is very small. At $\sqrt{s} = 14$ TeV the cross section $\sigma^{NNLO}(gg \to hh) = 40.2$ fb with $(10-15)\,\%$ accuracy [2]. For the final states with the reasonable signal/background ratios double h production will be found and triple coupling will be measured [3] only at the HL-LHC. We are looking for the extensions of the SM scalar sector in which the double h production is enhanced so it can be tested at the LHC in the next couple of years.

One of the well-motivated examples of non-minimal scalar sector is provided by the see-saw type II mechanism of the neutrino mass generation [4]. In this mechanism a scalar isotriplet $(\Delta^{++}, \Delta^{+}, \Delta^{0})$ with hypercharge $Y_\Delta = 2$ is added to the SM. The vacuum expectation value (vev) of the neutral component v_Δ generates Majorana masses of the left-handed neutrinos. In this model we get an additional mechanism of the double h production at the LHC in the mode with intermediate new heavy scalar H. The H production cross section and its decays widths are proportional to v_Δ^2 so to enhance double h production we need v_Δ to be as large as possible.

Since the nonzero value of v_Δ violates the well checked equality of the strength of charged and neutral currents at tree level, v_Δ should be less than a few GeV. Due to this bound the contribution of H decays to cross section of double Higgs production is small and comparable to SM cross section [5].

The bound on v_Δ stressed above is removed in the Georgi-Machacek (GM) model [6], in which in addition to $\vec{\Delta}$ a scalar isotriplet with $Y = 0$ is introduced. Bounds on v_Δ come from the measurement of the 125 GeV boson couplings to vector bosons and fermions, which would deviate from their SM values. Since the accuracy of the coupling measurements is poor, v_Δ as large as 30 GeV is allowed and $\sigma(gg \to H)$ can reach 2 pb value which makes it accessible with the integrated luminosity $\int \mathcal{L}dt = 300$ fb^{-1} prior to the HL-LHC run. In this paper we are mainly focused on the GM model.

If H is produced with large cross section then in principle it can be discovered in ZZ (WW) final state. Direct searches in this mode at the LHC [7] can set limits on model parameters which in some ranges of M_H can be stronger

than that from h couplings. However it is not the case in the GM model since we show that $\mathrm{Br}(H \to ZZ) < 1\%$ could occur.

The talk is based on results presented in papers [5, 8] written in collaboration with M.I. Vysotsky and E.V. Zhemchugov, where more details and references can be found.

THE MODEL

In the GM model (see [9] for a detailed review of this model [10]) in addition to SM Higgs doublet

$$\Phi^{(0)} = \begin{bmatrix} \Phi^+ \\ \Phi^0 \end{bmatrix}, \tag{1}$$

two isotriplets with hypercharges $Y = 0$ and $Y = 2$ are introduced:

$$\xi = \begin{bmatrix} \xi^+ \\ \xi^0 \\ \xi^- \end{bmatrix}, \qquad \Delta = \begin{bmatrix} \Delta^{++} \\ \Delta^+ \\ \Delta^0 \end{bmatrix}. \tag{2}$$

We took the potential in the following form (for a detailed description see [9]):

$$V = \frac{\mu_2^2}{2}\mathrm{Tr}\left(\Phi^\dagger\Phi\right) + \lambda_1\left[\mathrm{Tr}\left(\Phi^\dagger\Phi\right)\right]^2 + \frac{\mu_3^2}{2}\mathrm{Tr}\left(X^\dagger X\right) - M_1\mathrm{Tr}\left(\Phi^\dagger\tau^a\Phi\tau^b\right)\left(UXU^\dagger\right)_{ab}, \tag{3}$$

where $\Phi^{(0)}$, ξ and Δ are combined into matrices Φ and X:

$$\Phi = \begin{bmatrix} \Phi^{0*} & \Phi^+ \\ -\Phi^{+*} & \Phi^0 \end{bmatrix}, \qquad \langle\Phi\rangle = \tfrac{1}{\sqrt{2}}\begin{bmatrix} v_\phi & 0 \\ 0 & v_\phi \end{bmatrix}, \tag{4}$$

$$X = \begin{bmatrix} \Delta^{0*} & \xi^+ & \Delta^{++} \\ -\Delta^{+*} & \xi^0 & \Delta^+ \\ \Delta^{++*} & -\xi^{+*} & \Delta^0 \end{bmatrix}, \qquad \langle X\rangle = \begin{bmatrix} v_\Delta & 0 & 0 \\ 0 & v_\Delta & 0 \\ 0 & 0 & v_\Delta \end{bmatrix}, \tag{5}$$

U is a rotational matrix:

$$U = \begin{bmatrix} -\frac{1}{\sqrt{2}} & 0 & \frac{1}{\sqrt{2}} \\ -\frac{i}{\sqrt{2}} & 0 & -\frac{i}{\sqrt{2}} \\ 0 & 1 & 0 \end{bmatrix}, \tag{6}$$

$\tau^a = \sigma^a/2$ where σ^a are Pauli matrices. Let us note that we consider simplified potential which corresponds to $\lambda_2, \lambda_3, \lambda_4, \lambda_5, M_2 = 0$ choice in the potential considered in paper [9].

The value of v_Δ is generated by the term proportional to M_1 and the following relations are useful:

$$v_\Delta = \frac{M_1 v_\Phi^2}{4\mu_3^2}, \qquad v_\phi^2 + 8v_\Delta^2 = (246\ \mathrm{GeV})^2\,. \tag{7}$$

In paper [5] v_Δ is defined to be $\sqrt{2}$ times larger.

Since the potential is written in the way that vevs of two triplets are the same then the custodial symmetry is preserved and the relation between W and Z boson masses at tree level is the same as in the SM [11]. It means that main restrictions originate from the measurement of h couplings to SM particles. Since the accuracy of these measurements is not very good at the moment, these restrictions are not very tough and v_Δ up to approximately 30 GeV is allowed.

Only one scalar, a combination of ξ^0 and Δ^0, mixes with neutral component Φ^0 of SM doublet forming mass eigenstates, h and H, which correspond to the scalar discovered at LHC (so $M_h = 125$ GeV) and new heavy scalar. Since this new scalar H has doublet admixture, it couples to quarks and therefore it can be produced in gluon-gluon fusion so its production cross section at LHC can be much larger than that for the other scalars of the GM model which can be produced only in electroweak processes. It was stressed in [5] that in some region of parameters space H decays can provide great enhancement of double h production at LHC.

HEAVY SCALAR DECAYS

According to papers [9, 13] the couplings of H boson to hh, WW, and ZZ are the following:

$$g_{Hhh} = 24\lambda_1 c_\alpha^2 s_\alpha v_\phi - \frac{\sqrt{3}}{2} M_1 c_\alpha \left(3c_\alpha^2 - 2\right), \tag{8}$$

$$g_{HWW} = c_W^2 g_{HZZ} = \frac{g^2}{6}\left(8\sqrt{3}c_\alpha v_\Delta + 3 s_\alpha v_\phi\right), \tag{9}$$

where $c_W = \cos\Theta_W$, Θ_W is the weak mixing angle, $c_\alpha = \cos\alpha$, $s_\alpha = \sin\alpha$, α is the mixing angle between h and H.

According to the potential (3) α is defined as following:

$$\sin 2\alpha = \frac{-\sqrt{3} v_\phi M_1}{M_H^2 - M_h^2}, \tag{10}$$

where M_H is the mass of H.

Using coupling constants (8) and (9), for the partial widths of H decays we get

$$\Gamma_{H\to hh} \approx \frac{v_\Delta^2}{v_\phi^4}\frac{3M_H^3}{8\pi}\left[\frac{1+2\left(\frac{M_h}{M_H}\right)^2}{1-\left(\frac{M_h}{M_H}\right)^2}\right]^2 \sqrt{1-4\frac{M_h^2}{M_H^2}}, \tag{11}$$

$$\Gamma_{H\to ZZ} \approx \frac{v_\Delta^2}{v_\phi^4}\frac{M_H^3}{24\pi}\left[\frac{1-4\left(\frac{M_h}{M_H}\right)^2}{1-\left(\frac{M_h}{M_H}\right)^2}\right]^2 \left(1-4\frac{M_Z^2}{M_H^2}+12\frac{M_Z^4}{M_H^4}\right)\sqrt{1-4\frac{M_Z^2}{M_H^2}}, \tag{12}$$

$$\Gamma_{H\to WW} \approx \frac{v_\Delta^2}{v_\phi^4}\frac{M_H^3}{12\pi}\left[\frac{1-4\left(\frac{M_h}{M_H}\right)^2}{1-\left(\frac{M_h}{M_H}\right)^2}\right]^2 \left(1-4\frac{M_W^2}{M_H^2}+12\frac{M_W^4}{M_H^4}\right)\sqrt{1-4\frac{M_W^2}{M_H^2}}. \tag{13}$$

Deriving these formulae we used the approximation $v_\phi \gg v_\Delta$, i.e. $\sin 2\alpha \approx 2\sin\alpha$, $\mu_3 \approx M_H$, and $8\lambda_1 v_\phi^2 \approx M_h^2$. For $v_\Delta = 20$ GeV we get $\sin\alpha = -0.35$.

In paper [5] it was found that $H \to hh$ decays can provide large enhancement of double Higgs boson production. For $M_H = 300$ GeV and $v_\Delta \approx 20$ GeV we get $\sigma(gg \to H) = \sin^2\alpha \times \sigma\left(gg \to H^{\rm SM}\right) \approx 1.4$ pb at $\sqrt{s} = 14$ TeV. Using (11), (12), and (13) for $M_H = 300$ GeV we get $\mathrm{Br}\,(H \to hh) \approx 98\%$ while $\mathrm{Br}\,(H \to ZZ) \approx 0.6\%$. It means that in spite of large H production cross section the enhancement in ZZ final state is negligible so the search for H in this mode at LHC will not lead to new limits on model parameters.

At the same time recent progress in search for hh production [14] makes $H \to hh$ mode the most promising way to search for heavy H in this region of parameter space of the GM model.

CONCLUSIONS

It was shown that though in the GM model new heavy neutral scalar H can be produced with large cross section at the LHC, ZZ and WW decay modes can be very suppressed (if $H \to hh$ decays are kinematically allowed and M_H is not significantly larger than 300 GeV) so direct searches for H in these decay modes will not lead to its discovery. This is a peculiar feature of the GM model.

ACKNOWLEDGMENTS

The author is grateful to the Organizers for the opportunity to give a talk at the LHCP2015.

SG is partially supported under the grants RFBR No. 14-02-00995, 16-32-60115, 16-02-00342 and Russian Federation Government under grants NSh-6792.2016.2, MK-4234.2015.2 and No. 11.G34.31.0047. In addition, SG is grateful to Dynasty Foundation for the support.

REFERENCES

[1] G. Aad *et al* [ATLAS Collaboration], Phys. Lett. B **716**, 1 (2012);
S. Chatrchyan *et al* [CMS Collaboration], Phys. Lett. B **716**, 30 (2012).

[2] D. de Florian, J. Mazzitelli, DESY-14-080, LPN-14-073, arXiv:1405.4704.

[3] J. Baglio, PoS DIS2014 120 (2014), arXiv:1407.1045.

[4] J. Schechter, J. W. F. Valle, Phys. Rev. D **22**, 2227 (1980);
T. P. Cheng, L. F. Li, Phys. Rev. D **22**, 2860 (1980);
M. Magg, Ch. Wetterich, Phys. Lett. B **94**, 61 (1980);
R. N. Mohapatra, G. Senjanovic, Phys. Rev. D **23**, 165 (1981).

[5] S.I. Godunov, M.I. Vysotsky, E.V. Zhemchugov, JETP **120**, 369-375 (2015).

[6] H. Georgi, M. Machacek, Nucl. Phys. B **262**, 463 (1985).

[7] V. Khachatryan *et al.* [CMS Collaboration], JHEP **1510**, 144 (2015), CMS-HIG-13-031, CERN-PH-EP-2015-074.

[8] S.I. Godunov, M.I. Vysotsky, E.V. Zhemchugov, Phys. Lett. B **751**, 505 (2015).

[9] K. Hartling, K. Kumar, H. E. Logan, Phys.Rev.**D90**, 015007 (2014).

[10] We follow the notations used in [9] with minor change: $\chi \leftrightarrow \Delta$, $v_\chi \leftrightarrow v_\Delta$.

[11] Loop corrections can change this relation due to modification of h couplings. Bounds on deviations of h couplings from the SM is discussed in [12]. In the GM model in the limit $v_\Delta \ll v_\phi$ the coupling of h to weak bosons is modified in the following way: $\kappa_V \approx 1 + 6(v_\Delta/v_\phi)^2$ (see Eqs (59) and (61) from [9]). For $v_\Delta = 30$ GeV we obtain $\kappa_V \approx 1.09$, and for $v_\Delta = 20$ GeV we find $\kappa_V \approx 1.04$. According to Section 3.4 of [12] it is consistent with experimental data on EWPO.

[12] M. Ciuchini, E. Franco, S. Mishima and L. Silvestrini, JHEP **1308**, 106 (2013).

[13] Ch.-W. Chiang, K. Yagyu, JHEP **1301**, 026 (2013).

[14] G. Aad *et al.* [ATLAS Collaboration], Phys. Rev. D **92**, 092004 (2015).

Proceedings of the LHCP2015 Conference, St. Petersburg, Russia, August 31 - September 5, 2015

Editors: V.T. Kim and D.E. Sosnov

Higgs Boson Properties at the LHC: Mass, Spin and Parity

Manuela Venturi

Department of Physics and Astronomy, University of Victoria, British Columbia, Canada

On behalf of the ATLAS and CMS Collaborations

Abstract. The individual and combined measurements of the mass, spin and parity properties of the Higgs boson, obtained with the ATLAS and CMS detectors, using up to 25 fb^{-1} of 7 TeV and 8 TeV pp collision data, are reviewed.

INTRODUCTION

The discovery of a particle compatible with the long-sought Higgs boson at a mass around 125 GeV, has been announced in 2012 by the ATLAS [1] and CMS [2] collaborations at the Large Hadron Collider (LHC) at CERN. After establishing the discovery, the next step consists in measuring the properties of the new particle; here, the latest measurements of its mass, spin and parity quantum numbers are reviewed, from the individual experiments and from their combination when available. The datasets used by each experiment correspond to about 25 fb^{-1} of proton-proton collisions at $\sqrt{s}$ = 7 and 8 TeV energy in the center of mass (collectively referred to as LHC Run 1).

MASS MEASUREMENT

Besides being a fundamental parameter of the Standand Model (SM), an improved knowledge of the Higgs boson mass (m_H) leads to more precise predictions for other Higgs boson properties, such as the couplings, and is a test of consistency for the SM itself. The measurement of m_H by the ATLAS [3] and CMS [4] collaborations is performed in a model-independent way, fitting the spectra of the reconstructed invariant masses of the final state. Both collaborations rely on the so-called golden channels, $H \to \gamma\gamma$ and $H \to ZZ^\star \to 4\ell$, which offer the best mass resolution. The analyses maximize the profile-likelihood ratios $\Lambda(\alpha) = L(\alpha, \hat{\hat{\theta}}(\alpha))/L(\hat{\alpha}, \hat{\theta})$, in the asymptotic regime, where L represents the likelihood function, α the parameter of interest and θ the nuisance parameters of the fit. The maximization is done with varying α in the numerator, and with respect to the best-fit α and θ in the denominator. The likelihood functions are constructed using probability density functions (PDFs), based on signal and background expected distributions.

The $H \to \gamma\gamma$ channel

The diphoton channel profits from the large number of events in the final state, despite the small signal-to-background ratio (a few percent). It is characterized by a narrow signal peak over a large continuum background. To maximize the sensitivity and the mass resolution, both experiments split the events into several categories, depending on the event topology (converted/uncoverted photons for ATLAS, production mode signature for CMS), the kinematics for ATLAS (photon momenta and pseudorapidities) and a Boosted Decision Tree (BDT) classifier for CMS.

The fit is combined over all categories; the discriminating variable is the diphoton mass and the background PDFs are derived from a fit to the data. Figure 1 shows the diphoton mass spectra for (a) ATLAS and (b) CMS, for the combined Run 1 dataset.

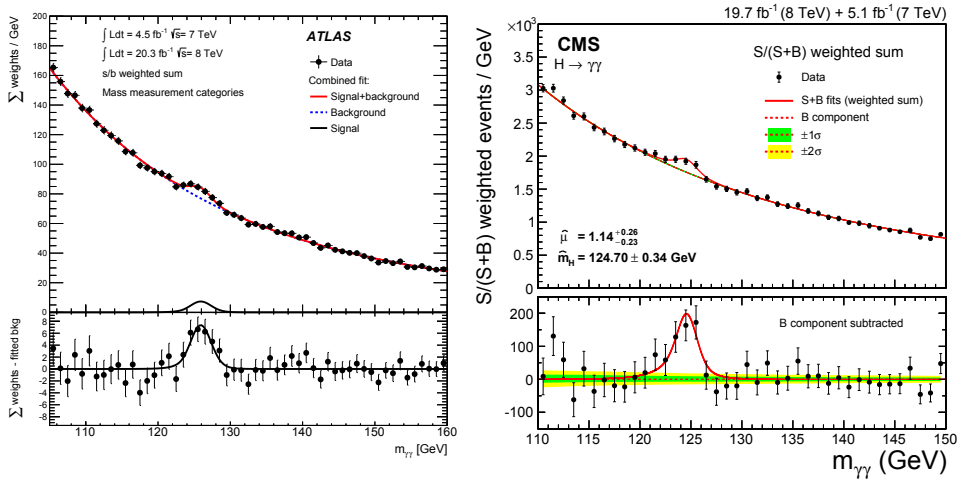

FIGURE 1. Diphoton mass spectra from the (a) ATLAS [3] and (b) CMS [4] collaborations, in the $H \to \gamma\gamma$ channel, showing the expected background and signal distributions, together with the observed data events, weighted by the significance. The lower boxes display the deviation from the background-only hypothesis.

The $H \to ZZ^\star \to 4\ell$ channel

Contrary to the $H \to \gamma\gamma$ channel, the $H \to ZZ^\star \to 4\ell$ ($\ell = e, \mu$) channel is characterized by a large signal-to-background ratio (around two) in the mass window of interest, and a much smaller number of events overall.

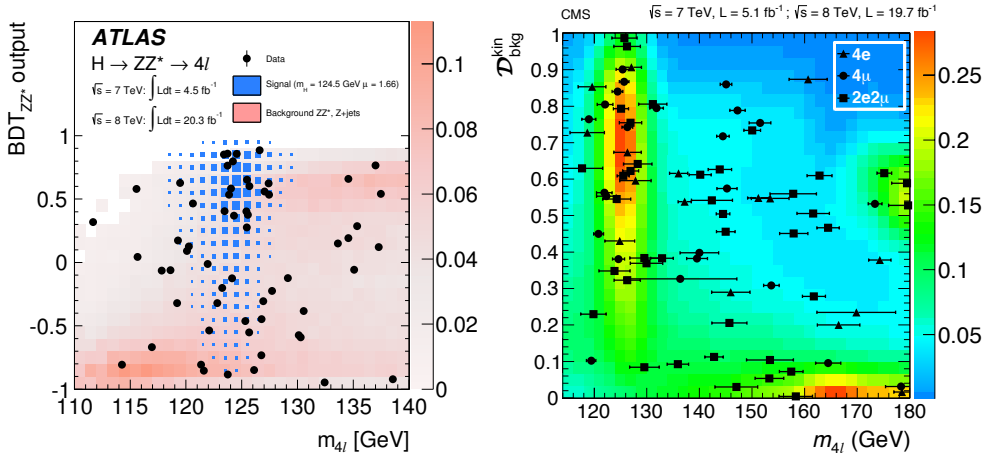

FIGURE 2. Four-lepton mass spectra from the (a) ATLAS [3] and (b) CMS [4] collaborations, in the $H \to ZZ^\star \to 4\ell$ channel, showing the expected and observed signal and background contributions. For ATLAS, $m_{4\ell}$ is shown as a fuction of the BDT discriminant, for CMS of the kinematic discriminant (whereas the fit uses also the per-event mass resolution in the latter case).

Both experiments make use of multivariate techniques to further enhance the sensitivity. In particular, ATLAS employs a BDT discriminant ($\mathrm{BDT}_{ZZ^\star}$), trained against the irreducible $ZZ^\star$ background, which contains a Matrix Element (ME) discriminant as one of the input variables, while CMS defines a kinematic variable, $\mathcal{D}^{\mathrm{kin}}$, from the masses of the dilepton pairs, the decay angles and a ME discriminant. Both analyses fit the multivariate discriminant together with the four-lepton mass ($m_{4\ell}$, with the addition of the information on the per-event mass resolution for CMS). Figure 2 shows the inputs for the 2D fits for the two experiments. The background estimation is data-driven for the reducible components (top quark and Z+jets) and taken from Monte Carlo (MC) simulation for $ZZ^\star$; the signal production modes are not distinguished in the analyses.

Combination of the $H \to \gamma\gamma$ and $H \to ZZ^\star \to 4\ell$ channels

To combine the ATLAS and CMS $H \to \gamma\gamma$ and $H \to ZZ^\star \to 4\ell$ analyses briefly described above, three signal strength parameters are introduced, namely $\mu^{\gamma\gamma}_{gg\mathrm{F}+t\bar{t}H}$, $\mu^{\gamma\gamma}_{\mathrm{VBF}+VH}$ and $\mu^{4\ell}$, which scale respectively the production rates through fermions and vector bosons for the $\gamma\gamma$ channel, and the total production rate for the $ZZ^\star$ channel. The three signal strenghts are assumed to be the same for ATLAS and CMS. The dominant uncertainties are also the same: electromagnetic energy scale and resolution, muon momentum scale and resolution, while theory uncertainties are negligible in all cases. The combined measurement yields a mass for the Higgs boson of:

$$m_H = 125.09 \pm 0.24(\mathrm{GeV}) = 125.09 \pm 0.21(\mathrm{stat}) \pm 0.11(\mathrm{syst})\ (\mathrm{GeV})\ [5]. \quad (1)$$

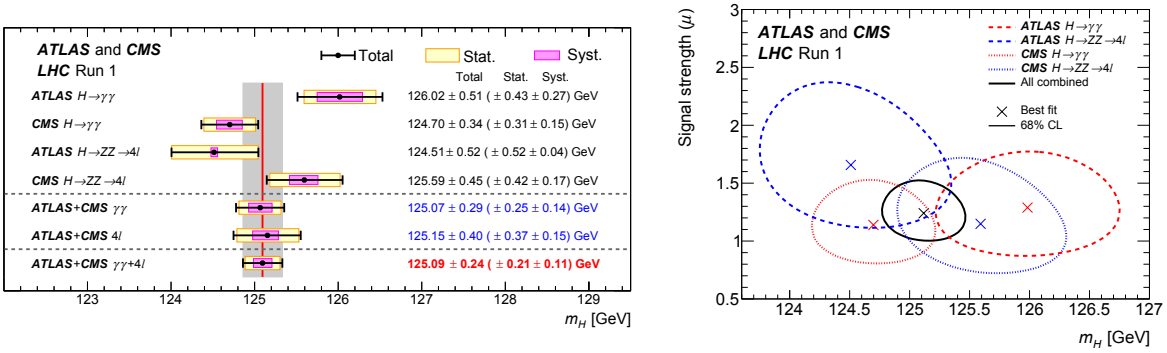

FIGURE 3. (a) Summary of the individual and combined mass measurements, from the ATLAS and CMS collaborations, for the $H \to \gamma\gamma$ and $H \to ZZ^\star \to 4\ell$ channels, and (b) their compatibility, shown as a function of the fitted signal strength. Both plots from [5].

Figure 3 shows a summary of (a) the individual measurements and (b) their compatibility, which is found to be of 10%.

SPIN AND PARITY MEASUREMENTS

The SM assigns a spin-parity value of $J^P = 0^+$ to the Higgs boson, which can be tested against alternative hypotheses for the newly discovered resonance: in particular, assignements of $J^P = 0^+_h$, 0^-, $1^\pm$ and 2^+ have been studied by the ATLAS [6] and CMS [7] collaborations (0^+_h being a model with higher-order operators). All the bosonic final states ($\gamma\gamma$, $ZZ^\star$ and $WW^\star$) are used, apart from $\gamma\gamma$ being excluded for $J = 1$, due to the Landau-Yang theorem, and for negative parity, due to poor discrimination. ATLAS does not consider the spin-1 hypothesis, after the previous publication where it was excluded with more than 99% CL. For spin-2 models, both universal (graviton-like) and non-universal couplings to quarks and gluons are tested, scanning over various k_q, k_g fractions. In addition to the fixed-hypothesis tests, the possible mixing of a SM Higgs boson with a Beyond-the-Standard-Model (BSM) spin-0 component is explored, which would result in CP violation in the Higgs sector.

All analyses rely only on the shape of the discriminating variables, and not on the rate prediction for BSM couplings, to avoid losing generality. The test statistic used to distinguish between the two spin-parity hypotheses is based on the ratio of their profile likelihoods; many thousands of MC pseudo-experiments are generated to obtain the test statistic distributions. The exclusion probability of the alternative J^P_{alt} hypothesis in favour of the SM one, is evaluated in terms of the modified confidence level estimator, $\mathrm{CL_S} = p(J^P_{\mathrm{alt}})/(1 - J^P_{\mathrm{SM}})$.

Spin and parity in ATLAS

The ATLAS parametrization follows the Higgs characterization model, which is an effective theory valid up to a cutoff scale of $\Lambda = 1$ TeV. Apart from the resonance under study, any other BSM particle would exist at a scale larger than Λ. For non-universal couplings, since NLO effects would lead to an unitarity-violating tail in the spectrum of the

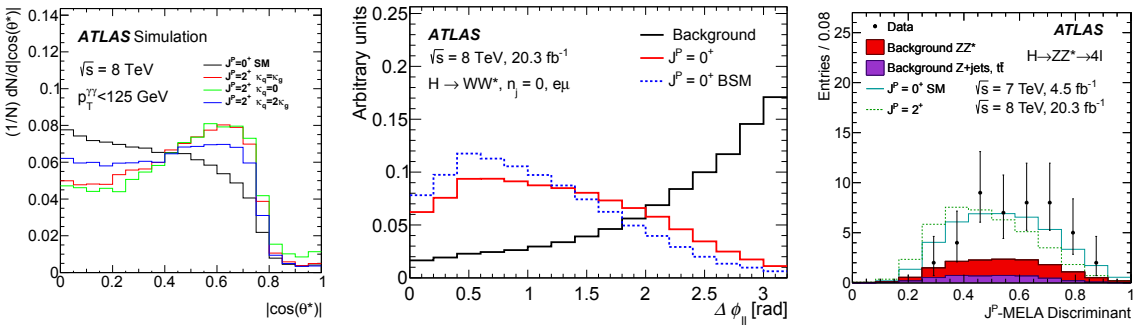

FIGURE 4. Examples of spin-parity sensitive variables from the ATLAS collaboration [6]. (a) Expected distributions of the polar angle in the Collins-Soper frame, for the SM and various spin-2 hypotheses, in the $H \to \gamma\gamma$ channel. (b) Expected distributions of the azimuthal difference between the charged leptons, for the SM and BSM 0^+ hypotheses, in the $H \to WW^\star$ channel [8]. (c) Expected and observed distributions of the MELA discriminant, for the SM and spin-2 hypothesis (with universal couplings), in the $H \to ZZ^\star \to 4\ell$ channel.

Higgs transverse momentum, p_T^H, a cut on this variable is performed, in two scenarios: $p_T^H < 125$ GeV (the mass of the resonance) and $p_T^H < 300$ GeV, which is one third of Λ.

The $H \to \gamma\gamma$ analysis follows what was described for the mass measurement, as for background determination, selection and categorization; kinematic variables sensitive to the spin of the resonance are the transverse momentum of the diphoton pair, $p_T^{\gamma\gamma}$, and the production angle between the two photons, measured in the Collins-Soper frame. Figure 4 (a) shows the expected angular distributions for the SM signal and various spin-2 hypotheses. The $H \to WW^\star$ analysis [8] uses only the $e\mu$ final state, which is the most sensitive, with up to one jet (only zero jets for parity studies), and combines the spin-parity sensitive variables into pairs of BDT discriminants: in the spin-2 case, BDT_0 (BDT_2) is obtained training the SM signal hypothesis (the alternative spin hypothesis) versus the background, while in the spin-0 case (both fixed-hypothesis and CP mixing) the second BDT discriminat is obtained training the two signal hypotheses one against the other. This approach ensures at the same time the best background suppression and signal discrimination. The most sensitive variable is found to be $\Delta\phi_{e\mu}$, the azimuthal difference between the charged leptons, depicted in Fig. 4 (b) for the total background, the SM signal and the BSM 0^+ hypothesis. In the $H \to ZZ^\star \to 4\ell$ case, the entire decay topology can be reconstructed, for a total of five spin-parity sensitive variables (the decay angles and the masses of the intermediate Z bosons) and three background-suppressing variables. A ME discriminant (MELA) is obtained in a tight mass window around m_H and then fitted to the data. Figure 4 (c) shows an example of the MELA discriminant for the spin-2 case.

Results for the fixed-hypotheses analyses are shown in Fig. 5 (a), for spin-0 and one representative spin-2 model, for the individual bosonic channels and their combination. In summary, all non-SM hypotheses are excluded with more than 99% CL.

For CP-mixing studies, the couplings k_{SM}, k_{HVV} and k_{AVV} are defined, corresponding to the interaction of a SM, BSM CP-even and BSM CP-odd spin-0 particle with WW or ZZ pairs, together with the mixing angle α for the CP-odd case. A scan on the ratios of couplings is performed and minimized to data, as shown in Fig. 6 for observed likelihoods, for (a) the CP-even case and (b) the CP-odd case. No significant deviation from a pure SM-composition is found.

Spin and parity in CMS

The CMS collaboration parametrizes the various BSM spin-parity scenarios using the anomalous-couplings approach, where the $A(HVV)$ amplitude is expanded in terms of the SM coupling, a_1^{VV}, and the BSM CP-even and CP-odd couplings, a_2^{VV} and a_3^{VV}, respectively. Results are given as a function of the effective fractional cross sections f_{ai}, bound between 0 and 1, and the phases ϕ_{ai}. The spin-2 analysis includes both the so-called "minimal" spin-2 model, 2^+_{m}, with a scan over the production fraction in the $q\bar{q}$ mode, and on several models with higher-dimension operators.

The $H \to \gamma\gamma$ analysis relies on the polar angle in the Collins-Soper frame, shown in Fig. 7 (a). For what concerns the $H \to WW^\star$ analysis, only the $e\mu$ final state is considered, with zero or one jet, as described for ATLAS before. Two discriminating variables are taken into account, the invariant mass of the dilepton pair, $m_{e\mu}$, and the transverse mass

Tested Hypothesis	$p^{\rm alt}_{{\rm exp},\mu=1}$	$p^{\rm alt}_{{\rm exp},\mu=\hat{\mu}}$	$p^{\rm SM}_{\rm obs}$	$p^{\rm alt}_{\rm obs}$	Obs. CL_s (%)
0^+_h	$2.5 \cdot 10^{-2}$	$4.7 \cdot 10^{-3}$	0.85	$7.1 \cdot 10^{-5}$	$4.7 \cdot 10^{-2}$
0^-	$1.8 \cdot 10^{-3}$	$1.3 \cdot 10^{-4}$	0.88	$< 3.1 \cdot 10^{-5}$	$< 2.6 \cdot 10^{-2}$
$2^+(\kappa_q = \kappa_g)$	$4.3 \cdot 10^{-3}$	$2.9 \cdot 10^{-4}$	0.61	$4.3 \cdot 10^{-5}$	$1.1 \cdot 10^{-2}$
$2^+(\kappa_q = 0;\ p_{\rm T} < 300GeV)$	$< 3.1 \cdot 10^{-5}$	$< 3.1 \cdot 10^{-5}$	0.52	$< 3.1 \cdot 10^{-5}$	$< 6.5 \cdot 10^{-3}$
$2^+(\kappa_q = 0;\ p_{\rm T} < 125GeV)$	$3.4 \cdot 10^{-3}$	$3.9 \cdot 10^{-4}$	0.71	$4.3 \cdot 10^{-5}$	$1.5 \cdot 10^{-2}$
$2^+(\kappa_q = 2\kappa_g;\ p_{\rm T} < 300GeV)$	$< 3.1 \cdot 10^{-5}$	$< 3.1 \cdot 10^{-5}$	0.28	$< 3.1 \cdot 10^{-5}$	$< 4.3 \cdot 10^{-3}$
$2^+(\kappa_q = 2\kappa_g;\ p_{\rm T} < 125GeV)$	$7.8 \cdot 10^{-3}$	$1.2 \cdot 10^{-3}$	0.80	$7.3 \cdot 10^{-5}$	$3.7 \cdot 10^{-2}$

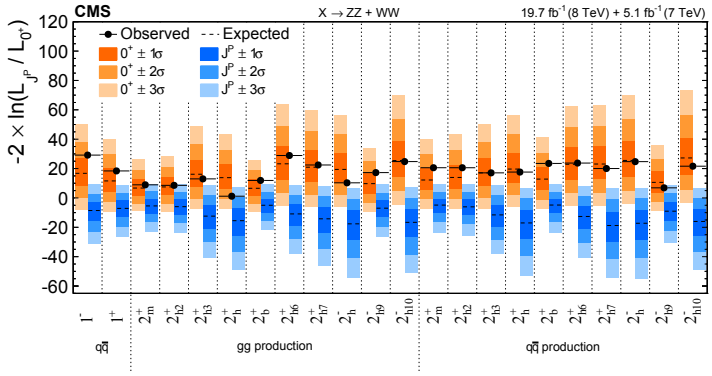

FIGURE 5. Summary of the fixed-hypothesis results from (a) ATLAS [6] and (b) CMS [7] collaborations, showing the expected and observed exclusion confidence levels for the several models under study.

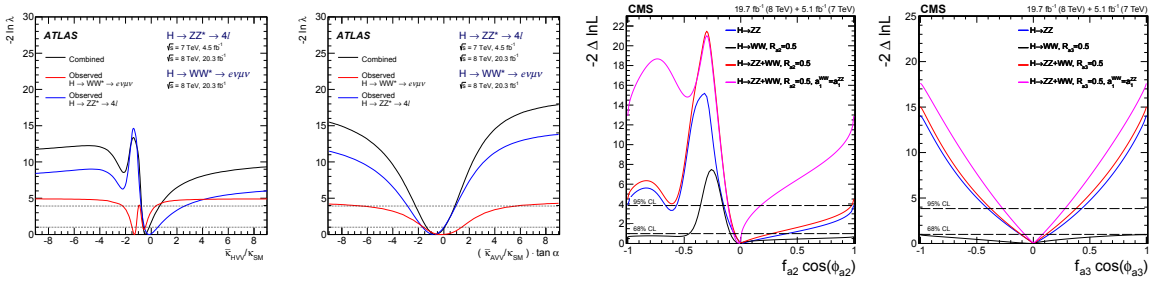

FIGURE 6. Scans over the strength multiplier of a possible BSM CP-even (a,c) or CP-odd (b,d) Higgs-boson component, compared with a pure SM composition. All results are shown on data and combined over the WW and ZZ channels. The ATLAS results [6] are shown in (a,b), the CMS ones [7] in (c,d).

of the full system, m_T, shown in Fig. 7 (b) for one representative case, while the azimuthal difference is disregarded since correlated to the previous ones. Finally, the $H \to ZZ^\star \to 4\ell$ analysis combines the eight observables of the final state, already mentioned for ATLAS, into a MELA discriminant, which provides templates for the background and the various signal hypotheses. One of these discriminants is shown in Fig. 7 (c), for the CP-odd case.

A complete summary of expected and observed results when testing the SM versus alternative spin-1 and spin-2 hypotheses, is given in Fig. 5 (b), for the individual bosonic channels and their combination; all non-SM hypotheses are excluded with more than 99% CL. Figure 6 shows the scan on the observed effective fractional cross sections, for (c) the CP-even case and (d) the CP-odd case. Again, no significant deviation from a pure SM-composition is found.

CONCLUSIONS

A review of the latest results on the mass, spin and parity properties of the Higgs boson has been presented.

The final Run 1 measurement of the mass of the Higgs boson has been derived from a combination of the ATLAS and CMS results, in the $H \to \gamma\gamma$ and $H \to ZZ^\star \to 4\ell$ final states. The measured value of the Higgs boson mass is $m_H = 125.09 \pm 0.24\,{\rm GeV} = 125.09 \pm 0.21({\rm stat}) \pm 0.11({\rm syst})$ GeV, and corresponds to a 10% compatibility among the

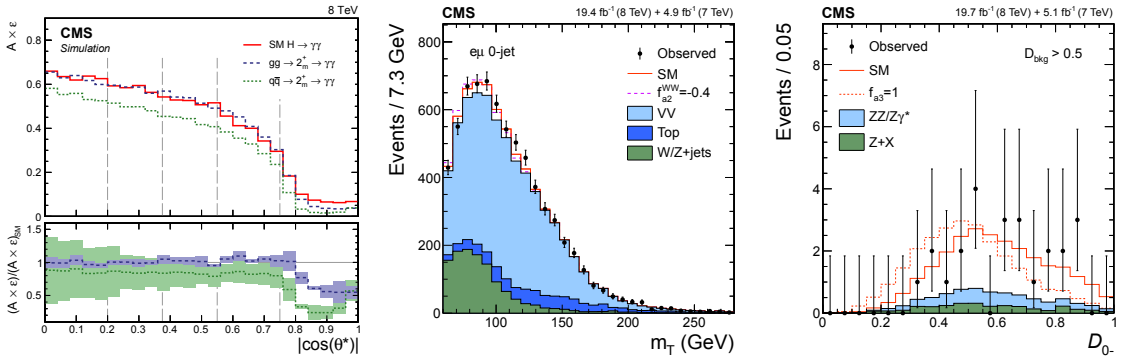

FIGURE 7. Examples of spin-parity sensitive variables from the CMS collaboration [7]. (a) Expected distributions of the polar angle in the Collins-Soper frame, for the SM and various spin-2 hypotheses, in the $H \to \gamma\gamma$ channel. (b) Expected distributions of the transverse mass, for the SM and BSM 0^+ hypotheses (CP-mix case), in the $H \to WW^\star$ channel. (c) Expected and observed distributions of the MELA discriminant, for the SM and the CP-odd hypotheses, in the $H \to ZZ^\star \to 4\ell$ channel.

individual results.

The spin and parity quantum numbers of the resonance have also been investigated, testing them against alternative models, both in the fixed-hypothesis and in the CP-mix scenarios, where the observed particle would violate the CP symmetry. In particular, the $J^P = 0^+_h$, 0^-, $1^\pm$ and 2^+ hypotheses have been studied by the ATLAS and CMS collaborations, using all bosonic channels. No significant deviation from a pure SM composition has been found.

REFERENCES

[1] ATLAS Collaboration, Phys. Lett. **B716**, 1–29 (2012), arXiv:1207.7214 [hep-ex] .
[2] CMS Collaboration, Phys. Lett. **B716**, 30–61 (2012), arXiv:1207.7235 [hep-ex] .
[3] ATLAS Collaboration, Phys. Rev. **D90**, p. 052004 (2014), arXiv:1406.3827 [hep-ex] .
[4] CMS Collaboration, Eur. Phys. J. **C75**, p. 212 (2015), arXiv:1412.8662 [hep-ex] .
[5] ATLAS and CMS Collaborations, Phys. Rev. Lett. **114**, p. 191803 (2015), arXiv:1503.07589 [hep-ex] .
[6] ATLAS Collaboration, Eur. Phys. J. **C75**, p. 476 (2015), arXiv:1506.05669 [hep-ex] .
[7] CMS Collaboration, Phys. Rev. **D92**, p. 012004 (2015), arXiv:1411.3441 [hep-ex] .
[8] ATLAS Collaboration, Eur. Phys. J. **C75**, p. 231 (2015), arXiv:1503.03643 [hep-ex] .

Proceedings of the LHCP2015 Conference, St. Petersburg, Russia, August 31 - September 5, 2015

Editors: V.T. Kim and D.E. Sosnov

Higgs Physics with Heavy New Physics

DAVID MARZOCCA

Physik-Institut, Universität Zürich, CH-8057 Zürich, Switzerland

marzocca@physik.uzh.ch

Abstract. We introduce a set of pseudo-observables (PO), defined from on-shell amplitudes, characterizing the properties of Higgs decays in generic extensions of the Standard Model with no new particles below the Higgs mass. These PO provide a generalization of the *kappa*-framework used by the LHC experiments and allow for the systematic inclusion of higher order QED corrections. Symmetries of the new-physics sector, such as CP invariance, lepton-universality, and custodial symmetry imply relations among the PO, that could be tested directly from Higgs data. The same assumption of heavy new physics, augmented by assuming that the Higgs is part of an electroweak doublet, allows for the introduction of the linear effective field theory (SMEFT) for describing the effect of new physics at low energy. In this context, the PO can be matched to the Wilson coefficients of the SMEFT, providing a way to test experimentally the SMEFT predictions.

1 INTRODUCTION

One of the main goals of Higgs studies at the LHC Run-2 and at future colliders will be a more precise and complete characterization of all its properties. Given we presently do not know the specific theory lying beyond the SM, it is important to develop a framework capable of collecting all the experimental information which will be available on the Higgs with the least possible theoretical bias. At the same time, a good framework should condensate the experimental information in a few well-defined quantities of easy theoretical interpretation.

Pseudo-observables (PO), defined directly from physical properties of on-shell amplitudes, are perfectly suited for this goal. Experimentally, PO correspond to some idealized observables, stripped of collider and soft radiation effects. Theoretically, they are well defined objects in quantum field theory, related to physical properties of the process in question. In this context, we define a set of PO capable of describing in great generality all Higgs boson decays.

In this proceedings contribution we summarize the main results, referring to published works for the details [1, 2, 3, 4]. In Sect. 2 we present the PO relevant to Higgs decays to two fermions while in Sect. 3 we describe the PO necessary to characterize the decays to vector currents, such as $h \to \gamma\gamma$ and $h \to 4f$, and how QED radiative corrections are a necessary – and sufficient – ingredient in order to reach the percent precision. In Sect. 4 and in Sect. 5 we study the predictions which follow from assuming specific symmetries of the new physics sector, or an underlying linear effective field theory.

2 HIGGS DECAYS TO TWO FERMIONS

The kinematics of two-body decays is fixed by momentum conservation. This implies that, if the polarization of the final state is not observed, the only accessible observable is the decay rate. The Higgs PO relevant to decays into two fermions are defined by the amplitude [1, 5]

$$\mathcal{A}(h \to f\bar{f}) = -i\frac{y_{\text{eff}}^{f,\text{SM}}}{\sqrt{2}}\bar{f}\left(\kappa_f + i\lambda_f^{\text{CP}}\gamma_5\right)f \,. \tag{1}$$

where $f = b, \tau, c, \mu$ and, if h is a CP-even state, λ_f^{CP} are CP-violating PO. As in the widely used κ-formalism, the best SM prediction for the decay rate is recovered in the $\kappa_f \to 1$, $\lambda_f^{\text{CP}} \to 0$ limit. With this notation, the inclusive decay

rates are

$$\Gamma(h \to f\bar{f})_{(\text{incl})} = \left[\kappa_f^2 + (\lambda_f^{\text{CP}})^2\right] \Gamma(h \to f\bar{f})^{(\text{SM})}_{(\text{incl})} \,, \tag{2}$$

where $\Gamma(h \to f\bar{f})^{(\text{SM})}_{(\text{incl})}$ is the best SM prediction for the decay rate, see e.g. Ref. [6], which fixes the parameter $y_{\text{eff}}^{f,\text{SM}}$. The ratio $\lambda_f^{\text{CP}}/\kappa_f$ can be probed only if the polarization of the final state fermions is accessible.

3 HIGGS DECAYS TO SPIN-1 CURRENTS

A very important class of Higgs decays, thanks to the rich kinematics they offer, are those into two spin-1 currents. This class includes two-body on-shell decays into gauge bosons such as $h \to \gamma\gamma$ and $h \to Z\gamma$, as well as $h \to f\bar{f}\gamma$ and all $h \to 4f$ decays. The $h \to 4f$ amplitudes are particularly interesting since they allow us to probe the effective hW^+W^- and hZZ interaction terms, which cannot be probed on-shell.

All the physical information on these processes is contained in the three-point correlation functions of the Higgs boson and two fermion currents (either both neutral or charged),

$$\langle 0|\mathcal{T}\left\{J_f^\mu(x), J_{f'}^\nu(y), h(0)\right\}|0\rangle \,, \tag{3}$$

where all the states are on-shell. These are probed by the experiments in $h \to 4f$ decays, as well as in Higgs associated production ($pp \to h + W, Z$) and in Higgs production via vector-boson fusion. In the following we focus on the decays, the implementation of PO in these Higgs production processes has been recently discussed in Ref. [7].

The correlation functions of Eq. (3) contain physical poles corresponding to the propagation of intermediate electroweak (EW) gauge bosons, i.e. non-local terms in which $x, y \neq 0$. Generic heavy new physics also generates local terms in which x and/or $y = 0$. The Higgs PO are defined directly from the residues of these different poles. This implies they are gauge-invariant quantities defined at all orders in perturbation theory. Extracting this kinematical (pole) structure from data would allow us both to determine the effective coupling of h to all the SM gauge bosons, as well as to investigate possible couplings of h to new massive states.

The explicit expansion of the amplitude and the definition of the PO can be found in Refs. [1, 5].[1] We present here a summary of all the Higgs decay processes (into on-shell particles) contained in this class and the PO necessary to describe each of them:

Process	PO
$h \to \gamma\gamma$	$\kappa_{\gamma\gamma},\ \lambda^{\text{CP}}_{\gamma\gamma}$
$h \to Z\gamma$	$\kappa_{Z\gamma},\ \lambda^{\text{CP}}_{Z\gamma}$
$h \to \gamma 2\nu$	$\kappa_{Z\gamma},\ \lambda^{\text{CP}}_{Z\gamma}$
$h \to \gamma 2\ell$	$\kappa_{\gamma\gamma},\ \lambda^{\text{CP}}_{\gamma\gamma},\ \kappa_{Z\gamma},\ \lambda^{\text{CP}}_{Z\gamma}$
$h \to Z 2\ell$	$\kappa_{ZZ},\ \epsilon_{ZZ},\ \epsilon^{\text{CP}}_{ZZ},\ \kappa_{Z\gamma},\ \lambda^{\text{CP}}_{Z\gamma},\ \epsilon_{Z\ell_L},\ \epsilon_{Z\ell_R}$
$h \to 2\ell 2\ell'$	$\kappa_{ZZ},\ \epsilon_{ZZ},\ \epsilon^{\text{CP}}_{ZZ},\ \kappa_{Z\gamma},\ \lambda^{\text{CP}}_{Z\gamma},\ \kappa_{\gamma\gamma},\ \lambda^{\text{CP}}_{\gamma\gamma},\ \epsilon_{Z\ell_L},\ \epsilon_{Z\ell_R},\ \epsilon_{Z\ell'_L},\ \epsilon_{Z\ell'_R}$
$h \to 4\ell$	$\kappa_{ZZ},\ \epsilon_{ZZ},\ \epsilon^{\text{CP}}_{ZZ},\ \kappa_{Z\gamma},\ \lambda^{\text{CP}}_{Z\gamma},\ \kappa_{\gamma\gamma},\ \lambda^{\text{CP}}_{\gamma\gamma},\ \epsilon_{Z\ell_L},\ \epsilon_{Z\ell_R}$
$h \to \bar{\ell}\ell 2\nu$	$\begin{cases} \kappa_{ZZ},\ \epsilon_{ZZ},\ \epsilon^{\text{CP}}_{ZZ},\ \kappa_{Z\gamma},\ \lambda^{\text{CP}}_{Z\gamma},\ \epsilon_{Z\ell_L},\ \epsilon_{Z\ell_R},\ \epsilon_{Z\nu} \\ \kappa_{WW},\ \epsilon_{WW},\ \epsilon^{\text{CP}}_{WW},\ \epsilon_{W\ell},\ \phi_{W\ell} \end{cases}$
$h \to \bar{\ell}\ell' 2\nu$	$\kappa_{WW},\ \epsilon_{WW},\ \epsilon^{\text{CP}}_{WW},\ \epsilon_{W\ell},\ \phi_{W\ell},\ \epsilon_{W\ell'},\ \phi_{W\ell'}$

In this table $\ell = e, \mu, \tau$ while ν indicates any of the three neutrino species. The W boson contact terms are in general complex numbers: $\epsilon_{W\ell} e^{i\phi_{W\ell}}$. The λ_x^{CP}, ϵ_x^{CP} and $\phi_{W\ell}$ terms describe CP-violating interactions if the Higgs is a CP-even state. Since many PO enter in more than one process, the best constraints will be obtained by combining different Higgs decay channels.

Radiative corrections

While the PO, defined from the correlation function in Eq. (3), describe in full generality the *short-distance* physics of $h \to 4\ell$ decays, in order to compare this amplitude decomposition with data also the *long-distance* contribution due to soft and collinear photon emission (i.e. the leading QED radiative corrections) must be taken into account.

[1] Here we use the same notation for the PO as in [5].

By assuming that these long-distance effects are free from new physics contribution, they can be implemented via universal convolution functions (or, equivalently, QED showering algorithms), independently on the short-distance contributions to the amplitude.

In Ref. [3] we showed that soft and collinear QED radiation induces a $\sim$ 15% effect on the di-lepton invariant mass spectrum. This enhancement is due both to the $\sim \log(m_h^2/m_*^2)$ factor, where m_* is the infrared cutoff, and to the presence of the Z boson peak in the spectrum. Including such effects is thus necessary in order to reach $\sim$ 10 % precision on the PO. Moreover, by comparing our results to the full next-to-leading-order (NLO) computation of the amplitude in the SM, we showed that the inclusion of QED effects is sufficient to within an accuracy of $\sim$ 1%. The inclusion of soft and collinear QED corrections allows to match the PO to some specific theory at NLO accuracy. The same QED radiation effects can be obtained, on an event-by-event basis, also by showering algorithms such as PHOTOS or PYTHIA and thus can be easily implemented in phenomenological analysis.

Tools

In order to facilitate the experimental analysis of Higgs decays in this framework, we implemented the Higgs PO presented here in a FeynRules model, *HiggsPO* [5]. This package can be used to generate Higgs decay events within MadGraph5_aMC@NLO. The Higgs production part, as well as final state showering effects, can be simulated by other dedicated codes.

4 SYMMETRY LIMITS

Symmetries of the new physics sector predict relations among the PO. On the one hand, these relations can be used, by assuming some symmetry, to reduce the number of independent PO to be studied. On the other hand, and more importantly, testing directly these relations from Higgs data would provide a precious insight into the symmetries of the new physics sector [1].

Flavor universality. This corresponds to enlarging the flavor symmetry to the $U(3)^5$ group. In terms of Higgs PO it implies that the contact terms are independent on the generation.

$$\epsilon_{Z\ell_L} = \epsilon_{Z\ell'_L}\,, \qquad \epsilon_{Z\ell_R} = \epsilon_{Z\ell'_R}\,, \qquad \epsilon_{Z\nu_\ell} = \epsilon_{Z\nu_{\ell'}}\,, \qquad \epsilon_{W\ell_L} = \epsilon_{W\ell'_L}\,, \qquad \phi_{W\ell_L} = \phi_{W\ell'_L}\,. \tag{4}$$

CP conservation. If the Higgs is a CP-even state and CP is conserved, then various PO vanish:

$$\lambda^{\rm CP}_{\gamma\gamma} = \lambda^{\rm CP}_{Z\gamma} = \epsilon^{CP}_{ZZ} = \epsilon^{CP}_{WW} = \phi_{We_L} = \phi_{W\mu_L} = 0\,. \tag{5}$$

Custodial symmetry. This is an accidental approximate symmetry of the SM, explicitly broken only by the hypercharge and by the small Yukawa couplings. It protects the electroweak ρ parameter from receiving sizable corrections. If the new physics sector also respects this symmetry then some relations among the PO can be obtained, see Refs. [1, 8]:

$$\epsilon_{WW} = c_w^2\epsilon_{ZZ} + 2c_w s_w \epsilon_{Z\gamma} + s_w^2\epsilon_{\gamma\gamma}\,, \tag{6}$$

$$\epsilon^{CP}_{WW} = c_w^2\epsilon^{CP}_{ZZ} + 2c_w s_w \epsilon^{CP}_{Z\gamma} + s_w^2\epsilon^{CP}_{\gamma\gamma}\,, \tag{7}$$

$$\kappa_{WW} - \kappa_{ZZ} = -\frac{2}{g}\left(\sqrt{2}\epsilon_{W\ell^i_L} + 2c_w\epsilon_{Z\ell^i_L}\right)\,, \tag{8}$$

$$\epsilon_{W\ell^i_L} = \frac{c_w}{\sqrt{2}}(\epsilon_{Z\nu^i_L} - \epsilon_{Z\ell^i_L})\,. \tag{9}$$

5 HIGGS PO IN THE LINEAR EFT

If the Higgs boson, h, is part of a $SU(2)_L$ doublet and the new physics is above the EW scale, a good description of deformations from the SM at the EW scale is provided by the Standard Model linear effective field theory (SMEFT). Under these assumptions, many processes involving the Higgs can be related to EW precision observables, well measured at LEP, which do not involve the physical Higgs particle. Testing if such relations are satisfied represents a very powerful tool to test the SMEFT assumption. Working at the leading order in the effective theory, the Higgs PO

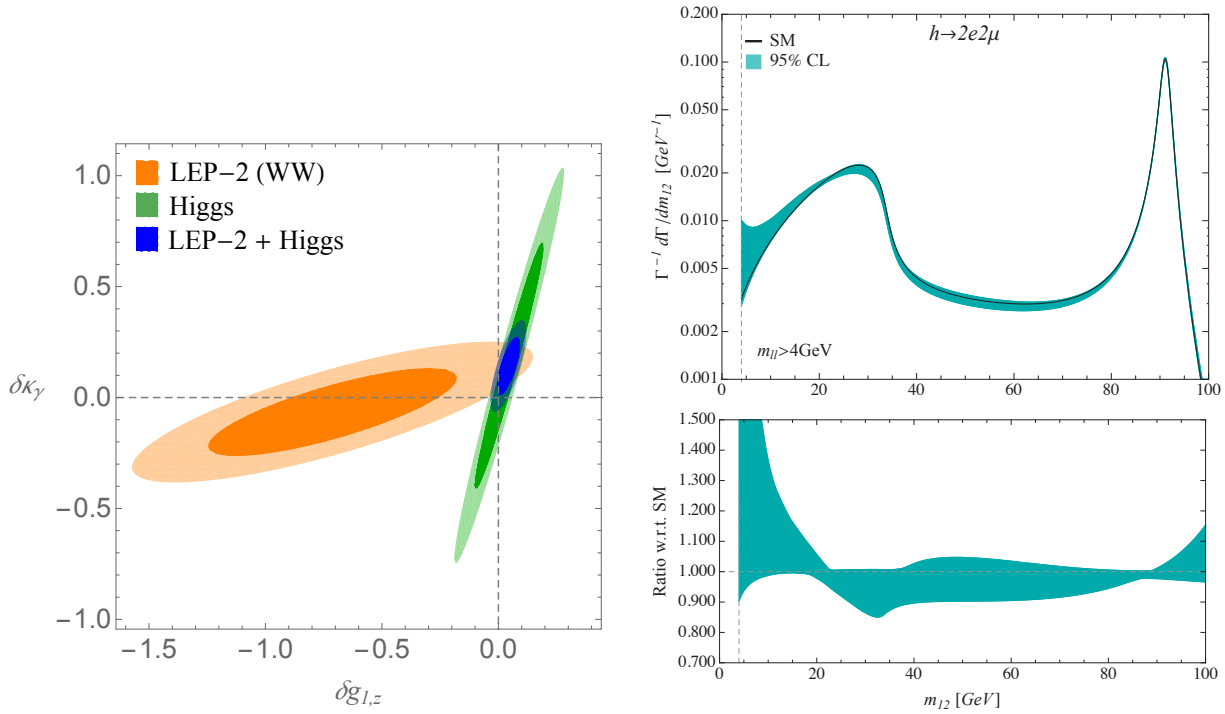

FIGURE 1. Left: Allowed 68% and 95% CL region in the $\delta g_{1,z}$-$\delta\kappa_\gamma$ plane after considering LEP-2 WW production data (TGC), Higgs data, and the combination of both datasets. **Right:** Allowed variation of the normalized differential decay rate $h \to 2e2\mu$ in m_{ee} (or, equivalently, $m_{\mu\mu}$) when varying all the PO withing the 95% CL bounds from our combined LEP-2 plus Higgs fit.

can be expressed as linear combinations of the Wilson coefficients of the dimension-6 operators [1, 2]. Analogously, the EW pseudo-observables, in particular the Z- and W-pole effective couplings, the W mass, and the anomalous triple gauge boson couplings (TGC), can be expressed as linear combinations of the same Wilson coefficients. By inverting these linear combinations it is possible to derive basis-independent relations between Higgs and EW PO [9, 1, 2].

One the one hand, this allows to combine Higgs data with LEP-I and LEP-II data (mainly WW production) in order to derive strong and robust bounds on the EFT coefficients, in particular the TGC. In Ref. [4] we performed a combined fit of LEP-II WW production data [10] and Higgs data from the LHC Run-I in the context of the SMEFT, assuming minimal flavor violation. In Fig. 1 (left) we show the bounds we obtain in two TGC parameters, when all other coefficients entering the fit are profiled. While both LEP-II and Higgs data present a flat directions in this plane when taken separately, the combination of the two datasets allows to cast strong bounds on all TGC. On the other hand, via this global analysis it is possible to derive strong bounds on the Higgs PO [2, 4] and study the size of the allowed effects in the $h \to 4\ell$ phenomenology, in particular in the decay rate and in the 4ℓ spectrum distributions. Our study shows that flavor non-universal effects are strongly suppressed due to the LEP-I bounds and that the deviations in the di-lepton invariant mass spectrum are constrained to be smaller than ~ 10 %, as shown in Fig. 1 (right). Such bounds can be interpreted as predictions of the linear EFT approach, which can be tested by Higgs data. Any observation of deviations from these predictions would have deep consequences for our understanding of the NP sector: it would imply that the Higgs is not part of an $SU(2)_L$ doublet (at least in part), or could also signal deviations from flavour universality in the lepton sector.

ACKNOWLEDGMENTS

I am grateful to M. Bordone, M. Gonzalez-Alonso, A. Greljo, A. Falkowski, G. Isidori and A. Pattori for the stimulating collaboration on the works presented in this talk. The author is supported in part by the Swiss National Science Foundation (SNF) under contract 200021-159720.

REFERENCES

[1] M. Gonzalez-Alonso, A. Greljo, G. Isidori and D. Marzocca, Eur. Phys. J. C **75** (2015) 3, 128 [arXiv:1412.6038 [hep-ph]].

[2] M. Gonzalez-Alonso, A. Greljo, G. Isidori and D. Marzocca, Eur. Phys. J. C **75** (2015) 7, 341 [arXiv:1504.04018 [hep-ph]].

[3] M. Bordone, A. Greljo, G. Isidori, D. Marzocca and A. Pattori, Eur. Phys. J. C **75** (2015) 8, 385 [arXiv:1507.02555 [hep-ph]].

[4] A. Falkowski, M. Gonzalez-Alonso, A. Greljo and D. Marzocca, arXiv:1508.00581 [hep-ph].

[5] A. Greljo, G. Isidori and D. Marzocca, *HiggsPO*, www.physik.uzh.ch/data/HiggsPO .

[6] S. Heinemeyer *et al.* [LHC Higgs Cross Section Working Group Collaboration], arXiv:1307.1347 [hep-ph].

[7] A. Greljo, G. Isidori, J. M. Lindert and D. Marzocca, arXiv:1512.06135 [hep-ph].

[8] R. Contino, M. Ghezzi, C. Grojean, M. Muhlleitner and M. Spira, JHEP **1307** (2013) 035 [arXiv:1303.3876].

[9] A. Pomarol, arXiv:1412.4410 [hep-ph].

[10] A. Falkowski and F. Riva, JHEP **1502** (2015) 039 [arXiv:1411.0669 [hep-ph]].

Proceedings of the LHCP2015 Conference, St. Petersburg, Russia, August 31 - September 5, 2015

Editors: V.T. Kim and D.E. Sosnov

Extended Higgs Sector: 2HDM, MSSM and NMSSM

E. BOOS[1,a)] and R. NEVZOROV[2,3,b)]

[1]*Skobeltsyn Institute of Nuclear Physics, Lomonosov Moscow State University, Moscow, Russia.*
[2]*ARC Centre of Excellence for Particle Physics at the Terascale and CSSM, Department of Physics, The University of Adelaide, Adelaide SA 5005, Australia.*
[3]*Institute for Theoretical and Experimental Physics, B. Cheremushkinskaya ulitsa 25, Moscow 117 259, Russia.*

[a)]Corresponding author: boos@theory.sinp.msu.ru
[b)]roman.nevzorov@adelaide.edu.au

Abstract. We review some aspects of Higgs phenomenology within the Two Higgs Model (2HDM), Minimal Supersymmetric Standard Model (MSSM) and Next–to–Minimal Supersymmetric Standard Model (NMSSM).

INTRODUCTION

Nowadays there are compelling indications that a new particle with a mass around $\sim$ 125 GeV discovered at the LHC in 2012 is consistent with the Standard Model (SM) Higgs boson. At the moment, the measured signal strengths into $\gamma\gamma$, WW, ZZ channels favour the interpretation of the observed particle as a neutral scalar state with spin-0. Nevertheless in order to assess its nature thoroughly more data is needed. The more detailed analysis of the signal strengths in different channels can in principle reveal discrepancies from the predictions of the SM that would provide a smoking gun signal of the new physics. Indeed, there are serious reasons to believe that the SM with the minimal Higgs content is not the ultimate theoretical structure responsible for electroweak (EW) symmetry breaking since it is unable to address many fundamental questions. For example, one can expect that at ultra–high energies the SM gets embedded in an underlying theory that provides a framework for unification of all interactions including gravity. Such underlying theory should also explain the weakness of gravitational force at low energies as compared with the strong and EW interactions. However, if the SM is embedded in a more fundamental theory characterized by the Planck scale $M_{Pl} \approx 10^{19}$ GeV, then the SM Higgs mechanism suffers from a stability crisis. In other words because of the quadratical scale dependence of the radiative corrections , the Higgs boson tends to acquire a mass of order of M_{Pl}. Practically all extensions of the SM predict more complicated Higgs sector leading to the presence of other neutral and/or charged Higgs bosons. An observation of any of such new states provides another possible smoking gun indication of the new physics.

Low–scale supersymmetry (SUSY) stabilizes the scale hierarchy. The Higgs sector of the Minimal Supersymmetric Standard Model (MSSM) involves two Higgs doublets. The inclusion of the superfields associated with the second Higgs doublet allows to achieve anomaly cancellation and induce masses for all quarks and leptons. In the MSSM there exists an upper limit on the lightest Higgs boson mass of about 130 – 135 GeV (see *e.g.* [1] and references therein). Thus the MSSM can be consistent with a 125 – 126 GeV SM-like Higgs boson. The local version of SUSY (supergravity) leads to a partial unification of the SM gauge interactions with gravity near the Planck scale. When SUSY partners of ordinary particles have TeV scale masses the lightest SUSY particle in the MSSM can be stable and play the role of dark matter. The unification of gauge coupling constants, which takes place in the MSSM and its simplest extensions at high energies, makes possible the incorporation of the EW and strong gauge interactions within Grand Unified Theories (GUTs) [2] based on simple gauge groups such as $SU(5)$, $SO(10)$ or E_6 that permits to explain the peculiar assignment of $U(1)_Y$ charges postulated in the SM and to address the observed mass hierarchy of quarks and leptons.

TWO HIGGS DOUBLET EXTENSION OF THE SM

As has been already mentioned in the Introduction, SUSY extensions of the SM contain two Higgs doublets. Both doublets may survive down to the EW scale. The most general renormalizable $SU(2)_W \times U(1)_Y$ gauge invariant potential of the two Higgs doublet model (2HDM) is given by [3]

$$V(\Phi_1,\Phi_2) = m_{11}^2\Phi_1^\dagger\Phi_1 + m_{22}^2\Phi_2^\dagger\Phi_2 - \left(m_{12}^2\Phi_1^\dagger\Phi_2 + h.c.\right) + \frac{\lambda_1}{2}(\Phi_1^\dagger\Phi_1)^2 + \frac{\lambda_2}{2}(\Phi_2^\dagger\Phi_2)^2 + \lambda_3(\Phi_1^\dagger\Phi_1)(\Phi_2^\dagger\Phi_2) \qquad (1)$$

$$+\lambda_4(\Phi_1^\dagger\Phi_2)(\Phi_2^\dagger\Phi_1) + \left\{\frac{\lambda_5}{2}(\Phi_1^\dagger\Phi_2)^2 + \left[\lambda_6(\Phi_1^\dagger\Phi_1) + \lambda_7(\Phi_2^\dagger\Phi_2)\right](\Phi_1^\dagger\Phi_2) + h.c.\right\}.$$

It is easy to see that the number of couplings in the 2HDM potential compared with the SM grows from two to ten. Furthermore, four of them m_3^2, λ_5, λ_6 and λ_7 can be complex, inducing CP–violation in the Higgs sector. At the physical minimum of the scalar potential (1) the Higgs fields Φ_1 and Φ_2 develop vacuum expectation values (VEVs) v_1 and v_2 respectively. When CP is conserved one can use the following parametrisation for Φ_1 and Φ_2

$$\Phi_a = \begin{pmatrix} \phi_a^+ \\ (v_a + \rho_a + i\,\eta_a)/\sqrt{2} \end{pmatrix}, \qquad a = 1,2\,. \qquad (2)$$

The non–zero VEVs v_1 and v_2 break the $SU(2)_W \times U(1)_Y$ gauge symmetry to $U(1)_{em}$ associated with electromagnetism. The combination of the Higgs VEVs $v = \sqrt{v_1^2 + v_2^2}$ is fixed by the Fermi scale, i.e. $v = 246\,\mathrm{GeV}$. On the other hand the ratio of the Higgs VEVs remains arbitrary. Hence it is convenient to introduce $\tan\beta = v_2/v_1$.

Initially the Higgs sector of the two Higgs doublet extension of the SM involves eight degrees of freedom. Three of them become massless Goldstone modes which are swallowed by the $W^\pm$ and Z gauge bosons. As a consequence the $W^\pm$ and Z bosons gain masses $M_W = g_2 v/2$ and $M_Z = \bar{g}v/2$ where $\bar{g} = \sqrt{g_2^2 + g_1^2}$ while g_2 and g_1 are the gauge couplings of the $SU(2)_W$ and $U(1)_Y$ interactions. When CP is conserved the remaining five physical degrees of freedom form two charged, one CP–odd and two CP-even Higgs states.

The Yukawa interactions of the Higgs doublets Φ_1 and Φ_2 with quarks and leptons may generate non–diagonal flavour transitions. In order to avoid flavor changing neutral currents (FCNC) one applies Glashow-Weinberg-Paschos condition: all fermions with the same quantum numbers couple to the same Higgs multiplet [4, 5]. The common way to realize the GWP condition is to impose a certain protecting custodial Z_2 symmetry ($\Phi_1 \to \Phi_1$, $\Phi_2 \to -\Phi_2$) that forbids potentially dangerous couplings of the Higgs fields to quarks and leptons.

Such a custodial symmetry implies that the Higgs couplings λ_6 and λ_7 vanish. This symmetry also requires the down-type quarks to couple to just one Higgs doublet, Φ_1 say, while the up-type quarks couple either to the same Higgs doublet Φ_1 (Type I) or to the second Higgs doublet Φ_2 (Type II) but not both. In addition the right down-type lepton may couple to the first or second Higgs doublet oppositely to the right down-type quarks leading to the models of Type 3 (Lepton-specific) or Type 4 (Flipped) [6]. The custodial Z_2 symmetry also forbids the mixing term $m_{12}^2(\Phi_1^\dagger\Phi_2)$ in the Higgs potential (1). However usually a soft violation of the Z_2 symmetry by dimension–two terms is allowed, since it does not induce Higgs–mediated tree–level FCNC.

There are many scenarios in 2HDM parameter space still allowed by all the measurements and constrains, in particular, by the Higgs coupling measurements. As an example one can mention recently refreshed [7] so called alignment without decoupling scenario, in which the other Higgs scalars with masses not significantly larger than m_h are not decoupled.

HIGGS SECTOR OF THE MSSM

At the tree level the couplings of the Higgs doublets in the MSSM are basically the same as in the 2HDM of type II. Nevertheless the structure of the tree level Higgs potential is considerably simpler in the MSSM than in the 2HDM of type II. Since the Lagrangian of SUSY models is fully determined by the structure of the gauge interactions and by the superpotential of the model under consideration the quartic Higgs couplings are not independent parameters. In

the MSSM the quartic part of the Higgs potential is set by the contribution of D–terms. Therefore at the tree level the quartic Higgs couplings are given by

$$\lambda_1 = \lambda_2 = \frac{\bar{g}^2}{4}, \qquad \lambda_3 = \frac{g_2^2 - g'^2}{4}, \qquad \lambda_4 = -\frac{g_2^2}{2}, \qquad \lambda_5 = \lambda_6 = \lambda_7 = 0\,. \tag{3}$$

As a consequence in these relations the masses and couplings of the Higgs states can be parametrised in terms of the mass of the pseudoscalar Higgs boson m_A and $\tan\beta$ only. The dependence of Higgs boson masses as a function of m_A at various $\tan\beta$ including loop corrections is shown explicitely in [8]. In particular, the analytic expressions for the masses of the charged and CP–even Higgs eigenstates takes the form

$$m^2_{H^\pm} = m_A^2 + M_W^2\,, \qquad m^2_{h,H} = \frac{1}{2}\left(M_{11}^2 + M_{22}^2 \mp \sqrt{(M_{22}^2 - M_{11}^2)^2 + 4M_{12}^4}\right), \tag{4}$$

where

$$M_{11}^2 = M_Z^2 \cos^2 2\beta\,, \qquad M_{12}^2 = -\frac{1}{2} M_Z^2 \sin 4\beta\,, \qquad M_{22}^2 = m_A^2 + M_Z^2 \sin^2 2\beta\,.$$

The qualitative pattern of the Higgs spectrum depends very strongly on m_A. With increasing m_A the masses of all the Higgs particles grow. At very large values of m_A ($m_A^2 \gg v^2$), the lightest Higgs boson mass approaches its theoretical upper limit $\sqrt{M_{11}^2}$, while the heaviest CP–even, CP–odd and charged states are almost degenerate around m_A. Thus at the tree–level m_h is always less than $M_Z \cos 2\beta$. When the Higgs spectrum is rather hierarchical, i.e. $m_A^2 \gg v^2$, the couplings of the lightest CP–even Higgs state are almost the same as the ones of the Higgs boson within the SM.

The inclusion of loop corrections raises the mass of the SM–like Higgs boson in the MSSM. In the simplest SUSY extensions of the SM the dominant contribution to m_h comes from the loops involving the top–quark and its superpartners because of their large Yukawa coupling h_t. When SUSY breaking scale M_S is considerably larger than M_Z and the masses of the superpartners of the top quark $m_{t_1} \simeq m_{t_2} \simeq M_S \gg v$ the contribution of the one–loop corrections to m_h^2 in the leading approximation can be written as

$$m_h^2 \approx M_Z^2 \cos^2 2\beta + \Delta m_h^2, \qquad \Delta m_h^2 \simeq \frac{3 m_t^4}{2\pi^2 v^2}\left[\frac{X_t^2}{M_S^2}\left(1 - \frac{1}{12}\frac{X_t^2}{M_S^2}\right) + \ln\left(\frac{M_S^2}{m_t^2}\right)\right], \tag{5}$$

where X_t is a stop mixing parameter and m_t is the running top quark mass . From Equation (5) it follows that the sufficiently large loop corrections to the SM–like Higgs mass can be obtained only if $M_S \gg m_t$ and the ratio $|X_t/M_S|$ is also large. The contribution of the one–loop corrections (5) attains its maximal value for $X_t^2 = 6\, M_S^2$. This is the so–called maximal mixing scenario. Simple estimations show that in order to raise the mass of the SM–like Higgs state to 125 GeV we need at large values of $\tan\beta$ a total loop contribution of $\Delta m_h^2 \simeq (85\,\mathrm{GeV})^2$ which is nearly as large as the value of the tree level mass. So large contribution of loop corrections to m_h implies that stops are substantially heavier than M_Z. As a consequence a tuning at least of order 1% in the MSSM is required to ensure the stabilisation of the EW scale. The value 125 GeV is somewhat smaller than the upper limit on the lightest Higgs mass one can achieve in the maximal mixing scenario. Scenarios with relaxed values for X_t called m_h^{mod+} and m_h^{mod+} where formulated and worked out in [9] and intensively used in experimental analyses [10, 11]. Simple approxiative formulas for relations between the Higgs masses including corrections are given recently in [12] assuming the the mass of the lightest Higgs fixed at 125 GeV. The approximation is valid for rather low $\tan\beta$. Corresponding scenario called hMSSM has been also considered in experimental searches (see [11]).

NATURAL NMSSM HIGGS BOSONS

In the simplest extension of the MSSM, the Next–to–Minimal Supersymmetric Standard Model (NMSSM), the superpotential is invariant with respect to the discrete transformations $\Phi_i \to e^{2\pi i/3}\Phi_i$ of the Z_3 group (for recent review see [13]). The term $\mu(H_u H_d)$ does not meet this requirement. Therefore it is replaced in the superpotential by

$$W_H = \lambda S\,(H_1 H_2) + \frac{1}{3}\kappa S^3\,, \tag{6}$$

where S is an additional superfield which is a singlet with respect to $SU(2)_W$ and $U(1)_Y$ gauge transformations. A spontaneous breakdown of the $SU(2)_W \times U(1)_Y$ symmetry gives rise to the non–zero VEV of singlet field $< S >= s/\sqrt{2}$ and an effective μ parameter is generated ($\mu_{eff} = \lambda s/\sqrt{2}$).

The NMSSM Higgs potential can be written as a sum

$$V = V_F + V_D + V_{soft} + \Delta V\,, \tag{7}$$

$$V_F = \lambda^2|S|^2(|H_1|^2 + |H_2|^2) + \lambda^2|(H_1H_2)|^2 + \lambda\kappa\left[S^{*2}(H_1H_2) + h.c.\right] + \kappa^2|S|^4\,, \tag{8}$$

$$V_D = \frac{g_2^2}{8}\left(H_1^+\sigma_a H_1 + H_2^+\sigma_a H_2\right)^2 + \frac{g'^2}{8}\left(|H_1|^2 - |H_2|^2\right)^2\,, \tag{9}$$

$$V_{soft} = m_1^2|H_1|^2 + m_2^2|H_2|^2 + m_S^2|S|^2 + \left[\lambda A_\lambda S(H_1H_2) + \frac{\kappa}{3}A_\kappa S^3 + h.c.\right]. \tag{10}$$

At the tree level the Higgs potential (7) is described by the sum of the first three terms. V_F and V_D are the F and D terms. Their structure is fixed by the superpotential (6) and the EW gauge interactions. The soft SUSY breaking terms are collected in V_{soft}. The set of soft SUSY breaking parameters involves soft masses m_1^2, m_2^2, m_S^2 and trilinear couplings A_κ, A_λ. The last term in Eq. (7), ΔV, corresponds to the contribution of loop corrections.

At the physical vacuum of the Higgs potential (7) H_1, H_2 and S acquire non-zero VEVs. The equations for the extrema of the full Higgs boson effective potential (7), i.e.

$$\frac{\partial V}{\partial s} = 0\,, \qquad \frac{\partial V}{\partial v_1} = 0\,, \qquad \frac{\partial V}{\partial v_2} = 0\,, \tag{11}$$

can be used to express soft scalar masses m_S^2, m_1^2, and m_2^2 in terms of other parameters and Higgs VEVs. As a result at the tree-level, the spectrum of the NMSSM Higgs bosons and their couplings can be parametrised in terms of the six parameters: $\lambda, \kappa, \tan\beta, A_\kappa, A_\lambda$ and μ_{eff}. Relations between masses of neutral Higgs states are shown in [14].

It is well known that the fine-tuning of the MSSM could be ameliorated in the NMSSM. The theoretical upper bound on the mass of the lightest Higgs boson in this SUSY model is given by

$$m_h^2 \;\approx\; M_Z^2\cos^2 2\beta + \frac{\lambda^2 v^2}{2}\sin^2 2\beta + \Delta m_h^2. \tag{12}$$

Contrary to the MSSM, for $\lambda v > M_Z$, the tree-level contributions to m_h are maximized for moderate values of $\tan\beta$. For example, setting $\lambda = 0.6$ and $\tan\beta = 2$, these tree-level contributions raise the Higgs boson mass to about 100 GeV requiring $\Delta m_h^2 \simeq (75\,\text{GeV})^2$ in order to match the 125 GeV Higgs mass value [15]. Thus with a 125 GeV Higgs boson, due to the fine-tuning of the MSSM, the NMSSM has emerged as a more natural alternative.

Motivated by the fine-tuning consideration it is worth to focus on large values of λ, i.e. $\lambda \gtrsim 0.6$, and the moderate values of $\tan\beta$, i.e. $\tan\beta = 1.5 - 3$, that result in the relatively large values of the top quark Yukawa coupling h_t at low energies. The growth of Yukawa couplings h_t, λ and κ at the EW scale entails the increase of their values at the Grand Unification scale M_X resulting in the appearance of the Landau pole that spoils the applicability of perturbation theory at high energies [16]–[18]. The requirement of validity of perturbation theory up to the scale M_X sets an upper limit on the low energy value of $\lambda(M_Z)$ for each fixed set of $\kappa(M_Z)$ and $h_t(M_t)$ (or $\tan\beta$). In particular, the large value of $\lambda(M_Z) \gtrsim 0.6$ implies that $|\kappa(M_Z)| \lesssim 0.3$ [19].

When $\lambda \gg \kappa$, the Higgs spectrum in the NMSSM has a hierarchical structure and all Higgs matrices can be diagonalised using the perturbation theory [20]-[22]. In this case the heaviest CP–even, CP–odd and charged states are almost degenerate. Their mass scale is set by $\mu_{eff}\tan\beta$ [23]-[25]. Two other CP–even Higgs states and the lightest Higgs pseudoscalar tend to be considerably lighter than the heaviest Higgs bosons. In order to investigate the discovery prospects for the NMSSM Higgs bosons at the High-Energy LHC in this scenario the following part of the parameter space associated with

$$0.6 \le \lambda \le 0.7, \quad -0.3 \le \kappa \le 0.3, \quad 1.5 \le \tan\beta \le 2.5, \quad 100\text{GeV} \le |\mu_{eff}| \le 185\text{GeV}, \tag{13}$$

$$-2\text{TeV} \le A_\lambda, A_\kappa, A_t \le 2\text{TeV}, \quad 100\ \text{GeV} \le M_1 \le 1\ \text{TeV}, \quad 200\ \text{GeV} \le M_2 \le 1\ \text{TeV}, \quad 1.3\ \text{TeV} \le M_3 \le 3\ \text{TeV}$$

was scanned over [26]. In Equation (13) M_1, M_2 and M_3 are the masses of the $U(1)_Y$, $SU(2)_W$ and $SU(3)_C$ gauginos. The value of the effective μ parameter was chosen to be sufficiently low to minimize the fine-tuning. The masses of the

first and second generation sfermions as well as the mass of the right-handed sbottom were set to be equal to 3 TeV. All other soft scalar masses were varied from 600 GeV to 3 TeV. It was required that at least one CP–even Higgs state has a mass between 124 GeV and 127 GeV and lead to the signal rates which were consistent with the ones observed by ATLAS and CMS [26]. Only the scenarios that result in the relic dark matter densities which are not larger than $\Omega_c h^2 = 0.1187 \pm 0.0017$ were taken into consideration.

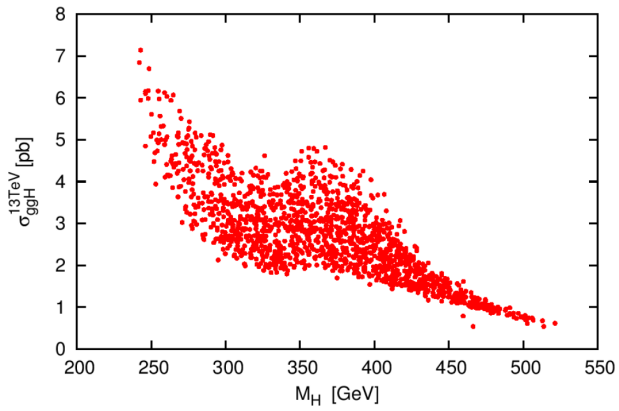

FIGURE 1. The gluon fusion production cross section at $\sqrt{s} = 13$ TeV for H as a function of its mass (see also [26]).

The numerical analysis indicated that in the parameter space under consideration the second lightest CP–even Higgs boson, $H_2 \equiv h$, is SM-like. The heavier CP-even and CP-odd Higgs bosons, $H_3 \equiv H$ and $A_2 \equiv A$, are predominantly a superposition of the components of the Higgs doublets (MSSM-like states). The lightest scalar and pseudoscalar Higgs states, $H_1 \equiv H_s$ and $A_1 \equiv A_s$, are singlet dominated. The almost degenerate heaviest CP-even, CP-odd and charged Higgs states have masses below about 530 GeV, so that they should still be light enough to be observed at the 13 TeV LHC. The H and A gluon fusion production cross sections range between 0.5 pb and a few pb, as shown in Figure 1.

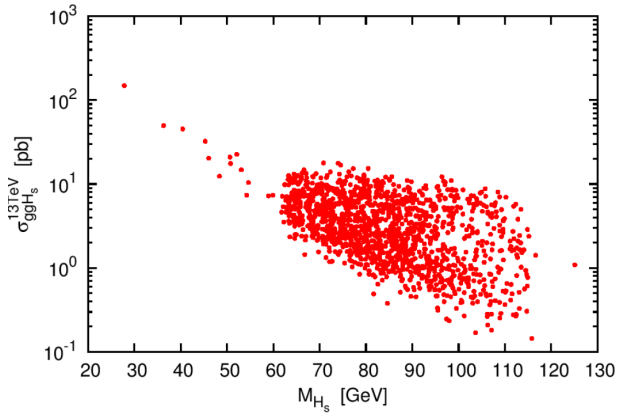

FIGURE 2. The gluon fusion production cross section at $\sqrt{s} = 13$ TeV for H_s as a function of its mass (see also [26]).

Due to the substantial mixing between the SM-like Higgs state and the singlet dominated CP-even state caused by the large value of λ the production cross section of H_s is sufficiently large. The Natural NMSSM scenario discussed here implies the existence of a CP-even Higgs state H_s that has a mass of $62\text{GeV} \lesssim M_{H_s} \lesssim 117\text{GeV}$ and of a CP-odd state A_s with $62\text{GeV} \lesssim M_{A_s} \lesssim 300\text{GeV}$. If masses of H_s and A_s are lower than 62GeV then the SM-like h can decay into these final states and this would reduce signal rates away from the measured values. Figure 2 shows the gluon fusion production cross section for H_s at $\sqrt{s} = 13$ TeV. The lightest pseudoscalar production cross section tend to be

an order of magnitude smaller as compared with the one for H_s.

If the light Higgs bosons H_s and A_s are very singlet-like their gluon fusion production rates can be rather small but they may still be produced via the decays of the heaviest Higgs states, because of the large λ value. Indeed, H can decay into pairs H_sH_s, H_sh and A_sA_s resulting in four fermion final state including $(2\tau)(2b)$ and 4τ final state as well as $(2\gamma)(2b)$ final state. Singlet Higgs bosons can be also produced from heavy pseudoscalar A decays into H_sA_s or hA_s. In summary, all Higgs bosons of the Natural NMSSM should in general be accessible at the high-energy LHC (for the detailed analysis, see [26]).

CONCLUDING REMARKS

Higgs-like boson is found at the LHC being in an agreement with the SM Higgs. However a precision of various signal strength measurements is still not good enough leaving many possibilities (points) in parameter space of new models containing extended Higgs sectors, in particular, 2HDM, MSSM, NMMSM, which satisfy all the constrains from EW precision observables, flavor, unitarity, perturbativity, vacuum stability, and searches for dark matter In some scenarios, when one of the Higgs states is 125 GeV CP even scalar boson the other Higgs(es) could be heavier or lighter, or nearly degenerate. Very difficult task is to cover all areas in model parameter spaces and to exclude completely discussed extensions. Well motivated way to proceed is a consideration of benchmark scenarios. Such an approach is under intensive discussion in the framewrok of the BSM Higgs Working Group (Heavy Higgs and Beyond Standard Model subgroup) [27].

ACKNOWLEDGMENTS

E.B. would like to thank the organisers of LHCP15 for the invitation to give the talk and a partial support. E.B. was also supported in part by the Grant No. 14-12-00363 of the Russian Science Foundation. The work of R.N. was supported by the University of Adelaide and the Australian Research Council through the ARC Center of Excellence in Particle Physics at the Terascale.

REFERENCES

[1] A. Djouadi, Phys. Rept. **459**, 1-241 (2008).
[2] H. Georgi and S. L. Glashow, Phys. Rev. Lett. **32**, 438 (1974).
[3] J. F. Gunion, H. E. Haber, G. L. Kane and S. Dawson, Front. Phys. **80**, 1 (2000).
[4] S. L. Glashow and S. Weinberg, Phys. Rev. D **15**, 1958 (1977).
[5] E. A. Paschos, Phys. Rev. D **15**, 1966 (1977).
[6] G. C. Branco, P. M. Ferreira, L. Lavoura, M. N. Rebelo, M. Sher and J. P. Silva, Phys. Rept. **516**, 1 (2012)
[7] J. Bernon, J. F. Gunion, H. E. Haber, Y. Jiang and S. Kraml, Phys. Rev. D **92**, no. 7, 075004 (2015)
[8] E. Boos, A. Djouadi, M. Muhlleitner and A. Vologdin, Phys. Rev. D **66**, 055004 (2002)
[9] M. Carena, S. Heinemeyer, O. Stl, C. E. M. Wagner and G. Weiglein, Eur. Phys. J. C **73**, no. 9, 2552 (2013)
[10] V. Khachatryan *et al.* [CMS Collaboration], JHEP **1410**, 160 (2014)
[11] G. Aad *et al.* [ATLAS Collaboration], JHEP **1511**, 206 (2015)
[12] A. Djouadi, L. Maiani, A. Polosa, J. Quevillon and V. Riquer, JHEP **1506**, 168 (2015)
[13] U. Ellwanger, C. Hugonie and A. M. Teixeira, Phys. Rept. **496**, 1 (2010).
[14] C. Beskidt, W. de Boer and D. I. Kazakov, Phys. Lett. B **726**, 758 (2013)
[15] S. F. King, M. Mhlleitner, R. Nevzorov and K. Walz, Nucl. Phys. B **870**, 323 (2013).
[16] R. Nevzorov and M. Trusov, Phys. Atom. Nucl. **64**, 1299 (2001).
[17] R. Nevzorov and M. Trusov, Phys. Atom. Nucl. **65**, 335 (2002).
[18] R. Nevzorov and M. Trusov, Phys. Atom. Nucl. **64**, 1513 (2001).
[19] S. F. King, M. Muhlleitner and R. Nevzorov, Nucl. Phys. B **860**, 207 (2012)
[20] P. Kovalenko, R. Nevzorov and K. A. Ter-Martirosian, Phys. Atom. Nucl. **61**, 812 (1998).
[21] R. Nevzorov and M. Trusov, J. Exp. Theor. Phys. **91**, 1079 (2000).
[22] R. Nevzorov, K. A. Ter-Martirosyan and M. A. Trusov, Phys. Atom. Nucl. **65**, 285 (2002).
[23] D. J. Miller, R. Nevzorov and P. M. Zerwas, Nucl. Phys. B **681**, 3 (2004).
[24] R. Nevzorov and D. J. Miller, [arXiv:hep-ph/0411275].
[25] D. J. Miller, S. Moretti and R. Nevzorov, [arXiv:hep-ph/0501139].
[26] S. F. King, M. Mhlleitner, R. Nevzorov and K. Walz, Phys. Rev. D **90**, 095014 (2014)
[27] https://twiki.cern.ch/twiki/bin/view/LHCPhysics/LHCHXSWGBSM

Proceedings of the LHCP2015 Conference, St. Petersburg, Russia, August 31 - September 5, 2015

Editors: V.T. Kim and D.E. Sosnov

Searches for Neutral 2HDM, MSSM and NMSSM Higgs Bosons at the LHC

MATTHIAS SCHRÖDER

KIT — Karlsruher Institut für Technologie
Institut für Experimentelle Kernphysik
Hermann-von-Helmholtz-Platz 1, 76344 Eggenstein-Leopoldshafen, Germany

matthias.schroeder@kit.edu

On behalf of the ATLAS and CMS Collaborations

Abstract. After a Higgs boson with a mass of 125 GeV has been discovered, it is still unclear whether this is the Higgs boson of the Standard Model or whether it is part of an extended Higgs sector, which is predicted by various models of new physics such as the minimal supersymmetric extension to the Standard Model. Recent results of direct searches for additional, neutral Higgs bosons by the ATLAS and CMS experiments are reviewed, which are based on pp collision data collected at centre-of-mass energies of 7 and 8 TeV corresponding to integrated luminosities of approximately 5 and 20 fb^{-1}, respectively.

Introduction

While the Higgs boson with a mass of 125 GeV [1] is consistent with the Standard Model (SM) expectations, non-SM couplings are only excluded up to branching ratios of $\approx 30\%$ with the current data [2]. Furthermore, numerous beyond-the-SM (BSM) models predict extended Higgs sectors, which may contain a SM-like Higgs boson.

Their phenomenology is described generically in Two-Higgs-Doublet-Models (2HDMs), which are effective extensions to the SM that add another Higgs doublet [3]. After electroweak symmetry breaking, five physical states remain: a light and a heavy CP-even boson h and H, an CP-odd boson A, all of which are neutral and collectively denoted ϕ, and two charged bosons $\text{H}^{\pm}$. The light state h is typically identified with the 125 GeV Higgs boson. If in addition the non-existence of flavour-changing neutral currents is imposed, the 2HDMs are defined by six free parameters: the masses m_{H}, m_{A}, $m_{\text{H}^{\pm}}$ of the additional Higgs bosons, the ratio $\tan\beta$ of the vacuum expectation values of the two doublets, and the mixing angle α of the two CP-even states h and H. Different types of 2HDMs are distinguished, depending on their Yukawa-coupling structure. For this article, type-II models are of interest, where one Higgs doublet couples to the up-type and the other to the down-type fermions.

The minimal supersymmetric extension to the SM (MSSM) is an example of a concrete model whose Higgs sector is described by a type-II 2HDM. In this case, however, the supersymmetry poses additional constraints on the Higgs sector, which, at tree level, is then completely defined by two parameters, conventionally chosen as m_{A} and $\tan\beta$ [4].

Other models feature more complex Higgs sectors, such as the Next-to-MSSM (NMSSM), which introduces an additional singlet field resulting in seven physical Higgs bosons. The light bosons can have masses below 125 GeV without violating the experimental constraints if their singlet component is large enough. The NMSSM is theoretically appealing because it solves the small fine-tuning problem introduced in the MSSM by the $m_{\text{h}} = 125$ GeV requirement [5].

In this article, recent results of direct searches for additional Higgs bosons performed by the ATLAS and CMS experiments [6, 7] at the LHC are reviewed, focusing on searches for neutral Higgs bosons as predicted in the MSSM, the 2HDMs, and the NMSSM. The analyses are performed with 4.9 and 19.7 fb^{-1} of pp collision data collected at centre-of-mass energies of 7 and 8 TeV, respectively.

Searches for Heavy Neutral MSSM Higgs Bosons

The heavy neutral MSSM Higgs bosons H and A are expected to be predominantly produced either in gluon-gluon fusion (ggF) or b-quark associated (bA) production at the LHC. Since the Yukawa-coupling to down-type fermions is enhanced by $\tan^2\beta$ relative to the SM over the whole m_A range, the latter production mode dominates for not-too-small values of $\tan\beta$ above approximately 10. Likewise, the branching fractions ($\mathcal{B}$) to charged leptons and down-type fermions are enhanced [8]. Searches performed by ATLAS and CMS probe all relevant and experimentally accessible channels $b\bar{b}$, $\tau\tau$, and $\mu\mu$.

CMS has performed a search for $\phi \to b\bar{b}$ using the $19.7\,\text{fb}^{-1}$ of 8 TeV data [9]. With a branching ratio of often up to 90%, this channel has the by far largest production rate but suffers from an overwhelming QCD-multijet background. Events are therefore selected by requiring the three leading jets (the three jets with highest transverse momentum p_T) to be identified as initiated by b-quarks (b-tagged). This selection targets at the typically dominant bA signal-production and largely reduces the QCD-multijet contribution. In order to cope with the huge event rate, dedicated triggers have been developed that perform online b-tagging. The signal is expected to manifest as a single resonance in the invariant-mass distribution m_{12} of the leading two jets, which is caused by the degenerate contributions of the A and H bosons. The remaining SM background consists almost entirely of QCD-multijet events with three real b jets or with two b jets and one mis-tagged light-flavour jet, leading to a non-resonant m_{12} distribution determined by the trigger turn-on and multijet production cross-section. The background is determined with a data-driven procedure, fitting a superposition of templates for each of the different flavour combinations of the three leading jets to the data. The template shapes are derived from a data control-sample of events with two b-tagged jets, which are weighted by the b-tag probability of the un-tagged jet.

The observed data are well described by the background-only expectation. In absence of a signal, model-independent upper limits are derived on the resonance production rate $\sigma(pp \to b\phi + X) \times \mathcal{B}(\phi \to b\bar{b})$, which range from 250 to 1 pb for signal-mass hypotheses from 100 to 900 GeV, respectively. The results, combined with the results of a previous analysis based on 7 TeV data [10], are also interpreted as constraints on the MSSM parameters, expressed as limits at 95% confidence level (C. L.) in $(\tan\beta, m_A)$ space. The other MSSM parameters are chosen to be fixed at certain benchmark values, where in addition to the traditionally used m_h^{max} benchmark scenario also several other recently proposed scenarios are considered, that are compatible with either h or H having a mass of 125 GeV in most parts of the parameter space [11]. This is not the case in the m_h^{max} scenario, which is therefore disfavoured by the data. The sensitivity in the $m_h^{\text{mod+}}$ scenario, for example, reaches up to $m_A = 500$ GeV and down to $\tan\beta = 14$ at low m_A, cf. Fig. 1 (left). The $\phi \to b\bar{b}$ channel is expected to be particularly sensitive to the higgsino-mass parameter μ of the MSSM [11]. This is evident in Fig. 1 (right), where the limit is compared for different values of μ, varying from $\tan\beta = 30$ for $\mu = -500$ GeV to beyond 60 for $\mu = +500$ GeV at $m_A = 500$ GeV.

Both ATLAS and CMS have performed searches in the $\phi \to \tau\tau$ channel, which contributes with $\mathcal{B} \approx 10\%$ [13, 14, 15]. The analyses deploy data at 7 and 8 TeV, and up to five $\tau\tau$ final-states — $e\tau_h$, $e\mu$, $\mu\tau_h$, $\mu\mu$, and $\tau_h\tau_h$ — are considered. Events are generally selected by requiring two oppositely charged, well isolated leptons. Additional, channel-dependent selection criteria are applied to suppress contributions from SM background processes; for example, in the $\mu\tau_h$ channel the transverse mass of the μ and the missing transverse momentum ($\not{E}_T$) is restricted to reject W+jets events. Depending on the analysis, the selected events are categorised according to the number of b-tagged jets, the τ-p_T, the employed trigger selection, and the signal-mass hypothesis in order to enhance the sensitivity and to distinguish between the different production modes. The invariant mass of the di-τ system is reconstructed using different estimators that are based on the leptons and on the $\not{E}_T$ to infer the neutrino momenta, which results into a relative mass resolution of typically 20% at 100 GeV. One of the dominant SM background contributions arises from $Z \to \tau\tau$ events; where important, it is determined from data with an embedding technique, in which the muons in $Z \to \mu\mu$ events are replaced by simulated τ-decay products. Further important backgrounds are due to W+jets and QCD-multijet events with jets mis-identified as τ_h and μ and are estimated from signal-depleted control regions in data.

In all channels, the observed data agree well with the SM-only expectation. Thus, model-independent upper limits on the resonance production rates $\sigma(pp \to \phi + X) \times \mathcal{B}(\phi \to \tau\tau)$ for the different production modes as well as limits on the MSSM parameters $\tan\beta$ and m_A are derived. The limits in the $m_h^{\text{mod+}}$ scenario obtained by CMS are shown in Fig. 1 (left); they reach up to $m_A = 1$ TeV (the plot shows only the range up to $m_A = 500$ GeV for better readability) and down to $\tan\beta = 5$ at low m_A. In this channel, sensitivity is reached also to the h state at 125 GeV, and therefore, the signal hypothesis is tested against a background plus SM-Higgs hypothesis. A similar result is obtained by ATLAS [14].

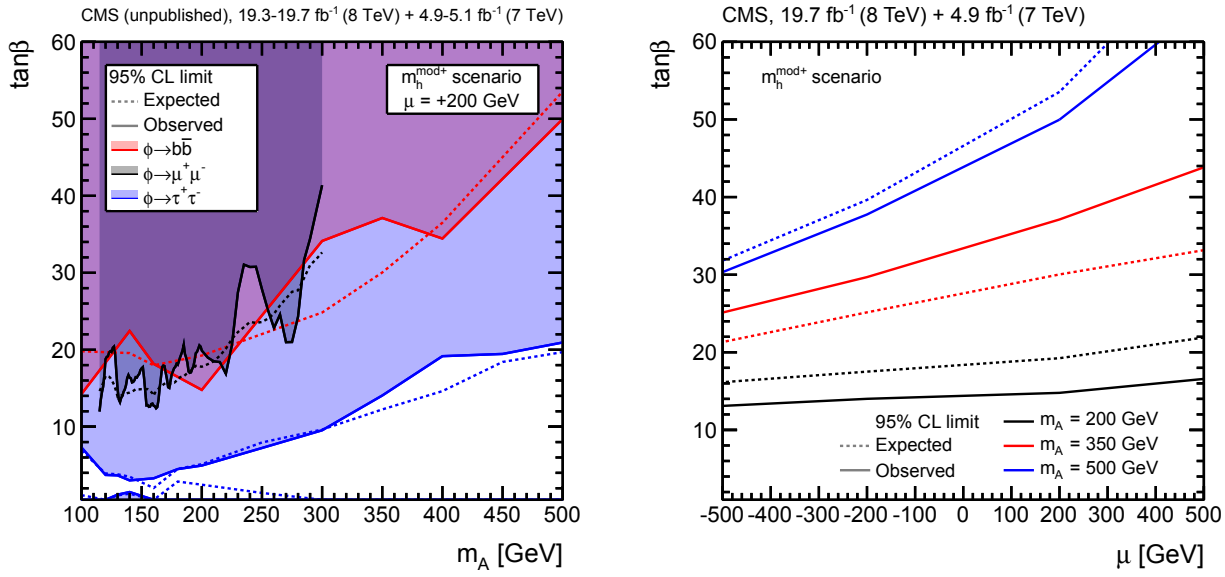

FIGURE 1. Expected (dashed lines) and observed (solid lines) upper limits at 95% C. L. on the MSSM parameter $\tan\beta$ in the $m_h^{\text{mod+}}$ benchmark scenario. Shown is (left) a comparison of the $\tan\beta$ limits versus m_A obtained in different final states $b\bar{b}$ [9], $\mu\mu$ [12], and $\tau\tau$ [13], with $\mu = +200$ GeV. The excluded parameter space (observed limit) is indicated by the shaded areas. The limit in the $\tau\tau$ final state extends to $m_A = 1$ TeV but is shown here only up to 500 GeV for better readability. Also shown (right) is a comparison of the $\tan\beta$ limits versus the higgsino-mass parameter μ obtained for three different values of m_A in the $b\bar{b}$ final state [9].

CMS has also performed a search in the di-μ final state using the 25 fb^{-1} of data at 7 and 8 TeV [12]; ATLAS has performed a similar search with 7 TeV data [16]. Although the branching fraction of this channel is below 10^{-3}, it benefits from the excellent relative mass resolution of approximately 1% at 125 GeV. Events are selected requiring two oppositely charged, well isolated muons. In order to suppress the $t\bar{t}$ background, events with $\not{E}_T > 35$ GeV and two or more b-tagged jets are rejected. The selected events are further categorised into events with one or zero b-tagged jets to enhance the sensitivity to the bA and ggF production processes, respectively. The di-μ invariant mass spectrum of the SM-background processes, which are dominated by Drell-Yan production, is modelled with an analytic function. The signal is expected to manifest as narrow resonances, which are parametrized by Voigt profiles, the shape of which are determined from simulation. In case of the MSSM interpretation, the signal model consists of two narrow resonances, one due to the h and the second one due to the degenerate A and H contributions, and their relative normalisation is fixed according to the choice of m_A and $\tan\beta$. The signal yield is extracted from fitting a linear combination of the signal and background models to the data.

No evidence of a signal is found, and the results are expressed as model-independent upper limits on $\sigma(pp \to \phi + X) \times \mathcal{B}(\phi \to \mu\mu)$ for the different production modes as well as on the MSSM parameters $\tan\beta$ and m_A in different benchmark scenarios. In the $m_h^{\text{mod+}}$ scenario, the exclusion at 95% C. L. on $\tan\beta$ reaches as low as 15 in the low-m_A region and to above 30 at m_A =300 GeV, cf. Fig. 1 (left).

As evident from Fig. 1 (left), the reviewed analyses probe the MSSM Higgs sector in different channels and complement each other. The most stringent limits arise from the $\tau\tau$ channel; the sensitivity in $\tan\beta$ is similar in the $b\bar{b}$ and $\mu\mu$ channels, where $\mu\mu$ has the lowest reach in m_A. The mass resolution is best in the $\mu\mu$ and worst in the $\tau\tau$ channel.

Searches for Pseudoscalar Higgs Bosons in 2HDMs

In most 2HDMs, the decay A → Zh of the pseudoscalar Higgs boson A into a Z boson and the Higgs boson at 125 GeV often has a large branching fraction for masses m_A above the kinematic threshold up to where the decay into two top quarks opens up and even beyond. In the MSSM, this is the case for low values of $\tan\beta$ [17].

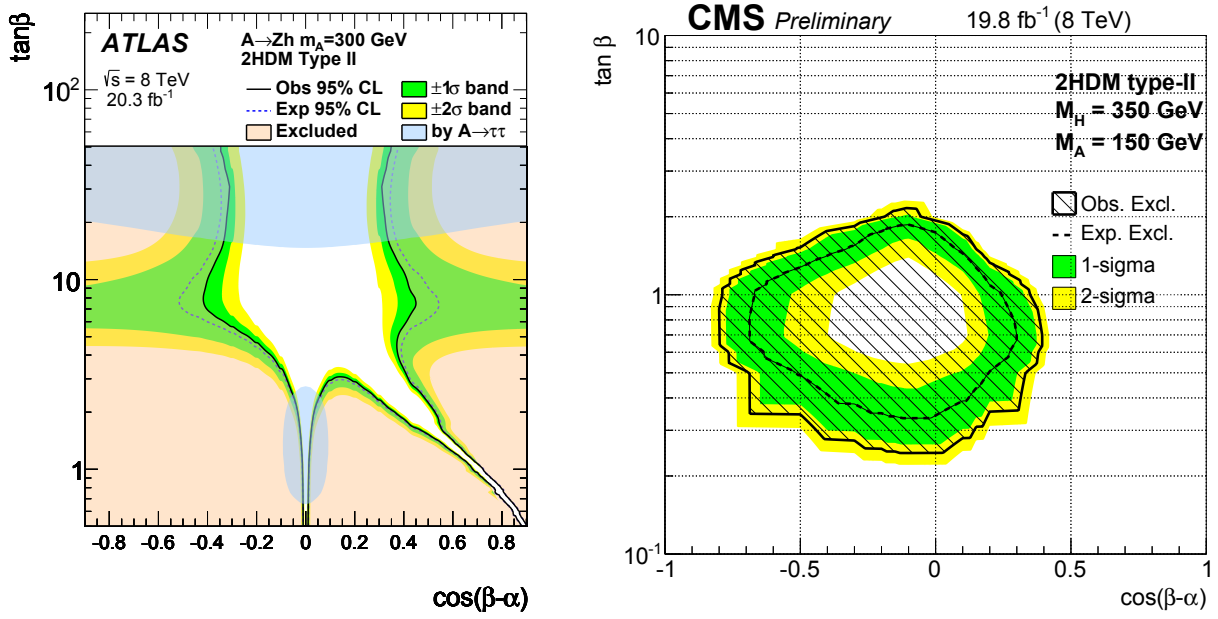

FIGURE 2. Expected (dashed lines) and observed (solid lines) limits at 95% C. L. on the parameters $\tan\beta$ and $\cos(\beta-\alpha)$ of the type-II 2HDM obtained for $m_A = m_H = m_{H^\pm} = 300\,\text{GeV}$ by the $A \to Zh$ search [18] (left) and for $m_A = 150\,\text{GeV}$, $m_H = m_{H^\pm} = 350\,\text{GeV}$ by the $H \to ZA$ search [20] (right). Excluded regions (observed limit) are marked by the light shaded (left) and hatched (right) areas; the dark shaded area (left) shows the exclusion obtained by a reinterpretation of the $\phi \to \tau\tau$ search described in the text [14].

Both ATLAS and CMS have performed searches for A-boson production in ggF with $A \to Zh$ in final states where the Z boson decays into two electrons or muons and the h boson into two b quarks or tau leptons, using the $20\,\text{fb}^{-1}$ of data collected at 8 TeV [18, 19, 20]. The leptonic Z decay offers a clean signature for triggering, while the $h \to b\bar{b}/\tau\tau$ rate is typically high. ATLAS also considers the $Z \to \nu\nu$ decay, which improves the sensitivity at high signal masses. A peak search is performed in the invariant-mass spectrum of the two leptons and b quarks/τ leptons, and the mass resolution is improved by deploying a constraint of 125 GeV on the di-b-jet/di-τ mass in the reconstruction. Different additional procedures are performed to improve the signal-to-background discrimination. For example, CMS employs the output of a boosted-decision tree classifier that takes into account b-tagging and angular information of the Z decay products. Important SM backgrounds arise from Z+jets and $t\bar{t}$ production and are determined from different control regions in data.

In the absence of a signal, the results are interpreted as constraints on the parameters of different 2HDMs, expressed as limits at 95% C. L. in $(\tan\beta, \cos(\beta-\alpha))$ space. Small contributions to the expected signal from bA production together with the combinatorics due to additional b jets are taken into account in the limit setting procedure. The limits obtained by ATLAS in the type-II 2HDM for $m_A = m_H = m_{H^\pm} = 300\,\text{GeV}$ are shown in Fig. 2 (left). Large parts of the parameter space are excluded, also at high values of $\tan\beta$. The sensitivity is reduced in the 'alignment limit' at $\cos(\beta-\alpha) \to 0$, where the h boson becomes SM like and the branching fraction $\mathcal{B}(A \to Zh)$ vanishes, as well as in a narrow region in phase space towards $\cos(\beta-\alpha) = 1$ at small $\tan\beta$, where $\mathcal{B}(h \to b\bar{b}/\tau\tau)$ becomes small. Sensitivity to the region of the alignment limit is to some extent obtained by a reinterpretation of the results of the MSSM $\phi \to \tau\tau$ search [14] described above, as indicated in the figure. CMS has found similar limits.

Access to the interesting region of the alignment limit is also gained with a complementary analysis by CMS, where the light Higgs boson at 125 GeV is not explicitly required in the final state [20]. Instead, a search for $A/H \to ZH/A$ events is conducted, and either mass hierarchy of the heavy Higgs bosons A and H is considered in the interpretation. The resulting limits on the type-II 2HDM parameters $\tan\beta$ and $\cos(\beta-\alpha)$ are shown in Fig. 2 (right) for $m_A = 150\,\text{GeV}$ and $m_H = m_{H^\pm} = 350\,\text{GeV}$.

Searches for Light Pseudoscalar NMSSM Higgs Bosons

The lightest pseudoscalar Higgs boson a of the NMSSM can have masses below 125 GeV without violating the experimental constraints by the SM Higgs-boson searches [5]. ATLAS has performed two searches for the decay $H \to aa$, where H is assumed to be either the 125 GeV boson or a second CP-even state, which is dominantly produced in ggF. Both searches employ 20.3 fb^{-1} of pp collision data collected at 8 TeV.

The first analysis targets events where one a boson decays to two muons and the other to two τ leptons, one of which decays leptonically [21]. It is assumed that the a boson only decays via the $\mu\mu$ or $\tau\tau$ channel. The search is performed for masses m_a of the a boson between 3.7 and 50 GeV with $m_H = 125$ GeV, and for different values of m_H between 100 and 500 GeV assuming $m_a = 5$ GeV. While the choice of the $m_a \to \mu\mu$ final-state leads to a low expected signal rate, it results in a high trigger efficiency, low signal-to-background ratio, and a narrow di-μ invariant mass resonance, which is used to identify a signal.

The two a bosons are expected to be produced back-to-back in the transverse plane with a high boost in most parts of the probed parameter space. Events are selected requiring two oppositely-charged, well-isolated muons constituting an $m_a \to \mu\mu$ candidate with $p_T > 40$ GeV. Further, an electron or muon well-separated in azimuth from the a candidate is required and there must be up to three additional tracks within a cone around the lepton, the leading of which has opposite charge to the lepton, which aims at reconstructing the $m_a \to \tau\tau$ decay. Additional isolation and quality criteria are imposed to suppress background events faking the τ signature. The expected signal di-μ mass distribution is modelled with a double-sided Crystal Ball (CB) function plus a Gaussian with different mean to describe small contributions due to $a \to \tau\tau \to \mu\mu + 4\nu$ decays. The SM background is dominated by Drell-Yan events and, at higher masses, $t\bar{t}$ events, which are parametrized essentially with exponential functions. Additional resonant contributions due to J/Ψ, Ψ', Υ_{1S}, Υ_{2S}, and Υ_{3S} mesons are modelled with CB functions, where the same mass-dependent resolution as for the signal model are assumed. The parameters of the signal and background model as well as the signal strength are determined in a simultaneous fit to the data in the signal region and in two background-enhanced control regions, which are selected by requiring the presence of additional light- or heavy-flavour jets in the events.

The data are well described by the background-only hypothesis. Thus, upper limits are set at 95% C. L. on the resonance production rate $\sigma(gg \to h) \times \mathcal{B}(h \to aa)$, which are shown in Fig. 3 (left) relative to the SM Higgs-boson ggF production rate as a function of m_a for $m_h = 125$ GeV. The result is scaled by $\mathcal{B}^2(a \to \tau\tau)$ to allow reinterpretation of the results given the $\mathcal{B}(a \to \tau\tau) + \mathcal{B}(a \to \mu\mu) = 1$ assumption.

The second analysis targets $H \to aa \to 4\gamma$ events where both a bosons decay into two photons [22]. The search

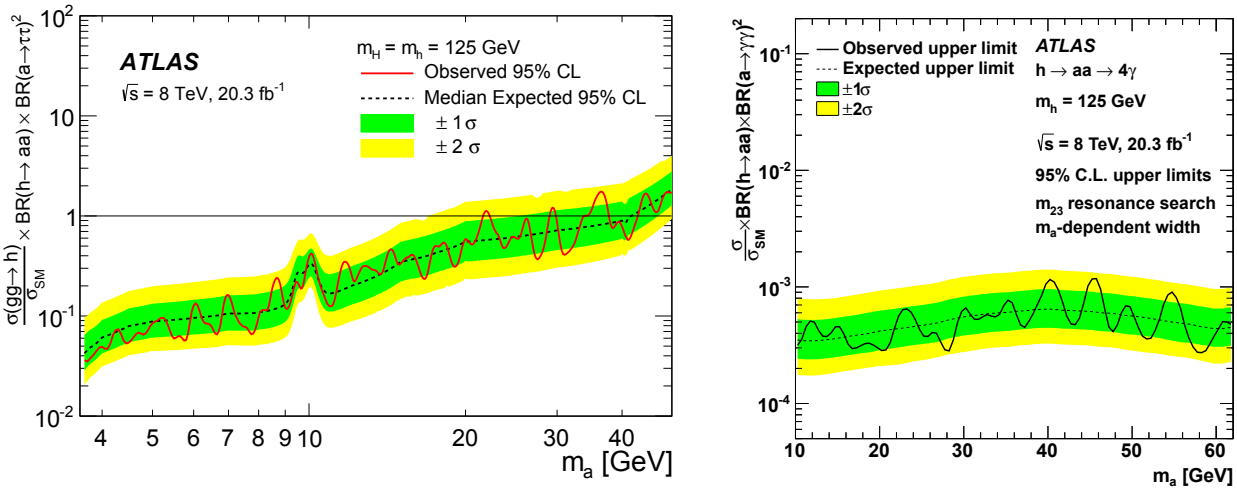

FIGURE 3. Observed (solid line) and expected (dashed line) upper limits on the $\sigma(gg \to h) \times \mathcal{B}(h \to aa)$ production relative to the SM Higgs-boson gluon-gluon fusion production rate as a function of m_a for $m_h = 125$ GeV. Shown are the results obtained in the $\mu\mu\tau\tau$ (left) and 4γ (right) final states, which are scaled by the appropriate branching fractions of the a boson final-states [21, 22]. The former limit is scaled by $\mathcal{B}^2(a \to \tau\tau)$ to account for the assumed branching ratios and allow reinterpretation of the results.

is performed for masses m_a of the a boson between 10 and 62 GeV with $m_H = 125$ GeV, and also for larger values of m_H with an adjusted m_a range up to the kinematic threshold.

Events are selected requiring at least three isolated photons, which provides sensitivity also to other BSM processes such as $Z \to \gamma a(\gamma\gamma)$ and rare SM processes such as $Z \to 3\gamma$. A resonance search is performed in the two-photon invariant mass distribution m_{23} of the second and third highest-p_T photons, which results in the best sensitivity to the $H \to aa \to 4\gamma$ process. The signal is modelled with a Gaussian. The dominant background arises from rare SM processes with three or more prompt photons as well as processes including electrons or jets misidentified as photons. It is determined from data with a fit in m_{23} side-band regions, where the background distributions is modelled by a fourth-order polynomial.

The observed data is well described by the background-only hypothesis, and thus, upper limits are set at 95% C. L. on the resonance production rate $\sigma(gg \to h) \times \mathcal{B}(h \to aa) \times \mathcal{B}^2(a \to \gamma\gamma)$. They are shown in Fig. 3 (right) relative to the SM Higgs-boson ggF production rate as a function of m_a for $m_h = 125$ GeV.

Conclusions

ATLAS and CMS have performed a wide variety of searches for additional Higgs bosons. In this article, recent searches for neutral Higgs bosons as predicted by the MSSM, 2HDMs, and NMSSM have been discussed, which have been performed with up to 25 fb^{-1} of 7 and 8 TeV data. No significant deviation from the SM is observed, and the results are used to derive stringent, complementary constraints on the BSM-Higgs parameter space.

REFERENCES

[1] ATLAS and CMS Collaborations, Phys. Rev. Lett. **114**, p. 191803 (2015), arXiv:1503.07589 [hep-ex] .
[2] ATLAS and CMS Collaborations, (2015), ATLAS-CONF-2015-044, CMS-PAS-HIG-15-002 .
[3] G. C. Branco et al., Phys. Rept. **516**, 1–102 (2012), arXiv:1106.0034 [hep-ph] .
[4] H. P. Nilles, Phys. Rept. **110**, 1–162 (1984).
[5] R. Dermisek and J. F. Gunion, Phys. Rev. **D76**, p. 095006 (2007), arXiv:0705.4387 [hep-ph] .
[6] ATLAS Collaboration, JINST **3**, p. S08003 (2008).
[7] CMS Collaboration, JINST **3**, p. S08004 (2008).
[8] LHC Higgs Cross Section Working Group, (2013), 10.5170/CERN-2013-004, arXiv:1307.1347 [hep-ph] .
[9] CMS Collaboration, JHEP **11**, p. 071 (2015), arXiv:1506.08329 [hep-ex] .
[10] CMS Collaboration, Phys. Lett. **B722**, 207–232 (2013), arXiv:1302.2892 [hep-ex] .
[11] M. S. Carena et al., Eur. Phys. J. **C73**, p. 2552 (2013), arXiv:1302.7033 [hep-ph] .
[12] CMS Collaboration, Phys. Lett. **B752**, 221–246 (2016), arXiv:1508.01437 [hep-ex] .
[13] CMS Collaboration, (2015), CMS-PAS-HIG-14-029 .
[14] ATLAS Collaboration, JHEP **11**, p. 056 (2014), arXiv:1409.6064 [hep-ex] .
[15] CMS Collaboration, JHEP **10**, p. 160 (2014), arXiv:1408.3316 [hep-ex] .
[16] ATLAS Collaboration, JHEP **02**, p. 095 (2013), arXiv:1211.6956 [hep-ex] .
[17] A. Djouadi and J. Quevillon, JHEP **10**, p. 028 (2013), arXiv:1304.1787 [hep-ph] .
[18] ATLAS Collaboration, Phys. Lett. **B744**, 163–183 (2015), arXiv:1502.04478 [hep-ex] .
[19] CMS Collaboration, Phys. Lett. **B748**, 221–243 (2015), arXiv:1504.04710 [hep-ex] .
[20] CMS Collaboration, submitted to Phys. Lett. B (2015), CMS-PAS-HIG-15-001 .
[21] ATLAS Collaboration, Phys. Rev. **D92**, p. 052002 (2015), arXiv:1505.01609 [hep-ex] .
[22] ATLAS Collaboration, submitted to EPJC (2015), arXiv:1509.05051 [hep-ex] .

Proceedings of the LHCP2015 Conference, St. Petersburg, Russia, August 31 - September 5, 2015

Editors: V.T. Kim and D.E. Sosnov

Searches for Charged Higgs Bosons in pp collisions with the ATLAS and CMS detectors

PIETRO VISCHIA[1,2]

[1]*LIP*[*]
[2]*Instituto Superior Técnico*

pietro.vischia@cern.ch
URL: http://cern.ch/vischia

On behalf of the ATLAS and CMS Collaborations

Abstract. Results for charged Higgs boson searches performed by the ATLAS and CMS Collaborations using data collected at the LHC with a center-of-mass energy of 8 TeV are presented. The major production modes and decay channels are overviewed, and results are compared for the production modes and decay channels that have been explored by both Collaborations. The first results for the direct search for a charged Higgs boson decaying into a top quark and a bottom antiquark are presented.

INTRODUCTION

In 2012, a neutral boson with a mass of approximately 125 GeV was discovered by the CMS and ATLAS experiments [1, 2, 3] at the CERN LHC. The properties of the new boson are consistent with those predicted by the standard model (SM) Higgs boson [4, 5, 6, 7, 8, 9]. Models with an extended Higgs sector are constrained by the measured mass, CP quantum numbers, and production rates of the new boson. The discovery of another scalar boson, neutral or charged, would represent unambiguous evidence for the presence of physics beyond the SM. Furthermore, such models might explain experimental observations such as baryon asymmetry, dark matter, and neutrino oscillations.

Charged Higgs bosons are predicted in models including at least two Higgs doublets. The simplest of such models are the two-Higgs-doublet models (2HDM) [10], such as the Minimal Supersymmetric Standard Model (MSSM) [11]. Two Higgs doublets result in five physical Higgs bosons: light and heavy CP-even Higgs bosons h^0 and H^0, a CP-odd Higgs boson A, plus two charged Higgs bosons $H^{\pm}$. All throughout this paper, the charged Higgs bosons will be referred to as H^+: charge conjugation will be always implied. The discovery of the neutral boson $h^0(125)$ implies that the MSSM parameter space can be described fully by using two parameters, such as the charged Higgs boson mass and the $\tan\beta$ parameter that represents the ratio between the vacuum expectation values of the neutral Higgs bosons [12].

The main search channels for a charged Higgs boson are described in this paper and involve production and decay either via vector bosons or via top quarks.

The channels involving vector bosons may feature the production of a charged Higgs from the decay of a heavy neutral Higgs boson H^0, or the production via vector boson fusion. Decays may involve only vector bosons, or cascade decays involving also a $h^0(125)$ neutral Higgs boson.

The channels involving top quark decays include charged Higgs produced either as decay products of the top quark (if $M_{H^+} < M_t - M_b$) or produced in association with top and bottom quarks (if $M_{H^+} > M_t - M_b$).

The region in which $M_{H^+} \sim M_t$ is driven by interference terms between production and decay modes, and its proper theoretical treatment is still under study: because of this lack of a proper theoretical description, this region has not yet been probed experimentally.

The results described in this paper have been obtained using the ATLAS and CMS detectors: a detailed description of the apparatuses can be found elsewhere [13, 14].

[*]with funding by FCT grant SFRH/BD/52067/2012 (IDPASC program)

Multi-Higgs boson cascade

The ATLAS Collaboration has explored the production of a charged Higgs boson in the context of a cascade decay starting from a heavy neutral Higgs boson H^0 [15].

In this analysis, the observed neutral scalar boson $h^0(125)$, with its properties, is assumed, whereas no particular model is assumed for additional bosons. The examined decay chain involves a charged Higgs boson produced in association with a W boson, $H^0 \to W^-H^+$, with subsequent decay of the charged Higgs into a W vector boson and a $h^0(125)$ scalar boson, $W^-H^+ \to h^0W^-W^+ \to b\bar{b}W^-W^+$. A leptonic decay is assumed for one of the W bosons, and a hadronic decay is assumed for the other one, yielding a final state characterized by four jets, out of which at least two coming from a b quark, one lepton, and missing energy: events are selected using criteria taking these objects into account in order to select the desired final state topology.

After the event selection described above, a Boosted Decision Tree (BDT) method is used in order to build a continuous discriminator to be used to separate signal from background. For each signal mass point hypothesis the BDT is retrained in order to optimally exploit the different features of the kinematics for heavier or lighter charged Higgs bosons. By cutting on the BDT discriminator value, signal regions with enhanced signal-to-background ratio are selected. An example of the obtained separation power is shown in Figure 1(a) for the $M_{H^0} = 1025$ GeV, $M_{H^+} = 625$ GeV signal mass point.

The final yields for signal and all backgrounds, after the event selection and the BDT cuts, are given as input to the limit computation procedure. 95% C.L. limits are obtained in the phase space defined by the H^0 and H^+ masses. Figure 1(b) shows the observed limits in terms of signal cross section: better limits are obtained for high masses for both neutral and charged Higgs, reflecting the better signal-to-background power obtainable for that region. Figure 1(c) shows the interpretation of the limits in terms of exclusion limits on the $gg \to H^0$ production cross section $\sigma(gg \to H^0)$: the observed limits are, for all mass points, larger than the NNLO predictions for $gg \to H^0$ production at the SM rate; hence, no exclusion region can be obtained.

$H^+ \to W^+Z$ in vector boson fusion

The decay of a charged Higgs boson into a couple of vector bosons, $H^+ \to W^+Z$, is allowed at tree level in Higgs Triplet Models [16, 17], and is examined by the ATLAS Collaboration [18]. The vector boson fusion production mechanism ensures the possibility of tagging the event by using the very energetic forward jets that radiate the vector bosons: by selecting a decay mode featuring leptonic decay of the Z boson, $Z \to \ell^+\ell^-$, $\ell = e, \mu$, and a hadronic decay of the W boson, $W^+ \to qq'$, a final state characterized by four jets and two isolated leptons can be chosen.

In order to selected the chosen final state, at least four jets are required in the event: first, the two highest-p_T non-b-tagged jets are required to be in opposite hemishpheres (to be identified with the tag jets of the vector boson fusion production mechanism). Among the remaining jets, the two highest-p_T ones are assumed to come from the $W^+ \to qq'$ decay, and consequently their invariant mass is required to be close to the W boson mass, $60 < M_{qq'} < 95$ GeV. Exactly two isolated leptons are required in the event, and their invariant mass is required to be close to the Z boson mass, $83 < M_{\ell\ell} < 99$ GeV.

The distribution of the invariant mass of the four-body system constituted by the two leptons (assumed coming from a Z boson decay) and the two jets assumed coming from the W boson decay, denoted $M_{\ell\ell jj}$, is used to set 95% C.L. limits on $\sigma_{VBF} \times \mathcal{B}(H^+ \to W^+Z)$ of 31–1020 fb for charged Higgs masses $200 < M_{H^+} < 1000$ GeV. Such limits are shown in Figure 2(a). When assuming $\mathcal{B}(H^+ \to W^+Z) = 1$, the results can be interpreted in the Georgi-Machacek Higgs Triplet Model [16]: the assumption is reasonable, because the branching ratio is predicted to be very high when the charged Higgs mass is above the W^+Z production threshold. The fraction of M_W^2 and M_Z^2 generated by the triplet vacuum expectation value can be described by a parameter, s_H^2, that turns out to be proportional to the cross section and the charged Higgs width: 95% CL exclusion limits are set on s_H^2 as a function of the charged Higgs mass, as shown in Figure 2(b).

Charged Higgs searches involving top quark production and decays

A charged Higgs boson can be produced in top quark decays if $M_{H^+} < M_t - M_b$: for $\tan\beta < 1$, charmed final states are dominant, whereas for higher values of $\tan\beta$ the dominant decay mode involves the decay into a tau lepton, $H^+ \to \tau\nu_\tau$. If $M_{H^+} > M_t - M_b$, the charged Higgs can be produced in association with top quarks, with or without extra b quarks in the final state.

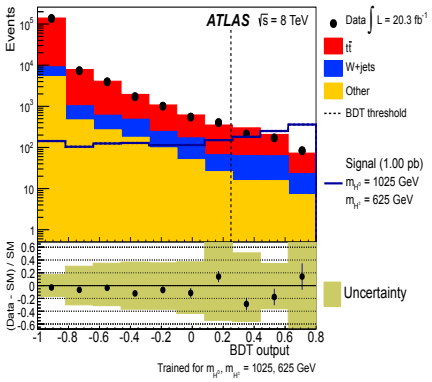

(a)

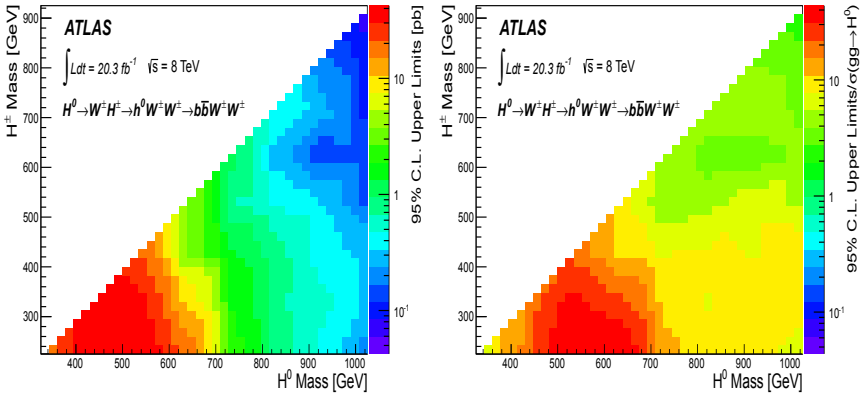

(b) (c)

FIGURE 1. (a) BDT discriminator trained for the $M_{\mathrm{H}^0} = 1025$ GeV, $M_{\mathrm{H}^+} = 625$ GeV signal mass point. The optimal threshold selected for defining the final signal region is shown as a vertical dashed line. (b) Observed 95% C.L. limits on the signal cross section in the phase space defined by the H^0 and H^+ masses. (c) Observed 95% C.L. limits on the signal production cross section divided by the NNLO predictions for $gg \to \mathrm{H}^0$ at the SM rate. Values lower than one would identify exclusion regions for the H^0 production. All figures are taken from [15].

Light charged Higgs searches for $\tan\beta < 1$

The $\mathrm{c\bar{s}}$ decay mode has been probed by the ATLAS and CMS Collaborations [19, 20] in the lepton+jets final state. In one leg of the SM top quark pair production, $\mathrm{t} \to \mathrm{W}^+\mathrm{b}$, the W boson is substituted by a charged Higgs boson. If the charged Higgs boson decays into a charm quark and a strange quark, the dijet invariant mass can be compared with the SM $\mathrm{W} \to \mathrm{qq}'$ case. The final state is reconstructed by assigning the missing transverse energy and the lepton to the leptonic decay of the top leg containing a W, whereas the two non-b-tagged jets are assigned to the hadronic decay of the W boson (for SM background production) or of the charged Higgs boson (for the signal production).

Events are selected in both analyses by requiring one isolated lepton (the CMS Collaboration also vetoes additional leptons in the event), at least four jets, at least two b-tagged jets, and missing transverse energy. The ATLAS Collaboration introduces also a cut on the transverse mass of the system constituted by the lepton and the missing transverse energy.

Figure 3 shows the obtained 95% C.L. limit on $\mathcal{B}(\mathrm{t} \to \mathrm{H}^+\mathrm{b})$ for the (a) ATLAS and (b) CMS analyses.

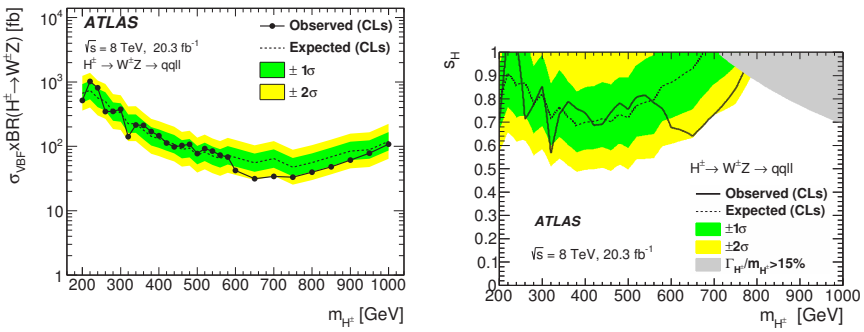

(a) (b)

FIGURE 2. (a) 95% C.L. limits on $\sigma_{VBF} \times \mathcal{B}(\mathrm{H}^+ \to \mathrm{W}^+\mathrm{Z})$, for charged Higgs masses $200 < M_{\mathrm{H}^+} < 1000$ GeV. (b) 95% C.L. limits on s_H^2, for charged Higgs masses $200 < M_{\mathrm{H}^+} < 1000$ GeV, in the context of the Georgi-Machacek Higgs Triplet Model. All figures are taken from [18].

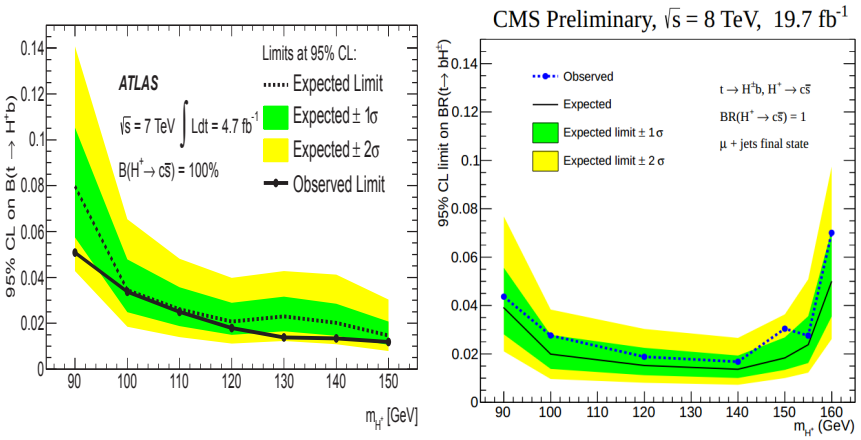

(a) (b)

FIGURE 3. The 95% C.L. exclusion limits on $\mathcal{B}(\mathrm{t} \to \mathrm{H}^+\mathrm{b})$ for the (a) ATLAS [19] and (b) CMS [20] results obtained in the ℓ+jets final state for the $\mathrm{H}^+ \to \mathrm{c\bar{s}}$ decay mode.

Light H^+ searches for $\tan\beta > 1$, and heavy H^+ searches in the τ_h+jets final state

For $M_{\mathrm{H}^+} < M_t - M_b$ and $\tan\beta > 1$, the dominant decay mode is $\mathrm{H}^+ \to \tau\nu_\tau$. This decay mode is also present for $M_{\mathrm{H}^+} > M_t - M_b$, although not the dominant one. This decay mode can be probed by selecting hadronic decay of the τ lepton, in the $\ell\tau_h$ and $\tau_h + jets$ final states. Although the $\ell\tau_h$ final state has been probed by the CMS Collaboration [21] with the 7 TeV data, this final state is not competitive anymore with the increased center-of-mass energy of 8 TeV.

The $\tau_h + jets$ has been analyzed by the ATLAS and CMS Collaborations [22, 23], by employing slightly different techniques. The missing transverse energy, in this final state, can be assigned univocally to the charged Higgs decay, thus enabling the computation of the charged Higgs transverse mass M_T.

The events are selected in a similar way, according to the event topology, by requiring one hadronically decaying τ lepton, three or four jets, missing transverse energy, and by vetoing the presence of isolated leptons in the event. The dominant backgrounds (electroweak EWK and multijet productions) are measured in data by using a fit of the M_T in control regions (ATLAS) and via angular cuts peculiar of the τ kinematics (CMS).

In this final state, events resulting from any decay mode of the charged Higgs different from $\mathrm{H}^+ \to \tau\nu_\tau$ would be measured in data together with the EWK and multijet backgrounds, and consequently the exclusion limits obtained are truly model-independent, not needing any assumption on the branching ratio of the charged Higgs to other final

states.

Figure 4 and Figure 5 show the 95% C.L. exclusion limits computed for a light or heavy charged Higgs boson, respectively, using the M_T distributions after the data driven background estimate, for the (a) ATLAS and (b) CMS analyses. The respective papers include also interpretations of the limits in different MSSM scenarios. In particular, the "low-m_H" scenario is completely excluded by both Collaborations.

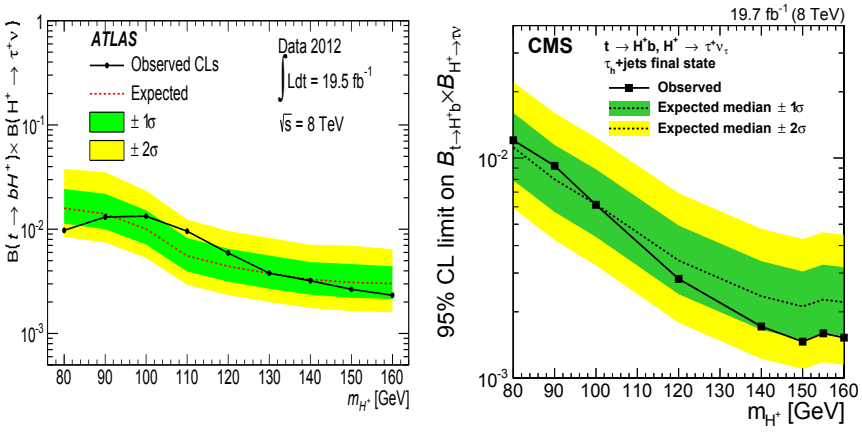

(a) (b)

FIGURE 4. The 95% C.L. exclusion limits on $\mathcal{B}(\mathrm{t} \to \mathrm{H}^+\mathrm{b}) \times \mathcal{B}(\mathrm{H}^+ \to \tau\nu_\tau)$ for a light charged Higgs boson for the (a) ATLAS [22] and (b) CMS [23] analyses.

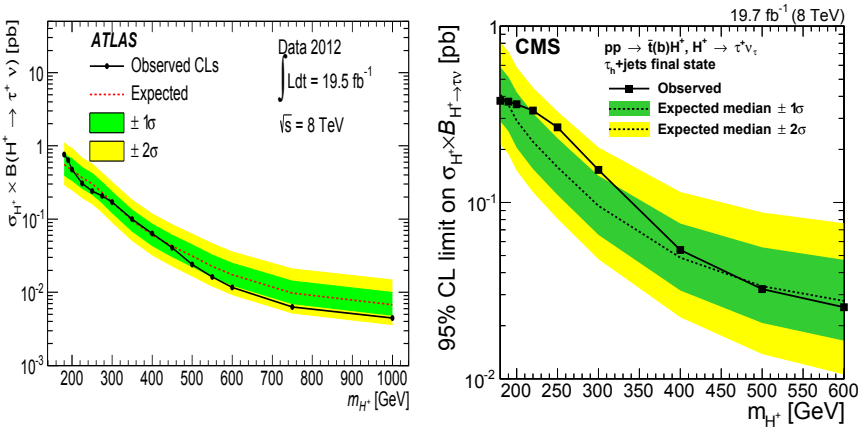

(a) (b)

FIGURE 5. The 95% C.L. exclusion limits on $\sigma_{\mathrm{H}^+} \times \mathcal{B}(\mathrm{H}^+ \to \tau\nu_\tau)$ for a heavy charged Higgs boson for the (a) ATLAS [22] and (b) CMS [23] analyses of the τ_h+jets final state.

Heavy charged Higgs searches - the $\ell\tau_h$, dilepton, and ℓ+jets final states

The $\ell\tau_h$ final state is sensitive mainly to the $\mathrm{H}^+ \to \tau\nu_\tau$ decay mode, whereas the dilepton final state is sensitive mainly to the $\mathrm{H}^+ \to \mathrm{t\bar{b}}$ decay mode. The ℓ+jets final state, instead, is sensitive only to the $\mathrm{H}^+ \to \mathrm{t\bar{b}}$: events with a charged Higgs decaying into τ leptons contribute only negligibly to this final state. Such final states have been studied by the CMS Collaboration [23].

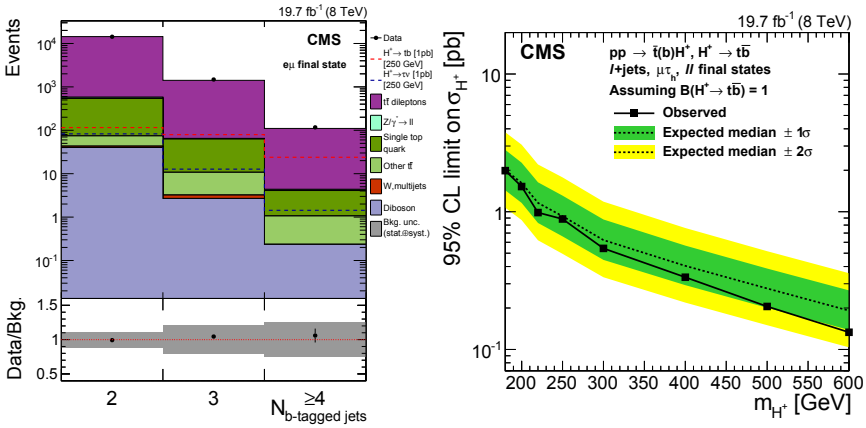

(a) (b)

FIGURE 6. (a) b-tagged jets multiplicity distribution for the eμ final state, after the full event selection. This distributions is used to set limits on σ_{H^+}. (b) 95% C.L. exclusion limits on σ_{H^+} for the combination of the $\mu\tau_h$, eμ, ee, $\mu\mu$, and ℓ + *jets* final states, for charged Higgs masses $180 < M_{H^+} < 600$ GeV. All figures are taken from [23].

The $\ell\tau_h$ final state had been studied for a light charged Higgs boson [21], and features as main background events in which a jet is misidentified as a τ_h: the data driven estimate is improved in [23] by taking into account the different composition of the backgrounds, in terms of quark jets and gluon jets, in the control and signal regions.

The ℓ+*jets* final state selects event with one isolated lepton, at least two jets, at least one b-tagged jet, and missing tranverse energy, yielding a final state dominated by $t\bar{t}$ and W+light/heavy flavours: backgrounds are estimated via a simultaneous fit from data in control regions.

The dilepton final state has been the first public result ever for a direct search of $H^+ \to t\bar{b}$, and proceeds by requiring two opposite sign leptons (with Z mass veto for the same flavour final states), at least two jets, missing transverse energy, and at least two b-tagged jets. The b-tagged jets multiplicity distribution (shown in Figure 6(a) for the eμ final sate) is expected to be biased towards higher multiplicity for the heavy charged Higgs production, in contrast to the SM top pair production, and is consequently used to set limits on σ_{H^+}.

Figure 6(b) shows the 95% C.L. exclusion limits on σ_{H^+} obtained combining the $\mu\tau_h$, eμ, ee, $\mu\mu$, and ℓ + *jets* final states, under the assumption that only the $H^+ \to t\bar{b}$ decay mode contributes to the signal yields (i.e. $\mathcal{B}(H^+ \to \tau\nu_\tau) = 0$). This is the first direct search ever for the $H^+ \to t\bar{b}$ decay mode.

Summary

Charged Higgs bosons have been searched for, by the ATLAS and CMS Collaboration, in a large spectrum of production and decay modes. The ATLAS Collaboration explored the cascade decay modes involving $h^0(125)$ and the vector boson fusion production, setting limits of 0.065–43 pb on $\sigma(gg \to H^0) \times \mathcal{B}(H^0 \to W^\mp H^\pm \to W^\pm W^\mp h^0 \to W^\pm W^\mp b\bar{b})$ [15], and of 31–1020 fb on $\sigma_{VBF} \times \mathcal{B}(H^\pm \to W^\pm Z)$ [18]. The $H^+ \to c\bar{s}$ decay mode has been examined by both Collaborations in the low tanβ regime, yielding limits of 4–2% on $\mathcal{B}(t \to H^+ b)$ [19, 20]. The $H^+ \to \tau\nu_\tau$ decay mode using the τ_h+jets final state has been probed by the ATLAS and CMS Collaborations for a vast range of masses, $M_{H^+} = 90 - 1000$ GeV, with the ATLAS result being more sensitive for $M_{H^+} > 400$ GeV and the CMS one more sensitive for $M_{H^+} = 90 - 400$ GeV [22, 23]. The CMS Collaboration obtained results for the first-ever direct search for the $H^+ \to t\bar{b}$ decay mode, yielding 95% C.L. exclusion limits of $\sigma(pp \to \bar{t}(b)H^+) \leq 4 - 0.5$ pb (assuming $\mathcal{B}(H^+ \to t\bar{b}) = 1$) [23]. The ATLAS and CMS Collaborations have interpreted their results in different MSSM scenarios, extending the region of phase space experimentally excluded for many of them. In particular, the low-M_H scenario has been completely ruled out by both Collaborations [22, 23].

REFERENCES

[1] ATLAS Collaboration, Observation of a new particle in the search for the Standard Model Higgs boson with the ATLAS detector at the LHC. *Phys. Lett. B*, 716 (2012), 1. [arxiv:1207.7214, doi:10.1016/j.physletb.2012.08.020]

[2] CMS Collaboration, Observation of a new boson at a mass of 125 GeV with the CMS experiment at the LHC. *Phys. Lett. B*, 716 (2012), 30. [arxiv:1207.7235, doi:10.1016/j.physletb.2012.08.021]

[3] CMS Collaboration, Observation of a new boson with mass near 125 GeV in pp collision at $\sqrt{s}$ = 7 and 8 TeV. *JHEP*, 06 (2013), 081. [arxiv:1303.4571, doi:10.1007/JHEP06(2013)081]

[4] ATLAS Collaboration, Measurements of Higgs boson production and couplings in diboson final states with the ATLAS detector at the LHC. *Phys. Lett. B*, 726 (2013), 88. [arxiv:1307.1427, doi:10.1016/j.physletb.2013.08.010]

[5] ATLAS Collaboration, Evidence for the spin-0 nature of the Higgs boson using ATLAS data. *Phys. Lett. B*, 726 (2013), 120. [arxiv:1307.1432, doi:10.1016/j.physletb.2013.08.026]

[6] CMS Collaboration, Study of the Mass and Spin-Parity of the Higgs Boson Candidate via its Decay to Z Boson Pairs. *Phys. Rev. Lett.*, 110 (2013), 081803. [arxiv:1212.6639, doi:10.1103/PhysRevLett.110.081803]

[7] CMS Collaboration, Measurement of the properties of a Higgs boson in the four-lepton final state. *Phys. Rev. D*, 88 (2014), 88, 081803. [arxiv:1312.5353, doi:10.1103/PhysRevD.89.092007]

[8] CMS Collaboration, Constraints on the Higgs boson width from off-shell production and decay to Z-boson pairs. *Phys. Lett. B*, 736 (2014), 64. [arxiv:1405.3455, doi:10.1016/j.physletb.2014.06.077]

[9] CMS Collaboration, Precise determination of the mass of the Higgs boson and tests of compatibility of its couplings with the standard model predictions using proton collisions at 7 and 8 TeV. *Eur. Phys. J. C*, 75 (2015), 212. [arxiv:1412.8662, doi:10.1140/epjc/s10052-015-3351-7]

[10] Lee, T. D., A Theory of Spontaneous T Violation. *Phys. Rev. D*, 8 (1973), 1226. [doi:10.1103/PhysRevD.8.1226]

[11] Djouadi, A., The Anatomy of Electro-Weak Symmetry Breaking. II: The Higgs bosons in the Minimal Supersymmetric Model. *Phys. Rep.*, 459 16 (2008), 1. [doi:10.1016/j.physrep.2007.10.005]

[12] Djouadi, A., Maiani, L., Moreau, G., Polosa, A., Quevillon, J., Riquer, V., The post-Higgs MSSM scenario: habemus MSSM?. *Eur. Phys. J. C*, 73 (2012), 2650. [doi:10.1140/epjc/s10052-013-2650-0]

[13] ATLAS Collaboration, The ATLAS Experiment at the CERN Large Hadron Collider. *J. Inst.* 3 (2008), S08003. [doi:10.1088/1748-0221/3/08/S08003]

[14] CMS Collaboration, The CMS experiment at the CERN LHC. J. Inst. 3 (2008), S08004. [doi10.1088/1748-0221/3/08/S08004]

[15] ATLAS Collaboration, Search for a multi-Higgs-boson cascade in $W^+W^-b\bar{b}$ events with the ATLAS detector in pp collisions at $\sqrt{s}$ = 8 TeV. *Phys. Rev. D*, 89 (2014), 032002. [doi:10.1103/PhysRevD.89.032002]

[16] Georgi, H., and Machacek, M., Doubly charged Higgs bosons. *Nucl. Phys. B* 262 (1985), 463. [doi:10.1016/0550-3213(85)90325-6]

[17] Cheung, K., and Ghosh, D. K., Triplet Higgs boson at hadron colliders. *J. High Energy Phys.* 11 (2002), 048. [doi:10.1088/1126-6708/2002/11/048]

[18] ATLAS Collaboration, Search for a Charged Higgs Boson Produced in the Vector-Boson Fusion Mode with Decay $H^\pm \to W^\pm Z$ using pp Collisions at $\sqrt{s}$ = 8 TeV with the ATLAS Experiment. *Phys. Rev. Lett.* 114 (2015), 231801. [doi:10.1103/PhysRevLett.114.231801]

[19] ATLAS Collaboration, Search for a light charged Higgs boson in the decay channel $H^+ \to c\bar{s}$ in $t\bar{t}$ events using pp collisions at $\sqrt{s}$ = 7 TeV with the ATLAS detector. *Eur. Phys. J. C* 73-6 (2013), 2465. [doi:10.1140/epjc/s10052-013-2465-z]

[20] CMS Collaboration, Search for H^+ to cs-bar decay. *CMS-PAS-HIG-13-035*, [CDS:1728343]

[21] CMS Collaboration, Updated search for a light charged Higgs boson in top quark decays in pp collisions at $\sqrt{s} = 7\ TeV$. *CMS-PAS-HIG-12-052*, [CDS:1502246]

[22] ATLAS Collaboration, Search for charged Higgs bosons decaying via $H^\pm \to \tau^\pm\nu$ in fully hadronic final states using pp collision data at $\sqrt{s} = 8TeV$ with the ATLAS detector. *J. High Energy Phys.* 03 (2015) 88. [doi:10.1007/JHEP03(2015)088]

[23] CMS Collaboration, Search for a charged Higgs boson in pp collisions at $\sqrt{s}$ = 8 TeV. *Submitted to J. High Energy Phys.*, [arXiv:1508.07774]

Proceedings of the LHCP2015 Conference, St. Petersburg, Russia, August 31 - September 5, 2015

Editors: V.T. Kim and D.E. Sosnov

Rare and Exotic decays of the Higgs boson at the LHC

YUTA TAKAHASHI

European Organization for Nuclear Research (CERN)

Yuta.Takahashi@cern.ch

On behalf of the ATLAS and CMS Collaborations

Abstract. The recent LHC searches on rare and exotic Higgs boson decays are presented. The analyses are individually performed by the ATLAS and CMS collaborations, using LHC run-1 dataset with an integrated luminosity of ~ 20 fb^{-1}. The standard model rare Higgs decays, such as $H \to \mu\mu$, $H \to ee$, and $H \to Z/\gamma^*(\to \ell\ell) + \gamma$ are reviewed first, followed by exotic decays, such as lepton-flavour violating decays ($H \to \mu\tau, e\tau, e\mu$) and decays into a pair of pseudoscalar Higgs bosons ($H \to 2a_1$).

Introduction

The Higgs boson was discovered in 2012 by the ATLAS and CMS collaborations [1, 2]. The observed properties of this particle, e.g. its couplings to fermions and bosons and its spin and parity, are consistent with those of the Standard Model (SM) Higgs boson with a mass near 125 GeV [3, 4, 5, 6]. However, as implied by the current constraints on the Higgs boson branching ratio to non-SM particles, $\mathcal{B}(H \to \text{BSM}) < 34\%$ @ 2σ [7], there is still plenty of room left for the possible contributions from physics beyond the SM. This motivates direct searches for rare and exotic Higgs decays at the LHC.

In this note, searches for the rare SM Higgs boson decays (H$\to ee, \mu\mu$ and $H \to Z/\gamma^*(\to \ell\ell)\gamma$) are reviewed first, followed by recent searches for exotic decays such as lepton-flavor violating Higgs decays (H$\to \mu\tau, e\tau$ and $e\mu$) and decays to a pair of light pseudoscalar neutral Higgs bosons, as predicted by next-to-minimal supersymmetric standard model [8]. References corresponding to the analysis described here can be found in [9, 10].

Rare Higgs decays

$H \to ee, \mu\mu$

In the SM, the decay rate of the Higgs boson into fermions is proportional to m_f^2, where m_f is the fermion mass. As such, the branching ratio of the Higgs boson decaying into $\tau\tau$ final state is by far the largest among Higgs leptonic decay (6%), while $\mu\mu$ (0.02%) and ee (5×10^{-7}%) are much smaller. Given the fact that the $\tau\tau$ final state is already observed with 5.5σ significance by combining the ATLAS and CMS results [7], non-observation of the $\mu\mu$ and ee final states will be the direct evidence that the Higgs leptonic coupling is not flavour universal, unlike $Z \to \ell\ell$.

The basic strategy of the analysis is to reconstruct di-lepton invariant mass (m_{ll}) and look for a narrow di-lepton resonance on top of the large Drell-Yan background, whose contribution is typically three orders of magnitude larger than the signal. In order to increase the analysis sensitivity, the event categorization is performed based on number of jets, p_T of the di-lepton system and the η of the lepton. Figure 1 shows the di-muon invariant mass distribution in one of the most sensitive category, the VBF (Vector Boson Fusion) category with more than 2 jets satisfying $m_{jj} > 500$ GeV, $|\eta_{j1} - \eta_{j2}| > 3$ and $\eta_{j1} \times \eta_{j2} < 0$.

The obtained $m_{\ell\ell}$ distributions are fitted by signal and background templates, where an analytic function is used for the background modelings. Since no excess is observed, 95% C.L upper limits are set on the $H \to \mu^+\mu^-$ signal strength in units of the signal expected in the SM: 7.0 (obs) / 7.2 (exp) in the ATLAS analysis (assuming $m_H = 125.5$ GeV), while 7.4 (obs) / 6.5 (exp) in the CMS analysis (assuming $m_H = 125$ GeV). The CMS collaboration

also puts the upper limit on the cross-section times $H \to ee$ branching ratio: 0.0041 pb. These results imply that the Higgs leptonic coupling is indeed not flavour universal. The $H \to \mu\mu$ final state is expected to become accessible with 400 fb^{-1} of data at $\sqrt{s} = 13$ TeV, which will be the scope of high-luminosity LHC.

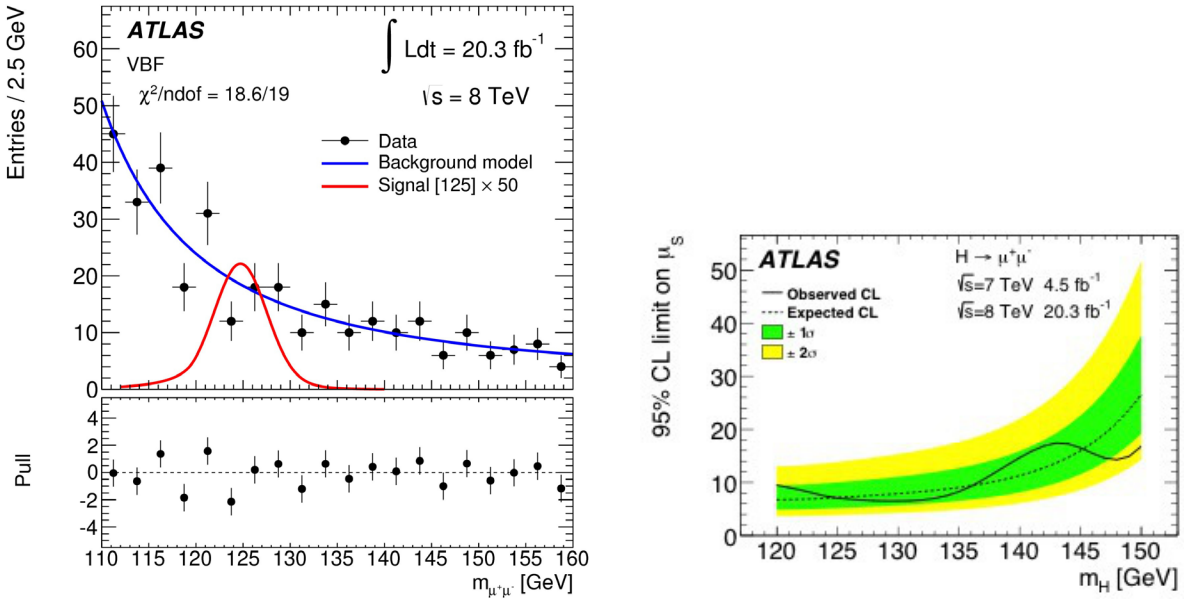

FIGURE 1. (left) di-muon invariant mass distribution in the VBF category, i.e. events with more than 2 jets with $m_{jj} > 500$ GeV, $|\eta_{j1} - \eta_{j2}| > 3$ and $\eta_{j1} \times \eta_{j2} < 0$. (right) observed (solid) and expected (dashed) 95% confidence level upper limits on the $H \to \mu^+\mu^-$ signal strength as a function of m_H. The green and yellow band shows $\pm 1\sigma$, $\pm 2\sigma$, respectively.

$H \to Z/\gamma^*(\to \ell\ell)\gamma$

The other important rare decay of the Higgs boson is $H \to Z/\gamma^* + \gamma$ [11, 12, 13]. Because of the exploitation of the $Z/\gamma^* \to \ell\ell$ decay in the analysis, the relative production rate of the $Z\gamma \to \ell\ell\gamma$ ($\gamma^*\gamma \to \ell\ell\gamma$) is merely 2.2% (4.0%) compared to the $H \to \gamma\gamma$ decay. However, observation of this final state is motivated, as a large enhancement of the branching ratio can be expected by heavy charged particles in the loop, just as for the $H \to \gamma\gamma$ decay.

The analysis proceeds by selecting events with opposite-sign lepton pairs (ee or $\mu\mu$) with one isolated photon. In order to increase the analysis sensitivity, an event categorization based on the η of the lepton, η of the photon, and shower shape variable are used in the CMS analysis. ATLAS exploits the categorization based on the $\Delta\eta(Z, \gamma)$ and Higgs p_T with respect to the thrust axis of the event. Further improvement has been obtained, in the ATLAS analysis, by using Z mass constraint fit to the lepton kinematics, which leads to 20% better $\ell\ell\gamma$ mass resolution.

As a discriminant variable, the invariant mass of the $\ell\ell\gamma$ system was used. Concerning the $H \to Z\gamma$ analysis, an additional requirement on the di-lepton mass is applied, e.g. $m_{\ell\ell} > m_Z - 10$ GeV. The dominant backgrounds come from irreducible initial-state radiation SM $Z\gamma$ production, which is modeled by an analytic function. Since no excess above the backgrounds was found, the upper limit on the signal strength is set to be $\mu < 11$ (obs) / 9 (exp) in ATLAS, and $\mu < 9.5$ (obs) / 10 (exp) in CMS analysis.

CMS also performed searches, targeting $H \to \gamma^*(\to \ell\ell)\gamma$ decay. To ensure that the di-lepton comes from low-mass γ^*, $m_{\ell\ell} < 20$ GeV is additionally required. Events with di-muon mass in the range $2.9 < m_{\mu\mu} < 3.3$ GeV and $9.3 < m_{\mu\mu} < 9.7$ GeV, however, are rejected to avoid $J/\psi \to \mu\mu$ and $\Upsilon \to \mu\mu$ contributions. Figure 2 shows the $m_{\mu\mu\gamma}$ spectra for the 8 TeV data and shows no excess above the expected backgrounds. The upper limit is set on the μ value as a function of m_H and at 125 GeV, $\mu < 7.7$ (exp. 6.4) is obtained. It should be noted that events consistent with $J/\psi \to \mu\mu$ in di-muon invariant mass are also used to set a 95% C.L limit on the branching ratio, $\mathcal{B}(H \to (J/\psi)\gamma) < 1.5 \times 10^{-3}$, although that is 540 times the SM prediction for $m_H = 125$ GeV [12].

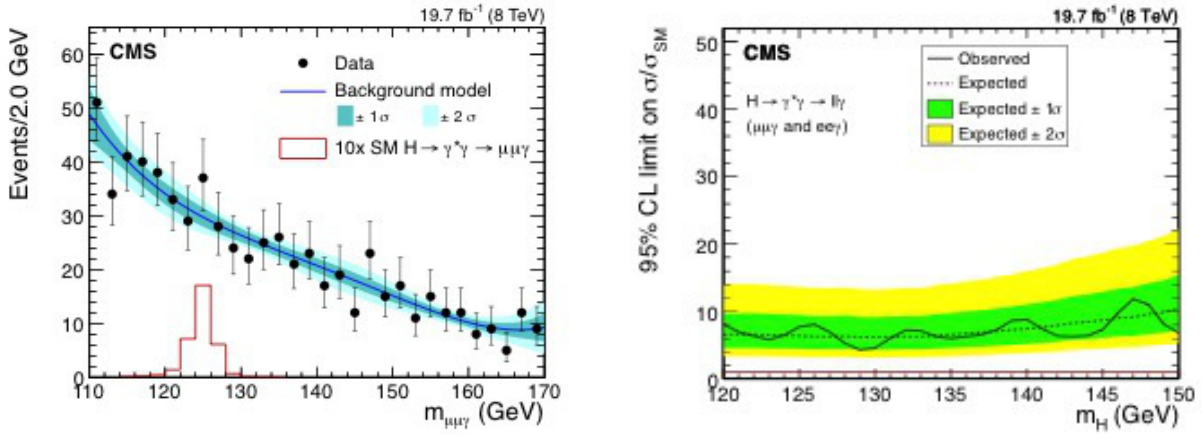

FIGURE 2. (left) $m_{\mu\mu\gamma}$ spectra at 8TeV, together with the result of a background-only fit to the data. (right) 95% C.L upper limit on the μ-value as a function of m_H.

Exotic Higgs decays

Lepton Flavour Violating decay : $H \to e\tau, \mu\tau, e\mu$

Within the SM, the leptonic-flavour violating decays of the Higgs boson are forbidden. However, such decays can naturally occur in supersymmetric models [14], composite Higgs models [15], models with flavour symmetries [16], Randall-Sundrum models [17], and many others. The pre-LHC limits on such decays are $\mathcal{B}(H \to e\mu) < 10^{-8}$, obtained from null search results on $\mu \to e\gamma$, and $\mathcal{B}(H \to \mu\tau, e\tau) < O(10\%)$, obtained from $\tau \to \mu\gamma, e\gamma$, other rare τ decays, and muon $g-2$ experiments. The weak constraints on $H \to \mu\tau$ and $H \to e\tau$ motivate direct searches at the LHC.

The analysis strategy is similar to that of the SM $H \to \tau\tau$ search. However, as depicted in Figure 3, there are striking differences in kinematic variables which can be exploited to select the events. For example, one can expect harder lepton p_T spectrum and the collinearity between the missing transverse energy (E_T^{miss}) and the lepton in the lepton-flavour violating decay.

After a set of event selections, CMS adopts the collinear mass as the final discriminant for the $H \to \mu\tau$ and $H \to e\tau$ analysis, while the $e\mu$ invariant mass is used for the $e\mu$ channel. ATLAS analyzed $H \to \mu\tau_{had}$ final state and uses a mass estimator, $m_{\mu\tau}^{MMC}$, reconstructed by the observed muon, hadronic τ and E_T^{miss}. The dominant backgrounds depend on the categories, but in general, come from Drell-Yan $Z \to \tau\tau$. To increase the analysis sensitivity, CMS categorizes the events based on the number of reconstructed jets, while ATLAS uses the transverse mass, $m_T(\mu, E_T^{miss})$ and $m_T(\tau, E_T^{miss})$ to define the signal region. Figure 4 shows discriminant variable distributions in recent papers [18, 19, 20].

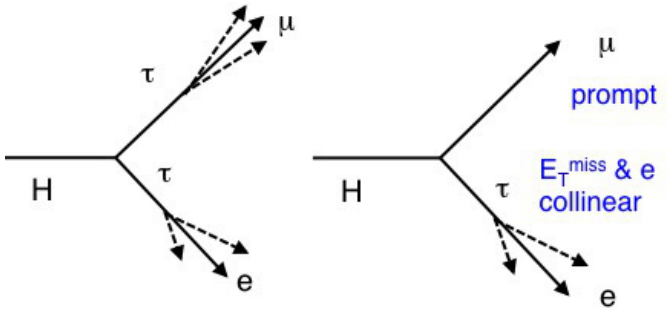

FIGURE 3. Schematic difference in the (left) SM $H \to \tau_\mu\tau_e$ decay and (right) lepton-flavour violating $H \to \mu\tau_e$decay.

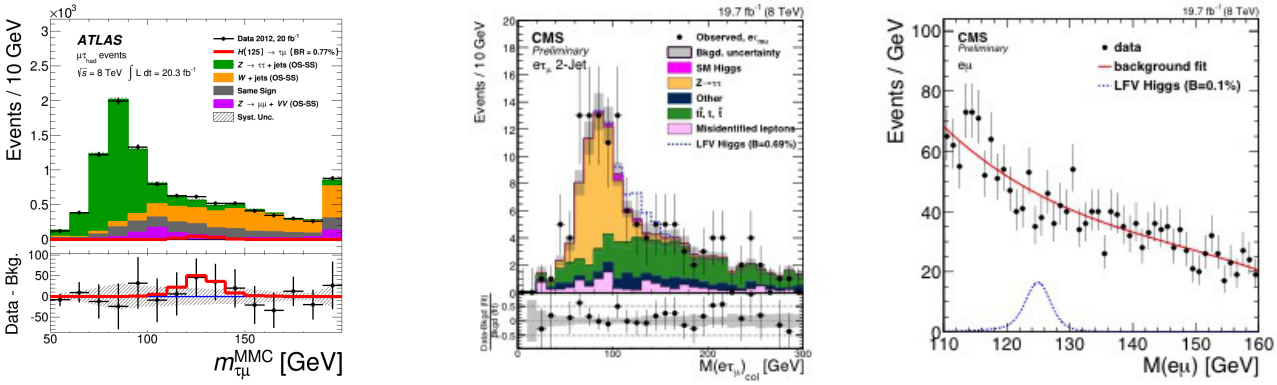

FIGURE 4. From left to right, post-fit combined $m^{MMC}_{\mu\tau_{had}}$ distribution obtained by adding individual distributions in signal regions (ATLAS), collinear $e\tau$ mass distribution in the 2 jet category (CMS), and invariant $e\mu$ mass distribution (CMS).

Table 1 summarizes obtained upper limit on the branching ratio for the lepton-flavour violating decays. The obtained limits in $e\tau$ and $\mu\tau$ channels are 0.7-1.9% level, which improves current indirect bounds by an order of magnitude. These limits are subsequently used to constrain the $\mu\tau$, $e\tau$ and $e\mu$ Yukawa coupling, which is $\sqrt{|Y_{\mu\tau}|^2 + |Y_{\tau\mu}|^2} < 3.6 \times 10^{-3}$, $\sqrt{|Y_{e\tau}|^2 + |Y_{\tau e}|^2} < 2.41 \times 10^{-3}$, and $\sqrt{|Y_{e\mu}|^2 + |Y_{\mu e}|^2} < 5.43 \times 10^{-4}$, respectively. Given the slight excess in the $H \to \mu\tau$ channel in both ATLAS (1.3σ) and CMS (2.4σ) analysis, it will be interesting to pursue with LHC run-2 data.

TABLE 1. Observed / expected upper limit on the lepton-flavour violating Higgs decay and its best fit value.

	ATLAS		CMS	
channel	$\mu\tau_{had}$	$\mu\tau$	$e\tau$	$e\mu$
obs. (exp.) limit	$< 1.85\%(1.24\%)$	$< 1.51\%(0.75\%)$	$< 0.69\%(0.75\%)$	$< 0.036\%(0.048\%)$
Best fit	$0.77 \pm 0.62\%$	$0.84^{+0.39}_{-0.37}\%$	$-0.10^{+0.37}_{-0.36}\%$	—

Light pseudoscalar decay : $H \to a_1 a_1 \to 4\mu$

In the next-to-minimal supersymmetric standard model (NMSSM), the Higgs sector is extended to have three CP-even Higgs bosons $h_{1,2,3}$, two CP-odd neutral Higgs bosons $a_{1,2}$ and a pair of charged Higgs bosons $H^{\pm}$. The h_1 or h_2 can decay via $h_{1,2} \to 2a_1$. where either the h_1 or h_2 can be the observed Higgs boson. If the a_1 mass lies within $2m_\mu < m_{a_1} < 2m_\tau$, the decay, $a_1 \to \mu^+\mu^-$ will be the dominant one. This motivates searches for 4μ final states [21].

The events are selected if there is a pair of low-mass di-muons with similar invariant mass. Figure 5 shows the 2D correlation plot between the 1st and 2nd di-muon invariant mass. The signal region is defined as the diagonal component of this plot, denoted by the white dashed lines. The dominant backgrounds come from SM $b\bar{b}$ production.

The off-diagonal sideband region, which lies outside the white dashed lines, is used to estimate the expected background in the signal region. Together with small backgrounds arising from electroweak production of four muons and direct $J\psi$ production, the expected background in the signal region is estimated to be 2.2 ± 0.7, while 1 event is observed at $m_{1,\mu\mu} = 0.33$ GeV, $m_{2,\mu\mu} = 0.22$ GeV. Since the observed yield is consistent with background expectation, the limit was set in the context of the next-to-minimal supersymmetric standard model, and in scenarios containing a hidden sector, including those predicting a non-negligible light boson lifetime.

Light pseudoscalar decay : $H \to a_1 a_1 \to \mu\mu\tau\tau$

Similarly to the 4μ analysis, one can also target the a_1 mass range $2m_\tau < m_{a_1}$ [22]. ATLAS performed such searches with $\mu\mu\tau\tau$ final state. Although the production rate of $\mu\mu\tau\tau$ final state is roughly 1/100, compared to the 4τ final state, one can benefit from a larger S/B ratio in this channel. In this analysis, at least one of the τ-leptons is required to decay leptonically.

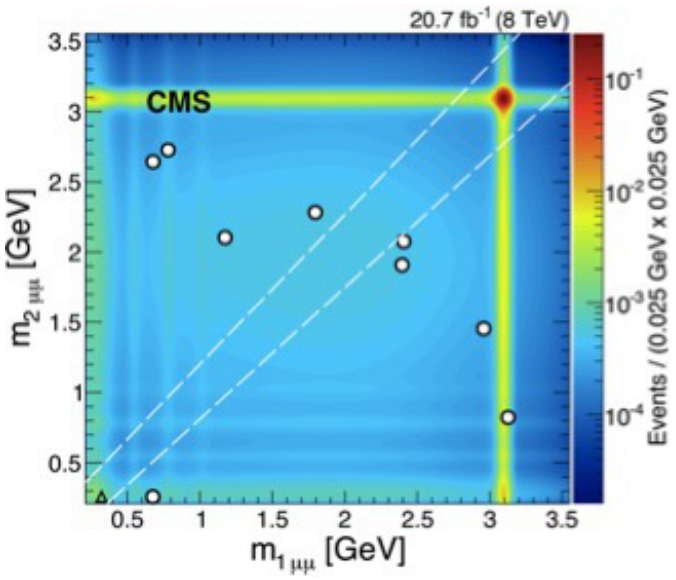

FIGURE 5. Distribution of the invariant masses $m_{1,\mu\mu}$ and $m_{2,\mu\mu}$ for the isolated di-muon pair events. The signal region is outlined as a white dashed lines, containing one data event (triangle) at $m_{1,\mu\mu} = 0.33$ GeV, $m_{2,\mu\mu} = 0.22$ GeV.

The analysis proceeds by selecting events with opposite-charge muons, with $p_T(\mu\mu) > 40$ GeV and $2.8 < m_{\mu\mu} < 70$ GeV. The high p_T requirement on the di-muon system stems from the fact that the two a_1 bosons are expected to be produced back-to-back in the transverse plane. The event must contain a third lepton (muon or electron) that is coming from the τ-lepton decay.

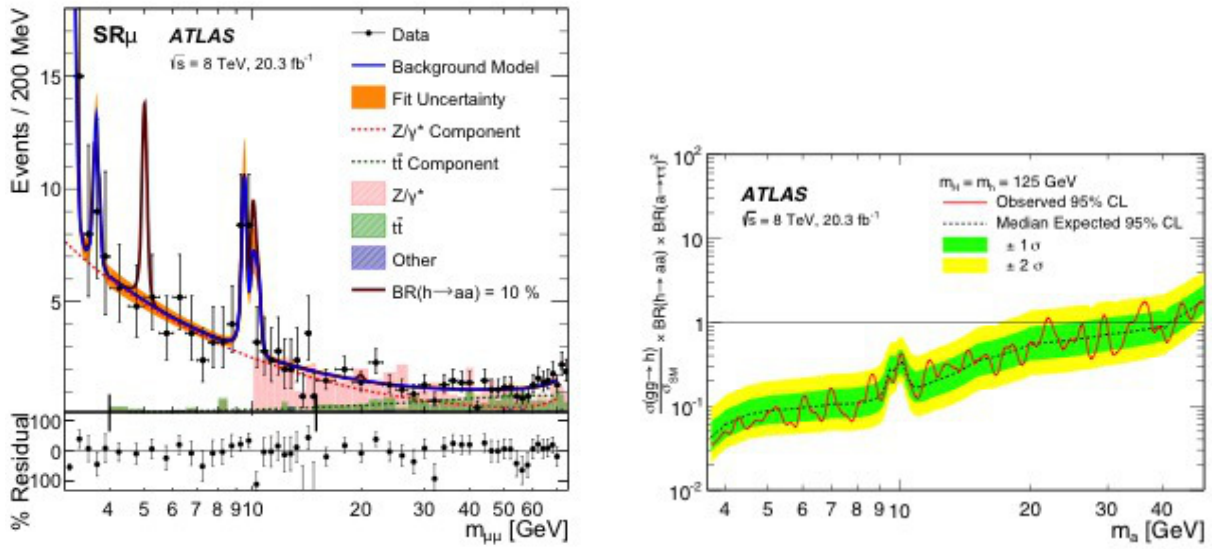

FIGURE 6. observed $m_{\mu\mu}$ distribution in the signal region and the background-only fit. The expected signal distribution from a signal with $\mathcal{B}(h \to aa) = 10\%$ is shown for three different m_a hypothesis (5, 10, and 20 GeV).

After a set of event selections, the di-muon invariant mass distribution is used to evaluate the possible excess, as shown in Figure 6. The full background model consists of six SM resonances ($J/\psi, \psi', \Upsilon_{1S}, \Upsilon_{2S}, \Upsilon_{3S}$ and Z), $t\bar{t}$ components and continuum Drell-Yan backgrounds. The signal and each SM resonances are modeled by double-sided Crystal Ball functions, and an un-binned log-likelihood fit is performed on the observed di-muon invariant mass

spectra to a combination of background and signal models. No excess of data is observed in the di-muon mass range from 3.7 GeV to 50 GeV. Upper limits are placed on the production of $H \to a_1 a_1$ relative to the SM $gg \to H$ production. Assuming no coupling of the a boson to quarks, the most stringent limit is placed at 3.5% for m_a = 3.75 GeV.

Summary

Since the discovery of the Higgs-like boson, searches have been made for rare and exotic Higgs decays by the ATLAS and CMS collaborations. The rare Higgs decays, such as $H \to ee, \mu\mu$, $H \to Z/\gamma^* + \gamma$, have not been observed yet with the run-1 dataset (19.7 fb^{-1}), as expected by the standard model. The current upper limit on the signal strength lies 7-11 times the SM values, and these channels are expected to become visible with high-luminosity LHC data. The exotic Higgs decays, e.g. lepton-flavour violating decays, decays into a pair of light pseudoscalar in the $\mu\mu\mu\mu$ or $\mu\mu\tau\tau$ final states, depending on the a_1 mass range, have been also explored using LHC run-1 dataset. Although there is a mild excess in the $H \to \mu\tau$ decay, there are, in general, no surprises up to now.

It should be noted that there is still plenty of room left for the contributions from physics beyond the SM, that is compatible with the observed Higgs boson. The current weak constraint on the Higgs branching ratio to the non-SM particles, $\mathcal{B}(H \to BSM) < 34\%$ (2σ), encourages to continue these interesting searches throughout LHC run-2.

REFERENCES

[1] ATLAS Collaboration, Phys. Lett. B 716 (2012) 1-29
[2] CMS Collaboration, Phys. Lett. B 716 (2012) 30-61
[3] ATLAS Collaboration, Phys. Lett. B 726 (2013) 88-119
[4] ATLAS Collaboration, Phys. Lett. B 726 (2013) 120-144
[5] CMS Collaboration, Phys. Rev. D 92 (2015) 012004
[6] CMS Collaboration, Eur. Phys. J. C 75 (2015) 212
[7] ATLAS and CMS Collaborations, Measurements of the Higgs boson production and decay rates and constraints on its couplings from a combined ATLAS and CMS analysis of the LHC pp collision data at $\sqrt{s}$ = 7 and 8 TeV, ATLAS-CONF-2015-044, CMS-PAS-HIG-15-002
[8] U. Ellwanger, M. Rausch de Traubenberg, and C. A. Savoy, Phenomenology of supersymmetric models with a singlet, Nucl. Phys. B 492 (1997) 21,
[9] All ATLAS Higgs Physics Public Results, presented in this note, can be found at `https://twiki.cern.ch/twiki/bin/view/AtlasPublic/HiggsPublicResults`
[10] All CMS Higgs Physics Public Results, presented in this note, can be found at `http://cms-results.web.cern.ch/cms-results/public-results/publications/HIG/index.html`
[11] CMS Collaboration, Phys. Lett. B 726 (2013) 587-609
[12] CMS Collaboration, Search for a Higgs boson decaying into $\gamma^*\gamma \to \ell\ell\gamma$ with low dilepton mass in pp collisions at $\sqrt{s}$ = 8 TeV, arXiv:1507.03031, CMS-HIG-14-003
[13] ATLAS Collaboration, Phys. Lett. B 732C (2014), 8-27
[14] J. L. Diaz-Cruz and J. J. Toscano, Lepton flavor violating decays of Higgs bosons beyond the standard model, Phys. Rev. D 62 (2000) 116005
[15] K. Agashe and R. Contino, Composite Higgs-mediated FCNC, Phys. Rev. D 80 (2009) 075016
[16] H. Ishimori et al., Non-Abelian Discrete Symmetries in Particle Physics, Prog. Theor. Phys. Suppl. 183 (2010) 1
[17] S. Casagrande et al., Flavor physics in the Randall-Sundrum Model I. Theoretical setup and electroweak precision tests, JHEP 10 (2008) 094
[18] CMS Collaboration, Phys. Lett. B 749 (2015) 337
[19] CMS Collaboration, Search for lepton-flavour-violating decays of the Higgs boson to $e\tau$ and $e\mu$ at $\sqrt{s}$ = 8 TeV, CMS-PAS-HIG-14-040
[20] ATLAS Collaboration, Search for lepton-flavour-violating $H \to \mu\tau$ decays of the Higgs boson with the ATLAS detector, arXiv:1508.03372, CERN-PH-EP-2015-184
[21] CMS Collaboration, A search for pair production of new light bosons decaying into muons, arXiv:1506.00424, CMS-HIG-13-010
[22] ATLAS Collaboration, Phys. Rev. D92 (2015) 052002

Proceedings of the LHCP2015 Conference, St. Petersburg, Russia, August 31 - September 5, 2015

Editors: V.T. Kim and D.E. Sosnov

Search for Invisible Decays of the Higgs boson at the LHC

ANDREW P. WHITE

Physics Department, University of Texas at Arlington, Arlington, TX76019, USA

awhite@uta.edu

On behalf of the ATLAS and CMS Collaborations

Abstract. Results are presented from the ATLAS and CMS experiments on searches for invisible decays of the Higgs boson using data from Run 1 at the CERN Large Hadron Collider.

INTRODUCTION

Results on Higgs boson couplings to date indicate that the discovered particle at M_h = 125 GeV is consistent with Standard Model expectations. However, within the current experimental uncertainties, there still remains the possibility that the Higgs boson could have a significant branching ratio to non-Standard Model particles [1]. A natural question is then whether the Standard Model Higgs boson, which is assumed to be ubiquitous in our universe, could be coupled to as yet undiscovered particles, such as those making up the Dark Matter. If indeed the Higgs boson does couple to Dark Matter, then the limit on the associated branching fraction can be used to set a limit on the Dark Matter-nucleon interaction mediated by the Higgs boson.

This paper presents the results of several analyses by ATLAS [2]and CMS [3]which set limits on the branching ratio of the Higgs boson into invisible final states. The results, interpreted in terms of WIMP(Weakly Interacting Massive Particle)-nucleon scattering cross-section limits, are compared with results from direct WIMP searches.

The various search channels for Higgs boson to invisible decays are described, followed by details of each type search. The results from all searches are then summarized, and the limits compared with the results of direct WIMP-nucleon dark matter search experiments.

Higgs boson to Invisible Search Channels

Three types of physics processes have been used to establish limits on the branching ratio for Higgs boson invisible decays: associated production of a Z boson and Higgs boson with the Z boson decaying to charged leptons or b-bar, the production of a W or Z boson with a Higgs boson with the W or Z bosons decaying to jet(s), and the production of a Higgs boson via vector-boson fusion with associated forward and backward jets with a large rapidity gap. The associated Feynman diagrams for these processes are shown in Figure 1. In all cases, the basic technique is to isolate and measure the rate of events that could result from production of the Higgs boson, with decay to invisible particles, and with the rest of the event recoiling against the unseen Higgs boson.

Searches via ZH production

ATLAS ZH - with Z boson decay to charged leptons [4]

ATLAS uses a single and dilepton triggers and, after a requirement of the lepton pair to be consistent with a Z boson, requires missing transverse momentum E_T^{miss} >90 GeV to take advantage of the steeply falling E_T^{miss} for the Z boson background. A selection is applied to follow the expected signal characteristics - the invisibly decaying Higgs boson

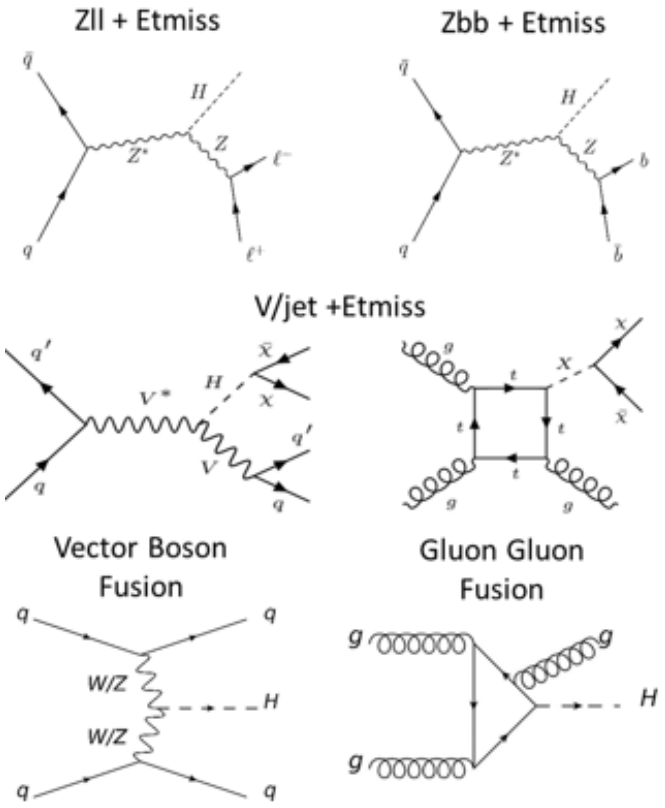

FIGURE 1. Feynman diagrams for the search channels for Higgs boson to Invisible Decays.

should be opposite the Z, a small di-lepton opening angle from a boosted Z, and no reconstructed jets with P_T >25 GeV and $|\eta|$ <2.5. The dominant backgrounds from ZZ and WZ are estimated from simulation, and other backgrounds with a genuine lepton pair are estimated from data. Figure 2 shows the E_T^{miss} for the 8 TeV data after the full selection. The results of a maximum likelihood fit to E_T^{miss} sets an upper limit on the Higgs boson to invisible branching ratio of 75% at 95% confidence level with an expected limit of 62%.

CMS ZH - with Z boson decay to charged leptons [5]

CMS also uses a single and dilepton triggers, but accepts events with 0 or 1 jet. The two jet categories are treated separately as they have different signal to background ratios. Events with two or more jets with P_T >30 GeV are rejected to suppress Drell-Yan + jets events. Backgrounds from WZ and ZZ events are estimated from simulation, while residual Drell-Yan events are estimated from a gamma + jets sample. Other backgrounds from top, tW, WW, W+jets, and Z $\rightarrow \tau\tau$ are estimated using a control sample of like-sign e-mu events. The main systematic uncertainties from the signal and background theoretical estimates are at the level of 8-9%. The limit on the Higgs boson to invisible branching ratio was obtained from a profile likelihood fit to 2-dimensional distributions of the azimuthal opening angle between the charged leptons and the transverse mass of the di-lepton and system, see Figure 3. The result is an observed limit of 83% at 95% confidence level with 86% expected.

CMS ZH - with Z boson decay to $b\,\bar{b}$ [5]

For this channel CMS uses an E_T^{miss} trigger and several E_T^{miss} plus jets triggers. The basic selection is for events with large E_T^{miss}, a jet pair consistent with Z $\rightarrow$ b bar with jets tagged by the CSV algorithm, large azimuthal separation between the Z boson and E_T^{miss}, and a relatively low di-jet invariant mass <250 GeV. The data is divided into three

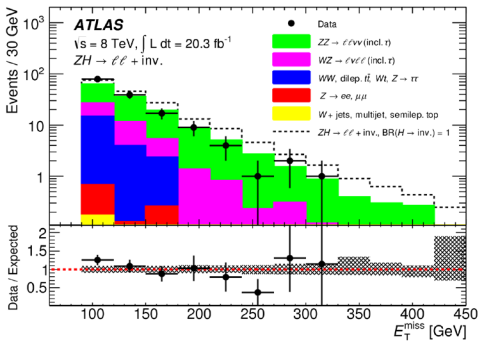

FIGURE 2. ATLAS E_T^{miss} after full selection for ZH, with Z boson decay to charged leptons [4].

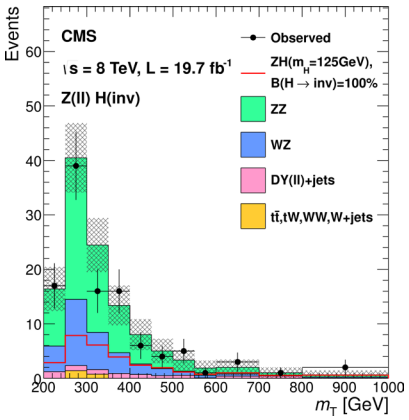

FIGURE 3. Transverse mass of the di-lepton and E_T^{miss} system [5].

regions of low, intermediate and high E_T^{miss}. Prominent backgrounds result from events with Z and/or W bosons decaying to b quarks, or produced in association with b quarks. A boosted decision tree (BDT) approach is used to enhance selection of heavy flavor, and identify a high boost Higgs boson. The limit on Higgs boson to invisible decays is determined by a fit to the BDT output distribution - shown in Figure 4. The limit is 182% with 199% expected. When combined with the CMS result above with the Z boson decaying to charged leptons, the limit is 81% at 95% confidence level with 83% expected.

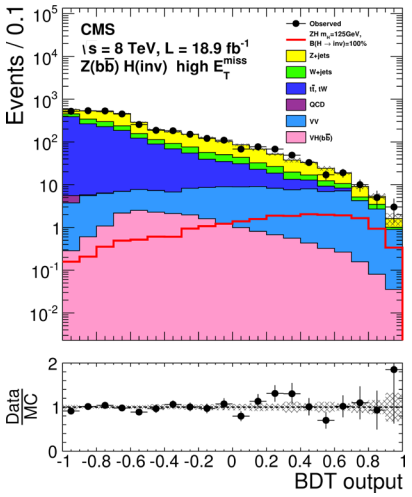

FIGURE 4. CMS BDT output distribution for high E_T^{miss} [5].

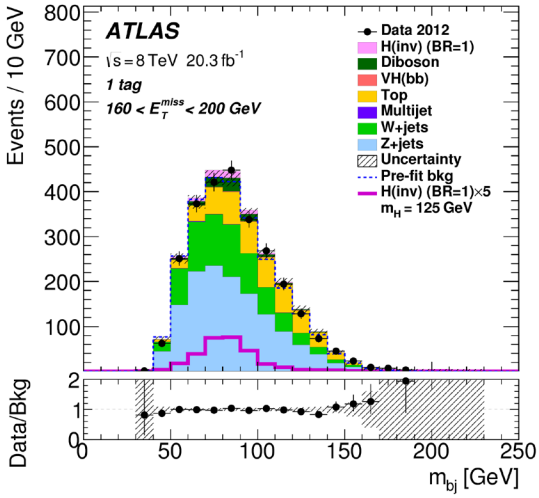

FIGURE 5. Post-fit distribution of M(bj) for one b-tag events [6].

Searches via Vector Boson production with decays to jets

ATLAS VH - with V decay to jets [6]

Data are taken with an E_T^{miss} trigger, requiring at least 80 GeV. Analysis selection requires a di-jet mass consistent with W or Z boson with ΔR(jj) restricted for boosted W or Z bosons. Signal regions are defined by the presence of 0, 1 or 2 b-tags. The analysis is optimized in four regions of E_T^{miss}, with separate requirements on ΔR(jj) and M(jj) for each region. The main backgrounds are from vector-boson plus jet production and from top production. The vector-boson

plus jets background is estimated from regions enhanced in W+jets or Z+jets with the simulated events reweighted to match the data. The limit is extracted from a fit to the E_T^{miss} distributions for signal and sidebands (events failing the M(jj) requirement), and vector-boson P_T distributions for the control regions. Figure 5 shows an example of a post-fit distribution for the case of single b-tag events. An upper limit is set on invisible Higgs boson decays of 78% at 95% confidence level with 86% expected.

CMS - Vector boson or monojet plus E_T^{miss} [7]

The search for new physics in mono-jet and mono-vector-boson channels is interpreted to give a limit for Higgs boson to invisible decays. Data were taken using various E_T^{miss} triggers. Events are selected if they have large E_T^{miss}, one or more jets, and no well-identified charged lepton or photon with P_T >10 GeV (15 GeV for taus). Three categories of events are identified using a multivariate vector-boson tagging technique: an unresolved (boosted) single fat jet with 60 GeV <M <110 GeV, two resolved jets with 60 GeV <M(jj) <110 GeV and E_T^{miss} >250 GeV, a monojet with no tag, large P_T, and large E_T^{miss}. Backgrounds come from W bosons with a missed charged lepton) or Z $\rightarrow \nu\nu$ plus jets are estimated using control regions. E_T^{miss} spectra for the vector-boson plus jets backgrounds are corrected by simultaneous likelihood fits across all control regions. The resulting reweighted events are used to give E_T^{miss} templates in the signal region. Finally, the limit is extracted from a template fit to E_T^{miss}. Figure 6 shows the E_T^{miss} distribution for the resolved jet category. A limit of 53% at 95% confidence level is set with 62% expected.

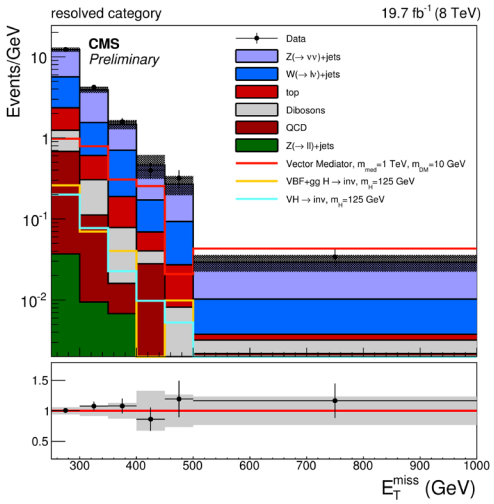

FIGURE 6. E_T^{miss} for the resolved jet category [7].

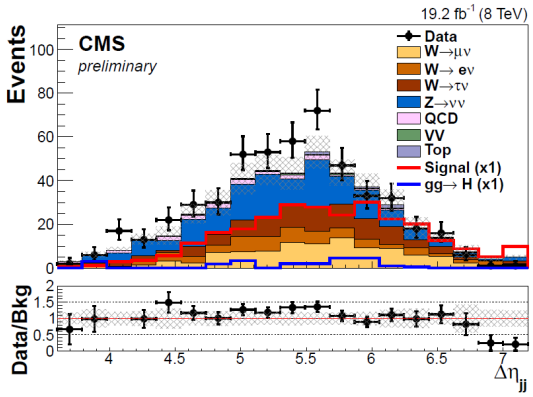

FIGURE 7. $\Delta\eta$(jj) for the CMS VBF search [8].

Searches via Vector-boson fusion (VBF)

CMS - VBF [8]

The basic trigger for this search is an E_T^{miss} requirement of 40 GeV at the first level, plus a particle flow jet pair with requirements on jet P_T, M(jj), and $\Delta\eta$(jj) which varied with the data taking period. Event selection is aimed at the VBF topology of significant E_T^{miss} from the invisible Higgs boson decay paired with forward-backward jets. The selection also aims to reduce the multijet background from fake and genuine E_T^{miss}. The main backgrounds from W and Z bosons plus jets are estimated from simulation, normalized to data in independent control regions with inverted lepton requirements. The multijet background is estimated from data using a non-isolated E_T^{miss} region with normalization from a sideband region. Figure 7 shows the $\Delta\eta$(jj) distributions for signal (BR = 100%) and backgrounds after the full selection. An upper limit of 57% at 95% confidence level is set with 40% expected.

ATLAS - VBF [9]

The ATLAS VBF search starts with an E_T^{miss} trigger (>80 GeV). Three orthogonal signal regions are defined, the primary one requiring large M(jj) >1000 GeV, and $\Delta\eta$(jj) >4.8, the other regions being motivated by a search with monojet plus E_T^{miss}. Angular requirements using the direction of jets and E_T^{miss} are applied to suppress the multijet background and a veto on charged leptons reduces backgrounds from processes with W and Z bosons. The backgrounds from W boson plus jets is estimated from a W boson control region, while the background from Z $\rightarrow \nu\nu$ plus jets is estimated from both W and Z bosons control regions. The multijet background is estimated from data using a control region with an inversion of the requirement that no jet points along the direction of the E_T^{miss}. Efficiencies of cuts from this control region are then applied to the signal region. The limit on invisible Higgs boson decays is computed using a maximum likelihood fit to yields in the signal regions and the W and Z bosons control regions. A limit of 28% at 95% confidence level is set, with 31% expected, with most of the sensitivity coming from the primary signal region. Figure 8 shows the final E_T^{miss} distribution in the primary signal region after the full selection.

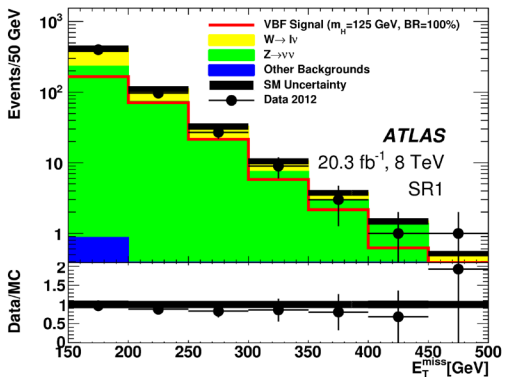

FIGURE 8. The final E_T^{miss} distribution from the primary signal region for the ATLAS VBF search [9].

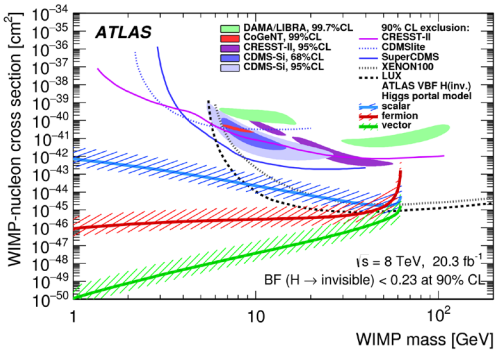

FIGURE 9. Limits on Dark Matter (WIMP) Nucleon cross section from the ATLAS VBF search and from direct search experiments [9].

Summary and Conclusions

Table 1 summarizes the limits obtained on Higgs boson to invisible decays for all the analyses described above. The best limit is from the ATLAS VBF search. This limit is further improved by the inclusion of the ATLAS limit from visible decays (which includes photons, charged leptons, b-quarks, and vector bosons). The combined limit is 23% at 95% confidence level with 24% expected [1]. CMS also has a combined search result (from gluon fusion, vector boson fusion, and vector boson associated production) with a limit of 36% at 95% confidence level with 30% expected.

TABLE 1. Result of ATLAS and CMS Searches for Higgs Boson to Invisible Decays.

Process	Experiment	Observed limit	Expected limit
Z(→ ll)	ATLAS	75%	62%
Z(→ ll)	CMS	83%	86%
Z(→ bbar)	CMS	182%	199%
V(W/Z → jets)	ATLAS	78%	86%
V/jet +E_T^{miss}	CMS	53%	62%
VBF	CMS	57%	40%
VBF	ATLAS	28%	31%

The limits on the Higgs boson to invisible decays can be interpreted in terms of upper limits on the spin-independent Dark-Matter nucleon cross-section. This result is compared with the limits from direct searches in Fig-

ure 9 [9] using the result from the ATLAS VBF search.

ACKNOWLEDGMENTS

Support from the U.S. Department of Energy under award number DE-SC0011686 is gratefully acknowledged.

REFERENCES

[1] ATLAS Collaboration, CERN-PH-EP-2015-191 arXiv:1509.00672 [hep-ex]
[2] ATLAS Collaboration, JINST 3 S08003 (2008).
[3] CMS Collaboration, JINST 3 S08004 (2008).
[4] ATLAS Collaboration, Phys. Rev. Lett. 112 201802 (2014) arXiv:1402.3244 [hep-ex].
[5] CMS Collaboration, EPJC 74 2980 (2014) arXiv:1404.1344 [hep-ex].
[6] ATLAS Collaboration, EPJC 75 337 (2015) arXiv:1504.04324 [hep-ex].
[7] CMS Collaboration, CMS-PAS-EXO-12-055, http://cdsweb.cern.ch/record/2036044
[8] CMS Collaboration, CMS-PAS-HIG-14-038, http://cdsweb.cern.ch/record/2007270
[9] ATLAS Collaboration, CERN-PH-EP-2015-186, arXiv:1508.07869 [hep-ex].
[10] L. Caminada et al, CMS Collaboration, www.physik.uzh.ch/reports/jb/2014/section13.pdf

Exotic physics: parallel talks

Proceedings of the LHCP2015 Conference, St. Petersburg, Russia, August 31 - September 5, 2015

Editors: V.T. Kim and D.E. Sosnov

Searches for Light Exotics at LHCb

FEDERICO LEO REDI

Imperial College, London

On behalf of the LHCb Collaboration

Abstract. We report on the latest direct searches for light exotics at LHCb, conducted during Run I of LHC. This proceedings are divided into two sections, the first part will cover the search for the lepton number violating decay $B \to \pi^+\mu^-\mu^-$ while the second part will cover the search for a low mass dark boson in the decay $B^0 \to K^{*0}\chi$, with $\chi \to \mu^+\mu^-$ and $K^{*0} \to K^+\pi^-$. The data used in these searches correspond to integrated luminosities of 1.0 and 2.0 fb^{-1} collected in pp collisions at centre of mass energies of $\sqrt{s}$ = 7 and 8 TeV in pp collisions with the LHCb detector.

Introduction

The LHCb detector is one of the four main detectors that operate at the Large Hadron Collider (LHC) at CERN. The LHCb detector consists of a single-arm forward spectrometer operating in the region of pseudorapidity, $1.9 < \eta < 4.9$. The detector was originally designed to study the production and decay of hadrons containing b and c quarks and indirectly probing the strength of the Standard Model (SM). The LHCb detector is now playing a fundamental role also in other areas of research, such as direct searches of rare SM decays and exotica. Exotica searches at LHCb primarily consist in Higgs physics and direct searches for beyond the SM particles. Many theoretical models predict the existence of new particles: their existence can be detected either directly through the production of on-shell particles or indirectly through virtual contributions in loop processes.

During Run I of the LHC, LHCb recorded data at a centre of mass energy $\sqrt{(s)}$ = 7 TeV (for 2010 and 2011) and 8 TeV (for 2012) corresponding to an integrated luminosity of 1.0 and 2.0 fb^{-1} respectively.

The SM is an incomplete theory. Not only the SM is in conflict with the observations of non-zero neutrino masses, the excess of matter over antimatter in the Universe, and the presence of non-baryonic dark matter but it also presents a number of fine-tuning problems (such as the hierarchy and strong CP problems). Beyond the SM (BSM) physics has been searched for at the LHC without success so far. Nevertheless LHCb is an ideal experiment to probe unique regions BSM phase space thanks to the detector unique particle identification capabilities, precise secondary vertex reconstruction and accurate measurements of lifetime, momentum and invariant mass. Throughout this document charge conjugation is implied unless explicitly stated otherwise and $c = 1$.

Search for Majorana Neutrinos in $B \to \pi^+\mu^-\mu^-$ Decays at LHCb

The nature of neutrinos in the SM has not been defined yet: neutrinos could either be Dirac fermions or their own antiparticle. In the latter case they are called "Majorana" particles [1]. Some of the most economical theories that can account simultaneously for neutrino masses and oscillations, baryogenesis, and dark matter, extend the SM by requiring the existance of a fourth neutrino generation. Since a fourth neutrino generation can couple with SM particles there exist many ways of searching for such particles, one of them being the neutrino-less double β decay. The approach followed by LHCb is different and complementary, which performs a direct search in heavy flavour decays, similar to what has been done in the past [2, 3, 4, 5].

The LHCb experiment has performed many studies for Majorana Neutrino produced in B^- decays, probing a wide range of masses and lifetimes; these searches were performed for the lepton flavour violating decays $B^- \to h^+\mu^-\mu^-$,

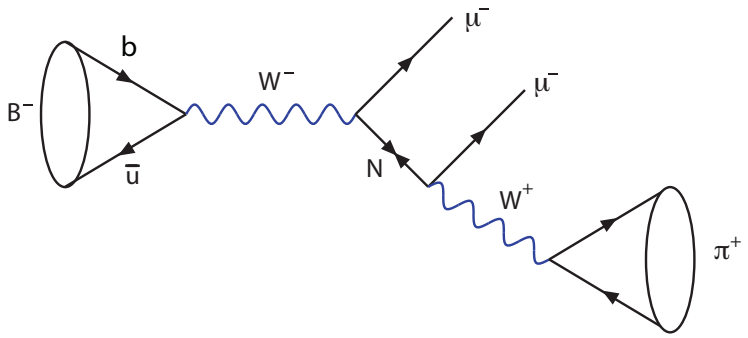

FIGURE 1. Feynman diagram for $B^- \to \pi^+\mu^-\mu^-$ decay mediated by a Majorana neutrino (N). Reproduced from [8].

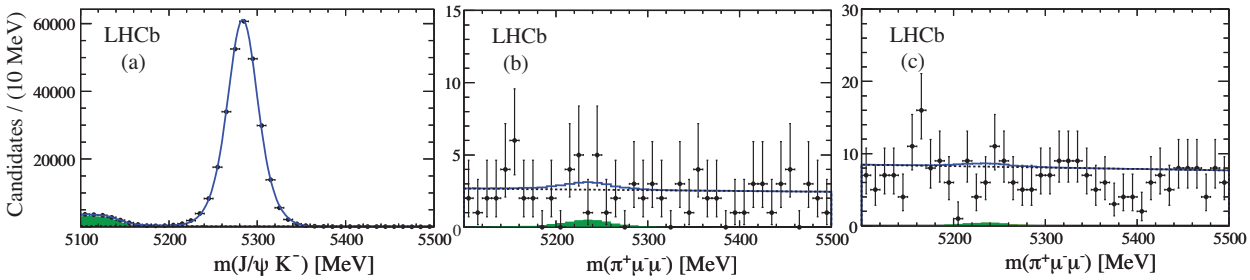

FIGURE 2. Invariant mass distributions with fits overlaid of candidate mass spectra for (a) $J/\psi\, K^-$, (b) $\pi^+\mu^-\mu^-$ ($\mathcal{S}$) , and (c) $\pi^+\mu^-\mu^-$ ($\mathcal{L}$). Where $\mathcal{S}$ $\mathcal{L}$ indicates the two different data samples one for short τ_N and another for τ_N up to 1000 ps. Peaking backgrounds are (green) shaded. The dotted lines show the combinatorial backgrounds only. The solid line shows the sum of both backgrounds [8].

where h is a hadron. These types of decays are prohibited by the SM but can happen thanks to production of on-shell Majorana neutrinos. The LHCb collaboration published three papers using different final states and different data sets:

- $h^+ = K^+$ or π^+, with ~36 pb^{-1} ($\sqrt{s}$ =7 TeV) [6].
- $h^+ = D^+$, D^{*+}, D_s^+ and $D^0\pi^+$, with ~410 pb^{-1} ($\sqrt{s}$ =7 TeV) [7].
- $h^+ = \pi^+$, with 3.0 fb^{-1} ($\sqrt{s}$ =7 TeV + $\sqrt{s}$ =8 TeV) [8].

This proceedings will concentrate on the latter paper, being the most recent of the three.

A Feynman diagram for the lepton number and flavour violating decay $B^- \to \pi^+\mu^-\mu^-$ is shown in Fig. 1. This decay is prohibited by the SM but can happen thanks to production of on-shell Majorana neutrinos, it has been chosen as it is one of the most sensitive way to look for Majorana neutrinos in B decays [8]. This decay, which has been theoretically modelled in Ref. [9], is sensitive to contributions from both on- and off-shell Majorana neutrino. More specifically if the mass of the Majorana neutrino, m_N, is smaller than $m_B - m_\mu$ then it can be produced on-shell with a finite lifetime in the detector. If, on the other hand, m_N is larger then it can still contribute to the decay as a virtual particle.

The selection is designed to maximise the efficiency squared divided by the background yield. This allows for decay products to be detached from the B^- decay vertex, therefore τ_N can span from few picoseconds up to ~ 1000 ps. Because for lifetimes ~ 1 ps, the $\pi^+\mu^-$ vertex can be significantly detached from the B^- decay vertex two different strategies are used: one for short τ_N ($\mathcal{S}$) and another for τ_N up to 1000 ps ($\mathcal{L}$).

In order to reduce the systematic uncertainty and to convert the yield into a branching fraction, the normalisation channel $B^- \to J/\psi\, K^-$ (with $J/\psi \to \mu^+\mu^-$) was chosen. For the $\mathcal{S}$ category and the normalisation channel the $\mu^-\mu^-\pi^+$ candidate combinations must, when reconstructed, form a common vertex. For the $\mathcal{L}$ category the $\pi^+\mu^-$ pair can be significantly displaced from the B^- vertex. A B^- candidate decay vertex is searched for by tracing back a neutrino N candidate to another μ^- in the event, which must form a vertex.

Figure 2 shows the mass spectra for the selected candidates. No signal is observed in both the $\mathcal{S}$ and $\mathcal{L}$ samples.

In order to set upper limits the Confidence Level method is used [10]. The signal region is defined as the mass interval within $\pm 2\sigma$ of the B^- mass where σ is the mass resolution. Because no evidence for a signal is found, upper

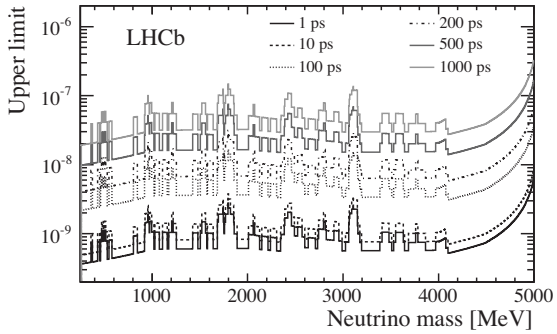

FIGURE 3. Upper limits on $\mathcal{B}(B^- \to \pi^+\mu^-\mu^-)$ at 95% C.L. as a function of m_N, in 5 MeV intervals, for specific values of τ_N [8].

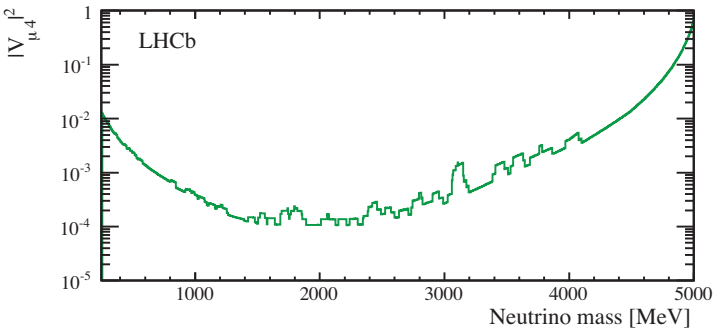

FIGURE 4. Upper limits at 95% C.L. on the fourth generation neutrino coupling to the muon $|V_{\mu 4}|^2$ are shown as a function of the mass of the Majorana neutrino m_N for the events in the displaced region [8].

limits are set by scanning across the m_N window. The efficiency is highest for τ_N of a few ps, then it decreases rapidly until $\tau_N \sim 200$ ps when it levels off until $\tau_N \sim 1000$ ps. After this value, the efficiency decreases to ~ 0 because most of the decays happen outside of the vertex detector. The multi-dimensional plot of the upper limit on $\mathcal{B}(B^- \to \pi^+\mu^-\mu^-)$ is shown in Fig. 3.

A model dependent upper limit on the coupling of a single fourth-generation Majorana neutrino to muons, $|V_{\mu 4}|$, for each value of m_N, is calculated using an expansion of the formula used by Ref. [9]. The resulting 95% C.L. limit on $|V_{\mu 4}|^2$ is extracted as a function of m_N and is shown in Fig. 4.

A Search for the Decay of a Hidden Sector Particle $\chi \to \mu^+\mu^-$ in $B^0 \to K^{*0}\chi$ at LHCb

In particle physics, the term hidden-sector refers to the set of predicted particles that do not interact via the gauge boson forces of the SM. Interest in hidden-sector SM extensions has increased [11] due to the lack of any new TeV scale particles and missing evidence for a dark matter candidate that could solve the open questions in high energy physics [12, 13, 14, 15, 16, 17, 18]. As for the Majorana neutrino, coupling between the SM and hidden-sector particles may arise via mixing between the hidden-sector field and any SM field with an associated particle that is not charged under the electromagnetic or strong interaction. This mixing could provide a portal through which a hidden-sector particle, χ, may be produced when kinematically allowed. This proceedings will concentrate on the search performed by LHCb for a hidden-sector boson produced in the decay $B^0 \to K^{*0}\chi$, with $\chi \to \mu^+\mu^-$ and $K^{*0} \to K^+\pi^-$ (throughout this proceedings, $K^{*0} \equiv K^*(892)^0$) [19].

As shown in Fig. 5, the $b \to s$ transition is mediated by a top quark loop at leading order. For this reason, χ boson with a sizeable top quark coupling, *e.g.* obtained via mixing with the Higgs sector, could be produced at a substantial rate in such decays. The dataset used for this analysis is the same used for the Majorana neutrino search reported in the previous chapter.

The search is conducted, as outlined in Ref. [20], by scanning the $m(\mu^+\mu^-)$ distribution for an excess of χ signal

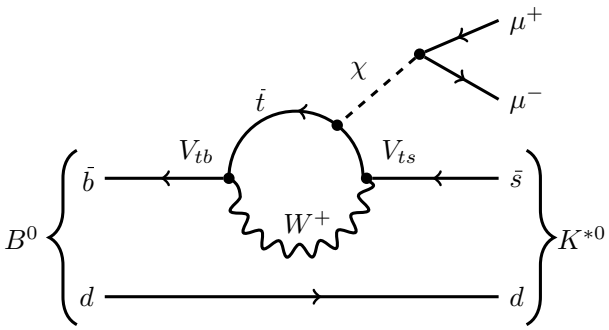

FIGURE 5. Feynman diagram for the decay $B^0 \to K^{*0}\chi$, with $\chi \to \mu^+\mu^-$ [19].

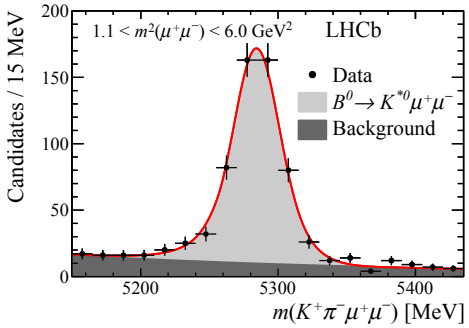

FIGURE 6. Invariant mass spectrum with fit overlaid [19].

candidates over the expected background. The $\chi \to \mu^+\mu^-$ decay vertex is permitted, but not required, to be displaced from the $B^0 \to K^{*0}\chi$ decay vertex. Two regions of reconstructed dimuon lifetime, $\tau(\mu^+\mu^-)$, are defined for each $m(\chi)$ considered in the search: a prompt region and a displaced region. Narrow resonances are vetoed by excluding the regions near the ω, ϕ, J/ψ, $\psi(2S)$ and $\psi(3770)$ resonances. These regions are removed in both the prompt and displaced samples to avoid contamination from unassociated dimuon and K^{*0} resonances.

The branching fraction product $\mathcal{B}(B^0 \to K^{*0}\chi(\mu^+\mu^-)) \equiv \mathcal{B}(B^0 \to K^{*0}\chi) \times \mathcal{B}(\chi \to \mu^+\mu^-)$ is measured relative to $\mathcal{B}(B^0 \to K^{*0}\mu^+\mu^-)$, where the normalisation sample is taken from the prompt region. Figure 6 shows the $K^+\pi^-\mu^+\mu^-$ control channel mass distribution for all prompt candidates that satisfy the full selection. An extended unbinned likelihood fit is performed on the control channel to the mass spectrum.

The $m(\mu^+\mu^-)$ distributions in both the prompt and displaced regions for candidates with an invariant mass that lies in a window of 50 MeV around the known B^0 mass are shown in Fig. 7. The p-value of the no-signal hypothesis is 80%, showing no evidence for a hidden-sector boson. Because no signal events are found, Fig. 8 shows the upper limits on $\mathcal{B}(B^0 \to K^{*0}\chi(\mu^+\mu^-))$, relative to $\mathcal{B}(B^0 \to K^{*0}\mu^+\mu^-)$, set at the 95% C.L. for different values of $\tau(\chi)$. As the Figure shows, the limits become less stringent for $\tau(\chi) \gtrsim 10$ ps, as the probability of the dark boson decaying within the vertex locator decreases. The branching fraction $\mathcal{B}(B^0 \to K^{*0}\mu^+\mu^-) = (1.6 \pm 0.3) \times 10^{-7}$ [21] is used to obtain upper limits on $\mathcal{B}(B^0 \to K^{*0}\chi(\mu^+\mu^-))$, which are also shown in Fig. 8.

Conclusions

In these proceedings we have provided two examples of direct searches for light exotics in the LHCb detector. This shows how LHCb can make contributions in the intensity frontier searches for BSM physics, where light particles are rarely coupling to the SM filed. As an example, Fig. 9 shows the existing experimental limits for the mixing parameter $|V_{\mu 4}|$ as a function of the Majorana neutrino candidate mass. It is striking that DELPHI was the last experiment to set a limit in the region of phase space above the charm quark mass. This means that LHCb is one of the few experiments, up to date, able to further constrain the phase space for this parameter.

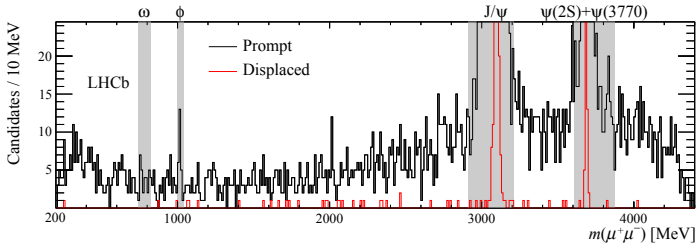

FIGURE 7. Distribution of $m(\mu^+\mu^-)$ in the (black) prompt and (red) displaced regions. The shaded bands denote regions where no search is performed due to (possible) resonance contributions. The J/ψ, $\psi(2S)$ and $\psi(3770)$ peaks are suppressed to better display the search region [19].

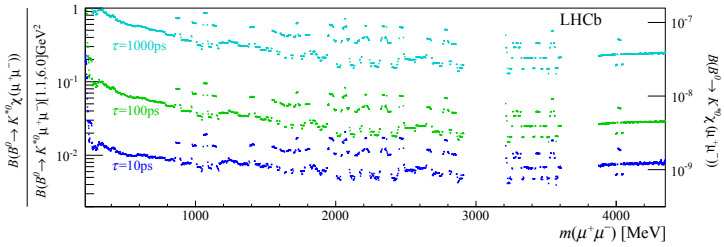

FIGURE 8. Upper limits at 95% CL for (left axis) $\mathcal{B}(B^0 \to K^{*0}\chi(\mu^+\mu^-))/\mathcal{B}(B^0 \to K^{*0}\mu^+\mu^-)$, with $B^0 \to K^{*0}\mu^+\mu^-$ in $1.1 < m^2(\mu^+\mu^-) < 6.0\,\mathrm{GeV}^2$, and (right axis) $\mathcal{B}(B^0 \to K^{*0}\chi(\mu^+\mu^-))$ [19].

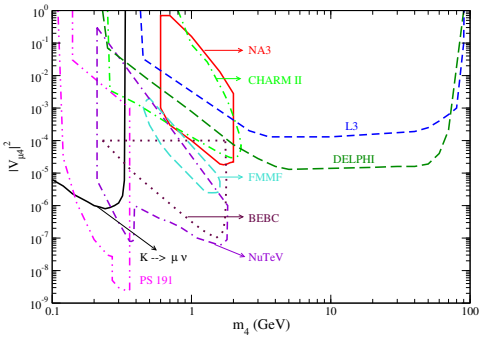

FIGURE 9. Limits on $|V_{\mu 4}|$ as a function of m_4 as set by previous non LHCb results. The area indicated by dotted lines are at 95% confidence level. Reproduced from [9].

REFERENCES

[1] E. Majorana, *Teoria simmetrica dell 0 elettrone e del positrone*, Nuovo Cim. **14** (1937) 171.

[2] LHCb collaboration, R. Aaij *et al., Searches for Majorana neutrinos in B^- decays*, Phys. Rev. **D85** (2012) 112004, arXiv:1201.5600.

[3] LHCb collaboration, R. Aaij *et al., Search for the lepton number violating decays $B^+ \to \pi^-\mu^+\mu^+$ and $B^+ \to K^-\mu^+\mu^+$*, Phys. Rev. Lett. **108** (2012) 101601, arXiv:1110.0730.

[4] BaBar collaboration, J. P. Lees *et al., Search for lepton-number violating $B^+ \to X^-\ell^+\ell^+$ decays*, arXiv:1310.8238.

[5] BELLE collaboration, O. Seon *et al., Search for lepton-number-violating $B^+ \to D^-\ell^+\ell'^+$ decays*, Phys. Rev. **D84** (2011) 071106, arXiv:1107.0642.

[6] LHCb collaboration, R. Aaij *et al., Search for lepton number violating decays $B^+ \to \pi^-\mu^+\mu^+$ and $B^+ \to K^-\mu^+\mu^+$*, Phys. Rev. Lett. **108** (2012) 101601, arXiv:1110.0730.

[7] LHCb collaboration, R. Aaij *et al., Searches for Majorana neutrinos in B decays*, Phys. Rev. **D85** (2012) 112004, arXiv:1201.5600.

[8] LHCb collaboration, R. Aaij *et al., Search for Majorana neutrinos in $B^- \to \pi^+\mu^-\mu^-$ decays*, Phys. Rev. Lett. **112** (2014) 131802, arXiv:1401.5361.

[9] A. Atre, T. Han, S. Pascoli, and B. Zhang, *The search for heavy Majorana neutrinos*, JHEP **05** (2009) 030, arXiv:0901.3589.

[10] T. Junk, *Confidence level computation for combining searches with small statistics*, Nucl. Instrum. Meth. **A434** (1999) 1435.

[11] R. Essig *et al., Working Group Report: New Light Weakly Coupled Particles, in Community Summer Study 2013: Snowmass on the Mississippi (CSS2013) Minneapolis, MN, USA, July 29-August 6, 2013*, 2013. arXiv:1311.0029.

[12] G. Weidenspointner *et al., The sky distribution of positronium annihilation continuum emission measured with spi/integral*, Astron. Astrophys. **450** (2006) 1012, arXiv:astro-ph/0601673.

[13] J. Chang *et al., An excess of cosmic ray electrons at energies of 300-800 GeV*, Nature **456** (2008) 362.

[14] PAMELA collaboration, O. Adriani *et al., An anomalous positron abundance in cosmic rays with energies 1.5-100 GeV*, Nature **458** (2009) 607, arXiv:0810.4995.

[15] PAMELA collaboration, O. Adriani *et al., The cosmic-ray electron flux measured by the PAMELA experiment between 1 and 625 GeV*, Phys. Rev. Lett. **106** (2011) 201101, arXiv:1103.2880.

[16] PAMELA collaboration, O. Adriani *et al., Cosmic-Ray Positron Energy Spectrum Measured by PAMELA*, Phys. Rev. Lett. **111** (2013) 081102, arXiv:1308.0133.

[17] Fermi-LAT collaboration, M. Ackermann *et al., Measurement of separate cosmic-ray electron and positron spectra with the Fermi Large Area Telescope*, Phys. Rev. Lett. **108** (2012) 011103, arXiv:1109.0521.

[18] AMS collaboration, M. Aguilar *et al., Electron and Positron Fluxes in Primary Cosmic Rays Measured with the Alpha Magnetic Spectrometer on the International Space Station*, Phys. Rev. Lett. **113** (2014) 121102.

[19] LHCb collaboration, R. Aaij *et al., Search for hidden-sector bosons in $B^0 \to K^{*0}\mu^+\mu^-$ decays*, Phys. Rev. Lett. **115** (2015) 161802, arXiv:1508.04094.

[20] M. Williams, *Searching for a particle of unknown mass and lifetime in the presence of an unknown non-monotonic background*, JINST **10** (2015), no. 06 P06002, arXiv:1503.04767.

[21] LHCb collaboration, R. Aaij *et al., Differential branching fraction and angular analysis of the decay $B^0 \to K^{*0}\mu^+\mu^-$*, JHEP **08** (2013) 131, arXiv:1304.6325.

Proceedings of the LHCP2015 Conference, St. Petersburg, Russia, August 31 - September 5, 2015

Editors: V.T. Kim and D.E. Sosnov

Theory Motivation For Exotic Signatures: Prospects and Wishlist for Run II

DANIEL STOLARSKI

Theory Division, Physics Department, CERN, CH-1211 Geneva 23, Switzerland

daniel.stolarski@cern.ch

Abstract. Here I give some motivations for exotic signatures to search for at Run II of the LHC, focusing on displaced phenomena. I will discuss signatures arising from various different kinds of models including theories of dark matter and those with exotic decays of the Higgs.

WHAT IS EXOTICS?

I was given the charge of motivating exotics searches in Run II without being given a definition of exotics. ATLAS and CMS have exotics groups, and looking at the searches within these groups, the common theme appears to be signals that do not appear in supersymmetry (SUSY). Yet, nearly every exotic search can be rewritten in terms of a SUSY model. For example, leptoquark searches look for the operator

$$\mathcal{L} = LQ\, q\, \ell \tag{1}$$

where q and ℓ are the Standard Model (SM) quark and lepton, and LQ is the particle being searched for. But if we simply relabel $LQ \to \tilde{d}$, then the operator in Equation 1 is exactly the operator that appears in the R-parity violating superpotential in SUSY: $W = \lambda' L\, Q\, D$.

Another example of exotics secretly being SUSY is a search for a diboson resonance which has received a great deal of attention lately [1]. Supersymmetric extensions of the Standard Model often have a problem of predicting a Higgs mass much lighter than the observed value. In the MSSM for example, at tree level $m_h \leq m_Z$. One of the most elegant solutions to this problem is "non-decoupling D-terms" [2, 3] which require a new gauge force and therefore new heavy vector bosons. These bosons must couple to the Higgs to raise the Higgs mass, and therefore should also couple to W and Z bosons, so such a model of non-decoupling D-terms could fit a potential excess in a diboson search [4]. See also [5] for another SUSY explanation of such an excess presented at LHCP.

Therefore, I use a very different and much more experimentally based definition of exotics: new experimental objects that cannot be produced in the SM. In this talk, I will consider a subset of this definition and focus on displaced signatures, those arising from decays of *long-lived* exotic particles somewhere in the detector but away from the interaction point. Finally, I will give a disclaimer that even with this narrow focus, I only give a few examples of scenarios that give rise to these signatures.

The simplest motivation for exotics is that it could be there, and if it is, we do not want to miss any new physics discoveries. Furthermore, the majority of searches for new physics are looking under the lamppost, namely they are looking for theories for which perturbation theory can be used to make precise predictions. Yet, nature need not be so kind as to allow us to use perturbation theory, so we need to explore as many types of theories as possible. Below I give some more concrete motivations for exotics, but we must keep a broad perspective in our experimental searches.

DARK MATTER

Cosmological observations give extremely strong evidence for the existence of dark matter and for it making up about one quarter of the energy budget of the universe. Yet, the particle physics properties of dark matter are still completely

unknown. A well studied example of a dark matter candidate is the weakly interacting massive particle (WIMP), but searches at both the LHC and in direct detection experiments have thus far only placed limits on WIMP scenarios. Therefore, considering other scenarios for dark matter is extremely well motivated.

Freeze-In

In the WIMP scenario, dark matter is in equilibrium with the SM thermal bath until the temperature drops below its mass when the annihilation of dark matter freezes out and sets the present day abundance. An alternative scenario is the so-called freeze-in mechanism [6], where dark matter is never in thermal equilibrium with the SM, but couples very weakly so that the SM thermal bath slowly leaks energy into the dark sector. This small coupling sets the abundance, and it was recently shown [7] that the size of this small parameter naturally implies long-lived particles that decay within the detector at LHC experiments.

In these models, the process is $B \to A_{\rm SM} X$ where X is dark matter with a mass of at most 100 GeV, but it could be orders of magnitude lighter. B is a new state with large couplings to the SM but small couplings to dark matter that sets the freeze-in abundance, so the B field is naturally long lived. $A_{\rm SM}$ can be virtually any SM state such as h, Z, $\ell^+\ell^-$, $q\bar{q}$, γ,..., so these models give a motivated scenario to search for virtually any SM state originating in any or all of the sub-detector regions.

Asymmetric Dark Matter and Emerging Jets

The ratio of the energy density of dark matter to baryons in our universe is about five, but it could have been orders of magnitude larger or smaller. In the WIMP paradigm, there is no explanation for why these energy densities are similar. An alternative is asymmetric dark matter: the number density of dark matter is controlled by the fact that there are more dark matter particles than anti-dark matter particles, much like the baryon asymmetry of our universe. This is an old idea [8] reviewed in [9]. If the same physics controls the dark matter and baryon asymmetry, then you naturally get that the number density of dark matter and baryons is comparable. But in most of the models that do this, the mass of the dark matter is a free parameter that needs to be set to be similar to the proton mass by hand, and therefore these models do not fully explain the coincidence of dark matter and baryons energy density.

The mass of the proton is explained by dimensional transmutation, so a theory of dark matter that has a QCD-like sector whose confinement scale is similar to that of QCD could then explain this coincidence, and such a model was presented in [10]. In such a theory, there is a whole zoo of hadrons in the dark sector that will also have GeV scale masses.

If there exists a heavy (TeV scale) mediator that couples to SM fields and dark quarks, something that automatically happens in the model of [10], then one could produce dark quark pairs at the LHC. Because the mediator is much heavier than the confinement scale, this process would result in jets of dark sector hadrons. The existence of the mediator also causes the dark pions to decay back into SM fields, and the natural length scale of this decay is O(cm). Therefore, the jet which starts out completely invisible at short distance slowly appears with each dark hadron decaying in a different place and creating a different displaced vertex. We have termed this structure *emerging jets* [11], and the signatures at the LHC are quite spectacular with a discovery potential for mediators well into the TeV scale, as shown in Figure 1.

OTHER MOTIVATIONS FOR DISPLACED SIGNATURES

Exotic Higgs Decays

The usual gauge hierarchy, the quadratic sensitivity of the Higgs mass to high scale physics is most problematic for the top quark loop. The hierarchy problem is solved and the top loop is cancelled by fermionic (scalar) top partners in theories of composite Higgs (supersymmetry). The dominant production mechanism of these partners at the LHC occurs because they are coloured, but they do not need to be! Twin Higgs [12] (folded SUSY [13]) models have uncoloured fermionic (scalar) top partners that can still cancel the SM top loop.

In order for these mechanisms to work, there still needs to be a colour factor in the loop, so many of these models have a twin colour gauge group that confines at the GeV scale. Some models have signatures that are similar to emerging jets discussed above, but the mediator can be the SM Higgs, motivating searches for exotics Higgs decays with displaced vertices. The signatures can be quite rich depending on the spectrum of the different confined twin

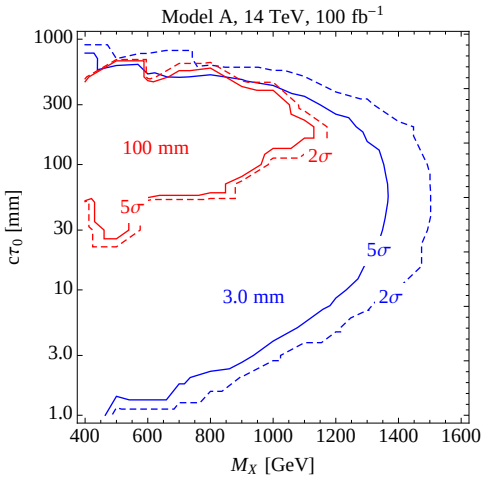

FIGURE 1. (Figure 10 from [11]) Discovery reach for the emerging jets scenario presented in [11]. The horizontal axis is the mediator mass which controls the production cross section, and the vertical is the dark pion lifetime.

states, and some of the possibilities are detailed in Figure 2 [14]. Other possibilities are studied in [15], and other models that give displaced Higgs decays as well as their prospects for the LHC are given in [16].

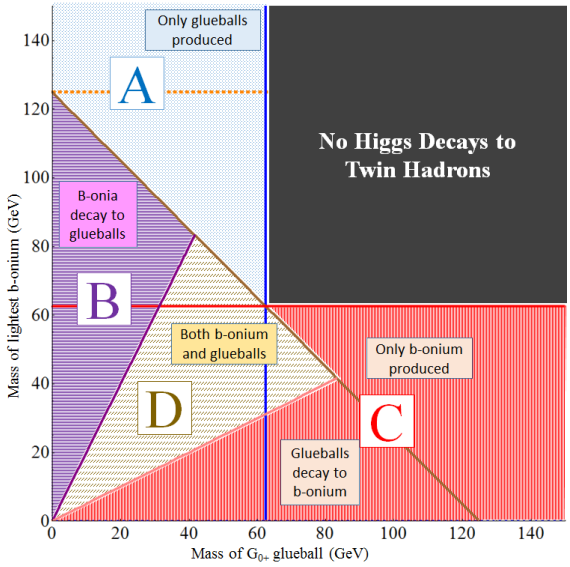

FIGURE 2. (Figure 5 from [14]) A description of the different kinds of exotic Higgs decays in twin Higgs models as a function of the mass of the lightest twin glueball and the lightest twin bottomonium state.

Quirks

Most of the models described in this talk involve positing an additional confining gauge group near the GeV scale. The confinement scale of a gauge theory, Λ is exponentially sensitive to high-scale parameters, so one can easily imagine such a theory where the confinement scale is many orders of magnitude lower, corresponding to a macroscopic length scale. If we further add fermions charged under this confining group that are also charged under the SM and at the TeV scale, so called quirks [17], then this very innocuous modification in theory space leads to extremely dramatic signatures at the LHC.

These quirks will be produced at the LHC and fly apart until they are separated by a distance Λ^{-1}, and then they will be pulled back together by the confining string. Therefore there will be charged particles taking very strange oscillating paths through an LHC detector. Some of the possibilities are shown in Figure 3.

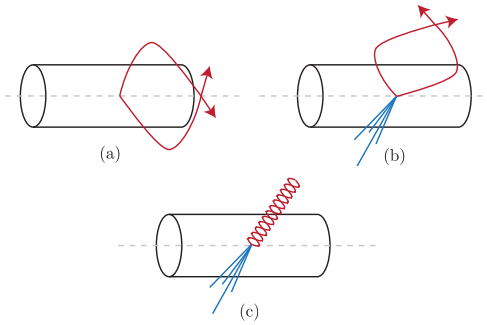

FIGURE 3. (Figure 5 from [17]) A pictorial representation of some possible quirk signatures.

A Note on Triggers

Both ATLAS and CMS have triggers designed to look specifically for different kinds of exotic signatures, and these are an important component of the search program. The LHC, however, is a hadron machine, so jets are quite plentiful. Therefore, standard triggers that look for jets or even leptons can be have a reasonable efficiency for various new physics models. This strategy is already used in mono-jet searches where the new physics is completely invisible, but this strategy can be generalized.

In [16], an excellent example of this was given in models where the Higgs decays to long lived neutrals. They compare the trigger efficiencies of three standard triggers: Vector Boson Fusion (VBF), VBF plus b's, and isolated lepton, to two exotic triggers: those for displaced jets and for trackless jets. While those exotic triggers were designed with this sort of new physics in mind, in many regions of parameter space the standard triggers do as well or better than the exotic ones. That is because the new physics sometimes happens to produced in conjunction with jets or gauge bosons, so the triggers can pick up those objects and leave the search for new physics to the analysis level.

WISHLIST FOR RUN II

My personal wishlist for exotic searches in Run II:

- More searches for distinct collider objects such as emerging jets or quirks.
- Searches for different SM states originating in different places in the detector.
- More general use of triggers including multi-jet and VBF.
- Keep searches as model independent as possible, trying not to use the details of any particular model for physics beyond the SM.

With this, if new physics exists in an exotic form, it is more likely to be found by the LHC's search program.

ACKNOWLEDGMENTS

I would like to thank the organizers of LHCP for the invitation to give this talk, and particularly Andreas Weiler for his feedback on my talk.

REFERENCES

[1] G. Aad *et al.* (ATLAS), (2015), arXiv:1506.00962 [hep-ex] .

[2] P. Batra, A. Delgado, D. E. Kaplan, and T. M. P. Tait, JHEP **02**, p. 043 (2004), arXiv:hep-ph/0309149 [hep-ph] .

[3] A. Maloney, A. Pierce, and J. G. Wacker, JHEP **06**, p. 034 (2006), arXiv:hep-ph/0409127 [hep-ph] .

[4] J. H. Collins and W. H. Ng, (2015), arXiv:1510.08083 [hep-ph] .

[5] C. Petersson and R. Torre, (2015), arXiv:1508.05632 [hep-ph] .

[6] L. J. Hall, K. Jedamzik, J. March-Russell, and S. M. West, JHEP **03**, p. 080 (2010), arXiv:0911.1120 [hep-ph] .

[7] R. T. Co, F. D'Eramo, L. J. Hall, and D. Pappadopulo, (2015), arXiv:1506.07532 [hep-ph] .

[8] S. Nussinov, Phys. Lett. **B165**, p. 55 (1985).

[9] K. Petraki and R. R. Volkas, Int. J. Mod. Phys. **A28**, p. 1330028 (2013), arXiv:1305.4939 [hep-ph] .

[10] Y. Bai and P. Schwaller, Phys. Rev. **D89**, p. 063522 (2014), arXiv:1306.4676 [hep-ph] .

[11] P. Schwaller, D. Stolarski, and A. Weiler, JHEP **05**, p. 059 (2015), arXiv:1502.05409 [hep-ph] .

[12] Z. Chacko, H.-S. Goh, and R. Harnik, Phys. Rev. Lett. **96**, p. 231802 (2006), arXiv:hep-ph/0506256 [hep-ph] .

[13] G. Burdman, Z. Chacko, H.-S. Goh, and R. Harnik, JHEP **02**, p. 009 (2007), arXiv:hep-ph/0609152 [hep-ph] .

[14] N. Craig, A. Katz, M. Strassler, and R. Sundrum, JHEP **07**, p. 105 (2015), arXiv:1501.05310 [hep-ph] .

[15] D. Curtin and C. B. Verhaaren, (2015), arXiv:1506.06141 [hep-ph] .

[16] C. Csaki, E. Kuflik, S. Lombardo, and O. Slone, Phys. Rev. **D92**, p. 073008 (2015), arXiv:1508.01522 [hep-ph] .

[17] J. Kang and M. A. Luty, JHEP **11**, p. 065 (2009), arXiv:0805.4642 [hep-ph] .

Proceedings of the LHCP2015 Conference, St. Petersburg, Russia, August 31 - September 5, 2015

Editors: V.T. Kim and D.E. Sosnov

Searches for Long-Lived Particles with Displaced Signatures at the LHC

DANIELA SALVATORE

Universita' della Calabria and INFN - Cosenza, Dipartimento di Fisica, ponte P. Bucci, 87036 Rende (CS) Italy.

daniela.salvatore@cern.ch

On behalf of the ATLAS and CMS Collaborations

Abstract. This contribution focuses on the most recent results from the ATLAS and CMS Collaborations on the searches for Long-Lived Particles at the Large Hadron Collider. These searches exploit the full dataset collected in 2012 from proton–proton collisions at a center-of-mass energy of 8 TeV. Results can be interpreted in terms of R-parity conserving or violating SUSY models, split SUSY, stealth SUSY and exotic scenarios like Hidden Valley. All the observations are compatible with background expectations and upper limits are set for the cross sections of the different decay modes.

RESULTS FROM THE ATLAS COLLABORATION

In this section, results from searches performed by the ATLAS experiment [1] are reported.

Search for Multitrack Displaced Vertices or Displaced Lepton Pairs

Many extensions of the Standard Model (SM) posit the existence of heavy particles with long lifetimes. This search, which is detailed in [2], focuses on events containing two gluinos or two squarks created in the pp collision and at least one long-lived particle (LLP) that decays at distances of the order of mm to tens of cm from its production point, with lifetimes of the order of ps to ns. In the supersymmetric scenarios involving R-parity violation (RPV) and gauge mediation, the LLP is the lightest neutralino ($\tilde{\chi}_1^0$); in the split supersymmetry (split SUSY) the LLP is the gluino. The decay channels under investigation are into two leptons or into five or more charged particles: in the latter case, events are selected using associated lepton candidates, jets or missing transverse momentum ($E_{\mathrm{T}}^{\mathrm{miss}}$). In some of the search channels, the trigger and search strategy are based only on the decay products of individual LLP, irrespective of the rest of the event. In these cases, the provided limits can easily be reinterpreted in different scenarios.

Displaced vertices (DV) are searched starting from the ATLAS standard tracking algorithms, but recovering lost tracks with looser impact parameters. DVs that are situated within regions of dense detector material are vetoed using a three-dimensional map of the detector within the fiducial region (Fig. 1 (left)). The invariant mass m_{DV} of all the tracks in the vertex must be greater than 10 GeV. The number of tracks forming the DV is required to be greater than 2 in the di-lepton case and greater than 5 in the multitrack channel.

An example of distribution of events inside or outside the signal region is given at Fig. 1 (right). No events are observed in any of the signal regions in events corresponding to an integrated luminosity of 20.3 fb^{-1}, and limits are set on model parameters within the aforementioned scenarios.

Search for Long-Lived Particles in the Hadronic Calorimeter

In the Hidden Valley (HV) scenario [3] [4] a SM-sector scalar boson Φ (that may not necessarily be the SM Higgs boson (H)) mixes with Φ_{hs}, a hidden sector scalar boson which can decay to v-quarks (q_{v}). The hidden sector consists of a confining gauge group that makes v-hadrons out of its v-quarks, in analogy with QCD. The v-quarks then hadronize to v-particles that can decay back to SM particles. The lightest HV particles π_{v} are pair-produced and each decays to a pair of SM fermions. The lifetime of the π_{v} is unconstrained and could be quite long.

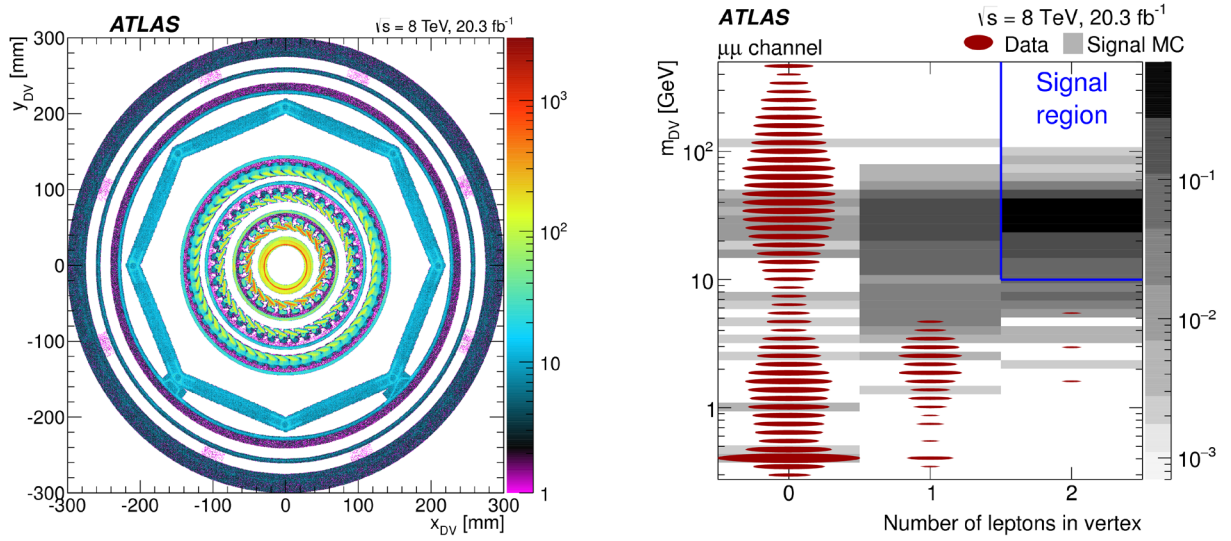

FIGURE 1. [2] (left) Transverse-plane density (in arbitrary units) of vertices with fewer than five tracks in material regions that are excluded by the material veto in the region $|z| < 300$ mm. The innermost circle corresponds to the beam pipe. This is surrounded by the three pixel layers. The octagonal shape and outermost circles are due to support structures separating the pixel and SCT detectors. (right) The distribution of dimuon-vertex candidates in terms of the vertex mass versus the number of lepton candidates in the vertex. The data distributions are shown with red ovals, the area of the oval being proportional to the logarithm of the number of vertex candidates in that bin. The gray squares show the $\tilde{g}(600\ \text{GeV}) \to q\bar{q}\ [\tilde{\chi}_1^0(50\ \text{GeV}) \to \mu\mu\nu]$ signal MC sample.

This search [5] focuses on the decay of a scalar boson to a pair of π_v that, in turn, decay at the outer edge of the ATLAS electromagnetic calorimeter (ECal) or inside the hadronic calorimeter (HCal). The π_v are reconstructed as a jet with an unusual energy signature that most traditional searches reject as having poor data quality. This characteristic signature was used to design the dedicated *CalRatio* trigger [6], which looks specifically for LLPs that decay near the outer radius of the ECal or within the HCal. Jets must satisfy $E_T > 35$ GeV and $\log_{10}(E_H/E_{EM}) > 1.2$, where (E_H) is the energy in the HCal and (E_{EM}) the energy in the ECal. Also they must have no tracks with transverse momentum $(p_T) > 1$ GeV in the region 0.2×0.2 $(\Delta\eta \times \Delta\phi)$ around their axes. Figures 2(a) and (b) show the track multiplicity and the $\log_{10}(E_H/E_{EM})$ for the signal and background samples.

The signal region is then defined as two simultaneous jets with low electro-magnetic fraction (EMF). No significant excess of events is observed with respect to QCD multi-jet and cosmic ray background events. Limits are reported on the product of the scalar boson production cross section times branching ratio into LLP as a function of the proper lifetime $(c\tau)$ of the particles, for boson masses from 100 GeV to 900 GeV, and a LLP mass from 10 GeV to 150 GeV.

Search for Long-Lived Particles in the Inner Detector and in the Muon Spectrometer

The HV model considers also a massive communicator, Z', produced by quark-antiquark annihilation decays into the hidden sector via $q\bar{q} \to Z' \to q_v\bar{q}_v$. The v-quarks hadronize into showers of π_v particles where the $\pi_v^{\pm}$ lifetime is a free parameter. If a π_v decays in the inner detector (ID) or in the muon spectrometer (MS), it can be reconstructed as a non-standard DV. The stealth SUSY [7] [8] scenario, a class of R-parity-conserving SUSY models that do not have large E_T^{miss} signatures, involves adding a hidden-sector (stealth) singlet superfield S at the electroweak scale, which has a superpartner singlino $\tilde{S}$. The SUSY decay chain ends with $\tilde{S}$ decaying to a singlet plus a low-mass gravitino $(\tilde{G})$, where $\tilde{G}$ carries off very little energy and the singlet promptly decays to two gluons. The effective decay processes are $\tilde{g} \to \tilde{S}g$ (prompt), $\tilde{S} \to S\tilde{G}$ (not prompt), and $S \to gg$ (prompt). This scenario results in one prompt gluon and two displaced gluon jets per gluino decay resulting in two DVs.

This analysis [9] employs techniques for reconstructing decay vertices of LLP decaying to jets in the ID and MS. Signal events require at least two reconstructed vertices: the dedicated "MuonRoiCluster" trigger [6] is used for the HV scalar boson and stealth SUSY benchmark models decays, where at least one DV must be reconstructed in the MS. A jet + E_T^{miss} trigger is used for the HV Z' benchmark model, for all the combinations of DV in the ID and MS.

No significant excess over the expected background is found and limits as a function of the LLP $c\tau$ are reported.

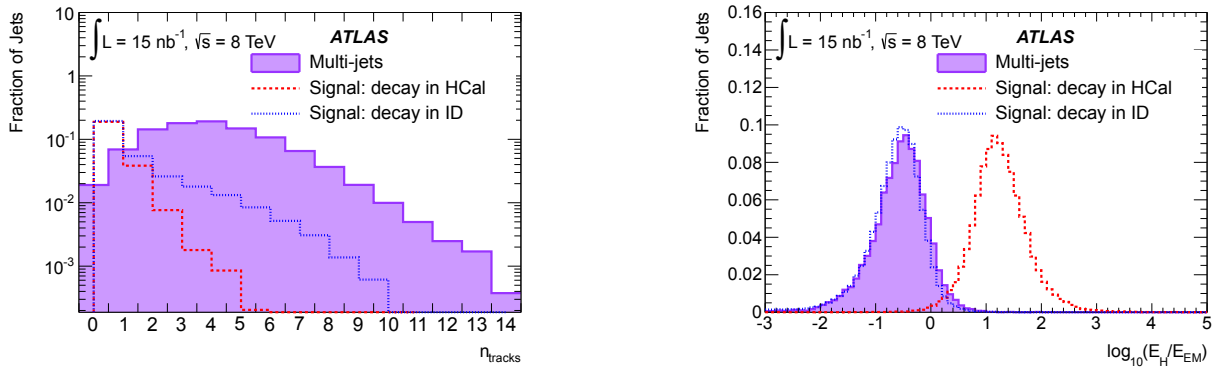

FIGURE 2. [5] (left) Number of good tracks (n_{tracks}) with $p_{\mathrm{T}} > 1$ GeV and $\Delta R < 0.2$ around the jet axis and (right) jet $\log_{10}(E_{\mathrm{H}}/E_{\mathrm{EM}})$ with jet $|\eta| < 2.5$, $p_{\mathrm{T}} > 40$ GeV. The π_{v} jets decaying in the HCal or in the inner detector are taken from the m_{H}= 126 GeV, $m_{\pi v}$= 10 GeV sample. Events are required to satisfy $E_{\mathrm{T}}^{\mathrm{miss}}$< 50 GeV.

The first results for displaced decays in Z' and Stealth SUSY models are presented (Fig. 3). For the scalar boson scenario, the upper bounds of the excluded $c\tau$ are the most stringent to date. Since the current Higgs boson measurement uncertainties do not exclude non-SM decay modes at the 30% or more level, the decay of the SM 125 GeV Higgs boson to a pair of long-lived scalars or pseudo scalars was also explored.

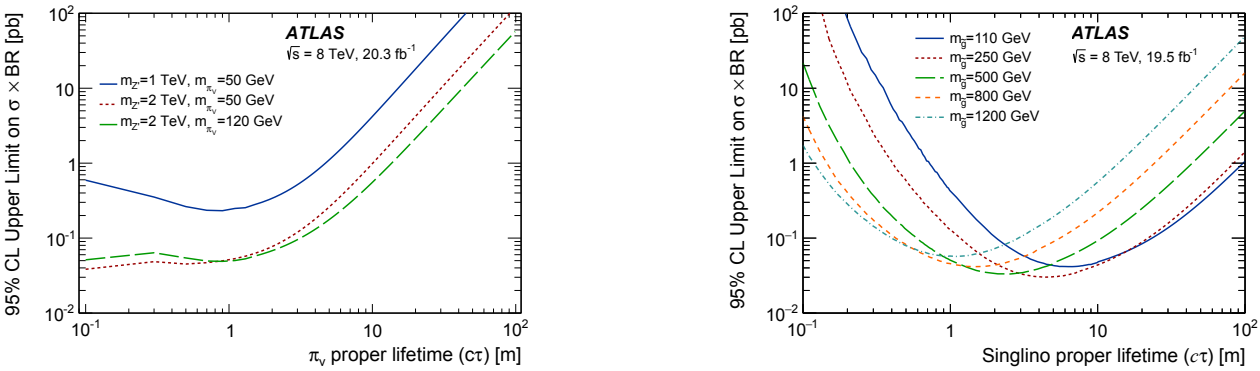

FIGURE 3. [9] Observed 95% CL limits on $\sigma\times$ BR for the (left) Z' samples and (right) Stealth SUSY samples.

Search for Lepton-Jets

In the scenario where the hidden sector and the SM couple via the vector portal, a light hidden photon (dark photon, γ_{d}) mixes kinetically with the SM photon. If the hidden photon is the lightest state in the hidden sector, it decays back to SM particles. From γ_{d} decays, collimated jet-like structures containing pairs of electrons and/or muons and/or charged pions (lepton jets, LJs), and which are produced far from the primary vertex of the event, may arise [10].

A search for LJs in a sample of 20.3 fb^{-1} is performed and described in detail in [11]. Three topologies are defined and shown at Fig. 4: LJ-type 0, LJ-type 1 and LJ-type 2. LJ-type 0 select LJs with all γ_{d} decaying to muons, with γ_{d} decays beyond the pixel detector up to the first trigger plane of the MS. LJ-type 1 select LJs with one γ_{d} decaying to a muon pair and one γ_{d} decaying to an electron/pion pair. The range of decay distances targeted by LJ-type1 extends from the last ID pixel layer up to the end of the HCal, for γ_{d} decaying into an electron/pion pair, and from the last ID pixel layer up to the first trigger plane of the MS, for the γ_{d} decays to muons. LJ-type 2 select all γ_{d} decaying to electron/pion pairs in the HCal. The requirement of low EMF is needed to reduce the SM multi-jet background.

The two Falkowski-Ruderman-Volansky-Zupan (FRVZ) models [10] predict non-SM Higgs boson decays to LJs and are used as benchmark samples. Since observed events are consistent with background expectations, upper limits

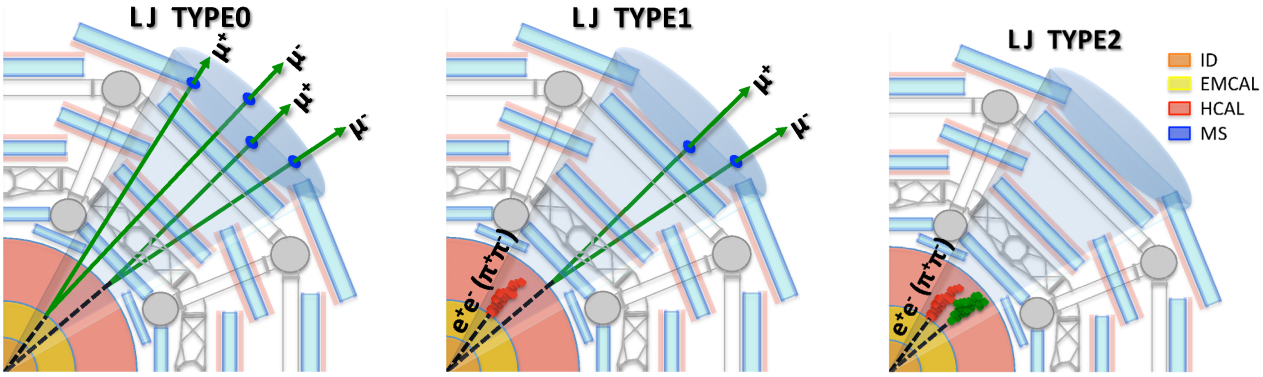

FIGURE 4. [11] Schematic picture of the LJ classification according to the γ_d decay final states: left TYPE0 LJ (only muons), centre TYPE1 LJ (muons and jets), right TYPE2 LJ (only jets). LJs containing only one γ_d contribute only to TYPE0 and TYPE2.

are derived as a function of the LLP cτ. The range of excluded cτ is 52 – 85 mm for the H $\rightarrow$ 4 γ_d + X model: if LJ-type 2 are excluded, this range extends to 15 – 260 mm and is 14 – 140 mm for the H $\rightarrow$ 2 γ_d + X model.

RESULTS FROM THE CMS COLLABORATION

In this section, results from searches performed by the CMS experiment [12] are reported.

Search for Long-Lived Particles Decaying into Quark Pairs

A search is performed for massive neutral LLP decaying to quark-antiquark pairs [13]. Quarks fragment and hadronize into jets of particles: therefore, the experimental signature is a distinctive topology of a pair of jets, originating at a secondary vertex that lies within the volume of the CMS tracker and is significantly displaced from the colliding beams. A DV is required to have at least a track from each jet, where constraints are put on the number of tracks with little impact parameters, and a $m_{\mathrm{DV}} > 4$ GeV. A candidate event is shown in Fig. 5.

Results are presented in the context of a HV model [4] where a long-lived, scalar, neutral exotic particle, X, in the mass range of 50 to 350 GeV, decays to $q\bar{q}$. The LLP is pair-produced in the decay of a non-SM Higgs boson in the mass range of 200 to 1000 GeV (i.e. $H \rightarrow 2X, X \rightarrow q\bar{q}$), where the H boson is produced through gluon-gluon fusion. In the second model, the LLP is a $\tilde{\chi}_1^0$ which decays into two quarks and a muon through an RPV coupling. The $\tilde{\chi}_1^0$ are produced in events containing a pair of squarks, where a squark can decay via the process $\tilde{q} \rightarrow q\,\tilde{\chi}_1^0 \rightarrow qq'\bar{q}''\mu$ [14]. The event selection is optimized for best sensitivity to the H model.

No significant excess is observed above SM expectations in events corresponding to an integrated luminosity of 18.5 fb^{-1}. Upper limits at 95% CL are set on the production cross sections for both models. For X with $c\tau$ of 0.4 to 200 cm, the upper limits are typically 0.5 – 200 fb. For pair production of squarks that promptly decay to $\tilde{\chi}_1^0$ with $c\tau$ of 2 – 40 cm, the upper limits on the cross section are typically 0.5 – 3 fb.

Search for Long-Lived Particles Decaying into Di-leptons

A search is performed for LLP that decay into final states that include a pair of electrons or a pair of muons [15]. In the first benchmark model, the LLP is a spinless boson X, which has a nonzero branching fraction to dileptons. The X is pair-produced in the decay of a non-SM Higgs boson, $H \rightarrow XX, X \rightarrow \ell^+\ell^-$ [4], where the Higgs boson is produced through gluon-gluon fusion and ℓ represents either an electron or a muon. In the second model, the LLP is a $\tilde{\chi}^0$which can decay via RPV couplings into a neutrino and two charged leptons [14], [16]. The $\tilde{\chi}^0$is produced in events containing a pair of squarks, where a squark can decay via the process $\tilde{q} \rightarrow q\,\tilde{\chi}^0, \tilde{\chi}^0 \rightarrow \ell^+\ell^-\nu$.

The experimental signature is a distinctive topology consisting of a pair of charged leptons originating from a secondary DV. To reject promptly produced particles, the tracks are required to have a transverse impact parameter significance with respect to the primary vertex of $|d_0|/\sigma_d$ >12, where σ_d is the uncertainty on d_0. This value is chosen to give an expected background significantly below one event, which gives the best signal sensitivity for the vast majority of the LLP lifetimes considered. The signed difference in azimuthal angles, $\Delta\phi$, between the dilepton

momentum vector, $\bar{p}_{\ell\ell}$, and the vector from the primary vertex to the dilepton vertex, $\bar{v}_{\ell\ell}$, must satisfy $\Delta\phi < \pi/2$, where $\Delta\phi$ is measured in the range $0 < \Delta\phi < \pi$. A comparison between $|d_0|/\sigma_d$ in signal MC and data is reported in Fig. 6.

No significant excess is observed above SM expectations in events corresponding to an integrated luminosity of 19.6 (20.5) fb^{-1}in the electron (muon) channel. Upper limits on the product of the cross section and branching fraction of such a signal are presented as a function of the LLP $c\tau$. The limits are presented in an approximately model-independent way, allowing them to be applied to a wide class of models yielding the above topology. In the specific case of a model in which a Higgs boson in the mass range 125 – 1000 GeV decays into a pair of long-lived neutral bosons in the mass range 20–350 GeV, each of which can then decay to dileptons, the upper limits obtained are typically in the range 0.2–10 fb for LLP $c\tau$ in the range 0.01–100 cm. In the case of the lowest Higgs mass considered (125 GeV), the limits are in the range 2–50 fb. These limits are sensitive to Higgs boson branching fractions as low as 10^{-4}.

Search for Long-Lived Particles in the Muon Chamber only

This study, described in [17], is closely related to the analysis described right above, since similar analysis techniques are employed to search for the same signal topology. While the previous analysis relied on electrons or muons whose trajectories were reconstructed in the silicon tracker, this study is based on information from muon tracks reconstructed in the CMS muon chambers only, which are able to reconstruct muons produced an order of magnitude farther away from the beam-line than what the silicon tracker can. This search improves sensitivity to particles that are especially long-lived and is fully complementary to the tracker-based one, since it explicitly excludes any muon whose trajectory is reconstructed in the silicon tracker and combined results from the two searches are presented.

No events corresponding to an integrated luminosity of 20.5 fb^{-1}pass the selection criteria for each of the two specific aforementioned benchmark models. Upper limits on the product of the cross section and branching fraction of such a signal are presented as a function of the LLP $c\tau$. For the first model, where a Higgs boson with mass in the range 125 – 1000 GeV decays to pairs of neutral LLP with masses in the range 20 – 350 GeV, that can decay to dimuon pairs, the limits are typically in the range 1 – 50 fb, and can weaken to a few pb for the lowest masses and longest lifetimes. Upper limits are given for lifetimes in the range $1 < c\tau < 10000$ cm.

Search for Events with an Electron and a Muon with Large Impact Parameters

A search for new LLP decaying to leptons is presented [18], using an integrated luminosity of 19.7 fb^{-1}. This search does not make any assumptions about the event topology beyond the requirement that the event contain an isolated electron and isolated muon with large impact parameters (between 0.02 and 2 cm) and opposite charges. It does not require, or exclude, hadronic activity or $E_{\mathrm{T}}^{\mathrm{miss}}$, neither that the reconstructed displaced tracks form a vertex. It does not require that the displaced tracks are collimated. In this way, the analysis has sensitivity to a wide variety of still viable beyond SM scenarios.

No excess is observed above background for displacements up to 2 cm. The results are interpreted in the context of a "displaced supersymmetry" model [19] with a pair-produced top squark decaying into an e-μ final state via RPV

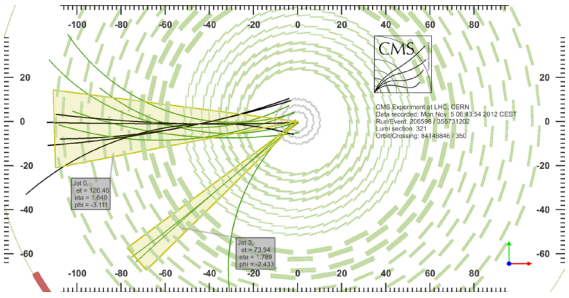

FIGURE 5. [13] Event display of a candidate in data, where only the selected dijet pair (yellow cones) and the tracks associated to both jets (curved lines) are shown, other objects being removed. The black tracks fit the secondary vertex which contains 5 tracks (5 from one jet and 2 from the other, while 2 tracks are associated to both jets) and is transversely displaced by 44 cm from the event primary vertex. The invariant mass of the dijet system is 75 GeV.

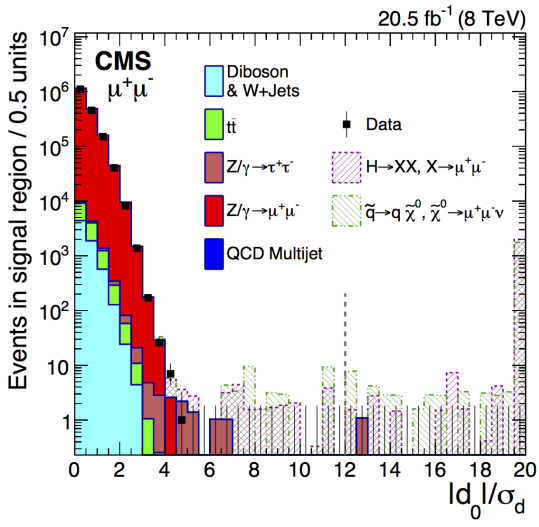

FIGURE 6. [15] The $|d_0|/\sigma_d$ distribution for the muon channels for events in the signal region $|\Delta\phi| < \pi/2$. Of the two leptons forming a candidate, the distribution of the one with the smallest $|d_0|/\sigma_d$ is plotted. The solid points indicate the data, the shaded histograms are the simulated background, and the hashed histograms show the simulated signal. The histogram corresponding to the $H \to XX$ model is shown for m_{H}=1000 GeV and m_{X}=350 GeV. The histogram corresponding to the $\tilde{\chi}^0 \to \ell^+\ell^-\nu$ model is shown for $m_{\tilde{\mathrm{q}}}$=350 GeV and $m_{\tilde{\chi}^0}$=140 GeV. The background histograms are stacked, and each simulated signal sample is independently stacked on top of the total simulated background. The d_0 corrections for residual tracker misalignment, discussed in the text, have been applied. The vertical dashed line shows the selection requirement $|d_0|/\sigma_d$ >12. Any entries beyond the right-hand side of a histogram are shown in the last visible bin of the histogram.

interactions, having a lifetime $0.02 < c\tau < 100$ cm. Limits are placed at 95% CL on this model as a function of top squark mass and lifetime. For a lifetime hypothesis of $c\tau = 2$ cm, top squark masses up to 790 GeV are excluded.

REFERENCES

[1] ATLAS Collaboration, JINST 3, S08003 (2008).
[2] ATLAS Collaboration, Phys. Rev. D 92, 072004 (2015).
[3] M. J. Strassler and K. M. Zurek, Phys. Lett. B 651 (2007) 374–379.
[4] M. J. Strassler and K. M. Zurek, Phys. Lett. B 661 (2008) 263–267.
[5] ATLAS Collaboration, Phys. Lett. B 743 (2015) 15–34.
[6] ATLAS Collaboration, JINST 8 (2013) P07015.
[7] J. Fan, M. Reece, and J. T. Ruderman, JHEP 1111 (2011) 012.
[8] J. Fan, M. Reece, and J. T. Ruderman, JHEP 1207 (2012) 196.
[9] ATLAS Collaboration, Phys. Rev. D 92 (2015) 012010.
[10] A. Falkowski, J.T. Ruderman, T. Volansky and J. Zupan, JHEP 05 (2010) 077.
[11] ATLAS Collaboration, JHEP 11(2014) 088.
[12] CMS Collaboration, JINST 3 S08004 (2008).
[13] CMS Collaboration, Phys. Rev. D 91 (2015) 012007.
[14] R. Barbieri et al., Phys. Rep. 420, 1 (2005).
[15] CMS Collaboration, Phys. Rev. D 91 (2015) 052012.
[16] B. C. Allanach et al., Phys. Rev. D 75, 035002 (2007).
[17] CMS Collaboration, CMS PAS EXO-14-012 (2014).
[18] CMS Collaboration, PRL 114, 061801 (2015).
[19] P. W. Graham et al., JHEP 07 (2012) 149.
[20] M. Cacciari, G. P. Salam and G. Soyez, JHEP 0804 (2008) 0633.
[21] A. Read, J. Phys. G 28 (2002) 2693.
[22] ATLAS Collaboration, ATLAS-CONF-2010-069.

Proceedings of the LHCP2015 Conference, St. Petersburg, Russia, August 31 - September 5, 2015

Editors: V.T. Kim and D.E. Sosnov

Searches for heavy stable charged particles and other exotic signatures with large ionization at the LHC

MAŁGORZATA KAZANA

National Centre for Nuclear Research, Hoża 69, 00-681 Warsaw, Poland

malgorzata.kazana@cern.ch

On behalf of the ATLAS and the CMS Collaborations

Abstract. The signature of the large ionization is used to search for signals of heavy stable charged particles or other new particles foreseen by models beyond the Standard Model. The related searches in proton-proton collisions at the Large Hadron Collider (LHC) are reviewed. No excess events were found. Results obtained by two LHC experiments ATLAS and CMS with data at a centre-of-mass energy of 7 and 8 TeV collected in 2011 and 2012 are presented in terms of exclusion limits on the mass and the production cross section of hypothetical particles.

INTRODUCTION

Many models of the physics beyond the Standard Model (SM) anticipate the existence of long-lived particles (LLP) like stau or slepton in Gauge-Mediated SUSY breaking (GMSB), R-hadrons (hadronized long-lived squarks or gluinos) in Split SUSY or nearly mass-degenerate chargino and neutralino in Anomaly-Mediated SUSY (AMSB). These particles which are massive (heavy) compared to known particles, neutral or electrically or magnetically charged. LLP can have speed $v = \beta \cdot c$ significantly less than the speed of light c. With lifetimes greater than few nanoseconds, these particles can travel distances comparable to the size of modern detectors and thus appear to be stable. While crossing the detector LLPs may have an abnormal ionization (dE/dx) if they are charged and an extended time-of-flight (TOF) with respect to SM particles. The measurements of dE/dx and TOF allows for particle's velocity (β) determination and provide mass estimate ($m = p\sqrt{(1-\beta^2)}/\beta$). The search for LLPs is challenging and interesting. It requires non-standard measurements and techniques of reconstructions and triggering. The LHC experiments performed the signature based searches which have been interpreted in the context of different models. Results obtained by the ATLAS [1] and CMS [2] experiments based on data collected in proton-proton collisions at centre-of-mass energy 7 TeV in 2011 and 8 TeV in 2012 will be reviewed.

SEARCHES with dE/dx in CMS

The CMS experiment has performed a wide search [3] for long-lived particles using two main signatures of the LLP, an abnormal ionization and an extended time-of-flight. Results were obtained with the full data set of pp collisions at the centre-of-mass energy 7 and 8 TeV for an integrated luminosity of 5.0 fb^{-1} and 18.8 fb^{-1}, respectively. Main discriminants in the analysis were energy depositions in the inner tracker and the time-of-flight (TOF) in the muon system. From individual energy depositions in the inner tracker, a discriminator I_as [3] measuring incompatibility with the minimum ionizing particle and an estimator I_h (which is related to the mass and momentum measurement in the following way $I_h = K \cdot m^2/p^2 + C$ where parameters K and C are determined from data) were constructed. The expected behaviour of the estimator for data and simulated signal is shown in Fig.1 (left). TOF measurement was performed in the muon detector. The particle's velocity β was obtained from the formula: $1/\beta = 1 + c \cdot \delta_t/L$, where δ_t was a measured time difference of a hit in the muon chamber relative to that expected for a $\beta = 1$ particle and L is the flight distance from the interaction point. Analysis used various combinations of signatures depending

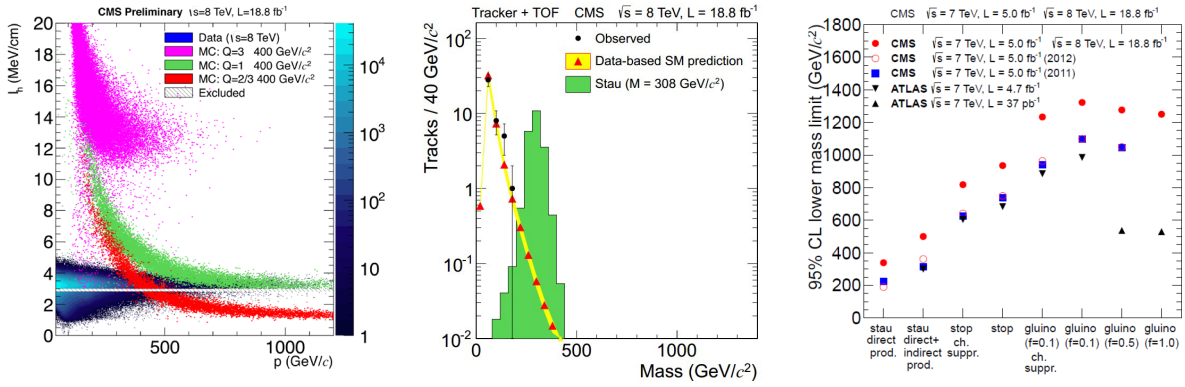

FIGURE 1. Distribution of a dE/dx estimator, I_h, versus particle momentum for 8 TeV data and MC simulated LLP candidates of different charges ([3] left). Observed and predicted mass spectrum for candidates entering the tracker and TOF ([3] middle) signal region for the final selection. Lower mass limits at 95 % CL for various models compared with previously published results. The model type is given on the x-axis ([3] right).

on the nature of the LLP under investigation. There are five following paths of search for LLPs: (i) for charged LLP: tracker and TOF were used to measure: measure transverse momentum p_T, dE/dx discriminator and $1/\beta$; (ii) for becoming neutral LLP: tracker-only was used to measure: p_T, dE/dx; (iii) for neutral LLP in the tracker, becoming charged: muon-only to p_T; (iv) for fractionally charged LLP: tracker-only to measure: p_T, dE/dx, which should be smaller then for SM particles; (v) for multiply charged LLP: tracker and TOF to measure: dE/dx and not p_T, because algorithms to reconstruct momentum work only for singly charged particles. Events were triggered either by a muon candidate with high $p_T > 40$ GeV or large missing transverse energy, $MET > 150$ GeV. Preselection criteria on the inner tracker track and the muon track allowed to select well reconstructed object. For all of the analyses, results were based upon a comparison of the number of candidates passing the final section criteria with the number of background events estimated using an $ABCD$ method. The number of background events in the signal region (A) was estimated using control regions (B, D, and C). For each analysis, fixed selections on the appropriate set of two or three variables, dE/dx discriminators, p_T, and $1/\beta$ were used to define the final signal region (and the regions for prediction).

These values were chosen to give an optimal discovery potential. For the tracker-only + tracker and TOF analyses, an additional requirement on the reconstructed mass is applied. Fig.1 (middle) shows the observed and predicted mass distributions for the tracker + TOF analysis with the final selection. The data were found consistent with the expected background, and lower limits were set on the mass of searched for long-lived particles. The summary of all exclusion mass limits is presented in Fig. 1. The tracker-only analysis excluded two kind of gluino masses below 1322 and 1233 GeV. Stop masses below 935 (818) GeV were excluded for the cloud (charge suppressed) models. In addition, the tracker and TOF analysis excluded stau $\widetilde{\tau}_1$ masses below 500 (339) GeV for the indirect (direct only) production. Drell-Yan signals as shown in Fig. 2 (left) for fractionally charged particles with $Q = 2e/3$ and $Q = 1e$ were excluded below 220 and 574 GeV respectively.

The results of the CMS search [3] for LLP described above have been reanalyzed [4] to set constraints on the phenomenological minimal supersymmetric standard model (pMSSM) which predict the existence of long-lived massive particles in certain regions of their parameter space. A novel technique for estimating the signal acceptance with an accuracy of 10% was introduced [4]. The limits are set on the long-lived sector of the pMSSM sub-space that covers SUSY particle masses up to about 3 TeV. The related region of the pMSSM parameter's space is shown in Fig. 2 (middle). In this sub-space, 95.9% of the points with a chargino lifetime greater than 10 ns are excluded by the including constraints from the results of the CMS analysis, as presented in Fig. 2 (right). The method described can be used to set constraints on other models with long-lived charged particles.

HEAVY STABLE CHARGED PARTICLES in ATLAS

The ATLAS experiment performed a search [5] for massive long-lived charged particles using full data sample of 19.1 fb^{-1} of proton-proton data at centre-of-mass energy of 8 TeV. The search was based entirely on signatures of the LLP, but it has been optimized for the different experimental signatures of sleptons, charginos and R-hadrons. Events

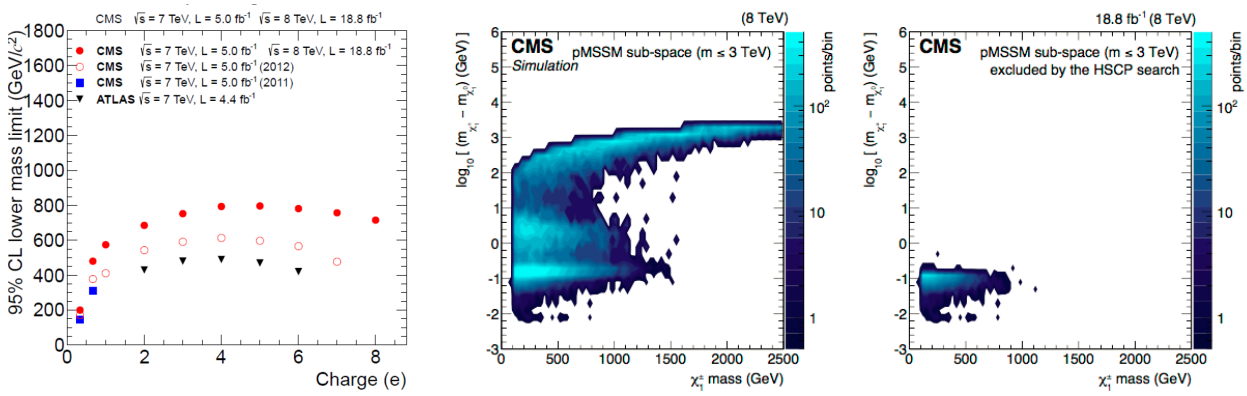

FIGURE 2. Lower mass limits at 95 % CL for various models for Drell-Yan like production of fractionally, singly, and multiply charged particles ([3] left). Number of pMSSM parameter points in the sub-space covering sparticle masses up to about 3 TeV for with long-lived charginos ([4] middle) and the set of points excluded by the CMS analysis ([4] right).

were selected online by trigger requirements either on the presence of muons with $p_T > 24$ GeV or large missing transverse energy, at least $MET > 60$ GeV. Offline candidates were selected with $p_T > 70\,GeV$ and $MET > 100$ GeV. Different requirements on p_T and p were placed in the various types of analyzes. The parameter β was calculated from the measured TOF in muon system and calorimeter, whereas the parameter $\beta\gamma$ was deduced from the specific energy loss dE/dx measured in the pixel detector. The background was reduced by additional requirements on β and the particle's mass specific for the final signature. Backgrounds which have remained consisted mainly of high-p_T muons with mismeasured β and/or large ionization. For all cases, it have been estimated from the data. One type of searches for sleptons is illustrated in Fig. 3 (left), where the mass distribution observed in data together with the background estimate, its systematic uncertainty and examples of expected signal as stau from the gauge-mediated symmetry breaking (GMSB) model are shown.

No indication of signal above the expected background was observed, and limits on new physics scenarios were set using the CLs prescription. Mass limits were derived by comparing the obtained cross-section limits to the lower edge of the $\pm\sigma$ band around the theoretically predicted cross-section for each process as shown in Fig. 3 (middle) for direct stau production. All results as a lower mass limits from various types of searches are summarized in Fig. 3 (right). Long-lived GMSB staus were excluded up to masses between 440 and 385 GeV for tanβ between 10 and 50, with a 289 GeV limit in the case where only direct tau slepton production was considered. In the context of simplified LeptoSUSY models, where sleptons were stable and have a mass of 300 GeV, squark and gluino masses were excluded up to a mass of 1500 and 1360 GeV, respectively. Directly produced charginos, in simplified models, where they were nearly degenerate with the lightest neutralino, were excluded up to a mass of 620 GeV. R-hadrons, composites containing a gluino, bottom squark or top squark, were excluded up to a mass of 1270, 845 and 900 GeV, respectively, using the full detector; and up to a mass of 1260, 835 and 870 GeV using an approach disregarding information from the muon spectrometer.

The ATLAS mass limit obtained for a direct production of stau pairs, $m_{\tilde{\tau}_1} > 289$ GeV, can be compared with the CMS limit [3], which excludes staus below 336 GeV.

HEAVY meta STABLE CHARGED PARTICLES in ATLAS

The search for stable long-lived particles [5] in the ATLAS detector has been extended [6] to search for meta-stable non-relativistic long-lived charged particles with lifetimes from 0.6 ns to 30 ns. Results were presented in the context of SUSY models assuming the existence of R-hadrons and in AMSB models for the case of long-lived charginos. The analysis used 18.4 fb^{-1} of data at $\sqrt{s} = 8$ TeV collected by the ATLAS detector. The key variable was an anomalous specific ionization energy loss in the pixel detector (dE/dx), which had allowed for the mass determination of particle crossing the detector. Events were selected using the lowest threshold unprescaled calorimetric trigger ($MET >$ 80 GeV), since there have been no trigger based on main observables. For signal events, the MET had originated from jets from QCD initial state radiation and, whenever relevant, by the LLP decays to undetected neutralinos. The

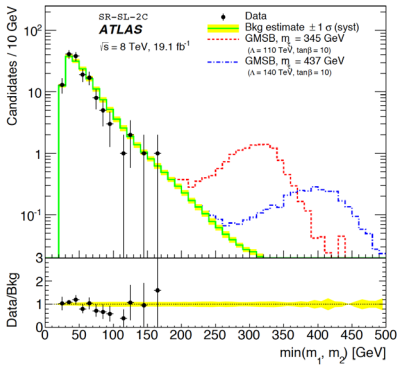

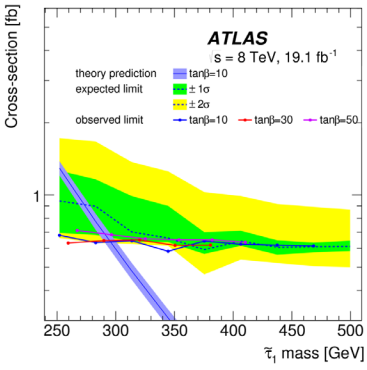

Search	Lower mass limit [GeV]
GMSB sleptons	
· $\tan\beta = 10, 20, 30, 40, 50$	440, 440, 430, 410, 385
· direct $\tilde{\ell}$ production ($m_{\tilde{\ell}} - m_{\tilde{\tau}_1} = 2.7$–$93$ GeV)	377–335
· direct $\tilde{\tau}_1$ production	289
· $\tilde{\chi}_1^0\tilde{\chi}_1^\pm$ decaying to stable $\tilde{\tau}_1$	537
LeptoSUSY	
· $\tilde{q}$, $\tilde{g}$	1500, 1360
Charginos	
· $\tilde{\chi}_1^\pm$	620
R-hadrons	
· $\tilde{g}$, $\tilde{b}$, $\tilde{t}$ (full-detector)	1270, 845 and 900
· $\tilde{g}$, $\tilde{b}$, $\tilde{t}$ (MS-agnostic)	1260, 835 and 870

FIGURE 3. The mass distribution for the observed data, background estimate and expected signal in the slepton search for the lower of the two masses (m_1, m_2) in the two-candidate signal region ([5] left). Cross-section upper limits as a function of the $\widetilde{\tau}_1$ mass for direct stau production and three values of tanβ, where the theoretical cross-section prediction for tanβ=10 does not vary significantly for the other *tanβ* values ([5] middle). The summary of the lower mass limits (95% CL) from the various searches ([5] right).

trigger efficiency have depended not only on the kind and mass of LLPs but also on their lifetime and has varied between 0.2% (for stable charginos) to 95% (for R-hadron gluinos with $\tau = 10$ ns). The LLP candidates should have appeared as high transverse momentum ($p_T > 150$ GeV) isolated particles with large dE/dx. Tracks identified as electrons were vetoed. In the search for meta-stable particles, tracks that were matched with a muon were rejected. The mass distribution was used to look for an excess of events, compatible with the expected measurement resolution for particles that have been selected as LLP candidates as shown in Fig. 4 (left). A data-driven approach was used to estimate the background. The method has used the data to fit distributions of key variables (p, dE/dx, η), taking into account their interdependence, and then to generate a large random sample of background events based on the same distributions. The Standard Model background expectation shows the agreement with observed data. Therefore, lifetime-dependent upper limits on R-hadrons and chargino production are set, and summarized in Fig. 4. Gluino R-hadrons with 10 ns lifetime and masses up to 1185 GeV were excluded at 95% confidence level. The exclusion for charginos was weaker and set for particles with 15 ns lifetime and masses up to 482 GeV.

Multi-charged particles in ALTAS

Multi-charged particles (MCPs) producing anomalously high ionization, consistent with long-lived massive particles with electric charges $|q| = ze$, where z = 2-6, were searched for in the ATLAS detector [7]. Data collected in 2012 at $\sqrt{s} = 8$ TeV from pp collisions corresponding to an integrated luminosity of 20.3 fb^{-1} were examined. Events were

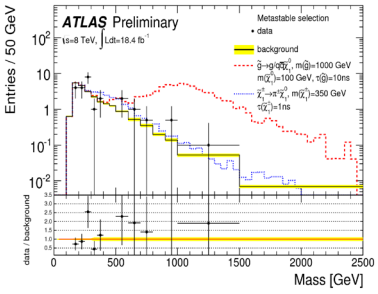

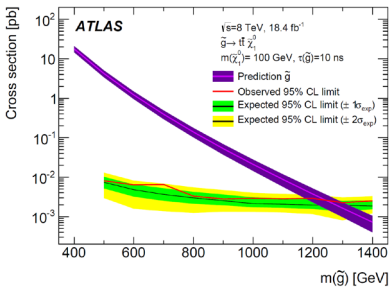

Particle	Decay	$m(\tilde{\chi}_1^0)$ [GeV]	τ [ns]	$m >$ [GeV]
$\tilde{g}$ R-hadron	stable	–	–	1115
$\tilde{b}$ R-hadron	stable	–	–	751
$\tilde{t}$ R-hadron	stable	–	–	766
chargino	stable	–	–	534
$\tilde{g}$ R-hadron	$g/q\bar{q}$	100	10	1185
$\tilde{g}$ R-hadron	$g/q\bar{q}$	$m(\tilde{g}) - 100$	10	1099
$\tilde{g}$ R-hadron	$t\bar{t}$	100	10	1182
$\tilde{g}$ R-hadron	$t\bar{t}$	$m(\tilde{g}) - 480$	10	1157
$\tilde{g}$ R-hadron	$g/q\bar{q}$	100	1.0	869
$\tilde{g}$ R-hadron	$g/q\bar{q}$	$m(\tilde{g}) - 100$	1.0	821
$\tilde{g}$ R-hadron	$t\bar{t}$	100	1.0	836
$\tilde{g}$ R-hadron	$t\bar{t}$	$m(\tilde{g}) - 480$	1.0	836
chargino	$\tilde{\chi}_1^0 + \pi^\pm$	$m(\tilde{\chi}_1^\pm) - 0.14$	1.0	239
chargino	$\tilde{\chi}_1^0 + \pi^\pm$	$m(\tilde{\chi}_1^\pm) - 0.14$	15	482

FIGURE 4. The distribution of the mass of selected candidates, derived from the specific ionization loss, for data, background, and examples of gluino R-hadron and chargino signals, for searches of metastable particles ([5] left). Upper limits on the production cross section as a function of mass for metastable gluino R-hadrons, with lifetime $\tau = 10$ ns, decaying into $t\bar{t}$ and a 100 GeV mass neutralino ([5] middle). The summary of the lower mass limits (95 % CL) for stable and decaying R-hadrons and charginos ([5] right).

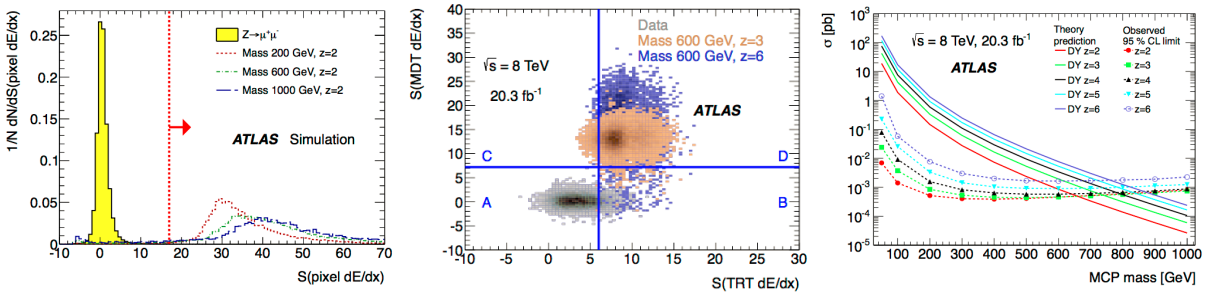

FIGURE 5. Normalized distributions of the dE/dx significance S in the pixel system for simulated muons from $Z \rightarrow \mu\mu$ events and MCPs passing the preselection requirements and hypothetical signals with high masses ([7] left). The distributions of the parameters S(MDT) versus S(TRT) for data and simulated signal samples used the the background estimation with $ABCD$ method ([7] middle). Observed 95 % CL cross-section upper limits and theoretical cross-sections as functions of the MCP's mass for values of z between 2 and 6 ([7] right).

collected with a single-muon (for $p_T/z > 36\,\text{GeV}$) or calorimetric trigger ($MET > 80\,\text{GeV}$). For the multi-charged particle, a purely electromagnetic coupling, proportional to its electric charge was assumed. MCPs were produced in pairs via the Drell-Yan (DY) process with only photon exchange included. It was assumed that the momentum measured in the detector had been inversely proportional to the charge of MCP, $p_T^{measured} = p_T/z$. MCPs would have an unique signature of high ionization in the detector, because the particle's energy loss has increased quadratically with its charge, which is large for MCPs. Estimates of dE/dx were evaluated for the pixel, the Transition Radiation Tracker (TRT) and the Monitored Drift Tube (MDT) of the muon system. The significance of the dE/dx variable in each sub-detector was defined by comparing the observed signal, dE/dx^{track}, with signal expected from a highly relativistic muon: $S = \frac{dE/dx^{track} - <dE/dx_\mu>}{\sigma(dE/dx_\mu)}$, where $< dE/dx_\mu >$, $\sigma(dE/dx_\mu)$ represent, respectively, the mean and the root-mean-square width of the dE/dx distribution for such muons in data. The S variable allowed for a good separation between Standard Model particles and MCPs, as illustrated in Fig. 5 (left). In the final step of the search, S(MDT dE/dx) and S(TRT dE/dx) were used to estimate background by the $ABCD$ method with the final selection cuts as shown in Fig. 5 (middle). Less than one background event was expected and no events were observed. Upper limits were derived on the production cross-sections and were interpreted as mass exclusion limits (Fig. 5 (right)) for a DY production model from 50 GeV up to 660, 740, 780, 785, and 760 GeV for charges $|q| = 2e, 3e, 4e, 5e$, and $6e$, respectively. Those results are comparable to limits obtained by the CMS collaboration (shown in Fig. 2 (left)), which were 685, 752, 793, 796, 781 GeV, respectively. The sensitivity of both LHC experiments to MCPs is similar.

HIGHLY IONIZING PARTICLES in ATLAS

An unique search for highly ionizing particles (HIP) [8] has been performed in the ATLAS experiment. HIP signatures are foreseen, for example, in theories predicting magnetic monopoles. The lightest magnetic monopole would be stable and carry a magnetic charge that is a multiple of the Dirac charge g_D, i.e., in Gaussian units, $\frac{g_D}{e} = \frac{1}{\alpha_e} \approx 68.5.$, where α_e is the fine structure constant. In terms of ionization energy loss at high velocity, a monopole with the Dirac charge corresponds to an electrically charged particle with charge $|z| = 68.5$. A monopole would thus manifest itself as a HIP, as would any highly charged stable particle.

HIPs were searched in the mass range of 200-2500 GeV and charges in ranges of $10 \leq |z| \leq 60$ and $0.5g_D \leq |g| \leq 2.0g_D$. A customized trigger has made monopoles with $|g| > 1.0\,g_D$ accessible in the ATLAS detector. This trigger was based on the electromagnetic calorimeter energy deposit with no energy deposits after the first calorimeter layer accompanied by the large fraction of the TRT tracker hits passing a high threshold (HT), $N_{HT} > 20$ and $f_{HT} > 0.37$. The ATLAS experiment deployed this trigger for four months in 2012 and collected the pp 8 TeV data corresponding to an integrated luminosity of $7.0\,\text{fb}^{-1}$. The final selection was based on several variables which identify low energy deposits in the calorimeter by a fraction of the energy contained in the most energetic cells in calorimeter (EM dispersion w) and associate them with a region with a high fraction of HT hits in the TRT (f_{HT}). A fully data-driven background estimate was performed in this search. The $ABCD$ method was applied for w and f_{HT}, assumed to be independent, as shown in Fig. 6 (left). No events were found in the signal region, leading to production cross-section upper limits on magnetic monopoles (Fig. 6 (middle)) and stable particles with large electric charge

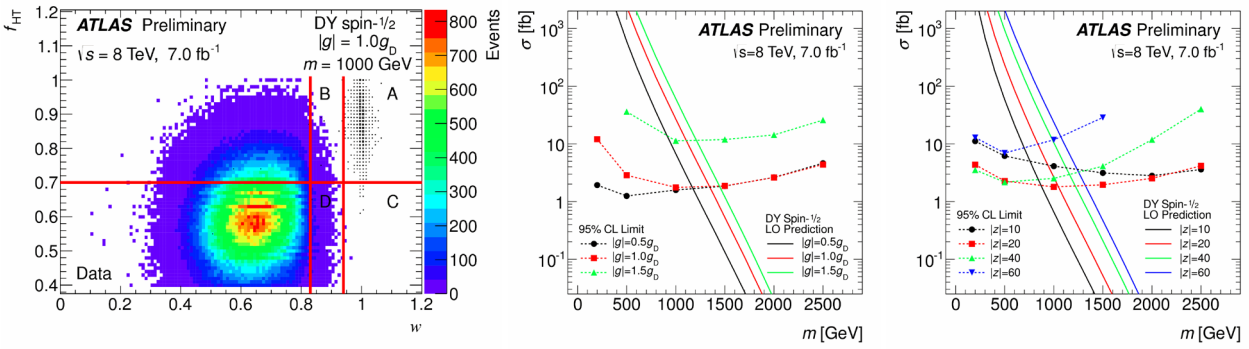

FIGURE 6. The background estimation for the HIP analysis. Candidates in data (inn color) and in a representative simulated signal sample (in black) are shown in the f_{HT} versus w plane at the last stage of the event selection. The number of background events in the signal region (A) is estimated using the left and bottom bands (B, D, and C) as control regions ([8] left). Cross-section upper limits at 95 % confidence level for spin 1/2 DY HIP production as a function of HIP mass in various scenarios ([8] middle and right plots).

(Fig. 6 (right)).

Lower mass limits at 95% confidence level in models of spin-1/2 DY HIP pair production were following: 1180 GeV for $0.5g_D$, 1340 GeV for $1.0g_D$, 1210 GeV for $1.5g_D$ and 780 GeV for $|z| = 10$, and 1070 GeV for $|z| = 60$.

SUMMARY

The LHC experiments ATLAS and CMS performed wide searches with large ionization for long-lived particles using pp data collected at the centre-of-mass energy of 7 and 8 TeV. Different final states including heavy stable charged particles were considered allowing to set a limit on the masses and lifetimes of hypothetical particles, since there was no evidence of such objects. Long-lived particles are interesting from the point of view of many extensions of the Standard Model and searches for LLPs will be continued with higher energies in LHC.

This work is supported by the Polish National Science Centre (NCN) grants UMO-2014/14/M/ST2/00428 and UMO-2014/15/B/ST2/03998.

REFERENCES

[1] ATLAS Collaboration. The ATLAS Experiment at the CERN Large Hadron Collider. *JINST*, 3:S08003, 2008.
[2] CMS Collaboration. The CMS experiment at the CERN LHC. *JINST*, 3:S08004, 2008.
[3] CMS Collaboration. Searches for long-lived charged particles in pp collisions at $\sqrt{s} = 7$ and 8 TeV. *JHEP*, 07:122, 2013.
[4] CMS Collaboration. Constraints on the pMSSM, AMSB Model and on Other Models from the Search for Long-Lived Charged Particles in Proton-Proton Collisions at $\sqrt{s} = 8$ TeV. *Eur. Phys. J.*, C75(7):325, 2015.
[5] ATLAS Collaboration. Searches for heavy long-lived charged particles with the ATLAS detector in proton-proton collisions at $\sqrt{s} = 8$ TeV. *JHEP*, 01:068, 2015.
[6] ATLAS Collaboration. Search for metastable heavy charged particles with large ionisation energy loss in pp collisions at $\sqrt{s} = 8$ TeV using the ATLAS experiment. *Eur. Phys. J.*, C75(9):407, 2015.
[7] ATLAS Collaboration. Search for heavy long-lived multi-charged particles in pp collisions at $\sqrt{s} = 8$ TeV using the ATLAS detector. *Eur. Phys. J.*, C75:362, 2015.
[8] ATLAS Collaboration. Search for magnetic monopoles and stable particles with high electric charges in 8 TeV pp collisions with the ATLAS detector. *CERN-PH-EP-2015-174*, 2015.

Proceedings of the LHCP2015 Conference, St. Petersburg, Russia, August 31 - September 5, 2015

Editors: V.T. Kim and D.E. Sosnov

Search for new physics in dijet resonant signatures and recent results from Run 2 with the CMS experiment

GIULIA D'IMPERIO

Università La Sapienza and INFN Roma

On behalf of the CMS Collaboration

Abstract. A search for narrow resonances in proton-proton collisions at a center-of-mass energy of $\sqrt{s}$ = 13 TeV is presented. The dijet invariant mass distribution of the two leading jets is measured with the CMS detector using early data from Run 2 of the Large Hadron Collider. The dataset presented here was collected in July 2015 and corresponds to an integrated luminosity of 42 pb^{-1}. The highest observed dijet mass is 5.4 TeV. The spectrum is well described by a smooth parameterization and no evidence for new particle production is observed. Upper limits at a 95% confidence level are set on the cross section of narrow resonances with masses above 1.3 TeV. When interpreted in the context of specific models the limits exclude: string resonances with masses below 5.1 TeV; scalar diquarks below 2.7 TeV; axigluons and colorons below 2.7 TeV; excited quarks below 2.7 TeV; and color octet scalars below 2.3 TeV.

Introduction

Deep inelastic proton-proton (pp) collisions often produce two or more energetic jets when the constituent partons are scattered with large transverse momenta (p_T). The invariant mass of the two jets with the largest p_T in the event (the dijet) has a spectrum that is predicted by quantum chromodynamics (QCD) to fall steeply and smoothly with increasing dijet mass (m_{jj}) [1].

Many extensions of the standard model predict the existence of resonances at the TeV scale that couple to partons (quarks and/or gluons), and therefore accessible at the proton-proton collisions of the Large Hadron Collider (LHC). The object of this search are narrow resonances, with small natural width compared to the experimental resolution, decaying to a pair of partons. The two partons will result in the detector as a pair of back-to-back hadronic jets in the transverse plane. If they come from the decay of a resonance, a bump corresponding to the mass of the resonance over the smoothly falling dijet mass distribution of the QCD processes will appear.

The search is extremely powerful and promising at the beginning of LHC run 2, since the new center-of-mass energy of $\sqrt{s}$ = 13 TeV is almost twice with respect to the past.

The increase in energy corresponds to much larger cross sections, especially at high mass, as can be seen in Fig. 1 left, where the ratio of the parton luminosity factor between 13 and 8 TeV is shown as a function of the resonance mass M_X. The results presented here make use of a 42 pb^{-1} dataset collected by the CMS experiment [2] in the first three weeks of data taking in July 2015. These data already exceed the sensitivity of the 2012 dijet search for resonance masses greater than about 5 TeV, as it is shown in Fig. 1 right.

Figure 1 right [3] and represents an estimate of the system mass that can be probed in BSM searches at one collider setup ("collider 2", e.g. LHC 8 TeV with 20 $fb^{-}1$) given an established system mass reach of some other collider setup ("collider 1", e.g. LHC 13 TeV with ≈0.04 fb^{-1}.). The mass where the grey diagonal line crosses the green (different green lines for different final states), indicates the point where the two setups have the same sensitivity. Where the green lines go below the grey, the 13 TeV datasets start to be more statistically powerful than the 8 TeV full dataset. This happens around 5 TeV if we consider the average of all partonic channels.

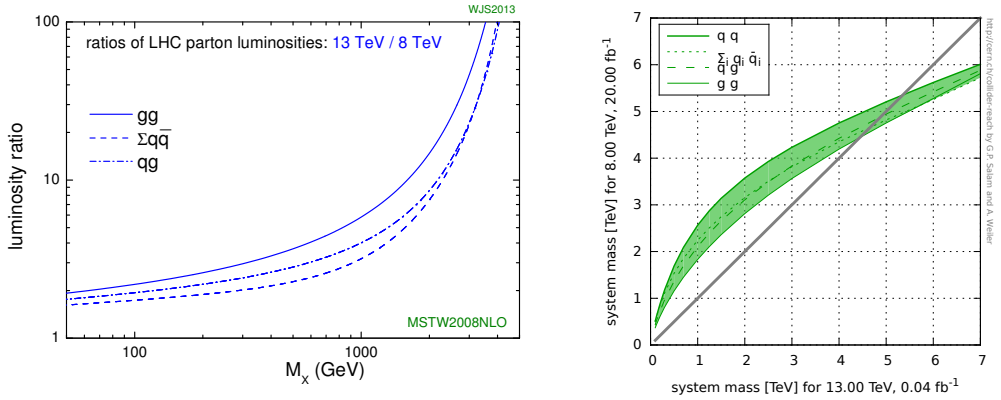

FIGURE 1. Left: the parton luminosity ratio between $\sqrt{s}$ = 13 TeV and 8 TeV as a function of the resonance mass M_X for qq, qg and gg final states. The ratio increases quickly at high dijet mass. Right: estimate of the system mass that can be probed in BSM searches at LHC run 1 setup (on y-axis $\sqrt{s}$ = 8 TeV with 20 fb^{-1}) given the system mass reach of run 2 setup (on x-axis $\sqrt{s}$ = 13 TeV with ≈0.04 fb^{-1}). The different green lines indicates the different final states (qq, qg, gg).

Jet reconstruction

The dijet analysis uses Particle Flow [4] jets with anti-k_T algorithm [5] and width parameter $\Delta R = \sqrt{\Delta\eta^2 + \Delta\phi^2} = 0.4$ (PF ak4 jets). This definition satisfies the requirements of infrared and collinear safety, and the jet energy is corrected using MC and data-based techniques in order to take into account the pile-up extra energy, the non-uniformity of the response across the detector and the residual difference in the absolute scale of the energy between data and MC.

CMS has developed jet quality criteria ("Jet ID") for PF jets which are found to retain the vast majority of real jets in the simulation while rejecting most fake jets arising from calorimeter and/or readout electronics noise. In addition to the Jet ID, all the PF ak4 jest are required to have a minimum $p_T > 30$ GeV and to be in the tracker coverage region $|\eta| < 2.5$. For the leading jet the p_T cut is $p_T > 60$ GeV.

The dijet analysis choice, as in the past, is to recluster in a larger cone the corrected PF ak4 jets that pass the selection described above, and use wide jets to reconstruct the invariant mass of the dijet system. This allows to contain better the energy of the hadrons in presence of final state radiation (FSR), and thus improves the dijet mass resolution with the resonance peak resulting both closer to the nominal mass and narrower. In the phase of the analysis preparation the optimization of the cone width has been studied in order to minimize the expected upper limits on the cross sections and the value $\Delta R = 1.1$ is found to be optimal.

Event selection and trigger studies

The most relevant selection criteria are:

i The dijet mass calculated using wide jets $m_{jj}^{Wide} > 1.2TeV$. During run 1 this cut was set to 890 GeV.

ii The angular separation between the two wide jets $|\Delta\eta_{jj}^{Wide}| < 1.3$. During run 1 this cut was the same. Optimization studies on 13 TeV Monte Carlo indicate that this value is still optimal.

The reason of (i) is that the trigger turn-on curve is complete around 1.2 TeV (see below in this section). The requirement (ii) is a cut on the $|\Delta\eta_{jj}^{Wide}|$ between the jets. This quantity is related to the emission angle of the final partons with respect to the beam line in the center-of-mass reference frame (the scattering angle θ^*):

$$\cos\theta^* = \tanh(\frac{\Delta\eta}{2}) \tag{1}$$

and the cut $|\Delta\eta_{jj}^{Wide}| < 1.3$ corresponds to $\cos\theta^* < 0.57$. This criterion is introduced to improve the signal over background ratio, excluding the region close to $\cos\theta^* = 1$ where most of the QCD processes concentrates. The analysis, with this choice, remains inclusive with respect to different new physics hypotheses.

The event with the highest dijet mass passing the full selection is shown in Fig. 2 left. The dijet mass of this clean dijet event is 5.4 TeV, greater then the highest mass event observed in 2012 (of 5.2 TeV), confirming that this analysis exceeds the run 1 sensitivity above ≈5 TeV.

The PFHT800 is the main unprescaled trigger that is used for this analysis. The trigger selection is based on the scalar sum of the transverse momenta of all the jets in the event (H_T) with a threshold around 800 GeV and carries a large part of the fully hadronic physics at CMS. The PFHT475 is a prescaled path, based on the same H_T selection of the main unprescaled one, with a lower threshold (around 450 GeV). It used as reference to study the relative trigger efficiency, since its turn-on region is far enough from the one of PFHT800, and it has a relatively small prescale ($O(100)$), that allows to collect a sufficient statistics to study the turn on region of the main trigger. The turn on curve as a function of m_{jj}^{Wide} is shown in Fig. 2 right.

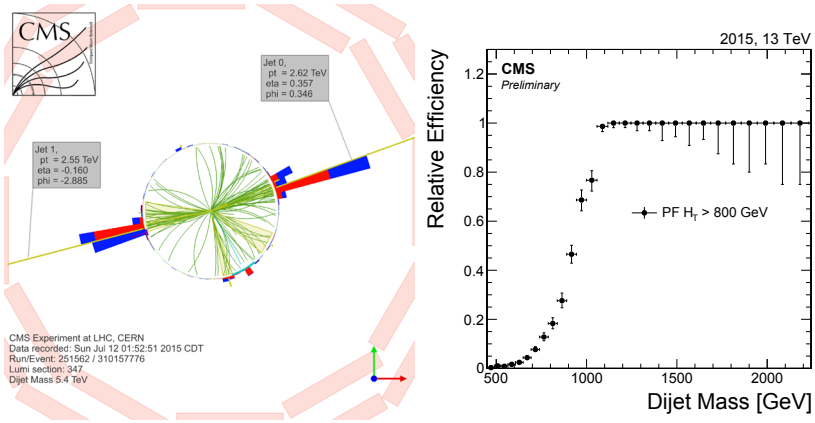

FIGURE 2. Left: display of the highest dijet mass event in the ρ-ϕ view of the CMS detector. Right: Trigger relative efficiency as function of m_{jj}^{Wide}.

The study of the trigger efficiency curve is important to decide where the fit to the dijet mass distribution in data can start, without having distortions in the low mass region due to the trigger turn on. The turn on curve of the PFHT800 trigger is complete for m_{jj}^{Wide} greater than about 1.2 TeV.

Data quality checks

The most relevant analysis variables are compared to a leading-order (LO) QCD Monte Carlo (MC) prediction from Pythia8 (v205) [6] with the CUETP8M1 tune [7, 8], including a GEANT 4 based [9] simulation of the CMS detector. To check the quality and stability of data some jet and event-related quantities are also monitored as a function of time.

Figure 3 shows:

- the data-MC comparison for the kinematic variables of the two leading jets: transverse momentum (p_T), pseudorapidity (η) and azimuthal angle (ϕ);
- the data-MC comparison for the main dijet event variables: the separation in pseudorapidity ($\Delta\eta$) and in the azimuthal angle ($\Delta\phi$) between the two leading jets;
- the observed dijet cross section as a function of time (run index).

The Monte Carlo simulation is scaled to the integral of data. The shapes of p_T, η and ϕ of the two leading jets and the angular distance between them result in good agreement with simulation. The measured dijet cross section is flat versus time, confirming that the data are stable and we do not observe unexpected features.

Analysis strategy

We search for narrow resonances in the dijet mass spectrum. For *narrow* we mean that the natural resonance width is small compared to the CMS dijet mass resolution.

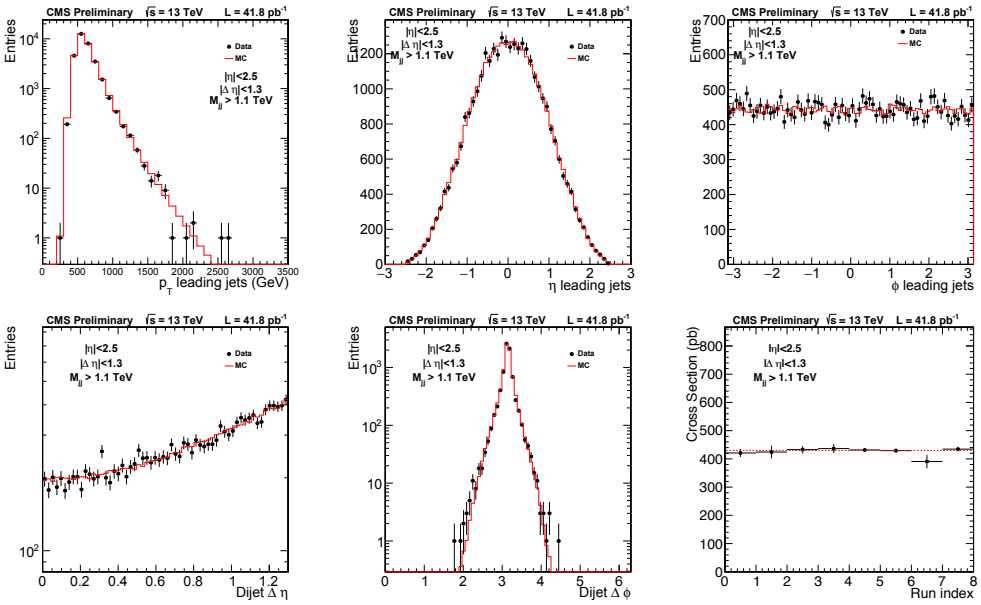

FIGURE 3. Top: kinematic distributions of the two leading jets (p_T, η, ϕ) in data and QCD simulation. Bottom: the dijet angular separation $\Delta\eta$ (left) and $\Delta\phi$ (middle) in data and QCD simulation, and the observed dijet cross section as a function of the run index (right).

Figure 4 shows the dijet mass distributions for these signals using Pythia 8 and the CMS detector simulation. The predicted mass distributions have a Gaussian core coming from the jet energy resolution and a tail towards lower mass values coming primarily from QCD radiation. The contribution of this low-mass tail to the line-shape depends on the parton content of the resonance (qq, qg, or gg). Resonances containing gluons, which are more susceptible to QCD radiation than quarks, have a more pronounced tail. For high-mass resonances, there is also another significant contribution depending on both PDFs and the natural width of the Breit-Wigner resonance shape. For resonances produced by interactions of non-valence partons in the proton, the low-mass component of the Breit-Wigner resonance shape is amplified by the rise of the parton probability distribution at low fractional momentum. This effect causes a large tail at low mass values.

Figure 5 shows the measured differential cross section as a function of dijet mass in predefined bins corresponding to the dijet mass resolution [10]. The data are compared to a LO QCD Monte Carlo prediction (the same used for Fig. 3).

To test the smoothness of our measured cross section as a function of dijet mass, we fit the data with the parameterization

$$\frac{\mathrm{d}\sigma}{\mathrm{d}m_{jj}} = \frac{P_0(1-x)^{P_1}}{x^{P_2}}\,, \tag{2}$$

with $x = m_{jj}/\sqrt{s}$ and three free parameters P_0, P_1, P_2. This functional form is a modified version of the 4-parameter function used in previous searches [10–20] to describe both data and QCD predictions. With a Fisher-test [21] it has been proved that the 4^{th} parameter is not necessary to describe the dataset od 42 pb^{-1} presented here. In Fig. 5 we show the result of the binned maximum likelihood fit, which has a chi-squared (χ^2) of 24 for 27 degrees of freedom when excluding the empty bins. The difference between the data and the fit is also shown at the bottom of Fig. 5, and that difference is normalized to the statistical uncertainty of the data in each bin. The data are well described by the fit.

Results

Figure 6 shows the model-independent observed and expected upper limits at a 95% confidence level (CL) on $\sigma \times B \times A$, i.e. the product of the cross section (σ), the branching fraction (B), and the acceptance (A), for the kinematic

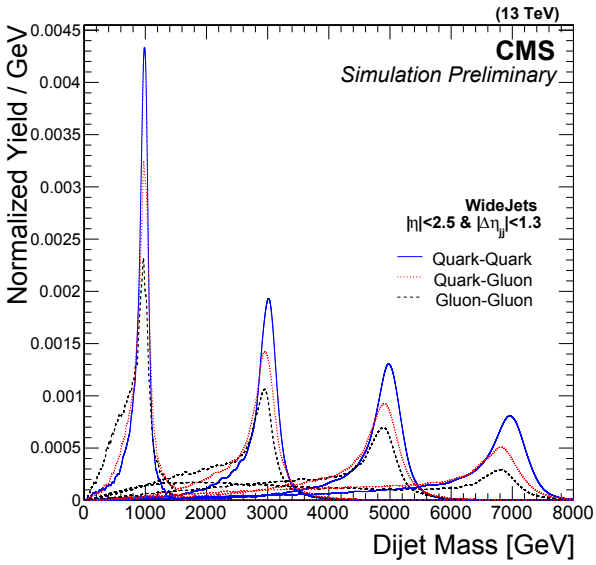

FIGURE 4. The reconstructed resonance mass spectrum generated with the Pythia MC simulation for quark-quark resonances modeled by the process qq → RS graviton → qq (solid), for quark-gluon resonances modeled by qg → excited quark → qg (dotted), and for gluon-gluon resonances modeled by gg → RS graviton → gg (dashed) for resonance masses of 1, 3, 5 and 7 TeV.

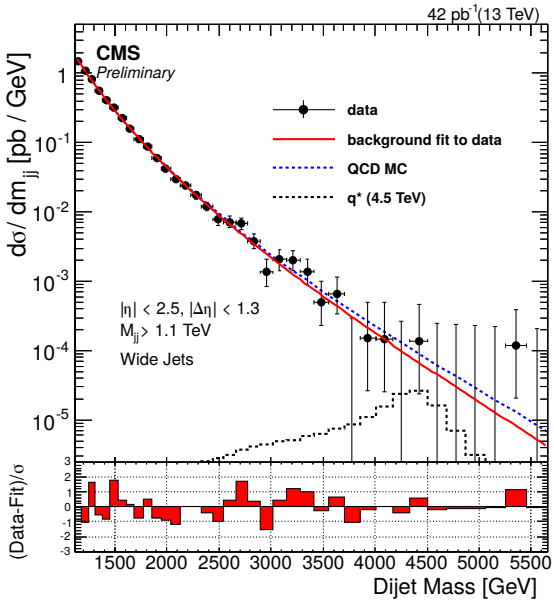

FIGURE 5. Dijet mass spectrum using wide jets (points) compared to a smooth fit (solid line) and to predictions [6] including detector simulation of QCD (dashed line) and expectations of one narrow resonance signal at the value of resonance mass excluded by this analysis with 95% CL. The QCD prediction has been normalized to the data. The error bars are statistical only. The bin-by-bin fit residuals divided by the uncertainty of the data, (data − fit)/σ_{data}, are shown at the bottom.

requirements $|\Delta\eta_{jj}^{Wide}| < 1.3$ and $|\eta| < 2.5$, for narrow qq, qg, and gg resonances.

Resonances with mass less than 1.3 TeV, are too close to the lower edge of our dijet mass spectrum to produce a peak distinguishable from the background, and are therefore not considered.

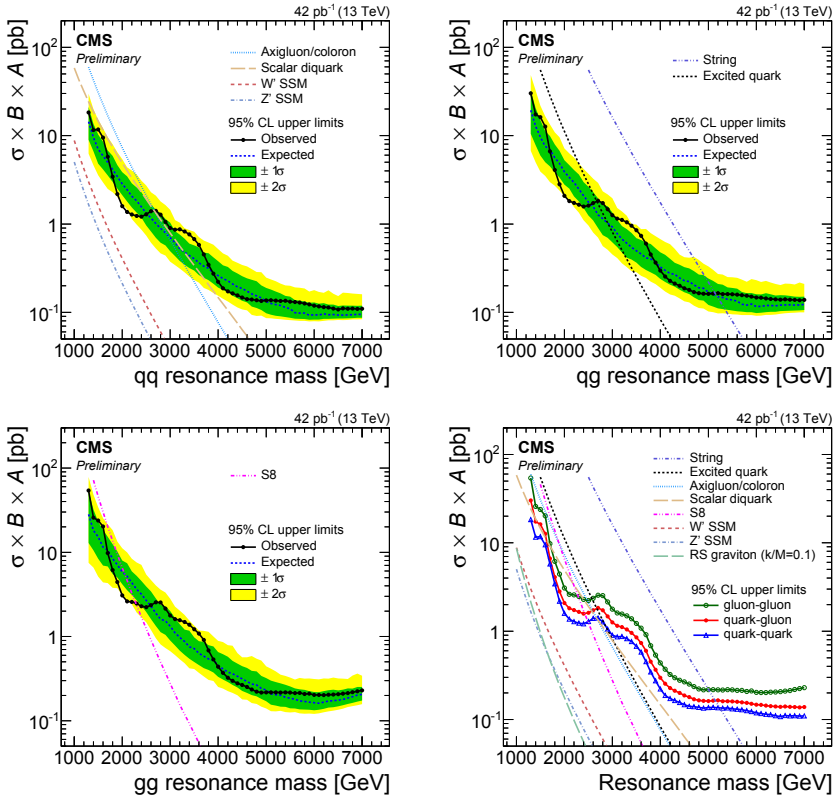

FIGURE 6. The observed and expected 95% upper limits on $\sigma \times B \times A$ for dijet resonances of the type (from top left) quark-quark, quark-gluon, gluon-gluon, summary of observed limits for the 3 final states. The observed limits are shown as points connected by solid curves. The expected limits are shown as dotted curves and their variation at the 1σ and 2σ levels with shaded bands. Limits are compared to predicted cross sections of string resonances [22, 23], scalar diquarks [24], excited quarks [25, 26], axigluons [27, 28], colorons [28, 29], color octet scalars S8 [30], new gauge bosons and [31], and RS gravitons [32].

The expected limits are estimated with pseudo-experiments generated using background-only hypotheses. The generated mass spectra are further fitted with a background-plus-signal model to extract expected upper limits. The difference in the limits for qq, qg, and gg resonances at the same resonance mass originate from the difference in their shapes. All upper limits presented can be compared to the parton-level predictions of $\sigma \times B \times A$, without any detector simulation, in order to determine mass limits on new particles. Acceptance can be evaluated at the parton level for the resonance decay to two partons. The model predictions shown in Fig. 6 are calculated in narrow-width approximation [33] using CTEQ6L1 [34] PDFs at leading order and a next to leading order k-factor is included for the W', Z', axigluon, and coloron models [28].

New particles are excluded at a 95% in mass regions for which the theory curve lies at or above the observed upper limit for the appropriate final state in Fig. 6. For string resonances the observed mass limit of 5.1 TeV already extends the previous CMS limit of 5.0 TeV, confirming again that this search is more sensitive then run 1 for masses greater than 5 TeV. For the other models, the previous run 1 limits are still more stringent [15]: for scalar diquarks the observed mass limit is 2.7 TeV, compared to 4.7 TeV set in run 1; for axigluons and colorons the observed mass limit is 2.7 TeV, compared to 3.7 TeV set in run 1; for excited quarks we exclude up to 2.7 TeV, compared to 3.5 TeV set in run 1; for a color octet scalar the observed mass limit of 2.3 TeV, compared to 2.7 TeV limit set in run 1. With the current dataset we cannot set mass limits on W', Z' bosons or RS Gravitons. The most stringent limits on the cross section of dijet resonance models are set from the recent results of CMS [35] and ATLAS [36], based on the full

dataset of 2015 at $\sqrt{s}$ = 13 TeV (respectively 2.4 fb^{-1} and 3.6 fb^{-1}).

REFERENCES

[1] Serguei Chatrchyan et al. Measurement of the differential dijet production cross section in proton-proton collisions at $\sqrt{s}$ = 7 TeV. *Phys. Lett. B*, 700:187, 2011.

[2] S. Chatrchyan et al. The CMS experiment at the CERN LHC. *JINST*, 3:S08004, 2008.

[3] Gavin Salam and Andreas Weiler. Collider reach. `http://collider-reach.web.cern.ch/collider-reach/`.

[4] CMS Collaboration. Commissioning of the particle-flow event reconstruction with the first LHC collisions recorded in the CMS detector. CMS Physics Analysis Summary CMS-PAS-PFT-10-001, 2010.

[5] Matteo Cacciari, Gavin P. Salam, and Gregory Soyez. The anti-k_t jet clustering algorithm. *JHEP*, 04:063, 2008.

[6] Torbjörn Sjöstrand, Stephen Mrenna, and Peter Skands. A brief introduction to PYTHIA 8.1. *Comp. Phys. Comm.*, 178:852, 2008.

[7] CMS Collaboration. Underlying Event Tunes and Double Parton Scattering. CMS Physics Analysis Summary CMS-PAS-GEN-14-001, 2014.

[8] Peter Skands, Stefano Carrazza, and Juan Rojo. Tuning PYTHIA 8.1: the Monash 2013 tune. *Eur. Phys. J. C*, 74:3024, 2014.

[9] S. Agostinelli et al. Geant4: A simulation toolkit. *Nucl. Instrum. Meth. A*, 506:250, 2003.

[10] Vardan Khachatryan et al. Search for Dijet Resonances in 7 TeV pp Collisions at CMS. *Phys. Rev. Lett.*, 105:211801, 2010. [Erratum 10.1103/PhysRevLett.106.029902].

[11] T. Aaltonen et al. Search for new particles decaying into dijets in proton-antiproton collisions at $\sqrt{s}$ = 1.96 TeV. *Phys. Rev. D*, 79:112002, 2009.

[12] Serguei Chatrchyan et al. Search for resonances in the dijet mass spectrum from 7 TeV pp collisions at CMS. *Phys. Lett. B*, 704:123, 2011.

[13] Serguei Chatrchyan et al. Search for narrow resonances and quantum black holes in inclusive and b-tagged dijet mass spectra from pp collisions at $\sqrt{s}$ = 7 TeV. *JHEP*, 01:013, 2013.

[14] Serguei Chatrchyan et al. Search for narrow resonances using the dijet mass spectrum in pp collisions at $\sqrt{s}$ = 8 TeV. *Phys. Rev. D*, 87:114015, 2013.

[15] V. Khachatryan et al. Search for resonances and quantum black holes using dijet mass spectra in proton-proton collisions at $\sqrt{s}$ = 8 TeV. *Phys. Rev. D*, 91:052009, 2015.

[16] G. Aad et al. Search for New Particles in Two-Jet Final States in 7 TeV Proton-Proton Collisions with the ATLAS Detector at the LHC. *Phys. Rev. Lett.*, 105:161801, 2010.

[17] Georges Aad et al. Search for new physics in dijet mass and angular distributions in pp collisions at $\sqrt{s}$ = 7 TeV measured with the ATLAS detector. *New J. Phys.*, 13:053044, 2011.

[18] Georges Aad et al. Search for new physics in the dijet mass distribution using 1 fb^{-1} of pp collision data at $\sqrt{s}$ = 7 TeV collected by the ATLAS detector. *Phys. Lett. B*, 708:37, 2012.

[19] Georges Aad et al. ATLAS search for new phenomena in dijet mass and angular distributions using pp collisions at $\sqrt{s}$ = 7 TeV. *JHEP*, 01:029, 2013.

[20] G. Aad et al. Search for new phenomena in the dijet mass distribution using pp collision data at $\sqrt{s}$ = 8 TeV with the ATLAS detector. *Phys. Rev. D*, 91:052007, 2015.

[21] Richard G. Lomax and Debbie L. Hahs-Vaughn. *Statistical concepts: A second course*. Routledge Academic, 2007.

[22] Luis A. Anchordoqui, Haim Goldberg, Dieter Lüst, Satoshi Nawata, Stephan Stieberger, and Tomasz R. Taylor. Dijet signals for low mass strings at the LHC. *Phys. Rev. Lett.*, 101:241803, 2008.

[23] Schuyler Cullen, Maxim Perelstein, and Michael E. Peskin. TeV strings and collider probes of large extra dimensions. *Phys. Rev. D*, 62:055012, 2000.

[24] JoAnne L. Hewett and Thomas G. Rizzo. Low-energy phenomenology of superstring-inspired E(6) models. *Phys. Rept.*, 183:193, 1989.

[25] U. Baur, I. Hinchliffe, and D. Zeppenfeld. Excited quark production at hadron colliders. *Int. J. Mod. Phys. A*, 2:1285, 1987.

[26] U. Baur, M. Spira, and P. M. Zerwas. Excited quark and lepton production at hadron colliders. *Phys. Rev. D*, 42:815, 1990.

[27] Paul H. Frampton and Sheldon L. Glashow. Chiral color: An alternative to the standard model. *Phys. Lett. B*, 190:157, 1987.
[28] R. Sekhar Chivukula, Arsham Farzinnia, Jing Ren, and Elizabeth H. Simmons. Hadron collider production of massive color-octet vector bosons at next-to-leading order. *Phys. Rev. D*, 87:094011, 2013.
[29] Elizabeth H. Simmons. Coloron phenomenology. *Phys. Rev. D*, 55:1678, 1997.
[30] Tao Han, Ian Lewis, and Zhen Liu. Colored resonant signals at the LHC: largest rate and simplest topology. *JHEP*, 12:085, 2010.
[31] E. Eichten, I. Hinchliffe, Kenneth D. Lane, and C. Quigg. Supercollider physics. *Rev. Mod. Phys.*, 56:579, 1984.
[32] Lisa Randall and Raman Sundrum. An alternative to compactification. *Phys. Rev. Lett.*, 83:4690, 1999.
[33] Robert M. Harris and Konstantinos Kousouris. Searches for dijet resonances at hadron colliders. *Int. J. Mod. Phys. A*, 26:5005, 2011.
[34] Jonathan Pumplin, Daniel Robert Stump, Joey Huston, Hung-Liang Lai, Pavel Nadolsky, and Wu-Ki Tung. New generation of parton distributions with uncertainties from global QCD analysis. *JHEP*, 07:012, 2002.
[35] Vardan Khachatryan et al. Search for narrow resonances decaying to dijets in proton-proton collisions at sqrt(s) = 13 TeV. 2015.
[36] Search for New Phenomena in Dijet Mass and Angular Distributions with the ATLAS Detector at $\sqrt{s}$ = 13 TeV. 2015.
[37] CMS Collaboration. CMS luminosity based on pixel cluster counting - summer 2013 update. *CMS Physics Analysis Summary* CMS-PAS-LUM-13-001, (2013).
[38] F. Abe et al. Search for new particles decaying to dijets in $p\bar{p}$ collisions at $\sqrt{s}$ = 1.8 TeV. *Phys. Rev. Lett.*, 74:3538, 1995.
[39] R. Sekhar Chivukula, Arsham Farzinnia, Elizabeth H. Simmons, and Roshan Foadi. Production of massive color-octet vector bosons at next-to-leading order. *Phys. Rev. D*, 85:054005, 2012.
[40] Tomasz Skwarnicki. A study of the radiative cascade transitions between the upsilon-prime and upsilon resonances. DESY-F31-86-02, 1986.
[41] CMS Collaboration. Cms luminosity based on pixel cluster counting - summer 2012 update. *CMS Physics Analysis Summary*, CMS-PAS-LUM-12-001, 2012.
[42] Particle Data Group and K. Nakamura. Review of Particle Physics. *J. Phys. G*, 37:075021, 2010. [See Ch. 33, Statistics].
[43] Zoltan Nagy. *Phys. Rev. D*, 68:094002, 2003.
[44] F. Abe et al. Search for new particles decaying to dijets at CDF. *Phys. Rev. D*, 55:5263, 1997.
[45] CMS Collaboration. Search for dijet resonances in the dijet mass distribution in 7 TeV pp collisions at CMS. *CMS Physics Analysis Summary*, http://cdsweb.cern.ch/record/1287571CMS-PAS-EXO-10-010, 2010.
[46] K. Nakamura et al. Review of particle physics. *J. Phys. G*, 37:075021, 2010.
[47] The PYTHIA6 Z2 tune is identical to the Z1 tune described in [**?**] except that Z2 uses the CTEQ6L PDF while Z1 uses CTEQ5L.

Proceedings of the LHCP2015 Conference, St. Petersburg, Russia, August 31 - September 5, 2015

Editors: V.T. Kim and D.E. Sosnov

Search For High Mass Dilepton And Diphoton Resonances At The Large Hadron Collider

OTMAN CHARAF

University of Alabama at Tuscaloosa

Otman.Charaf@cern.ch

On behalf of the ATLAS and CMS Collaborations

Abstract. The search for new physics at the TeV scale is one of the major aspects of the ATLAS and CMS experimental programmes. This includes a myriad of theoretical models involving resonances that can can decay to leptons or photons. An overview of such analyses is presented in this paper. All analyses presented here use the full 2012 dataset, corresponding to an integrated luminosity of $\sim 20\ fb^{-1}$, depending on the channel, recorded in proton-proton collisions at $\sqrt{s} = 8$ TeV with the ATLAS and CMS detectors at the CERN LHC. Unless otherwise stated, all electron, photon and muon identifications use a combination of shower shape and isolation criteria. No sign of new physics is observed and limits are set on the various model parameters.

Introduction

The recent discovery by the ATLAS [1] and CMS [2] Collaborations of a particle compatible with the Standard Model (SM) predictions for the Higgs boson [3, 4] enhanced our understanding of the electroweak symmetry (EW) breaking mechanism. But the large difference between the EW scale and the Planck scale, i.e. the hierarchy mass problem, stills remains unsolved. In many theoretical extensions of the SM, larger gauge groups are introduced to unify the electroweak and strong interactions [5, 6, 7, 8, 9] . Other models [10, 11, 12] introduce additional spatial dimensions of space-time, involving the existence of a so-called tower of Kaluza-Klein (KK) excitations of the known SM bosons or the hypothetical graviton. All these beyond the SM (BSM) theories therefore predict the existence of new massive resonances that could manifest at the TeV scale. Such resonances would appear as a peak over a continous background coming from the SM processes.

ATLAS Dilepton resonances [13]

Resonances such as the Sequential Standard Model Z' (Z'_{SSM}) with couplings to fermions equivalent to those of the SM Z boson, the $Z'_{\psi,\chi}$ predicted by E_6 gauge group grand unified theories [5, 6], or the Randall-Sundrum [12, 11, 10] graviton (G_{RS}) are probed in the dielectron and the dimuon channel. In addition, resonances such as the Z^* [9] or the minimal Z' [8] are also probed. Most of the background contributions are derived from Monte-Carlo simulations (Drell-Yan, $t\bar{t}, WW, WZ, ZZ$) except the fake contributions which are estimated, in the dielectron channel, from data using a fake rate method[1]. The total background contribution is normalized to the region $80 < M_{ll} < 110$ GeV. The systematic uncertainties amount to 4% for the signal in both channels and to 44% (23%) for the background in the dielectron (dimuon) channel for a dilepton mass of 3 TeV, the main contribution being the uncertainty on the Drell-Yan background due to PDF and α_S. Uncertainties smaller than 3% are neglected in the statistical analysis. Fig. 1 (left) and (middle) present the invariant mass spectra of the selected dielectron and dimuon pairs respectively, compared with the sum of the different background components. Excellent agreement is observed. To extract upper limits on the various model cross sections, a statistical interpretation tool is built based on a likelihood bayesian technique. A

[1] This source of background is negligible in the dimuon channel.

subtlety relies here in the fact that interference effects between the Drell-Yan process and a possible resonance are accounted in the minimal Z' models only. The parameter of interest is the cross-section times branching ratio if no interference effects are included and the coupling strength otherwise. The combination between the dielectron and dimuon channels is performed assuming lepton universality. Fig. 1(right) gives the 95% CL limits as a function of the dilepton invariant mass for the Z'_{ψ} and Z'_{SSM} models. A Z'_{SSM} is excluded below 2900 GeV, the Z'_{ψ}, Z'_{χ} and Z^* below 2510, 2620, 2850 GeV respectively. RS gravitons are excluded below 2680 (2280) GeV for couplings of 0.10 (0.05), all at 95% CL.

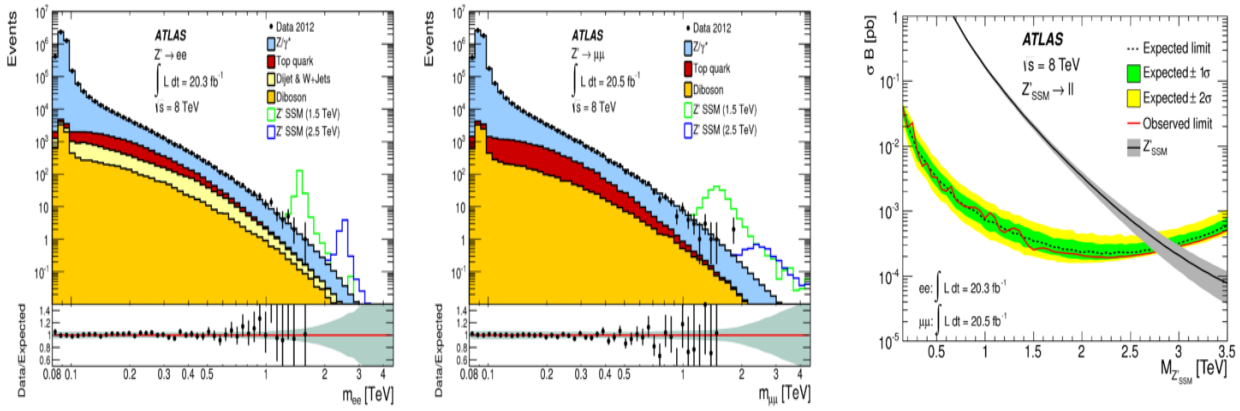

FIGURE 1. Dielectron (left) and dimuon (middle) invariant mass (m_{ll}) distributions after event selection, with two selected Z' signals overlaid, compared to the stacked sum of all expected backgrounds, and the ratios of data to background expectation [13]. Median expected (dashed line) and observed (solid red line) 95% CL upper limits on cross-section times branching ratio (σB) in the combined dilepton channel, along with predicted σB for Z'_{SSM} production (right) [13].

CMS Dilepton resonances [14]

The corresponding CMS analysis focuses on the Z'_{SSM}, the Z'_{ψ} and the RS graviton. In order for the analysis to be robust, different data-driven background estimation techniques and cross-check methods have been derived. For the Drell-Yan contribution, the mass spectrum shape is derived from Monte-Carlo simulations and normalized to the number of events in data in the region $60 < M_{ll} < 120$ GeV. The $t\bar{t}$, tW, WW, WZ and $\tau\tau$ contributions are derived from Monte-Carlo simulations and cross-checked using the data-driven $e\mu$ method which exploits the flavour-symmetric nature of such processes. Finally, the QCD multijet component is estimated using a data-driven fake rate method[2]. Fig. 2 (left) and (middle) present the invariant mass spectra of the selected dielectron and dimuon pairs respectively, compared with the sum of the different background components. Excellent agreement is observed. The statistical interpretation tool employs an unbinned likelihood bayesian technique. It has the specificity of (a) combining both channels and (b) setting limits on the cross section ratio $R_{\sigma} = \sigma_{Z'}/\sigma_Z$ allowing therefore to cancel some systematic uncertainties. Fig. 2(right) gives the 95% CL limits as a function of the dilepton invariant mass for the Z'_{ψ} and Z'_{SSM} models. A Z'_{SSM} is excluded below 2900 GeV and the Z'_{ψ} below 2570 GeV. RS gravitons are excluded below 2730, 2350 and 1270 GeV for couplings of 0.10, 0.05 and 0.01, respectively, all at 95% CL.

ATLAS diphoton resonances [15]

Randall-Sundrum gravitons, can also decay to a diphoton pair. The main, irreducible background comes from the Born and Box processes which are evaluated from Monte-Carlo predictions. The reducible background contributions arise from γ+jet and multijet contributions where at least one jet fakes a photon. They are estimated using templates extracted in control regions which are then extrapolated to the signal region using a smooth function. The total background is normalized to the region $179 < M_{\gamma\gamma} < 409$ GeV. Fig. 3 (left) presents the invariant mass spectrum of the

[2]This source of background is negligible in the dimuon channel.

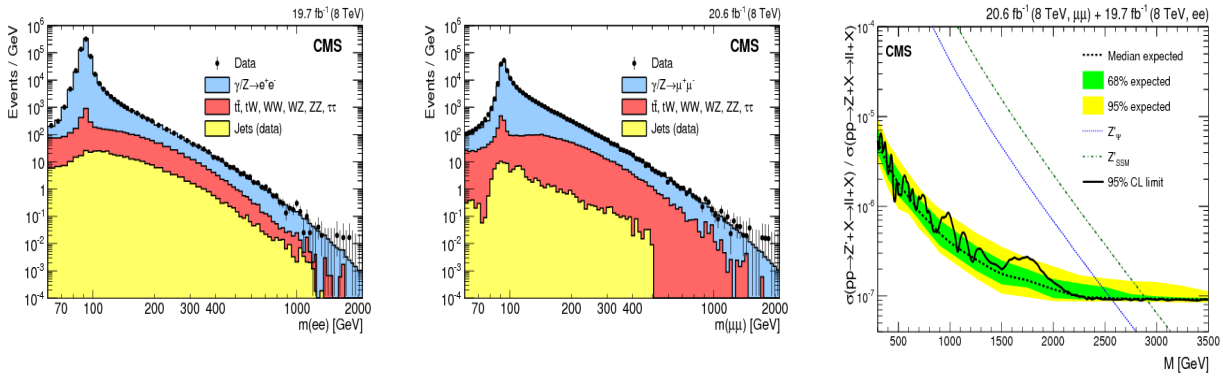

FIGURE 2. The invariant mass spectrum of $\mu^+\mu^-$ (left) and ee (right) events [14]. The points with error bars represent the data. The histograms represent the expectations from SM processes: Z/γ^*, $t\bar{t}$, and other sources of prompt leptons (tW, dibosons, $Z/\gamma^* \rightarrow \tau^+\tau^-$), as well as the multijet backgrounds. Upper limits as a function of the resonance mass M on the ratio of the product of cross section and branching fraction into lepton pairs relative to that of Z bosons, for final-state spins of 1 [14].

selected diphoton pairs, compared to the sum of the background estimations, where very good agreement is observed. The main systematic uncertainty is coming from the shape of the irreducible SM diphoton background contribution, mostly due to PDF effects. The most significant excess is found in the region $494 < M_{\gamma\gamma} < 745$ GeV and corresponds to a background-only hypothesis p-value of 58%. The statistical analysis follows a Bayesian approach with a flat positive prior for the cross section and Gaussian priors for the nuisance parameters associated to the systematic uncertainties. Fig. 3 (right) presents the 95% CL expected and observed upper limits on k/M_{Pl} as a function of the assumed value of the graviton mass. RS gravitons are excluded at 95% CL below 2660 GeV (1410 GeV) for a k/M_{Pl} value of 0.1 (0.01).

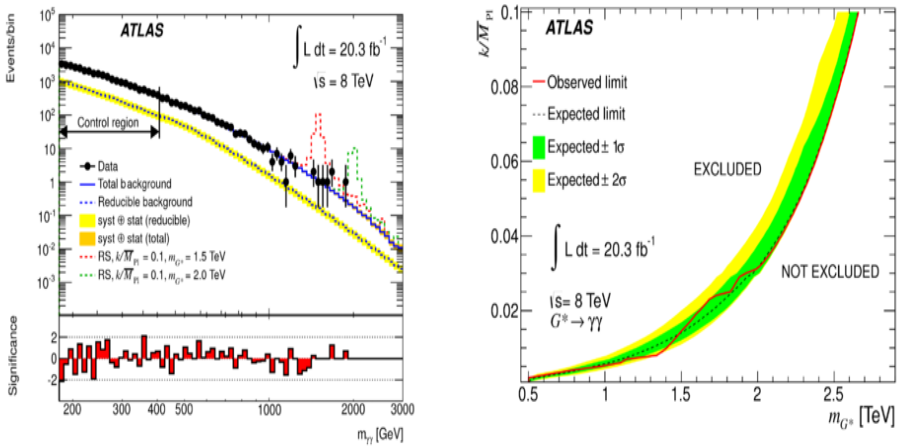

FIGURE 3. Observed invariant mass distribution (left) of the selected diphoton events (black dots; the vertical and horizontal axes on logarithmic scales) [15]. Superimposed are the SM background prediction including irreducible and reducible components and two examples of signal predictions. (Bottom insert) Bin-by-bin significance of the difference between data and background expectation. Expected and observed upper limits on k/M_{Pl} (right) expressed at 95% CL, as a function of the assumed value of the graviton mass [15].

CMS diphoton resonances [16]

The corresponding analysis in CMS uses no control region. The irreducible SM diphoton background contributions are estimated from Monte-Carlo predictions weighted by a K factor using the 2γNNLO [17, 18] program. The γ+jet and dijet contributions are estimated from data using a fake rate method. The Drell-Yan production of dielectron pairs is shown to be negligible. The invariant mass spectrum of the selected diphoton pairs is compared (Fig. 4 (left)) to the sum of the expected background contributions and very good agreement is observed. The method used to set limits on the RS model parameters is an unbinned likelihood constructed from the sum of probability density functions for the signal and background. Fig. 4 (right) presents the observed excluded region in the parameter space of the Randall-Sundrum model (k/M_{Pl} value as a function of the assumed graviton mass). RS gravitons are excluded at 95% CL below 1450, 2310 and 2780 GeV for k/M_{Pl} values of 0.01, 0.05 and 0.10, respectively.

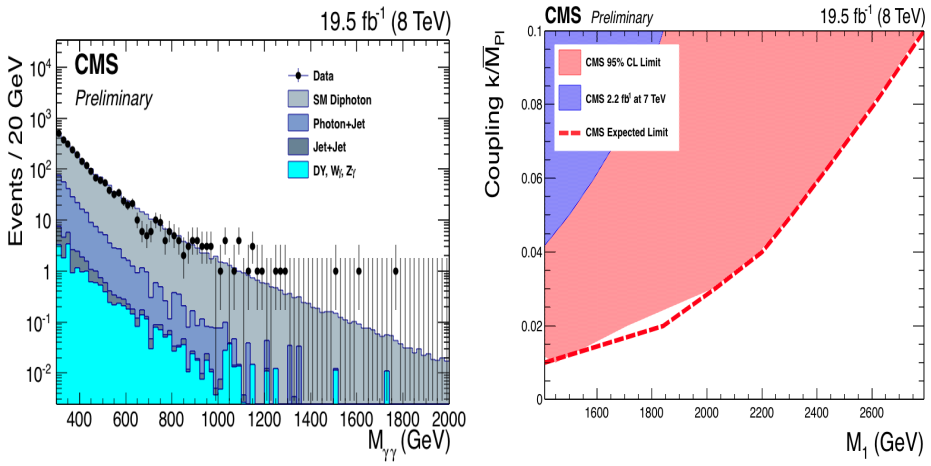

FIGURE 4. Diphoton invariant mass distribution for data (black dots) compared to the background predictions (left) [16]. Observed excluded region (right) in the parameter space of the Randall-Sundrum model [16]. The dashed red curve shows the expected limit.

ATLAS $\tau\tau$ resonances [19]

Resonances, as studied in dilepton analyses, can also decay to a pair of τ leptons. In addtion, some models [20] involve so-called non universal Z' (Z'_{NU}) which couple preferentially to third generation fermions. The search is performed in two channels: the $\tau_{had}\tau_{had}$ channel and the $\tau_{lep}\tau_{had}$ channel, where the lepton is either an electron or a muon. The dominant source of background, in both channels, is the Drell-Yan process ($Z/\gamma^* \rightarrow \tau\tau, ll$), which is estimated from Monte-Carlo simulations. Other sources of background come from QCD multijet and $W/Z/\gamma$+jets processes as well as $t\bar{t}$, tW and diboson (WZ, ZZ, WW) processes. The hadronic τ selection relies on a boosted decision tree based on shower shape and tracking information. The leptonic τ selection is based on isolation with an additional shower shape criterion for electrons. Events are selected containing two opposite sign and back to back τ leptons with a missing transverse energy criterion. The transverse mass of two reconstructed objetcs p^A and p^B, with transverse momenta p_T^A and p_T^B and with an angle $\Delta\phi(p^A, p^B)$ in the transverse plane, is defined as $m_T(p^A, p^B) = \sqrt{2p_T^A p_T^B(1 - \cos\Delta\phi(p^A, p^B))}$. Transverse mass thresholds, optimized separately for each signal mass and found to be the same for all channels, are applied. The total transverse mass is then defined as: $m_T^{tot}(\tau_1, \tau_2, \not{E}_t) = \sqrt{m_T^2(\tau_1, \tau_2) + m_T^2(\tau_1, \not{E}_t) + m_T^2(\tau_2, \not{E}_t)}$ where τ_1 and τ_2 denote the reconstructed visible decay products of the two τ leptons. Fig. 5 present the m_T^{tot} distributions after event selection, compared to the sum of the SM contributions, for the (left) $\tau_{had}\tau_{had}$ and (middle) $\tau_{lep}\tau_{had}$ channels. The statistical analysis employs the Bayesian Analysis Toolkit [21] and combines both channels. The main systematic uncertainties come from the τ identification efficiency and energy scale in the $\tau_{had}\tau_{had}$ channel and the statistical uncertainty on the background from fake factor estimates in $\tau_{lep}\tau_{had}$ channel. Fig. 5 (right) gives the combined upper

limits at 95% CL on the cross section times ditau branching ratio for a Z' from different theoretical scenarios. A Z'_{SSM} is excluded below 2020 GeV at 95% CL.

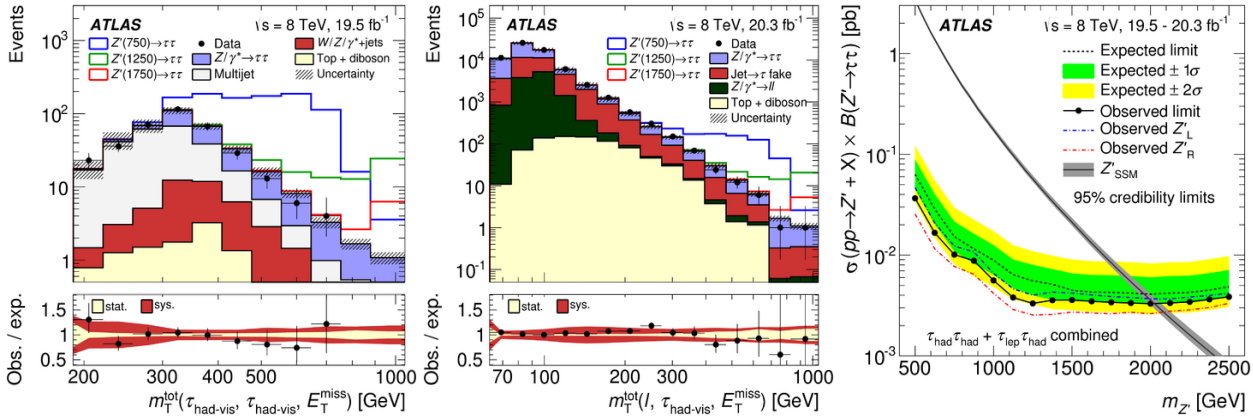

FIGURE 5. The m_T^{tot} distribution after event selection in the (left) $\tau_{had}\tau_{had}$ and (middle) $\tau_{lep}\tau_{had}$ channels [19]. The estimated contributions from SM processes are stacked and appear in the same order as in the legend. The inset shows the ratio of the observed events over the total expected SM contribution. Bayesian 95% credibility combined upper limits (right) on the cross section times ditau branching fraction for a Z'_{SSM} with an overlay of the impact of the Z'_L/Z'_R models [19].

CMS $\tau\tau$ resonances [22]

The corresponding analysis from CMS focuses on the final state where one τ decays to an electron and the other τ to a muon with the presence of missing transverse energy. The Z'_{SSM} and the GUT-inspired E_6 model Z'_ψ are investigated. The event selection requires well identified and isolated electron and muon with opposite charge and back to back in the transverse plane. The missing tranverse momentum $\not{E}_t$ is required to be higher than 20 GeV and its direction be consistent with originating from τ decays using the "CDF-ζ" [23] variable. This reduces the contamination of events containing a W boson. In addition no b-jets are allowed in the selected events. The visible tau decay products and the $\not{E}_t$ are used to reconstruct the mass: $M(\mu, e, \not{E}_t) = \sqrt{(E_\mu + E_e + \not{E}_t)^2 - (\vec{p_\mu} + \vec{p_e} + \vec{\not{E}_t})^2}$. The dominant source of background comes from the $t\bar{t}$ process and is evaluated in a control region defined by the presence of b-tagged jets. The QCD mulijet contribution is estimated in a high purity multijet sample considering like-sign $\tau\tau$ candidates where the contamination from non-multijet processes is subtracted based on Monte-Carlo expectations. The Drell-Yan background contribution is extracted from Monte-Carlo after comparing with the data in a low mass region with good agreement. A similar approach is used for the WW and W+jets contributions. The main systematic uncertainty is related to the data-driven background estimates, due mostly to the limited statistics in the control regions. Fig. 6 (left) presents the ditau mass $M(\mu, e, \not{E}_t)$ compared to the sum of the expected background contributions. The statistical analysis follows a Bayesian approach and uses as inputs the M(μ,e,$\not{E}_t$) distributions from signal, background and data. Fig. 6 (right) presents the observed 95% CL upper limits on the cross section times branching ratio for a Z' from different theoretical scenarios. The observed 95% CL lower limits of the Z'_{SSM} and Z'_ψ are 1300 and 810 GeV, respectively.

Conclusion

Results from searches for new massive resonances, in the dilepton and diphoton channels, using the ATLAS and CMS detectors, were presented, including a variety of theoretical models. No significant deviation from the corresponding SM processes is observed. Limits on the various model parameters were set at 95% CL. Those results were not, at the time of the conference, superseded yet by the results from Run II data.

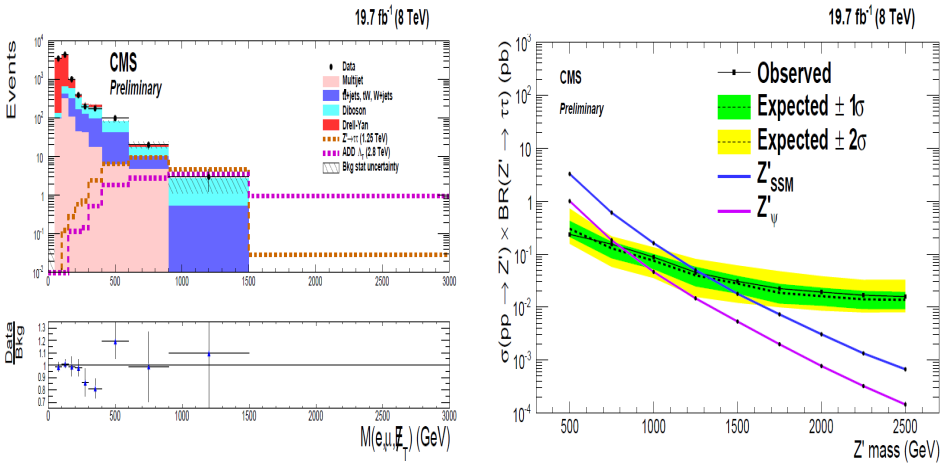

FIGURE 6. Distribution of the ditau mass (left), $M(e,\mu,\not{E}_t)$ [22]. The black points represent the observed data and the stack histogram the background expected from the SM. The lower plot shows the ratio of the data to the total SM background expectation. Error bars represent the statistical uncertainties only. Observed 95% CL upper limit (right) on $\sigma(pp \to Z') \times B(Z' \to \tau\tau)$) having analysed the final state with an electron and a muon, as a function of Z' mass (solid black line) [22].

REFERENCES

[1] JINST **3**, p. S08003 (2008).
[2] JINST **3**, p. S08004 (2008).
[3] JHEP **06**, p. 081 (2013), arXiv:1303.4571 [hep-ex] .
[4] Phys. Lett. **B716**, 1–29 (2012), arXiv:1207.7214 [hep-ex] .
[5] A. Leike, Phys. Rept. **317**, 143–250 (1999), arXiv:hep-ph/9805494 [hep-ph] .
[6] J. L. Hewett and T. G. Rizzo, Phys. Rept. **183**, p. 193 (1989).
[7] P. Langacker, Rev. Mod. Phys. **81**, 1199–1228 (2009), arXiv:0801.1345 [hep-ph] .
[8] E. Salvioni, G. Villadoro, and F. Zwirner, JHEP **11**, p. 068 (2009), arXiv:0909.1320 [hep-ph] .
[9] M. V. Chizhov, V. A. Bednyakov, and J. A. Budagov, *Results and perspectives in particle physics. Proceedings, 24th Rencontres de Physique de la Vallee d'Aoste, La Thuile, Italy, February 28-March 6, 2010*, Nuovo Cim. **C033N5**, 343–350 (2010), arXiv:1005.2728 [hep-ph] .
[10] L. Randall and R. Sundrum, Phys. Rev. Lett. **83**, 3370–3373 (1999), arXiv:hep-ph/9905221 [hep-ph] .
[11] W. D. Goldberger and M. B. Wise, Phys. Rev. Lett. **83**, 4922–4925 (1999), arXiv:hep-ph/9907447 [hep-ph] .
[12] L. Randall and R. Sundrum, Phys. Rev. Lett. **83**, 4690–4693 (1999), arXiv:hep-th/9906064 [hep-th] .
[13] Phys. Rev. **D90**, p. 052005 (2014), arXiv:1405.4123 [hep-ex] .
[14] JHEP **04**, p. 025 (2015), arXiv:1412.6302 [hep-ex] .
[15] Phys. Rev. **D92**, p. 032004 (2015), arXiv:1504.05511 [hep-ex] .
[16] "Search for High-Mass Diphoton Resonances in pp Collisions at $\sqrt{s}$ = 8 TeV with the CMS Detector," CMS Physics Analysis Summary CMS-PAS-EXO-12-045 (CERN, 2015).
[17] S. Catani, L. Cieri, D. de Florian, G. Ferrera, and M. Grazzini, Phys. Rev. Lett. **108**, p. 072001 (2012), arXiv:1110.2375 [hep-ph] .
[18] S. Catani and M. Grazzini, Phys. Rev. Lett. **98**, p. 222002 (2007), arXiv:hep-ph/0703012 [hep-ph] .
[19] JHEP **07**, p. 157 (2015), arXiv:1502.07177 [hep-ex] .
[20] D. J. Muller and S. Nandi, Phys. Lett. **B383**, 345–350 (1996), arXiv:hep-ph/9602390 [hep-ph] .
[21] A. Caldwell, D. Kollar, and K. Kroninger, Comput. Phys. Commun. **180**, 2197–2209 (2009), arXiv:0808.2552 [physics.data-an] .
[22] "Search for high-mass resonances and large extra dimensions with tau-lepton pairs decaying into final states with an electron and a muon at $\sqrt{s}$ = 8 TeV," CMS Physics Analysis Summary CMS-PAS-EXO-12-046 (CERN, 2015).
[23] A. Abulencia *et al.* (CDF), Phys. Rev. Lett. **96**, p. 011802 (2006), arXiv:hep-ex/0508051 [hep-ex] .

Proceedings of the LHCP2015 Conference, St. Petersburg, Russia, August 31 - September 5, 2015

Editors: V.T. Kim and D.E. Sosnov

Searches for Direct Production of Dark Matter at the LHC

GEORGIA KARAPOSTOLI

Université Libre de Bruxelles, Brussels, Belgium

Georgia.Karapostoli@cern.ch

On behalf of the ATLAS and CMS Collaboration

Abstract. This article reports on searches for new phenomena through direct production of dark matter (DM) particles at the LHC. Searches for DM made public by Summer 2015 by the CMS [1] and ATLAS [2] collaborations, are presented and categorized according to the event topology characteristics. The data collected in proton-proton collisions at a center-of-mass energy of 8 TeV, correspond to an integrated luminosity of 19.7 fb^{-1} and 20.3 fb^{-1} for CMS and ATLAS respectively. The analyses find no excess of events above the Standard Model expectations and the results are interpreted in terms of 90% confidence limits on the DM-nucleon scattering cross-section, as a function of the DM particle mass, for both spin-dependent and spin-independent scenarios. We find that LHC collider searches provide a complementary probe of WIMPs to direct detection experiments, and give strong constraints on light DM particles.

INTRODUCTION

The existence of dark matter in the Universe is highly motivated by many astrophysical and cosmological observations. However, nearly nothing is known of its underlying particle nature. One of the best motivated candidates for a DM particle is a weakly interacting massive particle (WIMP) which is expected to couple to standard model (SM) particles through a generic weak interaction. Such a new particle would result in the correct relic density values for nonrelativistic matter in the early universe, as measured by the PLANCK [3] and WMAP [4] satellites.

Weakly interacting massive particles are one such class of particle candidates that can be searched for at the LHC. Because WIMPs interact so weakly that they do not deposit energy in the calorimeter, their production leads to signatures with missing transverse momentum, the magnitude of which is called E_T^{miss} . Here, WIMPs are assumed to be produced in pairs and the events are identified via observation of large E_T^{miss} recoiling against a visible final-state object X, which may be a hadronic jet, photon, or W/Z boson. The interaction of WIMPs with SM particles is described using an effective field theory (EFT) approach, as a contact interaction mediated by a single new heavy particle or particles with mass too large to be produced directly at the LHC (see fig. 1). Such interactions can be described by contact operators with:

$$L_{\text{int}} = \text{C}\,(\bar{q}\Gamma^q q)\,(\bar{\chi}\Gamma^\chi \chi) \tag{1}$$

where C represents the coupling constant, which usually depends on the mass of the DM particle, m_χ , and the effective mass scale of the interaction, $M_\star$, and the operator Γ describes the type of the interaction, including scalar ($\Gamma = 1$), pseudoscalar ($\Gamma = \gamma^5$), vector ($\Gamma = \gamma^\mu$), axial vector ($\Gamma = \gamma^\mu\gamma^5$) and tensor interactions. In this formalism, EFT provides a framework for comparing LHC results to existing direct or indirect DM searches. However, although the EFT approach is more model-independent, it is not valid when the typical momentum transfer approaches the scale of the high-mass particles that have been integrated out. For this reason, the pair production of WIMPs is also investigated within the so-called simplified models [5], where a pair of WIMPs couples to a pair of quarks explicitly via a new mediator particle. Simplified models do not suffer from the concerns related to EFT, but include more assumptions by design and are therefore less generic. The two approaches are thus complementary and both are considered here.

FIGURE 1: Feynman diagrams for the production of weakly interacting massive particle pairs $\chi - \bar{\chi}$ associated with a jet from initial-state radiation of a gluon, g. Left: a contact interaction described with effective operators. Right: a simplified model with a Z' boson. Taken from Ref. [6].

THE MONO-JET SEARCH

Events with an energetic jet and large missing transverse momentum in the final state constitute a clean and distinctive signature in searches for production of dark matter particles at colliders. Such signatures are referred to as monojet-like. In this section we describe the relevant search [6] which uses 20.3 fb^{-1} of $\sqrt{s}$ = 8 TeV data collected in 2012 with the ATLAS detector at the LHC. The expected background to the monojet-like signature is dominated by Z($\rightarrow \nu\bar{\nu}$) + jets and W+jets production (with W($\rightarrow \tau\nu$) + jets being the dominant among the W+jets backgrounds), and includes small contributions from Z/$\gamma^{\star}$($\rightarrow \ell^{+}\ell^{-}$) + jets ($\ell = e, \mu, \tau$), multijet, $t\bar{t}$, single-top, and diboson (WW, WZ, ZZ, Wγ, Zγ) processes.

Monojet-like topologies in the final state are selected by requiring to have at least one jet with $p_T > 20$ GeV, no leptons, whereas the leading-jet p_T and the E_T^{miss} satisfy $p_T / E_T^{miss} > 0.5$. Nine signal regions (SRs) are considered with increasing missing transverse momentum requirements between $E_T^{miss} > 150$ GeV and $E_T^{miss} > 700$ GeV. The main irreducible backgrounds of the analysis, namely the W+jets and Z($\rightarrow \nu\bar{\nu}$) + jets backgrounds, are estimated using Monte Carlo (MC) event samples normalized using data in selected control regions. The remaining SM backgrounds from Z/$\gamma^{\star}$ ($\rightarrow \ell^{+}\ell^{-}$) + jets, $\bar{t}t$, single top, and dibosons are determined using MC simulated samples, while the multijet background contribution is extracted from data.

The data observed in the different signal regions are compared with the SM expectations for the total number of events in the different signal regions and a very good agreement is found. These results are translated into limits on the pair production of WIMPs. The $M_{\star}$ limits for a scalar and vector type of operator within the EFT approach are shown in Figure 2 down to WIMP masses of 10 GeV, as extracted from the signal regions that exhibit the best expected sensitivity.

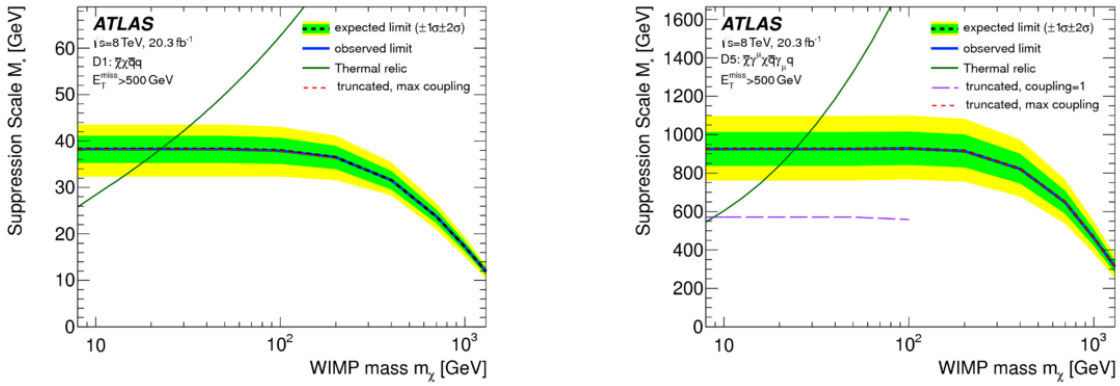

FIGURE 2: Lower limits at 95% CL on the suppression scale $M_{\star}$ are shown as a function of the WIMP mass m_{χ} for left: scalar and right: vector type of operators, in each case for the most sensitive SRs. Taken from Ref. [6].

DM SEARCHES IN MONO-OBJECT (V/JET) + MET TOPOLOGIES

The canonical "monojet" search strategy presented in the previous section, provides model-independent means of exploring scenarios where production of DM particles proceeds via a mediator with couplings to the SM. Related mono-V (V=W/Z) searches target the associated production of DM with SM vector bosons, which can be enhanced in theories with non-universal DM couplings.

Monojet and hadronic mono-V channels

This search targets the hadronic decay modes of the vector bosons in the mono-V channels. The CMS analysis [7] explores the mono-V production at high boost utilising recently developed techniques designed to exploit information available in the sub-structure of jets. The analysis incorporates both monojet and mono-V final states in a combined search, categorized according to the nature of the jets in the event. The DM signal extraction is performed by considering the shape of the E_T^{miss} distribution in each event category, which potentially provides improved sensitivity compared to the previous monojet analysis. The signature of monojet and hadronic mono-V production is a large value of missing E_T^{miss} recoiling against jets. The largest backgrounds are due to Z+jet production in which the Z decays to neutrinos, and leptonically decaying W+jet production where the charged lepton falls outside of the detector acceptance or fails the reconstruction criteria, thus producing real E_T^{miss} .

The presence of a signal is searched for by an excess of events with respect to the expectations for the SM backgrounds in a region at high missing transverse energy. The accuracy with which the shapes for the major backgrounds (V+jets) is estimated is an essential part of this analysis. Data from control regions are utilised in order to determine both the shape and normalization for the V+jets backgrounds in the signal region. The comparisons between data and background in the E_T^{miss} distributions, for each of the event categories, show a very good agreement between the expected SM backgrounds and data, at the percent level. The results of this analysis are interpreted in terms of upper limits on the DM pair-annihilation cross-section. Within the EFT approach, for a vector mediator, the direct-detection bounds dominate above $m_\chi = 6$ GeV, while for the axial-vector, scalar, pseudo-scalar mediator models, the bounds from this analysis dominate over the whole region.

The corresponding ATLAS analysis [8] identifies "large-radius" jets which are supposed to capture the hadronic products of both quarks from W or Z boson decay. Two signal regions are defined by two thresholds in E_T^{miss} : 350 and 500 GeV. The three irreducible backgrounds are estimated by extrapolation from a common data control region in which the selection is identical to that of the signal regions except that the muon veto is inverted and W/Z+jets with muon decays are the dominant processes. The data agree well with the background estimate for each E_T^{miss} threshold. Exclusion limits are set on the dark matter signals using the CLs method. Figures 3 and 4 show direct-detection bounds at 90% confidence level vs m_χ .

Leptonic mono-V channels

Further CMS and ATLAS analyses ([9] and [10] respectively) assume the scenario of a Z boson recoiling against two DM particles, where the Z boson subsequently decays into two leptons producing a clean dilepton signature along with missing transverse energy.

The relevant CMS analysis selects events with exactly two well-identified, isolated leptons with the same flavor and opposite charge (e^+e^- or $\mu^+\mu^-$) with $p_T > 20$ GeV each and invariant mass within ±10 GeV of the nominal mass of the Z boson. The final selection is optimized for DM signals to obtain the best expected limit at 95% confidence level using the variables: E_T^{miss} and $\Delta\phi(\ell\ell, E_T^{miss})$ among others. The ZZ and WZ backgrounds are modeled using MC simulation whereas remaining non-resonant backgrounds are estimated via data-driven methods. It is worth mentioning that the dominant background, $ZZ \to \ell^+\ell^-\bar{\nu}\nu$, contributes the largest theoretical uncertainties which are derived from generator differences. After a preselection of events, the distribution of E_T^{miss} shows a good agreement between data and background prediction in both the di-e and di-μ channels.

Figures 3 and 4 show combined upper limits at 90% CL which are set on the DM-nucleon scattering cross sections as a function of DM particle mass for both spin-dependent and spin-independent cases, as reported by the CMS and ATLAS analyses respectively. These limits are less stringent than the lower limits for dark matter candidates recoiling against a W or Z boson decaying to hadrons which are also shown superimposed.

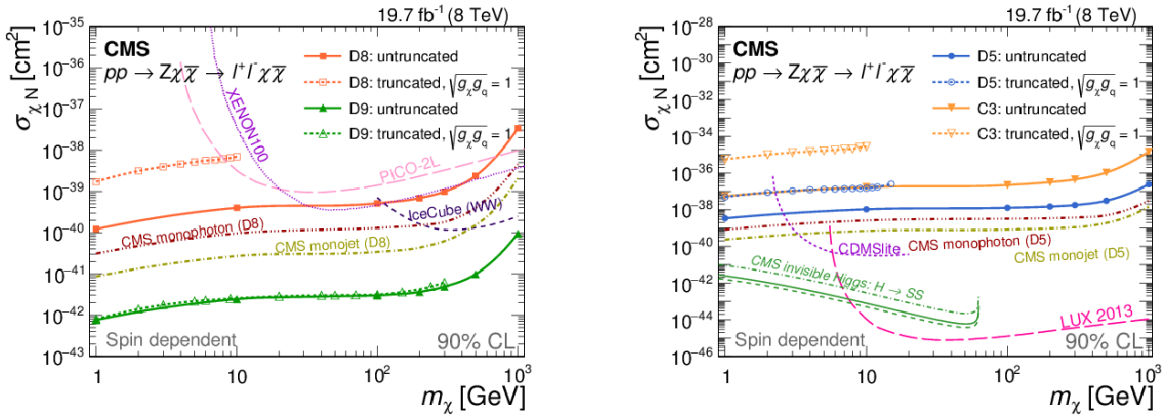

FIGURE 3: The 90% CL upper limits on the DM-nucleon cross section as a function of m_χ for left: spin-dependent limits for axial-vector and tensor coupling of Dirac fermion DM candidates, and right: spin-independent limits for vector coupling of complex scalar and Dirac fermion DM candidates. Taken from Ref. [9].

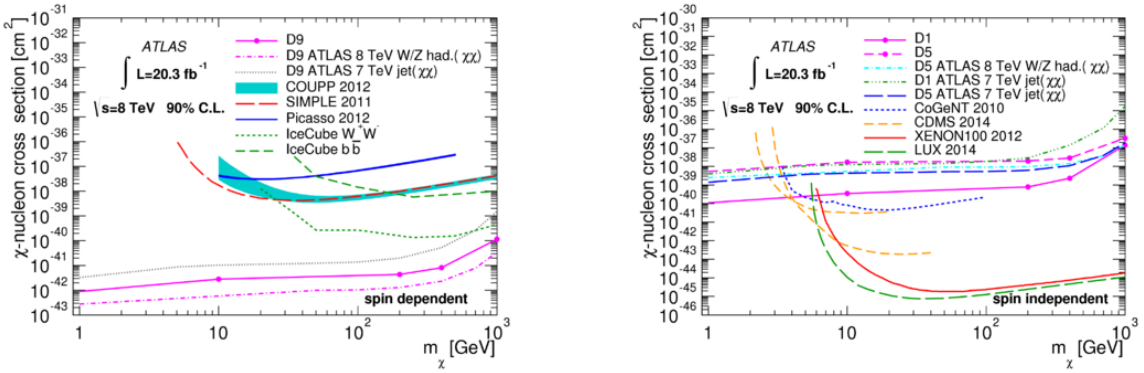

FIGURE 4: Observed 90% C.L. upper limits on the DM-nucleon scattering cross section as a function of m_χ for left: spin-independent and right: spin-dependent effective operators mediating the interaction of the dark matter particles with the qq initial state. Taken from Ref. [10].

DM SEARCHES IN HEAVY-FLAVOR TOPOLOGIES

Previous monojet search results have shown that the exclusion limits for a scalar type of interaction is the least stringent among all types which have been probed. This is because in this interaction the coupling strength is proportional to the mass of the quark. As a consequence, couplings to light quarks are suppressed and inclusive monojet searches are not optimal. It is therefore expected that the sensitivity for the scalar interaction can be improved by searching for final states with third generation quarks.

The presented CMS analysis [11] searches for the associated production of dark matter particles with a pair of top quarks in the single-lepton channel. The dominant standard model background processes for this analysis are production of tt+jets, tt + g/W/Z, W+jets, single top, di-boson (WW, WZ and ZZ) and Drell-Yan. Signal events are selected by requiring exactly one identified isolated lepton, at least three jets and at least one b-tagged jet. Additional requirements on $E_T^{miss} > 320$ GeV and the transverse mass $M_T > 160$ GeV are applied to increase the discrimination of the background with respect to the signal. Standard model backgrounds for this analysis are estimated from simulation, with data-to-simulation scale factors applied to the dominant backgrounds of tt+jets and W+jets.

The analysis observes no excess of events in the search region, and interpreting the results in the context of a scalar interaction between dark matter particles and top quarks, it sets lower limits on the interaction scale $M_\star$, shown in Figure 5, left, showing an improvement of at least a factor 2 with respect to the previously most stringent limits. Figure 5, right, shows the observed 90% CL upper limits on the dark matter-nucleon cross sections as a function of the

dark matter mass for the scalar operator considered. More stringent limits are obtained from this analysis compared to direct dark matter searches in the low mass region of less than about 6 GeV, which are excluded for dark matter-nucleon cross sections higher than $1-2\times10^{-42}\mathrm{cm}^2$, corresponding to 10 – 20 fb. Comparable limits are obtained with the corresponding ATLAS analysis [12] by obtaining sensitivities of approximately $\sigma^{\mathrm{SI}}_{\chi-N} = 10^{-42}\mathrm{cm}^2$ for $m_\chi = 10$ GeV.

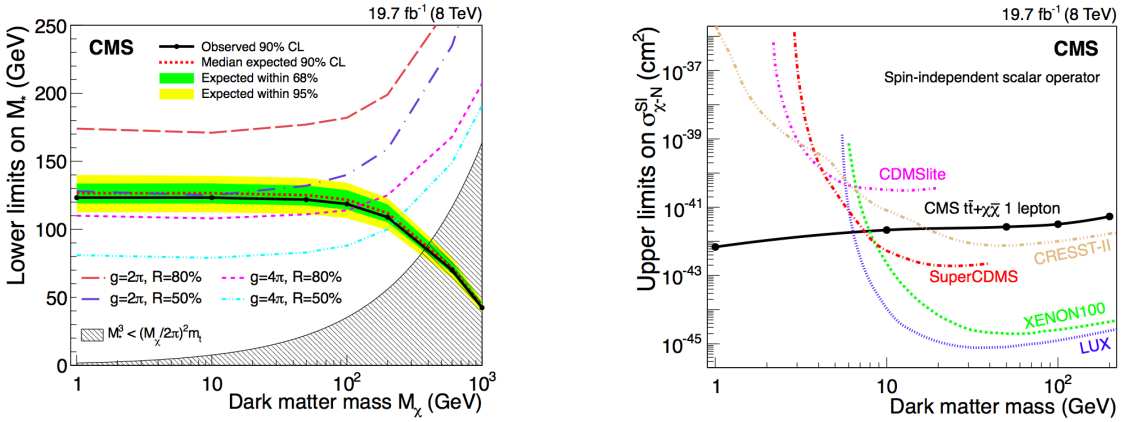

FIGURE 5: Left: observed exclusion limits in the plane of DM particle mass and interaction scale, with the region below the solid curve excluded at a 90% CL. Right: the 90% CL upper limits on the DM-nucleon spin-independent scattering cross sections as a function of the DM particle mass for the scalar operator considered in this paper. Taken from Ref. [11].

In the same context of scenarios that possible new particles favor coupling to massive SM particles, such as the top quark, additional searches look for mono-top events, in which a potential dark matter particle is produced in association with a top quark. The relevant CMS and ATLAS analyses ([13], [14]) report no evidence of new physics and calculate exclusion limits on the mass of dark matter candidates at 95% CL. Scalar and vectorial dark matter particles with masses below 327 GeV and 655 GeV respectively, are excluded.

DM INTERACTING THROUGH HIGGS

Direct observation of DM can also be searched for through the decays of the Higgs boson to invisible particles. The study of the properties of a Higgs boson discovered by the ATLAS and CMS collaborations in 2012, does not exclude a sizeable branching ratio for its decay to invisible particles. It also opens up the question of whether a Higgs-like scalar field plays an important role in describing the interaction between dark and ordinary matter in the universe. In particular, possible decays to weakly interacting particles, are predicted by many extensions of the SM, e.g. Higgs boson portal models.

The ATLAS collaboration has performed an independent search [15] for the H → inv. decay in final states with two or more jets and large E_T^{miss} , motivated by Higgs boson production in association with a vector boson V (V = W or Z): $q\bar{q}' \rightarrow VH$. For the discovered Higgs boson at $m_H = 125$ GeV, an observed (expected) upper limit of 78% (86%) at 95% CL on the branching ratio of the Higgs boson to invisible particles is set. These limits are derived assuming SM production and combining contributions from VH and gluon-fusion processes.

However, if the mass of the DM particle is larger than $m_H/2$, the invisible Higgs searches are not sensitive, and approaches such as analyses of H + E_T^{miss} events are required such as the ATLAS search cited [16]. Here, the $H \rightarrow \gamma\gamma$ decay mode is used exclusively, as the small branching ratio is mitigated by the distinct diphoton resonance signature and the low expected number of background events with significant E_T^{miss} . Limits on DM production are derived from the cross section limits at a given DM mass m_χ , and expressed as 95% CL limits on the suppression scale $M_\star(\Lambda)$ for EFT operators; see Fig. 6 for limits for a vector operator. For the lowest m_χ region not excluded by results from searches for invisible Higgs boson decays near $m_\chi = m_H/2$, values of Λ up to 60 GeV are excluded for the vector operators.

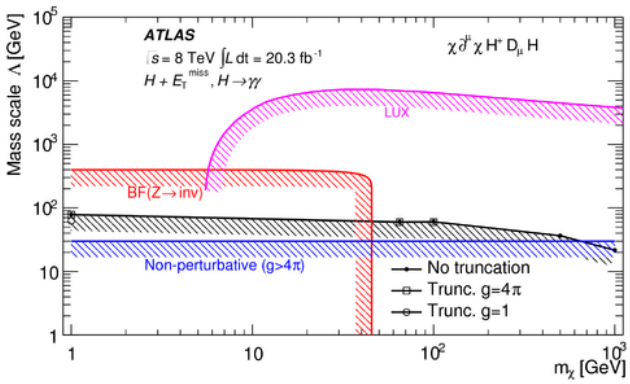

FIGURE 6: Limits at 95% CL on the mass scale Λ as a function of the DM mass (m_χ) for one of the four EFT models considered. Solid black lines are due to H + E_T^{miss} analysis. Taken from Ref. [16].

SUMMARY

Searches for evidence for DM production have been presented in the monojet and other mono-object plus missing transverse energy topologies, using the dataset corresponding to an integrated luminosity of 19.7 fb^{-1} and 20.3 fb^{-1} of pp collisions collected by the CMS and ATLAS detectors respectively at a center-of-mass energy of 8 TeV at the LHC. The observed data are consistent with SM expectations and the results are translated into upper limits at 90% CL on the DM-nucleon scattering cross sections as a function of the DM particle mass. Most stringent limits are obtained by the mono-jet and hadronic mono-V channels. Under the assumptions made in the EFT approach, the LHC collider DM limits are particularly relevant in the low DM mass region, and remain important over the full m_χ range covered.

REFERENCES

[1] CMS Collaboration, *The CMS experiment at the CERN LHC*, JINST 3:S08004, 2008.
[2] ATLAS Collaboration, *The ATLAS experiment at the CERN LHC*, JINST 3:S08003, 2008.
[3] Planck Collaboration, P. Ade et al., Astron. Astrophys. 571 (2014) A16, arXiv:1303.5076 [astro-ph].
[4] G. Hinshaw et al., ApJS 208 (2013) 19, arXiv:1212.5226 [astro-ph].
[5] The ATLAS/CMS Dark Matter Forum, arXiv:1507.00966 [hep-ex].
[6] ATLAS Collaboration, EPJC 75 (2015) 299, arXiv:1502.01518 [hep-ex].
[7] CMS Collaboration, CMS PAS EXO-12-055.
[8] ATLAS Collaboration , PRL 112, 041802 (2014), arXiv:1309.4017 [hep-ex].
[9] CMS Collaboration, CMS PAS EXO-12-054.
[10] ATLAS Collaboration, PRD 90, 012004 (2014), arXiv:1404.0051 [hep-ex].
[11] CMS Collaboration, JHEP 06 (2015) 121, arXiv:1504.03198 [hep-ex].
[12] ATLAS Collaboration, EPJC 75 (2015) 92, arXiv:1410.4031 [hep-ex].
[13] CMS Collaboration, Phys. Rev. Lett. 114 (2015) 101801, arXiv:1410.1149 [hep-ex].
[14] ATLAS Collaboration, Eur. Phys. J. C (2015) 75:79, arXiv:1410.5404 [hep-ex].
[15] ATLAS Collaboration, Eur. Phys. J. C (2015) 75:337, arXiv:1504.04324 [hep-ex].
[16] ATLAS Collaboration, PRL 115, 131801 (2015), arXiv:1506.01081 [hep-ex].

Proceedings of the LHCP2015 Conference, St. Petersburg, Russia, August 31 - September 5, 2015

Editors: V.T. Kim and D.E. Sosnov

Generalized Solution for RS Metric and LHC Phenomenology

A.V. KISSELEV

Institute for High Energy Physics, NRC "Kurchatov Institute", 142281 Protvino, Russian Federation.

alexandre.kisselev@ihep.ru

Abstract. The new generalization of the Randall-Sundrum (RS) solution for the warp factor $\exp[\sigma(y)]$ is proposed. In contrast to the well-known RS1 expression, the generalized function $\sigma(y)$ is *explicitly* periodic in variable y. This solution is symmetric with respect to the branes. It obeys the orbifold symmetry $y \to -y$ and reproduces jumps of its derivative on both branes. It is noted that $\sigma(y)$ is defined by Einstein-Hilbert's equations up to a constant C. It is shown that different values of C results in theories with quite different spectra of the Kaluza-Klein gravitons. An application of this theoretical framework to LHC phenomenology is considered.

INTRODUCTION

The 5-dimensional space-time with an extra coordinate y, non-factorizable geometry and two branes was suggested by Randall and Sundrum (RS) [1] as an alternative to the ADD model with flat extra dimensions (EDs) [2]. The RS model is a model of gravity in the AdS_5 space-time compactified to the orbifold S^1/Z_2. It means that the periodicity condition, $(x^\mu, y) = (x_\mu, y + 2\pi r_c)$, is imposed on y, and points (x^μ, y) and $(x^\mu, -y)$ are identified. In the RS1 scenario there exist two branes at the orbifold fixed points $y = 0$ and $y = \pi r_c$, where r_c is the size of the compactified ED.

The background warped metric is given by

$$ds^2 = e^{-2\sigma(y)}\,\eta_{\mu\nu}dx^\mu dx^\nu - dy^2, \tag{1}$$

where $\eta_{\mu\nu}$ is the Minkowski tensor ($\mu = 0, 1, 2, 3$) with the signature $(1, -1, -1, -1)$, and the action is taken in the following form [1]:

$$S = \int d^4x \int_{-\pi r_c}^{\pi r_c} dy\ \sqrt{G}\,(2\bar{M}_5^3\,\mathcal{R} - \Lambda) + \int d^4x\,\sqrt{|g^{(1)}|}\,(\mathcal{L}_1 - \Lambda_1) + \int d^4x\,\sqrt{|g^{(2)}|}\,(\mathcal{L}_2 - \Lambda_2)\,. \tag{2}$$

Here $G_{MN}(x, y)$ is the 5-dimensional metric ($M, N = 0, 1, 2, 3, 4$), $g_{\mu\nu}^{(i)}$ are the induced metrics on the branes ($i = 1, 2$), Λ is the 5-dimensional cosmological constant, and Λ_i are the brane tensions. The parameter $\bar{M}_5$ is the 5-dimensional reduced Planck scale.

The set of Einstein-Hilbert's equations looks like

$$6\sigma'^2(y) = -\frac{\Lambda}{4\bar{M}_5^3}\,, \quad 3\sigma''(y) = \frac{1}{4\bar{M}_5^3}\,[\Lambda_1\,\delta(y) + \Lambda_2\,\delta(\pi r_c - y)]\,. \tag{3}$$

In ref. [1] the following solution of these equation was proposed:

$$\sigma_{\rm RS}(y) = \kappa|y|\,, \tag{4}$$

where κ is a parameter with a dimension of mass, with the fine tuning relations:

$$\Lambda_{\rm RS} = -24\bar{M}_5^3\kappa^2\,, \quad (\Lambda_1)_{\rm RS} = -\,(\Lambda_2)_{\rm RS} = 24\bar{M}_5^3\kappa\,. \tag{5}$$

The RS1 model predicts an existence of heavy Kaluza-Klein (KK) gravitons. These massive resonances are intensively searched for by the LHC collaborations (see, for instance, [3]).

The function $\sigma_{\rm RS}(y)$ (4) is consistent with the orbifold symmetry, $y \to -y$. However, it is not symmetric with respect to both branes. The jump of $\sigma'(y)$ on the brane $y = \pi r_c$ does not *directly* follow from eq. (4). It can be reproduced only if one takes into account the periodicity condition. Moreover, (4) does not contain a constant term allowed by differential equations (3).

GENERALIZATION OF RS1 SOLUTION

In refs. [11] the generalization of the solution (4) was obtained which is is symmetric with respect to the interchange of the branes:

$$\sigma(y) = \frac{\kappa}{2}(|y| - |\pi r_c - y|) + \frac{|\kappa|\pi r_c}{2} - C \ , \tag{6}$$

where C is a constant ($0 \leqslant C \leqslant |\kappa|\pi r_c$). It also obeys the orbifold symmetry $y \to -y$ and explicitly reproduces the jumps of its derivative on *both* branes. The only disadvantage of the expression (6) (as well as of the RS1 expression (4)) is that the periodicity condition is not realized in it *explicitly*. Everybody has to keep this condition in "mind" in order to demonstrate that (6) is consistent with the orbifold symmetry (for details, see [11]).

That is why, we propose a new solution of Einstein-Hilbert's equations (3) which is both symmetric with respect to the branes and *periodic* function of its variable y:

$$\sigma(y) = \frac{\kappa r_c}{2}\left[\left|\mathrm{Arccos}\left(\cos\frac{y}{r_c}\right)\right| - \left|\pi - \mathrm{Arccos}\left(\cos\frac{y}{r_c}\right)\right|\right] + \frac{\pi|\kappa|r_c}{2} - C \ . \tag{7}$$

Here and in what follows Arccos(z) is a *principal value* of the multivalued inverse trigonometric function arccos(z). It is define by the inequality (see, for instance, ref. [5]):

$$0 \leqslant \mathrm{Arccos}(z) \leqslant \pi \ , \quad -1 \leqslant z \leqslant 1 \ . \tag{8}$$

It means that [5]

$$\mathrm{Arccos}(\cos x) = \begin{cases} x - 2n\pi, & 2n\pi \leqslant x \leqslant (2n+1)\pi \ , \\ -x + 2(n+1)\pi, & (2n+1)\pi \leqslant x \leqslant 2(n+1)\pi \ , \end{cases} \tag{9}$$

where $n = 0, 1, \ldots$ It follows from (9) that for $0 \leqslant y \leqslant \pi r_c$ (here and below it is assumed that $\kappa > 0$):

$$\sigma(y) + C = \frac{\kappa}{2}(|y| - |\pi r_c - y|) + \frac{\kappa\pi r_c}{2} = \kappa y \ . \tag{10}$$

For $\pi r_c \leqslant y \leqslant 2\pi r_c$ we get:

$$\sigma(y) + C = \frac{\kappa}{2}(|2\pi r_c - y| - |y - \pi r_c|) + \frac{\kappa\pi r_c}{2} = \kappa(2\pi r_c - y) \ , \tag{11}$$

and so on. As a result, we obtain a graphic representation for the function $\sigma(y)$ shown in Fig. 1.

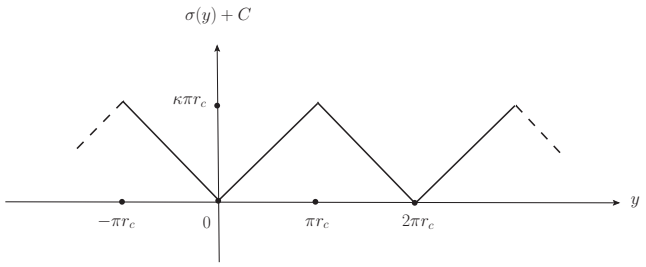

FIGURE 1. Warp function $\sigma(y)$ on the orbifold S_1/Z_2.

The function $\sigma(y)$ (7) has the explicit Z_2 symmetry,

$$\sigma(-y) = \sigma(y) \ . \tag{12}$$

By differentiating both sides of eq. (7), we get:

$$\sigma'(y) = \frac{\kappa}{2}\left[\varepsilon\left(\mathrm{Arccos}\left(\cos\frac{y}{r_c}\right)\right) + \varepsilon\left(\pi - \mathrm{Arccos}\left(\cos\frac{y}{r_c}\right)\right)\right]\frac{\sin(y/r_c)}{|\sin(y/r_c)|} \ , \tag{13}$$

where

$$\varepsilon(x) = \theta(x) - \theta(-x) = \begin{cases} +1, & x > 0 \ , \\ -1, & x < 0 \ . \end{cases} \tag{14}$$

Here and below the *prime* denotes the derivative with respect to variable y. Since[1]

$$\varepsilon(\mathrm{Arccos}(\cos x)) + \varepsilon(\pi - \mathrm{Arccos}(\cos x)) = 2 \ , \tag{15}$$

for all $x \neq \pm\pi n$ ($n = 0, 1, \ldots$), we can write:

$$\sigma'(y) = \kappa\,\varepsilon(\sin(y/r_c)) \ , \quad y \neq \pm\pi r_c, \pm 2\pi r_c, \ldots \ . \tag{16}$$

At the points $y = \pm\pi r_c n$ ($n = 0, 1, \ldots$) the function $\sigma'(y)$ *is not defined* (left and right derivatives of $\sigma(y)$ do not coincide). The jumps of $\sigma'(y)$ at these points are:

$$\begin{aligned} &\sigma'(2n\pi r_c + \epsilon) - \sigma'(2n\pi r_c - \epsilon) = 2\sigma'(2n\pi r_c + \epsilon) = 2\kappa \ , \\ &\sigma'((2n+1)\pi r_c + \epsilon) - \sigma'((2n+1)\pi r_c - \epsilon)2\sigma'((2n+1)\pi r_c + \epsilon) = -2\kappa \ . \end{aligned} \tag{17}$$

It follows from (16) that $\sigma'(y)$ is the periodic function and

$$\sigma'(-y) = -\sigma'(y) \ . \tag{18}$$

By using equation

$$\delta(f(z)) = \sum_k \frac{1}{|f'(z_k)|}\,\delta(z - z_k) \ , \tag{19}$$

where z_k are ordinary zeros of the function $f(z)$, we obtain from (16):

$$\sigma''(y) = 2\kappa\sum_{n=-\infty}^{\infty}\left[\delta(y + 2\pi n r_c) - \delta(y - \pi r_c + 2\pi n r_c)\right] \ . \tag{20}$$

The periodicity of the function $\sigma''(y)$ in variable y is obvious from this formula.

To demonstrate its Z_2 symmetry, let us note that σ depends on a dimensionless variable

$$x = y/r_c \tag{21}$$

and dimensionless parameter κr_c as follows:

$$\sigma(x) = \frac{\kappa r_c}{2}\left[|\mathrm{Arccos}(\cos x)| - |\pi - \mathrm{Arccos}(\cos x)|\right] + \frac{\pi\kappa r_c}{2} - C \ . \tag{22}$$

Then we can rewrite (20) in the form:

$$\sigma''(x) = \frac{2\kappa}{r_c}\sum_{n=-\infty}^{\infty}\left[\delta(x + 2n\pi) - \delta(x - \pi + 2n\pi)\right] \ , \tag{23}$$

[1] Note that $0 < \mathrm{Arccos}(\cos x) < \pi$ for all $x \neq \pm\pi n$.

and make the following transformations:

$$\begin{aligned}\sigma''(x) &= \frac{2\kappa}{r_c}\sum_{n=-\infty}^{\infty}\left[\delta(x+2n\pi)-\delta(x-\pi+2n\pi)\right] = \frac{2\kappa}{r_c}\sum_{m=-\infty}^{\infty}\left[\delta(x-2m\pi)-\delta(x-\pi-2(m-1)\pi)\right] \\ &= \frac{2\kappa}{r_c}\sum_{m=-\infty}^{\infty}\left[\delta(-x+2m\pi)-\delta(-x-\pi+2m\pi)\right]. \end{aligned} \tag{24}$$

Thus, $\sigma''(y) = \sigma''(-y)$.

We conclude that eqs. (7), (16) and (20) are consistent with Fig. 1. On the interval $0 \leqslant y \leqslant \pi r_c$ we have:

$$\sigma''(y) = 2\kappa[\delta(y) - \delta(y-\pi r_c)] , \tag{25}$$

that means:

$$\Lambda_1 = -\Lambda_2 = 24\bar{M}_5^3\kappa . \tag{26}$$

As for 5-dimensional cosmological constant, one can see from eqs. (3) and (16) that

$$\Lambda = -24\bar{M}_5^3\kappa^2 , \tag{27}$$

for $0 < y < \pi r_c$, but Λ (as well as $\sigma'(y)$) *is not defined* at the end points $y = 0,\ \pi r_c$.

LHC PHENOMENOLOGY

The warp extra dimension can be searched for at the LHC in processes defined by subprocesses mediated by s-channel KK gravitons $h^{(n)}$:

$$a\bar{a} \to h^{(n)} \to b\bar{b} , \tag{28}$$

where $a = q, g$, and $b = q, g, l$ or γ. The *universal* part of their matrix elements is defined by the sum [6]:

$$\mathcal{S}(\hat{s}) = \frac{1}{\Lambda_\pi^2}\sum_{n=1}^{\infty}\frac{1}{\hat{s} - m_n^2 + i\, m_n\Gamma_n} , \tag{29}$$

Here $\sqrt{\hat{s}}$ is the invariant energy of the *partonic* subprocess, Λ_π is the coupling of the massive gravitons to the SM fields:

$$\mathcal{L}_{\rm int} = -\frac{1}{\bar{M}_{\rm Pl}}\, h_{\mu\nu}^{(0)}(x)\, T_{\alpha\beta}(x)\, \eta^{\mu\alpha}\eta^{\nu\beta} - \frac{1}{\Lambda_\pi}\sum_{n=1}^{\infty} h_{\mu\nu}^{(n)}(x)\, T_{\alpha\beta}(x)\, \eta^{\mu\alpha}\eta^{\nu\beta} , \tag{30}$$

where $T_{\alpha\beta}(x)$ is the energy-momentum tensor of the SM fields. $\Gamma_n \simeq 0.1\, m_n^3/\Lambda_\pi^2$ denotes the total width of the graviton with the KK number n and mass m_n [6].

The hierarchy relation,

$$\bar{M}_{\rm Pl}^2 = \frac{\bar{M}_5^3}{\kappa}e^{2C}\left(1 - e^{-2\pi\kappa r_c}\right) \simeq \frac{\bar{M}_5^3}{\kappa}\, e^{2C} , \tag{31}$$

defines the fundamental gravity scale $\bar{M}_5$ and the curvature parameter κ as functions of the constant C (we assume that $\pi\kappa r_c \gg 1$). By taking different values of C, we come to quite diverse *physical scenarios* [7].

The case $C = 0$ is in fact the RS1 model, in which $M_5 \sim \kappa \sim \bar{M}_{\rm Pl}$ [1]. For non-zero C, the geometry with the small curvature of the 5-dimensional space-time ($\kappa \ll M_5 \sim 1$ TeV) can be realized [8]-[9]. In particular, for $C = \kappa\pi r_c$ the graviton spectrum is predicted to be similar to that of the ADD model [2]. In such a case, the graviton masses are

$$m_n = \kappa x_n , \tag{32}$$

where x_n is nth zero of the Bessel function $J_1(x)$. By using LHC data on diphoton and dilepton production at 7 and 8 TeV, the following lower bound on M_5 was obtained [10]-[11]:

$$M_5 > 6.4 \text{ TeV} . \tag{33}$$

Let us put $C = \kappa\pi r_c/2$. If an effective energy of colliding partons at the LHC $\hat{s}$ is large enough, the sum in eq. (29) can be calculated analytically [7]:

$$\mathcal{S}(\hat{s}) = -\frac{1}{2\Lambda_\pi^3\sqrt{\hat{s}}}\left(\frac{\bar{M}_5}{\kappa}\right)^{3/2}\frac{J_2(z)}{J_1(z)}\,, \tag{34}$$

where

$$z = \frac{\sqrt{\hat{s}}}{\Lambda_\pi}\left(\frac{\bar{M}_5}{\kappa}\right)^{3/2}. \tag{35}$$

The values of the parameters M_5 and κ can be chosen in such a way that the gravitons with the masses

$$m_n = 3.7x_n \text{ MeV} \tag{36}$$

form almost continuous spectrum, and [7]

$$|\mathcal{S}(\hat{s})| = \frac{\mathrm{O}(1)}{(1\text{TeV})^3\sqrt{\hat{s}}}\,. \tag{37}$$

Thus, we come to TeV physics at the LHC energies.

CONCLUSIONS

To conclude, let us underline that our main theoretical formula (7):

- is symmetric with respect to the branes: $\sigma(y)$ remains unchanged if $y \to \pi r_c - y$, $k \to -k$;[2]
- obeys the orbifold Z_2-symmetry: $\sigma(y) = \sigma(-y)$;
- reproduces the jumps of $\sigma'(y)$ on both branes: $\sigma''(y) = 2\kappa[\delta(y) - \delta(y - \pi r_c)]$;
- is the periodic function of the extra coordinate: $\sigma(y + 2\pi r_c n) = \sigma(y)$, $n = \pm1, \pm2, \ldots$

It is important to note that the periodicity property of the solution of Einstein-Hilbert's equations (3) is realized *analytically* (7) for the first time.

REFERENCES

[1] L. Randall and R. Sundrum, Phys. Rev. Lett. **83** (1999) 3370 [hep-ph/9905221].

[2] N. Arkani-Hamed, S. Dimopoulos and G. Dvali, Phys. Lett. B **429** (1998) 263 [hep-ph/9803315]; Phys. Rev. D **59** (1999) 086004 [hep-ph/9807344]; I. Antoniadis, N. Arkani-Hamed, S. Dimopoulos and G. Dvali, Phys. Lett. B **436** (1998) 257 [hep-ph/9804398].

[3] J. Zhu, *Exotics Searches at the LHC*, in Proceedings of the Third Annual Conference on Large Hadron Collider Physics (LHCP 2015), August 31-September 5, 2015, St. Petersburg, Russia.

[4] A.V. Kisselev, Phys. Rev. D **88** (2013) 095012 [arXiv:1311.5316]; *General solution for the warp function in the RS scenario*, arXiv:1403.2238, 2014.

[5] I.S. Gradshteyn and I.M. Ryzhik, *Table of Integrals, Series, and Products*, Eighth Edition, Eds. D. Zwillinger and V. Moll, Academic Press, US, 2014, pp. 55-56.

[6] A.V. Kisselev, Phys. Rev. D **73** (2006) 024007 [hep-th/0507145].

[7] A.V. Kisselev, *Physical models within the framework of the Randall-sundrum scenari*o, arXiv:1403.5469, 2014.

[8] G. F. Giudice, T. Plehn and A. Strumia, Nucl. Phys. B **706** (2005) 455 [hep-ph/0408320].

[9] A.V. Kisselev and V.A. Petrov, Phys. Rev. D **71** (2005) 124032 [hep-ph/0504203].

[10] A.V. Kisselev, JHEP **09** (2008) 039 [arXiv:0804.3941].

[11] A.V. Kisselev, JHEP **04** (2013) 025 [arXiv:1210.3238]; Particles and Nuclei, Letters **11** (2014) 1112 [arXiv:hep-ph/1306.5402].

[2] Under the replacement $y \to \pi r_c - y$ the positions of the branes are interchanged ($y = 0 \rightleftarrows y = \pi r_c$), while under the replacement $k \to -k$ their tensions are interchanged ($\Lambda_1 \rightleftarrows \Lambda_2$).

Beyond the Standard Model physics: plenary talks

Proceedings of the LHCP2015 Conference, St. Petersburg, Russia, August 31 - September 5, 2015

Editors: V.T. Kim and D.E. Sosnov

Dark Matter Searches at the Large Hadron Collider

ANNAPAOLA DE COSA

Physik Institut, Universität Zürich, Witerthurerstrasse 190, CH-8057 Zürich, Switzerland

annapaola.de.cosa@cern.ch

On behalf of the ATLAS and CMS Collaborations

Abstract. A search for Dark Matter particles directly produced in pair at the Large Hadron Collider is presented. The search is performed using the full LHC Run-I dataset recorded with the CMS and ATLAS detectors in proton-proton collisions at a center-of-mass energy of 8 TeV. Dark Matter production is searched for looking for an excess of events with a large missing transverse momentum in association with energetic light or heavy flavour quark production, or in association with energetic leptons. The search is interpreted within the framework of an effective field theory, as well as of simplified models. No deviation from standard model background expectation is found and exclusion limits on Dark Matter production cross section are obtained.

INTRODUCTION

There is clear evidence of an abundance of matter in the Universe that cannot be explained by the visible matter. This excess, named Dark Matter (DM), accounts for about the 25% of the content of the Universe, while the ordinary matter accounts only for at most 5%. Proof of evidence for Dark Matter comes already in 1970's from the observation of the effects of its gravitational interaction with atomic matter. Despite the overwhelming evidence of the existence of Dark Matter brought to light during the last decades, its nature is still unknown.

Dark Matter is today one of the most compelling indirect evidence for new physics beyond the standard model (SM).

Several theoretical models predict the production of DM at colliders and explain their interaction with SM particles [1][2]. One of the most promising candidates for DM are the Weakly Interactive Massive Particles (WIMPs). Although this is not the unique relevant hypothesis on DM nature, these proceedings will consider only the WIMP-DM models.

The hunt for the WIMPs involves a variety of experiments looking for non-gravitational interaction of DM with SM particles. They can be mainly classified in three categories according to the way in which they look for DM-SM interaction.

- **Direct detection experiments** look for the Dark Matter particle producing recoil energies in the keV energy scale caused by the DM scattering off the target nucleus. Underground experiments look for such kind of signature in the recoil spectrum of single scattering events.
- **Indirect detection experiments** search for products of DM annihilation in dense region of the Universe. DM annihilation is expected to yield standard models particles such as photons and leptons. The predicted branching ratio to different final states depends on the WIMP model assumed. Indirect detection experiments look for an excess in DM-annihilation products.
- **Collider experiments** look for DM pair production in SM particle collisions.

Direct, indirect detection and collider experiments provide complementary approaches to the search for DM as they probe different kinds of WIMP-SM interaction (Fig. 1) in different regions of the phase space.

This paper summarises the results of searches for direct production of Dark Matter at the Large Hadron Collider, LHC, with the CMS (Compact Muon Solenoid) [3] and ATLAS (A Toroidal LHC ApparatuS) [4] experiments, using proton-proton collisions at 8 TeV centre-of-mass energy collisions collected during Run-1.

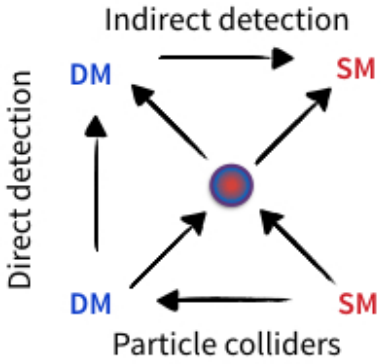

FIGURE 1: View of complementary approach of direct, indirect detection and collider searches to DM-SM interaction.

Searching for Dark Matter at the LHC

If WIMPs produce signal in direct detection experiments, they have to couple to nucleons as well, thus allowing a production of WIMPs in SM-SM collisions. Under this assumption, the large interactions of WIMPs with SM particles implies detectable rates of DM production in the high energy interactions at colliders.

The low DM-mass phase space is particularly suitable for searches at colliders, since a typical collision involving quarks and gluons has a cross section which rapidly falls with the mass of produced states. Therefore, production of light states is favoured, whereas production of massive particles is suppressed.

The WIMP particles are assumed to be stable on collider timescale. This implies a preclusion for the WIMPs to decay within the detector volume: similarly to neutrinos, if produced in SM particle collisions, DM would escape the detector without interacting with it and leaving sign of its passage. Therefore, WIMPs would appear as imbalance of energy in the plane transverse to colliding beams.

Their production can be inferred by measuring the amount of missing energy in the event and looking for the presence of other visible particles recoiling against it. A such clear signature with a high p_T particle and missing energy in the final state is used to flag the interaction and identify it. A rich phenomenology is explored at the LHC looking for Dark Matter, involving final states with energetic jets from light flavour quarks, high p_T leptons as well as jets from heavy flavour quarks.

THEORETICAL APPROACH

Effective Field Theory

Although the nature of the particles mediating the interaction between WIMPs and SM is an essential ingredient to describe the interaction itself, a good simplification can be done in first instance when the mediating particles are heavy compared to the momentum involved in the process. Under this assumption the mediator can be integrated out and the interaction described as contact interaction according to an effective field theory (EFT) approach. Figure 2 shows the diagram pf the DM production in association to a jet from initial state radiation, in the framework of the EFT. While this approach does not provide a complete description of the phenomenology in the whole phase space, still it provides a good approximation for a class of similar models and makes possible a comparison among different kinds of searches in a common framework.

The effective field theory description has also the advantage to be characterised only by three parameters of the theory: the type of interaction between DM and SM (e.g. vector, axial-vector, scalar, pseudoscalar), the mass of the Dark Matter particle, m_χ, and the energy scale of the interaction, often identified as either M^* or Λ, which is related to the mediator mass, M_ϕ, and to the couplings to DM and quarks, g_χ and g_q, by the relation:

$$M^* = \frac{M_\phi}{\sqrt{g_\chi g_q}} \tag{1}$$

The EFT operators were largely employed to interpret results from Run-1 DM searches at the LHC. However, the EFT approach is not a complete theory. It assumes that there are no other new particles accessible at the LHC. It is valid only under the assumption that the momentum transferred in the process is low enough to prevent the mediator to be produced on-shell. At the energies probed at the LHC this may not be the case, and the reliability of the EFT is not guaranteed anymore.

Truncation techniques are exploited to present EFT results. Such techniques consist in rejecting the fraction of events not satisfying the minimum validity requirement for EFT assumption. The transferred momentum is required to be smaller than the mediator mass, $Q_{tr} < M_{\phi}$. This operation weakens the limits leading to less constraining results.

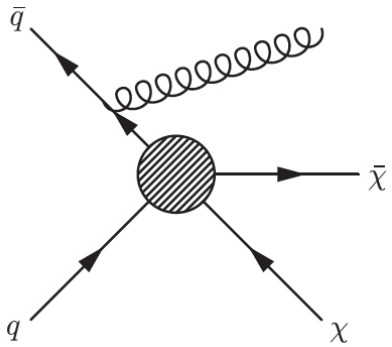

FIGURE 2: Dark Matter production in association with a single jet in the approximation of contact interaction.

Simplified Models

As previously explained, the EFT description holds in cases in which the DM-SM interaction mediator is very heavy compared to the energies involved in the interaction itself. This restricts the phase space that can be covered by this interpretation. Already at the energies reached in Run-1 proton-proton collisions at the LHC, the validity of the assumptions behind the EFT approach is limited. The contact interaction validity issue together with the prospect of much higher energies explored during LHC Run-2 collisions, leads to the need of reconsidering the benchmark models used to interpret the DM searches in Run-1. For cases in which the mediator is not so heavy, or the energy interaction is sufficiently high to produce the mediator on shell, more advanced models are needed that include explicitly the mediator in the theory.

Simplified models are not a complete theory but provide a faithful description of the kinematics of the DM production in the considered processes overcoming the limitations of the EFT approach and giving direct access to the interaction mediator. ATLAS and CMS collaborations, together with the theorist community, have established in September 2014 a forum, the LHC DM Forum, to agree upon the definition of a set of simplified models for the interpretation of results from early Run-2 DM searches. The outcome of this collaboration was summarised in the report of the Forum and made public in July 2015 [5]. An example of simplified model diagrams considered for single-jet plus $\not{E}_T$ signature is shown in Fig. 3. Some of Run-1 searches consider simplified models in addition to EFT for results interpretation in terms of DM production.association

EXPERIMENTAL APPROACH

As anticipated, the production of WIMPs at LHC through the process

$$pp \rightarrow \chi\bar{\chi} \tag{2}$$

is worthless as a discovery mode because it provides no signs for identification of production process. For this reasons processes in which WIMP particles are produced together with additional visible particles radiated off initial partons are considered to infer DM production.

In this way the SM particles are used to flag the interaction and the WIMPs are identified as the missing momentum recoiling against.

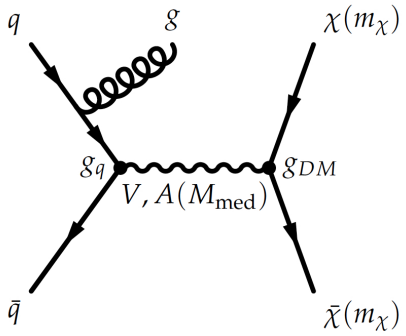

FIGURE 3: Representative Feynman diagram showing the pair production of WIMP particles in association to a single jet from initial state radiation via vector or axial-vector mediator.

Different signatures are exploited for this purpose: WIMPs produced in association with a high transverse momentum jet of hadrons from initial state radiation, or with an energetic electroweak vector boson (γ, W, Z), but also with one or more heavy flavour quarks (top or bottom).

The signature of signal production is an imbalance of energy in the transverse plane, therefore the key variable for all DM searches at LHC is the missing transverse momentum reconstructed in the detector. The main SM physics backgrounds consist of electroweak processes such as the production of Z or W bosons with jets, where the Z decays to neutrinos ($Z \rightarrow \nu\nu$) and the W decays to a neutrino and a charged lepton ($W \rightarrow l\nu$), where the lepton does not fall within the acceptance. Other important source of backgrounds derive from the production of $t\bar{t}$ events producing W bosons and QCD multijet events in which mis-reconstruction of jets leads to fake missing transverse momentum.

To minimize the contribution of non-genuine missing energy from jet mis-measurement and missing energy from non-reconstructed leptons and neutrinos from W or Z decay, specific requirements are applied depending on the signal signature. The selections applied to reject these kinds of backgrounds are described in the next sections together with some sophisticated techniques employed to identify vector boson decays in their low and high momentum regimes.

It is not possible to completely reject background events, thus, a good understanding of the missing transverse momentum distribution for SM backgrounds is essential. The presence of a signal is indeed revealed by an excess of events with respect to the SM background expectation in the high missing transverse momentum region.

To improve the understanding of the background contribution in the tails of high missing transverse momentum, the technique used for the different searches is to define regions enriched in background, called control regions (CRs), and use data distribution in these regions to predict background behaviour in signal region: control-to-signal region transfer factors (TFs) are defined to derive data-driven corrections to background expectation in signal region. A more specific example will be given in the following section for the monojet analysis case.

Monojet searches

Given the high cross section of gluon production from initial state radiation, events with a jet and missing transverse momentum are the most sensitive for most Dark Matter benchmark models proposed. Both ATLAS and CMS have looked for DM production in association with an high-p_T jet [6] [7], events with this signature are also named monojet events. Events selected in this search are required to have one central, high-p_T jet (150/120 GeV in CMS/ATLAS selection) and high $\not{E}_T$ ($\not{E}_T$ >200/150 GeV for CMS/ATLAS). Background events with genuine $\not{E}_T$ from W-decay neutrinos are suppressed by vetoing isolated leptons. Different strategies are employed by ATLAS and CMS to reject multijet events from QCD with non-genuine $\not{E}_T$ du to jet energy mis-measurement. CMS allows a second jet in the event if it is close to the leading one ($\Delta\phi(j_1,j_2)$<2.5), in order to include the frequent cases where initial state radiation yields to two jets. ATLAS allows the presence of even more than two jets, but only if they are produced far from the missing energy ($\Delta\phi(j_i,\not{E}_T)$>1.0).

The dominant backgrounds remaining after the selection described above are $Z \rightarrow \nu\nu + jets$ and $W \rightarrow l\nu + jets$, when the lepton is not reconstructed.

Data-driven techniques are employed to constraint the background in the region where the signal-to-background ratio is high, i.e. in the high missing energy region. A template fit in then performed over the full considered range of

missing energy spectrum.

In order to determine both shape and normalization for the $V + jets$ backgrounds in the signal region, data in background-enriched control samples are defined and used. Control-to-signal region transfer factors are derived as a function of $\not{E}_T$ bins in order to get the background prediction in the signal region applying a correction to data in control regions.

The similarity of Z-decay to neutrinos and to a pair of muons is exploited by defining a dimuon-enriched control sample. The $Z \to \nu\nu + jets$ is hence modelled using the dimuon control region in data. Due to the difference in branching ratio between the two processes (branching ratio of $Z \to \nu\nu$ is about 6 times larger than $Z \to \mu^+\mu^-$ branching ratio), the statistical uncertainty on dimuon template becomes a dominant systematics. A complementary approach used to overcome this issue is to define a regione enriched in $\gamma + jets$ events. The kinematics of this process is very similar to $Z \to \nu\nu + jets$ at large boson transverse momentum. This technique allows to further constrain $Z(\nu\nu) + jets$ background in signal region.

Similarly to what done for Z+jets background, W+jets is corrected by defining a single-muon control region.

The V+jets expectation in signal region is then corrected by performing a simultaneous likelihood fit to the signal and control regions across all the bins. The expected background yields in the i-th bin ($\mu^{Z\to\nu\nu}$ and $\mu^{W\to l\nu}$) in signal region are free parameters of the fit and are constrained from control regions through bin-dependent transfer factors, R_i^V:

$$\mu^{Z\to\nu\nu} = N_i^{Z_{\mu\mu}|\gamma} \cdot R_i^{Z|\gamma} \tag{3}$$

and

$$\mu^{W\to l\nu} = N_i^W \cdot R_i^W, \tag{4}$$

where N_i is the expected number of background events in a given bin i for a specific control region. The transfer factors R_i accounts for differences in signal and control regions for each background process and are derived as the ratio of the number of $Z(\nu\nu) + jets$ events in the signal region to that of $Z(\mu\mu) + jets$ and $\gamma + jets$ events in control regions, or as the ratio of $W(l\nu) + jets$ events in the signal and control region.

The systematic uncertainties are treated as nuisance parameters of the fit, and the transfer factors are allowed to vary within uncertainty.

The pre-fit and post-fit distribution of the $\not{E}_T$ in the signal region for SM backgrounds is shown in Fig. 4 compared to observed $\not{E}_T$ distribution.

The background determination technique described above is adopted by CMS. ATLAS employs a similar procedure to determine background expectation.

Data is found to be in good agreement with SM background expectation from the two experiments: no significant excess is observed in the tails of the distribution. Figure 5 shows the $\not{E}_T$ distribution for background expectation and data as found by the ATLAS experiment.

CMS monojet search does not include multijet events. A dedicated analysis is performed making use of razor variables. The razor variables are used to quantify the transverse imbalance of the jet momenta in events with more jets including b-tagged jets. This category of events gives extra-sensitivity to monojet search, even though the cross section is lower, the di-jet topology provide good discrimination against SM background.

The razor variables employed in this search are defined for dijet events according to the following definition:

$$M_R = \sqrt{(|\vec{p_{J_1}}| + |\vec{p_{J_2}}|)^2 - (p_Z^{J_1} + p_Z^{J_2})^2} \tag{5}$$

and

$$M_T^R = \sqrt{\frac{\not{E}_T(p_T^{J_1} + p_T^{J_2})^2 - \vec{\not{E}_T} \cdot (\vec{p_T}^{J_1} + p_T|\vec{J_2})^2}{2}} \tag{6}$$

where J_1 and J_2 are two mega-jets built from 2 or more jets. These variables were employed to look for the production of invisible particles in cascade decays of heavier particles, and were found to be sensitive to DM direct production as well, as suggested in [8].

Events are classified according to the number of b-tagged jet multiplicity and M_R value. Background expectation is derived from data building single and dimuon categories according to the signal region categorization.

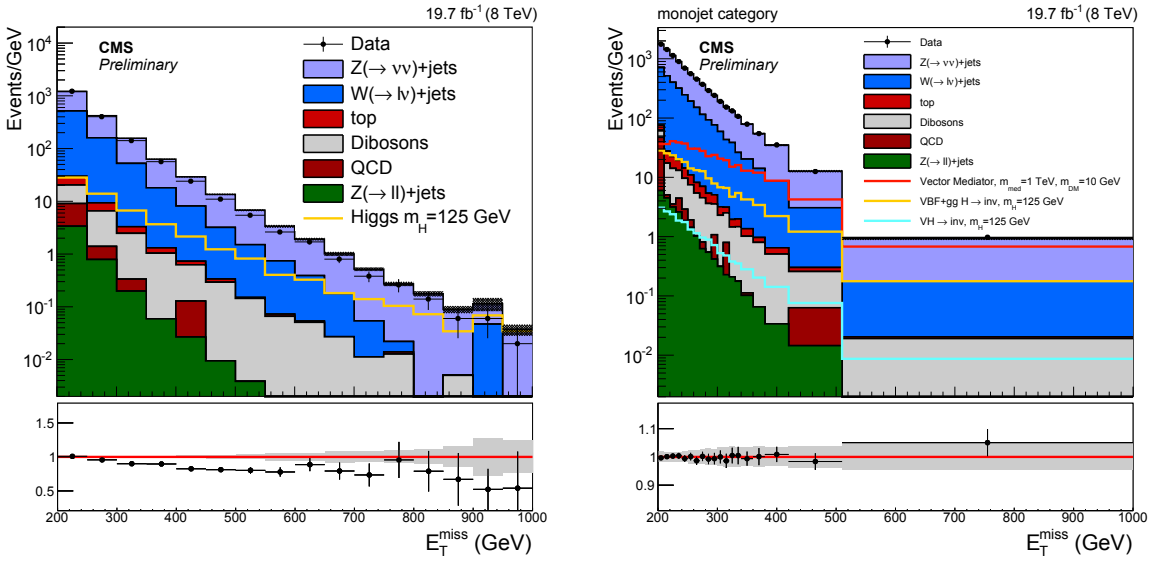

FIGURE 4: Distribution of the $\not{E}_T$ distribution in simulated events (filled coloured histograms) and data (black dots) after the signal selection for the CMS monojet search. Left: Pre-fit distribution. Right: Post-fit distribution. The grey band indicates the statistical uncertainty from MC simulation in the pre-fit plot and the post-fit uncertainty on background in the plot on the right. The expected distribution for a Higgs boson with mass 125 GeV is shown, assuming 100% branching ratio to invisible particles [7].

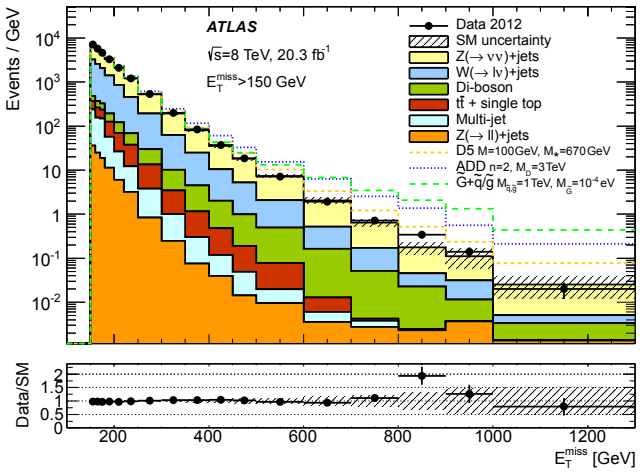

FIGURE 5: Missing transverse momentum distribution for the ATLAS monojet search, showing background expectation (filled coloured histograms) and data (black dots) in the signal region [6].

Figure 6 shows the R^2 distribution for the most sensitive category ($M_R > 600$ GeV). The main systematic uncertainty for this search comes from initial state radiation modelling. No significant excess was observed in this channel.

Mono-V searches

Although the monojet signature is the most sensitive signature for the majority of benchmark models used to interpret the results in terms of DM production, other DM production processes are worth to investigate. Among them signatures with high $\not{E}_T$ and electroweak vector bosons have lower cross section with respect to monojet signature but also

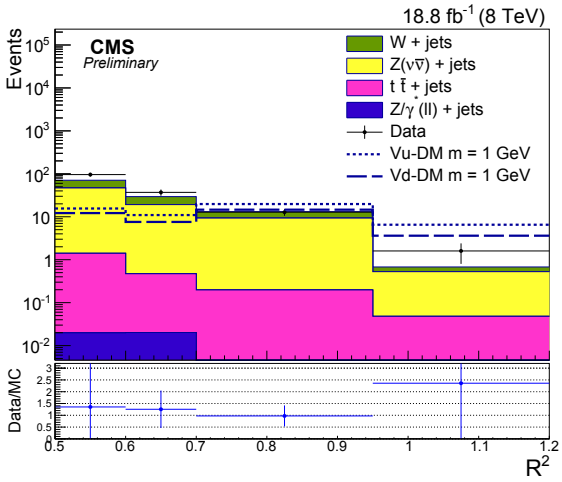

FIGURE 6: Comparison of observed yields and the data-driven prediction in the very high M_R category for the CMS multijet search with razor variables. Background contributions are represented in filled coloured histograms, while data are represented with black dots. Two signal benchmark models are shown, in an EFT model with different vector coupling to up and down quarks [8].

lower background. Mono-W, mono-Z and mono-γ searches are carried out at ATLAS and CMS.

The search for a vector boson recoiling against high $\not{E}_T$ has been performed in both hadronic and leptonic channels. The hadronic channel is quite challenging because of the overwhelming background but it is favoured by the large branching fraction of W and Z boson decay to a pair of quarks, and hence jets. Advanced techniques exploiting informations from the sub-structure of jets are employed to explore mono-V production in the boosted regime. In this region of the phase space the two jets stemmed by the vector boson are produced very close to each other, leading to a unique large jet reconstructed rather than two single jets. Both experiments make use of such techniques to isolate signal-like events from background events.

ATLAS [9] search looks for events with a central, high-p_T, massive jet (*fat jet*) with substructure consistent with two merged jets originated from a W or a Z boson, and with mass consistent with W/Z boson mass. The reconstruction of hadronic V-decay in a fat jet is validated defining a $t\bar{t}$-enriched control region requiring one muon, one fat jet and two additional, well separated narrow jets, out of which at least one b tagged and $\not{E}_T$ >250 GeV. The fat jet mass distribution in the top control region is shown in Fig. 7 comparing predicted backgrounds with data. It is clearly visible the W mass peak and a tail due to the partial or total inclusion of the b jet in the fat jet. The internal structure of a fat jet produced by V decay is characterised by a momentum balance between the two leading subjets, therefore the event is required to satisfy this characteristic in order to reduce background contamination. The momentum balance is defined as:

$$\sqrt{y} = min(p_{T1}P_{T2})\frac{\Delta R}{m_{jet}} \tag{7}$$

and it is required to be larger than 0.4.

Background from SM $t\bar{t}$ events and multijet events is suppressed rejecting events with additional narrow jets not overlapping with the fat jet, or overlapping with the $\not{E}_T$. W + jets background is reduced by vetoing the presence of lepton candidates in the event.

Events are classified in inclusive signal regions with increasing threshold on missing energy: $\not{E}_T > 250$ GeV and $\not{E}_T > 500$ GeV. Similarly to monojet search, the remaining backgrounds arise from $Z \to \nu\nu$ and $W \to l\nu$ production in association with jets, with the latter process begin source of background when the lepton fails identification requirements. These backgrounds are estimated from background-enriched data control regions. Extrapolation factors from control-to-signal region are derived from simulation as a function of m_{jet} and applied to data in control region to get an estimate of expected background in the region of interest.

The fat jet mass distribution in the two $\not{E}_T$ bins in signal region is shown in Fig. 8 for data and expected background as from data-driven prediction.

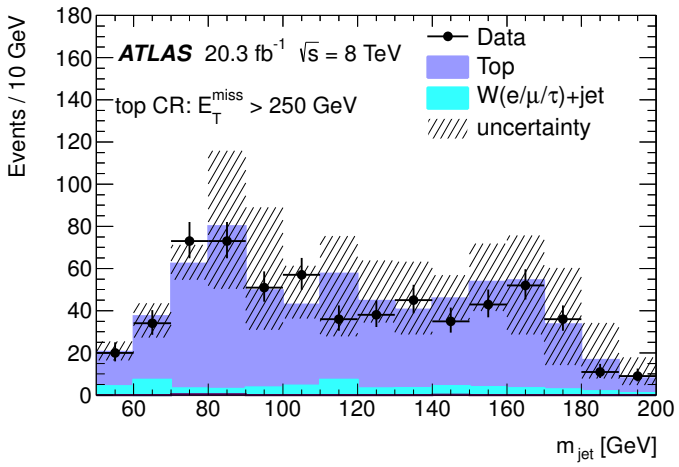

FIGURE 7: Distribution of m_{jet} in the data and for the predicted background in the top control region for the ATLAS search. The region is defined by asking one muon, one fat-jet, two narrow jets and at least one b-tag jet. A requirement on the missing transverse momentum is applied: $\not{E}_T$ >250 GeV. Uncertainties include statistical and systematic sources [9].

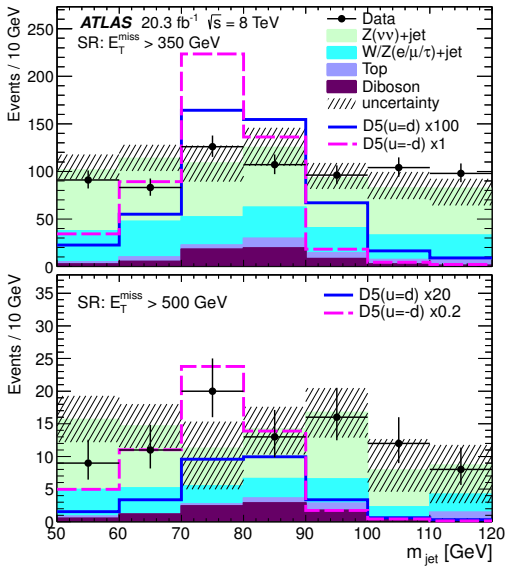

FIGURE 8: Distribution of m_{jet} in the data and for the predicted background in the signal regions with $\not{E}_T$ >350 GeV (top) and $\not{E}_T$ >500 GeV (bottom) for the ATLAS search. Uncertainties include statistical and systematic sources [9].

The major sources of systematic uncertainties affecting the search are due to the limited statistics in the control samples and the theoretical uncertainties in the simulated samples used to derive transfer factors. Uncertainties on jet energy calibration and momentum resolution for the fat jet have also a relevant effect on the final limit.

A fair agreement between data and simulation is observed in the two signal bins defined by different cuts on $\not{E}_T$.

The strategy adopted by CMS [7] differs mainly in the way in which informations on jet substructure are used: CMS looks at how much the fat jet is likely to be originated from 2 quarks using the N-subjettiness [10] variable, τ_N, which quantifies how likely the N-jet structure hypothesis is. The ratio τ_2/τ_1 is a valuable discriminating variable for the boosted-V topology. Figure 9 (left) shows the τ_2/τ_1 distribution in data and simulation.

CMS looks also in the low p_T region of V production to maximise the significance of the search making use

of multivariate techniques to identify the combination of jets originating from V decay. In this regime the two jets stemmed from V-quarks are not merged but rather fully reconstructed. Properties of individual and jets and of di-jet system are exploited to isolate signal-like events.

The mass of the di-jet system is required to be consistent with an weak boson mass ($60 < m_{jj} < 110\ GeV$). The combinatorial background is still dominant after this selection and to resolve the ambiguity picking up the right pair of jets, the multivariate resolved V-tagger is applied.

The V-tagging discriminant is built using as input variables:

- **Quark-Gluon Likelihood Discriminant** value for each jet. This discriminant distinguishes between jets stemmed from quarks and gluons.
- **Jet Pull Angle.** Vector bosons are color-singlet and therefore the two originated quarks are color connected. The color connection of the two jets is exploited looking at the pull angle of the trailing jet with respect to the leading jet and viceversa.
- **Mass Drop.** The mass drop variable is defined from the mass of each jet as well as of the di-jet system and from the distance between the two jets:

$$\frac{\max(m_{j_1}, m_{j_2})}{m_{j_1 j_2}} \Delta R_{j_1 j_2} \tag{8}$$

  This variable is quite helpful in rejecting background given its characteristic to be smaller for dijets from vector boson decay compared to dijets from combinatorial background.
- **Dijet** $p_T(j_1 j_2)/m_{j_1 j_2}$**.** This variable was found to perform nicely against combinatorial background.

The multivariate discriminator defined as described above is used to tag resolved V-tagged events and to choose the best dijet candidate as V candidate. The distribution of the V-tag discriminator is shown in Fig. 9 (right). Events with jets recognised as originating from b are rejected to reduce contamination from top backgrounds.

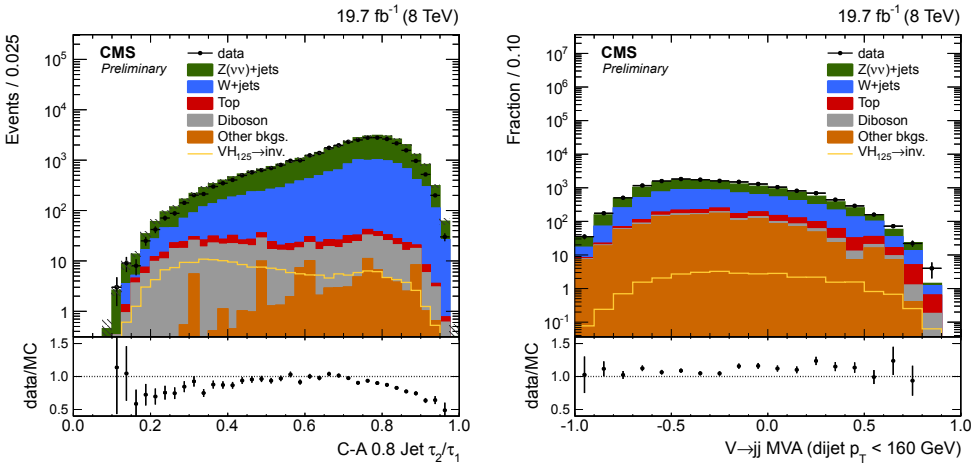

FIGURE 9: Left: Distribution of τ_2/τ_1 variable used in CMS search before the jet mass cut for events in data and MC simulation in the boosted-V event category. Right: CMS resolved V-tagger variable distribution in data is overlaid to expected backgrounds after all other signal region cuts are applied, for dijet p_T <160 GeV [7].

The data-driven strategy adopted by CMS to constraint backgrounds in the signal region for resolved and boosted V + $\not{E}_T$ searches is the same as applied in monojet search.

Data are found to be compatible with SM background expectation and no excess is observed.

Signature with leptonic-decay channels of weak vector bosons are also considered for DM production search. The monolepton search looks for DM pair produced with a W boson radiated off an incoming quark with the W decaying leptonically. Events for this signature are selected if an isolated lepton with $p_T > 100/45$ GeV (electron/muon) [11] is present. A large azimuthal opening angle between the lepton and the $\not{E}_T$ is imposed to discriminate signal from QCD

multijet background. After this selection the major irreducible background is due to $W \rightarrow l\nu$ decay. The W transverse mass, m_T, defined as:

$$m_T = \sqrt{2p_T^l \not{E}_T (1 - cos(\Delta\phi_{l,\not{E}_T}))} \tag{9}$$

has a natural endpoint at M_W, if the $\not{E}_T$ originates only from W neutrino. This is the main discriminating variable against this kind of background. In Fig. 10 (left side), the m_T distribution for SM background expectation and data is shown. ATLAS performs a similar search in this final state [12].

The $Z(ll)+\not{E}_T$ search relies on a clear dilepton signature plus missing energy from WIMP particles. ATLAS search [13] is performed looking for dilepton events with two opposite-sign, same-flavour, isolated leptons, with invariant mass, m_{ll} consistent with M_Z ($76 < m_{ll} < 106$ GeV). The dilepton candidate is required to be produced far from the $\not{E}_T$ in order to reject events where the $\not{E}_T$ originates from mis-reconstructed jets: $\Delta\phi(\not{E}_T, p_T^{ll}) > 2.5$. Top quark background is suppressed by vetoing the presence of reconstructed jets in the event. Similarly events containing a third lepton are removed to reduce diboson background. Nevertheless, the $ZZ \rightarrow l^+l^-\bar{\nu}\nu$ is the dominant background after selection and it is determined from simulation samples. The search looks for an excess of events in the tails of the missing transverse momentum spectrum. Figure 10 (right side) shows distribution of $\not{E}_T$ for data and simulated backgrounds.

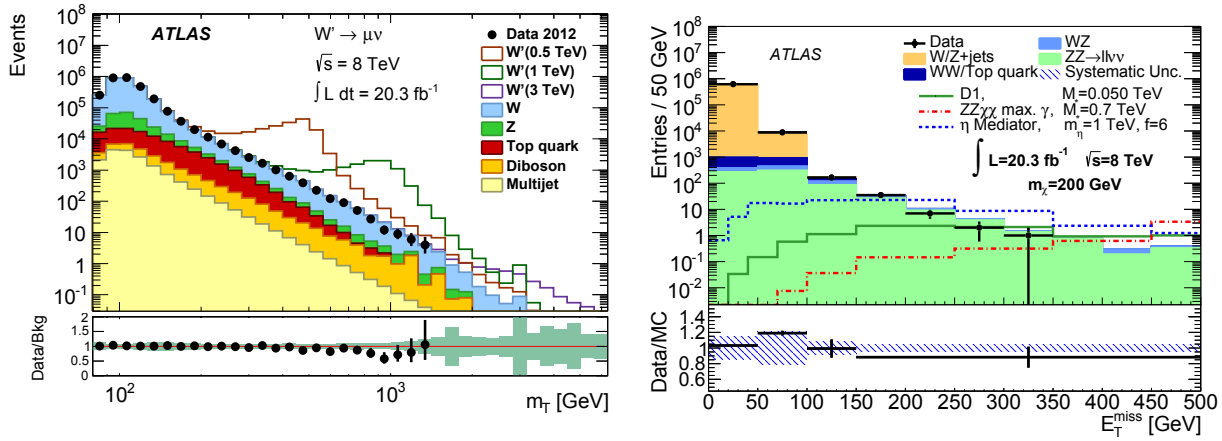

FIGURE 10: Left: Transverse mass spectrum for the muon channel after the event selection of the ATLAS mono-lepton search [12]. Right: missing transverse momentum distribution after all selection for the ATLAS mono-Z search for observed data and background, as estimated from simulation [13].

A similar search is performed by CMS [14], which makes use of the m_T spectrum for the statistical analysis. The m_T variable is defined as:

$$m_T = \sqrt{2p_T^{ll} \not{E}_T (1 - cos(\Delta\phi_{ll,\not{E}_T}))} \tag{10}$$

Signal events are expected to accumulate in the tails. No excess is observed by the two experiments. Data are compatible with the background-only expectation.

Interpretation of Mono-X results

The observations of ATLAS and CMS experiments in the mono-X searches is found to be consistent with background-only hypothesis. Exclusion limits are set on the Dark Matter production cross section and, in the framework of EFT interpretation the limits are translated into lower constraints on the energy scale M^* as a function of the DM mass, for each considered EFT interaction operator. Lower limits on the energy suppression scale are reported in Fig. 11 for the multijet analysis with razor variables. A translation to the DM-nucleon elastic cross section versus Dark Matter mass plane is performed [15] to allow a comparison of LHC results to direct detection experiments.

The 90% CL upper limits on the DM-nucleon scattering cross section for spin independent (vector) and spin dependent (axial vector) interactions is shown in Fig. 12 as a function of the WIMP mass. Comparisons are made with

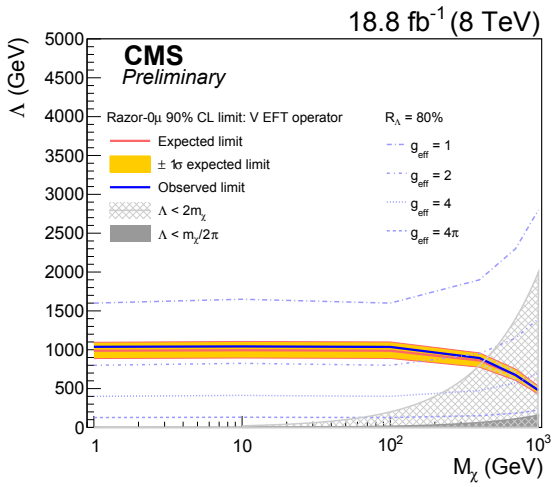

FIGURE 11: Lower limit at 90% CL on the suppression scale M* (Λ) as a function of the WIMP particle mass in the case of vector current. The validity of the EFT is quantified by $R_\Lambda = 80\%$ contours, corresponding to different values of the effective couplings g_{eff} [8].

results from direct detection experiments, showing a complementarity between collider and direct searches. Collider searches are more sensitive at low values of DM mass. This is due to a limitation of direct detection experiments in the low mass region where the recoil signal becomes too soft to be effectively detected. For spin-independent interactions, collider searches provide complementary coverage up to intermediate mass points.

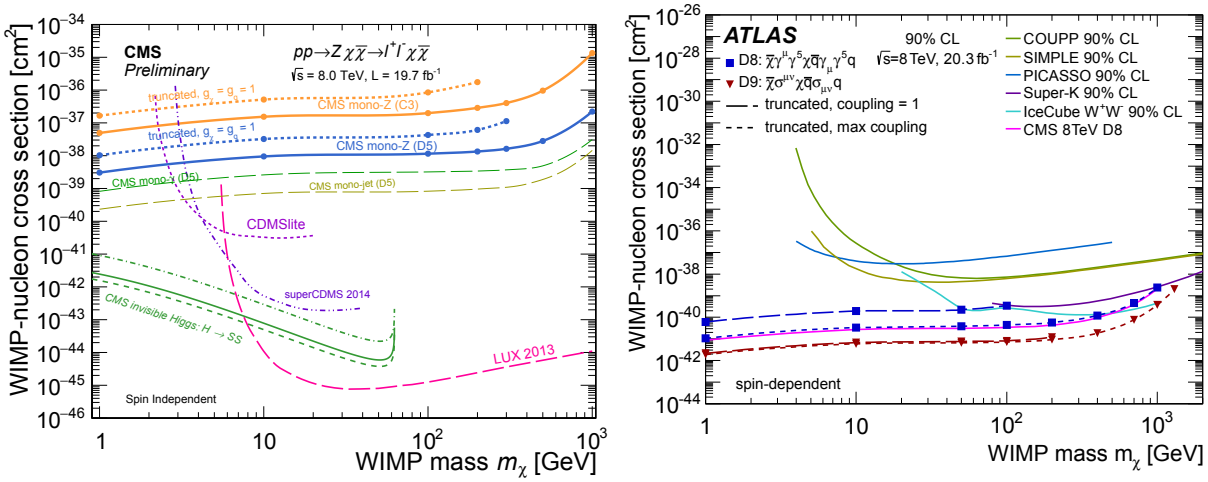

FIGURE 12: Upper limits at 90% CL limit on spin-independent (left) [14] and spin-dependent (right) [6] elastic WIMP-nucleon scattering cross section as a function of DM particle mass for different operators compared to results from direct searches.

The Run-1 results from monojet and monoV analyses are interpreted also in terms of simplified models. In view of 13 TeV LHC collisions, ATLAS and CMS collaborations have established a set of common benchmark simplified models to use for the interpretation of DM search results.

CMS monojet and mono-V searches are interpreted in terms of simplified models following recommendations from the LHC DM Forum.

The mono-V hadronic channel is actually combined with the monojet in CMS search. The events are classified in resolved V-tagged plus $\not{E}_T$, boosted V-tagged plus $\not{E}_T$ and monojet categories, as described above, in order to be orthogonal.

The events fill in the category in cascade, this method assures that the three categories are completely independent.

The 90% CL upper limits are calculated considering the simplified models in terms of exclusion in the $m_\chi - m_\phi$ plane, assuming four different mediators (vector, axial-vector, scalar, pseudo-scalar). The results are summarised in Fig. 13 for vector and axial vector interactions.

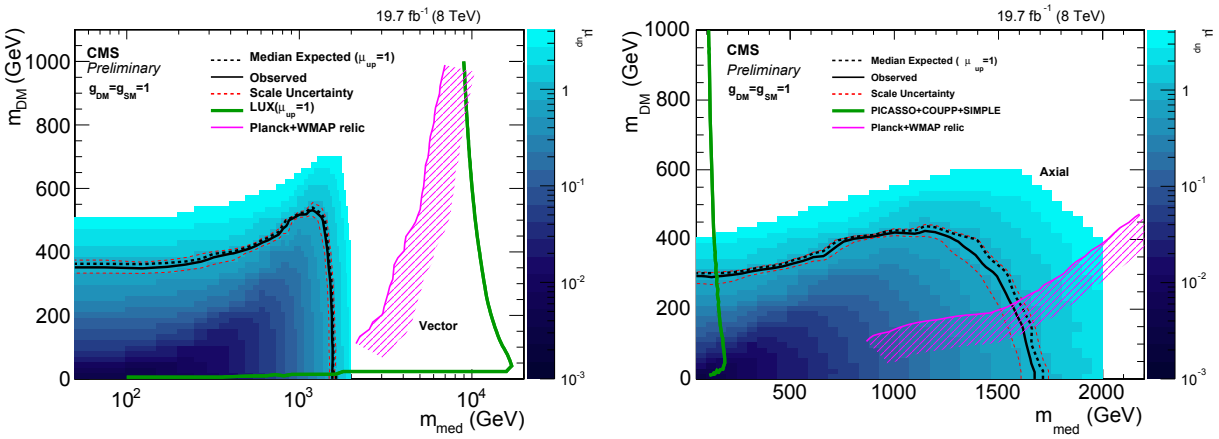

FIGURE 13: Observed 90% CL limits on the signal strength μ, defined as the ratio of the measured cross section to the theoretical cross section, in the $m_\phi - m_\chi$ plane, assuming a vector (left) and axial-vector (right) mediator. A combination of results from monojet, resolved and boosted mono-V categories is used to set limits [7].

DM search in heavy flavour channels

Mono-X searches put stringent bounds on vector interaction, but not on scalar interaction. Coupling to heavy flavour quarks is favoured in case of scalar (pseudoscalar) interaction, given the dependence of the cross section on the mass of quark. Coupling to light flavour quarks is suppressed with respect to top and bottom quarks.

Other Dark Matter searches have been carried out by ATLAS and CMS to further constraint this kind of interactions: final states with missing transverse momentum and a single or a pair of top/bottom quarks have been investigated.

Many models beyond the standard model propose the monotop production in association to an invisible state. Such models can be classified in two categories: resonant and non resonant production. CMS presented results for the monotop production in its hadronic decay channel [16]. ATLAS focused on the signature with a single lepton in the final state [17].

The hadronic channel takes the advantage of the large branching ratio of the top decay to jets. This search looks for events with 3 jets, out of which at least one b tagged, and with invariant mass of the three jets being consistent with the top mass, and large missing transverse momentum. The dominant background comes from V+jets events. The expectation of this process in the signal region is extracted from data in control regions throughout control-to-signal region transfer factors.

Additionally, a lepton veto is applied to suppress backgrounds with genuine $\not{E}_T$ from W decay into leptons.

The semi-leptonic search look for events with exactly one isolated lepton and one b-tagged jet, together with missing energy. The W transverse mass, m_T, and the azimuthal opening angle between the lepton and the b jet are constrained in order to reject background events from multijet QCD with mis-identified leptons and $\not{E}_T$ from jet mis-reconstruction.

The resonant and non-resonant models are partially or totally excluded assuming different values of couplings. Fig. 14 shows the upper limit plot on the invisible state production cross section for the non-resonant model from hadronic channel (left). The resonant model from single lepton channel is excluded in the full mass range for the couplings assumed. In both channels data are found to be compatible with background-only hypothesis. No excess is observed on top of the background expectation and limits on production cross section are set.

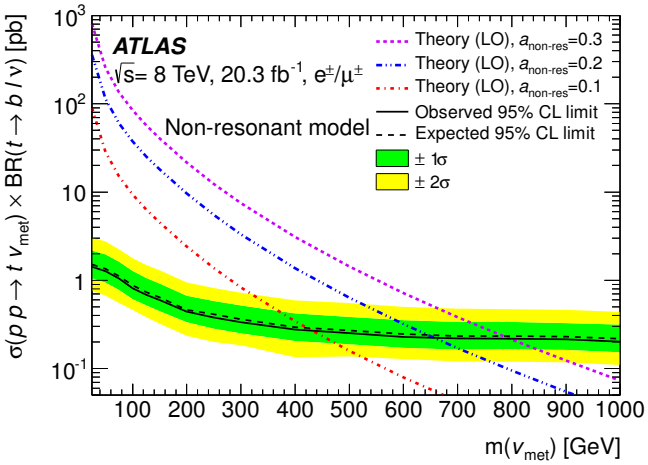

FIGURE 14: Upper limits at 95% CL on monotop production cross section under non-resonant hypothesis. Depending on the assumption on the coupling, states with mass up to 800 GeV are excluded [17].

Beside the monotop search, ATLAS and CMS have searched for a DM pair production in association with a pair of top quarks: ATLAS in the all-hadronic and single-lepton channels [18], while CMS in the semileptonic and dileptonic channels [19][20]. The most sensitive final state is the single-lepton channel, followed by the full hadronic and the dilepton. Events of single lepton topology are identified by requiring exactly one isolated lepton in the event and at least three jets, out of which one identified as b jet. The missing transverse momentum and the pair of leading jets are required to have large azimuthal opening separation, $\Delta\phi(j_{1,2}, \not{E}_T)$, and so to have been produced in different directions, to suppress SM top background. The main backgrounds remaining after the selection are dileptonic $t\bar{t}$ events. These kind of events are rejected applying a requirement on the M_{T2}^W [21]. The contribution from W + jets process is reduced by applying a requirement on the W transverse mass, m_T. The dominant processes, $t\bar{t}$ and W + jets are normalised to data from control regions. A single bin counting experiment is performed in the signal region defined by $\not{E}_T > 350$ GeV and lower limits are placed on the interaction scale at 95% CL for DM-SM scalar interaction (Fig. 15). An analogue search is performed by ATLAS and described in [18]: the $\not{E}_T$ distribution after full selection for the hadronic channel is shown in Fig. 15 (left).

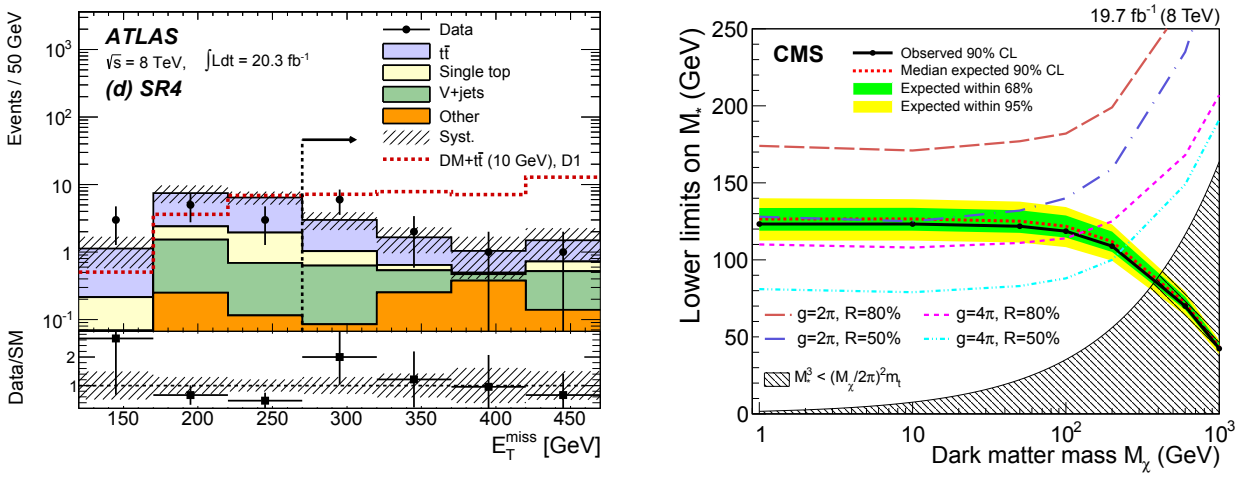

FIGURE 15: Comparison of data and expected SM background for the $\not{E}_T$ distribution in the hadronic channel of ATLAS $t\bar{t} + DM$ search [18], signal for a specific DM scenario is superimposed (left). Lower limits at 90% CL on the interaction scale M^* as a function of WIMP particle mass as resulting from CMS $t\bar{t} + DM$ search [19].

CONCLUSIONS

The ATLAS and CMS Dark Matter searches covered a huge range of final states during the LHC Run-1 data-taking looking for evidence of WIMP particles. The observation is consistente with the SM background expectation in all the channels, and bound have been set on the production cross section considering different models. Results from these searches have been compared to those from direct detection experiments in the framework of an EFT approach. It is clear a complementarity of the two: collider searches are more powerful in constraining the low DM-mass region with respect to direct detection experiments for spin-independent searches where the direct detection suffers a lack of sensitivity. However, the EFT models employed to interpret DM search results, suffer of validity limitation in the high-energy regime. Thus, new models, simplified models, in which the mediator is explicitly considered instead of integrated out, have been employed. These models provide a more fair description of the interaction itself and overcome the limitations of the EFT approach. the simplified models will be the approach followed to interpret the new results coming from LHC Run-2 data taking.

REFERENCES

[1] G. Bertone, D. Hooper, and J. Silk, Phys. Rept. **405**, 279–390 (2005), arXiv:hep-ph/0404175 [hep-ph] .

[2] D. Bauer *et al.* (Snowmass 2013 Cosmic Frontier Working Groups 14), "Dark Matter in the Coming Decade: Complementary Paths to Discovery and Beyond," (2015), pp. 16–23, arXiv:1305.1605 [hep-ph] .

[3] S. Chatrchyan *et al.* (CMS Collaboration), JINST **3**, p. S08004 (2008).

[4] G. Aad *et al.* (ATLAS Collaboration), JINST **3**, p. S08003 (2008).

[5] D. Abercrombie *et al.*, (2015), arXiv:1507.00966 [hep-ex] .

[6] G. Aad *et al.* (ATLAS Collaboration), Eur. Phys. J. **C75**, p. 299 (2015), [Erratum: Eur. Phys. J.C75,no.9,408(2015)], arXiv:1502.01518 [hep-ex] .

[7] V. Khachatryan *et al.* (CMS Collaboration), "Search for New Physics in the V/jet + MET final state," Tech. Rep. CMS-PAS-EXO-12-055 (CERN, Geneva, 2015).

[8] V. Khachatryan *et al.* (CMS Collaboration), "Search for dark matter direct production using razor variables in events with two or more jets in pp collisions at 8 TeV," Tech. Rep. CMS-PAS-EXO-14-004 (CERN, Geneva, 2015).

[9] G. Aad *et al.* (ATLAS Collaboration), Phys. Rev. Lett. **112**, p. 041802 (2014), arXiv:1309.4017 [hep-ex] .

[10] V. Khachatryan *et al.* (CMS Collaboration), "V Tagging Observables and Correlations," Tech. Rep. CMS-PAS-JME-14-002 (CERN, 2014).

[11] V. Khachatryan *et al.* (CMS Collaboration), Phys. Rev. **D91**, p. 092005 (2015), arXiv:1408.2745 [hep-ex] .

[12] G. Aad *et al.* (ATLAS Collaboration), JHEP **09**, p. 037 (2014), arXiv:1407.7494 [hep-ex] .

[13] G. Aad *et al.* (ATLAS Collaboration), Phys. Rev. **D90**, p. 012004 (2014), arXiv:1404.0051 [hep-ex] .

[14] V. Khachatryan *et al.* (CMS Collaboration), (2015), arXiv:1511.09375 [hep-ex] .

[15] Goodman *et al.*, Phys. Rev. **D82**, p. 116010 (2010), arXiv:1008.1783 [hep-ph] .

[16] V. Khachatryan *et al.* (CMS Collaboration), Phys. Rev. Lett. **114**, p. 101801 (2015), arXiv:1410.1149 [hep-ex] .

[17] G. Aad *et al.* (ATLAS Collaboration), Eur. Phys. J. **C75**, p. 79 (2015), arXiv:1410.5404 [hep-ex] .

[18] G. Aad *et al.* (ATLAS Collaboration), Eur. Phys. J. **C75**, p. 92 (2015), arXiv:1410.4031 [hep-ex] .

[19] V. Khachatryan *et al.* (CMS Collaboration), JHEP **06**, p. 121 (2015), arXiv:1504.03198 [hep-ex] .

[20] V. Khachatryan *et al.* (CMS Collaboration), "Search for the Production of Dark Matter in Association with Top Quark Pairs in the Di-lepton Final State in pp collisions at $\sqrt{s} = 8$ TeV," Tech. Rep. CMS-PAS-B2G-13-004 (2014).

[21] C. G. Lester and D. J. Summers, Phys. Lett. **B463**, 99–103 (1999), arXiv:hep-ph/9906349 [hep-ph] .

[22] G. Aad *et al.* (ATLAS Collaboration), "Search for dark matter pair production in events with a hadronically decaying W or Z boson and missing transverse momentum in pp collision data at $\sqrt{s} = 8$ TeV with the ATLAS detector," Tech. Rep. ATLAS-CONF-2013-073 (CERN, 2013).

[23] N. F. Bell, Y. Cai, J. B. Dent, R. K. Leane, and T. J. Weiler, Phys. Rev. **D92**, p. 053008 (2015), arXiv:1503.07874 [hep-ph] .

Proceedings of the LHCP2015 Conference, St. Petersburg, Russia, August 31 - September 5, 2015

Editors: V.T. Kim and D.E. Sosnov

Supersymmetry: Experimental Status

KEITH A. ULMER

Texas A&M University, Department of Physics and Astronomy, College Station, TX, 77843, USA.

ulmer@tamu.edu

On behalf of the CMS and ATLAS Collaborations

Abstract. This talk presents results from the CMS and ATLAS Collaborations from searches for physics beyond the Standard Model motivated by supersymmetry from Run 1 of the LHC. Representative searches are described to illustrate the diverse nature of the search program in both background estimation techniques and final state topologies. The status of preparation for Run 2 searches at 13 TeV is also presented.

INTRODUCTION

The Standard Model of particle physics accurately describes the interactions of all known fundamental particles in the universe, and has remained the prevailing paradigm in the field for over forty years. Despite its success, the Standard Model remains an incomplete theory of fundamental particles and interactions. It does not include a description of gravity, nor does it explain the compelling astronomical evidence for dark matter. Of the proposed extensions to the Standard Model, supersymmetry (SUSY) has remained among the most popular for decades. It provides exactly the needed compensation to stabilize the Higgs mass, while additionally providing an ideal candidate for dark matter with a stable weakly interacting lightest supersymmetric particle (LSP).

The CMS [1] and ATLAS [2] experiments at the CERN Large Hadron Collider are general purpose detectors built to explore the fundamental nature of the universe. Among the results from the two experiments are many searches for supersymmetry, which have thus far yielded null results [3, 4]. The search programs in both experiments are based on a wide arrange of techniques to measure standard model background contributions as well as a diverse range of possible final states. In this talk, a sample of results are shown to illustrate techniques deployed in these searches. By no means are all relevant results discussed or presented.

In the first section, a series of general searches in different final states are described. The second section contains a discussion of more targeted searches focused on dedicated final state topologies, while the third section discussed difficult to reach signatures. The forth section attempts to put the full set of searches performed into a global context, while the final section shows progress toward new searches in the LHC Run 2 with 13 TeV proton-proton collisions.

INCLUSIVE SEARCHES

Unlike the Standard Model Higgs boson, supersymmetry has many free parameters, which can give rise to a great variety of signatures. Further, the unknown mass spectrum can also give rise to a great variety of production cross sections and final state kinematics. With such a broad range of possible signatures, a fruitful class of supersymmetry searches is performed with inclusive sensitivity. Here I describe four such examples in different final states.

The classic jets plus missing energy signature is searched for in a three dimensional binned analysis taking advantage of sensitivity in different bins of missing energy (MET), the sum of jet transverse momenta (HT), and the number of jets tagged as bottom quarks [5]. Events are selected by removing those with an identified electron or muon and then requiring at least three jets and at least one tagged b-quark jet. The main Standard Model backgrounds derive from $t\bar{t}$, W + jets, Z + jets, and QCD multijet events. The contribution from each category of background is measured from data control samples to minimize the reliance on accurate simulation. In particular, single lepton events are used

to predict the $t\bar{t}$ and W + jets backgrounds, and dilepton events are used to predict the Z + jets backgrounds with Z decays to neutrinos. The QCD multijet contribution is predicted by utilizing a kinematic sideband enriched in QCD events where a jet and MET are aligned.

No significant excess of events above the Standard Model predictions is observed. Fig. 1 (left) shows the data compared to the expected Standard Model contribution after selecting events with at least 3 b-quark jets. The search results are interpreted in several benchmark SUSY models, including gluino pair production with each gluino decaying to two b-quarks and the LSP. Fig. 1 (right) shows that such models are excluded for gluino masses as high as around 1.2 TeV.

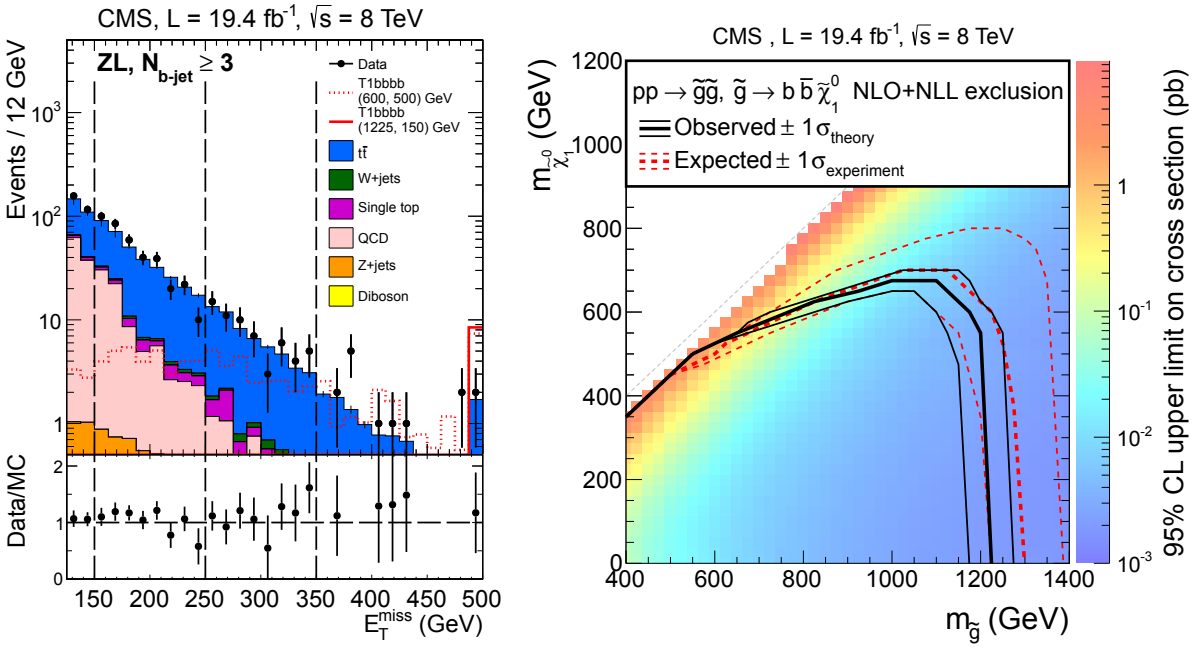

FIGURE 1. MET distribution in hadronic search with at least 3 b-jets (left) and limits from the search for gluino to bbLSP production (right). Taken from Ref. [5].

A similarly broad search was performed with complementary events selected with exactly one muon or electron in [6]. Minimal requirements on MET and the transverse mass (MT) of the lepton and MET are used to select SUSY-like events. Sensitivity to a variety of models is obtained by classifying search regions into large and small jet multiplicity. Backgrounds arise predominately from W + jets and $t\bar{t}$ events. The size of the Standard Model contributions are predicted by identifying data control regions enriched in each background. MC simulation is then used with the overall normalization taken from the data control region to predict the background in each signal region.

The MET distribution for a signal region with five or more jets is show in Fig. 2 (left) with data compared to the background estimation. No significant signal is observed in any of the search regions and 95% CL upper limits are set on a variety of simplified models. Fig. 2 (right) shows the limits for gluino pair production with both gluinos decaying into two top quarks with limits reaching beyond 1.3 TeV for light LSPs.

Next, a search was performed based on events with two electrons or muons with the same electric charge [7]. Such events are rare in the Standard Model, but can occur readily in many new physics signatures. The leptons are required to be well isolated to select prompt leptons from W or Z decays and remove those associated with jets, for example from semi-leptonic b decays. The main backgrounds arise from events with a non-prompt lepton that mistakenly passes the isolation criteria in addition to another prompt lepton or from events with two true prompt leptons arising from such rare processes as diboson production. The background from non-prompt leptons is determined by measuring the so-called "fake rate" of the likelihood of a non-prompt lepton to pass the isolation criteria in a data control sample, as shown in Fig. 3 (left). The contributions from rare backgrounds are taken from simulation. As with the other inclusive searches, signal regions are defined in a number of bins of MET, HT, and number of b-tagged jets to ensure sensitivity to a variety of possible signal models and parameter space. No significant excess of events is observed above the

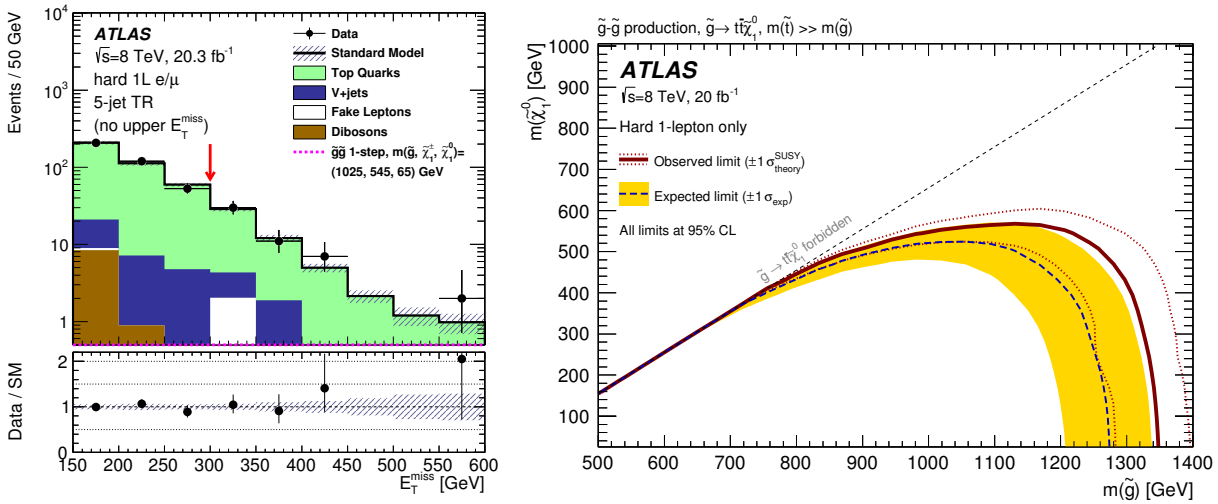

FIGURE 2. MET distribution for the W + jets control region for the inclusive 1L search (left) and results from the search for gluino to $t\bar{t}$LSP production (right). Taken from Ref. [6].

expected Standard Model backgrounds. Fig. 3 (right) shows the observed limit for sbottom pair production with each sbottom decaying to t, W, and the LSP.

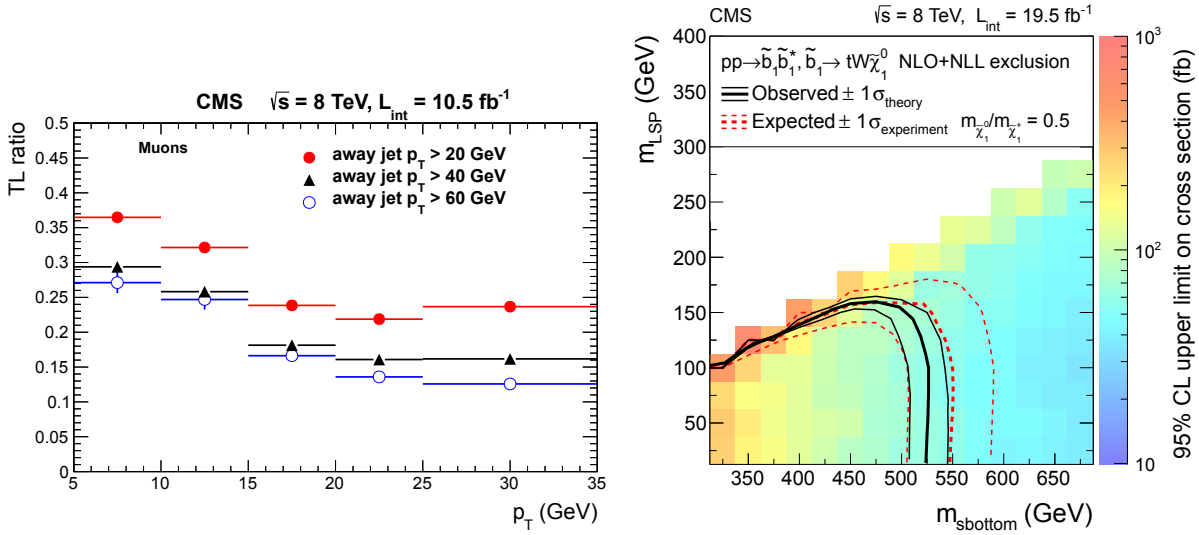

FIGURE 3. Tight to loose isolation ratio used to measure non-prompt lepton fake rate (left) and results from same-sign dilepton search for sbottom pair production (right). Taken from Ref. [7].

The final inclusive search described in this talk is based on events with two high p_T photons [8]. Such a signature is common in gauge mediated (GMSB) SUSY scenarios where the LSP is a gravitino and the lightest neutralino decays into a photon and the gravitino. Sensitivity to strong and electroweak production is achieved with search bins in low and high MET and jet multiplicity. The main backgrounds arise from combinatorial diphoton production and from photon + jets events where one of the jets is mistaken as an isolated photon. The missing energy in such background events is generally the result of mismeasured jets. Since the MET does not come from the photons themselves, data control samples composed of events from the photon isolation sidebands can be used to measure the expected MET shape. The MET shape is then normalized to the low MET region in the true two photon sample to predict the

background in the signal region. Fig. 4 (left) shows the MET distribution for a signal region with MET > 200 GeV where the signal extends to higher MET than the remaining backgrounds. No significant excess of signal events is observed. Fig. 4 (right) shows the upper limits on gluino production in a GMSB scenario with a bino-like neutralino.

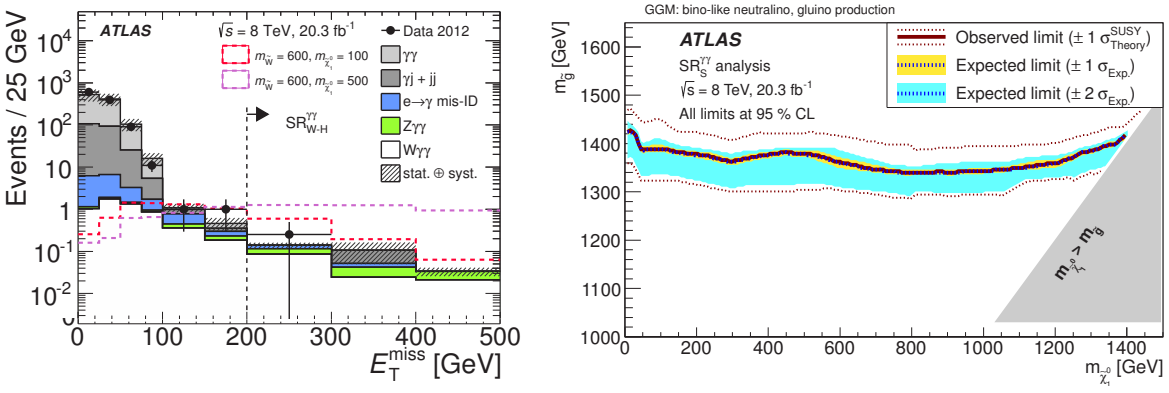

FIGURE 4. MET distribution for inclusive diphoton search signal region (left) and results for gluino production GMSB model (right). Taken from Ref. [8].

TARGETED SEARCHES

In addition to generic inclusive searches, some SUSY signatures are sufficiently well motivated to demand dedicated searches targeting a more specific model. Here two such targeted searches are described. The first is for stau pair production, while the second targets direct stop production.

Direct stau pair production is well motivated, in particular by its potential connection to cosmological scenarios to describe the early evolution of the universe. While generic dilepton searches are often sensitive to stau production through the stau decays to electrons or muons, a dedicated search is required to capture sensitivity to hadronic stau decays which have the largest branching fraction. In [9] events with two hadronic tau candidates with opposite charge are selected. Z boson candidates are vetoed to reject Z to $\tau\tau$ events, and events with a b-tagged jet are rejected to remove $t\bar{t}$ events. The remaining background is dominated by QCD multijet events. To select signal from this background, a multivariate boosted decision tree (BDT) is trained and only events with high BDT score are retained. After such selection, the main backgrounds remaining are W + jets and diboson events. The W + jets background is measured by identifying a data control sample enriched in W + jets and normalizing the MC simulation prediction to the yield in this control sample. Fig. 5 (left) shows a plot of the MT2 distribution in this control sample. No significant excess of events is observed about the background predictions and 95% CL upper limits are set. Even after stringent selection and significant background rejection, only the lightest staus are excluded with masses around 100 GeV, as shown in Fig. 5 (right).

Another very well motivated SUSY scenario is direct stop production, as the stop plays a key role in the cancelation of quadratic divergences to the Higgs mass from top quark loops. The search in [10] utilizes the all hadronic final state to target stop pair production with stop to top, LSP decays with both tops decaying hadronically. The analysis uses a customized jet algorithm to identify two hadronic top decay candidates. Events with an isolated electron, muon, or tau are removed. The most significant background arrises from $t\bar{t}$ events with MET from a leptonic W decay where the charged lepton is lost. The separation of signal and background is achieved with a BDT trained to select signal events. Kinematic variables such as the angle between the MET and the jets in the sub-leading top candidate as shown in Fig. 6 (left) are used in the BDT. After the selection, MC simulation is used to estimate the total background contribution in each signal region. The MC is corrected to achieve good agreement with data in several key kinematic distributions and the background prediction is validated in the BDT sidebands. No significant excess of data over background is observed and limits are set on direct stop production. As shown in Fig. 6 (right) stop masses up to around 800 GeV are excluded for light LSPs.

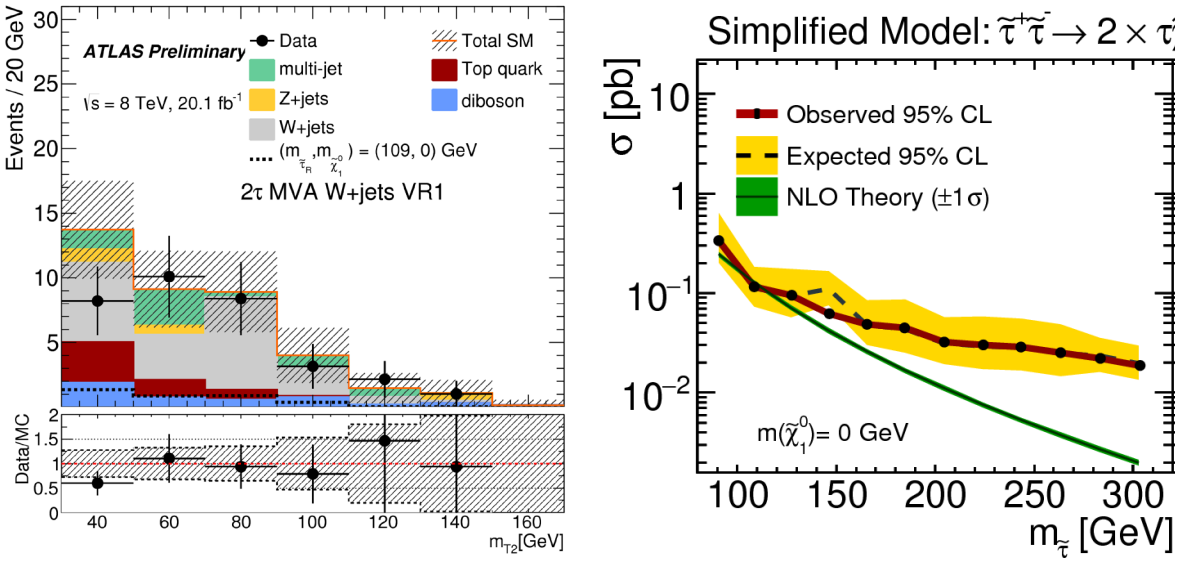

FIGURE 5. Stau search W + jets validation region (left) and stau exclusion limits (right). Taken from Ref. [9].

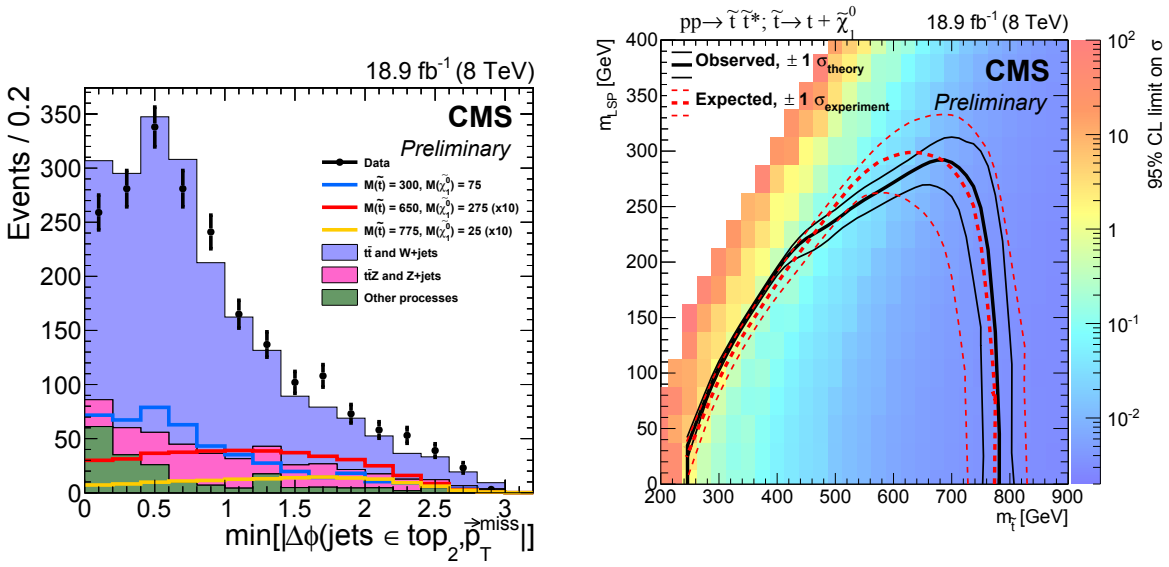

FIGURE 6. Minimum $\Delta\phi$ distribution between MET and subleading top candidate jets (left) and stop to top, LSP production limits (right) from the hadronic stop search. Taken from Ref. [10].

EXPLORING GAPS

As more and more SUSY searches have yielded null results, an increasing effort has been placed on considering where a signal may yet be hiding in space accessible with current LHC data. This section describes four such searches that explore regions not covered by more conventional SUSY searches.

One such gap in SUSY sensitivity occurs when the stop has a mass very close to that of the top and LSP is very light. In this scenario, stop pair production looks very similar kinematically to top pair production and the signal can be very difficult to dig out. One approach is to use a precision measurement of the top cross section and compare

it to the theoretically predicted cross section from the Standard Model. If excess events exist, they could be from the presence of stops. Additionally, the spin correlations of the scalar stops are somewhat different from that of the spin 1/2 tops. The search in [11] exploits this difference to gain sensitivity to stop production in this difficult region. Dileptonic $t\bar{t}$ events are used to compare the observed angular difference between the leptons with that expected from $t\bar{t}$ and stop pair production, as shown in Fig. 7 (left). No deviation from the expected Standard Model distribution is observed and limits are set on stop pair production, as shown in Fig. 7 (right).

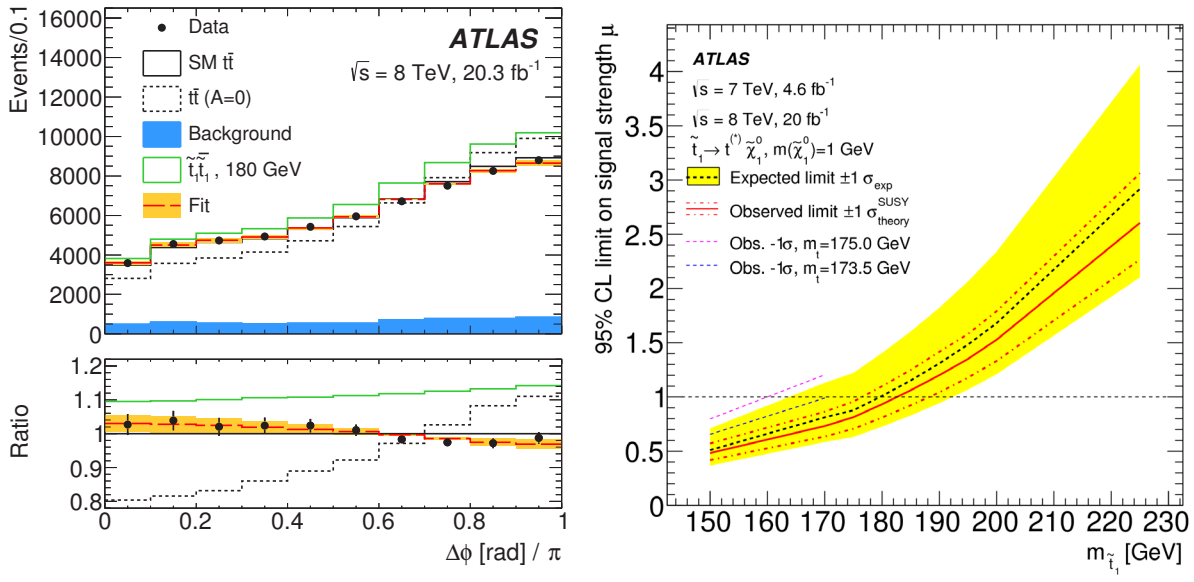

FIGURE 7. Angle between two leptons in dileptonic $t\bar{t}$ cross section measurement compared to SUSY stop signal (left) and resulting exclusion limit for stop production (right). Taken from Ref. [11].

Another difficult to access region occurs when SUSY particle masses are nearly degenerate. These so called "compressed" spectra can result in SUSY decays with little missing energy if the LSP is close in mass the parent particle. As in direct dark matter searches with the monojet topology, compressed SUSY can be searched for in events where the SUSY system recoils against an ISR jet. The compressed spectrum then produces missing energy when it is boosted. Such a technique is employed in [12] where the ISR jet and missing energy are searched for in combination with one or two low p_T leptons, which can originate from stop or chargino decays. The resulting lepton p_T spectrum is soft, as shown in Fig. 8 (left) for compressed decays. After selecting only events with low p_T isolated leptons much of the background is removed and sensitivity to this difficult region is obtained, as shown in Fig. 8 (right).

The search in [9] extends the soft lepton plus ISR topology even further in searching in events with three or more low p_T leptons plus large MET. This allows for sensitivity to such SUSY signatures as chargino or neutralino production decaying to a neutralino LSP with intermediate sleptons, which can give up to four leptons in the final state. The Standard Model background for three or more isolated leptons plus large MET and a high p_T ISR jet is very low. Figure 9 (left) shows the single observed signal event in one of the search regions compared to the background prediction, while Fig. 9 (right) shows the results of the search when combined with same-sign dilepton and high p_T multilepton searches.

Another alternative to ISR to boost the compressed SUSY spectrum is vector boson fusion (VBF). The pair of VBF jets serves the same purpose of providing a boost to the SUSY system, which would otherwise have very low MET. The search in [13] exploits the VBF topology to search for compressed SUSY with complementary sensitivity to the ISR searches. As an additional discriminating variable, the mass of the VBF dijet system can be utilized to select high mass events more typical of signal. Figure 10 (left) shows the dijet mass distribution for background compared to signal. The observed distribution is consistent with the Standard Model expectation and no evidence for SUSY is found. Figure 10 (right) shows the search results interpreted as limits on compressed sbottom pair production as well as direct dark matter production.

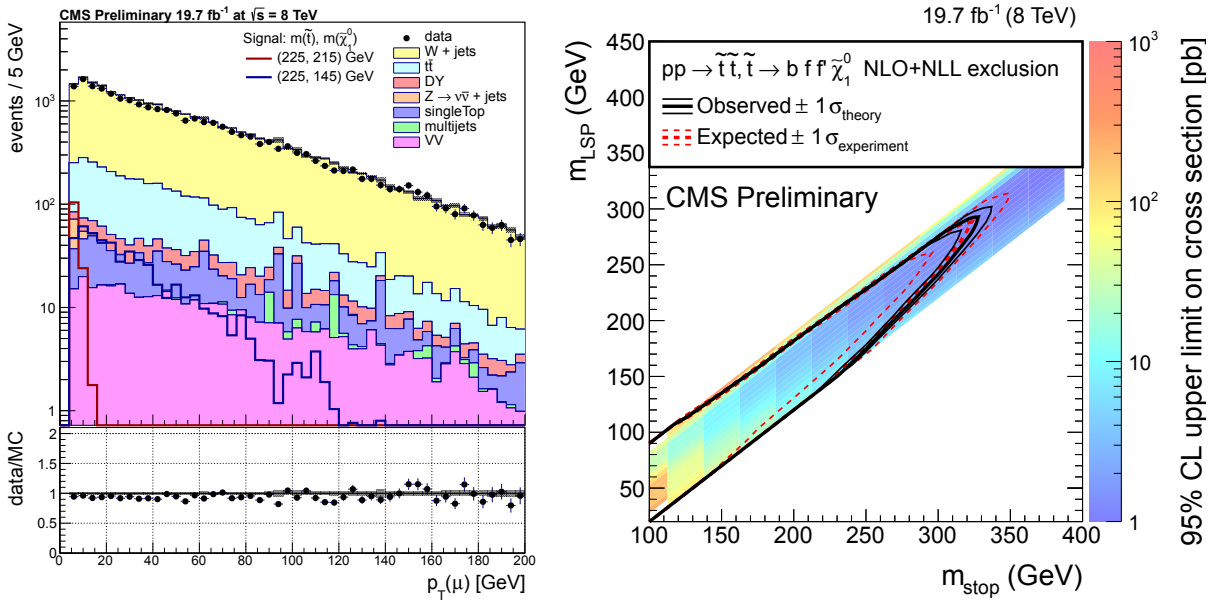

FIGURE 8. Muon p_T distribution (left) and compressed stop search limits (right) in soft muon SUSY search. Taken from Ref. [12].

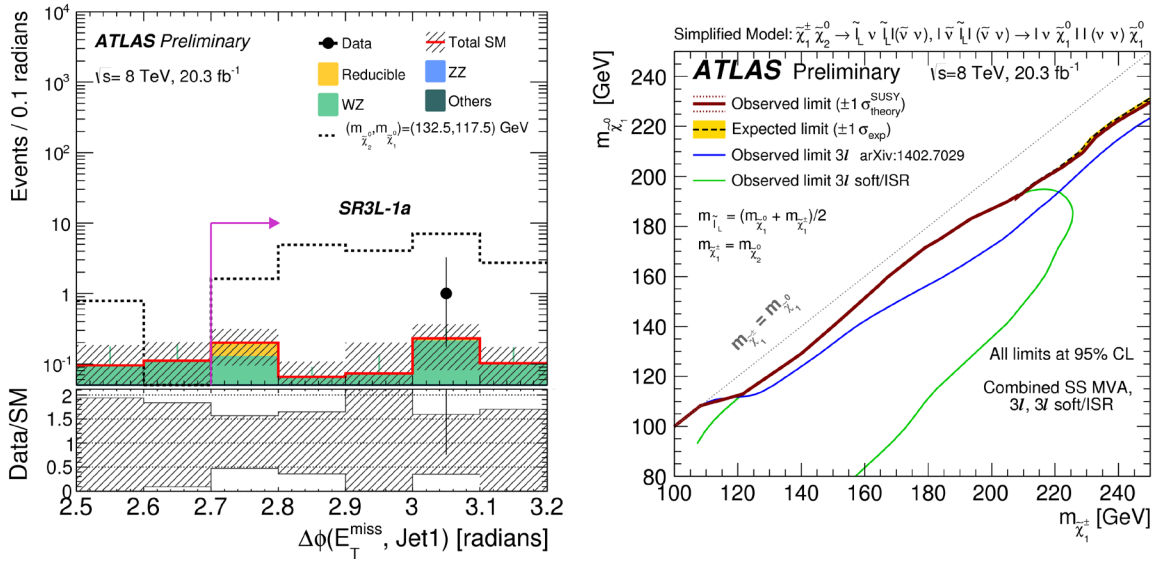

FIGURE 9. Angular separation between lead jet and MET in the three soft lepton + ISR search (left) and resulting limits on electroweak SUSY production (right). Taken from Ref. [9].

THE BROAD PICTURE

With the plethora of possible SUSY signatures and searches performed at the LHC, it is important to put the entirety of the search program together to assess where things stand. Many different searches can be sensitive to the same model. When mutually exclusive final states provide complementary sensitivity, a combination of the results of the different relevant searches can extend the overall reach. For example, in Fig. 11 (left) the results from searches using five different final states are shown along with the combination of the five searches, which extends the sensitivity beyond any of the individual searches alone. Alternatively, different searches can be designed to be sensitive to different

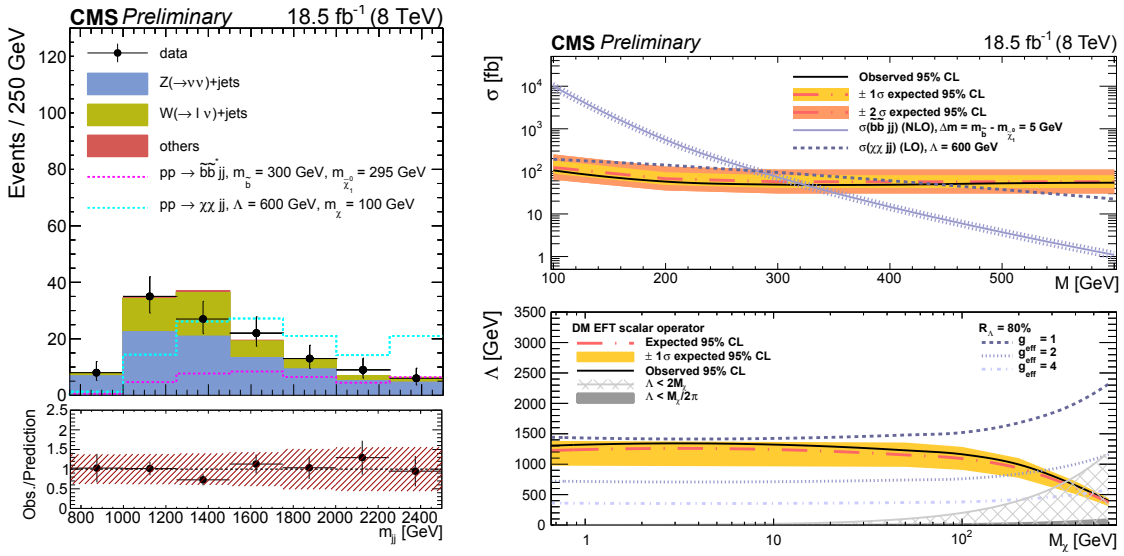

FIGURE 10. Dijet mass distribution comparing signal and background (left) and limits for sbottom pair and dark matter production (right) from the VBF SUSY search. Taken from Ref. [13].

regions of parameter space for a given model. When the exclusion regions for each individual search are overlaid, the total exclusion can show significant coverage. For example, Fig. 11 (right) shows the exclusions from eight different searches targeting direct stop production. In total, they exclude a very significant region of the plane. Such summary plots also serve to highlight regions where gaps exist in the current sensitivity and can motivate future efforts.

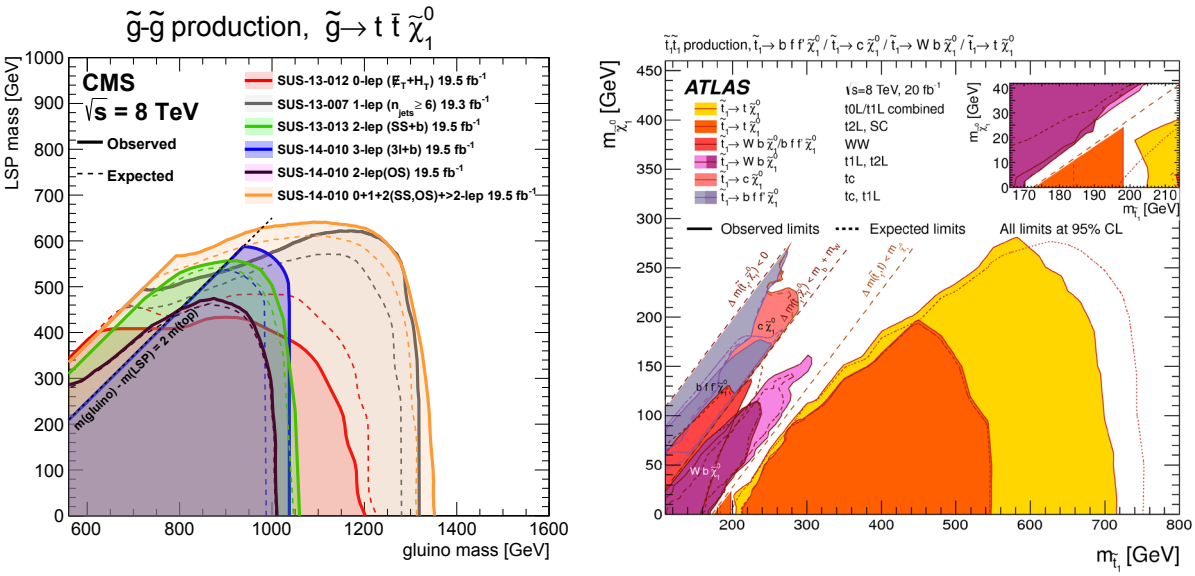

FIGURE 11. Summary plots of various search results from gluino-mediated stop production (left) from [3] and direct stop production (right) from [4].

An alternative approach to assess the overall state of the SUSY search program is to consider full SUSY models. A popular approach is to utilize the parameterized minimal supersymmetric standard model (pMSSM) which parameterizes SUSY with 19 free parameters after making several experimentally well motivated assumptions. Many SUSY signal points are then generated based on scanning the 19 parameters to provide a set of possible SUSY mass spectra.

In [14] and [15] scans of pMSSM points are compared to a variety of results from the CMS and ATLAS collaborations, respectively. The points are then classified into those which are excluded by at least one of the searches and those that remain viable. The fraction of excluded points for gluino and slepton production from [15], for example, are show in Fig. 12. As expected, the lower mass points are more likely to be excluded and the results generally compare well to the simplified model results. However, certain of the pMSSM points that remain allowed can be studied in further detail to understand how to better design searches to capture sensitivity to these points in future searches.

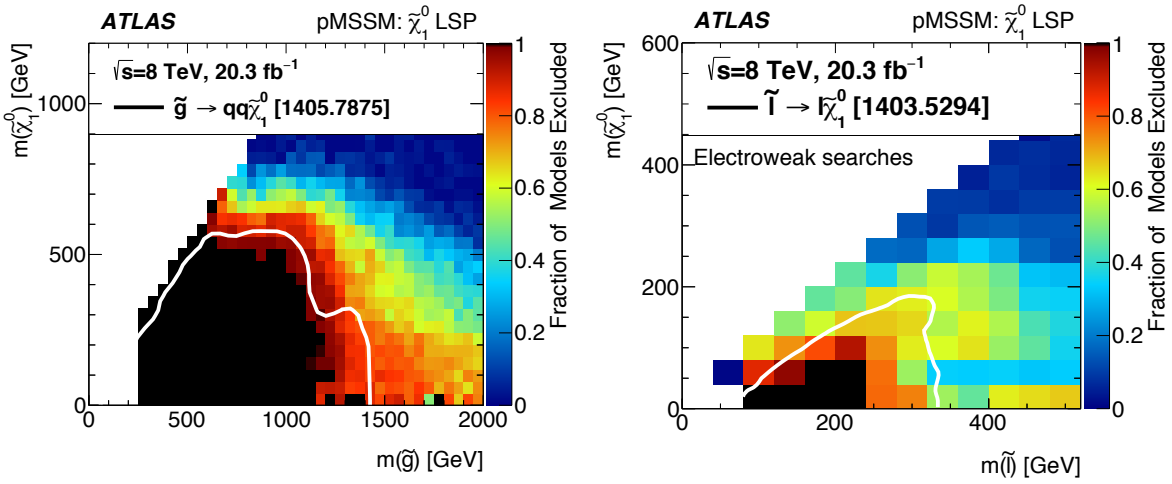

FIGURE 12. Results for gluino (left) and slepton (right) exclusions from the pMSSM parameter scan points. Taken from Ref. [15].

PREPARATION FOR 13 TeV

The year 2015 saw the restart of the LHC after "long shutdown 1" in 2013-2014. The shutdown allowed for the successful retuning of the LHC to achieve a record collision energy of $\sqrt{s}$ = 13 TeV. At the time of the LHCP conference, each experiment had collected a few dozen pb^{-1} worth of 13 TeV data, which was used to commission the 13 TeV SUSY searches [16, 17, 18]. In this section, results of these commissioning exercises are shown.

Figure 13 shows the trigger efficiencies as measured in 13 TeV data for triggers based on HT and MET. Such triggers are utilized for hadronic SUSY searches. Figure 14 shows distributions of sensitive SUSY variables in single lepton control samples compared to MC simulation. In the left plot, a sample with no b-tagged jets is selected to test the modeling of the W + jets background, while in the right plot, a single muon sample is selected and visible energy templates are used to predicted the hadronic tau background. In both cases, the 13 TeV is is observed to be in good agreement with expectation from MC.

In Fig. 15 (left) dilepton control sample events are plotted compared to simulation to test the understanding of Z + jets background prediction techniques. In Fig. 15 (right), the distribution of MET/ $\sqrt{\text{HT}}$ is plotted comparing 13 TeV data and MC simulation for multijet events, showing good understanding of the QCD multijet background prediction methods. Figure 16 shows 13 TeV data commissioning results for the same-sign dilepton search. In the left plot, the isolation distribution for identified muons is plotted, showing good agreement between data and simulation. In the right plot, the di-electron mass is shown for same-sign and opposite-sign dilepton events, which is a key ingredient in measuring the rate of wrong charge assignment in electrons.

In summary, the 13 TeV data are remarkably well understood only a short period after data taking. Both experiments are well on track for producing SUSY search results when a sufficient amount of 13 TeV is available. First results are expected based on the full 2015 dataset.

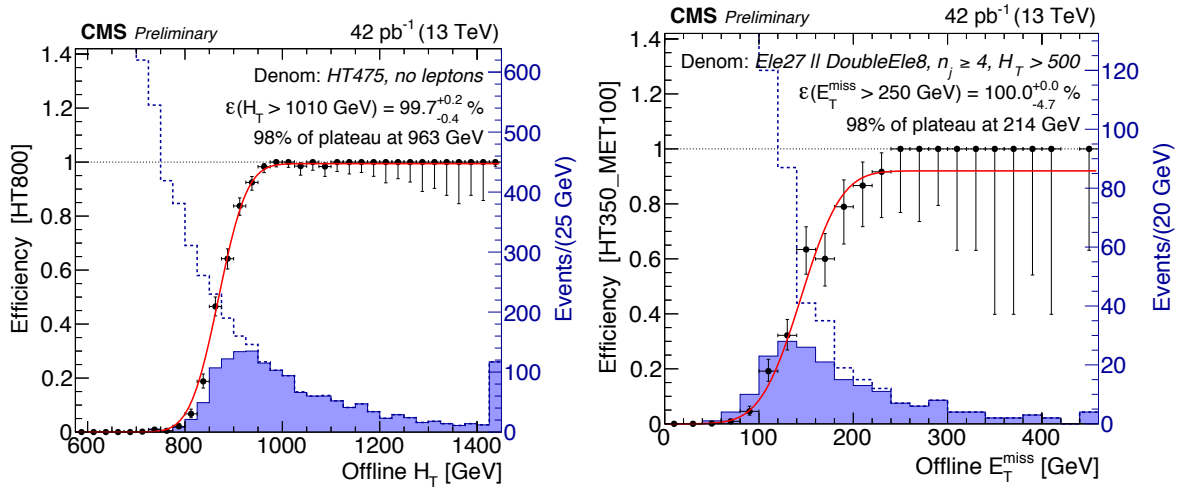

FIGURE 13. Early 13 TeV data commissioning plots for SUSY triggers based on HT (left) and MET (right). Taken from Ref. [16].

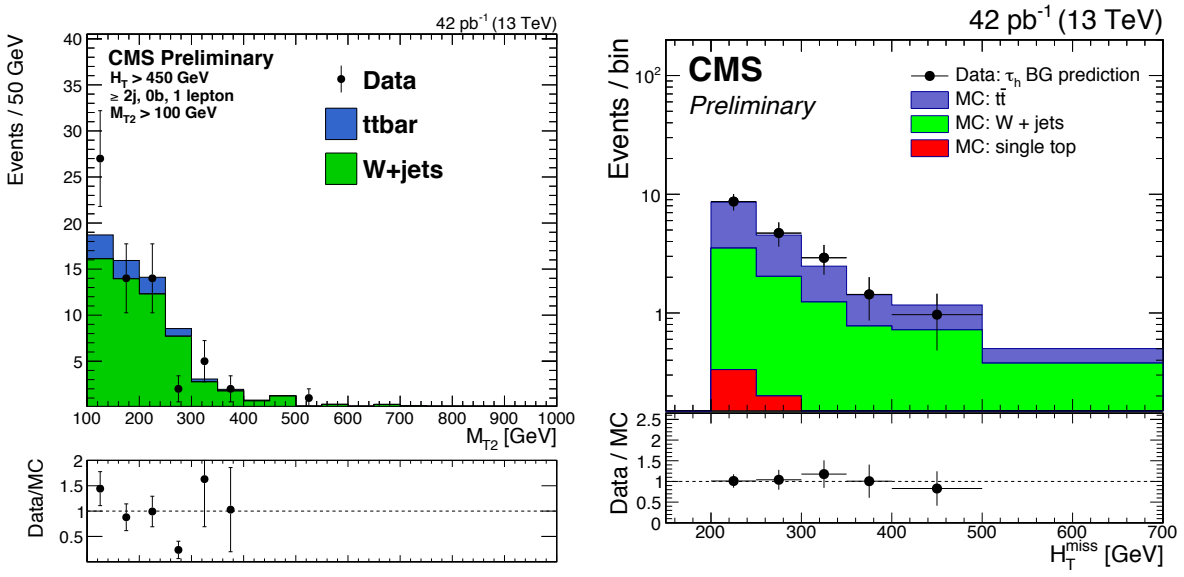

FIGURE 14. Early 13 TeV data commissioning plots for lost lepton (left) and hadronic tau (right) backgrounds for hadronic SUSY searches. Taken from Ref. [16].

CONCLUSIONS

Supersymmetry remains among the most popular extensions to the Standard Model. This talk reviews a sample of SUSY results from Run 1 of the LHC at 8 TeV. The CMS and ATLAS experiments have each produced a large number of SUSY results, with no significant deviations from Standard Model expectations yet observed. Data taking has begun for Run 2 at 13 TeV. Early commissioning results show that both experiments are on track to produce exciting new results with this data in the near future. Exciting times are ahead.

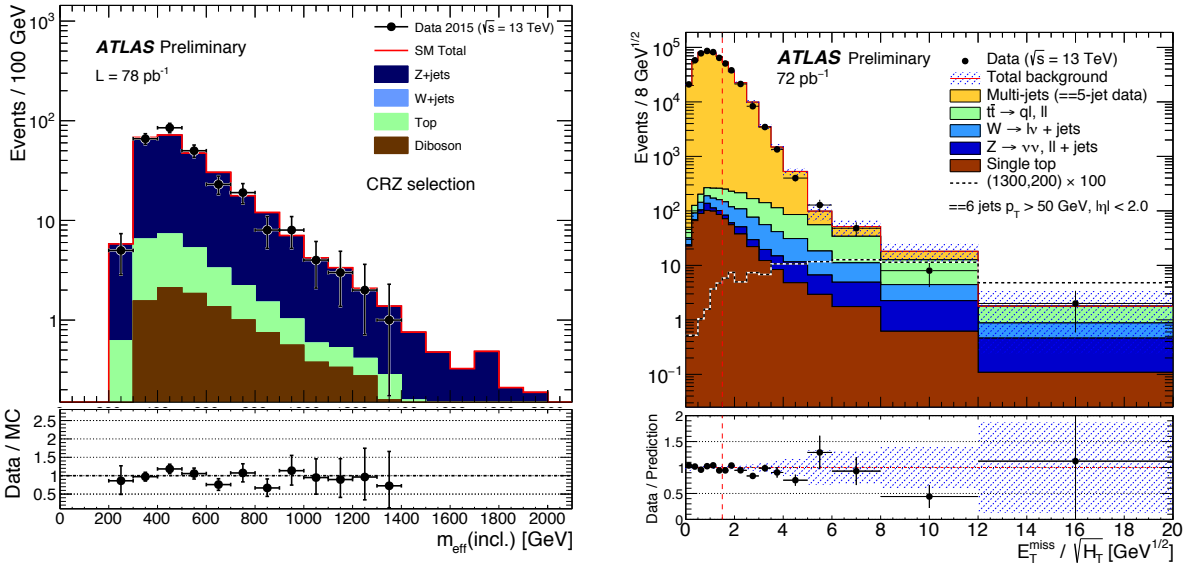

FIGURE 15. Early 13 TeV data commissioning plots for Z (left) from [17]and QCD multijet (right) from [18] backgrounds for hadronic SUSY searches.

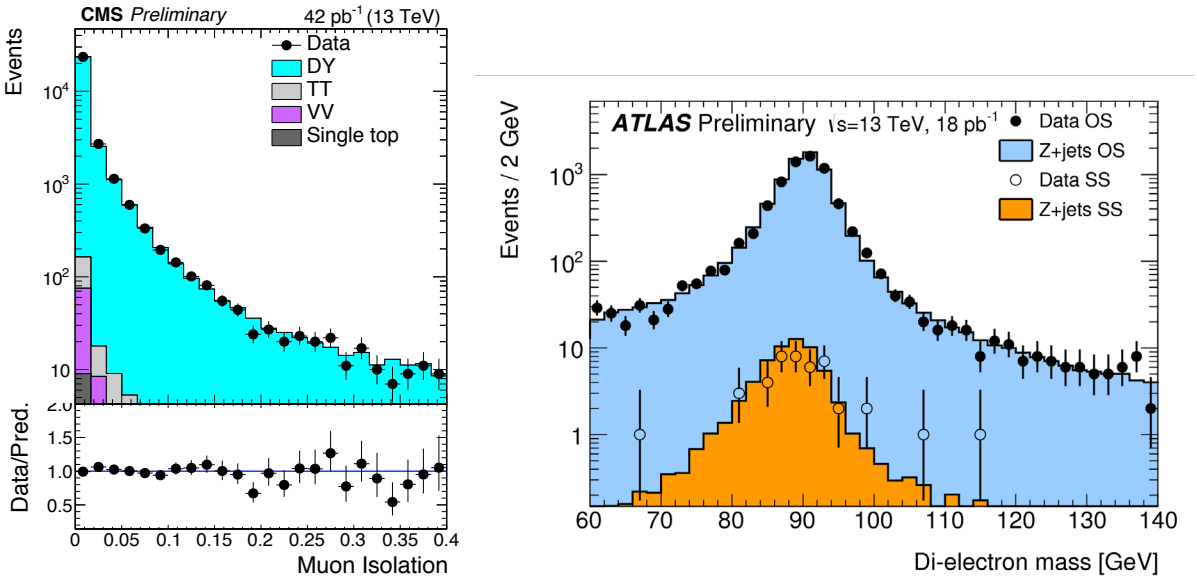

FIGURE 16. Early 13 TeV data commissioning plots for muon isolation (left) from [16] and di-electron mass (right) from [17] used to predict non-prompt and wrong charge backgrounds, respectively, in same-sign dilepton SUSY searches.

REFERENCES

[1] CMS Collaboration, JINST **3**, S08004 (2008).
[2] ATLAS Collaboration, JINST **3**, S08003 (2008).
[3] CMS Collaboration, "CMS Supersymmetry Physics Results," `https://twiki.cern.ch/twiki/bin/view/CMSPublic/PhysicsResultsSUS`.
[4] ATLAS Collaboration, "ATLAS Supersymmetry searches" `https://twiki.cern.ch/twiki/bin/view/AtlasPublic/SupersymmetryPublicResults`.
[5] CMS Collaboration, Phys. Lett. B **725**, 243 (2013) [arXiv:1305.2390 [hep-ex]].
[6] ATLAS Collaboration, JHEP **1510**, 054 (2015) [arXiv:1507.05525 [hep-ex]].
[7] CMS Collaboration], JHEP **1401**, 163 (2014) [JHEP **1501**, 014 (2015)] [arXiv:1311.6736, arXiv:1311.6736 [hep-ex]].
[8] ATLAS Collaboration, Phys. Rev. D **92**, no. 7, 072001 (2015) [arXiv:1507.05493 [hep-ex]].
[9] ATLAS Collaboration, arXiv:1509.07152 [hep-ex].
[10] CMS Collaboration, CMS-PAS-SUS-13-023, `http://cds.cern.ch/record/2044441` (2015).
[11] ATLAS Collaboration, Phys. Rev. Lett. **114**, no. 14, 142001 (2015) [arXiv:1412.4742 [hep-ex]].
[12] CMS Collaboration, CMS-PAS-SUS-14-021, `http://cds.cern.ch/record/2010110` (2015).
[13] CMS Collaboration, CMS-PAS-SUS-14-019, `http://cds.cern.ch/record/2046988` (2015).
[14] CMS Collaboration, CMS-PAS-SUS-15-010, `http://cds.cern.ch/record/2063744` (2015).
[15] ATLAS Collaboration, JHEP **1510**, 134 (2015) [arXiv:1508.06608 [hep-ex]].
[16] CMS Collaboration, "Commissioning the performance of key observables used in SUSY searches with the first 13 TeV data," CMS-DP-2015-035, `http://cds.cern.ch/record/2049757` (2015) .
[17] ATLAS Collaboration, ATL-PHYS-PUB-2015-028, `https://atlas.web.cern.ch/Atlas/GROUPS/PHYSICS/PUBNOTES/ATL-PHYS-PUB-2015-028` (2015).
[18] ATLAS Collaboration, ATL-PHYS-PUB-2015-030, `https://atlas.web.cern.ch/Atlas/GROUPS/PHYSICS/PUBNOTES/ATL-PHYS-PUB-2015-030` (2015).

Proceedings of the LHCP2015 Conference, St. Petersburg, Russia, August 31 - September 5, 2015

Editors: V.T. Kim and D.E. Sosnov

Status of Beyond Standard Model Higgs searches at the LHC

P. BRÜCKMAN DE RENSTROM*

Institute of Nuclear Physics, Polish Academy of Sciences, ul. Radzikowskiego 152, 31-342, Poland

pawel.bruckman.de.renstrom@cern.ch

On behalf of the ATLAS and CMS Collaborations

Abstract. An overview of searches for Beyond Standard Model physics phenomena in the Higgs sector from the ATLAS and the CMS experiments in LHC Run 1 is given. Both indirect limits as well as direct searches for various extensions of the scalar sector are covered. The review presents a wide scope of results and concentrates on the most recent analyses.

INTRODUCTION

The Brout-Englert-Higgs (BEH) electroweak (EW) symmetry breaking mechanism[1, 2] is, within the Standard Model (SM), a theory described by only two parameters defining the shape of the scalar field potential. The vacuum expectation value of the Higgs field is fixed by the measured masses of the electroweak gauge bosons, leaving the model with only one free parameter, which determines the mass of the unique physical state predicted by the model, the neutral Higgs boson scalar.

July 4th, 2012 brought a breaking news of a discovery of a Higgs-like particle which coupled to gauge bosons [3, 4]. By now, the BEH mechanism has been firmly confirmed via precision measurements of the Higgs boson mass, its couplings to electroweak bosons and heavy fermions (t, b quarks and τ lepton) as well as its most likely J^{CP} quantum numbers.

Fixing the model by measuring the Higgs boson mass, completes the SM electroweak symmetry breaking scenario. Couplings to all SM particles, proportional to their mass for fermions and to their mass squared for bosons, are exhaustively determined by the model. So far all measured properties of the discovered scalar state are consistent with the Higgs boson particle predicted in the Standard Model. However, this alone does not rule out variety of Beyond Standard Model (BSM) scenarios. Our current quest includes questions whether the observed Higgs boson state is the only one or maybe there exists an extended scalar sector, whether the Higgs boson is responsible for the entire mass of the SM particles and, finally, whether it is a fundamental particle. In order to answer these questions one has to select models of interest. The most popular ones include an additional EW singlet [5, 6], the whole family of Two Higgs Doublet Models (2HDM) [7, 8], notably the Minimal Supersymmetric Standard Model (MSSM) [9, 10, 11, 12, 13], Next to MSSM (NMSSM) [14, 15, 16], composite Higgs [17, 18], etc. All above allow for SM-like light Higgs phenomenology with smaller or larger modifications to the couplings. Furthermore, most models predict additional, usually heavier, states in the scalar sector.

The Higgs boson mass measurements from the ATLAS [19] and CMS [20] experiments, in fully reconstructed $H \to ZZ \to 4l$ and $H \to \gamma\gamma$ channels, are now combined. The resulting LHC average value is $m_H = 125.09 \pm 0.21(\text{stat}) \pm 0.11(\text{syst})$ GeV[21]. The measured mass puts firm constraints on certain BSM scenarios, notably the Minimal Supersymmetric Standard Model (MSSM), due to radiative corrections necessary to elevate the physical mass of the lightest Higgs boson above the mass of the Z boson [11].

The ATLAS and CMS determination of the Higgs couplings to SM particles was first announced at this conference [22]. The combined results include Higgs couplings to W and Z bosons, t, b and τ fermions, as well as an upper limit for the muon coupling. The latter allows to establish that lepton couplings to the Higgs boson are not universal, but rather consistent with being proportional to the mass. The combination is based on the measured $\sigma \times \text{BR}(H \to XX)$

*supported in part by the Polish Government NCN grant 2012/07/B/ST2/03680

for all investigated Higgs decay modes, i.e. $H \to ZZ$, $H \to \gamma\gamma$, $H \to WW$, $H \to b\bar{b}$, $H \to \tau\tau$ and $H \to \mu\mu$. Additional event categorization (number of jets, b-tagged jets, leptons, etc.) allows to distinguish between different Higgs boson production modes that is gluon-gluon fusion (ggF), vector boson fusion (VBF), production associated with electroweak bosons (WH, ZH), and production in association with a top quark pair (ttH). Available theoretical calculations (at NNLO or NLO) allow to infer effective couplings of the Higgs particle to different SM particle species. As the Higgs boson decay to $t\bar{t}$ is not kinematically allowed, the coupling to the top quark is obtained indirectly from the signal strength of the ggF process involving the top quark loop in the production vertex. Measurements of the couplings constitute a stringent probe of various BSM Higgs scenarios. So far, all measured values remain consistent with their SM predictions and follow the expected mass scaling.

The same decay channels were used to determine the overall strength of the Higgs boson signal, μ, defined as the ratio of the actually observed signal event rate to the one predicted by the Standard Model. The combined result yields $\mu = 1.09^{+0.11}_{-0.10}$ where error includes statistical and systematic experimental uncertainties as well as systematic uncertainties on theoretical predictions for both the signal and the underlying background. The observed signal strength being nine percent above the predicted value, still remains compatible with the latter within its uncertainty. It has to be noted, that the upward fluctuation strengthens exclusion limits for many BSM scenarios, which predict reduced couplings to the presumably observed light neutral Higgs boson state.

Both experiments also performed analyses probing multiple J^{CP} scenarios of the observed Higgs boson using the kinematic distributions of the decay products. The $ZZ \to 4l$ decay channel gives access to the full kinematics of the final state providing the most stringent constraints. The $WW \to lvlv$ decays retain partial sensitivity via variables such as the invariant mass, transverse momentum or the transverse plane opening angle of the lepton pair and the transverse mass of the leptons plus the missing momentum. The $\gamma\gamma$ decays allow to analyze the di-photon angular distribution in the Collins-Soper frame. The results clearly favor the vacuum quantum numbers (0^{++}) at the 99% confidence level (CL) [23, 24].

The current experimental road-map naturally splits in two complementary approaches.

1. Precision measurements of the properties of the discovered Higgs boson state: A: production rates in different channels such as ggF, VBF, WH, ZH associated production, ttH associated production and searches for yet unobserved Higgs boson pair production (HH) or associated production (tH, bbH); B: widths of the observed decay modes ($\gamma\gamma$, ZZ^*, WW^*, bb, $\tau\tau$) and searches for rare ones ($\mu\mu$, $Z\gamma$, etc.); C: combination of these measurements to infer couplings of the Higgs to SM particles; D: spin and parity quantum numbers of the Higgs; E: searches for rare Higgs decays, such as LFV decays, invisible decays or decays to light yet unobserved particles.
2. Direct searches for new states expected within the extended Higgs sector. A: heavy neutral CP-even and CP-odd states in their decays to $\gamma\gamma$, ZZ^*, WW^*, bb, $\tau\tau$, HH, HZ and tt; B: heavy charged Higgs decaying to $\tau\nu$, tb, WZ, cs, etc.

Both approaches try to answer common questions: Are all observations consistent with the SM predictions? How much of the BSM scenario phases-space can current data exclude? Clearly, the answer is highly model dependent.

A selection of results indirectly probing the BSM Higgs sector is discussed in section entitled **Exploring the 125** GeV **Higgs**. Direct searches for additional states of the extended scalar sector are reviewed in section entitled **Direct searches for BSM scalars**.

Exploring the 125 GeV Higgs

One of the basic and model-independent integrity tests consists of fitting the parameterized dependence of the coupling scale factor, $\kappa_{f,i}$ for ferminos and $\kappa_{V,j}$ for vector bosons. For that purpose, a simple parameterisation has been proposed [25]: $\kappa_{f,i} = v\frac{m^{\epsilon}_{f,i}}{M^{1+\epsilon}}$ and $\kappa_{V,j} = v\frac{m^{2\epsilon}_{V,j}}{M^{1+2\epsilon}}$ for fermions and bosons, respectively. v denotes the SM Higgs vacuum expectation value (246 GeV). M, the "VEV parameter", and ϵ, the "mass scaling parameter" probing the strength and the mass scaling of the Higgs couplings, are free in the fit. The SM is realized for $\epsilon = 0$ and $M = v$ which give SM couplings for all particles, $\kappa_{f,i} = \kappa_{V,j} = 1$. The fit assumes same production and decay modes as predicted by the SM. The results obtained by the two collaborations are shown in Figure 1 and demonstrate exemplary agreement with the SM prediction.

One of the simplest involves addition of one scalar electroweak singlet field to the Higgs doublet of the SM, both of which acquire non-zero vacuum expectation values [5, 6]. Mixing between the singlet state and the surviving state of the doublet field results in two CP-even Higgs bosons, where h (H) is the lighter 125 GeV(heavier) of the pair. The

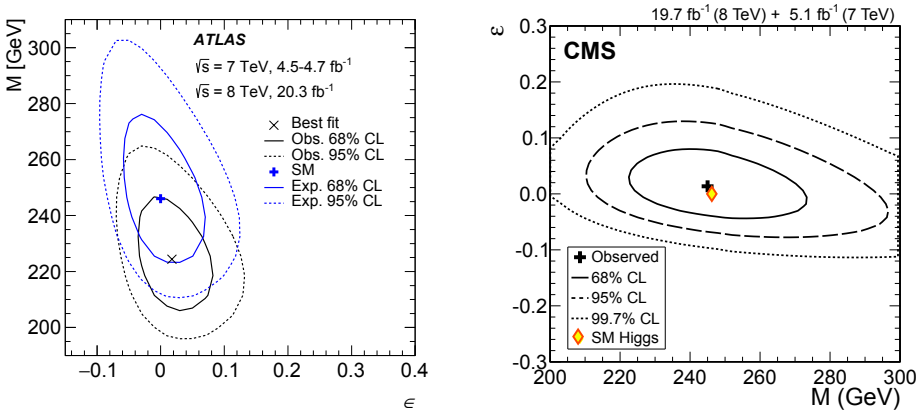

FIGURE 1. Fit to the mass scaling parameter ϵ and the VEV parameter M compared to the SM expectation from ATLAS [26] and CMS [27] Collaborations.

unitarity requirement infers that $\kappa^2 + \kappa'^2 = 1$, where κ and κ' are coupling strength modifiers relative to the SM. In particular one has $\sigma_h = \kappa^2 \times \sigma_{h,\mathrm{SM}}$. The observed Higgs boson signal strength sets a limit on the coupling strength of the singlet state to SM particles at $\kappa'^2 < 0.12$ at 95% CL, while the expected limit was 0.23. The result can be converted into the limit in the μ_H–$\mathrm{BR}_{H,\mathrm{new}}$ plane, where the parameters are the heavy Higgs signal strength and its branching to yet unobserved particles, respectively. They are related by $\mu_H = \kappa'(1 - \mathrm{BR}_{H,\mathrm{new}})$. The limit is shown on the left plot in Figure 2

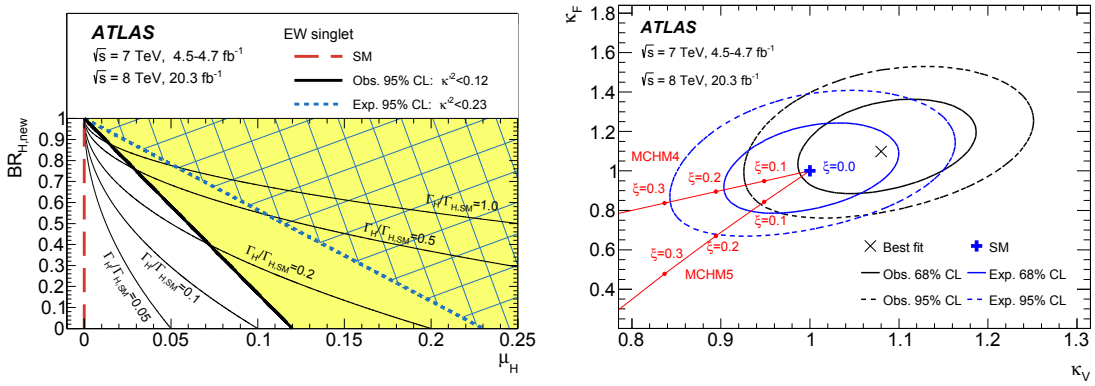

FIGURE 2. Limits on the additional Higgs singlet model (left) and the MCHM4, MCHM5 models (right) from ATLAS [26].

Another simple class of models are the Minimal Composite Higgs Models (MCHM), which represent a possible explanation for the scalar naturalness problem, wherein the Higgs boson is a composite, pseudo-Nambu-Goldstone boson rather than an elementary particle. Compositeness leads to a reduction of couplings to SM fermions and bosons which takes slightly different form, depending on specific model realization. Two most common types were considered, so called MCHM type four and five. MCHM4 [17] features a common scaling for fermions and bosons $\kappa = \kappa_V = \kappa_F = \sqrt{1-\xi}$ while MCHM5 [17] assumes $\kappa_V = \sqrt{1-\xi}$ and $\kappa_F = (1-2\xi)/\sqrt{1-\xi}$. In both variants $\xi = v^2/f^2$, where v is the Higgs VEV and f is the compositeness scale. The SM phenomenology is recovered under $f \longrightarrow \infty$. The right plot in Figure 2 shows the resulting limit together with its expected bounds. For both MCHM4 and MCHM5 ATLAS is able to exclude compositeness at a scale below some 700 GeV.

Two Higgs Doublet Model (2HDM) is a generic class of models implementing a second Higgs doublet [7, 8]. Depending on the choice of couplings to SM particles there are four distinct realizations fulfilling the Glashow-Weinberg condition [28]:

Type I	One doublet couples to vector bosons, the other couples to fermions.
Type II	One doublet couples to up-type quarks,the other to down-type quarks and leptons.
Lepton-specific	Couplings to quarks as in the Type I model and to leptons as in Type II.
Flipped	Couplings to quarks as in the Type II model and to leptons as in Type I.

Notably, Type II is most commonly considered as it is realized by the Supersymmetry. Generic 2HDM models are conventionally parameterized by $\tan\beta = V_2/V_1$, the ratio of the VEV of the two doublets, and $\cos(\beta-\alpha) = g^{\mathrm{2HDM}}_{HVV}/g^{\mathrm{SM}}_{HVV}$, the ratio of the heavy CP-even Higgs state coupling to electroweak vector bosons. Unitarity additionally implies that $v_1^2 + v_2^2 = v^2 \approx (246\ \mathrm{GeV})^2$. The SM phenomenology is recovered in the limit of $\cos(\beta-\alpha) \longrightarrow 0$, called "alignment". Figure 3 shows the observed and expected limits on parameters of 2HDM models of Type I and Type II resulting from the ATLAS measurements of 125 GeV couplings. The results clearly favor the scenario of near alignment leaving,

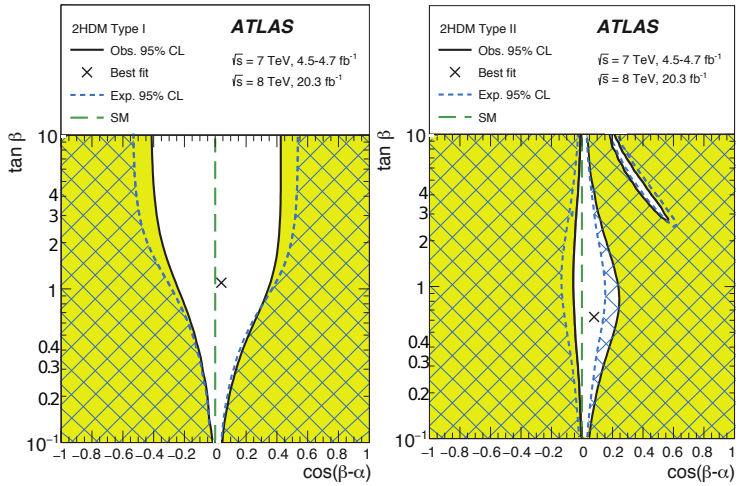

FIGURE 3. Limits on the 2HDM models of Type I (left) and Type II (right) from ATLAS [26]. The unconstrained petal on the right of Type II exclusion corresponds to sign-flipped couplings to down-type fermions (τ, b).

however, phase-space for new physics.

The actually observed Higgs boson of 125 GeV, when assumed to be the light Higgs state of the Minimal Supersymmetric Standard Model (MSSM), h, can provide valuable constraints via the radiative corrections to its mass. These may become restrictive under further assumptions. In the hMSSM model the dominant top and stop radiative corrections to h mass are used to infer its effective couplings [11, 12, 13]. Within the model, the couplings depend exclusively on the mass of the CP-odd Higgs state m_A and $\tan\beta$ and follow from the diagonalization of the light and the heavy CP-even Higgs mass matrix. Results overlaid with various exclusions from direct searches are shown on the left plot of Figure 4. ATLAS is able to exclude $m_A < 370$ GeV (expected 310 GeV) uniformly in a wide range of $\tan\beta$.

Apart from the limits inferred from the observed Higgs boson coupling strength, a very attractive source of information is offered by searches for Higgs decays which are highly suppressed in the SM. In the following, we report on two such searches, a search for invisible Higgs decays and a search for lepton flavor violating (LFV) decays of the Higgs.

Invisible decays ($H \to$ inv.) of the Higgs boson have been studied carefully by both experiments. This includes: a) vector boson fusion (VBF) with subsequent $H \to$ inv. Main signature involves two jets with a large pseudorapidity gap and a large invariant di-jet mass, accompanied by large missing transverse momentum ($E_{\mathrm{T}}^{\mathrm{miss.}}$) [29, 30]; b) ZH associated production, with $Z \to ll$, $Z \to b\bar{b}$ and $H \to$ inv. tagged by two leptons with opposite sign charge and same flavor (OSSF) (e or μ) forming the Z invariant mass together with a large $E_{\mathrm{T}}^{\mathrm{miss.}}$ [31, 32]; c) VH ($V = W$ or Z), where $V \to jj$ and $H \to$ inv.. The signature is the dijet mass consistent with m_V and a large $E_{\mathrm{T}}^{\mathrm{miss.}}$ [33]. The CMS limit as a function of the Higgs mass from the VBF analysis is shown in Figure 5. For the 125 GeV Higgs the limit is $\mathrm{BR_{inv}} < 0.5$ at 95% CL (0.40 exp.) and when combined with the ZH analysis yields $\mathrm{BR_{inv}} < 0.47$ at 95% CL (0.35 exp.). ATLAS, on top of direct combined limit from VBF, ZH and VH analyses, claims a more restrictive limit which also takes into account the visible widths to $\gamma\gamma$, ZZ^*, WW^*, $Z\gamma$, bb, $\tau\tau$, $\mu\mu$. The combined result yields $\mathrm{BR_{inv}} < 0.25$ at 95% CL (0.27 exp.). The limit can be further converted to a constraint on couplings to hypothetical

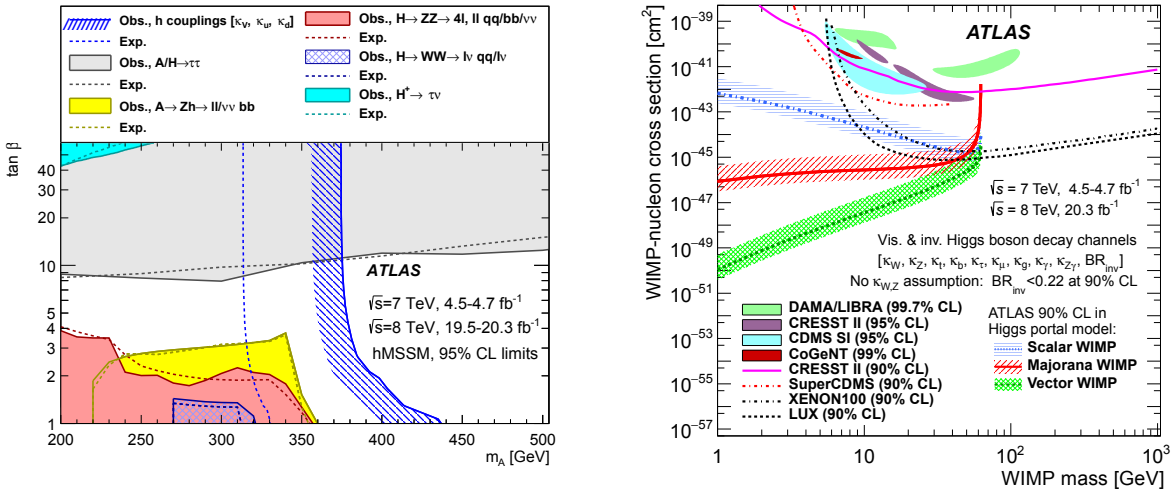

FIGURE 4. ATLAS exclusion limits on the hMSSM model inferred from radiative corrections to the mass of the observed 125 GeV h, overlaid with number of exclusions from direct searches (left). Limits on the WIMP-nucleon scattering cross-section as a function of WIMP mass inferred from the measured $\mathrm{BR_{inv}}$ of the 125 GeV Higgs boson. Limits from direct detection experiments are overlaid (right). [26]

weakly interacting massive particles (WIMP) [34, 35] for either scalar, Majorana fermion or vector particle hypothesis. These are then used to calculate the cross-section for WIMP-nucleon scattering, to be directly compared with direct dark matter (DM) detection experiments. The motivation arises from the models which assume the Higgs to be the only mediator between the SM particles and the WIMPs responsible for DM. The limits on the cross-section as a function of the assumed WIMP mass is shown on the right plot of Figure 4. The indirect limit has a natural threshold of $2m_{\mathrm{WIMP}} < m_H$. Nonetheless, the derived exclusion is highly competitive with all existing direct detection results in the entire accessible mass range (overlaid on the plot).

LFV decays of the Higgs are highly suppressed in the SM due to renormalizability requirement. Possibility of sizeable LFV is, however, predicted in various BSM models (2HDM, composite Higgs, Randall Sundrum warped extra dimensions (RS), etc.). Indirect limits on $\mathrm{BR}(H \to \tau\mu)$ come from searches for $\tau \to \mu\gamma$ decays and are weak, O(10%). CMS searched for $H \to \tau\mu$ in hadronic and electronic τ decay modes [36]. The combined best fit branching fraction yields $0.89^{+0.40}_{-0.37}\%$ and represents an excess of 2.5σ. ATLAS performed similar search but only in the $\tau_{\mathrm{had}}\mu$ decay channel which gave the best fit branching fraction of $0.77 \pm 0.62\%$ which allowed to put an upper limit of 1.85% at 95% CL [37]. LHC Run 2 will certainly follow up on these measurements.

This brings us to the last topic selected for this section i.e. looking for the Higgs boson pair production. In SM, the non-resonant double-Higgs (HH) production is expected e.g. in the s-channel due to the Higgs self-coupling. However, current experimental sensitivity is still far from the SM expected rates. An observation of signal would mean an enhanced cross-section and clearly sign BSM physics. The enhancement varies from up to three for composite Higgs models, through additional singlet model (up to 15) to 2HDM models predicting a factor up to 50. CMS has recently reported two analyses looking for Higgs pair production in $bbbb$ and $bb\gamma\gamma$ final states. The earlier, [38], presents a model independent search using four b-tagged jets. The main background originating from the QCD multi-jet events is estimated from data using control regions. The latter, [39], looks for two b-tagged jets and a pair of photons. Both analyses report limits up to mass of 1.1 TeV of the resonant state decaying to a pair of 125 GeV Higgses. No significant deviation from the SM background was observed. ATLAS has just published [40] a combination of recent search in $bbbb$ channel [41] with searches in $bb\tau\tau$, $bb\gamma\gamma$ and $WW\gamma\gamma$. The analyses assume SM decays of the light Higgs state h. The combined limit on the $\sigma(gg \to H) \times \mathrm{BR}(H \to hh)$ is shown on the left plot of Figure 6. The step at $m_H = 500$ GeV is due to high sensitivity of the $bbbb$ analysis which probes the region starting from 500 GeV. The observed limit is consistent with the expected one over the full Higgs boson mass range considered. The right plot shows an example exclusion for the hMSSM model resulting from the observed cross-section limit. There is currently no exclusion power for high $\tan\beta$ due to the suppressed $\mathrm{BR}(H \to hh)$. The analysis also provides an upper limit on

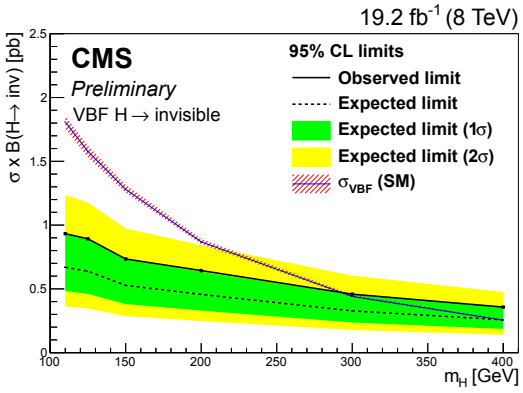

FIGURE 5. CMS exclusion limits on the invisible decays of the SM-like Higgs boson [30].

the non-resonant cross-section which yields $\sigma(gg \to hh) < 0.69$ pb (0.47 pb exp.), which should be compared to the SM prediction of 9.9 ± 1.3 fb.

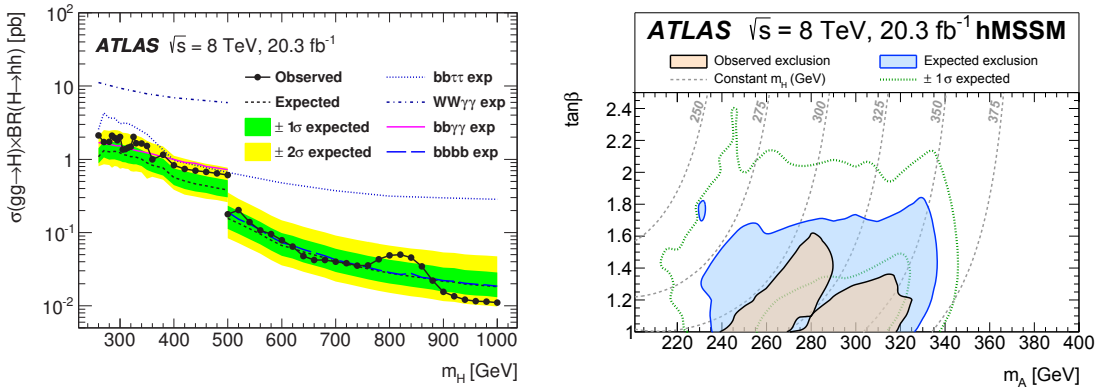

FIGURE 6. ATLAS combined limit on the $\sigma(gg \to H) \times \mathrm{BR}(H \to hh)$ from $bbbb$, $bb\tau\tau$, $bb\gamma\gamma$ and $WW\gamma\gamma$ analyses (left) and an example exclusion inferred on hMSSM (right) [40].

Before closing, let us also mention that the statistical sensitivity of both LHC experiments becomes sufficient to start studying differential cross-sections for Higgs boson production [42, 43] which can be source of valuable constraints for various BSM scenarios.

Direct searches for BSM scalars

Direct searches are motivated predominantly by the phenomenology of the 2HDM, notably the MSSM or its derivatives but can also provide valuable limits on other BSM scenarios like electroweak Higgs singlet, triplet model, etc. Searches include both CP-even and CP-odd heavy Higgses as well as charged Higgs bosons, which would very clearly sign the extended scalar sector. In this context, *heavy* means any new state with mass higher than the discovered 125 GeV boson.

CMS has recently published a comprehensive set of results of searches for the CP-even Higgs state H in its decay to ZZ or WW [44]. It encompasses variety of final states: $WW \to l\nu l\nu$, $l\nu qq$, $ZZ \to 2l2l$, $2l2q$, $2l2\nu$. The search is rather generic and covers the mass range from around 150 GeV up to one TeV. The left plot in Figure 7 shows the limit at the 95% CL on the observed cross-section normalized to the cross-section for the SM Higgs of the same mass σ_{SM}. Individual channels as well as the combined limit and its expectation are shown. The current combined sensitivity is better than the rate expected from the SM Higgs over the entire considered mass range. This allows to

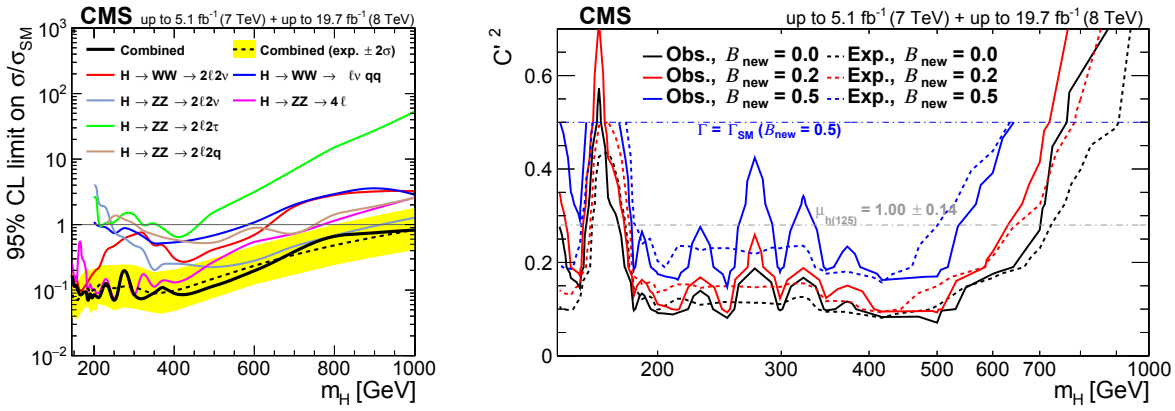

FIGURE 7. 95% CL limit on the cross-section for H production normalized to the cross-section for the SM Higgs of the same mass (left).The expected limit with $\pm 2\sigma$ error band is overlaid. 95% CL exclusion limit on the additional electroweak singlet model (right). B_{new} denotes the assumed decay branching to new particles. [44]

put exclusion limits on e.g. the additional electroweak singlet model as shown on the right of Figure 7. The limit is given in terns of C'^2, which is exactly equivalent to κ'^2 introduced in previous section in the context of the singlet model. Exclusion depends on the assumed branching fraction of the heavy Higgs boson to new particles B_{new}. Best limit, obtained assuming only SM decays ($B_{\text{new}} = 0$), excludes $C'^2 > 0.2$ at 95% CL up to nearly 700 GeV. It is worth noting, that the Higgs signal strength observed by CMS ($\mu_{\text{h(125)}} = 1.00 \pm 0.14$) excludes indirectly C'^2 above 0.28 regardless of the heavy state mass.

Similar results are reported by the ATLAS Collaboration. The $H \to ZZ$ search [45] considered $2l2l$, $2l2q$, $2l2\nu$ final states and reports limits for H masses up to 1 TeV which are then interpreted in terms of 95% exclusion limits on 2HDM $\cos(\beta - \alpha)$ vs. $\tan\beta$ parameter space. The search in the $H \to WW$ channel [46] involves $lvl\nu$, $lvqq$ final states and reports limits for H masses up to 1500 GeV. Both analyses optimized their sensitivity separately for the ggF and VBF production. Two example cross-section limits as a function of H mass are presented in Figure 8. The left plot shows the limit on the $\sigma \times \text{BR}(H \to ZZ)$ from the ggF analysis while the right plot shows the limit on the $\sigma \times \text{BR}(H \to WW)$ from the VBF analysis. More generally, all obtained limits are consistent with the expected ones over the entire range of considered H mass.

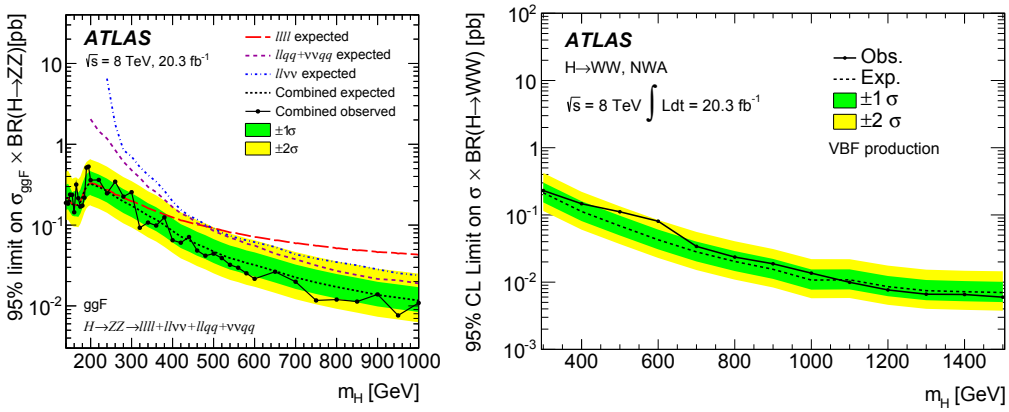

FIGURE 8. 95% CL limit on the cross-section times branching fraction for $H \to ZZ$ production via ggF [45] (left) and 95% CL limit on the cross-section times branching fraction for $H \to WW$ production via VBF [46] (right). The expected limit with one and two sigma error band is overlaid.

Another generic type of study is a search for a heavy state decaying into two photons. CMS has recently reported

results on $X \to \gamma\gamma$ search covering the mass range from 150 GeV to 850 GeV [47]. Both narrow and wide mass resonances are considered. Additionally, results are reported separately for spin 0 and spin 2 hypotheses. An example limit for spin 0 narrow hypothesis is shown in Figure 9. None of the four variants of the search reveals any significant deviation from the SM expectation. ATLAS published similar search [48] and observed no significant excess of events

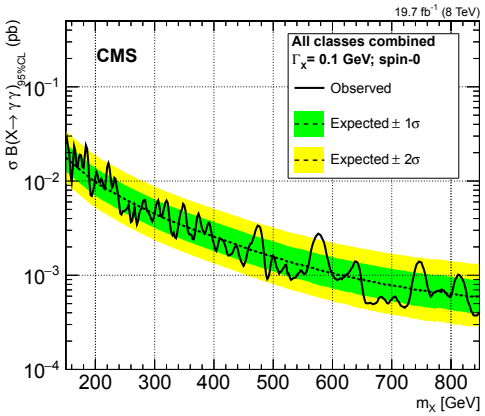

FIGURE 9. 95% CL limit on $\sigma \times \mathrm{BR}(X \to \gamma\gamma)$ for narrow spin 0 resonance hypothesis [47]. The expected limit with one and two sigma error band is overlaid.

above the SM background.

Finally, interesting exclusions on the MSSM type of models can be derived from searching for heavy Higgs boson in its decays to down-type fermions. Due to high mass and hence large coupling, $b\bar{b}$ and $\tau^+\tau^-$ final states are of main interest. Couplings to down-type fermions are enhanced in MSSM for high values of $\tan\beta$. This is why signal limits to these final states can constrain the high $\tan\beta$ part of the MSSM parameter space.

A nice probe for Higgs boson coupling to b quarks comes from CMS, which performed a generic search for a boson produced in association with a b-quark and subsequently decaying into a $b\bar{b}$ pair. The signature of three b-tagged jets is used to put limit on $\sigma(pp \to b\Phi + X) \times \mathrm{BR}(\Phi \to b\bar{b})$ in the wide range of Φ masses from 100 to 900 GeV [49]. The results are shown on the right plot of Figure 10 together with the limit expected in absence of the signal. The two are in good agreement over the entire mass range. This has been converted into 95 % CL limits on the

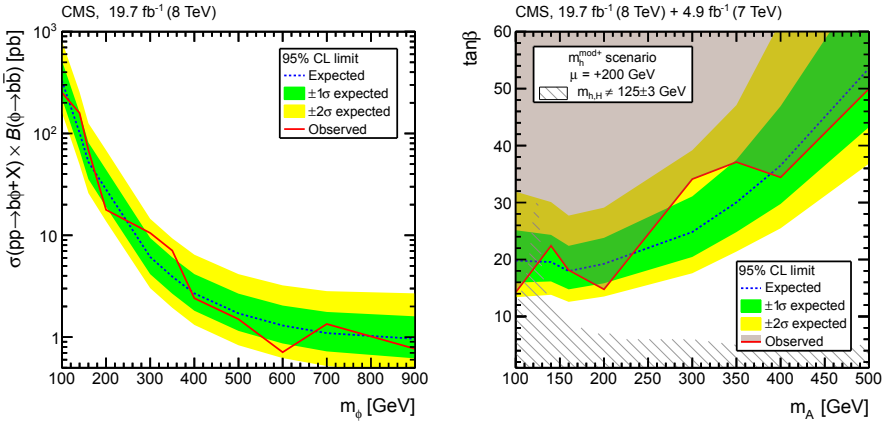

FIGURE 10. 95% CL limits on $\sigma(pp \to b\Phi + X) \times \mathrm{BR}(\Phi \to b\bar{b})$ (left) and on the m_A–$\tan\beta$ plane for the $\mathrm{m_h^{mod+}}$ scenario (right). [49]

MSSM models. The right plot shows the exclusion inferred on the $\mathrm{m_h^{mod+}}$ scenario on the m_A–$\tan\beta$ plane. Values of $\tan\beta > 20$ are excluded for low m_A masses (< 250 GeV) with the exclusion rising to 50 around $m_A = 500$ GeV.

Both experiments extensively searched for h, H, A neutral scalars decaying into a pair of τ leptons [50, 51], beyond the experimentally established boson of mass 125 GeV. Three τ decay mode combinations were used in

both cases, the $\tau_e\tau_\mu$, $\tau_{\rm lep}\tau_{\rm had}$ and $\tau_{\rm had}\tau_{\rm had}$. CMS additionally searched in the $\tau_\mu\tau_\mu$ channel and used event categories with higher multiplicity of b-jets in order to probe for $bb\Phi$ associated production. None of the searches observed a significant deviation from the SM background prediction. This allowed to put 95% CL exclusion limits on MSSM scenarios. Figure 11 shows limits on the m_A–tanβ plane for the $m_h^{\rm mod+}$ scenario obtained by the two experiments.

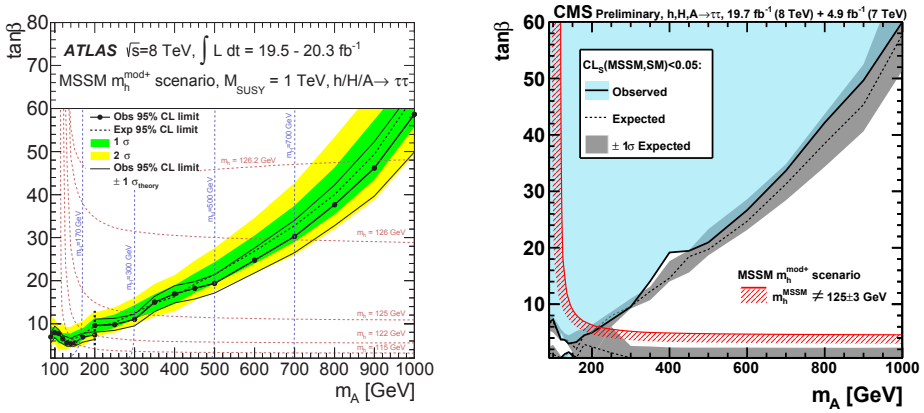

FIGURE 11. 95% CL exclusion limits on m_A–tanβ plane for the $m_h^{\rm mod+}$ scenario from ATLAS [50] (left) and CMS [51] (right) searches for $h, H, A \to \tau^+\tau^-$.

A natural way to look for 2HDM signatures is searching for cascade decays of the CP-odd state A to the lightest h and a Z boson. Such searches have been performed by both the ATLAS [52] and the CMS [53, 54] Collaborations, yielding no evidence for BSM signal. Here, we report on a recent, analysis from the CMS Collaboration, which performed a generic search, allowing for any mass hierarchy, for either $H \to AZ$ or $A \to HZ$, with subsequent leptonic decay of the Z boson ($Z \to ll$, $l = e, \mu$) and the lighter Higgs boson decaying to a pair of either τ leptons or b quarks ($A/H \to b\bar{b}, \tau^+\tau^-$) [55]. Such decays are expected irrespective of possible *alignment* and are therefore complementary to the indirect searches reported in the previous section. All combinations of leptonic and hadronic τ decays were considered. Figure 12 shows an example pair of exclusion plots. The left figure gives the 95% CL limit

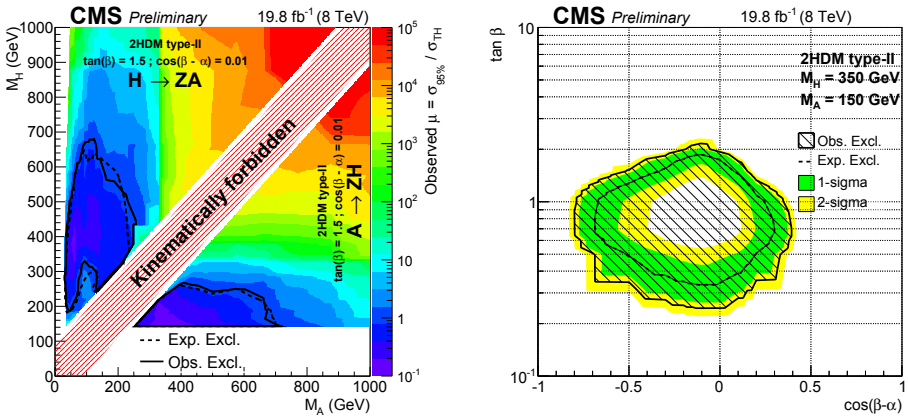

FIGURE 12. Left: 95% CL exclusion limits on $\rm M_A - M_H$ plane from a generic search for the cascade decay $H/A \to A/HZ$ with subsequent $Z \to ll$, $l = e, \mu$ and $A/H \to b\bar{b}, \tau^+\tau^-$. Right: a resulting exclusion limit on the cos$(\beta - \alpha)$–tanβ plane for an example choice of $\rm M_A$ and M_H. [55]

on the observed signal strength $\mu = \sigma_{95\%}/\sigma_{\rm TH}$ on the $\rm M_A - M_H$ plane. Both the expected and observed limits are indicated, showing a good agreement. The diagonal band is kinematically forbidden in the presence of an on-shell Z produced in the decay. The $\rm M_H$ is truncated, representing the lower mass limit corresponding to the observed 125 GeV Higgs boson. Sensitivity of the analysis drops rapidly when the $t\bar{t}$ decay channel for the lighter Higgs state opens. On

the other hand, highly boosted topologies, expected for large mass difference, suffer from reconstruction inefficiencies. The right plot in Figure 12 demonstrates that interesting exclusion on the $\cos(\beta-\alpha)$–$\tan\beta$ plane can be inferred under given M_A, M_H mass assumptions.

Existence of a charged scalar would spectacularly sign BSM physics. A charged state is predicted in models with more than one Higgs doublet, notably in Supersymmetry. In the context of MSSM, $H^+ \to \tau\nu$ dominates the charged Higgs decay for $m_{H^+} < m_t$ and remains significant in a large range of masses for high $\tan\beta$. For low $\tan\beta$ $H^+ \to tb$ dominates if $m_{H^+} > m_t$. Channels searched for comprise $\tau_{\rm had}\nu$, $\tau_{\rm lep}\nu$ with accompanying $t \to l\nu b$, tb, cs, and WZ. The latter was considered in the context of Higgs Triplet Model, where such a vertex is allowed at the tree level. Here, we report on results for $H^+ \to \tau\nu$ decay which is a flagship channel for the charged Higgs search at low and intermediate masses. For $m_{H^+} < m_t$ the search is done in $t\bar{t}$ events where one of the top quarks decays to a b quark emitting a H^+. At higher masses, the associated production with the top is assumed. Search for an excess in the $\tau_{\rm vis.} - E_{\rm T}^{\rm miss}$ transverse mass gives the cross-section limits which are subsequently converted into exclusion on the $m_{H^+} - \tan\beta$ parameter plane. An example exclusion obtained by CMS is shown in Figure 13 for the two H^+ mass ranges considered [56].

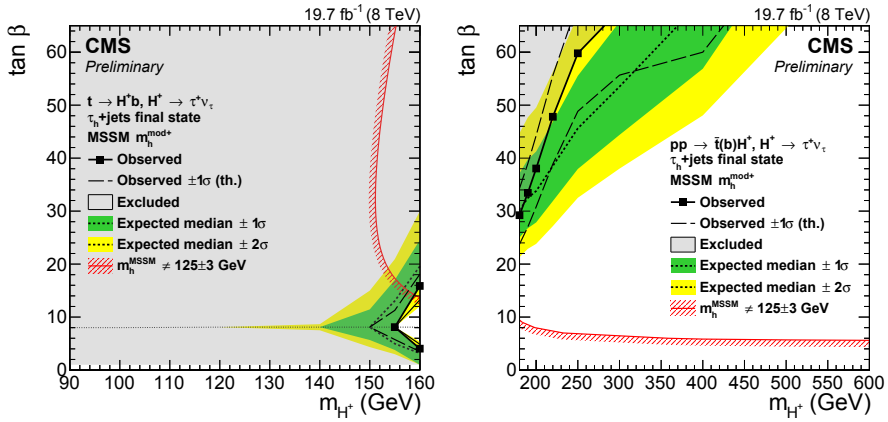

FIGURE 13. 95% CL exclusion limits on m_H^+–$\tan\beta$ plane for the $m_h^{\rm mod+}$ scenario from searches for $H^+ \to \tau\nu$ decays [56]. The light Higgs ($m_{H^+} < m_t$) and the heavy Higgs ($m_{H^+} < m_t$) limits are shown on separate plots. The red delimiting line indicates the region excluded within the model by the mass of the observed light neutral Higgs ($m_h = 125 \pm 3$ GeV).

The exclusion is slightly weaker than the expected limit for masses around 250 GeV, but the excess of events is not significant. The sensitivity reported by the ATLAS Collaboration [57] is very similar and the observed exclusion limit is consistent with the expected one for the entire mass range considered. A new paper has recently emerged from CMS combining searches in $\tau\nu$ and tb channels [58]. It is covered in detail by another article in this volume [59].

A more exotic scenario has been studied by ATLAS in the $H^+ \to WZ$ channel [60]. The charged Higgs couples to WZ at tree level in the Georgi-Machacek Higgs Triplet Model (GMHTM) [61]. This is why VBF has been assumed as the H^+ production. The $H^+ \to WZ$ is searched in the leptonic decay of the Z and hadronic decay of the W resulting in the $lljj$ final state. The search covers H^+ masses in the range 240 GeV $< m_{H^+} <$ 700 GeV. Above 700 GeV the signal width becomes too large to be detectable ($\Gamma/\sigma > 15\%$). The search excludes a charged Higgs boson originating from GMHTM alone in the entire considered mass range, assuming that the Higgs decays exclusively to WZ. Figure 14 shows the distributions of the discriminant variable m_{lljj} for data, simulated background and hypothetical signal of 400 GeV charged Higgs (left) together with the GMHTM exclusion limit on the $m_{H^+} - S_H$ plane. S_H is the assumed contribution of GMHTM to the electroweak symmetry breaking.

Before concluding, let us recall yet another considered scenario, which derives from the MSSM. The Next to Minimal Supersymmetric Standard Model (NMSSM) [14, 15, 16] introduces an additional Higgs singlet on top of the usual two electroweak doublets. The additional degree of freedom relaxes constraints from the observed mass of the light neutral Higgs state which turns out to be considerably larger than m_Z. The latter puts stringent constraints on the MSSM models via the radiative corrections necessary to raise the h mass to the experimentally observed 125 GeV (e.g. $m_h^{\rm mod+/-}$). NMSSM predicts another pseudo-scalar state a which can be light is and produced in the decay of either heavier H or the 125 GeV h state. It can subsequently decay e.g. to a pair of photons. Such scenario has been search for by ATLAS for both $H \to aa \to 4\gamma$ and $h_{125} \to aa \to 4\gamma$ hypothesis [62]. In the earlier case it was assumed that 300 GeV $< m_H <$ 600 GeV and $m_a <$ 250 GeV. The experimental signature consisted of at least three isolated

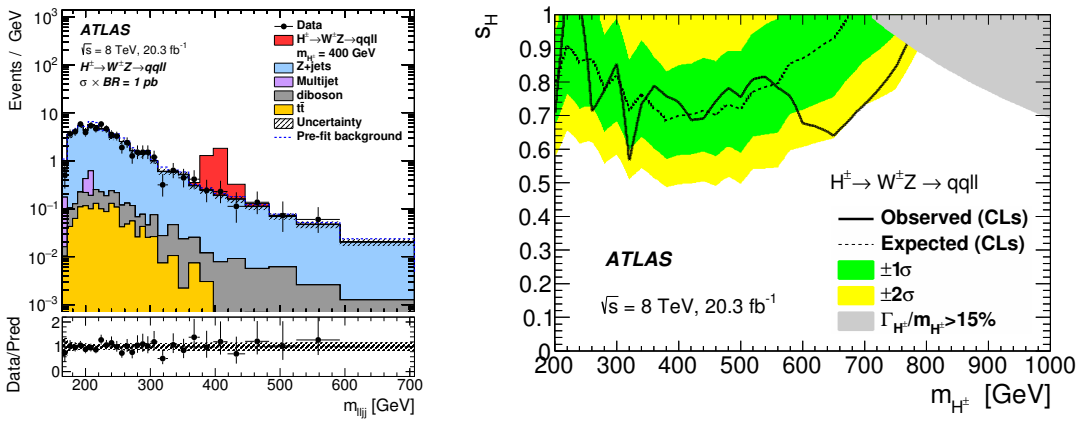

FIGURE 14. ATLAS search for the Georgi-Machacek Higgs Triplet Model [60]. Expected and observed mass of the $lljj$ system together with hypothetical signal of $m_{H^+} = 400$ GeV (left) and the exclusion limit on the S_H parameter (see text for explanation), assuming BR($H^+ \to WZ$) = 100% (right).

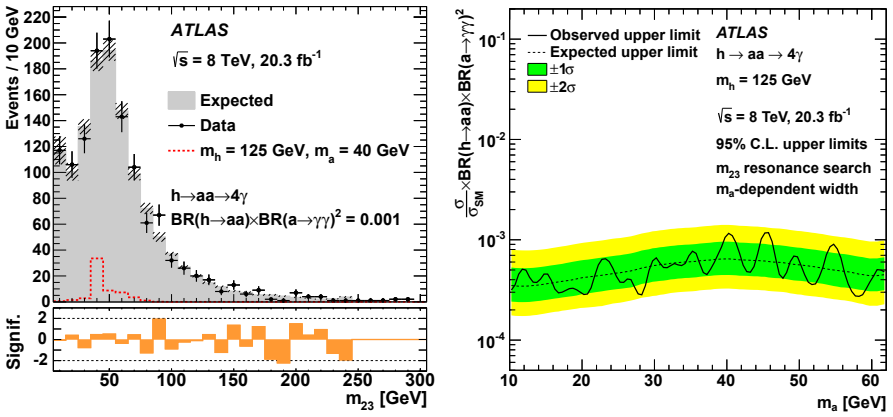

FIGURE 15. Search for the NMSSM light pseudo-scalar a from ATLAS. The expected and observed m_{23} spectrum (left) and the limit $\sigma/\sigma_{\rm SM} \times {\rm BR}(H/h \to aa) \times /{\rm BR}(a \to \gamma\gamma)^2$ for $m_h = 125$ GeV (right). [62]

photons. Invariant mass of the pair $m_{23} = m(\gamma_2\gamma_3)$ was used to search for a resonance corresponding to the pseudo-scalar a. The left plot in Figure 15 shows the observed m_{23} compared to the SM expectation. No significant excess is observed. This allowed to put exclusion limits on $\sigma/\sigma_{\rm SM} \times {\rm BR}(H/h \to aa) \times /{\rm BR}(a \to \gamma\gamma)^2$. An example exclusion for $m_h = 125$ GeV is shown on the right plot in Figure 15. A similar search, but in the $\mu\mu\tau\tau$ final state [63], revealed no deviation from the background-only hypothesis, either.

Summary

We presented a brief overview of the latest results on the search for Beyond Standard Model extensions of the Higgs sector. The searches can be divided in two categories. The first approach consists of precision measurements of the properties of the experimentally established 125 GeV Higgs boson. These include its mass, production rates and branching fractions and J^{CP}. Differential cross-sections start to be experimentally accessible, too. The second way are generic searches for heavier members of the extended Higgs sector, be it CP-even and CP-odd neutral bosons or charged scalars.

Within the current experimental uncertainties the 125 GeV Higgs looks very SM-like. No firm evidence for BSM phenomena in the scalar sector is visible. A large variety of analyses managed to place exclusion limits on various

BSM scenarios. Increase of the LHC pp energy from 8 to 13 TeV marks an increase of σ_H by more than factor two. Together with a larger integrated luminosity expected in the LHC Run 2, the VBF and the W, Z associated production await to be fully explored. Even larger factors are expected for the ttH associated production and the production of HH pairs. These will allow for direct measurement of the top-Higgs coupling as well as probing the HH cross-section, which are highly sensitive to extended Higgs scenarios. The cross-section for production of heavier states is naturally increased at 13 TeV extending the discovery potential.

There seems to be no Beyond Standard Model excitement yet, but the LHC Run 2 has a large potential to reveal new physics.

REFERENCES

[1] F. Englert and R. Brout, *Broken symmetry and the mass of gauge vector mesons*, *Phys. Rev. Lett.* 13 (1964) 321.

[2] P. W. Higgs, *Broken symmetries and the masses of gauge bosons*, *Phys. Rev. Lett.* 13 (1964) 508.

[3] ATLAS Collaboration, *Observation of a new particle in the search for the Standard Model Higgs boson with the ATLAS detector at the LHC*, *Phys. Lett.* B 716 (2012) 1.

[4] CMS Collaboration, *Observation of a new boson at a mass of 125 GeV with the CMS experiment at the LHC*, *Phys. Lett.* B 716 (2012) 30.

[5] A. Hill and J. van der Bij, *Strongly interacting singlet-doublet Higgs model*, *Phys. Rev.* D 36 (1987) 3463.

[6] G. M. Pruna and T. Robens, *Higgs singlet extension parameter space in the light of the LHC discovery*, *Phys. Rev.* D 88 (2013) 115012.

[7] J. F. Gunion and H. E. Haber, *The CP conserving two Higgs doublet model: The approach to the decoupling limit*, *Phys. Rev.* D 67 (2003) 075019.

[8] G. Branco et al., *Theory and phenomenology of two-Higgs-doublet models*, *Phys. Rept.* 516 (2012) 1.

[9] J. Gunion and H. E. Haber, *Higgs Bosons in Supersymmetric Models (I)*, *Nucl. Phys.* B 272 (1986) '1, Erratumibid. 402 (1993) 567568.

[10] A. Djouadi, *The anatomy of electro-weak symmetry breaking. Tome II: The Higgs bosons in the minimal supersymmetric model*, *Phys. Rept.* 459 (2008) 1.

[11] L Maiani, A. D. Polosa and V Riquer, *Bounds to the Higgs Sector Masses in Minimal Supersymmetry from LHC Data*, *Phys. Lett.* B 724 (2013) 274

[12] M. Carena et al., *Higgs Boson Searches at the LHC: Benchmark Scenarios after the Discovery of a Higgs-like Particle*, *Eur. Phys. J.* C73 (2013) 2552.

[13] A. Djouadi et al., *Fully covering the MSSM Higgs sector at the LHC*, *JHEP* 06 (2015) 168.

[14] U. Ellwanger, J. F. Gunion, and C. Hugonie, *Establishing a No-Lose Theorem for NMSSM Higgs Boson Discovery at the LHC*, (2001) arXiv:hep-ph/0111179 [hep-ph].

[15] R. Dermisek and J. F. Gunion, *The NMSSM Solution to the Fine-Tuning Problem, Precision Electroweak Constraints and the Largest LEP Higgs Event Excess*, *Phys. Rev.* D 76 (2007) 095006.

[16] D. Curtin et al. *Phys. Rev.* D 90, 075004 (2014).

[17] K. Agashe, R. Contino and A. Pomarol, *The minimal composite Higgs model*, *Nucl. Phys.* B 719 (2005) 165

[18] R. Contino, L. Da Rold and A. Pomarol, *Light custodians in natural composite Higgs models*, *Phys. Rev.* D 75 (2007) 055014

[19] ATLAS Collaboration, *The ATLAS Experiment at the CERN Large Hadron Collider*, *JINST* 3 S08003 (2008).

[20] CMS Collaboration, *The CMS experiment at the CERN LHC*, *JINST* 3 S08004 (2008).

[21] ATLAS and CMS Collaborations, *Combined Measurement of the Higgs Boson Mass in pp Collisions at* $\sqrt{s}$ = 7 *and* 8 TeV *with the ATLAS and CMS Experiments*, *Phys. Rev. Lett.* 114 (2015) 191803.

[22] ATLAS and CMS Collaborations, *Measurements of the Higgs boson production and decay rates and constraints on its couplings from a combined ATLAS and CMS analysis of the LHC pp collision data at* $\sqrt{s}$ = 7 *and* 8 TeV , ATLAS-CONF-2015-044/CMS-PAS-HIG-15-002 (2015).

[23] ATLAS Collaboration, *Study of the spin and parity of the Higgs boson in diboson decays with the ATLAS detector*, *Eur. Phys. J.* C75 (2015) 476.

[24] CMS Collaboration, *Constraints on the spin-parity and anomalous HVV couplings of the Higgs boson in proton collisions at 7 and 8* TeV, *Phys. Rev.* D 92 (2015) 012004.

[25] J. Ellis and T. You, *Updated Global Analysis of Higgs Couplings*, *JHEP* 06 (2013) 103.

[26] ATLAS Collaboration, *Constraints on new phenomena via Higgs boson couplings and invisible decays with the ATLAS detector*, (2015) arXiv:1509.00672 [hep-ex].

[27] CMS Collaboration, *Precise determination of the mass of the Higgs boson and tests of compatibility of its couplings with the standard model predictions using proton collisions at* 7 *and* 8 TeV, *Eur. Phys. J.* C75 (2015) 212.

[28] S. L. Glashow and S. Weinberg, *Natural conservation laws for neutral currents*, *Phys. Rev.* D 15 (1977) 1958.

[29] ATLAS Collaboration, *Search for invisible decays of a Higgs boson using vector-boson fusion in pp collisions at* $\sqrt{s}$ = 8TeV *with the ATLAS detector*, (2015), arXiv:1508.07869 [hep-ex].

[30] CMS Collaboration, *Search for invisible decays of Higgs bosons in the vector boson fusion production mode*, CMS-PAS-HIG-14-038 (2015).

[31] ATLAS Collaboration, *Search for Invisible Decays of a Higgs Boson Produced in Association with a Z Boson in ATLAS*, *Phys. Rev. Lett.* 112 (2014) 201802

[32] CMS Collaboration, *Search for invisible decays of Higgs bosons in the vector boson fusion and associated ZH production modes*, *Eur. Phys. J.* C74 (2014) 2980.
[33] ATLAS Collaboration, *Search for invisible decays of the Higgs boson produced in association with a hadronically decaying vector boson in pp collisions at* $\sqrt{s}$ = 8 TeV *with the ATLAS detector*, *Eur. Phys. J.* C75 (2015) 337.
[34] S. Kanemura et al., *Can WIMP Dark Matter overcome the Nightmare Scenario?*, *Phys. Rev.* D 82 (2010) 055026.
[35] A. Djouadi et al., *Implications of LHC searches for Higgsportal dark matter*, *Phys. Lett.* B 709 (2012) 65.
[36] CMS Collaboration, *Search for lepton-flavour-violating decays of the Higgs boson*, *Phys. Lett.* B 749 (2015) 337
[37] ATLAS Collaboration, *Search for lepton-flavour-violating* $H \to \mu\tau$ *decays of the Higgs boson with the ATLAS detector*, (2015) arXiv:1508.03372 [hep-ex].
[38] CMS Collaboration, *Search for resonant pair production of Higgs bosons decaying to two bottom quark-antiquark pairs in proton-proton collisions at* 8 TeV, *Phys. Lett.* B 749 (2015) 560.
[39] CMS Collaboration, *Search for resonant HH production in 2gamma+2b channel*, CMS-PAS-HIG-13-032 (2014).
[40] ATLAS Collaboration, *Searches for Higgs boson pair production in the* $hh \to bb\tau\tau$, $\gamma\gamma WW^*$, $\gamma\gamma bb$, $bbbb$ *channels with the ATLAS detector*, *Phys. Rev.* D 92, 092004 (2015).
[41] ATLAS Collaboration, *Search for Higgs boson pair production in the* $b\bar{b}b\bar{b}$ *final state from pp collisions at* $\sqrt{s}$ = 8 TeV *with the ATLAS detector*, *Eur. Phys. J.* C75 (2015) 412.
[42] ATLAS Collaboration, *Constraints on non-Standard Model Higgs boson interactions in an effective Lagrangian using differential cross sections measured in the* $H \to \gamma\gamma$ *decay channel at* $\sqrt{s}$ = 8 *TeV with the ATLAS detector*, (2015) arXiv:1508.02507 [hep-ex].
[43] CMS Collaboration, *Measurement of inclusive and differential fiducial cross sections for Higgs boson production in the* $H \to 4$ *decay channel in pp collisions at* $\sqrt{s}$ = 7 *and* 8 TeV , CMS-PAS-HIG-14-028 (2015).
[44] CMS Collaboration, *Search for a Higgs boson in the mass range from 145 to 1000* GeV*decaying to a pair of W or Z bosons*, (2015) arXiv:1504.00936 [hep-ex].
[45] ATLAS Collaboration, *Search for an additional, heavy Higgs boson in the* $H \to ZZ$ *decay channel at* $\sqrt{s}$ = 8 TeV *in pp collision data with the ATLAS detector*, (2015) arXiv:1507.05930 [hep-ex].
[46] ATLAS Collaboration, *Search for a high-mass Higgs boson decaying to a W boson pair in pp collisions at* $\sqrt{s}$ = 8 TeV *with the ATLAS detector*, (2015) arXiv:1509.00389 [hep-ex].
[47] CMS Collaboration, *Search for diphoton resonances in the mass range from 150 to 850* GeV *in pp collisions at* $\sqrt{s}$ = 8 TeV, (2015) arXiv:1506.02301 [hep-ex].
[48] ATLAS Collaboration, *Search for Scalar Diphoton Resonances in the Mass Range 65-600* GeV *with the ATLAS Detector in pp Collision Data at* $\sqrt{s}$ = 8 TeV, *Phys. Rev. Lett.* 113, (2014) 171801.
[49] CMS Collaboration, *Search for neutral MSSM Higgs bosons decaying into a pair of bottom quarks*, (2015) arXiv:1506.08329 [hep-ex].
[50] ATLAS Collaboration, *Search for neutral Higgs bosons of the minimal supersymmetric standard model in pp collisions at* $\sqrt{s}$ = 8 TeV *with the ATLAS detector*, *JHEP* 11 (2014) 056.
[51] CMS Collaboration, *Search for additional neutral Higgs bosons decaying to a pair of tau leptons in pp collisions at* $\sqrt{s}$ = 7 *and* 8 TeV, CMS-PAS-HIG-14-029 (2015).
[52] ATLAS Collaboration, *Search for a CP-odd Higgs boson decaying to Zh in pp collisions at* $\sqrt{s}$ = 8 *TeV with the ATLAS detector*, *Phys. Lett.* B 744 (2015) 163-183.
[53] CMS Collaboration, *2HDM scenario, H to hh and A to Zh*, *Phys. Rev.* D 90 (2014) 112013.
[54] CMS Collaboration, *Search for a pseudoscalar boson decaying into a Z boson and the 125* GeV *Higgs boson in* $l^+l^-b\bar{b}$ *final states*, *Phys. Lett.* B 748 (2015) 221.
[55] CMS Collaboration, *Search for H/A decaying into Z + A/H, with Z to ll and A/H to fermion pair*, CMS-PAS-HIG-15-001 (2015).
[56] CMS Collaboration, *Search for charged Higgs bosons with the* H^+ *to tau nu decay channel in the fully hadronic final state at* $\sqrt{s}$ = 8 TeV, CMS-PAS-HIG-14-020 (2015).
[57] ATLAS Collaboration, *Search for charged Higgs bosons decaying via* $H^{+-} \to \tau^{+-}\nu$ *in fully hadronic final states using pp collision data at* $\sqrt{s}$ = 8 TeV *with the ATLAS detector*, *JHEP* 03 (2015) 088.
[58] CMS Collaboration, *Search for a charged Higgs boson in pp collisions at* $\sqrt{s}$ = 8 TeV, (2015) arXiv:1508.07774 [hep-ex].
[59] P. Vischia, in this Volume.

[60] ATLAS Collaboration, *Search for a Charged Higgs Boson Produced in the Vector-boson Fusion Mode with Decay $H^{\pm} \to W^{\pm}Z$ using pp Collisions at $\sqrt{s} = 8$ TeV with the ATLAS Experiment*, *Phys. Rev. Lett.* 114, (2015) 231801.

[61] H. Georgi and M. Machacek, *Doubly Charged Higgs Bosons*, *Nucl. Phys.* B262 (1985) 463.

[62] ATLAS Collaboration, *Search for new phenomena in events with at least three photons collected in pp collisions at $\sqrt{s} = 8$ TeV with the ATLAS detector*, (2015) arXiv:1509.05051 [hep-ex].

[63] ATLAS Collaboration, *Search for Higgs bosons decaying to aa in the $\mu\mu\tau\tau$ final state in pp collisions at $\sqrt{s} = 8$ TeV with the ATLAS experiment* , *Phys. Rev.* D 92 (2015) 052002.

SuperSymmetry: plenary talks

Proceedings of the LHCP2015 Conference, St. Petersburg, Russia, August 31 - September 5, 2015

Editors: V.T. Kim and D.E. Sosnov

Multiphoton Signatures of Multisector Gauge Mediation

GABRIELE FERRETTI

Department of Fundamental Physics,
Chalmers University of Technology,
Fysikgården 1, 41296 Göteborg, Sweden

ferretti@chalmers.se

Abstract. We report on a study of models of gauge mediation with multiple hidden sectors. In such models, the neutralino sector is augmented with an additional pseudo-goldstino for each sector. This leads to modified decay chains with extra photons in the final state. In the case where the lightest ordinary SUSY particle is a Bino, this gives rise to multiphoton plus missing energy signatures at the LHC. We present the number of signal events expected in the case of slepton pair production in both RUN 1 and in the current 2015 data sample, as well as a preliminary, Montecarlo based, estimate of the background. Our conclusion is that a targeted multiphoton plus MET search would be quite sensitive to this type of models already with the present data.

INTRODUCTION

Supersymmetry [1] (SUSY) is a very appealing idea that potentially explains the hierarchy problem, provides dark matter candidates and facilitates grand-unification. Sadly, there has been no sign of SUSY at the LHC after RUN-1. This has led to the exclusion of large regions of parameter space for the prototypical minimal scenarios. For the class of SUSY models of direct relevance for this work – those based on the mechanism of gauge mediation (GM) – the strongest limits to-date are found in [2] and [3].

For those of us who are not ready to give up on SUSY yet, these negative results indicate the need to broaden the search to non-minimal scenarios and non-standard signatures in RUN-2, in order to cover the largest possible region of the SUSY terrain and ensure that we do not miss any of its possible incarnations. Here we discuss the particular example of multiphoton ($n_\gamma \geq 3$) + MET signatures that can expose models of Gauge Mediation with multiple Hidden Sectors while weakening current constraints.

In the context of supergravity, models with multiple hidden sectors have been studied in [4]. The first theoretical investigation of multiple hidden sectors in the context of GM was done in [5]. The collider phenomenology of GM with goldstini was discussed in [6], for the case where the Lightest Observable-Sector Particle (LOSP) was a gaugino-like neutralino or a stau, and in [7] for the case of higgsino LOSP. In all these investigations the attention was focused mainly on the case of two SUSY breaking sectors. (Further work on electro-weak production can be found in [8].)

New phenomena arise in the case of more than two sectors and they were discussed in [9]. This last aspect will be the focus of this note.

GAUGE MEDIATED SUSY BREAKING

In models of GM [10], SUSY is broken spontaneously by a hidden sector and mediated to the MSSM (or possibly a larger observable sector) by gauge interactions. This has the main advantage of suppressing unacceptable flavor changing interaction.

GM is characterized by a low SUSY breaking scale $\sqrt{f}$ and the gravitino (of mass $m_{3/2} = f/\sqrt{3}M_{\rm P}$) is necessarily the LSP. Since the gravitino is almost massless we can use the equivalence theorem [11] and treat it as a spin $1/2$ goldstino $\tilde{G}$. Since the decay to the goldstino is suppressed by $1/f$, typically only the NLSP (which does not have any other choice in R-parity preserving theories) decays into it. The distinguishing signature of models of gauge

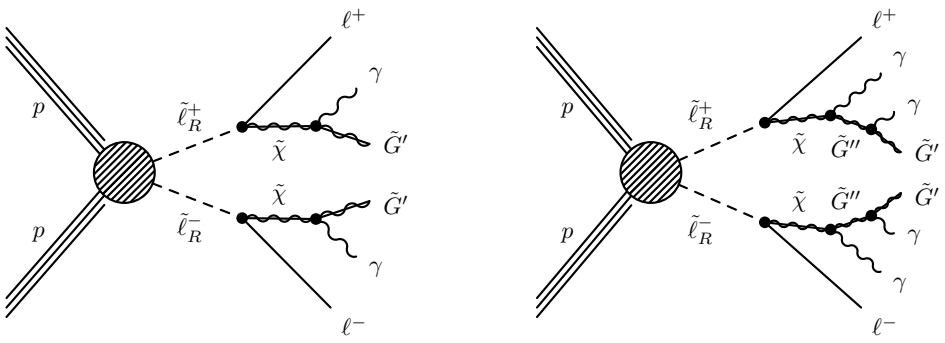

FIGURE 1. The processes relevant at the LHC in the (left) two- and (right) three-sector models. Picture taken from [9].

mediation is thus given by the last (prompt) decay where the NLSP decays into a goldstino and a SM particle. In this talk for brevity we focus only on the typical scenario

$$\tilde{\chi}_1^0 \text{ (mostly Bino)} \ \to \gamma\, \tilde{G} \tag{1}$$

In the case where many hidden sectors contribute to SUSY breaking [9], the massless goldstino is only one particular linear combination of the goldstini η_i from each sector $\tilde{G} \approx (f_1\tilde{\eta}_1 + \ldots f_n\eta_n)/f, \quad (f^2 \equiv f_1^2 + \ldots f_n^2)$. The remaining mass eigenvectors $\tilde{G}'$, $\tilde{G}''$ ... are the pseudo-goldstini (pGLD). They acquire masses ($\lesssim 100$ GeV) at tree and loop level [5].

Just like the goldstino, these pGLD have negligible direct production cross section, so they can only be produced in the decay chain involving the LOSP. In our scenario the LOSP is the Bino and decays preferably to the heaviest pGLD. The pGLD successively decays to lighter pGLD: $\tilde{G}'' \to \gamma\, \tilde{G}'$. A numerical analysis of the decay rates shows that the only relevant (prompt) decay mode is $\tilde{G}'' \to \gamma\, \tilde{G}'$ ($\tilde{G}'' \to V\, V\, \tilde{G}'$ and $\tilde{G}'' \to f\, \bar{f}\, \tilde{G}'$ are never competitive, $\tilde{G}'' \to Z\, \tilde{G}'$ is phase-space suppressed, if allowed at all.) Moreover, one can have at most one such additional prompt decay. Thus, the simplified model with three sectors, with $\tilde{G}'$ collider stable, captures all the collider phenomenology of these models. Setting $m_{\tilde{G}'} = 0$ or $m_{\tilde{G}''} = m_{\tilde{G}'} = 0$ reduces this simplified model to the two-sector model or to the ordinary case.

More specifically, the decay $\tilde{G}'' \to \gamma\, \tilde{G}'$ is mediated by the dimension five operator

$$\propto \ \tilde{G}''\sigma^\mu\bar{\sigma}^\nu\tilde{G}'F_{\mu\nu} \tag{2}$$

This operator arises from the last term in the SUSY operator

$$-\int d^2\theta \frac{M_{B(i)}}{2f_i} X_i WW \supset -\frac{M_{B(i)}}{2}\left(\tilde{B}\tilde{B} - \frac{\sqrt{2}}{f_i}\tilde{\eta}_i\tilde{B}D_Y - \frac{i}{\sqrt{2}f_i}\tilde{B}\sigma^\mu\bar{\sigma}^\nu\tilde{\eta}_i B_{\mu\nu}\right) \tag{3}$$

after rotating all fields to their mass eigenbasis. Note that a term such as (2) vanishes if $\tilde{G}' = \tilde{G}''$. In particular it vanishes in the standard scenario with only one sector.

SLEPTON PAIR PRODUCTION

In [9] we studied the production mode via right-handed sleptons. We considered both the case where the neutralino LOSP decays to a collider stable pGLD as in Fig. 1(left) as well as the case when the pGLD undergoes a further decay an is Fig. 1(right). The former process has the same topology as the ordinary GM one but with what effectively behaves as a "massive goldstino". The latter entails a new topology giving rise to up to four high p_T prompt photons. For the three sector case we considered the four benchmark points indicated in Table 1

For these models, the most relevant search at the time was the ATLAS diphoton + MET search [12]:

$$4.8 \text{ fb}^{-1},\ 7 \text{ TeV}: \quad p_T^{\gamma_{1,2}} > 50 \text{ GeV}, \quad \text{MET} > 100,\ 125,\ 200 \text{ GeV} \tag{4}$$

TABLE 1. Benchmarks for the three sector case.

M_{ℓ_R}	M_χ	$M_{G''}$	$M_{G'}$
200	150	100	50
200	150	100	0
200	150	50	0
200	100	50	0

This search is now superseded by [3]

$$20.3\ \text{fb}^{-1},\ 8\ \text{TeV}: \quad p_T^{\gamma_{1,2}} > 75\ \text{GeV}, \quad \text{MET} > 150,\ 200,\ 250\ \text{GeV} \tag{5}$$

However, due to the small amount of MET and the softness of the photons, these searches are poorly sensitive to these models. In particular, the four benchmarks for the three sector model are still not excluded by these searches. We also accounted for the searches [13] and [14] which also include leptons in their final states, and are thus relevant to the chosen production mode. These searches turned out to be less sensitive than [12].

On the other hand, searches with $\geq 3\ \gamma\ +$ MET in the final state would be very sensitive to these models. As an illustration, in Table 2 we give the number of signal events expected with 20 fb^{-1} of data at 8 TeV for our simplified model with right-slepton production, requiring loose cuts on the photons.

$$p_T^{\gamma_{1,2,3,(4)}} > 20\ \text{GeV}, \quad |\eta| < 2.5, \quad \Delta R > 0.4 \tag{6}$$

TABLE 2. Number of expected events with 20 fb^{-1} of data at 8 TeV for the four benchmark models in Table 1 after the cuts (6).

final state	MET	150-100-50	150-100-0	150-50-0	100-50-0
3γ	>50 GeV	45	56	46	36
	> 100 GeV	11	19	14	9.0
final state	MET	150-100-50	150-100-0	150-50-0	100-50-0
4γ	> 50 GeV	18	27	19	12
	> 100 GeV	3.4	8.3	5.6	3.0

In Table 3 we also report the number of expected events (abridged from [9]) with $n_\gamma \geq 4$ and MET > 50 GeV, still with the requirements (6), to be expected after 3 fb^{-1} at 13 TeV as we stand roughly at the end of the 2015 run. We see that even with fairly low luminosity one still would get a handful of events.

TABLE 3. Number of expected events with 3 fb^{-1} of data at 13 TeV for the four benchmark models in Table 1 after the cuts (6) imposing $n_\gamma \geq 4$ and MET > 50 GeV.

150-100-50	150-100-0	150-50-0	100-50-0
6.1	8.4	6.2	4.1

The main open issues at this point is a reliable estimate of the background as well as the extension of the analysis to other production modes. We report now preliminary results on both of these point.

For an estimate of the background, we have generated Montecarlo samples using MadGraph5 [15], Pythia6 [16], FastJet [17] and Delphes3 [18] with the ATLAS standard detector specification modified only by setting the jet radius parameter to 0.4. This is not enough for a quantitatively reliable estimate as it does not take into account pile-up and other detector effects. However it should give an idea of the severity of the problem.

The main sources of background are diphoton and triphoton plus jets, where one of the jets is faking a photon, as well as SM processes with irreducible missing energy, such as invisible Z decay or leptonic W decay, in addition to photons and jets.

We have simulated the purely QED+QCD background (photons and jets only) in two ways. First we generated the $q\,\bar{q} \to \gamma\,\gamma$ and $q\,\bar{q} \to \gamma\,\gamma\,\gamma$ processes at partonic level and subsequently showered with Pythia (the $q\,\bar{q} \to \gamma\,\gamma\,\gamma\,\gamma$ process has a negligible cross section). As a second attempt, we generated the above processes, together with up to two jets at partonic level and performed MLM matching [19]. In this second case, in order to provide a hard scale for the matching, we required the p_T of the leading photon to be at least 70 GeV. The second sample gave the larger contribution to the background, with 3 events at 8 TeV with 20 fb^{-1} in the case of MET > 50 GeV and $n_\gamma \geq 3$ photons with the same p_T and $|\eta|$ requirements as in (6) and a negligible contribution in the remaining cases of Table 2.

The largest contribution from a process containing a vector boson came from a leptonically decaying W together with 2 photons and up to one matched jet. Here there was no need to impose additional requirements on the p_T of the leading photon since the W provided the hard scale for the matching algorithm. We obtained 0.7 events at 8 TeV with 20 fb^{-1} in the case MET > 50 GeV and $n_\gamma \geq 3$ photons and, again, a negligible result in the other cases.

A similar study has been performed at 13 TeV with 3 fb^{-1} and similar conclusions have been reached. in particular the background should be negligible for the case presented in Table 3.

Although a more reliable estimate of backgrounds of this type should come from a data driven analysis perhaps supplemented by a full detector simulation for the vector boson case, we take these results as an indication that the background can in fact be brought under control and that the proposed searches are sensitive to the signal even for such low values of p_T and MET.

The scope of the signal generation using slepton pair production is rather limited given the low cross section and a full analysis will require considering strong and electroweak production modes as well. In order to accomplish this, we have made a minor modification at the UFO level [20] of the pre-existing code for gauge mediated SUSY [21] by adding the second goldstino with the interaction (2) together with non-zero masses and widths for all the particles involved. We have validated the code on some benchmark processes and we now plan to start the generation of signal samples for both strong and electroweak production as well as different LOSP candidates. We hope to report on the results in the near future.

CONCLUSIONS

In this contribution we reported on a study [9] of models of gauge mediation with multiple hidden sectors. We discussed the non-standard signatures that are to be expected in the case of a Bino LOSP, namely multiphoton final states accompanied by some amount of MET. Due to the different kinematic the leading photon spectrum is softer than in the usual case and the MET signature is reduced. We showed the number of signal events expected in the case of slepton pair production as well as a preliminary, Montecarlo based, estimate of the background. Our conclusion is that a targeted multiphoton plus MET search would be quite sensitive to this type of models already with the 8 TeV results and also in the new 13 TeV run.

We conclude this short note by stressing the two main qualitative points that have driven this investigation and should have a broader significance in the context of gauge mediated SUSY breaking:

First, do not necessarily assume that the "Goldstino/Gravitino" is nearly massless. The LOSP could be decaying to a heavy "impostor"–the pseudo-goldstino. This is what happens generically in models with more than one hidden sector and looking at such non-minimal models is more motivated now that the most commonly expected SUSY signals have failed to turn up in LHC searches.

Secondly, do not necessarily assume that the "impostor" is collider stable. There is still room for one prompt decay into a photon and a lighter (pseudo)-goldstino. This occurs in fairly generic regions of the parameter space of multi-sector models. Further decays or other decays modes such as $\tilde{G}'' \to \tilde{G}'\,\gamma\,\gamma$ or $\tilde{G}'' \to \tilde{G}'\,l^+\,l^-$ have however too small a partial width to be of interest for collider phenomenology.

ACKNOWLEDGMENTS

It is a pleasure to thank my colleagues R. Argurio, K. De Causmaecker, A. Mariotti, K. Mawatari, C. Petersson and Y. Takaesu for a very enjoyable collaboration and the organizers of the conference for the invitation and the fabulous hospitality.

REFERENCES

[1] H. Miyazawa, Prog. Theor. Phys. **36** (1966) 6, 1266. P. Ramond, Phys. Rev. D **3** (1971) 2415. A. Neveu and J. H. Schwarz, Nucl. Phys. B **31** (1971) 86. Y. A. Golfand and E. P. Likhtman, JETP Lett. **13** (1971) 323 [Pisma Zh. Eksp. Teor. Fiz. **13** (1971) 452]. D. V. Volkov and V. P. Akulov, Phys. Lett. B **46** (1973) 109. J. Wess and B. Zumino, Nucl. Phys. B **70** (1974) 39.

[2] V. Khachatryan *et al.* [CMS Collaboration], Phys. Rev. D **92** (2015) 7, 072006 [arXiv:1507.02898 [hep-ex]].

[3] G. Aad *et al.* [ATLAS Collaboration], Phys. Rev. D **92** (2015) 7, 072001 [arXiv:1507.05493 [hep-ex]].

[4] K. Benakli and C. Moura, Nucl. Phys. B **791** (2008) 125 [arXiv:0706.3127 [hep-th]]. C. Cheung, Y. Nomura and J. Thaler, JHEP **1003** (2010) 073 [arXiv:1002.1967 [hep-ph]]. C. Cheung, J. Mardon, Y. Nomura and J. Thaler, JHEP **1007** (2010) 035 [arXiv:1004.4637 [hep-ph]].

[5] R. Argurio, Z. Komargodski and A. Mariotti, Phys. Rev. Lett. **107** (2011) 061601 [arXiv:1102.2386 [hep-th]].

[6] R. Argurio, K. De Causmaecker, G. Ferretti, A. Mariotti, K. Mawatari and Y. Takaesu, JHEP **1206** (2012) 096 [arXiv:1112.5058 [hep-ph]].

[7] T. Liu, L. Wang and J. M. Yang, Phys. Lett. B **726** (2013) 228 [arXiv:1301.5479 [hep-ph]].

[8] T. Liu, L. Wang and J. M. Yang, JHEP **1502** (2015) 177 [arXiv:1411.6105 [hep-ph]]. K. i. Hikasa, T. Liu, L. Wang and J. M. Yang, JHEP **1407** (2014) 065 [arXiv:1403.5731 [hep-ph]].

[9] G. Ferretti, A. Mariotti, K. Mawatari and C. Petersson, JHEP **1404** (2014) 126 [arXiv:1312.1698 [hep-ph]].

[10] M. Dine and W. Fischler, Phys. Lett. B **110** (1982) 227. L. Alvarez-Gaume, M. Claudson and M. B. Wise, Nucl. Phys. B **207** (1982) 96. M. Dine and A. E. Nelson, Phys. Rev. D **48** (1993) 1277 [hep-ph/9303230]. M. Dine, A. E. Nelson and Y. Shirman, Phys. Rev. D **51** (1995) 1362 [hep-ph/9408384]. M. Dine, A. E. Nelson, Y. Nir and Y. Shirman, Phys. Rev. D **53** (1996) 2658 [hep-ph/9507378]. S. Dimopoulos, G. F. Giudice and A. Pomarol, Phys. Lett. B **389** (1996) 37 [hep-ph/9607225]. S. P. Martin, Phys. Rev. D **55** (1997) 3177 [hep-ph/9608224]. E. Poppitz and S. P. Trivedi, Phys. Lett. B **401** (1997) 38 [hep-ph/9703246]. P. Meade, N. Seiberg and D. Shih, Prog. Theor. Phys. Suppl. **177** (2009) 143 [arXiv:0801.3278 [hep-ph]].

[11] P. Fayet, Phys. Lett. B **70** (1977) 461.

[12] G. Aad *et al.* [ATLAS Collaboration], Phys. Lett. B **718** (2012) 411 [arXiv:1209.0753 [hep-ex]].

[13] ATLAS Collaboration, ATLAS-CONF-2012-144.

[14] CMS Collaboration, CMS-PAS-SUS-13-006.

[15] J. Alwall, M. Herquet, F. Maltoni, O. Mattelaer and T. Stelzer, JHEP **1106** (2011) 128 [arXiv:1106.0522 [hep-ph]].

[16] T. Sjostrand, S. Mrenna and P. Z. Skands, JHEP **0605** (2006) 026 [hep-ph/0603175].

[17] M. Cacciari, G. P. Salam and G. Soyez, Eur. Phys. J. C **72** (2012) 1896 [arXiv:1111.6097 [hep-ph]].

[18] J. de Favereau *et al.* [DELPHES 3 Collaboration], JHEP **1402** (2014) 057 [arXiv:1307.6346 [hep-ex]].

[19] M. L. Mangano, M. Moretti, F. Piccinini and M. Treccani, JHEP **0701** (2007) 013 [hep-ph/0611129].

[20] C. Degrande, C. Duhr, B. Fuks, D. Grellscheid, O. Mattelaer and T. Reiter, Comput. Phys. Commun. **183** (2012) 1201 [arXiv:1108.2040 [hep-ph]].

[21] N. D. Christensen *et al.*, Eur. Phys. J. C **73** (2013) 10, 2580 [arXiv:1308.1668 [hep-ph]].

Proceedings of the LHCP2015 Conference, St. Petersburg, Russia, August 31 - September 5, 2015

Editors: V.T. Kim and D.E. Sosnov

Inclusive Searches for Squarks and Gluinos with the ATLAS Experiment at LHC

J. MAURER

Horia Hulubei National Institute for R&D in Physics and Nuclear Engineering (IFIN-HH), Str. Reactorului no.30, P.O.BOX MG-6, Bucharest - Magurele, Romania.

jmaurer@cern.ch

On behalf of the ATLAS Collaboration

Abstract. The ATLAS experiment at LHC has conducted searches for the supersymmetric partners of quarks and gluons in the proton-proton collision data collected in 2012, at a centre-of-mass energy of 8 TeV and with an integrated luminosity of 20.3 fb^{-1}, using various topologies corresponding to different decay modes. No significant excess above SM predictions was observed, and exclusion limits were set on the squark and gluino masses in various scenarios. For light neutralinos, the experimental sensitivity reached gluino masses up to 1.3 TeV, and squark masses up to 850 GeV.

INTRODUCTION

Supersymmetry (SUSY) [1] is one of the most studied frameworks to extend the Standard Model (SM) beyond the electroweak scale. In its minimal realization (MSSM) it predicts a new bosonic (fermionic) partner for each fundamental SM fermion (boson). The partners of the SM quarks and gluons (referred to as squarks and gluinos), that carry SU(3) colour charges, can be pair-produced in proton-proton collisions with sizable cross-sections. Dedicated experimental searches have therefore been conducted at the Large Hadron Collider (LHC) [2] during its first phase of exploitation, at a centre-of-mass energy of 7 then 8 TeV. The ATLAS experiment [3] in particular has extensively searched for squarks and gluinos, and the latest results [4, 5] obtained with the 2012 dataset (integrated luminosity of 20.3 fb^{-1}) are reported in this document.

The results presented here focus on scenarios in which an additional discrete symmetry (R-parity), introduced to prevent large flavour-violating couplings, is preserved in the interactions. The lightest superpartner (LSP) is then stable, and is a viable dark matter candidate. It is generally considered to be either the lightest neutralino[1] $\tilde{\chi}_1^0$ or the gravitino[2] $\tilde{G}$. The squarks or gluinos produced in the hard scattering event decay in cascade up to the LSP, which leads to a final state with energetic jets and large missing transverse momentum $E_{\mathrm{T}}^{\mathrm{miss}}$. The latter constitutes the typical minimal signature for squarks and gluinos searches at LHC, which might be completed by other striking features depending on the intermediate particles involved in the decay chain. Several ATLAS searches have thus been conducted targeting different decay modes, mainly distinguished by the multiplicities of charged leptons, b jets or photons. Often, the different experimental signatures provide complementary approaches to probe a particular decay channel. In a recent review of its 8 TeV searches [4], the ATLAS collaboration summarized the current situation in terms of experimental sensitivity to various decay channels, and provided in a few cases a statistical combination of several searches to improve it. In the absence of any significant excess over SM in observed data, exclusion limits were set on the masses of SUSY particles. These constraints are presented here in the context of simplified scenarios in which only gluino (squark) pair production is considered, with a 100% branching ratio assumed for the decay channels of interest; the other SUSY particles not involved in the decay process are assigned arbitrarily large masses.

[1] Neutral mass eigenstates $\tilde{\chi}_{1,2,3,4}^0$ (in increasing mass) of the mixed superpartners of the SM Higgs and electroweak gauge bosons.

[2] Physical state formed by the graviton's superpartner absorbing the Goldstone fermionic degrees of freedom induced by the SUSY breaking.

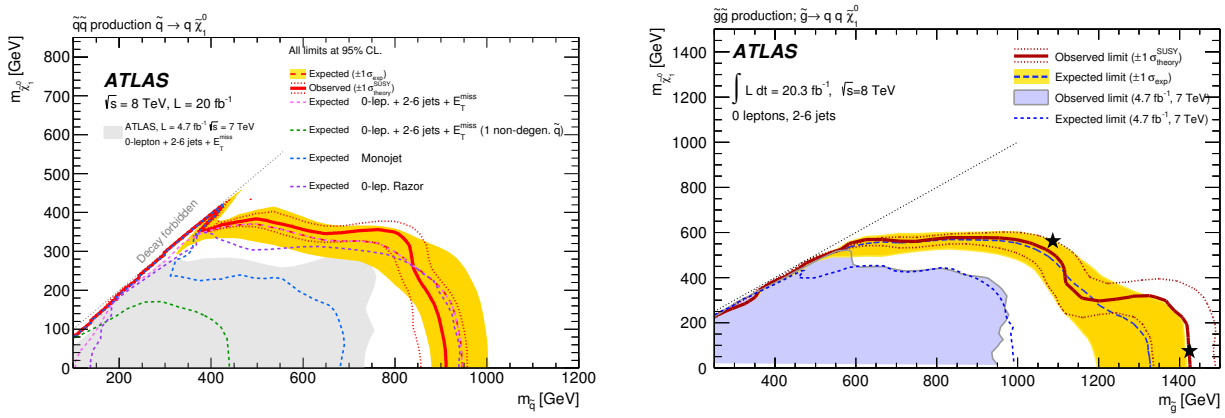

(a) $\tilde{q}\tilde{q}^*$ production, $\tilde{q} \to q\tilde{\chi}_1^0$ (b) $\tilde{g}\tilde{g}$ production, $\tilde{g} \to q\bar{q}\tilde{\chi}_1^0$

FIGURE 1. 95% CL_S exclusion limits on four-flavour-degenerate squark-antisquark (a) and gluino-gluino (b) pair production with direct decays into LSP and SM quarks, as a function of the squark (gluino) and LSP masses. Ref. [4].

GENERAL SEARCH STRATEGY

The experimental searches performed by the ATLAS Collavoration follow generally similar strategies for the background estimates and the interpretation of the results. Backgrounds from the main SM processes (W/Z+jets, $t\bar{t}\ldots$) are estimated with the help of control regions enriched in the relevant process, with kinematic requirements close to those employed in the signal regions but with limited signal contamination. Monte-Carlo (MC) simulations are then used to extrapolate the background yields from the control to the signal regions. Rarer SM processes are directly predicted from MC and rely on the best theoretical knowledge of their production cross-section. Experimental backgrounds of various natures are estimated through methods relying on data; these include for example fake $E_{\mathrm{T}}^{\mathrm{miss}}$ from mismeasured jet energy, or misidentified leptons.

Exclusion limits are set by comparing signal prediction to the expected background yields in the signal regions, either in a single bin or by fitting the observed distribution of a discriminant variable; sometimes, orthogonal signal regions are statistically combined to improve sensitivity. Limits are provided as 95% confidence level intervals in the CLs formalism [6], using the HistFitter framework [7] which performs statistical test relying on a profile likelihood ratio [8].

INCLUSIVE SEARCHES

Direct squark and gluino decays to LSP

The most inclusive SUSY search [9] targets direct decays of squarks and gluinos to quarks and LSP, by selecting events with jets and $E_{\mathrm{T}}^{\mathrm{miss}}$, vetoing the presence of identified electrons or muons. The overwhelming QCD background is reduced by stringent requirements on $E_{\mathrm{T}}^{\mathrm{miss}}$ and the effective mass m_{eff}, the scalar sum of the transverse momentum of selected jets and $E_{\mathrm{T}}^{\mathrm{miss}}$. Seventeen signal regions are defined with varying tightness of the cuts, and are split by the numbers of required jets, which varies from ≥ 2 to ≥ 6.

The exclusion limits set by this search on the squarks and gluino masses as function of the LSP mass can be seen on Fig. 1. In the case of mass-degenerate $\tilde{u}$, $\tilde{d}$, $\tilde{s}$ and $\tilde{c}$ squarks, masses up to 800 GeV are excluded for LSP masses smaller than 300 GeV, while there is little sensitivity for greater LSP masses. For very close squark and LSP masses, the quarks produced in the decay are too soft to seed the reconstruction of jets; this region of the phase space can nevertheless be explored by tagging events in which the pair-produced $\tilde{q}\tilde{q}^*$ recoils significantly against a jet from initial state radiation, leading to a monojet + $E_{\mathrm{T}}^{\mathrm{miss}}$ signature [10]. The reinterpretation of this search to direct squark decays, proposed in Ref. [4] and also shown in Fig. 1, provides a good complement to the inclusive search, allowing to exclude squarks and LSPs of equal mass up to 400 GeV.

Gluino masses up to 1.3 TeV are excluded for a light LSP, the limit reducing to 1.1 TeV for LSP masses of 200

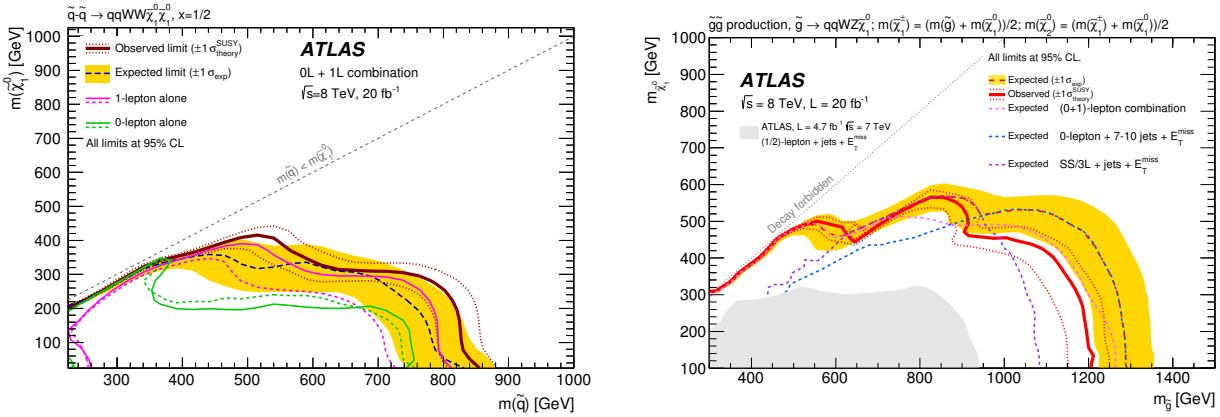

(a) $\tilde{q}\tilde{q}^*$ production, $\tilde{q} \to q'W\tilde{\chi}_1^0$ via $\tilde{\chi}_1^\pm \to W^\pm\tilde{\chi}_1^0$ (b) $\tilde{g}\tilde{g}$ production, $\tilde{g} \to q\bar{q}'WZ\tilde{\chi}_1^0$ via $\tilde{\chi}_1^\pm \to W^\pm\tilde{\chi}_2^0$

FIGURE 2. 95% CL_S exclusion limits on four-flavour-degenerate squark-antisquark production with $\tilde{\chi}_1^\pm$-mediated decays (a) and gluino-gluino production with a two-step decay (b), as a function of the squark (gluino) and LSP masses. Ref. [4].

GeV, and with little sensitivity for LSP masses above 500 GeV. The exclusion limit is obtained by choosing in each point of the phase space the most suitable signal region in terms of expected sensitivity. One can for example identify from the shape of the exclusion limit in Fig. 1 a region at $m_{\tilde{g}} > 1.2$ TeV in which the exclusion is driven by a signal region with ≥ 4 jets and tight kinematic requirements, and a region at $m_{\tilde{g}} < 1.1$ TeV which relies on a signal region with ≥ 5 jets and much looser m_{eff} requirements.

Cascade decays, signatures with leptons

More complex cascade decays may occur through the contribution of light neutralinos/ charginos[3], or sleptons, which leads to final states enriched in SM gauge bosons and leptons. The simplest case is a one-step decay through a chargino, $\tilde{q}/\tilde{g} \to q(q)\tilde{\chi}_1^\pm \to q(q)W^\pm\tilde{\chi}_1^0$. The sensitivity of the inclusive zero-lepton search to this scenario is complemented by a search requiring at least one electron or muon, together with several jets and $E_{\text{T}}^{\text{miss}}$ [11]. In addition, in the most recent results [4] signal regions identifying the presence of a hadronically decaying W boson (either with a resolved decay into two jets, or through a single jet substructure when significantly boosted) were added to the inclusive search. Figure 2a shows the exclusion limits on the squarks masses in this scenario, as function of the LSP mass. Being statistically orthogonal due to the lepton requirements, the inclusive and one-lepton searches were combined in [4], allowing to exclude squarks masses up to 800 GeV for a light LSP, thus representing a 50 GeV improvement over the performance of either of the analysis considered alone. Overall, the region of the phase space the searches are sensitive to is similar than for direct decays (Fig.1a).

To probe decay channels that lead to larger amount of particles in the final states, several other searches were performed, requiring notably no lepton and $\geq 7-10$ jets [12], or two leptons and jets [11], or at least two leptons of identical charge and jets [13]. The increased rarity of these final states for SM processes allows to relax the tight kinematic requirements imposed in the more inclusive searches. For example, typical $E_{\text{T}}^{\text{miss}}$ requirements are about 500 GeV for the zero-lepton and 300 GeV for the one-lepton searches, but reduced to about 100 and 150 GeV for [12] and [13], the latter even featuring a signal region without any $E_{\text{T}}^{\text{miss}}$ cut. This notably helps improving the sensitivity to SUSY scenarios with compressed mass spectra. Figure 2b shows for example exclusion limits on the gluino mass in the context of a two-step decay $\tilde{g} \to qq'\tilde{\chi}_1^\pm \to qq'W^\pm\tilde{\chi}_2^0 \to qq'W^\pm Z\tilde{\chi}_1^0$. Several of the searches mentioned above are sensitive to this final state, and their complementarity is illustrated by an improvement of the exclusion limit by about 50 GeV on the LSP mass compared to inclusive searches alone. The overall sensitivity is here again similar to the one seen for direct gluino decays (Fig.1b), with gluino masses excluded up to 1150 GeV for a light LSP.

[3] Charged mass eigenstates $\tilde{\chi}_{1,2}^\pm$ (in increasing mass) of the mixed superpartners of the SM Higgs and electroweak gauge bosons.

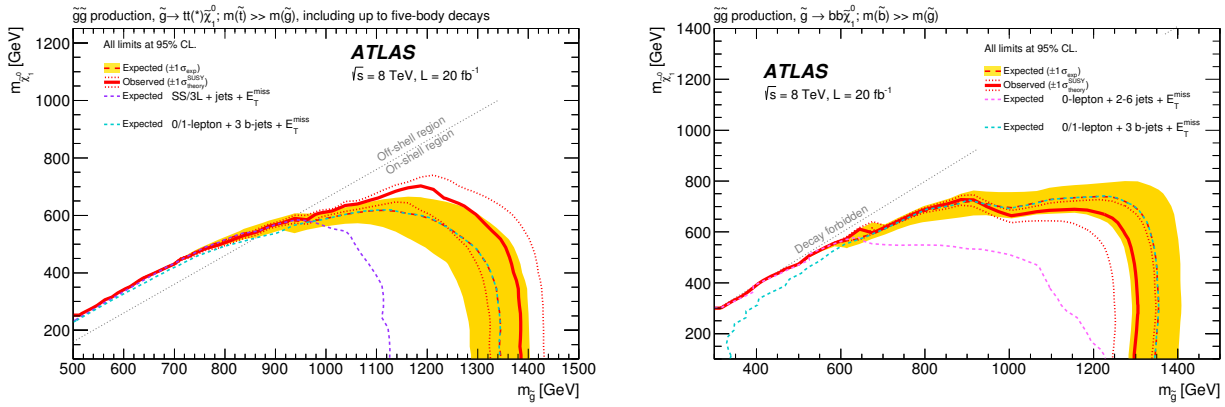

(a) $\tilde{g}\tilde{g}$ production, $\tilde{g} \to t\bar{t}\tilde{\chi}_1^0$ (b) $\tilde{g}\tilde{g}$ production, $\tilde{g} \to b\bar{b}\tilde{\chi}_1^0$

FIGURE 3. 95% CL_S exclusion limits on gluino-gluino pair production with $\tilde{t}$- (left) or $\tilde{b}$-mediated (right) decays to LSP and a $t\bar{t}$ ($b\bar{b}$) pair, as a function of the gluino and LSP masses. Ref. [4].

More specific discriminant variables

In addition to the searches mentioned so far, which relied on rather simple discriminant variables to build signal regions, other searches used more involved techniques, based on specific characteristics of the considered final states. Beside providing complementarity to the simpler approaches, these techniques could have brought further information about the properties of BSM events, in the case of an observed excess, helping characterize the nature of the underlying process. For example, the Razor variables described in [14] were employed for zero-lepton and two-lepton final states [4, 11], in which they notably replace $E_{\mathrm{T}}^{\mathrm{miss}}$ requirements. The sensitivity of the former to direct squark decays is shown on Fig. 1a, the performance of this search being very similar to the "standard" zero-lepton search relying on $E_{\mathrm{T}}^{\mathrm{miss}}$.

Another search [15] scrutinized the dilepton invariant mass line shape for pairs of opposite-charge electrons or muons, either identifying Z bosons present e.g. in $\tilde{g} \to q\bar{q}\tilde{\chi}_1^0 \to q\bar{q}Z\tilde{G}$ decays, or looking for non-resonant edges in the lineshape such as those caused by slepton-mediated $\tilde{g} \to q\bar{q}\tilde{\ell}\ell \to q\bar{q}\ell^+\ell^-\tilde{\chi}_1^0$ decays. This search reported the largest deviation with respect to SM among the ATLAS searches for squarks and gluinos, quoting an excess with a significance of three standard deviations in the signal region selecting events with on-shell $Z \to \ell\ell$.

Finally, exclusive production of charm squarks with direct decays $\tilde{c} \to c\tilde{\chi}_1^0$ has been looked for in Ref. [16] through the tagging of c-quark jets, leading to excluded charm squark masses below 500 GeV for a light LSP, a performance similar to the one obtained for generic squark searches (Fig.1a).

FINAL STATES WITH B JETS, TAU LEPTONS OR PHOTONS

The decay chains presented so far were rather generic in terms of the flavour of the (s)quarks and (s)leptons involved in the intermediate and final states. However, in many SUSY models, third generation sleptons and squarks can play an enhanced role in the decay chains, because of their lighter masses. For example, even if one assumes flavour unification at large energy scales, the large Yukawa couplings of the t, b quarks and τ leptons compared to the first two fermion generations can lead to lighter top, bottom squarks or tau sleptons [1] through increased contributions to the running masses in the renormalization group equations, as well as a larger induced mixing of the superpartners of the left- and right-handed chiral degrees of freedom. This can lead to signatures often containing t or b quarks, or taus.

Most of the decay chains also assume SUGRA-like scenarios, in which the LSP is the lightest neutralino. But in gauge-mediated SUSY breaking scenarios, the LSP is instead the gravitino, enforcing e.g. signatures with photons or taus if the next-to-LSP (NLSP) is a bino-like neutralino ($\tilde{\chi}_1^0 \to \gamma\tilde{G}$) or a stau ($\tilde{\tau} \to \tau\tilde{G}$).

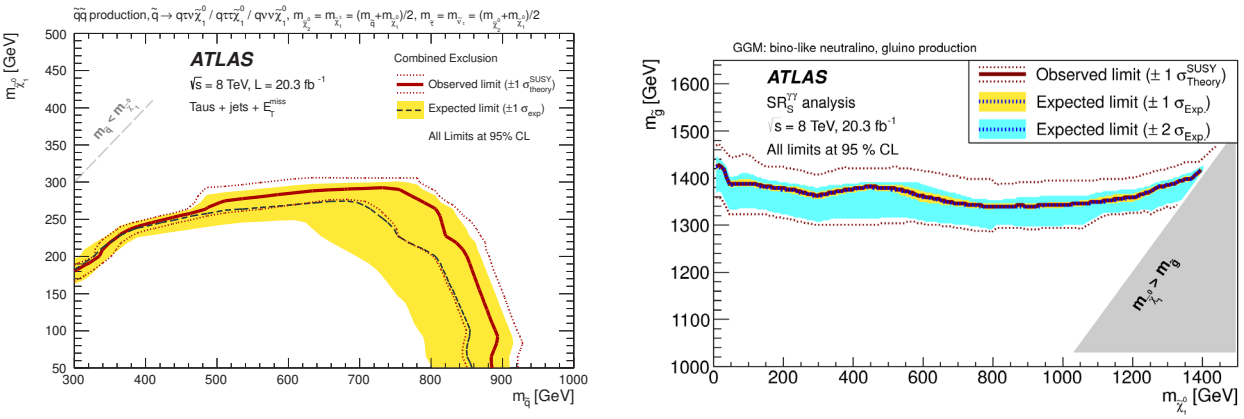

(a) $\tilde{q}\tilde{q}^*$ production, $\tilde{q} \to q'\tau\nu\tilde{\chi}_1^0$ / $q\tau\tau\tilde{\chi}_1^0$ / $q\nu\nu\tilde{\chi}_1^0$ (b) $\tilde{g}\tilde{g}$ production, $\tilde{g} \to q\bar{q}\tilde{\chi}_1^0 \to q\bar{q}\gamma\tilde{G}$

FIGURE 4. 95% CL_S exclusion limits on quark-antisquark production with $\tilde{\tau}$-mediated decay to LSP (left), and gluino-gluino production in a GGM scenario with a $\tilde{\chi}_1^0 \to \gamma\tilde{G}$ decay (right), as a function of the gluino and neutralino masses. Refs. [4, 5].

Final states with *b* jets

Light top squarks are further favored by constraints enforced by the resolution of the SM hierarchy problem in the frame of SUSY models, which require their masses not to exceed the TeV scale. Masses of bottom squarks are also limited to some extent, being related to top squarks through $SU(2)$ invariance. While the direct production of third generation squarks is the subject of dedicated ATLAS searches [17], gluino decays mediated by top or bottom squarks, such as $\tilde{g} \to t\bar{t}\tilde{\chi}_1^0$ or $\tilde{g} \to b\bar{b}\tilde{\chi}_1^0$, might also be significantly enhanced. Such decays lead to peculiar final states with four bottom or top quarks.

A search was performed [18] to specifically target these final states, selecting events with at least three *b*-tagged jets. Figure 3 shows exclusion limits on the gluino mass as function of the LSP mass in the two decay scenarios mentioned previously. Gluino masses up to 1.3 TeV are excluded, similarly to the case of decays into light flavour quarks (Fig. 1b). However, thanks to the lower SM background for *b*-enriched final states, the sensitivity to regions of the phase space with large LSP masses is significantly improved, allowing exclusion for LSP masses up to 600 GeV.

Final states with tau leptons

The largely increased rates of tau leptons with respect to electrons or muons in final states associated to scenarios with a tau slepton as NLSP lead to a dedicate search [19], which selected for events with at least one tau, jets and $E_{\mathrm{T}}^{\mathrm{miss}}$, and further categorized them as function of the number of taus and other light leptons. A reinterpretation of the analysis results was proposed recently in Ref. [4], in the context of squarks or gluino decays to a neutralino LSP via tau sleptons, $\tilde{q} \to q(\tilde{\chi}_1^{\pm}|\tilde{\chi}_2^0)$ with $\tilde{\chi}_1^{\pm} \to (\tilde{\tau}\nu|\tau\tilde{\nu})\tilde{\chi}_1^0$ and $\tilde{\chi}_2^0 \to (\tilde{\tau}\tilde{\tau}|\tilde{\nu}\tilde{\nu})\tilde{\chi}_1^0$, leading to final states with up to four taus. The corresponding exclusion limits on the gluino mass is shown on Fig. 4a, reaching here again 850 GeV for a light LSP.

Final states with photons

Searches with photons and jets in the final state [5] are mainly motivated by the presence of a $\tilde{\chi}_1^0 \to \gamma\tilde{G}$ decay within the squark or gluino decay, which occurs in gauge-mediated SUSY breaking scenarios. Events with at least one photon are selected, and are categorized depending on the presence of additional features (another photon, lepton, *b*-tagged jet), with additional requirements on $E_{\mathrm{T}}^{\mathrm{miss}}$ varying from 100 to 300 GeV.

Figure 4b shows the exclusion limits on the gluino mass in the simplest scenario, with a direct decay $\tilde{g} \to q\bar{q}\tilde{\chi}_1^0$ which relies on a signal region built from events with at least two photons and jets. In that case, gluino masses up to 1.3 Tev are excluded, independently of the neutralino mass which this time acts only as an intermediate state in the decay chain. Other signal regions requiring leptons or *b*-tagged jets allow to probe scenarios with concurrent decay channels, for example $\tilde{\chi}_1^0 \to h\tilde{G}$ with $h \to b\bar{b}$, or $\tilde{\chi}_1^0 \to Z\tilde{G}$ with $Z \to \ell\ell$. Exclusion limits are provided in Ref. [5] on minimal gauge-mediated models that feature such decays, which also lead to exclude gluino masses below O(1 TeV).

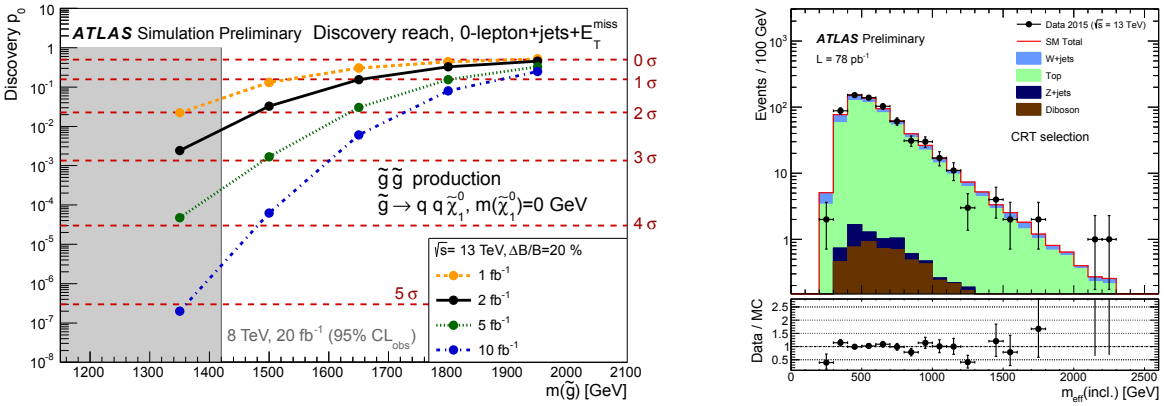

(a) (b)

FIGURE 5. Projection at $\sqrt{s} = 13$ Tev of the sensitivity to gluino pair production (a), and first 2015 data / Monte-Carlo comparisons (b), for the inclusive search with zero lepton, jets and $E_{\mathrm{T}}^{\mathrm{miss}}$. Refs. [20, 21].

CONCLUSION

The ATLAS experiment has conducted several searches for squarks and gluinos using various topologies corresponding to different decay modes, that included final states requiring leptons, *b*-tagged jets, taus or photons. No significant excess above SM predictions was observed, and exclusion limits were set on the squark and gluino masses in various scenarios. For light neutralinos, the experimental sensitivity reached gluino masses up to 1.3 TeV, and squark masses up to 900 GeV. In general, the constraints are not varying much with the decay mode, except for heavy LSPs where particular topologies with low expected SM background can lead to an improvement of the sensitivity.

The focus is now set on the second phase of exploitation of the LHC at an increased center-of-mass energy of 13 TeV and a higher integrated luminosity, for which a large improvement in sensitivity to gluino and squarks production is foreseen (Fig. 5a).

REFERENCES

[1] S. P. Martin, Adv. Ser. Direct. High Energy Phys. **21**, 1153 (2010).
[2] L. Evans and P. Bryant, JINST **3**, p. S08001 (2008).
[3] ATLAS Collaboration, JINST **3**, p. S08003 (2008).
[4] ATLAS Collaboration, JHEP **10**, p. 054 (2015).
[5] ATLAS Collaboration, Phys. Rev. **D92**, p. 072001 (2015).
[6] A. L. Read, Journal of Physics G: Nuclear and Particle Physics **28**, p. 2693 (2002).
[7] M. Baak, G. Besjes, D. Cte, A. Koutsman, J. Lorenz, et al., Eur.Phys.J. **C75**, p. 153 (2015).
[8] G. Cowan, K. Cranmer, E. Gross, and O. Vitells, Eur. Phys. J. **C71**, p. 1554 (2011), [Erratum: Eur. Phys. J.C73,2501(2013)].
[9] ATLAS Collaboration, JHEP **09**, p. 176 (2014).
[10] ATLAS Collaboration, Phys. Rev. **D90**, p. 052008 (2014).
[11] ATLAS Collaboration, JHEP **04**, p. 116 (2015).
[12] ATLAS Collaboration, JHEP **10**, p. 130 (2013), [Erratum: JHEP01,109(2014)].
[13] ATLAS Collaboration, JHEP **06**, p. 035 (2014).
[14] C. Rogan, 2010, arXiv hep-ex/1006.2727.
[15] ATLAS Collaboration, Eur. Phys. J. **C75**, p. 318 (2015).
[16] ATLAS Collaboration, Phys. Rev. Lett. **114**, p. 161801 (2015).
[17] ATLAS Collaboration, Eur. Phys. J. **C75**, p. 510 (2015).
[18] ATLAS Collaboration, JHEP **10**, p. 24 (2014).
[19] ATLA Collaboration, JHEP **09**, p. 103 (2014).
[20] ATLAS Collaboration, 2015, ATL-PHYS-PUB-2015-005.
[21] ATLAS Collaboration, 2015, ATL-PHYS-PUB-2015-028, ATL-PHYS-PUB-2015-029, ATL-PHYS-PUB-2015-030.

Proceedings of the LHCP2015 Conference, St. Petersburg, Russia, August 31 - September 5, 2015

Editors: V.T. Kim and D.E. Sosnov

CMS: Searches For Third Generation Squarks

LARA LLORET IGLESIAS

LIP-Lisboa Av. Elias Garcia 14, 1000−149 Lisbon (Portugal)

lara@cern.ch

On behalf of the CMS Collaboration

Abstract. Summary of the main searches for third generation squarks produced directly in the hard scattering with the CMS detector at a center of mass energy of 8 TeV.

INTRODUCTION

Supersymmetry (SUSY) [1][2] is a possible extension of the standard model (SM). It provides a symmetry between fermions and bosons such that a supersymmetric particle (generically referred to as a *sparticle* or *superpartner* is proposed for each SM particle. A sparticle has the same properties as its SM counterpart except that its spin quantum number differs by a half-integer. Spin 1/2 SM fermions, (quarks and leptons) are thus paired with spin 0 SUSY sfermions (the squarks and sleptons). There is a similar, but slightly more complicated pairing for bosons; SUSY models have extended Higgs sectors that contain neutral and charged higgsinos that mix with the SUSY partners of the neutral and charged electroweak gauge bosons, respectively. The resulting mixed states are referred to as neutralinos and charginos. In many instances of SUSY with conservation of R-parity [8], the neutralino, $\tilde{\chi}_1^0$, is weakly interacting. It is also stable because it is the lightest SUSY particle (LSP), and thus an excellent candidate for Dark MatterSUSY protects the Higgs mass against divergent quantum corrections associated with virtual SM particles by providing cancellations via the corresponding corrections for virtual superpartners. Since no sparticles have been observed thus far, they are generally expected to be more massive than their SM counterparts. On the other hand, sparticle masses cannot be arbitrarily large if they are to stabilise the Higgs mass without an unnatural level of fine-tuning. This is particularly important for the partners of the third generation SM particles. Searches are performed for signatures that are in common to many scenarios. One likely feature of SUSY is that third generation squarks are lighter than squarks of the first and second generation. Squarks can either be produced directly in the hard scattering or via a gluino decay. Only results from direct production will be the scope of this article. These processes present a small production cross section and often lead to signatures with large SM backgrounds. The results of the CMS searches are interpreted in simplified models where the parameter space is reduced to two or three parameters by restricting it to one production and decay chain.

THIRD GENERATION SQUARK SEARCHES

The CMS collaboration has performed several searches which are sensitive to third generation squark production at 8 TeV. The following sumarizes some of the most relevant searches which interpret their results in models of third generation squark production.

All hadronic MVA

The data sample of proton-proton collisions used in this analysis [3] corresponds to an integrated luminosity of 18.9 fb^{-1} at $\sqrt{s} = 8$ TeV. The search features novel background suppression and prediction methods, including a dedicated top-quark pair reconstruction algorithm referred to as the Comprehensively Optimized Resonance Reconstruction

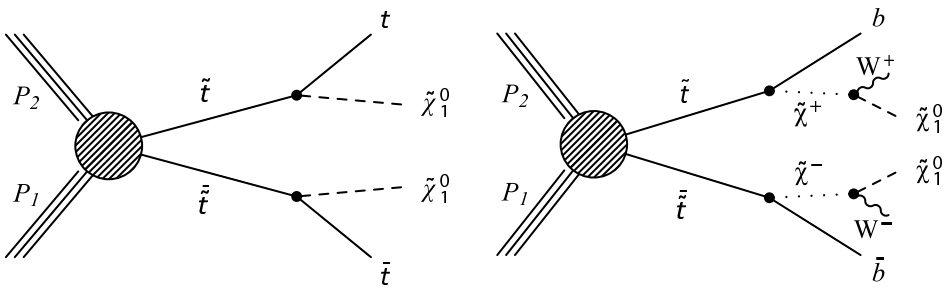

FIGURE 1. Diagrams representing two simplified models of direct top squark pair production: T2tt with top squark decay via an on-shell top quark (left) and T2bW with top squark decay via an intermediate chargino (right).

ALgorithm (CORRAL). Kinematic properties of the reconstructed top candidates are then exploited to further improve the discrimination of signal from background. The algorithm starts by clustering jets with the Cambridge/Aachen algorithm [7] with distance metric R=1 to produce what will be referred to as proto-jets. Then each fat jet is considered for division into a pair of subjets. A MVA 'picky' metric is then used to determine if it is more appropriate to associate the particles with the two subjets than with the fat jet. Jets passing a set of criteria that separate the highest p_T jet from a top quark decay from all other jets in the event are labeled seed jets. Three-jet top quark candidates are then constructed from all combinations of three jets in the event that include at least one seed jet. They must pass the 'top candidate' MVA. The most important input variables are the W and top invariant masses and the b-tagging discriminator value. Other variables such as the angular separations of the jets are included for additional discrimination. A final list of top pairs contains all combinations of two high quality top candidates with independent jets. The reconstructed top pair used in the analysis is the one with the highest discriminator value from a BDT that is trained with variables similar to those used in the candidate selection as well as information regarding correlations between the top candidates. The CORRAL algorithm reconstructs at least one top pair in nearly 100% events that have six or more picky jets.

Once the top pairs have been reconstructed kinematics are used to discriminate signal from background. Figure 2 illustrates the signal separation gained by exploiting differences in the kinematics of the reconstructed top pairs in signal relative to top pair candidate in SM background.

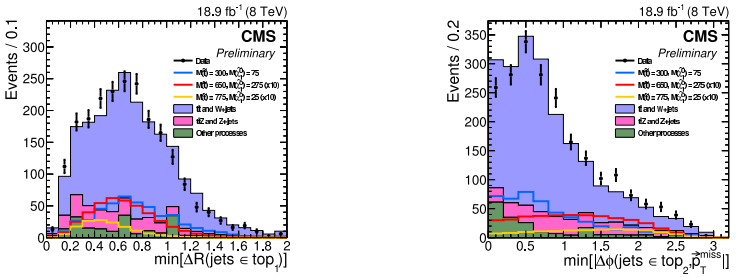

FIGURE 2. The distributions of properties of reconstructed top pairs are shown for data together with signal and background MC data samples for three choices of MStop and MLSP after the baseline selection. The left plot shows the minimum angular separation between any two jets in the leading reconstructed top, defined as the top candidate of the pair with the highest discriminator value, while the right plot shows the minimum separation in ϕ between each jet and the missing p_T in the sub-leading reconstructed top.

Results

The data are found to be in agreement with the predicted backgrounds. Exclusion limits are set in simplified SUSY models with the top squark decaying to jets and an undetected neutralino, either through an on-shell top quark or through an intermediate chargino. Models with the top squark decaying via an on-shell top quark are excluded for top squark masses up to 755 GeV in the case of neutralino masses below 200 GeV. Models with an intermediate chargino are excluded in some scenarios for top squark masses up to 650 GeV. Figure 3 shows the observed and expected

limits for the T2tt signal topology.

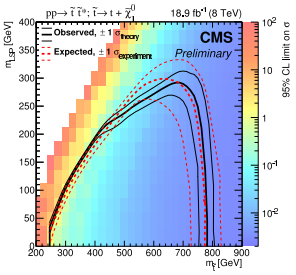

FIGURE 3. Observed and expected 95% CL limit on the $\tilde{t}\bar{\tilde{t}}$ production cross section and exclusion areas in the $m_{\tilde{t}} - m_{\chi_1^0}$ plane for the T2tt signal topology.

Monojet searches

Given the lack of observation of a SUSY signature in more conventional searches, it is important to search for SUSY with compressed mass spectra, i.e. SUSY scenarios in which the parent sparticles are close in mass to the daughter sparticles. Small mass splittings between the top or bottom squark and the LSP leave little visible energy in the detector, making signal events difficult to distinguish from SM background. However, events with an energetic initial state ration (ISR) jet recoiling against the missing p_T vector from the LSP can provide a clear signal for compressed events. The dominant decay mode is the flavour changing neutral-current process $\tilde{t} \to c\chi_1^0$. In the case of the b, the kinematically similar decay $\tilde{b} \to b\chi_1^0$ dominates for compressed scenarios, so the monojet topology is used to search for both top and bottom squarks. Figure 4 shows the Feynman diagrams taken into account for the monojet search.

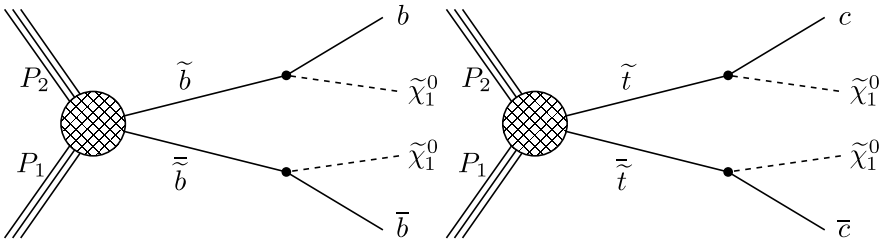

FIGURE 4. Feynman diagram showing the pair production of bottom squarks followed by their decays via $\tilde{b} \to b\chi_1^0$ (left) and via $\tilde{t} \to c\chi_1^0$ (right)

A search [6] is performed for events with a single jet and significant missing p_T. The main backgrounds are due to Z($\nu\nu$)+jets and W(lν) processes. These backgrounds are estimated from data, using a control sample of μ+jets events in which Z ($\mu\mu$) and W($\mu\nu$) events are used to estimate the Z($\nu\nu$)+jets and W($l\nu$) backgrounds, respectively. Small contributions from diboson, QCD multijet, and $t\bar{t}$ events are estimated using simulation corrected for any differences between simulation and data. Very small backgrounds arising from single top quark and Z$\to l^+l^-$ processes are taken from simulation directly.

Results

Figures 5 and 6 show the expected and observed 95% CL exclusion limits in the (msbottom, mLSP) mass plane for bottom-squark pair production assuming a 100% branching fraction to the decay $\tilde{b} \to b\chi_1^0$ and $\tilde{t} \to c\chi_1^0$ respectively.

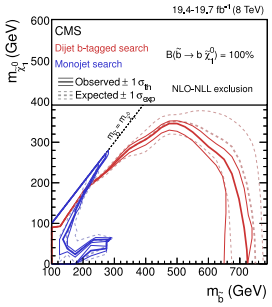

FIGURE 5. Expected and observed 95% CL exclusion limits in the (msbottom, mLSP) mass plane for bottom-squark pair production, assuming 100% branching fraction to the decay $\tilde{b} \to b\chi_1^0$. The $\pm\sigma_{exp}$ and $\pm\sigma_{th}$ limit curves are also shown. Limits for the dijet b-tagged search and monojet searches are superimposed, to illustrate where in the parameter space each search dominates. The black diagonal line marks the border of the kinematically allowed region.

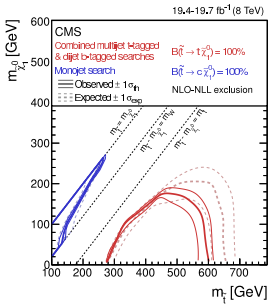

FIGURE 6. Expected and observed 95% CL mass exclusion limits in the (mstop, mLSP) mass plane for top-squark pair production, assuming 100% branching fraction to the decay $\tilde{t} \to t\chi_1^0$, or, in the case of a highly compressed spectrum, to $\tilde{t} \to c\chi_1^0$. The $\pm\sigma_{exp}$ and $\pm\sigma_{th}$ limit curves are also shown. The combined results from the dijet b-tagged and multijet t-tagged searches and the result from the monojet search are displayed separately. The dashed black diagonal lines mark the borders of the various kinematic regimes leading to different top squark decays as described in the text.

1 lepton stop MVA

This search [4] covers the pair production of top squarks in events with a single isolated electron or muon, jets, large missing transverse energy, and large transverse mass. The data sample corresponds to an integrated luminosity of $19.5 fb^{-1}$ of pp collisions collected in 2012 by the CMS experiment at a center-of-mass energy $\sqrt{(s)} = 8$ TeV. The results are interpreted in the context of supersymmetric models with pair production of top squarks that decay either to a top quark and a neutralino (t2tt) or to a bottom quark and a chargino (t2bW) for different x values where x is defined as $m_{\tilde{\chi}^\pm} = x \cdot m_{\tilde{t}} + (1-x) \cdot m_{\tilde{\chi}_1^0}$. These processes are expected to have large branching fractions if kinematically accessible. The signature of the signal process includes high transverse momentum jets, including two b-jets, and missing ET. Exactly one isolated, high pT electron or muon, at least 4 jets, at least one b-tagged jet, and large missing ET and transverse mass (MT) are required. The requirement of large MT strongly suppresses backgrounds from semi-leptonic decays of top quark pairs, and from W+jets. The dominant background in this kinematic region is dilepton decays of top quark pairs, where one of the leptons is not identified. The primary results of the search use boosted decision tree (BDT) techniques, and a cut-based analysis is pursued as a cross-check. Several BDT and cut-based signal regions are defined, in order to be sensitive to a range of signal kinematics, which depend on the masses of the supersymmetric particles produced in the signal events. Backgrounds are estimated from Monte Carlo, with scale factors (where necessary) and uncertainties derived from data control regions.

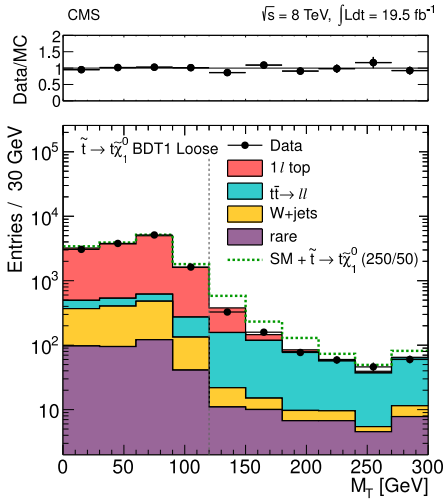

FIGURE 7. Comparison of the MT distributions in data vs. MC for events satisfying the loosest t2tt BDT signal region requirements (BDT1 loose). The distribution for the t2tt model with m(t) = 250 GeV and m(tt) = 50 GeV is overlaid. The vertical dashed line indicates the corresponding signal region requirement.

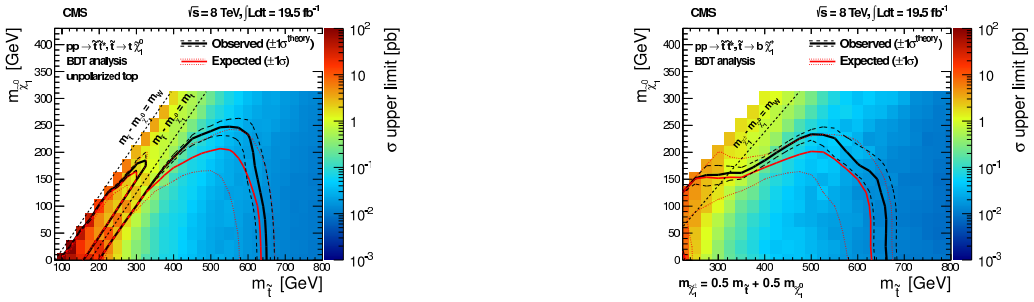

FIGURE 8. Interpretations using the primary results from the BDT method for the t2tt model (left) and t2bW for x=0.50 (right). The color scale indicates the observed cross section upper limit. The observed, median expected, and ±1 standard deviation (σ) expected exclusion contours are indicated.

Results

The data is consistent with the expected backgrounds in the signal regions. The results are interpreted in the context of models of top squark pair production where the top squark decays either to a top quark and a neutralino or to a bottom quark and a chargino. These results probe top squarks up to about 650 GeV, depending on the decay. Figure 8 shows the interpretation using the BDT results for both the t2tt aand t2bW model (x=0.50).

Combination with 0 leptons Razor

The razor variables are defined in the context of pair production of heavy particles each decaying to a visible system of particles and a weakly interacting particle. Details about the different variables can be found in [5]. Figure 9 shows the combined limits of the 0 leptons razor results with the 1 lepton stop MVA. The 1 lepton analysis dominates for low stop masses and the 0 leptons razor one for the high stop masses.

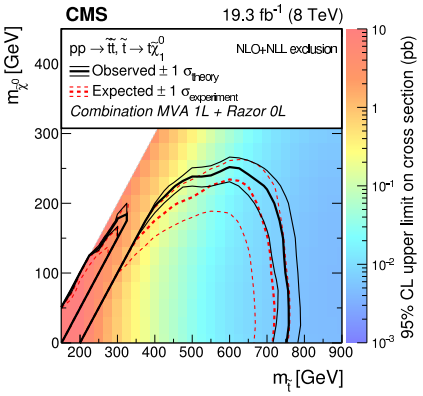

FIGURE 9. Interpretations using the primary results from the BDT method for the t2tt model (left) and t2bW for x=0.50 (right). The color scale indicates the observed cross section upper limit. The observed, median expected, and ±1 standard deviation (σ) expected exclusion contours are indicated.

REFERENCES

[1] Barbieri, R., Ferrara, S., Savoy, C. A. (1982). Gauge models with spontaneously broken local supersymmetry. Physics Letters B, 119(4), 343-347.

[2] Dawson, S., Eichten, E., Quigg, C. (1985). Search for supersymmetric particles in hadron-hadron collisions. Physical Review D, 31(7), 1581.

[3] CMS Collaboration, A Search for Scalar Top Quark Production and Decay to All Hadronic Final States in pp Collisions at $\sqrt(s)$ = 8 TeV, SUS-13-023, https://cds.cern.ch/record/2044441

[4] Puljak, I., Kadija, K., Antunovic, Z., Morovic, S., Luetic, J., Duric, S., Brigljevic, V. (2013). Search for top-squark pair production in the single-lepton final state in pp collisions at $\sqrt(s)$ = 8 TeV. European physical journal C: particles and fields, 73, 2677-1.

[5] Khachatryan, V., Sirunyan, A. M., Tumasyan, A., Adam, W., Bergauer, T., Dragicevic, M., Hartl, C. (2015). Search for supersymmetry using razor variables in events with b-tagged jets in p p collisions at s= 8 TeV. Physical Review D, 91(5), 052018.

[6] Khachatryan, V., Besancon, M., Couderc, F., Dejardin, M., Denegri, D., Fabbro, B., Givernaud, A. Searches for third generation squark production in fully hadronic final states in proton-proton collisions at sqrt (s)= 8 TeV.

[7] Dokshitzer, Y. L., Leder, G. D., Moretti, S., Webber, B. R. (1997). Better jet clustering algorithms. Journal of High Energy Physics, 1997(08), 001.

[8] Wess, J., Zumino, B. (1974). Supergauge transformations in four-dimensions. Nucl. Phys. B, 70(3), 9.

Proceedings of the LHCP2015 Conference, St. Petersburg, Russia, August 31 - September 5, 2015

Editors: V.T. Kim and D.E. Sosnov

Search for "Electroweakinos" with the ATLAS Detector at the LHC

ALEXANDER MANN

Ludwig-Maximilians-Universität München, Fakultät für Physik, Am Coulumbwall 1, 85748 Garching bei München.

A.Mann@LMU.de

On behalf of the ATLAS Collaboration

Abstract. Supersymmetry is one of the most popular extensions of the Standard Model of particle physics, as it offers solutions to several shortcomings of the Standard Model. Natural supersymmetric models favor masses for the new particles which are predicted by supersymmetry in the range of hundreds of GeV, well within the reach of the Large Hadron Collider at CERN. If squarks and gluinos are much heavier, the production of charginos and neutralinos may be the dominant production mode for supersymmetric particles. These proceedings present results from new searches for the production of charginos and neutralinos, focusing on the recent paper by the ATLAS collaboration that summarizes and extends the searches for the electroweak production of supersymmetric particles using data from Run-1 of the LHC.

INTRODUCTION

Supersymmetry (SUSY) [1–9] is one of the most popular extensions of the Standard Model of particle physics, as it can provide solutions to a number of problems or short-comings of the Standard Model. It introduces a new space-time symmetry between fermions and bosons and predicts essentially a doubling of the number of elementary particles contained in the model. A large number of searches have been designed and carried out in the past to find traces of these particles in collider experiments. These proceedings discuss the search for electroweakinos with the ATLAS detector [10], one of the two large multi-purpose detectors at the Large Hadron Collider (LHC) [11] at CERN. Electroweakinos comprise the supersymmetric charginos $\widetilde{\chi}_i^{\pm}$ $(i = 1, 2)$ and neutralinos $\widetilde{\chi}_j^0$ $(j = 1, \ldots, 4)$, which are mixtures of the bino, the wino triplet and the higgsinos, which in turn are the superpartners of the $\mathrm{U}(1)_Y$ and $\mathrm{SU}(2)_L$ gauge bosons and Higgs doublets of supersymmetry.

The primary motivation for the search for electroweakinos comes from its complementarity to the strong-production searches. In fact, electroweak production may be the dominant production mode for supersymmetric particles at the LHC if the squarks and gluinos are sufficiently heavy. Another motivation is naturalness [12, 13]: Natural models of supersymmetry suggest that the masses of the lightest charginos and neutralinos fall into a range that is well accessible at the LHC.

All searches for supersymmetry have produced null results so far, as no significant excess beyond the event yields expected from Standard Model processes has been observed. These null results can be translated into limits on the masses of supersymmetric particles in simplified models, which for strongly produced particles reach beyond 1 TeV, whereas in the case of electroweak production they are of the order of several hundreds of GeV. Recent results from the electroweak analyses carried out by the ATLAS collaboration include a search for exotic decays of the observed 125 GeV Higgs boson into light neutralinos and possibly gravitinos. This yields final states with photons and large missing transverse momentum ($E_{\mathrm{T}}^{\mathrm{miss}}$) and is motivated from Gauge-Mediated Supersymmetry Breaking and Next-to-Minimal Supersymmetry extensions of the Standard Model [14]. Then there is another analysis which does somewhat the opposite and looks for the production of a chargino $\widetilde{\chi}_1^{\pm}$ and a neutralino $\widetilde{\chi}_2^0$ decaying via a W boson and the 125 GeV Higgs boson [15]. The latest result from the ATLAS collaboration on the search for electroweakinos is the electroweak summary paper [16]. This paper will be the focus of these proceedings.

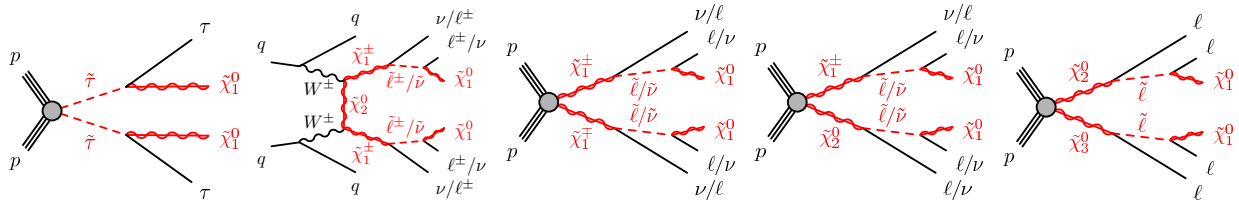

FIGURE 1. Diagrams illustrating the production of supersymmetric particles and their decays modes in the five simplified models that are employed in the interpretation of the results in the electroweak summary paper.

THE SEARCH FOR ELECTROWEAKINOS

The goal of the electroweak summary paper is to summarize and to extend the searches for electroweak supersymmetry with the ATLAS detector using the data taken during the first run (Run-1) of the LHC, corresponding to 20 fb^{-1} of pp collisions at a center-of-mass energy $\sqrt{s} = 8$ TeV. It is not only a summary but also includes five new analyses that have not been published before. These analyses look for two- or three-lepton final states and strive to extend the reach of earlier analyses by lowering the thresholds on the transverse momenta (p_{T}) of the leptons, by exploiting initial-state radiation (ISR) or vector-boson fusion (VBF) event topologies, or through the application of multi-variate analysis (MVA) techniques. In addition to these five new analyses, statistical combinations of the new and the existing searches are performed to extend the excluded mass ranges, adding also new combinations and reinterpretations of existing searches. Furthermore, the impact of the assumption for the mass of the intermediate slepton in simplified models on the exclusion reach is studied. One particular focus of the new analyses is to improve the sensitivity of the searches for supersymmetry scenarios with compressed mass spectra, where small mass differences between the particles in the supersymmetry decay chains lead to low-energetic decay products. Due to their low energy and momentum, these decay products may fail trigger or offline thresholds and may thus not be reconstructed. This deteriorates the signal acceptances and reduces the sensitivity of the analyses.

The results of the searches described in the electroweak summary paper are interpreted in two classes of models. The first class are simplified models, where only one specific production mode and decay chain for the supersymmetric particles is considered, and the branching ratios for the decays are assumed to be 100 %. Five simplified models are employed in the interpretation of the results in the electroweak summary paper as shown in Fig. 1 (from left to right): Production of stau pairs, production of same-sign chargino pairs in a VBF topology, chargino-pair production, associated production of the lightest chargino ($\widetilde{\chi}_1^{\pm}$) and the second-lightest neutralino ($\widetilde{\chi}_2^0$), and production of $\widetilde{\chi}_2^0$ together with $\widetilde{\chi}_3^0$. In all cases, the decays of the electroweak gauginos may proceed via all three slepton or sneutrino generations. The second class of models are phenomenological models: In the electroweak phenomenological Minimal Supersymmetric extension of the Standard Model (pMSSM), only the direct production of charginos and neutralinos is considered, which results in a small number of only four parameters. The two-parameter Non-Universal Higgs Masses model (NUHM2) is basically a constrained MSSM with two additional parameters that allow to tune the Higgs masses. The third phenomenological model used in the paper is a scenario with Gauge-Mediated Supersymmetry Breaking (GMSB), where the lightest supersymmetric particle (LSP) is the gravitino. This is different from all other models that are considered, where the LSP is always the lightest neutralino $\widetilde{\chi}_1^0$. For the GMSB scenario, electroweak production dominates for large values of the parameter Λ, the supersymmetry-breaking mass scale felt by the low-energy sector. In all models discussed in these proceedings, R-parity is assumed to be conserved.

Two of the five new analyses are independent from the others as their selections have little overlap with the other analyses and their results are interpreted in models specific to these analyses. These two analyses are the two-tau analysis using an MVA technique and the search for two same-sign (SS) leptons in a vector-boson fusion topology. They will therefore be discussed, including their results and interpretations, separately from the others.

2τ (MVA) Analysis

The *two-tau (MVA)* analysis is an update of an earlier analysis, which targets the direct production of charginos, neutralinos and staus in final states with at least two hadronically decaying tau leptons and missing transverse momentum [17]. In contrast to the simpler, cut-based analysis, the updated version makes use of a boosted-decision tree (BDT) to improve the sensitivity, and the results are interpreted in a simplified model with direct-stau production, where the

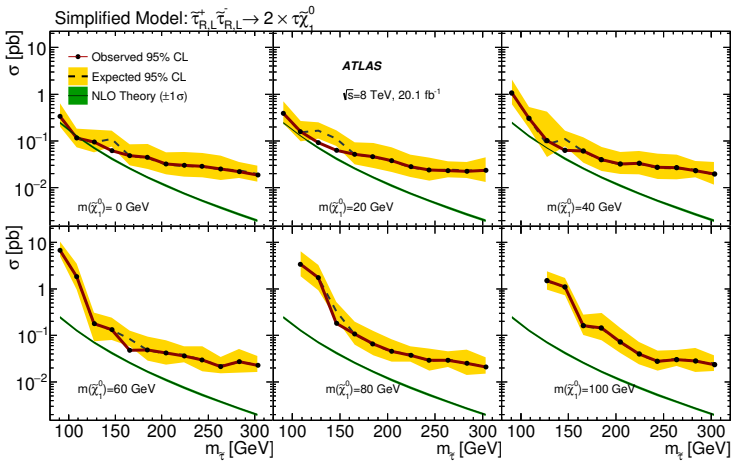

FIGURE 2. For six different masses of the LSP, these plots show the 95 % CL exclusion limits on the cross sections for combined pair production of left- and right-handed staus as a function of the stau mass [16].

cut-based analysis had practically no sensitivity. In the two-tau (MVA) analysis, events with exactly two taus with opposite charge are selected. Events that contain a *b*-tagged jet or where the two taus have an invariant mass that is compatible with the assumption that the taus are coming from a *Z*-boson decay are rejected. A boosted decision tree is trained on twelve input variables, which are based on kinematic properties of the two taus and $E_{\mathrm{T}}^{\mathrm{miss}}$ and have good discriminatory power. A cut on the output value of the BDT is then used to define one signal region (SR). Good agreement of the distribution of the BDT output variable in data and its expected distribution from the Standard Model background prediction is found prior to the signal-region cut, and no excess is observed in the signal region. This allows to interpret the analysis in terms of limits on the production cross section for stau pairs as a function of the mass of the stau and the LSP, as shown in Fig. 2. The best limit is found for a stau mass around 110 GeV and a massless LSP.

2 SS ℓ (VBF) Analysis

The second analysis from the summary paper to be presented here looks at final states with two light leptons with the same charge. It specifically targets a scenario where supersymmetric particles are produced via vector-boson fusion (VBF) as shown in the second diagram in Fig. 1. This reduces the production cross section considerably but on the other hand makes it easier to separate signal and background by requiring the presence of the two additional VBF jets. The jets also often cause the chargino to be boosted, yielding energetic decay products even in compressed spectra. In addition to two light leptons with the same charge, events selected in this analysis are required to have two jets and missing transverse momentum above 120 GeV in order to be in the plateau of the $E_{\mathrm{T}}^{\mathrm{miss}}$ trigger that is used in this analysis. (This is a unique feature of this analysis. In contrast, all of the other four analyses use combinations of single, double, and triple lepton triggers.) One cut-based signal region is defined, exploiting the VBF topology by requiring that the two jets be well-separated and in opposite hemispheres of the ATLAS detector and have a large invariant mass. Additional cuts suppress the remaining Standard Model backgrounds, mainly diboson and top quark production. No excess is observed in the SR, thus limits are set on the VBF $\widetilde{\chi}_1^{\pm}\widetilde{\chi}_1^{\pm}$ production cross section. The limits obtained from the 2012 dataset remain above the theoretical predictions by at least a factor three, i. e. this analysis is not yet sensitive to VBF $\widetilde{\chi}_1^{\pm}\widetilde{\chi}_1^{\pm}$ production. Exclusion plots for two different assumptions on the mass of the lighter chargino $\widetilde{\chi}_1^{\pm}$ and as function of the mass splitting $\Delta m(\widetilde{\chi}_1^{\pm},\widetilde{\chi}_1^0)$ can be found in the paper [16]. CMS recently made public a search that is able to set limits on the electroweak production of supersymmetric particles in a VBF scenario [18]. The main differences are that the CMS search does not only consider same-sign chargino production but combines several production modes, assumes larger mass splittings between the chargino and the neutralino, and decays to happen via staus only.

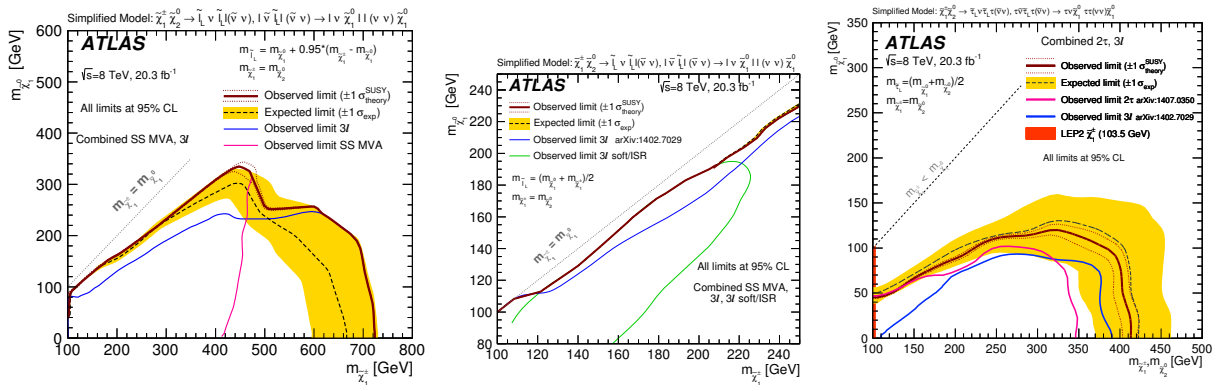

FIGURE 3. The 95 % CL exclusion limits on $\widetilde{\chi}_1^{\pm}\widetilde{\chi}_2^0$ production from the combinations of several analyses [16]. Left: $\widetilde{\ell}_L$-mediated decays with sleptons close in mass to the $\widetilde{\chi}_2^0$, middle: zoom of the compressed region, $\widetilde{\ell}_L$-mediated decays with sleptons masses halfway between $\widetilde{\chi}_2^0$ and $\widetilde{\chi}_1^0$, right: $\widetilde{\tau}_L$-mediated decays with stau mass halfway between $\widetilde{\chi}_2^0$ and $\widetilde{\chi}_1^0$.

Compressed Spectra With Two- and Three-Lepton Final States

In the following part, the remaining three of the five new analyses are discussed, before then coming the a joint presentation of their results and interpretations. These three analyses look at final states with two or three light leptons and aim to extend the reach of earlier searches for the production of electroweakinos [19, 20] for compressed supersymmetry scenarios.

The *2 OS ℓ (ISR)* analysis extends the earlier search for supersymmetry in final states with two leptons [19] to small mass splittings $\Delta m(\widetilde{\chi}_1^{\pm},\widetilde{\chi}_1^0)$ between the lightest chargino $\widetilde{\chi}_1^{\pm}$ and neutralino $\widetilde{\chi}_1^0$ by exploiting initial-state radiation jets. The ISR jet boosts the leptons from the supersymmetric decay chain, which otherwise may have too low momentum to pass the trigger or reconstruction thresholds. Events which have exactly two light leptons with opposite charge (OS leptons) and an ISR jet with high transverse momentum are selected, excluding events that contain b-tagged or forward jets, or in which the invariant mass of the two light leptons is close to the Z-boson mass. Two signal regions are defined based on "super-razor variables" [21] with good discriminatory power in compressed spectra and the ratio R_2 of the missing transverse momentum and the sum of missing transverse momentum and the transverse momenta of the leptons. ISR jets are also used in the *3ℓ (ISR)* analysis, which extends the corresponding earlier search [20] to small mass splittings $\Delta m(\widetilde{\chi}_2^0,\widetilde{\chi}_1^0)$ between the second-lightest neutralino $\widetilde{\chi}_2^0$ (or lightest chargino $\widetilde{\chi}_1^{\pm}$) and the lightest neutralino $\widetilde{\chi}_1^0$. Moreover, three-lepton triggers are now included which allow to go lower in lepton p_{T} (*soft leptons*). Events must have exactly three light leptons, including one pair with same flavor but opposite charge (SFOS). After a veto on events with b-tagged jets or where a SFOS lepton pair comes from an Υ meson decay, four signal regions are defined which either veto or require a jet with large p_{T} and differ in the allowed window for the value of the minimum mass of the SFOS pairs. Finally, the *2 SS ℓ (MVA)* analysis complements the search for three-lepton final states in case one of the three leptons is missed, selecting events with exactly two light leptons with the same charge sign. This analysis makes use of eight boosted decision trees which are trained independently to define the same number of signal regions, optimized for four different mass-splitting scenarios $\Delta m(\widetilde{\chi}_2^0,\widetilde{\chi}_1^0)$, each with and without the presence of ISR jets. The output of the BDT is also used to define validation regions that demonstrate that the Standard Model backgrounds are well understood. All three analyses observe good agreement between the event counts in data and their Standard Model predictions and no significant excess in any of the signal regions. These results are interpreted in terms of exclusion limits, combining analyses where they have comparable sensitivity.

INTERPRETATIONS

The exclusion limits on the mass parameters $m(\widetilde{\chi}_1^0)$ and $m(\widetilde{\chi}_1^{\pm}) = m(\widetilde{\chi}_2^0)$ for the simplified model with $\widetilde{\chi}_1^{\pm}\widetilde{\chi}_2^0$ production are shown in the plots in Fig. 3. Both $\widetilde{\chi}_1^{\pm}$ and $\widetilde{\chi}_2^0$ are assumed to be pure wino, whereas the $\widetilde{\chi}_1^0$ is pure bino. The resulting observed limits from combinations of both the new analyses and the ones published earlier as indicated in the plots, are given by the thick red lines and compared against the earlier exclusion limits, drawn as thinner lines.

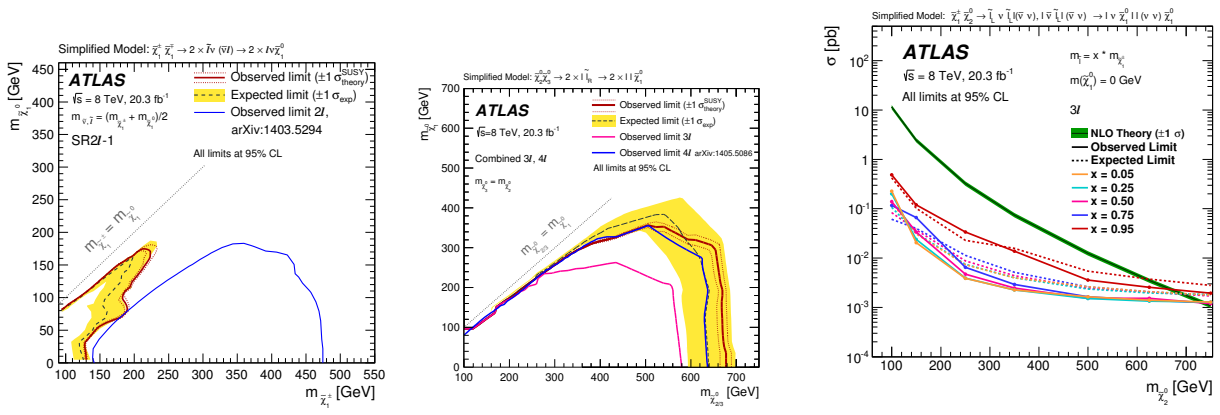

FIGURE 4. The 95 % CL exclusion limits on $\widetilde{\chi}_1^{\pm}\widetilde{\chi}_1^{\mp}$ production (left) and $\widetilde{\chi}_2^0\widetilde{\chi}_3^0$ production (middle) with slepton-mediated decays. The right-hand plot shows the impact of the intermediate slepton mass on the exclusion limit [16].

The left plot in the Figure shows the complementarity of the new 2 SS ℓ (MVA) analysis and the earlier 3ℓ analysis. In the middle, a zoom-in of the compressed region close to the diagonal is shown, which highlights the improvement of the limit in this difficult region that is obtained from the new 3ℓ (ISR / soft-leptons) analysis. Note that the assumption on the mass of the sleptons here is different from the one in the left plot. The 2 SS ℓ (MVA) analysis is also included in the combination but has no sensitivity in this region by itself and thus no exclusion line is shown. The right-hand plot of Fig. 3 shows a new combination of the existing 2τ and 3ℓ analyses in a scenario where the gaugino decays are mediated via staus only.

The left plot in Fig. 4 demonstrates the complementarity of the new 2 OS ℓ (ISR) analysis and the earlier 2ℓ analysis in the exclusion limits for the $\widetilde{\chi}_1^{\pm}\widetilde{\chi}_1^{\mp}$ simplified model with $\widetilde{\ell}_L$-mediated decays, where the new analysis fills the gap between the existing exclusion contour and the diagonal kinematic boundary. Again, the $\widetilde{\chi}_1^{\pm}$ is a pure wino and the $\widetilde{\chi}_1^0$ a pure bino in this simplified model. The plot in the middle shows a new combination of the existing 3- and 4-lepton analyses in the simplified model with $\widetilde{\chi}_2^0\widetilde{\chi}_3^0$ production and decays mediated via $\widetilde{\ell}_R$. Here, the $\widetilde{\chi}_2^0$ and $\widetilde{\chi}_3^0$ are assumed to be pure higgsino and mass-degenerate. This combination improves the earlier limits on the mass of the initial supersymmetric particles from the 4-lepton analysis by about 30 GeV. For all three simplified models, $\widetilde{\chi}_1^{\pm}\widetilde{\chi}_1^{\mp}$, $\widetilde{\chi}_1^{\pm}\widetilde{\chi}_2^0$, and $\widetilde{\chi}_2^0\widetilde{\chi}_3^0$, the impact of the assumption for the intermediate slepton mass on the exclusion reach has been checked for a massless LSP by varying the slepton mass between 5 and 95 % of the mass of the decaying gaugino. The impact is found to be small, as can be seen in the right plot of Fig. 4 for the case of $\widetilde{\chi}_1^{\pm}\widetilde{\chi}_2^0$.

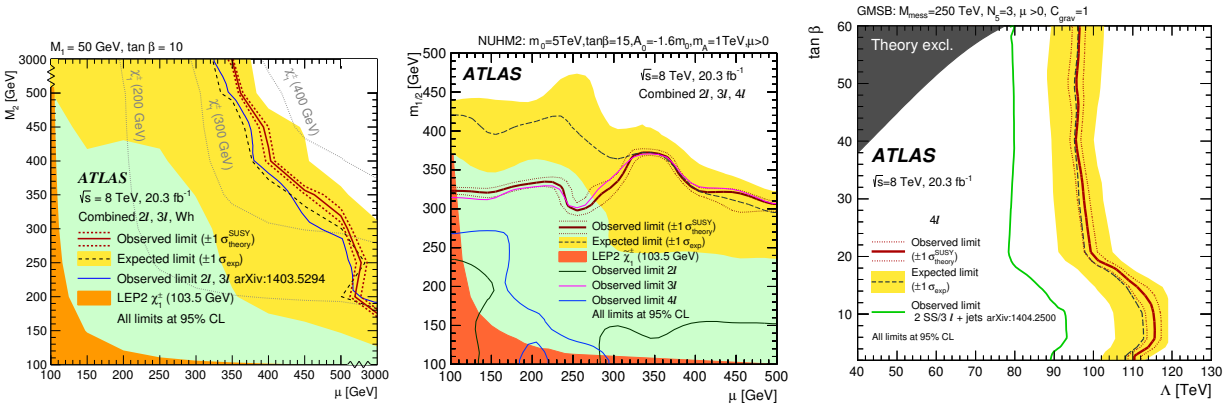

FIGURE 5. 95 % CL exclusion limits from the searches for electroweakinos in phenomenological models: pMSSM (left), NUHM2 (middle), and GMSB (right) [16].

The results of the electroweak analyses have also been interpreted in terms of exclusion limits on parameters of

phenomenological models. These limits are shown in Fig. 5. The 95 % CL exclusion limit on the pMSSM parameters μ and M_2 is obtained by combining the Wh analysis [15] with the results from the 2ℓ and 3ℓ analyses [19, 20] and is shown in the left plot. The limits on the NUHM2 parameters μ and $m_{1/2}$ come from a new combination of the existing 2ℓ, 3ℓ, and 4ℓ analyses and are shown in the middle plot in Fig. 5. It can be seen that the 3ℓ analysis drives the exclusion limit in this scenario. The right plot shows that a new reinterpretation of the 4ℓ analysis [22] yields an improvement of 15 to 20 TeV with respect to an earlier combination [23]. The electroweak summary paper also has two plots which compare all earlier and new exclusion contours in the mass-parameter planes of the respective simplified models, providing separate comparisons for slepton- and W / Z / h-boson mediated decays. For the latter decay modes, the sensitivity of the new analyses is small, thus no combination has been attempted.

CONCLUSION

In conclusion, now that the searches for supersymmetry in the data from the first run of the LHC have been wrapped up, no strong signs for physics beyond the Standard Model have emerged from the Run-1 data. Still, a large number of supersymmetry analyses have been made public that constrain the parameter space of supersymmetric models. In these proceedings, the new electroweak summary paper has been discussed, which contains the final ATLAS limits on the electroweak production of supersymmetric particles at a center-of-mass energy of $\sqrt{s} = 8$ TeV. It should be stressed that this paper is not only a summary, but also includes completely new analyses, explores several new analysis techniques, and includes new combinations.

The second run of the LHC has started, and a dataset of around $4\,\text{fb}^{-1}$ of integrated luminosity from proton-proton collisions at the increased center-of-mass energy of $\sqrt{s} = 13$ TeV has been collected in 2015. As the cross sections for the production of heavy particles grows stronger than linearly with the center-of-mass energy, the higher the relevant mass ranges, the stronger the benefit from the increased center-of-mass energy for the expected reach of a search. The first results with the new data will thus come from the strong-production searches, which benefit a lot more from the higher center-of-mass energy as the larger cross sections for strong production allow them to go higher in mass than the electroweak searches. Electroweak searches in general need more data to improve upon with the existing Run-1 results. However, they will be able to build upon lots of experience gained during Run-1, and on the long term will also profit from the higher integrated luminosity to be collected in the three years of Run-2, which is expected to exceed the integrated luminosity from Run-1 by a factor around four.

REFERENCES

[1] H. Miyazawa, Prog. Theor. Phys. **36 (6)**, 1266–1276 (1966).
[2] P. Ramond, Phys. Rev. **D3**, 2415–2418 (1971).
[3] Y. A. Gol'fand and E. P. Likhtman, JETP Lett. **13**, 323–326 (1971).
[4] A. Neveu and J. H. Schwarz, Nucl. Phys. **B31**, 86–112 (1971).
[5] A. Neveu and J. H. Schwarz, Phys. Rev. **D4**, 1109–1111 (1971).
[6] J. Gervais and B. Sakita, Nucl. Phys. **B34**, 632–639 (1971).
[7] D. V. Volkov and V. P. Akulov, Phys. Lett. **B46**, 109–110 (1973).
[8] J. Wess and B. Zumino, Phys. Lett. **B49**, 52–54 (1974).
[9] J. Wess and B. Zumino, Nucl. Phys. **B70**, 39–50 (1974).
[10] ATLAS Collaboration, JINST **3**, S08003 (2008).
[11] L. Evans and P. Bryant, JINST **3**, S08001 (2008).
[12] R. Barbieri and G. Giudice, Nucl.Phys. **B306**, 63–76 (1988).
[13] B. de Carlos and J. Casas, Phys.Lett. **B309**, 320–328 (1993), arXiv:hep-ph/9303291 [hep-ph] .
[14] ATLAS Collaboration, ATLAS-CONF-2015-001, `https://cds.cern.ch/record/1988425`.
[15] ATLAS Collaboration, Eur. Phys. J. C **75:208** (2015).
[16] ATLAS Collaboration, *submitted to Phys. Rev. D* (2015), arXiv:1509.07152 [hep-ex] .
[17] ATLAS Collaboration, Journal of High Energy Physics **1410** (2014), 096.
[18] CMS Collaboration, CMS-PAS-SUS-14-005, `https://cds.cern.ch/record/2002647`.
[19] ATLAS Collaboration, Journal of High Energy Physics **1405** (2014), 071.
[20] ATLAS Collaboration, Journal of High Energy Physics **1404** (2014), 169.
[21] M. R. Buckley *et al.*, Phys. Rev. D **89**, p. 055020 (2014).
[22] ATLAS Collaboration, Phys. Rev. D **90**, p. 052001 (2014).
[23] ATLAS Collaboration, Journal of High Energy Physics **1406** (2014), 035.

Proceedings of the LHCP2015 Conference, St. Petersburg, Russia, August 31 - September 5, 2015

Editors: V.T. Kim and D.E. Sosnov

Search for electroweak SUSY production at the CMS experiment

HAMED BAKHSHIANSOHI

Institute for Research in Fundamental Sciences, Tehran, Iran

Hamed.Bakhshian@cern.ch

On behalf of the CMS Collaboration

Abstract. A review of recent results from CMS on searches for the electroweak production of supersymmetry particles is presented. All possible production scenarios including $\chi^{\pm}\chi^{\mp}$, $\chi^{0}\chi^{\pm}$, $\chi^{0}\chi^{0}$, $\tilde{l}\tilde{l}$ and also the vector boson fusion (VBF) production mechanism are investigated. The full 2012 data sample which comprises 19.6 fb^{-1} of proton-proton collisions at $\sqrt{s}$ = 8 TeV is used. In all studied decay modes, the observed yields agree well with the expectation of the standard model (SM) predictions and limits are set on the rates of the direct production of charginos, neutralinos and sleptons.

Introduction

Most of the searches for Super Symmetry (SUSY) [1] at the Compact Muon Solenoid (CMS) [2] have focused on the production of gluinos and squarks productions, the SUSY partners of the gluon and quarks, via strong interactions [3, 4, 5]. Observing no evidence of new physics, the strongly-interacting SUSY particles up to a mass scale of ~1 TeV are excluded. If squarks and gluinos are heavy, direct electroweak production of charginos and neutralinos, the SUSY partners of the $W^{\pm}$, Z, and Higgs bosons, may be dominated at the LHC. Although the electroweak SUSY production may suffer from the very low rate, the clean leptonic final state and the QCD-free selection makes this study possible.

Search for $\tilde{\chi}^{\pm}\tilde{\chi}^{0}_{2}$ productions

The production of a chargino and a neutralino has the highest rate among electroweak SUSY productions. The masses of $\tilde{\chi}^{\pm}$ and $\tilde{\chi}^{0}_{2}$ are assumed to be equal for this study. The results of these studies are documented in [6]. Different decay scenarios for this study are considered.

The first scenario is for the slepton mass between $\tilde{\chi}^{\pm}$ and LSP ($\tilde{\chi}^{0}_{1}$) masses. In this case the parent SUSY particle decays to leptons via sleptons. The final state of such decay would be three leptons together with missing transverse energy ($\vec{E}^{\text{miss}}_{\text{T}}$). For selecting signal events, all events with 3 leptons and $\vec{E}^{\text{miss}}_{\text{T}} > 50$ GeV are selected. To suppress $t\bar{t}$ events, events with at least one b-tagged jet are discarded. The WZ contribution is estimated using simulated samples where a data driven fake rate method is exploited to estimate the remaining $t\bar{t}$ background. Events are classified based on lepton flavors, the invariant mass of the leptons and $\vec{E}^{\text{miss}}_{\text{T}}$ [6].

For the compressed spectrum, when the slepton mass is close to the LSP mass, the produced lepton could be so soft that escapes detection. To cover this part of the phase space, a search for events with two same-sign leptons plus missing energy is also performed [6].

Another possible decay scenario which has been considered is the case in which the SUSY parent particles decay to Z and W bosons because their decay to sleptons is forbidden and the neutralino is bino-like (Fig. 1 (left)). The leptonic decay of the Z boson together with leptonic and hadronic decays of the W boson are taken into account for this study. For the leptonic decay of the W boson, the 3 lepton selection which is described in the previous part is used.

Discovering the SM Higgs boson motivates the search for a Higgsino-like neutralino (Fig. 1 (right)). The leptonic decay of the W boson along with different Higgs decays are studied [6]. For the Higgs bosons decaying to $b\bar{b}$, events

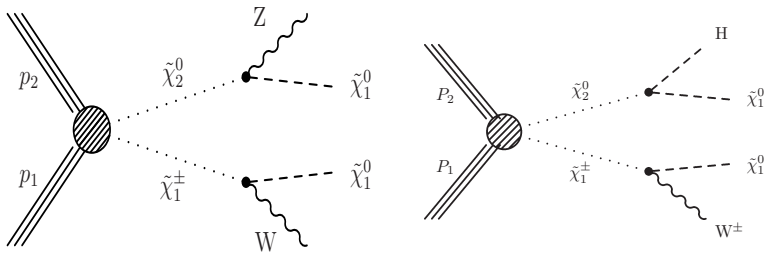

FIGURE 1. When sleptons are heavier than chargino and neutralino, they decay to SM bosons [6].

with one lepton and exactly two b-tagged jets are selected. Moderate cuts on $\vec{E}_{\mathrm{T}}^{\mathrm{miss}}$ and the transverse mass of the lepton are applied. All the backgrounds are estimated using simulation. A peak is searched for in the invariant mass of the $b\bar{b}$ system.

To search for $H \rightarrow W(l\nu)W(jj)$, events with two same-sign leptons and two jets are selected. For backgrounds from fake leptons, a data driven method is employed. All backgrounds with two prompt same-sign leptons are taken from MC. In the invariant mass of the lepton and two jets a search is performed to find the Higgs peak. As no evidence of new physics is observed, the results are used to set exclusion limits on the mass of chargino and neutralino (Fig 2 (right))

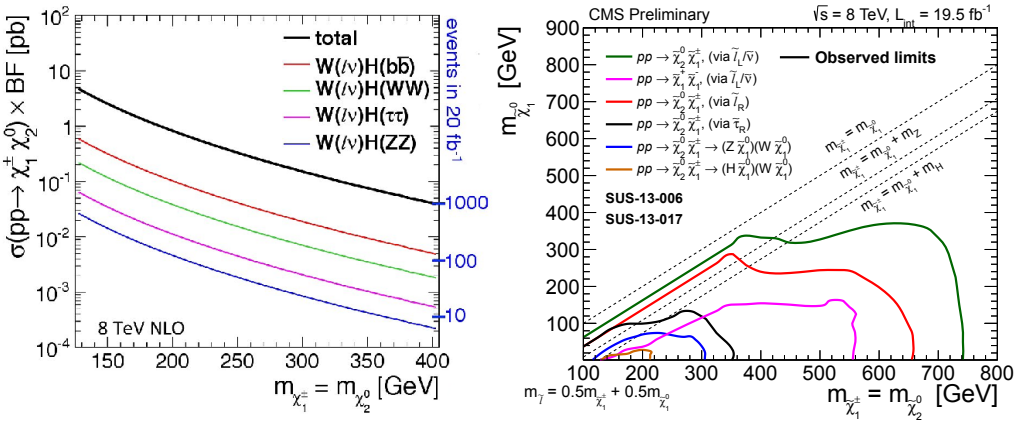

FIGURE 2. Cross section of WH via SUSY electroweak production vs. the $\tilde{\chi}^{\pm}$ mass for different branching fractions (left) and the exclusion limits on the mass of the chargino and neutralino in $\tilde{\chi}^{\pm}\tilde{\chi}_2^0$ searches by the CMS collaboration (right) [6].

Search for $\tilde{\chi}^0\tilde{\chi}^0$ production

When $\tilde{\chi}^0$ and $\tilde{\chi}^{\pm}$ are both wino-like, the production of $\tilde{\chi}^0\tilde{\chi}^0$ is very suppressed. In gauge-mediated-SUSY-breaking (GMSB) models [7, 8, 9] the production rate of this process is enhanced. LSP in this model is an almost massless gravitino. For the case of Higgsino-like $\tilde{\chi}^0$, two produced $\tilde{\chi}^0$s decay to two Higgs bosons and $\vec{E}_{\mathrm{T}}^{\mathrm{miss}}$ according to Fig. 3.

As the Higgs boson decays in 60% of cases into two b-quarks, only the $H \rightarrow b\bar{b}$ decay is considered for this search [10]. Events with four or five jets in the final state are selected among which at least three jets must be tagged as b-quark jet. To reconstruct the Higgs bosons, the combination of jets minimizing $|\Delta m_{jj}| \equiv |m_{jj,1} - m_{jj,2}|$ is selected. To select events with $m_{jj,1}$ and $m_{jj,2}$ consistent with the SM Higgs mass, two cuts are applied : $100 < \langle m_{jj} \rangle < 140$ GeV and $|\Delta m_{jj}| < 20$ GeV. To estimate the backgrounds which is mostly $t\bar{t}$, the $\langle m_{jj} \rangle$ and $|\Delta m_{jj}|$ variables are used to define the signal and control regions.

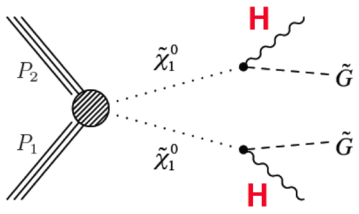

FIGURE 3. The $\tilde{\chi}^0\tilde{\chi}^0$ decay to two Higgs bosons and $\vec{E}_{\mathrm{T}}^{\mathrm{miss}}$

Yields in different $\vec{E}_{\mathrm{T}}^{\mathrm{miss}}$ ranges are compared to the background expectation and no sign of new physics is observed. However, because of a slight excess of data events compared to the background expectation we are unable to exclude the signal hypothesis for any value of Higgsino mass [10]. Figure 4 shows the results in terms of the signal

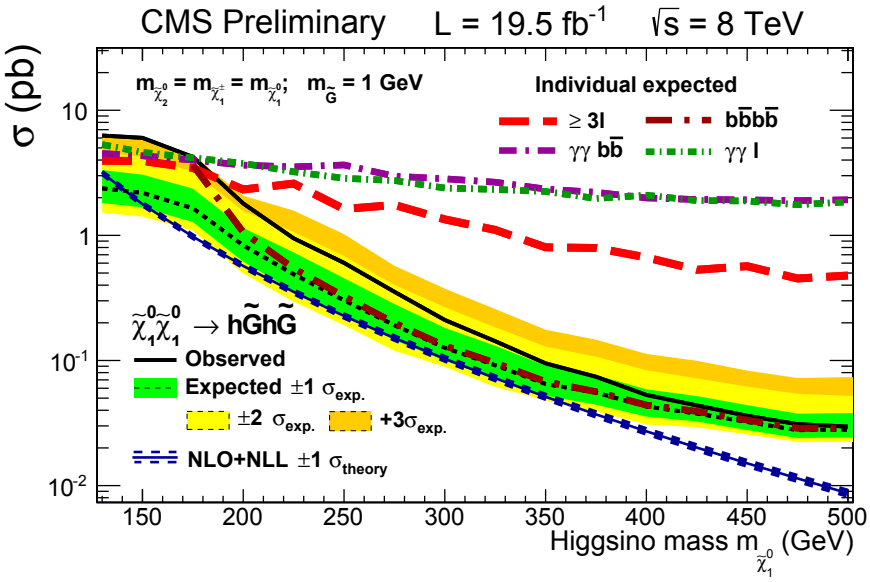

FIGURE 4. The expected and observed upper limits on the cross section of the $\tilde{\chi}^0\tilde{\chi}^0$ production for $HH + \vec{E}_{\mathrm{T}}^{\mathrm{miss}}$ studies [10].

model cross section.

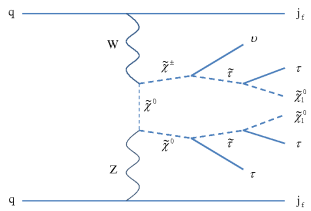

FIGURE 5. Feynman diagram of the SUSY electroweak production via VBF mechanism.

Search for electroweak SUSY with VBF tagging

The most recent result published by the CMS experiment, studies scenarios in which two electroweakino particles are produced via the vector boson fusion mechanism [11]. The Feynman diagram of such process is shown in Fig. 5. The specific signature of this signal is the production of two jets which are produced in the forward region of the detector. Requesting for two jets with $p_T > 30$ GeV in the opposite forward directions ($\eta_1 * \eta_2 < 0$ and $|\Delta\eta| > 4.2$) and applying a tight requirement on their invariant mass ($m(jj) > 250$ GeV) discard considerably the standard model backgrounds. For the central region, events with two isolated leptons are selected. Here in addition to electrons and muons, the

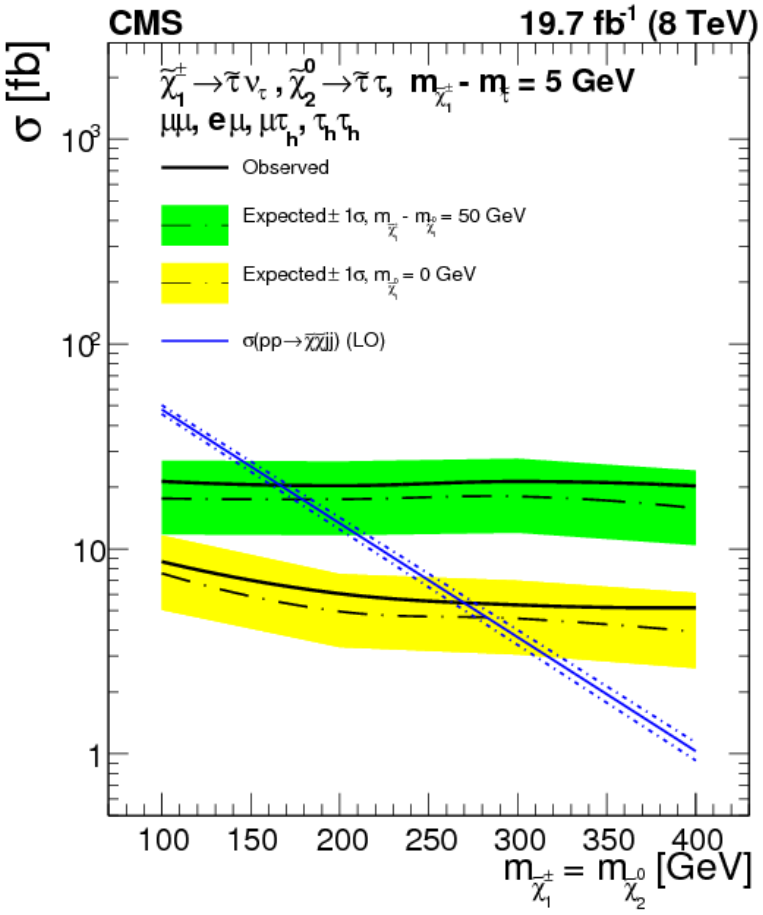

FIGURE 6. The exclusion limit on the cross section of this process vs. the χ^{pm} mass when $m_{\chi} - m_{\tilde{\tau}} = 5$ GeV [11].

hadronic decay of the τ leptons (τ_h) are also included. In addition, a moderate cut on $\vec{E}_{\mathrm{T}}^{\mathrm{miss}}$ is applied. To reject the $t\bar{t}$ background, events with exactly zero b-tagged jet are selected. Dividing events according to their lepton content

(eμ, $\mu\mu$, $\mu\tau_h$ and $\tau_h\tau_h$) and their charges (same sign (SS) and opposite sign (OS)), leads to 8 different categories. Backgrounds in all categories are estimated using data-driven techniques. As no difference between the estimated backgrounds and the observed data is seen, upper limit on the cross section vs. the $\chi^{\pm}$ mass is evaluated. The excluded region for the case where the mass difference of the $\chi^{\pm}$ and $\tilde{\tau}$ is only 5 GeV is shown in the Fig. 6.

REFERENCES

[1] Yu.A. Golfand and E.P. Likhtman. Extension of the algebra of poincare group generators and violation of p invariance. *JETP Lett.*, 13:323, 1971.

[2] CMS Collaboration. The cms experiment at the cern lhc. *Journal of Instrumentation*, 3(08):S08004, 2008. URL `http://stacks.iop.org/1748-0221/3/i=08/a=S08004`.

[3] CMS Collaboration. Search for new physics in events with same-sign dileptons and b-tagged jets in pp collisions at $\sqrt{s}$ = 7 TeV. *JHEP*, 08:110, 2012. doi: 10.1007/JHEP08(2012)110.

[4] CMS Collaboration. Search for new physics in events with opposite-sign leptons, jets, and missing transverse energy in pp collisions at $\sqrt{s}$ = 7 TeV. *Phys. Lett. B*, 718:815–840, 2013. doi: 10.1016/j.physletb.2012.11.036.

[5] CMS Collaboration. Search for new physics with same-sign isolated dilepton events with jets and missing transverse energy. *Phys. Rev. Lett.*, 109:071803, 2012. doi: 10.1103/PhysRevLett.109.071803.

[6] CMS Collaboration. Searches for electroweak production of charginos, neutralinos, and sleptons decaying to leptons and W, Z, and Higgs bosons in pp collisions at 8 TeV. Technical Report arXiv:1405.7570. CMS-SUS-13-006. CERN-PH-EP-2014-098, May 2014. URL `http://cds.cern.ch/record/1704963`. Comments: Published in European Physical Journal C.

[7] Konstantin T. Matchev and Scott D. Thomas. Higgs and Z boson signatures of supersymmetry. *Phys. Rev. D*, 62:077702, 2000. doi: 10.1103/PhysRevD.62.077702.

[8] Patrick Meade, Matthew Reece, and David Shih. Prompt decays of general neutralino NLSPs at the Tevatron. *JHEP*, 05:105, 2010. doi: 10.1007/JHEP05(2010)105.

[9] Joshua T. Ruderman and David Shih. General neutralino NLSPs at the early LHC. 2011.

[10] CMS Collaboration. Searches for electroweak neutralino and chargino production in channels with Higgs, Z, and W bosons in pp collisions at 8 TeV. *Phys. Rev. D*, 90:092007, Nov 2014. doi: 10.1103/PhysRevD.90.092007. URL `http://link.aps.org/doi/10.1103/PhysRevD.90.092007`.

[11] CMS Collaboration. Search for supersymmetry in the vector-boson fusion topology in proton-proton collisions at $\sqrt{s}$ = 8 TeV. *JHEP*, 11:189, 2015. doi: 10.1007/JHEP11(2015)189.

Proceedings of the LHCP2015 Conference, St. Petersburg, Russia, August 31 - September 5, 2015

Editors: V.T. Kim and D.E. Sosnov

R-Parity Violating SUSY Results from ATLAS and CMS

NORA EMILIA PETTERSSON

Tokyo Institute of Technology, Ookayama 2-12-1, Meguro-Ku, Tokyo 152-8550

nora.emilia.pettersson@cern.ch

On behalf of the ATLAS and CMS Collaborations

Abstract. Experimental searches for Supersymmetry (SUSY) at the Large Hadron Collider (LHC) often assume R-Parity Conservation (RPC) to avoid theoretical and experimental issues with rapid proton decay. A consequence of RPC is that it implies the existence of a stable SUSY-particle that cannot decay. The search strategies are strongly based on the hypothesis of weakly interacting massive particles escaping without detection - yielding missing transverse energy (MET) to the collision events. It is vital to explore all possibilities considering that no observation of SUSY has been made and that strong exclusion limits have already been placed on RPC-SUSY scenarios. Introducing individual baryon- and lepton-number violating couplings in R-Parity Violating (RPV) models would avoid rapid proton decay. The strong mass and cross-section exclusion set for RPC-SUSY are weakened if RPV couplings are allowed in the SUSY Lagrangian - as these standard searches lose sensitivity due to less expected MET. A summary of a few of the experimental searches for both prompt and long-lived RPV scenarios conducted by the ATLAS and CMS Collaborations will be presented in this document.

INTRODUCTION

Supersymmetry (SUSY) is a concept that introduces a symmetry between fermions and bosons. Numerous theories based on the SUSY framework have been developed in the last decades, making SUSY the most popular way to describe Beyond Standard Model (BSM) physics. Lepton Number (L) and Baryon Number (B) conservations are not enforced in SUSY, instead a new quantity named R-Parity (P_{R}) is introduced. R-Parity relates the Lepton Number (L) and the Baryon Number (B) with the particle's spin (s) (Eq. 1).

$$P_{\mathrm{R}} = (-1)^{3(\mathrm{B}-\mathrm{L})+2\mathrm{s}}. \tag{1}$$

The SM particles have $P_{\mathrm{R}} = 1$ while SUSY particles (sparticles) have $P_{\mathrm{R}} = -1$. Most SUSY theories abide by R-Parity Conservation (RPC) to avoid causing the protons to decay rapidly and have interesting effects on the experimental signatures of sparticle productions and decays. In RPC, sparticles must be created in pairs, and decay to at least one lighter sparticle. This effectively leads to the consequence that there must exist a Lightest Supersymmetry Particle (LSP) that cannot decay further due to the lack of any lighter sparticle to decay to. Experimentally, this means that in RPC scenarios there is a weakly interacting LSP that escapes the detector without decaying and gives the event large amounts of missing transverse energy $E_{\mathrm{T}}^{\mathrm{miss}}$ - and indeed, the majority of SUSY searches at the Large Hadron Collider (LHC) includes requirements on events to contain high $E_{\mathrm{T}}^{\mathrm{miss}}$. However, after the completion of the first run of proton-proton collisions at the LHC, the gaping hole of any signs of new physics and strict exclusion limits set from several experimental searches might suggest that the assumption of a stable LSP is not correct - to say the least it is vital to investigate other possibilities, such as R-Parity Violating (RPV) scenarios.

$$\mathscr{L}_{\Delta\mathrm{L}=1} = \frac{1}{2}\lambda^{ijk} L_i L_j \bar{e}_k + \lambda'^{ijk} L_i Q_j \bar{d}_k + \mu'^{i} L_i H_u, \tag{2}$$

$$\mathscr{L}_{\Delta\mathrm{B}=1} = \frac{1}{2}\lambda''^{ijk} \bar{u}_i \bar{d}_j \bar{d}_k, \tag{3}$$

SUSY contains both L violating and B violating terms in the SUSY-Lagrangian; given in Eq. 2 and Eq. 3 respectively. The L and e signify leptons; doublet and singlet respectively. Quarks are denoted by the Q, u, and d; for the quarks, up-type, and down-type respectively. RPV interactions including the Higgs are shown by the H contribution. In all of the L and B violating terms, the interaction strengths are characterized by the couplings λ^{ijk}, λ'^{ijk}, λ''^{ijk}, and μ'^{i}, where the indices ijk denote the generations of the leptons or quarks involved.

Typically, only one of the terms in either Eq. 2 or Eq. 3 is set to non-zero values, while the rest remains zero to avoid contradicting observations of the proton's lifetime. Decays through the different RPV couplings give specific experimental signatures. Sparticle decaying through the first $\Delta L = 1$ term λLLe yields final states with multiple leptons (dropping indices). The second term $\lambda' LQd$ contains both lepton and quarks and decays through this coupling will therefore give final states of both leptons and jets. Finally, the last term in Eq. 2, is a bilinear term yielding signatures of lepton-gaugino mixing. Multi-jets are to be expected when sparticles are allowed to decay through the B-violating couplings (Eq. 3).

Several experimental searches at the LHC for RPV SUSY have been conducted both by the ATLAS Experiment [1] and the CMS Experiment [2] during LHC's Run-1, targeting a diverse set of production processes, LSPs, and RPV couplings. Mostly, the LSPs are assumed to decay promptly but a handful analyses expect the LSP to be long-lived, giving different signatures.

EXPERIMENTAL SEARCH TECHNIQUES FOR RPV SUSY

A few examples from both experiments are reviewed, dividing the searches into six categories; Lepton Number Violating Re-Interpretation, Resonance Searches, Lepton and Jet Searches, Multi-Lepton Searches, Multi-Jet Searches, and Long-Lived Searches.

Run-1 Lepton Number Violating Re-Interpretation

A re-interpretation of Run-1 RPC and RPV searches on a specific simplified RPV model has been performed by the ATLAS experiment [3], similar re-interpretations by the CMS experiment can be found in Ref. [4]. Certain searches for RPC SUSY have loose requirements on $E_{\mathrm{T}}^{\mathrm{miss}}$ and can therefore be adapted on RPV scenarios. Moreover, the analyses targeting RPV often focus on a single coupling with set indices e.g. λ^{112}, greatly limiting the potential of the analysis to constrain a larger area of parameter-space of a given model. Five analyses are combined to cover four models of SUSY targeting all the Lepton Number Violating (LNV) RPV couplings. The result is that by performing a combination of several searches one obtains stricter exclusions limits.

Three simplified SUSY models are adapted, targeting the trilinear couplings λ^{ijk}, λ'^{ijk}, while for the bilinear coupling μ'^{i}, a fourth, phenomenological Minimal Supersymmetric Standard Model (pMMSM) is considered. Throughout, the neutralino $\tilde{\chi}_1^0$ is the LSP and decays promptly through λ^{ijk}, λ'^{ijk}, or μ'^{i} exclusively to SM particles. For all cases the LSP decay limits are split into planes of Branching Ratios (BRs) dependent on the number of heavy leptons or quarks from the LSP decay. For example, a BR plane for LSP decays through λ^{ijk} to two leptons is defined as the ratio of light (electrons, muons) to heavy (taus) leptons. Allover, both gluino and squark production are considered. Kinematics of the events, and especially of the decay itself, depend on the ratio R of the mass between the Next to Lightest Sparticle (NLSP) and the LSP; three values $R = 0.1, 0.5, 0.9$ are studied. Each of the analyses included has its strong points and dominates a certain area of the BR planes. Signal regions and significant backgrounds vary from analysis to analysis and the details will not be reviewed here.

Resonance Searches

Recreating the mass of a decaying particle by its daughter products is a powerful way to search for new particles, referred to as mass resonances. One such search that looks for resonances in the 3-jet invariant mass spectrum has been performed by the CMS experiment [5]. In this analysis, gluinos ($\tilde{g}$) are produced in pairs and are assumed to decay promptly through one of the Baryon Number Violating (BNV) couplings, λ''^{112}, λ''^{113}, or λ''^{223}, to three quarks. Events with multiple (≥ 6) high transverse momentum (p_{T}) jets are selected. The invariant mass M_{jjj} is formed by all possible 3-jet combination out of the six highest p_{T} jets in the event. Placing demands on event structures helps reduce the number of allowed combinations for the targeted $\tilde{g}$ decay. Signal events will form a Gaussian peak on top of the mass spectrum from wrongly combined jets. The latter contains the largest background that is Quantum ChromoDynamical (QCD) multijets.

The ATLAS experiment has conducted RPV resonance searches, for instance, one analysis looks for resonances in the dilepton invariant mass spectrum. This search targets production of tau sneutrinos ($\tilde{\nu}_\tau$) from $d\bar{d}$ annihilations, where the $\tilde{\nu}_\tau$ decay to lepton pairs [6].

Lepton and Jet Searches

Especially decays by the RPV coupling λ' produce both leptons and quarks, giving rise to lepton and jet event signatures. Searches, therefore, often rely on both on selecting high p_{T} jets and leptons. A search for a top squark ($\tilde{t}$) has been conducted by the CMS experiment [7]. The $\tilde{t}$ are assumed to be pair produced and decay as $\tilde{t} \to b\tilde{\chi}^{\pm} \to \tilde{\nu}_{e/\mu}e^{\pm}/\mu^{\pm}$. The sneutrino decays through λ' to pair of quarks. This search selects events containing opposite signed lepton pairs (same flavour) and at least five jets, one of them is required to contain a b quark (b-jet). The invariant mass of the lepton pairs must be larger than 130 GeV. The search is sensitive to eight RPV couplings; λ'^{i11}, λ'^{i12}, λ'^{i21} and λ'^{i22}. The target couplings are divided into muon and electron selection with index $i = 1$ and $i = 2$ respectively. The major backgrounds come from fully leptonic decays of $t\bar{t}$. Other background contributions are events containing Drell-Yan but these are suppressed by the signal requirement of at least one b-jet. CMS has also performed a complementary search where the muon and electron sneutrinos are replaced by tau sneutrinos. The targeted RPV coupling are then $i = 3$, λ'^{3jk} [8].

The BNV coupling λ'' could potentially yield lepton and jet signatures. The ATLAS experiment has searched for pair produced $\tilde{g}$ decaying to a top and a top squark, where the latter decays through λ''^{323} to a b and a s quark [9]. The search then looks for events with two same-charge leptons or three leptons. The events are also required to have three or more b-jets. Similarly, the CMS collaboration performed a search for nearly the same signature, but assuming direct decay of the $\tilde{g}$ through λ''^{323} to b and s quarks [10]. Additional examples of searches targeting lepton plus jet signatures can be found in references [11, 12].

Multi-Lepton Searches

Final states with multiple leptons are expected from sparticles decaying through the LNV coupling λ. A search from the ATLAS collaboration targets a simplified RPV model with a bino-like neutralino $\tilde{\chi}_1^0$ and is assumed to be the LSP. Four different production mechanism of $\tilde{\chi}_1^0$ are considered (all assumed to be the NLSP in that scenario); $\tilde{g}$, $\tilde{\chi}^{\pm}$, $\tilde{l}_{L/R}$, and $\tilde{\nu}_{L/R}$. The LSP decays to a combination of isolated electrons, muons and taus; $\tilde{\chi}_1^0 \to ll\nu$ [13]. The analysis is sensitive to several λ_{ijk} by allowing all generations of leptons to be present in the final state. Six signal regions are defined; requiring final states with at least four leptons and minimal requirements of $E_{\mathrm{T}}^{\mathrm{miss}} > 50$ to 100 GeV. The four leptons are divided into groups depending on how many taus are identified in the event. Lastly, to reduce background, each signal region requires a Z-boson veto. The backgrounds in the analysis are from combinations of multiple Z/W-bosons, or t quarks plus Z/W bosons, or Higgs boson decays. These are divided into "reducible" and "irreducible" contributions depending on whether they have less than four prompt leptons or at least four prompt leptons. The reducible backgrounds are estimated by a "weighting method" where the fake rates to have misidentified leptons are derived from Monte Carlo (MC) based simulations and applied to a control sample extracted from data, orthogonal to the signal region. The irreducible backgrounds are quantified by use of MC simulations.

Multi-Jet Searches

Signatures with multiple jets are to be expected with decays through the BNV coupling λ''. A dedicated search from the ATLAS collaboration looks for decays of $\tilde{g} \to tsb$ with BNV decays through λ''^{323} [14]. The $\tilde{g}$ is the LSP and pairs of $\tilde{g}$ are produced in proton-proton collisions. Signal regions are defined by requirements on the event's jet-multiplicity; 6, 7 or ≥ 8. Moreover, one lepton, either an electron or a muon is required to be present in a signal event. Each signal region is binned in the number of b-jets; from zero up to five. Dominant backgrounds vary depending on the number of b-jets but are mostly $t\bar{t}$+jets.

An ATLAS analysis is targeting the same coupling but here the top squark is assumed to be the LSP, decaying to b and s jets [15]. The search strategy is to look for boosted, merged jets from the $\tilde{t}$ decays, with high p_{T} but low mass. A more general analysis, in which one is targeting several of the λ''^{ijk} couplings, has been performed by the ATLAS collaboration [16], defining several signal regions depending on the flavour of the quarks in the final states.

Long-Lived Searches

In case the RPV couplings are relatively small, the LSP could become long-lived. Both the ATLAS and the CMS experiments have looked for displaced vertex signatures from a Long-Lived Particle (LLP) decaying within the detector, the results from these analyses are interpreted using several RPV couplings. The ATLAS analysis attempts to reconstruct the decay point in the tracking volume of the detector [17], while the CMS analysis searches for events containing a pair of jets originating from a displaced vertex [18]. In both cases, the expected SM background is comparatively small due to the exotic signature. Another LLP CMS search looks for events containing long-lived stops decaying through λ' to a lepton and a b quark [19]. Events are selected if they contain isolated electrons and muons,

where the tracks linked to the leptons should be displaced, i.e. have large impact parameters relative to the primary interaction point.

RESULTS

No excesses above the SM expectations are seen in any of the analyses. In the absence of any signal, limits are set, given an RPV coupling, on the production cross section and the mass of production particle. The CL_s method [20] is used by both experiments to present exclusions, set at 95% confidence level. Results reviewed here are example of one analysis from each category, further results are found within the references provided in the previous sections.

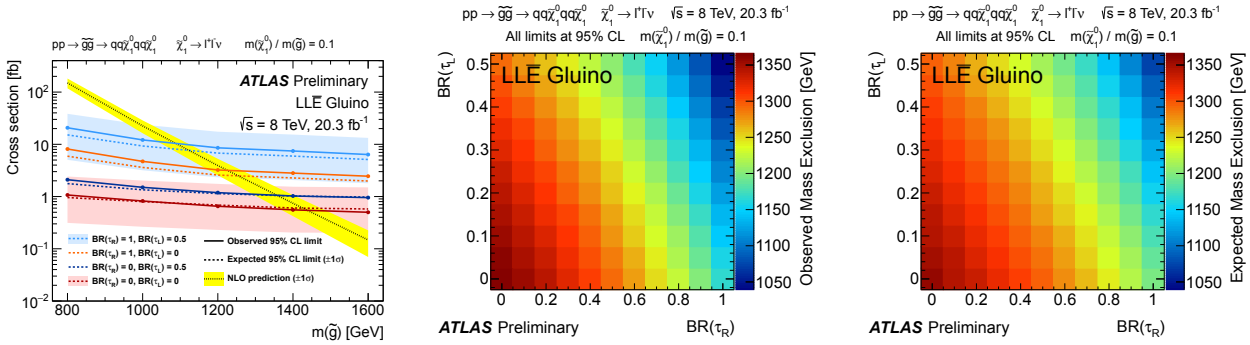

(a) (b) (c)

FIGURE 1. Exclusion limits on the cross section as a function of the gluino mass. The solid and dashed lined represent the observed and expected limits at 95% Confidence level. The mass ratio between the NLSP and LSP are set to 0.1, and the LSP is assumed to decay to two leptons and a neutrino. The colored lines correspond to different points in the BR-planes. In the worse case (a), the gluino mass can be excluded up to 1040 GeV. The observed and expected mass exclusion for several points on the BR grid are shown in (b) and (c) respectively [3].

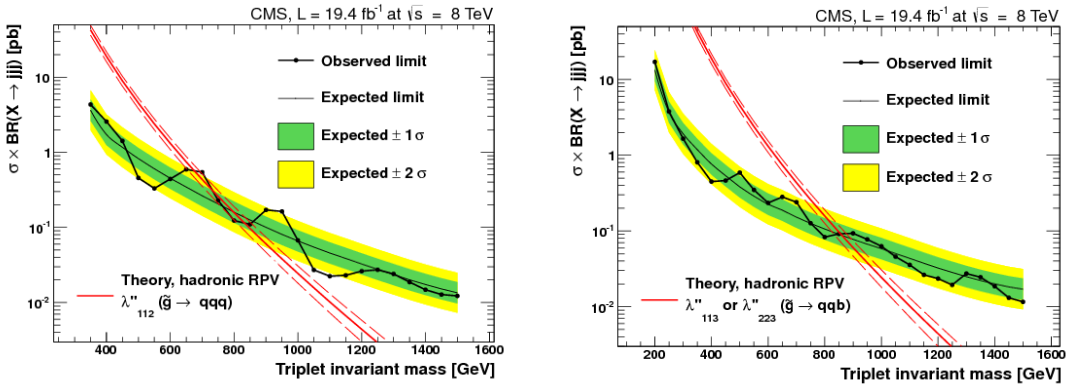

(a) (b)

FIGURE 2. Observed and expected exclusions on the cross section times the BR are shown as a function of the triplet invariant mass of the three jets. The limits are set for light flavor jets (a) and heavy flavor jets (b) and are shown for the expectation $\pm 1\sigma$ in green and $\pm 2\sigma$ in yellow. The red lines shows the NLO+NLL predictions and the theoretical uncertainty at 1σ confidence level are illustrated by the red dashed lines [5].

The results from the Run-1 interpretations [3] are given as upper limits on the cross section as a function of the NLSP mass. As an example, Figure 1 (a) shows the limits set for λ where R=0.1, where the black line and yellow band corresponds to the Next to Leading Order (NLO) prediction. The solid and dashed colored lines show the observed and expected values given 4 different relations between the branching ratios of number of right and left handed taus.

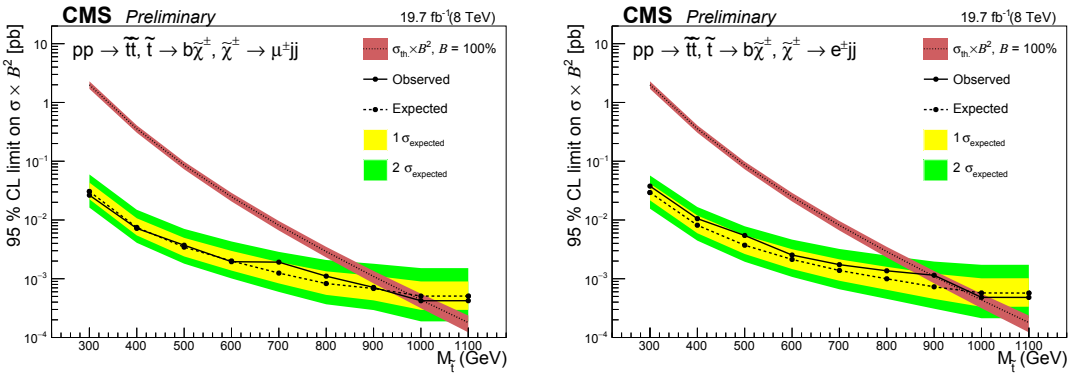

(a) (b)

FIGURE 3. Observed and expected limits for the cross section as a function of the stop mass, solid and dashed black lines respectively. The yellow and green error bands corresponds to a $\pm 1\sigma$ and $\pm 2\sigma$ interval. The red line shows the theoretical cross section expectations for the stop at NLO+NLL. Limits for events with muons are shown in (a) while electrons are shown in (b) [7].

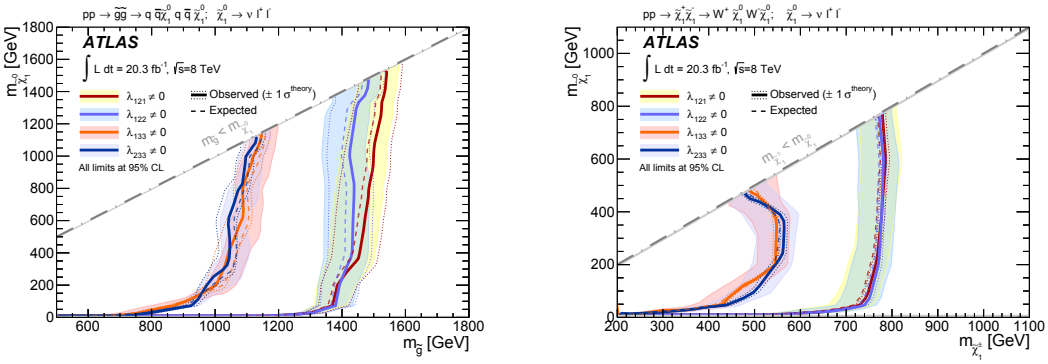

(a) (b)

FIGURE 4. Exclusion limits at 95% confidence level are shown as the excluded masses of the NLSP and LSP in RPV simplified models. The various colors shows the limits for a set of four different RPV scenarios where different couplings are set to non zero values. The solid lines show the observed values while the dashed lines show the expectations. Limits for gluino production are shown in (a) while the limits for chargino production are shown in (b) [13].

The limits on the observed and expected exclusions are shown in (b) and (c) in the form of the BR-plane. In the worst case (light blue line), a mass of $\tilde{g}$ less than 1040 GeV is excluded. Observed and expected limits on the cross sections as a function of the mass of the three jet resonance [5] are shown for light and heavy flavour jets in Fig 2 (a) and (b) respectively. Gluino mass of up to 650 GeV is excluded for light flavor jets, while the exclusion is made for 200 to 835 GeV considering heavy flavor jets for the given decay process. Figure 3 shows the results for chargino-mediated stop decay [7], in form of limits on the cross section times the branching ratio squared, as a function of the $\tilde{t}$ mass. The stop mass is excluded up to 1000 GeV for muons (Fig. 3 (a)) and 890 GeV for electrons (Fig. 3 (b)). Results from the multi-lepton analysis [13] are given as mass exclusions of the LSP mass versus the NLSP mass (Fig 4). The analysis excludes $\tilde{g}$ masses up to 1350 GeV (Fig 4 (a)) and $\tilde{\chi}^{\pm}$ masses up to 750 GeV (Fig 4 (b)). More exclusion plots are found within the given reference. The multi-jet search [14] produce results in the form of cross section time BR as a function of the $\tilde{g}$ mass, exclusions are set assuming 100% BR for the decay $\tilde{g} \rightarrow tbs$. Mass of the gluino up to 1036 GeV is excluded (Fig. 5). In case of the LLP search [17] the limits are set on the cross section of the targeted production and decay process as a function of average lifetime $c\tau$, and for the optimal range the exclusions are set to values from 0.5 fb to 5 fb.

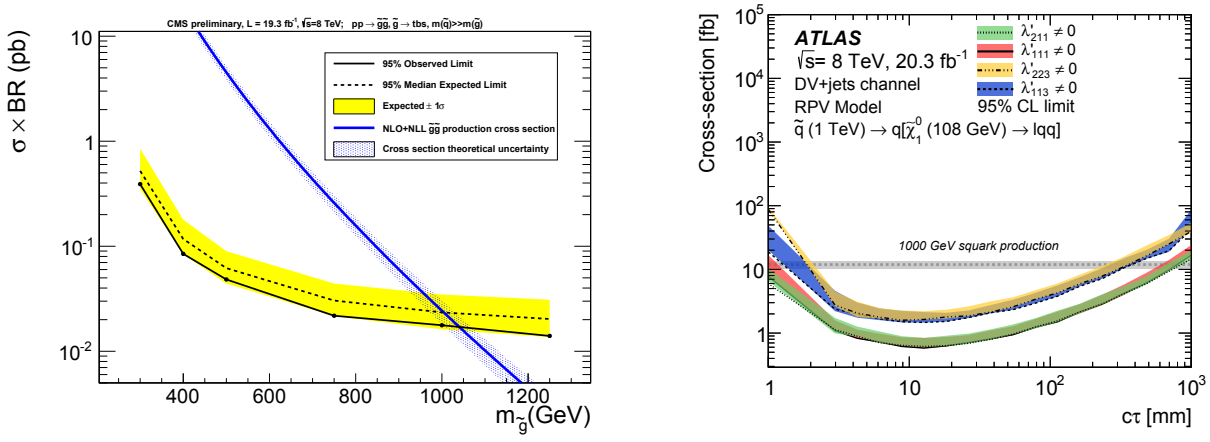

(a) (b)

FIGURE 5. Cross section times the BR exclusions at a 95% confidence level as a function of the mass of the gluino pair production (a). The observed and expected limits are drawn with solid and dashed lines, respectively. The theoretically caculated cross section is shown by the blue line with given uncertainties [14]. Upper limits on the cross section as a function of $c\tau$ for the long-lived particle (b). For the given scenario, where a neutalino decays to a lepton and two quarks, the limits are shown for four different RPV couplings, targeting both light and heavy flavour jets [17].

CONCLUSION

RPV SUSY are in LHC searches explored to a lesser extent than RPC scenarios. The requirement on large amount of $E_{\mathrm{T}}^{\mathrm{miss}}$ implemented with the assumption of a stable LSP makes the currently set RPC limits not applicable on RPV SUSY. However, there exist dedicated experimental searches for RPV SUSY, adopting a wide variety of search strategies for a decaying LSP. A few examples have been reviewed; A large scale Run-1 re-interpretation for LNV RPV, Resonance searches, Lepton and Jet searches, Multi-lepton searches, Multi-jet searches and long-lived searches. The analyses cover different production mechanisms and RPV couplings and even lifetimes of the SUSY particles. Limits are set on the masses of the NLSP or the LSP given a specific RPV coupling strength and decay chain.

REFERENCES

[1] ATLAS Collaboration, JINST **3**, p. S08003 (2008).
[2] CMS Collaboration, JINST **3**, p. S08004 (2008).
[3] ATLAS Collaboration, ATLAS-CONF-2015-018, 2015, https://cds.cern.ch/record/2017303.
[4] CMS Collaboration, CMS-PAS-SUS-12-027, 2012, https://cds.cern.ch/record/1494689.
[5] CMS Collaboration, Phys. Rev. Lett. **730**, 193–214 (2014), arXiv:1311.1799 [hep-ex].
[6] ATLAS Collaboration, Phys. Rev. Lett. **115**, p. 031801 (2015), arXiv:1503.04430 [hep-ex].
[7] CMS Collaboration, CMS-PAS-EXO-14-013, 2015, https://cds.cern.ch/record/2032167.
[8] CMS Collaboration, Phys. Lett. **B739**, p. 229 (2014), arXiv:1408.0806 [hep-ex].
[9] ATLAS Collaboration, JHEP **06**, p. 035 (2014), arXiv:1404.2500 [hep-ex].
[10] CMS Collaboration, JHEP **01**, p. 163 (2014), arXiv:1311.6736 [hep-ex].
[11] ATLAS Collaboration, ATLAS-CONF-2015-015, 2015, https://cds.cern.ch/record/2002885.
[12] CMS Collaboration, Phys. Rev. Lett. **111**, p. 221801 (2013), arXiv:1306.6643 [hep-ex].
[13] ATLAS Collaboration, Phys. Rev. **D90**, p. 052001 (2014), arXiv:1405.5086 [hep-ex].
[14] CMS Collaboration, CMS-PAS-SUS-12-015, 2013, https://cds.cern.ch/record/1632190.
[15] ATLAS Collaboration, ATLAS-CONF-2015-026, 2015, https://cds.cern.ch/record/2037653.
[16] ATLAS Collaboration, Phys. Rev. **D91**, p. 112016 (2015), arXiv:1502.05686 [hep-ex].
[17] ATLAS Collaboration, Phys. Rev. **D92**, p. 072004 (2015), arXiv:1504.05162 [hep-ex].
[18] CMS Collaboration, Phys. Rev. **D91**, p. 012007 (2015), arXiv:1411.6530 [hep-ex].
[19] CMS Collaboration, Phys. Rev. Lett. **114**, p. 061801 (2015), arXiv:1409.4789 [hep-ex].
[20] A. L. Read, J. Phys. **G28**, p. 2693 (2002).

ElectroWeak physics and Quantum ChromoDynamics: plenary talks

Proceedings of the LHCP2015 Conference, St. Petersburg, Russia, August 31 - September 5, 2015

Editors: V.T. Kim and D.E. Sosnov

Precision Measurements of Electroweak Parameters with Z Bosons at the Tevatron

ARIE BODEK

Department of Physics and Astronomy, University of Rochester, Rochester, NY. 14627, USA

bodek@pas.rochester.edu

On behalf of the CDF and D0 Collaborations

Abstract. We report on the extraction of $\sin^2\theta^{\rm lept}_{\rm eff}(M_Z)$ and an indirect measurement of the mass of the W boson from the forward-backward asymmetry of dilepton events in the Z boson mass region at the Tevatron. The data samples of e^+e^- and $\mu^+\mu^-$ events collected by the CDF detector correspond to the full 9.4 fb^{-1} run II sample and yield an effective electroweak mixing angle $\sin^2\theta^{\rm lept}_{\rm eff}(M_Z) = 0.23222 \pm 0.00046$. The corresponding result reported by the D0 collaboration with the full 9.4 fb^{-1} e^+e- sample is $\sin^2\theta^{\rm lept}_{\rm eff}(M_Z) = 0.23146 \pm 0.00047$. The CDF collaboration also extracts the on-shell electroweak mixing angle $\sin^2\theta_W = 0.22401 \pm 0.00044$ which corresponds to an indirect measurement of the W boson mass M_W(indirect) = 80.327 ± 0.023 GeV. The quoted uncertainties include both statistical and systematic contributions.

INTRODUCTION

The effective $\sin^2\theta_W$ coupling at the lepton vertex, denoted as $\sin^2\theta^{\rm lept}_{\rm eff}(M_Z)$, has been accurately measured at the LEP-1 and SLD e^+e^- colliders. The combined average of six individual LEP-1 and SLD measurements[1] yields $\sin^2\theta^{\rm lept}_{\rm eff}(M_Z) = 0.23153 \pm 0.00016$. However, there is tension between the two most precise individual measurements: the combined LEP-1 and SLD b-quark forward-backward asymmetry ($A^{0,b}_{\rm FB}$) yields $\sin^2\theta^{\rm lept}_{\rm eff}(M_Z) = 0.23221 \pm 0.00029$, and the SLD polarized left-right asymmetry ($\mathcal{A}_\ell$) yields $\sin^2\theta^{\rm lept}_{\rm eff}(M_Z) = 0.23098 \pm 0.00026$. These two measurements differ by 3.2 standard deviations. In order to help resolve this difference new measurements of $\sin^2\theta^{\rm lept}_{\rm eff}(M_Z)$ should have uncertainties similar to SLD or LEP ($\approx \pm 0.0003$).

In addition, now that the Higgs boson mass (M_H) is known, the Standard Model (SM) is over constrained. Any inconsistency between precise measurements of SM parameters could be indicative of new physics. Fig.1 (a) (from ref.[2]) shows the current world average[3] of direct measurements of the mass of the W boson (M_W=80.385 ± 0.015 GeV) versus the 2014 average[4] of the direct measurements of the mass of the top quark (M_t = 173.34 ± 0.76 GeV).

The average of the Tevatron measurements of M_t in 2014 is M_t=174.34 ± 0.37(stat) ± 0.52(syst) GeV (or 174.34±0.64). If we also include the 2014 measurements of ATLAS and CMS the combined 2014 world average [4] (CDF, D0, CMS, ATLAS) is M_t=173.34 ± 0.27(stat) ± 0.71(syst) GeV (or 173.34 ± 0.76 GeV) as shown in Fig.1 (a). Also shown in green is the expectation from the SM with M_H = 125.6 ± 0.7 GeV. The average of all direct measurements of M_W is about 1.5 standard deviation higher than the prediction of the standard model. Predictions of supersymmetric models for M_W are also higher [5] than the predictions of the standard model.

The most recent measurement of M_t at the LHC are somewhat lower than at the Tevatron. The ATLAS[6] measurement published in 2015 is M_t= 172.99 ± 0.91 GeV. The CMS[7] 2015 measurement M_t=172.44 ± 0.13(stat) ± 0.47(syst) GeV (or 172.44 ±0.48 GeV) is the most precise measurement to date and supersedes all previous CMS results. There is about a two standard deviation tension between the 2015 CMS measurement of M_t and the earlier Tevatron measurements. However, both are consistent with the world average. The lower value of M_t as measured by CMS would imply a somewhat larger deviation of M_W from the prediction of the SM as shown in Fig. 1 (b). The parameter that needs to be measured more precisely is M_W. The current experimental uncertainties in the direct measurements of the W boson mass (M_W^{direct}) by D0 and CDF at the Tevatron are about ±20 MeV per experiment.

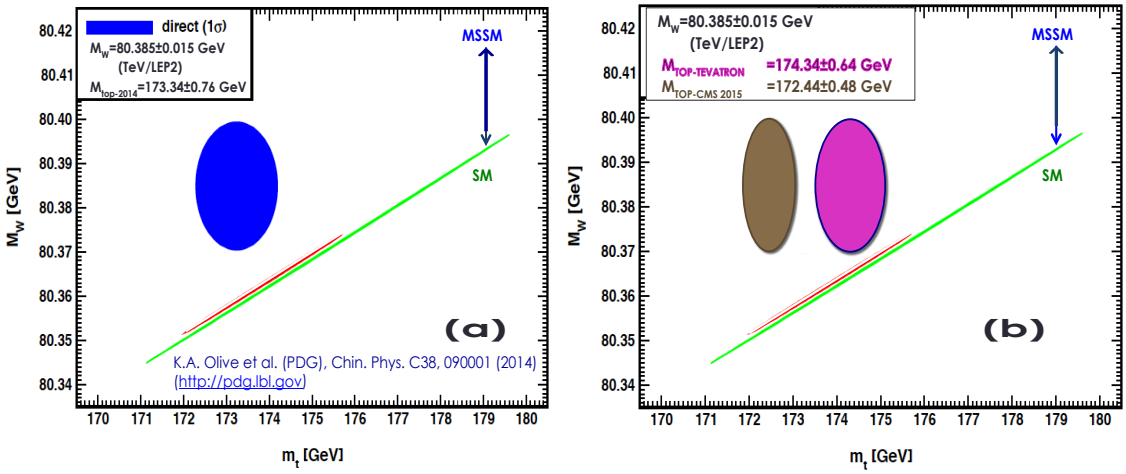

FIGURE 1. (a) World average of all direct measurements of M_W (CDF, D0, LEP2) versus the average of all M_t measurements (CDF, D0, CMS, ATLAS) in 2014. The green line is the expectation from the SM (with $M_H = 125.6 \pm 0.7$ GeV). Supersymmetry models predict values which are above the SM line. (b) Same as (a) but with the CMS measurement of M_t in 2015 as compared to the Tevatron measurement of M_t.

Equivalently one can also measure the on-shell[8] weak mixing angle, $\sin^2\theta_W = 1 - M_W^2/M_Z^2$. An error of ± 0.0004 in the on-shell $\sin^2\theta_W$ is equivalent to an indirect measurement of the W boson mass ($M_W^{indirect}$) to a precision of ± 20 MeV.

The angular distribution for the production of deletions in hadron colliders is proportional to

$$1 + \cos^2\theta + \frac{A_0}{2}(1 - 3\cos^2\theta) + A_4\cos\theta,$$

where θ is the polar angle in the Collins-Soper frame[9]. The coefficient $A_0(P_T)$ is small and vanished for dilepton transverse momentum $P_T = 0$. The integrated forward-backward asymmetry $A_{\rm fb}(M)$ is equal to $3A_4(M)/8$,

Precise extractions of $\sin^2\theta_{\rm eff}^{\rm lept}(M_Z)$ and $\sin^2\theta_W = 1 - M_W^2/M_Z^2$ using the forward-backward asymmetry ($A_{\rm fb}$) of dilepton events produced in $p\bar{p}$ and pp collisions are now possible for the first time because of four new innovations:

- A new technique [10] for calibrating the muon and electron energy scales as a function of detector η and ϕ (and sign), thus greatly reducing systematic uncertainties from the energy scale. These technique is used at CDF and CMS. A similar technique is used by D0 for electrons.
- A new event weighting technique[11]. With this technique all experimental uncertainties in acceptance and efficiencies cancel (by measuring the $\cos\theta$ coefficient A_4 and using the relation $A_{\rm fb} = 3A_4/8$). Similarly, additional weights can be included for antiquark dilution, which makes the analysis independent of the acceptance in dilepton rapidity. These technique is used by CDF and is currently being implemented at CMS.
- The implementation[12] in 2012 of Z fitter Effective Born Approximation (EBA) electroweak radiative corrections into the theory modified predictions of POWHEG and RESBOS which allows for a measurement of both $\sin^2\theta_{\rm eff}^{\rm lept}(M_Z)$ and $\sin^2\theta_W = 1 - M_W^2/M_Z^2$. These EBA electroweak radiative corrections were implemented in CDF analyses[12, 13, 14] since 2013. Recently, an official version of POWHEG with electroweak radiative corrections has been released. Similarly, electroweak radiative corrections have been implemented in other theory predictions. Comparisons of different implementation of EW radiative corrections are now possible..
- A new technique [15] that reduces Parton Distribution Function (PDF) uncertainties by incorporating additional constraints from the mass and rapidity dependence of Drell-Yan $A_{\rm fb}$. The use of Drell-Yan $A_{\rm fb}(M, y)$ χ^2 weighting was first proposed in ref. [15]) for additional constraints on PDFs. The χ^2 weighting technique reduces the PDF uncertainty in the measurements of $\sin^2\theta_{\rm eff}^{\rm lept}(M_Z)$, $\sin^2\theta_W$, and in the indirect and direct measurements of M_W. This technique has been used in CDF[14] and is currently being implemented in CMS.

Momentum-energy scale corrections

This new technique[10] is used in CDF (for both muons and electrons) and also in CMS. In CMS it is used to get a precise measurement of the Higgs boson mass in the four lepton channel. A similar technique is used by D0 for electrons. The technique used in CDF and CMS relies on the fact that the Z boson mass is well known as follows:

- Any correlation between the scales of the two leptons is removed by getting an initial calibration using Z events. It is done by requiring that the mean $\langle 1/P_T \rangle$ of each lepton in bins of detector η, ϕ and charge is equal to the expected value for generated Z events, smeared by the momentum/energy resolution.
- The Z boson mass is is used as a second order correction. The measured Z boson mass as a function of detector η, ϕ and charge of the lepton is required to be equal to the value for generated Z events (smeared by the momentum/energy resolution). Additionally the measured J/ψ and Υ masses as a function of η of the lepton are also used.

The scale corrections are determined for both data events and reconstructed hit level Monte Carlo events. After corrections, the reconstructed Z boson mass as a function η, ϕ and charge for both the data and hit level MC agrees with the generator level Monte Carlo (smeared by resolution, and with experimental acceptance cuts). All charge bias is removed. For muons, the following calibration constants are extracted for each bin in η and ϕ

- A multiplicative calibration correction in the quantity $1/P_T$ which accounts for possible mis-calibration of the magnetic field.
- A calibration correction which is additive in $1/P_T$ which accounts for tracker mis-alignments.
- For very low energy muons, the J/ψ and Υ masses are used to determine a small additional calibration constant to tune the dE/dx energy loss in the amount of material in the tracker as a function of detector η.

When the technique is used for electrons, the multiplicative correction accounts for tower mis-calibration and there is no additive correction since the tracker is not used in the reconstruction of the electron energy.

The event weighting technique

The forward-backward $A_{\rm fb}$ asymmetry of leptons measured with this technique[11] is insensitive to the acceptance and lepton detection efficiency. Therefore, the raw $A_{\rm fb}$ which is measured using this technique is automatically corrected for efficiency and acceptance. The only corrections that need to be made are corrections for momentum/energy resolution which lead to event migration between different bins in dilepton mass. All experiment dependent systematic uncertainties cancel to first order. This technique is used in the CDF analysis for muons and electrons, and is currently being implemented at CMS.

The event weighting technique utilizes two kinds of weights. Angular weights are used to remove the sensitivity to acceptance and lepton detection efficiency as a function of $\cos\theta$. In the CDF (and CMS) analyses, only angular weights are used. For proton-proton collisions at the LHC, one can also include weights which correct for the rapidity dependent dilution and therefore removes the sensitivity to the acceptance in dilepton rapidity.

Electroweak radiative corrections

ZGRAD-type EW radiative corrections - used by D0

An approximate method that only corrects for the flavor dependence of $\sin^2\theta_{\rm eff}$ has been proposed by Baur and collaborators [18]. The flavor dependence is approximately: $\sin^2\theta_{\rm eff}^{\rm u-quark} = sin^2\theta_{\rm eff}^{\rm lept} - 0.0001$ and $\sin^2\theta_{\rm eff}^{\rm d-quark} = sin^2\theta_{\rm eff}^{\rm lept} - 0.0002$.

We refer to these EW corrections (which have been implemented in RESBOS) as ZGRAD-type corrections. These corrections are used by D0. The D0 collaboration reports[19] that $\sin^2\theta_{\rm eff}^{\rm lept}(M_Z)$ extracted using RESBOS (with CTEQ 6.6 -NLO PDFs) including ZGRAD-type radiative corrections is +0.00008 larger than the value of $\sin^2\theta_{\rm eff}^{\rm lept}(M_Z)$ extracted using PYTHIA 6.323 [20] with the same PDF set and no EW radiative corrections. The PYTHIA matrix elements are QCD leading order as compared to RESBOS matrix elements which are NLO. However, as reported by D0, the estimated correction due to higher order QCD effects is negligibly small.

The above procedure partially corrects for the flavor dependence of $\sin^2\theta_{\rm eff}$. It does not account for the mass dependence of $\sin^2\theta_{\rm eff}$ (shown in Fig. 2(c)) nor does it account for the complex mass dependent form factors. As described below, a more complete treatment of EW radiative corrections factors is needed in order yield a measurement of the on-shell $\sin^2\theta_W = 1 - M_W^2/M_Z^2$.

Effective Born approximation (EBA) electroweak radiative corrections - used by CDF

These radiative corrections have been implemented in CDF[12] (for modified versions of POWHEG, RESBOS and Tree level calculations). The corrections are derived from the approach adopted at LEP[16]. The Z-scattering-amplitude form factors are calculated by ZFITTER 6.43 [16] which has been used by LEP-1 and SLD measurements for precision tests of the standard model [17].

$A_{fb}(M)$ in the region of the mass of the Z boson is sensitive to the effective weak mixing angle $\sin^2\theta_{\rm eff}(M, flavor)$, where M is the dilepton mass. Here, $\sin^2\theta_{\rm eff}$ is related to the on-shell[8] electroweak mixing angle $\sin^2\theta_W = 1 - M_W^2/M_Z^2$ via complex mass and flavor (weak isospin) dependent electroweak radiative corrections form factors. The massless-fermion approximation is used.

The parameter which is measured at LEP and SLD is $\sin^2\theta^{\rm lept}_{\rm eff}(\mathrm{M}_Z)$. Previous extraction of $\sin^2\theta^{\rm lept}_{\rm eff}(\mathrm{M}_Z)$ from Drell-Yan A_{fb} neglected the dependence of $\sin^2\theta_{\rm eff}$ on flavor and dilepton mass. The input to the theory predictions has been one value of $\sin^2\theta_{\rm eff}$ which on average was assumed to be independent of mass or flavor and has been interpreted as $\sin^2\theta^{\rm lept}_{\rm eff}(\mathrm{M}_Z)$.

When the full EBA EW radiative corrections are included, the input to the theory prediction templates for $A_{\rm fb}(M)$ is the on-shell $\sin^2\theta_W = 1 - M_W^2/M_Z^2$. The templates are compared to the data and the best fit value of $\sin^2\theta_W$ is extracted. From the best fit value of $\sin^2\theta_W$ and the full complex EBA radiative corrections form factors we can then extract $\sin^2\theta^{\rm lept}_{\rm eff}(M_Z)$ which is the effective leptonic EW mixing angle at the mass of the Z boson. With the EBA radiative corrections used at CDF it is found that $\sin^2\theta^{\rm lept}_{\rm eff}(M_Z) \approx 1.037\sin^2\theta_W$.

If the EBA EW radiative corrections are included, the extracted value of $\sin^2\theta^{\rm lept}_{\rm eff}(M_Z)$ is higher by +0.00023 than the value extracted with no EW radiative corrections. About +0.00008 originate from accounting for the flavor dependence of $\sin^2\theta^{\rm lept}_{\rm eff}(M)$, +0.00006 originates from accounting for the mass dependence of $\sin^2\theta^{\rm lept}_{\rm eff}(M)$, and +0.00009 originate from accounting for the mass dependent complex EW Fitter form factors.

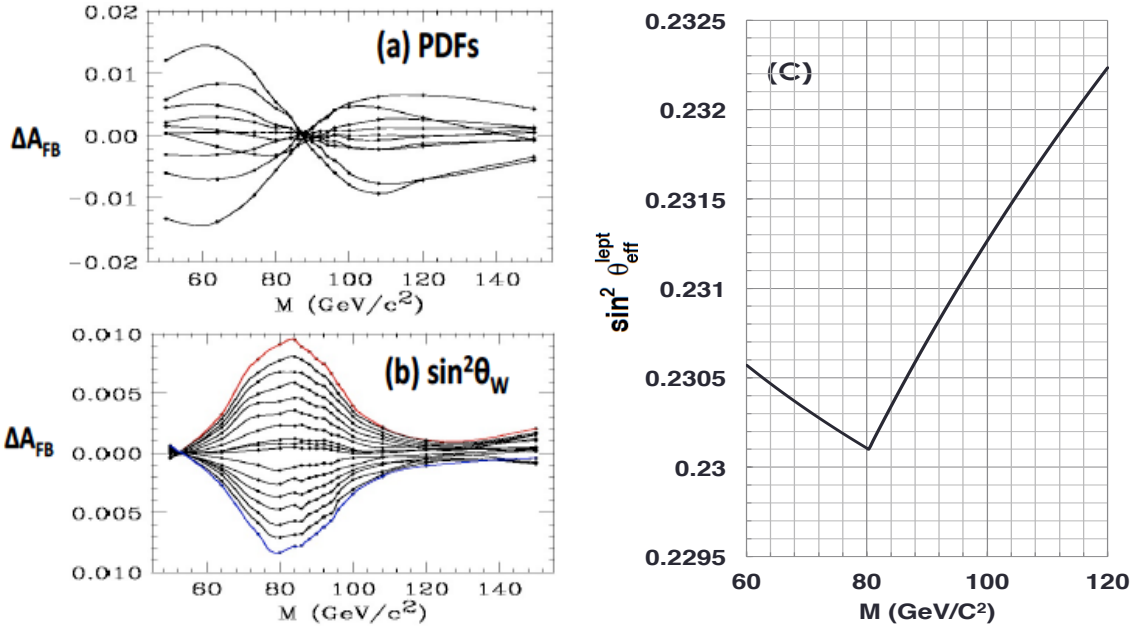

FIGURE 2. Tevatron: (a) The difference between $A_{\rm fb}(M)$ for 10 NNPDF3.0 (NNLO) replicas and $A_{\rm fb}(M)$ calculated for the default NNPDF3.0 (NNLO) (261000). Much of the difference originates form the different dilution factors for each of the NNPDF replicas. Here $\sin^2\theta_W$ is fixed at a value of 0.2244. (b) The difference between $A_{\rm fb}(M)$ for different values of $\sin^2\theta_W$ ranging from 0.2220 (shown at the top in red) to 0.2265 (shown on the bottom in blue), and $A_{\rm fb}(M)$ for $\sin^2\theta_W$=0.2244. Here $A_{\rm fb}(M)$ is calculated with the default NNPDF3.0 (NNLO). (Figures (a) and (b) are from Ref. [15]). (c) Scale dependence of $\sin^2\theta^{\rm lept}_{\rm eff}(M)$. The minimum of $\sin^2\theta^{\rm lept}_{\rm eff}(M)$ is at the mass of the W boson (from Ref. [2]).

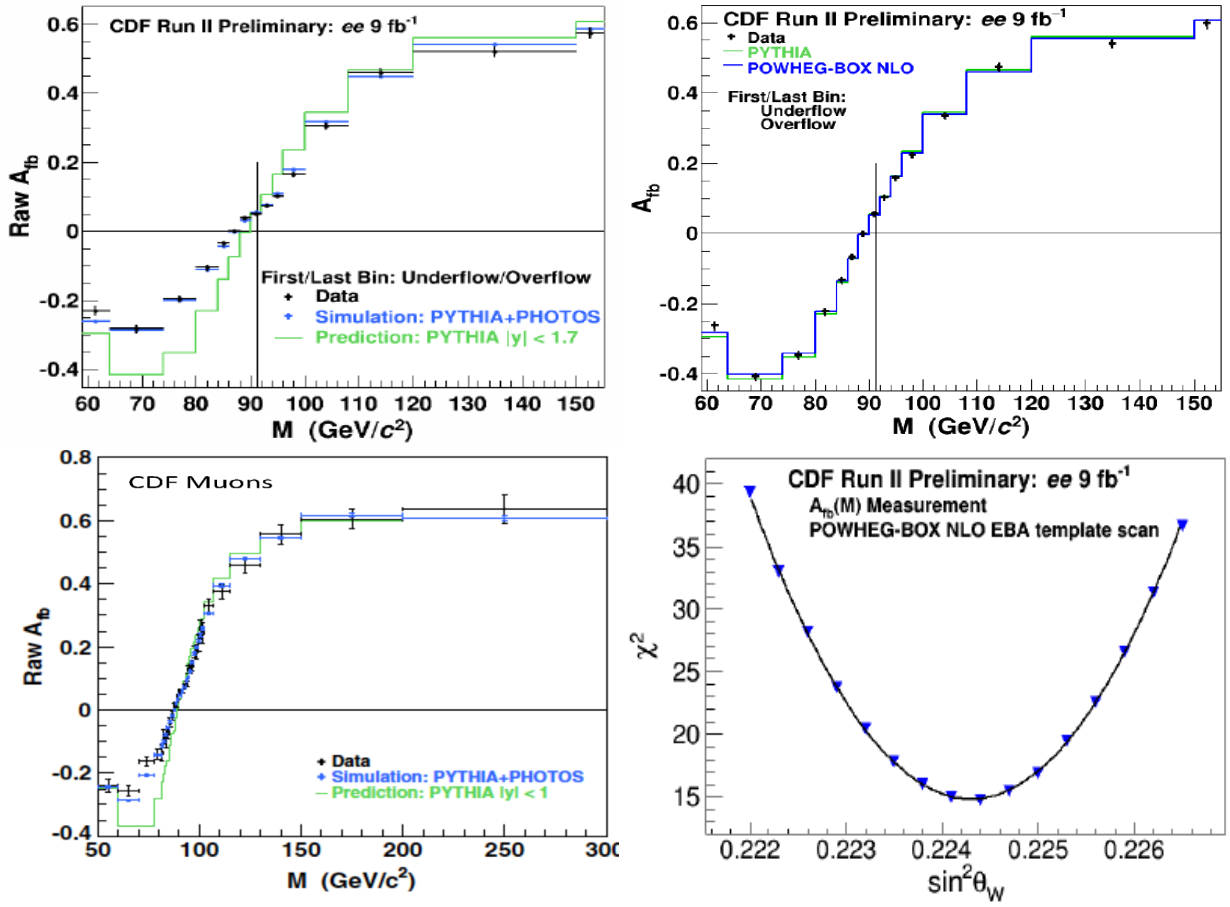

FIGURE 3. Top-Left: CDF raw $A_{\rm fb}(M)$ measurement in bins of e^+e^- invariant mass. Only statistical uncertainties (bin-by-bin unfolding) are shown. The Monte Carlo simulation (PYTHIA) includes the effect of resolution smearing and FSR. The PYTHIA $|y| < 1.7$ asymmetry curve does not. Top-Right: $A_{\rm fb}(M)$ for e^+e^- events unfolded for resolution and QED-FSR. The PYTHIA calculation uses $\sin^2\theta^{\rm lept}_{\rm eff} = 0.232$. The EBA-based RESBOS and POWHEG calculations uses $\sin^2\theta_W = 0.2233$ ($\sin^2\theta^{\rm lept}_{\rm eff}(M_Z) = 0.2315$). Bottom-Left: Same as Top-Left for the $\mu^+\mu^-$ sample (here $|y| < 1$). Bottom-Right: χ^2 vs. $\sin^2\theta_W$ for the CDF e^+e^- sample.

Analysis of CDF $\mu^+\mu^-$ and e^+e^- full 9.4 fb^{-1} run II sample

After applying the calibrations and muon and electron scale corrections to the experimental and simulated data, $A_{\rm fb}(M)$ is measured in bins of $\mu^+\mu^-$[13] for and e^+e^-[14] invariant mass using the event-weighting method. This measurement is denoted as the raw $A_{\rm fb}(M)$ measurement because the event-weighting method provides a first-order acceptance correction, but does not include resolution unfolding and final-state (FSR) QED radiation. The raw $A_{\rm fb}$ measurements in bins of the $\mu^+\mu^-$ and e^+e^- invariant mass are shown on the left part of Fig. 3. Only statistical uncertainties are shown. The Monte Carlo simulation (PYTHIA+PHOTOS) includes the effect of resolution smearing and FSR. To illustrate the effects of resolution smearing and FSR, the PYTHIA $|y| < 1$ and $|y| < 1.7$ asymmetry curves do not include the effect of resolution smearing or FSR.

With the event weighting technique, the events near $\cos\theta$=0 are assigned zero weight. Therefore, the migration of events between positive and negative $\cos\theta$ is negligible. Resolution smearing and FSR primarily transfer events between bins in invariant mass. The raw $A_{\rm fb}$ in bins of e^+e^- and $\mu^+\mu^-$ invariant mass is unfolded[13] for resolution smearing and FSR using a transfer matrix which is obtained from the Monte Carlo simulation. The unfolded $A_{\rm fb}(M)$ for electrons is shown in the top-right panel of Fig. 3.

The electroweak (EWK) mixing parameters $\sin^2\theta^{\rm lept}_{\rm eff}(M_Z)$ and $\sin^2\theta_W$ are extracted from the fully unfolded

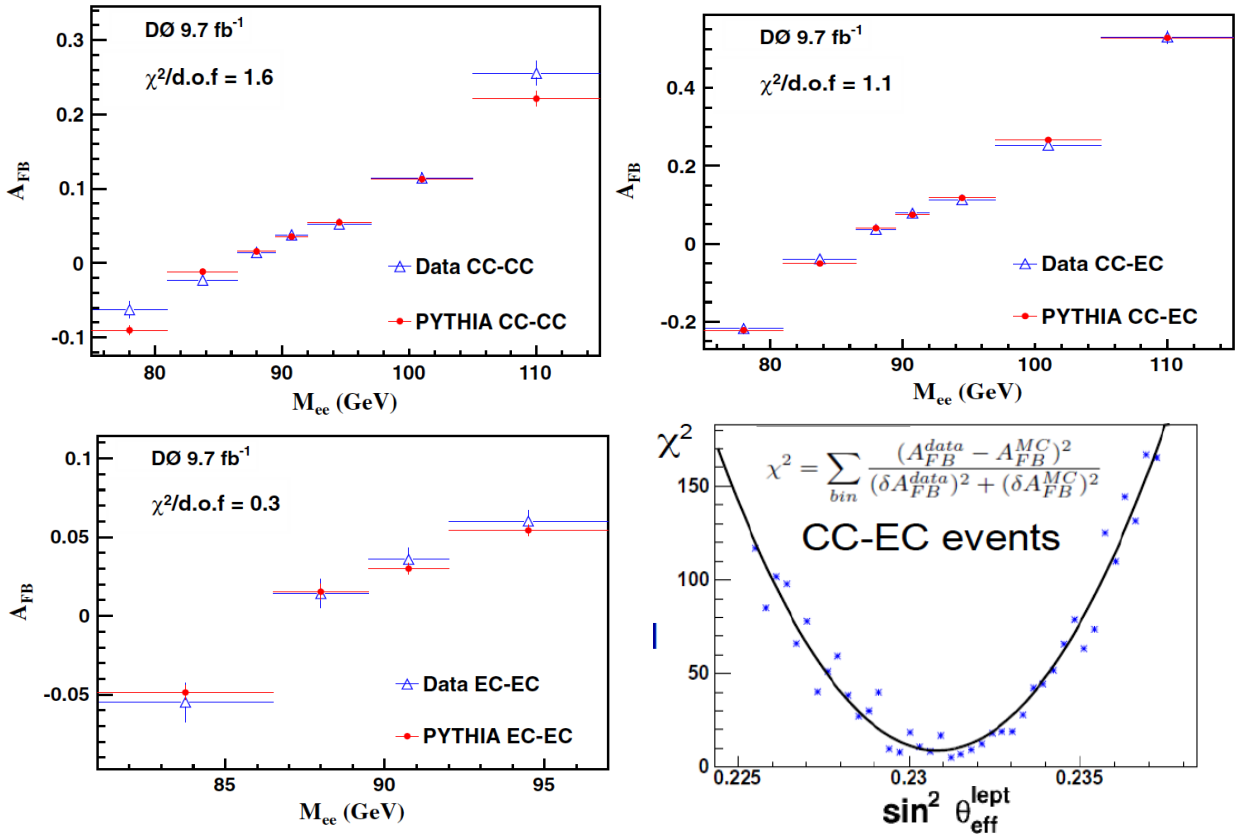

FIGURE 4. D0 raw $A_{\rm fb}(M)$ measurement in bins of e^+e^- invariant mass for Central-Central calorimeters (CC-CC), Central-Endcap calorimeters (CC-CE), and Endcap-Endcap calorimeters (EC-EC) event topologies. Also shown is the χ^2 vs. $\sin^2\theta^{\rm lept}_{\rm eff}(M_Z)$ for the D0 $A_{\rm fb}(M)$ CC-CE topology.

$A_{\rm fb}(M)$ measurements using $A_{\rm fb}(M)$ templates calculated with different values of $\sin^2\theta_W$. Three QCD calculations are used: LO (tree), RESBOS NLO, and POWHEG-BOX NLO. The three calculations were modified to include EWK radiative correction[12] using the Effective Born Approximation (EBA).

The $A_{\rm fb}(M)$ measurement is directly sensitive to the effective-mixing parameters $\sin^2\theta^{\rm lept}_{\rm eff}(M)$ which are combinations of the form-factors and $\sin^2\theta_W$. Most of the sensitivity to $\sin^2\theta^{\rm lept}_{\rm eff}(M_Z)$ comes from the Drell-Yan $A_{\rm fb}(M)$ near the Z pole, where $A_{\rm fb}$ is small. In contrast, $A_{\rm fb}(M)$ at higher mass values where $A_{\rm fb}$ is large, is mostly sensitive to the axial coupling, which is known. While the extracted values of the effective-mixing parameter $\sin^2\theta^{\rm lept}_{\rm eff}(M_Z)$ are independent of the details of the EBA model, the interpretation of the best-fit value of the on-shell $\sin^2\theta_W$ and its corresponding form factors depend on the details of the EBA model.

Calculations of the $A_{\rm fb}(M)$ templates with different values of the electroweak-mixing parameter are compared with the measurement to determine the value of the parameter that best describes the data. The calculations include both quantum chromodynamic and EBA electroweak radiative corrections. The measurement and templates are compared using the χ^2 statistic evaluated with the $A_{\rm fb}$ measurement error matrix. Each template provides a scan point for the χ^2 function $(\sin^2\theta_W, \chi^2(\sin^2\theta_W))$. The scan points are fit to a parabolic χ^2 functional form. For the CDF e^+e^- analysis, the χ^2 distribution of the scan over templates from the POWHEG NLO calculation (with NNPDF3.0) is shown in the bottom right panel of Fig. 3. For the e^+e^- analysis the EBA-based POWHEG box NLO NNPDF3.0 calculations of $A_{\rm fb}(M)$ are used to extract the central value of $\sin^2\theta_W$. For the CDF $\mu^+\mu^-$ analysis the EBA-based RESBOS (CTEQ6.6M) NLO calculations of $A_{\rm fb}(M)$ are used to extract the central value of $\sin^2\theta_W$. The other calculations are used to estimate the systematic uncertainty from the electroweak radiative corrections and QCD NLO radiation.

Analysis of D0 e^+e^- full 9.4 fb^{-1} run II sample

In the published D0 analysis[19], $A_{\rm fb}(M)$ measurements in bins of e^+e^- invariant mass are done for several event topologies as shown in Fig.4. Electrons and positrons are detected in in the Central Calorimeter (CC) and in the Endcap Calorimeter (EC). The event topologies correspond to Central-Central (CC-CC), Central-Endcap (CC-CE), and Endcap-Endcap (EC-EC). The effects of acceptance, FSR and resolution smearing are all incorporated into MC templates with different values of $\sin^2\theta^{\rm lept}$. The RESBOS templates (calculated with NNPDF2.3 NLO PDFs) are compared to the data for the three topologies and the best fit values of $\sin^2\theta^{\rm lept}$ are extracted. The χ^2 vs. $\sin^2\theta^{\rm lept}_{\rm eff}(M_Z)$ for the D0 $A_{\rm fb}(M)$ CC-CE topology is shown in the bottom right panel of Fig.4.

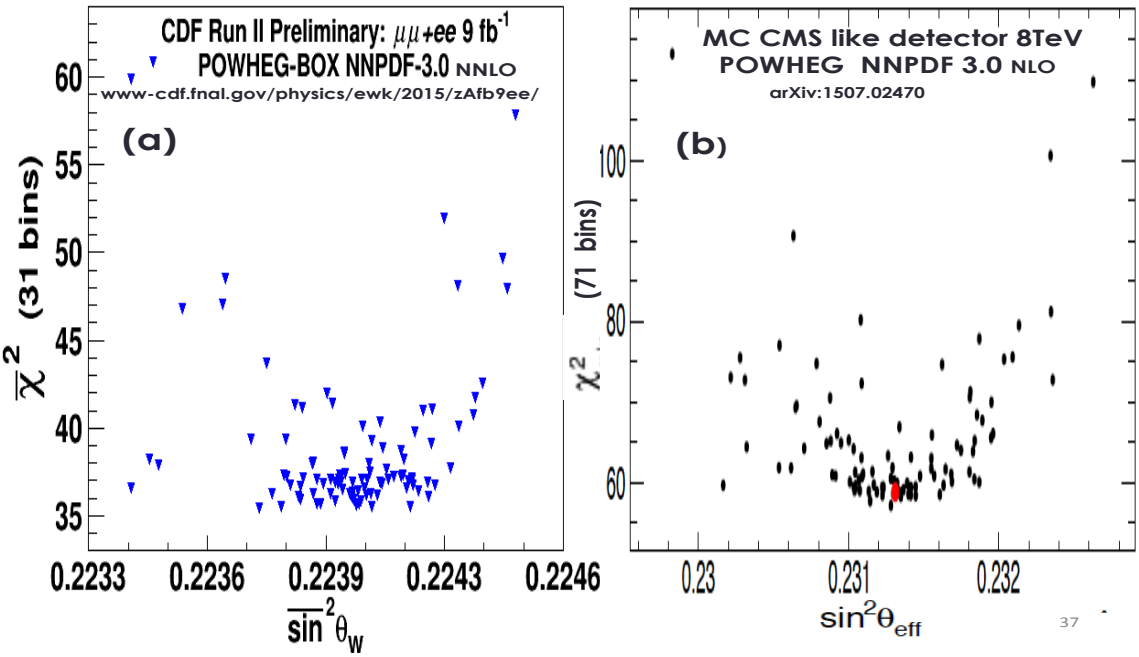

FIGURE 5. (a) CDF data: Best χ^2 versus $\sin^2\theta_W$ (from ref. [14]). (b) Best χ^2 versus $\sin^2\theta^{\rm lept}_{\rm eff}(M_Z)$ for MC simulation of a CMS like detector with 15 fb^{-1} at 8 TeV (from ref. [15] (arXiv:1507.02470).

Constraining PDFs through χ^2 weighting

This technique which was first proposed in ref. [15] has been implemented in the most recent CDF analysis[14]. At the Tevatron the technique reduces the PDF uncertainty in $\sin^2\theta_W$ by 20%. The reduction of the PDF uncertainty in $\sin^2\theta_W$ with this technique at the LHC is much more significant[15]. Fig. 2 (a) from Ref.[15] shows the difference between $A_{\rm fb}(M)$ for 10 NNPDF3.0 (NNLO) replicas and $A_{\rm fb}(M)$ calculated for the default NNPDF3.0 (NNLO) (261000). Much of the difference originates form the different dilution factors for each of the NNPDF replicas. Here $\sin^2\theta_W$ is fixed at a value of 0.2244. Fig.2(b) shows the difference between $A_{\rm fb}(M)$ for different values of $\sin^2\theta_W$ ranging from 0.2220 (shown at the top in red) to 0.2265 (shown on the bottom in blue), and $A_{\rm fb}(M)$ for $\sin^2\theta_W$=0.2244. Here $A_{\rm fb}(M)$ is calculated with the default NNPDF3.0 (NNLO).

Fig. 5(a) shows the χ^2 for the best fit value of $\sin^2\theta_W$ at CDF extracted using each of the 100 PDF replicas for the NNPDF3.0 (NNLO) PDF set[21]. As shown in Fig.2(b) different values of $\sin^2\theta_W$ raise or lower $A_{\rm fb}$(M) for all values of dilepton mass. In contrast, as shown in Fig.2(a) PDFs which raise the value of $A_{\rm fb}(M)$ for dilepton mass above the mass of the Z boson, reduce $A_{\rm fb}(M)$ below the mass of the Z bosons. The sensitivity of $A_{\rm fb}(M)$ to $\sin^2\theta_W$ is very different from the sensitivity to PDFs. Therefore, PDFs with a high value of χ^2 are less likely to be correct. As shown in ref. [15], this information can be incorporated into the analysis by weighting the PDF replicas by $e^{-\chi^2/2}$. This reduces the weights of PDFs with large values of χ^2. In addition to the measurements of $\sin^2\theta^{\rm lept}_{\rm eff}(M_Z)$ and the on-shell

$\sin^2\theta_W = 1 - M_W^2/M_Z^2$, these $A_{\rm fb}(M)$ constrained PDF weights can also be used to reduce the PDF uncertainties in other Tevatron measurements such as the direct measurement of M_W.

Results

The Tevatron results with the full 9.4 fb^{-1} sample are:

- D0: $\sin^2\theta^{\rm lept}_{\rm eff}(M_Z)$=0.23147± 0.00043 (stat) ±0.00008(syst)±0.00017 (NNPDF2.3 NLO PDFs),
  or $\sin^2\theta^{\rm lept}_{\rm eff}(M_Z)^{D0}$ = 0.23147± 0.00047
- CDF: $\sin^2\theta^{\rm lept}_{\rm eff}(M_Z)$=0.23222± 0.00042 (stat) ±0.00008(syst)±0.00016 (NNPDF3.0 NNLO PDFs),
  or $\sin^2\theta^{\rm lept}_{\rm eff}(M_Z)^{CDF}$ = 0.23222± 0.00046
- CDF: $M_W^{indirect}$ = 80.327±0.021(stat) ±0.010(sys) GeV,
  or $M_W^{indirect}$ = 80.327±0.023 GeV

The left panel of Fig.6 shows a comparison of $\sin^2\theta^{\rm lept}_{\rm eff}(M_Z)$ measurement from the Tevatron and other experiments, including the latest LHC results from CMS[22], ATLAS[23] and LHCb[25]. The LEP-1+SLD Z-pole entry is the combination of their six Z-pole measurements. The right panel of Fig.6 shows a comparison of CDF $M_W^{indirect}$ measurements to measurements by other experiments. The TeV and LEP-2 value is the world average of the direct measurements[3] of M_W (M_W^{direct} = 80.385 ± 0.015 GeV). All the others are indirect W-mass measurements that use the standard model (on-shell scheme). The indirect measurement labeled NuTeV[24] is the Tevatron neutrino neutral current measurement[24]. The indirect measurement labeled LEP1+SLD(M_t) is from standard model fits to all Z pole measurements[1] in combination with the Tevatron top-quark mass measuremen[4].

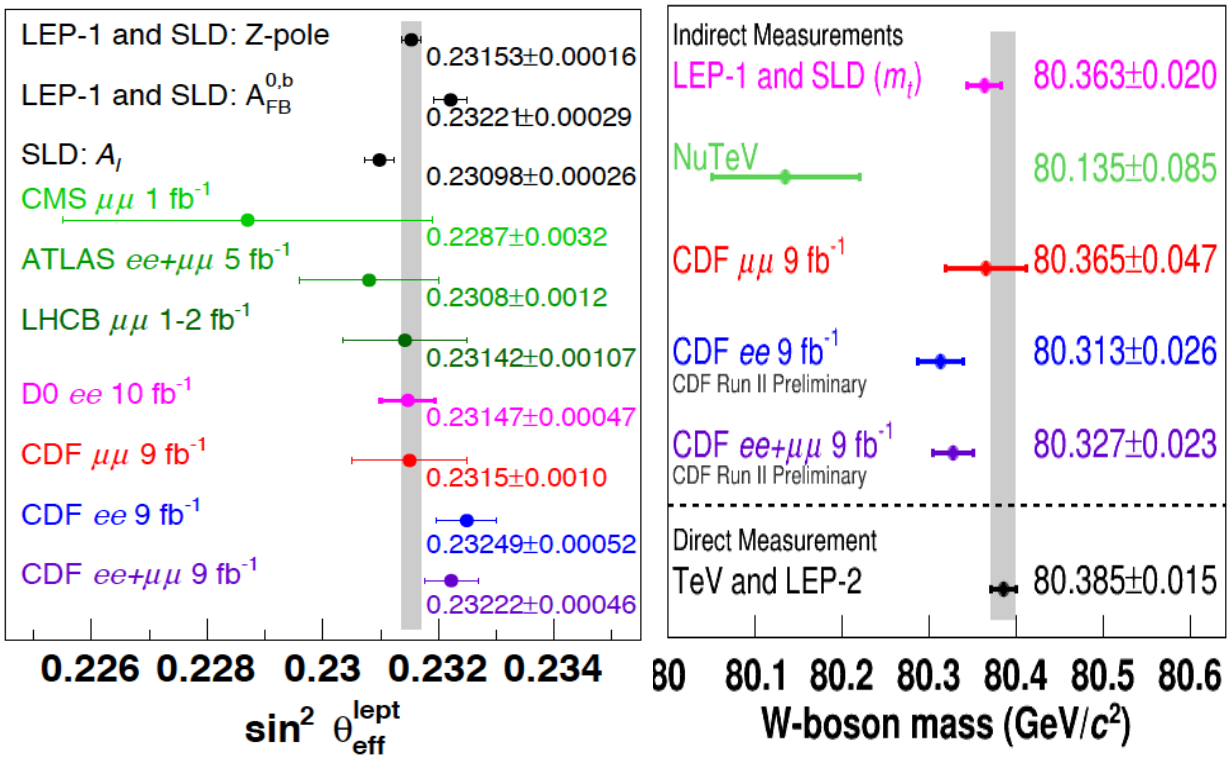

FIGURE 6. Left panel: Comparison of $\sin^2\theta^{\rm lept}_{\rm eff}(M)_Z$ measurements. that includes the latest LHC results from CMS[22], ATLAS[23] and LHCb[25]. The LEP-1+SLD Z-pole entry is the combination of their six Z-pole measurements. Right panel: M_W measurements. All except for 'TeV and LEP-2' are indirect W-mass measurements that use the standard model (on-shell scheme). NuTeV is the Tevatron neutrino neutral current measurement[24].

REFERENCES

[1] The ALEPH, DELPHI, L3, OPAL, SLD Collaborations, the LEP Electroweak Working Group, the SLD Electroweak and Heavy Flavour Groups, Phys. Rept. 427, 257 (2006); the ALEPH, DELPHI, L3, OPAL Collaborations, the LEP Electroweak Working Group, Phys. Rept. 532, 119 (2013)

[2] K.A. Olive et al. (PDG) *Chin. Phys.* **C38**, 090001 (2014). (http://pdg.lbl.gov)

[3] T. Aaltonen et al. (CDF, D0) Phys. Rev. D 88, 052018 (2013), (arXiv:1307.7627).

[4] ATLAS, CDF, CMS and D0 Collaborations, *"First combination of Tevatron and LHC measurements of the top-quark mass"*, arXiv:1403.4427 (ATLAS-CONF-2014-008; CDF Note 11071; CMS PAS TOP-13-014; D0 Note 6416).

[5] Heinemeyer, W. Hollik, G. Weiglein, L. Zeune, JHEP12, 084 (2013) (arXiv:1311.1663).

[6] ATLAS Collaboration, *"Measurement of the top quark mass in the* $t\bar{t} \rightarrow$ lepton + jets *and* $t\bar{t} \rightarrow$ dilepton *channels using* $\sqrt{s} = 7$ *TeV ATLAS data"*, Eur. Phys. J. C (2015) 75:330 (arXiv:1503.05427).

[7] CMS Collaboration, *"Measurement of the top quark mass using proton-proton data at* $\sqrt{s} = 7$ *and 8 TeV"* (arXiv:1509.04044).

[8] A. Sirlin, Phys. Rev. D 22, 971 (1980).

[9] J. C. Collins and D. E. Soper, Phys. Rev. D 16, 2219 (1977).

[10] A. Bodek et al., Eur. Phys. J. C72, 10 (2012), *"Extracting Muon Momentum Scale Corrections for Hadron Collider Experiments"* (arXiv:1208.3710).

[11] A. Bodek, Eur. Phys. J. C67, 321 (2010), *A simple event weighting technique for optimizing the measurement of the forward-backward asymmetry of Drell-Yan dilepton pairs at hadron colliders* (arXiv:0911.2850).

[12] Aaltonen et. al., (CDF collaboration), Phys, Rev. D88, 072002 (2013), *Indirect measurement of* $\sin^2\theta_W$ *(or* M_W*) using* e^+e^- *pairs in the Z-boson region with* $p\bar{p}$ *collisions at a center-of-momentum energy of 1.96 TeV* (arXiv:1307.0770).

[13] Aaltonen et. al., (CDF collaboration) Phys.Rev. D89, 072005 (2014) *Indirect measurement of* $\sin^2\theta_W$ *(or* M_W*) using* $\mu^+\mu^-$ *pairs from* γ^*/Z *bosons produced in* $p\bar{p}$ *collisions at a center-of-momentum energy of 1.96 TeV* (arXiv:1402.2239).

[14] http://www-cdf.fnal.gov/physics/ewk/2015/zAfb9ee/

[15] A. Bodek, J. Han, A. Khukhunaishvili, W. Sakumoto, *"Using Drell-Yan forward-backward asymmetry to reduce PDF errors in the measurement of electroweak parameters"* (arXiv:1507.02470).

[16] D. Bardin, M. Bilenky, T. Riemann, M. Sachwitz, and H. Vogt, Comput. Phys. Commun. 59, 303 (1990); D. Bardin, P. Christova, M. Jack, L. Kalinovskaya, A. Olchevski, S. Riemann, and T. Riemann, Comput. Phys. Commun. 133, 229 (2001); A. Arbuzov, M. Awramik, M. Czakon, A. Freitas, M. Grnewald, K. Monig, S. Riemann, and T. Riemann, Comput. Phys. Commun. 174, 728 (2006).

[17] S. Schael et al. (ALEPH, DELPHI, L3, OPAL, and SLD collaborations; LEP Electroweak Working Group; and SLD Electroweak and Heavy Flavour Groups), Phys. Rep. 427, 257 (2006) *Precision electroweak measurements on the Z resonance*

[18] U. Baur, O. Brein, W. Hollik, C. Schappacher, and D. Wackeroth, Phys. Rev. D 65, 033007, 2002, *Electroweak Radiative Corrections to Neutral-Current Drell-Yan Processes at Hadron Colliders* (arXiv:0108274).

[19] V. M. Abazov et al. (D0 collaboration) Phys. Rev. Lett. 115, 041801 (2015), *Measurement of the effective weak mixing angle in* $p\bar{p} \rightarrow Z/\gamma^*\ e^+e^-$ *events* (arXiv:1408.5016).

[20] T. Sjostrand, P. Eden, C. Feriberg, L. Lonnblad, G. Miu, S. Mrenna, and E. Norrbin, Comp. Phys. Commun. 135, 238 (2001) PYTHIA version v6.323 is used by D0.

[21] R. D. Ball et al., Nucl. Phys. B867, 244 (2013), *Parton distributions with LHC data,* NNPDFS.

[22] The CMS collaboration, Phys. Rev D84 112002 (2011), *"Measurement of the weak mixing angle with the Drell-Yan process in proton-proton collisions at the LHC"* (arXiv:1110.2682).

[23] The ATLAS collaboration,HEP09, 049 (2015), *"Measurement of the forward-backward asymmetry of electron and muon pair-production in pp collisions at* $\sqrt{(}s)$*= 7 TeV with the ATLAS detector"* (arXiv:1503.03709).

[24] G. P. Zeller et. al. (NuTeV), Phys. Rev. Lett. 88, 091802 (2002) and Phys. Rev. Lett, 90, 239902(E) (2003).

[25] LHCb collaboration, *"Measurement of the forward-backward asymmetry in* $Z \rightarrow \mu\mu$ *decays and determination of the effective weak mixing angle"* (arXiv:1509.07645).

Proceedings of the LHCP2015 Conference, St. Petersburg, Russia, August 31 - September 5, 2015

Editors: V.T. Kim and D.E. Sosnov

Forward EW Physics at the LHC

STEPHEN FARRY

Department of Physics, University of Liverpool, L69 7ZE, United Kingdom.

stephen.farry@cern.ch

On behalf of the CMS and LHCb Collaborations

Abstract. Measurements of electroweak production in the forward region at the LHC provide unique and complementary information to those performed in the central region. Studies have been performed not just by LHCb, a dedicated forward detector, but also by ATLAS and CMS, which are primarily situated in the central region but can exploit forward calorimetry coverage to contribute to the understanding of SM processes in the forward region.

INTRODUCTION

Studies of the production and decay of electroweak bosons in the forward region provide both complementary and unique information to those performed in the central region. The measurements can be used to provide constraints on the parton distribution functions (PDFs) as they probe a distinct region of (x, Q^2) phase space, where x is the longitudinal momentum fraction of the proton carried by the parton, and Q^2 is the energy scale of the interaction. As forward bosons are produced through the annihilation of two partons with asymmetric longitudinal proton momentum fractions, studies of their production simultaneously probes the low- and high-x regions of the (x, Q^2) plane. This is illustrated in the left diagram of Figure 1, where the different regions explored by the LHC experiments at a centre-of-mass energy of 8 TeV are shown.

The extension of measurements into the forward region is also particularly relevant for the electroweak production of W and Z bosons. The signature for these process is the production of the boson in association with two jets with a large rapidity gap arising from colour flow considerations. The inclusion of forward jets in the measurements allows for a greater phase space with which to identify these rapidity gaps.

At a proton-proton collider such as the LHC, the forward region is also a more sensitive probe of the forward-backward asymmetry in Z decays. Z bosons produced in the forward region are more likely to follow the initial quark direction and consequently suffer less from the dilution of the parton level asymmetry observed in the central region. This is discussed in more detail later in the text.

The approximate rapidity coverage of the ATLAS [1], CMS [2] and LHCb [3] experiments is shown in the right diagram of Figure 1. LHCb is an experiment optimised for the study of $\mathcal{CP}$ violation in heavy flavour decays, and consequently is fully instrumented in the forward region. This includes tracking coverage in the pseudorapidity range between 2.0 and 5.0, as well as electromagnetic and hadronic calorimetry up to approximately 4.5. The ATLAS and CMS detectors are instrumented in the central region, and consequently their tracking coverage is limited to $|\eta| < 2.4$. However, both experiments have calorimetry coverage further forward which allows them to identify jets and electrons in the forward region. In particular, the ATLAS forward calorimeters provide both hadronic and electromagnetic calorimeter coverage up to $\eta = 4.9$, while the CMS electromagnetic calorimeter coverage extends up to $\eta = 3.0$ with hadronic calorimetry coverage up to $\eta = 5.0$.

Measurements of inclusive W and Z production at LHCb are discussed first, followed by measurements of W and Z boson production in association with inclusive jets and W production in association with heavy flavour jets. Finally the electroweak production of W and Z bosons is presented followed by measurements of the forward-backward asymmetry in $Z \to \ell\ell$ events.

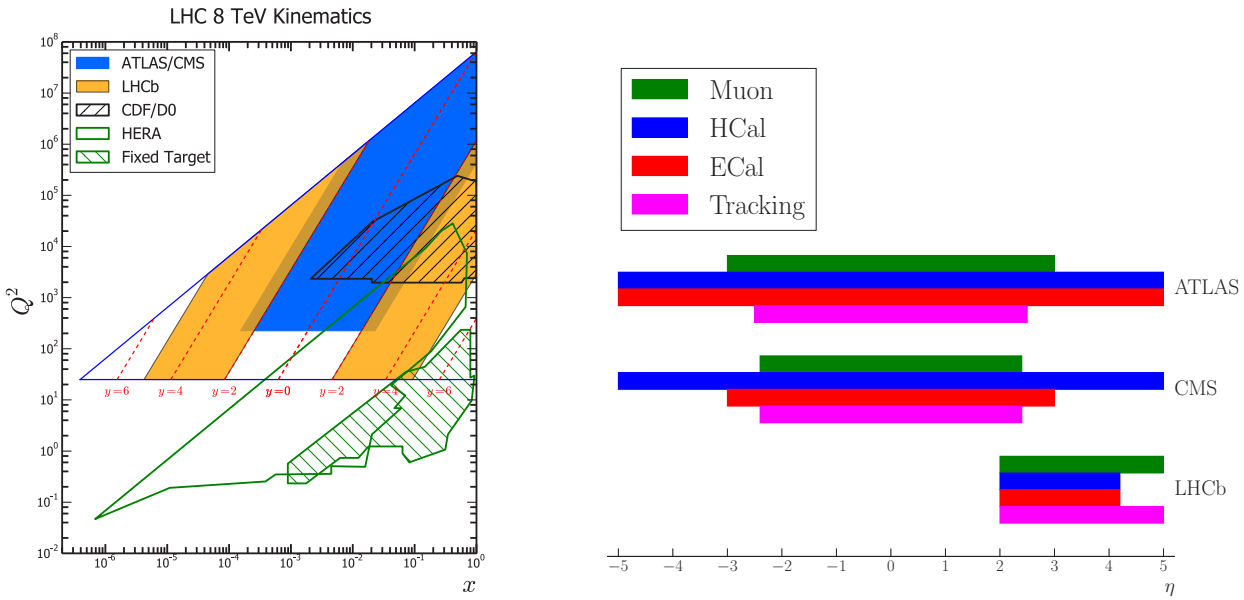

FIGURE 1. (Left) The region of the (x, Q^2) space probed by previous experiments as well as ATLAS, CMS and LHCb at a centre-of-mass energy of 8 TeV. (Right) The approximate rapidity coverage of the different components of the ATLAS, CMS and LHCb detectors.

Inclusive W and Z Production

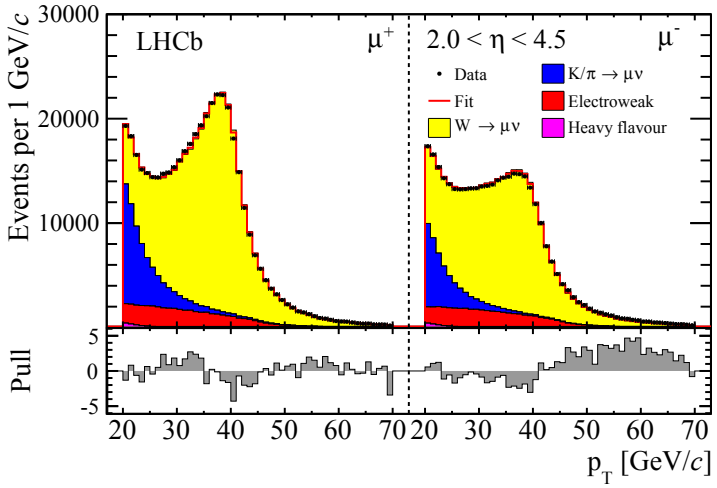

FIGURE 2. Fit to the muon p_T spectrum for W^+ (left) and W^- (right) candidates for purity extraction [4].

Measurements of the inclusive production of W and Z bosons in the forward region have recently been performed by the LHCb experiment at $\sqrt{s} = 7$ TeV in the muon channel [4, 5] and of Z production at both $\sqrt{s} = 7$ and 8 TeV in the electron channel [6, 7]. The measurement of W production is performed by selecting muons which have a transverse momentum of greater than 20 GeV and a pseudorapidity in the region $2.0 < \eta < 4.5$. The purity of the W boson sample is determined by performing a template fit to the p_T of the selected events using signal and background shapes obtained from both data and simulation. The signal shape and the dominant background,

arising from muons produced through the decay-in-flight of pions and kaons, are allowed to float in the fit, with the other backgrounds normalised using data-driven techniques. The fit is shown for both positive and negative muons in Figure 2 with a purity of approximately 77% achieved for both W^+ and W^-. The extracted yields are corrected for detector reconstruction and selection efficiency, as well as final state radiation in order to facilitate a comparison with fixed order QCD predictions. The differential cross-sections and lepton charge asymmetry are shown in Figure 3 as a function of lepton pseudorapidity. The results are compared to predictions obtained at NNLO in perturbative QCD using the FEWZ [8] generator and a number of different PDF sets with a good level of agreement observed. The experimental precision is dominated by the luminosity measurement, as well as the effect of the beam energy uncertainty, with both sources contributing uncertainties of 1.16 and $\sim$ 1% respectively. The presence of a small overlap in the coverage of the ATLAS, CMS and LHCb detectors also allows a comparison to be made between the three experiments. This comparison is shown in Figure 4 for ATLAS [9] and CMS [10] where in both cases the LHCb data is corrected using theoretical predictions to account for differences in the chosen measurement fiducial volumes. In order to perform measurements of Z boson production, the same kinematic selection is applied as in the case of W production (with electrons also selected) and a second, opposite-sign lepton is also required to be present with the pair forming an invariant mass in the region of the Z peak. In the dimuon channel, this mass range is chosen to be between 60 and 120 GeV, while for the electron channel, incomplete bremsstrahlung recovery results in the smearing of the mass spectrum to lower masses, and so the dielectron invariant mass is required to be larger than 40 GeV. The purity in both channels is determined using data-driven methods, and is over 99% for the dimuon channel, and approximately 95% in the electron channel. The measurements are presented and compared to SM predictions using a range of different PDF sets as a function of boson rapidity in Figure 5, with a similar level of agreement observed as in the case of W boson production. Uncertainties on the overall normalisation due to the luminosity and the beam energy uncertainty are again seen to dominate. It should be noted that the beam energy is only applied to the $Z \to \mu\mu$ measurement, where a more precise measurement of the luminosity is exploited. Measurements of W and Z production in the muon channel at 8 TeV are not discussed here but have also since been performed by LHCb [11].

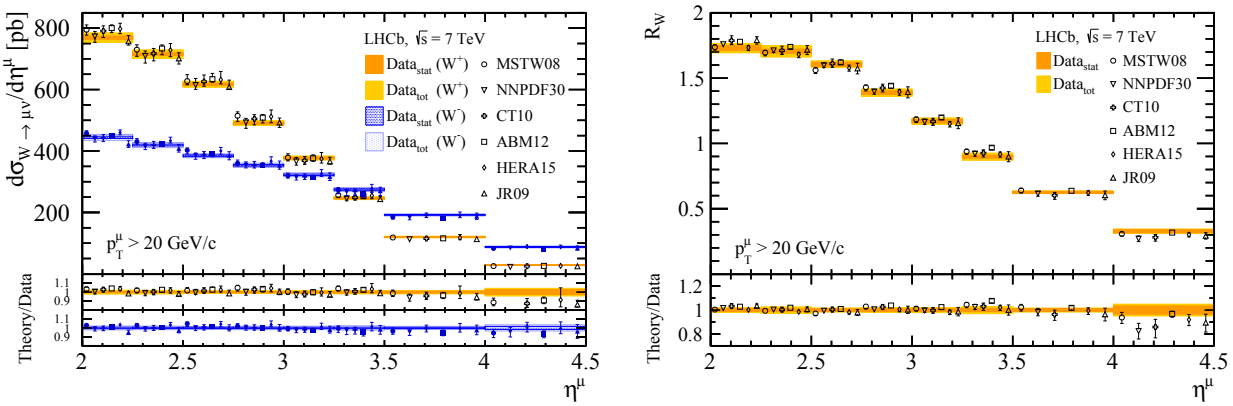

FIGURE 3. Measurements of (left) the W boson production cross-section and (right) the lepton charge asymmetry at LHCb, where both are shown as a function of lepton pseudorapidity and compared to NNLO QCD predictions using a variety of PDF sets [5].

W and Z Production in Association with Jets

The ATLAS collaboration has performed measurements of W [12] and Z [13] production in association with jets (Wj, Zj) where the bosons are reconstructed in both the muon and electron decay modes. The muons (electrons) are required to satisfy $|\eta| < 2.4(2.47)$ and the jets extend up to forward rapidities of 4.4. The leptons are required to have a p_{T} in excess of 25 GeV for W events, and to be greater than 30 GeV for Z events, where they are also required to have a dilepton mass range between 66 and 112 GeV. The W candidates are selected by vetoing on additional leptons in the final state, and requiring a missing transverse momentum, $E_{\mathrm{T}}^{\mathrm{miss}}$, in excess of 25 GeV and a transverse mass, m_{T}, of greater than 40 GeV.

The jets are reconstructed using the anti-k_{T} algorithm with a distance parameter of 0.4 and are required to have

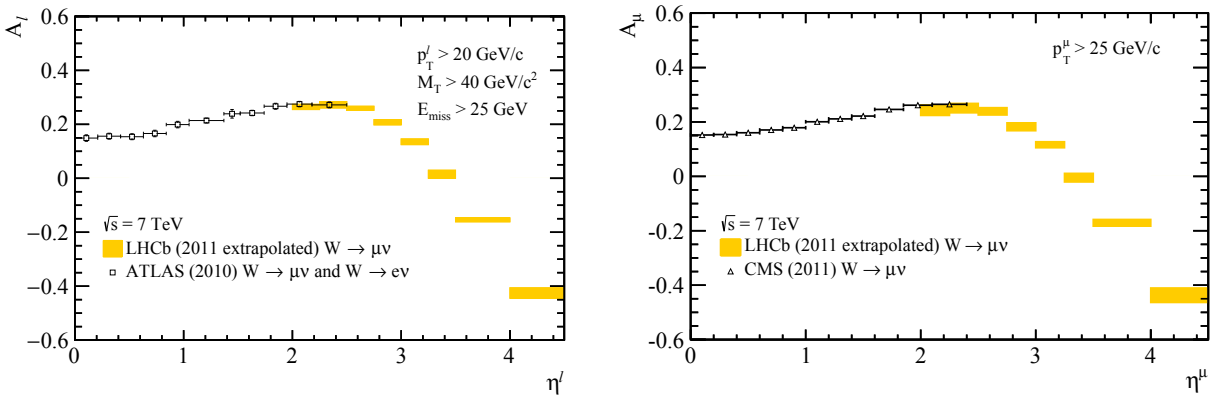

FIGURE 4. Comparisons of the measured inclusive W lepton charge asymmetry between (left) LHCb and ATLAS, and (right) LHCb and CMS. In both cases the LHCb measurement is extrapolated to match the ATLAS/CMS fiducial volume using theoretical predictions [5].

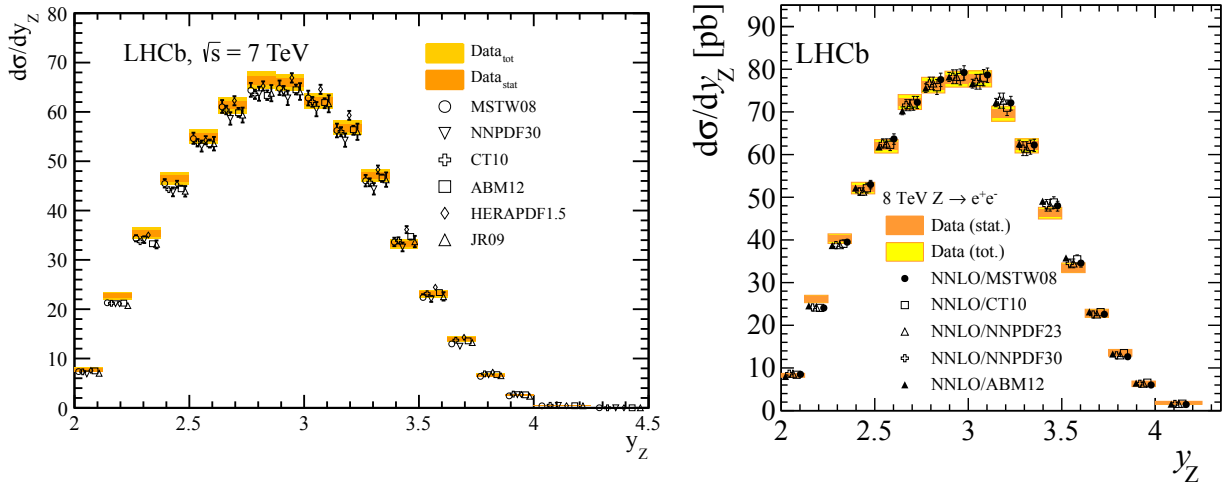

FIGURE 5. Measurements of the Z boson production cross-section measured at LHCb for the (left) muon and (right) electron decay mode. Comparisons are made to NNLO QCD predictions with a range of PDF sets [5, 7].

transverse momenta in excess of 30 GeV and to be separated from the leptons by a radius of 0.5 in $\eta - \phi$ space. The background contributions from QCD multi-jet and $t\bar{t}$ production are estimated using data-driven methods while the remaining backgrounds are taken from simulation The cross-section is measured as a function of a number of kinematic variables, and for jet multiplicities of up to seven. Of particular interest here are the measurements of the cross-sections versus jet rapidity and the rapidity separation of the two leading jets (for events with jet multiplicities of greater than one). These distributions are shown in Figure 6 and Figure 7 for Wj production and Figure 8 for Zj production. A general good level of agreement is observed although some of the predictions show a slight overestimation of the measured cross-sections at high rapidities.

W boson production in association with heavy flavour jets

As the LHCb experiment is optimised for the selection of heavy flavour decays in the forward region, it is uniquely suited to perform heavy flavour tagging of jets in the forward region. This is achieved using a tagging algorithm which identifies heavy flavour jets through the presence of a secondary vertex with a radial separation, $\Delta R < 0.5$ between its

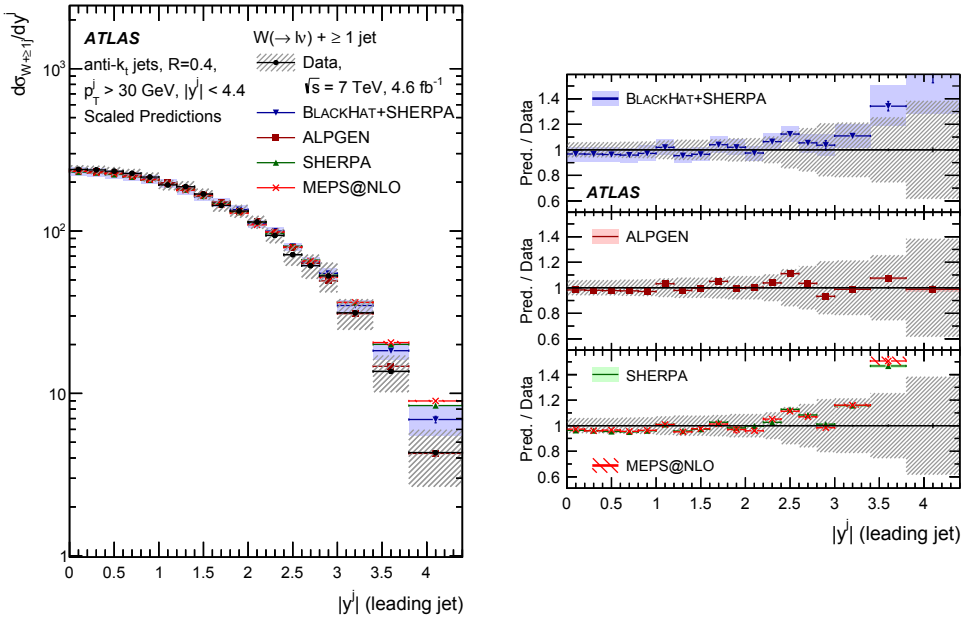

FIGURE 6. Measurements of the cross-section for $W\,j$ production at ATLAS shown for the rapidity of the leading jet. Deviations from the SM predictions are observed in the most forward bins [12].

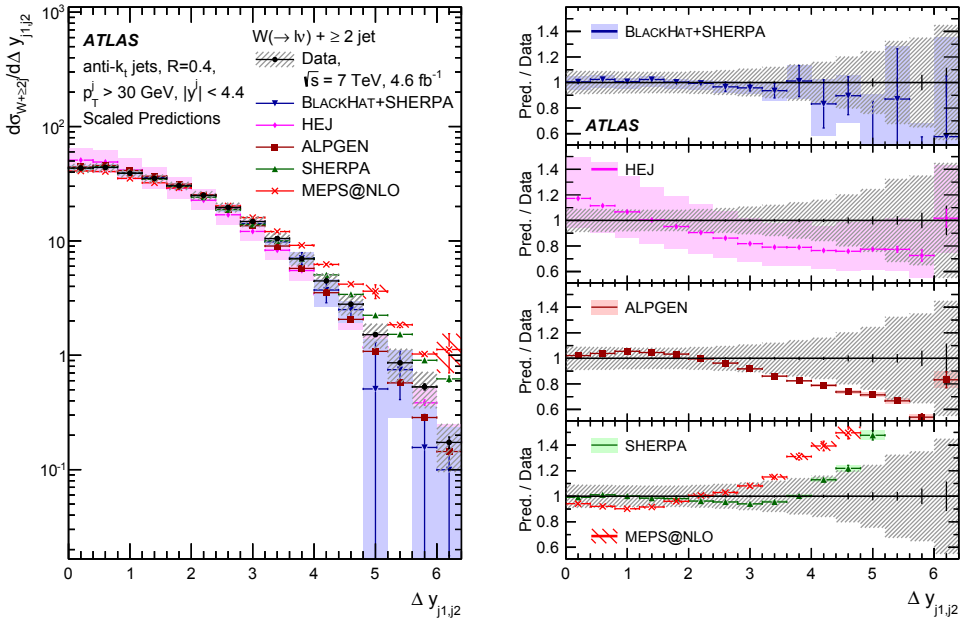

FIGURE 7. Measurements of the cross-section for $W\,j$ production at ATLAS shown for the the rapidity separation of the leading and subleading jet in events with at least two jets [12].

direction of flight and that of the jet axis. Two boosted decision trees (BDTs) are trained using characteristics of both the jet and the secondary vertex to separate light jets from heavy flavour jets, and $b-$jets from $c-$jets. More details on the secondary vertex tagging algorithm can be found in Reference [14].

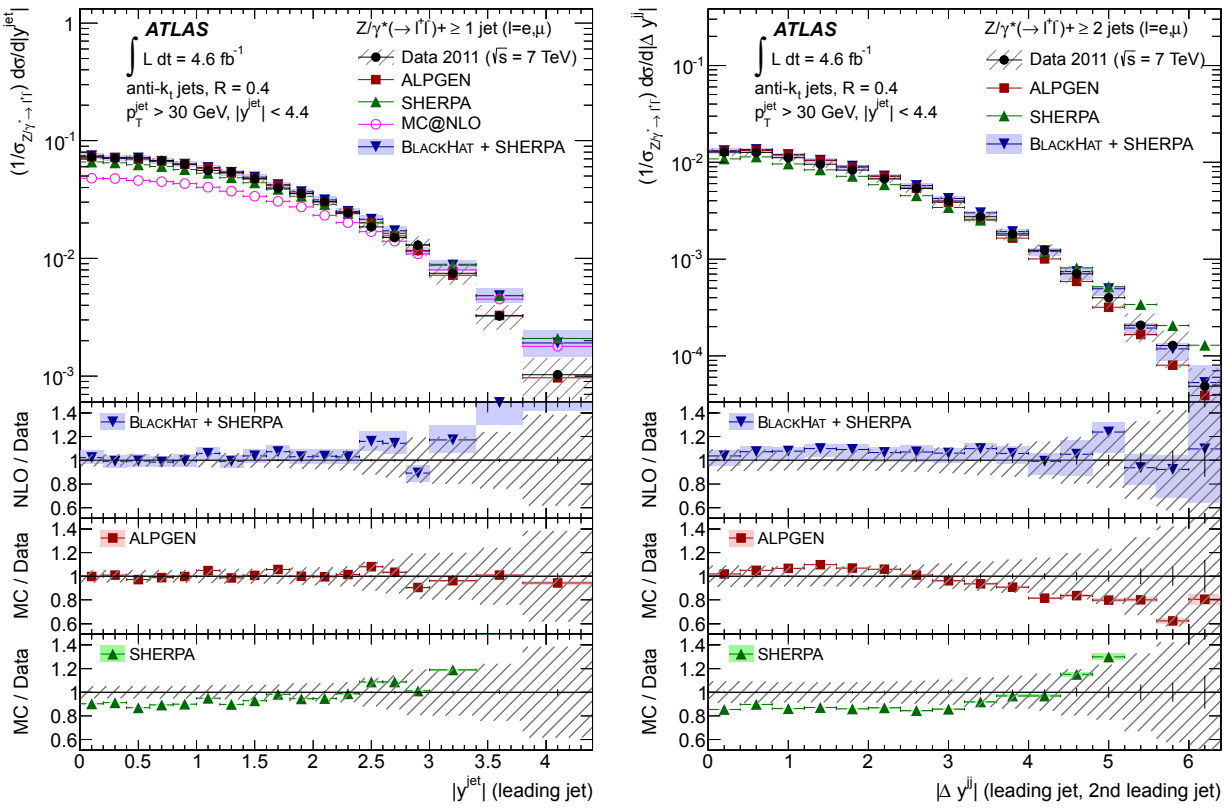

FIGURE 8. Measurements of the cross-sections for Zj production at ATLAS shown for (left) the rapidity of the leading jet and (right) the rapidity separation of the leading and subheading jet in events with at least two jets. Deviations from the SM predictions are observed in the most forward bins [13].

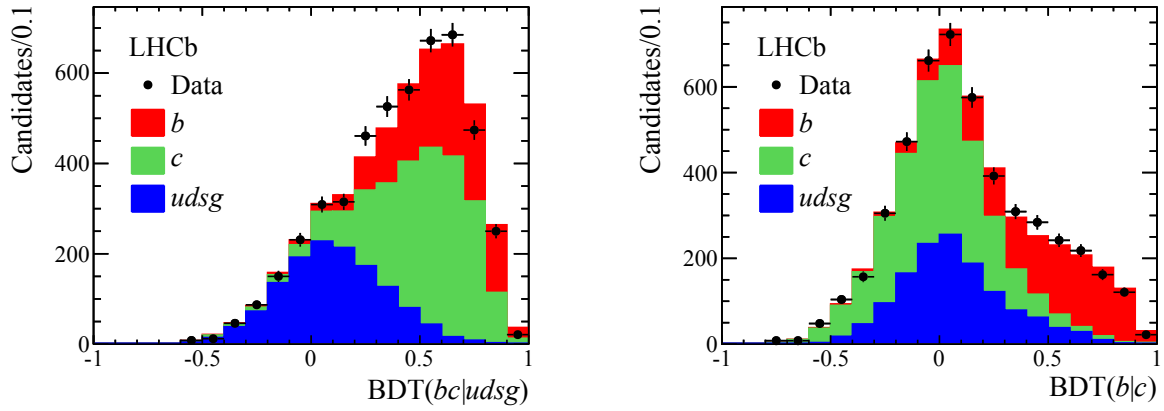

FIGURE 9. Shown are the BDT distributions used to separate (left) light jets from heavy flavour jets and (right) b-jets from c-jets in order to measure W production in association with $b-$ or $c-$jets [14].

These heavy flavour tagging capabilities are applied to measurements of W boson production in association with b- and c-jets [15]. The W boson is reconstructed using a similar selection to that described earlier, and a jet is additionally required to be present with a p_{T} in excess of 20 GeV and a pseudorapidity between 2.2 and 4.2. The events are also required to satisfy $p_{\mathrm{T}}(j_\mu + j) > 20$ GeV, where j_μ is a reconstructed jet containing the muon candidate. The observable

is expected to be large for W+jet events due to the missing neutrino in the final state and consequently improves the signal purity by rejecting backgrounds arising from di-jet production where the jet momenta are balanced. The purity is extracted using a fit to an isolation variable defined as the ratio of $p_{\mathrm{T}}(\mu)/p_{\mathrm{T}}(j_\mu)$ which is representative of the isolation of the muon. The background to the sample arising from QCD backgrounds, such as the mis-identification of pions or kaons, or the semi-leptonic decay of heavy flavour mesons is then determined using fits to this variable. The b and c-jet yields are extracted by performing a fit to the two-dimensional BDT distributions in each bin. Additional backgrounds are considered from other electroweak processes, such as $Z \to \mu\mu$, $Z \to \tau\tau$, $W \to \tau\nu_\tau$ and top production are subtracted using data-driven techniques. Fits to the $p_{\mathrm{T}}(\mu)/p_{\mathrm{T}}(j_\mu)$ distribution and the two-dimensional BDT distribution in the $p_{\mathrm{T}}(\mu)/p_{\mathrm{T}}(j_\mu) > 0.9$ bin are shown in Figure 9.

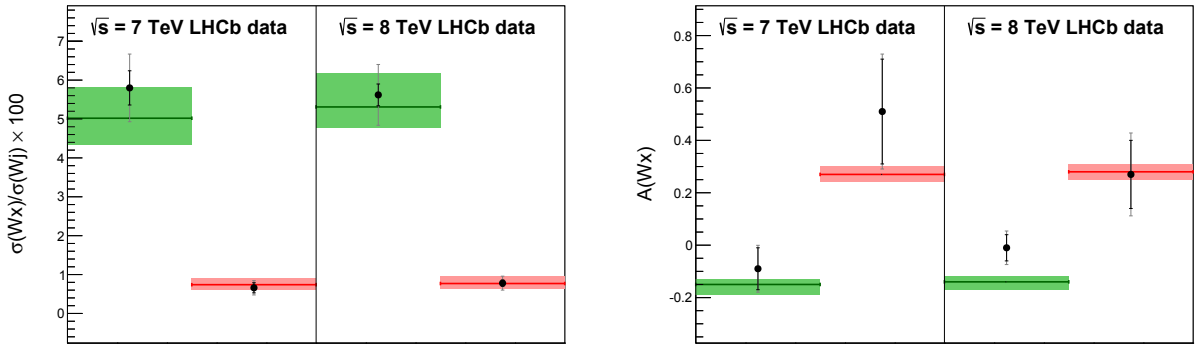

FIGURE 10. Comparisons of measurements performed at 7 and 8 TeV for Wc (green) and Wb (red) compared to theoretical predictions for (left) the ratio of Wb/Wc to Wj production and (right) Wb/Wc charge asymmetries [15].

The extracted signal yields are then corrected for detector efficiency and other reconstruction effects and measurements are performed at both 7 and 8 TeV. The ratios of Wb and Wc production to inclusive Wj production, and their charge asymmetries are shown in Figure 10 and compared to the SM predictions obtained at NLO using MCFM [16] and the CT10 PDF set. A good agreement is in general observed.

Electroweak W and Z boson production

While the dominant mechanism for the production of W and Z bosons is through the annihilation of quark-anti-quark pairs, a contribution from the purely electroweak t-channel exchange of electroweak bosons, known as electroweak production, is also present. These amplitudes include contributions from vector-boson fusion which is of particular interest due to its similarities with Higgs boson production as well as a probe of anomalous WWZ triple gauge couplings. Electroweak boson production is characterised by a boson produced in association with a pair of jets separated by a rapidity gap and with a large di-jet invariant mass. These properties can be used to distinguish it from $q\bar{q}$ annihilation and the extra phase space afforded by including jets produced in the forward region allows the signal purity to be increased by extending the rapidity gap to large values of rapidity separation, $|\Delta\eta_{jj}|$.

The CMS collaboration has reported measurements of electroweak Zjj production at both 7 [17] and 8 TeV [18]. Z bosons are selected through both their electronic and muonic decay modes where the leptons are required to have $p_{\mathrm{T}} > 20$ GeV and a combined invariant mass of greater than 50 GeV. Two jets are then required to be present with transverse momenta $p_{\mathrm{T}}^{j} > 25$ GeV, a di-jet invariant mass, M_{jj} of greater than 120 GeV and jet pseudorapidities, η_j of up to 4.7. Both analyses exploit multi-variate algorithms in order to separate signal from background. A BDT is trained using a number of discriminating variables, including $|\Delta\eta_{jj}|$, and the signal contribution is estimated by a template fit to the BDT response where the signal and the Drell-Yan background are free to float in the fit and the other contributions are fixed using simulation. The 8 TeV analysis makes use of three different analysis strategies, where different kinematic requirements are applied and different variables are input to the BDT. The resultant distributions for the measurements at 7 and 8 TeV for the dimuon channel are shown in Fig. 11. with just one analysis strategy

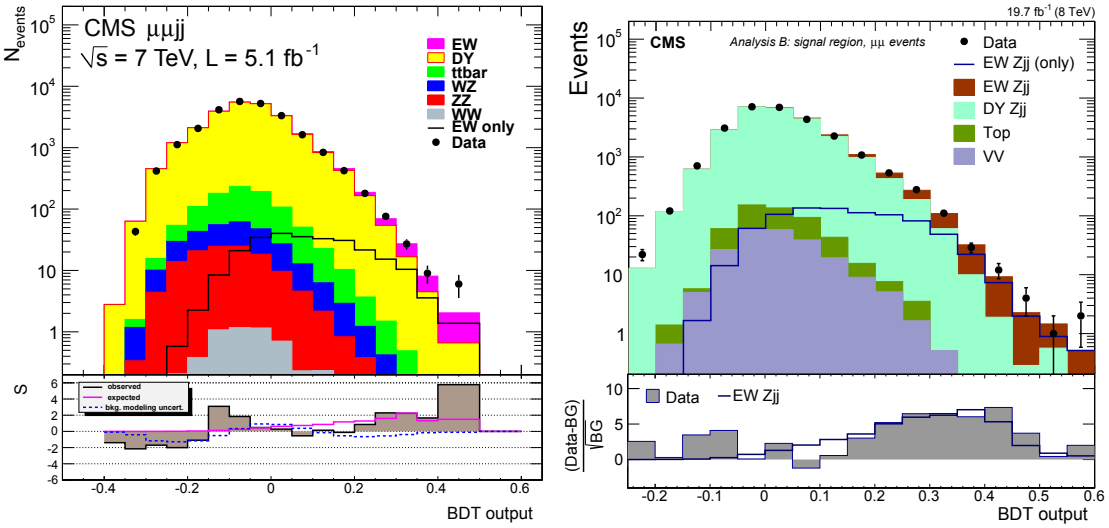

FIGURE 11. The observed BDT responses for the dimuon channel at (left) 7 [17] and (right) 8 TeV [18] where the electroweak Zjj component is visible at high BDT response values. Only one of the analysis classes is shown for the 8 TeV measurement.

for the 8 TeV analysis shown for clarity. The cross-sections are extracted at both centre-of-mass energies with good agreement observed with SM predictions.

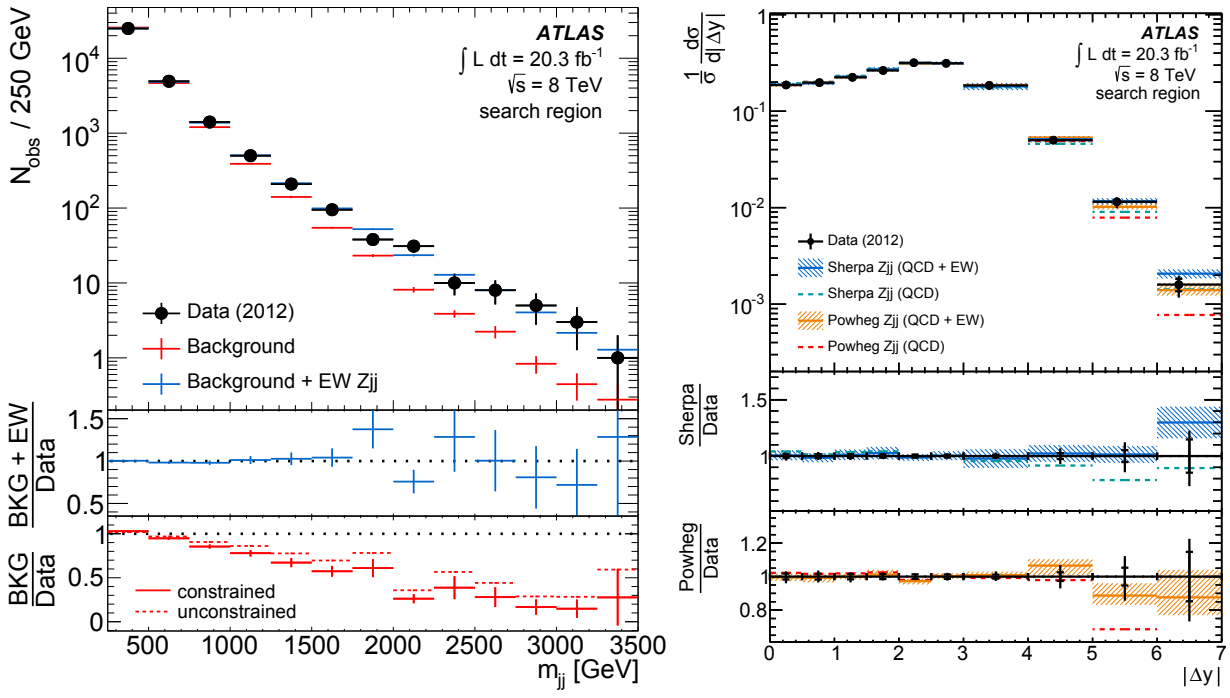

FIGURE 12. (left) the number of observed data events compared to the expected background and signal contributions as a function of m_{jj} (right) the measured cross-section as a function of $|\Delta y|$ compared to theoretical predictions [19].

The ATLAS collaboration has reported measurements of electroweak Zjj production at 8 TeV [19].The analysis is also performed using both the electron and muon decay modes of the Z, with both the leptons and jets required

to have a p_{T} of greater than 25 GeV, where the jets extend up to rapidities of 4.4. The Zjj signal contribution, and subsequently the cross-section, is extracted from a fit to the dijet invariant mass in five separate fiducial regions. One of these regions, known as the "search" region, is chosen specifically to enhance the electroweak component by requiring a balanced Zjj system in addition to a di-jet invariant mass of greater than 250 GeV and a jet rapidity gap between the two selected jets. The distributions for the search region are shown as a function of the rapidity separation and the di-jet invariant mass in Figure 12. A good agreement is observed between the measured cross-sections and the SM predictions in the different fiducial regions, while the measurements are also used to set limits on anomalous triple gauge couplings.

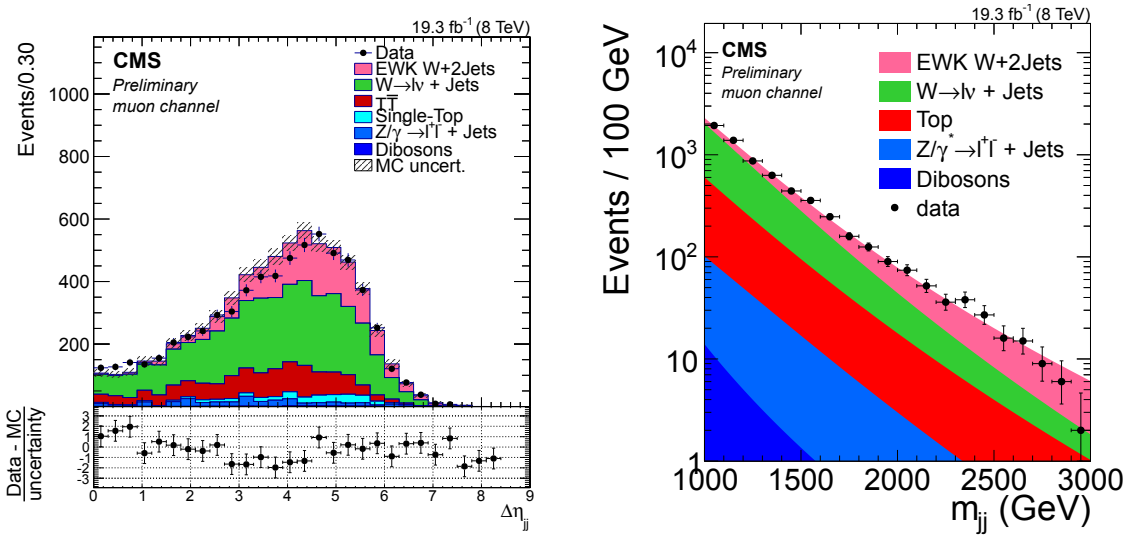

FIGURE 13. (left) the pseudorapidity separation of the two leading jets as observed in data and compared to expectations (right) the fit used to extract the electroweak component of Wjj production [20].

CMS have additionally performed a measurement of electroweak Wjj production [20] in both the muon and electron decay mode where slightly different kinematic requirements are performed compared to the Zjj measurement. Muons (electrons) are required to have p_{T} greater than 25 (30) GeV and $|\eta| < 2.1(2.5)$. Two jets are also required with a pseudorapidity of less than 4.7 where the leading jet has a p_{T} of greater than 60 GeV and the sub-leading jet has a p_{T} of greater than 50 GeV. The transverse missing energy is required to be greater than 25(30) GeV for the muon(electron) channel. The cross-section is extracted from a fit to the M_{jj} spectrum, shown in Figure 13 along with the $\Delta\eta_{jj}$ distribution observed in data and compared to expectations. A good agreement is observed with the SM predictions.

Forward-Backward Asymmetry and extraction of $\sin^2\theta_W$ in $Z \to \ell\ell$ events

The annihilation process $q\bar{q} \to \ell^+\ell^-$ exhibits a forward-backward asymmetry, A_{FB}, due to the presence of both vector and axial-vector amplitudes. The asymmetry is observed when considering the distribution of the polar angle of the positive lepton, measured with respect to the quark direction in the $q\bar{q}$ rest frame. It shows a strong dependence on the dilepton invariant mass near the Z resonance. As the LHC is a symmetric pp collider, the quark direction is not known and the forward direction is alternatively defined with respect to the z component of the Z boson momentum. This results in a dilution of the asymmetry in cases where the Z boson does not follow the direction of the initial quark. As the valence quarks are more prominent in the forward region, a consequence of the higher x-region probed, the parton level asymmetry is more pronounced in this region.

The ATLAS, CMS and LHCb experiments have performed measurements of A_{FB} as a function of dilepton invariant mass using Run-I data. ATLAS has performed the measurement at 7 TeV [21] while CMS has performed the measurement at both 7 and 8 TeV [22, 23] where the 7 TeV result does not include forward electrons and consequently is not discussed here. The measurements have been performed in both the dimuon and dielectron channels where the

TABLE 1. A summary of the different leptonic decay modes and kinematic ranges used by the LHCb, CMS and ATLAS collaborations to study the forward-backward asymmetry. ATLAS and CMS both explore "central-forward" regions, where one of the leptons is required to be central and the other to be in the forward region.

Exp.	Channel	$M_{\ell\ell}$	p_{T}^{ℓ}	η^{ℓ}
LHCb	dimuon	60 – 160 GeV	> 20 GeV	$2 < \eta < 4.5$
CMS	dimuon	40 – 2000 GeV	> 20 GeV	$\lvert\eta\rvert < 2.4$
CMS	dielectron	40 – 2000 GeV	> 20 GeV	$\lvert\eta\rvert < 2.4$
CMS	central-forward electron	40 – 300 GeV	> 30, 20 GeV	$\lvert\eta\rvert < 2.4$, $3.0 < \eta < 5$
ATLAS	dimuon	40 – 2000 GeV	> 25 GeV	$\lvert\eta\rvert < 2.4$
ATLAS	dielectron	40 – 1000 GeV	> 25 GeV	$\lvert\eta\rvert < 2.47$
ATLAS	central-forward electron	40 – 250 GeV	> 25 GeV	$\lvert\eta\rvert < 2.47$, $2.5 < \eta < 4.9$

final state leptons are required to be in the central region. Additionally, in order to access the more sensitive forward region, the dielectron channel is extended by requiring that one of the electrons be reconstructed in the central region, and the second be reconstructed in the forward calorimeters. LHCb has performed the measurement in the dimuon channel at 7 and 8 TeV [24], where both muons are reconstructed in the forward region. A summary of the different channels and kinematic regions explored by the three experiments is shown in Table 1.

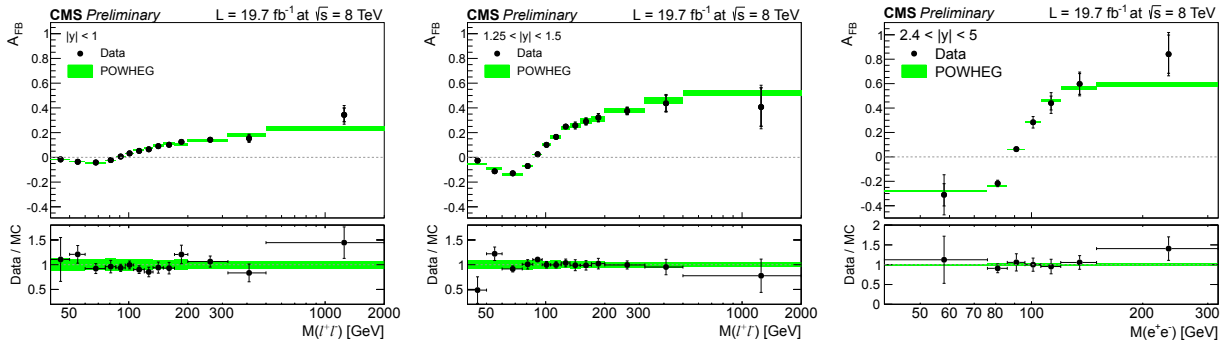

FIGURE 14. The forward backward asymmetry as measured by the CMS collaboration in three different rapidity bins. The muon and electron channels are combined in the central region, while the measurement in the forward region is only performed in the electron channel [23].

The distributions obtained from data are corrected for background contributions, as well as unfolded for detector effects to obtain the true asymmetry distributions. In the case of the ATLAS measurement, the distribution is additionally corrected for the effects of dilution using Pythia [25] simulation. The ATLAS and LHCb result is performed as a function of dilepton invariant mass, while CMS performs the measurement double-differentially as a function of invariant mass and rapidity. The forward-backward asymmetry as measured by CMS is shown for three different rapidity bins in Figure 14 where the increasing asymmetry is evident moving from the central to the forward region. The results for LHCb and ATLAS are shown in Figure 15, where the central-forward region is shown for ATLAS.

Extraction of $\sin^2\theta_W^{\mathrm{eff}}$

As A_{FB} is sensitive to the effective weak mixing angle, $\sin^2\theta_W^{\mathrm{eff}}$, both ATLAS and LHCb have extended the measurement to extract the value of $\sin^2\theta_W^{\mathrm{eff}}$ through a template fit to the measured asymmetry. Predictions are obtained using a range of values of $\sin^2\theta_W^{\mathrm{eff}}$ and a χ^2 minimisation is performed in order to determine the best fit value. The templates are generated using Powheg [26] for LHCb and Pythia for ATLAS. A comparison of the results, in addition to other measurements is shown in Figure 16. The dominant source of systematic uncertainty for both measurements is due to the description of the PDFs, which is lower for LHCb due to the higher values of boson rapidity probed than the central or forward-central measurements performed at ATLAS. The PDFs also represent the largest uncertainty on the ATLAS measurement, while the LHCb measurement is limited by the available statistics.

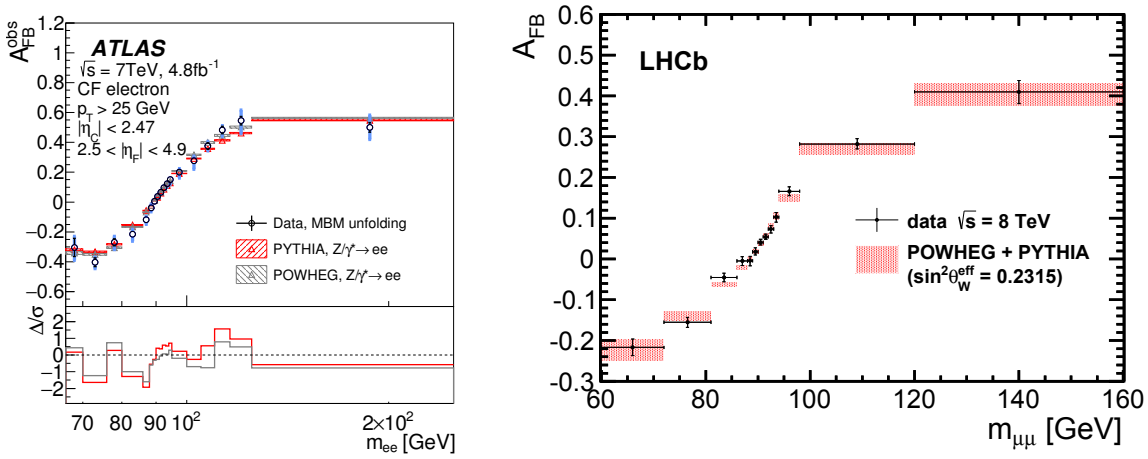

FIGURE 15. The forward backward asymmetry measured by (left) ATLAS in the central-forward region [21] and (right) LHCb [24]. The ATLAS measurement is shown before correction for dilution and is compared to predictions generated using both PYTHIA and POWHEG while the LHCb measurement is compared to POWHEG.

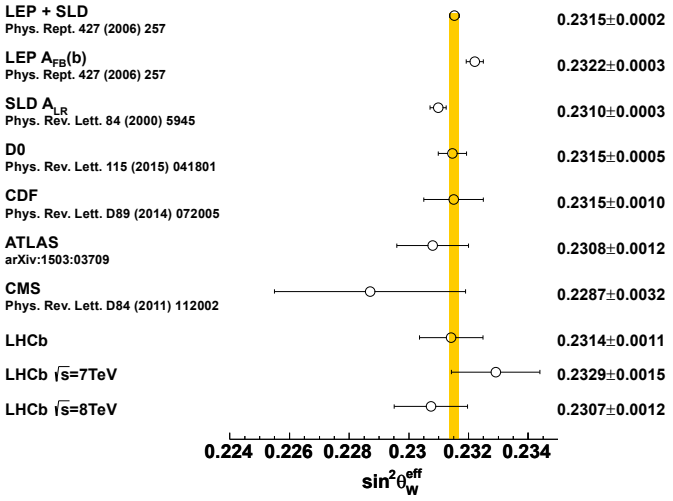

FIGURE 16. Comparison of measurements of $\sin^2\theta_W$ as performed by ATLAS, LHCb and a number of different experiments [21].

Conclusion

Measurements have been presented of electroweak production in the forward region, where the final state involves forward leptons and/or jets in the final state. The LHCb detector, situated in the forward region, has performed measurements of both inclusive and associated W and Z boson production. The ATLAS and CMS collaboration have both performed measurements including forward jets for the the study of the electroweak production of electroweak bosons, while ATLAS has additionally performed measurements of W and Z production in association with forward jets. All three experiments have performed measurements of the forward-backward asymmetry in $Z \to \mu\mu$ events, where LHCb selects dilepton pairs in the forward region, and ATLAS and CMS exploit both the central, and "central-forward" regions, where calorimeters are used to select dielectron events with one electron in the forward region.

REFERENCES

[1] ATLAS collaboration, JINST **3**, p. S08003 (2008).
[2] CMS collaboration, JINST **3**, p. S08004 (2008).
[3] LHCb collaboration, JINST **3**, p. S08005 (2008).
[4] LHCb collaboration, JHEP **12**, p. 079 (2014), arXiv:1408.4354 [hep-ex] .
[5] LHCb collaboration, JHEP **08**, p. 039 (2015), arXiv:1505.07024 [hep-ex] .
[6] LHCb collaboration, JHEP **02**, p. 106 (2013), arXiv:1212.4620 [hep-ex] .
[7] LHCb collaboration, JHEP **05**, p. 109 (2015), arXiv:1503.00963 [hep-ex] .
[8] R. Gavin, Y. Li, F. Petriello, and S. Quackenbush, Comput. Phys. Commun. **182**, 2388–2403 (2011), arXiv:1011.3540 [hep-ph] .
[9] ATLAS collaboration, Phys. Rev. **D85**, p. 072004 (2012), arXiv:1109.5141 [hep-ex] .
[10] CMS collaboration, JHEP **10**, p. 132 (2011), arXiv:1107.4789 [hep-ex] .
[11] LHCb collaboration, (2015), arXiv:1511.08039 [hep-ex] .
[12] ATLAS collaboration, Eur. Phys. J. **C75**, p. 82 (2015), arXiv:1409.8639 [hep-ex] .
[13] ATLAS collaboration, JHEP **07**, p. 032 (2013), arXiv:1304.7098 [hep-ex] .
[14] LHCb collaboration, JINST **10**, p. P06013 (2015), arXiv:1504.07670 [hep-ex] .
[15] LHCb collaboration, (2015), arXiv:1505.04051 [hep-ex] .
[16] J. M. Campbell and R. K. Ellis, Phys. Rev. **D62**, p. 114012 (2000), arXiv:hep-ph/0006304 [hep-ph] .
[17] CMS collaboration, JHEP **10**, p. 062 (2013), arXiv:1305.7389 [hep-ex] .
[18] CMS collaboration, Eur. Phys. J. **C75**, p. 66 (2015), arXiv:1410.3153 [hep-ex] .
[19] ATLAS collaboration, JHEP **04**, p. 031 (2014), arXiv:1401.7610 [hep-ex] .
[20] CMS collaboration, "Measurement of the cross section of the electroweak production of a W boson with two jets in pp collisions at sqrt(s) = 8TeV," Tech. Rep. CMS-PAS-SMP-13-012 (CERN, Geneva, 2015).
[21] ATLAS collaboration, JHEP **09**, p. 049 (2015), arXiv:1503.03709 [hep-ex] .
[22] CMS collaboration, Phys. Lett. **B718**, 752–772 (2013), arXiv:1207.3973 [hep-ex] .
[23] CMS collaboration, "Forward-backward asymmetry of Drell-Yan lepton pairs in pp collisions at 8 TeV," Tech. Rep. CMS-PAS-SMP-14-004 (CERN, Geneva, 2015).
[24] LHCb collaboration, JHEP **11**, p. 190 (2015), arXiv:1509.07645 [hep-ex] .
[25] T. Sjostrand, S. Mrenna, and P. Z. Skands, JHEP **05**, p. 026 (2006), arXiv:hep-ph/0603175 [hep-ph] .
[26] S. Alioli, P. Nason, C. Oleari, and E. Re, JHEP **07**, p. 060 (2008), arXiv:0805.4802 [hep-ph] .

Proceedings of the LHCP2015 Conference, St. Petersburg, Russia, August 31 - September 5, 2015

Editors: V.T. Kim and D.E. Sosnov

Probing PDFs and soft QCD at the LHC

GRIGORY SAFRONOV

Institute for Theoretical and Experimental Physics, 117218, Moscow, B. Cheryomushkinskaya 25

On behalf of the ATLAS and CMS Collaborations

Abstract. LHC has delivered 30 fb^{-1} of proton-proton collisions at the center-of-mass energies of 7 and 8 TeV in 2010-2012 during the LHC Run I. Run II has started in 2015 and approximately 200 pb^{-1} of proton-proton collisions at $\sqrt{s}$ = 13 TeV have been delivered by September. An important part of physics program in the ATLAS and CMS experiments are precision studies of the quantum chromodynamics. Parton density functions are an essential part of calculation of any process at a hadron collider. Detailed studies of soft proton-proton interactions and production of soft particles allows to improve phenomenology of processes in non-perturbative QCD domain. A selection of measurements probing PDFs and soft QCD based on the Run I data as well as early results from the Run II are presented in this review.

INTRODUCTION

The appropriate theory to describe interactions of hadrons is the Quantum Chromodynamics (QCD). A fundamental property of QCD is the strong dependence of the coupling constant, α_s, on the energy scale of the interaction, Q. Processes involving large Q: $Q \gg \Lambda_{QCD} \sim 200$ MeV can be described by means of the calculations based on the perturbation theory in QCD (pQCD) because the coupling constant is small, such processes are usually referred to as hard processes. Softer processes cannot be calculated perturbatively and are described by various QCD-based models with parameters fitted to the data. Monte Carlo generators widely used to simulate final states at LHC exploit such models for a simulation of a soft processes occurring in the hadron scattering such as hadronisation or multiple parton interactions.

Parton density functions (PDFs) is an essential component for calculation of any process at a hadron collider. Due to the soft nature of processes governing the state of partons inside the nucleon it cannot be calculated in the pQCD framework. It is the QCD factorization theorem which allows to factorize the total process cross-section into the hard matrix element involving interacting partons and to the probabilities to find such partons inside the proton or parton density functions which are extracted from an experiment. PDFs are parametrised as a function of the fraction of total proton momentum carried by the parton, x, and the momentum transfer in the interaction, Q. Parametrisations of PDFs are fitted to various observables using theory predictions involving leading order (LO), next-to-leading order (NLO) or next-next-to-leading order (NNLO) matrix elements.

LHC has delivered a total of approximately 30 fb^{-1} of proton-proton collisions at $\sqrt{s}$ =7 and 8 TeV during the Run I. Also data at $\sqrt{s}$ = 900 GeV and 2.76 TeV is available. The LHC Run II started in 2015 and approximately 200 pb^{-1} of proton-proton collisions at $\sqrt{s}$ = 13 TeV have been delivered by September. In this report the selection of ATLAS and CMS measurements based on the above data and sensitive to soft QCD processes and PDFs is presented.

ATLAS AND CMS DETECTORS

ATLAS and CMS are large multi-purpose detectors at the LHC collider. Tracking system of ATLAS (A Toroidal LHC ApparatuS) [1] consists of the silicon pixel, silicon micro-strip and transition radiation detectors. These detectors are surrounded by the super-conducting solenoid which provides magnetic field of 2 T. For the Run II, a new innermost layer of the silicon pixel tracker, called insertable B-layer (IBL) [2, 3], has been inserted at a radial distance of 3.3 cm from the beam line. ATLAS has Lead/Liquid Argon (*LAr*) sampling electromagnetic calorimeter which covers

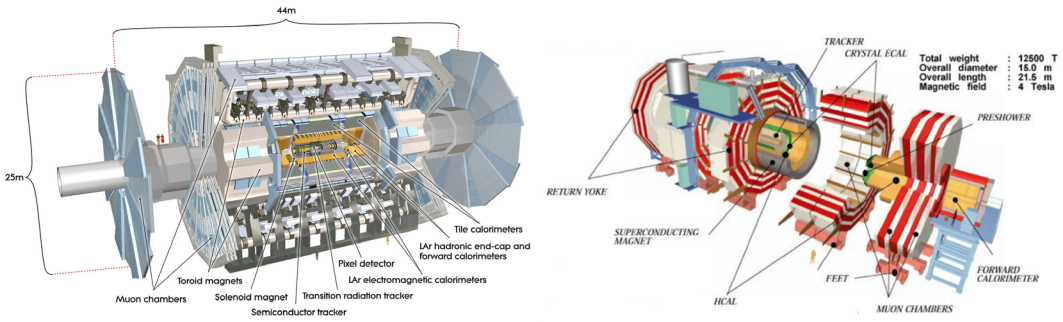

FIGURE 1. ATLAS (left) and CMS (right) detectors

pseudorapidity (η) range $|\eta| < 3.2$. The hadron calorimeter consists of iron/scintillator barrel region ($|\eta| < 1.475$). The endcap ($|\eta| < 3.2$) and forward ($|\eta| < 4.9$) regions are covered by *LAr* calorimeters. The ATLAS muon system is based on three large toroidal magnets with 8 coils each providing magnetic field of 2.0-7.5 T. Inside the magnets system of precision tracking chambers is located.

CMS (Compact Muon Solenoid) [4] detector is based on the super-conducting magnet providing magnetic field of 4 T. Inside the magnet the tracking system, electromagnetic and hadronic calorimeters are located. CMS tracking system consists of the pixel vertex detector and the silicon strip tracker. The electromagnetic calorimeter is made of $PbWO_4$ crystals and covers pseudorapidity range $|\eta| < 3.0$. The barrel and endcap hadronic calorimeters are sampling brass/scintillator and also cover the pseudorapidity range $|\eta| < 3.0$. The forward calorimeter covering range $|\eta| < 5.0$ is steel absorber/quartz fiber, Cerenkov light emitted in quartz fibers aligned along the beam axis is collected with photomultipliers. The magnet is surrounded by the iron return yoke with the muon drift chambers embedded into it.

SOFT QCD

Measurements of soft processes at LHC are special in a sense that they require special datasets. Data for mainstream measurements like the Higgs boson production, rare standard model processes and searches beyond the standard model is delivered with large number of pp interactions (tens) occurring in the same bunch-crossing referred to as pileup. Soft processes are extremely hard to study in the high-pileup environment because it is often not possible to distinguish objects produced in the same pp interaction. At the same time many soft measurements are not luminosity-demanding. Thus soft QCD probes are made using special low-pileup data delivered during a limited number of special low-pileup LHC fills or on other occasions.

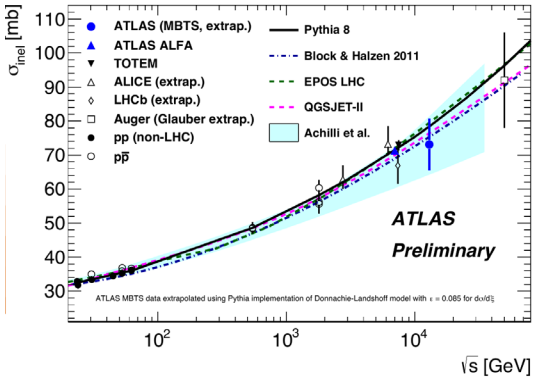

FIGURE 2. Inelastic cross-section measurement at 13 TeV by ATLAS collaboration [10]. Results from previous measurements are also shown. Data points are compared to predictions from PYTHIA8 and cosmic ray MC generators EPOS and QGSJET-II.

Cross-section of pp interactions

The milestone measurement for each energy of the LHC collisions is the pp interaction cross-section. Total cross-section cannot be calculated from the first principles but follows a number of fundamental relations one of them is the optical theorem which states that imaginary part of the forward elastic scattering amplitude is proportional to the total pp cross-section. ATLAS ALFA detector and TOTEM experiment installed in CMS cavern have precision coordinate detectors which can be moved very close to the beam ($\sim 10\sigma$ beam transverse size) and thus measure the cross-section for elastic scattering of protons differentially by Mandelstam $|t|$ variable and later extrapolate to $|t| = 0$ to make use of the optical theorem and determine the total cross-section. Measurements for 7 and 8 TeV collision energies are available from these devices based on the Run I data e.g. [5, 6, 7]. Limited in acceptance inelastic cross-section measurements are also available both from the ATLAS and CMS Collaborations from the Run I data [8, 9]. Most recent inelastic cross-section measurement was performed by the ATLAS Collaboration for 13 TeV pp collisions [10]. Inelastic scattering incorporates dissociation of at least one of the scattered protons by means of color exchange or exchange by colorless object called Pomeron, latter class of events is referred to as diffraction. Limited geometrical acceptance allows to measure cross-section in the fiducial region which is usually defined in terms of variable $\xi = M_X^2/s$, where M_X is higher mass of two observed dissociation systems. For the ATLAS measurement events were selected with the system of Minimum Bias Trigger Scintillators (MBTS) covering range of $2.07 < |\eta| < 3.86$ which provide an access to $\xi > 10^{-6}$. The fiducial cross-section was extrapolated then to the full acceptance region using different Monte-Carlo models which give a spread of ±4.7% in the final cross-section value. Final result (Fig. 2) demonstrates agreement with previous measurements although it struggles from large uncertainty of preliminary integrated luminosity measurement.

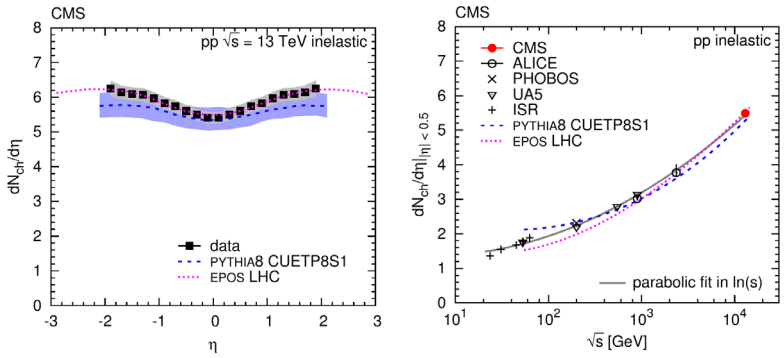

FIGURE 3. CMS results [14]. Angular distribution of charged particle density (left) in pp collisions at 13 TeV. Collision energy dependence of charged particle density in the central region (right). Measurement was performed with the 0 T magnetic field. Presented result is based on counting of straight tracks. Results were cross-checked with the method based on counting triplets of hits. Events were recorded with the Zero Bias trigger. Results are compared to the PYTHIA 8 and cosmic ray MC EPOS predictions. EPOS predictions demonstrate good agreement with the data.

Soft particle production

Angular or transverse momentum distributions of soft charged particles produced in proton-proton collisions are non-demanding measurements in terms of the number of events needed and thus can be performed at a very early stage of data-taking. Soft particle production observables allow to test models for hadronisation or multiple-parton interactions (MPI) as implemented in various Monte Carlo generators. They provide valuable input to new tunes of model parameters (along with other observables). Both ATLAS and CMS experiments have performed measurements of soft particle production in the beginning of Run I [11, 12]. Also remarkable combined measurement of soft particle production by CMS and TOTEM experiments at $\sqrt{s} = 8$ TeV is available [13] where charged particle density in pseudorapidity bins ($dN_{ch}/d\eta$) is measured up to $|\eta| = 7.0$. Recently CMS has published the paper with $dN_{ch}/d\eta$ measurement at 13 TeV (Fig. 3) [14] which is based on the data taken in special run in May 2015 with the pileup of 0.05. The preliminary results from ATLAS [15] are somewhat more extended: $dN_{ch}/d\eta$, multiplicity and transverse momentum (p_T) spectrum measurements are available, some of them are presented at Fig. 4.

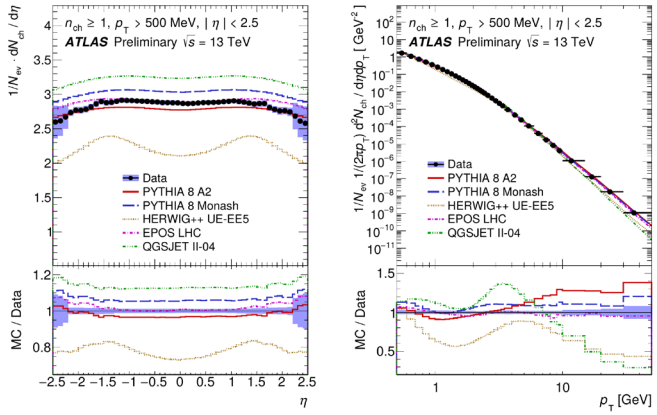

FIGURE 4. ATLAS measurement of soft particle production [15]. Charged particle density as a function of η (left) and as a function of p_T (right). Measurement was performed with 170 μb^{-1} of 13 TeV pp collisions taken in the beginning of the Run II of the LHC. Events were selected with MBTS system. Tracks with $p_T > 500$ GeV are selected for the measurement.

An interesting feature of the presented results is that EPOS MC generator [16] used for cosmic ray physics demonstrates the best agreement with the data in the wide range of pseudorapidity and p_T while well-known PYTHIA8 and HERWIG++ show some disagreements. EPOS is based on the parton-based Gribov-Regge theory and describes pp interaction in analogue to the heavy ion interaction with subsequent stages from quark-gluon plasma to freeze-out. The key observable for fit to data is the total cross-section and the inelastic cross-section. Although fits to other soft observables are also used [16].

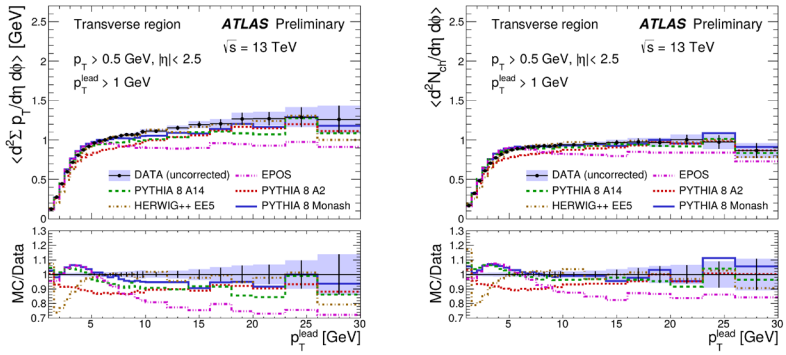

FIGURE 5. ATLAS underlying event measurement [21]. The density of scalar p_T sum (left) and the multiplicity density (right) in the transverse region as a function of the leading track transverse momentum, p_T^{lead}. Sample of 170 μb^{-1} was used for the measurement. The data points are not corrected for the detector effects. The data is compared to MC predictions passed through the full ATLAS detector simulation.

The key measurement for understanding soft activity in the presence of a hard probe and thus for tuning of the Monte-Carlo generators which incorporate hard physics like PYTHIA8 or HERWIG++ is the underlying event (UE) measurement. The underlying event activity consists of particles emerging from hadronisation of soft initial- and final- state radiation, products of MPI and beam remnants. Understanding of UE is important for many new physics searches and precision studies of the standard model. In particular UE contaminates isolation variables and creates an offset to the jet energy measurement. An event topology in transverse to the beam plane is divided to "toward" and "away" regions defined by the leading jet (or particle) direction and "transverse" region in which the underlying event properties are measured. Normally the number of particles and average p_T per unit of solid angle are measured as a function of the transverse momentum of the leading jet (or particle), p_T^{lead}. The underlying event was first defined and measured by the CDF collaboration in $p\bar{p}$ collisions at $\sqrt{s} = 1.8$ TeV [17] and since then has been widely used for

tuning of general-purpose MC generators. ATLAS and CMS provided UE measurements based on the 0.9, 2.76 and 7 TeV data [18, 19, 20] which were used for Run I -based MC tunes. Recently the measurement from ATLAS based on 13 TeV data [21] has become available. Results of the measurement are presented at Fig. 5, they are not corrected for the detector effect and thus compared to the Monte Carlo predictions passed through the full detector simulation. The PYTHIA 8 tunes A2, A14 and Monash were used for comparison. The former two tunes were developed by the ATLAS collaboration and are aimed at the description of a soft particle production observables (A2) or an underlying event- and parton shower- sensitive observables (A14). Monash tune was developed by the PYTHIA 8 authors and is optimized for the description of energy dependence of soft particle production and underlying event data. HERWIG++ tune UEE5 is optimized for the good description of the underlying event at 7 TeV. Data points are well-described by the PYTHIA 8 and HERWIG++ tunes except for the region of the plateau onset: $1 < p_T^{lead} < 5$ GeV. The EPOS MC fails as the hardness of the probe object increases.

Two-particle correlations

A study of particle correlations provide further insight into the nature of soft QCD processes in particular about collective effects during the collision of protons. Angular two-particle correlations studied as 2-dimensional correlation function in $\Delta\eta - \Delta\phi$ coordinates are discussed in this paragraph. The strong particle correlation referred to as "long-range far-side" correlation is demonstrated for $\Delta\phi \sim \pi$ due to the momentum conservation law. It was the remarkable result of the LHC Run I when CMS has observed the correlation of particles produced with similar ϕ (or $\Delta\phi \sim 0$) along the η coordinate in proton-proton collisions with large particle multiplicity [22]. Such correlation referred to as "long-range near-side" has been observed earlier in heavy ion collisions e.g. by PHOBOS collaboration [23]. The observation has received wide attention from theory community and a broad range of models was suggested to explain the correlation [24]. Preliminary ATLAS Collaboration results on the two-particle correlations in pp collisions at 13 TeV are available in [25] and by the time of the writing the updated results have become available in [26], Fig. 6. The measurement was performed with 14 nb^{-1} of the low-pileup pp collisions. Dedicated trigger which required at least 60 tracks with $p_T > 0.4$ GeV was used to select the events. The two-particle correlation was measured in bins of the charged particle multiplicity, N_{ch}^{rec}. Which is defined as the number of tracks with $p_T > 0.4$ GeV originating from the vertex with the largest Σp_T^2 in the event. The correlation function is defined as $C(\Delta\phi, \Delta\eta) = S(\Delta\phi, \Delta\eta)/B(\Delta\phi, \Delta\eta)$ where S and B correspond to charged particle pairs taken from the same event and from mixed events respectively. In addition the yield of particles per selected particle, Y, was measured. The yield quantifies strength of the correlation and represents the number of particles associated with each trigger particle in a given $\Delta\phi/\Delta\eta$ interval. An excess of the yield over uncorrelated background integrated over the "ridge" area, Y_{int} (Fig. 6), is consistent with zero for $N_{ch}^{rec} < 40$ and increases rapidly with N_{ch}^{rec} for $N_{ch}^{rec} > 40$. ATLAS measurement of Y_{int} is consistent with the CMS 7 TeV result. This suggests a statement that the strength of the correlation in the "ridge" does not depend on the collision energy.

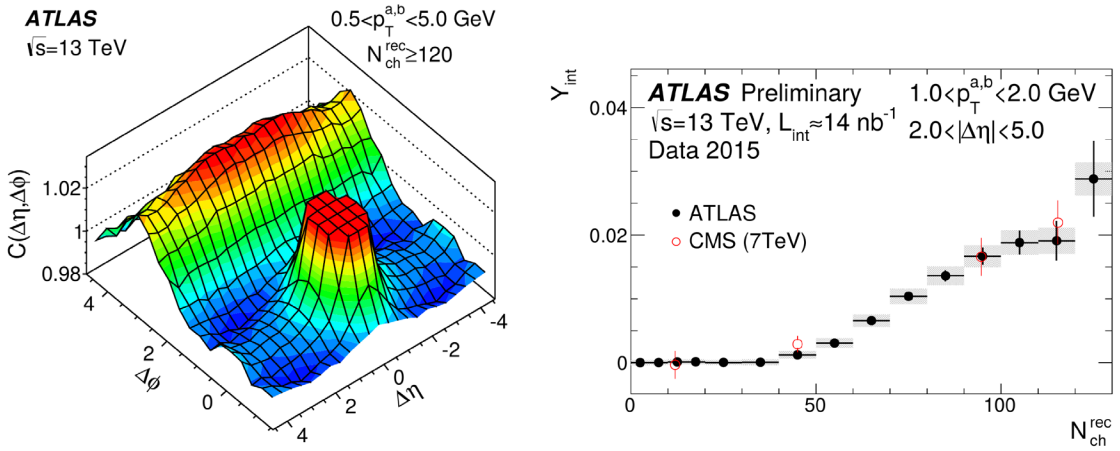

FIGURE 6. Measurement of the two-particle correlations from ATLAS. The two-dimensional correlation function, $C(\Delta\phi, \Delta\eta)$ from [26] (left). The integrated yield of particles within the ridge per selected particle with subtracted uncorrelated background from [25] (right) . An agreement with the 7 TeV CMS data is demonstrated.

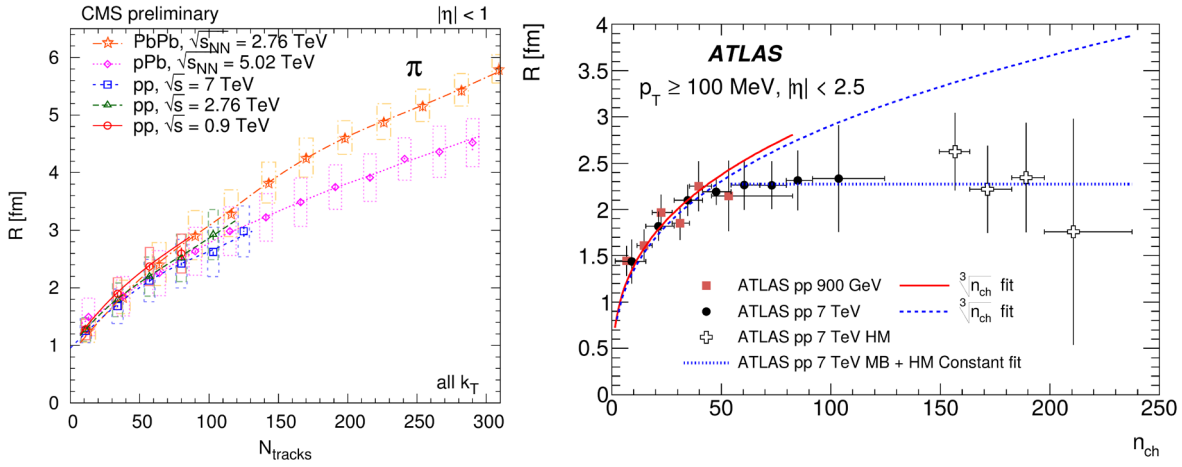

FIGURE 7. Measurements of the Bose-Einstein correlations. The CMS results from [30] (left) show that interaction region size, R, as a function of the multiplicity of charged tracks (N_{tracks}) is the same for heavy ion and pp collisions and for different energies. In the ATLAS results from [29] (right) the saturation of R is observed for pp collisions and the charged particle multiplicity, n_{ch}, greater than 55.

Due to the fact that wave function of 2-boson system is symmetric under the interchange of particles the probability to observe two identical bosons is increased. This statement makes basis for the long-standing "Bose-Einstein correlation " (BEC) method for the determination of size of a boson-emitting source used in the astrophysics and particle physics. CMS has measured BEC in 900 GeV, 2.76 and 7 TeV data [27, 28]. ATLAS has measurements at 900 GeV and 7 TeV [29]. Bose-Einstein correlations are measured in terms of the correlation function: $C = \rho(p_1, p_2)/\rho_0(p_1, p_2)$, where ρ is the spatial density of particles close in momentum space while ρ_0 is the same density for the so-called reference sample which should include all types of particle correlations except for the BEC. Different methods for constructing the reference sample are being used. CMS in [27] has used particles harvested from different events while ATLAS in [29] used opposite-sign pairs. Both collaborations use the ratio of the correlation function to the analogous function obtained from MC simulation which does not include BEC effects to correct for detector effects and resonance decays. Both collaborations study BEC as a function of charged particle multiplicity. CMS both in [28] and [27] has proved that the interaction region size, R, does not depend on the collision energy. In [30] CMS compared BEC results for the pp, pPb and $PbPb$ collisions [30] and found that the size of interaction region does not depend on whether nucleons or nuclei collide (Fig. 7 left). ATLAS in [29] has extended the measurement for pp collisions to larger multiplicities and observed the saturation of interaction region size for charged particle multiplicity greater than 55 (Fig. 7 right).

PDF PROBES

The parton density functions are of vital importance for theory predictions for any LHC measurement. Pre-LHC PDF sets are mostly constrained by the data from the HERA and Tevatron colliders. For proton-proton collisions at high values of x quark PDF dominates over gluon while at low x gluon PDF dominates. PDF uncertainties are large at very high x which is a constraining factor for new physics searches with heavy-mass states. For medium x PDF uncertainty is smaller but still gives a sizable contribution to precision studies of standard model parameters. PDF in low-x region are dominated by gluons and have large uncertainty while this region could be used for pQCD resummation studies such as applicability of DGLAP and BFKL approaches to PDF evolution description. Many PDF-sensitive measurements are available from the LHC Run I. Many of them have been incorporated into new PDF sets [31]. Recent new PDF sets CT14 [32], NNPDF3.0 [33] and MMHT14 [34] include ATLAS, CMS and LHCb data into global fits. Review of the selection of PDF-sensitive measurements from ATLAS and CMS is given below.

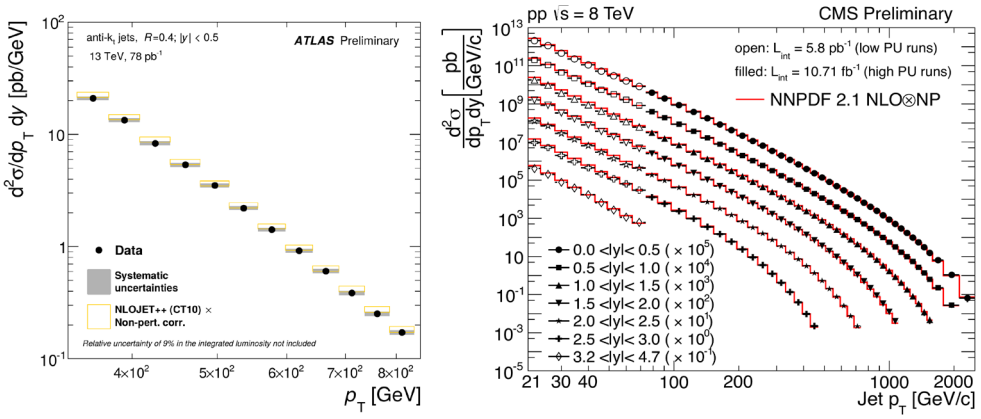

FIGURE 8. Inclusive jet measurements at 13 TeV from ATLAS [39] (left) and at 8 TeV from the CMS [37, 38] (right)

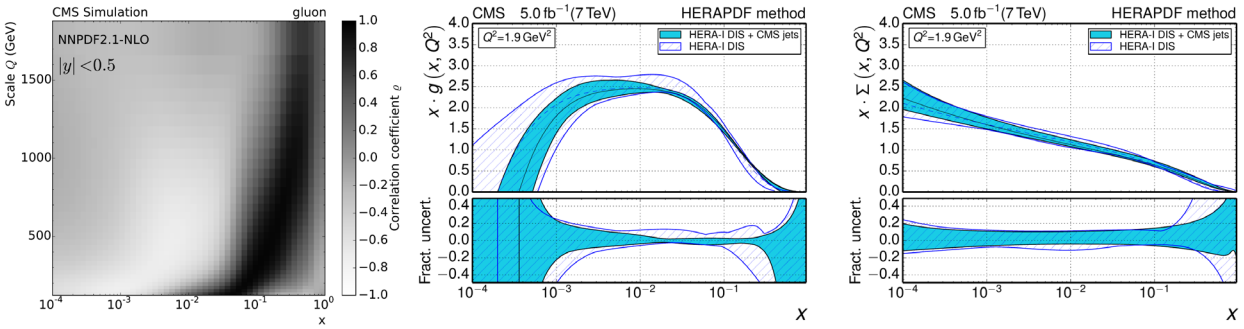

FIGURE 9. Results of PDF fit performed by CMS collaboration with 7 TeV inclusive jet data combined with HERA DIS data [40]. PDFs evolved to Q^2=1.9 GeV are shown. Significant reduction of gluon pdf (left) and quark (pdf) uncertainty is observed

Inclusive jet cross-sections

The inclusive jet cross-section provides an access to a wide range of x. Lower x jet production is dominated by gluons while for the large x jet production is dominated by quark jets. Many Run I data - based jet measurements are available from ATLAS and CMS. Both ATLAS and CMS have measured inclusive jet cross-section up to $p_T \sim 2$ TeV using the full 7 TeV collision energy dataset [35, 36]. Combination of 8 TeV CMS results for low p_T jets measured with low-pileup data [37] and high-p_T jets [38] is available (Fig. 8 right). ATLAS Collaboration has preliminary 13 TeV result [39] (Fig. 8 left). Results are compared to NLO calculation corrected for non-perturbative effects, good agreement of theory predictions with the data is observed.

Both Collaborations have used an inclusive jet data for their own extractions of the PDFs and strong coupling constant [40, 41]. Such studies although not being part of any PDF set give important information on the PDF sensitivity of chosen observables. At Fig. 9 (left) the correlation between the inclusive jet cross-section and the value of gluon PDF is shown, as obtained by CMS in [40]. Gluon PDF is strongly correlated with the cross-section except for the largest x where the jet cross-section is determined by quarks. CMS has performed PDF extraction from combined CMS 7 TeV and HERA DIS data. Results are presented at Fig. 9 (center and right). Gluon PDF uncertainty is reduced in the wide range of x, while for quark PDF uncertainty improvement is demonstrated for large x.

ATLAS has used the inclusive jet cross-section measurement [36] in combination with the jet cross-section measured in 0.2 pb^{-1} of 2.76 TeV collisions for the PDF extraction [41]. Fig. 10 shows the ratio of cross-sections at 7 TeV and at 2.76 TeV, ρ, divided by theory predictions obtained with CT10 PDF set. Systematic uncertainty on the ratio is very small which is the result of partial cancellation of correlated detector-related uncertainties. Thus combined data might bring new constraint on the PDF. At Fig. 11 results of the combined fit for HERA DIS data and the ATLAS jet

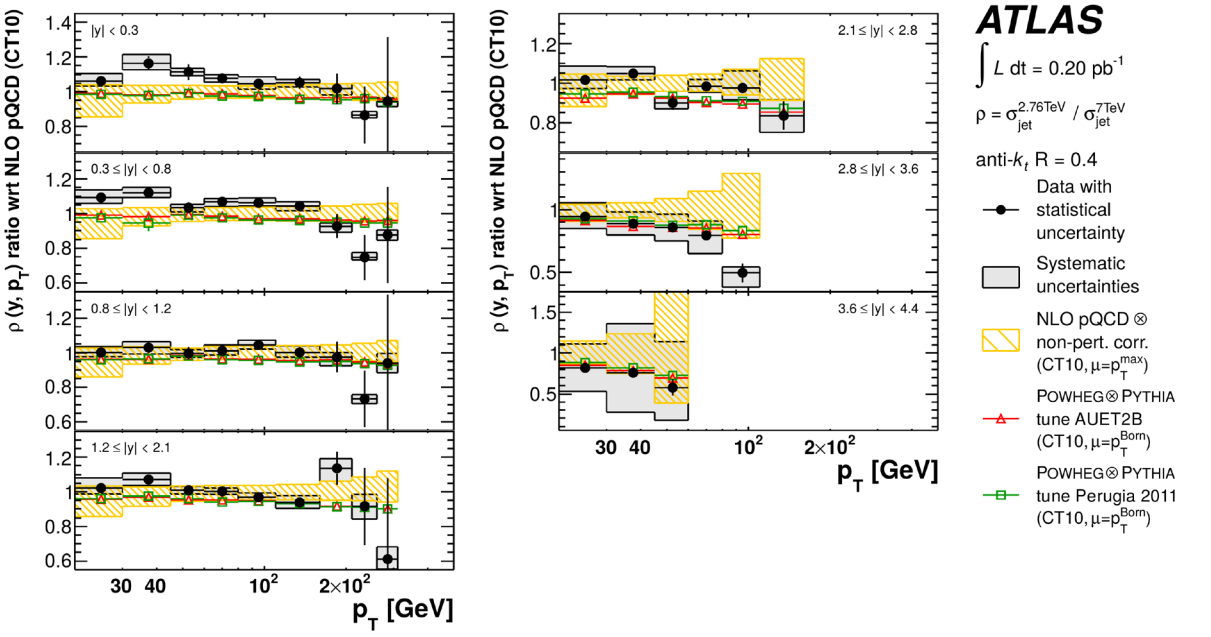

FIGURE 10. ATLAS measurement of the ratio of inclusive jet cross-section at different energies [41]. Ratio of the inclusive jet cross section at $\sqrt{s} = 2.76$ TeV to cross-section at $\sqrt{s} = 7$ TeV divided by the ratio obtained in NLO calculation with CT10 PDF set shown as a function of the jet p_T in bins of the jet rapidity y. The 4.3% uncertainty from the luminosity measurement is not shown.

data for gluon PDF is shown. Combined fit brings shift to central value and improvement in PDF uncertainty.

CMS has measured the inclusive jet cross-section at 2.76 TeV for 2013 dataset of 5 pb^{-1} and obtained the ratio to 8 TeV inclusive cross-section measured using 8 TeV dataset (10.71 fb^{-1}) [38].

Finally both ATLAS [42, 43] and CMS [44] have measured the double jet and tri-jet cross-sections which also can be used for the extraction of PDFs.

W, Z production

The W and Z boson production cross-sections and rapidity distributions are used for the PDF constraints since Tevatron. The ATLAS and CMS have measured W, Z cross-sections with the 13 TeV data [45, 46]. ATLAS measurements in [45] were done with 85 pb^{-1}. The total W and Z cross sections in electron and muon channels were measured as well as the ratios of cross-sections W^+/W^- and $W^\pm/Z$. The W^+/W^- ratio probes difference between valence u and d quark distributions while $W^\pm/Z$ ratio is sensitive to the strange quark content. The ratios benefit from experimental uncertainty cancellation. In general NNLO theoretical predictions with various PDF sets showed an agreement with the data except for the case of CT10 NNLO PDF set which showed moderate discrepancy for W^+/W^- ratio.

An interesting channel which allows to directly probe strange quark content inside the proton is the W + charm quark production. Production of W from u-quark is Cabibbo-suppressed and contributes few % to the total cross-section. Measurement of the $W + c/W + \bar{c}$ cross-section ratio can provide info on $s/\bar{s}$ content asymmetry. CMS has measured the cross-section and the cross-section ratio using 5 fb^{-1} of 7 TeV data [47] both integrated and differential in pseudorapidity of the lepton from W decay. Differential measurement provides an access to PDF for different values of x. W's were reconstructed in e or μ decay channel.

Similar results from ATLAS for the 4.7 fb^{-1} of 7 TeV data are available [48]. In the work [49] ATLAS has performed fit of the differential distributions with HERAPDF set with free parameter reflecting s/d quark content ratio. ATLAS data suggests that content of s and d quarks is symmetric for wide range of x (Fig. 12 left). CMS has performed fit of ratio of s quark content to those of u and d quarks in the work [50] using both the W muon charge asymmetry and the W+charm measurements. While the QCD analysis performed by ATLAS collaboration suggests a symmetric composition in the light-quark sea at the low x region, the fit result using the CMS measurements suggests

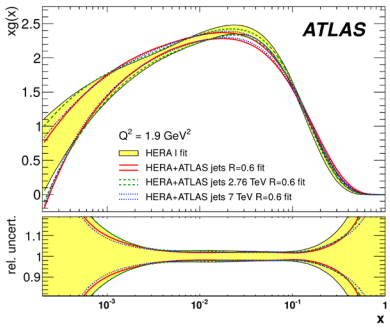

FIGURE 11. Results of combined PDF fit of to ATLAS 2.76 and 7 TeV data and to HERA DIS data [41]

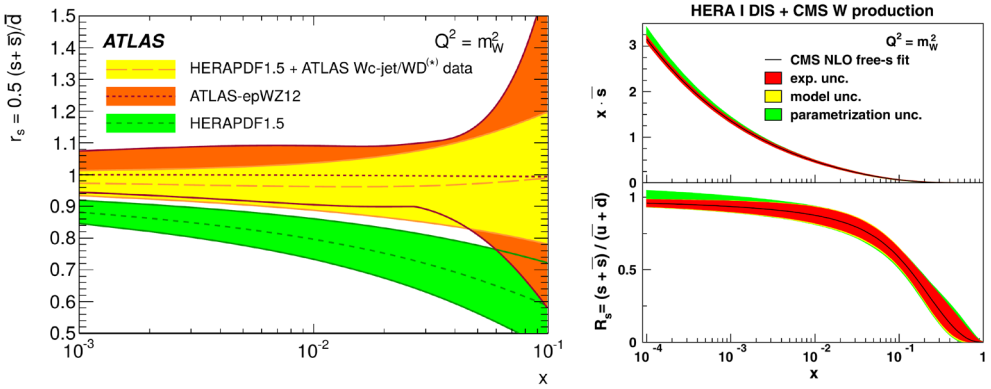

FIGURE 12. Results for the strange quark / light quark PDF extraction. ATLAS fit of $W + c$ data [48] (left), no strange quark suppression with respect to light quarks is observed. CMS fit of muon asymmetry data [50] (right), s-quark PDF is suppressed with respect to light quark PDF for medium and large x.

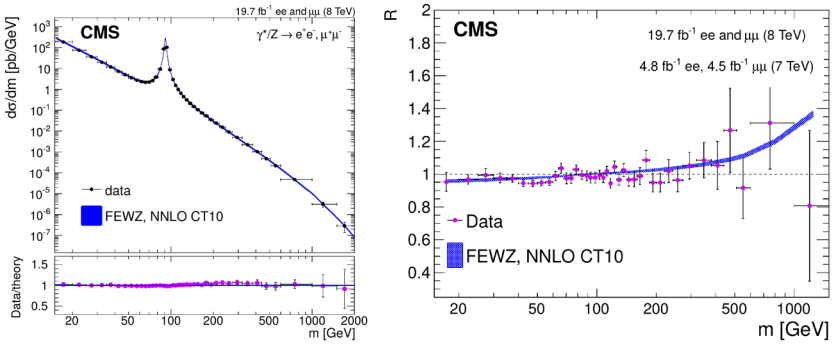

FIGURE 13. CMS results on the Drell-Yan production [54]. Cross-section (left) and the ratio of 7 and 8 TeV normalized cross-sections (right) differential in lepton pair mass.

that the strange sea quark distribution is suppressed in the medium to high x region, consisting with the prediction from global PDFs (Fig. 12 right).

Drell-Yan

Along with the DIS Drell-Yan (DY) process have been used since long time for PDF extraction in dedicated fixed-target experiments. DY process is production of lepton pair in hadronic interactions via s-channel γ^*/Z boson production. Differential distributions in mass or rapidity of the produced lepton pair can be calculated up to NNLO in the perturbation theory. Rapidity and mass of the lepton pair give an access to Q and x of the interaction. Measurements of these distributions allow to probe PDFs in particular for large x. At the same time LHC energy provides an access to large values of Q never probed before. DY production has been investigated in detail both by ATLAS [51, 52] and CMS [53, 54] collaborations. Recent CMS measurement is made on the sample of 8 TeV collisions as large as 20 fb^{-1} [54]. Differential distributions of both electron and muon pairs are obtained for the mass range $m_{ll} > 15$ GeV. Differential distributions and total cross-section in the Z-peak region are compared to pQCD NNLO calculations with CT10 NNLO PDFs set. Total cross-section for the Z-peak are calculated for $60 < m_{ll} < 120$ GeV region and are found to be consistent between electron and muon channels and NNLO calculations. In the same work along with absolute cross-section CMS has measured the ratio of normalized 8 and 7 TeV cross-sections. In paper [52] ATLAS collaboration has measured differential cross-section in bins of DY mass for the very low mass range. In addition to the measurement itself the fit of PDF to measured observables using NLO and NNLO pQCD calculations was performed in the ATLAS work.

CONCLUSIONS

The selection of the soft QCD measurements from the ATLAS and CMS collaborations has been discussed. Results for a many basic measurements are available for the 13 TeV pp collisions. Monte-Carlo generators tuned using Run I data show good performance with respect to the 13 TeV data. New results for two-particle correlations were discussed. The "ridge" observation in pp-collisions made by the CMS at $\sqrt{s} = 7$ TeV was for the first time confirmed by the ATLAS experiment in pp collisions at 13 TeV. An independence of strength of correlation in the ridge region on collisions energy was demonstrated. At the same time earlier CMS measurements of Bose-Einstein correlations for lower $\sqrt{s}$ showed that the size of the interaction region in pp collisions does not depend on collision energy. Recent Bose-Einstein correlation measurement from ATLAS reveals new interesting feature of collective effects in pp collisions - the saturation of interaction region size for the large multiplicities of final state charged particles.

Along with the Higgs-boson discovery Run I of the LHC has delivered many precision results which sharpen methods for theoretical calculations within the framework of the standard model. In particular the LHC data has significant impact on the global PDF fits. A number of new PDF sets which incorporate LHC Run I data have been produced and are being used for Run II analyses. New measurements with pp collisions at 13 TeV sensitive to PDF start to appear.

REFERENCES

[1] ATLAS Collaboration, JINST **3**, S08003 (2008)
[2] M. Capeans, *et al.* (ATLAS IBL Collaboration), CERN-LHCC-2010-013, ATLAS-TDR-19
[3] ATLAS Collaboration CERN-LHCC-2012-009, ATLAS-TDR-19-ADD-1
[4] CMS Collaboration, JINST **3**, S08004 (2008)
[5] G. Antchev, *et al.* (TOTEM Collaboration), Europhys. Lett. **101**, 21002 (2013)
[6] G. Antchev, *et al.* (TOTEM Collaboration), Nucl. Phys. B **899**, 527 (2015), *arXiv:1503.08111 [hep-ex]*
[7] ATLAS Collaboration, Nucl. Phys. B **889**, 486 (2014) *arXiv:1408.5778 [hep-ex]*
[8] ATLAS Collaboration, Nature Commun. **2**, 463 (2011), *arXiv:1104.0326 [hep-ex]*
[9] CMS Collaboration, Phys. Lett. B **722**, 5 (2013), *arXiv:1210.6718 [hep-ex]*
[10] ATLAS collaboration, ATLAS-CONF-2015-038
[11] ATLAS Collaboration, New J. Phys. **13**, 053033 (2011), *arXiv:1012.5104 [hep-ex]*
[12] CMS Collaboration, Phys. Rev. Lett. **105**, 022002 (2010), *arXiv:1005.3299 [hep-ex]*
[13] CMS and TOTEM Collaborations, Eur. Phys. J. C **74**, no. 10, 2053 (2014), *arXiv:1405.0722 [hep-ex]*
[14] CMS Collaboration, Phys. Lett. B **751**, 143 (2015), *arXiv:1507.05915 [hep-ex]*
[15] ATLAS collaboration, ATLAS-CONF-2015-028
[16] T. Pierog, *et al.* Phys. Rev. C **92**, no. 3, 034906 (2015), *arXiv:1306.0121 [hep-ph]*
[17] T. Affolder *et al.* (CDF Collaboration), Phys. Rev. D **65**, 092002 (2002)

[18] ATLAS Collaboration, Phys. Rev. D **83**, 112001 (2011), *arXiv:1012.0791 [hep-ex]*
[19] CMS Collaboration, JHEP **1304**, 072 (2013), *arXiv:1302.2394 [hep-ex]*
[20] CMS Collaboration, JHEP **1109**, 109 (2011), *arXiv:1107.0330 [hep-ex]*
[21] ATLAS Collaboration, ATL-PHYS-PUB-2015-019
[22] CMS Collaboration, JHEP **1009**, 091 (2010)
[23] B. Alver, *et al.* (PHOBOS Collaboration), Phys. Rev. C **81**, 024904 (2010), *arXiv:0812.1172 [nucl-ex]*
[24] W. Li, Mod. Phys. Lett. A **27**, 1230018 (2012), *arXiv:1206.0148 [nucl-ex]*
[25] ATLAS collaboration, ATLAS-CONF-2015-027
[26] ATLAS Collaboration, CERN-PH-EP-2015-251, *arXiv:1509.04776 [hep-ex]*
[27] CMS Collaboration, CMS-PAS-FSQ-13-002
[28] CMS Collaboration, Phys. Rev. Lett. **105**, 032001 (2010), *arXiv:1005.3294 [hep-ex]*
[29] ATLAS Collaboration, Eur. Phys. J. C **75**, no. 10, 466 (2015), *arXiv:1502.07947 [hep-ex]*
[30] CMS Collaboration, CMS-PAS-HIN-14-013
[31] J. Rojo, *et al.*, J. Phys. G **42**, 103103 (2015), *arXiv:1507.00556 [hep-ph]*
[32] S. Dulat, *et al.*, *arXiv:1506.07443 [hep-ph]*
[33] R. D. Ball, *et al.*, JHEP **1504**, 040 (2015), *arXiv:1410.8849 [hep-ph]*
[34] L. A. Harland-Lang, *et al.*, Eur. Phys. J. C **75**, no. 5, 204 (2015), *arXiv:1412.3989 [hep-ph]*
[35] CMS Collaboration, Phys. Rev. D **87**, no. 11, 112002 (2013), *arXiv:1212.6660 [hep-ex]*
[36] ATLAS Collaboration, JHEP **1502**, 153 (2015), *arXiv:1410.8857 [hep-ex]*
[37] CMS Collaboration, CMS-PAS-FSQ-12-031
[38] CMS Collaboration, CMS-PAS-SMP-12-012
[39] ATLAS collaboration, ATLAS-CONF-2015-034
[40] CMS Collaboration, Eur. Phys. J. C **75**, no. 6, 288 (2015), *arXiv:1410.6765 [hep-ex]*
[41] ATLAS Collaboration, Eur. Phys. J. C **73**, no. 8, 2509 (2013), *arXiv:1304.4739 [hep-ex]*
[42] ATLAS Collaboration, Eur. Phys. J. C **75**, no. 5, 228 (2015), *arXiv:1411.1855 [hep-ex]*
[43] ATLAS Collaboration, JHEP **1405**, 059 (2014), *arXiv:1312.3524 [hep-ex]*
[44] CMS Collaboration, Eur. Phys. J. C **75**, no. 5, 186 (2015), *arXiv:1412.1633 [hep-ex]*
[45] ATLAS collaboration, ATLAS-CONF-2015-039
[46] CMS Collaboration, CMS-PAS-SMP-15-004
[47] CMS Collaboration, JHEP **1402**, 013 (2014), *arXiv:1310.1138 [hep-ex]*
[48] ATLAS Collaboration, JHEP **1405**, 068 (2014), *arXiv:1402.6263 [hep-ex]*
[49] ATLAS Collaboration, Phys. Rev. Lett. **109**, 012001 (2012), *arXiv:1203.4051 [hep-ex]*
[50] CMS Collaboration, Phys. Rev. D **90**, no. 3, 032004 (2014), *arXiv:1312.6283 [hep-ex]*
[51] ATLAS Collaboration, Phys. Lett. B **725**, 223 (2013), *arXiv:1305.4192 [hep-ex]*
[52] ATLAS Collaboration, JHEP **1406**, 112 (2014), *arXiv:1404.1212 [hep-ex]*
[53] CMS Collaboration, JHEP **1312**, 030 (2013) *arXiv:1310.7291 [hep-ex]*
[54] CMS Collaboration, Eur. Phys. J. C **75**, no. 4, 147 (2015), *arXiv:1412.1115 [hep-ex]*

Proceedings of the LHCP2015 Conference, St. Petersburg, Russia, August 31 - September 5, 2015

Editors: V.T. Kim and D.E. Sosnov

High p_T QCD at the LHC

MONICA DUNFORD

Kirchhoff Institut für Physik, Heidelberg Universität

monica.dunford@cern.ch

On behalf of the ATLAS and CMS Collaborations

Abstract. At the Large Hadron Collider, measurements of jet production cross sections are important tests of the Standard Model in a new unexplored energy region. In addition, the study of jets is of great relevance to searches for new particles and new interactions as Standard Model processes often represent a significant background. In this work, results on the inclusive, di-jet, multi-jet and vector boson+jet cross sections are presented. The properties of events with jets are discussed, such as multi-jet topologies and kinematic distributions for $b\bar{b}$ production in association with a Z boson. Overall the theoretical distributions are able to model most distributions but tensions exist in several places.

Introduction

The study of jet production cross sections is an important test of quantum chromodynamics (QCD), the theory of the strong interactions. At the Large Hadron Collider (LHC), jet cross sections and jet properties can be measured in a new, unexplored energy region including a larger jet rapidity range, an extended jet transverse momentum (p_T) range and greater di-jet invariant masses. In addition, jets in association with vector bosons are also produced at high rates at LHC allowing for detailed measurements of these processes in a new energy regime. Differential measurements of rare processes, such as Z+bb production, now become possible. Finally, with these large data samples, the strong coupling constant (α_s) can be extracted with high precision.

In recent years, there has also been tremendous progress on the theoretical predictions of QCD interactions. Better modeling of these processes directly impacts both measurements of QCD and also searches for new physics as Standard Model processes are often a significant background. Leading-order generators describe many of the basic kinematic distributions of jet production well. However these generators are plagued with large theoretical uncertainties. To reduce these uncertainties and improve the modeling, a plethora of next-to-leading order calculations, such as BlackHat+SHERPA and Powheg are now available.

Jet Production

Jet production in proton-proton collisions at the LHC allows the exploration of the theory of QCD at the TeV-scale. In this theory, jets can be interpreted as the fragmentation of quarks and gluons produced in the hard scattering process, followed by their hadronization. Production cross sections of jets with high transverse momenta can be perturbatively calculated in QCD. The measurement of such cross sections therefore provides a test of the validity of perturbative QCD (pQCD) as well as tests the interplay between perturbative and non-perturbative effects, such as hadronization. In addition these measurements probe the dynamics of QCD over many orders of magnitude in jet energy.

As a first test of pQCD predictions at a new center-of-mass energy, the ATLAS collaboration measured the cross section for inclusive-jet production using 78 pb^{-1} of data at a 13 TeV center-of-mass energy [1, 2]. The inclusive-jet cross section is measured differentially as a function of the jet p_T in a jet rapidity range of $|y| < 0.5$. The theoretical predictions from next-to-leading order pQCD calculations with corrections for non-perturbative effects are compared to the measured cross section. As seen in Figure 1, the predictions are consistent with the data over the full p_T range.

The ratio of the inclusive-jet cross section at two different center-of-mass energies is a powerful test of pQCD predictions as many of the dominant theoretical and experimental uncertainties cancel in this ratio. In a recent analysis from the CMS collaboration this ratio of cross sections was measured at center-of-mass energies of 2.76 GeV and 8 GeV [3, 4]. The ratio of jets with $|y| < 0.5$ is shown in Figure 1 as a function of the jet p_T. The observed cross section ratio values are in the range 0.1-14% and tend to decrease with the increase in jet p_T. Overall there is good agreement between the data and next-to-leading order predictions.

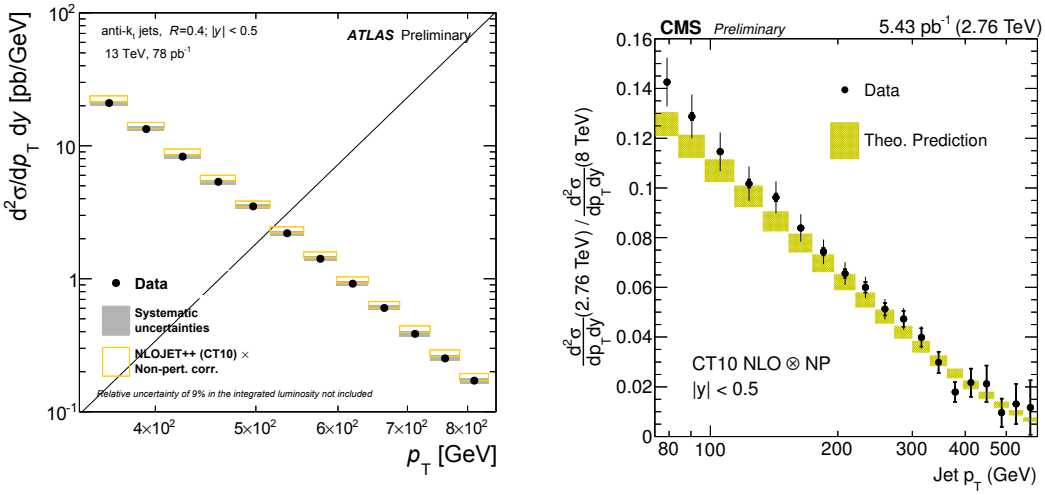

FIGURE 1. Left: Inclusive-jet cross sections as a function of the jet p_T in $|y| < 0.5$, for anti-kt jets with R = 0.4, shown in a range of $346 \geq p_T \geq 838$ GeV [2]. The vertical error bars indicate the statistical uncertainties and the filled area indicates the experimental systematic uncertainties. Next-to-leading order pQCD predictions, shown by the open boxes, are compared to the data. Right: The ratio of inclusive-jet cross sections at $\sqrt{s} = 2.76$ GeV and 8 TeV for the rapidity bin $|y| < 0.5$ [4]. The data are compare to next-to-leading order pQCD predictions. The statistical and total experimental uncertainties are indicated with the inner thick and the outer thin vertical error bars, respectively, while the systematic uncertainties due to theoretical sources are shown as hatched yellow area.

To study multi-jet topologies, measurements of the di-jet azimuthal decorrelations provide insight into production of multiple jets without actually measuring beyond the two jets with the largest p_T. The azimuthal angular separation between the two leading jets is defined as $\Delta\phi_{\text{dijet}} = |\phi_{\text{jet1}} - \phi_{\text{jet2}}|$. When only two jets are present in the event, this separation is π. For 3-jet events, the smallest possible angular separation value is $2\pi/3$. If more than three jets are found, the azimuthal angle between the two leading jets can approach zero, although very small angular separations are suppressed because of the finite size for a particular jet algorithm and jet radius. A recent analysis from the CMS collaboration measured the angular separation for different ranges of the leading jet p_T, using 19.7 fb^{-1} of data at an 8 TeV center-of-mass energy [5]. The results were compared to leading-order and next-to-leading order predictions. There is overall good agreement to the data, however there are some deviations for predictions which use PYTHIA6 for the modeling of the parton showering.

As an additional test of multi-jet topologies, a recent publication from the CMS collaboration studied several topological variables for 3-jet and 4-jet events, using 5.1 fb^{-1} of data at a 7 TeV center-of-mass energy [6]. One such variable for events with 3-jets is the scaled energy, x_3, which is defined as $x_3 = 2E_3/\sqrt{\hat{s}_{345}}$. In this definition E_3 is the energy of the most energetic outgoing jet and $\sqrt{\hat{s}_{345}}$ is the center-of-mass energy of the hard scattering process. Figure 2 shows the comparison of the data to several leading-order predictions. The distribution peaks close to 1 and the peak gets sharper with increasing jet p_T. The x_3 value is expected to follow a linear rise from 2 to 1 for a phase space model that includes only energy-momentum conservation, while QCD predicts a deviation from linearity at higher values of x_3. This feature is observed in the data, particularly for higher p_T bins. Multi-leg leading-order predictions, such as MADGRAPH+PYTHIA6, are needed to model this distribution correctly.

A study of 4-jet events was undertaken by the ATLAS collaboration using 20.3 fb^{-1} of data at an 8 TeV center-of-mass energy [7]. The cross sections as a function of the jet momenta, invariant masses, minimum and maximum opening angles and other kinematic variables are compared between data and next-to-leading order predictions. Fig-

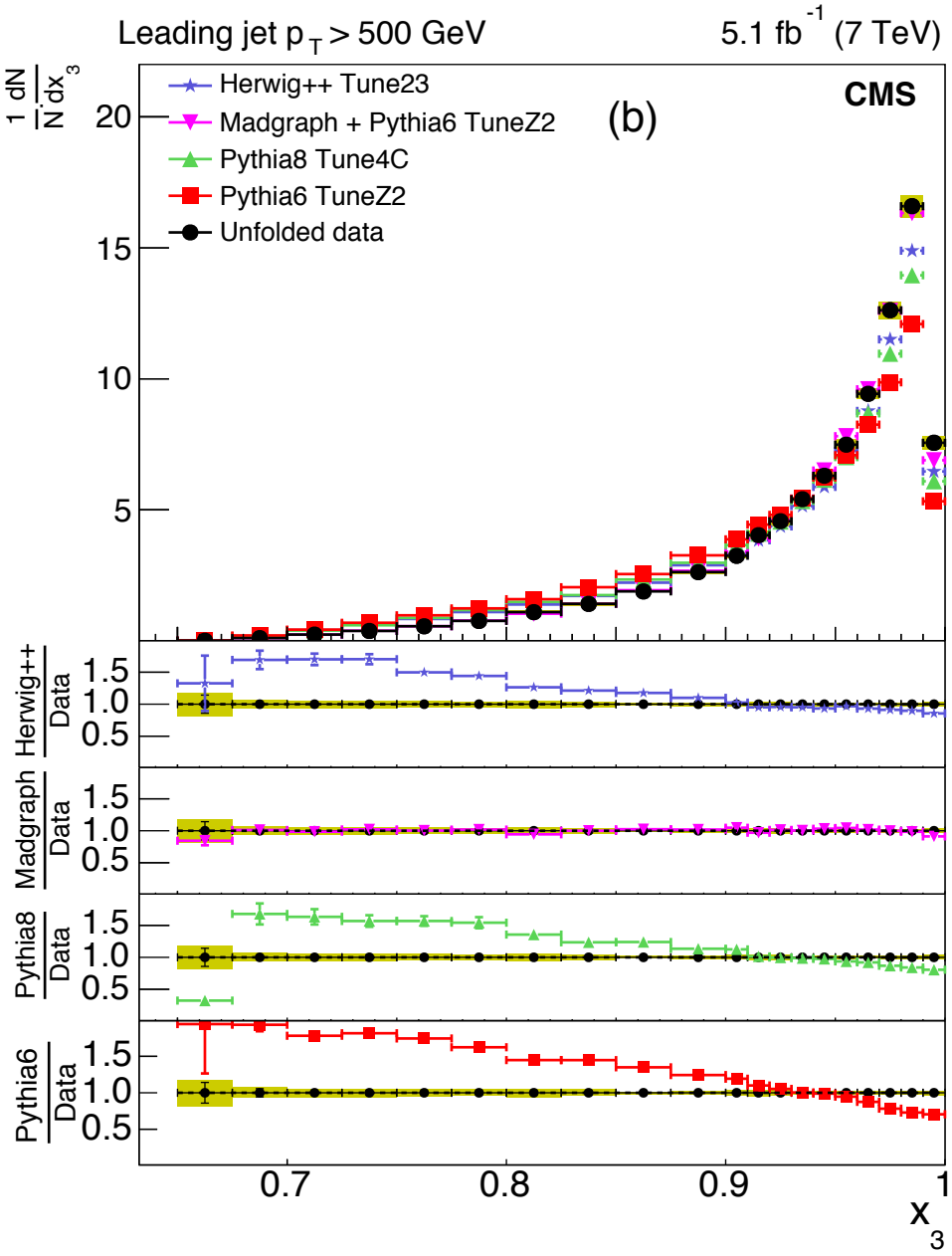

FIGURE 2. Corrected normalized distribution of the scaled energy of the leading-jet in the inclusive three-jet sample [6]. Predictions from leading-order models are also shown. The distributions are obtained from an inclusive three-jet sample with the jets restricted in the region of $0.0 < |y| < 2.5$ and with leading jet p_T between 190 and 300 GeV. The data points are shown with statistical uncertainty only and the bands indicate the statistical and systematic uncertainties combined in quadrature. The lower panels show the ratios of predictions to the data. The ratios are shown with statistical uncertainty in the data as well as in the predictions, while the band shows combined statistical and systematic uncertainties.

ure 3 shows the $\sum p_T^{\text{central}}$ value. For 4-jet events, this variable is defined as the summed p_T of the two jets which fall into the rapidity gap of the two jets with the largest rapidity separation in the event. This variable is of particular interest as it, or a variation of, is often used as a means of rejecting QCD jet events in measurements of vector boson fusion processes. The data are compared to several higher-order predictions in four different jet p_T ranges. Overall all predictions describe the data well, however $2 \rightarrow 2$ leading-order predictions (not shown here) have difficulties modeling this distribution.

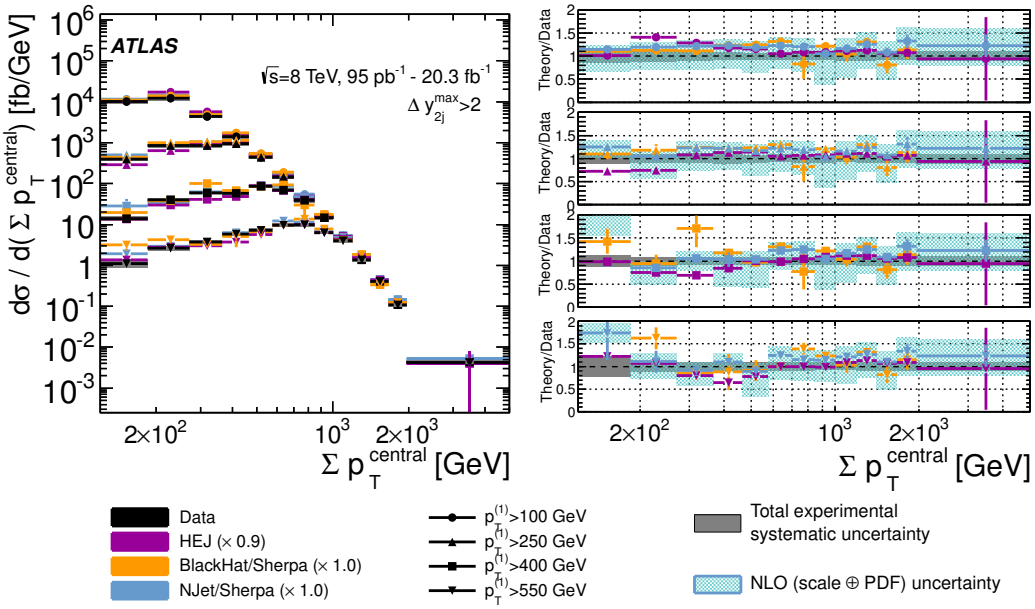

FIGURE 3. Unfolded four-jet differential cross section as a function of $\sum p_T^{\text{central}}$ with $y_{\text{max}} > 2$, compared to different theoretical predictions [7]. For better comparison, the predictions are multiplied by the factors indicated in the legend. The left panel shows the full spectra and the right panel the ratios of the different predictions to the data. The solid band represents the total experimental systematic uncertainty centered at one. The patterned band represents the theory uncertainties. The scale uncertainties for the HEJ predictions are not drawn.

Vector Boson+Jet Production

Recent Vector Boson+Jets Results

The ATLAS collaboration recently published a comprehensive comparison of data to theory predictions for W+jet production [8]. These measurements, which used 4.6 fb^{-1} of data at a 7 TeV center-of-mass energy, accessed for the first time jet transverse momenta up to 1 TeV. In this kinematic region, higher-order electroweak (EWK) effects can become as important as those from higher-order pQCD corrections. Figure 4 compares the leading jet p_T distribution between detector-corrected data and various predictions. The predictions from SHERPA and ALPGEN, which are both leading-order calculations, show generally good agreement to the data. The higher-order predictions of BlackHat+SHERPA, LoopSim and MEPS@NLO all tend to underestimate the cross section at high values of the jet p_T. None of these predictions include EWK corrections. However, the effects from EWK corrections are expected to be significant and negative at large values of jet p_T, which would worsen the agreement between data and the higher-order theory predictions. This publication also compared data and predictions in several other jet observables such as jet rapidity, the scalar sum of all jets and the angular distributions between the leading two jets. No theoretical prediction is able to describe all of the measured distributions.

Using Z+jet events, the CMS collaboration also probed regions of phase space where EWK corrections and QCD effects are expected to be large [9]. At high jet energies, EWK corrections and QCD processes can introduce a dependence of the cross section on logarithmic terms of the form $\ln(p_T^Z/m_Z)$, which can become large and pose a

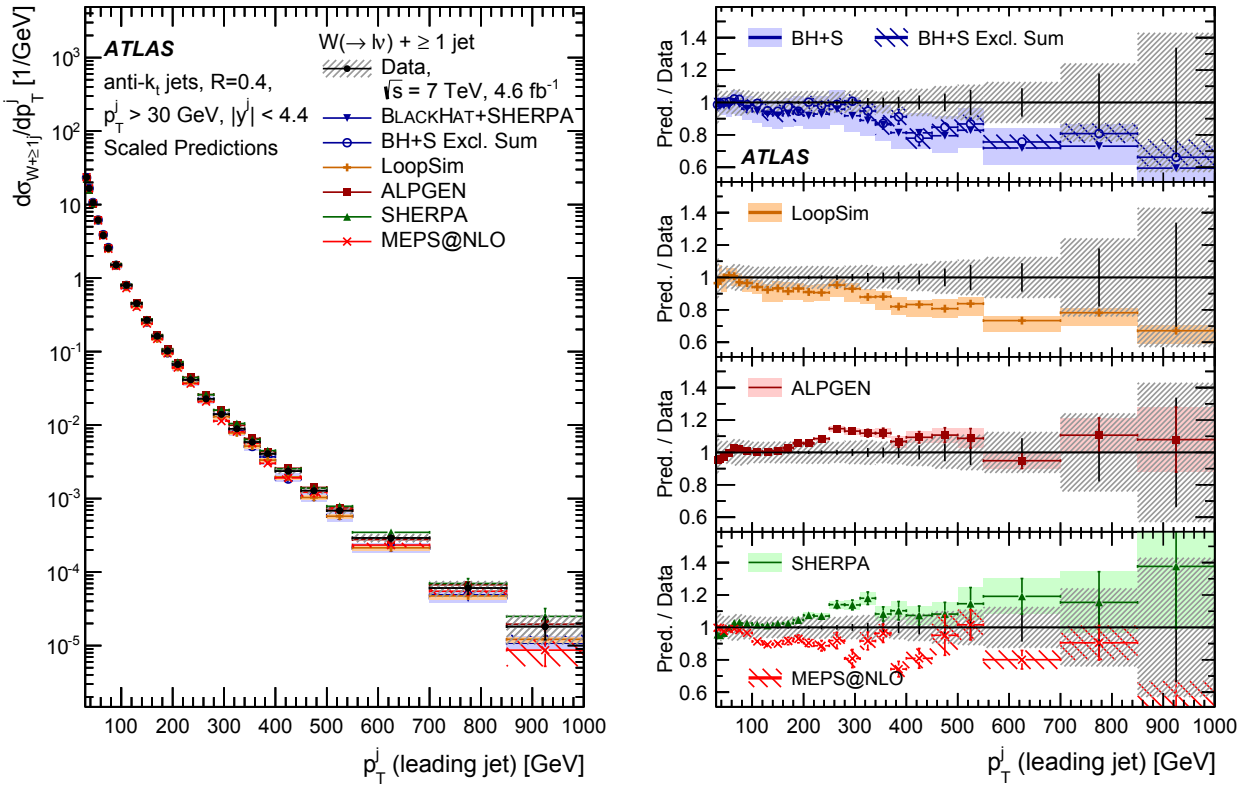

FIGURE 4. Cross section for the production of W+jets as a function of the leading-jet p_T in $N_{\text{jets}} \geq 1$ events [8]. For the data, the statistical uncertainties are shown by the vertical bars, and the combined statistical and systematic uncertainties are shown by the black-hashed regions. The data are compared to predictions from BlackHat+SHERPA, BlackHat+SHERPA including the exclusive summing, LoopSim, ALPGEN, SHERPA and MEPS@NLO. BH+S is an abbreviation for BlackHat+SHERPA. The left-hand plot shows the differential cross sections and the right-hand plot shows the ratios of the predictions to the data. The theoretical predictions have been scaled in order to compare the shapes of the distributions. The theoretical uncertainties, which differ for the various predictions, are described in Ref. [8]

challenge for perturbative calculations such as BlackHat. Using 19.7 fb^{-1} of data at an 8 TeV center-of-mass energy, the cross section of Z+jet production as a function of the $\log_{10} p_T^Z/P_T^{j1}$ for $N_{\text{jets}} \geq 2$ can be seen in Figure 5. For events with exactly one jet, the p_T of the jet should balance against the p_T of the Z boson and this distribution would peak around zero. In multi-jet events where the Z boson p_T is larger than any other jet, the value will be positive. The leading-order predictions of MADGRAPH+PYTHIA6 and SHERPA model this distribution well. However, the next-to-leading order BlackHat predictions underestimate the cross section for positive values. At these values, contributions from higher jet multiplicities become important; since BlackHat here only includes next-to-leading order predictions up to two jets and a leading-order prediction for three jets, it is not expected to model this region well. This publication also include the $(pp \to Z\text{+jets})/(pp \to \gamma\text{+jets})$ cross section ratio, which provides important information about the higher-order effects of these large logarithmic corrections at higher p_T.

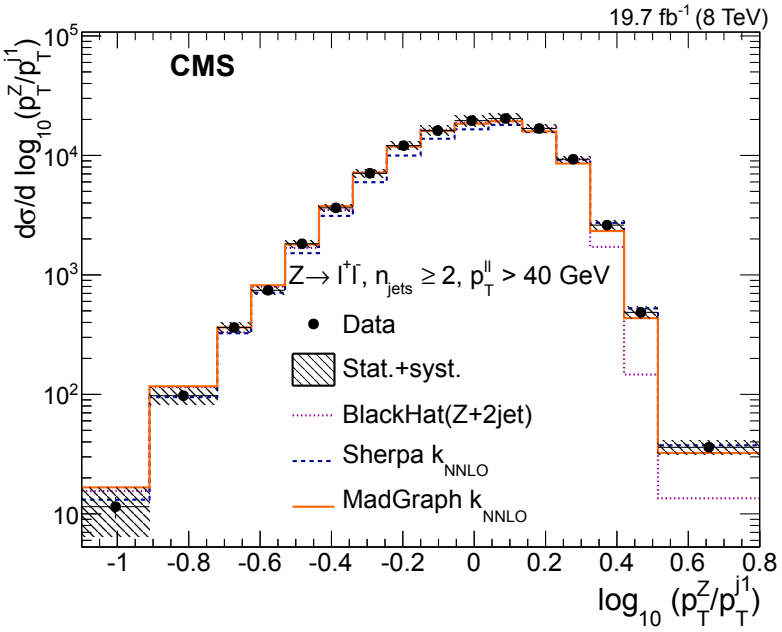

FIGURE 5. Cross section for the production of Z+jets for $N_{\text{jets}} \geq 2$ as a function of the $\log_{10} p_T^Z/P_T^{j1}$ [9]. The detector-corrected data are compared with estimations from MADGRAPH+PYTHIA6, SHERPA, and BlackHat.

Recent Vector Boson+Heavy Flavor Results

Measurements of W boson production in association with c and b quarks is an important test of the Standard Model. A result from the D0 collaboration showed the production of $W + c$ and $W + b$ production, using 8.7 fb^{-1} of data at a 1.96 TeV center-of-mass energy [10]. For $W + c$ production, the dominant processes are $qg \to Wc$ and $q\bar{q} \to Wg$ where $g \to c\bar{c}$. The first process is sensitive to quark and gluon parton density functions, while the second process is sensitive to gluon splitting. Additionally, the later process becomes more dominant with larger jet p_T. For $W + b$ production, the dominant process is $q\bar{q} \to Wg$ where $g \to b\bar{b}$ and is therefore largely sensitive to gluon splitting. Both the $W + c$ and $W + b$ cross sections where measured as a function of the leading jet p_T. For $W + c$ production, the next-to-leading order predictions agree with the data for the lowest values of jet p_T (20-30 GeV) but disagree at higher values. This disagreement may arise from many sources, for example, from missing higher-order corrections, an underestimated contribution from gluon splitting, or possible enhancement in the strange quark PDF. For $W + b$ production, the next-to-leading order predictions underestimate the data in all p_T bins, which is suggestive of missing higher-order corrections.

With the large datasets available from the LHC detailed studies of previously rare processes such as Z boson production in association with at least one b-jet can now be performed. An analysis from the CMS collaboration showed the production of a Z boson in association with at least one jet originating from a b quark using 19.8 fb^{-1} of data at an 8 TeV center-of-mass energy [11]. Measurements of Z boson production in association with two b-jets are

of particular interested as they are sensitive the gluon splitting. Figure 6 shows the cross section of $Z + bb$ production as a function of the ΔR between the two b-jets. The MADGRAPH and Powheg predictions all agree well with the data. However, this good agreement is in tension with previous measurements from ATLAS and CMS [12, 13] which showed significant deviations between data and predictions at the smallest values of ΔR. Future studies are needed to better understand these differences.

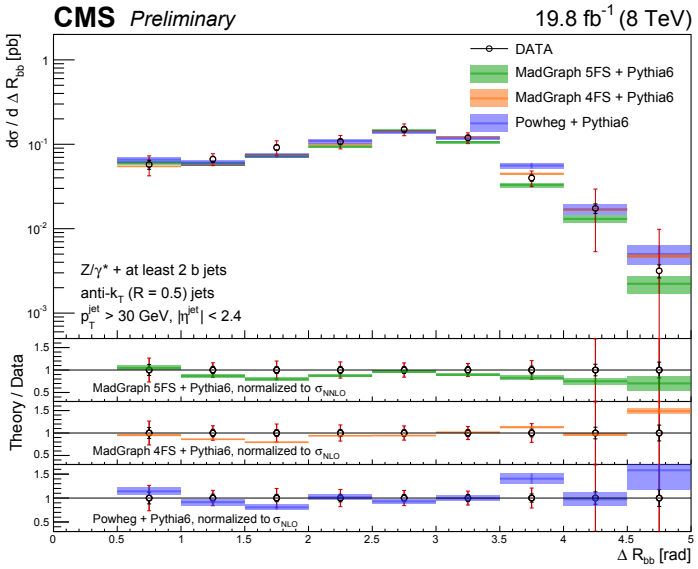

FIGURE 6. Differential $Z + bb$ cross section as a function of the ΔR_{bb}, compared with the MADGRAPH 5FS, MADGRAPH 4FS and Powheg theoretical predictions (shaded bands), normalized to the theoretical cross sections [11]. For each data point the statistical and the total (statistical plus systematic) uncertainty are represented by the double error bar. The width of shaded bands represents the statistical error on the theoretical predictions.

Measurements of α_s

A wide range of measurements of α_s are now available using LHC data including studies using inclusive-jets, 3-jet events and $t\bar{t}$ events (see Figure 7). Using event shape variables that were first developed in e^+e^- experiments, the ATLAS collaboration has an updated measurement of α_s using 158 pb^{-1} of data at a 7 TeV center-of-mass energy [14]. The jet-based transverse energy-energy correlation is defined as

$$\frac{1}{\sigma}\frac{d\sum}{d(\cos\phi)} = \frac{1}{\sigma}\sum_{ij}\int \frac{d\sigma}{dx_{Ti}dx_{Tj}d(\cos\phi)} x_{Ti}x_{Tj}dx_{Ti}dx_{Tj}$$

where the sum runs over all pairs of jets in the final state with an azimuthal angular difference ϕ and $x_{Ti} = E_{Ti}/E_T$ is the transverse energy carried by the i-th jet in units of the sum of the jet transverse energies $E_T = \sum_i E_{Ti}$. Figure 7 shows the energy-energy correlation for data and next-to-leading order predictions. The distribution peaks at $\cos\phi = 1$ (due to self-correlations) and at $\cos\phi = -1$. The central region is expected to be dominated by hard radiation processes while soft radiation is expected to be important in the $\cos\phi \approx \pm 1$ regions. The shape of the next-to-leading order predictions is sensitive to the value of α_s used, and χ^2 minimization is used to extract the best value of α_s with respect to the data. The comparison of the value of α_s extracted from the energy-energy correlation is compared to other measurements in Figure 7. This measurement is dominated by theoretical uncertainties, thereby showing the need for next-to-next-to-leading order calculations.

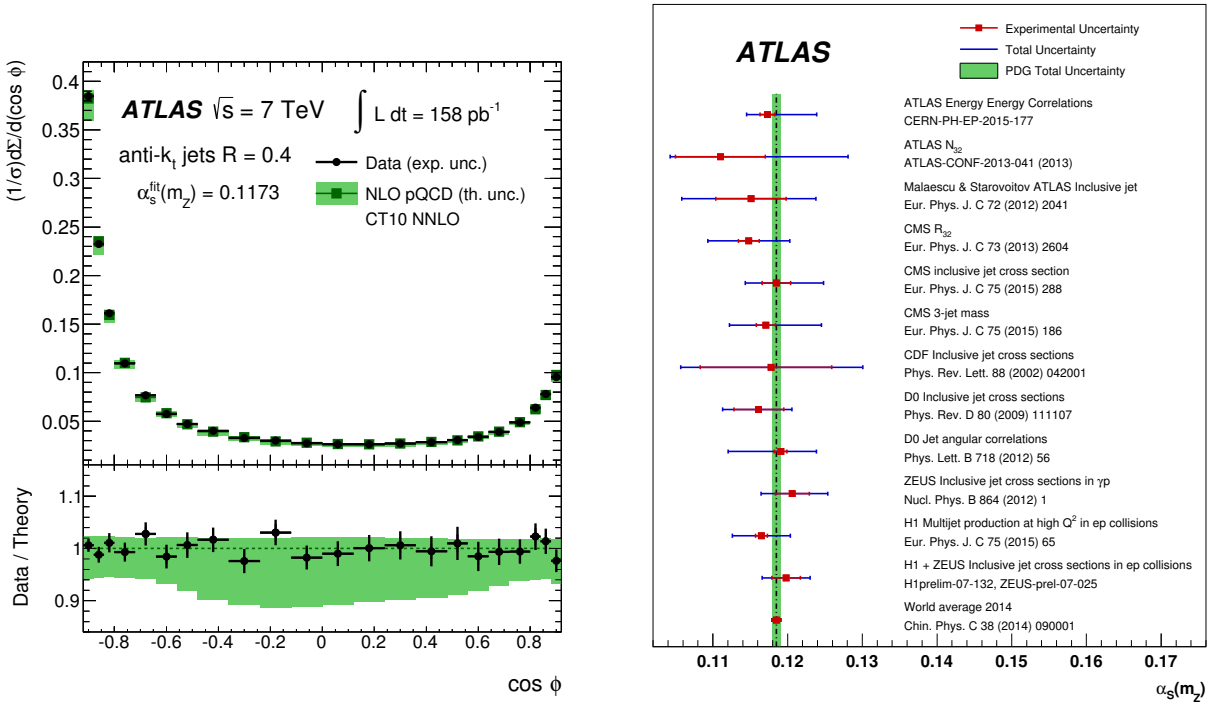

FIGURE 7. Left: The unfolded distributions for transverse energy-energy correlation compared with the results of a fit to pQCD next-to-leading order calculations including non-perturbative corrections [14]. The green shaded band indicates the uncertainty on the theoretical predictions, which includes the sum in quadrature of uncertainties associated with scale, α_s and PDFs. The statistical uncertainties on the predictions are indicated by green error bars. The solid error bars on the data points (in black) indicate the experimental uncertainties taking into account the correlations between them. Right: Comparison of the value of $\alpha_s(m_Z)$ obtained in this analysis with values from jet observables measured by other experiments in hadron-hadron and ep colliders. The red error bar represents the experimental uncertainties, while the blue bar includes both experimental and theoretical errors. The vertical green band represents the PDG world average for 2014.

Conclusions

Using the large datasets available from the LHC, we have made tremendous progress in our understanding of QCD, both in the breadth of available measurements and the improved precision of the calculations. Future improvements include next-to-next-to-leading order calculations for processes with jets and vector bosons in associations with jets, continuing to measure the corners of phase space such as events with very energetic jets and continuing to explore the kinematic distributions of rare processes such as vector bosons in association with heavy flavor jets. The increased center-of-mass energy to 13 TeV will be a new energy regime to continue to test and explore jet physics.

REFERENCES

[1] ATLAS Collaboration, JINST **3**, p. S08003 (2008).
[2] ATLAS Collaboration, ATLAS-CONF-2015-034 (2015).
[3] CMS Collaboration, JINST **3**, p. S08004 (2008).
[4] CMS Collaboration, CMS-PAS-SMP-14-017 (2015).
[5] CMS Collaboration, CMS-PAS-SMP-14-015 (2015).
[6] CMS Collaboration (CMS), Eur. Phys. J. **C75**, p. 302 (2015), arXiv:1502.04785 [hep-ex] .
[7] ATLAS Collaboration (ATLAS), submitted to JHEP (2015), arXiv:1509.07335 [hep-ex] .
[8] ATLAS Collaboration (ATLAS), Eur. Phys. J. **C75**, p. 82 (2015), arXiv:1409.8639 [hep-ex] .
[9] CMS Collaboration (CMS), JHEP **10**, p. 128 (2015), arXiv:1505.06520 [hep-ex] .
[10] D0 Collaboration (D0), Phys. Lett. **B743**, 6–14 (2015), arXiv:1412.5315 [hep-ex] .
[11] CMS Collaboration, CMS-PAS-SMP-14-010 (2015).
[12] CMS Collaboration (CMS), JHEP **12**, p. 039 (2013), arXiv:1310.1349 [hep-ex] .
[13] ATLAS Collaboration (ATLAS), JHEP **10**, p. 141 (2014), arXiv:1407.3643 [hep-ex] .
[14] ATLAS Collaboration (ATLAS), Phys. Lett. **B750**, 427–447 (2015), arXiv:1508.01579 [hep-ex] .

Proceedings of the LHCP2015 Conference, St. Petersburg, Russia, August 31 - September 5, 2015

Editors: V.T. Kim and D.E. Sosnov

QCD selected results from ALICE and LHCb

EUGENIO SCAPPARONE

INFN-Bologna, Via Irnerio 46, 40126 Bologna(Italy)

scapparone@bo.infn.it

On behalf of the ALICE and LHCb Collaborations

Abstract. Data collected during LHC Run 1 in pp, p-Pb and Pb-Pb interactions led to outstanding results, allowing us to go deeper in the comprehension of QCD related phenomena. ALICE and LHCb have a broad physics program, including several studies where QCD manifests in different ways. In this proceeding a few selected results obtained by ALICE and LHCb will be presented.

INTRODUCTION

LHC Run 1 gave us the possibility to study the interaction of three different hadron systems (pp, p-Pb and Pb-Pb) at a centre of mass energy per nucleon pair ranging from $\sqrt{s_{NN}}$=0.9 to $\sqrt{s_{NN}}$=13 TeV. Many important QCD results were obtained, making a comprehensive review of this subject beyond the aim of this proceeding. Here I will focus on the new results obtained by the ALICE and the LHCb Collaborations, putting emphasis on the interplay of hard and soft processes, and the search for gluon saturation using vector meson photo-production. Several important QCD studies as jets or high p_T physics will not be discussed, being the subject of other talks in the same conference session.

SOFT AND HARD PROCESS INTERPLAY

Although the bulk of particle production at the LHC is dominated by soft hadrons, hard scatterings at TeV energies play an important role too. The dependence of the charged particle multiplicity density on the system size and on the centre of mass energy per nucleon pair ($\sqrt{s_{NN}}$) reflects the interplay between hard parton-parton scattering and soft processes. The contribution of these two processes is explicitly taken into account in the Glauber model, where the charged particle multiplicity has two distinct contributions. The charged particle multiplicity is expected to scale as $\mathrm{d}N_{ch}/\mathrm{d}\eta \propto \sqrt{s}^{\lambda}$ in the models relying on parton saturation. The charged particle multiplicity as a function of the centre of mass energy $\sqrt{s}$ can be fit to a power law, s^{α}. It's quite impressive, using the λ parameter obtained at HERA by fitting at low Bjorken-x the gluon PDF ($xg(q^2, x) \propto x^{-\lambda}, \lambda \simeq 0.25-0.3$) and multiplying by 1/2, one obtains the charged multiplicity grows as $s^{0.12-0.15}$, that is quite close to the experimental values [1], ranging from $s^{0.10}$ for protons to $s^{0.15}$ for Pb-Pb interactions.

The difference in the exponent from pp to p-Pb and Pb-Pb collisions stimulated a lot of theoretical work. It can be explained by different values of the saturation scale Q_S folded with gluon initiated jet charged multiplicity ([2]) or by a different energy dependence of the saturation scale value for protons and nuclei [3], due to the behaviour of the DGLAP gluon distribution, whose x dependence gets steeper at higher Q and at higher A.

Taking advantage of the large mass of the c,b quarks, heavy quark production cross section can be successfully calculated using pQCD: Next to Leading Order (NLO) models reproduce within (large) uncertainties the $c\bar{c}$ cross section as a function of $\sqrt{s}$ in a wide energy range, from 10 GeV to 10 TeV. Theoretical expectations for the production cross section of charmed hadrons have been calculated in the Generalized Mass Variable Flavour Scheme (GMVFNS) model and using Fixed Order Next to Leading Logarithm (FONLL) approach.

The differential charmed meson cross section as a function of the p_T in pp collisions at the LHC has been measured by LHCb [4] at $\sqrt{s}$= 7 TeV: data are properly reproduced by GMVFNS (slightly above data) and FONLL (slightly below data) models. The GMVFNS model reproduces the Λ_c baryon production cross section too; in this

case, differently from charmed meson production, the experimental data are slightly larger than predictions. Similar results have been obtained by the ALICE Collaboration [5]

Open and hidden charm and beauty production are a footprint of high p_t events, while the bulk of hadron production is connected to soft processes. Studying charmed meson production as a function of the event charged multiplicity is therefore the most straightforward way to study the soft and hard interplay in hadronic collisions.

In the past a first attempt was made by the NA27 experiment using a 400 GeV/c proton beam. By using a fruitful merging of the hadron detailed tracking offered by a hydrogen bubble chamber and the reliability of a high resolution muon spectrometer, they compared the charged multiplicity distribution for events with or without charm production [6]. Events with charm showed a different distribution with a larger average multiplicity (<N>=11.0±0.5) compared to those without charm (<N>=8.98±0.01). The explanation of this result was based on the collision centrality: high centrality events have a higher probability to produce both J/Ψ and a large number of charged hadrons.

After more than twenty years a new analysis was performed by the ALICE collaboration using data collected in the 2010 pp run at $\sqrt{s}$=7 TeV. As a result a linear increase of the relative J/Ψ yield as a function of charged particle multiplicity density $(\mathrm{d}N/\mathrm{d}\eta)/\langle \mathrm{d}N/\mathrm{d}\eta \rangle$ was found [7]. The observed behaviour cannot be understood by J/Ψ directly produced in 2→2 hard partonic scattering: a prediction by PYTHIA 6.4.25 in the Periugia 2011 tune, where only J/Ψ produced in hard scatterings were considered, showed an opposite trend, i.e. a decrease of the J/Ψ multiplicity with respect to the event multiplicity. This evidence suggests other mechanisms are at work in the bulk of charmed event production.

MULTIPARTON INTERACTIONS AND COLOUR RECONNECTION

The last result shown in the previous section is not surprising, considering at high energy is unrealistic to expect the bulk of the interactions comes from single parton interactions(SPI). Collisions at the LHC are characterized by a large number of processes: Hard scattering, gluon radiation, fragmentation, QED bremsstrahlung and secondary particle production. Considering the large density of quark and gluons and the composite nature of incoming partons, as pointed out by T. Sjostrand [8], it is inevitable that multiparton interaction (MPI) plays an important role. A manifestation of this effects is the long tail in the charged particle multiplicity distribution in the minimum-bias event, where hard jets play a modest role. The $c\bar{c}$ creation is proportional to the hard scattering cross section σ_{hard} and the total multiplicity has a substantial contribution from MPI . If MPI contributes to the hard scattering too, this may explain the linear growth of the relative J/Ψ yield as a function of charged particle multiplicity density reported above.

The dominant QCD processes involve t-channel gluon exchange: the hard cross section grows at small p_T as $\mathrm{d}p_T^2/p_T^4$, leading to a divergence for $p_T \to 0$ (regularized by dampening to $\mathrm{d}p_T^2/(p_{T0}^2 + p_T^2)^2$. Comparing TOTEM data [9] to the perturbative hard cross section shows the latter is larger than the experimentally measured inelastic cross section at transverse momentum ranging from $p_t \simeq 2$ GeV/c at $\sqrt{s}$= 0.9 TeV to $p_t \simeq 5$ GeV/c at $\sqrt{s}$= 13 TeV [10].

The simplest explanation is that each hadron-hadron collision contains more than one partonic 2→2 scattering. In a naive representation of MPI, the number of hard scattering in each event follows a poisson distribution, whose average is given by $< n_{hard} > \simeq \sigma_{hard}/\sigma_{inel}$. Nevertheless MPIs in the same event could be not independent among them.

An intriguing process is the so called Double Parton Scattering (DPS), where two independent types of scattering take place in the same event. This cross section can be written as

$$\sigma_{DPS} = \frac{m\sigma_A\sigma_B}{\sigma_{eff}}, \tag{1}$$

where A and B are two independent processes, σ_{eff} is a geometrical scale cross section, m=1/4 if C_A and C_B are identical and non-self-conjugate (e.g. D^0D^0), m= 1 if C_A and C_B are different and either C_A and C_B is self-conjugate (e.g. $J/\Psi D^0$), and m=1/2 otherwise.

CMS and ATLAS measured the cross section of (W + 2 jets) associated production events. The obtained σ_{eff} was 20.7±0.8(stat)±6.6(syst) mb [11] and $15.0\pm3.0(\mathrm{stat})^{+5.0}_{-3.3}(\mathrm{syst})$ mb [12], in good agreement with the CDF result at the Fermilab Tevatron $14.5\pm1.7(\mathrm{stat})^{+1.7}_{-2.3}(\mathrm{syst})$ mb [13]. LHCb went a step forward, measuring the DPS in events with J/Ψ accompanied by open charm, and pairs of open charm hadrons [14, 15]. This study includes a large number of processes, as J/Ψ D, D^+D^-, D^0D^0, $D^0\Lambda_c^+$, etc. The peculiarity of these systems is that they dominate over single parton scattering cross section, i.e. the process has a high purity. pQCD models using SPS fail to reproduce the cross

sections of the $J/\Psi\, D^0$, $J/\Psi\, D^+$, $J/\Psi\, D_s^+$, and $J/\Psi\Lambda_c^+$ channels, while the DPS qualitatively agree with them (figure 1). Using equation 1 to obtain σ_{eff} gives results in agreement with those from ATLAS, CDF and CMS quoted above. The present statistical accuracy does not allow to draw a conclusion on the effective cross section possible independence on system and energy.

Future runs at the LHC will be important for this study: higher energies will allow the study of the simultaneous production of Υ mesons and charm hadrons and the study of triple parton scattering too.

In the most naive picture, each MPI is independent, giving separated singlets. This is of course unphysical, since hadron remnants need colour connection too: at least a colour connection between partons and remnants is therefore required. In the so called "Leading colour" scheme, each parton is colour connected to another (single) parton only. This picture worked quite well at LEP, but it's questionable at the LHC, where Colour Reconnection (RC) is expected to play a significant role. In the RC inspired models colours carried by partons are reshuffled just before the hadronization. The colour configuration transformation is based on three principles: the SU(3) colour rules determine if two strings are compatible. Then a simplified space-time picture checks causal contact between strings. The string-length measure (λ- measure) represents the rapidity span of a string: this key parameter decides if a possible

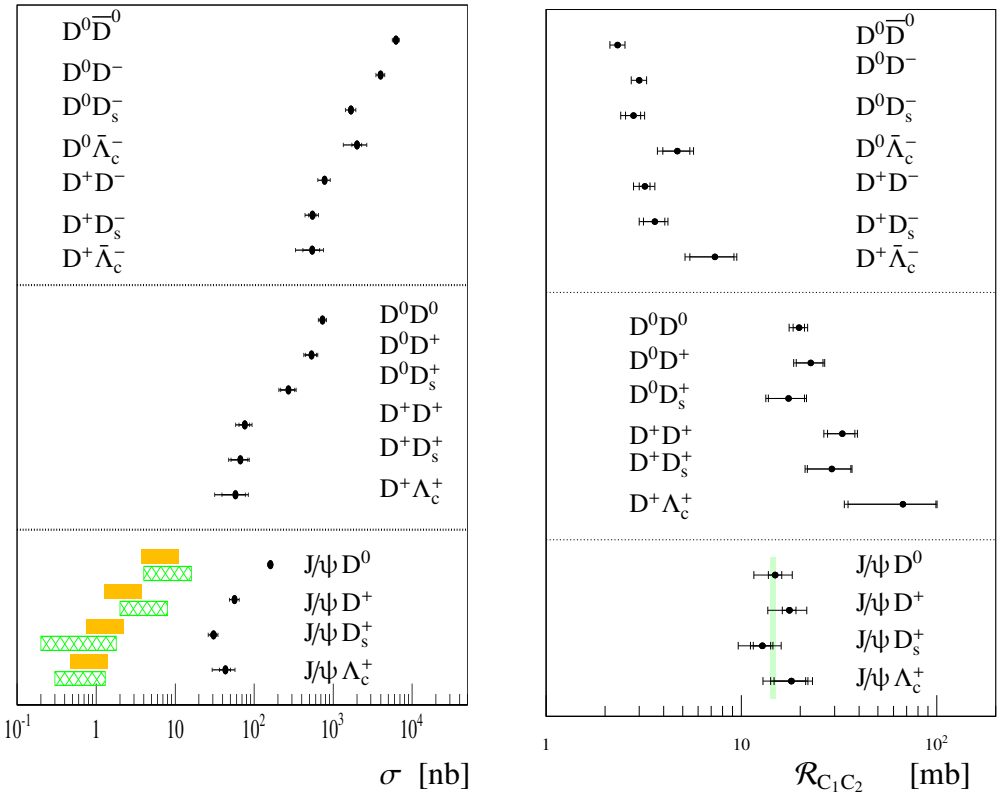

FIGURE 1. LHCb measured ratios (ref [4]) $\mathcal{R}_{C_1C_2}$ (points with error bars) in comparison with the expectations from DPS using the cross-section measured at Tevatron for multi-jet events (light green shaded area). For the J/ψC case the outermost error bars correspond to the total uncertainties including the uncertainties due to the unknown polarization of the prompt J/Ψ mesons. Right: LHCb measured cross-sections (ref [4]) $\sigma_{J/\psi c}$, σ_{cc} and $\sigma_{c\bar{c}}$ (points with error bars) are compared, in J/ψC channels, to the calculations in Refs. [17, 18] (hatched areas) and Ref. [19] (shaded areas).

reconnection is favoured. Final partons are colour connected so that the λ-measure becomes as short as possible. As a consequence the transverse momentum of the partons is shared by a minimum number of hadrons. If each MPI produces particle independently of each other, then their p_T should be independent of the number of MPIs, and hence

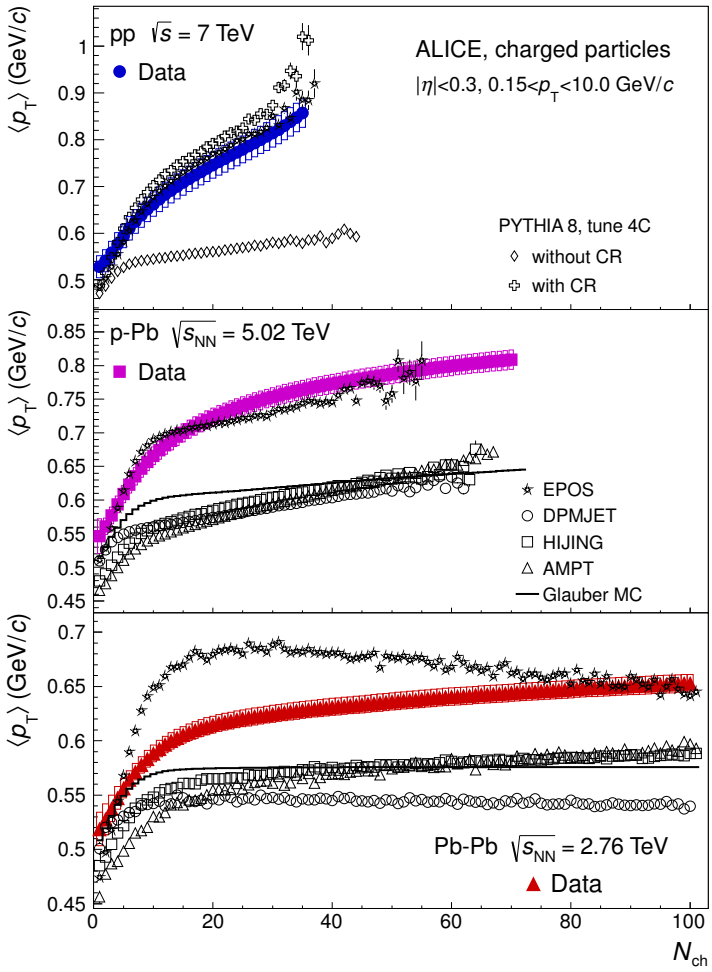

FIGURE 2. Average transverse momentum as a function of charged-particle multiplicity measured by ALICE (ref. [20]) in pp (upper panel), p-Pb (middle panel), and Pb-Pb (lower panel) collisions in comparison to model calculations. The data are compared to calculations with the DPMJET, HIJING, A MPT, and EPOS Monte Carlo event generators. For pp collisions, calculations with PYTHIA 8 [42] with tune 4C are shown with and without the colour reconnection (CR) mechanism. The lines show calculations in a Glauber Monte Carlo approach.

of the total number of charged particles N_{ch}.

The distribution of the average transverse momentum $< p_T >$ as a function of the charged multiplicity N_{ch} was studied by ALICE in pp, p-Pb and Pb-Pb collisions [20]. PYTHIA 8 fails to reproduce pp data if CR is not included, while it works successfully when CR is included (figure 2). In p-Pb interactions the EPOS code is much closer to data with respect to HIJING, AMPT, Glauber models and DPMJET. Nevertheless it has a different trend at $N_{ch}< 20$ and fails in Pb-Pb interactions. An alternative explanation with respect to CR is given by models based on the Colour Glass Condensate [23]. The model introduced by Razaeian [24] reproduces quite well the $< p_T >$ as a function of N_{ch} for all of the three systems.

Although introduced in 1987, the CR is still in evolution. Recently extra string topologies, including new types of connections between partons, have been introduced in [27]. LHCb measured the ratio $\bar{\Lambda}/K^0_S$ at $\sqrt{s}$=0.9 TeV [21]: data were poorly reproduced by PYTHIA 6 (Perugia0 tuning). CMS studied the ratio Λ/K^0_S at $\sqrt{s}$= 0.9 and 7 TeV [22]: a poor agreement with PYTHIA 8 and PYTHIA 6 (Perugia0 tuning) was confirmed. The new CR model [27], available in PYTHIA 8.21, improved considerably the comparison to data, giving a satisfactory agreement in the Λ/K^0 ratio up to 4-5 GeV/c.

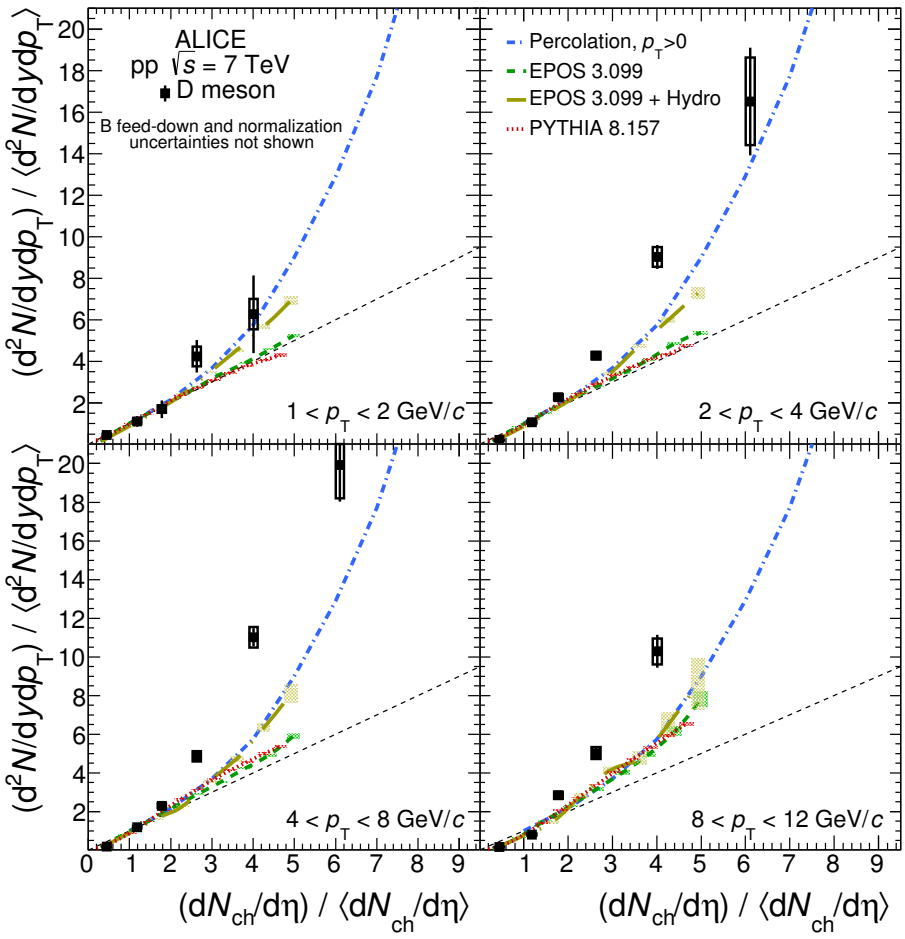

FIGURE 3. Average D-meson relative yield as a function of the relative charged-particle multiplicity at central rapidity in different p_T intervals measured by ALICE (ref. [16]). Different calculations are presented: PYTHIA 8.157 [30, 31], EPOS 3 with and without hydro [71, 72] and a p_T-integrated percolation model [41, 73]. The coloured lines represent the calculation curves, whereas the shaded bands represent their statistical uncertainties at given values of $(dN_{ch}/d\eta/\langle dN_{ch}/d\eta \rangle)$.

Another observable to test colour reconnection capability in reproducing experimental data is given by the study of the charmed meson relative yield, $(d^2N/dy\ dp_T)/(\langle d^2N/dy\ dp_T \rangle$ as a function of the charged multiplicity density $(dN_{ch}/d\eta)/\langle dN_{ch}/d\eta \rangle$. ALICE results [16] obtained in pp collisions at $\sqrt{s}$=7 TeV, showed a growth faster than linear at high multiplicity. A similar increase is obtained both for J/Ψ and non-prompt J/Ψ (from b quark decay). Open charm, open beauty and hidden charm hadron show a similar increase. This trend is therefore related to c,b quark production process, and is not influenced strongly by hadronization. PYTHIA 8, implementing colour reconnection shows a linear growth, as EPOS 3.099: they look adequate at low multiplicity but they cannot reproduce the faster growth observed at high multiplicity (figure 3), while EPOS with hydrodynamics is closer to the data.

It is worth noting models based on percolation can also reproduces the fast rise at large multiplicity density. In this class of models, the number of charmed particles produced in the event, is proportional to the number of strings, while the soft component is expected to be proportional to the number of participant nucleons. The charmed particle multiplicity distribution is also proportional to the multiplicity of a single string in the rapidity range and to a damping factor, representing the string interaction. This damping factor decreases with the string density $\rho = N_S \sigma_0/\sigma$, where N_s is the number of string, σ_0 is the string transverse area and σ is the collision transverse area. Under these assumptions, it is easy to show the relation between the charmed particle and the charged multiplicity density is linear at low ρ and is quadratic at high ρ, reproducing thus the faster than linear trend observed experimentally. Somehow the high number

of strings, directly related to the number of available partons, screens the charged particle multiplicity, introducing a phenomenology close to the so called parton saturation.

Colour Glass Condensate inspired models, relying on parton saturation, can reproduce several observables measured in pp, p-Pb and Pb-Pb collisions at the LHC. These models, as showed in [32], can also reproduce HERA data at Bjorken-x lower than 10^{-2}. On the other end HERA data can also be explained by alternative models. As an example, the geometrical scaling, which can be smartly explained by models relying on parton saturation, is also generated by linear DGLAP evolution, as pointed out in [31]. Parton saturation is therefore an intriguing subject: in the second part of this proceeding the studies on proton saturation performed at the LHC will be presented.

ULTRA PERIPHERAL COLLISIONS

When the interaction between two hadrons takes place at large impact parameters ($b > R_A + R_B$, where R_A and R_B are the two hadron radii), hadronic interactions are strongly suppressed and electromagnetic processes dominate. These processes are often called Ultra Peripheral Collisions (UPC). As an example the two hadrons may just exchange one or more photons; events with two virtual photons (one from each hadron) may give a lepton-antilepton pair in the final state. The process can be just partially mediated by the electromagnetic field: an hadron may radiate a photon that fluctuates into a virtual $q\bar{q}$ pair. The quark-pair may interact with the strong field of the other hadron, giving a real vector meson.

The importance of this physics in fact relies on the possibility to shed light on a given target inner structure: the probability the virtual quark-pair turns into a real vector meson depends on the strong field. At leading order the cross section to produce a J/Ψ is proportional to the square of the gluon PDFs. Pb-Pb collisions give informations on the nucleus coloured strong field, allowing to measure the difference between the effective field experienced by the quark-antiquark pair with respect to the naive hypothesis of a simple superposition of the A nucleon fields (gluon shadowing). At the LHC a Bjorken-x ranging from 10^{-2} to 10^{-5}, can be explored, depending on the process, rapidity and centre of mass energy. This wide region is very interesting due to the large gluon PDFs uncertanties. Heavy vector meson production in p-p or p-Pb interactions allow to study the gluon PDF in the proton and search for saturation effects.

The process e+p→e+p+J/Ψ was studied in detail at HERA. As a result the cross section of the process γ+p→J/Ψ+ p as a function of the photon-proton centre of mass energy ($W_{\gamma p}$) was found to grow as a power law. The fit to a power law, $\sigma \propto W_{\gamma p}^{\delta}$, in the range $20 < W_{\gamma p} < 300$ GeV, gave δ=0.69±0.02(stat)±0.03(syst) (ZEUS) [33] and δ=0.67±0.03(stat+syst) (H1) [34, 35]. The growth of the cross section was interpreted by pQCD inspired models as an increase of the gluon density approaching smaller Bjorken-x.

J/ψ and Ψ(2s) vector meson production

ALICE studied J/Ψ photo-production [30] up to $W_{\gamma p} \simeq 700$ GeV, using p-Pb data collected at $\sqrt{s_{NN}}$=5.02 TeV. In this case the Pb nucleus acts as photon emitter in more than 95% of the events. This allows to give an unambiguous determination of the event rapidity y and therefore of $W_{\gamma p}$. During the 2013 p-Pb run, the beam direction was reversed, allowing the study of two different rapidity ranges.

The obtained cross section was σ(p+Pb→J/Ψ+p+Pb)=6.42±0.43(stat)±0.61(syst) μb at $2.5 < y < 4$ and σ(p+Pb→J/Ψ+p+Pb)=2.46±0.31(stat)$^{+0.24}_{-0.28}$(syst) μb at $-3.6 < y < -2.6$. The above cross section is related to the photon-proton cross section γ+p→J/Ψ +p through the photon flux, $\frac{dn}{dk}$, where k is the photon energy, which is determined by the J/Ψ mass and rapidity,

$$k = \frac{1}{2} M_{J/\psi}\, e^{-y}. \tag{2}$$

Figure 4 shows the cross section measured by the ALICE muon spectrometer at four different $W_{\gamma p}$. Two calculations are available from the JMRT group [28]: the first one referred to as LO is based on a power law description of the process, while the second model is labeled as NLO, and includes contributions which mimic effects expected from the dominant NLO corrections. Because both JMRT models have been fitted to the same data, the resulting energy dependences are very similar. ALICE data support their extracted gluon distribution up to $x \simeq 2\cdot10^{-5}$. The STARLIGHT parameterization [38] is based on a power law fit using only fixed-target and HERA data, giving δ= 0.65±0.02. Figure 4 also shows predictions from the b-Sat eikonalized model [36] which uses the Color Glass Condensate approach to incorporate saturation, constraining it to HERA data alone. The results from the models mentioned above are within

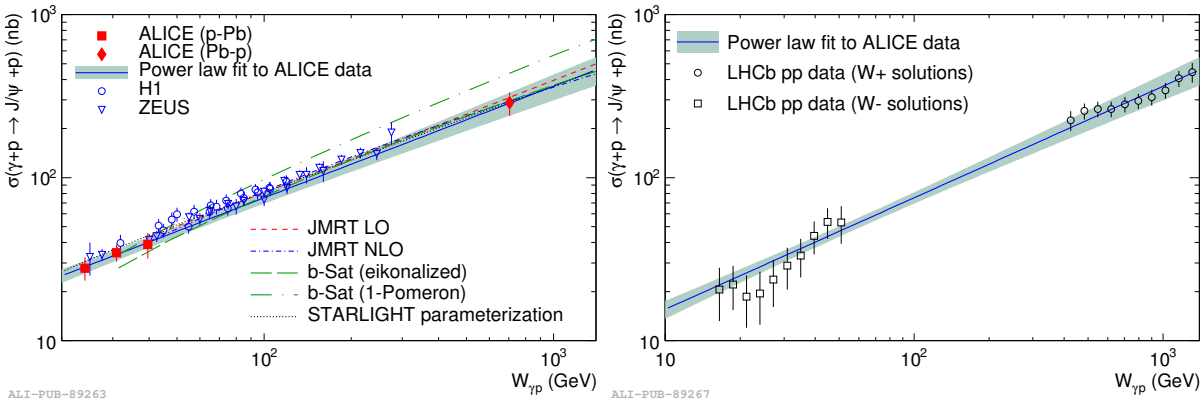

FIGURE 4. Coherent γ+p $\rightarrow$J/ψ +p cross section obtained by ZEUSS and H1 at HERA and by ALICE(ref. [30]) at the LHC in p-Pb collisions(left). The LHCb point obtained in pp collisions at $\sqrt{s}$= 7 TeV(right) are compared to the fit obtained using ALICE data in p-Pb collisions at $\sqrt{s}$=5.02 TeV.

one sigma of ALICE measurement. The b-Sat 1-Pomeron prediction taken from [37] also agrees with the ALICE low energy data points, but it is about 4 sigmas above measurement at the highest energy.

ALICE data are successfully fitted to a power law giving δ=0.68$\pm$0.06(stat+sys) in good agreement with the results found at HERA. This result shows there is no change of the cross section behaviour, within the errors, between the HERA and the LHC energies.

J/ψ and Ψ(2s) production in ultra peripheral collisions was studied by LHCb in pp collisions at $\sqrt{s}$= 7 TeV [29]. Identical hadron interactions do not allow to distinguish which one of the two hadrons emitted the photon and therefore an ambiguity on the rapidity is present: as a consequence each event has two possible $W_{\gamma p}$ solutions. In this case extracting the γ+p$\rightarrow J/\Psi$ +p cross section from the measured p+p$\rightarrow J/\Psi$ +p+p measured cross section is not trivial. The analysis required 2 tracks in an otherwise empty detector. Invariant mass distribution showed clear J/Ψ and $\Psi(2s)$ peaks. After correcting for acceptance and efficiency, the $0.93 pb^{-1}$ integrated luminosity gave a cross section in the pseudorapidity interval 2.0<$\eta_{\mu^{\pm}}$<4.5, σ(p+p$\rightarrow J/\Psi$+p+p)=291$\pm$7(stat)$\pm$19(syst) pb and σ(p+p$\rightarrow\Psi(2s)$ +p+p)=6.5$\pm$0.9(stat)$\pm$0.4(syst) pb. The extraction of the γ+p$\rightarrow$ V+p (V=J/Ψ, Ψ(2s) or Υ) cross section was obtained by using a power law to connect the two cross sections:

$$\frac{d\sigma(p+p\rightarrow V+p+p)}{dy} = S^2(W_+)(k_+\frac{dn}{dk_+})\sigma^{th}_+(\gamma p) + S^2(W_-)(k_-\frac{dn}{dk_-})\sigma^{th}_-(\gamma p), \quad (3)$$

where S is the gap survival probability, k is the photon energy, $k\frac{dn}{dk}$ is the photon flux and $\sigma_{+,-}(\gamma p)$ are the cross section of the process γ+p$\rightarrow J/\Psi$+ p, corresponding to the two different $W_{\gamma p}$ solutions. S is the probability no other process in the event affect the existence of the gap in the particle distribution. In fact, besides the quark-antiquark pair, the other spectator partons might participate in the interaction, and destroy the rapidity gap(s) in the final state, for instance by exchanging gluons with the partons of the other hadron. This quantity has not be measured experimentally at the LHC and one has therefore to rely on Monte Carlo simulation. According to an eikonal model [28] it depends on the vector meson mass, rapidity and center of mass energy. As far as $\Upsilon(J/\Psi)$ is concerned at $\sqrt{s}$=7 TeV, S^2 ranges from $\simeq$0.81($\simeq$ 0.87) at $y \simeq 2$ and $\simeq$0.47(4$\simeq$0.68) at $y \simeq 4.5$ [28]. Models including saturation [39] reproduce within the error the J/ψ and Ψ(2s) cross section measured by LHCb as a function of the rapidity. The differential J/Ψ and Ψ(2s) cross section both agree better with the NLO rather than LO predictions of [28]. Comparing the ALICE and LHCb results (figure 4, right panel) shows the cross sections measured by LHCb at different $W_{\gamma p}$ agree within the error with the ALICE fit quoted above.

LHCb observed [40] exclusive double charmed meson production in pp collisions at $\sqrt{s}$= 7 and 8 TeV too. The main contribution to these processes comes from double pomeron exchange: different topologies may contribute to the total scattering amplitude, depending on the relative gluon hardness. Using an integrated luminosity of $3 fb^1$, LHCb measured a cross section σ=58$\pm$10(stat)$\pm$6(syst) pb and $\sigma=63^{+27}_{-18}$(stat)$\pm$10(syst) pb, for J/Ψ J/Ψ and J/Ψ Ψ(2s), respectively. Data and theoretical expectactions agree within the large prediction uncertainties (factor two or three), due to gluon PDF that enters with the fourth power.

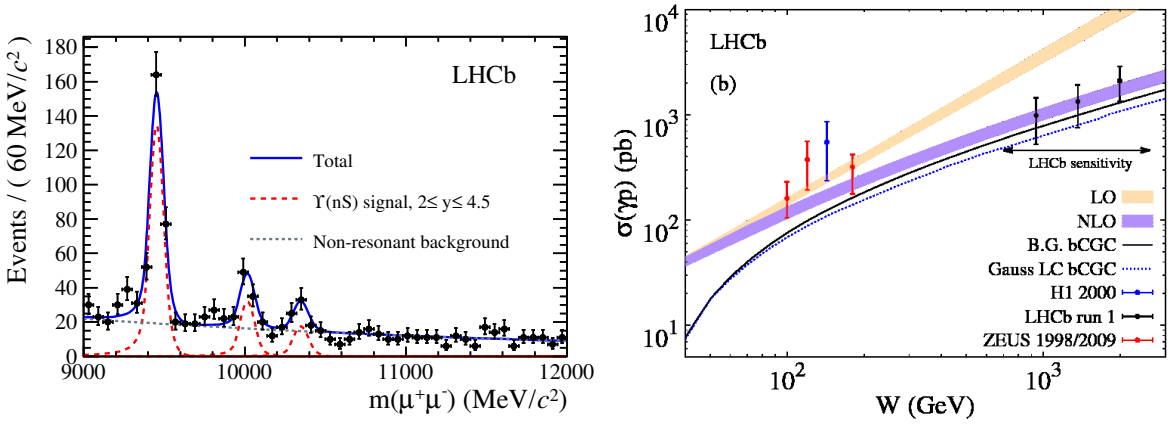

FIGURE 5. Left panel: LHCb invariant di-muon mass distribution for 7 TeV and 8 TeV data in the rapidity range 2.0<y<4.5 (ref. [41]). Right panel: photon-proton cross section extracted from the LHCb results compared to LO and NLO predictions [28] and to a CGC inspired model [42].

Υ vector meson production

The LHCb collaboration recently published [41] the first study of Υ photo-production in pp collisions at the LHC. Given the low statistics, data collected at $\sqrt{s}$=7 and 8 TeV were combined, giving a total integrated luminosity L=580 pb^{-1} after pile-up subtraction. The three peaks (figure 5, left) corresponding to the $\Upsilon(1s)$, $\Upsilon(2s)$ and $\Upsilon(3s)$ vector mesons, are clearly visible in the invariant mass spectrum. The most important backgrounds in this analysis, performed at 2.0<$\eta_{\mu^\pm}$<4.5, come from $\chi_b \rightarrow \Upsilon + \gamma$ decay and from inelastic interactions that involve undetected products of proton dissociation or gluon radiation. The cross sections for Υ(1s), Υ(2s), Υ(3s) are σ=9.0±2.1(stat)±1.7(syst) pb, σ=1.3±0.8(stat)±0.3(syst) pb and σ <3.4 pb (95% C.L.), respectively. The contribution to the total cross section from the W_- is expected to be small and is therefore neglected (see equation 1).

The dominant W_+ solutions are therefore estimated assuming that they dominate the cross section, and are shown in Figure 5, right panel. As a result both the NLO model [28] and the impact parameter dependent CGC model [42] properly reproduce the data.

Conclusions

In a paper published in 1987 [43], where a realistic model for particle production in hadron-hadron collisions was presented, T. Sjostrand and M. van Zijl wrote in the conclusions *"if the measure of success is the degree of simplicity achieved, then ours is a complete failure"*.

Their model was detailed and accurate, and was a terrific step forward in reproducing several experimental results. The above lapidary sentence stigmatized how challenging and laborious was the modelling of a QCD inspired model, requiring the implementation of many details in order to reproduce in a satisfactory way the various experimental observables. LHC Run 1 provided a large number of accurate measurements in three different colliding systems, that can be often reproduced by properly tuned models, inspired by different theories.

Nevertheless LHC events are of daunting complexity: several mechanisms are at play and we still miss a simple event generator that predicts (or at least reproduces) simultaneously all the hadron production observables. Hydrodynamics may reproduce the ridge features, but while it's widely accepted in A-A collisions the ridge may be originated by various harmonic flow components, generated by strong hydrodynamic response to initial conditions, it's not straightforward similar arguments can be applied to the ridge seen in small systems, as pp interactions. Colour Glass Condensate inspired models are a smart approach to reproduce several observables, although elliptic flow mass ordering is not obviously obtained. In addition gluon saturation is required by these models and a compelling, unambiguous experimental evidence is still missing. Future projects as the Electron Ion Collider (EIC) will play a decisive role in exploring this important QCD area.

In addition satisfactory explanation is still pending for few intriguing results: as an example ALICE showed the first direct evidence of gluon shadowing in the nucleus by measuring the exclusive J/Ψ cross section in Pb-Pb collisions at $x \simeq 10^{-2} - 10^{-3}$ [44]. The favored gluon shadowing fit, EPS09, gives a satisfactory agreement when used to reproduce the J/Ψ nuclear modification factor $R^{J/\psi}_{pPb}$ in p-Pb collisions measured by ALICE [45] and by LHCb [46]. Surprisingly the use of the same fit does not give a satisfactory prediction for the nuclear modification factor of the $\Psi(2s)$ vector meson, showing in this case the inital state effects are not enough to reproduce experimental the data [47, 48].

The next LHC runs will make available data collected at higher centre of mass energies and with higher integrated luminosity. QCD modelling is not trivial and will require several efforts, but LHC is an outstanding machine: it will continue to offer a great opportunity to shed light on this complex and intriguing scenario and will stimulate more theoretical and phenomenological invaluable work.

REFERENCES

[1] K. Aamodt et al. (ALICE Collaboration), Phys. Rev. Lett. 105, 252301.
[2] E. Levin and H. Rezaeian, Phys. Rev. D83 (2011) 114001.
[3] T. Lappi, EPJ C71 (2011) 1699.
[4] R. Aaij et al. (LHCb Collaboration), Nucl. Phys. B871 (2013) 1.
[5] B. Abelev et al. (ALICE Collaboration), JHEP 11 (2012) 065.
[6] NA27 Collaboration, Z.Phys. C41 (1988) 19.
[7] K. Aamodt et al. (ALICE Collaboration), Phys. Lett. B712 (2012) 165.
[8] T. Sjostrand, Phys. Scripta T158 (2013) 014002.
[9] G. Antchev et al., (TOTEM Collaboration), Phys. Rev. Lett. 111 (2013) 012001.
[10] P. Skands et al., Arxiv: 1404.5630.
[11] S. Chatrchyan et al . (CMS COllaboration) JHEP 03 (2014) 032.
[12] G. Aad et al. (ATLAS COllaboration) New J. Phys. 15 (2013) 033038.
[13] F. Abe et al., (CDF Collaboration) Phys. Rev. D56 (1997) 3811.
[14] R. Aaij et al. (LHCb Collaboration) JHEP 06 (2012) 141.
[15] R. Aaij et al. (LHCb Collaboration) JHEP 03 (2014) 108.
[16] J. Adam et al. (ALICE Collaboration) JHEP 1509 (2015) 148.
[17] A. V. Berezhnoy et al., Phys. Rev.D57 (1998) 4385.
[18] S. P. Baranov, Phys. Rev. D73 (2006) 074021.
[19] J.-P. Lansberg, Eur. Phys.J.C61 (2009) 693.
[20] B. B. Abelev et al., (ALICE Collaboration), Phys. Lett. B727 (2013) 371.
[21] R. Aaij et al., (LHCb Collaboration) JHEP 08 (2011) 034.
[22] S. Chatrchyan et al . (CMS COllaboration) JHEP 05 (2011) 064.
[23] E. Iancu and R. Venugopalan, arXiv:hep-ph/0303204.
[24] A. H. Rezaeian, Phys. Lett. B 727 (2013) 218.
[25] R. Aaij et al., (LHCb Collaboration) JHEP 08 (2011) 034.
[26] V. Khachatryan et al. (CMS Collaboration), JHEP 05 (2011) 064.
[27] J. R. Christiansen and P. Z. Skands, JHEP 1508 (2015) 003.
[28] S.P. Jones et al., JHEP 1311 (2013) 085.
[29] R. Aaij et al., (LHCb Collaboration), J. Phys. G41, 055002 (2014).
[30] B. B. Abelev et al., (ALICE Collaboration) Phys. Rev. Lett. 113 (2014) 232504.
[31] F. Caola et. al., Nucl. Phys. A854 (2011) 32.
[32] E. Iancu, Nucl. Phys. B191 (2009) 281.
[33] S. Chekanov et al.(ZEUS Collaboration), Eur. Phys. J. C24, 345 (2002).
[34] A. Aktas et al. (H1 Collaboration), Eur. Phys. J. C46, 585(2006).
[35] C. Alexa et al. (H1 Collaboration), Eur. Phys. J. C73, 2466 (2013).
[36] H. Kpwalski et al., Phys. Rev. D74 (2006) 074016
[37] J.L. Abelleira Fernandez et al., arXiv:1211.4831.
[38] website, http://starlight.hepforge.org/
[39] M. B. Ducati et al., Phys. Rev. D88 (2013) 017504.
[40] R. Aaij et al., (LHCb Collaboration) J. Phys. G. 41 (2014) 115002.
[41] R. Aaij et al., (LHCb Collaboration) JHEP 09 (2015) 084.

[42] V.P. Goncalves et al., Phys. Lett B742 (2015) 172.
[43] T. Sjostrand and M. van Zijl, Phys. Rev. D36 (1987) 2006.
[44] E. Abbas et al., (ALICE Collaboration), Eur. Phys. J C73 (2013) 2617.
[45] B. Abelev et al., (ALICE Collaboration), JHEP 02 (2014) 073.
[46] R. Aaij et al., (LHCb Collaboration), JHEP 02 (2014) 72.
[47] B. Abelev et al., (ALICE Collaboration), JHEP 12 (2014) 073.
[48] R. Aaij et al., (LHCb Collaboration), LHCb-CONF-2015-006, CERN-LHCb-CONF-2015-006.

Standard Model – ElectroWeak physics: parallel talks

Proceedings of the LHCP2015 Conference, St. Petersburg, Russia, August 31 - September 5, 2015

Editors: V.T. Kim and D.E. Sosnov

Vector boson production at the LHC: transverse-momentum resummation and leptonic decay

GIANCARLO FERRERA

Dipartimento di Fisica, Università di Milano and INFN, Sezione di Milano, I-20133 Milan, Italy.

giancarlo.ferrera@mi.infn.it

Abstract. We present results for the transverse-momentum (q_T) distribution of W and Z/γ^* bosons produced in hadronic collisions. At small value of q_T, the logarithmically-enhanced perturbative QCD contributions are resummed up to next-to-next-to-leading logarithmic accuracy. Resummed results are consistently combined with the complete $O(\alpha_S^2)$ fixed-order result at small, intermediate and large values of q_T. The leptonic decay of the vector boson is explicitly included with the corresponding spin correlations, the finite-width effects and the full dependence on the final-state lepton(s) kinematics. The recoil due to the transverse momentum of the vector boson is consistently and explicitly treated in the resummed calculation. We present a comparison of some of the available LHC data with the results obtained with the numerical program `DYRes`, which allows the user to apply arbitrary kinematical cuts on the final-state leptons and to compute the corresponding distributions in the form of bin histograms.

Introduction

The production of W and Z/γ^* bosons in hadronic collisions, through the Drell–Yan (DY) mechanism [1], is a process of great importance for physics studies within and beyond the Standard Model.

Accurate theoretical predictions for the DY production cross section and related kinematical distributions require the evaluation of QCD radiative corrections. The total cross section [2] and the rapidity distribution [3] of the vector boson are known up to the next-to-next-to-leading order (NNLO). Two independent fully differential NNLO calculations, which include the leptonic decay of the vector boson, have been performed [4, 5, 6]. Electroweak (EW) [7] and mixed QCD-EW [8] corrections have also been considered.

An observable which is particularly relevant is the vector boson transverse-momentum (q_T). In the region of large q_T ($q_T \sim m_V$, where m_V is the vector boson mass), fixed-order QCD corrections are known analytically up to $O(\alpha_S^2)$ [9, 10, 11, 12, 13] and numerically at $O(\alpha_S^3)$ [14, 15].

Nonetheless the bulk of the vector boson cross section lies in the small-q_T region ($q_T \ll m_V$), where the reliability of the fixed-order expansion is spoiled by the presence of large logarithmic corrections, $\alpha_S^n\ (m_V^2/q_T^2)\ln^m(m_V^2/q_T^2)$ (with $0 \le m \le 2n-1$), due to soft and collinear parton emissions. The reliability of perturbation theory at small q_T can be restored by resumming these logarithmically-enhanced terms to all orders [16]–[25]. Resummed and fixed-order calculations can be consistently matched to achieve a uniform accuracy from small to large values of q_T.

The resummed calculation up to next-to-next-to-leading logarithmic (NNLL) accuracy performed in Refs. [26, 27] have been extended in Ref. [28] to W and Z/γ^* boson. Moreover in Ref. [28] the leptonic decay of the vector boson with the corresponding spin correlations has been explicitly included [1].

The inclusion of the vector boson leptonic decay is particularly important because hadron collider experiments can directly measure only the decay products of vector bosons in finite kinematical regions. By retaining the kinematics of the final-state leptons it is possible to apply in the theoretical calculation the kinematical selection cuts of the corresponding experimental analyses.

The spin of the vector boson dynamically correlates the decaying lepton momenta with the transverse momentum acquired by the vector boson through its production mechanism. Through the resummation procedure at fixed lepton momenta, higher-order contributions due to soft and collinear multiparton radiation dynamically produce a finite value

[1] A detailed discussion of the resummation formalism we have employed can be found in Refs. [21, 22, 23, 25]

of the transverse momentum q_T of the lepton pair which, once distributed between the lepton momenta, affects the lepton angular distribution. This q_T-recoil effect is a non-singular contribution to the q_T cross section at small values of q_T and, therefore, cannot be unambiguously computed through the transverse-momentum resummation formalism. Therefore the inclusion of the full dependence on the lepton decay variables in the resummed calculation requires the implementation of a q_T-recoil prescription [2].

The vector boson computation of Ref. [28] is implemented in the numerical code `DYRes`, which allows the user to apply arbitrary kinematical cuts on the final-state leptons and to compute the corresponding relevant distributions in the form of bin histograms [3]. The code `DYRes` is publicly available and it can be downloaded from the URL address `http://pcteserver.mi.infn.it/~ferrera/dyres.html` .

Numerical results at the LHC

We consider the processes $pp \to Z/\gamma^* \to l^+l^-$ and $pp \to W^\pm \to l\nu_l$ at LHC energies. We present our resummed results at NNLL+NNLO and NLL+NLO accuracy [4], and we compare them with some of the available LHC data. The hadronic cross sections is computed by using the NNPDF3.0 [37] parton densities functions (PDFs) with $\alpha_S(m_Z^2) = 0.118$. The input electroweak parameters in the G_μ scheme (G_F, m_Z, m_W) are taken from the PDG 2014 [38].

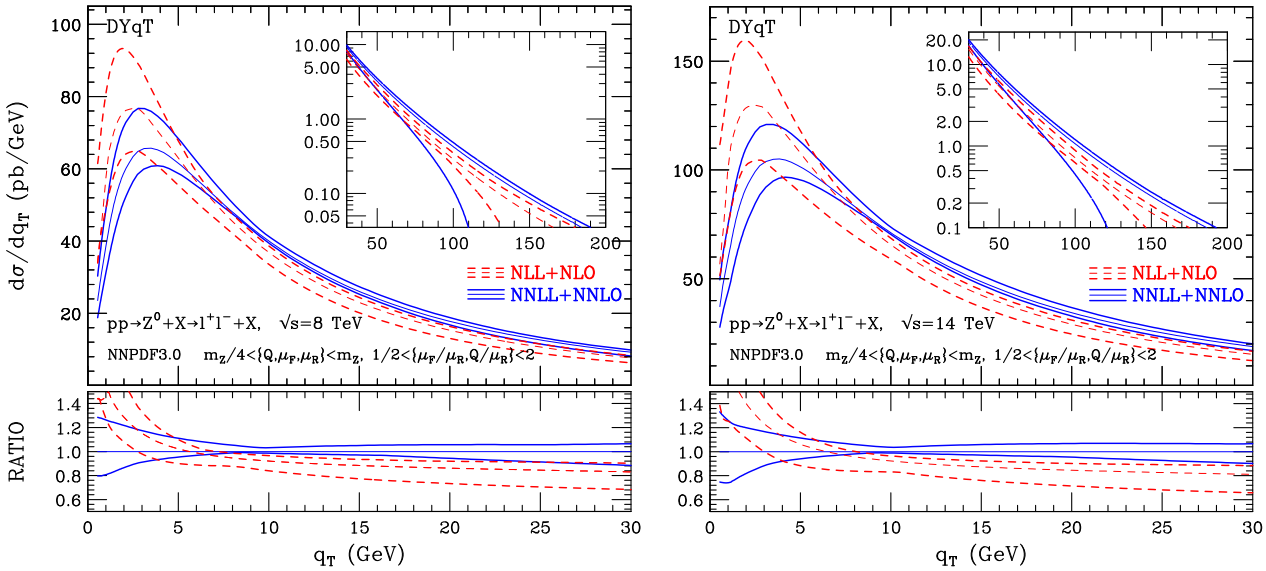

FIGURE 1. NLL+NLO (red dashed) and NNLL+NNLO (blue solid) results for the q_T spectrum of Z bosons at the LHC with energies $\sqrt{s}$ =8 TeV (left panel) and $\sqrt{s}$ =14 TeV (right panel). The lower panel presents the ratio of the scale-dependent NLL+NLO and NNLL+NNLO results with respect to the NNLL+NNLO result at the central value of the scales.

We start the presentation from the inclusive results for the q_T spectrum. The numerical results are obtained by using the `DYqT` code [26, 27] [5].

The NLL+NLO and NNLL+NNLO results for the q_T spectrum of on-shell Z boson produced at the LHC with $\sqrt{s}$ =8 TeV and $\sqrt{s}$ =14 TeV are presented in Fig. 1. At each logarithmic accuracy we present the result at the central value factorization, renormalization and resummation [39] scales, $\mu_F = \mu_R = Q = m_Z/2$, and a corresponding uncertainty band obtained through independent variations of μ_F, μ_R and Q in the range $m_Z/4 \le \{\mu_F, \mu_R, Q\} \le m_Z$ with the constraints $0.5 \le \mu_F/\mu_R \le 2$ and $0.5 \le Q/\mu_R \le 2$. The lower panels in Fig. 1 present the ratio of the

[2] A general and consistent procedure that is directly applicable to q_T resummed calculations for generic production processes of high-mass systems in hadron collisions has been introduced and discussed in Ref. [28].

[3] Analogous calculations were performed for Higgs boson [35] and diboson production [36].

[4] The label NNLO (NLO) refers to the fixed-order perturbative accuracy in the small-q_T region and for the total cross section, the corresponding perturbative accuracy in the large-q_T region is NLO (LO).

[5] The code `DYqT` is publicly available and it can be downloaded from `http://pcteserver.mi.infn.it/~ferrera/dyqt.html` .

scale-dependent NLL+NLO and NNLL+NNLO results with respect to the NNLL+NNLO result at the central value $\mu_F = \mu_R = Q = m_Z/2$ of the scales.

The region of small and intermediate values of q_T is shown in the main panels of Fig. 1. At fixed centre–of–mass energy the NNLL+NNLO q_T spectrum is harder than the spectrum at NLL+NLO accuracy. At fixed value of q_T the cross section sizeably increases by increasing the centre–of–mass energy from 8 TeV to 14 TeV. The shape of the NNLL+NNLO q_T spectrum is slightly harder at the higher energy. The NLL+NLO scale-variation band is wider than the NNLL+NNLO band. The NLL+NLO and NNLL+NNLO bands overlap at small transverse momenta and remain very close by increasing q_T. The NNLL+NNLO (NLL+NLO) scale dependence is about ±10% (±20%) at the peak, it decreases to about ±2% (±7%) at $q_T \simeq 10$ GeV and increases to about ±6% (±10%) at $q_T \sim 25$ GeV.

The inset plots show the cross section in the large-q_T region. The resummation results obtained with `DYqT` and reported in the inset plots are presented for illustrative purposes. At large values of q_T ($q_T \gtrsim m_Z$) the resummed result looses predictivity, and its perturbative uncertainty becomes large. In this region the resummation cannot improve the predictivity of fixed-order calculations and the resummed result has to be replaced by the standard fixed-order prediction.

We have estimated the non perturbative (NP) effects, related to the intrinsic transverse-momentum of partons inside the colliding hadrons, with a simple model which include a free parameter and we have studied the uncertainties related to the parton distribution functions (PDFs). In summary, from our brief analysis on the possible impact of NP effects for vector boson production at the LHC, we conclude that our conservative) estimate leads to quantitative effects that are small and well within the perturbative scale variation dependence, still in the very low q_T region. A quantitatively similar conclusion applies to the effect of PDF uncertainties. Based on these observations we limit ourselves to considering only the perturbative calculation and the corresponding scale variation uncertainties.

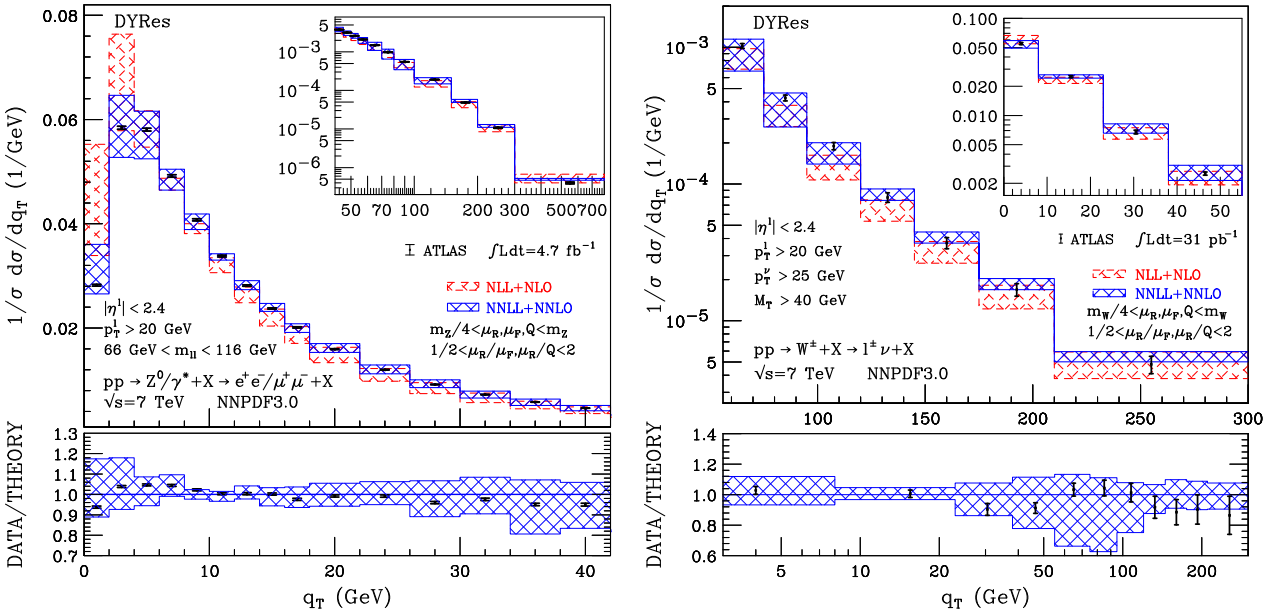

FIGURE 2. Vector boson production at the LHC with lepton selection cuts. The NLL+NLO (red) and NNLL+NNLO (blue) normalized q_T spectra compared with the ATLAS data: Z/γ^* production [40] (left panel) and $W^\pm$ production [42] (right panel). The inset plot shows the ratio of the data and of the scale dependent NNLL+NNLO result with respect to the NNLL+NNLO result at central values of the scales.

We now consider the measurement of the q_T spectrum of dilepton pairs at the LHC with $\sqrt{s} = 7$ TeV, as reported by the ATLAS [40] Collaboration with an integrated luminosity of 4.7 fb^{-1} [6]. The cuts that define the fiducial region in which the measurement is performed (our corresponding calculation is carried out in the same region) are as follows. The invariant mass m_{ll} of the lepton pair is required to be in the range 66 GeV $< m_{ll} <$ 116 GeV, and the leptons must

[6] An analogous measurement of the q_T distribution at the LHC was reported by the CMS Collaboration [41] with a smaller integrated luminosity of 36 pb^{-1}.

be in the central rapidity region, with pseudorapidity $|\eta^l| < 2.4$, and they have a transverse momentum $p_T^l > 20$ GeV.

The results of our resummed calculation are shown in Fig. 2 (a). The blue-solid (red-dashed) histogram is the NNLL+NNLO (NLL+NLO) prediction for the q_T spectrum, which is normalized to the cross section in the fiducial region, and the points are the data with the corresponding experimental errors. The inset plot shows the high-q_T region while the lower panel shows the data and the scale dependent NNLL+NNLO prediction normalized to the NNLL+NNLO result at central values of the scales ($\mu_F = \mu_R = Q = m_Z/2$). The scale dependence band of the perturbative calculation is computed by varying μ_F, μ_R and Q as previously discussed. We see that our perturbative calculation is consistent with the data within the uncertainties and that the scale variation bands at NLL+NLO and NNLL+NNLO accuracy overlap. Moreover, in going from NLL+NLO to NNLL+NNLO accuracy the perturbative uncertainty is reduced and the agreement between experimental data and theory prediction is improved. The perturbative uncertainty at NNLL+NNLO accuracy is about ±10% at the peak, it decreases to about ±4% at $q_T \sim 10$ GeV, and it increases again to about ±10% at $q_T = 40$ GeV.

In Fig. 2 (b) we consider the q_T spectrum of $W^\pm$ bosons. We present a comparison of our resummed results with the $pp \to W \to l\nu$ data collected by the ATLAS Collaboration [42] with an integrated luminosity of 31 pb^{-1} at $\sqrt{s} = 7$ TeV. The fiducial region is defined as follows: the charged lepton has transverse momentum $p_T^l > 20$ GeV and pseudorapidity $|\eta^l| < 2.4$, the missing transverse energy is $p_T^\nu > 25$ GeV, and transverse mass $m_T = \sqrt{2p_T^l\, p_T^\nu(1-\cos(\phi^l - \phi^\nu))}$ is constrained in the region $m_T > 40$ GeV. In the small q_T region, the bin sizes of the experimental data are rather large and in Fig. 2 (b) we focus on the large q_T region 55 GeV $< q_T <$ 300 GeV (the small q_T region is shown in the inset plot). The lower panel of Fig. 2 (b) presents the ratio of both data and theoretical results with respect to the reference theoretical result. The ratio and the scale variation bands are computed as in the case of Fig. 2. We see that our NNLL+NNLO calculation describes the W production data within the perturbative uncertainties. The NNLL+NNLO perturbative uncertainty is about ±8% at the peak, it decreases to about ±4% at $q_T \sim 15$ GeV, and it increases again to about ±15% at $q_T = 50$ GeV.

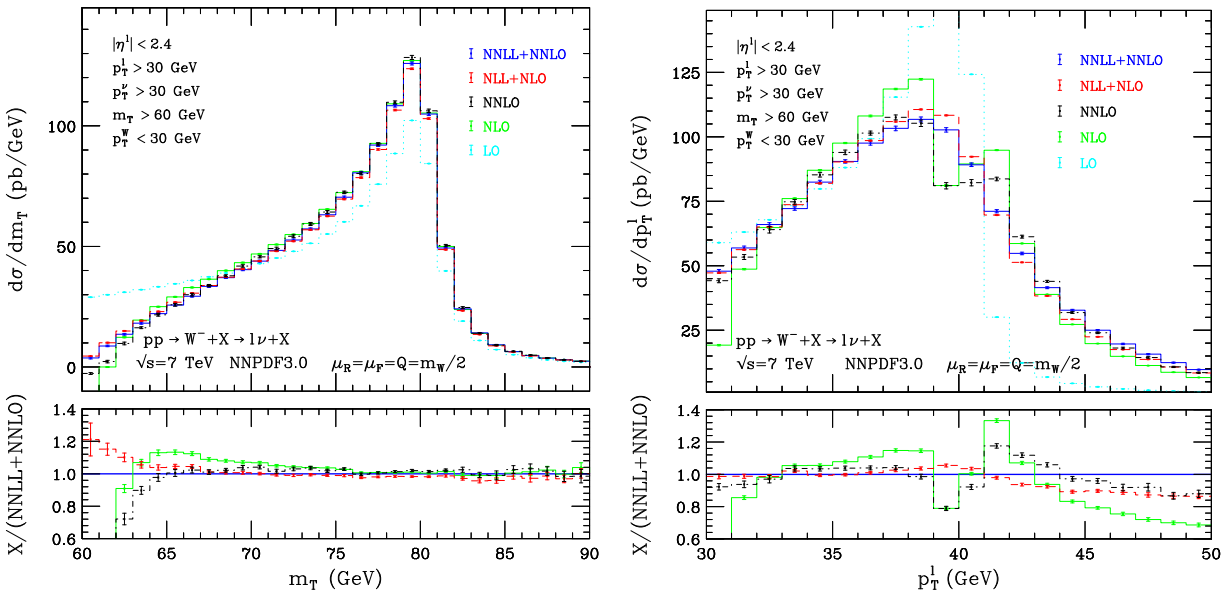

FIGURE 3. Effect of q_T resummation for $pp \to W^- \to l^-\bar{\nu}_l$ production at the LHC: (a) transverse-mass (m_T) distribution and (b) lepton p_T distribution. Comparison of results of the fixed-order calculation at LO (cyan dotted), NLO (green solid) and NNLO (black dot-dashed) with the resummed calculation at NLL+NLO (red dashed) and NNLL+NNLO (blue solid) accuracy. The lower panel shows the ratio between the various results (excluding the LO result) and the NNLL+NNLO result.

We finally study the impact of q_T resummation on some kinematical distributions that are relevant for the measurement of the W mass. We consider $pp \to W^- \to l^-\bar{\nu}_l$ with $\sqrt{s} = 7$ TeV and we apply the following selection cuts: the charged lepton has transverse momentum $p_T^l > 30$ GeV and rapidity $|\eta^l| < 2.4$, the missing transverse momentum is $p_T^\nu > 30$ GeV, and the transverse mass is $m_T > 60$ GeV. We also apply a cut on the transverse momentum p_T^W of the

W boson, $p_T^W < 30$ GeV. The results of our calculation of the m_T distribution and of the lepton momentum distributions are presented in Fig. 3. The reference scale choice of the calculation is $\mu_F = \mu_R = Q = m_W/2$. We present the results of the fixed-order calculation at LO (cyan dotted), NLO (green solid) and NNLO (black dot-dashed) accuracy and we compare them with the results of the q_T resummed calculation at NLL+NLO (red dashed) and NNLL+NNLO (blue solid) accuracy. The lower panel shows the ratio between the various results (excluding the LO result) and the NNLL+NNLO result.

The m_T distribution in the range $m_T < 90$ GeV is presented in Fig. 3 (a). We can consider two regions: the large-m_T region, around $m_T \sim m_W$ and the small-m_T region. In the large-m_T region, we see that the perturbative prediction is extremely stable against radiative corrections. This is a consequence of the well known fact that the transverse mass is weakly sensitive to the transverse momentum of the W boson. On the contrary, in the small-m_T region, we observe that the fixed-order predictions become unreliable. This is due to the fact that the kinematical constraints $p_T^l > 30$ GeV and $p_T^\nu > 30$ GeV produce an unphysical boundary (and a stepwise behaviour) of the m_T distribution at $m_T = 60$ GeV in the LO calculation. The boundary is due to the LO kinematics ($q_T = 0$) and it disappears at higher orders. The LO boundary induces (integrable) logarithmic singularities [43] which are resummed to all order by q_T resummation, and the the resummed prediction is well behaved at the LO boundary.

In Fig. 3 (b) we present the p_T^l distribution. In the limit in which the W boson is produced on shell, this distribution has an LO kinematical boundary at $m_W/2$. The finite width of the W boson (partially) smears this effect: at LO both the p_T^l and p_T^ν distributions are strongly peaked at $m_W/2$ (Jacobian peak) and quickly drop for $p_T \gtrsim m_W/2$. The almost stepwise behaviour of the LO distribution produces large radiative corrections at NLO and beyond [43]. The NLO and NNLO distributions indeed display an unphysical peak at $p_T \sim 42$ GeV, which is an artifact of such large corrections. The resummed predictions at NLL+NLO and NNLL+NNLO accuracy are free of such instabilities and display a smooth *shoulder* behaviour around the LO boundary for on-shell production. The perturbative instabilities of the fixed-order calculation at small values of p_T are analogous to those that we have previously discussed in the case of the m_T distribution in the region $m_T \sim 60$ GeV. The resummed calculation is perturbatively stable in the small-p_T region, and the differences between the NLL+NLO and NNLL+NNLO results are small throughout the entire region with $p_T \lesssim 45$ GeV. In the large-p_T region ($p_T \gtrsim 45$ GeV) the NLO calculation is essentially the first perturbative order at which both the p_T^l distribution is non vanishing and therefore in this region the p_T^l distribution display relatively large radiative corrections.

Summary

We have presented the calculation of the transverse-momentum (q_T) distribution of Drell–Yan high-mass lepton pairs performed in Ref. [28], which is based on the transverse-momentum resummation formalism developed in Refs. [21, 22, 23]. We have performed a perturbative QCD study up to next-to-next-to-leading logarithmic (NNLL) accuracy, combining small-q_T resummation with the complete $O(\alpha_S^2)$ fixed-order result at small, intermediate and large values of q_T. In particular, the calculation exactly reproduces the complete NNLO total cross section after integration over q_T. This leads to theoretical predictions with a controllable and uniform perturbative accuracy over the region from small up to large values of q_T.

In the case of vector boson production at LHC energies, we have estimated the theoretical uncertainties due to uncalculated higher-order QCD corrections by performing a systematic study on factorization, renormalization and resummation scale dependence with the `DYqT` code [26, 27].

We have explicitly included the leptonic decay of the Z/γ^* and W vector bosons with the corresponding spin correlations, the finite-width effects and the full dependence on the final-state leptonic variables, and we have consistently treated in the resummation procedure the q_T recoil due to the transverse momentum of the vector boson.

We have compared our resummed results for Z/γ^* and W production with some of the available LHC data applying the same kinematical cuts on final state leptons that are considered in the experimental analyses. We find that the data are well described by our predictions within the perturbative uncertainties. We have also considered the impact of transverse-momentum resummation on observable, which are different from the vector boson q_T, that depend on the lepton kinematical variables, such as the leptonic transverse-momentum, and the transverse-mass distributions in W production.

Our calculation is implemented in the publicly available parton-level Monte Carlo numerical code `DYRes` which allows the user to apply arbitrary kinematical cuts on the vector boson and the final-state leptons, and to compute the corresponding relevant distributions in the form of bin histograms.

REFERENCES

[1] S. D. Drell and T. M. Yan, Phys. Rev. Lett. **25** (1970) 316 [Erratum-ibid. **25** (1970) 902].
[2] R. Hamberg, W. L. van Neerven and T. Matsuura, Nucl. Phys. B **359** (1991) 343 [Erratum-ibid. B **644** (2002) 403]; R. V. Harlander and W. B. Kilgore, Phys. Rev. Lett. **88** (2002) 201801.
[3] C. Anastasiou, L. J. Dixon, K. Melnikov and F. Petriello, Phys. Rev. D **69** (2004) 094008.
[4] K. Melnikov and F. Petriello, Phys. Rev. Lett. **96** (2006) 231803, Phys. Rev. D **74** (2006) 114017; R. Gavin, Y. Li, F. Petriello and S. Quackenbush, Comput. Phys. Commun. **182** (2011) 2388.
[5] S. Catani, L. Cieri, G. Ferrera, D. de Florian and M. Grazzini, Phys. Rev. Lett. **103** (2009) 082001.
[6] S. Catani, G. Ferrera and M. Grazzini, JHEP **1005** (2010) 006.
[7] S. Dittmaier and M. Kramer, Phys. Rev. D **65** (2002) 073007; U. Baur and D. Wackeroth, Phys. Rev. D **70** (2004) 073015; V. A. Zykunov, Phys. Atom. Nucl. **69** (2006) 1522 [Yad. Fiz. **69** (2006) 1557]; A. Arbuzov et al., Eur. Phys. J. C **46** (2006) 407 [Erratum-ibid. C **50** (2007) 505]; C. M. Carloni Calame, G. Montagna, O. Nicrosini and A. Vicini, JHEP **0612** (2006) 016; U. Baur, O. Brein, W. Hollik, C. Schappacher and D. Wackeroth, Phys. Rev. D **65** (2002) 033007; V. A. Zykunov, Phys. Rev. D **75** (2007) 073019; C. M. Carloni Calame, G. Montagna, O. Nicrosini and A. Vicini, JHEP **0710** (2007) 109; A. Arbuzov et al., Eur. Phys. J. C **54** (2008) 451.
[8] A. Kotikov, J. H. Kuhn and O. Veretin, Nucl. Phys. B **788** (2008) 47; W. B. Kilgore and C. Sturm, Phys. Rev. D **85** (2012) 033005; R. Bonciani, PoS EPS **-HEP2011** (2011) 365; S. Dittmaier, A. Huss and C. Schwinn, Nucl. Phys. B **885** (2014) 318.
[9] R. K. Ellis, G. Martinelli and R. Petronzio, Nucl. Phys. B **211** (1983) 106.
[10] P. B. Arnold and M. H. Reno, Nucl. Phys. B **319** (1989) 37 [Erratum-ibid. B **330** (1990) 284].
[11] R. J. Gonsalves, J. Pawlowski and C. F. Wai, Phys. Rev. D **40** (1989) 2245.
[12] E. Mirkes, Nucl. Phys. B **387** (1992) 3.
[13] E. Mirkes and J. Ohnemus, Phys. Rev. D **51**, 4891 (1995).
[14] R. Boughezal, C. Focke, X. Liu and F. Petriello, Phys. Rev. Lett. **115** (2015) 6, 062002 doi:10.1103/PhysRevLett.115.062002.
[15] A. G. D. Ridder, T. Gehrmann, E. W. N. Glover, A. Huss and T. A. Morgan, arXiv:1507.02850 [hep-ph].
[16] Y. L. Dokshitzer, D. Diakonov and S. I. Troian, Phys. Lett. B **79** (1978) 269, Phys. Rep. **58** (1980) 269; G. Parisi and R. Petronzio, Nucl. Phys. B **154** (1979) 427; G. Curci, M. Greco and Y. Srivastava, Nucl. Phys. B **159** (1979) 451.
[17] J. C. Collins and D. E. Soper, Nucl. Phys. B **193** (1981) 381 [Erratum-ibid. B **213** (1983) 545].
[18] J. C. Collins and D. E. Soper, Nucl. Phys. B **197** (1982) 446.
[19] J. C. Collins, D. E. Soper and G. Sterman, Nucl. Phys. B **250** (1985) 199.
[20] J. Kodaira and L. Trentadue, Phys. Lett. B **112** (1982) 66, report SLAC-PUB-2934 (1982), Phys. Lett. B **123** (1983) 335.
[21] S. Catani, D. de Florian and M. Grazzini, Nucl. Phys. B **596** (2001) 299.
[22] G. Bozzi, S. Catani, D. de Florian and M. Grazzini, Nucl. Phys. B **737** (2006) 73.
[23] G. Bozzi, S. Catani, D. de Florian and M. Grazzini, Nucl. Phys. B **791** (2008) 1.
[24] S. Catani and M. Grazzini, Nucl. Phys. B **845** (2011) 297.
[25] S. Catani, L. Cieri, D. de Florian, G. Ferrera and M. Grazzini, Nucl. Phys. B **881** (2014) 414.
[26] G. Bozzi, S. Catani, G. Ferrera, D. de Florian and M. Grazzini, Nucl. Phys. B **815** (2009) 174.
[27] G. Bozzi, S. Catani, G. Ferrera, D. de Florian and M. Grazzini, Phys. Lett. B **696** (2011) 207.
[28] S. Catani, D. de Florian, G. Ferrera and M. Grazzini, JHEP **1512** (2015) 047.
[29] S. Catani, L. Cieri, D. de Florian, G. Ferrera and M. Grazzini, Eur. Phys. J. C **72** (2012) 2195.
[30] S. Catani, E. D'Emilio and L. Trentadue, Phys. Lett. B **211** (1988) 335.
[31] D. de Florian and M. Grazzini, Phys. Rev. Lett. **85** (2000) 4678, Nucl. Phys. B **616** (2001) 247.
[32] S. Catani and M. Grazzini, Eur. Phys. J. C **72** (2012) 2013 [Eur. Phys. J. C **72** (2012) 2132].
[33] T. Gehrmann, T. Luebbert and L. L. Yang, JHEP **1406** (2014) 155.
[34] S. Catani and M. Grazzini, Phys. Rev. Lett. **98** (2007) 222002.
[35] D. de Florian, G. Ferrera, M. Grazzini and D. Tommasini, JHEP **1111** (2011) 064, JHEP **1206** (2012) 132.
[36] L. Cieri, F. Coradeschi and D. de Florian, JHEP **1506** (2015) 185; M. Grazzini, S. Kallweit, D. Rathlev and M. Wiesemann, JHEP **1508** (2015) 154.
[37] R. D. Ball *et al.* [NNPDF Collaboration], JHEP **1504** (2015) 040.
[38] K. A. Olive *et al.* [Particle Data Group Collaboration], Chin. Phys. C **38** (2014) 090001.
[39] G. Bozzi, S. Catani, D. de Florian and M. Grazzini, Phys. Lett. B **564** (2003) 65.
[40] G. Aad *et al.* [ATLAS Collaboration], JHEP **1409** (2014) 145.
[41] S. Chatrchyan *et al.* [CMS Collaboration], Phys. Rev. D **85** (2012) 032002.
[42] G. Aad *et al.* [ATLAS Collaboration], Phys. Rev. D **85** (2012) 012005.
[43] S. Catani and B. R. Webber, JHEP **9710** (1997) 005.

Proceedings of the LHCP2015 Conference, St. Petersburg, Russia, August 31 - September 5, 2015

Editors: V.T. Kim and D.E. Sosnov

Measurements of Single Electroweak Boson Production in 13 TeV pp Collisions with the ATLAS Detector

JASON NIELSEN

Santa Cruz Institute for Particle Physics, University of California, Santa Cruz 95064 U.S.A.

On behalf of the ATLAS Collaboration

Abstract. The $W \to \ell\nu$ and $Z \to \ell^+\ell^-$ production cross sections have been measured in pp collisions at 13 TeV using 85 pb^{-1} of data recorded with the ATLAS experiment at the LHC. Results are presented for the total cross section and for the cross section in a restricted fiducial phase space. The total inclusive $W^{\pm}$ cross section times single-flavor lepton branching ratio is 19350 ± 20 (stat.) ± 760 (syst.) ± 1740 (lumi.) pb, and the total inclusive Z cross section times leptonic branching ratio is 1869 ± 7(stat.)±42(syst.)±(lumi.) pb. Theoretical predictions of W and Z production, using different PDF sets and Monte Carlo generators, are compared to the ATLAS measurements at 13 TeV.

INTRODUCTION

Measurements of electroweak boson production in hadron-hadron collisions provide a benchmark for our understanding of electroweak (EW) interactions and quantum chromodynamics (QCD). The large cross sections and clean experimental signatures make these measurements a precision test of the Standard Model. Recent calculations include contributions at NNLO in QCD with NLO EW corrections. The measurements at $\sqrt{s} = 13$ TeV represent deep probes into the proton structure and can be used to constrain parton distribution functions at low-x and high Q^2. Ratios of the production cross sections feature reduced experimental uncertainties and offer even more precise comparisons with higher-order calculations.

The cross section for W boson production and decay to a single lepton flavor can be written as

$$\sigma^{\text{tot}}_{W^{\pm}} = \sigma_W \cdot BR(W \to \ell\nu) = \frac{N^{\text{sig}}_W}{A_W \cdot C_W \cdot \mathcal{L}} \tag{1}$$

and similarly for the Z cross section. In this equation, N^{sig}_W represents the number of data events after background subtraction, A_W represents the geometric and kinematic acceptance factor, and C_W represents the correction factor due to experimental efficiencies. The corresponding W fiducial cross section is defined as

$$\sigma^{\text{fid}}_{W^{\pm}} = \sigma^{\text{tot}}_{W^{\pm}} \cdot A_W = \frac{N^{\text{sig}}_W}{C_W \cdot \mathcal{L}} \tag{2}$$

with a similar equation for the Z cross section. The acceptance factors and correction factors are calculated with dedicated Monte Carlo calculations.

The ATLAS experiment [1] collected high-quality data from pp collisions at $\sqrt{s} = 13$ TeV, corresponding to an integrated luminosity of 85 pb^{-1} during June-July 2015. During that period, the LHC circulated 6.5 TeV proton beams with 50 ns bunch spacing. The mean number of additional pp interactions per bunch crossing (pileup) was $\langle\mu\rangle = 19$. The relative uncertainty on the integrated luminosity is estimated to be 9%, using the method described in Ref. [2].

The data are compared to distributions generated with Monte Carlo simulations. Nearly all of the expected distributions were generated with the Powheg-Box v2 Monte Carlo program [3], specifically the codes for single boson production [4], interfaced with the Pythia v.8.186 parton shower program [5]. The programs used the CT10

PDF set [6] and the AZNLO CTEQL1 set of modeling parameters configured for POWHEG+PYTHIA v.8 [7]. All Monte Carlo samples were processed with the GEANT4-based simulation [8] of the ATLAS detector [9].

FIDUCIAL REGION DEFINITION AND EVENT SELECTION

The fiducial region definition emphasizes a common phase space across the electron and muon channels. For W production, the fiducial region is defined by the following: $p_{\mathrm{T}}^{\ell} > 25$ GeV, $p_{\mathrm{T}}^{\nu} > 25$ GeV, $|\eta_{\ell}| < 2.5$, and the transverse mass $m_{\mathrm{T}} > 50$ GeV. For Z production, the fiducial region is defined by $p_{\mathrm{T}}^{\ell} > 25$ GeV, $|\eta_{\ell}| < 2.5$, and $66 < m_{\ell\ell} < 116$ GeV. The geometrical and kinematic acceptances for W and Z production are calculated using the FEWZ 3.1 generator [10, 11] with the CT10NNLO PDFs [6].

Events in the electron and muon channels are selected using triggers that require at least one electron or muon with $p_{\mathrm{T}} > 24$ or 20 GeV, respectively. The electron candidates are identified using a likelihood algorithm based on the measurements of calorimeter shower shapes and measurements of track properties. Electrons are required to be isolated in terms of the electromagnetic calorimeter deposits and charged particle tracks. The electron isolation is tuned so that the efficiency is at least 90% for all $p_{\mathrm{T}} > 25$ GeV. The muon candidates are also required to pass a similar cone-based isolation test, based on both calorimeter and tracking information. The muon isolation is also tuned to maintain 90% efficiency in the same range as the electrons.

The W event selection requires exactly one electron or muon candidate with $p_{\mathrm{T}} > 25$ GeV, missing transverse momentum $E_{\mathrm{T}}^{\mathrm{miss}} > 25$ GeV, and W transverse mass $m_{\mathrm{T}}^{W} > 50$ GeV. The Z event selection requires exactly two electrons or muons of opposite charge with invariant mass $66 < m_{\ell\ell} < 116$ GeV. For inclusive production measurements, no explicit requirements are applied to the hadronic jets that may be present in the events.

BACKGROUND ESTIMATES

Contributions from electroweak backgrounds and top-quark backgrounds are estimated using simulated Monte Carlo samples. The multijet background, which is a dominant background in the W event selection, is calculated by fitting the transverse mass distribution in data. The systematic uncertainty is estimated by using different multijet template distributions in the fit.

The kinematic distributions resulting from the W event selection are shown in Fig. 1. The background distributions, including the multijet background, match the selected data within uncertainties. The kinematic distributions resulting from the Z event selection are shown in Fig. 2. In both figures, the signal normalization is taken from the NNLO FEWZ calculation with the CT10 PDF fit.

CROSS SECTION RESULTS

The central values of the C_W and C_Z correction factors are computed from a combination of simulated samples and data samples. Experimental efficiencies, such as lepton reconstruction, identification, and trigger efficiencies, have been measured with Monte Carlo samples and corrected by data-driven scale factors to take into account differences between data and simulation.

The major systematic uncertainties in the calculation of C_W and C_Z are the electron reconstruction and identification efficiencies, the electron and muon trigger efficiencies, and the jet energy scale and resolution. The uncertainty on the integrated luminosity is not included in these factors but is applied as a separate uncertainty in the cross section calculation.

Because the W and Z production cross sections in the electron and muon channel are expected to reflect the same underlying physics, and because the measured cross sections agree well within uncertainties, the two channels are combined for the fiducial and total cross section results. The combination is performed for the W^+, W^-, and Z boson cross sections simultaneously using the HERAVERAGER program [13]. Correlations between the separate systematic uncertainties are included in the combination.

The combined results of the fiducial and total cross sections for W^+, W^-, $W^{\pm}$, and Z production are shown in Table 1. The total cross section results have been extrapolated from the fiducial results using the corresponding A_W and A_Z acceptance factors.

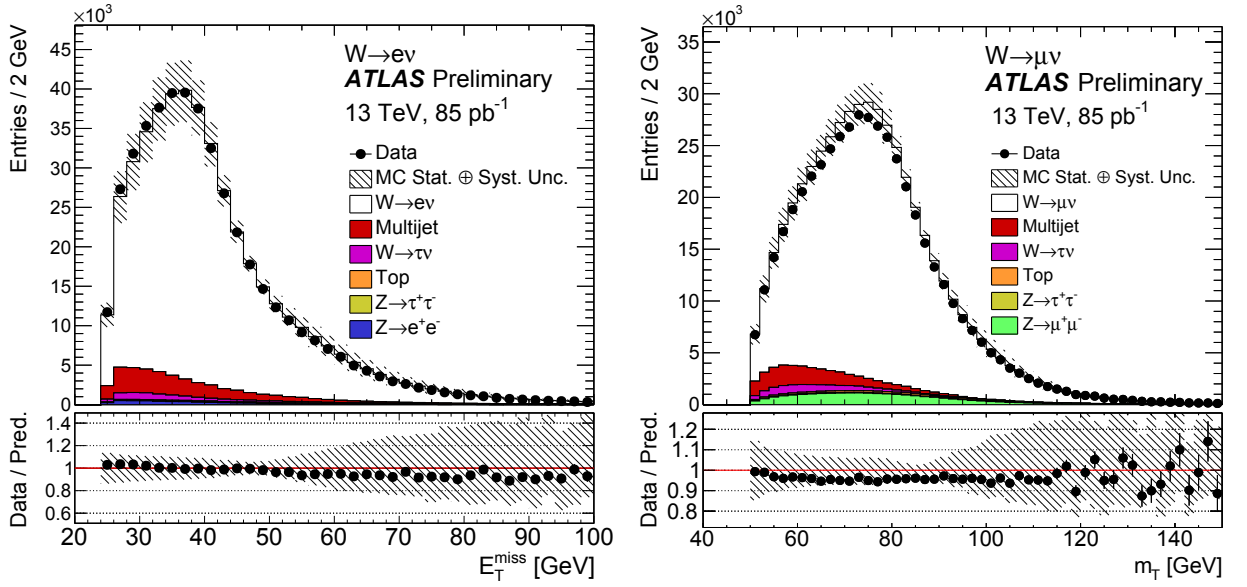

FIGURE 1. Missing transverse momentum distribution from the $W \to e\nu$ selection (left) and transverse mass distribution from the $W \to \mu\nu$ selection (right) [12]. The expected contributions from all backgrounds are estimated with Monte Carlo simulations, except for the multijet background which is estimated with a data-driven method. Combined systematic and statistical uncertainties, not including the luminosity uncertainty, are shown as a shaded band.

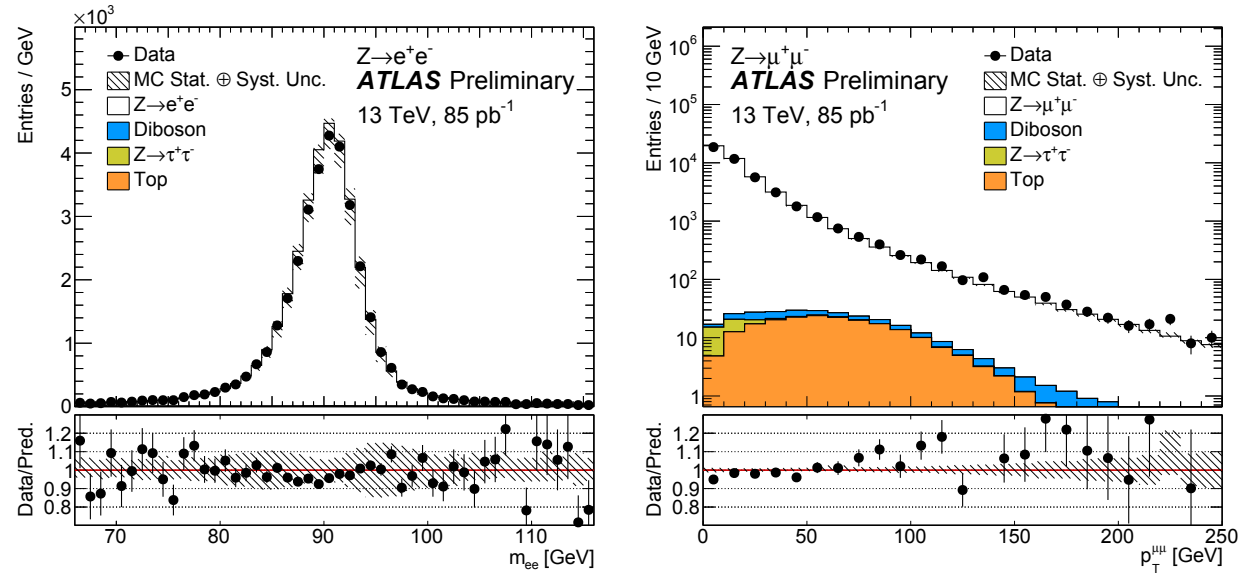

FIGURE 2. Di-electron invariant mass distribution from the $Z \to e^+e^-$ selection (left) and di-muon transverse momentum distribution from the $Z \to \mu^+\mu^-$ selection (right) [12]. The expected contributions from all backgrounds are estimated with Monte Carlo simulations. Combined systematic and statistical uncertainties, not including the luminosity uncertainty, are shown as a shaded band.

TABLE 1. Combined measurements of the fiducial and total cross sections for single boson production in electron and muon channels [12].

Channel	Fiducial cross section value ± stat ± syst ± lumi [pb]	Total cross section value ± stat ± syst ± lumi [pb]
W^-	3344 ± 6 ± 113 ± 301	8380 ± 20 ± 350 ± 750
W^+	4340 ± 7 ± 138 ± 391	10960 ± 20 ± 440 ± 990
$W^\pm$	7684 ± 9 ± 232 ± 692	19350 ± 20 ± 760 ± 1740
Z	746 ± 3 ± 13 ± 67	1869 ± 7 ± 42 ± 168

The measured cross section values can be compared to predictions from the higher-order calculations using different PDF sets. The measurements agree well with predictions, as shown in Fig. 3 for the fiducial cross sections; however, the experimental measurements are dominated by the luminosity uncertainty, which is much larger than the other experimental uncertainties or the PDF uncertainties.

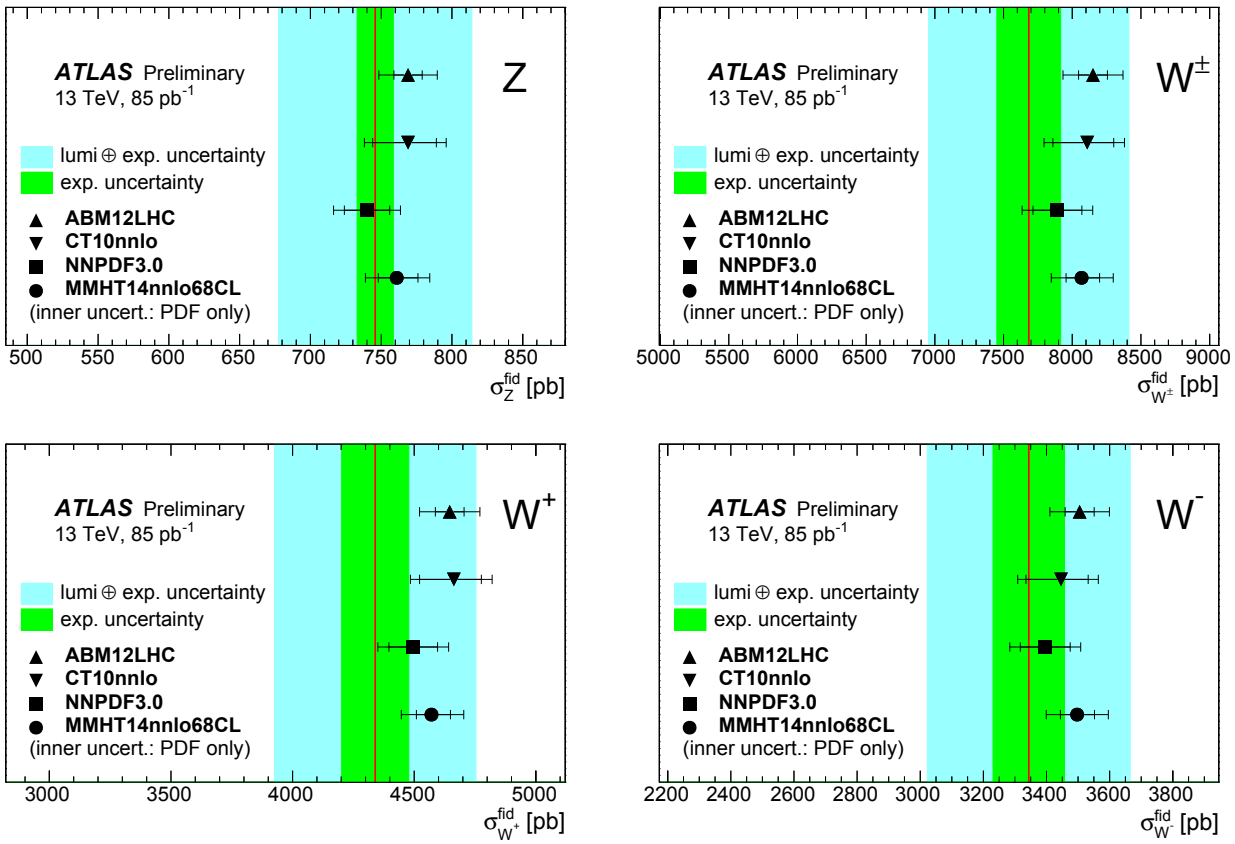

FIGURE 3. Predictions for the combined fiducial cross sections σ_Z^{fid} (top left) and $\sigma_{W^\pm}^{\text{fid}}$ (top right) with various PDF sets, compared to the ATLAS measurement (red line), and for the $\sigma_{W^+}^{\text{fid}}$ (bottom left) and for the $\sigma_{W^-}^{\text{fid}}$ (bottom right) cross sections [12]. The green and cyan bands correspond to the experimental uncertainties with and without the luminosity uncertainty, respectively. The central error bar for each prediction reflects the PDF uncertainty, and the outer error bar includes all systematic uncertainties.

The total production cross section measurements at $\sqrt{s} = 13$ TeV can be compared to measurements at other center-of-mass energies, as shown in Fig. 4. These include the first measurements from the UA1 [14] and UA2 [15] experiments at the CERN $S\bar{p}pS$ and the latest measurements at $\sqrt{s} = 7$ and 8 TeV from the ATLAS [16] and CMS [17, 18] experiments. The new measurements follow the predicted trend as a function of energy.

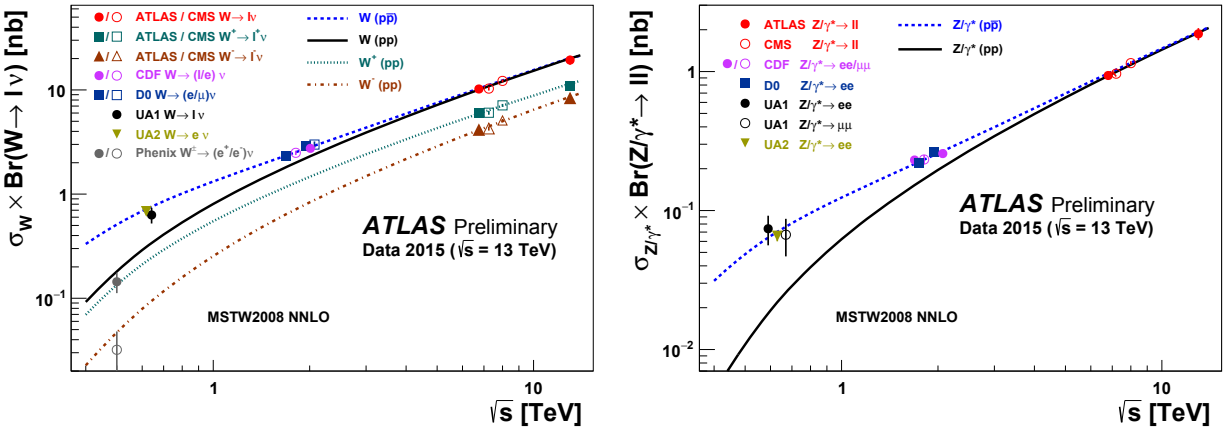

FIGURE 4. Measurements of total cross sections times branching ratios $\sigma_W^{\text{tot}} \times \text{BR}(\text{W} \to \ell\nu$ (left) and $\sigma_Z^{\text{tot}} \times \text{BR}(\text{Z} \to \ell^+\ell^-)$ (right) as a function of center-of-mass energy, compared to predictions from NNLO QCD calculations [12]. All data points are shown with total uncertainties.

The ratios of the measured cross sections feature partial cancellation of some experimental uncertainties. The reduced total uncertainty makes these ratios powerful tools for constraining PDF uncertainties and comparing PDF sets [19]. The ratio of W^+ to W^- boson cross sections is mostly sensitive to the difference of u_v and d_v valence-quark distributions at low Bjorken-x, while the ratio of $W^\pm$ to Z boson cross sections constrains the strange-quark distribution. There is a significant correlation between systematic uncertainties for measurements of the same lepton flavor, especially for the W^+/W^- ratio, and the cancellation of uncertainties is greatest there. The ratios of the W^+/W^- and $W^\pm/Z$ fiducial cross sections are shown in Fig. 5, along with the predictions from the ABM12LHC [20], CT10 [21], NNPDF3.0 [22], and MMHT14 [23] PDF sets.

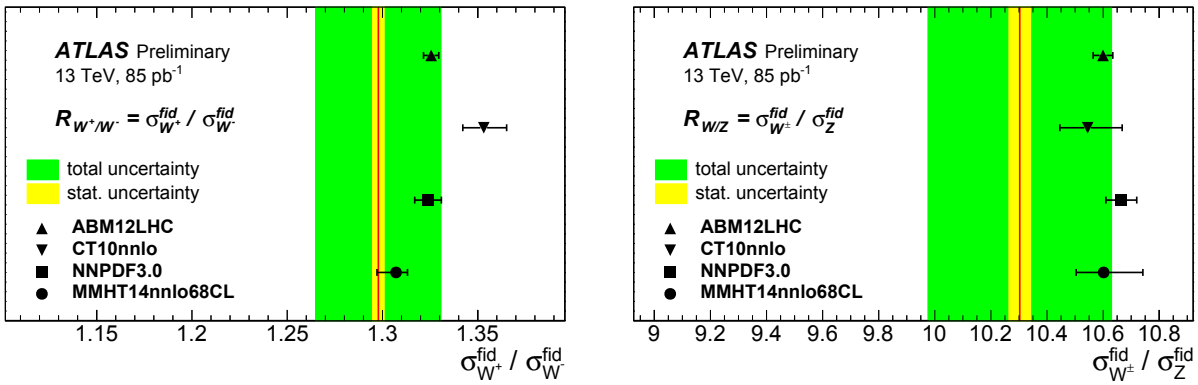

FIGURE 5. Ratio of W^+ to W^- combined fiducial production cross sections (left) and ratio of $W^\pm$ to Z-boson combined fiducial cross sections (right) [12]. The measurements, represented by the solid red lines, are compared to predictions based on various PDF sets. The yellow and green bands correspond to the statistical uncertainty and the total experimental uncertainty, respectively. The error bar for each prediction reflects the PDF uncertainty.

The ratio of W^+ and W^- cross sections, in particular, shows a spread in the predictions from the various PDF sets. The measured result is in agreement with the PDF fits that include LHC measurements from Run 1. The predicted ratio of $W^\pm$ and Z cross sections is consistent among the PDF sets and with the new measured value itself.

SUMMARY

The W and Z production cross sections have been measured in the ATLAS experiment at $\sqrt{s} = 13$ TeV. The results, from a dataset corresponding to an integrated luminosity of $85\,\mathrm{pb}^{-1}$, agree well with the latest NNLO calculations and PDF sets. The total inclusive $W^{\pm}$ cross section times single-flavor lepton branching ratio is $19350 \pm 20\,(\mathrm{stat.}) \pm 760\,(\mathrm{syst.}) \pm 1740\,(\mathrm{lumi.})$ pb, and the total inclusive Z cross section times leptonic branching ratio is $1869 \pm 7(\mathrm{stat.}) \pm 42(\mathrm{syst.}) \pm (\mathrm{lumi.})$ pb. Ratios of the measured cross section achieve partial cancellation of systematic uncertainties and can constrain PDF uncertainties at low-x and high-Q^2 needed for the LHC physics program. Additional details of the measurements can be found with supplementary materials at Ref. [12].

Acknowledgements

It is a pleasure to acknowledge the LHC operations team for the success of the 13 TeV pp run, and the conference organizers for the stimulating meeting environment. This work was supported in part by the U.S. Department of Energy under grant DE-FG02-13ER41983.

REFERENCES

[1] ATLAS Collaboration, JINST **3**, S08003 (2008).
[2] ATLAS Collaboration, Eur. Phys. J. C **73**, 2518 (2013).
[3] S. Alioli et al., JHEP **1006** (2010) 043.
[4] S. Alioli et al., JHEP **0807** (2008) 060.
[5] T. Sjöstrand, S. Mrenna and P. Z. Skands, Comput. Phys. Commun. **178** (2008) 852867.
[6] H.-L. Lai et al., Phys. Rev. D **82** (2010) 074024.
[7] ATLAS Collaboration, JHEP **1409** (2014) 145.
[8] S. Agostinelli et al., Nucl. Instrum. Meth. **A506** (2003) 250303.
[9] ATLAS Collaboration, Eur. Phys. J. C **70** (2010) 823,
[10] K. Melnikov and F. Petriello, Phys. Rev. D **74**, 114017 (2006).
[11] Y. Li and F. Petriello, Phys. Rev. D **86**, 094034 (2012).
[12] ATLAS Collaboration, ATLAS-CONF-2015-039,
https://atlas.web.cern.ch/Atlas/GROUPS/PHYSICS/CONFNOTES/ATLAS-CONF-2015-039.
[13] A. Glazov, AIP Conf. Proc. **792** (2005) 237240.
[14] C. Albajar et al., Phys. Lett. **B198** (1987) 271.
[15] J. Alitti et al., Phys. Lett. **B276** (1992) 365374.
[16] ATLAS Collaboration, Phys. Rev. D **85**, 072004 (2012).
[17] CMS Collaboration, JHEP **10**, 132 (2011).
[18] CMS Collaboration, Phys. Rev. Lett. **112**, 191802 (2014).
[19] J. Rojo et al., arXiv:1507.00556 [hep-ph].
[20] S. Alekhin, J. Blumlein, and S. Moch, Phys. Rev. D **89**, 054028 (2014).
[21] J. Gao et al., Phys. Rev. D **89**, 033009 (2014).
[22] R. D. Ball et al., JHEP **04** 040 (2015).
[23] L. A. Harland-Lang, A.D. Martin, P. Motylinski, and R. S. Thorne, Eur. Phys. J. C **75**, 204 (2015).

Proceedings of the LHCP2015 Conference, St. Petersburg, Russia, August 31 - September 5, 2015

Editors: V.T. Kim and D.E. Sosnov

Measurements of di-boson and tri-boson Production (involving photons) with ATLAS+CMS Detectors

SHU LI

Department of Physics, Duke University, Physics Bldg., Science Dr., Box 90305
Durham, NC 27708, United States of America

shuli@phy.duke.edu

On behalf of the ATLAS and CMS Collaborations

Abstract. We present a broad range of Standard Model measurements of di-boson and tri-boson (involving photons) production cross sections for various decay channels using proton-proton collision data with ATLAS and CMS detectors. The latest results are obtained at the center-of-mass energy of both 7 TeV and 8 TeV and cover the measurements of fiducial cross sections, differential cross sections and the comparison with leading-order/next-to-leading-order/next-to-next-to-leading-order theory predictions. Model-independent limits on anomalous gauge couplings and extra narrow resonances are presented.

INTRODUCTION

Di-boson and tri-boson productions involving photons have relatively larger cross sections than the other massive di-boson and tri-boson channels. The measurements of these processes at LHC experiments provide important tests for perturbative QCD, electroweak multi-boson interactions, electroweak symmetry breaking over a broad kinematic range and constraints for PDFs at TeV scale. In addition, the measurements also provide the direct estimate and understanding of such irreducible Standard Model (SM) backgrounds for Higgs and many other beyond SM (BSM) searches. Using the measured fiducial/differential cross section, model-independent new physics searches can be performed by probing anomalous Triple Gauge Couplings (aTGCs) or anomalous Quartic Gauge Couplings (aQGCs) using effective Lagrangian or effective field theory formalism.

We present the latest measurements of the following topics:

- Measurements of fiducial and differential cross sections of $W^{\pm}(\rightarrow \ell^{\pm}\nu)\gamma$ at $\sqrt{s} = 7$ TeV by both ATLAS and CMS and limits on $WW\gamma$ aTGCs.
- Measurements of fiducial and differential cross sections of $Z(\rightarrow \ell^{+}\ell^{-})\gamma$ and $Z(\rightarrow \nu\nu)\gamma$ at $\sqrt{s} = 7/8$ TeV by ATLAS/CMS and limits on $ZZ\gamma/Z\gamma\gamma$ aTGCs.
- Search for new resonances in $W\gamma/Z\gamma$ final states at $\sqrt{s} = 8$ TeV by ATLAS.
- Search for $W^{\pm}(\rightarrow \ell^{\pm}\nu)V(\rightarrow jj)\gamma$ SM production at $\sqrt{s} = 8$ TeV by CMS and limits on $WW\gamma\gamma/WWZ\gamma$ aQGCs.
- Measurements of fiducial cross sections of $W^{\pm}(\rightarrow \ell^{\pm}\nu)\gamma\gamma$ at $\sqrt{s} = 8$ TeV with first evidence by ATLAS and limits on $WW\gamma\gamma$ aQGCs.

Measurements of fiducial and differential cross sections of $W^{\pm}(\rightarrow \ell^{\pm}\nu)\gamma$ at $\sqrt{s} = 7$ TeV by ATLAS and CMS

The $W^{\pm}\gamma$ production cross section is measured in fully leptonic final states consisting of $W^{\pm} \rightarrow e^{\pm}\nu$ and $W^{\pm} \rightarrow \mu^{\pm}\nu$ decay channels. The measurement is performed in a fiducial region optimized to enrich the $W^{\pm}\gamma$ signal contribution with lepton/photon fake backgrounds suppressed.

ATLAS performed the measurement with 4.6 fb^{-1} of proton-proton (pp) collision data delivered by the LHC in the year of 2011 at $\sqrt{s} = 7$ TeV. A fiducial region is defined for the cross section to be measured by requiring exactly

one lepton with transverse momentum p_{T} greater than 25 GeV and pseudorapidity η up to 2.47, at least one isolated photon with E_{T} (transverse energy) greater than 15 GeV and $|\eta| < 2.37$, missing transverse energy $E_{\mathrm{T}}^{\mathrm{miss}}$ greater than 35 GeV both with and without associated high E_{T} jet (jet-inclusive and jet-exclusive). A separation of photons and charged leptons in the pseudorapidity-azimuthal plane of $\Delta R(\ell, \gamma) > 0.7$ is adopted so as to suppress the contribution from final state radiation (FSR). The fiducial cross sections are measured to be 2.77 ± 0.03 (stat.) ± 0.33 (syst.) ± 0.14 (lumi.) pb for jet-inclusive region and 1.76 ± 0.03 (stat.) ± 0.21 (syst.) ± 0.08 (lumi.) pb for jet-exclusive region, both of which are consistent with next-to-leading-order (NLO) calcuations by the MCFM generator. 1.96 ± 0.17 (syst.) pb (jet-inclusive) and 1.39 ± 0.13 pb (jet-exclusive). The differential cross sections are measured as a function of photon E_{T}, jet multiplicities and m_{T} (transverse mass) of the W boson. Please consult Ref. [1] for details.

CMS performs the measurement with 5.0 fb^{-1} of pp collision data collected in the year of 2011 at $\sqrt{s} = 7$ TeV. The measured fiducial region requires to have exactly one lepton with $p_{\mathrm{T}} > 35$ GeV and $|\eta| < 2.5$, at least one isolated photon with $E_{\mathrm{T}} > 15$ GeV and $|\eta| < 2.5$ as well as $m_{\mathrm{T}}^{W} > 70$ GeV cut for background suppression. The FSR rejection cut $\Delta R(\ell, \gamma) > 0.7$ is applied as in the ATLAS analysis. The measured fiducial cross section is 37.0 ± 0.8 (stat.) ± 4.0 (syst.) ± 0.8 (lumi.) pb in good agreement with the MCFM NLO prediction of 31.8 ± 1.8 (syst.) pb. The differential cross section is measured as a function of photon E_{T}. Please consult Ref. [2] for details.

Figure 1 shows the measured differential cross section as function of E_{T}^{γ} for both ATLAS and CMS.

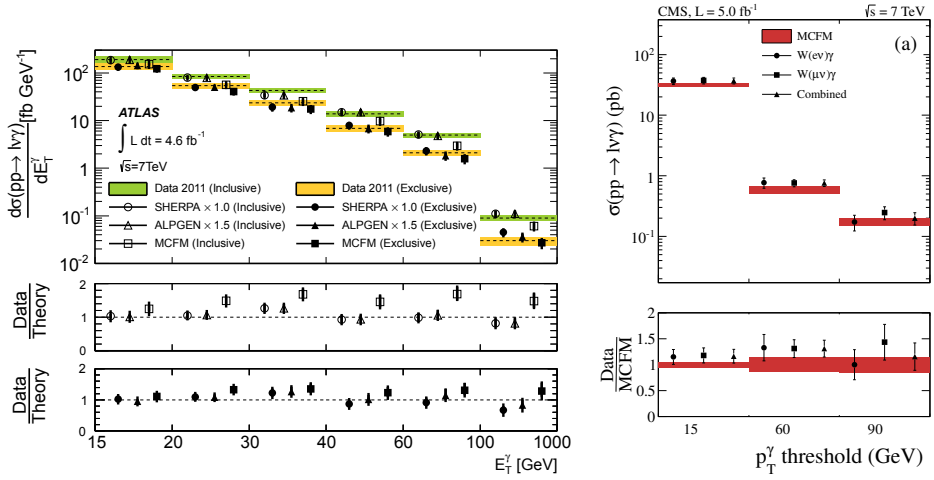

FIGURE 1. $W^{\pm}(\rightarrow \ell^{\pm}\nu)\gamma$ differential cross sections as a function of E_{T}^{γ} for ATLAS (left) and CMS (right). Taken from Ref. [1, 2].

Measurements of fiducial and differential cross sections of $Z(\rightarrow \ell^{+}\ell^{-})\gamma$ and $Z(\rightarrow \nu\nu)\gamma$ at $\sqrt{s} = 7/8$ TeV by ATLAS/CMS

The $Z\gamma$ production cross section is measured in both charged leptonic decay final states ($Z \rightarrow e^{+}e^{-}/\mu^{+}\mu^{-}$) and neutrino final state ($Z \rightarrow \nu\nu$). The fiducial regions are different between charged lepton channels and neutrino channel because of different signal and background characteristics.

ATLAS measures the $Z(\rightarrow \ell^{+}\ell^{-})\gamma$ and $Z(\rightarrow \nu\nu)\gamma$ production with 4.6 fb^{-1} of pp collision data delivered by the LHC in the year of 2011 at $\sqrt{s} = 7$ TeV. The fiducial regions for charged lepton channels are defined to have exactly two same-flavor (SF) opposite-charge (OC) leptons with $p_{\mathrm{T}}^{\ell} > 25$ GeV and $|\eta_{\ell}| < 2.47$, at least one isolated photon with $E_{\mathrm{T}}^{\gamma} > 15$ GeV and $|\eta| < 2.37$. The $\Delta R(\ell, \gamma) > 0.7$ cut is adopted for FSR rejection. Both jet-inclusive and jet-exclusive regions are defined the same way as the aforementioned $W^{\pm}(\rightarrow \ell^{\pm}\nu)\gamma$ measurement in ATLAS. The measured fiducial cross section of charged lepton channels is: 1.31 ± 0.02 (stat.) ± 0.11 (syst.) ± 0.05 (lumi.) pb for jet-inclusive region and 1.05 ± 0.02(stat.) ± 0.10 (syst.) ± 0.04 (lumi.) pb for jet-exclusive region, which is consistent with the MCFM NLO calculation: 1.18 ± 0.05 (syst.) pb for jet-inclusive region and 1.06 ± 0.05 (syst.) pb for jet-exclusive region. Please consult Ref. [1] for details. The differential cross sections of charged lepton channels are measured as a function of photon E_{T}, jet multiplicities and $Z\gamma$ invariant mass.

The fiducial region of $Z(\rightarrow \nu\nu)\gamma$ measurement in ATLAS requires exactly zero charged leptons with the same

charged lepton cuts as the charged lepton channels, $E_{\mathrm{T}}^{\mathrm{miss}}$ greater than 90 GeV and at least one photon with exactly the same η and photon/lepton separation cuts as charged lepton channels but higher E_{T} threshold of 100 GeV. The high $E_{\mathrm{T}}^{\mathrm{miss}}$ and higher E_{T}^{γ} cuts are introduced to suppress the background contamination from fake photon ($e \to \gamma$, $jet \to \gamma$) and fake $E_{\mathrm{T}}^{\mathrm{miss}}$. Both the jet-inclusive fiducial cross section of 0.133 ± 0.013 (stat.) ± 0.020 (syst.) ± 0.005 (lumi.) pb and 0.116 ± 0.010 (stat.) ± 0.013 (syst.) ± 0.004 (lumi.) pb and jet-exclusive fiducial cross section of 0.116 ± 0.010 (stat.) ± 0.013 (syst.) ± 0.004 (lumi.) pb are in good agreement with NLO theory predictions by MCFM, which are 0.156 ± 0.012 (syst.) pb and 0.115 ± 0.009 (syst.) pb, respectively. Please consult Ref. [1] for details.

CMS measures the $Z(\to \ell^+\ell^-)\gamma$ ($Z(\to \nu\nu)\gamma$) production with 19.5 fb^{-1} (19.6 fb^{-1}) of pp collision data collected in the year of 2012 at $\sqrt{s}$ = 8 TeV. The fiducial region for charged lepton channel measurements require to have at least one same-flavor opposite-charged lepton pair with $p_{\mathrm{T}}^{\ell} > 20$ GeV and $|\eta| < 2.5$, one isolated photon with $E_{\mathrm{T}}^{\gamma} > 15$ GeV and $|\eta| < 2.5$ as well as the same photon/lepton separation cut for FSR rejection as ATLAS. The measured fiducial cross section is: 2063 ± 19 (stat.) ± 98 (syst.) ± 54 (lumi.) fb for jet-inclusive in agreement with MCFM NLO prediction of 2100 ± 120 fb and 1770 ± 18 (stat.) ± 115 (syst.) ± 46 (lumi.) fb for jet-exclusive in agreement of MCFM NLO prediction of 1800 ± 120 fb. Figure 2 shows the measured differential cross section in the charged lepton channels by CMS in comparison with theory predictions. In the high E_{T}^{γ} region, the measurement is better described by the next-to-next-to-leading-order (NNLO) prediction and Sherpa leading-order (LO) prediction than MCFM NLO prediction. Please consult Ref. [3] for details.

In the neutrino channel ($Z(\to \nu\nu)\gamma$) of CMS, the fiducial region is defined to have higher E_{T} photon ($E_{\mathrm{T}}^{\gamma} > 145$ GeV) and $E_{\mathrm{T}}^{\mathrm{miss}} > 140$ GeV, which is similarly motivated as ATLAS for the purpose of higher background rejection power. In addition, photons are restricted to have $|\eta| < 1.44$ in the barrel region of the calorimeter which ensures a better purity for reconstructed photons. The measured fiducial cross section is: 52.7 ± 2.1(stat.) ± 6.4(syst.) ± 1.4(lumi.) fb which is consistent with the SM NNLO prediction of $50.0^{+2.4}_{-2.2}$ fb. Please consult Ref. [4] for details.

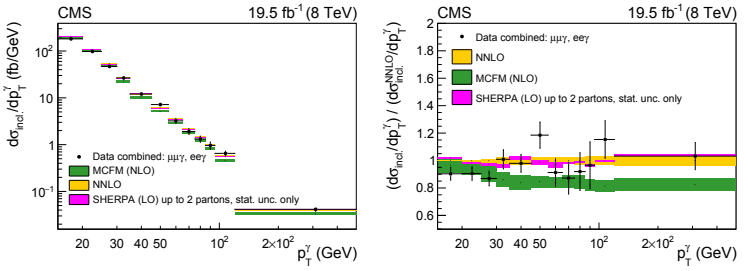

FIGURE 2. $Z(\to \ell^+\ell^-)\gamma$ differential cross sections as a function of E_{T}^{γ} for CMS (left) and its ratio of measurement versus theory prediction (right). Taken from Ref. [3].

Limits on the $WW\gamma/ZZ\gamma/Z\gamma\gamma$ aTGCs

As an extension and further theory implication of the SM measurements, the measured fiducial and differential cross sections can be used to provide model-independent constraints on the new physics using the effective lagrangian parameterizations for aTGCs. Based on the assumption of the C and P conservations separately, the aTGCs are parameterized as λ_γ and $\Delta\kappa_\gamma$ ($\Delta\kappa_\gamma = \kappa_\gamma - 1$) for the $WW\gamma$ vertex, h_3^Z and h_4^Z for the $ZZ\gamma$ vertex, and h_3^γ and h_4^γ for the $Z\gamma\gamma$ vertex. Any deviations of the aTGC parameters from the SM values would lead to an excess observed from data in high E_{T}^{γ} region.

ATLAS uses the measured 7 TeV exclusive fiducial cross section of $W^{\pm}(\to \ell^{\pm}\nu)\gamma$ and $Z(\to \nu\nu)\gamma$ with $E_{\mathrm{T}}^{\gamma} > 100$ GeV cut to set the limits on both the $WW\gamma$ aTGCs (λ_γ and $\Delta\kappa_\gamma$) and the $ZZ\gamma/Z\gamma\gamma$ aTGCs (h_3^Z, h_4^Z, h_3^γ and h_4^γ). Please consult Ref. [1] for details.

CMS sets the limits on the same $WW\gamma$ aTGCs parameters by counting the yield of events in bins of E_{T}^{γ} at $\sqrt{s}$ = 7 TeV with full 2011 pp collision data. Please consult Ref. [2] for details. The limits on the same $ZZ\gamma/Z\gamma\gamma$ aTGCs are set using the measured E_{T}^{γ} spectrum from $Z(\to \nu\nu)\gamma$ channel at $\sqrt{s}$ = 8 TeV with full 2012 pp collision data. Please consult Ref. [4] for details.

The latest 95% C.L. two-dimensional contour limits of $ZZ\gamma/Z\gamma\gamma$ aTGCs by CMS at $\sqrt{s} = 8$ TeV are shown in Figure 3. (Please consult Ref. [4] for details) The summary of all the current ATLAS/CMS $WW\gamma$ and $ZZ\gamma/Z\gamma\gamma$ aTGC limits in comparison with LEP and Tevatron results is shown in Figure 4. Please consult Ref. [5] for details.

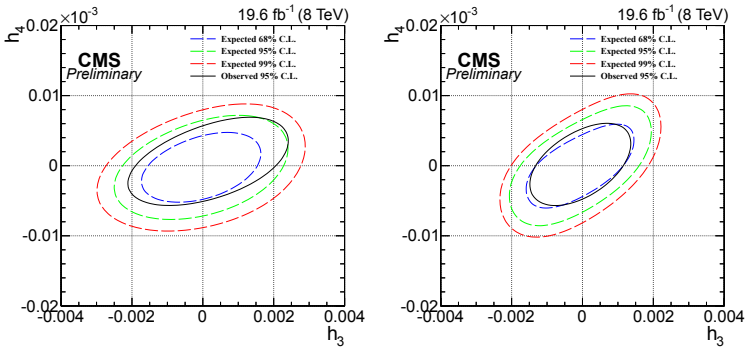

FIGURE 3. The 95% C.L. two-dimensional contour limits of $ZZ\gamma$ (left) and $Z\gamma\gamma$ (right) aTGCs by CMS. Taken from Ref. [4].

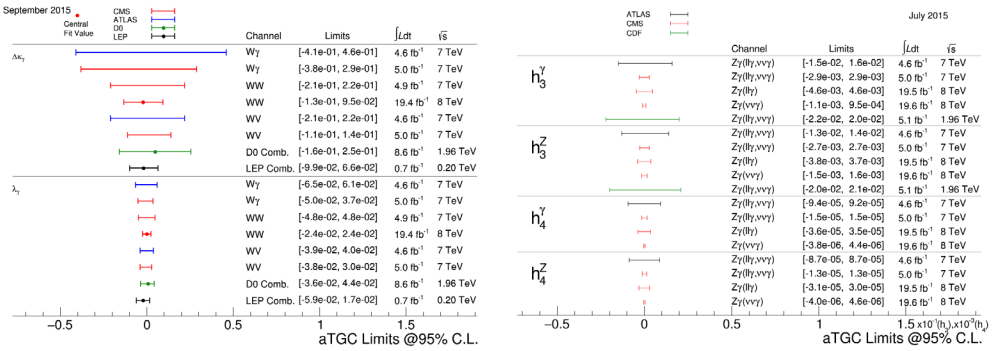

FIGURE 4. The comparison of $WW\gamma$ and $ZZ\gamma/Z\gamma\gamma$ aTGC limits between different experiments. Taken from Ref. [5].

Search for new resonances in $W\gamma/Z\gamma$ final states at $\sqrt{s} = 8$ TeV by ATLAS

In addition to the SM precision measurements of $W\gamma/Z\gamma$ cross sections and search for model-independent boson self-interactions via anomalous triple gauge couplings, ATLAS also provide a first search for narrow vector (spin-1) and scalar (spin-0) high mass resonances in the fully leptonic $W\gamma/Z\gamma$ final states at $\sqrt{s} = 8$ TeV with 20.3 fb^{-1} 2012 full dataset. Low-Scale Technicolor model is used as the benchmark model for the narrow vector resonances of $W\gamma/Z\gamma$. Higgs effective couplings inducing direct narrow scalar resonances of $Z\gamma$ is used to benchmark the scalar model. The three-body invariance mass spectrum of $\ell^+\ell^-\gamma$ is used to set limits on the high mass $Z\gamma$ narrow vector/scalar resonances while the three-body transverse mass spectrum of $\ell^\pm\nu\gamma$ is used to set limits on the the high mass $W^\pm\gamma$ narrow vector resonances. A double exponent function is adopted to fit the $W\gamma/Z\gamma$ mass shape and high mass tail extrapolation. No deviation with respect to SM is observed. The observed model independent limits on $\sigma_{fid} \times BR$ of narrow vector resonances are shown in Figure 5. Please consult Ref. [6] for details.

Search for $W^\pm(\to \ell^\pm\nu)V(\to jj)\gamma$ SM production at $\sqrt{s} = 8$ TeV by CMS and limits on $WW\gamma\gamma/WWZ\gamma$ aQGCs

CMS presents a first search for SM semileptonic $WV(V = W/Z)\gamma$ production at $\sqrt{s} = 8$ TeV with 19.3 fb^{-1} 2012 full dataset in the final state of a W boson decaying into a charged lepton (e/μ) and a neutrino, and a second W or Z boson decaying into hadrons, and a isolated photon. The production is measured in a fiducial region containing a photon with

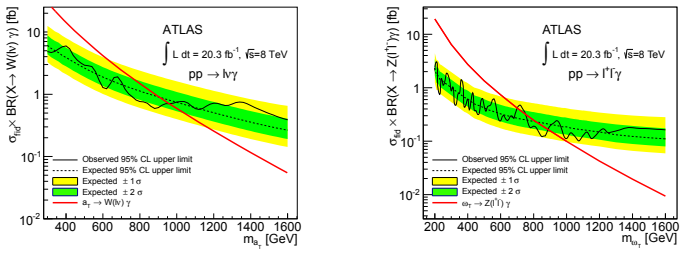

FIGURE 5. The observed model independent limits of narrow vector resonances in $W\gamma$ (left) and $Z\gamma$ (right) final states. Taken from Ref. [6].

$E_{\mathrm{T}} > 30$ GeV and $|\eta| < 1.44$. An upper limit of 311 fb is set on the measured fiducial cross section of semileptonic $WV\gamma$, which is approximately a factor of 3.4 larger than the SM prediction with NNLO QCD calculations. Please consult Ref. [7] for details. The measured $WV\gamma$ process provides a direct probe of BSM new physics signatures which can be parameterized as aQGCs (κ_0^W/Λ^2, κ_C^W/Λ^2, a_0^W/Λ^2, a_0^W/Λ^2 and $f_{T,0}/\Lambda^4$) modifying SM boson self-interactions and inducing high E_{T}^{γ} excesses. Please consult Ref. [8, 9, 10] for details. The measured photon E_{T} spectrum is used to set the limits on these aQGC parameters and binned over the range 30-450 GeV. Please consult Ref. [7] for details. The limits are compared with other experiments along with the latest aQGC limits of $W\gamma\gamma$ by ATLAS as shown in Figure 7. Please consult Ref. [11] for details.

Measurement of $W^{\pm}(\rightarrow \ell^{\pm}\nu)\gamma\gamma$ SM production at $\sqrt{s} = 8$ TeV with evidence by ATLAS and limits on $WWW\gamma$ QGC

ATLAS presents a first measurement of $W^{\pm}(\rightarrow \ell^{\pm}\nu)\gamma\gamma$ SM production at $\sqrt{s} = 8$ TeV with 20.3 fb^{-1} 2012 full dataset. The measured fiducial region is detailed in Table 1 and divided into jet-inclusive and jet-exclusive regions, which is similar to the inclusive $W\gamma/Z\gamma$ measurements in ATLAS. Figure 6 shows the kinematic distributions of $W\gamma\gamma$ with comparisons of data vs signal prediction and background estimates. The measured cross sections are $6.1^{+1.1}_{-1.0}$ (stat.) $\pm$ 1.2 (syst.) $\pm$ 0.2 (lumi.) fb for jet-inclusive region and $2.9^{+0.8}_{0.7}$ (stat.) $\pm^{+1.0}_{-0.9}$ (syst.) $\pm$ 0.1 (lumi.) fb for jet-exclusive region, both of which are in good agreement with MCFM NLO predictions: 2.90 $\pm$ 0.16 (syst.) fb (jet-inclusive) and 1.88 $\pm$ 0.20 (syst.) fb (jet-exclusive). Please consult Ref. [11] for details.

TABLE 1. $W^{\pm}(\rightarrow \ell^{\pm}\nu)\gamma\gamma$ fiducial definition. Taken from Ref. [11].

Definition of the fiducial region for $W^{\pm}(\rightarrow \ell^{\pm}\nu)\gamma\gamma$ measurement
$p_{\mathrm{T}}^{\ell} > 20$ GeV, $p_{\mathrm{T}}^{\nu} > 25$ GeV, $\lvert\eta_{\ell}\rvert < 2.5$
$m_{\mathrm{T}} > 40$ GeV
$E_{\mathrm{T}}^{\gamma} > 20$ GeV, $\lvert\eta_{\gamma}\rvert < 2.37$, iso. fraction $\epsilon_h^p < 0.5$
$\Delta R(\ell,\gamma) > 0.7$, $\Delta R(\gamma,\gamma) > 0.4$, $\Delta R(\ell/\gamma, j) > 0.3$
Exclusive: no anti-k_t jets with $p_{\mathrm{T}}^{jet} > 30$ GeV, $\lvert_{jet}\rvert < 4.4$

The aQGC limits are obtained using high dimension operators $f_{T,0}/\Lambda^4$, a_0^W/Λ^2 and a_0^W/Λ^2 (Please consult Ref. [8, 9, 10] for details) in the jet-exclusive fiducial region with additional cuts on $m_{\gamma\gamma} > 300$ GeV to enhance the sensitivity to the aQGCs of the $WW\gamma\gamma$ vertex. Please consult Ref. [11] for details. The non-unitarized limits are compared with other experiments based on the same parameterization formalism as shown in Figure 7.

SUMMARY

We present a summary of the latest di-boson and tri-boson production measurements by ATLAS and CMS and the corresponding BSM searches with both model-independent aTGC/aQGC parameterizations and high mass narrow resonances. The measured cross sections are presented and compared to high order theory predictions and found to be in good agreement, which provide stringent tests of the electroweak sector of SM. The current aTGC/aQGC limits

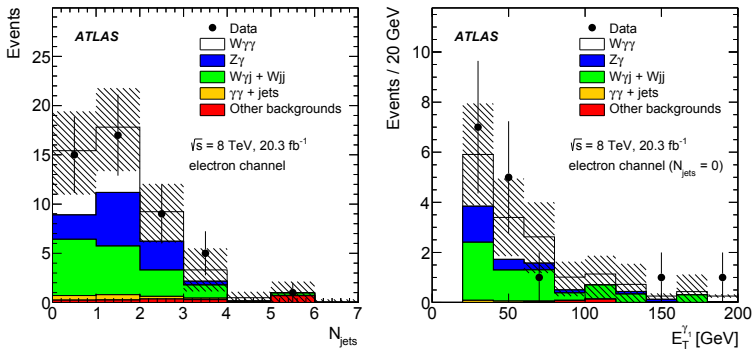

FIGURE 6. The kinematic distributions of $W\gamma\gamma$ candidates for jet multiplicities (left) and photon E_{T}^{γ} (right) spectra. Taken from Ref. [11].

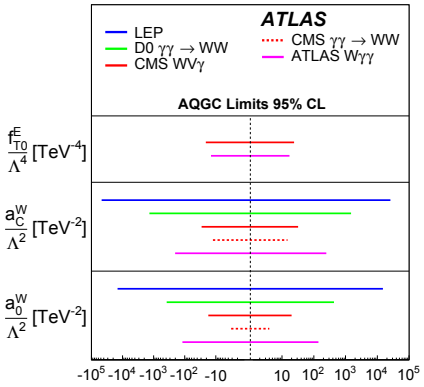

FIGURE 7. Comparisons of $f_{T,0}/\Lambda^4$, a_0^W/Λ^2 and a_0^W/Λ^2 aQGC limits between different experiments. Taken from Ref. [11].

either already surpass the limits from previous experiments such as Tevatron and LEP, or are getting competitive with the previous results.

ACKNOWLEDGMENTS

We thank CERN for the very successful operation of the LHC during Run 1, as well as the support staff from our institutions without whom ATLAS and CMS could not be operated efficiently and produce the outstanding precision measurements and new physics search results.

REFERENCES

[1] ATLAS Collaboration, Phys. Rev. **D91**, p. 112003 (2013).
[2] CMS Collaboration, Phys. Rev. **D89**, p. 092005 (2013).
[3] CMS Collaboration, JHEP **04**, p. 164 (2015).
[4] CMS Collaboration, CMS Note **CMS-PAS-SMP-14-019** (2015).
[5] Https://twiki.cern.ch/twiki/bin/view/CMSPublic/PhysicsResultsSMPaTGC.
[6] ATLAS Collaboration, Phys. Lett. **B738**, 428–447 (2014).
[7] CMS Collaboration, Phys. Rev. **D90**, p. 032008 (2014).
[8] O. J. P. Eboli, M. C. Gonzalez-Garcia, S. M. Lietti, Phys. Rev. **D69**, p. 095005 (2004).
[9] O. J. P. Eboli, M. C. Gonzalez-Garcia, J. K. Mizukoshi, Phys. Rev. **D74**, p. 073005 (2006).
[10] M. Baak *et al.*, (2013), arXiv:1310.6708 [hep-ph] .
[11] ATLAS Collaboration, Phys. Rev. Lett. **115** (2015).

Proceedings of the LHCP2015 Conference, St. Petersburg, Russia, August 31 - September 5, 2015

Editors: V.T. Kim and D.E. Sosnov

Production of heavy vector boson pairs: WW, WZ, ZZ

RICCARDO BELLAN

Università degli Studi di Torino and INFN, dipartimento di Fisica, via P. Giuria 1, 10125 Torino (IT).

On behalf of the ATLAS and CMS Collaborations

Abstract. This article summarises the status of the analysis of heavy vector boson pairs production at $\sqrt{s}$ = 7 TeV and 8 TeV made by the ATLAS and CMS Collaborations. The production of the WW, WZ and ZZ pairs in several decay modes is reported together with limits on anomalous triple gauge couplings, as presented at the LHCP 2015 conference.

INTRODUCTION

Despite the fact that the Standard Model (SM) of particle physics has been proven to be an extraordinary theory capable of predicting the production cross section of several processes spanning over eight order of magnitude, and in addition to that we discovered the Higgs boson, we still have to understand in detail the Electroweak Symmetry Breaking (EWSB) mechanism. The SM is based on a non-Abelian structure and its intimate nature, meaning the interaction among vector bosons, still needs to be fully explored. To do that, it is crucial to deeply understand the final states mediated by the heavy gauge boson pair production, such that the fundamental question to be answered become: do we master them, using our best Standard Model computation? To find a solution to this quest we need to pursue three main roads: measure with high precision the differential cross sections, measure exclusive multiboson production mechanism such as the vector boson scattering and the quartic gauge coupling mediated processes, and finally investigate the high di-boson mass region.

The ATLAS [1] and CMS [2] Collaborations have put in place a huge research program to analyse the production of all vector boson pair combinations, studying them in a plethora of final states, that sometime link together different vector boson production mechanism, as reported in Tab. 1.

TABLE 1. Final states investigated by the ATLAS and CMS and corresponding vector boson pair production.

$\ell\ell\ell'\ell'$	$\ell\ell\ell'\nu$	$\ell^{\pm}\ell^{\pm}\nu\nu$	$\ell\ell\nu\nu$	$\ell\ell b\bar{b}$	$\ell\nu b\bar{b}$	$\ell\nu jj$
ZZ	WZ	$W^{\pm}W^{\pm}$	WW ZZ	ZZ	WZ	WW WZ

In this article some of them are briefly presented.

SEARCH FOR VECTOR BOSON PAIR PRODUCTION IN THE $\ell\ell\ell'\ell'$ FINAL STATE

The primary final state to study the ZZ production is the one with four charged leptons. The ZZ system can be studied with high precision, because the two bosons can be fully reconstructed and the background is two orders of magnitude lower than the signal. The largest background comes from events where jets faking leptons are produced in association with two or three true leptons in the event, mainly originating from Drell-Yan, $t\bar{t}$ and WZ processes, and it is estimated from data. Other sources of background come from genuine, but rare, four-lepton processes like ttZ, WWZ, ttWW and are estimated using Monte Carlo generated events.

The ATLAS and CMS Collaborations, requiring two on-shell Z bosons (the mass windows are slightly different between the two experiments), measured the total production cross section and the differential cross-sections of the

ZZ production as a function of the invariant mass of the diboson system, the leading lepton, Z boson and ZZ pair p_T and other kinematic variables of the process [3, 4]. The results from both Collaborations are in a good agreement with the theoretical expectations, as reported in Fig. 1 (left and centre panel).

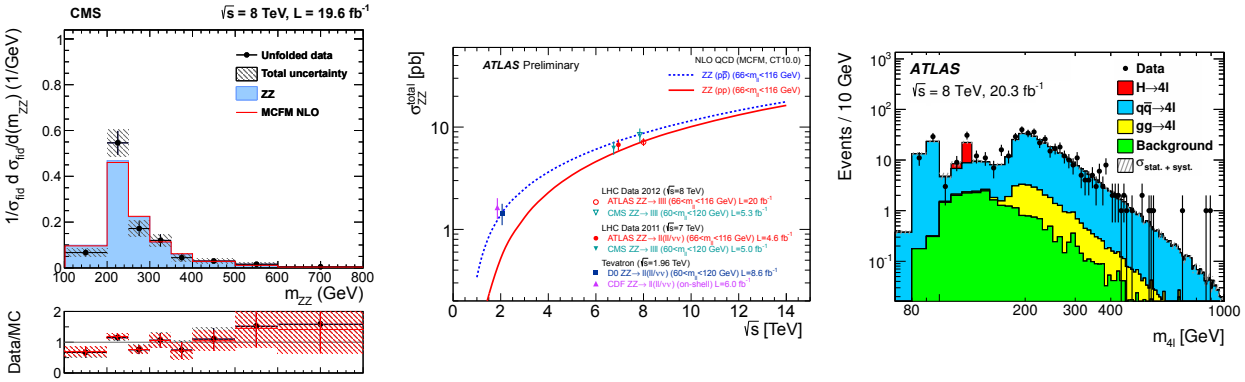

FIGURE 1. Left: Differential cross sections normalised to the fiducial cross section as a function of the invariant mass of the ZZ system, as measured by the CMS Collaboration [3]. Centre: Comparison of experimental measurements and theoretical predictions of the total ZZ production cross section as a function of centre-of-mass energy [4]. Right: Invariant mass distribution of the four-lepton system from data and expectations from different 4ℓ signal production processes plus the estimated background contributions, as measured by the ATLAS Collaboration [4].

ATLAS performed also an analysis of the four-lepton final state relaxing the requirement on the second vector boson mass window, letting it to be slightly off-shell [5]. The analysis selection strategy is similar to the one used for the Higgs boson search made both by the ATLAS [6] and CMS [7] experiments and allows therefore to see not only the ZZ continuum, but also the Higgs resonance and the Z→ 4ℓ decay (Fig. 1 right panel). In this analysis the ratio of the $gg \rightarrow ZZ$ cross section to the one calculated at the leading order is also measured, and the signal strength of the gluon-fusion component relative to its leading-order prediction is determined to be $\mu_{gg} = \sigma_{data}/\sigma_{LO} = 2.4 \pm 1.0(stat.) \pm 0.5(syst.) \pm 0.8(theo.)$.

SEARCH FOR VECTOR BOSON PAIR PRODUCTION IN THE $\ell\ell\ell'\nu$ FINAL STATE

The WZ production where the two bosons decay leptonically is a low background channel, despite the W boson cannot be fully reconstructed without additional external constraint. The understanding of the missing energy sources achieved by the experiments is impressive (Fig. 2) and helps to maintain the background level to be less than a third of the event in the signal region.

Also in this channel the largest background source (estimated from data) is from jets faking leptons and produced association with a weak boson or a top quark, while the second largest contribution comes from ZZ into 4 leptons events where a lepton is not identified as such. The latter is estimated with simulation.

Both the ATLAS and CMS Collaborations [8, 9] report a total cross section measurement compatible with the theoretical prediction at Next-To-Leading precision. For $\sqrt{s} = 8$ TeV: $\sigma_{WZ} = 20.3^{+0.8}_{-0.7}(stat.)^{+1.2}_{-1.1}(syst.)^{+0.7}_{-0.6}(lumi.)$ pb (measured by ATLAS with $66GeV < m_Z < 116GeV$ and $\sigma_{theo} = 20.3 \pm 0.8$ pb) [9], $\sigma_{WZ} = 24.61 \pm 0.76(stat.) \pm 1.13(syst.) \pm 1.08(lumi.)$ pb (measured by CMS with $71GeV < m_Z < 111GeV$ and $\sigma_{theo} = 21.91^{+1.17}_{-0.88} \pm 0.8$ pb) [8].

SEARCH FOR VECTOR BOSON PAIR PRODUCTION IN THE $\ell\ell\nu\nu'$ FINAL STATE

The largest production cross-section for a heavy vector boson pair is the one of WW. However, the inability to fully reconstruct the kinematics of the di-boson system and the contamination coming from processes with a very similar final states to the signal make this analysis more challenging than the ones that look for ZZ and WZ pairs. The complete phase space is dominated by events coming from $t\bar{t}$ decays, thus only the region with low jet multiplicity can be directly explored (Fig. 3 left panel).

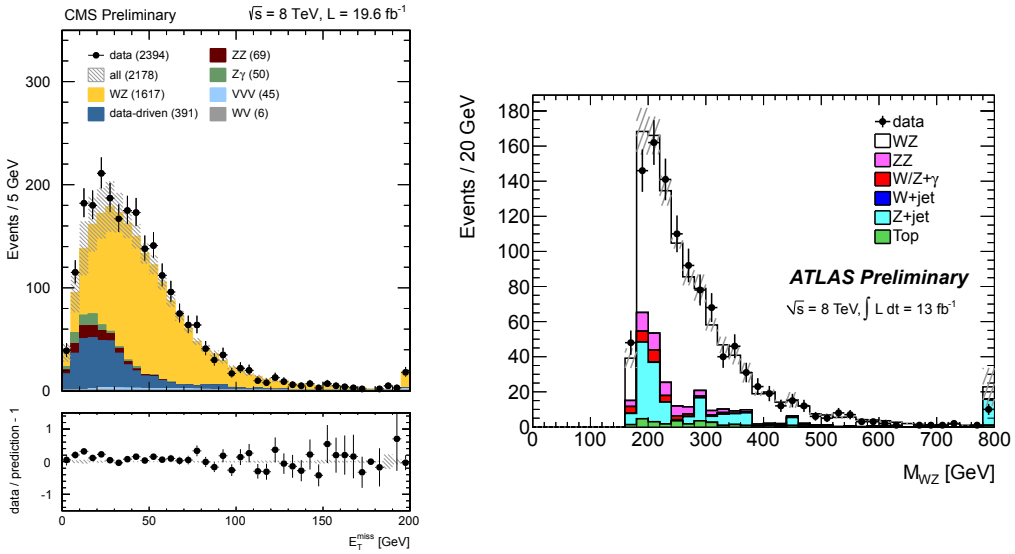

FIGURE 2. Left: Missing transverse energy in the WZ search region, as measured by the CMS Collaboration [8]. Right: Distributions of the invariant mass of the WZ system, as measured by the ATLAS Collaboration [9].

ATLAS [10] studied only the 0-jet region, applying a jet-veto to the analysis, while CMS [11] studied the final states with 0-jet and the 1-jet (Fig. 3 centre and right panel). Both ATLAS and CMS use theoretical calculation to extrapolate the cross-section measurement from the low (or vetoed) jet multiplicity region to the total phase space. CMS however modelled the dominant $q\bar{q}$ component by resumming the large higher-order corrections to the WW p_T, that indirectly corrects the jet p_T spectrum, thus improving the accuracy on the signal rate predicted theoretically in each single jet bin category. This could explain why the total WW production cross-section measured by CMS ($\sigma_{WW} = 60.1 \pm 0.9(stat.) \pm 3.2(exp.) \pm 3.1(theo.) \pm 1.6(lumi.)$ pb) is closer to the theoretical prediction made at Next-To-Next-Leading-Order precision ($\sigma_{theo} = 59.8^{+1.3}_{-1.1}$ pb) than the value measured by the ATLAS Collaboration ($\sigma_{WW} = 71.4 \pm 1.2(stat.)^{+5.0}_{-4.4}(syst.)^{+2.2}_{-2.1}(lumi.)$ pb).

The CMS Collaboration presented also the differential cross section as a function of several kinematic variables such as the leading lepton p_T, the transverse momentum of the dilepton system, the invariant mass $m_{\ell\ell}$ and the angular separation between leptons, and compared them with different Monte Carlo event generators such as MADGRAPH, POWHEG, and MC@NLO [11, ref. therein]. The final outcome is that none of the simulation taken into account perform better than the other in all variables, but each of them in turn can describe the shapes extracted from data (with the exception of $d\sigma_{WW}/d\Delta\phi_{\ell\ell}$ which is not well described by any of them).

HADRONIC DECAYS OF ONE OF THE VECTOR BOSON

Despite the low signal-to-background ratio compared to the fully leptonic channels, a diboson signal can still be clearly observed from events in which one boson decays leptonically and the other hadronically. ATLAS and CMS both use a template fit analysis to the invariant mass of the dijet system distribution to extract the signal from WV events, where V = W,Z and $W/Z \to jj$ [12, 13]. These analysis are done with 7 TeV data, where the surrounding jet activity is not yet prohibitive.

On 8 TeV data the CMS Collaboration studied also the VZ production where Z decays into a $b\bar{b}$ pair and V is either a W or a Z that decays leptonically [14]. This analysis uses control regions to normalise the simulation and then it exploit a boosted decision tree (BDT) technique to extract the signal.

Figure 4 shows the outcome of the inclusive jet-jet analysis (left) and the $b\bar{b}$ one (right).

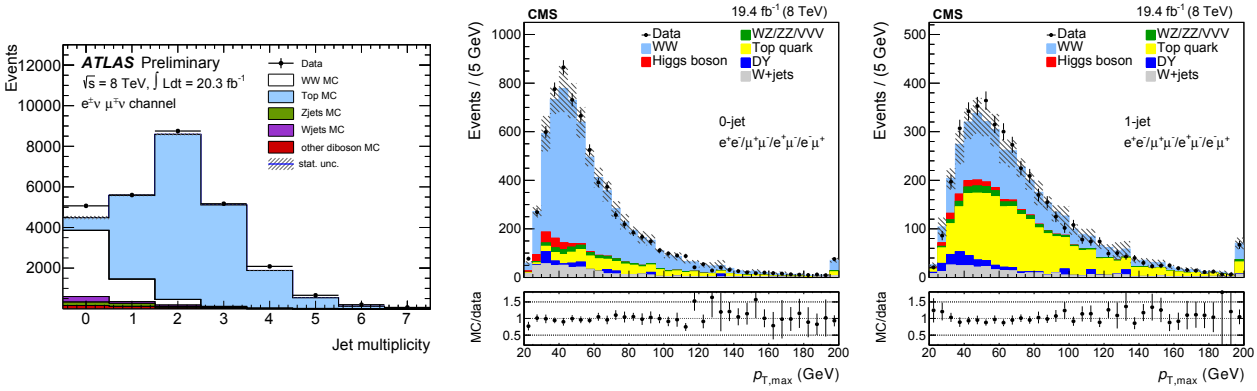

FIGURE 3. Jet multiplicity distributions for $e\mu$ events (left), as measured by the ATLAS Collaboration in the WW $\rightarrow \ell\ell\nu\nu'$ search analysis [10]. The data and MC distributions for the zero-jet category (centre) and one-jet category (right) of the leading lepton p_T, as measured by the CMS Collaboration [11].

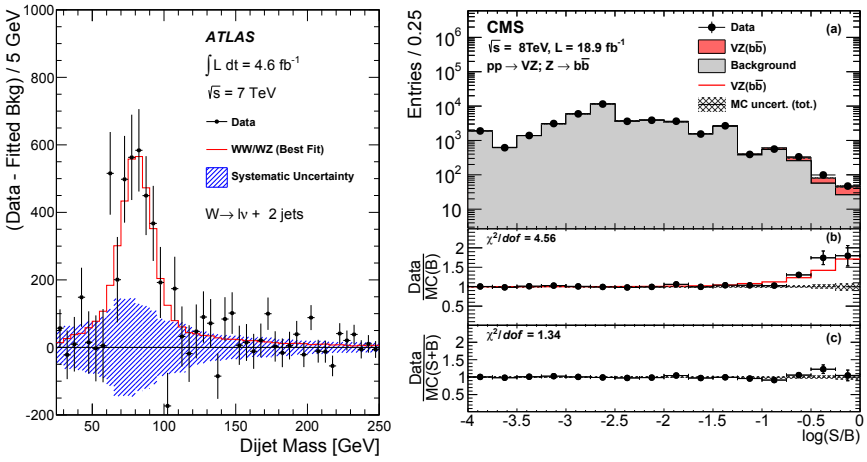

FIGURE 4. Left: Distribution of the background-subtracted data for the sum of the electron and muon channels of the di-jet invariant mass [13]. The superimposed histogram shows the fitted signal and the hatched band shows the systematic uncertainty on the background after profiling the nuisance parameters. Right: (a) Combined distribution for all channels in the value of the logarithm of the ratio of signal to background (S/B) discriminants in data and in Monte Carlo (MC) simulations, based on the outputs of the S and B BDT discriminants for each event [14]. The two bottom panels display (b) the ratio of the data and of the SM expectation relative to the background-only hypothesis, and (c) data relative to the expected sum of background and VZ signal.

aTGC

The study of the anomalous vector boson couplings enables the search for new physics phenomena at the same time as performing Standard Model electroweak measurements, looking for deviations from the Standard Model predictions in the tail of distributions such as the invariant mass of the diboson (m_{VV}), dilepton ($m_{\ell\ell}$) or dijet m_{jj} system, or the transverse momentum of the reconstructed vector boson ($p_{T,V}$). The new physics can be parametrised adding terms to the Standard Model lagrangian. Several possibilities can be implemented: the effective vertex approach [15], used in ZZ analysis; the effective lagrangian approach [16], used in WV analyses and the effective field theory approach [17], used in WW, vector boson scattering and triboson analyses. Usually the additional parameters in the lagrangian are varied one-by-one or at most two-by-two, as there is little correlation among them.

Neither ATLAS nor the CMS Collaboration reported any significant deviation from the Standard Model expectations. In the two tables displayed in Fig. 5 are reported the current limits on the anomalous triple gauge couplings.

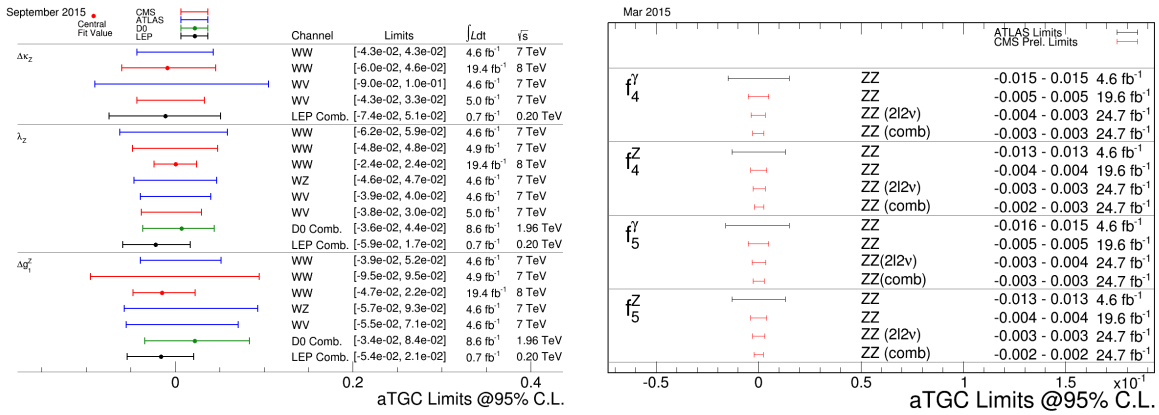

FIGURE 5. Left: Limits on WWZ aTGC couplings [11, 12, 13, 18, 19, 20, 21, 22]. Right: Limits on neutral aTGC ZZγ and ZZZ couplings are presented. In the Standard Model all neutral triple gauge couplings are zero at tree level [3, 23, 24].

CONCLUSIONS

We discovered a Higgs boson, yet the comprehension of the Electroweak Symmetry Breaking is not completed: understanding the multiboson production is the key point, because its complementary with the Higgs boson properties studies and high mass searches. The ATLAS and CMS Collaboration put in place a tremendous set of analyses on 7 and 8 TeV data to explore the multiboson final states setting limits on possible deviation from the Standard Model predictions.

The time of multiboson production is coming, the *new frontier* will be the study of VV+jets, vector boson scattering and triboson production processes: they will among of the hot topic of LHC Run II!

REFERENCES

[1] ATLAS Collaboration, JINST **3**, p. S08003 (2008).
[2] CMS Collaboration, JINST **3**, p. S08004 (2008).
[3] CMS Collaboration, Phys. Lett. B **740**, p. 250 (2015).
[4] ATLAS Collaboration, ATLAS-CONF-2013-020 (2013).
[5] ATLAS Collaboration, Phys. Lett. B **753**, p. 552 (2016).
[6] ATLAS Collaboration, Phys. Rev. D **91**, p. 012006 (2015).
[7] CMS Collaboration, Phys. Rev. D **89**, p. 092007 (2014).
[8] CMS Collaboration, CMS-PAS-SMP-12-006 (2012).
[9] ATLAS Collaboration, ATLAS-CONF-2013-021 (2013).
[10] ATLAS Collaboration, ATLAS-CONF-2014-033 (2014).
[11] CMS Collaboration, arXiv:1507.03268 (2015).
[12] ATLAS Collaboration, JHEP **01**, p. 049 (2015).
[13] CMS Collaboration, Eur. Phys. J. C **73**, p. 2283 (2013).
[14] CMS Collaboration, Eur. Phys. J. C **74**, p. 2973 (2014).
[15] K. Hagiwara *et al.*, Nucl. Phys. B **282**, 253–307 (1987).
[16] K. Hagiwara *et al.*, Phys. Rev. D **41**, 2113–2119 (1990).
[17] K. Hagiwara *et al.*, Phys. Rev. D **48**, p. 2182 (1993).
[18] ATLAS Collaboration, Phys. Rev. D **87**, p. 112001 (2013).
[19] CMS Collaboration, Eur. Phys. J. C **73**, p. 2610 (2013).
[20] ATLAS Collaboration, Eur. Phys. J. C **72**, p. 2173 (2012).
[21] D0 Collaboration, Phys. Lett. B **718**, p. 451 (2012).
[22] ALEPH, DELPHI, L3, OPAL, LEP Electroweak Collaboration, Phys. Rept. **532**, p. 119 (2013).
[23] ATLAS Collaboration, JHEP **03**, p. 128 (2013).
[24] CMS Collaboration, Eur. Phys. J. C **75**, p. 511 (2015).

Proceedings of the LHCP2015 Conference, St. Petersburg, Russia, August 31 - September 5, 2015

Editors: V.T. Kim and D.E. Sosnov

Vector Boson Scattering at LHC

LINDA FINCO

INFN and University of Torino, Via P. Giuria 1 Torino, Italy.

linda.finco@cern.ch

On behalf of the ATLAS and CMS Collaborations

Abstract. Vector boson scattering provides an important test of the Standard Model and of the dynamics of the electroweak symmetry breaking mechanism. An overview of measurements of vector boson scattering processes is presented. The analyzed data are collected at a center-of-mass energy of 7 and 8 TeV by the ATLAS and CMS detectors at the Large Hadron Collider. The results are compared with Standard Model predictions and are interpreted in terms of constraints on anomalous gauge couplings. Future projections of vector boson scattering analyses at the High-Luminosity LHC are also summarized.

INTRODUCTION

The Standard Model (SM) is the most detailed theory to explain the Modern Physics. Thanks to accurate theoretical predictions and good understanding of detector performances, the measurements of the SM processes are very precise. Nevertheless, there is still much to be done: the discovery of the Higgs boson in 2012 has opened up further questions that have to be addressed. After this discovery, the most urgent experimental task is to test if the Higgs boson is the only responsible for the electroweak symmetry breaking (EWSB) mechanism and, if it is not, understand which alternative theory is at work. The high energy vector boson scattering (VBS) plays a central role in answering these questions. In the following, the analyses on vector boson scattering processes carried out by both the ATLAS [1] and CMS [2] Collaborations at 7 and 8 TeV are summarized. Furthermore, future projections at the High-Luminosity LHC are reported.

VECTOR BOSON SCATTERING AND ANOMALOUS GAUGE COUPLINGS

The production processes involving the scattering of two massive vector bosons, VV→ VV with V = W or Z, provide useful information on the validity of the SM and, in particular, they could be the final test of the nature of the Higgs boson. Through the Higgs mechanism the W and Z bosons get mass and, consequently, they acquire also the longitudinal degree of freedom. From theoretical calculations it can be seen that the scattering amplitudes of longitudinally polarized vector bosons increase as a function of the center-of-mass energy $\sqrt{s}$ and violate unitarity at 1-1.5 TeV. Since unitarity is essentially the statement of conservation of total probability, it cannot be violated in nature and some phenomena must intervene. In the SM framework these divergences are totally canceled by the diagrams in which a Higgs boson is exchanged. The study of VBS processes is thus particularly important in order to probe the nature of the EWSB mechanism and check if the unitarity is completely restored by it.
Understanding which is the correct theory is therefore a crucial task and can be accomplished at hadron colliders. Here VBS can be idealized as an interaction of gauge bosons radiated from initial-state quarks, yielding a final state with two bosons and two jets in a purely electroweak process. Vector boson scattering interactions are rare, but carry a very peculiar hallmark which can be explored experimentally: the two jets produced in association with the boson pair are expected to have a very high energy. These jets, that originate from the fragmentation of the initial-state quarks in electroweak processes, are characterized also by a large separation in (pseudo)rapidity $(\Delta\eta_{jj})\Delta y_{jj}$ and a large invariant mass (m_{jj}). These features yield the best separation power with respect to the events produced via strong interactions, that are the main background.
The non-abelian nature of the electroweak sector predicts the self interaction of electroweak gauge bosons in the form

of triple and quartic gauge boson couplings (TGC and QGC). Triboson production and VBS are directly sensitive to QGCs and their in-depth analysis provides complementary ways to study them. If any deviation from the SM predictions is observed, independent tests of the triple and quartic gauge boson couplings can give important information on the type of new physics responsible for the departures from the SM. New physics can be searched using essentially two strategies [3]: by looking for new phenomena directly, or by looking for novel interactions of the known particles of the SM. Focusing on the latter method, one can extends the SM Lagrangian by adding higher-dimension operators:

$$\mathcal{L} = \mathcal{L}_{SM} + \sum_i \frac{c_i}{\Lambda_i^2} O_i + ..., \tag{1}$$

where O_i are the higher dimension operators proportional to inverse powers of Λ, the mass scale that characterizes the coefficients of these operators and can be regarded as the scale of new physics. By dimension analysis, the dimension-six operators are expected to be dominant and they may affect three- and four-boson vertices, while dimension-eight operators modify quartic-boson interactions only.

ANALYSES IN RUN 1

Using data at 7 and 8 TeV collected during the Run I, it is possible to start exploring vector boson scattering processes through the study of different interactions. In the following, a summary of the published results achieved by both ATLAS and CMS Collaborations is reported, in order to present the current state on this subject.

Z + Forward-Backward Jets (8 TeV)

This analysis investigates the electroweak production of a Z boson in association with 2 jets, which is not truly a vector boson scattering process, given that only a single boson (and not a pair of bosons) is produced. Nevertheless, it presents very interesting features: it has a comparable cross section and a very similar topology to the vector boson fusion production of the Higgs boson, it is sensitive to new physics since involves the WWZ triple vertex and the two jets produced in association with the Z boson have the same characteristics of the VBS tagging jets. This process can thus be exploited to refine forward-jet selection and is very useful for vector boson scattering analyses.
In proton-proton collisions at LHC the dominant source of production of a Z boson followed by a leptonic decay $Z \to \ell\ell$ in association with two jets is through mixed electroweak and strong processes of order $O(\alpha_{EW}^2 \alpha_S^2)$. Pure electroweak productions of the $\ell\ell jj$ final state, of order $O(\alpha_{EW}^4)$, are rarer and include vector boson fusion (VBF) processes, of particular interest because similar to the VBF production of a Higgs boson and sensitive to anomalous WWZ triple gauge couplings. This analysis is performed by both ATLAS and CMS Collaborations using the data-set collected at 8 TeV, with an integrated luminosity of about 20 fb^{-1} [4, 5]. In both analyses the signal is defined requiring a single Z boson decaying into a lepton pair ($Z \to e^+e^-, \mu^+\mu^-$) and two high energy jets, with large $\Delta\eta_{jj}$ (or Δy_{jj}) and m_{jj}. The ATLAS Experiment presents a measurement of fiducial cross sections and differential distributions of *inclusive* Z + 2 jets production, dominated by processes via strong interaction. These measurements are performed in five fiducial regions with different sensitivity to the electroweak component. The number of signal events produced via electroweak interaction is extracted by fitting the di-jet invariant mass reconstructed in the *search region*, the fiducial region in which the electroweak component is more enhanced. The corresponding fiducial cross section is $\sigma_{EW}^{search} = 54.7 \pm 4.6\ (stat.)^{+9.8}_{-10.4}\ (syst.) \pm 1.5\ (lumi.)$ fb. The theoretical prediction is $46.1 \pm 0.2\ (stat.)^{+0.3}_{-0.2}\ (scale) \pm 0.8\ (PDF) \pm 0.5\ (model)$ fb, which is in good agreement with the data. Figure 1 (left) shows the distribution of Δy_{jj} in the search region, measured by ATLAS.
The CMS Collaboration performs a similar analysis. The measurement is obtained by combining two different methods (a multivariate analysis and a data-driven procedure) and is $\sigma_{EW} = 226 \pm 26\ (stat.) \pm 35\ (syst.)$ fb. The result is in agreement with the theoretical cross section at NLO which is 239 fb and the difference with respect to the measurement obtained by the ATLAS Experiment is due to the different kinematic region selected. Figure 1 (right) reports the distribution of m_{jj} in the signal region and in the $Z \to \mu^+\mu^-$ decay channel, measured by CMS.

W + Forward-Backward Jets (8 TeV)

As the previous analysis, the electroweak production of a W boson in association with two jets is not actually a vector boson scattering process, but it is characterized by the presence of two VBS-like tagging jets and thus can be used to improve jet selection in VBS-related studies. This process is analyzed by the CMS Collaboration, using 19.3 fb^{-1} of data recorded at $\sqrt{s} = 8$ TeV [6]. The cross section of this process is measured requiring W bosons

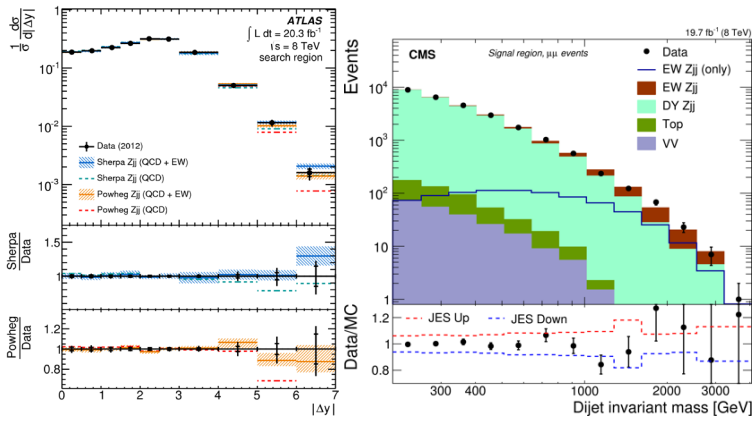

FIGURE 1. Z + Forward-Backward Jets analysis. Unfolded normalized differential cross-section distribution as a function of the rapidity separation between the leading jets in the search region measured by ATLAS (left) [4]. Distribution for m_{jj} for $\mu\mu$ events in the signal region measured by CMS (right) [5].

decaying into muons or electrons, produced centrally with two jets well separated in rapidity. In Fig. 2 (left), the distribution of the m_{jj} variable for the muon decay channel is reported. The number of signal events is extracted from the fit and used to compute the fiducial electroweak W + 2 jets cross section. The combined result of muon and electron channels is $\sigma_{EW}^{e+\mu} = 0.42 \pm 0.04\ (stat.) \pm 0.09\ (syst.) \pm 0.01\ (lumi.)$ pb, in agreement with SM prediction of $0.50 \pm 0.02\ (scale) \pm 0.02\ (PDF)$ pb.

$\gamma\gamma$-Production of W^+W^- (7 and 8 TeV)

The first VV → VV analysis carried out at the LHC is the study of exclusive two-photon production of W^+W^- in proton-proton collisions at $\sqrt{s} = 7$ [7] and 8 TeV [8]. This study is conducted by the CMS Collaboration using data collected in 2011 and 2012, with an integrated luminosity of 5.05 fb^{-1} (7 TeV) and 19.7 fb^{-1} (8 TeV). In order to select the signal, the $\mu^\pm e^\mp$ final state is used, following the decay $pp \to p^{(*)}\gamma\gamma p^{(*)} \to p^{(*)}W^+W^-p^{(*)} \to p^{(*)}\mu^\pm e^\mp p^{(*)}$. Since both very forward-scattered protons escape detection, such a production process is characterized by a primary vertex formed of a $\mu^\pm e^\mp$ pair with no other tracks, with large transverse momentum and large invariant mass. Examining the SM signal region, defined by events with zero extra tracks on the $\mu^\pm e^\mp$ vertex and $p_T(\mu^\pm e^\mp) > 30$ GeV, two events passing all selection requirements are observed at 7 TeV, compared to the expectation of 2.2 ± 0.4 signal events and 0.84 ± 0.15 background events. The measured cross section is $\sigma = 2.2^{+3.3}_{-2.0}(stat.)$ fb, with a significance of $\sim 1\sigma$, and corresponds to an upper limit at 95% C.L. of $\sigma < 10.6$ fb. At 8 TeV, 13 events are observed in the signal region, with an expected background of 3.5 ± 0.5 events, consistently with SM predictions (see Fig. 2, right). In this case, the measured cross section is $\sigma = 12.3^{+5.5}_{-4.4}(stat.)$ fb, with a significance of 3.6σ. Furthermore, this channel can be also sensitive to anomalous quartic gauge couplings of the gauge boson ($\gamma\gamma$WW vertex) and it can be used to look for any deviation from the SM. In this perspective, in the analysis at 7 TeV a tighter cut on the transverse momentum of the lepton pair ($p_T(\mu^\pm e^\mp) > 100$ GeV) is added. Zero data events are observed in this region, which is consistent with the SM expectation of 0.14. A limit is set on the partial cross section times branching fraction at 95% C.L. of $\sigma < 1.9$ fb. At 8 TeV several dimension-six and dimension-eight operators are studied. No significant deviations from the SM are observed and the resulting limits are interpreted in terms of improved constraints on aQGC.

Vector Boson Scattering in $W^\pm W^\pm$ + 2 Jets Channel (8 TeV)

The first evidence of VVjj electroweak production is reported in the study of vector boson scattering in events with two leptons of the same charge and two jets. This analysis is carried out by both ATLAS and CMS Experiments [9, 10] and uses the data sample collected at 8 TeV with an integrated luminosity of about 20 fb^{-1}. The strong production cross section is reduced by the same-sign requirement, making the experimental signature of same-sign di-lepton events with two jets an ideal topology for VBS studies. Candidate events have exactly two high-p_T leptons of the same charge, two jets with large rapidity separation and di-jet mass, and moderate missing transverse momentum. The final states considered are $\mu^\pm\mu^\pm\nu_\mu\nu_\mu jj$, $e^\pm e^\pm\nu_e\nu_e jj$ and $\mu^\pm e^\pm\nu_\mu\nu_e jj$.

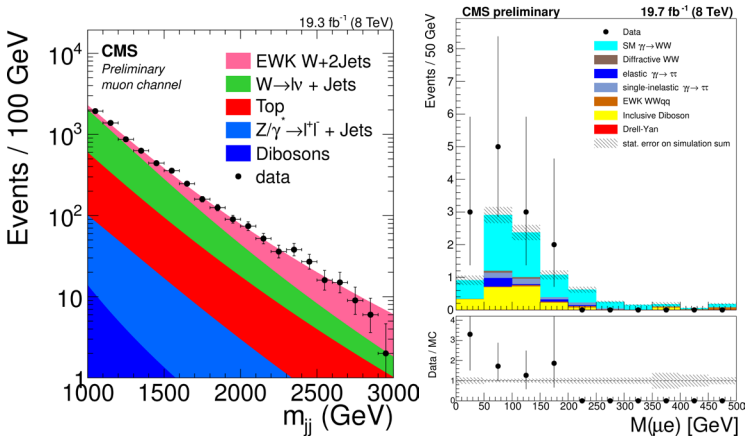

FIGURE 2. W + Forward-Backward Jets analysis: distribution of the m_{jj} for muon channel (right) [6]. $\gamma\gamma$-Production of W^+W^- analysis: $\mu^{\pm}e^{\mp}$ invariant mass for events in the signal region at 8 TeV (left) [8]. Both analyses are carried out by CMS.

In the ATLAS analysis, two fiducial regions are defined: the *inclusive region*, to study the combination of electroweak and strong production mechanisms, and the *VBS region*, to investigate the electroweak interactions alone. The latter region is a subset of the inclusive one and requires the two jets with largest p_T to be separated in rapidity by $|\Delta y| > 2.4$. The CMS analysis considers only the *VBS signal region* requiring $|\Delta\eta| > 2.5$, but measures the $W^{\pm}W^{\pm}jj$ production in an extended fiducial region. Several SM processes enter the signal regions as irreducible background processes or through instrumental effects. Figure 3 (left) shows the expected and observed $|\Delta y_{jj}|$ distribution after the inclusive region selection, measured by the ATLAS Collaboration. Results achieved by the CMS Experiment are presented in Figure 3 (right), in which the m_{jj} distribution in the signal region is reported. The ATLAS Collaboration observes

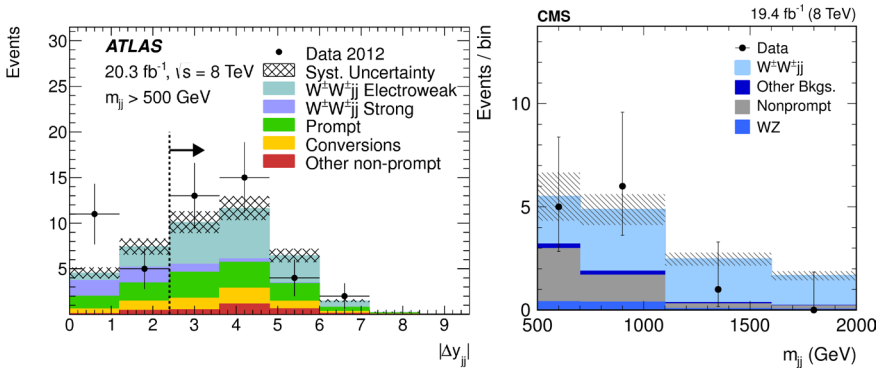

FIGURE 3. Vector Boson Scattering in $W^{\pm}W^{\pm}$ + 2 Jets Channel analysis. $|\Delta y_{jj}|$ distribution for events passing all inclusive region selections ($|\Delta y_{jj}|$ selection is indicated by a dashed line) measured by ATLAS (left) [9]. The distributions of m_{jj} in the signal region measured by CMS (right) [10].

an excess of events, obtaining a significance over the background-only hypothesis of 4.5(3.6) standard deviations in the inclusive(VBS) region. This excess is interpreted as $W^{\pm}W^{\pm}jj$ production. The fiducial cross sections in the two regions are $\sigma^{fid}_{incl} = 2.1 \pm 0.5(stat.) \pm 0.3(syst.)$ fb and $\sigma^{fid}_{VBS} = 1.3 \pm 0.4(stat.) \pm 0.2(syst.)$ fb. The measured cross sections are in agreement with the respective SM expectations of 1.52 ± 0.11 fb and 0.95 ± 0.06 fb. The cross section measured by CMS in a wider fiducial region is $\sigma^{fid}_{incl} = 4.0^{+2.4}_{-2.0}(stat.)\,^{+1.1}_{-1.0}(syst.)$ fb, with an expectation of 5.8 ± 1.2 fb. Additional contributions to $W^{\pm}W^{\pm}jj$ production can be expressed using higher-dimensional operators leading to anomalous QGC (aQGCs). For this measurement ATLAS uses the electroweak chiral Lagrangian approach, parameterizing SM deviations in terms of α_4 and α_5. Limits on aQGCs affecting vertices with four interacting W bosons are set, finding the one-dimensional projection at $\alpha_{4,5} = 0$ of $0.14 < \alpha_4 < 0.16$ and $0.23 < \alpha_5 < 0.24$ compared to an expected $0.10 < \alpha_4 < 0.12$ and $0.18 < \alpha_5 < 0.20$ (Fig. 4, left). CMS uses instead the effective field theory approach.

The expected and observed two dimensional limits on the operator coefficients $F_{T,0}/\Lambda^4$ and $F_{T,1}/\Lambda^4$ (coefficients of two of the effective dimension-eight operators) are presented in Fig. 4 (right).

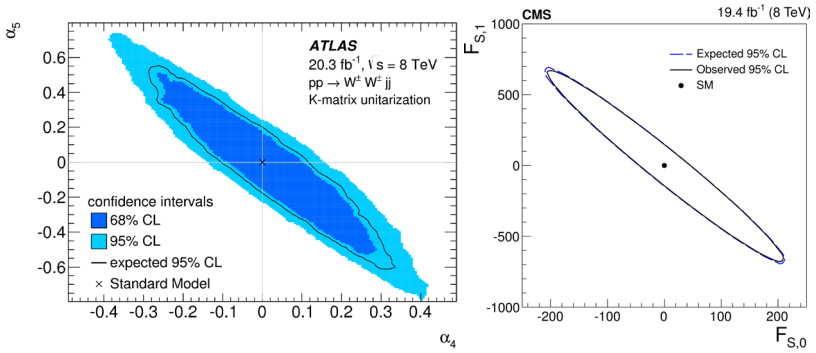

FIGURE 4. Vector Boson Scattering in $W^{\pm}W^{\pm}$ + 2 Jets Channel analysis. Limits on (α_4,α_5) measured by ATLAS (left) [9]. Observed and expected two-dimensional 95% CL limits for $F_{T,0}/\Lambda^4$ and $F_{T,1}/\Lambda^4$ measured by CMS (right) [10].

FUTURE PERSPECTIVES

In the following, a summary of several studies at 14 TeV published by both ATLAS and CMS Collaborations is reported [11, 12]. New physics contributions are studied using an effective field theory approach for modeling anomalous contributions to quartic gauge couplings, by investigating dimension-six and dimension-eight operators. For sufficiently heavy new particles, not directly detectable, the observed effect would be an anomalous enhancement of the cross section at higher scattering energies.

Vector Boson Scattering in ZZ + 2 Jets Channel (14 TeV)

This channel suffers from a small cross section, but provides a very clean final state, with two Z bosons decaying in four leptons. The ATLAS analysis selects two pairs of leptons of opposite charge and same flavor (electrons or muons) with a transverse momentum above 25 GeV. At least two jets with a transverse momentum above 50 GeV are required and the invariant mass of the two most highest-p_T jets must be above 1 TeV. In order to determine the expected sensitivity to beyond SM (BSM) ZZ contribution, the dimension-six operator $O_{\Phi W}$ is investigated through its coefficient $c_{\Phi W}/\Lambda^2$. Figure 5 (right) shows the reconstructed 4-lepton invariant mass distribution. In Table 1 the 5σ discovery potential is illustrated.

Vector Boson Scattering in WZ + 2 Jets Channel (14 TeV)

This channel presents a cross section times branching ratio larger than the $ZZjj$ final state, but the full kinematics reconstruction of the process is more difficult since a neutrino is produced in the decay. Both ATLAS and CMS have estimated up to which energy scale anomalous couplings could be observed at HL-LHC. The ATLAS (CMS) event selection requires exactly three high transverse momentum leptons (electrons or muons) with $p_T > 25$ (20) GeV. Two of them must be consistent with a Z boson. At least two jets with a transverse momentum above 50 GeV must be present and the di-jet invariant mass is required to be at least 1000 (600) GeV. The CMS analysis additionally requires that the two jets are separated by at least 4.0 in pseudorapidity.
Both Collaborations obtain the expected sensitivity to BSM WZ contribution, by studying a dimension-eight operator through its coefficient f_{T1}/Λ^4. Figure 5 (middle) shows the reconstructed WZ invariant mass distribution assuming $f_{T1}/\Lambda^4 = 1.0$ TeV^{-4} obtained by CMS. In Table 1 the 5σ discovery potential is illustrated for both experiments.

Vector Boson Scattering in $W^{\pm}W^{\pm}$ + 2 Jets Channel (14 TeV)

This channel has a cross section times branching ratio larger with respect to the previous final states, but the second neutrino makes the reconstruction of the full kinematics of the weak boson scattering system impossible. Only the ATLAS Collaboration has studied the sensitivity for this channel at HL-LHC. Exactly two leptons of the same charge, with $p_T > 25$ GeV are required in the selection, together with at least two jets with $p_T > 50$ GeV. The invariant mass

of the two selected highest-p_T jets must exceed 1 TeV. The distribution of the mass of the two jets and two leptons is used to discriminate signal from background. A dimension-eight operator is chosen to parameterize new physics in terms of the magnitude of the coefficient f_{S0}/Λ^4. Figure 5 (right) shows the $m_{\ell\ell jj}$ distribution and in Tab. 1 the 5σ discovery potential is illustrated.

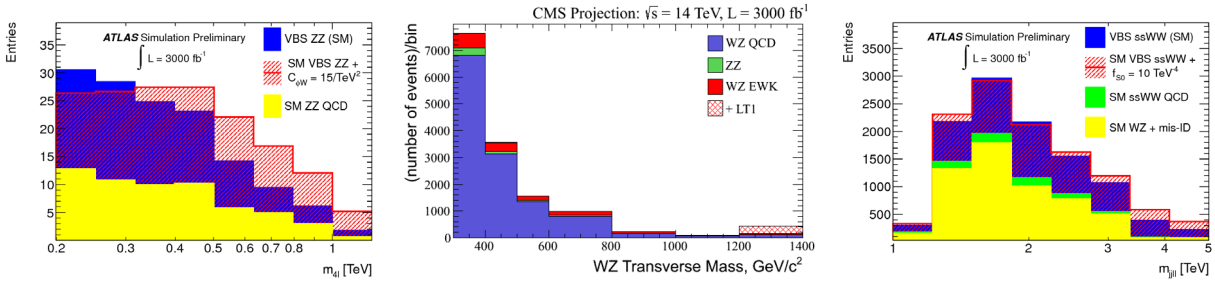

FIGURE 5. The reconstructed 4-lepton mass ($m_{4\ell}$) spectrum in the $pp \to ZZ + 2j \to 4\ell + 2j$ process (left) [11]. WZ transverse mass in the $pp \to WZ + 2j \to 3\ell\nu + 2j$ process (center) [12]. The reconstructed 4-body mass spectrum using the two leading leptons and jets in the $pp \to WW + 2j \to 2\ell 2\nu + 2j$ channel [11].

TABLE 1. Projected 5σ discovery achieved for the vector boson scattering analyses at HL-LHC, with $\mathcal{L} = 3000$ fb^{-1}.

Experiment	Final State	Parameter	Op. Dim	5σ-significance
ATLAS	$\ell^+\ell^-\ell^+\ell^- jj$	$c_{\Phi W}/\Lambda^2$	6	16 TeV^{-2}
CMS/ATLAS	$\ell^\pm\nu\ell^+\ell^- jj$	f_{T1}/Λ^4	8	0.55/0.6 TeV^{-4}
ATLAS	$\ell^\pm\nu\ell^\pm\nu jj$	$f_{S,0}/\Lambda^4$	8	4.5 TeV^{-4}

CONCLUSIONS

The vector boson scattering provides an important test of the Standard Model validity and of the Higgs boson role in the electroweak symmetry breaking mechanism. Analyses at 7 and 8 TeV carried out by both CMS and ATLAS Experiments have been summarized and the first evidence for a VBS dominated process at LHC in the $W^\pm W^\pm$ + 2 jets channel has been reported. However, even if it was possible to start exploring these processes at lower energies, we will be able to fully investigate these interactions only with higher integrated luminosity. Studies at 14 TeV are expected to increase the understanding of VBS and QGC.

REFERENCES

[1] G. Aad *et al.* (ATLAS Collaboration), JINST **3**, p. S08003 (2008).
[2] S. Chatrchyan *et al.* (CMS Collaboration), JINST **3**, p. S08004 (2008).
[3] C. Degrande *et al.*, Annals of Physics **335**, 21 – 32 (2013).
[4] G. Aad *et al.* (ATLAS Collaboration), Journal of High Energy Physics **2014** (2014), 10.1007/JHEP04(2014)031.
[5] V. Khachatryan *et al.* (CMS Collaboration), The European Physical Journal C **75** (2015), 10.1140/epjc/s10052-014-3232-5.
[6] Tech. Rep. CMS-PAS-SMP-13-012 (CERN, Geneva, 2015).
[7] S. Chatrchyan *et al.* (CMS Collaboration), Journal of High Energy Physics **2013** (2013), 10.1007/JHEP07(2013)116.
[8] Tech. Rep. CMS-PAS-FSQ-13-008 (CERN, Geneva, 2015).
[9] G. Aad *et al.* (ATLAS Collaboration), Phys. Rev. Lett. **113**, p. 141803 (2014).
[10] V. Khachatryan *et al.* (CMS Collaboration), Phys. Rev. Lett. **114**, p. 051801 (2015).
[11] Tech. Rep. ATLAS-PHYS-PUB-2013-006 (CERN, Geneva, 2013).
[12] Tech. Rep. CMS-PAS-FTR-13-006 (CERN, Geneva, 2013).

Proceedings of the LHCP2015 Conference, St. Petersburg, Russia, August 31 - September 5, 2015

Editors: V.T. Kim and D.E. Sosnov

NNLO Mixed QCD–EW Corrections to Drell–Yan Processes in the Resonance Region

STEFAN DITTMAIER[1], ALEXANDER HUSS[2] and CHRISTIAN SCHWINN[3,1,a)]

[1]*Albert-Ludwigs-Universität Freiburg, Physikalisches Institut, D-79104 Freiburg, Germany*
[2]*Institute for Theoretical Physics, ETH, CH-8093 Zürich, Switzerland*
[3]*Institute for Theoretical Particle Physics and Cosmology, RWTH Aachen University, D-52056 Aachen*

[a)]Corresponding author: schwinn@physik.rwth-aachen.de

Abstract. We review the application of the pole approximation to the QCD–electroweak corrections of $O(\alpha_s\alpha)$ to W- and Z-boson production at hadron colliders and present results for the numerically dominant corrections, which arise from the combination of the QCD corrections to the production with electroweak corrections to the decay of the W/Z boson. We compare our results to simpler approximations based on naive products of NLO QCD and electroweak correction factors or leading-logarithmic approximations for QED final-state radiation. Finally, we estimate the effect of the $O(\alpha_s\alpha)$ corrections on the measurement of the W-boson mass.

INTRODUCTION

The Drell–Yan-like production of W and Z bosons, $pp/p\bar{p} \to V \to l_1\bar{l}_2 + X$, is one of the most prominent classes of particle reactions at hadron colliders. The large production rate and the clean experimental signature of the leptonic vector-boson decay allow these processes to be measured with great precision and render them the most important "standard-candle" processes at the LHC. Of particular relevance for precision tests of the Standard Model is the potential of the Drell–Yan processes at the LHC for high-precision measurements in the resonance regions, where the effective weak mixing angle might be extracted from data with LEP precision. The W-boson mass M_W can be determined from a fit to the distributions of the lepton transverse momentum ($p_{T,l}$) and the transverse mass ($M_{T,vl}$) of the lepton pair, allowing for a sensitivity below 10 MeV (see Ref. [1] and references therein).

The Drell–Yan-like production of W or Z bosons is one of the theoretically best understood processes. The current state of the art includes QCD corrections at next-to-next-to-leading-order (NNLO) accuracy, supplemented by leading higher-order soft-gluon effects or matched to QCD parton showers up to NNLO, and electroweak (EW) corrections at next-to-leading order (NLO) and leading universal corrections beyond (see, e.g., references in Ref. [2]). Thus, in addition to the N^{3}LO QCD corrections, the next frontier in fixed-order computations is given by the mixed QCD–EW corrections of $O(\alpha_s\alpha)$, which can affect observables relevant for the M_W determination at the percent level. Currently these effects are approximated, e.g., in a parton-shower framework where the virtual NLO corrections and the first emitted photon or gluon are treated exactly, while further emissions are generated in the collinear approximation (see Refs. [3, 4] and references therein). However, a full NNLO calculation at $O(\alpha_s\alpha)$ is necessary for an ambiguity-free combination of NLO QCD and NLO EW corrections. Here some partial results for two-loop amplitudes [5, 6, 7] as well as the full $O(\alpha_s\alpha)$ corrections to the W/Z decay widths [8, 9] are known. A complete calculation of the $O(\alpha_s\alpha)$ corrections requires to combine the double-virtual corrections with the $O(\alpha)$ EW corrections to W/Z + jet production, the $O(\alpha_s)$ QCD corrections to W/Z + γ production, and the double-real corrections (see references in Ref. [2]).

In a series of two recent papers [2, 10], we have initiated the calculation of the $O(\alpha_s\alpha)$ corrections to Drell–Yan processes in the resonance region via the so-called *pole approximation* (PA). In this contribution we outline the salient features of the PA at $O(\alpha_s\alpha)$ and discuss our numerical results on the dominant corrections in this order, which are the "initial–final" factorizable corrections. We compare them to different versions of a naive product ansatz obtained by multiplying NLO QCD and EW correction factors, and to a leading-logarithmic treatment of photon radiation as provided by the structure-function approach or QED parton showers such as PHOTOS [11]. We further estimate the

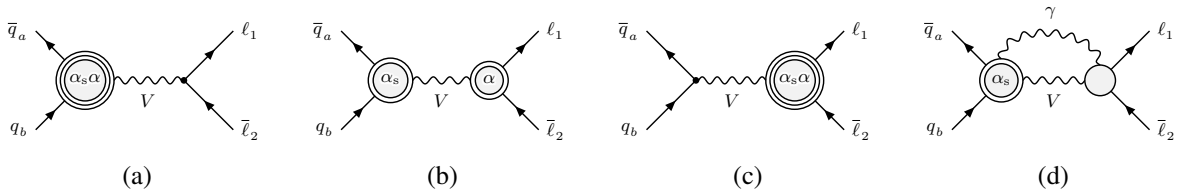

FIGURE 1. The four types of corrections that contribute to the mixed QCD–EW corrections in the PA illustrated in terms of generic two-loop amplitudes: factorizable corrections of initial–initial (a), initial–final (b), and final–final type (c), as well as non-factorizable corrections (d). Simple circles symbolize tree structures, double (triple) circles one-loop (two-loop) corrections.

effect of the NNLO $O(\alpha_s\alpha)$ corrections on the measurement of the W-boson mass.

POLE APPROXIMATION FOR THE MIXED QCD–EW CORRECTIONS

The PA is based on a systematic expansion of the cross section about the pole of the gauge-boson resonance and splits the corrections into factorizable and non-factorizable contributions. The former can be separately attributed to the production and the subsequent decay of the gauge boson, while the latter link the production and decay subprocesses by the exchange of soft photons. The PA has been applied to $O(\alpha)$ corrections in several variants [10, 12, 13] and shows agreement with the known NLO EW corrections up to fractions of 1% near the resonance, i.e. at a phenomenologically satisfactory level. In particular, the bulk of the NLO EW corrections near the resonance is due to the factorizable corrections to the W/Z decay subprocesses, while the factorizable corrections to the production process are mostly suppressed below the percent level, with the non-factorizable contributions being even smaller.

The quality of the PA at NLO motivates its application to the calculation of the NNLO mixed QCD–EW corrections. The structure of the PA for this case has been worked out in detail in Ref. [10] and provides a classification of the $O(\alpha_s\alpha)$ corrections into the four types of contributions shown in Fig. 1 for the case of the double-virtual corrections:[1]

(a) The initial–initial factorizable corrections are given by two-loop $O(\alpha_s\alpha)$ corrections to on-shell W/Z production and the corresponding one-loop real–virtual and tree-level double-real contributions, i.e. W/Z + jet production at $O(\alpha)$, W/Z + γ production at $O(\alpha_s)$, and the processes W/Z + γ + jet at tree level. Results for individual ingredients are known, however, a consistent combination of these building blocks using a subtraction scheme for infrared singularities at $O(\alpha_s\alpha)$ has not been performed yet.

(b) The factorizable initial–final corrections consist of the $O(\alpha_s)$ corrections to W/Z production combined with the $O(\alpha)$ corrections to the leptonic W/Z decay. Their computation is described in detail in Ref. [2]. The main results are presented below.

(c) Factorizable final–final corrections arise from the $O(\alpha_s\alpha)$ counterterms of the lepton–W/Z-vertices, which involve only QCD corrections to the W/Z self-energies [14]. They yield a relative correction below 0.1% [2] and have no impact on the shape of distributions, so that they are phenomenologically negligible.

(d) The non-factorizable $O(\alpha_s\alpha)$ corrections are given by soft-photon corrections connecting the initial state, the intermediate vector boson, and the final-state leptons, combined with QCD corrections to W/Z-boson production. They can be calculated in terms of soft-photon correction factors to squared tree-level or one-loop QCD matrix elements [10] and are numerically below 0.1%. Thus, for phenomenological purposes the $O(\alpha_s\alpha)$ corrections can be factorized into terms associated with initial-state and/or final-state corrections and their combination.

The factorizable initial–initial corrections (a) are the only currently missing $O(\alpha_s\alpha)$ corrections within the PA. Results of the PA at $O(\alpha)$ show that observables such as the $M_{T,\nu l}$ distribution for W production or the M_{ll} distributions for Z production are extremely insensitive to photonic initial-state radiation (ISR) [10]. Since these distributions also do not receive overwhelmingly large QCD corrections, we do not expect significant initial–initial NNLO $O(\alpha_s\alpha)$ corrections to such distributions. Furthermore, they would require $O(\alpha_s\alpha)$-corrected PDFs for a consistent evaluation, which are however not available. On the other hand, the factorizable corrections of the type"initial–final" (b) combine two types of corrections that are sizeable at NLO and deform the shape of differential distributions. Therefore we expect this class of the factorizable corrections to capture the dominant $O(\alpha_s\alpha)$ effects.

[1] For each class of contributions with the exception of the final–final corrections (c), also the associated real–virtual and double-real corrections have to be computed, obtained by replacing one or both of the labels α and α_s in the blobs in Fig. 1 by a real photon or gluon, respectively, and taking corresponding crossed partonic channels, e.g. with quark–gluon initial states, into account.

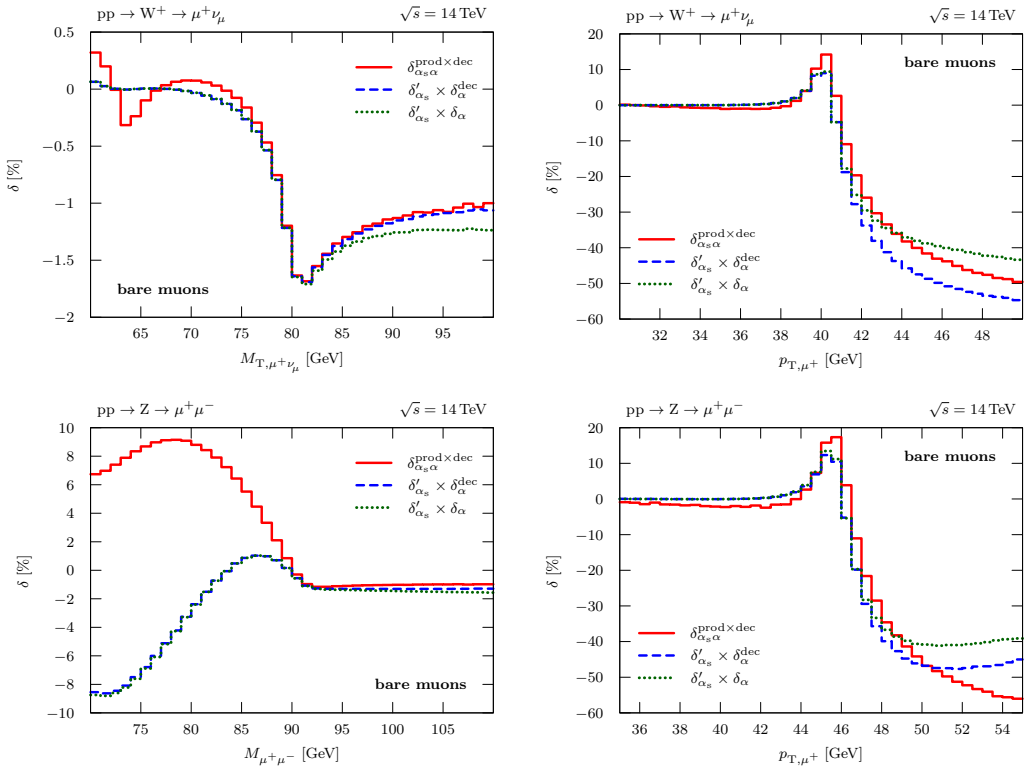

FIGURE 2. Relative factorizable corrections of $O(\alpha_s\alpha)$ induced by initial-state QCD and final-state EW contributions. Above: transverse-mass (left) and transverse-lepton-momentum (right) distributions for W^+ production at the LHC. Below: lepton-invariant-mass distribution (left) and a transverse-lepton-momentum distribution (right) for Z production at the LHC. The naive products of the NLO correction factors δ'_{α_s} and δ_α are shown for comparison. (Taken from Ref. [2].)

NUMERICAL RESULTS FOR THE DOMINANT $O(\alpha_s\alpha)$ CORRECTIONS

In the following we present our results for the dominant $O(\alpha_s\alpha)$ NNLO corrections to the Drell–Yan cross section in the resonance region, which are given by the initial–final factorizable corrections (Figure 1 (b)). We consider isolated ("bare") muons using the setup and input parameters of Ref. [2]. The corresponding corrections for "dressed leptons" using a recombination with collinear photons show the same features, but are typically smaller by a factor of two [2].

Our default prediction $\sigma^{\mathrm{NNLO_{s\otimes ew}}}$ is obtained by adding the factorizable initial–final NNLO corrections $\Delta\sigma^{\mathrm{NNLO_{s\otimes ew}}}_{\mathrm{prod\times dec}}$ to the sum $\Delta\sigma^{\mathrm{NLO_s}} + \Delta\sigma^{\mathrm{NLO_{ew}}}$ of the full NLO QCD and EW corrections, where all contributions are consistently evaluated with NLO PDFs. The numerically negligible non-factorizable and factorizable final–final corrections are not included. Figure 2 shows the numerical results for the relative $O(\alpha_s\alpha)$ initial–final factorizable corrections

$$\delta^{\mathrm{prod\times dec}}_{\alpha_s\alpha} \equiv \Delta\sigma^{\mathrm{NNLO_{s\otimes ew}}}_{\mathrm{prod\times dec}}/\sigma^{\mathrm{LO}} \tag{1}$$

for the $M_{\mathrm{T},\nu l}$ and the $p_{\mathrm{T},l}$ distributions for W^+ production at the LHC. For Z production, the results for the M_{ll} distribution and a transverse-lepton-momentum (p_{T,l^+}) distribution are displayed. In order to check the validity of simpler estimates of the NNLO QCD–EW corrections, the plots also show the product $\delta'_{\alpha_s}\delta_\alpha$ of the QCD and EW correction factors

$$\delta'_{\alpha_s} \equiv \Delta\sigma^{\mathrm{NLO_s}}/\sigma^{\mathrm{LO}}, \qquad \delta_\alpha \equiv \Delta\sigma^{\mathrm{NLO_{ew}}}/\sigma^{0}, \tag{2}$$

which arises in the relative difference of our default NNLO prediction $\sigma^{\mathrm{NNLO_{s\otimes ew}}}$ and a naive product ansatz $\sigma^{\mathrm{NNLO_{s\otimes ew}}}_{\mathrm{naive\ fact}} = \sigma^{\mathrm{NLO_s}}(1+\delta_\alpha)$. Note that the LO prediction σ^{LO} is evaluated with LO PDFs, whereas σ^0 is evaluated using NLO PDFs. The relative NLO EW corrections are defined in two different versions: First, based on the full $O(\alpha)$ correction (δ_α),

and second, based on the dominant EW final-state correction of the PA ($\delta_\alpha^{\mathrm{dec}}$). Any large deviations between $\delta_{\alpha_s\alpha}^{\mathrm{prod\times dec}}$ and $\delta'_{\alpha_s}\delta_\alpha^{(\mathrm{dec})}$ can be attributed to the double-real emission corrections, which do not take the reducible form of a product of two NLO corrections, in contrast to the other initial–final factorizable contributions [2]. The difference of the naive products defined in terms of $\delta_\alpha^{\mathrm{dec}}$ and δ_α indicates the impact of the missing $O(\alpha_s\alpha)$ corrections beyond the initial–final corrections considered in our calculation and therefore also provides an error estimate of the PA, and in particular of the omission of the corrections of initial–initial type.

For the $M_{\mathrm{T},\nu l}$ distribution for W^+ production (upper left plot in Figure 2), the mixed NNLO QCD–EW corrections amount to approximately -1.7 % around the resonance, which is about an order of magnitude smaller than the NLO EW corrections. Both variants of the naive product provide a good approximation to the full result in the region around and below the Jacobian peak, which is dominated by resonant W production. This can be attributed to well-known insensitivity of the observable $M_{\mathrm{T},\nu l}$ to ISR effects already seen for the NLO corrections [10]. For larger $M_{\mathrm{T},\nu l}$, the product $\delta'_{\alpha_s}\delta_\alpha$ based on the full NLO EW correction factor deviates from the other curves, which signals the growing importance of effects beyond the PA. However, the deviations amount to only few per-mille for $M_{\mathrm{T},\nu l} \lesssim 90$ GeV.

The corrections to the $p_{\mathrm{T},l}$ distributions (right plots in Figure 2) are small far below the Jacobian peak, but rise to about 15% (20%) on the Jacobian peak at $p_{\mathrm{T},l} \approx M_V/2$ for the case of the W^+ boson (Z boson) and then drop to almost -50% at $p_{\mathrm{T},l} = 50$ GeV. This enhancement of corrections above the Jacobian peak arises already in the NLO QCD results (see e.g. Fig. 8 in Ref. [10]) where the recoil due to real QCD radiation shifts events with resonant W/Z bosons above the Jacobian peak. The naive product ansatz deviates from the full result $\delta_{\alpha_s\alpha}^{\mathrm{prod\times dec}}$ by 5–10% at the Jacobian peak, where the PA is expected to be the most accurate. This can be attributed to the strong influence of the recoil induced by ISR on $p_{\mathrm{T},l}$, which implies a larger effect of the double-real emission corrections on this distribution, which are not captured correctly by the naive products. The two versions of the naive products display larger deviations than in the $M_{\mathrm{T},\nu l}$ distribution, which signals a larger impact of the missing $O(\alpha_s\alpha)$ initial–initial corrections.[2]

In the M_{ll} distribution for Z production (lower left plot in Figure 2), corrections up to 10% are observed below the resonance. This is consistent with the large NLO EW corrections from photonic final-state radiation (FSR) that shifts the reconstructed value of M_{ll} away from the resonance $M_{ll} = M_{\mathrm{Z}}$ to lower values. The naive products $\delta'_{\alpha_s}\delta_\alpha^{(\mathrm{dec})}$ approximate the full initial–final corrections $\delta_{\alpha_s\alpha}^{\mathrm{prod\times dec}}$ reasonably well for $M_{ll} \geq M_{\mathrm{Z}}$ but completely fail already a little below the resonance where they do not even reproduce the sign of the full correction $\delta_{\alpha_s\alpha}^{\mathrm{prod\times dec}}$. This failure can be understood from the fact that the appropriate QCD correction factor for the events that are shifted below the resonance by photonic FSR is given by its value at the resonance $\delta'_{\alpha_s}(M_{ll} = M_{\mathrm{Z}}) \approx 6.5\%$ [2], whereas the naive product ansatz simply multiplies the corrections locally on a bin-by-bin basis.

Approximating $O(\alpha_s\alpha)$ corrections by leading logarithmic final-state radiation

As is evident from Fig. 2, a naive product of the QCD and EW correction factors (2) is not adequate to approximate the NNLO QCD–EW corrections for all observables. A promising factorized approximation for the dominant initial–final corrections can be obtained by combining the full NLO QCD corrections to W/Z production with a leading-logarithmic (LL) approximation for FSR. For this purpose we have employed a structure-function approach [15] and a simulation of FSR using PHOTOS [11]. Both approaches take the interplay of the recoil effects from jet and photon emission properly taken into account, but neglect certain subdominant finite contributions. In order to compare to our result for the $O(\alpha_s\alpha)$ corrections, we only generate a single photon emission in both implementations of the LL approximation and use the same input-parameter scheme for α as in $\delta_{\alpha_s\alpha}^{\mathrm{prod\times dec}}$ (see Ref. [2] for details).

In Fig. 3 we compare our best prediction (1) for the factorizable initial–final $O(\alpha_s\alpha)$ corrections for W^+ and Z production to the combination of NLO QCD corrections with the two FSR approximations. For the structure-function approach (denoted by LL^1FSR), the intrinsic uncertainty of the LL approximation is illustrated by the band width resulting from varying the QED scale Q within the range $M_V/2 < Q < 2M_V$ for $V = \mathrm{W}, \mathrm{Z}$. We observe a clear improvement compared to the naive product approximations investigated above, in particular for the M_{ll} distribution in Z production, which is correctly modelled by both FSR approximations, whereas the naive products completely failed to describe this distribution. In the $M_{\mathrm{T},\nu l}$ spectrum of the charged-current process one also finds good agreement of the different results below the Jacobian peak and an improvement over the naive product approximations in Fig. 2. The description of the $p_{\mathrm{T},l}$ distributions is also improved compared to the naive product approximations, but some differences remain in the charged-current process.

[2] These deviations should be interpreted with care, since the peak region $p_{\mathrm{T},l} \approx M_V/2$ corresponds to the kinematic onset for V + jet production where fixed-order predictions break down and QCD resummation is required for a proper description.

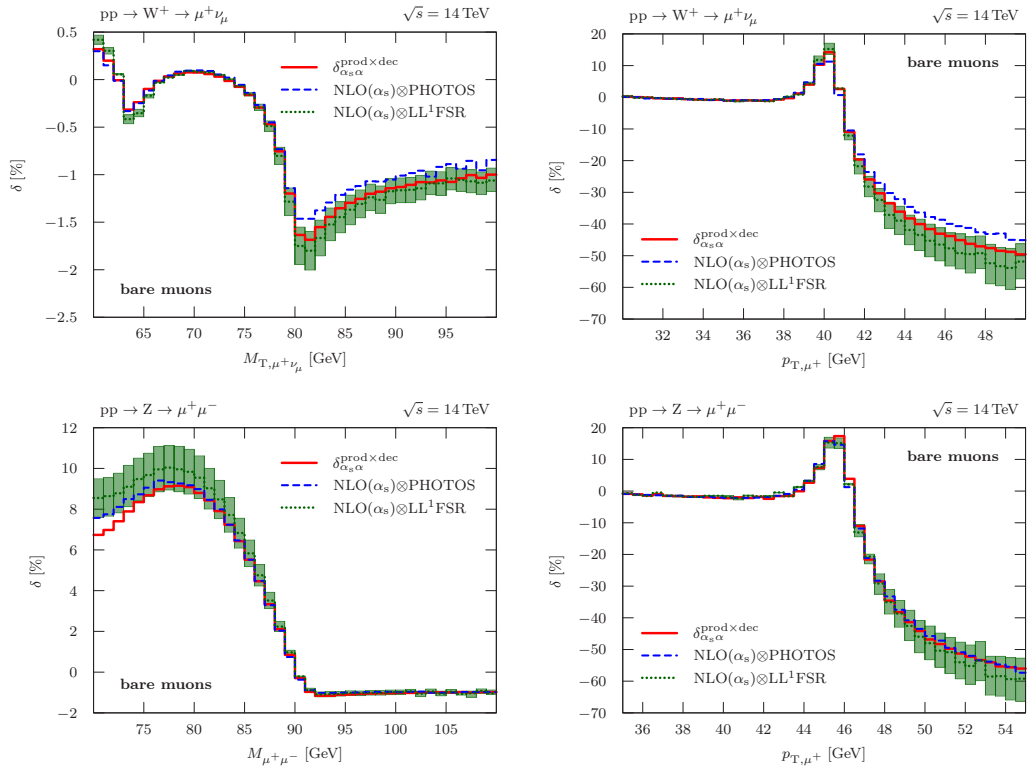

FIGURE 3. Comparison of the approximation obtained from PHOTOS and from the structure-function (LL^1FSR) approach for the relative $O(\alpha_s\alpha)$ initial-state QCD and final-state EW corrections to our best prediction $\delta^{\text{prod}\times\text{dec}}_{\alpha_s\alpha}$. Above: transverse-mass (left) and transverse-lepton-momentum (right) distributions for W^+ production at the LHC. Below: lepton-invariant-mass distribution (left) and a transverse-lepton-momentum distribution (right) for Z production at the LHC. (Taken from Ref. [2].)

Impact on the W-boson mass extraction

In order to estimate the effect of the $O(\alpha_s\alpha)$ corrections on the M_W measurement at the LHC we have performed a χ^2 fit of the $M_{T,\nu\ell}$ distribution in the interval $M_{T,\nu\ell} = [64, 91]$ GeV . We treat the $M_{T,\nu\ell}$ spectra calculated in various theoretical approximations for a reference mass $M_W^{OS} = 80.385$ GeV as "pseudo-data" that we fit with "templates" calculated using the LO predictions σ^0 for different values of M_W^{OS}. The best-fit value $M_W^{fit,th}$ quantifying the impact of a higher-order correction in the theoretical cross section σ^{th} is then obtained from the minimum of the function

$$\chi^2(M_W^{fit,th}) = \sum_i \left[\sigma_i^{th}(M_W^{OS}) - \sigma_i^0(M_W^{fit,th})\right]^2 / (2\Delta\sigma_i^2)\,, \tag{3}$$

where the sum over i runs over $M_{T,\nu l}$ bins in steps of 1 GeV. Here σ_i^{th} and σ_i^0 are the integrated cross sections in the i-th bin, uniformly rescaled so that the sum over all bins is identical for all cross sections. We assume a statistical error of the pseudo-data, taking $\Delta\sigma_i^2 \propto \sigma_i^{th}$. We do not attempt to model detector effects that are expected to affect the different theory predictions in a similar way and to cancel to a large extent in our estimated mass shift.

Using the prediction $\sigma^{NLO_{ew}}$ as the pseudo-data σ^{th} in (3) we estimate the mass shift due to the NLO EW corrections as $\Delta M_W^{NLO_{ew}} \approx -90$ MeV (-40 MeV) for bare muons (dressed leptons) [2]. We have also estimated the effect of multi-photon radiation and obtained a mass shift $\Delta M_W^{FSR} \approx 9$ MeV relative to the result of the fit to the NLO EW prediction for bare muons. These values are comparable to previous results reported in Ref. [16].[3] To estimate the impact of the initial–final $O(\alpha_s\alpha)$ corrections we consider the mass shift obtained by using our best prediction (1) relative to

[3]The results of Ref. [16] cannot be compared directly to our results, since different event-selection criteria are used. Note that the role of pseudo-data and templates is reversed in Ref. [16] so that the mass shift has the opposite sign.

that obtained for the sum of the NLO QCD and EW corrections. We obtain $\Delta M_{\mathrm{W}}^{\mathrm{NNLO}} \approx -14$ MeV (-4 MeV) for bare muons (dressed leptons) [2], which provides a simple estimate of the impact of the full $O(\alpha_{\mathrm{s}}\alpha)$ corrections on the M_{W} measurement.

CONCLUSIONS

The precision-physics program in Drell–Yan-like W- and Z-boson production at the LHC requires a further increase in the accuracy of the theoretical predictions, where the mixed QCD–electroweak corrections of $O(\alpha_{\mathrm{s}}\alpha)$ represent the largest component of fixed-order radiative corrections after the well established NNLO QCD and NLO electroweak corrections. In this contribution, we have reviewed the major results of our two recent papers [2, 10], where we have established a framework for evaluating the $O(\alpha_{\mathrm{s}}\alpha)$ corrections to Drell–Yan processes in the resonance region using the pole approximation and presented the calculation of the non-factorizable and most important factorizable corrections. The non-factorizable corrections [10] and the factorizable corrections corresponding solely to the W/Z decay subprocesses [2] turned out to be phenomenologically negligible. Moreover, an analysis of the NLO corrections in pole approximation suggests that the factorizable corrections corresponding to the production subprocess, which are yet unknown, will have a minor impact on the observables relevant for the W-boson mass measurement.

We have summarized our numerical results [2] of the dominant factorizable corrections of $O(\alpha_{\mathrm{s}}\alpha)$, which arise from the combination of sizeable QCD corrections to the production with large EW corrections to the decay subprocesses. Naive product approximations fail to capture these corrections in distributions that are sensitive to QCD initial-state radiation and therefore require a correct treatment of the double-real-emission part of the NNLO corrections. Naive products also fail to capture observables that are strongly affected by a redistribution of events due to final-state real-emission corrections, such as the invariant-mass distribution of the neutral-current process. A combination of the NLO QCD corrections and a collinear approximation of real-photon emission through a QED structure-function approach or a QED parton shower such as PHOTOS provides a significantly better agreement with our results. In particular, for the invariant-mass distribution in Z-boson production both collinear approximations model the redistribution of events due to final-state radiation, which is responsible for the bulk of the corrections in this observable.

We have estimated the effect of the $O(\alpha_{\mathrm{s}}\alpha)$ corrections on the M_{W} measurement to ≈ -14 MeV for the case of bare muons and ≈ -4 MeV for dressed leptons. These corrections therefore have to be properly taken into account in the W-boson mass measurements at the LHC, which aim at a precision of about 10 MeV.

ACKNOWLEDGMENTS

This project is supported by the German Research Foundation (DFG) via grant DI 784/2-1 and the German Federal Ministry for Education and Research (BMBF). Moreover, A.H. is supported via the ERC Advanced Grant MC@NNLO (340983). C.S. is supported by the Heisenberg Programme of the DFG.

REFERENCES

[1] M. Baak *et al.*, (2013), arXiv:1310.6708 [hep-ph] .
[2] S. Dittmaier, A. Huss, and C. Schwinn, (2015), to appear in Nucl. Phys. B, arXiv:1511.08016 [hep-ph] .
[3] L. Barzè *et al.*, JHEP **1204**, p. 037 (2012), arXiv:1202.0465 [hep-ph] .
[4] L. Barzè *et al.*, Eur.Phys.J. **C73**, p. 2474 (2013), arXiv:1302.4606 [hep-ph] .
[5] A. Kotikov, J. H. Kühn, and O. Veretin, Nucl.Phys. **B788**, 47–62 (2008), arXiv:hep-ph/0703013 [hep-ph] .
[6] W. B. Kilgore and C. Sturm, Phys.Rev. **D85**, p. 033005 (2012), arXiv:1107.4798 [hep-ph] .
[7] R. Bonciani, PoS **EPS-HEP2011**, p. 365 (2011).
[8] A. Czarnecki and J. H. Kühn, Phys.Rev.Lett. **77**, 3955–3958 (1996), arXiv:hep-ph/9608366 [hep-ph] .
[9] D. Kara, Nucl.Phys. **B877**, 683–718 (2013), arXiv:1307.7190 .
[10] S. Dittmaier, A. Huss, and C. Schwinn, Nucl.Phys. **B885**, 318–372 (2014), arXiv:1403.3216 [hep-ph] .
[11] P. Golonka and Z. Was, Eur.Phys.J. **C45**, 97–107 (2006), arXiv:hep-ph/0506026 [hep-ph] .
[12] U. Baur, S. Keller, and D. Wackeroth, Phys.Rev. **D59**, p. 013002 (1999), arXiv:hep-ph/9807417 [hep-ph] .
[13] S. Dittmaier and M. Krämer, Phys. Rev. **D65**, p. 073007 (2002), hep-ph/0109062 .
[14] A. Djouadi and P. Gambino, Phys.Rev. **D49**, 3499–3511 (1994), arXiv:hep-ph/9309298 [hep-ph] .
[15] E. A. Kuraev and V. S. Fadin, Sov. J. Nucl. Phys. **41**, 466–472 (1985).
[16] C. Carloni Calame *et al.* , Phys.Rev. **D69**, p. 037301 (2004), arXiv:hep-ph/0303102 [hep-ph] .

Standard Model – Quantum ChromoDynamics: parallel talks

Proceedings of the LHCP2015 Conference, St. Petersburg, Russia, August 31 - September 5, 2015

Editors: V.T. Kim and D.E. Sosnov

Jet Results from CMS

ALEXANDER A. SAVIN

Physics Dept., University of Wisconsin, 1150 University Ave., Madison WI 53706-1390, USA
on leave from NPI Moscow State University, Moscow, Russia

asavin@mail.cern.ch

On behalf of the CMS Collaboration

Abstract. Production of jets, measured with high experimental precision, allow for important tests of different theoretical predictions. These proceedings present a short overview of the recent jet results obtained with the CMS experiment at the LHC.

Introduction

A high cross section of the jet production at the LHC results in enourmous events yield that can be used for precise experimental measurements. Jet rates, normalized cross sections, correlation between jets and multidifferential jet cross sections, measured in proton-proton collisions, provide significant input for theoretical models and improve our understanding of the standard model. Parton density functions, strong coupling constant, modelling of hard interaction, parton shower algoritms and multiple interactions, fragmentation and hadronization, QED radiation - this is still not a full list of important physics topics that can be addressed with jet results.

Precission measurement requires not only significant number of data events, but also well understood detector performance, proper simulation of the detector responce and robust jet reconstruction algorithm. The anti-kt algoritm [1] that is used by CMS, to be run on the particles reconstructed using particle-flow algorithm [2], demonstrated a good performance and reliable treatment of underlying events. The jets at CMS are corrected for pileup (multiple beam interactions in single event) and also subject of different corrections. Still the energy scale uncertainty remains the dominant systematic uncertainty in all the jet-related measurements. These proceedings present only a short overview of the recent jet results from CMS.

Inclusive jet production cross section

The most general measurement that can be done with jets is the inclusive jet production cross section measurement. A huge jets yield at the LHC allows to perform an accurate double differential cross section measurement with fine binning, as demonstrated in Fig. 1 left, where inclusive jet cross section at $\sqrt{8}$ TeV, unfolded for detector effects, double-differential in jet p_T and y is compared to theoretical predictions [3, 4]. The NLO predictions are corrected for non-perturbative effects. The data are well described by the predictions over many orders of magnitude in cross section and for jet p_T up to 2.5 GeV.

To better explore the comparison of the data to different theoretical predictions, the ratio of the data to the prediction with CT10 PDF is shown together with five investigated PDF sets in Fig. 1 right. The total experimental systematic uncertainties are shown as band around one. The theory predictions describe the data generally well, the results from different PDF sets differ from each other mainly at high p_T. The best description of the data is obtained with predictions based on the CT10 PDF set.

Similar results were recently obtained by CMS at $\sqrt{s} = 2.76$ TeV [5]. Figure 2 left shows that the data are well described by the predictions over many orders of magnitude in cross section in slightly different kinematic regime than in the previous measurement. The ratio of cross sections obtained at different $\sqrt{s}$ provides even more

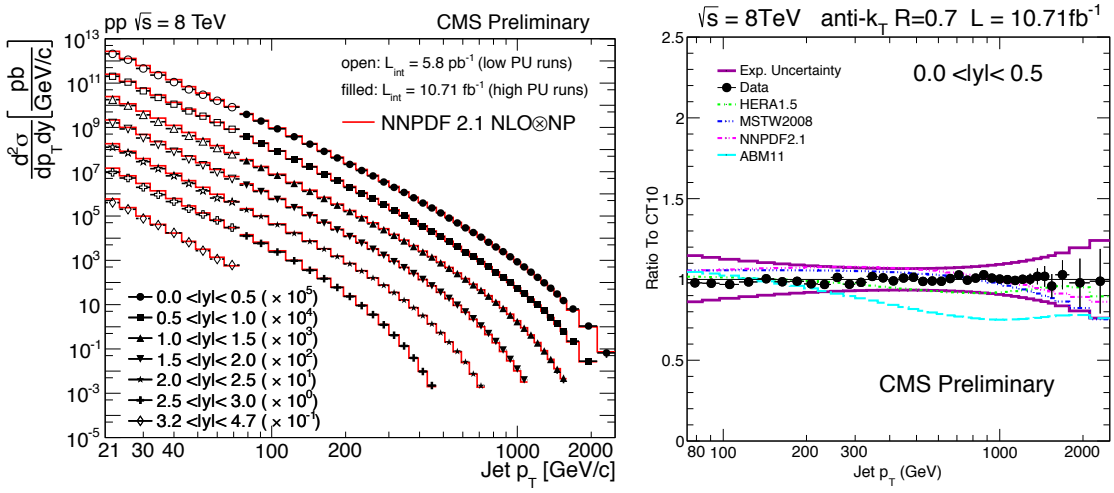

FIGURE 1. Left: inclusive jet cross section measurement from CMS. Right: the ratio of cross sections to the theory predictions for one representative y-bin.

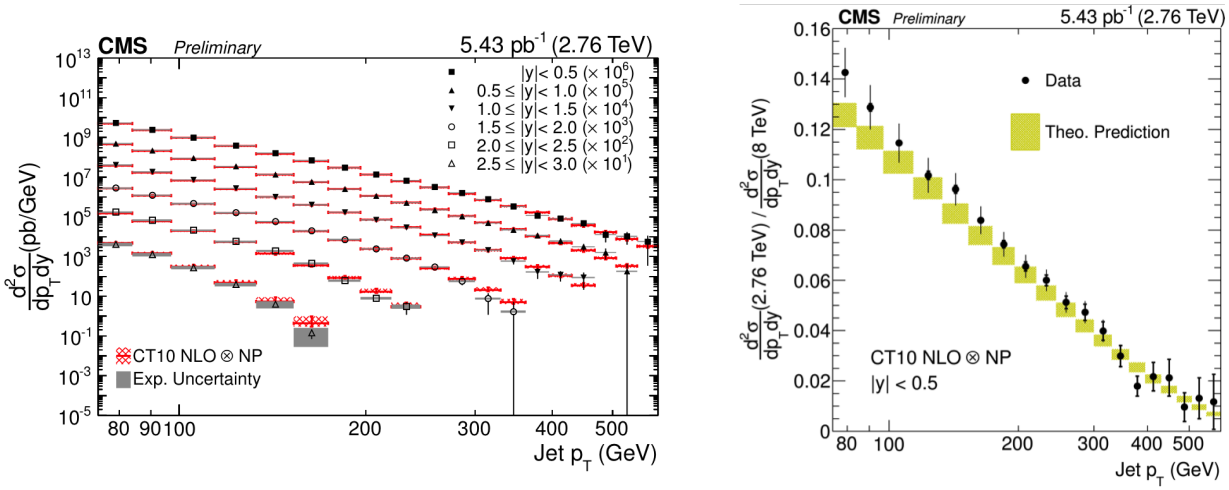

FIGURE 2. Left: inclusive jet cross section measurement from CMS at $\sqrt{s} = 2.76$ TeV. Right: the ratio of cross sections measured at different $\sqrt{s}$ for one representative $|y|$ bin

precise comparison to the theory, because many correlated uncertainties cancel for both measurement and predictions. Figure 2 right shows the ratio of the two measurements and demonstrates that at low jet p_{T} the predictions deviate from the observed behaviour by 1-1.5 σ.

Dijet production cross section and kinematics

Study of mutijet production is not only a natural continuation of the inclusive jet studies, it also allows to study correlations in jet kinematics that are extremely sensitive to NLO effects.

In Fig. 3 dijet cross section at $\sqrt{8}$ TeV, unfolded for detector effects, double-differential in jet p_T and y, is well described by the predictions [6]. The ratio of the data to the prediction with NNPDF PDF is shown together with other investigated PDF sets in Fig. 3 right. The theory predictions describe the data generally well, the conclusions based on this comparison are consistent with previously shown inclusive jet results.

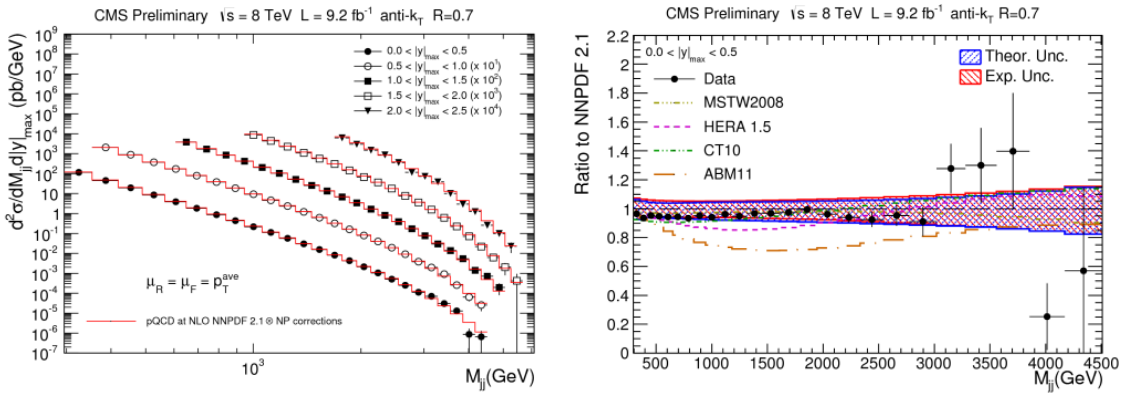

FIGURE 3. Left: inclusive dijet cross section measurement from CMS at $\sqrt{s}$ = 8 TeV. Right: the ratio of cross sections to predictions for one representative |y| bin.

Figure 4 presents the azimuthal correlation between two leading in p_T jets from CMS [7]. In the right plot the data are compared to fixed order prediction only in restricted $\Delta\phi$ range, since there is no prediction at fixed-order that can describe the whole region. The predictions are calculated for three jets NLO production, which is not valid at π, corresponding to LO dijet production, and also not valid after $\pi/2$, since here we would require NNLO prediction. In the region between $\pi/2$ and $2\pi/3$ the predictions do not describe data, since the three jets NLO calculations become effectively only LO in this regime. In the region where predictions are expected to work, the data are well described.

The same data are compared in Figure 4 left to predictions of different models, that reasonably describe the measurements over the whole $\Delta\phi$ range. The small observed differences are discussed in detail in Ref. [7].

Extraction of α_s

All jet measurements can be used to extract the value of the strong coupling constant, α_s. The predictions show high sensitivity to the α_s, thus allowing to use fits to measured distributions with α_s as a fit parameter, to extract its best value. Figure 5 left shows a summary of running α_s measurements for all published CMS results and results from Tevatron and HERA experiments. For CMS the measurements include the inclusive jets, ratio of the three- to two- jet production cross sections, studies of three-jet mass and $\mathrm{t\bar{t}}$ production. Overall all data demonstrate consistent values of α_s, that agree well with the CMS measurement [3], with $\alpha_s(M_Z) = 0.1185^{+0.0063}_{-0.0042}$, where the $\alpha_s(M_Z)$ values are evolved to the corresponding energy scale Q using the two-loop solution to the renormalization group equation within HOPPET.

The summary of the $\alpha_s(M_Z)$ values measured in different experiments compared to the world average in Fig. 5 right. Within the uncertainties all the measurements agree between each other and with the average value.

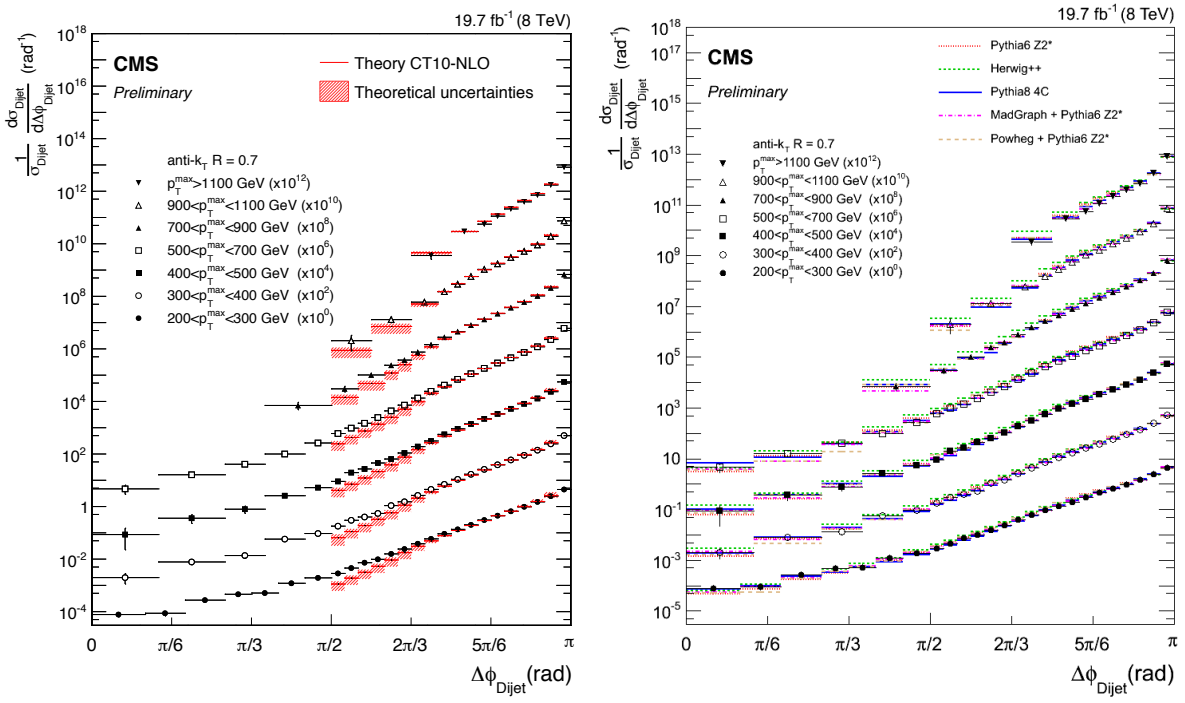

FIGURE 4. The normalized dijet cross section differential in $\Delta\phi_{Dijet}$ for seven p_T^{max} regions, scaled by multiplicative factors for presentation purposes. For $\pi > \Delta\phi_{Dijet} > \pi/2$ the data are compared to predictions from fixed-order calculations in pQCD in the left plot, and to different models in the right plot for the whole $\Delta\phi$ region.

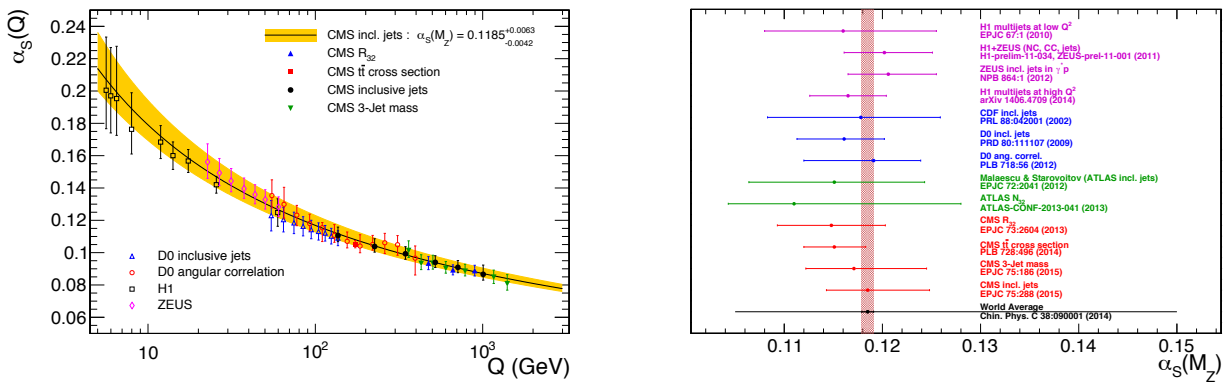

FIGURE 5. Left: the strong coupling $\alpha_s(Q)$ (solid line) and its total uncertainty (band) as determined in Ref. [3, 4]. Results from HERA and Tevatron experiments are also shown. Right: an overview of $\alpha_s(M_Z)$ measurements using hadrons.

Summary

Extremely interesting results from the LHC Run I data have contributed a lot to our understanding of underlying physics processes. Increasing luminosity and center-of-mass energy in the LHC Run II should allow for even more precise measurements in further extended kinematic regimes.

References

REFERENCES

[1] M. Cacciari, G. P. Salam, and G. Soyez, JHEP **04**, p. 063 (2008), arXiv:0802.1189 [hep-ph] .
[2] CMS Collaboration, CMS Physics Analysis Summary CMS-PAS-PFT-10-001 (2010).
[3] CMS Collaboration, CMS Physics Analysis Summary CMS-PAS-SMP-12-012 (2012).
[4] CMS Collaboration, CMS Physics Analysis Summary CMS-PAS-FSQ-12-031 (2012).
[5] CMS Collaboration, CMS Physics Analysis Summary CMS-PAS-SMP-14-017 (2014).
[6] CMS Collaboration, CMS Physics Analysis Summary CMS-PAS-SMP-14-002 (2014).
[7] CMS Collaboration, CMS Physics Analysis Summary CMS-PAS-SMP-14-015 (2014).

Proceedings of the LHCP2015 Conference, St. Petersburg, Russia, August 31 - September 5, 2015

Editors: V.T. Kim and D.E. Sosnov

ATLAS PDF Results

MARK STOCKTON

McGill University, Department of Physics, Montreal QC, Canada.

mark.stockton@cern.ch

On behalf of the ATLAS Collaboration

Abstract. Uncertainties from parton distribution functions can limit our measurements of new cross sections and searches beyond the standard model. Results are presented on recent ATLAS measurements which are sensitive to parton distribution functions. These cover a wide range of cross section measurements, including those from: jets, photons, W/Z bosons and top quarks.

INTRODUCTION

Standard model (SM) measurements at the LHC probe new phase space not explored before at colliders. The measurements also have small uncertainties due to the large data sample collected and well understood detectors, so can provide stringent tests of parton distribution functions (PDFs). This is crucial for new cross section measurements and searches beyond the SM as PDFs are often the dominant uncertainty. The ATLAS [1] measurements presented focus mainly on those that can be used in a global PDF fit, which would then aim to have a reduced PDF uncertainty. The measurements presented here are grouped by PDF impact, starting with results related to the gluon PDF, then heavy quarks and finally light quarks.

GLUON PDF

Jet measurements are a useful tool to measure the gluon PDF due to their large cross section. The analyses are carried out either as inclusive [2] (all jets), di-jet [3] (selecting two jets) or tri-jet [4] (selecting three jets). When comparing to next-to-leading-order (NLO) predictions it is important to use a range of jet radii (0.4 and 0.6) and to include non-perturbative and electroweak (EW) corrections (the latter are not available for tri-jet measurements yet). In all three results there is an overall good agreement between the measured cross section and that from NLO, especially with the large theoretical errors. The results are compared to many PDFs (CT, MSTW, NNPDF, HERAPDF, ABM and GJR), and only ABM11 shows any tension with the results. This tension is seen in all three measurements, and is shown in Fig. 1 for the inclusive jet measurement.

The overall experimental uncertainty is reduced in these measurements compared to those on 2010 data, but still the jet energy scale was the dominant experimental uncertainty. This can be reduced by taking a ratio between results, as measured [5] using data at 7 TeV and 2.76 TeV. This ratio reduces the total uncertainty from 20% to 5%, whilst still providing PDF sensitivity as the two center of mass energies probe different momentum fractions of the proton (x). The measured cross section is higher than predicted in the central rapidity and smaller in the forward rapidity regions. The resulting gluon PDF has reduced uncertainty and the distribution becomes harder. For sea quarks the distribution is softer, and gives a slightly larger error.

A similar but cleaner process to jet measurements is the inclusive photon cross section [6]. When measuring photons with an isolation requirement the results agree well with NLO, especially at high p_{T} where the fragmentation contribution is smaller. The study [7] carried out to investigate PDFs and MCFM in this process found the best shape came from ABM, but the other PDFs were well within errors. Figure 2 shows both the general good agreement of theory over the measured cross section and also the detailed comparison to several PDFs.

Swapping from photon p_{T} distributions to those from Z bosons [8] provides another probe of the gluon PDF. The results are compared to a range of predictions of differing orders where differences of 10% or more are observed,

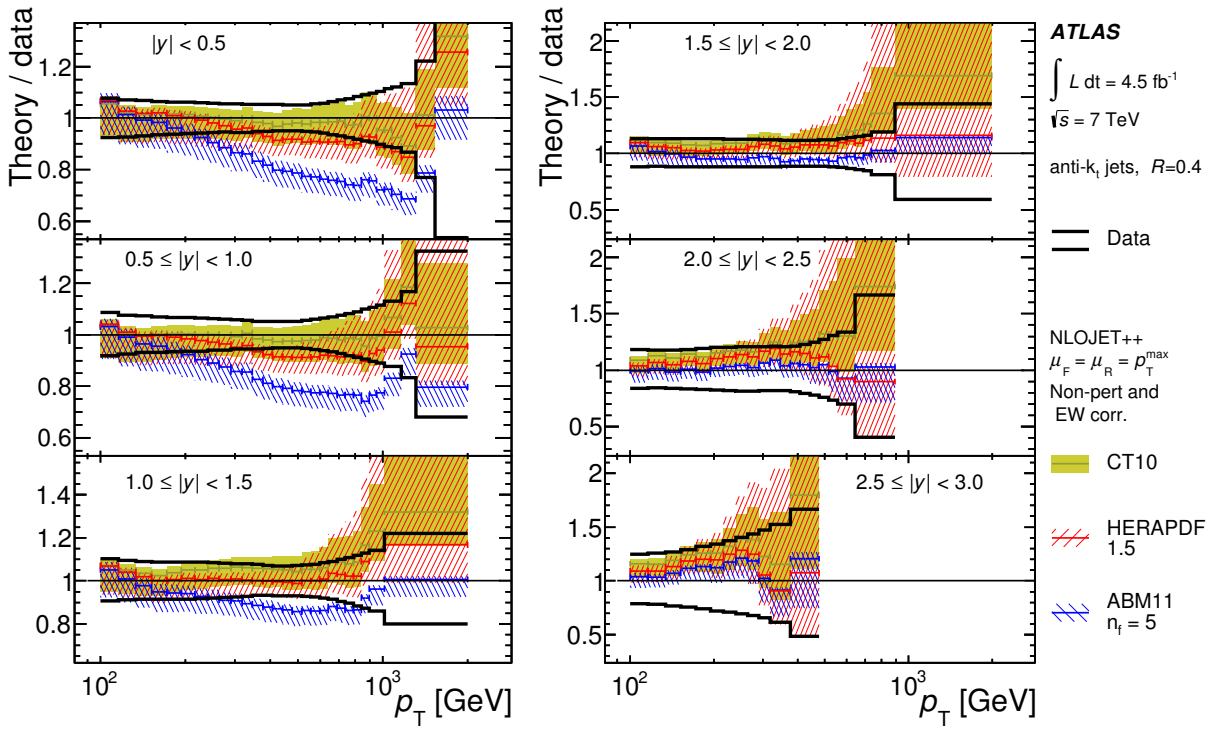

FIGURE 1. Figures of cross section ratios [2] with respect to data in different y regions from the inclusive jet measurement. A selection of the PDF comparisons are shown here, namely: CT10, HERAPDF1.5 and ABM11.

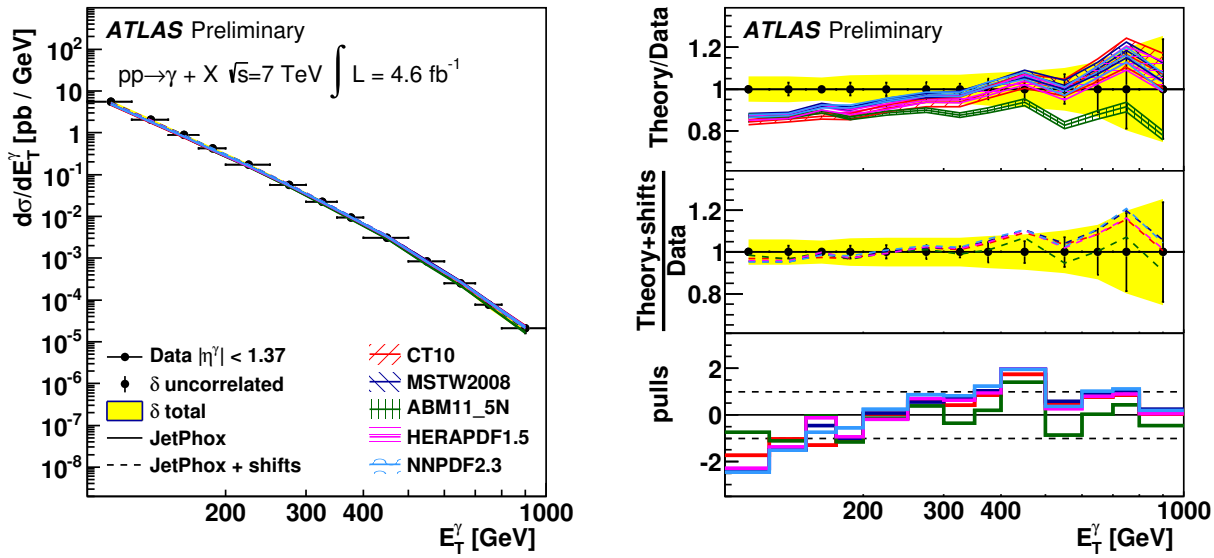

FIGURE 2. Figures of the PDF comparisons [7] showing the measured inclusive photon cross section (left) and cross section ratios (right), with the latter including both the nominal plus shifted PDF comparisons.

although the predictions from ResBos and NNLO+NLL (next-to-NLO plus next-to-leading-log) are within uncertainties. New NNLO Z/W plus one jet predictions may help these distributions to constrain PDFs, but the result has already been used to tune Pythia8 and Powheg+Pythia8.

A final probe of the gluon PDF can be provided by measuring the $t\bar{t}$ process, as done [9] in the one lepton and four jets channel (of which one is a b-tagged jet). By normalising the resulting cross sections, using the total cross section integrated over all bins, the systematic uncertainties are reduced. The results show sensitivity to different PDFs, as shown for some example distributions in Fig. 3, with HERAPDF providing the best agreement. However, the predictions don't include EW corrections so could limit sensitivity, and it is likely that NNLO predictions are important too.

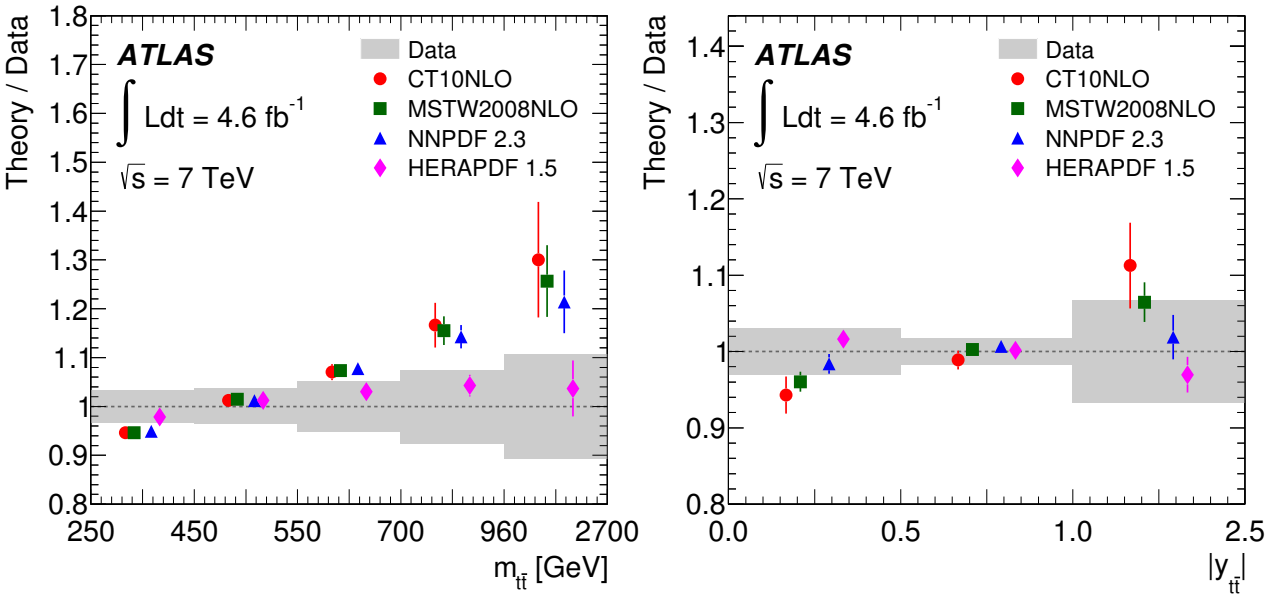

FIGURE 3. Normalised top cross section measurements [9] compared to several PDFs, for mass $m_{t\bar{t}}$ (left) and rapidity $|y_{t\bar{t}}|$ (right).

HEAVY QUARK PDF

In 2010 data a NNLO PDF fit was performed [10] from the cross section measurements as a function of lepton pseudorapidity (η) in W boson events and Z rapidity in Z boson events. This fit combines these measurements with data from HERA to create the PDF: ATLAS-epWZ12. This is done twice using either free or fixed $\bar{s}$, with the former performing better in the Z measurement but no difference is seen in the W case. From the free fit the ratio of the strange-to-down sea quark distributions (r_S) is obtained and compared to different PDFs (ABKM09, NNPDF2.1 MSTW08 and CT10 NLO) of which only CT10 is within uncertainties of the measured value.

This ratio can also be studied in W plus c events [11]. These are selected either by reconstructing a D meson or by requiring a c jet. The events are split depending on the geometry, same/opposite side (SS/OS respectively) of the lepton and c jet/D meson. When comparing the SS to OS cross section ratios to many PDFs, similar trends are observed in both measurements. These show the best agreement with ATLAS-epWZ12 and NNPDF2.3coll (the NNPDF fit from only collider data), with others showing tension to the measured results. Similar to above, the measurement of the lepton η cross section shows good agreement with aMC@NLO. A χ^2 minimisation is performed with HERAFitter resulting in a fit of r_S, as shown in Fig. 4, which again supports that strange is not suppressed.

Measurements related to the b PDF are made in Z plus jet events [12]. Templates of tagging variables are used to extract both the Z plus b and Z plus $b\bar{b}$ cross sections from the jets in these events. The best agreement is found when comparing to predictions from MCFM and aMC@NLO (when using 5 flavours). Unfortunately the theoretical scale errors dominate, which results in the measurement not having any PDF sensitivity currently.

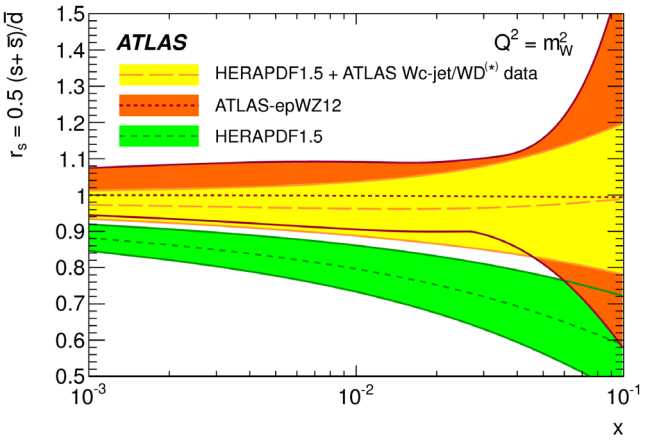

FIGURE 4. Distributions of r_S as a function of x [11], comparing the fit with the latest data to two previous PDFs.

LIGHT QUARK PDF

From the latest 13 TeV data taken at the LHC there have already been measurements of W and Z cross sections [13]. Total and fiducial cross sections are measured, all showing good agreement with the latest PDFs. The total cross sections are compared to results at previous center of mass energies and follow the expected trend of the cross section. Ratios are taken of the fiducial cross sections at 13 TeV, to reduce the systematic uncertainties. The comparisons to the predictions from FEWZ3.1 are shown in Fig. 5. These predictions include EW corrections from FEWZ3.1 itself for Z bosons and from SANC for W bosons. In these ratios the data favours the PDFs that include LHC data in their fit for the W^+/W^- ratio, with no preference seen in the $W^\pm/Z$ ratio.

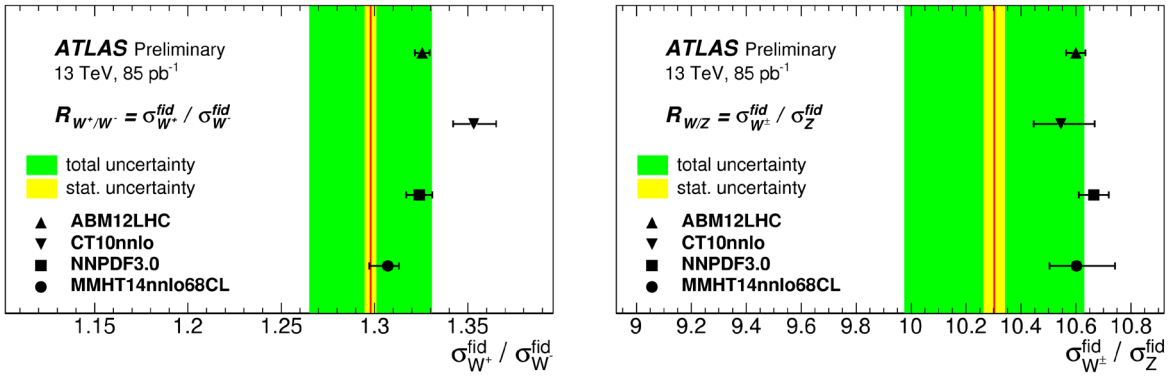

FIGURE 5. Ratios of the measured fiducial cross sections [13]: W^+/W^- (left) and $W^\pm/Z$ (right).

Another probe of light quark PDFs was performed by simultaneously measuring three cross sections [14]. The total cross sections from the three channels: WW, $t\bar{t}$ and $Z \to \tau\tau$ are used to form a contour of likelihood for each pair of results. The $t\bar{t}$ and $Z \to \tau\tau$ comparison to NNLO shows a better agreement with the data and the dominant theoretical uncertainty comes from the PDF, as shown in Fig. 6. Also shown there is the NLO comparison with the $t\bar{t}$ and WW cross sections, where the predictions underestimate data. This is true for all three pairs of cross sections at NLO, but at this order the dominant theoretical uncertainty comes from the scale choice.

Drell-Yan measurements are made at both high [15] and low [16] mass. The high mass range covers 116 GeV $< m_{ee} <$ 1.5 TeV, whereas the low mass covers 26 GeV $< m_{ll} <$ 66 GeV with an extension down to 12 GeV for the muon channel. At high mass the measured cross section is consistently above the predictions from all the PDFs, whereas at low mass there is good agreement with NNLO QCD fit. In all cases there is limited PDF sensitivity, however the high mass results were used in the fit for the photon PDF [17].

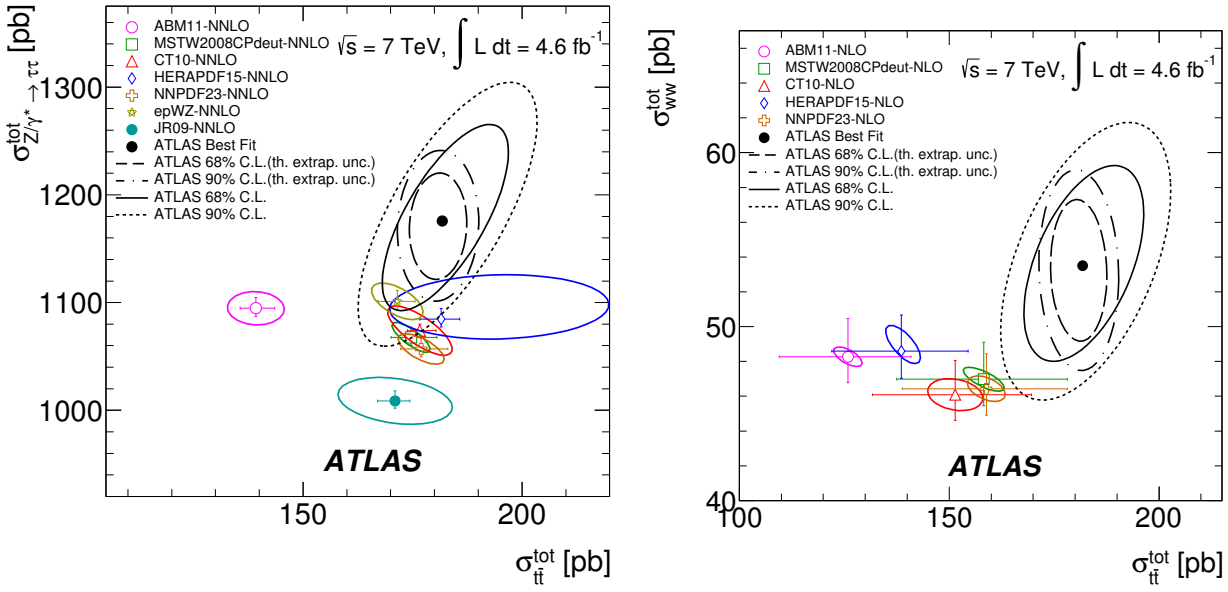

FIGURE 6. Figures of the likelihood contours produced from the measured cross sections [14] and theoretical predictions. Left: NNLO predictions for the $t\bar{t}$ and $Z \to \tau\tau$ cross sections. Right: for the NLO $t\bar{t}$ and WW cross sections.

Conclusion

The measurements presented probe many different areas of both the gluon and quark PDFs. Already 13 TeV results are being made and are of interest for studying PDFs. Many new analyses relevant to PDFs are also under study, an example of this is the four jet cross section [18] which currently has no direct input for PDFs but could do in the future.

REFERENCES

[1] ATLAS Collaboration, JINST **3**, p. S08003 (2008).
[2] ATLAS Collaboration, JHEP **02**, p. 153 (2015), [Erratum: JHEP 09, 141 (2015)], arXiv:1410.8857 [hep-ex] .
[3] ATLAS Collaboration, JHEP **05**, p. 059 (2014), arXiv:1312.3524 [hep-ex] .
[4] ATLAS Collaboration, Eur. Phys. J. **C75**, p. 228 (2015), arXiv:1411.1855 [hep-ex] .
[5] ATLAS Collaboration, Eur. Phys. J. **C73**, p. 2509 (2013), arXiv:1304.4739 [hep-ex] .
[6] ATLAS Collaboration, Phys. Rev. **D89**, p. 052004 (2014), arXiv:1311.1440 [hep-ex] .
[7] ATLAS Collaboration, Tech. Rep. ATL-PHYS-PUB-2013-018 (2013).
[8] ATLAS Collaboration, JHEP **09**, p. 145 (2014), arXiv:1406.3660 [hep-ex] .
[9] ATLAS Collaboration, Phys. Rev. **D90**, p. 072004 (2014), arXiv:1407.0371 [hep-ex] .
[10] ATLAS Collaboration, Phys. Rev. Lett. **109**, p. 012001 (2012), arXiv:1203.4051 [hep-ex] .
[11] ATLAS Collaboration, JHEP **05**, p. 068 (2014), arXiv:1402.6263 [hep-ex] .
[12] ATLAS Collaboration, JHEP **10**, p. 141 (2014), arXiv:1407.3643 [hep-ex] .
[13] ATLAS Collaboration, Tech. Rep. ATLAS-CONF-2015-039 (2015).
[14] ATLAS Collaboration, Phys. Rev. **D91**, p. 052005 (2015), arXiv:1407.0573 [hep-ex] .
[15] ATLAS Collaboration, Phys. Lett. **B725**, 223–242 (2013), arXiv:1305.4192 [hep-ex] .
[16] ATLAS Collaboration, JHEP **06**, p. 112 (2014), arXiv:1404.1212 [hep-ex] .
[17] R. D. Ball *et al.* (NNPDF), Nucl. Phys. **B877**, 290–320 (2013), arXiv:1308.0598 [hep-ph] .
[18] ATLAS Collaboration, Tech. Rep. CERN-PH-EP-2015-181, arXiv:1509.07335 (2015).

Proceedings of the LHCP2015 Conference, St. Petersburg, Russia, August 31 - September 5, 2015

Editors: V.T. Kim and D.E. Sosnov

LHCb PDF measurements

MIKA VESTERINEN

Physikalisches Institut, Im Neuenheimer Feld 226, 69120 Heidelberg.

mika.vesterinen@cern.ch

On behalf of the LHCb Collaboration

Abstract. The LHCb experiment covers a unique region of acceptance at forward rapidities in the high energy proton-proton collisions of the LHC. This means that measurements of particle production in LHCb are directly sensitive to the parton distribution functions at low Björken-x values. Several measurements of inclusive W and Z/γ^* production with the Run-I dataset are reported. Further measurements of W and Z/γ^* production in association with inclusive jets and b- and c-tagged jets are also reported.

Introduction

The search for new physics at the LHC and future hadron colliders is reliant on a precise understanding of the partonic structure of the proton, which is encoded in the parton distribution functions (PDFs). They are constrained by a mixture of hadron collider, fixed target and ep collider data on processes for which the perturbative partonic cross sections can be calculated to a high degree of precision. The LHC experiments themselves play a crucial role in constraining the PDFs. The LHCb experiment [1] covers a unique region of kinematic acceptance [2], having full tracking, calorimeter and particle identification capabilities in the pseudorapidity region $2 < \eta < 5$. In hadron-hadron collisions at a centre of mass energy of $\sqrt{s}$, the production of a state of mass M with rapidity y is initiated by partons of momentum fractions,

$$x_{1,2} = \frac{M}{\sqrt{s}} e^{\pm y}. \tag{1}$$

LHCb measurements of vector boson production are sensitive down to $x \sim 10^{-5}$. Several such measurements are reported in these proceedings. These are based on 1 fb^{-1} recorded at $\sqrt{s} = 7$ TeV in 2011, and 2 fb^{-1} recorded at $\sqrt{s} = 8$ TeV in 2012. In addition to its unique coverage of forward pseudorapidities, LHCb has the most precise luminosity determination at a hadron collider experiment. Using a combination of beam-gas imaging and van der Meer scans, the luminosities of the 7 and 8 TeV datasets are determined with relative uncertainties of 1.7% and 1.12%, respectively [3].

Inclusive W and Z/γ^* cross section at $\sqrt{s} = 7$ TeV

In [4], LHCb reports on a measurement of the cross section for inclusive $Z/\gamma^* \to \mu^+\mu^-$ production. The muons must have transverse momenta in excess of 20 GeV/c, and be reconstructed in the region $2 < \eta < 4.5$. Candidates are considered within a dimuon invariant mass range between 60 and 120 GeV/c^2. At least one of the muons must be matched to a single muon line at all stages of the trigger. Roughly 60k signal candidates are obtained, with less than 1% background contamination. The signal yields are corrected for the muon trigger, reconstruction and selection efficiencies, which are measured using $Z/\gamma^* \to \mu^+\mu^-$ candidates with special requirements. For example, the muon identification efficiencies are measured with a sample in which these requirements are only imposed on one of the muons. Integrated over the kinematic acceptance defined by the above requirements, the following cross section is obtained,

$$\sigma(pp \to Z/\gamma^* \to \mu^+\mu^-) = 76.0 \pm 0.3_{\text{stat}} \pm 0.5_{\text{syst}} \pm 1.0_{\text{beam}} \pm 1.3_{\text{lumi}} \text{ pb},$$

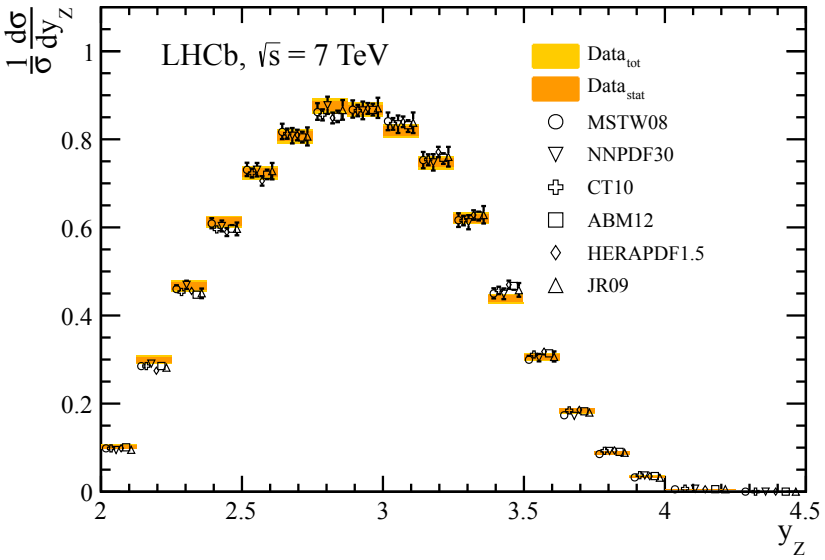

FIGURE 1. The $Z/\gamma^* \to \mu^+\mu^-$ cross section as a function of rapidity [4].

where the third uncertainty relates to the knowledge of the LHC collision energy. The cross section is also measured as a function of the transverse momentum, ϕ^*_η [5], and rapidity of the dimuon pair. The latter is shown in Figure 1, in comparison to predictions from the FEWZ NNLO generator [6, 7] with the ABM12 [8], CT10 [9], HERA1.5 [10], JR09 [11], MSTW08 [12] and NNPDF3.0 [13]. LHCb has also measured $Z/\gamma^* \to e^+e^-$ production at $\sqrt{s} = 7$ TeV [14] and 8 TeV [15], and $Z/\gamma^* \to \tau^+\tau^-$ production at $\sqrt{s} = 7$ TeV [16].

LHCb reports a measurement of W production at $\sqrt{s} = 7$ TeV [17]. The kinematic requirements on the muon are the same as those that are applied to the muons in the Z/γ^* study. Further isolation requirements are needed to control the level of background from the in-flight decays of hadrons to muons. Candidates are vetoed if another high p_T muon is present in the event, in order to suppress the background from $Z/\gamma^* \to \mu^+\mu^-$. The signal yields are extracted by fitting the muon p_T spectra as shown in Figure 2. The signal purity is around 70%. The signal yields are corrected for all sources of inefficiency using the same methods described above in the context of the $Z/\gamma^* \to \mu^+\mu^-$ study. Integrated over the kinematic acceptance defined above, the following cross sections are measured,

$$\sigma(pp \to W^+ \to \mu^+\nu) = 861.0 \pm 2.0_{\text{stat}} \pm 11.2_{\text{syst}} \pm 14.7_{\text{lumi}} \text{ pb},$$

$$\sigma(pp \to W^- \to \mu^-\bar{\nu}) = 675.8 \pm 1.9_{\text{stat}} \pm 8.8_{\text{syst}} \pm 11.6_{\text{lumi}} \text{ pb},$$

and the following ratio is obtained,

$$\frac{\sigma(pp \to W^+ \to \mu^+\nu)}{\sigma(pp \to W^- \to \mu^-\bar{\nu})} = 1.274 \pm 0.005_{\text{stat}} \pm 0.009_{\text{syst}}.$$

Figure 3 shows the two separate cross sections as a function of the muon η, compared to predictions with the same six PDF sets described above. Four different cross section ratios of W^+, W^- and Z/γ^* are reported [4]. These are determined with higher experimental precision due to cancelling systematic uncertainties, notably in the luminosity and in the muon reconstruction efficiencies. These ratios will help to constrain the flavour structure of the proton, in particular the strange quark content and symmetry.

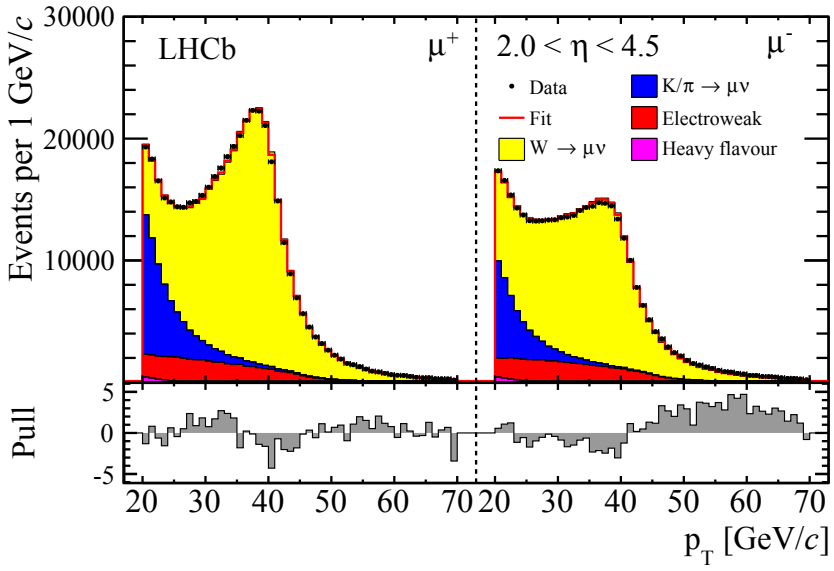

FIGURE 2. The muon p_T spectrum in the (left) $W^+ \to \mu^+\nu$ and (right) $W^- \to \mu^-\bar{\nu}$ candidates [17].

Low mass Drell-Yan production.

In [18], LHCb reported a measurement of $\gamma^* \to \mu^+\mu^-$ production at $\sqrt{s} = 7$ TeV, and covering invariant masses as low as 5 GeV, which corresponds to x values below 10^{-5}. This measurement is based on a 37 pb^{-1} recorded during the 2010 run. The signal yield is extracted by fitting the muon isolation distributions to subtract the hadronic backgrounds. Figure 4 shows the measured cross section as a function of the dimuon invariant mass, which is in good agreement with the QCD calculations.

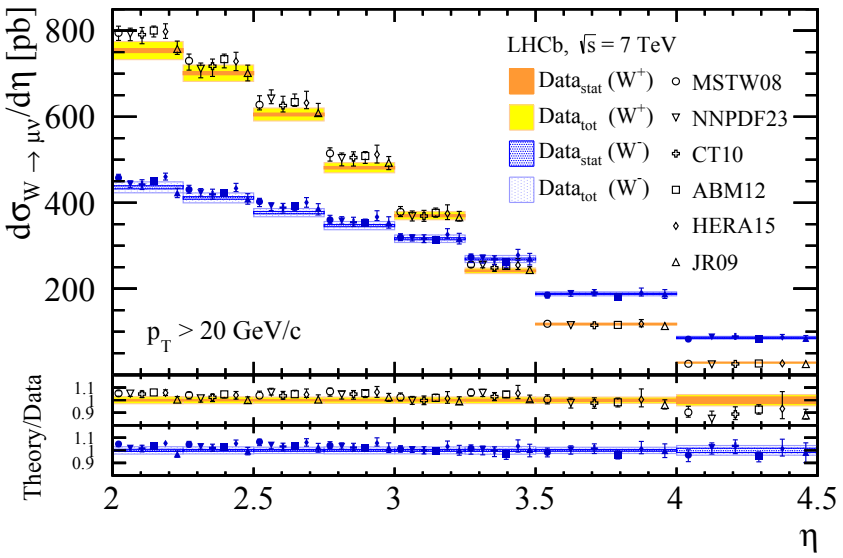

FIGURE 3. The $W^+ \to \mu^+\nu$ and $W^- \to \mu^-\bar{\nu}$ cross sections as a function of the muon η [17].

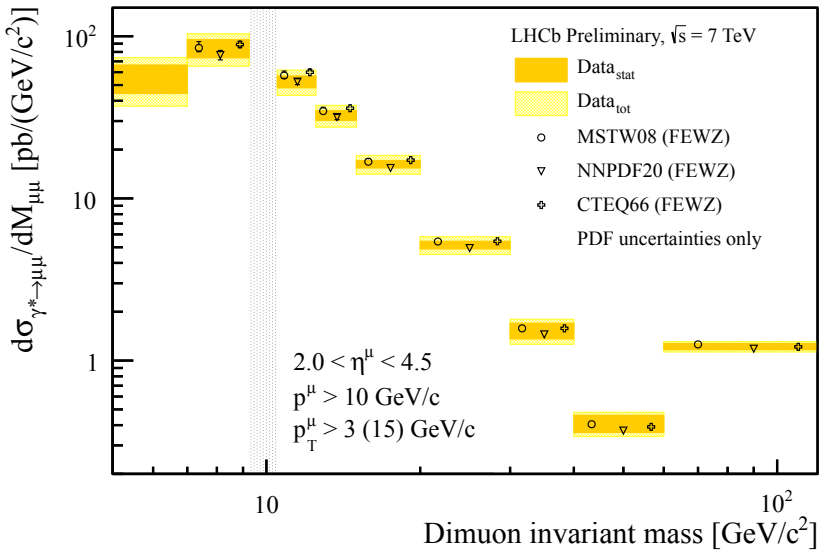

FIGURE 4. The Z/γ^* cross section as a function of the dimuon invariant mass [18]

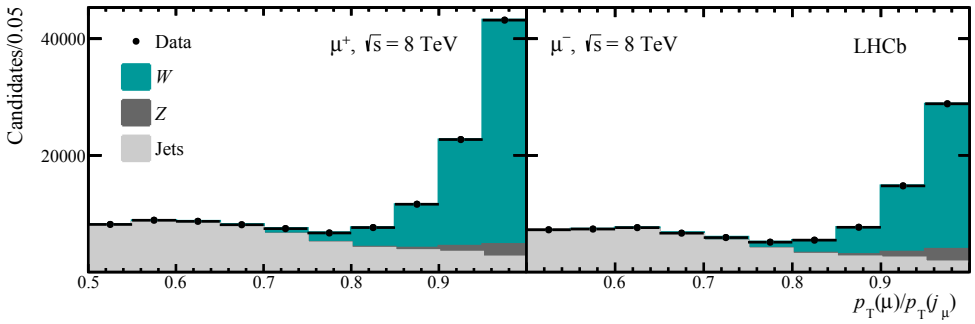

FIGURE 5. The $p_T(\mu)/p_T(\text{jet},\mu)$ distribution of (left) W^++jet and (right) W^-+jet candidates, in the 2012 dataset, corresponding to a centre of mass energy of 8 TeV. [24]

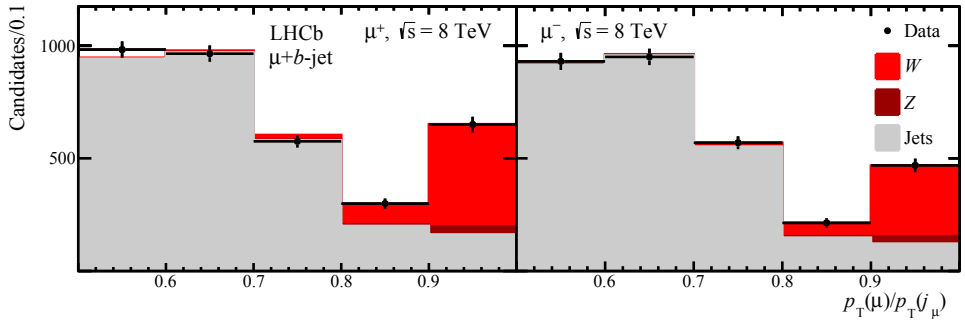

FIGURE 6. The $p_T(\mu)/p_T(\text{jet},\mu)$ distribution of (left) $W^+ + b$-jet and (right) $W^- + b$-jet candidates, in the 2012 dataset, corresponding to a centre of mass energy of 8 TeV. [24]

Vector boson production in association with jets

In [19] LHCb reports a measurement of Z/γ^* production in association with jets. The selection requirements on the $Z/\gamma^* \to \mu^+\mu^-$ candidates are the same as those applied in the inclusive measurement described above. The jets are reconstructed with the anti-k_T algorithm [20] with a cone size of 0.5, as implemented in the FASTJET package [21]. In [22] this measurement was extended to study $Z/\gamma^* + b$-jet production by searching for a secondary vertex within the jet. LHCb recently developed dedicated b- and c-jet identification algorithms [23]. A boosted decision tree is trained to distinguish b-jets from light jets, while another is trained to distinguish between b- and c-jets. For jets with $p_T > 20$ GeV/c and $2.2 < \eta < 4.2$, it is possible to identify b-jets with an efficiency of around 65% for a mis-id (from light jets) rate of 1%. For c-jets the corresponding efficiency with the same fake rate is around 25%. In [24] LHCb reported a measurement of W+jet production with the full Run-I dataset. The signal component is extracted with the use of an isolation variable that considers the p_T of the reconstructed jet which contains the muon. Figure 5 shows, for the 2012 part of the dataset, the $p_T(\mu)/p_T(\text{jet},\mu)$ distribution to which a fit is performed to determine the signal yield. Using the identification algorithms described above, the W+b and W+c components are extracted. The $p_T(\mu)/p_T(\text{jet},\mu)$ distributions are shown for b- and c-jet enriched regions in Figures 6 and 7, respectively. All of these measurements are in agreement with QCD calculations. The W+jet measurements will constrain the valence d-quark PDF, while the W+charm measurements will constrain the strange quark PDFs, and the W+beauty measurements will constrain the gluon PDF.

Conclusions

The study of particle production within the LHCb experiment probes the proton structure in a unique region of x and Q^2. Compared to the other LHC experiments, LHCb is the only one that has full tracking, calorimeter and particle

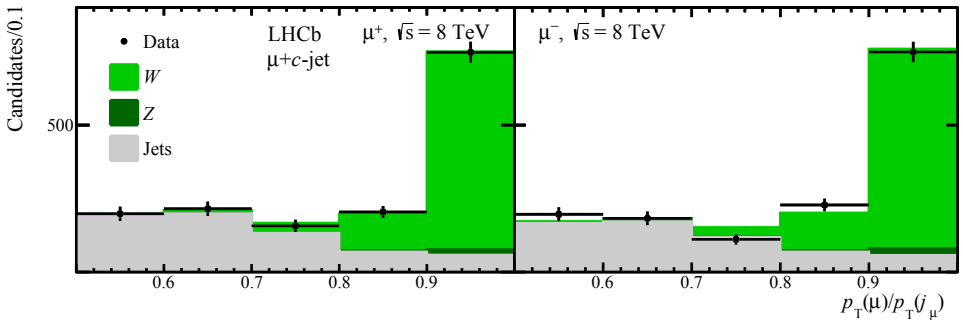

FIGURE 7. The $p_T(\mu)/p_T(\text{jet},\mu)$ distribution of (left) W^+ + c-jet and (right) W^- + c-jet candidates, in the 2012 dataset, corresponding to a centre of mass energy of 8 TeV. [24]

identification over the pseudorapidity range $2 < \eta < 5$. Several measurements of inclusive W and Z/γ^* production are reported. These are complemented by further measurements of associated production of W and Z/γ^* with inclusive jets, and with b- and c-tagged jets. These measurements have helped to constrain and reduce uncertainties on current PDF sets, while new measurements from LHCb will help to improve the precision of future PDF sets even further.

REFERENCES

[1] LHCb reoptimized detector design and performance: Technical Design Report, 2003, lHCb-TDR-009.

[2] R. S. Thorne, A. D. Martin, W. J. Stirling, and G. Watt, "Parton Distributions and QCD at LHCb," in *Proceedings, 16th International Workshop on Deep Inelastic Scattering and Related Subjects (DIS 2008)* (2008) p. 30, arXiv:0808.1847 [hep-ph] .

[3] R. Aaij *et al.* (LHCb), JINST **9**, p. P12005 (2014), arXiv:1410.0149 [hep-ex] .

[4] R. Aaij *et al.* (LHCb collaboration), JHEP **08**, p. 039 (2015), arXiv:1505.07024 [hep-ex] .

[5] A. Banfi, S. Redford, M. Vesterinen, P. Waller, and T. R. Wyatt, Eur. Phys. J. **C71**, p. 1600 (2011), arXiv:1009.1580 [hep-ex] .

[6] Y. Li and F. Petriello, Phys. Rev. **D86**, p. 094034 (2012), arXiv:1208.5967 [hep-ph] .

[7] R. Gavin, Y. Li, F. Petriello, and S. Quackenbush, Comput. Phys. Commun. **182**, 2388–2403 (2011), arXiv:1011.3540 [hep-ph] .

[8] S. Alekhin, J. Blumlein, and S. Moch, Phys. Rev. **D89**, p. 054028 (2014), arXiv:1310.3059 [hep-ph] .

[9] H.-L. Lai, M. Guzzi, J. Huston, Z. Li, P. M. Nadolsky, J. Pumplin, and C. P. Yuan, Phys. Rev. **D82**, p. 074024 (2010), arXiv:1007.2241 [hep-ph] .

[10] F. D. Aaron *et al.* (ZEUS, H1), JHEP **01**, p. 109 (2010), arXiv:0911.0884 [hep-ex] .

[11] P. Jimenez-Delgado and E. Reya, Phys. Rev. **D79**, p. 074023 (2009), arXiv:0810.4274 [hep-ph] .

[12] A. D. Martin, W. J. Stirling, R. S. Thorne, and G. Watt, Eur. Phys. J. **C63**, 189–285 (2009), arXiv:0901.0002 [hep-ph] .

[13] R. D. Ball *et al.* (NNPDF), JHEP **04**, p. 040 (2015), arXiv:1410.8849 [hep-ph] .

[14] R. Aaij *et al.* (LHCb), JHEP **02**, p. 106 (2013), arXiv:1212.4620 [hep-ex] .

[15] R. Aaij *et al.* (LHCb), JHEP **05**, p. 109 (2015), arXiv:1503.00963 [hep-ex] .

[16] R. Aaij *et al.* (LHCb), JHEP **01**, p. 111 (2013), arXiv:1210.6289 [hep-ex] .

[17] R. Aaij *et al.* (LHCb collaboration), JHEP **12**, p. 079 (2014), arXiv:1408.4354 [hep-ex] .

[18] Inclusive low mass Drell-Yan production in the forward region at $\sqrt{s} = 7$ TeV, Mar 2012.

[19] R. Aaij *et al.* (LHCb collaboration), JHEP **01**, p. 033 (2014), arXiv:1310.8197 [hep-ex] .

[20] M. Cacciari, G. P. Salam, and G. Soyez, JHEP **04**, p. 063 (2008), arXiv:0802.1189 [hep-ph] .

[21] M. Cacciari and G. P. Salam, Phys. Lett. **B641**, 57–61 (2006), arXiv:hep-ph/0512210 [hep-ph] .

[22] R. Aaij *et al.* (LHCb), JHEP **01**, p. 064 (2015), arXiv:1411.1264 [hep-ex] .

[23] R. Aaij *et al.* (LHCb), JINST **10**, p. P06013 (2015), arXiv:1504.07670 [hep-ex] .

[24] R. Aaij *et al.* (LHCb), Phys. Rev. **D92**, p. 052001 (2015), arXiv:1505.04051 [hep-ex] .

Proceedings of the LHCP2015 Conference, St. Petersburg, Russia, August 31 - September 5, 2015

Editors: V.T. Kim and D.E. Sosnov

Soft QCD models and general-purpose Monte Carlo simulation

ANDRZEJ SIÓDMOK[1,2]

[1]*Theoretical Physics Department, CERN, Geneva, Switzerland.*
[2]*The Henryk Niewodniczański Institute of Nuclear Physics Polish Academy of Sciences Radzikowskiego 152, 31-342 Kraków, Poland.*

andrzej.siodmok@cern.ch

Abstract. We begin with a brief description of the main building blocks of Monte Carlo event generators (MCEG) for the full simulation of hadron–hadron collisions. Next, we focus on soft QCD models and in particular on Multiple Partonic Interaction (MPI) models that are implemented in MCEG. Finally, we present a comparison of three main Monte Carlo event generators, Herwig++, PYTHIA and SHERPA, and also a cosmic-rays model EPOS to a range of LHC data sets which are sensitive to the MPI activity.

INTRODUCTION

Monte Carlo event generators (MCEG) are of crucial importance for particle physics. They provide fully exclusive simulations of high-energy collisions, therefore they are used by almost all experimental collaborations to plan their experiments and analyze their data, and by theorists to simulate the complex final states of the fundamental interactions which are essential in the search for Beyond the Standard Model physics. Currently there are three families of MCEG available which all offer suitable frameworks for LHC physics: Herwig(6/++/7) [1, 2, 3], Pythia(6/8)[4, 5] and Sherpa[6, 7]. In this short contribution we briefly discuss the main building blocks of a Monte Carlo event generation[1] and focus on soft QCD models and in particular Multiple Parton Interaction (MPI) models. MPI models are essential for a proper description of the minimum-bias (MB) and underlying event (UE) data from hadron colliders. The amount of UE activity at the LHC is measured, so it is tempting to think that the contribution of the UE is known. However, there are observables that depend on correlations or fluctuations away from average value of the UE, including, to varying extents, any measurement relying on jets or isolation criteria. In fact, almost every observable[2] that will be used for beyond the standard model searches or precision measurements falls into this class, so the correction must be represented by a model tuned to data, rather than by a single number measured from data.

Event Generation

The main building blocks of MCEG needed for a simulation of a proton-proton collision at the LHC are:

1. Hard process
2. Parton shower
3. Hadronization
4. Multiple Interactions
5. Decays of unstable hadrons

[1]For a detailed description of MCEG with much more information on the physics background we refer the reader to the MCnet review paper on Monte Carlo event generators [8] and the much shorter but more recent documents [9, 10].

[2]Some measurements based on boosted jet substructure techniques are examples of an exception in that respect, see for example [11, 12, 13].

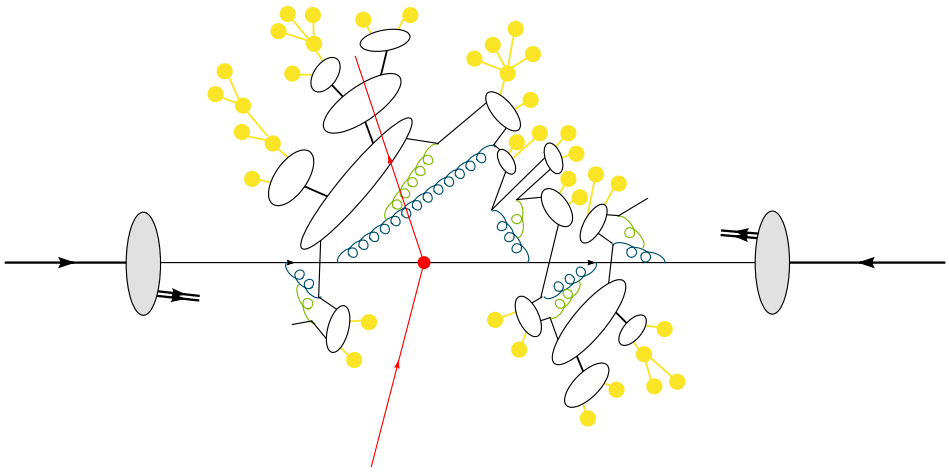

FIGURE 1. Drawing of the simulation of a pp collision shown in [14]. The MPI are not included in this figure.

In Fig. 1 we show a cartoon of the event generation (excluding MPI). The generation begins with a hard signal process, in the figure this is lepton pair production (red). Then the parton shower evolution (marked with the dark and light green gluon curly lines) starts from the hard process and evolves downwards in momentum scale to a point $\sim$ 1 GeV where perturbation theory breaks down. At this scale the partonic degrees of freedom are converted into hadrons (yellow circles) via a hadronization model. In the case of Fig. 1 the cluster hadronization model (white blobs) is presented. The cluster model [15] was introduced in Herwig and also implemented in Sherpa[16]. While Pythia's hadronization model is based on the famous Lund string model [17]. The last step of event generation is based on the fact that many of these hadrons (yellow blobs) are not stable particles and therefore decay. In addition to this sequence of steps, all initiated by the hard subprocess, there may be additional semi-hard processes, called multiple partonic interactions, which are the main subject of this note. These are mostly fairly soft QCD interactions that also undergo all of the steps described above for the hard process and produce additional particles in all the available phase space.

Multiple parton interactions

The first detailed Monte Carlo model for perturbative MPI was proposed in [18] and was the main model in Pythia for a long time. The models implemented in Herwig [19, 20] and the first model in Sherpa are based on a similar physical picture. There are however important details where the approach deviates from the formalism in Pythia. For example in the recent Pythia versions the additional hard scatters are interleaved with the parton shower [21, 22] which is not the case in Sherpa or Herwig++. This approach allows a picture where MPI and the parton shower radiation are interleaved in one common sequence of decreasing $p_\perp$ values. Before we highlight some other differences between the models let us first briefly describe the MPI model implemented in Herwig++ [23, 24]. The model is formulated in impact parameter space. At fixed impact parameter $\vec{b}$, multiple parton scatterings are assumed to be independent which leads to an expression for the average number of hard interactions:

$$\bar{n}(\vec{b}, s) = A(\vec{b}; \mu^2)\sigma^{\text{inc}}(s; p_t^{\text{min}}) \,, \tag{1}$$

where $A(\vec{b}; \mu^2)$ is a so-called overlap function describing the two colliding protons as a function of the impact parameter $\vec{b}$. In Herwig++ $A(\vec{b}; \mu^2)$ is modelled by the electromagnetic form factor, see Fig. 2(a). The parameter μ^2 appearing in the function is one of the main tuning parameters and can be interpreted as an effective inverse proton radius.In Pythia 8 there are five different options for the overlap function, including a double Gaussian matter distribution which is very similar to the one obtained from the electromagnetic form factor. In Herwig++, parton-parton scatterings ($\sigma^{\text{inc}}(s; p_t^{\text{min}})$) are divided into soft and hard by a parameter p_t^{min}, which is another main tuning parameter in the model. Above p_t^{min}, scatters are assumed to be perturbative and take place according to leading order QCD matrix elements. Below p_t^{min}, scatters are assumed to be non-perturbative, with "Gaussian" transverse momentum distribution and valence-like longitudinal momentum distribution, see Fig. 2(b). In Pythia in order to damp the cross

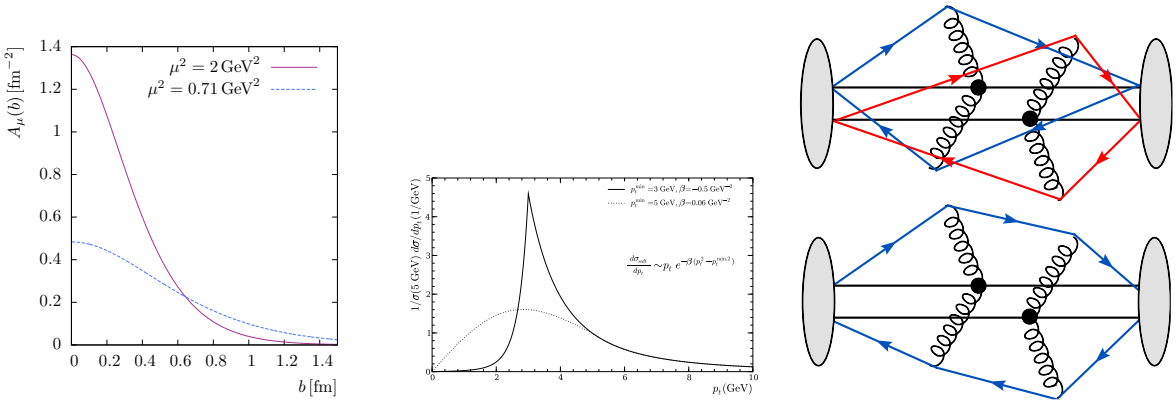

(a) The overlap function used in Herwig++ (two values of μ^2 parameter).

(b) Division of parton-parton scatterings into soft and hard in Herwig++.

(c) An example of two different colour connection of MPI.

FIGURE 2. Main building blocks of MPI model in Herwig++.

section at $p_T \to 0$, the cross section is multiplied by a regularization factor $(p_T^2/(p_T^2 + p_{T0}^2))^2$, and simultaneously the α_s is evaluated at a scale $p_T^2 + p_{T0}^2$, where p_{T0} is a free parameter of the model. It is interesting to mention that there is a CMS measurement [25] which gives some hints towards the mechanism by which the parton-parton cross sections are unitarised when approaching low-p_T. In both Herwig++ and Pythia p_{T0} and $p_t^{\min}$ vary with energy. In Herwig++ according to:

$$p_t^{\min}(s) = p_{\perp,0}^{\min}\left(\frac{\sqrt{s}}{E_0}\right)^b, \tag{2}$$

and, in principle, $p_{\perp,0}^{\min}$ and b are fitted to data, with $E_0 = 7$ TeV. A similar evolution of p_{T0} is implemented in Pythia. Finally, the last and the least understood building block of MPI models is so-called colour reconnection (CR), see Fig. 2(a). The idea behind CR is based on colour preconfinement [26], which implies that parton jets emerging from different partonic interactions are colour-connected (clustered in Herwig++) if they are located closely in phase space. As the MPI model does not take that into account, those colour connections have to be adapted afterwards by means of a CR procedure. In Herwig++ the CR model defines the distance between two partons based on their invariant mass, i.e the distance is small when their invariant mass (cluster mass) is small. Therefore, the aim of the CR model is to reduce the colour length $\lambda \equiv \sum_{i=1}^{N_{cl}} m_i^2$, where N_{cl} is the number of clusters in an event and m_i is the invariant mass of cluster i. A similar model of CR was implemented some time ago in Pythia [4] and recently there were new ideas of how to improve the model for example by going beyond leading colour approximation [27, 28]. In Fig. 3 we show an observable that is sensitive to CR: $\langle p_t \rangle$ vs N_{ch}. We expect that it should be almost flat when the MPI system hadronizes independently (i.e. without additional correlations due, to for example CR). In Fig. 3 (left panel) we see that the measured distribution is not flat and that all generators (except Sherpa which does not have a CR model) are able to describe $\langle p_t \rangle$ vs N_{ch} MB data collected at 7 TeV. In Fig. 3 (middle panel) we show charged-particle multiplicities as a function of the pseudorapidity, ATLAS MB data was collected at the new energy frontier 13 TeV [29] which means that it was not used for the tuning of MCEG. Pythia 8 seems to describe the data reasonably well, however the cosmic-rays model EPOS [30, 31] seems to describe the MB data even better. On the other hand we will see, that it fails to describe the UE data. Herwig++ fails to describe the MB data, one of the reasons for this is that it was only tuned to the UE data. However it is worth noticing that the older UE tune of Herwig++ gives a much better description of MB data, Fig. 3 (right panel) shows the potential of the model. This observation brings us to the point that in general MPI models have a problem describing both UE and MB data sets simultaneously (using the same tune). Similar tension is also visible in the disagreement of MPI models with the effective cross section for double-parton scattering σ_{eff} [32, 33]. However, in the recent publication [34] the authors provided a Herwig++ tune which is able to describe UE data over the range of energies in addition to σ_{eff} measured by the CDF and more modern experiments. The other type of measurements which are very sensitive to MPI activity are Underlying Event measurements which are made relative to a leading object (the hardest charged track or a jet). Then, the transverse

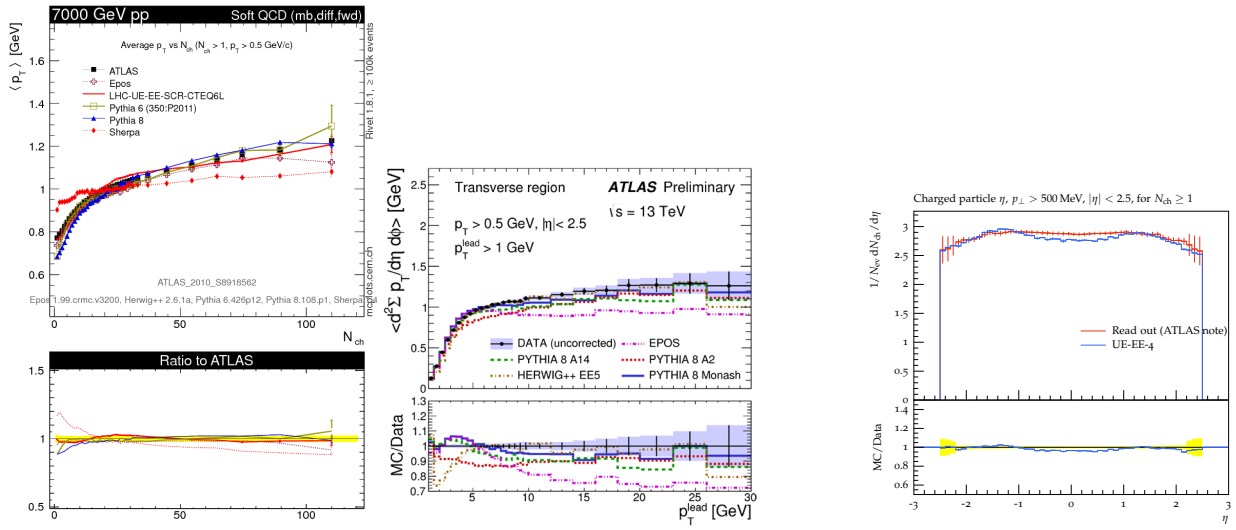

FIGURE 3. ATLAS MB data showing the average transverse momentum as a function of the number of charged particles at 7 TeV— [35] (left panel), charged-particle multiplicities as a function of the pseudorapidity at 13 TeV [29] (middle panel) and the same as the middle panel but with data compared to an older tune EE-4 of HERWIG++. The dots represent the data and the curves represent the predictions from different MC models.

plane is subdivided in azimuthal angle ϕ relative to this leading object at $\phi = 0$. The region around the leading object, $|\phi| < \pi/3$, is called the "towards" region and the opposite region, where we usually find a recoiling hard jet, $|\phi| > 2\pi/3$, is called the "away" region. The remaining region, transverse to the leading object and its recoil, where the underlying event is expected to be least 'contaminated' by activity from the hard subprocess, is called the "transverse" region. Therefore, in Fig. 4 we show the mean scalar $p_\perp$ sum of stable particles as a function of $p_\perp^{\rm lead}$ in the transverse

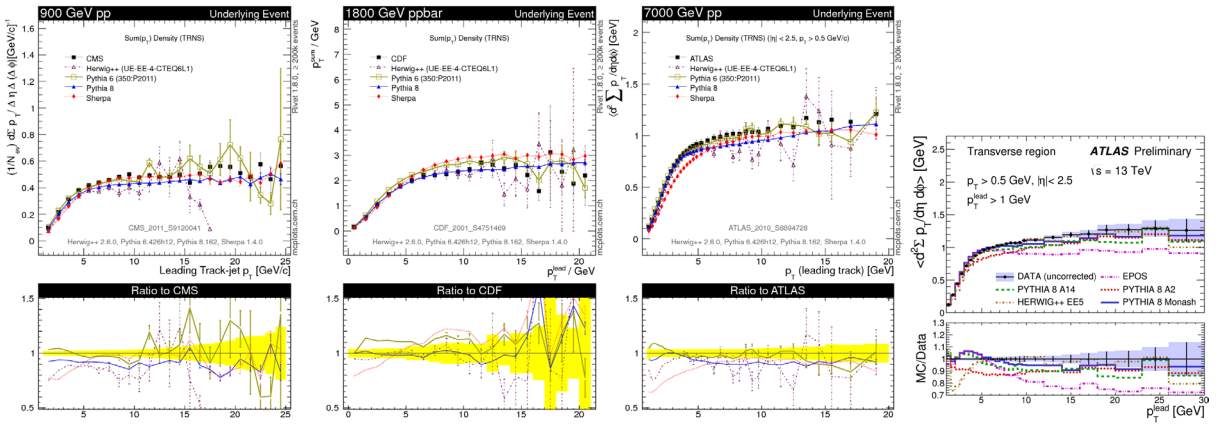

FIGURE 4. ATLAS data at 900GeV (1st column), CDF data at 1800GeV (2nd column), ATLAS data at 7TeV (3rd column) and 13TeV (4th column) showing the mean scalar $p_\perp$ sum of the stable charged particles in the "transverse" area as a function of $p_\perp^{\rm lead}$.

region measured at different energies (from 900 GeV to 13 TeV). The plateau at high p_T in Fig. 4 shows nicely that the transverse activity decouples from the leading object momentum for large momenta, hence the interpretation as underlying event activity is correct. We can also see that all MCEG describe the data collected at different collider energies reasonably well, which would not be possible without good modeling of MPI. In the last column we show new data collected at 13 TeV, this is not used in the tuning procedure and therefore can be used to test the predictions of the models. We can see that the models are in good agreement with the data, except, as mentioned before, EPOS. This is because EPOS currently has no hard component in the model. Finally, despite the significant success of MPI

models in describing a range of MB and UE there are still open problems. Let me show just one which is clearly visible in Fig. 5, taken from a CMS measurement of strange particle production in UE [36]. We can see that if we start to ask more detailed questions about the nature of the UE (for example asking about strange particles) some models have significant problems producing a correct answer. However, there is a constant effort to improve the MPI models and already there has been a first attempt [37] to solve the problem in Fig. 5. Finally, let me just mention that there is a new approach to MPI in SHERPA called SHRiMPS. It aims at a smooth inclusion of diffractive and soft interactions into the multiple iteraction picture, based on a Gribov–Regge formalism [38]. However it is not yet fully developed and tuned, therefore we don't show its results.

Conclusion

Amazing progress has been made in the development of MCEG over the previous decades. We have seen that a wide range of LHC data sensitive to soft QCD is well described by MCEG. The other LHC data sets triggered new developments of the MC event generators. Finally, there are data sets which show that there is still need for further development. As the LHC studies more subtle effects, generators must keep increasing their precision. This is only possible with an appropriate input from the experimental community which gives a solid basis for future developments of MCEG.

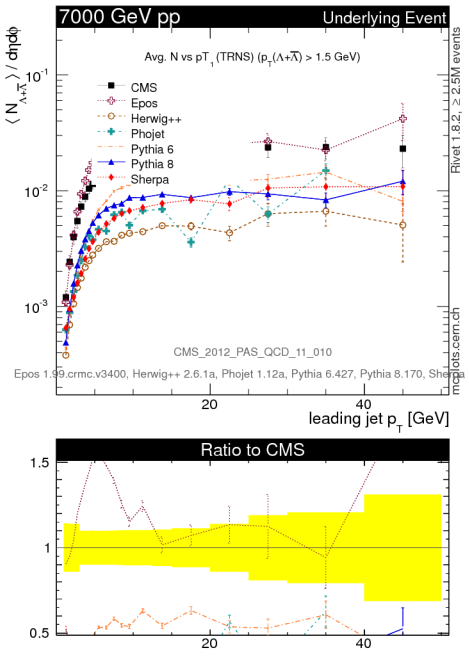

FIGURE 5. CMS data at at 7TeV showing the multiplicity density of the $\Lambda + \bar{\Lambda}$ particles in the "transverse" area as a function of $p_{\perp}^{\text{lead}}$.

ACKNOWLEDGMENTS

We thank the organizers for the very pleasant and fruitful conference. We wish to acknowledge Stephen Webster for his critical reading of these proceedings.

REFERENCES

[1] G. Corcella, I. G. Knowles, G. Marchesini, S. Moretti, K. Odagiri, P. Richardson, M. H. Seymour, and B. R. Webber, JHEP **01**, p. 010 (2001), arXiv:hep-ph/0011363 [hep-ph] .

[2] M. Bahr *et al.*, Eur. Phys. J. **C58**, 639–707 (2008), arXiv:0803.0883 [hep-ph] .
[3] J. Bellm *et al.*, (2015), arXiv:1512.01178 [hep-ph] .
[4] T. Sjostrand, S. Mrenna, and P. Z. Skands, JHEP **05**, p. 026 (2006), arXiv:hep-ph/0603175 [hep-ph] .
[5] T. Sjstrand, S. Ask, J. R. Christiansen, R. Corke, N. Desai, P. Ilten, S. Mrenna, S. Prestel, C. O. Rasmussen, and P. Z. Skands, Comput. Phys. Commun. **191**, 159–177 (2015), arXiv:1410.3012 [hep-ph] .
[6] T. Gleisberg, S. Hoeche, F. Krauss, A. Schalicke, S. Schumann, and J.-C. Winter, JHEP **02**, p. 056 (2004), arXiv:hep-ph/0311263 [hep-ph] .
[7] T. Gleisberg, S. Hoeche, F. Krauss, M. Schonherr, S. Schumann, F. Siegert, and J. Winter, JHEP **02**, p. 007 (2009), arXiv:0811.4622 [hep-ph] .
[8] A. Buckley *et al.*, Phys. Rept. **504**, 145–233 (2011), arXiv:1101.2599 [hep-ph] .
[9] M. H. Seymour and M. Marx, "Monte Carlo Event Generators," (2013) arXiv:1304.6677 [hep-ph] .
[10] A. Sidmok, Acta Phys. Polon. **B44**, 1587–1601 (2013).
[11] M. H. Seymour, Z. Phys. **C62**, 127–138 (1994).
[12] A. Altheimer *et al.*, Eur. Phys. J. **C74**, p. 2792 (2014), arXiv:1311.2708 [hep-ex] .
[13] M. Dasgupta, A. Powling, and A. Siodmok, JHEP **08**, p. 079 (2015), arXiv:1503.01088 [hep-ph] .
[14] S. Gieseke, Nucl. Phys. Proc. Suppl. **222-224**, 174–186 (2012).
[15] B. R. Webber, Nucl. Phys. **B238**, p. 492 (1984).
[16] J.-C. Winter, F. Krauss, and G. Soff, Eur. Phys. J. **C36**, 381–395 (2004), arXiv:hep-ph/0311085 [hep-ph] .
[17] B. Andersson, G. Gustafson, G. Ingelman, and T. Sjostrand, Phys. Rept. **97**, 31–145 (1983).
[18] T. Sjostrand and M. van Zijl, Phys. Rev. **D36**, p. 2019 (1987).
[19] J. M. Butterworth, J. R. Forshaw, and M. H. Seymour, Z. Phys. **C72**, 637–646 (1996), arXiv:hep-ph/9601371 [hep-ph] .
[20] I. Borozan and M. H. Seymour, JHEP **09**, p. 015 (2002), arXiv:hep-ph/0207283 [hep-ph] .
[21] T. Sjostrand and P. Z. Skands, JHEP **03**, p. 053 (2004), arXiv:hep-ph/0402078 [hep-ph] .
[22] T. Sjostrand and P. Z. Skands, Eur. Phys. J. **C39**, 129–154 (2005), arXiv:hep-ph/0408302 [hep-ph] .
[23] M. Bahr, S. Gieseke, and M. H. Seymour, JHEP **07**, p. 076 (2008), arXiv:0803.3633 [hep-ph] .
[24] M. Bahr, J. M. Butterworth, S. Gieseke, and M. H. Seymour, "Soft interactions in Herwig++," in *Proceedings, 1st International Workshop on Multiple Partonic Interactions at the LHC (MPI08)* (2009), pp. 239–248, arXiv:0905.4671 [hep-ph] .
[25] C. Collaboration (CMS), (2014).
[26] D. Amati and G. Veneziano, Phys. Lett. **B83**, p. 87 (1979).
[27] J. R. Christiansen and P. Z. Skands, JHEP **08**, p. 003 (2015), arXiv:1505.01681 [hep-ph] .
[28] J. R. Christiansen and T. Sjostrand, Eur. Phys. J. **C75**, p. 441 (2015), arXiv:1506.09085 [hep-ph] .
[29] "Charged-particle distributions in sqrt(s)=13 TeV p p interactions measured with the ATLAS detector at the LHC," Tech. Rep. ATLAS-CONF-2015-028 (CERN, Geneva, 2015).
[30] H. J. Drescher, M. Hladik, S. Ostapchenko, T. Pierog, and K. Werner, Phys. Rept. **350**, 93–289 (2001), arXiv:hep-ph/0007198 [hep-ph] .
[31] K. Werner, I. Karpenko, T. Pierog, M. Bleicher, and K. Mikhailov, Phys. Rev. **C82**, p. 044904 (2010), arXiv:1004.0805 [nucl-th] .
[32] F. Abe *et al.* (CDF), Phys. Rev. **D56**, 3811–3832 (1997).
[33] M. Bahr, M. Myska, M. H. Seymour, and A. Siodmok, JHEP **03**, p. 129 (2013), arXiv:1302.4325 [hep-ph] .
[34] M. H. Seymour and A. Siodmok, JHEP **10**, p. 113 (2013), arXiv:1307.5015 [hep-ph] .
[35] G. Aad *et al.* (ATLAS), New J. Phys. **13**, p. 053033 (2011), arXiv:1012.5104 [hep-ex] .
[36] "Measurement of Strange Particle Production in Underlying Events in proton-proton collisions at sqrt(s)," Tech. Rep. CMS-PAS-QCD-11-010 (CERN, Geneva, 2011).
[37] C. Bierlich and J. R. Christiansen, Phys. Rev. **D92**, p. 094010 (2015), arXiv:1507.02091 [hep-ph] .
[38] V. A. Khoze, F. Krauss, A. D. Martin, M. G. Ryskin, and K. C. Zapp, Eur. Phys. J. **C69**, 85–93 (2010), arXiv:1005.4839 [hep-ph] .
[39] "Leading Track Underlying Event at 13 TeV," Tech. Rep. ATL-PHYS-PUB-2015-019 (CERN, Geneva, 2015).

Proceedings of the LHCP2015 Conference, St. Petersburg, Russia, August 31 - September 5, 2015

Editors: V.T. Kim and D.E. Sosnov

Soft QCD at CMS

EKATERINA KUZNETSOVA

Petersburg Nuclear Physics Institute, Orlova Roscha, Gatchina, Leningrad district, 188300, Russia

Ekaterina.Kuznetsova@cern.ch

On behalf of the CMS Collaboration

Abstract. Soft QCD measurements play an important role in fundamental QCD studies as well as in tuning of corresponding Monte Carlo generator models for a good description of experimental data. The presented overview covers CMS studies on Underlying Event activity, transitions between perturbative and non-perturbative QCD regions, inclusive studies of diffractive production and recent measurements of the charged hadron multiplicity in inelastic production.

INTRODUCTION

The dominating fraction of proton-proton collision products are originating from soft and semi-hard QCD processes which are described with phenomenological models. Studies of kinematic distributions and particle multiplicities allow to validate the models and to tune model parameters for a better description of the experimental data. The presented overview covers CMS studies on Underlying Event activity, transitions between perturbative and non-perturbative QCD regions, measurements of inclusive single- and double- diffractive cross sections and recent measurements of the charged hadron multiplicity in inelastic production.

RESULTS OVERVIEW

Underlying Event studies at $\sqrt{s} = 2.76$ TeV

The Underlying Event (UE) measurements performed at $\sqrt{s} = 2.76$ TeV [1] supplement the earlier studies done for center-of-mass energy of 0.9 and 7 TeV [2]. The analysis was performed on a Mininum Bias data sample triggered with a coincidence of two opposite Beam Scintillator Counters ($3.23 < |\eta| < 4.65$) enhanced with a jet-triggered sample to cover a harder scale. The data were obtained during a dedicated run in year 2011 and correspond to an integrated luminosity of 0.3 nb^{-1} and low collision pile-up of 6.2%.

High quality charged tracks with $p_T > 0.5$ GeV and $|\eta| < 2.5$ are considered in the analysis. To support measurements with low-p_T jets, track-based jets were reconstructed from the preselected tracks using Sis-Cone algorithm with the distance parameter 0.5. Hard events were selected requiring at least one track-jet with transverse momentum p_T^{jet} above 1 GeV in the acceptance of $|\eta| < 2$. Underlying Event activity was studied in azimuthal transverse regions $60° < |\Delta\phi| < 120°$ defined with respect to the direction of a leading track-jet. The charged particle density corrected for detector effects, $\langle N_{ch}\rangle/(\Delta\eta\Delta(\Delta\phi))$, and the density of a scalar p_T-sum of charged particles, $\Sigma p_T/(\Delta\eta\Delta(\Delta\phi))$, were studied separately. For each quantity the two transverse regions were classified as regions with a maximal and a minimal activity, *transMAX* and *transMIN*. Such separation ensures the content of the *transMAX* region to be enhanced with initial- and final- state radiation while the *transMIN* region is dominated by Multiple Parton Interaction (MPI) and beam-beam remnants. At a fixed centre-of-mass energy these two components of UE are expected to have different behaviour with increasing hard scale - while the ISR ans FSR activity continuously increase with the hard scale, MPI is expected to saturate [3].

Figure 1 shows the measured charged particle density as a function of the transverse momentum of a leading track-jet for *transMAX* (left) and *transMIN* (right) regions compared to different Monte Carlo predictions. CUETP8S1

tune [4] of PYTHIA8 shows the best agreement with the data for both regions. The saturation of MPI activity is observed at about 8 GeV and the rise of activity in *transMAX* can be attributed to ISR/FSR.

The whole transverse region was considered to compare the UE measurements at $\sqrt{s} = 2.76$ TeV to the previous results obtained for 0.9 and 7 TeV. Figire 2 shows measured densities as functions of leading track-jet p_T. The corresponding MC predictions are in a reasonable agreement with the data.

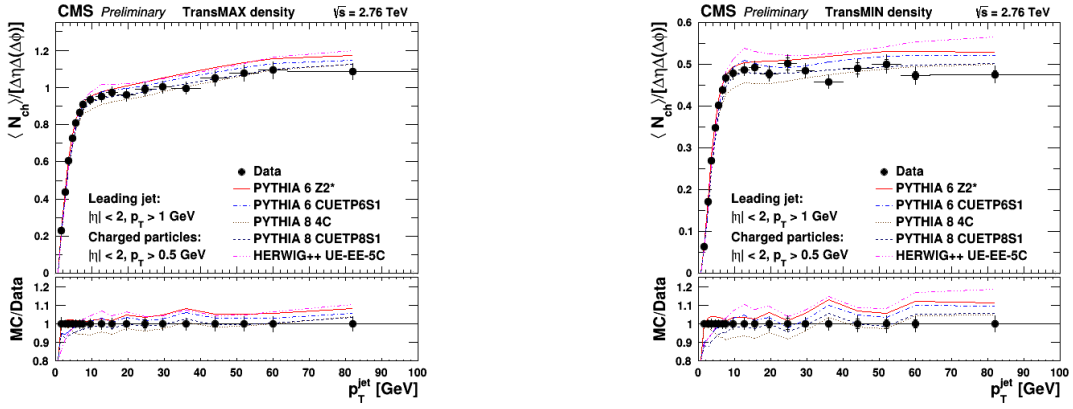

FIGURE 1. Measured charged particle density in the *txransMAX* (left) and *transMIN* (right) regions as functions of leading track-jet p_T shown together with various Monte Carlo predictions. The ratios of MC predictions to the measurements are shown on the bottom of the figures. The inner errors correspond to the statistical uncertainties and the outer errors represent the statistical and systematic uncertainties added in quadrature.

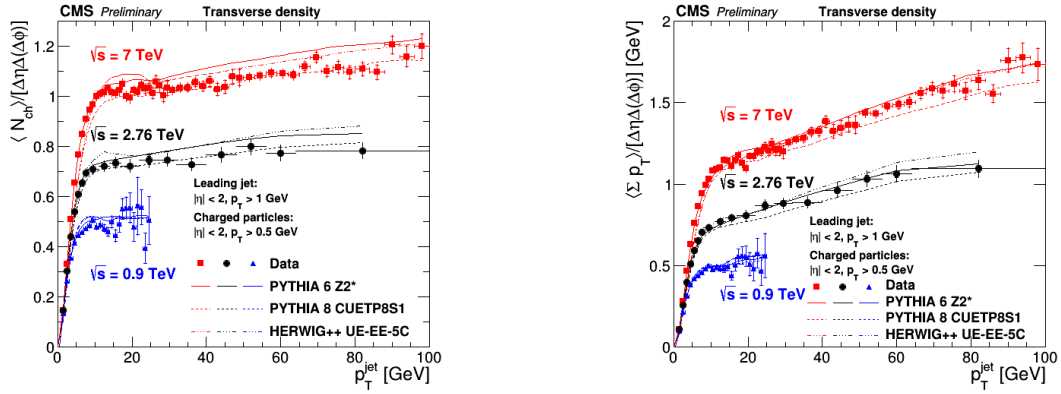

FIGURE 2. Measured charged particle density (left) and density of the scalar-p_T sum (right) as functions of leading track-jet p_T for $\sqrt{s} = 0.9$, 2.76 and 7 TeV and corresponding Monte Carlo predictions.

Leading charged particle and leading jet cross section at small transverse momenta

A transition between perturbative and non-perturbative domains can be studied measuring an integrated jet cross section approaching low values of the jet transverse momentum. Divergence of a parton-parton cross section at small p_T values, $d\sigma/dp_T^2 \sim \alpha_S^2/p_T^4$, causes the integrated cross section $\sigma(p_{T\,min}) = \int_{p_{T\,min}} p_T^2 d\sigma/dp_T^2$ to exceed the total inelastic cross section for $p_{T\,min}$ at the level of few GeV for the LHC energies [5]. In MC generators the low-p_T behaviour of the cross section is regularized with phenomenological models fitted to measurements of UE.

The low-p_T behaviour of the integrated cross section in a limited detector acceptance can be studied with transverse momentum distributions obtained for a leading charged particle or a leading jet and summed down to the $p_{T\,min}$ value: $\sigma(p_{T\,lead} > p_{T\,min})/\sigma_{vis} = 1/N \sum \Delta p_{T\,lead}(\Delta N_{lead}/\Delta p_{T\,lead})$, where $\Delta p_{T\,lead}$ is a bin width of the transverse

momentum distribution and N is the total number of preselected events. Leading charged particles and leading jets have different sensitivity of the integrated p_T distributions to UE so the two measurements are complementary [6].

The studies were performed on low pile-up (~5.4%) data obtained during a joined CMS+TOTEM data taking in July 2012 at $\sqrt{s}$ = 8 TeV center-of-mass energy. Minimum Bias data used in the analysis correspond to an integrated luminosity of 45 μb^{-1} and were triggered with the TOTEM T2 telescopes [7] located on both sides of the interaction point and covering $5.3 < |\eta| < 6.5$. Tracks with $p_T > 400$ MeV reconstructed in the acceptance of $|\eta| < 2.4$ were used to obtain the leading charged particle distribution as well as to form a track-jet for the leading jet study. For the leading charged particle distribution an additional cut $p_T > 0.8$ GeV was applied. The track-jets were reconstructed within $|\eta| < 1.9$ with the anti-k_t algorithm using a distance parameter of 0.5, and allow to approach a low p_T values of 1 GeV. The obtained results were corrected for detector effects.

Normalised integrated p_T distributions are shown in Fig. 3 as functions of $p_{T\,min}$ for leading track-jets (left, middle) and leading charged particles (right). The corresponding predictions from several Monte Carlo event generators normalised to the values measured for 14.3 (leading jets) and 9 GeV (leading charged particles) are shown for comparison. Fig. 3 (left) demonstrates saturation of the cross section at $p_{T\,min}$ of several GeV. The closest agreement to the data is obtained with EPOS event generator tuned to LHC data (Fig. 3, middle, right).

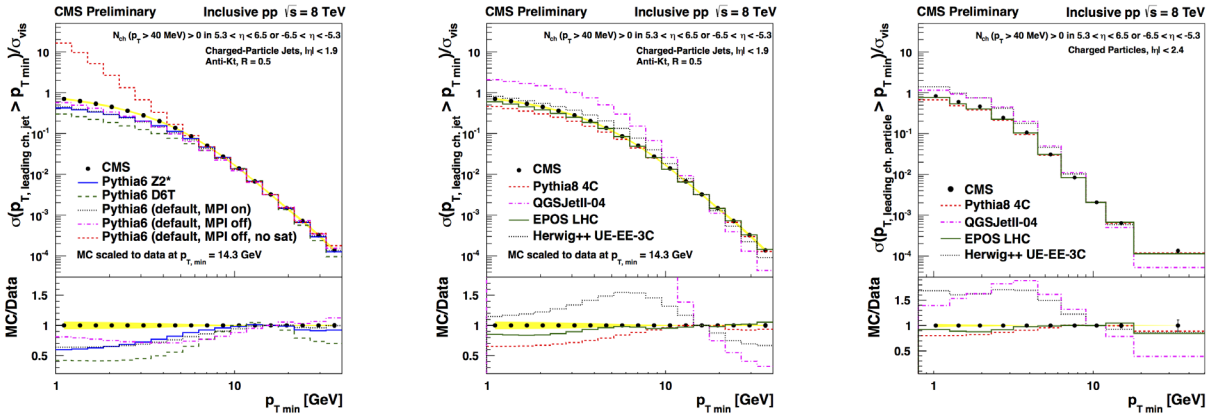

FIGURE 3. Normalised integrated event cross-sections as functions of $p_{T\,min}$ for a leading track-jet (left and middle plots) and a leading charged particle (right). The data are compared to predictions from various Monte Carlo event generators. The error bars indicate the statistical uncertainty and the shaded area the systematic uncertainty. The systematic uncertainties are only shown in the ratio plot.

Update on soft diffractive cross section measurements

Measurements of diffracive cross sections [8] were performed on a low-pileup Minimum Bias data recorded in year 2010 at $\sqrt{s}$ = 8 TeV center-of-mass energy. The data correspond to an integrated luminosity of 16.2 μb^{-1} and were triggered with any of two Beam Scintillator Counters. Event preselection was performed using a topology of diffractive events requiring presence of a Large Rapidity Gap in the acceptance of the central CMS detector ($|\eta| < 4.7$). Forward and central gap samples were preselected requiring a forward or central LRG of at least 4 or 3 pseudorapidity units respectively. CMS CASTOR calorimeter located at $-6.6 < \eta < -5.2$ was used in the analysis to separate SD- and DD-enhanced data samples according to the activity in the above acceptance. Thus three data samples were selected - an SD-enhanced sample with a forward LRG at the negative detector edge with no CASTOR activity, a DD-enhanced samples corresponding to a forward LRG observed at -Z edge of the central detector and accompanied with activity in the CASTOR acceptance, and a DD-enhanced sample corresponding to a central LRG.

MC-based studies using PYTHIA8-MBR [9] event generator allow to define the corresponding diffractive mass acceptance for the above samples as $1.1 \lesssim \log_{10}(M_X/\mathrm{GeV}) \lesssim 2.5$ for SD events (pp→pX) of the first sample, $\{1.1 \lesssim \log_{10}(M_X/\mathrm{GeV}) \lesssim 2.5, \quad 0.5 \lesssim \log_{10}(\mathrm{M_Y/GeV}) \lesssim 1.1\}$ for DD events (pp→XY) of the forward gap DD-enhanced sample, and $\{\log_{10}(M_X/\mathrm{GeV}) \lesssim 1.1, \quad \log_{10}(\mathrm{M_Y/GeV}) \lesssim 1.1\}$ for DD events of the central gap sample.

The SD-enhanced sample is contaminated mostly with DD events corresponding to $\log_{10}(M_Y/\text{GeV}) \lesssim 0.5$, while the dominating background for the DD-enhanced sample originates from non-diffractive events.

The differential cross-sections are obtained as functions of relative momentum loss of the intact proton ξ which is related to the mass of the diffractive system as $\xi = M^2/s$. At the detector level it can be obtained as $\xi^{\pm} = 1/\sqrt{s} \sum_i E^i \mp p_z^i$, summing over all Particle Flow objects reconstructed in the central detector, where E^i and p_z^i are the energy and corresponding longitudinal momentum, and the sign is defined by z direction of the diffractive system. Figure 4 shows the differential cross sections after MC-based corrections for detector effects and background contamination. Left and middle plots show the SD and DD cross sections obtained from the forward gap samples as functions of ξ_X, and the right plot shows the DD cross section for the central gap sample in units of $\Delta\eta = -\ln\xi$. The results are compared with MC predictions and the best description is obtained with PYTHIA8-MBR generator for the Pomeron trajectory intercept $\alpha_{I\!P}(0) = 1 + \epsilon = 1.08$. The visible SD integrated cross sections was found for the corresponding kinematics regions for both pp→pX and pp→pY contributions to be of $4.06 \pm 0.04(\text{stat})^{+0.69}_{-0.63}(\text{syst})$ mb. Joining the DD integrated cross sections obtained for forward and central gaps, σ^{DDvis}_{CASTOR} and σ^{DDvis}_{CG}, a visible DD cross section is defined as $\sigma^{DDvis} = 2\sigma^{DDvis}_{CASTOR} + \sigma^{DDvis}_{CG}$ and found to be $2.69 \pm 0.04(\text{stat})^{+0.29}_{-0.30}(\text{syst})$ mb.

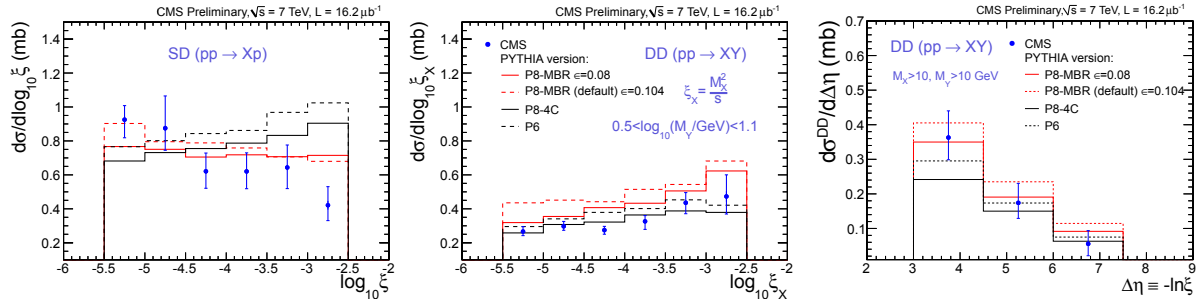

FIGURE 4. The SD (left) and DD (middle) cross sections obtained for the forward LRG samples as functions of ξ_X, and the DD cross section obtained for the central LRG sample as a function of $\Delta\eta$.

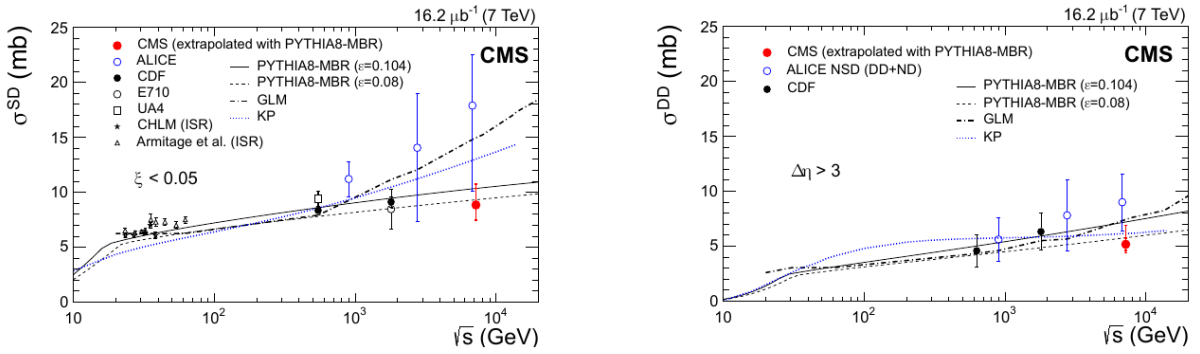

FIGURE 5. The SD (left) and DD (right) cross sections as functions of center-of-mass energy of pp and $p\bar{p}$ collisions obtained in different experiments for $\xi < 0.05$ (SD) and $\Delta\eta > 3$ (DD), and the corresponding predictions of PYTHIA8-MBR Monte-Carlo and phenomenological models.

To extrapolate the integrated cross sections evaluated for the studied acceptance regions to the commonly used acceptance of $\xi < 0.05$ for SD and $\Delta\eta > 3$ for DD, a MC-based extrapolation was performed using PYTHIA8-MBR generator with the intercept parameter $\epsilon = 0.08$. The observed extrapolated values $\sigma^{SD} = 8.84 \pm 0.08(\text{stat})^{+1.49}_{-1.38}(\text{syst})^{+1.17}_{-0.37}(\text{extrap})$ mb and $\sigma^{DD} = 5.17 \pm 0.08(\text{stat})^{+0.55}_{-0.57}(\text{syst})^{+1.62}_{-0.51}(\text{extrap})$ mb are shown in Fig. 5 together with the corresponding values obtained in other experiments as functions of center-of-mass energies. The data are compared to the predictions of PYTHIA8-MBR Monte-Carlo and to GLM [10] and KP [11] models.

Pseudorapidity distribution of charged hadrons in proton-proton collisions at $\sqrt{s} = 13$ TeV

Measurements of charged hadron multiplicity as a function of pseudorapidity, $dN_{ch}/d\eta$, were performed with early Run2 data obtained for $\sqrt{s} = 13$ TeV during a special low-pileup ($\lesssim 5\%$) run [12]. The data were recorded at 0 T magnetic field of the CMS solenoid. The analysis was performed on a Zero Bias data sample triggered with the beam pickup and timing devices (BPTX) on two opposite bunches crossing the interaction point.

CMS pixel tracker hits were used to reconstruct charged tracks. The barrel region of the silicon pixel tracker consists of three layers with 150 μm x 150 μm pixels covering radial region of 4.3 – 11 cm. Reconstruction of straight pixel tracks was performed using two different approaches based on hit pairs (tracklet method) and on hit triplets (track method).

Within the tracklet method, two hits from different pixel layers form a tracklet if they have a good correspondence of azimuthal coordinates and/or pseudorapidities. To find a primary vertex, all tracklets with a hit in the first layer found requiring $|\phi_i^{hit} - \phi_j^{hit}| < 0.05$ are extrapolated to the beam axis and corresponding points of the closest approach are clustered within $\Delta z < 0.12$ cm. A primary vertex is obtained as the most populated cluster. The method provides a good vertex reconstruction efficiency ranging from 80% for 3 hits in the first pixel layer up to 100% when the number of hits is above 8. Events with no primary vertex found are rejected from the further analysis.

The number of charged particles is derived from tracklets reconstructed within $|\Delta\eta| < 2$ and formed of hits with the best pseudorapidity correlation requiring each hit to be assigned to one tracklet only. Figure. 6 (left) shows the $\Delta\phi$ distribution for the obtained tracklets. The peak at $\Delta\phi = 0$ corresponds to charged hadrons originating from the primary vertex while the sideband is formed of uncorrelated hits. The combinatorial background is suppressed rejecting tracklets with $|\Delta\phi| > 1$ and $|\Delta\eta| > 0.1$ and the flat side region $1 < |\Delta\phi| < 2$ is used to estimate contribution of the tracklets reconstructed from uncorrelated hits. The number of charged particles is corrected for the combinatorial background for each η bin individually. The tracklet approach is sensitive to the charged tracks with a transverse momentum above 0.04 GeV/c. Corrections for secondary particles, tracklet acceptance and reconstruction efficiency were performed using MC studies with PITHIA8 CUETP8S1 generator tune. Additional corrections for detector geometry were applied as well.

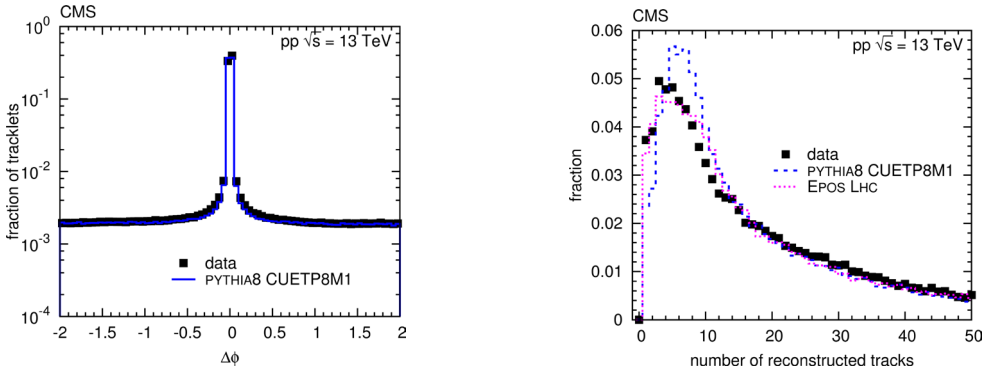

FIGURE 6. Left: $\Delta\phi$ distributions of hit pairs on tracklets in the data (squares) and from MC simulation (histogram) for the tracklet analysis. Right: the distributions of the number of reconstructed tracks per event from data and from simulations obtained in the track-based analysis.

The track method uses tracks reconstructed from a hit triplets approaching a straight line. The hits are combined requiring for an azimuthal alignment of hits from 1st and 2nd and for hits from 2nd and 3rd layers, $|\Delta\phi_{1,2}| < \alpha$ and $|\Delta\phi_{2,3}| < \alpha$, and for a correspondence of polar angles of the above di-hit combinations, $|\Delta\theta_{12,23}| < \alpha$. The best signal significance is achieved for $\alpha = 0.02$. The reconstructed tacks are fitted to a straight line. Z-position of a point of the closest track approach to the beam axis, z_0, is found assuming a zero impact parameter. Tracks are rejected if $|z_0| >$ 20 cm. Average deviation of track hits from the fitted track, $\overline{d}$, is used to estimate the uncertainty in z, $\sigma_z = \overline{d}/\sin\theta$. A primary vertex is found using the above quantities (z_0, σ_z) with agglomerative vertex reconstruction [13].

The events with a reconstructed primary vertex are used to define the charged hadron multiplicity. Figure. 6 (right) shows the distributions of the number of reconstructed tracks per event for the inelastic collisions. To observe the number of charge hadrons, the track distribution was corrected for the secondary particles and track reconstruction efficiency for η and event multiplicity bins.

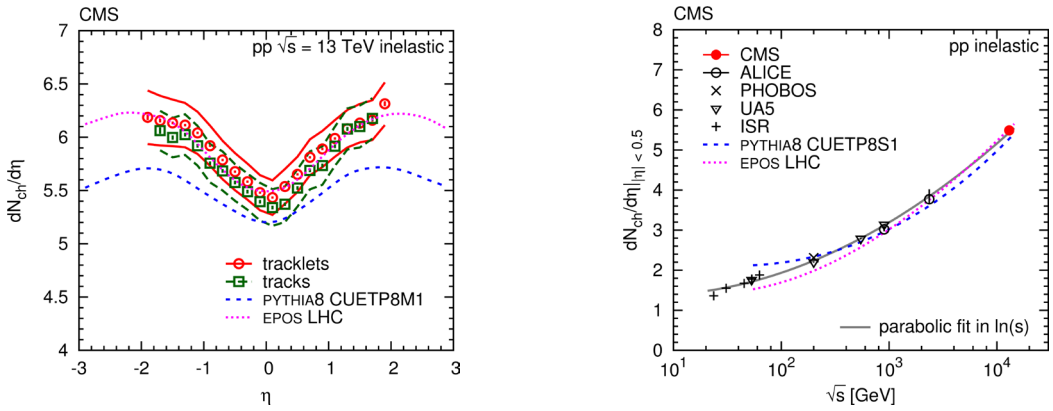

FIGURE 7. Left: distributions of the pseudorapidity density of charged hadrons in the region $|\eta| < 2$ for inelastic collision events, reconstructed using tracklets (open circles), and tracks (open squares), compared to PYTHIA8 CUETP8S1 and EPOS LHC predictions, shown as dashed and dotted curves, respectively. The solid and long-dashed lines encompassing the data points indicate the systematic uncertainties of the two reconstruction methods. Right: Center-of-mass energy dependence of $\mathrm{d}N_{ch}/\mathrm{d}\eta|_{|\eta|<0.5}$ including ISR, UA5, PHOBOS, ALICE and CMS data. The solid curve shows a second-order polynomial in $\ln(s)$ fit to the data points.

The charged hadron multiplicities obtained with the above approaches agree within 3% as shown in Fig. 7, left. The mean values were used to derive the charged hadron multiplicity averaged over the $|\eta| < 0.5$ range, $\mathrm{d}N_{ch}/\mathrm{d}\eta|_{|\eta|<0.5} = 5.49 \pm 0.01(\mathrm{stat}) \pm 0.17(\mathrm{syst})$, which is shown in Fig. 7 (right) together with corresponding results from other experiments as a function of center-of-mass energy. The predictions from PYTHIA8 CUETP8S1 and EPOS-LHC MC generators are shown for the comparison.

SUMMARY

Selected recent CMS results on soft QCD have been presented. The obtained results are shown in comparison to predictions of latest tunes of different MC generators. Though a good overall description of the data is demonstrated, various deviations are observed in distributions dominated with non-perturbative QCD processes. The presented results are expected to play an important role in the further development and tuning of the corresponding MC models.

REFERENCES

[1] V. Khachatryan *et al.* (CMS), JHEP **09**, p. 137 (2015), arXiv:1507.07229 [hep-ex] .
[2] S. Chatrchyan *et al.* (CMS), JHEP **09**, p. 109 (2011), arXiv:1107.0330 [hep-ex] .
[3] T. Sjostrand and M. van Zijl, Phys. Lett. **B188**, p. 149 (1987).
[4] CMS Collaboration (CMS), CMS-PAS-GEN-14-001 (2014).
[5] A. Grebenyuk, F. Hautmann, H. Jung, P. Katsas, and A. Knutsson, Phys. Rev. **D86**, p. 117501 (2012), arXiv:1209.6265 [hep-ph] .
[6] CMS Collaboration (CMS), CMS-PAS-FSQ-12-032 (2014).
[7] G. Anelli *et al.* (TOTEM), JINST **3**, p. S08007 (2008).
[8] V. Khachatryan *et al.* (CMS), Phys. Rev. **D92**, p. 012003 (2015), arXiv:1503.08689 [hep-ex] .
[9] R. Ciesielski and K. Goulianos, *Proceedings, 36th International Conference on High Energy Physics (ICHEP2012)*, PoS **ICHEP2012**, p. 301 (2013), arXiv:1205.1446 [hep-ph] .
[10] E. Gotsman, E. Levin, and U. Maor, Phys. Lett. **B716**, 425–429 (2012), arXiv:1208.0898 [hep-ph] .
[11] A. B. Kaidalov and M. G. Poghosyan, (2011), arXiv:1109.3697 [hep-ph] .
[12] V. Khachatryan *et al.* (CMS), Phys. Lett. **B751**, 143–163 (2015), arXiv:1507.05915 [hep-ex] .
[13] F. Sikler, Nucl. Instrum. Meth. **A621**, 526–533 (2010), arXiv:0911.2767 [physics.ins-det] .
[14] R. Ciesielski, "Diffraction, forward physics and soft QCD results from CMS," in *Proceedings, 2nd Conference on Large Hadron Collider Physics Conference (LHCP 2014)* (2014) arXiv:1409.5473 [hep-ex] .

Top quark physics: plenary talks

Proceedings of the LHCP2015 Conference, St. Petersburg, Russia, August 31 - September 5, 2015

Editors: V.T. Kim and D.E. Sosnov

The Top Quark Production at the LHC

ABIDEH JAFARI

Université Catholique de Louvain, Louvain-la-Neuve, Belgium

Abideh.Jafari@cern.ch

On behalf of the ATLAS and CMS Collaborations

Abstract. The top quark pair production at the LHC has been studied in details by ATLAS and CMS collaborations. In addition to the inclusive $t\bar{t}$ cross section, now measured with an unprecedented precision, the LHC Run I data are exploited to provide comprehensive modeling comparisons through differential measurements at particle and/or parton levels. Furthermore, the uncertainties related to extrapolations to the full phase space are constrained using the measurements within a fiducial volume of the detector. The $t\bar{t}$ events are investigated in boosted regimes using the jet substructure techniques. The production cross section of $t\bar{t}$ in addition to one or two b quarks is also measured. Finally, the LHC experiments have presented the very first $t\bar{t}$ measurements at $\sqrt{s} = 13$ TeV, performed using up to 80 pb^{-1} of the LHC Run II data.

INTRODUCTION

The top quark, observed for the first time in Tevatron [1, 2, 3, 4], is a unique particle in the framework of the standard model (SM) because of its large mass and short life time, providing an excellent testing ground to validate SM or to search for new physics. Thanks to the diversity of particles in the final state, the top quark events are also used as commissioning tools for early data. At hadron colliders, the top quark is produced dominantly through strong interactions in pairs and to lesser extent, singly via electroweak interactions. The overwhelming $t\bar{t}$ production at the LHC allows for ultimate precision in measuring the top quark properties as well as modeling studies and improvements through differential measurements.

Assuming $\mathcal{B}(t \to bW) \approx 1$, the $t\bar{t}$ events are categorized based on the decay products of the W boson. The lowest rate belongs to the dilepton final state where the two W bosons decay to either an electron or a muon. This final state is almost background free and is used for early inclusive measurements. The rate increases with one W boson decaying hadronically. The signal in lepton+jets final state is contaminated with a moderate amount of backgrounds. These events are exploited for early differential measurements. Measurements in the full-hadronic channel – the final state with both W bosons decaying to quarks – usually requires a large amount of data for a good precision because of the huge background contamination.

The ATLAS [5] and CMS [6] experiments rediscovered the top quark, produced in pairs, with only $\sim 3\,\text{pb}^{-1}$ of data at $\sqrt{s} = 7$ TeV Collaboration [7], CMS Collaboration [8]. The analyses were later superseded with more precise measurements in Run I [9, 10] with the systematic uncertainties, even though very small, being the limiting factors. The first LHC cross section measurement of the electroweakly produced top quark in t-channel is carried out using an integrated luminosity of 36 pb^{-1} at 7 TeV [11], followed by more elaborative analyses with more data [12, 13, 14, 15, 16]. The sub-dominant single-top production in association with a W boson is observed for the first time at the LHC [17, 18] while an evidence or an upper limit on cross section is reported for the rare s-channel production [19, 20].

The LHC data from Run I is still in use to explore the top quark sector while proton collisions at $\sqrt{s} = 13$ TeV are exploited for the early top quark measurements at the highest-ever-reached center-of-mass energy. In this article, the recent $t\bar{t}$ studies performed by the ATLAS and CMS collaborations are presented where the focus is on the production with or without additional jets, differential and fiducial measurements and boosted regimes.

INCLUSIVE CROSS SECTION MEASUREMENTS

The use of kinematic information in the lepton+jets final state with ATLAS at $\sqrt{s} = 8$ TeV

Events in this analysis [21] are required to pass a logical OR of isolated and nonisolated single-lepton (electron or muon) trigger conditions with $p_{\mathrm{T}} > 24$ GeV for isolated triggers and 60 (36) GeV for nonisolated ones. The offline E_{T} (p_{T}) threshold increases to 40 GeV for the electron (muon) where the candidate must be close to the primary vertex of the hard interaction, isolated and in the central part of the detector, $|\eta| < 2.47$ (2.5). The barrel-end cap transition region, $1.37 < |\eta| < 1.52$, is excluded for the electron. Events containing additional leptons with looser specifications are discarded. Jets, reconstructed using the anti-k_t algorithm [22, 23] with radius parameter $R = 0.4$, are selected if they meet $p_{\mathrm{T}} > 25$ GeV and $|\eta| < 2.5$ criteria. Events are required to have at least three selected jets of which one is likely to be originated from a b quark, according to a multivariate discriminating variable. Finally, the magnitude of missing transverse momentum, $E_{\mathrm{T}}^{\mathrm{miss}}$, and the transverse mass of the W boson, $m_{\mathrm{T}}(W)$ must exceed 30 GeV [21]. The majority of events in the selected sample contain prompt electrons or muons from vector boson decays. However, a small fraction of events include the so-called *fake leptons* which are nonprompt and artifacts of the reconstruction.

The signal yield is extracted using a template fit over a likelihood distribution, LHD. The LHD is constructed using the projective likelihood method [24] with the lepton pseudorapidity $|\eta_\ell|$ and the transformed aplanarity (an event shape variable) used as inputs. Figure 1 shows the distributions of LHD and its input variables in data and simulation. The templates for signal and all backgrounds except the fake lepton contamination are taken from simulation. The

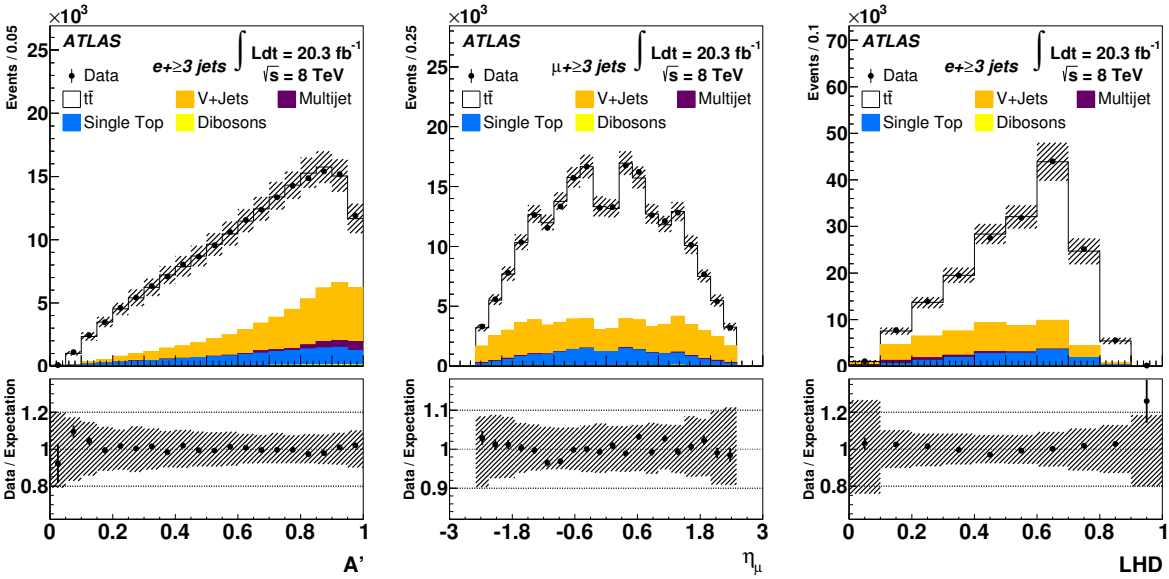

FIGURE 1. The distribution of the transformed aplanarity in the electron channel (a), lepton pseudorapidity in the muon channel (b) and the LHD in the electron channel (c) for data and simulations, using 20.3 fb^{-1} of 8 TeV collision data by ATLAS [21]. The hatched area corresponds to the statistical and systematic uncertainties.

fake lepton contamination is estimated by means of a matrix method using the information of a dedicated control region. The normalization of signal and the vector boson plus jets background are left free in the fit while single-top and fake lepton contributions are fixed to the theory calculations and the matrix method estimation, respectively. The measurement, using 20.3 fb^{-1} of 8 TeV data, yields $\sigma_{t\bar{t}}^{\ell j} = 258 \pm 1(\mathrm{stat.})^{+22}_{-23}(\mathrm{syst.}) \pm 8(\mathrm{lumi.}) \pm 4(\mathrm{beam})$ pb with the parton distribution function (PDF) being the dominant systematic uncertainty. The analysis is carried out with a top quark mass of $m_t = 172.5$ GeV where the top mass dependence of the measured cross section is determined to be $\frac{\Delta\sigma_{t\bar{t}}/\sigma_{t\bar{t}}}{\Delta m_t} = -1.1\%\,\mathrm{GeV}^{-1}$. The measurement in the fiducial volume is performed using the particle-level objects, i.e., stable particles from the full matrix element and parton shower generators without any interaction with the detector [21]. The particle-level object reconstruction and selection is very close to those of the detector level. The fiducial

analysis results in $\sigma_{t\bar{t}}^{\ell j,\text{fid}} = 22.8 \pm 0.1(\text{stat.})^{+1.9}_{-2.0}(\text{syst.}) \pm 0.7(\text{lumi.}) \pm 0.4(\text{beam})$ pb. Such measurements provide a more robust comparison to the theoretical prediction without extrapolating to regions outside of the detector acceptance.

Multi-differential approach in $e\mu$ final state with CMS at $\sqrt{s} = 7$ and 8 TeV

The presence of one electron and one muon is the main criterion for events in this analysis [10] to be selected. At HLT, one of the two leptons is required to have $p_{\text{T}} > 17$ GeV and the other $p_{\text{T}} > 8$ GeV for the 8 TeV data samples. The logical OR between this trigger and the one with the two leptons passing $p_{\text{T}} > 10$ GeV is considered for the 7 TeV study. For offline selection, the lepton p_{T} threshold is 20 GeV with $|\eta| < 2.4$ for both electron and muon. The two candidates must be isolated and close to the primary vertex of the hard interaction. In case of additional $e\mu$ pairs in the event, the one with the highest scalar p_{T} is considered. Jets are reconstructed using the ant-k_T algorithm with the distance parameter $R = 0.5$ and are required to have $p_{\text{T}} > 30$ GeV and $|\eta| < 2.4$. The b quark jet identification is performed using a multivariate discriminator [10]. No explicit requirement is placed on the number jets and b jets. Instead, events are categorized based on b-tagged jet and additional non-b-tagged jet multiplicities. Three classes are used for b-tagged jets (one, two and zero or more b-tagged jets) and four for additional jets (zero, one, two and three or more jets), leading in total to 12 different categories. A simultaneous maximum likelihood fit with systematic uncertainties as nuisance parameters is carried out over all categories in both 7 and 8 TeV center-of-mass energies where from each, the p_{T} distribution of the softest jet in the event enters the final fit. The procedure allows to control the effect of extra radiations in the event. The uncertainties are calculated taking into account the full correlation matrix of all categories and across center-of-mass energies. Figure 2 illustrates the post-fit distributions in different categories at 7 TeV. The measurement yields $\sigma_{t\bar{t}} = 174.5 \pm 2.1(\text{stat})^{+4.5}_{-4.0}(\text{syst}) \pm 3.8(\text{lumi})$ pb at $\sqrt{s} = 7$ TeV and $\sigma_{t\bar{t}} = 245.6 \pm$

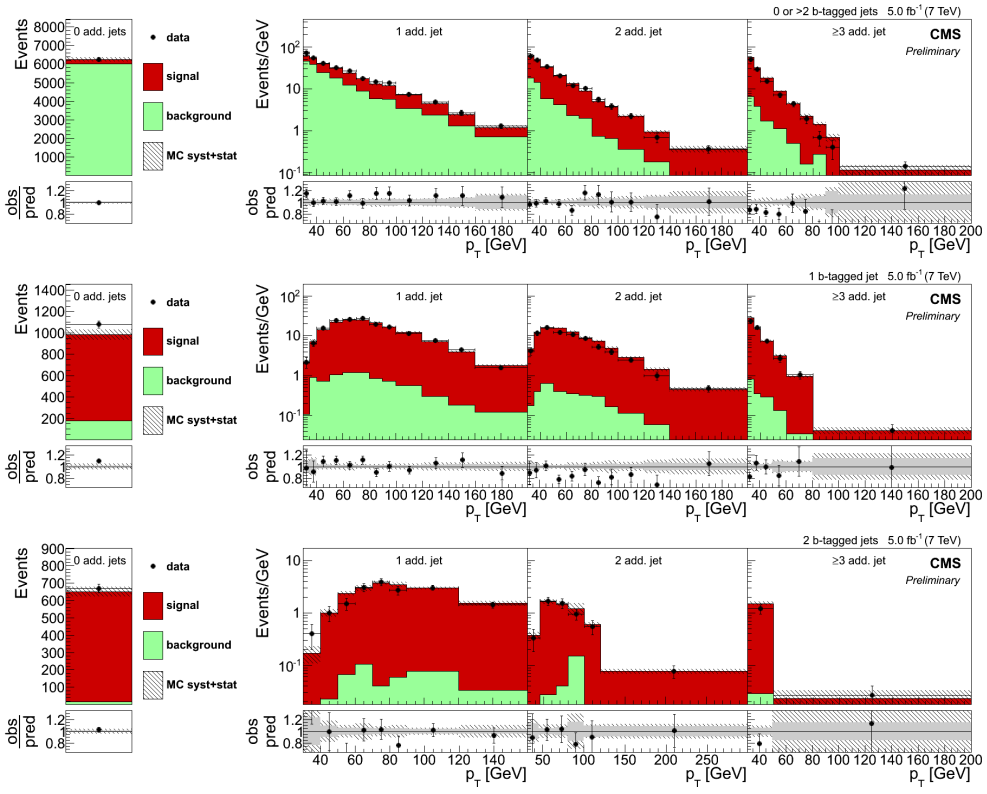

FIGURE 2. Fitted total event yield for zero additional non-b-tagged jets (left) and p_{T} of the least energetic additional non b-tagged jet in the event (right) for events with one, two, and at least three additional non b-tagged jets, and with zero or more than two (top), one (middle) and two (bottom) b-tagged jets, using 5.0 fb^{-1} of data at $\sqrt{s} = 7$ TeV by CMS [10]. The hatched bands correspond to the sum of statistical and systematic uncertainties in the event yield for the sum of signal and background predictions. The ratios of data to the sum of the predicted yields are shown at the bottom of each subplot. Here, the solid band represents the statistical uncertainty.

$1.3(\text{stat})^{+6.6}_{-5.5}(\text{syst}) \pm 6.5(\text{lumi})$ pb at $\sqrt{s} = 8$ TeV. The $t\bar{t}$ cross section is also measured in the fiducial region (visible phase space), defined by the acceptance requirements on the two charged leptons in the final state. It is determined to be $\sigma^{vis.}_{t\bar{t}} = 3.05 \pm 0.04(\text{stat})^{+0.08}_{-0.07}(\text{syst}) \pm 0.07(\text{lumi})$ pb at $\sqrt{s} = 7$ TeV and $\sigma^{vis.}_{t\bar{t}} = 4.24 \pm 0.02(\text{stat})^{+0.11}_{-0.10}(\text{syst}) \pm 0.11(\text{lumi})$ pb at $\sqrt{s} = 8$ TeV. The Drell-Yan background contamination together with the lepton identification are found to be the dominant systematic uncertainties in both measurements. Table 1 compares these results to the earlier measurement by ATLAS [25] with a similar precision as well as to the theory calculations. The signal modeling is the most pronounced systematic uncertainty in the ATLAS analysis.

TABLE 1. The $t\bar{t}$ cross section measurement in $e\mu$ final state at $\sqrt{s} = 7$ and 8 TeV from ATLAS [25] and CMS [10] experiments compared with the theoretical calculations.

	7 TeV	**8 TeV**	$\mathbf{R_{8/7}}$
	scale ± (PDF + α_s)		
Theory*	$177.3^{+4.7}_{-6.0} \pm 7.1$	$252.9^{+6.7}_{-8.6} \pm 11.7$	1.4 ± 0.01
ATLAS	182.9 ± 7.1	242.4 ± 10.3	1.33 ± 0.06
CMS	174.5 ± 6.2	245.6 ± 9.3	1.41 ± 0.06

*Calculated using the Top++ v2 program [26].

The $t\bar{t}b(b)$ cross section measurement with ATLAS at $\sqrt{s} = 8$ TeV

The study of $t\bar{t}$ production in association with b quarks allows for understanding the quantum chromodynamics (QCD) at next-to-leading order precision. The $t\bar{t}b(b)$ cross section measurements at the LHC [27, 28, 29] are performed in ℓ+jets and $\ell\ell$ final sates of $t\bar{t}$ where the b-jet identification variables are exploited to determine the flavour of additional jets. In the recent analysis by ATLAS [30], the $t\bar{t}b$ cross section in a fiducial volume is measured in events with exactly one lepton and at least five jets, of which at least three are identified as b-jets (ttb lepton-plus-jet) as well as events with an $e\mu$ pair and at least three b-jets (ttb dilepton). Events with two leptons and at least four b-jets are used for $t\bar{t}bb$ fiducial measurement (ttbb dilepton) where the result of a tight cut-based method is confirmed by a fit-based method with looser selection. Jets are ordered according to the multivariate b-jet identification discriminator, MV1c weight, and the template for the third and/or fourth jet(s) is used in the signal extraction fit. Templates are categorized based on the true flavour of jets (b, c and l) to discriminate between signal and backgrounds. While the profile likelihood fit in ttb lepton-plus-jet and $e\mu$ channels is based on the MV1c weight of the third jet, the maximum-likelihood fit in ttbb is performed in the 15 populated bins of the MV1c distribution for the jets with the third and fourth highest MV1c values. The $R_{ttbb} = \frac{\sigma_{ttbb}}{\sigma_{ttjj}}$ quantity is also measured to be 1.30% with 33% uncertainty. All measurements are summarized and compared to different generators and settings in Fig. 3.

DIFFERENTIAL CROSS SECTION MEASUREMENTS

Differential cross section measurements are carried out at the LHC to provide more elaborative comparisons with theory calculations. The distribution of the reconstructed top quark properties together with those of leptons and jets are studied after unfolding the detector effects to the level of partons or particles. Particle level objects are reconstructed as close as possible to those at detector level.

Differential $t\bar{t}$ cross section in $\ell\ell$ and ℓ+jets final states with CMS at $\sqrt{s} = 8$ TeV

In this analysis [31] events with exactly two opposite sign leptons, incompatible with the Z boson if they have the same flavour, are required to have at least two jets with at least one being b-tagged, to be selected for the dilepton final state. Single lepton channel contains events with exactly one electron or muon and at least four jets. At least two jets must be tagged as b-jets and two must be non-tagged. The normalized differential $t\bar{t}$ cross section is obtained by counting the number of $t\bar{t}$ signal events in bins of a given observable, correcting for detector effects and acceptance, and dividing by the measured total inclusive $t\bar{t}$ event rate. The total inclusive cross section is determined by integrating over all bins in each observable. Figure 4 shows the distributions of unfolded data, compared with different theory

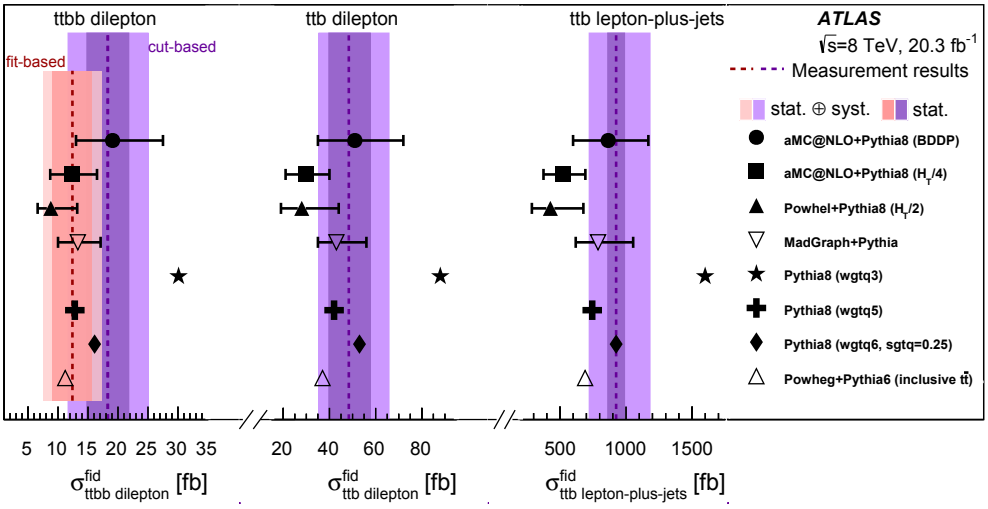

FIGURE 3. Comparison of the ATLAS $t\bar{t}b(b)$ measured cross sections [30] in the three fiducial phase-space regions with theoretical predictions obtained from a variety of different generators. The measurements, based on 20.3 fb^{-1} of data at 8 TeV, are shown with the contributions from $t\bar{t}V$ and $t\bar{t}H$ removed to allow direct comparison to the predictions containing only the pure QCD matrix elements. The coloured bands indicate the statistical and total uncertainties of the measurements. The errors on the theoretical prediction are obtained by simultaneously varying the renormalisation and factorisation scales by a factor of two.

predictions, for p_{T} of the lepton (ℓ+jets) and of the $t\bar{t}$ system ($\ell\ell$). The former is unfolded to particle level in a fiducial volume where the latter is unfolded to parton level in the full phase space. Generally good agreement is observed between data and simulation.

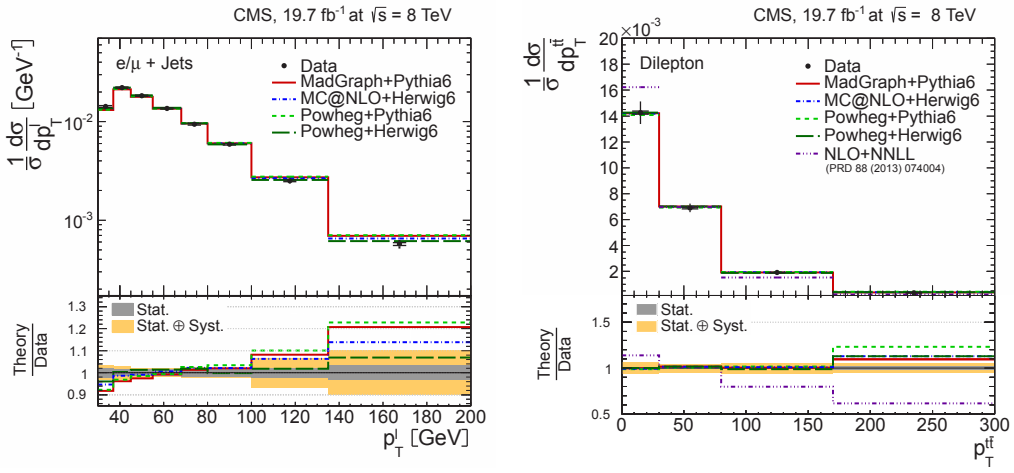

(a) (b)

FIGURE 4. The CMS normalized differential $t\bar{t}$ production cross section [31], using 19.7 fb^{-1} of 8 TeV data, in the ℓ+jets channels as a function of the p_{T}^{ℓ} (a) and in the dilepton channels as a function of $p_{\mathrm{T}}^{t\bar{t}}$ (b). The data points are placed at the midpoint of the bins. The inner (outer) error bars indicate the statistical (combined statistical and systematic) uncertainties. The measurements are compared to predictions. The lower part of each plot shows the ratio of the predictions to data.

Differential $t\bar{t}$ cross section in ℓ+jets final states with ATLAS at $\sqrt{s} = 7$ TeV

This measurement [32] is performed at particle level in a fiducial volume, using events with only one muon or electron together with at least four jets of which at least two are identified as b-jet. The $t\bar{t}$ system at particle level is reconstructed similar to the one at detector level, using the W boson mass constraint and the closest b-tagged jet for the leptonic side, and assigning the remaining jets to the hadronically decaying top quark. The differential cross section is evaluated after subtracting the backgrounds from data, and correcting for the reconstruction and the top quark mis-assignment effects. Figure 5 illustrates the unfolded rapidity distribution of the leptonically and hadronically decaying top quarks at particle level (pseudo-top) in comparison with predictions. Larger event yield is observed in simulation than in data. A similar feature in both ATLAS [32] and CMS [31] analyses is the softer top quark p_{T} spectrum in data than

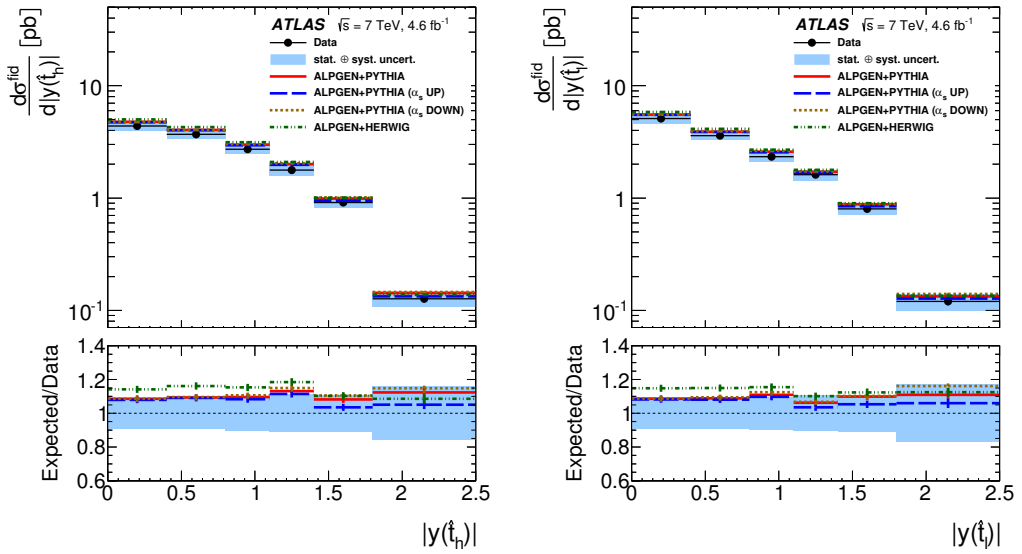

FIGURE 5. The ATLAS differential $t\bar{t}$ cross section [32] after channel combination, with 4.6 fb^{-1} of 7 TeV data, as a function of (a) the hadronic pseudo-top-quark y and (b) the leptonic pseudo-top-quark y. The data points are shown with a blue band which represents the total uncertainty (statistical and systematic). The model predictions from several LO multi-leg MC generators are superimposed.

simulation. Figure 6 shows that such behaviour is present at particle level in the fiducial volume as well as at parton level in the full phase space.

Differential $t\bar{t}$ cross section for high p_{T} tops with CMS at $\sqrt{s} = 8$ TeV

Events consistent with $t\bar{t}$ decays to ℓ+jets in boosted regimes are selected [33] based on the presence of a non-isolated electron or muon where additional requirements are applied to suppress the jet-lepton mis-identifications. In the same hemisphere as lepton, there must be at least one jet with small cone size ($R = 0.5$) reconstructed using the anti-k_t algorithm [34]. The small-R that are jets identified as b-jet are required to have non-zero secondary vertex mass (m_{vtx}). In the other hemisphere, the hadronically decaying top quark is reconstructed as a single, large-R ($R = 0.8$) jet and identified as a top-jet candidate using jet substructure techniques [35]. Events are classified into three groups based on the b-tagged and top-tagged jet multiplicities: $1t + 1b$, $1t + 0b$ and $0t$. All categories are fitted simultaneously using the m_{vtx} distribution from the first and the $|\eta_\ell|$ distribution from the last two groups. The fiducial cross section measurement at *particle level* results in $\sigma^{\mathrm{fid}}_{t\bar{t}} = 1.28 \pm 0.09(\mathrm{stat.+syst.}) \pm 0.1(\mathrm{PDF}) \pm 0.09(\mathrm{Q}^2) \pm 0.03(\mathrm{lumi})$ pb. At *parton level* the result is $\sigma^{\mathrm{fid}}_{t\bar{t}} = 1.44 \pm 0.1(\mathrm{stat.+syst.}) \pm 0.13(\mathrm{PDF}) \pm 0.15(\mathrm{Q}^2) \pm 0.04(\mathrm{lumi})$ pb. The prediction by PowHeg, being 1.49 (1.67) pb at particle (parton) level, is $\sim 14\%$ higher, corresponding to 1.3σ (1.0σ) deviation. The differential distributions are extracted from the combination of $1t$ categories. Figure 7 (a,b) illustrates the top quark p_{T} distribution after background subtraction and unfolding. The PowHeg event generator shows a trend to be harder

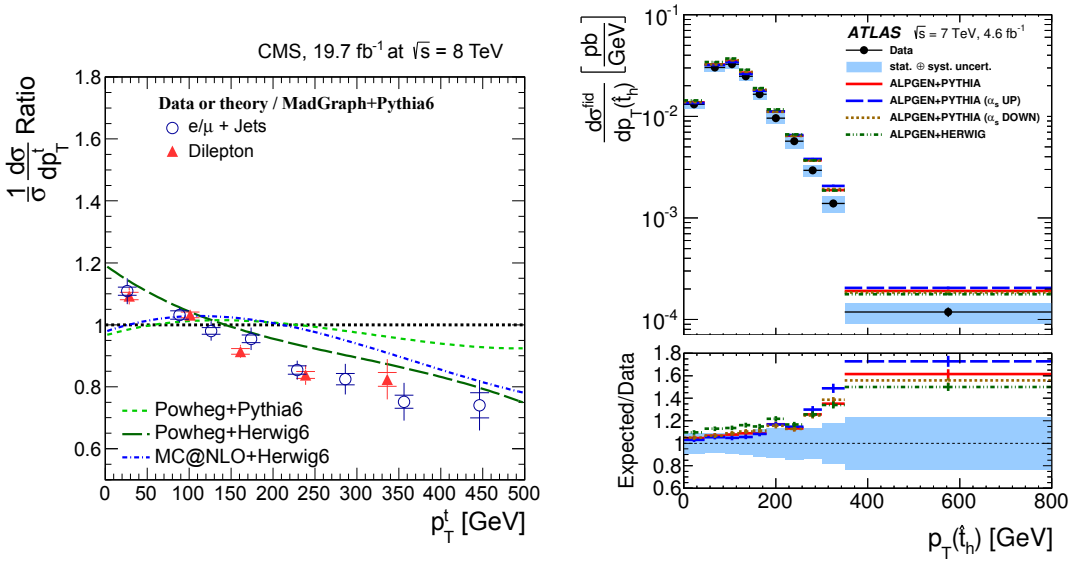

(a) (b)

FIGURE 6. Differential cross section after channel combination compared with predictions as a function of p_{T}^{t} by ATLAS [32] (4.6 fb^{-1}, 7 TeV) with the blue band representing the total (statistical and systematic) uncertainty (a) together with the normalized differential cross section ratio between the unfolded data and predictions by the CMS [31] (19.7 fb^{-1}, 8 TeV) with the inner (outer) error bars indicating the statistical (combined statistical and systematic) uncertainties (b).

than data where MadGraph prediction is consistent with data. A similar feature observed in the earlier measurement by ATLAS [36] where as shown in Fig. 7 (c,d), the overestimation exists in almost all generators and increases with top quark p_{T}.

LHC EARLY $t\bar{t}$ MEASUREMENTS AT $\sqrt{s} = 13$ TEV

ATLAS $t\bar{t}$ cross section measurement in $e\mu$ final state with 78 pb^{-1} of data

Using the first pp collisions at $\sqrt{s} = 13$ TeV, ATLAS has performed an in-situ measurement of the $\sigma_{t\bar{t}}$ and ϵ_b where the latter accounts for the acceptance and b-tagging efficiency [37]. Events with an $e\mu$ pair and one or two b-tagged jets enter the set of equations,

$$N_{1b} = L\,\sigma_{t\bar{t}}\,\epsilon_{e\mu}\,2\epsilon_b(1 - C_b\epsilon_b) + N_{1b}^{bkg}, \quad \text{and} \quad N_{2b} = L\,\sigma_{t\bar{t}}\,\epsilon_{e\mu}\,2\epsilon_b^2 + N_{2b}^{bkg}, \tag{1}$$

where lepton pair efficiency, $\epsilon_{e\mu}$, as well as the b-tagging correlation between top and anti-top and mis-tagged jets, C_b, are taken from simulation. The Drell-Yan background is validated in a data control region where the contribution from non-prompt leptons is estimated in a same-sign data sample, scaled by Monte-Carlo ratio of the opposite-sign to same-sign ratio. The $t\bar{t}$ cross section is determined to be $\sigma_{t\bar{t}} = 825 \pm 49\,(\mathrm{stat.}) \pm 60\,(\mathrm{syst.}) \pm 83\,(\mathrm{lumi})$ pb, consistent with the SM prediction. The hadronization of the signal sample together with the electron identification are dominant sources of uncertainties. The measured b-jet acceptance and identification efficiency, $\epsilon_b = 0.527 \pm 0.026\,(\mathrm{stat.}) \pm 0.006\,(\mathrm{syst.})$, is also compatible with Monte-Carlo expectation, $\epsilon_b^{\mathrm{MC}} = 0.543$.

CMS $t\bar{t}$ cross section measurement in $e\mu$ final state with 42 pb^{-1} of data

In this early analysis by CMS [38] events containing an $e\mu$ pair with $m_{e\mu} > 12$ GeV in addition to at least two jets are used with no b-tagging requirement. The expected Drell-Yan background contamination is corrected with $ee/\mu\mu$ control data within a Z boson mass window. The selected events are corrected for the acceptance, selection efficiency and branching ratios after the subtraction of backgrounds. The measured $t\bar{t}$ cross section is $\sigma_{t\bar{t}} = 769 \pm 60\,(\mathrm{stat.}) \pm 55\,(\mathrm{syst.}) \pm 92\,(\mathrm{lumi})$ pb. The dominant systematic uncertainties correspond to lepton trigger and identification. With a

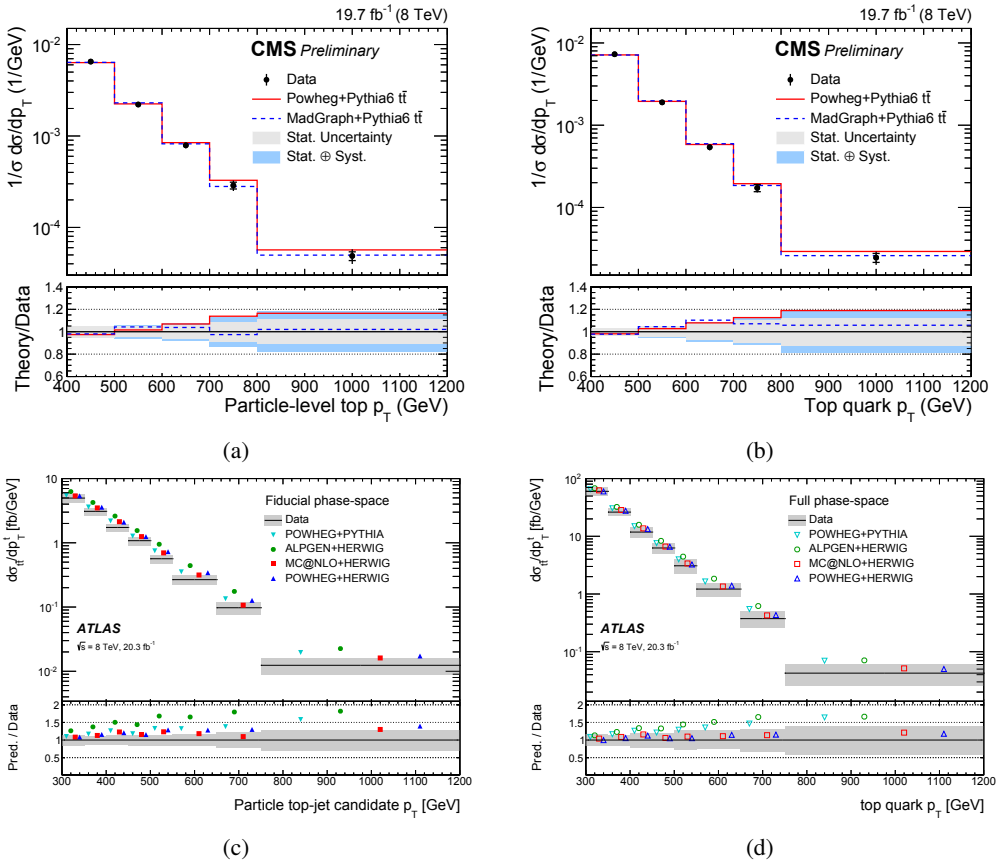

FIGURE 7. Differential cross section for the combined electron and muon channels in bins of particle level top jet (a,c) and parton level top quark (b,d) p_{T}, for CMS [33] (a,b) and ATLAS [36] (c,d) analyses in boosted regimes. Both analyses are performed at $\sqrt{s} = 8\,\mathrm{TeV}$, using the entire corresponding data sample. The particle (parton) level measurements are performed in the fiducial (full) phase space. The statistical and systematic components of the total uncertainty are shown separately and together for CMS and ATLAS, respectively. The points of the various predictions in the ATLAS measurement are spaced along the horizontal axis for presentation only; they correspond to the same p_{T} range.

linear parametrization of acceptance versus m_{top}, a reduction of $\approx 0.7\%$ is expected for $\sigma_{t\bar{t}}$ at $m_{\mathrm{top}} = 173.34\,\mathrm{GeV}$ [39]. The measurement in the fiducial volume results in $\sigma_{t\bar{t}}^{\mathrm{fid}} = 12.8 \pm 1.0\,(\mathrm{stat.}) \pm 1.0\,(\mathrm{syst.}) \pm 1.5\,(\mathrm{lumi})\,\mathrm{pb}$.

Differential $t\bar{t}$ cross section measurement with CMS in $\ell\ell$ final state using $42\,\mathrm{pb}^{-1}$ of data

The first differential measurement at $\sqrt{s} = 13\,\mathrm{TeV}$ [40] is carried out in the dilepton final state with $m_{\ell\ell} > 20\,\mathrm{GeV}$. To suppress the Z+jets background in the same-flavour channels, the dilepton invariant mass must be outside a Z boson mass window of $91 \pm 15\,\mathrm{GeV}$ and the magnitude of missing transverse momentum, $E_{\mathrm{T}}^{\mathrm{miss}}$, must exceed 40 GeV. The remaining part of the Z+jets background is corrected using the data within the Z boson mass window. The kinematic properties of top quarks are obtained through a kinematic reconstruction algorithm [31]. Figure 8 presents the top quark p_{T} and the mass of the $t\bar{t}$ system after unfolding to parton level in the full phase space. Within the uncertainties, good agreement is observed between data and predictions from different event generators.

Differential $t\bar{t}$ cross section measurement with CMS in ℓ+jets final state using $42\,\mathrm{pb}^{-1}$ of data

The CMS differential analysis in ℓ+jets [41] makes use of events with exactly one isolated muon or electron, at least two jets and at least one b-tagged jet where a harder p_{T} requirement is placed for at least one b jets. The leptonically decaying top quark is reconstructed through momentum conservation criteria, $(p_\ell + p_\nu)^2 = m_W^2$ and

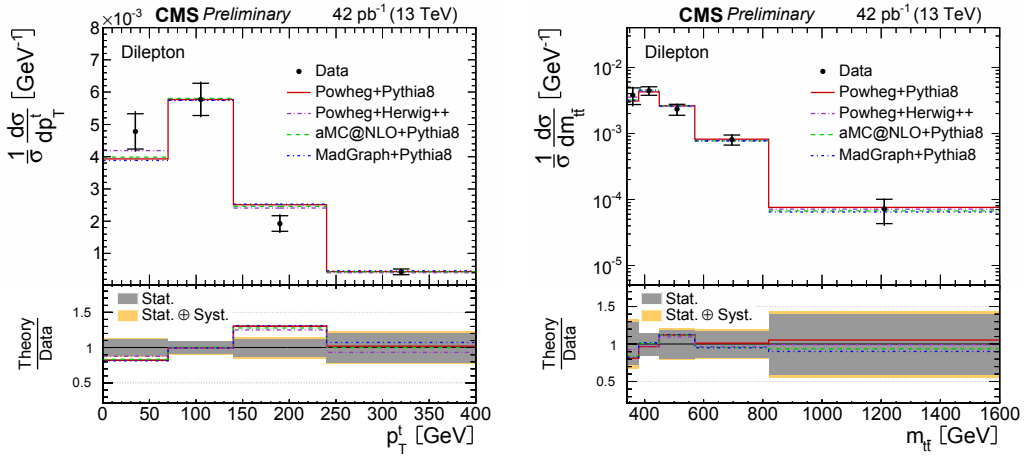

(a) (b)

FIGURE 8. The CMS normalized differential $t\bar{t}$ production cross section [40] as a function of the transverse momentum p_T of the top quark (a) and the invariant mass of the $t\bar{t}$ system (b), using 42 pb^{-1} of data at 13 TeV. The inner (outer) error bars indicate the statistical (combined statistical and systematic) uncertainty. The lower part of each plot shows the ratio of the predictions to data.

$(p_\ell + p_\nu + p_b)^2 = m_{top}^2$. For the hadronic side, the 2D probability of m_{jj} vs. m_{jjb}, being compatible with the W boson and top quark hypotheses, is maximized. Events with low 2D probability are rejected. The remaining non-$t\bar{t}$ backgrounds are small and are taken from simulation. The total $t\bar{t}$ cross section, $\sigma_{t\bar{t}} = 836 \pm 27\,(\text{stat.}) \pm 84\,(\text{syst.}) \pm 100\,(\text{lumi})$ pb, is obtained by performing the analysis in a single bin that includes all events. The b-tagging and PDF uncertainties are dominant in this measurement. Figure 9 shows the normalized differential cross section as a function of p_T of the leptonically and hadronically decaying top quarks. The data and simulations agree well within the uncertainties.

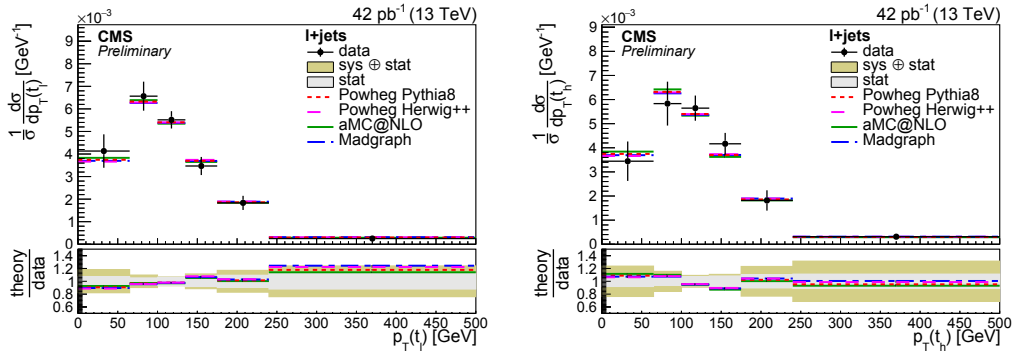

(a) (b)

FIGURE 9. The CMS normalized differential cross section [41] as a function of p_T of the leptonically (a) and hadronically (b) decaying top quarks, compared to different predictions. The analysis is based on 42 pb^{-1} of 13 TeV data.

SUMMARY

The LHC experiments studied the very first top quarks from proton-proton collisions at 13 TeV. The production rate of $t\bar{t}$ is measured inclusively and in bins of top quark properties together with lepton and jets. Precise results are also obtained using the full LHC data set in Run I where boosted regimes are also explored thanks to the large data sample. Figure 10 summarizes the inclusive $t\bar{t}$ cross section measurements from ATLAS and CMS experiments.

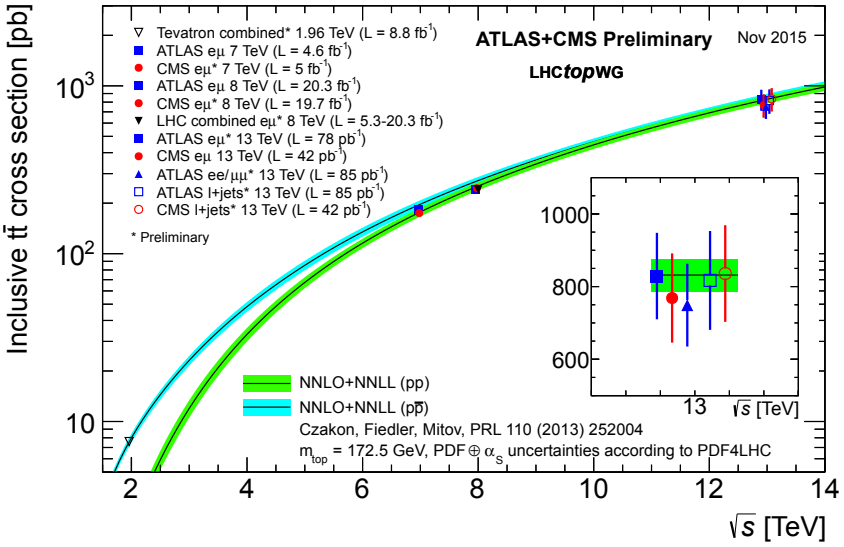

FIGURE 10. Summary of LHC and Tevatron measurements of the top-pair production cross-section as a function of the centre-of-mass energy compared to the NNLO QCD calculation complemented with NNLL resummation (Top++2.0). The theory band represents uncertainties due to renormalisation and factorisation scale, parton density functions and the strong coupling. The measurements and the theory calculation are quoted at $m_{top} = 172.5$ GeV. Measurements made at the same centre-of-mass energy are slightly offset for clarity.

ACKNOWLEDGMENTS

The author would like to thank the ATLAS and CMS collaborations for their excellent work in top quark physics.

REFERENCES

[1] CDF Collaboration. Observation of top quark production in $\bar{p}p$ collisions. *Phys. Rev. Lett.*, 74:2626–2631, 1995. doi: 10.1103/PhysRevLett.74.2626.

[2] D0 Collaboration. Observation of the top quark. *Phys. Rev. Lett.*, 74:2632–2637, 1995. doi: 10.1103/PhysRevLett.74.2632.

[3] CDF Collaboration. Observation of electroweak single top-quark production. *Phys. Rev. Lett.*, 103:092002, Aug 2009. doi: 10.1103/PhysRevLett.103.092002.

[4] D0 Collaboration. Observation of single top-quark production. *Phys. Rev. Lett.*, 103:092001, Aug 2009. doi: 10.1103/PhysRevLett.103.092001.

[5] ATLAS Collaboration. The ATLAS Experiment at the CERN Large Hadron Collider. *JINST*, 3:S08003, 2008. doi: 10.1088/1748-0221/3/08/S08003.

[6] CMS Collaboration. The CMS experiment at the CERN LHC. *JINST*, 3:S08004, 2008. doi: 10.1088/1748-0221/3/08/S08004.

[7] ATLAS Collaboration. Measurement of the top quark-pair production cross section withatlas in pp collisions at $\sqrt{s}$ = 7TeV. *The European Physical Journal C*, 71(3):1577, 2011. ISSN 1434-6044. doi: 10.1140/epjc/s10052-011-1577-6.

[8] CMS Collaboration. First measurement of the cross section for top-quark pair production in protonproton collisions at $\sqrt{s}$ = 7 TeV. *Physics Letters B*, 695(5):424 – 443, 2011. ISSN 0370-2693. doi: http://dx.doi.org/10.1016/j.physletb.2010.11.058.

[9] ATLAS Collaboration. Measurement of the $t\bar{t}$ production cross-section using $e\mu$ events with b-tagged jets in pp collisions at $\sqrt{s}$ = 7 and 8 TeV with the ATLAS detector. *The European Physical Journal C*, 74(10): 3109, 2014. ISSN 1434-6044. doi: 10.1140/epjc/s10052-014-3109-7.

[10] CMS Collaboration. Measurement of the $t\bar{t}$ production cross section in the $e\mu$ channel in pp collisions at 7 and 8 TeV. Technical Report CMS-PAS-TOP-13-004, CERN, Geneva, 2015.

[11] CMS Collaboration. Measurement of the t-channel single top quark production cross section in pp collisions at $\sqrt{s}$ = 7 TeV. *Phys. Rev. Lett.*, 107:091802, Aug 2011. doi: 10.1103/PhysRevLett.107.091802.

[12] ATLAS Collaboration. Comprehensive measurements of t-channel single top-quark production cross sections at $\sqrt{s}$ = 7 TeV with the atlas detector. *Phys. Rev. D*, 90:112006, Dec 2014. doi: 10.1103/PhysRevD.90.112006.

[13] CMS Collaboration. Measurement of the single-top-quark t-channel cross section in pp collisions at $\sqrt{s}$ = 7 TeV. *Journal of High Energy Physics*, 2012(12):35, 2012. doi: 10.1007/JHEP12(2012)035.

[14] ATLAS Collaboration. Measurement of t-Channel Single Top-Quark Production in pp Collisions at $\sqrt{s}$ = 8 TeV with the ATLAS detector. Technical Report ATLAS-CONF-2012-132, CERN, Geneva, Sep 2012. URL `http://cds.cern.ch/record/1478371`.

[15] CMS Collaboration. Measurement of the t-channel single-top-quark production cross section and of the $|v_{tb}|$ ckm matrix element in pp collisions at $\sqrt{s}$ = 8 TeV. *Journal of High Energy Physics*, 2014(6):90, 2014. doi: 10.1007/JHEP06(2014)090.

[16] CMS Collaboration. Fiducial t-channel single top-quark cross section at 8 TeV. Technical Report CMS-PAS-TOP-15-007, CERN, Geneva, 2015. URL `http://cds.cern.ch/record/2055528`.

[17] ATLAS Collaboration. Measurement of the production cross-section of a single top quark in association with a W boson at 8 TeV with the ATLAS experiment. *arXiv:1510.03752*, 2015.

[18] CMS Collaboration. Observation of the associated production of a single top quark and a w boson in pp collisions at $\sqrt{s}$ = 8 TeV. *Phys. Rev. Lett.*, 112:231802, Jun 2014. doi: 10.1103/PhysRevLett.112.231802.

[19] ATLAS Collaboration. Evidence for single top-quark production in the s-channel in proton-proton collisions at $\sqrt{s}$ = 8 TeV with the ATLAS detector using the Matrix Element Method. *arXiv:1511.05980*, 2015.

[20] CMS Collaboration. Search for s-channel single top-quark production in pp collisions at $\sqrt{s}$ = 8 TeV. Technical Report CMS-PAS-TOP-13-009, CERN, Geneva, 2013. URL `https://cds.cern.ch/record/1633190`.

[21] ATLAS Collaboration. Measurement of the top pair production cross section in 8 TeV proton-proton collisions using kinematic information in the lepton+jets final state with atlas. *Phys. Rev. D*, 91:112013, Jun 2015. doi: 10.1103/PhysRevD.91.112013.

[22] Matteo Cacciari and Gavin P. Salam. Dispelling the myth for the jet-finder. *Physics Letters B*, 641(1):57 – 61, 2006. ISSN 0370-2693. doi: http://dx.doi.org/10.1016/j.physletb.2006.08.037.

[23] Matteo Cacciari, Gavin P. Salam, and Gregory Soyez. The anti- k t jet clustering algorithm. *Journal of High Energy Physics*, 2008(04):063, 2008.

[24] A. Hoecker et al. TMVA - Toolkit for Multivariate Data Analysis. *ArXiv Physics e-prints*, March 2007.

[25] ATLAS Collaboration. Measurement of the $t\bar{t}$ production cross-section using $e\mu$ events with b -tagged jets in pp collisions at $\sqrt{s}$ = 7 and 8 TeV with the ATLAS detector. *Eur. Phys. J.*, C74(10):3109, 2014. doi: 10.1140/epjc/s10052-014-3109-7.

[26] Michal Czakon and Alexander Mitov. Top++: A Program for the Calculation of the Top-Pair Cross-Section at Hadron Colliders. *Comput. Phys. Commun.*, 185:2930, 2014. doi: 10.1016/j.cpc.2014.06.021.

[27] ATLAS Collaboration. Study of heavy-flavor quarks produced in association with top-quark pairs at $\sqrt{s}$ = 7 TeV using the atlas detector. *Phys. Rev. D*, 89:072012, Apr 2014. doi: 10.1103/PhysRevD.89.072012.

[28] CMS Collaboration. Measurement of the cross section ratio $\sigma_{t\bar{t}b\bar{b}}/\sigma_{t\bar{t}jj}$ in pp collisions at $\sqrt{s}$ = 8 TeV. *Physics Letters B*, 746:132–153, 2015. ISSN 0370-2693. doi: http://dx.doi.org/10.1016/j.physletb.2015.04.060.

[29] CMS Collaboration. Measurement of the ttbb cross section and the ratio ttbb/ttjj in the lepton+jets final state at 8 TeV with CMS detector. Technical Report CMS-PAS-TOP-13-016, CERN, Geneva, 2015. URL `http://cds.cern.ch/record/2038631`.

[30] ATLAS Collaboration. Measurements of fiducial cross-sections for $t\bar{t}$ production with one or two additional b-jets in pp collisions at $\sqrt{s}$ = 8 TeV using the ATLAS detector. *arXiv:1508.06868*, 2015.

[31] CMS Collaboration. Measurement of the differential cross section for top quark pair production in pp collisions at $\sqrt{s}$ = 8 TeV. *Eur. Phys. J.*, C75(11):542, 2015. doi: 10.1140/epjc/s10052-015-3709-x.

[32] ATLAS Collaboration. Differential top-antitop cross-section measurements as a function of observables constructed from final-state particles using pp collisions at $\sqrt{s}$ = 7 TeV in the ATLAS detector. *JHEP*, 06: 100, 2015. doi: 10.1007/JHEP06(2015)100.

[33] CMS Collaboration. Measurement of the differential ttbar production cross section for high-pt top quarks in e/mu+jets final states at 8 TeV. Technical Report CMS-PAS-TOP-14-012, CERN, Geneva, 2015. URL http://cds.cern.ch/record/2045404.

[34] Matteo Cacciari, Gavin P. Salam, and Gregory Soyez. The Anti-k(t) jet clustering algorithm. *JHEP*, 04:063, 2008. doi: 10.1088/1126-6708/2008/04/063.

[35] CMS Collaboration. Boosted Top Jet Tagging at CMS. Technical Report CMS-PAS-JME-13-007, CERN, Geneva, 2014. URL https://cds.cern.ch/record/1647419.

[36] ATLAS Collaboration. Measurement of the differential cross-section of highly boosted top quarks as a function of their transverse momentum in $\sqrt{s}$ = 8 TeV proton-proton collisions using the ATLAS detector. 2015.

[37] ATLAS Collaboration. Measurement of the $t\bar{t}$ production cross-section in pp collisions at 13 TeV using $e\mu$ events with b-tagged jets. Technical Report ATLAS-CONF-2015-033, CERN, Geneva, Jul 2015. URL http://cds.cern.ch/record/2038144.

[38] CMS Collaboration. Measurement of the top quark pair production cross section in proton-proton collisions at $\sqrt{s}$ = 13 TeV. 2015.

[39] CMS ATLAS, CDF and D0 Collaborations. First combination of Tevatron and LHC measurements of the top-quark mass. 2014.

[40] CMS Collaboration. First measurement of the differential cross section for $t\bar{t}$ production in the dilepton final state at $\sqrt{s}$ = 13 TeV. Technical Report CMS-PAS-TOP-15-010, CERN, Geneva, 2015. URL http://cds.cern.ch/record/2047866.

[41] CMS Collaboration. Measurement of the inclusive and differential tt production cross sections in lepton + jets final states at 13 TeV. Technical Report CMS-PAS-TOP-15-005, CERN, Geneva, 2015. URL http://cds.cern.ch/record/2048622.

Top quark physics: parallel talks

Proceedings of the LHCP2015 Conference, St. Petersburg, Russia, August 31 - September 5, 2015

Editors: V.T. Kim and D.E. Sosnov

Measurements of $t\bar{t}$ + X with the ATLAS and CMS Experiments

CARMEN DIEZ PARDOS

DESY, Notkestr. 85 22706 Hamburg (Germany)

carmen.diez@desy.de

On behalf of the ATLAS and CMS Collaborations

Abstract. Recent measurements of top quark pair production cross section in association with additional particles are presented. The results include measurements of differential cross sections for $t\bar{t}$+jet processes as well as inclusive cross sections for $t\bar{t}$ production in association with additional heavy-quark jets or additional bosons. The results are obtained by the ATLAS and CMS collaborations using data collected in proton-proton collisions at centre-of-mass energies of 7 TeV and 8 TeV.

INTRODUCTION

The top quark is the heaviest known elementary particle and the only quark that decays before hadronisation, and thus gives direct access to its properties. With its large mass, it plays a crucial role in electroweak loop corrections, providing indirect constraints on the mass of the Higgs boson. Top quark measurements also provide important input to QCD calculations. Moreover, various scenarios of physics beyond the standard model (SM) expect the top quark to couple to new particles.

In hadron colliders, top quarks are mostly produced in pairs via the strong interaction. At the LHC energies, the dominant mechanism is gluon-gluon fusion, corresponding to ~80% of the generation process. Top quarks decay almost exclusively via the $t \rightarrow bW$ and it is the decay of the W bosons that defines the final state. Therefore, $t\bar{t}$ signatures can be classified according to the combinatorics of the W boson decay. The $t\bar{t}$ measurements presented are performed using the final states that include events with two leptons, two neutrinos and two b jets (dilepton decay channels) and one lepton, one neutrino and four jets, out of which two arise from b quarks (lepton+jets), and requiring additional jets, leptons or a photon, depending on the process under study. Only the most recent results by the ATLAS ATLAS Collaboration [1] and CMS CMS Collaboration [2] experiments are discussed.

$t\bar{t}$+jets

At LHC energies, the fraction of $t\bar{t}$ events with additional hard jets in the final state is large, about half of the total number of $t\bar{t}$ events. The understanding of these processes is relevant to test higher order QCD calculations, in which contributions from initial and final state radiation are taken into account to achieve a good quantitative description of multijet processes. The correct description of these events is important not least because multijet processes constitute important backgrounds for many new physics searches and $t\bar{t}$+H processes.

CMS and ATLAS have performed several measurements of $t\bar{t}$ production differential measurements both in the dileptonic and l+jets channels, such as the cross section as a function of the jet multiplicity and properties of the jets in different kinematic ranges in $t\bar{t}$+jets topologies ATLAS Collaboration [3], CMS Collaboration [4].

The measurements are corrected for detector and hadronisation effects back to particle level, using a regularised unfolding procedure, and they are either absolute or normalised, so that systematic uncertainties correlated between all bins cancel in the ratio. Typically the measurements are performed in a fiducial volume to minimize model dependencies. Figure 1 shows the differential cross section as a function of jet multiplicity in the l+jets (ATLAS, 7 TeV ATLAS

Collaboration [3]) and dilepton (CMS, 8 TeV CMS Collaboration [4]) channels, compared to different generators at LO with up to 5 hard partons and with NLO matrix element computations. The largest uncertainties arise from the jet energy scale and MC modeling up to high multiplicities, where they are dominated by statistical uncertainty. In Fig. 2 the absolute cross sections are shown as a function of the transverse momentum (p_T) of the leading jet in the event (left), which is likely to come from the decay of the $t\bar{t}$ system, and the leading additional jet (right), arising from initial state radiation. In general good agreement is observed between data and predictions.

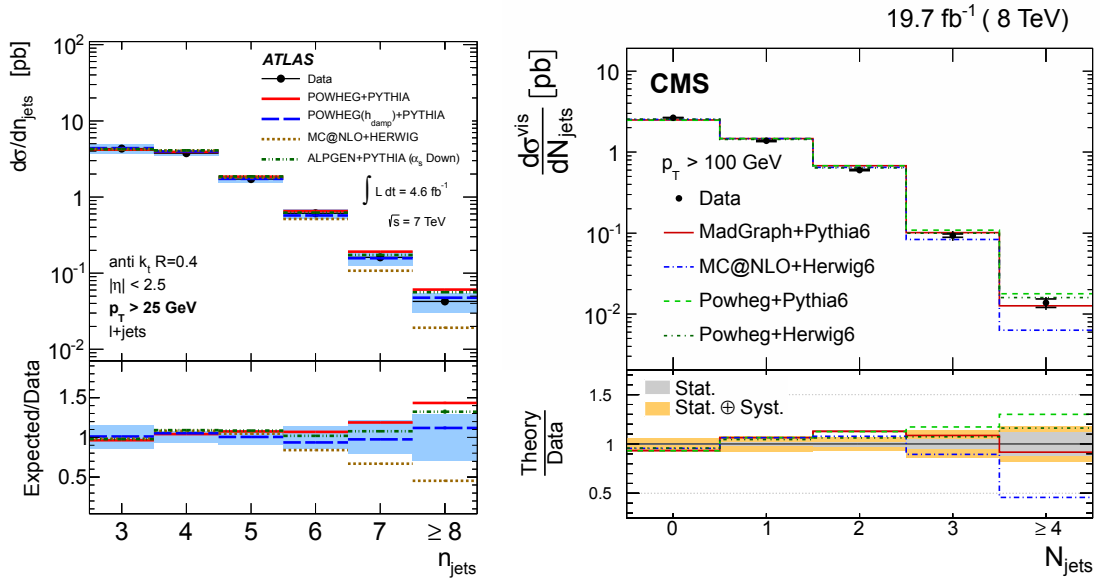

FIGURE 1. Absolute differential $t\bar{t}$ cross sections as a function of jet multiplicity in the event, at 7 TeV for jets with $p_T > 25$ GeV (left) ATLAS Collaboration [3] and at 8 TeV for jets with $p_T > 100$ GeV (right) CMS Collaboration [4].

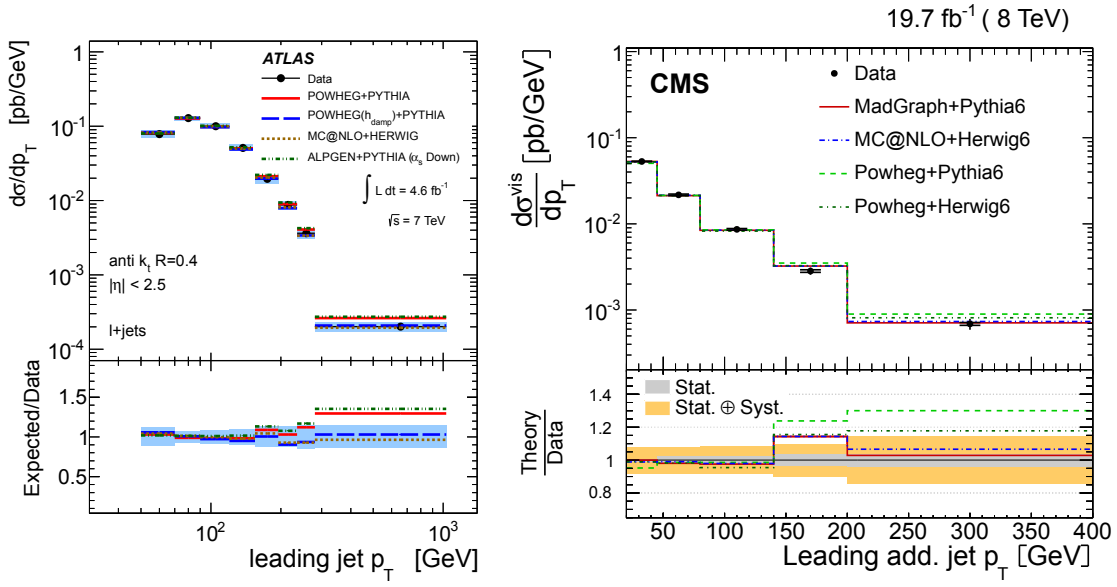

FIGURE 2. Absolute differential $t\bar{t}$ cross sections as a function of the p_T of the leading jet in the event (left) ATLAS Collaboration [3] and the leading additional jet not coming from the $t\bar{t}$ decay (right) CMS Collaboration [4] compared to different predictions.

$t\bar{t}$+heavy flavour

The production of $t\bar{t}$ in association with a pair of bottom quarks ($b\bar{b}$) is an irreducible background to the production of $t\bar{t}$+H, where the Higgs boson decays to $b\bar{b}$. A precise measurement of $\sigma(t\bar{t}b\bar{b})$ has the potential to reduce background uncertainty and thus, increase sensitivity. Both CMS and ATLAS collaborations have measured the cross section ratio $\sigma(t\bar{t}b\bar{b})/\sigma(t\bar{t}jj)$ using dilepton and l+jets decay channels. The most recent analysis in CMS is performed by selecting single lepton events CMS Collaboration [5]. The relative contribution from $t\bar{t}b\bar{b}$ is determined with a simultaneous template fit to the measured b-tagging algorithm discriminant of the jets in the event. An example is shown in Fig. 3 left. The result is $\sigma(t\bar{t}b\bar{b})/\sigma(t\bar{t}jj)$ =0.0117±0.0040(stat.)±0.0003(sys.), for jets with $p_T > 40$ GeV, where the flavor of generated jets is defined by the flavor of the leading quark in the jet. The results are in good agreement with NLO calculations and with a previous CMS measurement in the dilepton channel when the same jet definition is used CMS Collaboration [6].

Measurements of fiducial cross sections for $t\bar{t}$ production with one or two additional b-jets at $\sqrt{s} = 8$ TeV are also performed using the ATLAS detector ATLAS Collaboration [7]. The measurements of the absolute $t\bar{t}b$ and $t\bar{t}b\bar{b}$ cross sections make use of a likelihood fit to the distribution of the multivariate discriminant used for b-jet identification, in the l+jets and eμ channels. A cut-based analysis is also used to determine the cross section and $\sigma(t\bar{t}b\bar{b})/\sigma(t\bar{t}jj)$ in the dilepton channels. The results measured for particle-level jets with $p_T > 40$ GeV are summarised in Fig. 3 (right). The predictions containing NLO matrix elements for the pp→ $t\bar{t}b\bar{b}$ process, as well as the merged LO+PS prediction are in agreement with the measured cross sections within the measurement uncertainties. Different g→ $b\bar{b}$ splitting models affect significantly the $t\bar{t}b\bar{b}$ and $t\bar{t}b$ cross sections in the samples where all additional b jets come from the parton shower.

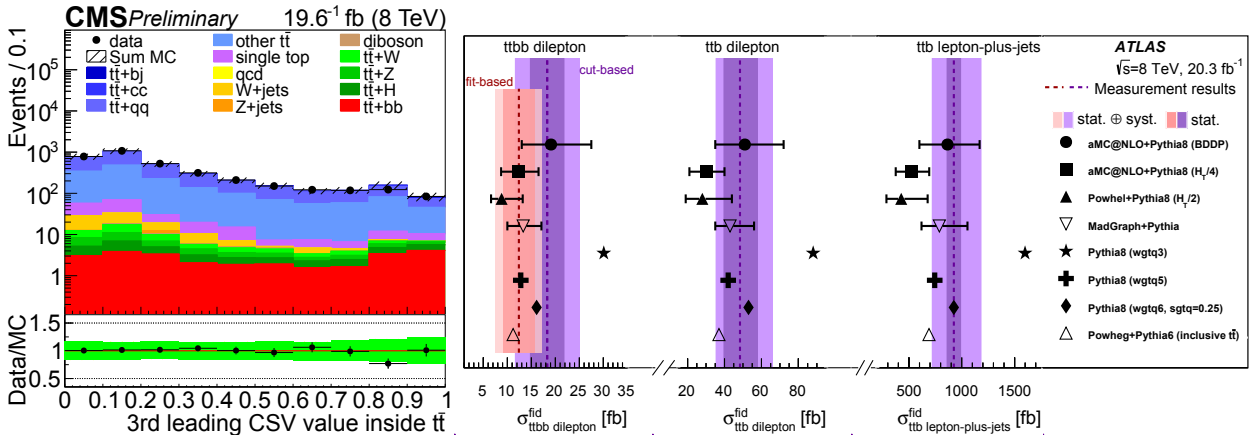

FIGURE 3. Left: Pre-fit distribution of the CSV b-tag discriminant for the jet categories of 4 jets and 0 b-tags of additional jets, in the muon channel. The errors include the statistical and systematic uncertainties CMS Collaboration [5]. Right: Comparison of the measured cross sections in the three fiducial phase-space regions with theoretical predictions obtained from a variety of different generators. The coloured bands indicate the statistical and total uncertainties of the measurements. The errors on the theoretical prediction are obtained by simultaneously varying the renormalisation and factorisation scales by a factor of two ATLAS Collaboration [7].

$t\bar{t}$ production in association with additional bosons

Measurement of $t\bar{t}$+W/Z

Measurements of the cross sections of $t\bar{t}$+W/Z processes are the first step towards measuring the coupling to bosons. They are also relevant because they could be enhanced by beyond the SM (BSM) contributions as well as they represent an important background for BSM searches, as some searches for SUSY or $t\bar{t}$+H. The analyses by both the ATLAS and CMS Collaborations are performed using the 8 TeV data. The general strategy is described in the following. The event sample is divided in categories depending on the number of charged leptons (2, 3 or 4 leptons), which yield different admixtures of ttW and ttZ processes: Same-sign dilepton analysis are enriched in $t\bar{t}$+W, while trilepton

and four-lepton topologies are dedicated to measure process. The signal is extracted simultaneously in a binned likelihood fit in the different signal categories. Additionally, the categories are further split depending on jet multiplicity, number of b-tagged jets and E_T^{miss}, optimised individually to increase sensitivity. The expected yields measured by ATLAS after the fit compared to data in the control regions and the signal regions are shown in Fig. 4 ATLAS Collaboration [8]. The measurement yields significances of 5σ and 4.2σ over the background-only hypothesis, for $t\bar{t}$+W and $t\bar{t}$+Z, respectively. The measured cross section result $\sigma(t\bar{t}W) = 369^{+100}_{-91}$ fb and $\sigma(t\bar{t}Z) = 176^{+58}_{-52}$ fb.

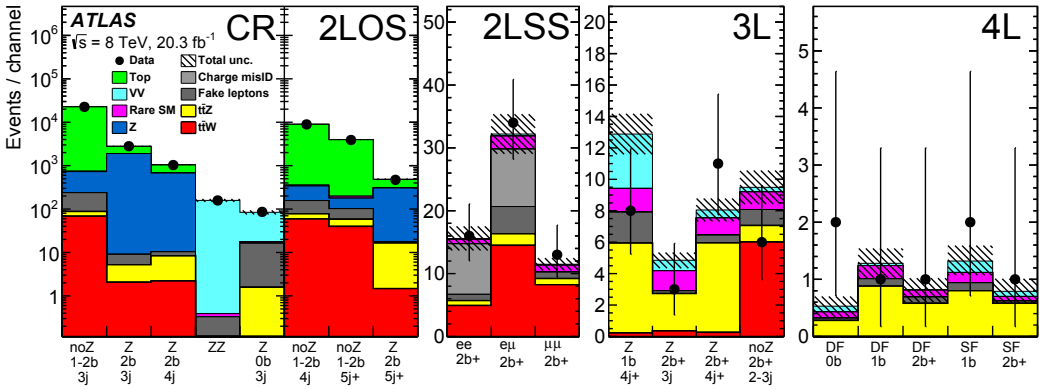

FIGURE 4. Expected yields after the fit compared to data in the five control regions (CR), used to constrain the backgrounds, the three signal regions in the opposite-sign dilepton channel (2LOS), the three signal regions in the same-sign dilepton channel (2LSS), the four signal regions in the trilepton channel (3L) and the five signal regions in the tetralepton channel (4L) ATLAS Collaboration [8].

The most recent analysis by CMS CMS Collaboration [9], extends the general analysis strategy by performing a kinematic reconstruction of the measured events under the $t\bar{t}$+W and $t\bar{t}$+Z process hypotheses, assigning the reconstructed jets and leptons to the individual particles of the process signatures. The information is then combined with other kinematic information to train Boosted Decision Trees (BDTs) that can be used to achieve an improved separation of the background and signal processes. Such trainings are performed in a variety of channels with differing numbers of jets, b tags and charged leptons. The $t\bar{t}$+W cross section is measured to be 382^{+117}_{-102} fb with a significance of 4.8 standard deviations, while the $t\bar{t}$+Z cross section is measured to be 242^{+65}_{-55} fb with a significance of 6.4 standard deviations from the background-only hypothesis. The results are summarized in Fig. 5.

Measurement of $t\bar{t}+\gamma$

The production cross section of $t\bar{t}$ associated with a photon has been recently measured at $\sqrt{s} = 7$ TeV by the ATLAS Collaboration ATLAS Collaboration [10]. This process is sensitive to the $t\gamma$ coupling and models with composite top quarks and excited top quark production ($t^\star \rightarrow t\gamma$). The $t\bar{t} + \gamma$ measurement is performed in the l+jets decay channel. Events are selected by requiring a photon with a transverse energy greater than 20 GeV and an angular distance between the photon and $|m_{e\gamma} - m_Z| > 5$ GeV, to suppress misidentified photons, in addition to the $t\bar{t}$ selection. Prompt photons are estimated from a template fit to the photon isolation variable. The transverse energy of the selected photons and the result of the template fit are shown in Fig. 6. The fiducial cross section is measured to be $\sigma_{t\bar{t}+\gamma} \cdot BR = 63 \pm 8(\text{stat})^{+17}_{-13}(\text{syst})\pm 1(\text{lumi})$ fb per lepton flavour, consistent with SM expectation ($\sigma(t\bar{t} + \gamma) = 48 \pm 10$fb). The production is observed with a significance of 5.3 standard deviations away from the null hypothesis. The measurement by the CMS Collaboration in the μ+jets channel can be found in Ref. CMS Collaboration [11].

Summary

Top quark measurements provide important information about the production process as described in QCD, as well as sensitivity to possible new physics. In the last years, the LHC has become a real 'top factory' and the large $t\bar{t}$ samples collected allowed to perform precise differential $t\bar{t}$+jets cross section measurements, first measurements of $t\bar{t}$+ heavy flavour, and the observation of $t\bar{t}$+W/Z/γ. The latter measurements will benefit from the data expected to be collected

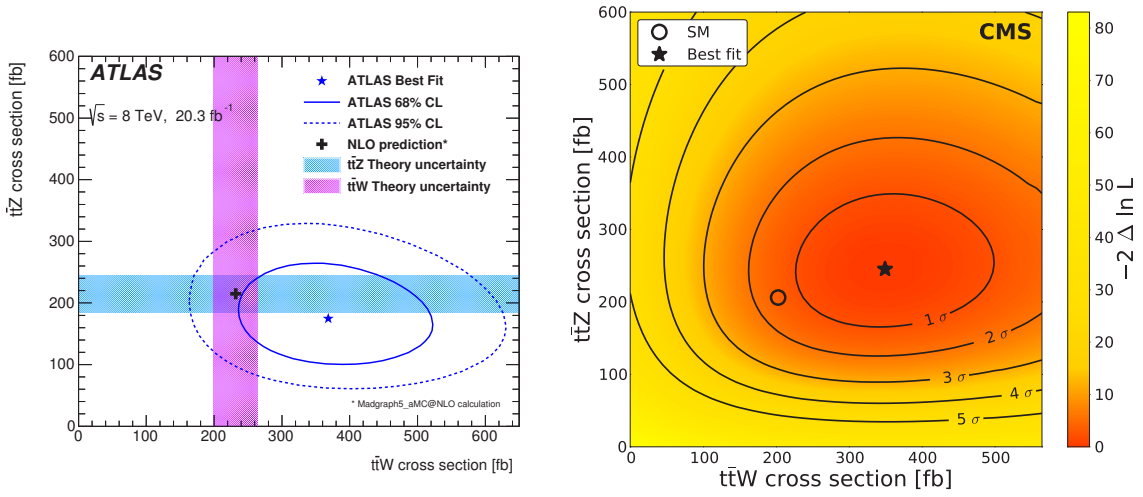

FIGURE 5. Left: The result by ATLAS of the simultaneous fit to the $t\bar{t}$+W and $t\bar{t}$+Z cross sections along with the 68% and 95% CL uncertainty contours ATLAS Collaboration [8]. Right: Profile likelihood as a function of the cross sections as measured by CMS. CMS Collaboration [9].

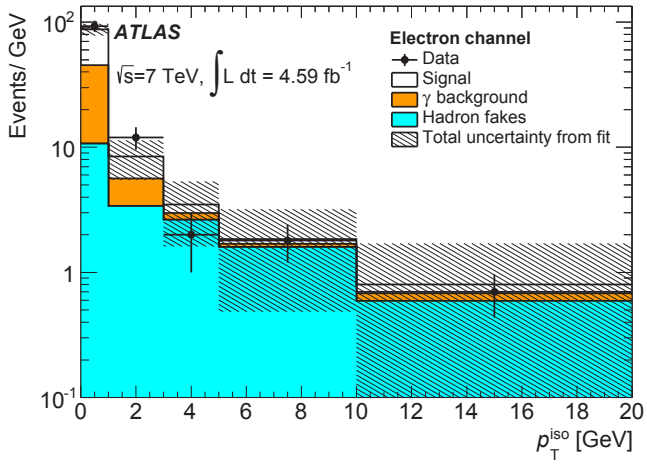

FIGURE 6. Results of the combined likelihood fit using the track-isolation distributions as the discriminating variable for the electron channel. The contribution from $t\bar{t} + \gamma$ events is labeled as 'Signal', prompt-photon background is labeled 'background', the contribution from hadrons misidentified as photons is labeled as 'Hadron fakes' ATLAS Collaboration [10].

during the full LHC Run2, which will allow to reduce the uncertainties significantly and thus to verify if couplings to the top quark are compatible with SM or altered by BSM effects.

REFERENCES

[1] ATLAS Collaboration, JINST **3**, p. S08003 (2008).
[2] CMS Collaboration, JINST **3**, p. S08004 (2008).
[3] ATLAS Collaboration, JHEP **01**, p. 020 (2015).
[4] CMS Collaboration, arXiv:1510.03072 [hep-ex] (2015).
[5] CMS Collaboration, CMS-PAS-TOP-13-016 (2015).
[6] CMS Collaboration, Phys. Lett. **B746**, p. 132 (2015).
[7] ATLAS Collaboration, arXiv:1508.06868 [hep-ex] (2015).
[8] ATLAS Collaboration, JHEP **11**, p. 172 (2015).
[9] CMS Collaboration, arXiv:1510.01131 [hep-ex] (2015).
[10] ATLAS Collaboration, Phys. Rev. **D91**, p. 072007 (2015).
[11] CMS Collaboration, CMS-PAS-TOP-13-011 (2014).

Proceedings of the LHCP2015 Conference, St. Petersburg, Russia, August 31 - September 5, 2015

Editors: V.T. Kim and D.E. Sosnov

Latest Developments in Differential Distributions at NNLO

DAVID HEYMES

Cavendish Laboratory, University of Cambridge, Cambridge CB3 0HE, UK

dheymes@hep.phy.cam.ac.uk

Abstract. Differential distributions for on-shell top-quark pair production at next-to-next-to-leading order in perturbative QCD for the Large Hadron Collider at $\sqrt{s} = 8$ TeV are presented and discussed. The theoretical framework of the calculation is summarized. By comparing the prediction to measurements, it turns out that next-to-next-to-leading order corrections are necessary in order to resolve a discrepancy between data and next-to-leading order predictions in the transverse momentum distribution of the top-quark.

INTRODUCTION

Top-quarks provide an excellent testing ground for the Standard Model and in particular Quantum Chromodynamics (QCD) at the Large Hadron Collider (LHC). The large number of top-quark pairs that have been produced at $\sqrt{s} = 7$ TeV and $\sqrt{s} = 8$ TeV allows for detailed studies of top-quark properties in different kinematical regions. Additionally, they are an important background for the main physics program measurements at the LHC at $\sqrt{s} = 13$ TeV, namely precision measurements of the Higgs-boson properties and searches for physics beyond the Standard Model. Precision predictions at a differential level for top-quark pairs are demanded in order to give a reliable interpretation of the measurements within and beyond the Standard Model.

In order to test the Standard Model down to the precision that can be achieved at the LHC, theoretical predictions at the same accuracy need to be provided. The total inclusive cross-section at next-to-next-to-leading order QCD [1, 2, 3, 4, 5, 6] shows a very good agreement with measurements at 7, 8 and 13 TeV [7, 8, 9, 10, 11]. Furthermore, only at this order of perturbation theory the theoretical uncertainty is at the same level as the precision of the measurement.

At a differential level, most measurements of the decay products of the top-quark, namely leptons and jets, are currently in good agreement with next-to-leading order predictions obtained using available Monte Carlo event generators. In contrast, the p_{T}-distribution of the top-quark itself reveals a discrepancy between measurements and next-to-leading order predictions at $\sqrt{s} = 7$, 8 and 13 TeV [12, 13, 14, 15, 16, 17, 18]. Since the top-quark is not measured directly, but reconstructed from its decay products using Monte Carlo generators, inaccuracies in the Standard Model description of the top-quark level process could cause a tensions. Higher-order QCD corrections will help to identify the origin of those discrepancies.

Several approximations of the next-to-next-to-leading order QCD corrections to differential top-quark pair production have been presented [19, 20, 21, 22, 23, 24]. These approximations are next-to-leading order accurate and, in addition, they capture contributions of the next-to-next-to-leading order result in specific kinematical regions, e.g. the partonic threshold of the top-quark pair.

In this write-up, full next-to-next-to-leading order differential distributions for top-quark pair production at the LHC at 8 TeV are discussed. First, an overview of next-to-next-to-leading order computations for top-quark pair production is presented. This is followed by results for the p_{T}-, $m_{t\bar{t}}$-, $y_{t\bar{t}}$- and y_t-distribution. Finally, the results are summarized and an outlook for further studies is given. For additional details please refer to the main publication [25].

Next-to-next-to-leading order computations for top-quark pairs

In order to perform numerical computations beyond leading order, a subtraction framework is needed to consistently cancel soft and collinear singularities between virtual and real contributions to the cross section. At next-to-leading

order general algorithms are established and allow an automated simulation of a large class of processes, that are relevant for the phenomenology at the LHC [26, 27]. At next-to-next-to-leading order different subtraction schemes have been proposed and applied to single processes.

In the context of top-quark pair production three approaches can be distinguished: The *antenna-subtraction* scheme has been used to calculate differential distributions in the leading colour approximation for the partonic contribution $q\bar{q} \to t\bar{t}$ [28, 29]. The q_{T}-*subtraction* scheme has been applied to top-quark pair production in [30] and results for the qq'-channel to the total inclusive cross section have been obtained.

The sector improved residue subtraction scheme, Stripper, has been proposed in [31] and subsequently successfully applied to the calculation of the total inclusive cross section for top-quark pair production [1, 2, 3, 4, 5, 6, 32]. The result includes all partonic processes without further approximations except the truncation of the perturbation series beyond next-to-next-to-leading order. Afterwards, the same framework has been used to predict the forward-backward asymmetry at the Tevatron [33], which has been the first differential prediction for on-shell top-quark pair production at next-to-next-to-leading order.

However, the first formulation of the subtraction scheme and its implementation for the Tevatron setup were not suited to provide robust differential results for the LHC on an adequate time-scale. A substantial diminution of the convergence of the Monte Carlo integration has been observed as the collider energy has been increased. This behaviour is due to large logarithms of ratios between the top-quark mass and the partonic center-of-mass energy in phase space integrals. Moreover, current and future demands of the LHC require a fast Monte Carlo generator, that provides reliable predictions at next-to-next-to-leading order, which can be flexibly adjusted to experimental setups.

In view of those requirements, a complete new implementation of Stripper has been developed, which is based on an improved four-dimensional formulation of the subtraction scheme [34]. The whole framework is general, since it exploits the process independent soft and collinear factorization of tree-level and one-loop matrix elements as well as the universal singular structure of virtual one-loop and two-loop amplitudes [32, 35, 36, 37, 38, 39, 40, 41, 42, 43, 44, 45, 46, 47, 48]. The remaining information about a specific process under consideration can be provided by interfacing the corresponding tree-level matrix elements as well as the finite parts of the one-loop and two-loop amplitudes. The implemented event generator includes concepts that have been proven and tested at next-to-leading order to increase speed and efficiency of the numerical calculation, e.g. Monte Carlo summation over partonic subprocesses and Monte Carlo summation over external polarizations. The software allows for a simultaneous calculation of different parton distribution functions, different renormalization and factorization scales and different observables.

For the specific case of top-quark pair production the tree-level matrix elements are obtained from Ref. [49]. The four-point one-loop amplitudes have been recomputed independently, but can be found in Refs. [50, 51, 52]. The five-point one-loop amplitudes are taken from the code used in Refs. [53, 54]. The two-loop amplitudes are numerically given in form of a dense grid [55, 56]. Partial analytic results for the two-loop amplitudes can be found in Refs. [57, 58, 59, 60].

RESULTS

The differential results presented in Figure 1 and Figure 2 are calculated using the following setup. The pole mass of the top-quark is set to $m_t = 173.3$ GeV. The distributions have been calculated using the MSTW2008 parton distribution function (PDF) set [61], where PDF uncertainties are not displayed. Each order includes the PDF set of the corresponding order. The theoretical uncertainties are obtained by varying the renormalization scale μ_{R} and factorization scale μ_{F} independently around the central scale $\mu_{\mathrm{R}} = \mu_{\mathrm{F}} = m_t$. The additional restriction, $0.5 < \mu_{\mathrm{R}}/\mu_{\mathrm{F}} < 2$, is imposed [62]. All results have been cross checked with available results: Integrals over the distributions reproduce the total cross section of Refs. [1, 2, 3, 4] to better than permil level. The next-to-leading order results are cross checked with the Monte Carlo event generator MCFM [63, 64].

Figure 1 shows the $p_{\mathrm{T},t}$, $m_{t\bar{t}}$ and $y_{t\bar{t}}$ differential distributions for the absolute normalization as well as the corresponding next-to-leading order and next-to-next-to-leading order K-factors. It should be noticed that the widths of bins of the calculation is much smaller than the widths of the bins that are currently used by the ATLAS and CMS collaborations, which allows to use these results for a variety of phenomenological analyses.

Each of the three distributions shows a good perturbative convergence. This behaviour, which has already been known for the total inclusive cross section, can be observed for each histogram bin separately. The central value lies within the error band of the previous order. This suggests that the theoretical predictions are robust within the stated error bands, while keeping in mind that the uncertainty of the PDF set is not included yet.

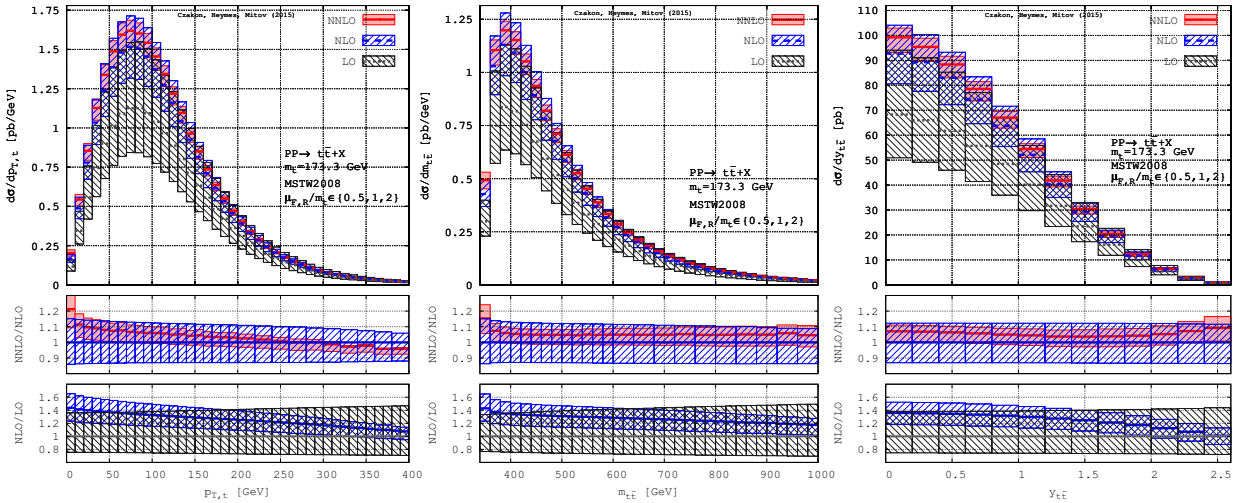

FIGURE 1. Top/antitop p_{T}-distribution (left), $m_{t\bar{t}}$-distribution (center) and $y_{t\bar{t}}$-distribution (right) in leading order (LO), next-to-leading order (NLO) and next-to-next-to-leading order (NNLO) QCD. Error bands are from scale variation [25].

A significant rise of the K-factors in the first bin of the $p_{\mathrm{T},t}$-distribution and to a lesser degree in the first bin of the $m_{t\bar{t}}$-distribution can be observed. However, this slight enhancement at low p_{T} and low $m_{t\bar{t}}$ is due to soft-gluon and Coulomb effects at the top-quark pair threshold, which are not captured within a fixed order calculation. Related work, in order to capture these effects to all orders can be found in Refs. [19, 20, 21, 22, 65, 66, 67, 68, 69]. A further investigation of these effects and matching resummed results to the fixed order prediction would be interesting.
The next-to-next-to-leading order K-factor shows a significant slope in the p_{T}-distribution, which, however, is within the next-to-leading error band. The $m_{t\bar{t}}$-distribution at next-to-next-to-leading order is remarkably stable with respect to the next-to-leading order prediction over the whole range of displayed values. It is therefore a well suited observable to look for new resonances beyond the Standard Model as suggested for example in Ref. [70]. The shape of the rapidity distribution of the top-quark pair at next-to-next-to-leading order changes slightly with respect to the next-to-leading order distribution, which is however not significant.
A first comparison of the p_{T}-distribution and the y_t-distribution of the top-quark with the CMS measurement in the lepton and jets channels from Ref. [15] is shown in Figure 2. Further comparisons with CMS data can be found in Ref. [71], while a comparison with the ATLAS measurements at $\sqrt{s} = 8$ TeV has been included in Ref. [72].
The distributions are normalized, such that integrating the displayed bins yields unity. Uncertainties due to scale variations for next-to-next-to-leading order distributions are shown exclusively. The lower panel displays the ratio of the Data, the leading order and the next-to-leading order distribution with respect to the next-to-next-to-leading order distribution. There is a slight mismatch between the normalization of the data and the prediction. The transverse momentum distribution of the data includes an additional bin, $400\mathrm{GeV} < p_{\mathrm{T}} < 500\mathrm{GeV}$, which contributes 4 permil to the normalization. In the rapidity distribution, the last bin of the theory prediction extends up to $|y_t| < 2.6$, while the last bin of the measurement extends only up to $|y_t| < 2.5$. This can be seen explicitly in Figure 2.
The first observation is that the tension between data and the next-to-leading order result for the p_{T}-distribution is resolved at next-to-next-to-leading order. In each bin the Standard Model prediction gets closer to the CMS data and an agreement within the displayed uncertainties can be observed. The normalized rapidity distribution of the top-quark is stable with respect to next-to-next-to-leading order corrections. Within the experimental uncertainty the data seems to be well described by the next-to-next-to-leading order prediction.

SUMMARY AND OUTLOOK

In this write-up, differential distributions for top-quark pair production at next-to-next-to-leading order QCD for the LHC at $\sqrt{s} = 8$ TeV have been presented. These results have been obtained using a complete independent implementation of the subtraction scheme Stripper and include all partonic channels, where no approximations have been

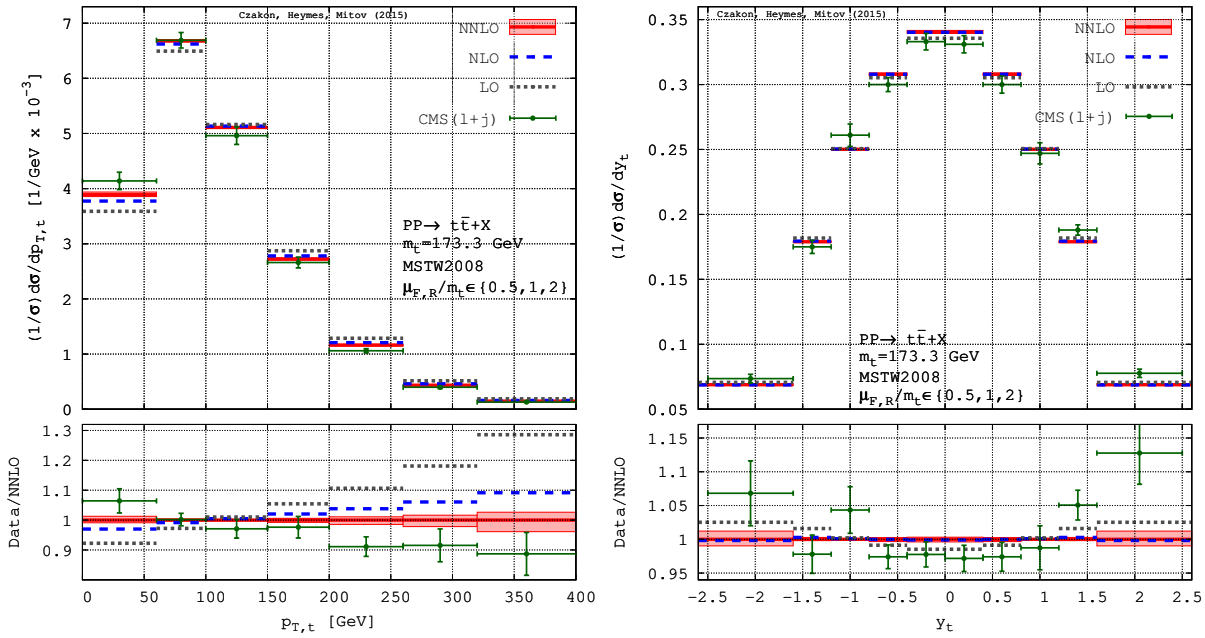

FIGURE 2. Normalised distribution for the p_{T} of the top/antitop-quark (left) and the rapdity y of the top/antitop-quark (right) in comparison with CMS measurements [15, 25]

made.

These results can be used for further phenomenological studies and tuning of Monte Carlo event generators in order to validate the estimated Standard Model background at the LHC. Moreover, they are valuable to constrain parton distribution functions using LHC data and to measure the strong coupling α_s. High precision Standard Model prediction allow to further explore limitations of the Standard Model and allow to constrain different scenarios beyond the Standard Model.

The presented results have been obtained for fixed scale settings $\mu_{\mathrm{F,R}} \in \{m_t, m_t/2, 2m_t\}$, which allowed for several cross checks of the final result with previous calculations, e.g. the total inclusive cross section. However, for differential predictions this setting may not be the most appropriate one. In the near future results will become available using several dynamical scales and will include different PDF sets and PDF error estimates.

The calculation will be extended to a center-of-mass energy of $\sqrt{s} = 13$ TeV. In this context, it would be interesting to extend the kinematic regime of the $m_{t\bar{t}}$- and p_{T}- distribution to higher values, since a significant number of top-quark pairs are produced in this so called *boosted* regime, $\sqrt{\hat{s}} \gg m_t$. In this regime large logarithm can be resummed to all order to improve a fixed order calculation [73, 74]. A first comparison of the resummed results matched to next-to-leading order QCD and the full next-to-next-to-leading order at result $\sqrt{s} = 8$ TeV has been presented in Ref. [75]. An investigation of how the resummed result could be matched to the full next-to-next-to-leading order prediction would be interesting.

Finally, a particle level comparison with data would be possible, once decays of the top-quark are included into the calculation at next-to-next-to-leading order. It should be noticed that next-to-next-to-leading order corrections for on-shell top-quark decays have already been presented in Refs. [76, 77].

ACKNOWLEDGMENTS

The work of D.H. is supported by the UK Science and Technology Facilities Council [grants ST/L002760/1 and ST/K004883/1].

REFERENCES

[1] P. Bärnreuther, M. Czakon and A. Mitov, Phys. Rev. Lett. **109**, 132001 (2012) [arXiv:1204.5201 [hep-ph]].
[2] M. Czakon and A. Mitov, JHEP **1212**, 054 (2012) [arXiv:1207.0236 [hep-ph]].
[3] M. Czakon and A. Mitov, JHEP **1301**, 080 (2013) [arXiv:1210.6832 [hep-ph]].
[4] M. Czakon, P. Fiedler and A. Mitov, Phys. Rev. Lett. **110**, no. 25, 252004 (2013) [arXiv:1303.6254 [hep-ph]].
[5] M. Cacciari, M. Czakon, M. Mangano, A. Mitov and P. Nason, Phys. Lett. B **710**, 612 (2014) [arXiv:1111.5869 [hep-ph]].
[6] M. Czakon and A. Mitov, Comput. Phys. Commun. **185**, 2930 (2014) [arXiv:1112.5675 [hep-ph]].
[7] S. Chatrchyan *et al.* [CMS Collaboration], JHEP **1211**, 067 (2012) [arXiv:1208.2671 [hep-ex]].
[8] S. Chatrchyan *et al.* [CMS Collaboration], JHEP **1402**, 024 (2014) [JHEP **1402**, 102 (2014)] [arXiv:1312.7582 [hep-ex], arXiv:1312.7582].
[9] G. Aad *et al.* [ATLAS Collaboration], Eur. Phys. J. C **74**, no. 10, 3109 (2014) [arXiv:1406.5375 [hep-ex]].
[10] V. Khachatryan *et al.* [CMS Collaboration], arXiv:1510.05302 [hep-ex].
[11] [ATLAS Collaboration] ATLAS-CONF-2015-049.
[12] S. Chatrchyan *et al.* [CMS Collaboration], Eur. Phys. J. C **73**, no. 3, 2339 (2013) [arXiv:1211.2220 [hep-ex]].
[13] G. Aad *et al.* [ATLAS Collaboration], Phys. Rev. D **90**, no. 7, 072004 (2014) [arXiv:1407.0371 [hep-ex]].
[14] G. Aad *et al.* [ATLAS Collaboration], JHEP **1506**, 100 (2015) [arXiv:1502.05923 [hep-ex]].
[15] V. Khachatryan *et al.* [CMS Collaboration], arXiv:1505.04480 [hep-ex].
[16] G. Aad *et al.* [ATLAS Collaboration], arXiv:1510.03818 [hep-ex].
[17] [CMS Collaboration] CMS-PAS-TOP-15-005.
[18] [CMS Collaboration] CMS-PAS-TOP-15-010.
[19] V. Ahrens, A. Ferroglia, M. Neubert, B. D. Pecjak and L. L. Yang, JHEP **1009**, 097 (2010) [arXiv:1003.5827 [hep-ph]].
[20] V. Ahrens, A. Ferroglia, M. Neubert, B. D. Pecjak and L. L. Yang, JHEP **1109**, 070 (2011) [arXiv:1103.0550 [hep-ph]].
[21] N. Kidonakis, Phys. Part. Nucl. **45**, no. 4, 714 (2014) [arXiv:1210.7813 [hep-ph]].
[22] N. Kidonakis, Phys. Rev. D **91**, no. 3, 031501 (2015) [arXiv:1411.2633 [hep-ph]].
[23] M. Guzzi, K. Lipka and S. O. Moch, JHEP **1501**, 082 (2015) [arXiv:1406.0386 [hep-ph]].
[24] A. Broggio, A. S. Papanastasiou and A. Signer, JHEP **1410**, 98 (2014) [arXiv:1407.2532 [hep-ph]].
[25] M. Czakon, D. Heymes and A. Mitov, arXiv:1511.00549 [hep-ph].
[26] S. Catani and M. H. Seymour, Nucl. Phys. B **485**, 291 (1997) [Nucl. Phys. B **510**, 503 (1998)] doi:10.1016/S0550-3213(96)00589-5 [hep-ph/9605323].
[27] S. Frixione, Z. Kunszt and A. Signer, Nucl. Phys. B **467**, 399 (1996) doi:10.1016/0550-3213(96)00110-1 [hep-ph/9512328].
[28] G. Abelof, A. Gehrmann-De Ridder and I. Majer, arXiv:1506.04037 [hep-ph].
[29] G. Abelof and A. Gehrmann-De Ridder, JHEP **1412**, 076 (2014) [arXiv:1409.3148 [hep-ph]].
[30] R. Bonciani, S. Catani, M. Grazzini, H. Sargsyan and A. Torre, arXiv:1508.03585 [hep-ph].
[31] M. Czakon, Phys. Lett. B **693**, 259 (2010) [arXiv:1005.0274 [hep-ph]].
[32] M. Czakon, Nucl. Phys. B **849** (2011) 250 [arXiv:1101.0642 [hep-ph]].
[33] M. Czakon, P. Fiedler and A. Mitov, Phys. Rev. Lett. **115**, no. 5, 052001 (2015) [arXiv:1411.3007 [hep-ph]].
[34] M. Czakon and D. Heymes, Nucl. Phys. B **890**, 152 (2014) [arXiv:1408.2500 [hep-ph]].
[35] S. Catani and M. Grazzini, Nucl. Phys. B **570** (2000) 287 [hep-ph/9908523].
[36] J. M. Campbell and E. W. N. Glover, Nucl. Phys. B **527**, 264 (1998) [hep-ph/9710255].
[37] S. Catani and M. Grazzini, Phys. Lett. B **446**, 143 (1999) [hep-ph/9810389].
[38] V. Del Duca, A. Frizzo and F. Maltoni, Nucl. Phys. B **568**, 211 (2000) [hep-ph/9909464].
[39] Z. Bern, L. J. Dixon, D. C. Dunbar and D. A. Kosower, Nucl. Phys. B **425**, 217 (1994) [hep-ph/9403226].
[40] Z. Bern, V. Del Duca and C. R. Schmidt, Phys. Lett. B **445**, 168 (1998) [hep-ph/9810409].
[41] D. A. Kosower, Nucl. Phys. B **552**, 319 (1999) [hep-ph/9901201].
[42] D. A. Kosower and P. Uwer, Nucl. Phys. B **563**, 477 (1999) [hep-ph/9903515].
[43] Z. Bern, V. Del Duca, W. B. Kilgore and C. R. Schmidt, Phys. Rev. D **60**, 116001 (1999) [hep-ph/9903516].
[44] G. Somogyi and Z. Trocsanyi, JHEP **0701**, 052 (2007) [hep-ph/0609043].
[45] S. Catani and M. Grazzini, Nucl. Phys. B **591**, 435 (2000) [hep-ph/0007142].
[46] S. Catani, S. Dittmaier and Z. Trocsanyi, Phys. Lett. B **500**, 149 (2001) [hep-ph/0011222].
[47] I. Bierenbaum, M. Czakon and A. Mitov, Nucl. Phys. B **856**, 228 (2012) [arXiv:1107.4384 [hep-ph]].

[48] A. Ferroglia, M. Neubert, B. D. Pecjak and L. L. Yang, JHEP **0911**, 062 (2009) [arXiv:0908.3676 [hep-ph]].
[49] M. Bury and A. van Hameren, Comput. Phys. Commun. **196** (2015) 592 [arXiv:1503.08612 [hep-ph]].
[50] J. G. Körner, Z. Merebashvili and M. Rogal, Phys. Rev. D **71**, 054028 (2005) [hep-ph/0412088].
[51] C. Anastasiou and S. M. Aybat, Phys. Rev. D **78**, 114006 (2008) [arXiv:0809.1355 [hep-ph]].
[52] B. Kniehl, Z. Merebashvili, J. G. Körner and M. Rogal, Phys. Rev. D **78**, 094013 (2008) [arXiv:0809.3980 [hep-ph]].
[53] S. Dittmaier, P. Uwer and S. Weinzierl, Phys. Rev. Lett. **98**, 262002 (2007) [hep-ph/0703120 [HEP-PH]].
[54] S. Dittmaier, P. Uwer and S. Weinzierl, Eur. Phys. J. C **59**, 625 (2009) [arXiv:0810.0452 [hep-ph]].
[55] M. Czakon, Phys. Lett. B **664** (2008) 307 [arXiv:0803.1400 [hep-ph]].
[56] P. Bärnreuther, M. Czakon and P. Fiedler, JHEP **1402**, 078 (2014) [arXiv:1312.6279 [hep-ph]].
[57] R. Bonciani, A. Ferroglia, T. Gehrmann, A. von Manteuffel and C. Studerus, JHEP **1312**, 038 (2013) [arXiv:1309.4450 [hep-ph]].
[58] R. Bonciani, A. Ferroglia, T. Gehrmann, A. von Manteuffel and C. Studerus, JHEP **1101**, 102 (2011) [arXiv:1011.6661 [hep-ph]].
[59] R. Bonciani, A. Ferroglia, T. Gehrmann and C. Studerus, JHEP **0908**, 067 (2009) [arXiv:0906.3671 [hep-ph]].
[60] R. Bonciani, A. Ferroglia, T. Gehrmann, D. Maitre and C. Studerus, JHEP **0807**, 129 (2008) [arXiv:0806.2301 [hep-ph]].
[61] A. D. Martin, W. J. Stirling, R. S. Thorne and G. Watt, Eur. Phys. J. C **63**, 189 (2009) [arXiv:0901.0002 [hep-ph]].
[62] M. Cacciari, S. Frixione, M. L. Mangano, P. Nason and G. Ridolfi, JHEP **0809**, 127 (2008) [arXiv:0804.2800 [hep-ph]].
[63] J. M. Campbell and R. K. Ellis, arXiv:1204.1513 [hep-ph].
[64] P. Nason, S. Dawson and R. K. Ellis, Nucl. Phys. B **303**, 607 (1988); Nucl. Phys. B **327**, 49 (1989) [Erratum-ibid. B **335**, 260 (1990)].
[65] N. Kidonakis and G. F. Sterman, Nucl. Phys. B **505**, 321 (1997) [hep-ph/9705234].
[66] E. Laenen, G. Oderda and G. F. Sterman, Phys. Lett. B **438**, 173 (1998) [hep-ph/9806467].
[67] N. Kidonakis, E. Laenen, S. Moch and R. Vogt, Phys. Rev. D **64**, 114001 (2001) [hep-ph/0105041].
[68] K. Hagiwara, Y. Sumino and H. Yokoya, Phys. Lett. B **666**, 71 (2008) [arXiv:0804.1014 [hep-ph]].
[69] Y. Kiyo, J. H. Kuhn, S. Moch, M. Steinhauser and P. Uwer, Eur. Phys. J. C **60**, 375 (2009) [arXiv:0812.0919 [hep-ph]].
[70] R. Frederix and F. Maltoni, JHEP **0901**, 047 (2009) doi:10.1088/1126-6708/2009/01/047 [arXiv:0712.2355 [hep-ph]].
[71] CMS Collaboration [CMS Collaboration], CMS-PAS-TOP-15-011.
[72] G. Aad *et al.* [ATLAS Collaboration], arXiv:1511.04716 [hep-ex].
[73] A. Ferroglia, B. D. Pecjak and L. L. Yang, Phys. Rev. D **86**, 034010 (2012) doi:10.1103/PhysRevD.86.034010 [arXiv:1205.3662 [hep-ph]].
[74] A. Ferroglia, S. Marzani, B. D. Pecjak and L. L. Yang, JHEP **1401**, 028 (2014) doi:10.1007/JHEP01(2014)028 [arXiv:1310.3836 [hep-ph], arXiv:1310.3836].
[75] A. Ferroglia, B. D. Pecjak, D. J. Scott and L. L. Yang, arXiv:1512.02535 [hep-ph].
[76] M. Brucherseifer, F. Caola and K. Melnikov, JHEP **1304**, 059 (2013) doi:10.1007/JHEP04(2013)059 [arXiv:1301.7133 [hep-ph]].
[77] J. Gao, C. S. Li and H. X. Zhu, Phys. Rev. Lett. **110**, no. 4, 042001 (2013) doi:10.1103/PhysRevLett.110.042001 [arXiv:1210.2808 [hep-ph]].

Proceedings of the LHCP2015 Conference, St. Petersburg, Russia, August 31 - September 5, 2015

Editors: V.T. Kim and D.E. Sosnov

Measurements of the top-quark mass in fixed schemes and with alternative methods using the ATLAS and CMS detectors at the LHC

TERESA BARILLARI

Max-Planck-Inst. für Physik Werner-Heisenberg-Institut – Föhringer Ring 6 D-80805 München, Germany

barilla@mppmu.mpg.de

On behalf of the ATLAS and CMS Collaboration

Abstract. Selected topics of the top-quark mass measurements in well-defined schemes are presented. The measurements have been performed using data recorded with the ATLAS and CMS detectors at the LHC at proton-proton centre-of-mass energies of 7 and 8 TeV. Precision theoretical QCD calculations for both inclusive top-antitop quark pair production and top-antitop quark pair production with an additional jet to extract the top quark mass in the pole-mass scheme have been used.

INTRODUCTION

The top quark is by far the heaviest known fermion and the heaviest known fundamental particle. It plays an important role in the Standard Model (SM). Precise measurements of the top-quark mass (m_t) provide a key input to consistency tests of the SM. The mass of the Higgs boson and the top quark are also important parameters in the determination of the vacuum stability [1, 2].

Nowadays, the most precise determinations of m_t have been achieved experimentally from kinematical reconstruction of the measured top-quark decay products, e.g. measuring the semi-leptonic decay channel of top-antitop quark pairs ($t\bar{t}$), where one top quark decays into a b quark, a charged lepton and its neutrino and the other top quark decays into a b quark and two u/d/c/s quarks, yielding a value of $m_t = 172.35 \pm 0.51$ GeV [3]. These m_t determinations, however, have not been linked so far in an unambiguous manner to a Lagrangian top-quark mass in a specific renormalization scheme as employed in perturbative calculations in quantum chromodynamics (QCD), electroweak fits, or any theoretical prediction in general [4, 5, 6]. The values of m_t extracted using these schemes are usually identified with the top-quark pole mass, m_t^{pole}. Present studies estimate differences between the two top-quark mass definitions, m_t and a theoretically well defined short-distance mass definition at a low scale (e.g. m_t^{pole}), of about 1 GeV.

In addition to direct m_t measurements as mentioned above, the mass dependence of the QCD prediction for the cross section ($\sigma_{t\bar{t}}$) can be used to determine m_t by comparing the measured to the predicted $\sigma_{t\bar{t}}$ [7, 8, 9, 10, 11, 12]. Although the sensitivity of $\sigma_{t\bar{t}}$ to m_t might not be strong enough to make this approach competitive in precision, it yields results affected by different sources of systematic uncertainties compared to the direct m_t measurements and allows for extractions of m_t in theoretically well-defined mass schemes. The values extracted using these methods are usually identified with the top-quark pole mass.

This distinction of the theoretical description of the measured parameter, e.g. either the parameter in the underlying Monte Carlo (MC) generator, m_t^{MC} (or simply m_t), the mass term in the top-quark propagator, m_t^{pole}, or the mass in a well defined low-scale short distance scheme [4, 13], is recently gaining in importance.

In the following, selected m_t^{pole} measurements performed by the ATLAS [14] and CMS [15] experiments at LHC [16] using data at proton-proton (pp) centre-of-mass energies of 7 and 8 TeV, are presented.

TOP-QUARK POLE MASS MEASUREMENTS

In contrast to the standard kinematical reconstruction of the measured top-quark decay product methods mentioned above, cross-section-like observables can be used to compare QCD predictions depending on m_t^{pole}, with unfolded data. The unfolding removes detector effects, and, in addition these measurements benefit from the larger independence from the mass definition in the used MC generators. For the total cross-section measurements, however, a 5% uncertainty translates into a 1% uncertainty in the top-quark mass [17] and the difference from going from next-to-leading order (NLO) to next-to-next-to-leading order (NNLO) predictions is even larger ($\sim$ 10%). Experimentally the challenges lie in the unfolding of the data and in the absolute normalization. Furthermore measurements of m_t^{pole} involving new shape-like observables as proposed in [18] can help reduce both theoretical and experimental uncertainties.

Measurements of Top-Quark Pole Mass in $t\bar{t}$ Di-Lepton Events

The measurements of the $t\bar{t}$ production cross-section, $\sigma_{t\bar{t}}$, together with the NNLO prediction in QCD including the resummation of next-to-next-to-leading-logarithmic (NNLL) soft gluon terms [19], are used to determine the top-quark pole mass. Most of such measurements are performed in the electron-muon (e - μ) channel, where each W boson from the top quark decays into a lepton and a neutrino. Events are required to contain an oppositely charged e - μ pair. The restriction to the di-lepton channel allows obtaining a particular clean $t\bar{t}$ event sample. The value of m_t^{pole} is determined from the $\sigma_{t\bar{t}}$ measurements in pp collisions at centre-of-mass energies of $\sqrt{s}$ = 7 TeV and $\sqrt{s}$ = 8 TeV with the CMS and ATLAS detector at LHC. Both experiments assume a top-quark mass of m_t^{MC} = 172.5 GeV in simulations to extract the reconstruction efficiency.

CMS Top-Quark Pole Mass Measurements

Compared to previous m_t^{pole} measurements at 7 TeV [20] and at 8 TeV [21] the latest CMS results [22] include the full CMS data samples with integrated luminosities of 5.0 fb^{-1} (7 TeV) and 19.7 fb^{-1} (8 TeV). The value of m_t^{pole} at NNLO+NNLL is extracted by confronting the measured cross section $\sigma_{t\bar{t}}$ at 7 and 8 TeV with predictions employing different parton density function (PDF) sets: NNPDF3.0 [23], CT14 [24], and MMHT2014 [25]. The obtained m_t^{pole} values are listed in Table 1. The contributions from uncertainties on the CT14 PDF set are scaled to 68% confidence level.

A weighted average is calculated, taking into account all systematic uncertainty correlations between the measured cross sections at 7 and 8 TeV and assuming 100% correlated uncertainties for the theory predictions at the two energies. The combined m_t^{pole} results are listed in Table 1 and are in good agreement with each other and the world average value [26]. Figure 1 shows the combined likelihood of the measured and predicted dependence of the $t\bar{t}$

TABLE 1. Top-quark pole mass measured by CMS at NNLO+NNLL extracted by confronting the measured $t\bar{t}$ production cross section at 7 and 8 TeV [20, 21, 22]. The obtained combined m_t^{pole} results are also listed ($\sqrt{s}$ = 7 + $\sqrt{s}$ = 8 TeV).

PDF	m_t^{pole} ($\sqrt{s}$ = 7 TeV) [GeV]	m_t^{pole} ($\sqrt{s}$ = 8 TeV) [GeV]	m_t^{pole} ($\sqrt{s}$ = 7 + $\sqrt{s}$ = 8 TeV) [GeV]
NNPDF3.0 [23]	$173.4 \pm^{2.0}_{2.0}$	$173.9 \pm^{1.9}_{2.0}$	$173.6 \pm^{+1.7}_{1.8}$
MMHT2014 [25]	$173.7 \pm^{2.0}_{2.1}$	$174.2 \pm^{1.9}_{2.2}$	$173.9 \pm^{+1.8}_{1.9}$
CT14 [24]	$173.9 \pm^{2.3}_{2.4}$	$174.3 \pm^{2.2}_{2.4}$	$174.1 \pm^{+2.1}_{2.2}$

production cross section on m_t^{pole} for 7 (left plot) and 8 TeV (right plot).

In another measurement at $\sqrt{s}$ = 8 TeV CMS [27] uses a folding technique to map fixed order QCD calculations depending on m_t^{pole} as implemented in the Monte Carlo for Femtobarn calculation MCFM [28], to predict the shape in m_{lb}^{min}. The top quark decay chain considered in this analysis is $t \to Wb$ followed by $W \to l\nu$. Neglecting both leptons and b-quark masses, at leading order the quantity m_{lb} is directly related to m_t and the mass of the W boson, m_W, as follows: $m_{lb}^2 = \frac{m_t^2 - m_w^2}{2}(1 - \cos\theta_{lb})$. Here, θ_{lb} is the opening angle between the lepton and the b quark in the W-boson rest frame. The distribution of m_{lb} has an end point at $max(m_{lb}) \sim \sqrt{m_t^2 - m_{W'}^2}$, i.e. around 153 GeV for a top-quark mass of 173 GeV. In the analysis, m_{lb} is reconstructed by choosing the permutation that minimizes the value of m_{lb} in each event and only the b-jet candidate with the highest transverse momentum $p_\perp$ is considered together with both

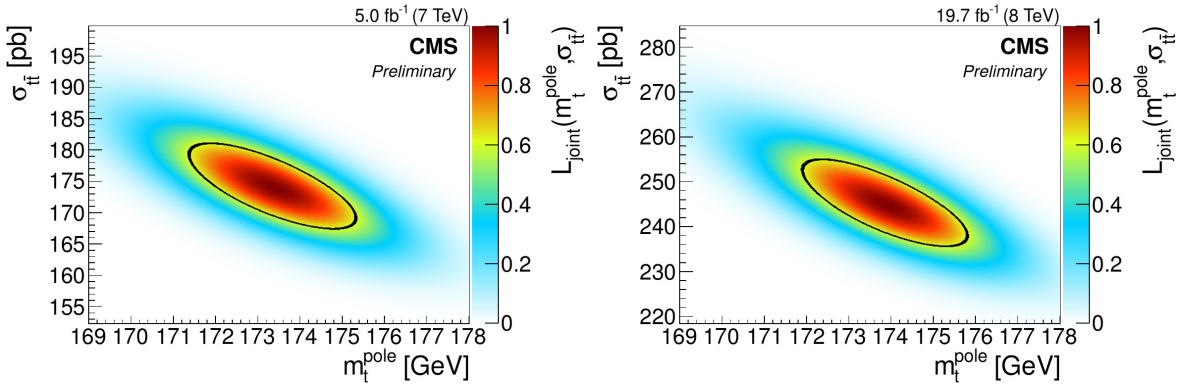

FIGURE 1. Combined likelihood of the measured and predicted dependence of the $t\bar{t}$ production cross section on the top-quark mass for 7 (left plot) and 8 TeV (right plot) in CMS [22]. The total one standard deviation uncertainty is indicated by a black contour.

leptons (e and μ). Only one top quark in each event is used. In this particular definition, the combination yielding the smallest m_{lb} in the event is kept, and referred to as m_{lb}^{min}, shown in Figure 2. The response matrices in m_{lb}^{min} are obtained from fully simulated events obtained using the matrix element generator MADGRAPH 5.1.5.11 [29] with MADSPIN [30] for the decay of heavy resonances, PYTHIA 6.426 [31] for parton showering; the MC events have been passed through a full simulation of the CMS detector based on GEANT [32] (combination called MADGRAPH + PYTHIA + GEANT). By using the information on the rate of events alone a value of $m_t = 171.4 \pm 0.4_{stat} \pm 1.0_{syst}$ GeV is measured. Combining the results obtained using rate+m_{lb}^{min} shape fits one is able to extract $m_t = 173.1^{1.9}_{1.8}$ GeV. These results can be compared to the mass extraction from the same dataset via the total cross-section calculated at NNLO.

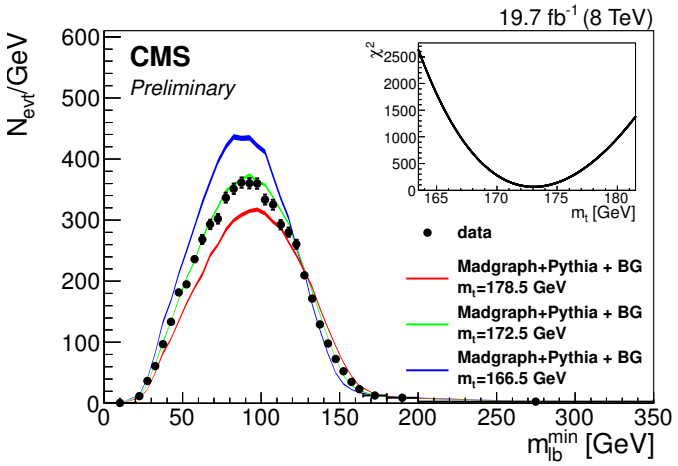

FIGURE 2. Normalized event yields obtained by CMS [27], for $t\bar{t}$ production at the LHC at $\sqrt{s}$ = 8 TeV, presented as a function of m_{lb}^{min}. The bullets are the experimental data points and the error bars indicate their statistical uncertainties. The inset shows the χ^2 distribution as a function of m_t as determined from the fit of the simulation to the shape of the data.

ATLAS Top-Quark Pole Mass Measurements

ATLAS also extracts m_t^{pole} at NNLO+NNLL by confronting the measured production cross section $\sigma_{t\bar{t}}$ at 7 and 8 TeV with predictions employing different PDF sets [33]: CT10 NLO [34], MSTW 2008 68% CL NLO [35], and NNPDF 2.3 NLO [36]. The extraction of m_t^{pole} is performed by maximizing a Bayesian likehood function separately

for each PDF set and centre-of-mass energy to give m_t^{pole} values shown in Table 2. Finally m_t^{pole} is extracted from

TABLE 2. Measurements performed by ATLAS of m_t^{pole} at NNLO+NNLL extracted by confronting the measured production cross section $\sigma_{t\bar{t}}$ with predictions employing different PDF sets.

PDF	ATLAS m_t^{pole} $\sqrt{s}$ = 7 TeV [GeV]	ATLAS m_t^{pole} $\sqrt{s}$ = 8 TeV [GeV]
C10 NNLOCT10 NLO [34]	171.4 ± 2.6	174.1 ± 2.6
MSTW 68 % NNLO [35]	171.2 ± 2.4	174.0 ± 2.5
NNPDF2.3 5f FFN [36]	$171.3^{+2.2}_{-2.3}$	174.2 ± 2.4

the combined $\sqrt{s}$ = 7 and $\sqrt{s}$ = 8 TeV dataset. The resulting value using the envelope of all three considered PDF sets is $m_t^{pole} = 172.9^{+2.5}_{-2.6}$ GeV. The results are shown in Figure 3, together with previous determinations using similar techniques from D0 [37] and CMS [38]. All extracted values are consistent with the average of measurements from

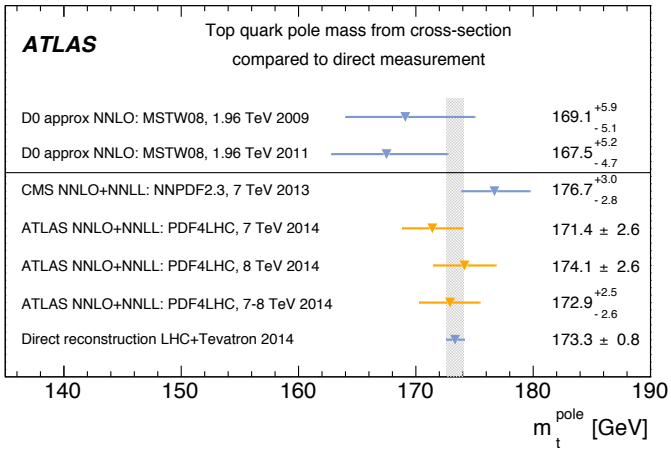

FIGURE 3. Comparison of m_t^{pole} values determined from ATLAS and previous measurements [33].

kinematic reconstruction of $t\bar{t}$ events of 173.34 ± 0.76 GeV [26], showing good compatibility of top-quark masses extracted using very different techniques and assumptions.

Measurements of Top-Quark Pole Mass in $t\bar{t}$ + 1-Jet Events

The normalized differential cross section for $t\bar{t}$ production in association with at least 1-jet is studied as a function of the inverse of the invariant mass of the $t\bar{t}$ + 1-jet system. This distribution is used by the ATLAS experiment [39] for a precise determination of m_t^{pole}. A new observable suggested in [18] is used in this measurement: $\mathcal{R}(m_t^{pole}, \rho_s) = \frac{1}{\sigma_{t\bar{t}+1\,jet}} \frac{d\sigma_{t\bar{t}+1\,jet}}{d\rho_s}(m_t^{pole}, \rho_s)$. The differential is taken in $\rho_s = 2m_0/\sqrt{s_{t\bar{t}j}}$, that is the ratio of an arbitrary mass scale in the vicinity of m_t, here set to m_0 = 170 GeV, over the invariant $t\bar{t}$ + 1 jet mass. $t\bar{t}$ events are selected at $\sqrt{s}$ = 7 TeV in a similar way as done for the the lepton+jets analysis [40], and an additional central jet with $p_\perp > 50$ GeV is added. An SVD unfolding [41] with a response matrix from POWHEG+PYTHIA+GEANT4 [31, 32, 42] maps the measured ρ_s to parton level. The unfolded distribution of $\mathcal{R}(m_t^{pole}, \rho_s)$ is shown in Figure 4 (left). The measurement of m_t^{pole} = 173.7 $\pm 1.5_{stat} \pm 1.4_{syst}$ GeV is then obtained in a χ^2-fit to $0.25 < \rho_s < 1$ with $\rho_s > 0.675$ being the most sensitive bin, as shown in Figure 4 (right).

CONCLUSIONS

Measurements of m_t^{pole} using alternative methods have been performed by both the ATLAS and CMS experiments using data collected at $\sqrt{s}$ = 7 and 8 TeV at LHC. The latest CMS [22] results obtained using di-lepton $t\bar{t}$ events at 7 and the 8 TeV give a $m_t^{pole} = 173.6 \pm^{+1.7}_{1.8}$ GeV. The normalized differential cross section for $t\bar{t}$ production in

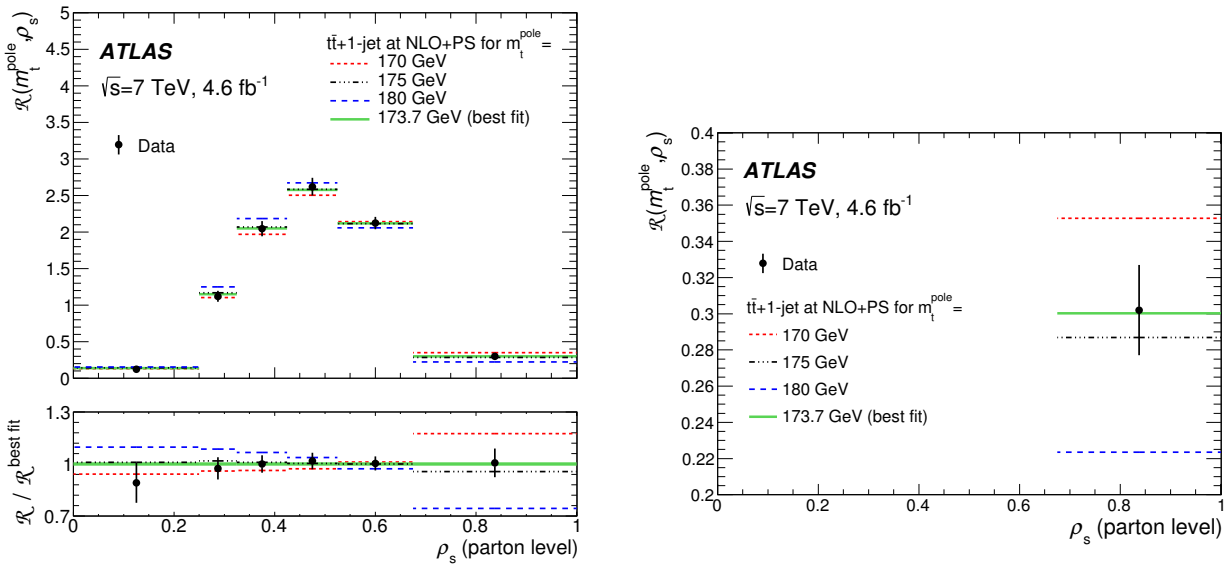

FIGURE 4. Unfolded $\mathcal{R}(m_t^{pole}, \rho_s)$ distribution as measured by ATLAS [39] (left). The predictions of the $t\bar{t}$ + 1-jet calculation at NLO+PS using three different masses (m_t^{pole} = 170, 175 and 180 GeV) are shown with the result of the best fit to the data, m_t^{pole} = 173.7 ± 1.5 (stat.) GeV. The value of the most sensitive interval of the $\mathcal{R}$-distribution $\rho_s > 0.65$ [39] (right). The black point corresponds to the data. The shaded area indicates the statistical uncertainty of this bin.

association with at least 1-jet studied by the ATLAS experiment [39] at 7 TeV give a measurement of m_t^{pole} = 173.7 $\pm 1.5_{stat} \pm 1.4_{syst}$ GeV. All the extracted values of m_t^{pole} are consistent with m_t measurements obtained using standard kinematic reconstruction of $t\bar{t}$ events.

ACKNOWLEDGMENTS

I would like to thank the ATLAS and CMS Collaborations for giving me the opportunity to give this talk at this conference and the top-quark groups conveners of both experiments for providing me the material presented here.

REFERENCES

[1] G. Degrassi *et al.*, JHEP **08**, p. 098 (2012), arXiv:1205.6497 [hep-ph] .
[2] M. Baak *et al.* (Gfitter Group), Eur. Phys. J. **C74**, p. 3046 (2014), arXiv:1407.3792 [hep-ph] .
[3] C. Collaboration, (2015), arXiv:1509.04044 [hep-ex] .
[4] S. Moch *et al.*, "High precision fundamental constants at the TeV scale," Tech. Rep. arXiv:1405.4781. MITP-14-036 (2014).
[5] A. Buckley *et al.*, Phys. Rept. **504**, 145–233 (2011), arXiv:1101.2599 [hep-ph] .
[6] A. H. Hoang, "The Top Mass: Interpretation and Theoretical Uncertainties," (2014) arXiv:1412.3649 [hep-ph] .
[7] S. Alekhin, A. Djouadi, and S. Moch, Phys. Lett. **B716**, 214–219 (2012), arXiv:1207.0980 [hep-ph] .
[8] V. Ahrens, A. Ferroglia, M. Neubert, B. D. Pecjak, and L. L. Yang, Phys. Lett. **B703**, 135–141 (2011), arXiv:1105.5824 [hep-ph] .
[9] U. Langenfeld, S. Moch, and P. Uwer, Phys. Rev. **D80**, p. 054009 (2009), arXiv:0906.5273 [hep-ph] .
[10] D0 Collaboration, V. M. Abazov *et al.*, Phys. Lett. **B703**, 422–427 (2011), arXiv:1104.2887 [hep-ex] .
[11] M. Beneke, P. Falgari, S. Klein, and C. Schwinn, Nucl. Phys. **B855**, 695–741 (2012), arXiv:1109.1536 [hep-ph] .
[12] M. Beneke *et al.*, JHEP **07**, p. 194 (2012), arXiv:1206.2454 [hep-ph] .

[13] A. H. Hoang and I. W. Stewart, Nucl. Phys. Proc. Suppl. **185**, 220–226 (2008), arXiv:0808.0222 [hep-ph] .
[14] ATLAS Collaboration, JINST **3**, p. S08003 (2008).
[15] CMS Collaboration, JINST **3**, p. S08004 (2008).
[16] L. Evans and P. Bryant, JINST **3**, p. S08001 (2008).
[17] S. Alekhin, J. Blumlein, and S. Moch, Phys. Rev. **D89**, p. 054028 (2014), arXiv:1310.3059 [hep-ph] .
[18] S. Alioli *et al.*, Eur. Phys. J. **C73**, p. 2438 (2013), arXiv:1303.6415 [hep-ph] .
[19] M. Czakon and A. Mitov, Comput. Phys. Commun. **185**, p. 2930 (2014), arXiv:1112.5675 [hep-ph] .
[20] CMS Collaboration, JHEP **11**, p. 067 (2012), arXiv:1208.2671 [hep-ex] .
[21] CMS Collaboration, JHEP **02**, p. 024 (2014), [Erratum: JHEP 02, 102 (2014)], arXiv:1312.7582 [hep-ex] .
[22] CMS Collaboration, "Measurement of the ttbar production cross section in the emu channel in pp collisions at 7 and 8 TeV," Tech. Rep. CMS-PAS-TOP-13-004 (CERN, Geneva, 2015).
[23] R. D. Ball *et al.* (NNPDF), JHEP **04**, p. 040 (2015), arXiv:1410.8849 [hep-ph] .
[24] S. Dulat *et al.*, (2015), arXiv:1506.07443 [hep-ph] .
[25] L. A. Harland-Lang, A. D. Martin, P. Motylinski, and R. S. Thorne, Eur. Phys. J. **C75**, p. 204 (2015), arXiv:1412.3989 [hep-ph] .
[26] ATLAS, CDF, CMS, D0 Collaboration, (2014), arXiv:1403.4427 [hep-ex], ATLAS-CONF-2014-008, CDF-NOTE-11071, CMS-PAS-TOP-13-014, D0-NOTE-6416, FERMILAB-TM-2582-E .
[27] CMS Collaboration, "Determination of the top-quark mass from the m(lb) distribution in dileptonic ttbar events at sqrt(s) = 8 TeV," Tech. Rep. CMS-PAS-TOP-14-014 (CERN, Geneva, 2014).
[28] J. M. Campbell and R. K. Ellis, Nucl. Phys. Proc. Suppl. **205-206**, 10–15 (2010), arXiv:1007.3492 [hep-ph] .
[29] J. Alwall, M. Herquet, F. Maltoni, O. Mattelaer, and T. Stelzer, JHEP **06**, p. 128 (2011), arXiv:1106.0522 [hep-ph] .
[30] P. Artoisenet, R. Frederix, O. Mattelaer, and R. Rietkerk, JHEP **03**, p. 015 (2013), arXiv:1212.3460 [hep-ph] .
[31] T. Sjostrand, S. Mrenna, and P. Z. Skands, JHEP **05**, p. 026 (2006), arXiv:hep-ph/0603175 [hep-ph] .
[32] S. Agostinelli *et al.* (GEANT4), Nucl. Instrum. Meth. **A506**, 250–303 (2003).
[33] ATLAS Collaboration, Eur. Phys. J. **C74**, p. 3109 (2014), arXiv:1406.5375 [hep-ex] .
[34] H.-L. Lai *et al.*, Phys. Rev. **D82**, p. 074024 (2010), arXiv:1007.2241 [hep-ph] .
[35] A. D. Martin, W. J. Stirling, R. S. Thorne, and G. Watt, Eur. Phys. J. **C63**, 189–285 (2009), arXiv:0901.0002 [hep-ph] .
[36] R. D. Ball *et al.*, Nucl. Phys. **B867**, 244–289 (2013), arXiv:1207.1303 [hep-ph] .
[37] D0 Collaboration, V. M. Abazov *et al.*, Phys. Rev. **D80**, p. 071102 (2009), arXiv:0903.5525 [hep-ex] .
[38] CMS Collaboration, Phys. Lett. **B728**, 496–517 (2014), [Erratum: Phys. Lett.B728, 526-528 (2014)], arXiv:1307.1907 [hep-ex] .
[39] ATLAS Collaboration, JHEP **10**, p. 121 (2015), arXiv:1507.01769 [hep-ex] .
[40] ATLAS Collaboration, Eur. Phys. J. **C75**, p. 330 (2015), arXiv:1503.05427 [hep-ex] .
[41] A. Hocker and V. Kartvelishvili, Nucl. Instrum. Meth. **A372**, 469–481 (1996), arXiv:hep-ph/9509307 [hep-ph] .
[42] S. Alioli, P. Nason, C. Oleari, and E. Re, JHEP **06**, p. 043 (2010), arXiv:1002.2581 [hep-ph] .

Proceedings of the LHCP2015 Conference, St. Petersburg, Russia, August 31 - September 5, 2015

Editors: V.T. Kim and D.E. Sosnov

Selected topics from the single top *t*-channel: cross section and other properties

BENEDIKT MAIER

Karlsruhe Institute of Technology (KIT) – D-76131 Karlsruhe, Germany

benedikt.maier@kit.edu

On behalf of the ATLAS and CMS Collaborations

Abstract. Measurements of the cross section and of the interactions happening at the tWb vertext are performed in the single top *t*-channel at center-of-mass energies of $\sqrt{s} = 7$ and 8 TeV. Results of both ATLAS and CMS collaborations are presented. No indications for new physics and no deviations from the Standard Model predictions within the experimental and theoretical uncertainties are found.

INTRODUCTION

The single top *t*-channel has the largest cross section of the three modes the electroweak production of a top quark at hadron colliders typically is devided into.[1] It therefore makes it an interesting place to look for potential new structures in the tWb coupling and to measure key parameters of the Standard Model (SM) such as the CKM matrix element V_{tb} that, in contrast to top quark pair production which is mediated by the strong interaction, appears already in the production. The leading order Feynman diagram of Figure 1 moreover suggests that the rates for the production of a top quark (t) are different from the anti-top ($\bar{t}$) quark in proton-proton collisions, because the incoming light quark is more likely to be a quark than its anti-partner. In turn this means the *t*-channel can also be used to constrain parton distribution functions (PDFs), which each predict a different $R = \sigma_t/\sigma_{\bar{t}}$ according to the respective energy and momenta distributions the partons are carrying.

CHANNEL TOPOLOGY AND ANALYSIS STRATEGY

Single top *t*-channel events have a distinct topology explained in the following: most characteristic is the upper outgoing quark line in Figure 1, representing a light quark which recoils against the exchanged virtual W boson. Upon hadronization it results in light jet with substantial transverse momentum, which tends to go in a forward direction. In a typical analysis the resonant top quark is required to decay leptonically, rejecting multi-jet background processes for which it is difficult to fake a prompt lepton. The sign of the lepton will also be used for distinguishing between t and $\bar{t}$ production. The top decay also features a b quark giving rise to a central b jet. The initial b quark is implied to stem from a gluon splitting. The $\bar{b}$ quark and its corresponding b jet however lie out of the tracker acceptance most of the time and thus cannot be tagged. Depending on whether one chooses the 5- or 4-flavor-scheme (5F, 4F) to describe the proton (in the latter the b quark is not considered a massless parton, but must be produced in a gluon splitting), the leading order formulation in terms of Feynman diagrams and calculus is either a $2 \to 2$ or $2 \to 3$ process. This has deep implications for the predictions and the modelling of the *t*-channel: for an all-orders-expansion the two schemes must give exactly the same results; in practice simulations at next-to-leading order are employed, and this circumstance leads to different predictions for the 4F and 5F. These can then be compared to experimental

[1] The separation into *t*-, tW- and *s*-channel makes most sense at leading order in the strong coupling constant α_S. At next-to-next-to-leading order at the latest, the definitions are not unambiguous anymore, and *t*- and *s*-channels start to interfere.

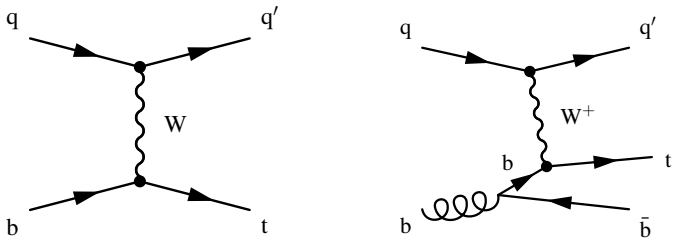

FIGURE 1. Leading order Feynman diagram of the *t*-channel in the 5F (left) and the 4F (right).

data, and conclusions can tried to be drawn on which model is the better. A detailed theoretical introduction into this subject is provided in [1].

The topology described above lends itself to a so called "2 jets 1 tag" selection (2j1t), which is widely employed in single top measurements and also consistently applied in every analysis presented here. Besides an isolated, hard lepton one expects one jet identified as b jet and a light, forward jet. In this signal enriched phase space it is typically the disciminator of a Neural Network trained with variables separating between single top production and the main background processes ($t\bar{t}$, W + jets and multi-jet production) or the pseudorapidity of the untagged jet, $|\eta_{j'}|$, that is used to extract the signal. The correct modelling of backgrounds is often verified in 2j0t or 3j2t control regions which are enriched in W + jets and $t\bar{t}$ events, respectively. This guarantees that all analysis ingredients are validated in phase spaces which are very close yet entirely orthogonal to the signal region.

CROSS SECTIONS

Inclusive

The CMS cross section measurement at $\sqrt{s} = 8\,\text{TeV}$ [2] is designed as a template analysis in $|\eta_{j'}|$, the pseudorapidity of the light recoil jet. It selects events with exactly one muon (electron) with $p_\text{T} > 26\,\text{GeV}$ (30 GeV) and $|\eta| < 2.1$ (2.5). Events with additional lepton candidates with looser selection criteria are rejected. For the muon channel a cut on the transverse mass of the reconstructed W boson $m_\text{T} > 50\,\text{GeV}$ is imposed[2]. In the electron channel it is a cut on the missing transverse energey of $E_\text{T}^\text{miss} > 45\,\text{GeV}$ that helps reject the QCD multi-jet background. By means of a range for the reconstructed top quark mass, which is $130 < m_{\ell\nu\text{b}} < 220\,\text{GeV}$, a signal (inside) and sideband (outside) region is defined.

The analysis exploits a 3j2t control region to determine the $t\bar{t}$ contribution in a semi-data driven way by looking at the $|\eta|$ templates of the untagged jet. Contributions for all other SM processes except for $t\bar{t}$ are subtracted from the data template, and bin-by-bin correction factors are derived by dividing the observed yields by the $t\bar{t}$ prediction as taken from simulation. This set of correction factors is then applied to the $t\bar{t}$ template in the 2j1t region, both in the signal and sideband regions. Since events in the 2j0t sample are predominantly stemming by W + jets production and hence these events have jets mostly coming from light quarks, this region is only used to perform a general validation of W + jets shapes and it is instead preferred to derive bin-by-bin correction factors for this background from the sidebands in 2j1t region. Predicted yields from all other processes are subtracted from the data $|\eta_{j'}|$ template and scale factors with respect to the W + jets simulation are obtained. The simulation is also used to derive additional corrections by extrapolating from the sideband into the signal region. QCD contributions are derived in a purely data driven manner from a region with inverted criteria on lepton isolation, but turn out to be very small.

The templates in the 2j1t region are simultaneously fit to data in $|\eta_{j'}|$ in both the electron and muon channel. The (semi-)data driven background estimations explained above come with uncertainties that are reflected by nuisance parameters in the maximum-likelihood fit; the signal normalization is left free to float. The left distribution of Figure 2 shows the post-fit distribution in the muon channel. A very good agreement between data and predictions is observed. The resulting cross section is $\sigma = 83.6 \pm 2.3\,(\text{stat.}) \pm 7.4\,(\text{syst.})\,\text{pb}$. The dominating systematics are related to the modelling of the signal process and the jet energy scale. Separating the events by the lepton charge and fitting the top and anti-top templates independently gives $\sigma_\text{t} = 53.8 \pm 1.5\,(\text{stat.}) \pm 4.4\,(\text{syst.})$ and $\sigma_{\bar{\text{t}}} = 27.6 \pm 1.3\,(\text{stat.}) \pm 3.7\,(\text{syst.})$.

[2]The definition for the transverse mass is $m_\text{T} = \sqrt{(p_\text{T}^\mu + E_\text{T}^\text{miss})^2 - (p_x^\mu + p_x^\text{miss})^2 - (p_y^\mu + p_y^\text{miss})^2}$. It relies on the missing transverse energy components to balance the sum of all observed momenta.

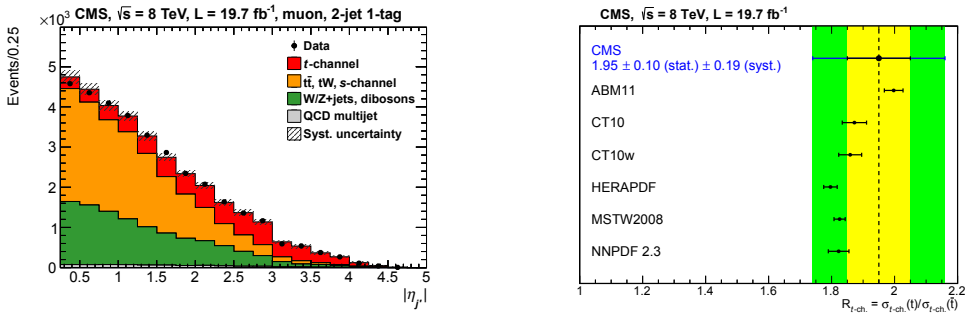

FIGURE 2. 2j1t distribution of the pseudorapidity of the untagged jet (left); R value predictions for different PDFs, which are all in agreement with the measured value within the uncertainties. Taken from the CMS cross section measurement at $\sqrt{s} = 8$ TeV [2].

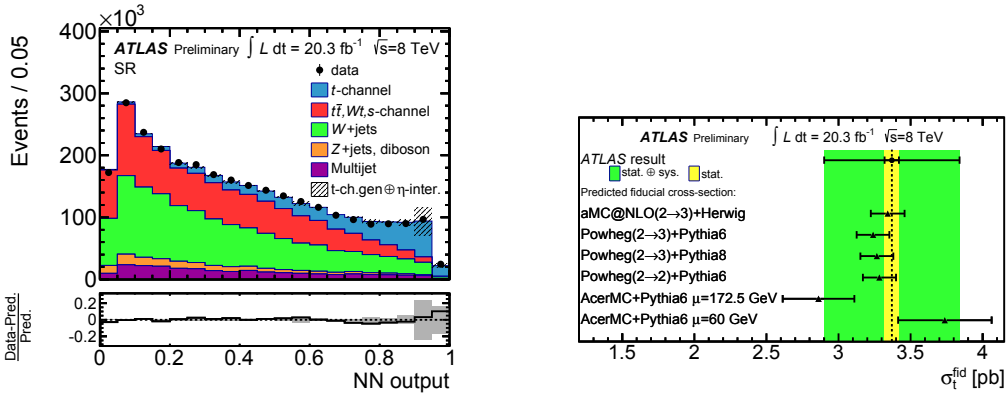

FIGURE 3. Results from the ATLAS fiducial cross section measurement at $\sqrt{s} = 8$ TeV [3]: post-fit NN output distribution in the 2j1t region (left). Fiducial cuts have been imposed on the simulations. The right figure compares the measured fiducial cross section with the predictions of various generation setups, disfavoring only the matched $2 \to 2/2 \to 3$ calculations.

Their ratio is $R = \sigma_t/\sigma_{\bar{t}} = 1.95 \pm 0.10\,(\text{stat.}) \pm 0.19\,(\text{syst.})$. This pseudo-observable is sensitive to which PDF has been used in the calculation of the hard interaction. The right figure of Figure 2 contrasts the measurement with different PDFs. The data does not really disfavor one of the sets within the uncertainties, but most of them predict a smaller R value than the one observed.

Fiducial

Compared to fully inclusive results, fiducial cross sections have the advantage that their dependence on the event generation (knobs to turn are e.g. matrix element generators, scale choices, hadronization models and PDFs) is reduced. Therefore differences related to the modelling are reduced to residual differences within the fiducial volume entirely covered by the experimental acceptance. Uncertainties stemming from the extrapolation from a visible into the inclusive phase space do not apply to such a measurement; moreover it is easier to re-interpret the results once better MC generators are available at some later point. Practically this is achieved my mimicking the selection imposed on reconstructed objects on behalf of cuts on stable particles at generator level. Consequently the following cuts are applied, defining a 2j1t signal region: exactly one lepton (muon or electron) with $p_T > 25\,\text{GeV}$ and $|\eta| < 2.5$. Jets are reconstructed within $|\eta| < 4.5$ and must have $p_T > 30\,\text{GeV}$ (or even $p_T > 35\,\text{GeV}$ if $2.75 < |\eta| < 3.5$). Exactly two jets need to be present, one of which must be identified as a b jet, either by deploying a multivariate algorithm for identifying secondary vertices on reconstruction level or by matching stable B hadrons to generated jets. The lepton must have a distance in the ϕ-η-plane of $\Delta R = \sqrt{\Delta\phi^2 + \Delta\eta^2} > 0.4$ to any jet. QCD multi-jet events are rejected by requiring $E_T^{\text{miss}} > 30\,\text{GeV}$ and $m_T > 50\,\text{GeV}$.

A Neural Network is trained with 14 variables, the three most relevant being the pseudorapidity of the untagged

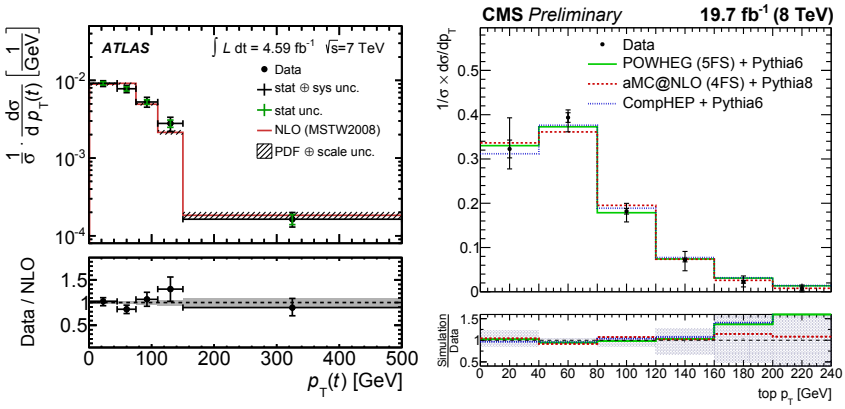

FIGURE 4. Normalized distributions of the top quark p_{T} have been measured by ATLAS (left) at $\sqrt{s} = 7$ [4] and by CMS (right) at 8 TeV [5].

jet, the reconstructed top quark mass and the invariant mass of the jet pair. The shape of the discriminator is validated in a $\mathrm{t\bar{t}}$ enriched 2j2t region and a 2j1t region with relaxed b tagging requirement, which makes it being dominated by W + jets events. Except for the QCD multi-jet production, which is estimated in a data driven technique, shapes of all backgrounds are taken from simulation, and the templates are normalized to the most precise available (N)NLO theory predictions. In Figure 3 a good agreement between data and simulation is found after a maximum-likelihood fit has been performed in the Neural Network discriminator. The fit results translate into a measured fiducial cross section $\sigma_{\mathrm{fid.}} = 3.37 \pm 0.05\,(\mathrm{stat.}) \pm 0.47\,(\mathrm{syst.}) \pm 0.09\,(\mathrm{lumi.})$. Figure 3 also shows a comparison of the result with predictions of various event generation setups, owing to the fact that, as mentioned in the introduction, the t-channel is a good place to constrain modelling aspects in the Monte-Carlo simulation. Except for the AcerMC setup, which is a calculation based on matching 4F and 5F events at leading order in α_{S} based of the p_{T} of the additional b quark, all setups give predictions that are well compatible with data. The inclusive cross section can easily be obtained – at the cost of larger uncertainties due to the extrapolation – by dividing the fiducial cross section by the selection effiency of the fiducial selection ($\sigma = (1/\epsilon_{\mathrm{fid}}) \cdot \sigma_{\mathrm{fid.}}$) and turns out to be $\sigma = 82.6 \pm 1.2\,(\mathrm{stat.}) \pm 11.4\,(\mathrm{syst.}) \pm 3.1\,(\mathrm{PDF}) + 2.3\,(\mathrm{lumi.})$. This information can be used to measure the CKM matrix element V_{tb}, which is $\simeq 1$ for the SM but whose value could be altered by new physics. Assuming $|V_{\mathrm{tb}}| \gg |V_{\mathrm{ts}}|, |V_{\mathrm{td}}|$ and $\mathcal{B}(\mathrm{t} \to \mathrm{bW}) = 1$, it is simply given by $|V_{\mathrm{tb}}| = \sqrt{\sigma/\sigma_{\mathrm{theor.}}}$ and numerically for this analysis $|V_{\mathrm{tb}}| = 0.97^{+0.09}_{-0.10}\,(\mathrm{exp.} + \mathrm{theor.})$, i.e. it is compatible with the SM prediction. More details are given in [3].

Differential

Both ATLAS and CMS have also measured a cross section differential in the p_{T} of the top quark [4, 5]. The analysis designs are similar: a Neural Network is trained in the 2j1t region for a better separation between the t-channel and background processes, and its discriminator is cut on in order to obtain a high-purity sample of single top events. After the background contributions are subtracted, the distributions are unfolded to parton level, where the kinematics of the top quark are understood to reflect the resonance before its decay and after radiation effects. The normalized p_{T} distributions are shown in Figure 4 for $\sqrt{s} = 7$ and 8 TeV, respectively, and display good agreement between data and simulation. The (dis)agreement in the tail of the 8 TeV distribution suggests that the 4F is able to model high p_{T} objects better than the 5F.

W BOSON HELICITY

The helicity of the W boson is usually subject to $\mathrm{t\bar{t}}$ analyses and is measured with a single top selection for the first time in the analysis presented here [6]. The helicity angle θ^*_ℓ is defined as the angle between the direction of the reconstructed W boson in the top quark rest frame and the direction of the lepton in the W boson rest frame. Its probability function (which is the same for $\mathrm{t\bar{t}}$ and single top events) is proportional to each helicity component (F_{L}: left-handed, F_0: longitudinal, F_{R}: right-handed) of the W boson,

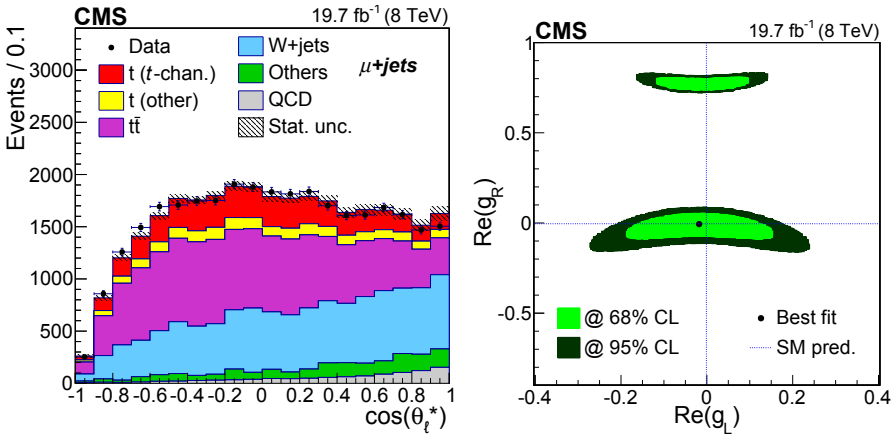

FIGURE 5. Distribution of $\cos\theta^*_\ell$ (left) and limits on real tensor components in the tWb coupling (right), taken from the 8 TeV CMS analysis [6].

$$\frac{1}{\Gamma}\frac{\mathrm{d}\Gamma}{\mathrm{d}\cos\theta^*_\ell} = \frac{3}{8}(1-\cos\theta^*_\ell)^2 F_\mathrm{L} + \frac{3}{4}\sin^2\theta^*_\ell F_0 + \frac{3}{8}(1+\cos\theta^*_\ell)^2 F_\mathrm{R}, \tag{1}$$

where Γ is the total width of the top quark decay. SM predictions are $F_\mathrm{L} = 0.311 \pm 0.005$, $F_0 = 0.687 \pm 0.005$ and $F_\mathrm{R} = 0.0017 \pm 0.0001$ [7]. In the analysis they are extracted from a maximum-likelihood fit in $\cos\theta^*_\ell$.

In terms of the event selection, it is closely following what has been done for the t-channel inclusive cross section measurement presented earlier. Since a boost in the top quark rest frame is required, a top quark candidate must be reconstructed. Two solutions for the z-component of the escaping neutrino arise when solving a quadratic equation for $p_{z,\nu}$. Events which only have two imaginary solutions are discarded, otherwise the one with the smallest absolute value is picked. Figure 5 shows the simulated $\cos\theta^*_\ell$ templates compared to data in the 2j1t muon channel. All single top events (t, s, tW) and $\mathrm{t\bar{t}}$ events contribute to the signal sample, since one can reconstruct a tWb vertices in all of them. The shape in $\cos\theta^*_\ell$ of the main background, W + jets, is taken from simulation, while the normalization is introduced as an unconstrained parameter and is fit simultaneously together with two of the three helicity fractions, F_L and F_0. The third component is obtained from the constraint $\Sigma_i F_i = 1$. Normalization estimates from [2] are used for all other backgrounds, whose shapes are either taken from simulation or taken from a control region in the case of multi-jet production. The fit results are $F_\mathrm{L} = 0.298 \pm 0.028\,(\mathrm{stat.}) \pm 0.032\,(\mathrm{syst.})$, $F_0 = 0.720 \pm 0.039\,(\mathrm{stat.}) \pm 0.037\,(\mathrm{syst.})$ and $F_\mathrm{R} = -0.018 \pm 0.019\,(\mathrm{stat.}) \pm 0.011\,(\mathrm{syst.})$, which is consistent with the SM predictions.

The above results can be re-interpreted in order to exclude potential tensor terms appearing in the tWb couplings, whose real parts are given by the parameters g_L and g_R in the extended Lagrangian

$$\mathcal{L}^{\mathrm{anom.}}_{\mathrm{tWb}} = -\frac{g}{\sqrt{2}}\bar{\mathrm{b}}\gamma^\mu(V_\mathrm{L}P_\mathrm{L} + V_\mathrm{R}P_\mathrm{R})\mathrm{tW}^-_\mu - \frac{g}{\sqrt{2}}\bar{\mathrm{b}}\frac{i\sigma^{\mu\nu}q_\nu}{m_\mathrm{W}}(g_\mathrm{L}P_\mathrm{L} + g_\mathrm{R}P_\mathrm{R})\mathrm{tW}^-_\mu + \mathrm{h.c.}, \tag{2}$$

assuming a purely left-handed interaction of the vector part, i.e. $V_\mathrm{L} = 1$, $V_\mathrm{R} = 0$. The reader is deferred to the publication for further information and more details. The best fit values are $g_\mathrm{L} = -0.017$ and $g_\mathrm{R} = -0.008$. As can be seen in Figure 5, this is consistent with the leading order SM prediction of 0. The signal modelling is the main source of systematic uncertainty.

TOP POLARIZATION

In the Standard Model the top quark is highly polarized along the direction of the light recoil quark, and its decay products bear information on the spin of the resonance. This can be used to construct an observable, $\cos\theta^*$, which is sensitive to the top quark polarization. It is defined as the angle between the lepton of the top quark decay and the light recoil jet, as seen from the top quark rest frame. Its differential distribution follows

$$\frac{1}{\Gamma}\frac{\mathrm{d}\Gamma}{\mathrm{d}\cos\theta^*} = \frac{1}{2}(1 + P_\mathrm{t}\alpha_\ell\cos\theta^*), \tag{3}$$

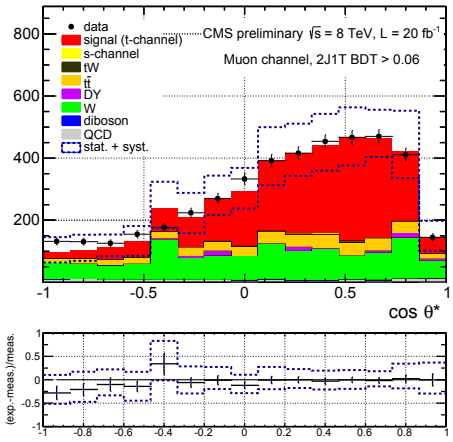

FIGURE 6. The CMS analyis [8] measures the $\cos\theta^*$ distribution at $\sqrt{s} = 8\,\text{TeV}$ in the muon channel after a cut on the BDT output.

where P_ℓ denotes the top quark polarization is α_ℓ is the degree of correlation of the angular distribution of ℓ with respect to the top quark spin (this analysis assumes $\alpha_\ell = 1$). The measured quantity finally is the asymmetry $A_\ell = (N(\cos\theta^* > 0) - N(\cos\theta^* < 0))/(N(\cos\theta^* > 0) + N(\cos\theta^* < 0))$, which is determined separately in both the electron and muon channel. A more detailed description of the applied cuts that enhance signal over background contributions is provided in [8], but it employs a 2j1t selection similar to [2]. The multi-jet background is derived from data in a control region enriched in QCD events that is obtained by inverting lepton isolation criteria. The default simulation setup for W + jets suffers from a bad description of $\cos\theta^*$ close to -1; another generator (Sherpa) which performs better in this region of phase space is used to correct the main MadGraph simulation. The shapes of $\text{t}\bar{\text{t}}$ templates are validated in a 3j1t and 3j2t control region. Finally a boosted decision tree (BDT) is trained in order to further separate single top production from the backgrounds. After a maximum-likelihood fit to its shape, in which the signal and background normalizations are determined, a cut on the BDT output is imposed to obtain a signal-enriched sample (see Figure 6). The background contributions are subtracted from data, and the distribution is unfolded to correct for detector effects. The asymmetry A_ℓ is calculated from the unfolded templates separately for the electron and the muon channel. Their combination gives $A_\ell = 0.41 \pm 0.06\,(\text{stat.}) \pm 0.07\,(\text{syst.})$, where the jet energy scale is the dominant source of systematic uncertainty. This results in a top quark polarization of $P_\text{t} = 0.82 \pm 0.12\,(\text{stat.}) \pm 0.32\,(\text{syst.})$.

REFERENCES

[1] F. Maltoni et al., "b-initiated processes at the LHC: a reappraisal", *J. High Energy Phys.* **07** (2012)

[2] CMS collaboration, "Measurement of the *t*-channel single-top-quark production cross section and of the $|V_{\text{tb}}|$ CKM matrix element in pp collisions at $\sqrt{s} = 8\,\text{TeV}$", *J. High Energy Phys.* **06** (2014)

[3] ATLAS collaboration, "Measurement of the Inclusive and Fiducial Cross-Section of Single Top-Quark *t*-Channel Events in pp Collisions at $\sqrt{s} = 8\,\text{TeV}$", *ATLAS-CONF-2014-007* (2014)

[4] ATLAS collaboration, "Comprehensive measurement of *t*-channel single top-quark production cross sections at $\sqrt{s} = 7\,\text{TeV}$ with the ATLAS detector", *Phys. Rev.* **D90** (2014)

[5] CMS collaboration, "Measurements of the differential cross section of single top-quark production in the *t*-channel in proton-proton collisions at $\sqrt{s} = 8\,\text{TeV}$", *CMS-PAS-TOP-14-004* (2014)

[6] CMS collaboration, "Measurement of the W boson helicity in events with a single reconstructed top quark in pp collisions at $\sqrt{s} = 8\,\text{TeV}$", *J. High Energy Phys.* **01** (2015)

[7] Czarnecki et al., "Helicity fractions of W bosons from top quark decays at NNLO in QCD", *Phys. Rev.* **D81** (2010)

[8] CMS collaboration, "Measurement of top-quark polarization in *t*-channel single-top production", *CMS-PAS-TOP-13-001* (2013)

Proceedings of the LHCP2015 Conference, St. Petersburg, Russia, August 31 - September 5, 2015

Editors: V.T. Kim and D.E. Sosnov

Observation of Top Quark Production in the Forward Region at LHCb

STEPHEN FARRY

Department of Physics, University of Liverpool, L69 7ZE, United Kingdom.

stephen.farry@cern.ch

On behalf of the LHCb Collaboration

Abstract. Forward top production is observed, in the $\mu + b$ final state, with the 3 fb^{-1} Run I dataset collected by the LHCb detector. The combined cross-section for $t\bar{t}$ and single top production at $\sqrt{s}$=7 TeV and $\sqrt{s}$=8 TeV is measured, for muons from the W boson with $p_{\rm T} > 25$ GeV in the pseudo-rapidity range 2.0< η <4.5 and with a b-tagged jet with $50 < p_{\rm T} < 100$ GeV in the pseudorapidity range 2.2< η <4.2. The production cross-sections are found to be in agreement with NLO predictions.

INTRODUCTION

The LHCb detector [1] is a dedicated forward detector at the LHC, fully instrumented in the pseudorapidity region $2.0 < \eta < 5.0$. It has been optimised to identify and reconstruct b and c hadron decays through precision tracking, vertexing and particle identification, and consequently is ideally suited to perform heavy flavour tagging of jets. The tagging of heavy flavour jets at LHCb, and specifically jets arising from b quarks, can be used to identify and measure the production of top quarks in the forward region. Such a measurement, originally proposed in order to measure the asymmetry of $t\bar{t}$ production [2], has the potential to reduce the uncertainties on the gluon PDF by up to 20% at large-x [3]. A study of the prospects for measuring top quark production at LHCb was performed in [4], with the number of events expected per fb^{-1} of data shown in Table 1. It should be noted that the predictions are made for a specific fiducial region which differs from that used in the final analysis, and so the numbers act only as a guide. As the LHCb experiment collects a lower rate of luminosity than the ATLAS and CMS experiments, and has a smaller fiducial acceptance, a significantly lower number of top quark events are expected to be produced at LHCb during Run-I data taking. The most statistically accessible final state is that of a lepton and a b-jet, which also suffers from the lowest purity due to the large contribution from direct Wb production. Nevertheless, this final state, and specifically that of a muon and a b-jet, is chosen to perform a measurement of top quark production in the forward rapidity region at LHCb [5], where top production includes contributions from both single top and $t\bar{t}$ production, with the latter contributing approximately 75% of events. The heavy flavour tagging techniques used at LHCb are described first, followed by the selection criteria and purity extraction before finally the results obtained are discussed.

Heavy Flavour Tagging

Heavy flavour tagging at LHCb is performed using the secondary vertex tagging algorithm outlined in [6]. Jets are tagged first by searching for a secondary vertex (SV) within the jet which satisfies specific track and vertex quality requirements. Two boosted decision trees (BDTs) are then trained on simulated b, c, and light jet samples using properties of the SV and the jet in order to separate light jets from heavy quark jets (BDT($bc|udsg$)), and $b-$jets from $c-$jets (BDT($b|c$)). The primary variables used are related to the $b-$ or $c-$hadron decay as these are expected to be well modelled in simulation. One parameter used to discriminate the jet types is the corrected mass, $M_{\rm cor}$, defined as

$$M_{\rm cor} = \sqrt{M^2 + p^2 \sin^2\theta} + p \sin\theta$$

TABLE 1. Summary of the expected top production cross-sections at LHCb in different final states for centre-of-mass energies of 7, 8 and 14 TeV. The table is reproduced from Reference [4]

$d\sigma$ (fb)	7 TeV	8 TeV	14 TeV
ℓb	285 ± 52	504 ± 94	4366 ± 663
$\ell b j$	97 ± 21	198 ± 35	2335 ± 323
$\ell b b$	32 ± 6	65 ± 12	870 ± 116
$\ell b b j$	10 ± 2	26 ± 4	487 ± 76
$\ell\ell$	44 ± 9	79 ± 15	635 ± 109
$\ell\ell b$	19 ± 4	39 ± 8	417 ± 79

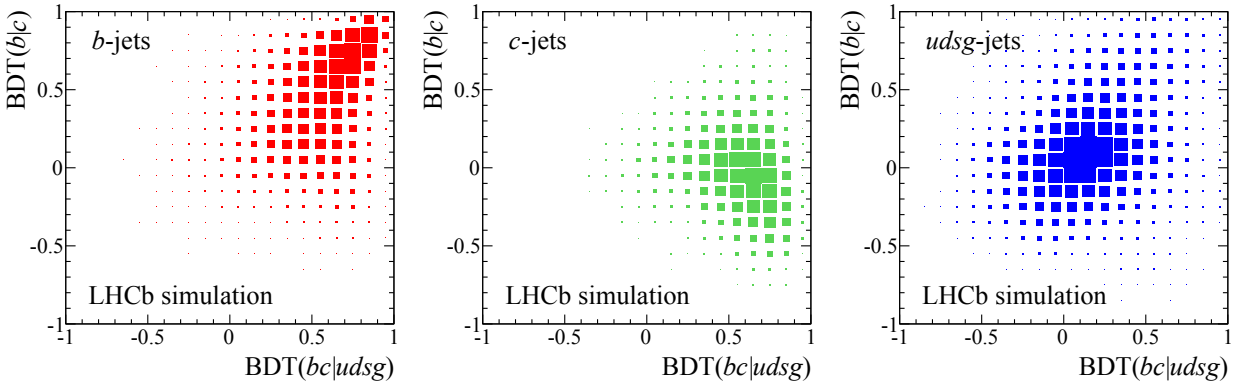

FIGURE 1. A two-dimensional representation of the BDT responses in simulation is shown for (left) b-jets, (middle) c-jets and (right) light-jets.

where M and p are the mass and momentum of the particles that form the SV and θ is the angle between the flight direction of the vertex and its momentum. It represents the minimum mass the long-lived object decaying at the vertex can have which is consistent with the flight direction. Other parameters include the fraction of the jet p_{T} carried by the particles forming the SV, as well as its multiplicity, net charge and flight distance. A two-dimensional representation of the BDT responses for b, c and light jets is shown in Figure 1. The output generated by the BDTs can then be used either to place requirements on the jets, or to perform a template fit to extract the relative amounts of b, c and light jets in a selected sample. Where requirements are placed on the BDT($bc|udsg$) response, the tagging efficiency versus light jet mis-tag rate is shown for b and $c-$jets in Figure 2.

Dataset and Selection

The measurement is performed using data collected at centre-of-mass energies of 7 and 8 TeV, corresponding to integrated luminosities of approximately 1 and 2 fb^{-1} respectively. The selection is based on previous studies of W production in association with b and $c-$jets performed at LHCb using the same dataset [7]. Events are selected which contain a muon with a transverse momentum, $p_{\mathrm{T}}(\mu)$, of greater than 25 GeV in the pseudorapidity region $2 < \eta < 4.5$, in addition to a jet satisfying $50 < p_{\mathrm{T}}(j) < 100$ GeV in the pseudorapidity range $2.2 < \eta < 4.2$. The inputs for jet reconstruction are selected using a particle flow algorithm as described in [8]and jet are clustered using the anti-k_{T} algorithm with distance parameter, $R = 0.5$. The muon and the jet are also required to be "unbalanced" in p_{T} by requiring that $p_{\mathrm{T}}(j_\mu + j)$, representing the p_{T} of the vectorial sum of j_μ and j is greater than 20 GeV, where j_μ is a reconstructed jet containing the muon candidate and j is the associated jet. The observable is expected to be large for W+jet events due to the missing neutrino in the final state and small for QCD di-jet production where the jet momenta are balanced. This represents a tighter fiducial selection than that used previously by LHCb to measure direct Wb production, and is specifically chosen to enhance the expected contribution from top quark production.

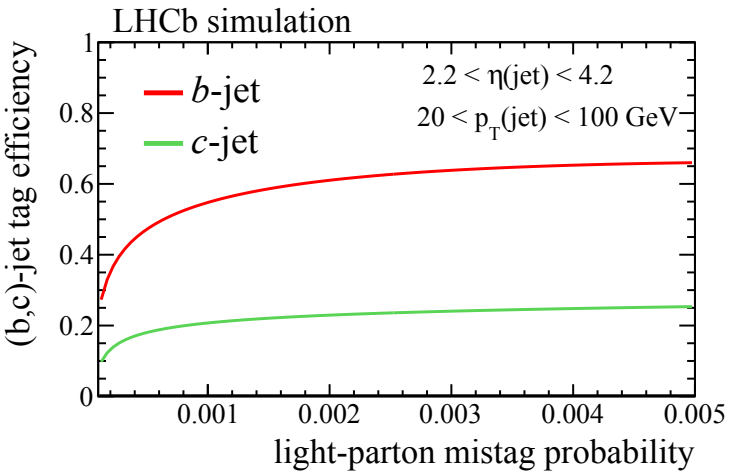

FIGURE 2. The efficiency for tagging b and $c-$jets versus the mis-tag probability for light jets obtained from simulation.

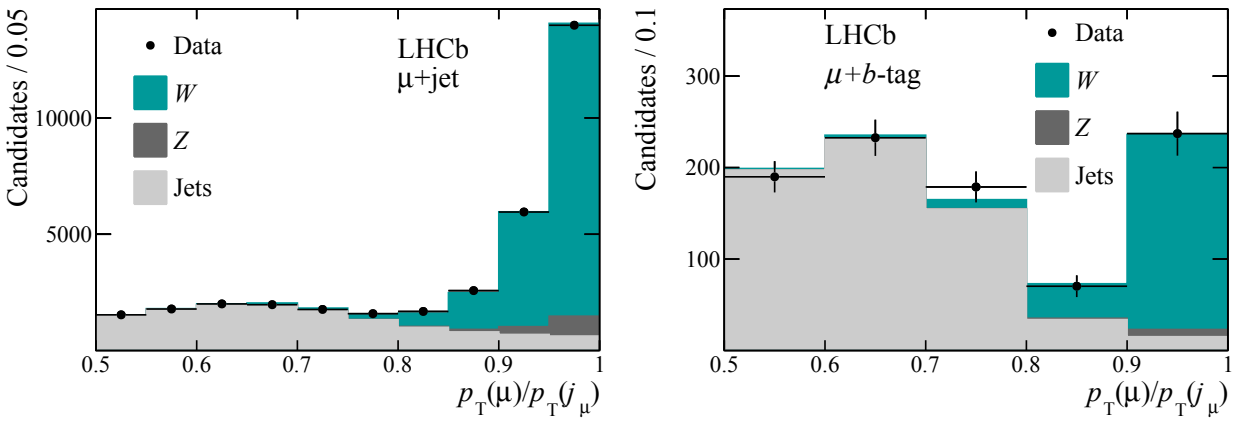

FIGURE 3. The combined fits used to extract the sample purity for (left) the total Wj sample and (right) the extracted Wb component.

Purity Determination

The purity is determined using a template fit to the isolation variable $p_{\mathrm{T}}(\mu)/p_{\mathrm{T}}(j_\mu)$, where $p_{\mathrm{T}}(\mu)$ is the transverse momentum of the muon in the final state, and $p_{\mathrm{T}}(j_\mu)$ is the transverse momentum of j_μ. This variable is expected to peak towards unity for signal events, and to be spread to lower values for backgrounds arising from QCD multi-jet processes. The electroweak template shapes are taken from simulation and corrected for differences between data and simulation using $Z \to \mu\mu$ events. The QCD background is estimated using a data-driven method. Events are selected in a sideband region obtained by requiring the muon and jet momenta are balanced ($p_{\mathrm{T}}(j_\mu + j)$ <20 GeV). This region is dominated by QCD events, and the events selected in this region are then reweighted in $p_{\mathrm{T}}(j_\mu)$ to match the shape obtained in the isolated signal region. In each bin of $p_{\mathrm{T}}(\mu)/p_{\mathrm{T}}(j_\mu)$, the contribution from b-jets is extracted by requiring that the jets contain an SV and performing a template fit to the resultant two-dimensional BDT distributions. The fits are performed separately for positive and negative muons, and for the different centre-of-mass energies. The combined fits are shown in Figure 3 for the full sample and the extracted b-jet component.

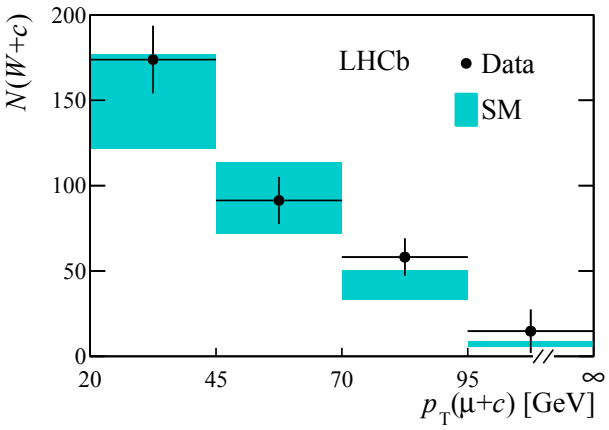

FIGURE 4. The observed Wc event yield compared with SM predictions obtained by first measuring Wj production and scaling by the SM expectation for $\sigma(Wc)/\sigma(Wj)$ and the expected $c-$tagging efficiency.

Results

The significance of the top quark contribution to the selected data sample is determined by comparing the observed event yield and charge asymmetry of Wb production to the SM prediction with and without the contribution from top quark production. The predictions are calculated at NLO in perturbative QCD using the MCFM generator and folded for detector effects. As predictions for the ratio of Wb to Wj production are approximately a factor of three more precise than for Wb production alone, the expected contribution from direct Wb production is obtained by first measuring the Wj cross-section in the chosen fiducial region, and then scaling it by the SM prediction for $\sigma(Wb)/\sigma(Wj)$ and the expected $b-$tagging efficiency. This approach is verified using the Wc channel, where no extra backgrounds are expected and good agreement is seen between the prediction obtained and the measurement, as shown in Figure 4. The observed event yield and charge asymmetry are shown in Figure 5 where a factor of three more events are observed than would be expected for the SM excluding top production, as well as a lower charge asymmetry. The statistical significance of the top quark contribution is calculated using a binned profile likelihood test to compare the data to the SM hypothesis without a top quark contribution and where contributions from both single top and $t\bar{t}$ production are included. A number of sources of systematic uncertainty are considered and are tabulated in Table 2, with the uncertainty on the $b-$tagging efficiency seen to dominate. The significance obtained is 5.4σ, confirming the observation of top quark production in the forward region. The excess is then used to calculate the cross-section for top quark production in the chosen fiducial region, which mirrors the kinematic selection, except for the requirement on $p_{\mathrm{T}}(j_\mu + j)$, which is alternatively applied to $p_{\mathrm{T}}(\mu + j)$. The cross-section includes contributions from both $t\bar{t}$ and single top production, and is determined to be

$$\begin{aligned}\sigma(\text{top})[7\text{TeV}] &= 239 \pm 53(\text{stat}) \pm 33(\text{syst}) \pm 24(\text{theory})\text{fb} \\ \sigma(\text{top})[8\text{TeV}] &= 289 \pm 43(\text{stat}) \pm 40(\text{syst}) \pm 29(\text{theory})\text{fb},\end{aligned}$$

where the first uncertainty is statistical, the second is systematic, and the third is due to uncertainties in the theoretical modelling. The results are in agreement with the SM predictions.

Conclusion

The first observation of top quark production is performed in the forward region using the Run-I dataset collected at LHCb. The measurement is performed in the $\mu + b-$jet final state and is found to be in good agreement with SM predictions. While measurements are currently statistically limited, a large increase in the top quark production cross-section is expected in Run-II at the higher centre-of-mass energy of 13 TeV. Consequently, a number of different final states will become statistically accessible and will allow a higher purity to be achieved as well as the separation of $t\bar{t}$ and single top production.

TABLE 2. Relative systematic uncertainties. The symbol † denotes an uncertainty that only applies to the cross-section measurement and not the significance determination.

source	uncertainty
GEC	2%
$p_T(\mu)/p_T(j_\mu)$ templates	5%
jet reconstruction	2%
SV-tag BDT templates	5%
b-tag efficiency	10%
trigger & μ selection	2%†
jet energy	5%†
$W \to \tau \to \mu$	1%†
luminosity	1–2%†
Total	14%
Theory	10%

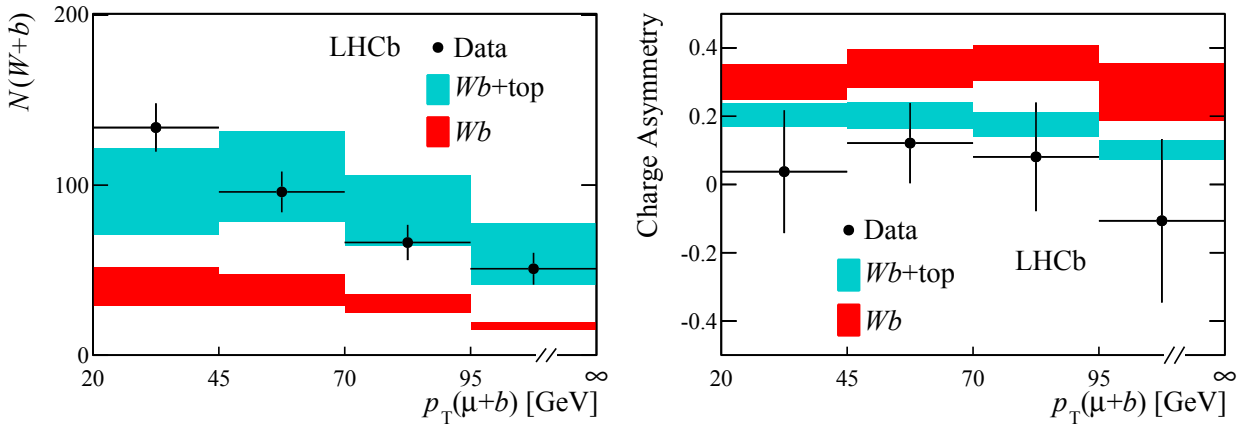

FIGURE 5. The observed (left) event yield and (right) charge asymmetry of Wb production compared to SM predictions calculated with and without the contribution from top quark production.

REFERENCES

[1] A. A. Alves, Jr. *et al.* (LHCb), JINST **3**, p. S08005 (2008).
[2] A. L. Kagan, J. F. Kamenik, G. Perez, and S. Stone, Phys. Rev. Lett. **107**, p. 082003Aug (2011).
[3] R. Gauld, JHEP **02**, p. 126 (2014), arXiv:1311.1810 [hep-ph] .
[4] R. Gauld, "Measuring top quark production asymmetries at LHCb," Tech. Rep. LHCb-PUB-2013-009. CERN-LHCb-PUB-2013-009 (CERN, Geneva, 2013).
[5] R. Aaij *et al.* (LHCb), (2015), arXiv:1506.00903 [hep-ex] .
[6] R. Aaij *et al.* (LHCb), JINST **10**, p. P06013 (2015), arXiv:1504.07670 [hep-ex] .
[7] R. Aaij *et al.* (LHCb), (2015), arXiv:1505.04051 [hep-ex] .
[8] R. Aaij *et al.* (LHCb), JHEP **01**, p. 033 (2014), arXiv:1310.8197 [hep-ex] .

Proceedings of the LHCP2015 Conference, St. Petersburg, Russia, August 31 - September 5, 2015

Editors: V.T. Kim and D.E. Sosnov

Golden Probe of the Top Yukawa

YI CHEN[1], DANIEL STOLARSKI[2,a)] and ROBERTO VEGA-MORALES[3]

[1]*Lauritsen Laboratory for High Energy Physics, California Institute of Technology, Pasadena, CA, USA*
[2]*Theory Division, Physics Department, CERN, CH-1211 Geneva 23, Switzerland*
[3]*CAFPE and Departamento de Fsica Terica y del Cosmos, Universidad de Granada, E-18071 Granada, Spain*

[a)]Corresponding author: daniel.stolarski@cern.ch

Abstract. We describe how the Higgs decay to four leptons can be used to probe the nature and CP structure of the top Yukawa coupling.

HIGGS DECAY TO FOUR LEPTONS

The discovery of the Higgs is the beginning of a long program to study its properties. Current state of the art characterizations of the boson usually involve looking at partial rates: comparing the frequency of different production and decay rates to the Standard Model (SM) prediction. In the Higgs decay to 4ℓ ($4e$, 4μ, $2e2\mu$), there is significantly more information than just how often this decay happens. Assuming that the Higgs is a scalar, there are five kinematic variables that describe each event. These can be parameterized, for example, using angles between a lepton and Z momentum, and the invariant mass of lepton pairs.

Shortly after the discovery, it was shown [1] that these kinematic variables encode information about the tensor structure of the Higgs coupling to gauge bosons. We compared three different possibilities:

$$h Z^\mu Z_\mu \quad \text{or} \quad h Z^{\mu\nu} Z_{\mu\nu} \quad \text{or} \quad h Z^{\mu\nu} F_{\mu\nu} \tag{1}$$

where h is the putative Higgs, $Z_{\mu\nu} = \partial_\mu Z_\nu - \partial_\nu Z_\mu$, and $F_{\mu\nu}$ is the equivalent field strength for the photon. We showed that with $O(50)$ events at the LHC, these different possibilities can be distinguished.

PROBING LOOP PROCCESSES

Having seen that kinematic distributions in $h \to 4\ell$ can be useful, we now turn our attention to measuring loop processes in this channel, namely the next-to-leading order (NLO) corrections to the tree level effect induced by the $h Z^\mu Z_\mu$ operator. The largest of these are shown in Figure 1, showing that this channel can be sensitive to the couplings of the Higgs to the top and W. Here we examine the sensitivity of this channel to the top Yukawa coupling, so we keep all other couplings (Higgs to W and Z and gauge boson couplings to fermions) at their SM values.

We parameterize the top Yukawa coupling as

$$h \bar{t} \left(y + i \tilde{y} \gamma^5 \right) t \, . \tag{2}$$

In the SM, $y \approx 1$ and $\tilde{y} \approx 0$. The pseudo-scalar operator is P and CP odd, so if both y and $\tilde{y}$ are non-zero, then CP is violated in the top Yukawa coupling. This effect is tiny in the SM, so a detection of this would be a clear sign of new physics.

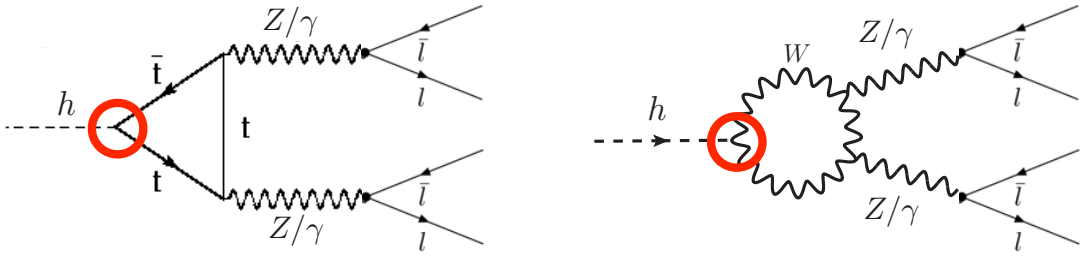

FIGURE 1. Feynman diagrams for the leading NLO corrections to $h \to 4\ell$. The coupling of the Higgs is circled to show which Higgs coupling can be probed, namely those to the top and W.

Other Probes of CP Violation

If there is CP violation in the top Yukawa coupling, this contributes to the electric dipole moments (EDM) of the electron, neutron, and Hg atom [2] at two loops. These bounds, particularly the electron EDM, constrain $\tilde{y}$ to be less than $O(1\%)$, with future experiments expected to reduce the bound to one in ten thousand.

The computations of EDM bounds assume SM couplings for other fields. In particular, the Yukawa coupling of the first generation fermions to the Higgs play a key role. As we have no direct experimental evidence that these couplings are SM-like, one could also consider the scenario where those couplings are zero, and in that case $O(1)$ values of $\tilde{y}$ are allowed. In this case, the neutron EDM is still somewhat sensitive due to the Weinberg operator, and future experiments are expected to bound $\tilde{y}$ at the per mille level, but they could also see a discovery. In that case, direct measurements of the top Yukawa coupling will be critical to characterizing the nature of CP violation responsible.

Experimental Sensitivity

In [3] we analyzed the experimental sensitivity of $h \to 4\ell$ to y and $\tilde{y}$. The sensitivity depends on the number of such decays which in turn depends on the integrated luminosity. To get an $O(1)$ precision on y and $\tilde{y}$, one needs about ten thousand events, which corresponds to a few thousand fb^{-1} of luminosity and depends on the experimental efficiencies. The scaling of the sensitivity is shown in Figure 2. From there, we see that the sensitivity to $\tilde{y}$ is better than to y, and this is because there is no SM contribution of the W to compete with in the P odd channel.

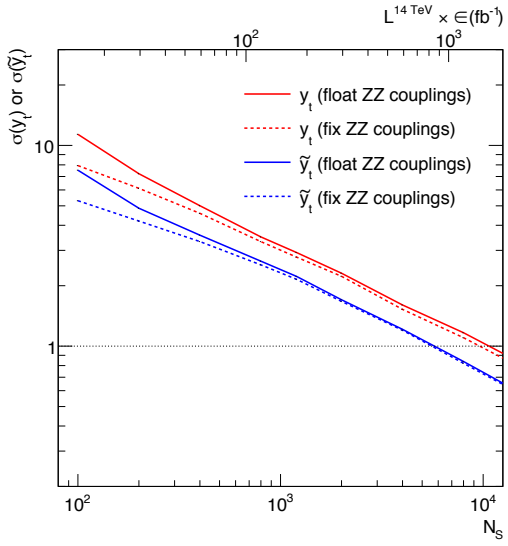

FIGURE 2. Sensitivity of the measurements described here in to y and $\tilde{y}$ as a function of the number of events. For details see text and [3].

The sensitivity depends on the experimental cuts used to collect $h \to 4\ell$. Current cuts are designed for discovery and to maximize the ratio of signal to background. As an example, they require one of the lepton pairs to have invariant mass bigger than 40 GeV at CMS. Since we already have the discovery, current measurements would be more sensitive to NLO effects if they aimed to maximize signal efficiency [4], even if that means having more background events in the sample. In particular, by loosening the invariant mass cut down to 4 GeV, the experiments will be much more sensitive to effects with photon intermediate states. This will increase the amount of background, but [4] showed that the sensitivity to loop effects is much improved even with background taken into account.

We can plot the the $1-\sigma$ contours in the $y-\tilde{y}$ plane for different numbers of events, and this is done Figures 3, 4, and 5. All our simulations use a crude modelling of detector effects including energy smearing described in [4]. We show three different contours for different assumptions about how events are collected. The outermost is using current CMS cuts, the middle is using the realistic "Relaxed-ϒ" cuts described in [4], and the innermost is with zero background, the theoretically best possible result. We see that definite improvements can be made relative to current cuts, but it is possible that a still better method exists.

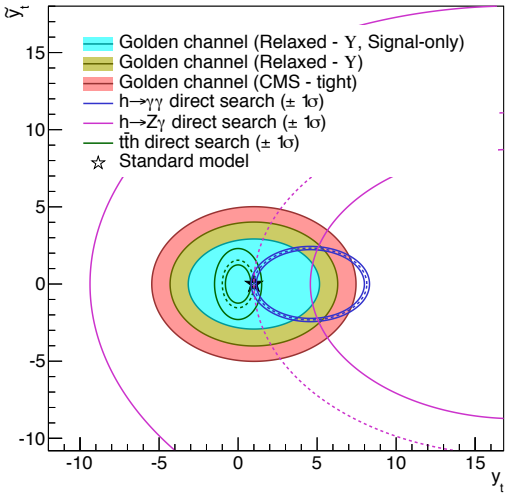

FIGURE 3. Sensitivity of the measurements described here in the $y-\tilde{y}$ plane with 800 events corresponding to approximately 300 fb^{-1}. For details see text and [3].

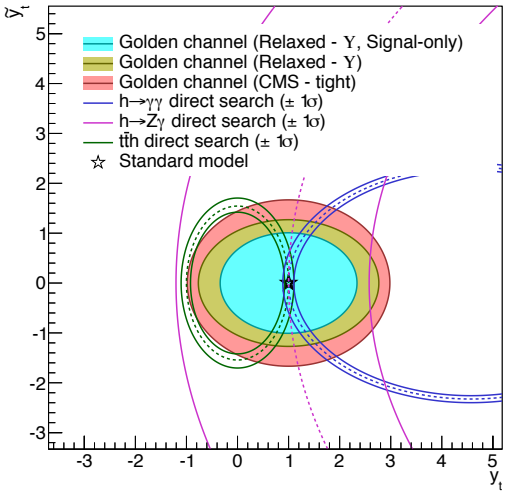

FIGURE 4. Same as Figure 3 but for 8,000 events corresponding to approximately 3,000 fb^{-1}.

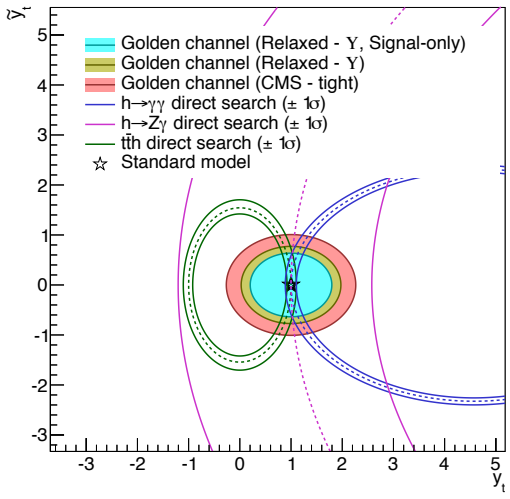

FIGURE 5. Same as Figure 3 but for 20,000 events corresponding to a putative 100 TeV collider with 3,000 fb^{-1}.

There are other measurements that are sensitive to the top Yukawa coupling, and we have put some of them in the figures for comparison. The green oval is the bound from $t\bar{t}h$ production which is quadratically sensitive to y and $\tilde{y}$. The thickness of the oval represents putative uncertainty of that measurement, but even with an infinitely precise measurement, $t\bar{t}h$ alone will never be able to determine at what point in the oval the true theory lies. The blue band is $h \to \gamma\gamma$, which is again an oval, but displaced from the origin because of the contribution from the W loop to that process. The pink curve is $h \to Z\gamma$ which is much less sensitive.

In Figure 3, we show the projected sensitivity with 800 events which corresponds to roughly 300 fb^{-1}, where we see the $h \to 4\ell$ measurement is only barely competitive with the others. On the other hand, with higher luminosity the other measurements do not gain much sensitivity, while $h \to 4\ell$ will always be statistics limited. Therefore we see in Figure 4, which corresponds to roughly 3,000 fb^{-1}, the high luminosity run of the LHC, that this measurement gets substantially better, allowing for strong constraints. Finally, we see that with 20,000 events, the measurement is even further improved, and this quantity of events could be achieved with a 100 TeV collider recording 3 ab^{-1}.

If $t\bar{t}h$ and $h \to \gamma\gamma$ are both measured to be SM-like in the asymptotic future of the LHC, then they can mutually break each others degeneracy in $y - \tilde{y}$ plane. On the other hand, there are assumptions about no other new physics that have to go into this measurement, particularly in the loop induced $h \to \gamma\gamma$ decay. Furthermore, if there is a deviation from the SM prediction in one or both of these measurements, then the $h \to 4\ell$ analysis described here will be crucial in characterizing the deviation.

CONCLUSIONS

The four lepton decay of the Higgs is an excellent channel to make detailed measurements. The four body final state gives rise to a rich structure of kinematic variables that can be exploited to measure the properties of the Higgs. This analysis is complementary to rate measurements and can give information not available in other ways. In particular, this channel is sensitive to NLO effects that interfere with the tree level contribution, giving access to the Higgs' coupling to the top quark and W boson. Furthermore, because the NLO effects interfere with the leading order, one can measure signs and phases of the Yukawa coupling. Therefore, this measurement can be used to place model independent bounds, or possibly even discover new physics.

ACKNOWLEDGMENTS

We would like to thank the organizers of LHCP and the top sessions for the invitation to give this talk. RVM is supported by MINECO, under grant number FPA2013-47836-C3-2-P.

REFERENCES

[1] D. Stolarski and R. Vega-Morales, *Directly Measuring the Tensor Structure of the Scalar Coupling to Gauge Bosons*, *Phys. Rev.* **D86** (2012) 117504 [1208.4840].

[2] J. Brod, U. Haisch and J. Zupan, *Constraints on CP-violating Higgs couplings to the third generation*, *JHEP* **11** (2013) 180 [1310.1385].

[3] Y. Chen, D. Stolarski and R. Vega-Morales, *Golden probe of the top Yukuwa coupling*, *Phys. Rev.* **D92** (2015), no. 5 053003 [1505.01168].

[4] Y. Chen, R. Harnik and R. Vega-Morales, *New opportunities in $h \to 4\ell$*, *JHEP* **09** (2015) 185 [1503.05855].

Proceedings of the LHCP2015 Conference, St. Petersburg, Russia, August 31 - September 5, 2015

Editors: V.T. Kim and D.E. Sosnov

Overview of FCNC Searches in Top Events from CMS and ATLAS

BORIS LEMMER

II. Physikalisches Institut, Georg-August-Universität Göttingen,
Friedrich-Hund-Platz 1, D-37077 Göttingen, Germany

boris.lemmer@cern.ch

On behalf of the ATLAS and CMS Collaborations

Abstract. The status of searches for flavor changing neutral currents (FCNCs) in top quark events from the ATLAS and CMS collaborations is presented. The results are quoted in terms of branching fractions $\mathcal{B}(t \to u/c + X)$ with X being a gluon, photon, Higgs or Z boson. Different decay signatures are probed and limits on $\mathcal{B}(t \to u/c + X)$ are shown. In an overview, these limits are compared to expectations for several beyond the Standard Model scenarios.

INTRODUCTION

Within the Standard Model (SM), flavor changing neutral currents do not exist at tree level and are highly suppressed at higher order due to the GIM mechanism [1]. However, in certain scenarios beyond the Standard Model (BSM) FCNCs can be significantly enhanced, reaching the level of experimental accessibility. The modeling of such FCNCs can be realized via effective Lagrangians. To avoid ambiguities due to different normalizations of the effective FCNC couplings, the branching ratios of the corresponding FCNC processes are used for a comparison. In the following, a set of analyses searching for FCNCs in top quark decays is presented. The analyses were performed by the ATLAS [2] and CMS [3] collaborations with data taken at the Large Hadron Collider [4] at center-of-mass energies of $\sqrt{s}$ = 7 TeV and 8 TeV. The results are presented in terms of branching fractions $\mathcal{B}(t \to u/c + X)$ with X being a gluon, photon, Higgs or Z boson. In a summary, the upper limits on these branching ratios are compared to expectations of several BSM scenarios, such as warped extra dimensions [5, 6], two-Higgs doublet models [7–9] and minimal supersymmetric models (MSSM) [10–12].

Presented Analyses

The type of boson involved in the FCNC process (g, γ, H or Z) and its possible subsequent decay determines the topology of the final state. The results are grouped into types of participating bosons. The strategies and results are compared in the following.

$t \to u/c + g$ (Single Top Events)

The CMS and ATLAS collaborations consider gluon mediated FCNCs in single top events. In both analyses, the initial state consists of a u/c quark and the gluon. In the CMS analysis [13] (dataset of 5 fb^{-1}, taken at $\sqrt{s}$ = 7 TeV) the FCNC process is assumed to occur at the final state vertex of the s-channel u/c quark (see Figure 1, left). Hence, the final state consists of a gluon and a top quark. Top quarks decaying leptonically into a muon are considered, which determines the event selection to be: one isolated muon and either one or two jets with $p_{\mathrm{T}} > 30$ GeV, of which one has to be tagged as b-jet (from top quark decay) and one must be un-tagged (FCNC gluon). Neural networks (NNs) are used to suppress multijet background and to separate FCNCs from SM final states. The observed (expected) 95% CL upper

limits for the branching ratios are $\mathcal{B}(t \to u+g) < 3.55 \cdot 10^{-4}$ $(1.58 \cdot 10^{-4})$ and $\mathcal{B}(t \to c+g) < 3.44 \cdot 10^{-3}$ $(1.05 \cdot 10^{-3})$, assuming the respective other branching ratio to be zero.

In contrast to the CMS analysis, the one carried by ATLAS assumes the FCNC process to occur in the initial state (see Figure 1, center), leading to a single quark in the final state without any extra particles [14]. In 20.3 fb^{-1} of data taken at $\sqrt{s} = 8$ TeV, top quarks decaying leptonically into a e/μ and the corresponding neutrino are selected, motivating to require an isolated e or μ ($p_{\mathrm{T}} > 25$ GeV), one b-tagged jet ($p_{\mathrm{T}} > 30$ GeV) as well as a cut on the missing transverse momentum $E_{\mathrm{T}}^{\mathrm{miss}}$ of 30 GeV and on the transverse W boson mass of 50 GeV for the event selection. Assuming the other of the two FCNC branching ratios to be zero, 95% CL upper limits are measured (predicted) as $\mathcal{B}(t \to u+g) < 4 \cdot 10^{-5}$ $(3 \cdot 10^{-5})$ and $\mathcal{B}(t \to c+g) < 17 \cdot 10^{-5}$ $(15 \cdot 10^{-5})$.

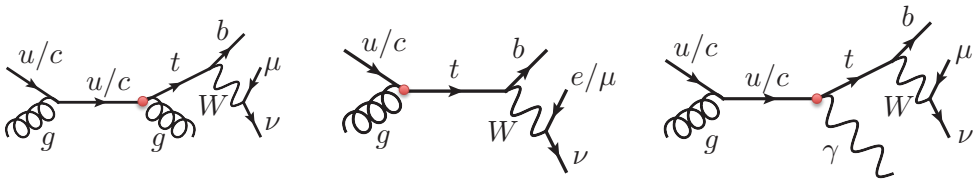

FIGURE 1: Gluon mediated FCNC at the initial state (left) and final state (center) vertex as well as photon mediated FCNC (right) in single top events.

$t \to u/c + \gamma$ (Single Top Events)

Assuming the same topology as in the $t \to u/c + g$ search, but replacing the gluon with a photon (see Figure 1, right), CMS analyzes 19.1 fb^{-1} of data taken at $\sqrt{s} = 8$ TeV to set limits on $\mathcal{B}(t \to u/c + \gamma)$ [15]. Events with one isolated muon with $p_{\mathrm{T}} > 26$ GeV, jets with $p_{\mathrm{T}} > 30$ GeV (not more than one being b-tagged), an isolated photon with $p_{\mathrm{T}} > 50$ GeV as well as $E_{\mathrm{T}}^{\mathrm{miss}} > 30$ GeV are selected. SM and FCNC contributions are separated using boosted decision trees (BDTs) to discriminate $tc\gamma$ and $tu\gamma$ FCNC signals individually from SM contributions. The yield of the main background, $W\gamma$+jets, is estimated with a data-driven method by fitting the $\cos(W,\gamma)$ distribution. Figure 2 (left) shows the BDT output with a scaled $tc\gamma$ distributions. The resulting (predicted) 95% CL upper limits are $\mathcal{B}(t \to u+\gamma) < 1.3 \cdot 10^{-4}$ $(1.9 \cdot 10^{-4})$ and $\mathcal{B}(t \to c+\gamma) < 1.7 \cdot 10^{-3}$ $(2.0 \cdot 10^{-3})$.

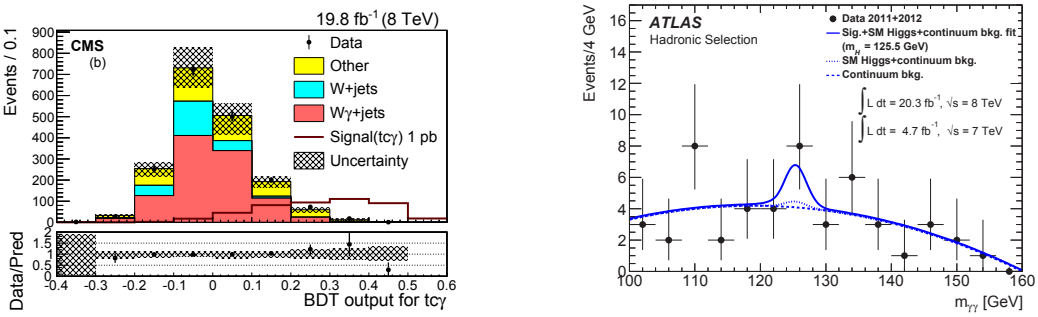

FIGURE 2: Left: BDT output in the photon-mediated FCNC search by CMS [15]. Right: Distribution of the invariant mass of the two photons from the $(H \to \gamma\gamma)$-mediated FCNC search by ATLAS [16], together with the fitted background and FCNC signal.

$t \to u/c + H$ ($t\bar{t}$ Events)

Higgs mediated FCNC signals are searched in events with $t\bar{t}$ pairs, focusing on multilepton and two-photon final states. The former final state is studied by CMS (three/two isolated e/μ with $p_{\mathrm{T}} > 20$ GeV for the first and $p_{\mathrm{T}} > 10$ GeV for the other leptons, same sign electric charge in case of two leptons, jets with $p_{\mathrm{T}} > 30$ GeV, cuts on $E_{\mathrm{T}}^{\mathrm{miss}}$, the scalar sum of the transverse energies of all jets passing the selection criteria, H_{T}, as well as a Z mass cut on the invariant mass of

the two-lepton-system, $m_{\ell\ell}$) using 19.7 fb^{-1} of data taken at $\sqrt{s}$ = 8 TeV [17]. Final states with $H \to WW, ZZ$ and $\tau\tau$ are considered. Possible final states are shown in Figure 3. Dominated by the dilepton channel, 95 % CL upper limits of $\mathcal{B}(t \to c + H) < 0.93\,\%$ (0.89 %) are observed (expected).

Both ATLAS and CMS provide FCNC limits for tHq couplings, obtained from events with $H \to \gamma\gamma$ decays and $t\bar{t}$ pairs of which the non-FCNC decay can occur hadronically or leptonically (see Figure 4, left). In the hadronic channel of the CMS analysis [18], two isolated photons ($p_T > 33$ GeV for the leading and 25 GeV for the sub-leading photon) are required next to at least four jets with $p_T > 20$ GeV, of which exactly one has to be b-tagged. In the leptonic channel, the same selection is applied but with an additional e/μ ($p_T > 20$ GeV) required and the number of jets lowered to at least two. In both channels, cuts on the masses of the top quark candidates are applied. The dominant non-resonant di-photon background is obtained from a fit to data, parametrized with the lowest possible bias. Using a dataset of 19.7 fb^{-1} taken at $\sqrt{s}$ = 8 TeV, observed (expected) limits of $\mathcal{B}(t \to u + H) < 0.42\,\%$ (0.65 %) and $\mathcal{B}(t \to c + H) < 0.47\,\%$ (0.71 %) are obtained at 95 % CL.

The ATLAS collaboration has also performed an analysis in the $H \to \gamma\gamma$ channel, using a larger dataset with 4.7 fb^{-1} at $\sqrt{s}$= 7 TeV and 20.3 fb^{-1} at $\sqrt{s}$= 8 TeV [16]. As in the CMS analysis, the analysis is split into leptonic and hadronic top decays. For the ATLAS analysis, the b-tag requirement is inclusive and an additional cut on the transverse W boson mass is applied in the leptonic channel. The limit on a combined tHc and tHu FCNC signal is measured via a fit to a data-driven non-resonant di-photon background in the hadronic channel (see Figure 2, right) and event counting in the leptonic channel. The latter one is used with 8 TeV data only. The measured (estimated) FCNC limit is determined as $\mathcal{B}(t \to q + H) < 0.79\,\%$ (0.51 %).

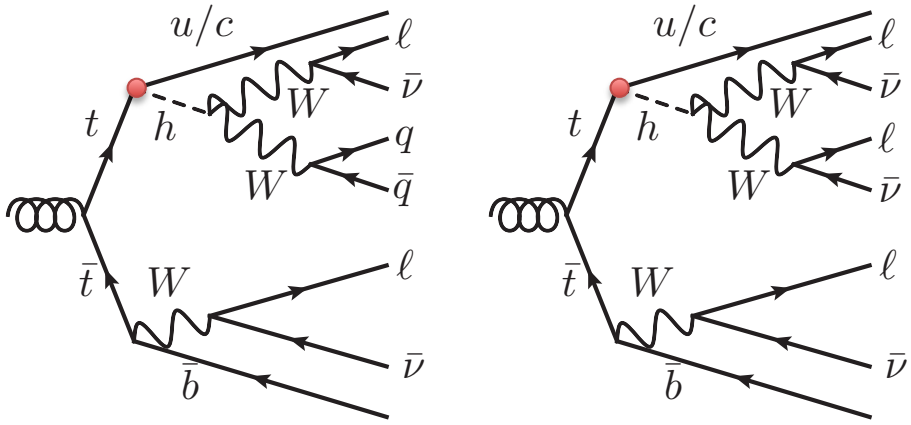

FIGURE 3: Higgs ($H \to WW$) mediated FCNC in $t\bar{t}$ events .

$t \to u/c + Z$ ($t\bar{t}$ Events)

The searches of FCNCs via tZq couplings closely follow the $t \to u/c + H$ analyses in the multilepton channels (see Figure 4, right). $t\bar{t}$ events in which one top is assumed to decay leptonically ($be\nu$ or $b\mu\nu$) and the other top via FCNC with a subsequent $Z \to ee$ or $Z \to \mu\mu$ decay. According to this topology, events are selected from 20.3 fb^{-1} of data taken at $\sqrt{s}$ = 8 TeV in the ATLAS analysis [19] by requiring three isolated electrons or muons with $p_T > 15$ GeV, two or three jets ($p_T > 35$ GeV) with one or two b-tags respectively as well as a cut on $E_T^{miss} > 20$ GeV and the χ^2 value of the top candidate mass fit. A tZc signal, which leads to a more conservative limit on the FCNC than tZu, is fitted to a simulated $t(\bar{t})Z$ and WZ background, leading to a 95 % CL upper limit of $\mathcal{B}(t \to q + Z) < 0.07\,\%$ (0.08 % expected).

In the corresponding CMS analysis [20], a very similar event selection is applied, requiring three isolated leptons ($p_T > 20$ GeV), at least two jets with $p_T > 30$ GeV with one being tagged as b-jet, as well as $E_T^{miss} > 30$ GeV and cuts on the top quark candidate masses. In contrast to ATLAS, CMS uses a data-driven background yield estimate by fitting b-tag channels with zero tags (diboson dominated), one tag (FCNC signal dominated) and two b-tags ($t\bar{t} + X$ dominated). For the FCNC limit measurement, the result is combined with a former one [21] using 5.0 fb^{-1} of 7 TeV

data, yielding to a 95 % CL upper limit of $\mathcal{B}(t \to q + Z) < 0.05\,\%$ (0.09 % expected). Searches for FCNC in the top

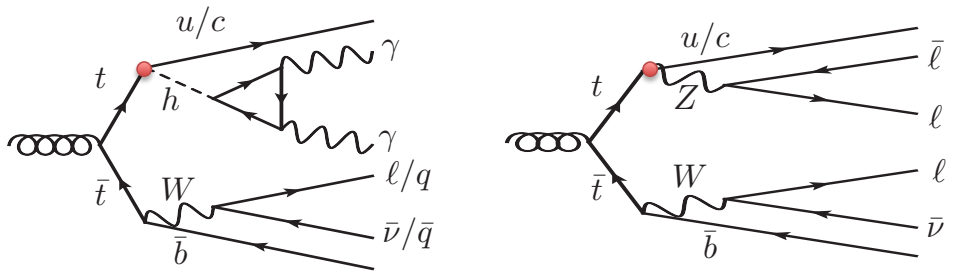

FIGURE 4: Higgs ($H \to \gamma\gamma$) mediated FCNC in $t\bar{t}$ events (left), Z ($Z \to \ell\ell$) mediated FCNCs in $t\bar{t}$ events (right).

quark sector, conducted by the ATLAS and CMS collaborations with centre-of-mass energies of $\sqrt{s} = 7$ and 8 TeV, were presented. So far, the measurements of the branching fractions $\mathcal{B}(t \to q + X)$ with $X = g, \gamma, Z$ or H have not yet reached sensitivity to the SM predictions [7]. Enhancements of these branching ratios are predicted for certain scenarios beyond the SM, e.g. warped extra dimensions, two-Higgs doublet models or minimal supersymmetric models. Reasonable upper limits – taking into account experimental results – on BSM driven branching ratio enhancements are quoted in [22] and references therein. Figure 5 summarizes the BR limits from ATLAS and CMS in the different FCNC models (g, γ, Z and H driven) and compares them to the SM predictions [7] and the BSM expectations [22]. So far, no FCNC measurement has reached sensitivity of any of the BSM scenarios.

The presented analyses contain complex final states and suffer from – next to the still limited statistics – the uncertainties on the modeling of the rare background processes.

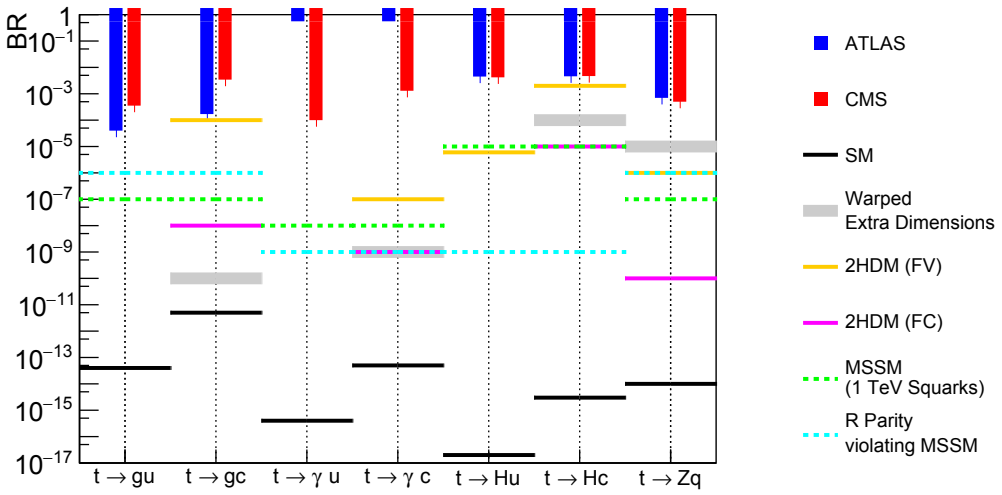

FIGURE 5: Summary of measured 95 % CL upper limits on the branching fraction $\mathcal{B}(t \to q + X)$ with $X = g, \gamma, Z$ or H, caused by FCNCs, measured by the ATLAS and CMS collaborations [13–20]. The limits are compared to the SM expectation for the branching fraction [7] as well as optimistic enhancements of the branching fraction in certain BSM scenarios (see [22] and references therein).

REFERENCES

[1] S. L. Glashow, J. Iliopoulos, and L. Maiani, Phys. Rev. D **2**, p. 1285 (1970).
[2] ATLAS Collaboration, JINST **3**, p. S08003 (2008).
[3] CMS Collaboration, JINST **3**, p. S08004 (2008).
[4] L. Evans and P. Bryant, JINST **3**, p. S08001 (2008).
[5] K. Agashe, G. Perez, and A. Soni, Phys. Rev. **D75**, p. 015002 (2007), arXiv:0606293 [hep-ph] .
[6] K. Agashe and R. Contino, Phys. Rev. **D80**, p. 075016 (2009), arXiv:0906.1542 [hep-ph] .
[7] J. A. Aguilar-Saavedra, Acta Phys. Polon. **B35**, p. 2695 (2004), arXiv:0409342 [hep-ph] .
[8] S. Bejar, "Flavor changing neutral decay effects in models with two Higgs boson doublets: Applications to LHC Physics," Ph.D. thesis, Barcelona, Autonoma U. 2006, arXiv:0606138 [hep-ph] .
[9] D. Atwood, L. Reina, and A. Soni, Phys. Rev. **D55**, p. 3156 (1997), arXiv:9609279 [hep-ph] .
[10] J. J. Cao, G. Eilam, M. Frank, K. Hikasa, G. L. Liu, I. Turan, and J. M. Yang, Phys. Rev. **D75**, p. 075021 (2007), arXiv:0702264 [hep-ph] .
[11] J. M. Yang, B.-L. Young, and X. Zhang, Phys. Rev. **D58**, p. 055001 (1998), arXiv:9705341 [hep-ph] .
[12] G. Eilam, A. Gemintern, T. Han, J. M. Yang, and X. Zhang, Phys. Lett. **B510**, p. 227 (2001), arXiv:0102037 [hep-ph] .
[13] CMS Collaboration, CMS-PAS-TOP-14-007 (2014), https://cds.cern.ch/record/1702400.
[14] ATLAS Collaboration, submitted to EPCJ (2015), arXiv:1509.00294 [hep-ph] .
[15] CMS Collaboration, submitted to JHEP (2015), arXiv:1511.03951 [hep-ex] .
[16] ATLAS Collaboration, JHEP **06**, p. 008 (2014), arXiv:1403.6293 [hep-ex] .
[17] CMS Collaboration, CMS-PAS-TOP-13-017 (2013), https://cds.cern.ch/record/2001934.
[18] CMS Collaboration, CMS-PAS-TOP-14-019 (2014), https://cds.cern.ch/record/2034227.
[19] ATLAS Collaboration, submitted to EPJC (2015), arXiv:1508.05796 [hep-ex] .
[20] CMS Collaboration, Phys. Rev. Lett. **112**, p. 171802 (2014), arXiv:1312.4194 [hep-ex] .
[21] CMS Collaboration, Phys. Lett. **B718**, 1252–1272 (2013), arXiv:1208.0957 [hep-ex] .
[22] K. Agashe *et al.* (Top Quark Working Group), "Working Group Report: Top Quark," in *Community Summer Study 2013: Snowmass on the Mississippi (CSS2013) Minneapolis, MN, USA, July 29-August 6, 2013* (2013) arXiv:1311.2028 [hep-ph] .
[23] K. Agashe and R. Contino, Phys. Rev. **D80**, p. 075016 (2009), arXiv:0906.1542 [hep-ph] .

Proceedings of the LHCP2015 Conference, St. Petersburg, Russia, August 31 - September 5, 2015

Editors: V.T. Kim and D.E. Sosnov

Wish-list for Run II top quark measurements (for BSM)

ROBERTO FRANCESCHINI

Theoretical Physics Department, CERN, Geneva, Switzerland

roberto.franceschini@cern.ch

Abstract. In this contribution I will highlight the new challenges for top quark physics at LHC Run II, focusing in particular on the interplay between precision studies on the top quark and searches for new physics. A new strategy to search for subtle scenarios of new physics is envisaged. The ability of compute and measure very accurately top quark properties such as its production rate, decay properties, *e.g* rates and distributions, and variables sensitive to the top quark mass is put at the center of this strategy to probe new physics.

INTRODUCTION

The Large Hadron Collider is known for being a "top quark factory", with a cross-section for top quark pair production nearing one *nb*, meaning millions of top quarks produced each year of running. Such a large rate for production of top quarks opens the way to *precision studies* of top quarks properties that were simply unattainable at previous machines. With such large top quark sample already recorded, or to be recorded in the next few years during Run II, statistical uncertainties are on their way to become less and less a limitation to the ultimate precision for experimental measurements. This prospect has stimulated a very intense effort for improving theory calculations to a level of precision that can match the foreseen experimental one. Presently it is possible to compute top quark production [1] and decay [2, 3] at NNLO in the strong coupling constant; huge progress has been made in matching NLO computations and parton showers [4] and computation of off-shell effects [5, 6, 7]; furthermore, automated NLO computations [8] can be used to produce distributions for any observable the experiments want to measure.

A similarly flourishing activity has taken place in many other areas of precision calculations for hadron collisions and the results of Run I of the Large Hadron Collider have yield a wonderful agreement between precision calculations of Standard Model processes and measurements by the Large Hadron Collider experiments, as witnessed by the summary of the Standard Model (sub)groups at this conference and their updates [9].

The great advances of precision measurements and precision calculations for hadron colliders is not only an enormous achievement *per se*, it also enables new strategies for the search of new physics at hadron colliders. In fact, hadron colliders are traditionally considered "discovery machines" for their ability to reach the highest energies and at the same time being able to scan for new phenomena on a vast range of energy scales. These features arise from the possibility to easily accelerate protons and effectively collide their constituents (quarks and gluons) with a large rate and a broad range of center of mass energies. At the same time the structure of the colliding protons poses a serious challenge to our ability to calculate, for instance because of possible interactions between initial states and final states of the collisions, and, in addition to this conceptual obstacle, perturbation theory of strong interactions converges rather slowly, hence several perturbative orders are sometimes needed to go seriously beyond an order of magnitude estimate of certain quantities.

The latest achievements in precision calculations have brought our understanding of hadronic collisions to a level that, as I will argue in the following, they can presently be used to spot new physics in subtle deviations from the predictions of precision calculations for observables that are sensitive to new physics. As a matter of fact, this use of precision calculations at hadron colliders opens the way for investigations of new physics with a mindset that is rather more typical of leptonic machines.

SUBTLE NEW PHYSICS AT RUN II

Despite the reduced beam energy compared to design at which the Large Hadron Collider has run in the past few years, already at this early stage of the life of the Large Hadron Collider a large amount of new physics scenarios have been tested. With supersymmetry being a leading candidate for the model of physics of the TeV scale, the impact of the Large Hadron Collider on new physics searches can be effectively summarized saying that colored superparticles are bound to be heavier than 1 TeV in most supersymmetric scenarios [10, 11, 12].

These tight bounds hold for a large class of models, however several possible ways out of this bound have been suggested. The details of the models that allow to alleviate the bounds that new physics scenarios receive from searches at the Large Hadron Collider cannot fit these pages, a sampler of options can be found in the literature [13, 14, 15, 16, 17, 18]. Nevertheless a unifying features of these models can be easily identified: all these models, in order to relax constraints from experimental searches, need to predict less apparent signatures of new physics, on which the experiments have a hard time to put bounds on. The increased difficulty to put bounds on these scenario can originate from *i)* lower production cross-section for the new physics states, which in turn can originate from having fewer new physics particles accessible at the Large Hadron Collider, or fewer available mediators for the production mechanisms (*e.g.* suppression of strong interaction production, removal of certain associated production mechanisms) *ii)* less visible signatures, which feature fewer leptons, softer missing momentum spectrum, a larger multiplicity of (softer) objects, or some combination of several of these "escape mechanisms".

Regardless of the precise cause of the looser bounds that apply in these models, all of them predict new physics not to show up (or at least not only) in very spectacular signatures, but in general they predict a large set of less spectacular signals, which tend to give rise to proton scattering final states that resemble very closely those of Standard Model scatterings. In view of such similarity of new physics events and Standard Model ones, it is extremely important to have under good theoretical control the predictions for Standard Model processes. Therefore the magnificent high-accuracy agreement between latest theory calculations and Run I measurements can be turned into a launch pad to attack the search of new physics with a new strategy, which leverages the precise knowledge of the Standard Model background, rather the absence of background.

A PRECISION OBSERVABLES PROGRAM ON THE TOP QUARK

Given that many extension of the Standard Model are built around, and motivated by, the peculiarities of the top-Higgs sector, the possibility to test with high precision the properties of the top quark at the Large Hadron Collider is very exciting. Also motivated by this perspective, the search of supersymmetric partners of the top quark (and of the bottom quark and Higgs boson) have become a standard theme of experimental investigation. Well organized summaries of the exclusion of simplified models with just a light stop and a light bino-like neutralino are routinely presented, e.g. in [19]. These summaries well exemplify how standard search strategies are in good position to cover most scenarios of new physics, still many scenarios remain difficult to attack. For instance for the stop-neutralino simplified model when stops become light, in the range of the top quark mass, the summary of Ref. [19] shows the shortcoming of simplest searches and models with mass spectra characterized by $m_{\tilde{t}} - m_{\chi} < m_t$ need to investigated with specially crafted strategies, *e.g.* looking for mono-jet signals, soft leptons and for signatures that insist of the W bosons, rather than the top quarks, to identify the decay products of the stops.

Despite these multiple attempts to attack this, after all pretty large, fraction of the parameter space of the stop-neutralino simplified model, large portions of the light stop parameter space are still uncovered. Given how basic is the simplified model under study, and also in view of its possible role of proxy towards a large domain of "top-like" new physics, full-coverage of this plane automatically emerges as a high priority task for Run II physics programs. To this end, as will be clear in a moment, precision top quark physics will be an essential asset to attain success in this endeavor.

A latest addition to the summary on the progress in search of new physics [20, 21], in fact, goes precisely in the direction of using precisely computable distributions of top quark physics observables, such as the angular separation of two leptons [22], to test the presence of top-like new physics with different spin. Also the measurement of the top pair total cross-section has been recently used to put bound on new physics that give rise to top-like final states and therefore affects the cross-section measurement [23, 24, 19]. For both these observables an extension of the present use can be envisaged for Run II, where a full exploration of bounds that can be obtained from these observables for generic stop mass (both below and above the top mass) and generic neutralino mass can be pursued.

It is worth to stress that the reach of searches for new physics in precision top quark observables, *e.g.* the aforementioned total cross-section and spin-correlation variables, goes much beyond that of model specific searches for new physics - though sometimes less powerful, this approach always probes a large set of new physics scenarios. In fact, any scenario that modifies significantly top quark production or decay has a chance to be observed, or excluded, looking at the fine details of these quantities well under theory control.

At Run II we can envision a new large class of observables to be used to test new physics in the top quark sample. These are the observables used for the determination of the top quark mass, which is presently extracted from Large Hadron Collider collisions to an astonishing sub-percent precision [25, 26]. The demonstrated capability to measure this standard Model parameter to such high accuracy embodies the great theoretical control on the Standard Model theory for the relevant observables and the superb performances of the experiments in measuring these observables. The achieved control sets an excellent stage for searching new phenomena in deviations from Standard Model predictions in the distributions that are presently used to measure the top quark mass.

Some types of new physics might induce a shift in the measured top quark mass [27], but this is not the sole possibility. In fact the top quark mass affects certain features of the relevant distributions, while new physics in general can present itself in several features of each distribution and in many distributions at the same time. Therefore a new physics search program, which cannot be reduced to a pure reinterpretation of the mass measurement, can be envisaged for Run II. In general this way to search new physics goes beyond, although gets started from, pure Standard Model measurements and the large amount of data that Run II will be the enabling factor for this kind of searches for new physics. In this respect the large and varied program of measurements of the top quark mass from many different quantities [28, 29, 30, 31, 32, 33, 34, 35, 36, 37, 38], is a precious asset to test the large landscape of new physics scenarios that can manifest at the Large Hadron Collider.

The effect of top-like new physics from supersymmetry can be very apparent in certain distribution. An example is represented for a stop-charigno-neutralino simplified model in Figure 1 for the decay

$$\tilde{t} \to \tilde{\chi}^{+} b \to \ell \nu \tilde{\chi}^{0} b$$

for a choice of masses $m_{\tilde{t}} = 200$ GeV, $m_{\tilde{\chi}^{+}} = 150$ GeV, $m_{\tilde{\chi}^{0}} = 100$ GeV, on which only very mild (and uncertain) bounds exists [39, 40, 41]. The new physics spectrum is characterized by mass splittings similar, but not identical, to those of the $t \to Wb \to \ell \nu b$ decay of the Standard Model. The similarity of the mass scale and mass splittings renders very difficult to single out this extra source of top-like events with gross-grained techniques, such as the search for an excess in a high-pT tail of a distribution. In fact this spectrum gives rise to softer decay products (in particular to softer b quarks) than ordinary top decay, which is a background for this search. Therefore, only using very precises probes of the mass splittings, such as the observables $m_{b,\ell}$ and E_b shown in Figure 1, one is able to highlight the subtle difference between top decay and its supersymmetric cousin $\tilde{t} \to \tilde{\chi}^{+} b \to \ell \nu \tilde{\chi}^{0} b$.

Further opportunities for testing new physics in a broad manner thanks to precise studies of top quark properties exists in several branches of top physics studies already carried out at the Large Hadron Collider. For instance the top quark decay into τ final states

$$t \to b \tau \nu$$

not mediated by a W boson, has reached sensitivity to decay modes with branching ratio a fraction of that of the Standard Model [43] and presently probes very effectively light charged Higgs boson that arise in supersymmetric models. The precise knowledge of the distributions that are used to test the light charged Higgs boson hypothesis can be used to test contact operators that mediate the same decay of the top quark, turning this search in a much broader scoped one. More in general the present status of this and other searches [44, 45], suggests that the present knowledge of top quark decay has reached a level that enables a broad search for new physics that embraces all Standard Model final states of top decay and new ones. In this perspective we can envisage a generalization of present global determinations of the Standard Model top quark branching rations [46] to encompass a broader set of observables and final states, to test more widely the presence of tiny deviations from the Standard Model in a *global analysis* of the properties of the top quark. The combined use of several observables, *e.g.* from the several final states measured, will be a point of strength of this global approach. In view of the results of Run I, this strategy will certainly be worth pursuing at Run II both to sharpen our knowledge of the top quark in the Standard Model and at the same time test a large class of new physics scenario, in particular those that might be *most elusive in standard searches*.

Many more opportunities wait to be caught exploiting the large amount of Run II top quark data. A particularly useful technique can be imagined to search new physics in top-like final states by exploiting one side of the $t\bar{t}$ event as trigger, for instance requiring a leptonic top, and scrutinizing the other half of the event in search for deviations of top

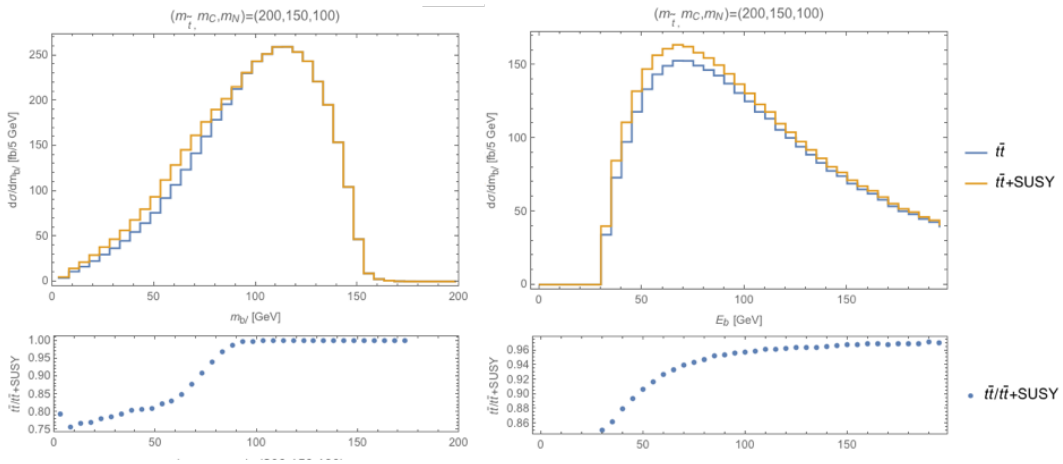

FIGURE 1. Possible deviation from the Standard Model shape of the lepton-b-jet invariant mass distribution and the b-jet energy distribution used for the top quark mass measurement in Ref. [42] and Ref. [28]. The bottom panel shows the ratio of the new physics over the Standard Model prediction. The effect of new physics is most apparent in certain regions of the distribution, allowing for calibration of the Standard Model prediction elsewhere in the data and test of the new physics hypothesis in the sensitive region.

quark properties from the Standard Model prediction. This strategy can highlight the presence of a small branching ratio of the top quark in supersymmetric particles, *e.g.* in light stop and neutralino (which can easily be at the percent level [47]):

$$t \to \tilde{t}\tilde{\chi}^0 \to jets\,,$$

which can arise for light stop and light neutralino in R-parity violating models with sizable UDD interactions. This type of decay might be highlighted by studies of standard Model properties such as Refs. [48, 46, 49], which, still being general searches for deviations from the Standard Model, can be suitably targeted towards this type of new physics, exploiting obvious features as the presence of a on-shell dijet resonance from the stop decay into jets, or the multi-jet decay of the neutralino, possibly enriched by a detectably displaced decay of the latter. On a similar note, the study of top quark decay can help to discover, or put bounds on, supersymmetric particles that do not carry color but experience a sizable LQD RPV interaction with the top quark, such as *staus* that can appear in the top quark decay

$$t \to b\tilde{\tau} \to b + jets\,.$$

CONCLUSIONS

The large production cross-section of the top quark at the Large Hadron Collider, together with the demonstrated capabilities of the experiments to measure top quark properties to high precision, and latest improvements of high precision theory calculations allow to envision a rich program of precision physics on the top quark at Run II of the Large Hadron Collider. Certain items of this physics program can be considered standard, for instance the study of top quark couplings and the production of top quarks in more rare reactions such as production in association with other states.

In this contribution I have argued that plenty of opportunities lays ahead if new physics is sought for in top quark properties, especially in scenarios of new physics that tend to be most elusive to the standard "high-pT" approach. These examples of new physics include new states with mass around that of the top quark, which have revealed severe limitations of the more generic (and more widespread) search approaches. I have identified a rich program of studies of the distributions that are presently used to measure the top quark mass, as to turn these distributions in precision tests for the presence of top-like new physics. Furthermore I have highlighted opportunities in the global study of the decay of top quark in all Standard Model channels, and new ones, as suggested by the addition of contact operators involving top quarks or by explicit models such as the examples in R-parity conserving and R-parity violating supersymmetry discussed above.

ACKNOWLEDGMENTS

RF thanks the organizers of the LHCP 2015 conference and the LHC Physics Centre at CERN for support. Furthermore RF thanks Gabriele Ferretti, Christoffer Petersson, Giacomo Polesello, and Riccardo Torre for discussions.

REFERENCES

[1] M. Czakon, D. Heymes, and A. Mitov, (2015), arXiv:1511.00549 [hep-ph] .
[2] J. Gao, C. S. Li, and H. X. Zhu, Physical Review Letters **110**, p. 042001January (2013), arXiv:1210.2808 [hep-ph] .
[3] M. Brucherseifer, F. Caola, and K. Melnikov, JHEP **4**, p. 59April (2013), arXiv:1301.7133 [hep-ph] .
[4] J. M. Campbell, R. K. Ellis, P. Nason, and E. Re, JHEP **04**, p. 114 (2015), arXiv:1412.1828 [hep-ph] .
[5] G. Heinrich, A. Maier, R. Nisius, J. Schlenk, and J. Winter, Journal of High Energy Physics **6**, p. 158June (2014), arXiv:1312.6659 [hep-ph] .
[6] G. Bevilacqua, M. Czakon, A. van Hameren, C. G. Papadopoulos, and M. Worek, Journal of High Energy Physics **2**, p. 83February (2011), arXiv:1012.4230 [hep-ph] .
[7] A. Denner, S. Dittmaier, S. Kallweit, and S. Pozzorini, JHEP **10**, p. 110October (2012), arXiv:1207.5018 [hep-ph] .
[8] J. Alwall, R. Frederix, S. Frixione, V. Hirschi, F. Maltoni, O. Mattelaer, H. S. Shao, T. Stelzer, P. Torrielli, and M. Zaro, JHEP **1407**, p. 079, arXiv:1405.0301v1 [hep-ph] .
[9] "https://atlas.web.cern.ch/Atlas/GROUPS/PHYSICS/CombinedSummaryPlots/SM/index.html," .
[10] M. Dine, Ann. Rev. Nucl. Part. Sci. **65**, 43–62Jan (2015), arXiv:1501.01035v1 [hep-ph] .
[11] N. Craig, ArXiv e-prints September (2013), arXiv:1309.0528 [hep-ph] .
[12] J. L. Feng, Ann.Rev.Nucl.Part.Sci. **63**, 351–382February (2013), arXiv:1302.6587 [hep-ph] .
[13] J. Serra, arXiv:1506.05110 [hep-ph] .
[14] A. Anandakrishnan, J. H. Collins, M. Farina, E. Kuflik, and M. Perelstein, arXiv:1506.05130 [hep-ph] .
[15] G. D. Kribs and A. Martin, Phys. Rev. **D85**, p. 115014March (2012), arXiv:1203.4821 [hep-ph] .
[16] M. Papucci, J. T. Ruderman, and A. Weiler, JHEP **09**, p. 035October (2012), arXiv:1110.6926 [hep-ph] .
[17] R. Franceschini, Advances in High Energy Physics **581038**, p. 16 (2015).
[18] D. Das, U. Ellwanger, and A. M. Teixeira, Journal of High Energy Physics **4**, p. 67April (2012), arXiv:1202.5244 [hep-ph] .
[19] ATLAS Collaboration, arXiv:1506.08616 [hep-ex] .
[20] CMS Collaboration (CMS Collaboration), CMS-PAS-TOP-14-023 (2015).
[21] G. Aad *et al.* (ATLAS Collaboration), (2014), arXiv:1412.4742 [hep-ex] .
[22] Z. Han, A. Katz, D. Krohn, and M. Reece, JHEP **8**, p. 083 (2012), arXiv:1205.5808 [hep-ph] .
[23] M. Czakon, A. Mitov, M. Papucci, J. T. Ruderman, and A. Weiler, Phys. Rev. Lett. **113**, p. 201803 (2014), arXiv:1407.1043 [hep-ph] .
[24] ATLAS Collaboration, Eur.Phys.J. **C74**, p. 3109June (2014), arXiv:1406.5375 [hep-ex] .
[25] "https://twiki.cern.ch/twiki/bin/view/lhcphysics/lhctopwgsummaryplots," .
[26] CMS Collaboration, ArXiv e-prints September (2015), arXiv:1509.04044 [hep-ex] .
[27] T. Eifert and B. Nachman, Phys. Lett. B **743**, p. 218 (2015), arXiv:1410.7025 [hep-ph] .
[28] CMS Collaboration, CMS-PAS-TOP-15-002 ().
[29] K. Agashe, R. Franceschini, and D. Kim, Phys. Rev. D **88**, p. 057701September (2013), arXiv:1209.0772 [hep-ph] .
[30] ATLAS Collaboration, ArXiv e-prints July (2015), arXiv:1507.01769 [hep-ex] .
[31] S. Alioli, P. Fernandez, J. Fuster, A. Irles, S.-O. Moch, P. Uwer, and M. Vos, ArXiv e-prints March (2013), arXiv:1303.6415 [hep-ph] .
[32] S. Kawabata, Y. Shimizu, Y. Sumino, and H. Yokoya, Phys. Lett. B **741**, 232–238 (2015), arXiv:1405.2395 [hep-ph] .
[33] Juste et al., arXiv:1310.0799 [hep-ph] .
[34] G. Cortiana, ArXiv e-prints October (2015), arXiv:1510.04483 [hep-ex] .
[35] G. Corcella, ArXiv e-prints November (2015), arXiv:1511.08429 [hep-ph] .
[36] S. Frixione and A. Mitov, JHEP **9**, p. 12September (2014), arXiv:1407.2763 [hep-ph] .
[37] "Mass determination in the t t-bar system with kinematic endpoints," Tech. Rep. CMS-PAS-TOP-11-027 (CERN, Geneva, 2012).

[38] CMS Collaboration, CMS-PAS-TOP-12-030 ().
[39] ATLAS Collaboration, ArXiv e-prints March (2014), arXiv:1403.4853 [hep-ex] .
[40] ATLAS Collaboration, ArXiv e-prints July (2014), arXiv:1407.0583 [hep-ex] .
[41] G. Aad *et al.* (ATLAS), JHEP **1310**, p. 189 (2013), arXiv:1308.2631 [hep-ex] .
[42] "Determination of the top-quark mass from the m(lb) distribution in dileptonic ttbar events at sqrt(s) = 8 TeV," Tech. Rep. CMS-PAS-TOP-14-014 (CERN, Geneva, 2014).
[43] "Updated search for a light charged Higgs boson in top quark decays in pp collisions at sqrt(s) = 7 TeV," Tech. Rep. CMS-PAS-HIG-12-052 (CERN, Geneva, 2012).
[44] CMS Collaboration, ArXiv e-prints October (2013), arXiv:1310.1618 [hep-ex] .
[45] S. Davidson, M. L. Mangano, S. Perries, and V. Sordini, ArXiv e-prints July (2015), arXiv:1507.07163 [hep-ph] .
[46] ATLAS Collaboration, ArXiv e-prints June (2015), arXiv:1506.05074 [hep-ex] .
[47] A. Djouadi, W. Hollik, and C. Jünger, Phys. Rev. D **54**, 5629–5635November (1996), hep-ph/9605340 .
[48] CMS Collaboration, ArXiv e-prints April (2014), arXiv:1404.2292 [hep-ex] .
[49] J. Alwall, R. Frederix, J.-M. Gérard, A. Giammanco, M. Herquet, S. Kalinin, E. Kou, V. Lemaitre, and F. Maltoni, European Physical Journal C **49**, 791–801February (2007), hep-ph/0607115 .
[50] ATLAS Collaboration, ArXiv e-prints August (2015), arXiv:1508.06868 [hep-ex] .

Heavy Flavour physics: plenary talks

Proceedings of the LHCP2015 Conference, St. Petersburg, Russia, August 31 - September 5, 2015

Editors: V.T. Kim and D.E. Sosnov

ATLAS/CMS: b-hadron production

ZHENG WANG

Institute of High Energy Physics, CAS., Beijing, China

Zheng.Wang@cern.ch

On behalf of the ATLAS and CMS Collaborations

Abstract. The ATLAS and CMS analyses of b-hadron production at $\sqrt{s}$ = 7 TeV and 8 TeV are summarized. The production cross section measurements include inclusive b production and exclusive production measurements of Υ(1S, 2S, 3S), B^+, B^0, B_s^0, $B_c^{\pm}$, Λ_b. The ATLAS and CMS search results of new b-quark states with RUN-I data are also introduced. Observation of the rare $B_s^0 \to \mu^+\mu^-$ decay from CMS and combined result of CMS and LHCb data are presented.

INTRODUCTION

Production of hadrons containing the b-quark has been predicted with NLO (Next-Leading Order) accuracy for more than twenty years. However, the dependence on the factorization and renormalization scales, and on the value of m_b results in theoretical uncertainties of up to 40%. The large production cross sections for b-hadron particles in pp collisions at LHC energies provides opportunities for testing the perturbative and non-perturbative QCD model predictions on the b-hadrons production and fragmentation accurately, and studying the dynamics of heavy quarks inside b-hadrons, decay models and spectroscopy. It is also possible for physicists to search for some quarkonium-like exotic states and other new physics phenomena.

The detailed description of the CMS and ATLAS detectors, together with a definition of the coordinate system used and the relevant kinematic variables, can be found in Refs. [1] [2] The ATLAS and CMS detectors have excellent capabilities to reconstruct b-hadron decays due to the highly efficient muon detection system and the high-resolution silicon tracker. For both experiments, the trackers have good momentum, impact parameter and vertex resolutions, and good b-tagging capability. ATLAS and CMS also have robust muon identification performance. Muon detection down to low p_T (transverse momentum) and low mis-identification of muon particle. In the LHC RUN-I running, ATLAS and CMS have collected the largest pp collision data samples, which corresponds to integrated luminosities of $\sim 5\ fb^{-1}$ at $\sqrt{s} = 7$ TeV and $\sim 20\ fb^{-1}$ at $\sqrt{s} = 8$ TeV, respectively. Therefore, ATLAS and CMS may fully exploit the highest Beauty Flavor production with high accuracy.

With the highest LHC luminosities, and access regimes and phase space, ATLAS and CMS analyses on B production are complementary to those by B factories [3], experiments on Tevatron [4] and LHCb [5].

MEASUREMENT OF PRODUCTION CROSS SECTION

This section introduces ATLAS and CMS results of inclusive and exclusive b-hardon reconstruction measurements, angular analysis of $B^0 \to K^{0*}\mu^+\mu^-$, measurements of the CP-violating weak phase ϕ_s and of the decay width difference $\Delta\Gamma_s$ using the $B_s^0 \to J/\psi\phi(1020)$ decay channel. The measurement of the parity-violating asymmetry parameter α_b and of the helicity amplitudes for the decay $\Lambda_b^0 \to J/\psi\Lambda^0$ at $\sqrt{s} = 7$ TeV and 8 TeV is also introduced.

Inclusive b production measurements

Inclusive b production measurements were performed by ATLAS and CMS at the beginning of LHC running from 2010. The typical data samples used for the inclusive process measurements are from $\sim nb^{-1}$ to $\sim pb^{-1}$. CMS mea-

sured differential production cross sections of inclusive b-hadron with muon with 85 nb^{-1} data at 7 TeV [6], the inclusive $b\bar{b} \to X \to \mu\mu X'$ with 27.9 pb^{-1} data at 7 TeV [7], and the inclusive b-jet production with 34 pb^{-1} data at 7 TeV [8]. ATLAS measured the production cross section of hadrons containing the b-quark using decays to $D^*\mu^- X$ final states [9], as well as the inclusive and di-jet cross-sections of b-jets at 7 TeV [10]. Differential cross sections have been measured as a function of muon (b-jet) transverse momentum and (pseudo)rapidity. The results of inclusive cross section measurement were compared with MC@NLO, POWHEG, Pythia predictions. Predictions are in agreement with ATLAS and CMS results within uncertainties.

Analyses of exclusive b-hadron production by ATLAS and CMS

Total and differential cross sections $d\sigma/dp_T^B$ and $d\sigma/dy^B$ for B^+ mesons produced in pp collisions at $\sqrt{s} = 7$ TeV are measured by CMS [11]. The data correspond to an integrated luminosity of 5.8 pb^{-1} collected by the CMS experiment. The exclusive decay $B^+ \to J/\psi K^+$, with $J/\psi \to \mu\mu$, is used to detect B^+ mesons and to measure the production cross section as a function of p_T^B and y^B. The total cross section for $p_T^{B^+} > 5$ GeV and $|y^{B^+}| < 2.4$ is measured to be $28.1 \pm 2.4(stat.) \pm 2.0(sys.) \pm 3.1(lum.)\, mb$. The result is in reasonable agreement with theoretical predictions in terms of shape, but has an absolute normalization approximately 1.5 times larger than the MC@NLO calculation. ATLAS as well measured B^+ differential production cross-section with 2.4 fb^{-1} data at $\sqrt{s} = 7$ TeV [12]. The integrated B^+ production cross-section in the kinematic range 9 GeV $< p_T <$ 120 GeV and $|y| < 2.25$ is measured to be $10.6 \pm 0.3(stat.) \pm 0.7(syst.) \pm 0.2(lumi.) \pm 0.4(Br)\, \mu b$. The next-to-leading-order QCD calculation is compatible with the measured differential cross-section. The predictions are obtained within the Powheg and MC@NLO frameworks and are quoted with an uncertainty from renormalization and factorization scales and b-quark mass of the order of 20%-40%. Within these uncertainties, Powheg+Pythia is in agreement with the measured integrated cross-sections and with the dependence on p_T and y. At low $|y|$, MC@NLO+Herwig predicts a lower production cross-section and a softer p_T spectrum than the one observed in data, while for $|y| > 1$ the predicted p_T spectrum becomes harder than observed in data. The FONLL calculation for $\sigma(pp \to bX)$ is compared to the data, assuming a hadronisation fraction $f_{\bar{b}\to B^+}$ of (40.1 ± 0.8)% [13], and is in good agreement with the measured differential cross-section $d\sigma/dp_T$, within the theoretical uncertainty.

The CMS measured of B^0 and B_s^0 differential production cross sections $d\sigma/dp_T^B$ and $d\sigma/dyB$ with 40 pb^{-1} data at $\sqrt{s} = 7$ TeV [14] [15]. The B^0 meson are reconstructed in the exclusive final state $J/\psi K_S^0$, with $J/\psi \to \mu\mu$ and $K_S^0 \to \pi^+\pi^-$, while B_s^0 are reconstructed from the decay $B_s^0 \to J/\psi\phi$ with $J/\psi \to \mu\mu$, $\phi \to K^+K^-$. The integrated B_s^0 cross section times $B_s^0 \to J/\psi\phi$ branching fraction in the range $8 < p_T^B < 50$ GeV/c and $|y^B| < 2.4$ is measured to be $6.9 \pm 0.6(stat.) \pm 0.6(sys.)\, nb$. For the B^0 with $p_T^B > 5$ GeV and $|y^B| < 2.2$, the total cross section is measured to be $33.2 \pm 2.5(stat.) \pm 3.5(sys.)\, \mu b$. The cross sections are compared with predictions based on perturbative QCD calculations at next-to-leading order. The B_s^0 result lies between the theoretical predictions of MC@NLO ($4.6^{+1.9}_{-1.7} \pm 1.4\, nb$) and PYTHIA ($9.4 \pm 2.8\, nb$), where the last uncertainty is from the $B_s^0 \to J/\psi\phi$ branching fraction. CMS cross-section measurements of B^+ and B^0 production in pp collisions at $\sqrt{s} = 7$ TeV gave values between the two theory predictions, indicating internal consistency amongst the three different B-meson (B^+, B^0 and B_s^0) results.

At ATLAS, the ratio of b-quark fragmentation fractions f_s/f_d was measured in pp collisions with 2.47 fb^{-1} data at $\sqrt{s} = 7$ TeV [16]. From the observed yields of $6640 \pm 100(stat) \pm 220(sys)$ $B_s^0 \to J/\psi\phi$ events and $36290 \pm 320(stat) \pm 650(sys)$ $B_d^0 \to J/\psi K^{*0}$ events, the quantity $\frac{f_s}{f_d} \frac{\mathcal{B}(B_s^0 \to J/\psi\phi)}{\mathcal{B}(B_d^0 \to J/\psi K^{*0})}$ is estimated to be $0.199 \pm 0.004(stat) \pm 0.010(sys)$. Figure 1, taken from [16], shows the measurements of f_s/f_d versus B meson p_T for CDF, LHCb, ATLAS and LEP experiments. ATLAS measurement agrees with results from LHCb, CDF, and the LEP average [17]. The ATLAS data show no dependence on p_T nor on $|\eta|$ within the kinematic range tested.

CMS measured the ratio $\mathcal{B}(B_s^0 \to J/\psi f_0(980))/\mathcal{B}(B_s^0 \to J/\psi\phi(1020))$ using the data of integrated luminosity of 5.3 fb^{-1} at $\sqrt{s} = 7$ TeV [18]. Total 873 ± 49 events of $B_s^0 \to J/\psi(\mu^+\mu^-)f^0(\pi^+\pi^-)$ and 8377 ± 107 events of $B_s^0 \to J/\psi(\mu^+\mu^-)\phi(K^+K^-)$ are observed. The ratio of the branching fraction of $B_s^0 \to J/\psi(\mu^+\mu^-)f^0(\pi^+\pi^-)$ to the branching fraction of $B_s^0 \to J/\psi(\mu^+\mu^-)\phi(K^+K^-)$, $R_{f_0/\phi}$, is determined to be $\frac{\mathcal{B}(B_s^0 \to J/\psi f_0)\mathcal{B}(f_0 \to \pi^+\pi^-)}{\mathcal{B}(B_s^0 \to J/\psi\phi)\mathcal{B}(\phi \to K^+K^-)} = 0.140 \pm 0.013(stat) \pm 0.018(syst)$. This result is consistent with the theoretical prediction of about 0.2 [19] and with previous measurements [20].

The $B_s^0 \to J/\psi\phi$ process is also a "golden" mode to explore CP violation because it is a flavor non-specific and experimentally clean final state. CMS measured the CP-violating weak phase ϕ_s of the B_s^0 meson and the decay width difference $\Delta\Gamma_s$ of the B_s^0 light and heavy mass eigenstates using a data sample of $B_s^0 \to J/\psi\phi(1020) \to \mu^+\mu^- K^+K^-$ decays at a centre-of-mass energy of 8 TeV [21]. A total of 49200 reconstructed B_s^0 decays are used to extract the

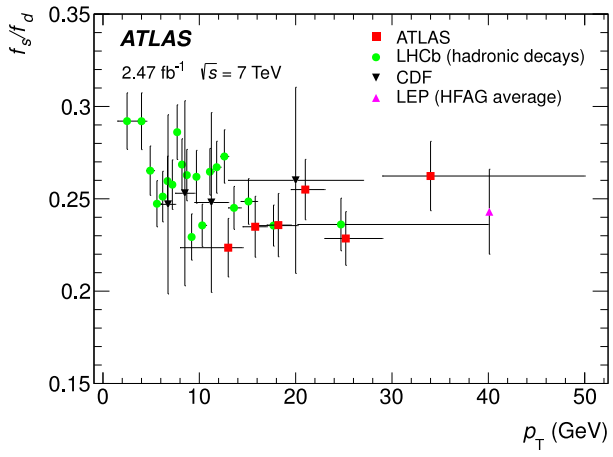

FIGURE 1. Measurements of f_s/f_d versus B meson p_T for CDF, LHCb and ATLAS [16], where the ATLAS data points are plotted at the average p_T of the events in each bin. The error bars show statistical and systematic errors added in quadrature. The LEP ratio, taken from Ref. [17], is plotted at an approximate p_T in Z decays.

values of ϕ_s and $\Delta\Gamma_s$ by performing a time-dependent and flavour tagged angular analysis of the $\mu^+\mu^- K^+K^-$ final state. ATLAS's measurement is based on 4.9 fb^{-1} of integrated luminosity at $\sqrt{s} = 7$ TeV. Table 1 shows the ATLAS, CMS, as well as LHCb [23] measurements of CP-violating weak phase ϕ_s and the decay width difference $\Delta\Gamma_s$. It may be seen that the measured value of ϕ_s agrees with the SM prediction [24], in which it is assumed that subleading contributions to the decay amplitude are negligible. Results confirm $\Delta\Gamma_s$ to be nonzero, with a value consistent with theoretical predictions. Three experiments provide independent reference measurements of ϕ_s and $\Delta\Gamma_s$, and contribute to improving the overall precision of these quantities and thereby probing the SM further.

TABLE 1. ATLAS, CMS and LHCb measurements of CP-violating weak phase ϕ_s and the decay width difference $\Delta\Gamma_s$.

Experiment	$\Delta\Gamma_s$ (ps^{-1})	ϕ_s **(rad)**
ATLAS (4.9 fb^{-1}) [22]	$0.053 \pm 0.021 \pm 0.010$	$0.12 \pm 0.25 \pm 0.5$
CMS (20 fb^{-1}) [21]	$0.095 \pm 0.013 \pm 0.007$	$-0.075 \pm 0.097 \pm 0.031$
LHCb (3 fb^{-1}) [23]	$0.0805 \pm 0.0091 \pm 0.0032$	$-0.058 \pm 0.049 \pm 0.006$

Using 20.5 fb^{-1} pp collision data at $\sqrt{s} = 8$ TeV, CMS studied the angular distributions and the differential branching fraction of the decay $B^0 \to K^{*0}\mu^+\mu^-$. In the analysis, The K^{*0} is reconstructed through its decay to $K^+\pi^-$, and the B^0 is reconstructed by fitting the two identified muon tracks and the two hadron tracks to a common vertex. From 1430 signal decays, the forward-backward asymmetry of the muons ($A_{\rm FB}$), the $K^*(892)^0$ longitudinal polarization fraction ($F_{\rm L}$), and the differential branching fraction are determined as a function of the dimuon invariant mass squared, dB/dq^2. Table 2 shows the measurements from CMS (the 7 TeV [25], 8 TeV results [26], and the combination), LHCb [27], BaBar [28], CDF [29], and Belle [30] of $F_{\rm L}$, $A_{\rm FB}$, and dB/dq^2 in the region $1 < q^2 < 6$ GeV^2 for the decay $B^0 \to K^{*0}\mu^+\mu^-$. CMS results are among the most precise to date and are consistent with Standard Model (SM) predictions and previous measurements.

For the B_c meson, CMS measured the ratio of the cross sections times branching fractions for $B_c^+ \to J/\psi\pi^+$ and $B^+ \to J/\psi K^+$ at a center-of-mass energy of 7 TeV and integrated luminosity of 5.1 fb^{-1} [33]. The analysis, performed for B_c^+ and B^+ mesons with $p_T > 15$ GeV and in the central rapidity region $|y| < 1.6$, gives a measured ratio of $R_{c/u} = [0.48 \pm 0.05(stat) \pm 0.03(syst) \pm 0.05(\tau_{B_c})]\%$. A similar measurement from LHCb in the kinematic region $p_T > 4$ GeV, $2.5 < \eta < 4.5$ gives $[0.68 \pm 0.10(stat) \pm 0.03(syst) \pm 0.05(\tau_{B_c})]\%$ [34]. The two measurements, performed in different kinematic regions, are expected to differ because of the softer p_T distribution of the B_c^+ with respect to that of the B^+, implying a lower value of the ratio at higher p_T. The measurements are consistent with this

TABLE 2. Measurements from CMS, LHCb, BaBar, CDF, and Belle of $F_{\rm L}$, $A_{\rm FB}$, and dB/dq^2 in the region $1 < q^2 < 6$ GeV^2 for the decay $B^0 \to K^{*0}\mu^+\mu^-$.

Experiment	$F_{\rm L}$	$A_{\rm FB}$	dB/dq^2 (10^{-8} **GeV**$^{-2}$)
CMS (7 TeV) [25]	$0.68 \pm 0.10 \pm 0.02$	$-0.07 \pm 0.12 \pm 0.01$	$4.4 \pm 0.6 \pm 0.4$
CMS (8 TeV) [26]	$0.72 \pm 0.05 \pm 0.05$	$-0.15^{+0.10}_{-0.08} \pm 0.03$	$3.6 \pm 0.3 \pm 0.3$
CMS (7 TeV + 8 TeV)	0.71 ± 0.06	$-0.12^{+0.07}_{-0.08}$	3.8 ± 0.4
LHCb [27]	$0.65^{+0.08}_{-0.07} \pm 0.03$	$-0.17 \pm 0.06 \pm 0.01$	$3.4 \pm 0.3^{+0.4}_{-0.5}$
BaBar [28]	–	–	$4.1^{+1.1}_{-1.0} \pm 0.1$
CDF [29]	$0.69^{+0.19}_{-0.21} \pm 0.08$	$0.29^{+0.20}_{-0.23} \pm 0.07$	$3.2 \pm 1.1 \pm 0.3$
Belle [30]	$0.67 \pm 0.23 \pm 0.05$	$0.26^{+0.27}_{-0.32} \pm 0.07$	$3.0^{+0.9}_{-0.8} \pm 0.2$
SM (LCSR) [31]	$0.79^{+0.09}_{-0.12}$	$-0.02^{+0.03}_{-0.02}$	$4.6^{+2.3}_{-1.7}$
SM (Lattice) [32]	$0.73^{+0.08}_{-0.10}$	$-0.03^{+0.04}_{-0.03}$	$3.8^{+1.2}_{-1.0}$

expectation. Measurements of the production cross section times branching fraction for $B_c^+ \to J/\psi l^+\nu$ relative to that for $B^+ \to J/\psi K^+$ are also available from the CDF experiment in the kinematic region $p_T > 4$ GeV and $|y| < 1$. With the present $B_c^+(p_T, |y|)$ coverage, these experimental results can give guidance to improve the theoretical calculations still affected by large uncertainties and constrain the various B_c^+ production models. The ratio of the $B_c^+ \to J/\psi\pi^+\pi^+\pi^-$ and $B_c^+ \to J/\psi\pi^+$ branching fractions has been measured to be $R_{B_c} = 2.55 \pm 0.80(stat) \pm 0.33(syst)^{+0.04}_{-0.01}(\tau_{B_c})$, which is in good agreement with the result from the LHCb experiment, $2.41 \pm 0.30(stat) \pm 0.33(syst)$ [35], and represents its first confirmation. This measurement can be compared with the theoretical predictions, which assume factorization into $B_c^+ \to J/\psi W^{+*}$ and $W^{+*} \to n\pi^+$ (n = 1, 2, 3, 4). In particular, Ref. [36] predicts 1.5 for the ratio, whereas Ref. [37] predicts three different values, 1.9, 2.0, and 2.3, depending on the chosen set of B_c^+ meson form factors. More precise measurements are needed to determine if one of the predictions is favored by the data. The model-independent method implemented for the efficiency evaluation of the five-body final state can be considered in future high-statistics analyses to reduce systematic uncertainties associated with the unknown multibody decay dynamics.

For the b-baryons, CMS measured the differential cross sections times branching fraction $d\sigma/dp_T^{\Lambda_b} \times \mathcal{B}(\Lambda_b \to J/\psi\Lambda)$ and $d\sigma/dy^{\Lambda_b} \times \mathcal{B}(\Lambda_b \to J/\psi\Lambda)$ for Λ_b baryons produced in pp collisions at $\sqrt{s} = 7$ TeV [38]. The measurements are given for $p_T^{\Lambda_b} > 10$ GeV and $|y^{\Lambda_b}| < 2.0$. The $p_T^{\Lambda_b}$ distribution falls faster than both the measured p_T spectra from b mesons and the predicted spectra from the NLO MC POWHEG and the leading-order MC PYTHIA. The measured value of $\sigma(\Lambda_b) \times \mathcal{B}(\Lambda_b \to J/\psi\Lambda)$ for $p_T^{\Lambda_b} > 10$ GeV and $|y^{\Lambda_b}| < 2.0$ is $1.16 \pm 0.06(stat.) \pm 0.12(sys.)$ nb, and the integrated $\sigma(\bar{\Lambda}_b)/\sigma(\Lambda_b)$ ratio is $1.02 \pm 0.07(stat.) \pm 0.09(sys.)$. The total cross section and rapidity distribution are consistent with both predictions within large uncertainties. The measured $\sigma(\bar{\Lambda}_b)/\sigma(\Lambda_b)$ ratio is consistent with unity and constant as a function of both $p_T^{\Lambda_b}$ and $|y^{\Lambda_b}|$.

At ATLAS, measurements of the parity-violating decay asymmetry parameter a_b and the helicity amplitudes for the decay $\Lambda_b^0 \to J/\psi(\mu^+\mu^-)\Lambda^0(p\pi^-)$ has been performed using the 4.6 fb^{-1} pp collisions data at a center-of-mass energy of 7 TeV [39]. The measured values of a_b, and the ratio parameters of the helicity amplitude k_+ and k_- are $a_b = 0.30 \pm 0.16(stat) \pm 0.06(syst)$, $k_+ = 0.21^{+0.14}_{-0.21}(stat) \pm 0.13(syst)$, $k_- = 0.13^{+0.20}_{-0.13}(stat) \pm 0.15(syst)$, corresponding to the value of helicity parameters $|a_+| = 0.17^{+0.12}_{-0.17}(stat) \pm 0.09(syst)$, $|a_-| = 0.59^{+0.06}_{-0.07}(stat) \pm 0.03(syst)$, $|b_+| = 0.79^{+0.04}_{-0.05}(stat) \pm 0.02(syst)$, $|b_+| = 0.08^{+0.13}_{-0.08}(stat) \pm 0.06(syst)$, The Λ_b^0 decay has large amplitudes $|a_-|$ and $|b_+|$, which means the negative-helicity states for Λ^0 are preferred. The Λ^0 and J/ψ from Λ_b^0 decay are highly polarized. Adding in quadrature the statistical and systematic uncertainties, the observed value of a_b is consistent with the measurement $a_b = 0.05 \pm 0.17(stat) \pm 0.07(syst)$ by LHCb [40] at the level of one standard deviation. However, it is not consistent with the expectation from pQCD (a_b in the range from -0.17 to -0.14) [41], and HQET ($a_b = 0.78$) [42] at a level of about 2.6 and 2.8 standard deviations, respectively.

The ATLAS experiment observed the decay $\Lambda_b^0 \to \psi(2S)\Lambda^0$ at $\sqrt{s} = 8$ TeV using an integrated luminosity of 20.6 fb^{-1} data [43]. The J/ψ and ψ(2S) mesons are reconstructed in their decays to a muon pair, while the $\Lambda^0 \to p\pi^-$

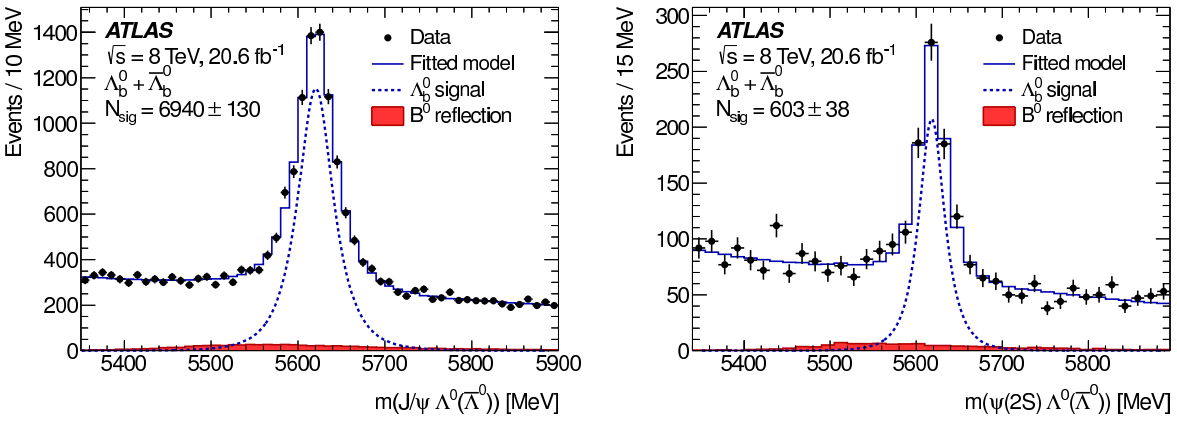

FIGURE 2. The invariant mass distributions for the combined sample of the selected Λ_b^0 and $\bar{\Lambda}_b^0$ candidates obtained after their fits to the $\Lambda_b^0 \to J/\psi\Lambda^0$ (left) and $\Lambda_b^0 \to \psi(2S)\Lambda^0$ (right) at ATLAS [43].

decay is exploited for the Λ^0 baryon reconstruction. The Λ_b^0 baryons are reconstructed with transverse momentum $p_T > 10$ GeV and pseudorapidity $|\eta| < 2.1$. Figure 2 shows the invariant mass distributions for the combined sample of the selected Λ_b^0 and $\bar{\Lambda}_b^0$ candidates obtained after their fits to the $\Lambda_b^0 \to J/\psi\Lambda^0$ and $\Lambda_b^0 \to \psi(2S)\Lambda^0$. The branching ratio of the $\Lambda_b^0 \to \psi(2S)\Lambda^0$ and $\Lambda_b^0 \to J\psi\Lambda^0$ decays has been measured to be $\Gamma(\Lambda_b^0 \to \psi(2S)\Lambda^0)/\Gamma(\Lambda_b^0 \to J\psi\Lambda^0) = 0.501 \pm 0.033(stat) \pm 0.016(syst) \pm 0.011(\mathcal{B})$. The ratio falls into the range 0.5-0.8, as found for the branching ratios of analogous B meson decays [44]. The only available theoretical expectation for the branching ratio of the two Λ_b^0 decays (0.8 ± 0.1 [45]) exceeds the measured value.

For the Υ production, ATLAS measured differential production cross sections and relative production rates for Υ(1S), Υ(2S), and Υ(3S) mesons in pp collisions at $\sqrt{s} = 7$ TeV at the LHC up to $p_T^{\Upsilon} < 70$ GeV in the rapidity interval $|y^{\Upsilon}| < 2.25$ [46]. The possible impact of the Υ spin alignment on these measured spectra is also quantified. These measurements are compatible with measurements by the CMS and LHCb collaborations. The integrated corrected cross sections multiplied by the $\Upsilon \to \mu^+\mu^-$ branching fractions within the rapidity region $|y^{\Upsilon}| < 2.25$ have been measured to be $8.01 \pm 0.02 \pm 0.36 \pm 0.31$ *nb*, $2.05 \pm 0.01 \pm 0.12 \pm 0.08$ *nb*, and $0.92 \pm 0.01 \pm 0.07 \pm 0.04$ *nb* for the Υ(1S), Υ(2S), and Υ(3S), respectively. Uncertainties correspond to statistical, systematic, and luminosity measurement effects. These cross sections are obtained assuming unpolarized production. If the production polarization is fully transverse or longitudinal with no azimuthal dependence in the helicity frame, the integrated cross sections may vary by up to (+19, -23)%, (+18, -21)%, and (+17, -19)%, respectively, for the Υ(1S), Υ(2S), and Υ(3S). If a nontrivial azimuthal dependence is considered, integrated cross sections may be significantly enhanced by a factor of 2 or more. ATLAS results compared to predictions from two theoretical approaches describing Υ production. Measurements find both the NNLO* CSM and the CEM predictions have some problems in describing the normalization and shape of the differential spectra. In particular, NNLO* dramatically underestimates the rate at high transverse momenta, where the data tend to agree better with the CEM. The inclusion of P-wave feed-down contributions in the theoretical calculation may help to improve the description. Large scale uncertainties in these predictions allow possible contributions from color-octet terms to contribute to the production rate in addition to singlet diagrams. The differential production ratios indicate that the increase in the production of higher Υ states as a function of p_T^{Υ} relative to the Υ(1S) observed previously begins to saturate at 30-40 GeV. Above ~ 40 GeV, the envelope of possible variations in the differential cross sections due to spin alignment is reduced to below ±10%. This, along with the expected reduction in feeddown contributions, results in a relatively well-controlled region in which to study quarkonium production without the dominant experimental and theoretical effects that complicate such studies at lower p_T.

CMS collaboration measured the differential production cross sections as a function of p_T for the Υ(1S), Υ(2S), and Υ(3S) at $\sqrt{s} = 7$ TeV based on a data sample corresponding to an integrated luminosity of 4.9 fb^{-1} in 2015 [47]. Figure 3 shows the $\Upsilon(n\mathrm{S})$ differential p_T cross sections times dimuon branching fractions at CMS. The analysis selects events with dimuon rapidity $|y| < 1.2$ and dimuon transverse momentum in the range $10 < p_T < 100$ GeV. Significantly improve the precision of the results in previously analyzed p_T ranges [46] [48], and also extend the maximum p_T range from 70 to 100 GeV. The measurements show a transition from an exponential to a power-law

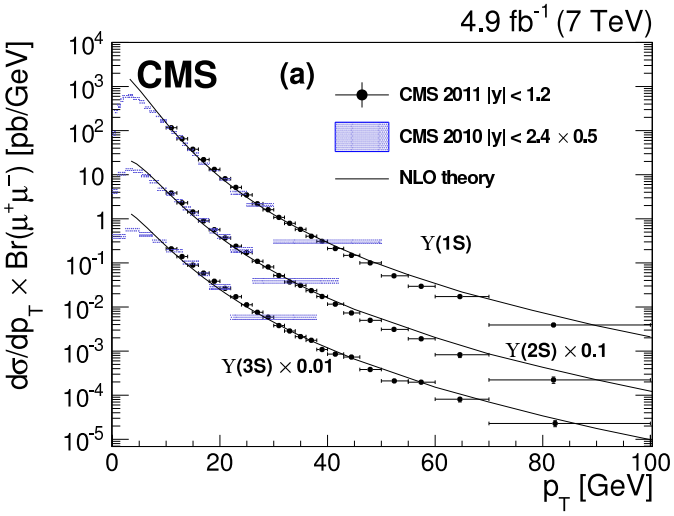

FIGURE 3. The $\Upsilon(n\mathrm{S})$ differential p_T cross sections times dimuon branching fractions for $|y| < 1.2$ by CMS [47]. The Υ(2S) and Υ(3S) measurements are scaled by 0.1 and 0.01, respectively, for display purposes.

behavior at $p_T \approx 20$ GeV for the three Υ states. Above that transition, the Υ(3S) spectrum is significantly harder than that of the Υ(1S). The ratios of the Υ(3S) and Υ(2S) differential cross sections to the Υ(1S) cross section show a rise as p_T increases at low p_T, then become flatter at higher p_T. Combined with the CMS Υ(nS) polarization results [49], the new bottomonium measurements are a formidable challenge to our theoretical understanding of the production of heavy-quark bound states.

SEARCH AND OBSERVATION FOR NEW b-STATES AND RARE DECAY

In the SM of particle physics, tree level diagrams do not contribute to flavor-changing neutral-current (FCNC) decays. However, FCNC decays may proceed through higher-order loop diagrams, and this opens up the possibility for contributions from non-SM particles. In the SM, the rare FCNC decays $B_s^0(B^0) \to \mu^+\mu^-$ have small branching fractions of $\mathcal{B}(B_s^0 \to \mu^+\mu^-) = (3.57 \pm 0.30) \times 10^{-9}$, corresponding to the decay-time integrated branching fraction, and $\mathcal{B}(B^0 \to \mu^+\mu^-) = (1.07 \pm 0.10) \times 10^{-10}$ [50] [51]. Several extensions of the SM, such as supersymmetric models with nonuniversal Higgs boson masses [52], specific models containing leptoquarks [53], and the minimal supersymmetric standard model with large tanβ [54], predict enhancements to the branching fractions for these rare decays. The decay rates can also be suppressed for specific choices of model parameters [55].

CMS searched the rare decays $B_s^0 \to \mu^+\mu^-$ and $B^0 \to \mu^+\mu^-$ in pp collisions at $\sqrt{s} = 7$ and 8 TeV [56], with data samples corresponding to integrated luminosities of 5 and 20 fb^{-1}, respectively. Fig 4 shows the weighted distribution of the dimuon invariant mass, $m_{\mu^+\mu^-}$ at CMS. An unbinned maximum-likelihood fit to the dimuon invariant mass distribution gives a branching fraction $\mathcal{B}(B_s^0 \to \mu^+\mu^-) = (3.0^{+1.0}_{-0.9}) \times 10^{-9}$, where the uncertainty includes both statistical and systematic contributions. An excess of $B_s^0 \to \mu^+\mu^-$ events with respect to background is observed with a significance of 4.3 standard deviations. For the decay $B^0 \to \mu^+\mu^-$, an upper limit of $\mathcal{B}(B^0 \to \mu^+\mu^-) < 1.1 \times 10^{-9}$ at the 95% confidence level is determined. Both results are in agreement with the expectations from the SM. The combined analysis [57] from CMS and LHCb [58], taking advantage of their full statistical power, establishes conclusively the existence of the $B_s^0 \to \mu^+\mu^-$ decay and provides an improved measurement of its branching fraction. The combined fit leads to the measurements $\mathcal{B}(B_s^0 \to \mu^+\mu^-) = (2.8^{+0.7}_{-0.6}) \times 10^{-9}$ and $\mathcal{B}(B^0 \to \mu^+\mu^-) = (3.9^{+1.6}_{-1.4}) \times 10^{-10}$, where the uncertainties include both statistical and systematic sources, the latter contributing 35% and 18% of the total uncertainty for the B_s^0 and B^0 signals, respectively. Using Wilks' theorem [59], the statistical significance in unit of standard deviations, σ, is computed to be 6.2 for the $B_s^0 \to \mu^+\mu^-$ decay mode and 3.2 for the $B^0 \to \mu^+\mu^-$ mode. The fit for the ratios of the branching fractions relative to their SM predictions yields $\mathcal{S}^{B_s^0}_{SM} = 0.76^{+0.20}_{-0.18}$ and $\mathcal{S}^{B^0}_{SM} = 3.7^{+1.6}_{-1.4}$. The measurements are compatible with the SM branching fractions of the $B_s^0 \to \mu^+\mu^-$ and $B^0 \to \mu^+\mu^-$ decays at the

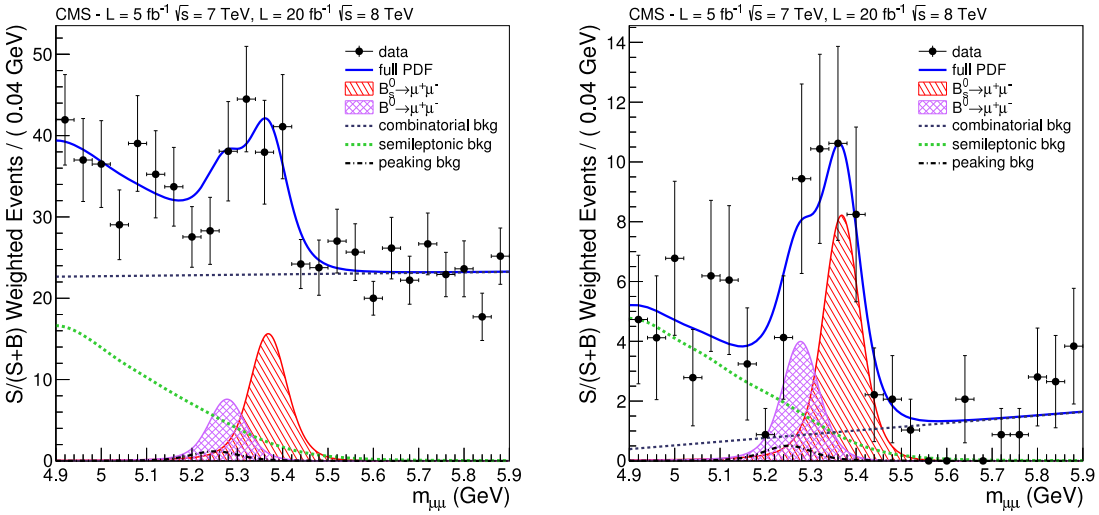

FIGURE 4. Weighted distribution of the dimuon invariant mass, $m_{\mu^+\mu^-}$ at CMS [56] by the categorized-BDT method (left) and the 1D-BDT method (right). For these plots, the individual categories are weighted with $S/(S+B)$, where S (B) is the signal (background) determined at the B_s^0 peak position. Details may be seen in the Ref. [56].

1.2σ and 2.2σ level, respectively, when computed from the one dimensional hypothesis tests. Finally, the fit for the ratio of branching fractions yields $\mathcal{R} = 0.14^{+0.08}_{-0.06}$, which is compatible with the SM at the 2.3σ level. This concludes a search that started more than three decades ago, and initiates a phase of precision measurements of the properties of this decay. It also produces three standard deviation evidence for the $B^0 \to \mu^+\mu^-$ decay.

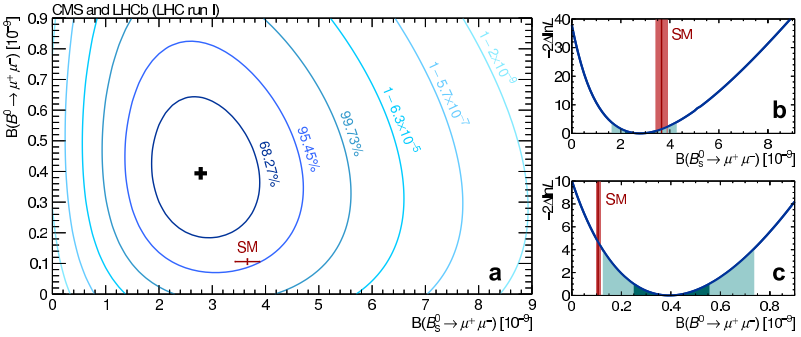

FIGURE 5. CMS and LHCb combination [57]: (left) Likelihood contours in the $\mathcal{B}(B^0 \to \mu^+\mu^-)$ versus $\mathcal{B}(B_s^0 \to \mu^+\mu^-)$ plane. (right) Variations of the test statistic $-2\Delta\ln L$ for $\mathcal{B}(B_s^0 \to \mu^+\mu^-)$ and $\mathcal{B}(B^0 \to \mu^+\mu^-)$.

The $B_c^\pm$ meson was observed by CDF and D0 experiments in the semileptonic decay and semileptonic decay, and then more decay modes have been observed by LHCb experiment in LHC. Excited states of the $B_c^\pm$ meson have not previously been observed. The spectrum and properties of the $B_c^\pm$ family are predicted by nonrelativistic potential models, perturbative QCD, and lattice calculations [60]. Measurements of the ground and excited states through fully reconstructed channels will provide tests of the predictions of these models and ultimately the opportunity to extract information on the strong interaction potential. ATLAS investigated the distribution of the mass difference $Q = m(B_c^\pm\pi^+\pi^-) - m(B_c^\pm) - 2m(\pi^\pm)$ for events with the $B_c^\pm$ meson reconstructed in its decay to $J/\psi\pi^\pm$ in pp collisions at the LHC [61]. The analysis is based on an integrated luminosity of 4.9 (19.2) fb^{-1} of pp collisions at a center-of-mass energy of 7 (8) TeV. The distributions of the mass difference Q in ATLAS 7 TeV and 8 TeV data are shown in Figure 6. A new state is observed at $Q = 288.3 \pm 3.5 \pm 4.1$ MeV (calculated as the error weighted mean of the 7 and 8 TeV mass values) corresponding to a mass of $6842 \pm 4(stat) \pm 5(syst)$ MeV. The significance of the observation is

5.2σ with the look elsewhere effect taken into account, and the local significance is 5.4σ. Within the uncertainties, the mass of the resonance corresponding to the observed structure is consistent with the predicted mass of the second S-wave state, $B_c^{\pm}(2S)$.

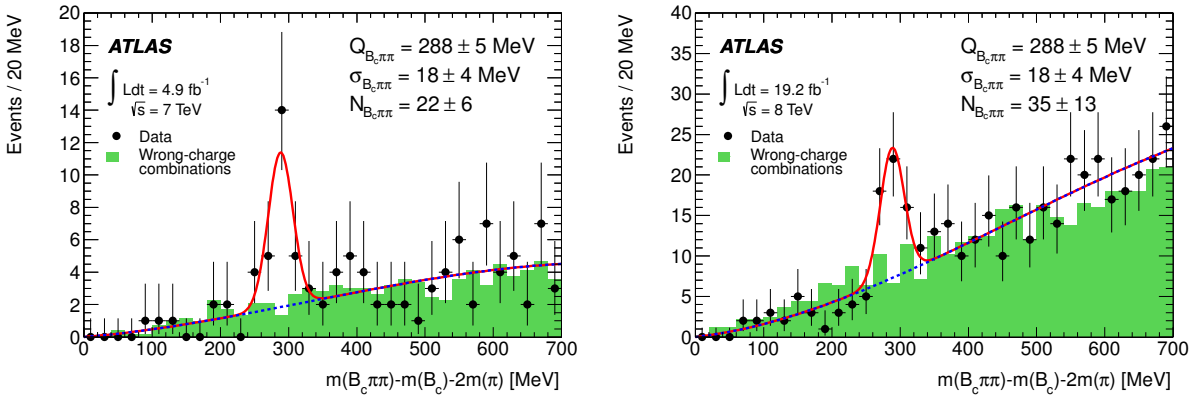

FIGURE 6. Distributions of the mass difference $Q = m(B_c^{\pm}\pi^+\pi^-) - m(B_c^{\pm}) - 2m(\pi^{\pm})$ for events with the $B_c^{\pm}$ meson reconstructed in it decay to $J/\psi\pi^{\pm}$ at 7 TeV (left) and 8 TeV (right) at ATLAS experiment [61].

For the $b\bar{b}$ system, the quarkonium states with parallel quark spins ($s = 1$) include the S-wave Υ and the P-wave χ_b states, where the latter each comprise a closely spaced triplet of $J = 0,\ 1,\ 2$ spin states: χ_{b0}, χ_{b1} and χ_{b2}. The $\chi_b(1P)$ and $\chi_b(2P)$, with spin-weighted mass barycenters of 9.90 and 10.26 GeV, respectively, can be readily produced in the radiative decays of $\Upsilon(2S)$ and $\Upsilon(3S)$. ATLAS studied the $\chi_b(nP)$ quarkonium state at $\sqrt{s} = 7$ TeV using a data sample corresponding to an integrated luminosity of 4.4 fb^{-1} [62]. The states are reconstructed through their radiative decays to $\Upsilon(1S, 2S)$ with $\Upsilon \to \mu^+\mu^-$, and the photon is reconstructed either through conversion to e^+e^- or by direct calorimetric measurement. In addition to the mass peaks corresponding to the decay modes $\Upsilon(1P, 2P) \to \Upsilon(1S)\gamma$, a new structure centered at a mass of $10.530 \pm 0.005(stat) \pm 0.009(syst)$ GeV is also observed, in both the $\Upsilon(1S)$ and $\Upsilon(2S)$ decay modes. This structure is interpreted as the $\chi_b(3P)$ system. At CMS, the production cross section ratio $\sigma(\chi_{b2}(1P))/\sigma(\chi_{b1}(1P))$ was measured with an integrated luminosity data of 20.7 fb^{-1} at $\sqrt{s} = 8$ TeV [63]. The χ_b states are detected by the radiative decays to a Υ(1S) and a photon, with the Υ(1S) decaying to two muons. Events are selected where the Υ(1S) and photon are emitted in the phase-space region defined by $|y^{\Upsilon}| < 1.5$ and $|\eta^{\gamma}| < 1.0$, in four bins of Υ(1S) p_T, spanning the range 7-40 GeV. The cross section ratio averaged over the Υ(1S) p_T range is measured to be $0.85 \pm 0.07(stat + syst) \pm 0.08$(BF), where the first uncertainty is the combination of the experimental statistical and systematic uncertainties and the second is from the uncertainty in the ratio of the χ_b branching fractions. The ratio does not show a significant dependence on the Υ(1S) p_T. This is the most precise measurement to date of the χ_{b2} and χ_{b1} relative production cross sections in hadron collisions, which complements and extends the LHCb results [64] obtained in the kinematic region $2.0 < y(\chi_b) < 4.5$, $5.0 < p_T(\Upsilon) < 25$ GeV.

For the b-baryons, CMS observed a new Ξ_b baryon in pp collisions at $\sqrt{s} = 7$ TeV with an integrated luminosity data of 5.3 fb^{-1} [65]. The new b baryon decays into $\Xi_b^-\pi^+$ (plus charge conjugates), the known Ξ_b^- baryon is reconstructed via the decay chain $\Xi_b^- \to J/\psi\Xi^- \to \mu^+\mu^-\Lambda^0\pi^-$, with $\Lambda^0 \to p\pi^-$. A peak is observed in the distribution of the difference between the mass of the $\Xi_b^-\pi^+$ system and the sum of the masses of the Ξ_b^- and π^+, with a significance exceeding 5 standard deviations. The measured $Q = M(J/\psi\Xi^-\pi^+) - M(J/\psi\Xi^-) - M(\pi)$ value is $14.84 \pm 0.74(stat) \pm 0.28(syst)$ MeV. Given the charged-pion and Ξ_b^- masses [66], the resulting b-baryon mass is $5945.0 \pm 0.7(stat) \pm 0.3(syst) \pm 2.7$ (PDG) MeV, where the last uncertainty reflects the accuracy of the Ξ_b^- mass from the Particle Data Group. While the width of the new baryon is not measured with good statistical precision, it is compatible with theoretical expectations [67]. Given its measured mass and decay mode, the new baryon is likely to be the Ξ_b^{*0}, with $J^P = 3/2^+$.

CMS observed peaking structures in the $J/\psi\phi$ mass spectrum from $B^+ \to J/\psi\phi K^+$ decays at $\sqrt{s} = 7$ TeV [68]. Picture 7 shows the distribution of mass difference $\Delta m = m(\mu^+\mu^-K^+K^-) - m(\mu^+\mu^-)$ in the CMS 7 TeV data. Two peaking structures are observed above the simulated phase-space (PS) continuum distribution shown by the dotted line. Assuming an S-wave relativistic BW lineshape for this structure above a three-body PS shape for the nonresonant background, a statistical significance of greater than 5 standard deviations is found. Adding the J/ψ mass to the

extracted Δm values, the mass and width are measured to be $m_1 = 4148.0 \pm 2.4(stat.) \pm 6.3(syst.)$ MeV and $\Gamma_1 = 28^{+15}_{-11}(stat.) \pm 19(syst.)$ MeV. The measured mass and width are consistent with the Y(4140) values reported by CDF experiment [69]. The relative branching fraction of this peaking structure with respect to the total number of $B^+ \to J/\psi\phi K^+$ events is estimated to be about 0.10, with a statistical uncertainty of about 30%. This is consistent with both the value measured by CDF of 15% ± 5% and the upper limit reported by LHCb (0.07) [70]. In addition, evidence for a second peaking structure is found in the same mass spectrum, with measured mass and width values of $m_2 = 4313.8 \pm 5.3(stat.) \pm 7.3(syst.)$ MeV and $\Gamma_2 = 38^{+30}_{-15}(stat.) \pm 16(syst.)$ MeV. Because of possible reflections from two-body decays, the statistical significance of the second structure cannot be reliably determined. The two structures are well above the threshold of open charm ($D\bar{D}$) decays and have relatively narrow widths. Conventional charmonium mesons with these masses would be expected to have larger widths and to decay predominantly into open charm pairs with small branching fractions into $J/\psi\phi$. Angular analyses of the $B^{\to} J/\psi\phi K^+$ decays would help to elucidate the nature of these structures.

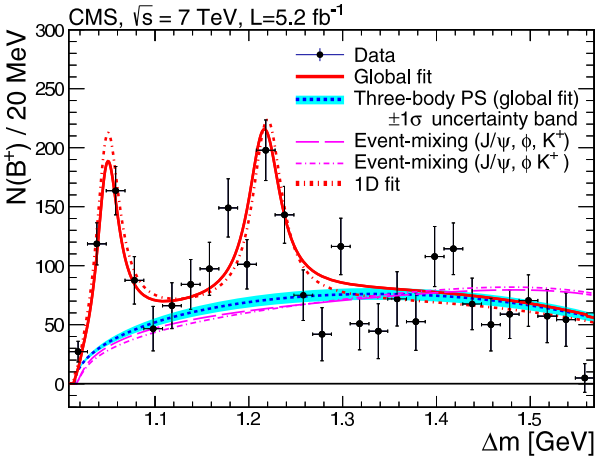

FIGURE 7. Distribution of mass difference $\Delta m = m(\mu^+\mu^- K+K-) - m(\mu^+\mu^-)$ in the CMS 7 TeV data [68]. Two peaking structures are observed above the simulated phase-space (PS) continuum distribution shown by the dotted line.

In the past decade, several unexpected charmonium states, such as the X(3872) and the Y(4260), have been discovered [71] and then confirmed [72] by the Belle and BaBar experiments. The X(3872) state has also been seen by hadron collider experiments [73]. The exotic resonance X(3872) was discovered in the final state $J/\psi\pi^+\pi^-$, and indicated that the X(3872) is produced not only through B-meson decays, but also through prompt production. A bottomonium counterpart of the X(3872), denoted as X_b, would be expected to decay through $X_b \to \Upsilon(1S)\pi^+\pi^-$. CMS searched for the exotic bottomonium state in the decay channel $X_b \to \Upsilon(1S)\pi^+\pi^-$, followed by $\Upsilon(1S) \to \mu^+\mu^-$, in pp collisions at $\sqrt{s} = 8$ TeV with an integrated luminosity data of 20.7 fb^{-1} [74]. Candidates were reconstructed from two identified muons and two additional charged tracks assumed to be pions. The search was conducted in the kinematic region $p_T(\Upsilon(1S)\pi^+\pi^-) > 13.5$ GeV and $|y(\Upsilon(1S)\pi^+\pi^-)| < 2.0$. The $\Upsilon(2S) \to \Upsilon(1S)\pi^+\pi^-$ process was used as a normalization channel, canceling many of the systematic uncertainties. Excluding the known $\Upsilon(2S)$ and $\Upsilon(1S)$ resonances, no significant excess above the background was observed for X_b masses between 10 and 11 GeV. The expected sensitivity of the analysis was greater than five standard deviations for the explored X_b mass range, if the relative signal strength is comparable to the corresponding value for the X(3872) of 6.56%. The resulting 95% confidence level upper limit on the ratio $\sigma(pp \to X_b \to \Upsilon(1S)\pi^+\pi^-)/\sigma(pp \to \Upsilon(2S) \to \Upsilon(1S)\pi^+\pi^-)$ is in the range 0.9-5.4%, depending on the assumed X_b mass. ATLAS also searched for the hidden-beauty analogue of the X(3872) by reconstructing $\pi^+\pi^-\Upsilon(1S)(\to \mu^+\mu^-)$ events in 16.2 fb^{-1} of pp collision data recorded at $\sqrt{s} = 8$ TeV [75]. No evidence for new narrow states is found for masses 10.05-10.31 GeV and 10.40-11.00 GeV. Upper limits are also set on the ratio $R = [\sigma(pp \to X_b)\mathcal{B}(X_b \to \Upsilon(1S)\pi^+\pi^-)]/[\sigma(pp \to \Upsilon(2S))\mathcal{B}(\Upsilon(2S) \to \Upsilon(1S)\pi^+\pi^-)]$, with results ranging from 0.8% to 4.0% depending on the X_b mass. The analogous ratio for the X(3872) is 6.56%: a value this large is excluded for all X_b masses considered. Separate fits to the $\Upsilon(1^3D_J)$ triplet, $\Upsilon(10860)$, and $\Upsilon(11020)$ also reveal no significant signals, and a CL_S upper limit of 0.55 is set on $\sigma(pp \to \Upsilon(1^3D_2))/\sigma(pp \to \Upsilon(2S))$.

SUMMARY

CMS and ATLAS collaborations extensively measured inclusive and exclusive B productions with LHC run-I data. CMS and ATLAS main achievements include precision measurements of B hadron production and decay properties; Observation of new B meson, baryon states and decay modes. For the rare processes, CMS observed long-sought $B_s \to \mu^+\mu^-$ decay. The results gave significant contribution to the stringent test of the Standard Model prediction, and new physics searches.

The higher energy, luminosity and pileup of coming LHC RUN-II runs will bring both challenges and new possibilities to ATLAS and CMS B physics studies.

ACKNOWLEDGMENTS

Congratulate colleagues in the CERN accelerator departments for the excellent RUN-I performance of the LHC and thank the technical and administrative staffs at CERN for their contributions to the success of the ATLAS and CMS effort. The author is supported by the Chinese Science Funds: 11061140514, 2013CB837801.

REFERENCES

[1] CMS Collaboration, *The CMS experiment at the CERN LHC*, JINST **3** (2008) S08004, doi:10.1088/1748-0221/3/08/S08004.

[2] ATLAS Collaboration, *The ATLAS Experiment at the CERN Large Hadron Collider*. JINST **3**, (2008) S08003.

[3] A. Abashian *et al*. (Belle Collaboration), Nucl. Instrum. Methods Phys. Res., Sect. A **479**, 117 (2002); also see detector section in J.Brodzicka *et al.*, Prog. Theor. Exp. Phys. **2012**, 04D001 (2012); B. Aubert, *et al*. (BABAR Collaboration), *The BABAR Detector: Upgrades, Operation and Performance*, Nucl. Inst. Meth. A **729**, 615 (2013), The BABAR Collaboration, *The BABAR Detector*, Nucl. Inst. Meth A **479**, 1 (2002).

[4] T. Aaltonen *et al*. (CDF Collaboration), Nucl. Instrum. Methods Phys. Res. Sect. A **526**, 249 (2004). V.M. Abazov *et al*. (D0 Collaboration), *The upgraded D0 detector*, Nucl. Instrum. Methods in Phys. Res. A **565**, 463 (2006).

[5] LHCb collaboration, A. A. Alves Jr. *et al.*, *The LHCb detector at the LHC*, JINST **3** (2008) S08005.

[6] CMS Collaboration, *Inclusive b-hadron production cross section with muons in pp collisions at* $\sqrt{s}$ *= 7 TeV*. J. High Energy Phys. **03** (2011) 090.

[7] CMS Collaboration, *Measurement of the cross section for production of* $b\bar{b}$ *X, decaying to muons in pp collisions at* $\sqrt{s}$ *= 7 TeV*. J. High Energy Phys. **06** (2012) 110.

[8] CMS Collaboration, *Inclusive b-jet production in pp collisions at* $\sqrt{s}$ *= 7 TeV*. J. High Energy Phys. **04** (2012) 084.

[9] ATLAS Collaboration, *Measurement of the b-hadron production cross section using decays to* $D^*\mu^-X$ *final states in pp collisions at* $\sqrt{s}$ *= 7 TeV with the ATLAS detector*. Nucl. Phys. B **864** (2012) 341.

[10] ATLAS Collaboration, *Measurement of the inclusive and dijet cross-sections of b-jets in pp collisions at* $\sqrt{s}$ *= 7 TeV with the ATLAS detector*. Eur. Phys. J. C **71** (2011) 1846.

[11] CMS Collaboration, *Measurement of the* B^+ *production cross section in pp collisions at* $\sqrt{s}$ = 7 *TeV*, Phys. Rev. Lett. **106** (2011) 112001. doi:10.1103PhysRevLett106.112001.

[12] ATLAS Collaboration, *Measurement of the differential cross-section of* B^+ *meson production in pp collisions at* $\sqrt{s}$ *= 7 TeV at ATLAS*, J. High Energy Phys. **10** (2013) 042.

[13] J. Beringer *et al.*, *Review of Particle Physics*, Phys. Rev. D **86** (2012) 010001

[14] CMS Collaboration, *Measurement of the* B^0 *production cross section in pp collisions at* $\sqrt{s}$ = 7 *TeV*, Phys. Rev. Lett. **106** (2011) 252001.

[15] CMS Collaboration, *Measurement of the* B_s^0 *production cross section with in* $B_s^0 \to \phi$ *decays pp collisions at* $\sqrt{s}$ = 7 *TeV*, Phys. Rev. D **84** (2011) 052008.

[16] ATLAS Collaboration, *Determination of the ratio of b-quark fragmentation fractions* f_s/f_d *in pp collisions at* $\sqrt{s}$ *= 7 TeV with the ATLAS detector*, arXiv:1507.08925, CERN-PH-EP-2015-165.

[17] LHCb Collaboration, *Measurement of the fragmentation fraction ratio f_s/f_d and its dependence on B meson kinematics*, J. High Energy Phys. **04** (2013) 001, arXiv:1301.5286 [hep-ex]; Y. Amhis *et al.*, Heavy Flavor Averaging Group, *Averages of b-hadron, c-hadron, and τ-lepton properties as of summer 2014* (2014), arXiv:1412.7515 [hep-ex]; CDF collaboration, *$BR(B_s^0 \to J/\psi\phi)$ measurement and extraction of the fragmentation fractions*, public CDF note 10795, 2012.

[18] CMS Collaboration, *Measurement of the ratio $\mathcal{B}(B_s^0 \to J/\psi f_0(980))/\mathcal{B}(B_s^0 \to J/\psi\phi(1020))$ at $\sqrt{s} = 7$ TeV* Submitted to Phys. Lett. B, arXiv:1501.06089.

[19] S. Stone and L. Zhang, *S-waves and the measurement of CP-violating phases in B_s decays*, Phys. Rev. D **79** (2009) 074024, doi:10.1103/PhysRevD.79.074024, arXiv:0812.2832.

[20] LHCb Collaboration, *First observation of $B_s^0 \to J/\psi f_0(980)$ decays*, Phys. Lett. B **698** (2011) 115, doi:10.1016/j.physletb.2011.03.006, arXiv:1102.0206; CDF Collaboration, *Measurement of branching ratio and B_s^0 lifetime in the decay $B_s^0 \to J/\phi f_0(980)$ at CDF*, Phys. Rev. D **84** (2011) 052012, doi:10.1103/PhysRevD.84.052012, arXiv:1106.3682; D0 Collaboration, *Measurement of the relative branching ratio of $B_s^0 \to J/\phi f_0(980)$ to $B_s^0 \to J/\psi\phi$*, Phys. Rev. D **85** (2012) 011103, doi:10.1103/PhysRevD.85.011103, arXiv:1110.4272.

[21] CMS Collaboration, *Measurement of the CP-violating weak phase ϕ_s and the decay width difference $\Delta\Gamma_s$ using the $B_s^0 \to J/\psi\phi(1020)$ decay channel in pp collisions at sqrts = 8 TeV*. arXiv:1507.07527, submitted to Phys. Lett. B.

[22] ATLAS Collaboration, *Flavor tagged time-dependent angular analysis of the $B_s^0 \to J/\psi\phi$ decay and extraction of ϕ_s and the weak phase $\Delta\Gamma_s$ in ATLAS*. Phys.Rev. D **90** (2014) 5, 052007.

[23] LHCb Collaboration, *Precision Measurement of CP Violation in $B_s^0 \to J/\psi K^+K^-$ Decays*. Phys. Rev. Lett. **114**, 041801 (2015).

[24] J. Charles *et al.*, Phys. Rev. D **84**, 033005 (2011); A. Lenz and U. Nierste, J. High Energy Phys. **06** (2007) 072; A. Badin, F. Gabbiani, and A. A. Petrov, Phys. Lett. B **653**, 230 (2007). A. Lenz and U. Nierste, *Proceedings of the CKM workshop 2010 in Warwick, Technische Universitat Munchen (Lenz) and Institut fur Theoretische Teilchenphysik (Nierste), 2010*, Reports No. TTP11-03 and TUM-HEP-792/11.

[25] CMS Collaboration, *Angular analysis and branching fraction measurement of the decay $B^0 \to K^{*0}\mu^+\mu^-$*. Phys. Lett. B **727** (2013) 77.

[26] CMS Collaboration, *Angular analysis of the decay $B^0 \to K^{*0}\mu^+\mu^-$ from pp collisions at $\sqrt{s} = 8$ TeV*. arXiv:1507.08126, submitted to Phys. Lett. B.

[27] LHCb Collaboration, *Differential branching fraction and angular analysis of the decay $B^0 \to K^{*0}\mu^+\mu^-$*. J. High Energy Phys. **08** (2013) 131.

[28] BaBar Collaboration, *Measurement of branching fractions and rate asymmetries in the rare decays $B^0 \to K^{*0}l^+l^-$*. Phys. Rev. D **86** (2012) 032012.

[29] CDF Collaboration, *Measurement of the angular distributions in the decays $B^0 \to K^{*0}\mu^+\mu^-$ at CDF.* Phys. Rev. Lett. **108** (2012) 081807; CDF Collaboration, *Measurement of the forward-backward asymmetry in the $B^0 \to K^{*0}\mu^+\mu^-$ decay and first observation of the $B_s^0 \to \phi\mu^+\mu^-$ decay.* Phys. Rev. Lett. **106** (2011) 161801.

[30] Belle Collaboration, *Measurement of the differential branching fraction and the forward-backward asymmetry for $B^0 \to K^*l^+l^-$*. Phys. Rev. Lett. **103** (2009) 171801.

[31] A.Khodjamirian, T.Mannel, A.A.Pivovarov, and Y.-M. Wang, *Charm-loop effect in $B \to K^{(*)}l^+l^-$ and $B \to K^*\gamma$*, J. High Energy Phys. **09** (2010) 089; A.Khodjamirian, T.Mannel, and Y.-M. Wang, *$B \to Kl^+l^-$ decay at large hadronic recoil*, J. High Energy Phys. **02** (2013) 010.

[32] R. R. Horgan, Z. Liu, S.Meinel, and M.Wingate, *Lattice QCD calculation of form factors describing the rare decays $B \to K^*l^+l^-$ and $B_s \to \phi l^+l^-$,* Phys. Rev. D **89** (2014), 094501.

[33] CMS Collaboration, *Measurement of the ratio of the production cross sections times branching fractions of $B_c^\pm \to J/\psi\pi^\pm$ and $B^\pm \to J/\psi K^\pm$ and $\mathcal{B}(B^\pm \to J/\psi\pi^\pm\pi^\pm\pi^\mp)/\mathcal{B}(B_c^\pm \to J/\psi\pi^\pm)$ in pp collisions at $\sqrt{s} = 7$ TeV*, J. High Energy Phys. **01** (2015) 063.

[34] LHCb Collaboration, *Measurement of B_c^+ production and mass with the $B_c^+ \to J/\psi\pi^+$ decay*, Phys. Rev. Lett. **109** (2012) 232001, doi:10.1103/PhysRevLett.109.232001, arXiv:1209.5634.

[35] LHCb Collaboration, *First observation of the decay $B_c^+ \to J/\psi\pi^+\pi^+\pi^-$*, Phys. Rev. Lett. **108** (2012) 251802, doi:10.1103/PhysRevLett.108.251802, arXiv:1204.0079.

[36] A. Rakitin and S. Koshkavev, *Hadronic B_c decays as a test of B_c cross section*, Phys.Rev. D **81** (2010) 014005.

[37] A. K. Likhoded and A. V. Luchinsky, *Light hadron production in $B_c \to J/\psi + X$ decays.*, Phys. Rev. D **81** (2010) 014015.

[38] CMS Collaboration, *Measurement of the Λ_b cross section and the $\bar{\Lambda}_b$ to Λ_b ratio with $J/\psi\Lambda$ decays in pp collisions at $\sqrt{s}$ = 7 TeV*. Phys. Lett. B **714** (2012) 136.

[39] ATLAS Collaboration, *Measurement of the parity-violating asymmetry parameter α_b and the helicity amplitudes for the decay $\Lambda_b^0 \to J/\psi\Lambda^0$ with the ATLAS detector*. Phys. Rev. D **89**, 092009 (2014).

[40] LHCb Collaboration, *Measurements of the $\Lambda_b^0 \to J/\psi\Lambda$ decay amplitudes and the Λ_b^0 polarisation in pp collisions at $\sqrt{s}$ = 7 TeV*. Phys. Lett. B **724**, 27(2013).

[41] C.-H. Chou, H.-H. Shih, S.-C. Lee, and H.-n. Li, Phys. Rev. D **65**, 074030 (2002).

[42] O. Leitner, Z. Ajaltouni, and E. Conte, Nucl. Phys. A **755**, 435 (2005); Z. Ajaltouni, E. Conte, and O. Leitner, Phys. Lett. B **614**, 165 (2005).

[43] ATLAS Collaboration, *Measurement of the branching ratio $\Gamma(\Lambda_b^0 \to \psi(2S)\Lambda^0)/\Gamma(\Lambda_b^0 \to J\psi\Lambda^0)$ with the ATLAS detector*. Phys.Lett. B **751** (2015) 63-80.

[44] K. A. Olive *et al*. (Particle Data Group), Chin. Phys. C **38** (2014) 090001.

[45] T. Gutsche *et al*., Phys. Rev. D **88** (2013) 114018, arXiv:1309.7879 [hep-ph]. The uncertainty of the branching fraction ratio $\Gamma(\Lambda_b^0 \to \psi(2S)\Lambda^0)/\Gamma(\Lambda_b^0 \to J\psi\Lambda^0)$ has been provided privately by the authors.

[46] ATLAS Collaboration, *Measurement of Upsilon production in 7 TeV pp collisions at ATLAS*. Phys. Rev. D **87** (2013) 052004.

[47] CMS Collaboration, *Measurements of the Υ(1S), Υ(2S), and Υ(3S) differential cross sections in pp collisions at $\sqrt{s}$ = 7 TeV*. Phys. Lett. B **749** (2015) 14-34.

[48] CMS Collaboration, *Measurement of the inclusive Υ production cross section in pp collisions at $\sqrt{s}$ = 7 TeV*, Phys. Rev. D **83** (2011) 112004; CMS Collaboration, *Measurement of the Υ(1S), Υ(2S), and Υ(3S) cross sections in pp collisions at Υ = 7 TeV*, Phys. Lett. B **727** (2013) 101.

[49] CMS Collaboration, *Measurement of the Υ(1S), Υ(2S) and Υ(3S) polarizations in pp collisions at $\sqrt{s}$ = 7 TeV*, Phys. Rev. Lett. **110** (2013) 081802.

[50] A. J. Buras, J. Girrbach, D. Guadagnoli, and G. Isidori, Eur. Phys. J. C **72**, 2172 (2012).

[51] K. De Bruyn, R. Fleischer, R. Knegjens, P. Koppenburg, M. Merk, A. Pellegrino, and N. Tuning, Phys. Rev. Lett. **109**, 041801 (2012).

[52] J. R. Ellis, K. A. Olive, Y. Santoso, and V. C. Spanos, J. High Energy Phys. **05** (2006) 063.

[53] S. Davidson and S. Descotes-Genon, J. High Energy Phys. **11** (2010) 073.

[54] S. R. Choudhury, A. S. Cornell, N. Gaur, and G. C. Joshi, Int. J. Mod. Phys. A **21**, 2617 (2006); J. K. Parry, Nucl. Phys. B **760**, 38 (2007).

[55] J. R. Ellis, J. S. Lee, and A. Pilaftsis, Phys. Rev. D **76**, 115011 (2007).

[56] CMS Collaboration, *Measurement of the $B_s^0 \to \mu^+\mu^-$ Branching Fraction and Search for $B^0 \to \mu^+\mu^-$ with the CMS Experiment*. Phys. Rev. Lett. **111**, 101804 (2013).

[57] CMS and LHCb collaborations, *Observation of the rare $B_s^0 \to \mu^+\mu^-$ decay from the combined analysis of CMS and LHCb data*. Nature **522** (2015) 68.

[58] LHCb Collaboration, Aaij, R. *et al*. *First evidence for the decay $B_s^0 \to \mu^+\mu^-$*. Phys. Rev. Lett. **110**, 021801 (2013); LHCb Collaboration, Aaij, R. *et al*. *Measurement of the $B_s^0 \to \mu^+\mu^-$ branching fraction and search for $B^0 \to \mu^+\mu^-$ decays at the LHCb experiment*. Phys. Rev. Lett. **111**, 101805 (2013).

[59] Wilks, S. S. *The large-sample distribution of the likelihood ratio for testing composite hypotheses*. Ann. Math. Stat. **9**, 60-62 (1938).

[60] S. Narison, Phys. Lett. B **210**, 238 (1988); W. Kwong and J. L. Rosner, Phys. Rev. D **44**, 212 (1991); Y.-Q. Chen and Y.-P. Kuang, Phys. Rev. D **46**, 1165 (1992); P. Jain and H. J. Munczek, Phys. Rev. D **48**, 5403 (1993); L. P. Fulcher, Z. Chen, and K. C. Yeong, Phys. Rev. D **47**, 4122 (1993); E. J. Eichten and C. Quigg, Phys. Rev. D **49**, 5845 (1994); S. S. Gershtein, V. V. Kiselev, A. K. Likhoded, and A. V. Tkabladze, Phys. Rev. D **51**, 3613 (1995); L. Motyka and K. Zalewski, Eur. Phys. J. C **4**, 107 (1998);M. Baldicchi and G. M. Prosperi, Phys. Rev. D **62**, 114024 (2000); N. Brambilla, A. Pineda, J. Soto, and A. Vairo, Phys. Rev. D **63**, 014023 (2000); A. Pineda and A. Vairo, Phys. Rev. D **63**, 054007 (2001); D. Ebert, R. N. Faustov, and V. O. Galkin, Phys. Rev. D **67**, 014027 (2003); S. Godfrey, Phys. Rev. D **70**, 054017 (2004); A. A. Penin, A. Pineda, V. A. Smirnov, and M. Steinhauser, Phys. Lett. B **593**, 124 (2004); S. Ikhdair and R. Sever, Int. J. Mod. Phys. A **20**, 4035 (2005); I. Allison, C. Davies, A. Gray, A. Kronfeld, P. Mackenzie, and J. Simone (HPQCD, Fermilab Lattice, and UKQCD Collaborations), Phys. Rev. Lett. **94**, 172001 (2005); D. Ebert, R. N. Faustov, and V. O. Galkin, Eur. Phys. J. C **71**, 1825 (2011); R. J. Dowdall, C. T. H. Davies, T. C. Hammant, and R. R. Horgan, Phys. Rev. D **86**, 094510 (2012).

[61] ATLAS Collaboration, *Observation of an Excited $B_c^{\pm}$ Meson State with the ATLAS Detector*. Phys. Rev. Lett. **113**, 212004 (2014).

[62] ATLAS Collaboration, *Observation of a New χ_b State in Radiative Transitions to $\Upsilon(1S)$ and $\Upsilon(2S)$ at ATLAS*. Phys. Rev. Lett. **108**, 152001 (2012)

[63] CMS Collaboration, *Measurement of the production cross section ratio $\sigma(\chi_{b2}(1P))/\sigma(\chi_{b1}(1P))$ in pp collisions at $\sqrt{s}$ = 8 TeV*. Phys. Lett. B **743** (2015) 383-402.

[64] LHCb Collaboration, *Measurement of the $\chi_b(3P)$ mass and of the relative rate of $\chi_{b1}(1P)$ and $\chi_{b2}(1P)$ production*, J. High Energy Phys. **10** (2014) 88.

[65] CMS Collaboration, *Observation of a New Ξ_b Baryon*. Phys. Rev. Lett. **108**, 252002 (2012).

[66] K. Nakamura *et al.*, J. Phys. G **37**, 075021 (2010).

[67] W. Detmold, C.-J. D. Lin, and S. Meinel, *Calculation of the heavy-hadron axial couplings g_1, g_2, and g_3 using lattice QCD*. Phys. Rev. D **85** 114508, 2012.

[68] CMS Collaboration, *Observation of a peaking structure in the $J/\psi\phi$ mass spectrum from $B^{\pm} \to J/\psi\phi K^{\pm}$*. Phys. Lett. B**734** (2014) 261-281.

[69] CDF Collaboration, *Evidence for a narrow near-threshold structure in the $J/\psi\phi$ mass spectrum in $B^+ \to J/\psi\phi K+$ decays*, Phys. Rev. Lett. **102** (2009),

[70] LHCb Collaboration, *Search for the X(4140)state in $B^+ \to J/\psi\phi K^+$ decays*, Phys. Rev. D **85** (2012).

[71] Belle Collaboration, *Observation of a narrow charmonium-like state in exclusive $B^{\pm} \to K^{\pm}\pi^+\pi^- J/\psi$ decays*, Phys. Rev. Lett. **91** (2003) 262001; BaBar Collaboration, *Observation of a broad structure in the $\pi^+\pi^- J/\psi$ mass spectrum around* 4.26 GeV/c^2, Phys. Rev. Lett. **95** (2005) 142001.

[72] BaBar Collaboration, *Study of the $B \to J/\psi K^-\pi^+\pi^-$ decay and measurement of the $B \to X(3872)K^-$ branching fraction*, Phys. Rev. D **71** (2005) 071103; Belle Collaboration, *Measurement of $e^+e^- \to \pi^+\pi^- J/\psi$ cross-section via initial state radiation at Belle*, Phys. Rev. Lett. **99** (2007) 182004.

[73] CDF Collaboration, *Observation of the narrow state $X(3872) \to J/\psi\pi^+\pi^-$ in $p\bar{p}$ collisions at $\sqrt{s}$ = 1.96 TeV*, Phys. Rev. Lett. **93** (2004) 072001; D0 Collaboration, *Observation and properties of the X(3872) decaying to $J/\psi\pi^+\pi^-$ in $p\bar{p}$ collisions at $\sqrt{s}$ = 1.96 TeV*, Phys. Rev. Lett. **93** (2004) 162002; LHCb Collaboration, *Observation of X(3872) production in pp collisions at $\sqrt{s}$ = 7 TeV*, Eur. Phys. J. C **72** (2012) 1972; CMS Collaboration, *Measurement of the X(3872) production cross section via decays to $J/\psi\pi^+\pi-$ in pp collisions at $\sqrt{s}$ = 7 TeV*, J. High Energy Phys. **1304** (2013) 154.

[74] CMS Collaboration, *Search for a new bottomonium state decaying to $\Upsilon(1S) \to \pi^+\pi^-$ in pp collisions at $\sqrt{s}$ = 8 TeV*. Phys. Lett. B **727** (2013) 57.

[75] ATLAS Collaboration, *Search for the X_b and other hidden-beauty states in the $\pi^+\pi^-\Upsilon(1S)$ channel at ATLAS*. Phys. Lett. B **740** (2015) 199-217.

Heavy Flavour physics: parallel talks

Proceedings of the LHCP2015 Conference, St. Petersburg, Russia, August 31 - September 5, 2015

Editors: V.T. Kim and D.E. Sosnov

ATLAS Heavy Flavor Production and Decay Properties

LIDIA SMIRNOVA[1,2]

[1]*Lomonosov Moscow State University (MSU), Faculty of Physics, Leninskie Gory, Moscow 119991, Russia*
[2]*Skobeltsyn Institute of Nuclear Physics (SINP MSU), 1(2), Leninskie gory, GSP-1, Moscow 119991, Russia*

Lidia.Smirnova@cern.ch

On behalf of the ATLAS Collaboration

Abstract. First measurements of non-prompt J/ψ fraction in pp collisions at $\sqrt{s}$ = 13 TeV and new results from RUN 1 data analysis are presented for heavy flavor production and decays. RUN 1 results include observation and measurement of the Z+J/ψ associated production, f_s/f_d measurements and the branching ratio measurement for Λ_b^0 decays to ψ(2S) +Λ^0 and J/ψ +Λ^0.

INTRODUCTION

The studies of heavy flavor production and decay properties at the ATLAS experiment [1] brought many important results, especially concerning measurements at the highest transverse momentum of produced heavy particles. The year 2015 has opened a new stage of studies with a successful start of Large Hadron Collider operation at $\sqrt{s}$ = 13 TeV of proton beam collisions. The first results with data collected by the ATLAS detector at the new energy for the lightest quarkonium state J/ψ production [2] are presented in this paper.

There are three new results from data collected in RUN 1, including observation and measurements of the associated J/ψ and Z boson production in pp collisions at $\sqrt{s}$ = 8 TeV [3], determination of the ration of b-quark fragmentation fractions f_s/f_d at $\sqrt{s}$ = 7 TeV [4] and measurement of the branching ratio $\Gamma\left(\Lambda_b^0 \to \psi(2S)\Lambda^0\right)/\Gamma\left(\Lambda_b^0 \to J/\psi\Lambda^0\right)$ [5].

EXPERIMENTAL RESULTS

Non-prompt J/ψ fraction in pp collisions at $\sqrt{s}$ = 13 TeV

The fraction of J/ψ mesons produced in pp collisions at energy 13 TeV that are products of b-hadron decays (non-prompt J/ψ) is measured with the total integrated luminosity of approximately 6.4 pb^{-1} [2]. The fraction is defined as the ratio of the number of J/ψ mesons produced in these decays to the total number produced. The non-prompt J/ψ are distinguished from the prompt ones by a longer decay time due to the primary b-hadron decay. This time is estimated from measurement of pseudo-proper decay time τ for di-muon vertexes. The calculations make use of the transverse momentum p_{T} of the two muons and the transverse decay length L_{xy} of the di-muon vertex, following the formula $\tau = L_{xy} m_{J/\psi}(\mathrm{PDG})/p_{\mathrm{T}}$, where the world average value [6] for the J/ψ mass $m_{J/\psi}$(PDG) is used. An unweighted two-dimensional unbinned maximum likelihood fit to the data in the di-muon invariant mass ($2.65 < m(\mu^+\mu^-) < 3.55$ GeV) and pseudo-proper decay time ($-5.0 < \tau < 15.0$ ps) is performed. It allows both background discrimination and separation of the prompt and non-prompt J/ψ mesons. The yields of non-prompt and prompt J/ψ production are extracted from the fit and the fraction of non-prompt J/ψ is calculated. Results for this fraction as a function of di-muon p_{T} and rapidity $|y|$ are presented in Fig. 1(a). This value increases from 0.25 to 0.65 within the p_{T} range from 8 GeV to 40 GeV and does not show significant dependence on rapidity within the precision of the measurement.

The centre-of-mass energy dependence of the fraction is shown in Fig. 1(b) for the J/ψ rapidity interval $|y| < 0.75$ with ATLAS results and CDF measurements for $|y| < 0.6$. The difference of intervals can be ignored as no rapidity dependence of the measured fraction has been observed. Finally, no significant change in the non-prompt fraction is

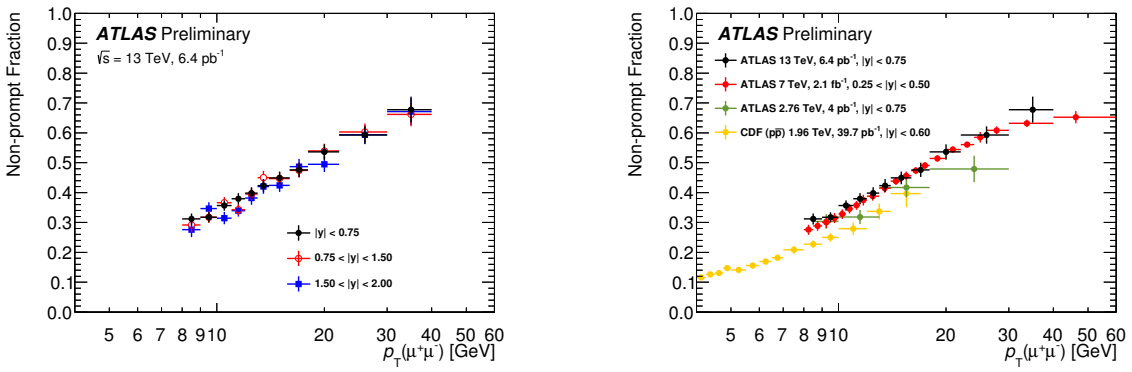

(a) (b)

FIGURE 1. Measured non-prompt J/ψ production fraction as a function of J/ψ p_{T} in three intervals of J/ψ rapidity (a); Non-prompt differential J/ψ production fraction for the most central rapidity interval $|y| < 0.75$ in comparison with similar measurements at lower energies (b) [2].

observed between the 7 and 13 TeV measurements, contrary to the significant difference between 7 TeV and lower energy measurements.

Z+J/ψ associated production

The production of a Z boson in association with a J/ψ meson in pp collisions allows for the studies of multiple parton scattering. First observation and measurements of the associated Z+J/ψ prompt and non-prompt productions are made with ATLAS detector in pp collisions at $\sqrt{s} = 8$ TeV and total integrated luminosity of 20.3 fb^{-1} [3]. An inclusive Z sample with the $\mu^+\mu^-$ and e^+e^- decay modes and J/ψ decaying to $\mu^+\mu^-$ indicates 290 candidate events for the associated production after the following cuts:

- Z decay leptons $p_{\mathrm{T}} > 25$ GeV (trigger lepton) and $p_{\mathrm{T}} > 15$ GeV (sub-leading lepton)
- their pseudorapidities $|\eta| < 2.5$
- J/ψ candidate invariant mass $2.6 \leq m_{J/\psi} \leq 3.6$ GeV,
- J/ψ p_{T} in range between 8 GeV and 100 GeV and its rapidity $|y| < 2.1$.

The associated Z+J/ψ production fractions relative to the Z inclusive production cross section in this phase volume is measured to be $(36.8 \pm 6.7 \pm 2.5) \cdot 10^{-7}$ and $(65.8 \pm 9.2 \pm 4.2) \cdot 10^{-7}$ for prompt and non-prompt produced J/ψ respectively. The azimuthal angle distributions between the Z boson and the prompt and non-prompt J/ψ mesons are presented in Fig. 2. The estimation of double parton scattering (DPS) contribution is calculated using parameter $\sigma_{\mathrm{eff}} = 15 \pm 3(\mathrm{stat.})^{+5}_{-3}(\mathrm{syst.})$ mb from ATLAS measurement of W + 2-jet events [7]. The DPS fraction is $(29 \pm 9)\%$ for the Z + prompt J/ψ signal and $(8 \pm 2)\%$ for the non-prompt signal. The pileup contribution is found to be two times smaller than DPS. Both are shown in Fig. 2 and used for estimation of single parton scattering (SPS) contribution to associated production.

The lowest bin in the azimuthal angle distribution in Fig. 2(a) is used for an independent calculation of the limit on maximum rate of the DPS contributions to the Z + prompt J/ψ production signal. This result is shown in Fig. 3. The lower limit on σ_{eff} is calculated to be 5.3 mb (3.7 mb) at 68% (95%) confidence level. This result is presented in Fig. 3(b) in comparison with earlier measurements.

The measured SPS Z + prompt J/ψ production rates are compared to theoretical predictions at LO and NLO for the colour-singlet and colour-octet prompt production processes. The sum of the rates for these processes is found to be lower than the measured values by factors from 2 to 5 within the J/ψ p_{T} range studied. The comparison of these results is shown in Fig. 4.

Measurement of the b-quark fragmentation fractions ratio f_s/f_d

The ratio of b-quark fragmentation fractions f_s/f_d is determined by the ATLAS experiment with an integrated luminosity of 2.47 fb^{-1} for pp collisions at $\sqrt{s} = 7$ TeV [4]. The exclusive decays $B_s \to J/\psi\phi$ and $B^0_d \to J/\psi K^{*0}$ are

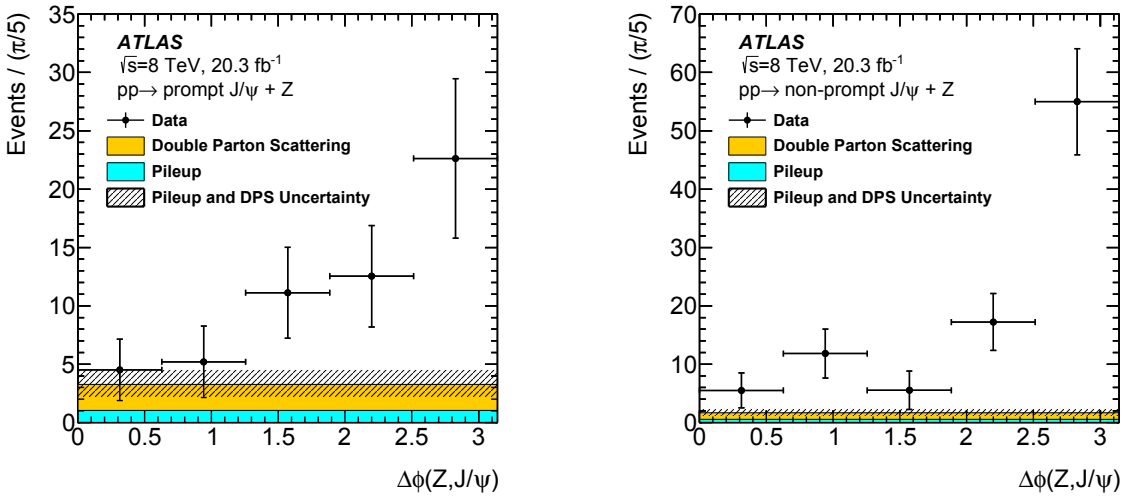

(a) (b)

FIGURE 2. Azimuthal angle between the Z boson and the prompt J/ψ meson (a) and such angle between the Z boson and the non-prompt J/ψ meson (b) distributions. The estimated DPS (yellow band) and pileup (cyan band) contributions to the data are overlaid [3].

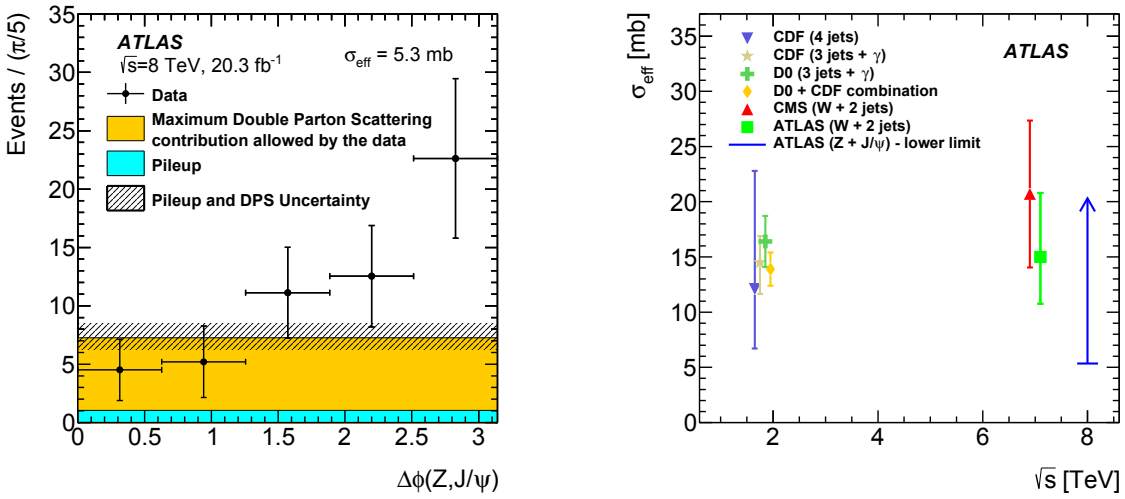

(a) (b)

FIGURE 3. Azimuthal angle between the Z boson and the prompt J/ψ meson and maximum DPS contribution (yellow band) (a); comparison of the σ_{eff} parameter value estimation with other measurements (b).

used for the analysis. The signal yields are found to be 6640 ± 100(stat) ± 220(syst) for the $B_s \to J/\psi\phi$ channel and 36290±320(stat)±650(syst) for $B_d^0 \to J/\psi K^{*0}$. The quantity $(f_s/f_d)\cdot(\text{BR}(B_s^0 \to J/\psi\phi)/\text{BR}(B_d^0 \to J\psi K^{*0}))$ is estimated to be 0.199 ± 0.004(stat) ± 0.010(syst). The ratio f_s/f_d is measured to be 0.240 ± 0.004(stat) ± 0.013(syst) ± 0.017(th) with the use of perturbative QCD predictions for branching ratios [8].

To investigate the p_{T} and η dependences of f_s/f_d the ratio is measured in six p_{T} bins in the range from 8 GeV to 50 GeV and four bins in η for $|\eta| < 2.5$. The results for different p_{T} are shown in Fig. 5(a) in comparison with the results of other experiments. No significant dependence on p_{T} or η is observed. The f_s/f_d ratio from the ATLAS measurement is compared with the LHCb [9], LEP [10] and CDF [11] results in Fig. 5(b). The ATLAS result is in agreement with the shown experiments.

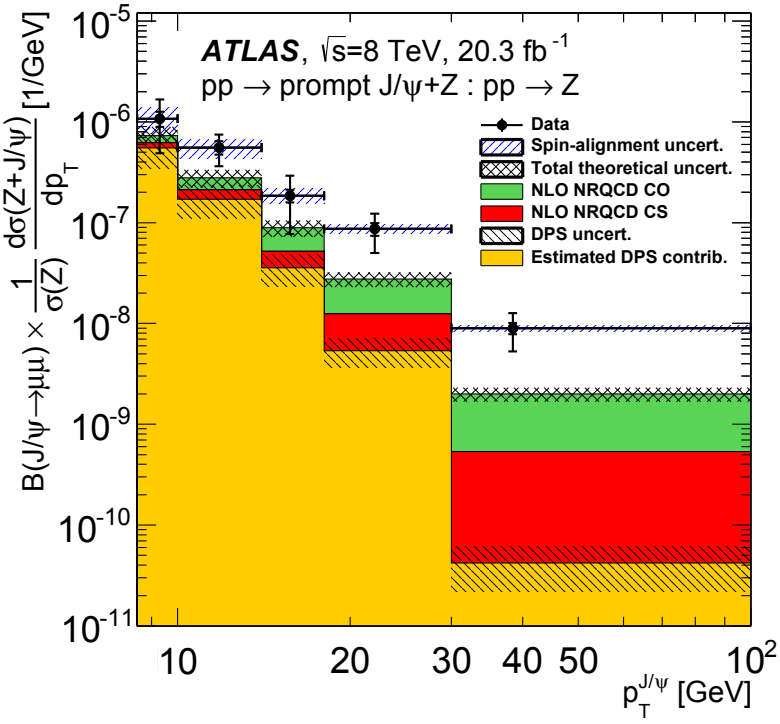

FIGURE 4. Production cross-section of prompt J/ψ in association with a Z boson as a function of p_{T} of the prompt J/ψ, normalized to the inclusive Z cross sections. Overlaid on the measurement is the contribution to the total signal originating from double parton scattering (DPS) interactions. Theoretical predictions at NLO accuracy for the single parton scattering (SPS) contributions from color-singlet (CS) and color-octet (CO) processes are added to the DPS estimate and presented in comparison to the data as solid line [3].

Measurement of the branching fractions ratio $\Gamma(\Lambda_b^0 \to \psi(2S)\Lambda^0)/\Gamma(\Lambda_b^0 \to J/\psi\Lambda^0)$

The Large Hadron Collider provides a possibility for the extensive studies of the Λ_b^0 barion properties. The observation of the $\Lambda_b^0 \to \psi(2S)\Lambda^0$ decay and measurement of the branching ratio of the $\Lambda_b^0 \to \psi(2S)\Lambda^0$ and $\Lambda_b^0 \to J\psi\Lambda^0$ decays are performed with the ATLAS detector in pp collisions at $\sqrt{s} = 8$ TeV using the total integrated luminosity of 20.6 fb^{-1} [5]. The Λ_b^0 barions are reconstructed with transverse momentum $p_{\mathrm{T}} > 10$ GeV and $|\eta| < 2.1$. The invariant mass distributions $m(J/\psi\Lambda^0)$ and $m(\psi(2S)\Lambda^0)$, calculated using tracks from Λ_b^0 topology fit, for combined sample of the Λ_b^0 and $\overline{\Lambda_b^0}$ barions are presented in Fig. 6. The invariant mass distributions $m(J/\psi K_{\mathrm{S}}^0)$ and $m(\psi(2S)K_{\mathrm{S}}^0)$ are shown also in the figures. The branching ratio of the two Λ_b^0 decays is calculated as

$$\frac{\Gamma(\Lambda_b^0 \to \psi(2S)\Lambda^0)}{\Gamma(\Lambda_b^0 \to J/\psi\Lambda^0)} = \frac{N_{\mathrm{cor}}(\Lambda_b^0 \to \psi(2S)(\mu^+\mu^-)\Lambda^0)}{N_{\mathrm{cor}}(\Lambda_b^0 \to J/\psi(\mu^+\mu^-)\Lambda^0)} \cdot \frac{\mathrm{BR}(J/\psi \to \ell\ell)}{\mathrm{BR}(\psi(2S) \to \ell\ell)},$$

where N_{cor} denotes the number of corresponding signal events after all the necessary corrections.

The BR values are used from [6]. The measured branching ratio of the two Λ_b^0 decays is $\Gamma(\Lambda_b^0 \to \psi(2S)\Lambda^0)/\Gamma(\Lambda_b^0 \to J/\psi\Lambda^0) = 0.501 \pm 0.033(\mathrm{stat}) \pm 0.016(\mathrm{syst}) \pm 0.011(\mathrm{BR})$. The measured ratio lies within the range $0.5 - 0.8$ found for the BR ratio of analogous B meson decays [6]. The only available theoretical prediction for this ratio 0.8 ± 0.1 [12] exceeds the measured value.

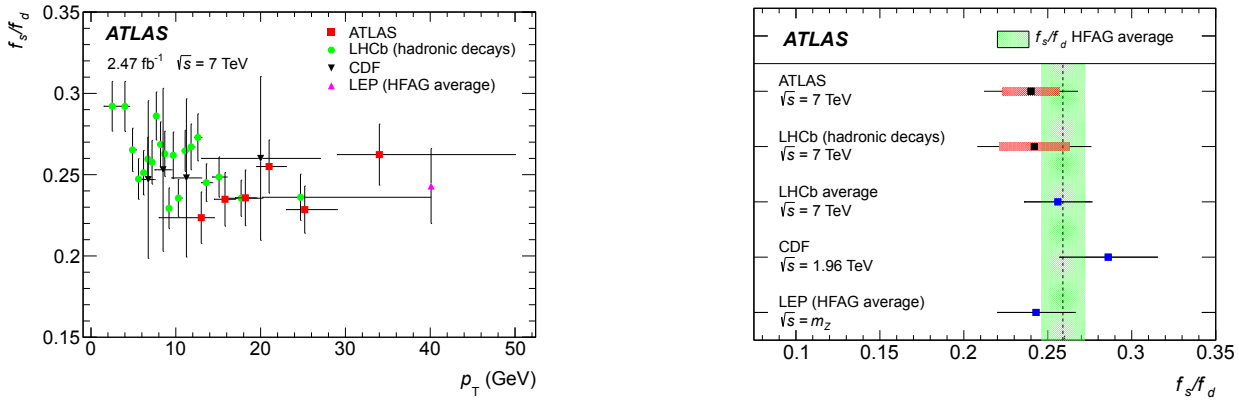

(a) (b)

FIGURE 5. The f_s/f_d ratio dependence on B-meson p_{T} (a) and the ATLAS f_s/f_d ratio in comparison with LHCb [9], LEP [10] average and CDF [11] results (b) [4].

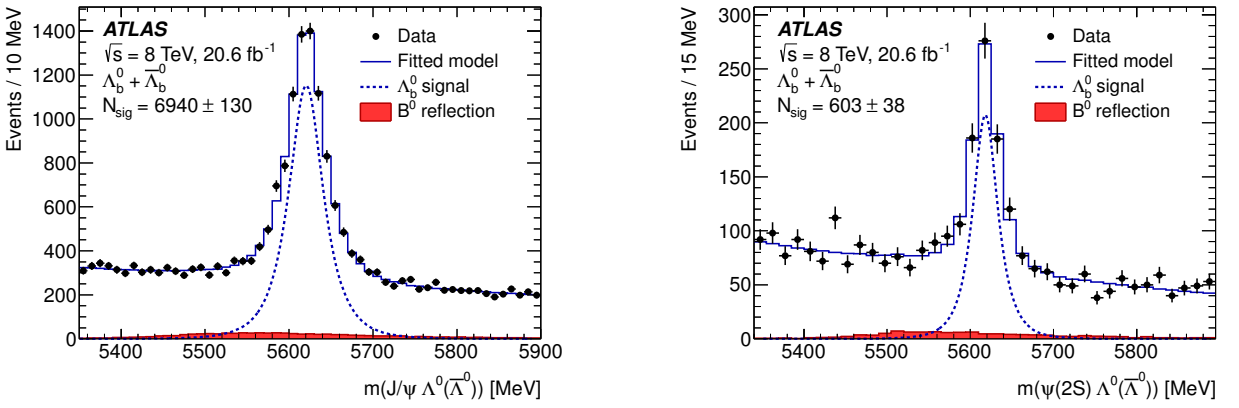

(a) (b)

FIGURE 6. The invariant mass distributions $m(J/\psi\Lambda^0)$ (a) and $m(\psi(2S)\Lambda^0)$ (b) for the combined sample of the selected Λ_b^0 and $\overline{\Lambda_b^0}$ candidates with B^0 decays reflections [5].

SUMMARY

The ATLAS experiment has successfully started the operation in RUN 2 at $\sqrt{s}$ = 13 TeV. The first RUN 2 measurements of the J/ψ non-prompt production are presented. New results for the heavy flavor production and decay properties with RUN 1 data are shown. They expand the set of results for B, B_s, B_c and Λ_b^0 hadrons in wide p_{T} regions from the ATLAS experiment presented on the collaboration website https://twiki.cern.ch/twiki/bin/view/AtlasPublic/BPhysPublicResults.

ACKNOWLEDGMENTS

Participation in the conference was partly supported by the Russian Foundation for Basic Research, grant 15-02-08133.

REFERENCES

[1] ATLAS Collaboration, *The ATLAS Experiment at the CERN Large Hadron Collider*, JINST **3** (2008) S08003.

[2] ATLAS Collaboration, *Measurement of the differential non-prompt J/ψ production fraction in $\sqrt{s}$ = 13 TeV pp collisions at the ATLAS experiment*, Tech. Rep. ATLAS-CONF-2015-030, CERN, Geneva, Jul, 2015.

[3] ATLAS Collaboration, *Observation and measurements of the production of prompt and non-prompt J/ψ mesons in association with a Z boson in pp collisions at $\sqrt{s}$ = 8 TeV with the ATLAS detector*, Eur. Phys. J. **C75** (2015) 229, arXiv:1412.6428 [hep-ex].

[4] ATLAS Collaboration, *Determination of the ratio of b-quark fragmentation fractions f_s/f_d in pp collisions at $\sqrt{s}$ = 7 TeV with the ATLAS detector*, arXiv:1507.08925 [hep-ex].

[5] ATLAS Collaboration, *Measurement of the branching ratio $\Gamma(\Lambda_b^0 \to \psi(2S)\Lambda^0)/\Gamma(\Lambda_b^0 \to J/\psi\Lambda^0)$ with the ATLAS detector*, Phys. Lett. **B751** (2015) 63–80, arXiv:1507.08202 [hep-ex].

[6] Particle Data Group Collaboration, K. A. Olive et al., *Review of Particle Physics*, Chin. Phys. **C38** (2014) 090001.

[7] ATLAS Collaboration, *Measurement of hard double-parton interactions in $W(\to l\nu)$+ 2 jet events at $\sqrt{s}$=7 TeV with the ATLAS detector*, New J. Phys. **15** (2013) 033038, arXiv:1301.6872 [hep-ex].

[8] X. Liu, W. Wang, and Y. Xie, *Penguin pollution in $B \to J/\psi V$ decays and impact on the extraction of the $B_s - \bar{B}_s$ mixing phase*, Phys. Rev. **D89** no. 9, (2014) 094010, arXiv:1309.0313 [hep-ph].

[9] LHCb Collaboration, R. Aaij et al., *Measurement of the fragmentation fraction ratio f_s/f_d and its dependence on B meson kinematics*, JHEP **04** (2013) 001, arXiv:1301.5286 [hep-ex].

[10] Heavy Flavor Averaging Group (HFAG) Collaboration, Y. Amhis et al., *Averages of b-hadron, c-hadron, and τ-lepton properties as of summer 2014*, arXiv:1412.7515 [hep-ex].

[11] CDF Collaboration, T. Aaltonen et al., *BR($B_s^0 \to J/\psi\phi$) measurement and extraction of the fragmentation fractions*, Public CDF note 10795, 2012, http://www-cdf.fnal.gov/physics/new/bottom/120420.blessed-BsJPsiPhi-BR/.

[12] T. Gutsche, M. A. Ivanov, J. G. Krner, V. E. Lyubovitskij, and P. Santorelli, *Polarization effects in the cascade decay $\Lambda_b \to \Lambda(\to p\pi^-) + J/\psi(\to \ell^+\ell^-)$ in the covariant confined quark model*, Phys. Rev. **D88** (2013) 114018, arXiv:1309.7879 [hep-ph].

Proceedings of the LHCP2015 Conference, St. Petersburg, Russia, August 31 - September 5, 2015

Editors: V.T. Kim and D.E. Sosnov

Theory perspective on rare $B_{d,s} \to \bar{\ell}\ell$ and $B \to K^{(*)}\bar{\ell}\ell$

CHRISTOPH BOBETH

Technische Universität München, Institute of Advanced Study, Garching, Germany

bobeth@ph.tum.de

Abstract. The current status is reviewed for theoretical predictions of rare B meson decays proceeding via $b \to s\bar{\ell}\ell$ transitions. The leptonic decays $B_{d,s} \to \bar{\ell}\ell$ are under excellent theoretical control, whereas for semi-leptonic decays $B \to K^{(*)}\bar{\ell}\ell$ hadronic contributions need to be further scrutinised in order to test the standard model and tighten constraints on nonstandard effects.

INTRODUCTION

In the course of the last decade the field of b-quark physics advanced hugely in the exploration of rare decays with measurements by Belle I and Babar at the B-factories, CDF at the Tevatron and recently with LHCb, CMS and ATLAS from Run I of the LHC (2011-2012). Especially LHCb provides first precise measurements of decays with branching fractions in the range of $O(10^{-6})$, such as flavour-changing neutral current (FCNC) decays mediated at the parton level by $b \to s\bar{\ell}\ell$: $B \to K^{(*)}\bar{\mu}\mu$ [1, 2, 3, 4, 5, 6], $B_s \to \phi\bar{\mu}\mu$ [7] and $\Lambda_b \to \Lambda\bar{\mu}\mu$ [8]. As an example of the reach, the very rare leptonic decay $B_s \to \bar{\mu}\mu$ presents the current edge of the advances, discovered by LHCb and CMS with a branching fraction of $O(10^{-9})$ [9]. For the first time data sets are sufficiently large in order to explore the wealth of phenomenological proposals. In principle, the unprecedented experimental precision enables us to perform novel tests of the standard model (SM) of particle physics at an advanced quantitative level as well as to strengthen constraints on its extensions, provided theoretical predictions are under control.

The control of theoretical predictions of $b \to s\bar{\ell}\ell$ decays depends usually on our capability to control the effects of the strong interaction and varies depending on the final state. In this respect, decays with only leptons, such as the rare leptonic decay $B_s \to \bar{\mu}\mu$, can be predicted most precisely, whereas decays with three- or four-body final states, as for example $B \to K\bar{\ell}\ell$ and $B \to K^*(\to K\pi)\bar{\ell}\ell$, are on less solid grounds. On the other hand, the latter decays are phenomenologically more interesting as they provide more observables in angular distributions of the final state.

The first experimental results from LHCb brought about also some first $(2-3)\,\sigma$ deviations from the SM expectations, which gave rise to many interpretations within extensions of the SM, but demand also for a critical assessment of theoretical uncertainties. In view of the experimental program for the next decade with the current Run 2 of LHCb and the future Run 3, as well as the run of Belle II, which will continue to increase the precision of experimental results, it will be important to revise the applied theoretical methods. Further, an improvement seems mandatory to test for tinier effects beyond the SM and to exploit the full potential of FCNC $b \to s\bar{\ell}\ell$ decays, such as

- test the SM and its inherent quark-mixing mechanism at the loop-level,
- constraints on effective right-handed, (pseudo-)scalar and tensorial $|\Delta B| = 1$ couplings $[\bar{s}\,\Gamma_{sb}\,b][\bar{\ell}\,\Gamma_{\ell\ell}\,\ell]$,
- search for non-standard CP-violation in $b \to s$, since in the SM they are $\propto V_{ub}$ and CP asymmetries $\lesssim 0.1\%$,
- test of lepton flavour universality (LFU) among $\ell = e, \mu, \tau$.

After an introductory section to the effective theory (EFT) of $|\Delta B| = 1$ decays, the current status will be shortly reviewed for theoretical predictions of $B_s \to \bar{\mu}\mu$ and related decays, and finally the theoretical treatment of $B \to K^{(*)}\bar{\ell}\ell$ will be summarised in the last section.

$|\Delta B| = 1$ EFFECTIVE THEORY

Within the SM, decays of quarks as constituents of some hadronic bound state proceed via the exchange of the rather heavy W bosons, such that a large mass hierarchy is present $m_H \ll m_W$ among the hadron masses $m_H \lesssim 5$ GeV and the W-boson mass $m_W \sim 80$ GeV, apart for top-quark decays. In a first step, this mass hierarchy justifies the decoupling of heavy degrees of freedom, such as W, Z, H-bosons and the top quark, giving rise to an EFT in the spirit of Fermi

$$\mathcal{L}_{\text{eff}} = \mathcal{L}_{\text{QCD}\times\text{QED}}(u,d,s,c,b,\,e,\mu,\tau) + \mathcal{L}_{\text{dim=6}} + \mathcal{L}_{\text{dim=8}} + \dots \tag{1}$$

with $SU(3)_c \times U(1)_{\text{em}}$ gauge interactions of light ($N_f = 5$) quarks and leptons of dim = 4. The second term represents the leading effect of flavour-changing operators O_k of dim = 6 that mediate $|\Delta B| = |\Delta S| = 1$ processes

$$\mathcal{L}_{\text{dim=6}} = \frac{4\,G_F}{\sqrt{2}}\left(V_{tb}V_{ts}^*\sum_i C_i(\mu_b)\,O_i + V_{ub}V_{us}^*\sum_j C_i(\mu_b)\,O_j\right) + \text{h.c.}, \tag{2}$$

whereas the higher dimensional operators (dim > 6) are currently neglected due to their suppression by $(m_b/m_W)^2 \sim 0.3\%$. The corresponding short-distance couplings C_i, the so-called Wilson coefficients, are evaluated at the scale $\mu_b \sim m_b$ of the order of the b-quark mass $m_b \sim 4$ GeV. They can be calculated reliably in perturbation theory at the parton level. Their initial conditions at the matching scale $\mu_0 \sim m_W$ are known up to NNLO in QCD [10, 11, 12] and NLO in electroweak (EW) interactions [13, 14, 15, 16]. The renormalisation group (RG) evolution from μ_0 to μ_b is also known to the respective orders [17, 18, 19, 20, 21, 22] and resums the largest logarithmic contributions of radiative corrections between the scales μ_0 and μ_b to all orders in couplings. The part $\propto V_{ub}V_{us}^*$, elements of quark-mixing matrix, gives rise to tiny CP asymmetries in the SM.

In the SM the most interesting operators for $b \to s\bar{\ell}\ell$ are the electric dipole operator $O_{7\gamma}$ and the semileptonic operators $O_{9,10}^{\ell\ell}$

$$O_{7\gamma} = \frac{e}{(4\pi)^2}m_b[\bar{s}\sigma_{\mu\nu}P_R b]F^{\mu\nu}, \qquad O_{9(10)}^{\ell\ell} = \frac{e^2}{(4\pi)^2}[\bar{s}\gamma_\mu P_L b][\bar{\ell}\gamma^\mu(\gamma_5)\ell]. \tag{3}$$

Due to operator mixing, also 4-quark current-current operators $O_{2(1)}^p = [\bar{s}\gamma_\mu P_L(\mathbf{T^a})p][\bar{p}\gamma^\mu P_L(\mathbf{T^a})b]$ with $p = (u,c)$ need to be considered. The $O_{1,2}^c$ are numerically the most relevant for $b \to s$ transitions and the evaluation of their contribution to three- and more-body $b \to s\bar{\ell}\ell$ decays constitutes the main theoretical complication. The $O_{1,2}^u$ are suppressed by $V_{ub}V_{us}^* \ll V_{tb}V_{ts}^*$, which is not anymore the case in $b \to d$ transitions as for example $B \to \pi\bar{\ell}\ell$ [23, 24]. Further contributions arise from QCD penguin and the chromo-magnetic dipole operators that are numerically suppressed by small Wilson coefficients for the majority of the observables[1] and at higher order in EW corrections also QED penguin operators have to be taken into account, as for example for the inclusive $B \to X_s\bar{\ell}\ell$ [19, 22].

The effective theory is the starting point for the evaluation of process-specific hadronic matrix elements. Currently all predictions are restricted to the LO in QED, which leads for example to the approximation of matrix elements of semileptonic operators $O_i^{\ell\ell} \propto [\bar{s}\Gamma_{sb}b][\bar{\ell}\Gamma_{\ell\ell}\ell]$ to $B(p_B) \to K^*(p_K)\bar{\ell}\ell$ as follows

$$\mathcal{M} \propto C_i(\mu_b)\left\langle\bar{\ell}\ell K_\lambda^*\middle|[\bar{s}\Gamma_{sb}b][\bar{\ell}\Gamma_{\ell\ell}\ell]\middle|B\right\rangle \overset{\text{LO QED}}{\approx} C_i(\mu_b)\left\langle\bar{\ell}\ell\middle|\bar{\ell}\Gamma_{\ell\ell}\ell\middle|0\right\rangle \otimes \left\langle K_\lambda^*\middle|\bar{s}\Gamma_{sb}b\middle|B\right\rangle \;=\; C_i(\mu_b)\,L\otimes F_\lambda(q^2) \tag{4}$$

where λ denotes the polarisation of the K^*, $q^2 = (p_B - p_K)^2$ is the dilepton invariant mass and $L \otimes F_\lambda$ stands for a Lorentz contraction of the leptonic tensor L with the $B \to K^*$ form factor F_λ, involving 4-vectors p_B, q and the polarisation vector of the K^*. Note that the μ_b dependence of the Wilson coefficient is cancelled by $L \otimes F_\lambda$, such that $\mathcal{M}$ is independent of μ_b to the considered order.

$B_{d,s} \to \bar{\ell}\ell$

The hadronic matrix element of leptonic decays $B_q \to \bar{\ell}\ell$, with $q = d,\ s$ and $\ell = e,\ \mu,\ \tau$, has an even simpler structure, which is obtained from (4) by the replacement $K_\lambda^* \to \textit{vacuum}$. As such, only operators with appropriate Γ_{sb} give

[1] These operators determine for example isospin asymmetries in $B \to K^*\gamma$ [25] and $B \to K^*\bar{\ell}\ell$ [26].

nonvanishing contributions via the decay constant of the B_q meson, f_{B_q}, defined as $\langle 0|\bar{q}\gamma^\mu\gamma_5 b|B_q\rangle = i f_{B_q} p_B^\mu$ and only if their leptonic tensor $L_\mu \neq [\bar{\ell}\gamma_\mu \ell]$, which would otherwise vanish upon contraction with p_B^μ. For this reason, in the SM only $O_{10}^{\ell\ell}$ contributes to $B_{d,s} \to \bar{\ell}\ell$ at LO in QED, whereas $O_9^{\ell\ell}$ or current-current $O_{1,2}^{u,c}$ do not, but additional (pseudo-)scalar operators $O_{S(P)}^{\ell\ell} \propto [\bar{s}\gamma_5 b][\bar{\ell}1(\gamma_5)\ell]$ could contribute beyond the SM. In consequence

$$\mathcal{M} \overset{\text{LO QED}}{\approx} C_{10}(\mu_b)\, f_{B_q}\, p^\mu\, [\bar{\ell}\gamma_\mu\gamma_5\ell] = C_{10}(\mu_b)\, f_{B_q}\, 2m_\ell\, [\bar{\ell}\gamma_5\ell] \tag{5}$$

where the equation of motion has been applied, giving rise to a helicity suppression by the lepton mass m_ℓ. The decay constant f_{B_q} is a nonperturbative quantity in QCD and can be calculated nowadays on the lattice with an accuracy of about 2% [27], however to leading order in QED only. On the level of the branching fraction $\mathcal{B} \propto |\mathcal{M}|^2$ this amounts to about 4% uncertainty. A reduction to 2% in the future is very likely, whereas further advances in accuracy require the consideration of higher order QED effects as well — some first steps towards this direction are discussed in [28]. Despite this, $\mathcal{B}(B_q \to \bar{\ell}\ell)$ is one of the most precisely predictable observables in b physics — as will become more clear below when discussing perturbative uncertainties — together with the mass difference of neutral B_q mesons, Δm_q, and the leptonic decay of charged $B^- \to \ell^-\bar{\nu}_\ell$. Prospects to extract the top-quark mass in the $\overline{\text{MS}}$ scheme or elements of the quark-mixing matrix are discussed in [29].

Nowadays, the NNLO QCD [12] and NLO EW [16] corrections to $C_{10}(\mu_b)$ have been included. The NNLO QCD corrections reduce the renormalisation scheme dependences from 1.8% to 0.2% at the level of $\mathcal{B}$. Note that NLO EW corrections are of two-fold origin: *i)* NLO corrections present in the SM at the scale μ_0 and *ii)* pure NLO QED corrections within the EFT between the scales μ_0 and μ_b. The renormalisation scheme dependences for EW contributions at the scale μ_0 cancel appropriately in $C_{10}(\mu_b)$. In fact they constituted the largest perturbative uncertainty of about ±8% at LO at the level of $\mathcal{B}$ and are reduced to 0.8% at NLO, where the final scheme dependence has been estimated from using three different renormalisation schemes [16]. The remaining NLO QED scheme dependences of $C_{10}(\mu_b)$ have been estimated to be about 0.3% by scale variation of $\mu_b \in [m_b/2, 2m_b]$. These will cancel upon inclusion of NLO QED corrections in (5) for scales below μ_b, which is complicated by their nonperturbative nature. Some of these corrections, namely soft final-state radiation [30] is accounted for on the experimental side [9, 31] and initial-state radiation can be safely neglected within the experimental signal windows [32]. The lacking NLO QED corrections are helicity suppressed and not enhanced by collinear logaritms.

The most recent SM predictions of the CP-averaged time-integrated branching ratio [33] of the leptonic FCNC decay $B_q \to \bar{\ell}\ell$, including corrections at NNLO in QCD and NLO in EW [34]

$$\begin{aligned}
\overline{\mathcal{B}}(B_s \to \bar{e}e) &= (8.54 \pm 0.55)\times 10^{-14}, & \overline{\mathcal{B}}(B_d \to \bar{e}e) &= (2.48 \pm 0.21)\times 10^{-15},\\
\overline{\mathcal{B}}(B_s \to \bar{\mu}\mu) &= (3.65 \pm 0.23)\times 10^{-9}, & \overline{\mathcal{B}}(B_d \to \bar{\mu}\mu) &= (1.06 \pm 0.09)\times 10^{-10},\\
\overline{\mathcal{B}}(B_s \to \bar{\tau}\tau) &= (7.73 \pm 0.49)\times 10^{-7}, & \overline{\mathcal{B}}(B_d \to \bar{\tau}\tau) &= (2.22 \pm 0.19)\times 10^{-8},
\end{aligned} \tag{6}$$

have uncertainties of 7% for $q = s$ and 9% for $q = d$, which are due to f_{B_q} and elements of the quark-mixing matrix. The latter are determined using the inclusive determination of $|V_{cb}|$ [35], which is larger than exclusive determinations. As $\mathcal{B}(B_s \to \bar{\ell}\ell) \propto |V_{cb}|^2$ the above values of the branching fractions can be simply rescaled for other values of $|V_{cb}|$. For $\ell = \mu$, the experimental averages of CMS and LHCb of their full LHC Run 1 data sets [9] are $\overline{\mathcal{B}}(B_s \to \bar{\mu}\mu) = (2.8^{+0.7}_{-0.6}) \times 10^{-9}$ and $\overline{\mathcal{B}}(B_d \to \bar{\mu}\mu) = (3.9^{+1.6}_{-1.4}) \times 10^{-10}$ with a statistical significance of $6.2\,\sigma$ and $3.2\,\sigma$, respectively. Only upper bounds exist for $\ell = e, \tau$.

$B \to K^{(*)}\bar{\ell}\ell$

Compared to the leptonic decay $B_q \to \bar{\ell}\ell$, the three- and four-body exclusive decays $B \to K^{(*)}\bar{\ell}\ell$ offer angular distributions with many observables that allow to test various combinations of Wilson coefficients. These are

$$\frac{1}{\Gamma}\frac{\mathrm{d}\Gamma}{\mathrm{d}\cos\theta_\ell} = \frac{3}{4}(1 - F_H)\sin^2\theta_\ell + \frac{1}{2}F_H + A_{\text{FB}}\cos\theta_\ell\,. \tag{7}$$

$$\begin{aligned}
\frac{8\pi}{3}\frac{\mathrm{d}^4\Gamma}{\mathrm{d}q^2\,\mathrm{d}\cos\theta_\ell\,\mathrm{d}\cos\theta_K\,\mathrm{d}\phi} &= (J_{1s} + J_{2s}\cos 2\theta_\ell + J_{6s}\cos\theta_\ell)\sin^2\theta_K + (J_{1c} + J_{2c}\cos 2\theta_\ell + J_{6c}\cos\theta_\ell)\cos^2\theta_K\\
&+ (J_3\cos 2\phi + J_9\sin 2\phi)\sin^2\theta_K\sin^2\theta_\ell + (J_4\cos\phi + J_8\sin\phi)\sin 2\theta_K\sin 2\theta_\ell + (J_5\cos\phi + J_7\sin\phi)\sin 2\theta_K\sin\theta_\ell\,,
\end{aligned} \tag{8}$$

with q^2-dependent F_H, $A_{\rm FB}$ in $B \to K\bar{\ell}\ell$ and the $J_i(q^2)$ in $B \to K^*(\to K\pi)\bar{\ell}\ell$. In combination with the corresponding measurement of the CP-conjugated decays, CP-averages and CP-asymmetries can be formed for each observable. In general, the twelve J_i are independent observables, but for example J_{6c} vanishes in the absence of scalar and tensorial $b \to s\bar{\ell}\ell$ couplings and the relations $J_{1s} = 3J_{2s}$ and $J_{1c} = -J_{2c}$ hold upon neglecting in addition also the lepton mass. For the moment all measurements of angular observables in $B \to K^*\bar{\ell}\ell$ are based on these two assumptions, which prevents in principle tests of scalar and tensorial couplings [36].

As outlined in (4), the matrix elements of semileptonic operators $O^{\ell\ell}_{9,10}$ and the electric dipole operator $O_{7\gamma}$ give rise to $B \to K^{(*)}$ form factors (FF) at LO in QED. The FF's are nonperturbative quantities, which can be calculated on the lattice (LQCD) [37, 38, 39, 40] for q^2 sufficiently large, i.e. in the so-called *high-q^2 region*, or with light-cone sum rules (LCSR) [41, 42, 43, 44] in the *low-q^2 region*. The current uncertainties of the FF's reach $(6-9)\%$ for LQCD and $(10-15)\%$ for LCSR predictions, which translate to twice on the branching fractions. There are approximate FF relations at low-q^2 [45, 46] and high-q^2 [47, 48] that relate certain FF's up to corrections of order $\Lambda_{\rm QCD}/m_b \sim 15\%$. These relations allowed to identify combinations of angular observables in $B \to K^*(\to K\pi)\bar{\ell}\ell$, which are to leading order in $\Lambda_{\rm QCD}/m_b$ free of FF's at low-q^2 [49, 50, 51] and high-q^2 [52], the so-called *optimised observables*

$$A_T^{(2)} \equiv P_1 \equiv \frac{J_3}{2\,J_{2s}}, \qquad A_T^{(\rm re)} \equiv 2\,P_2 \equiv \frac{J_{6s}}{4\,J_{2s}}, \qquad A_T^{(\rm im)} \equiv -2\,P_3 \equiv \frac{J_9}{2\,J_{2s}},$$
$$P_4' \equiv \frac{J_4}{\sqrt{-J_{2c}J_{2s}}}, \qquad P_5' \equiv \frac{J_5/2}{\sqrt{-J_{2c}J_{2s}}}, \qquad P_6' \equiv \frac{-J_7/2}{\sqrt{-J_{2c}J_{2s}}}, \qquad P_8' \equiv \frac{-J_8}{\sqrt{-J_{2c}J_{2s}}}. \tag{9}$$

The most prominent is the P_5' at low-q^2 where measurements show deviations from SM predictions with $(2-3)\,\sigma$ from the 1 fb^{-1} data set of LHCb [1] for most theory predictions [53, 54, 55, 56]. Below we will comment more on the details of theoretical uncertainties, since very conservative error estimates [57, 58] reach agreement with the measurements, observable by observable and q^2-bin by q^2-bin.

The nonleptonic (4-quark and chromomagnetic dipole) $|\Delta B| = 1$ operators contribute to $b \to s\bar{\ell}\ell$ at lowest order in QED via the matrix element of the time-ordered product of the electromagnetic current of quarks, $j_\mu^{\rm em}$, and the nonleptonic part of the weak Hamiltonian

$$\mathcal{M}_{\rm hadr} = \frac{\alpha_e}{4\pi}\frac{[\bar{\ell}\gamma^\mu\ell]}{q^2}\int {\rm d}^4x\, e^{i\,q\cdot x}\left\langle K^{(*)}_\lambda\middle|\,{\rm T}\Big\{\,j_\mu^{\rm em}(x),\ \sum_i C_i(\mu_b)\,O_i(0)\Big\}\middle|B(p)\right\rangle. \tag{10}$$

Different approaches have been used to evaluate this matrix element, depending on the kinematic regime of q^2.

In the high-q^2 region, starting at the open charm threshold $q^2 \gtrsim 15\ {\rm GeV}^2$, i.e. above the narrow resonances J/ψ and ψ', the dilepton mass $q^2 \sim m_b^2$ allows for a local OPE [59, 60, 61], corresponding to the limit $x \to 0$. The leading term is of dim = 3 and involves only $B \to K^{(*)}$ FF's, amenable to a calculation via LQCD. A dim = 4 term is further suppressed by m_s/m_b and numerically at the order of dim = 5 terms. Only the latter involve new FF's, which can be calculated in principle also via LQCD, however they are already suppressed by $(\Lambda_{\rm QCD}/m_b) \sim 2\%$. Apart from these systematically improvable terms, duality violating contributions beyond the OPE are not under theoretical control. They have been estimated with a model and their effect on the integrated rate was found to be about $\pm 2\%$ [61]. Duality violation is usually accounted for in SM predictions and global fits of rare B decays [55, 56, 62] by assigning an additional uncertainty of a few percent to the amplitudes. Moreover it was checked that allowing for large duality violation does not improve the goodness of global fits [56].

In the low-q^2 region with $q^2 \lesssim 6\ {\rm GeV}^2$, i.e. sufficiently below the narrow resonances, the recoil of the $K^{(*)}$ is large $E_{K^{(*)}} \sim m_b$. In this case QCD factorisation (QCDF) has been used to show that at leading order in $\Lambda_{\rm QCD}/m_b$ only FF- and hard-scattering contributions arise [63, 64]. Factorisation attempts failed so far at subleading order, where endpoint divergences are regulated model-dependently [26, 64], however, numerically the considered corrections are small for CP-averaged quantities compared to uncertainties. Further, soft-gluon emission is not accessible to QCDF and was considered in a light-cone OPE at $q^2 \ll 4m_c^2$ for the most important current-current operators $O^c_{1,2}$ [43]. The complete set of nonleptonic operators has been considered in [65] for $B \to K\bar{\ell}\ell$, but not yet to $B \to K^*\bar{\ell}\ell$. There the underlying idea consists of the use of a dispersion relation that relates the hadronic correlation function (10) in the physical region to the unphysical region $q^2 < 0$, where it is approximated by a partonic calculation under the assumption of local quark-hadron duality, justified by the large mass of the initial B meson and the large recoil of the final hadron. In this approach the leading QCDF corrections are incorporated together with soft-gluon contributions,

which can be expressed as shifts in the Wilson coefficients C_7 (only for $B \to K^*+(\gamma, \bar{\ell}\ell)$) and C_9. The effect of nonlocal hadronic corrections is smaller than uncertainties due to FF's for the rates of $B \to K^{(*)}\bar{\ell}\ell$ in $m_\phi^2 \lesssim q^2 \lesssim 6\,\text{GeV}^2$. Soft-gluon effects beyond QCDF have been also considered within a LCSR calculation [66, 67], but are numerically also too small [56] to play a role in global fits.

Schematically the amplitudes with polarisation λ receive various contributions at low q^2 due to semileptonic and nonleptonic operators

$$\mathcal{M}_\lambda \propto \left(\xi_i + \Delta F_9^{\alpha_s} + \Delta F_9^{1/m_b}\right)\left[C_9(\mu_b) \pm C_{10}(\mu_b)\right] + (9 \to 7) + \Delta^{non-fac} + \Delta^{\text{soft}}. \tag{11}$$

The use of FF relations introduces two universal FF's ξ_i ($i = \perp, \parallel$), with known order-α_s corrections $\Delta F_{7,9}^{\alpha_s}$ [46] and lacking subleading corrections $\Delta F_{7,9}^{1/m_b}$. The latter are ad-hoc parameterised $\propto a_i + b_i\,(q^2/m_B^2) + \ldots$ [57], assuming they are power corrections. The choice of the central values of a_i, b_i is the main origin of differences for SM predictions of optimised observables in [55, 56] versus [57, 58]. Whereas former groups[2] use central values given by LCSR calculations of the QCD FF's [44], the latter group fixes them to the heavy quark limit, i.e. setting them to zero. The comparison of the results shows that subleading corrections to FF relations are important for P_5' in the q^2-region of the zero crossing, where the differences are most pronounced. So-called *nonfactorisable* corrections, $\Delta^{non-fac}$ have been calculated in QCDF to leading order [26, 64] and soft-gluon effects Δ^{soft} in [43, 65]. For the purpose of SM predictions and in global fits, the lacking subleading nonfactorisable corrections (partially known [26, 64]) as well as the soft-gluon effects Δ^{soft} are parameterised in a similar fashion $\propto A_i + B_i\,(q^2/m_B^2) + C_i\,(q^4/m_B^4) + \ldots$. The parameters A_i, B_i, C_i are complex-valued and their size is chosen either to be of the order of a Λ_{QCD}/m_b subleading effect or to reproduce the size (but with arbitrary sign) of the calculation by [43, 65].

The SM predictions of $B \to K^{(*)}\bar{\ell}\ell$ observables in the literature use various procedures for estimates of uncertainties. The most conservative approach [58] determines the spread in each observable (and q^2-bin) by a simultaneous scan over all parameters within some ranges. In less conservative approaches parameters are divided into groups, where parameters belonging to each group are varied simultaneously and the spreads in the observables from the groups are added in quadrature [57, 55]. A bayesian motivated approach [53, 56, 62], assumes prior distributions (mostly gaussian) for the parameters, such that observables are calculated from a large sample of parameter values drawn according to these priors. The uncertainties are then determined from the 68% probability intervals of each observable. Further, a covariance matrix can be derived [56, 62], neglecting nongaussianities, which is used in global fits in order to include the correlations of observables due to the theory parameters, which is computationally much easier than a full bayesian fit [36, 53].

SUMMARY

The leptonic decays $B_q \to \bar{\ell}\ell$ are under excellent theoretical control. The CP-averaged and time-integrated branching fraction $\propto f_{B_q}^2/\Gamma_H^q \times (G_F m_W)^4\,|V_{tb}V_{tq}^*\,C_{10}(\mu_b)|^2$ suffers currently from 4 (7)% hadronic uncertainty from the B_s (B_d) decay constants f_{B_q} and 6 (9)% from V_{ts} (V_{td}). It can be expected that lattice progress will further decrease the uncertainties from decay constants below 2%. The only remaining uncertainty stems from quark-mixing parameters. Once the experimental precision suffices, $\mathcal{B}(B_q \to \bar{\ell}\ell)$ can be used in global CKM fits to get a better handle on V_{ts} (V_{td}) in the framework of the SM.

The three- and four-body decays $B \to K^{(*)}\bar{\ell}\ell$ are under less theoretical control. At high dilepton invariant mass q^2, the main uncertainties due to form factors (FF) are reducible in the future by lattice calculations. Duality violating corrections to the OPE at high q^2 are not accessible to theory and probably prevent the reach of a precision as in $B_q \to \bar{\ell}\ell$. Their size could be tested with data by search of large violations of relations between angular observables predicted by the OPE. At lowq^2, the factorisability of subleading corrections in QCDF has to be investigated as well as subleading corrections to FF relations. Further, soft-gluon effects have to be studied in more detail for the complete set of angular observables, where the refinement of the use of dispersion relations could be a next step to acquire more inside into such effects.

[2] Note that [56] does not use FF relations, i.e. the issue of $\Delta F_9^{1/m_b}$ does not arise at all, since it is assumed that LCSR allow to account for them.

ACKNOWLEDGMENTS

I am indebted to the organisers of *LHCP-2015* for the opportunity to present a talk and the kind hospitality in St. Petersburg.

REFERENCES

[1] R. Aaij *et al.* (LHCb), Phys. Rev. Lett. **111**, p. 191801 (2013), arXiv:1308.1707 [hep-ex] .
[2] R. Aaij *et al.* (LHCb), JHEP **06**, p. 133 (2014), arXiv:1403.8044 [hep-ex] .
[3] R. Aaij *et al.* (LHCb), JHEP **05**, p. 082 (2014), arXiv:1403.8045 [hep-ex] .
[4] R. Aaij *et al.* (LHCb), Phys. Rev. Lett. **113**, p. 151601 (2014), arXiv:1406.6482 [hep-ex] .
[5] R. Aaij *et al.* (LHCb), JHEP **09**, p. 177 (2014), arXiv:1408.0978 [hep-ex] .
[6] R. Aaij *et al.* (LHCb), JHEP **04**, p. 064 (2015), arXiv:1501.03038 [hep-ex] .
[7] R. Aaij *et al.* (LHCb), JHEP **09**, p. 179 (2015), arXiv:1506.08777 [hep-ex] .
[8] R. Aaij *et al.* (LHCb), JHEP **06**, p. 115 (2015), arXiv:1503.07138 [hep-ex] .
[9] V. Khachatryan *et al.* (LHCb, CMS), Nature **522**, 68–72 (2015), arXiv:1411.4413 [hep-ex] .
[10] C. Bobeth, M. Misiak, and J. Urban, Nucl. Phys. **B574**, 291–330 (2000), arXiv:hep-ph/9910220 [hep-ph] .
[11] M. Misiak and M. Steinhauser, Nucl. Phys. **B683**, 277–305 (2004), arXiv:hep-ph/0401041 [hep-ph] .
[12] T. Hermann, M. Misiak, and M. Steinhauser, JHEP **12**, p. 097 (2013), arXiv:1311.1347 [hep-ph] .
[13] A. J. Buras, P. Gambino, and U. A. Haisch, Nucl. Phys. **B570**, 117–154 (2000), arXiv:hep-ph/9911250 [hep-ph] .
[14] P. Gambino and U. Haisch, JHEP **09**, p. 001 (2000), arXiv:hep-ph/0007259 [hep-ph] .
[15] P. Gambino and U. Haisch, JHEP **10**, p. 020 (2001), arXiv:hep-ph/0109058 [hep-ph] .
[16] C. Bobeth, M. Gorbahn, and E. Stamou, Phys. Rev. **D89**, p. 034023 (2014), arXiv:1311.1348 [hep-ph] .
[17] K. G. Chetyrkin, M. Misiak, and M. Munz, Phys. Lett. **B400**, 206–219 (1997), [Erratum: Phys. Lett.B425,414(1998)], arXiv:hep-ph/9612313 [hep-ph] .
[18] P. Gambino, M. Gorbahn, and U. Haisch, Nucl. Phys. **B673**, 238–262 (2003), arXiv:hep-ph/0306079 [hep-ph] .
[19] C. Bobeth, P. Gambino, M. Gorbahn, and U. Haisch, JHEP **04**, p. 071 (2004), arXiv:hep-ph/0312090 [hep-ph] .
[20] M. Gorbahn and U. Haisch, Nucl. Phys. **B713**, 291–332 (2005), arXiv:hep-ph/0411071 [hep-ph] .
[21] M. Gorbahn, U. Haisch, and M. Misiak, Phys. Rev. Lett. **95**, p. 102004 (2005), arXiv:hep-ph/0504194 [hep-ph] .
[22] T. Huber, E. Lunghi, M. Misiak, and D. Wyler, Nucl. Phys. **B740**, 105–137 (2006), arXiv:hep-ph/0512066 [hep-ph] .
[23] C. Hambrock, A. Khodjamirian, and A. Rusov, Phys. Rev. **D92**, p. 074020 (2015), arXiv:1506.07760 [hep-ph] .
[24] R. Aaij *et al.* (LHCb), JHEP **10**, p. 034 (2015), arXiv:1509.00414 [hep-ex] .
[25] A. L. Kagan and M. Neubert, Phys. Lett. **B539**, 227–234 (2002), arXiv:hep-ph/0110078 [hep-ph] .
[26] T. Feldmann and J. Matias, JHEP **01**, p. 074 (2003), arXiv:hep-ph/0212158 [hep-ph] .
[27] S. Aoki *et al.*, Eur. Phys. J. **C74**, p. 2890 (2014), arXiv:1310.8555 [hep-lat] .
[28] N. Carrasco, V. Lubicz, G. Martinelli, C. T. Sachrajda, N. Tantalo, C. Tarantino, and M. Testa, Phys. Rev. **D91**, p. 074506 (2015), arXiv:1502.00257 [hep-lat] .
[29] G. F. Giudice, P. Paradisi, and A. Strumia, JHEP **11**, p. 192 (2015), arXiv:1508.05332 [hep-ph] .
[30] A. J. Buras, J. Girrbach, D. Guadagnoli, and G. Isidori, Eur. Phys. J. **C72**, p. 2172 (2012), arXiv:1208.0934 [hep-ph] .
[31] P. Golonka and Z. Was, Eur. Phys. J. **C45**, 97–107 (2006), arXiv:hep-ph/0506026 [hep-ph] .
[32] Y. G. Aditya, K. J. Healey, and A. A. Petrov, Phys. Rev. **D87**, p. 074028 (2013), arXiv:1212.4166 [hep-ph] .
[33] K. De Bruyn, R. Fleischer, R. Knegjens, P. Koppenburg, M. Merk, A. Pellegrino, and N. Tuning, Phys. Rev. Lett. **109**, p. 041801 (2012), arXiv:1204.1737 [hep-ph] .
[34] C. Bobeth, M. Gorbahn, T. Hermann, M. Misiak, E. Stamou, and M. Steinhauser, Phys. Rev. Lett. **112**, p. 101801 (2014), arXiv:1311.0903 [hep-ph] .
[35] A. Alberti, P. Gambino, K. J. Healey, and S. Nandi, Phys. Rev. Lett. **114**, p. 061802 (2015), arXiv:1411.6560 [hep-ph] .
[36] F. Beaujean, C. Bobeth, and S. Jahn, Eur. Phys. J. **C75**, p. 456 (2015), arXiv:1508.01526 [hep-ph] .
[37] C. Bouchard, G. P. Lepage, C. Monahan, H. Na, and J. Shigemitsu (HPQCD), Phys. Rev. **D88**, p. 054509 (2013), [Erratum: Phys. Rev.D88,no.7,079901(2013)], arXiv:1306.2384 [hep-lat] .
[38] R. R. Horgan, Z. Liu, S. Meinel, and M. Wingate, Phys. Rev. **D89**, p. 094501 (2014), arXiv:1310.3722 [hep-lat] .
[39] J. A. Bailey *et al.*, (2015), arXiv:1509.06235 [hep-lat] .
[40] R. R. Horgan, Z. Liu, S. Meinel, and M. Wingate, *Proceedings, 32nd International Symposium on Lattice Field Theory (Lattice 2014)*, PoS **LATTICE2014**, p. 372 (2015), arXiv:1501.00367 [hep-lat] .
[41] P. Ball and R. Zwicky, Phys. Rev. **D71**, p. 014015 (2005), arXiv:hep-ph/0406232 [hep-ph] .
[42] G. Duplancic and B. Melic, Phys. Rev. **D78**, p. 054015 (2008), arXiv:0805.4170 [hep-ph] .
[43] A. Khodjamirian, T. Mannel, A. A. Pivovarov, and Y. M. Wang, JHEP **09**, p. 089 (2010), arXiv:1006.4945 [hep-ph] .
[44] A. Bharucha, D. M. Straub, and R. Zwicky, (2015), arXiv:1503.05534 [hep-ph] .

[45] J. Charles, A. Le Yaouanc, L. Oliver, O. Pene, and J. C. Raynal, Phys. Rev. **D60**, p. 014001 (1999), arXiv:hep-ph/9812358 [hep-ph] .
[46] M. Beneke and T. Feldmann, Nucl. Phys. **B592**, 3–34 (2001), arXiv:hep-ph/0008255 [hep-ph] .
[47] N. Isgur and M. B. Wise, Phys. Rev. **D42**, 2388–2391 (1990).
[48] B. Grinstein and D. Pirjol, Phys. Lett. **B533**, 8–16 (2002), arXiv:hep-ph/0201298 [hep-ph] .
[49] F. Krüger and J. Matias, Phys. Rev. **D71**, p. 094009 (2005), arXiv:hep-ph/0502060 [hep-ph] .
[50] D. Becirevic and E. Schneider, Nucl. Phys. **B854**, 321–339 (2012), arXiv:1106.3283 [hep-ph] .
[51] S. Descotes-Genon, T. Hurth, J. Matias, and J. Virto, JHEP **05**, p. 137 (2013), arXiv:1303.5794 [hep-ph] .
[52] C. Bobeth, G. Hiller, and D. van Dyk, Phys. Rev. **D87**, p. 034016 (2013), arXiv:1212.2321 [hep-ph] .
[53] F. Beaujean, C. Bobeth, and D. van Dyk, Eur. Phys. J. **C74**, p. 2897 (2014), [Erratum: Eur. Phys. J.C74,3179(2014)], arXiv:1310.2478 [hep-ph] .
[54] T. Hurth, F. Mahmoudi, and S. Neshatpour, JHEP **12**, p. 053 (2014), arXiv:1410.4545 [hep-ph] .
[55] S. Descotes-Genon, L. Hofer, J. Matias, and J. Virto, JHEP **12**, p. 125 (2014), arXiv:1407.8526 [hep-ph] .
[56] W. Altmannshofer and D. M. Straub, Eur. Phys. J. **C75**, p. 382 (2015), arXiv:1411.3161 [hep-ph] .
[57] S. Jäger and J. Martin Camalich, JHEP **05**, p. 043 (2013), arXiv:1212.2263 [hep-ph] .
[58] S. Jäger and J. Martin Camalich, (2014), arXiv:1412.3183 [hep-ph] .
[59] G. Buchalla and G. Isidori, Nucl. Phys. **B525**, 333–349 (1998), arXiv:hep-ph/9801456 [hep-ph] .
[60] B. Grinstein and D. Pirjol, Phys. Rev. **D70**, p. 114005 (2004), arXiv:hep-ph/0404250 [hep-ph] .
[61] M. Beylich, G. Buchalla, and T. Feldmann, Eur. Phys. J. **C71**, p. 1635 (2011), arXiv:1101.5118 [hep-ph] .
[62] S. Descotes-Genon, L. Hofer, J. Matias, and J. Virto, (2015), arXiv:1510.04239 [hep-ph] .
[63] M. Beneke, T. Feldmann, and D. Seidel, Nucl. Phys. **B612**, 25–58 (2001), arXiv:hep-ph/0106067 [hep-ph] .
[64] M. Beneke, T. Feldmann, and D. Seidel, Eur. Phys. J. **C41**, 173–188 (2005), arXiv:hep-ph/0412400 [hep-ph] .
[65] A. Khodjamirian, T. Mannel, and Y. M. Wang, JHEP **02**, p. 010 (2013), arXiv:1211.0234 [hep-ph] .
[66] M. Dimou, J. Lyon, and R. Zwicky, Phys. Rev. **D87**, p. 074008 (2013), arXiv:1212.2242 [hep-ph] .
[67] J. Lyon and R. Zwicky, Phys. Rev. **D88**, p. 094004 (2013), arXiv:1305.4797 [hep-ph] .

Proceedings of the LHCP2015 Conference, St. Petersburg, Russia, August 31 - September 5, 2015

Editors: V.T. Kim and D.E. Sosnov

ATLAS CP Violation and rare B decays.

V.NIKOLAENKO

Institute for High Energy Physics, 142281, Protvino, Moscow region, Russian Federation

Vladimir.Nikolaenko@cern.ch

On behalf of the ATLAS Collaboration

Abstract. A new measurement of CP-violating parameters in $B_s \to J/\psi\phi$ decay is performed in ATLAS on full Run 1 statistics: $\phi_s = -0.094 \pm 0.083(stat) \pm 0.033(syst.)$ rad. and $\Delta\Gamma_s = 0.082 \pm 0.007$ ps^{-1}. Rare $B_s \to \mu^+\mu^-$ decay is analyzed on 2011 data at 7 TeV . The ratio of b-quark fragmentation functions measured, $f_s/f_d = 0.240 \pm 0.004(stat.) \pm 0.013(syst.) \pm 0.017(BR)$, this measurement helps to separate contributions from B^0 and B_s mesons into $\mu^+\mu^-$ final state in ongoing analysis on full Run 1 data.

Introduction.

B-physics results are based on statistics acquired mainly with di-muon triggers, with muons of different sign and requirements on muons transverse momentum p_{T} (mostly 4 GeV/c for both muons, for small fraction of events with high instantaneous luminosity the threshold was increased to 6 GeV/c).

Like the K^0 meson, the B_s meson can be produced in CP-even or CP-odd state with different lifetimes. $\Delta\Gamma_s$ is a difference between inverse lifetimes. CP-odd state has a longer lifetime than the CP-even one, the relative difference is $\sim$ 13 − 17%. There are observed ($b\bar{s} \leftrightarrow \bar{b}s$) oscillations via box diagrams with intermediate u, c, t $q\bar{q}$- pairs in t-channel and possibly New Physics. The mass difference between heavy (B^H) and light (B^L) CP-eigenstates leads to measured oscillation frequency $\Delta m_s \sim 17.77$ ps^{-1}.

CP-violating phase ϕ_s manifests itself in interference terms between mixing and decay amplitudes. In SM, phase $\phi_s \approx -2\beta_s$, where β_s is an angle in Kobayashi-Maskawa triangle,
$\beta_s = arg\frac{-V_{ts}V_{tb}^*}{V_{cs}V_{cb}^*}$. [1]

SM predictions: $\Delta\Gamma_s = 0.087 \pm 0.021$ ps^{-1}, $\phi_s = -0.0363 + 0.0016 - 0.0015$ *rad* [1]. Measurements of ϕ_s and $\Delta\Gamma_s$ test theoretical predictions. The analysis of data at 8 TeV is similar for published analysis of 7 TeV data [2]. The number of signal events at 8 TeV is greater by a factor of 3. Due to high statistics, more detailed study of acceptance, signal shape and background was performed. Also Electron tagging was applied. Finally, results at 8 and 7 TeV were statistically combined.

Effects from physics beyond Standard Model can cause a deviation from predicted $BR(B_s \to \mu^+\mu^-)$. This decay channel was recently observed in LHCb and CMS experiments. LHCb experiment also published interesting observations in differential distributions in $B^0 \to J/\psi K^*(890)$ decays. Both decays are under investigation in ATLAS, at full Run 1 statistics.

Analysis of $B_s \to J/\psi\phi$ decay.

The $B_s \to J/\psi\phi$ is registered in subsequent decays $J/\psi \to \mu^+\mu^-$ and $\phi \to K^+K^-$ (without kaon identification). B_s candidates were selected from events with $\mu^+\mu^-$ pair and mass $m(\mu^+\mu^-)$ close to the J/ψ mass. A Vertex fit of $\mu^+\mu^-$ tracks was performed and combined with two other opposite sign charged tracks with transverse momenta $p_{\mathrm{T}} > 1$ GeV and in pseudorapidity interval $|\eta| < 2.5$ taken with kaon mass. Kaon pair candidates with effective mass

[1] Caution: the angle β_s is NOT the same as angle β which is associated with another Kobayashi-Maskawa triangle, with d quark instead of s quark.

close to the $\phi(1020)$ mass, in interval $1008.5 < m(\mu^+\mu^-) < 1030.5\ MeV$ were selected. Then a four-track vertex fit was performed with fixed mass of $\mu^+\mu^-$ pair, and combinations with $\chi^2/NDF < 3.0$ were retained for further analysis. Details of selection requirements can be found in Ref.[2]. With reconstructed B_s vertex and the momentum vector, the primary vertex for lifetime measurement was selected as the vertex with smallest 3-dimensional impact parameter for reconstructed neutral track. Then the proper decay time was calculated:
$\tau = \frac{L_{xy} M_B}{p_{\mathrm{T_H}}}$, where L_{xy} denotes the impact parameter in transverse plane to the beam direction and M_B is the World Average mass value. Total 370000 B_s candidates were selected in the mass range from 5.150 to 5.650 GeV and subjected to further analysis.

No decay time cut was applied in the analysis.

Spin-zero B_s meson decays to two vector particles with 3 values of orbital momentum $L = 0, 1, 2$. P-wave decay corresponds to B_s in CP-odd state,while the CP-even state leads to S- and D-waves. Apart from 3 waves mentioned above, a 4-th wave was included in the analysis, where it takes into accound the background below the $\phi(1020)$ resonance, with (K^+K^-) system in the S-wave. The last wave corresponds to CP-odd state of B_s meson at the decay time.

A time-dependent Partial Wave Analysis with 4 waves was performed, using 3 angles between final state particles in Transversity basis. The coordinate system is defined as follows. x-axis is an unit vector in the direction of ϕ momentum in J/ψ rest frame, then XY-plane is defined by $\phi \to K^+K^-$ decay plane with positive projection of K^+ momentum on y-axis, then z-axis is perpendicular to both x and y and z-direction chosen according to convention of positive triplet.

Two polar angles were defined : 1) the ϕ_T is angle between projection of μ^+ momentum vector on (x,y) plane in the J/ψ rest frame and x-axis; 2) the ψ_T is angle between x-axis and K^+ momentum in the ϕ rest frame. The 3-rd θ_t angle is the angle between z-axis and μ^+ momentum vector in $J/\psi\phi$ rest frame.

A multi-dimensional fit to the data determine the following physical parameters: four amplitudes (A_0, A_{perp}, A_{par}, A_S), strong phases (δ_0, δ_{perp}, δ_{par}, δ_S, one of them can be fixed), as well as the mass of the B_s meson $m(B_s)$, ϕ_S, $\Delta\Gamma_s$ and the average inverse lifetime Γ_s. The mass spectrum used for separation of B_s signal from background, which is mainly the combinatorial one. There is also a small BG component from $B^0 \to J/\psi K^*$ decay due the to absence of pion identification.

An important ingredient of the analysis is tagging of b or $\bar{b}$ quark in B_s meson at the production time. The $b-$quark charge tagging significantly improves the precision of the ϕ_s measurement and helps in measurement of strong phases and resolution of ambigous solutions. If the tagging information is available, then new oscillating terms appear in time-dependent functions in partial waves, and amplitudes of new terms are proportional to $sin(\phi_s)$. It is known that the absolute value of ϕ_s angle is small, and new terms significantly improve the measurement precision. Information from opposite side tagging is used, i.e. leptons and/or jet charge from decay of 2nd B-hadron in the event. Methods were calibrated on B^{+-} -candidates in data after BG subtraction. Apart from methods based on combined muons, tagged muons and the jet charge used in the analysis of 7 TeV data, a new tagging method on electrons was developed and used in the analysis of data acquired at 8 TeV . Opposite-side charge distributions for different methods shown in Fig. 1, separately for B^+ and B^- calibration samples. Table 1 specifies the tagging power of different methods.

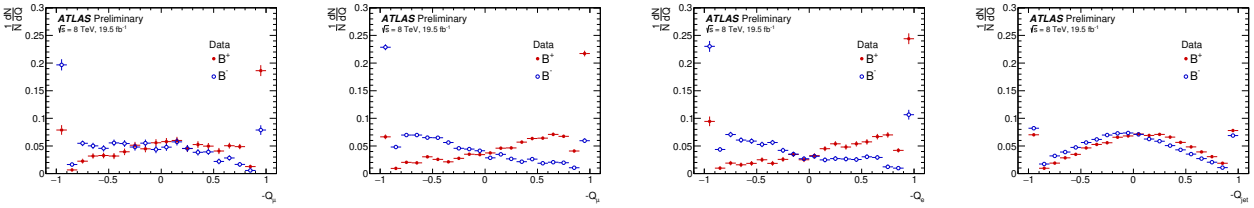

FIGURE 1. The opposite-side muon cone charge distribution for B^{+-} signal candidates for segment-tagged (left); combined muon (next); electron cone (next); jet charge(right)

Efficiency of B_s candidate reconstruction was estimated in specialy tuned Monte Carlo (MC) procedure, in several bins on transverse momentum p_{T} and pseudorapidity η.

A fit model was constructed and physical parameters were determined at the result of unbinned likelihod fit. A signal component of fit model contains a mass term (a Tripple Gaussian function), angular functions and time-dependent functions. Angular functions (4 diagonal and 6 non-diagonal) are multiplied by time-dependent functions

TABLE 1. Tagging power of different methods.

Tagger	Tagging Power [%]
Combined muon	0.92 ± 0.02
Electron	0.29 ± 0.01
Tagged muon	0.10 ± 0.01
Jet charge	0.19 ± 0.01
Total	1.49 ± 0.02

with dependencies on two exponential functions (smeared with experimental resolution) and also terms with tagginng probability distributions. Detailed description of angular and time-dependent function can be found in Ref. [1].

A background component of the Fit model consists of two parts, a combinatorial background component and a B^0 component. Combinatorial component contains a mass term (an exponential function). A time-dependent component contains 2 prompt exponents (including a tail to negative lifetime due to experimental resolution) and two non-prompt exponential functions. It worth mentioning that the error on time measurements was taken from reconstruction results in individual events and then multiplied by a scaling factor, which was also included as a fit parameter. This parameter was determined from the negative tail in time distributions of the data, due to absence of the lifetime cut. The angular distributions in this component were determined from fits in mass side bands. Finaly, the differences in tagging efficiency and lifetime uncertainties between signal and background regions were taken into account in so called Punzi terms.

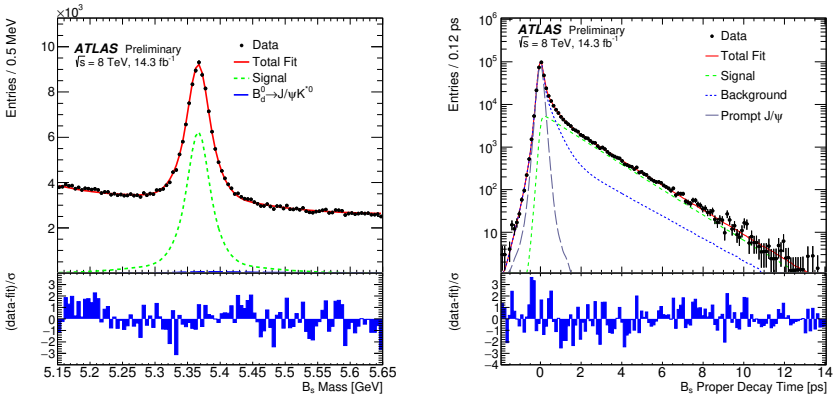

FIGURE 2. (Left) Mass fit projection for the $B_s^0 -> J/\psi\phi$. The red line shows the total fit, the dashed green line shows the signal component while the dotted blue line shows the contribution from $B^0 -> J/\psi K^*$ events. (Right) Proper decay time fit projection for the $B_s^0 -> J/\psi\phi$. The red line shows the total fit while the green dashed line shows the total signal. The total background is shown as a blue dashed line with a grey dotted line showing the prompt J/ψ background. Below each figure is a ratio plot that shows the difference between each data point and the total fit line divided by the statistical uncertainty (σ) of that point.

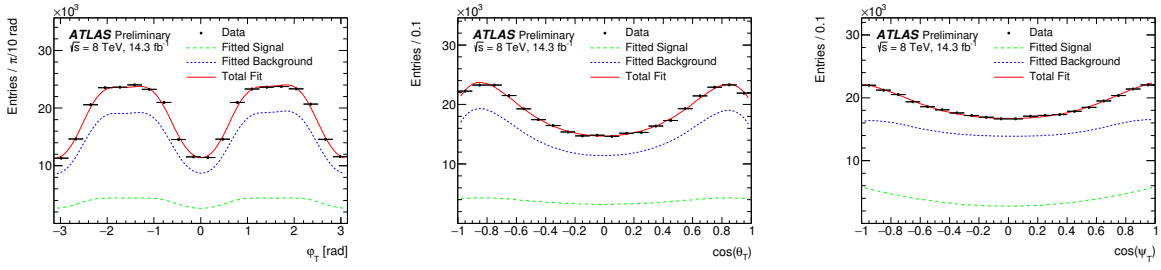

FIGURE 3. Fit projections for transversity angles. (Left): ϕ_T, (Right): $cos(\theta_T)$, (Center): $cos(\psi_T)$. In all three plots, the red line shows the total fit, the dashed green line shows the signal component and the dotted blue line shows the background contribution.

TABLE 2. Summary of systematic uncertainties assigned to the physics parameters.

	ϕ_s [rad]	$\Delta\Gamma_s$ [ps^{-1}]	Γ_s [ps^{-1}]	$\lvert A_\parallel(0)\rvert^2$	$\lvert A_0(0)\rvert^2$	$\lvert A_S(0)\rvert^2$	$\delta_\perp$ [rad]	$\delta_\parallel$ [rad]	$\delta_\perp - \delta_S$ [rad]
Tagging	0.026	0.003	$<10^{-3}$	$<10^{-3}$	$<10^{-3}$	0.001	0.238	0.014	0.004
Acceptance	$<10^{-3}$	$<10^{-3}$	$<10^{-3}$	0.003	$<10^{-3}$	0.001	0.004	0.008	$<10^{-3}$
Background angles model:									
Choice of p_T bins	0.02	0.006	0.003	0.003	$<10^{-3}$	0.008	0.004	0.006	0.008
Choice of mass interval	0.008	0.001	0.001	$<10^{-3}$	$<10^{-3}$	0.002	0.021	0.005	0.003
B_d^0 background model	0.008	$<10^{-3}$	$<10^{-3}$	0.001	$<10^{-3}$	0.008	0.007	$<10^{-3}$	0.005
Fit model:									
Default fit	0.001	0.002	$<10^{-3}$	0.002	$<10^{-3}$	0.002	0.025	0.015	0.002
Mass Signal model	0.004	$<10^{-3}$	$<10^{-3}$	0.002	$<10^{-3}$	0.001	0.015	0.017	$<10^{-3}$
Mass Background model	$<10^{-3}$	0.002	$<10^{-3}$	0.002	$<10^{-3}$	0.002	0.027	0.038	$<10^{-3}$
Time Resolution model	0.003	$<10^{-3}$	0.001	0.002	$<10^{-3}$	0.002	0.057	0.011	0.001
Total	0.036	0.007	0.003	0.006	0.001	0.013	0.25	0.05	0.01

Concerning the B^0 background component, the mass term was described by a Landau function with parameters tuned in a MC procedure. An exponential function smeared with per-candidate errors describes the time dependence, with lifetime value taken from PDG [3]. Angular distributions: taken from 3-dimensional fits to MC.

The mass fit projection and proper lifetime fit projection are shown at Fig.2. Fig.3 demonstrates fit projections for transversity angles. Table 2 presents a list of considered sources of systematics and preliminary evaluation of systematic errors for physics parameters.

It worth mentioning that the correlations between physics parameters are small, the largest correlation term between $\Delta\Gamma_s$ and Γ_s parameters is close to 0.4. Correlation between $(\phi_s, \Delta\Gamma_s) = 0.110$.

The following results were obtained from the analysis of data at 8 TeV :
$\phi_s = -0.119 \pm 0.088(stat.) \pm 0.036(syst.)$ *rad*.. $\Delta\Gamma_s = 0.096 \pm 0.013(stat.) \pm 0.007(syst.)$ ps^{-1}.

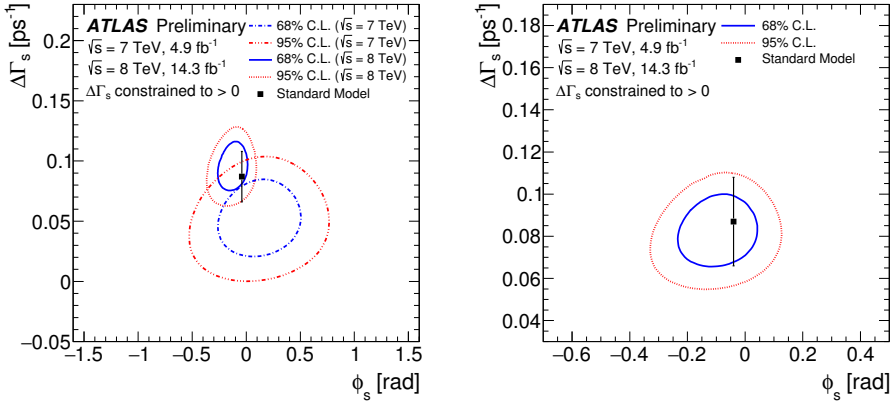

FIGURE 4. Likelihood contours in the $\phi_s - \Delta\Gamma_s$ plane for individual results from 7 TeV and 8 TeV data (left) and a final statistical combination of the results from 7 TeV and 8 TeV data (right). The blue line shows the 68% likelihood contour, while the red dotted line shows the 95% likelihood contour (statistical errors only). Points with errors indicate predictions from parametrisation in Standard Model.

At the next step, the results obtained on the data at 7 and 8 TeV were statistically combined. A Best Linear Unbiased Estimate (BLUE) procedure was used. A conservative approach was applied in treatment of correlations between systematic errors, assuming no correlations or 100% correlations and adding a difference to the final systematic error. Comparison between measurements at 7 and 8 TeV for ϕ_s and $\Delta\Gamma_s$ is presented in Fig.4, as well as the combined result. One can see that the analysis at 8 TeV yields more precise results in comparison with previous analysis at 7 TeV .

TABLE 3. Combined results for physics parameters.

Parameter	Value	Stat. err.	Syst. err.	
ϕ_s	-0.094	0.083	0.033	rad.
$\Delta\Gamma_s$	0.082	0.011	0.007	ps^{-1}
Γ_s	0.677	0.003	0.003	ps^{-1}
$\lvert A_{paral}(0)\rvert^2$	0.227	0.004	0.006	
$\lvert A_0(0)\rvert^2$	0.515	0.004	0.002	
$\lvert A_S(0)\rvert^2$	0.086	0.007	0.012	
δ_{perp}	4.13	0.34	0.15	rad.
δ_{paral}	3.16	0.13	0.05	rad.
$\delta_{perp} - \delta_S$	-0.08	0.03	0.01	rad.

Combined results for physics parameters are presented in Table 3.

Comparison of ATLAS Run 1 result with combination of other measurements is shown at Fig.5(left). Recent results from LHCb and CMS experiments can be found in Refs. [4, 5].

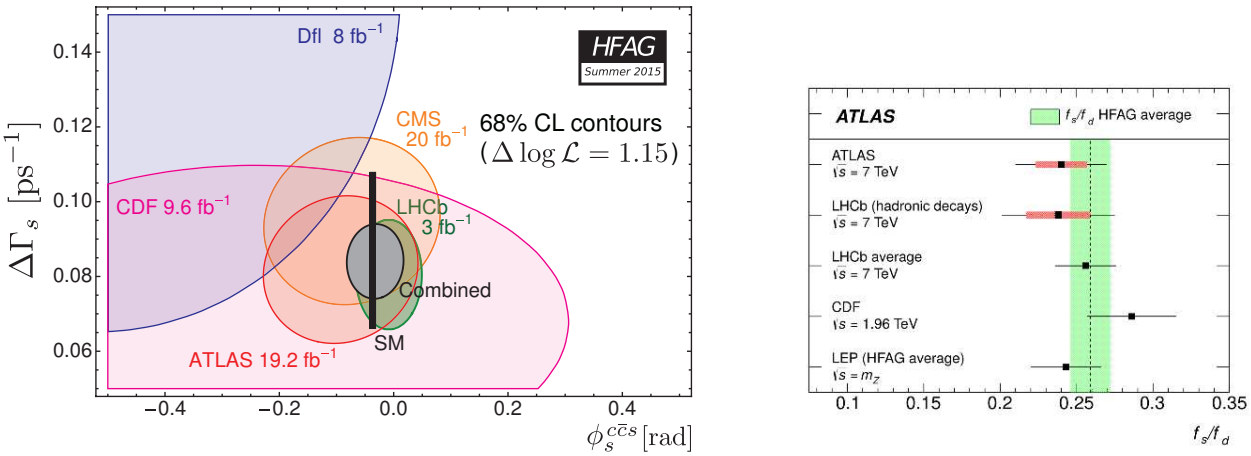

FIGURE 5. (Left) 68% conf. level contours in $(\phi_s, \Delta\Gamma_s)$ plane of ATLAS, CMS, CDF, D0 and LHCb results and their combined contour, as well as the Standard Model predictions (thin black rectangle). Taken from [6]. (Right) Compilation of measurements of b-quark fragmentation functions f_s/f_d .

Status of Rare decay studies in ATLAS.

Decays $B_s \to \mu^+\mu^-$ and $B^0 \to \mu^+\mu^-$ are suppressed in SM.
Recent predictions in SM: $BR(B_s \to \mu^+\mu^-) = (3.65 \pm 0.23)x10^{-9}$, $BR(B^0 \to \mu^+\mu^-) = (1.06 \pm 0.09)x10^{-10}$ [7].

Combined result from LHCb and CMS is recently published [8]:
$BR(B_s \to \mu^+\mu^-) = (2.8^{+0.7}_{-0.6})x10^{-9}$, $BR(B^0 \to \mu^+\mu^-) = (3.9^{+1.6}_{-1.4})x10^{-10}$.

ATLAS experiment put a limit on 7 TeV data with integrated luminosity of 4.9 fb^{-1} [9, 10]
$BR(B_s \to \mu^+\mu^-) < 19x10^{-9}$ at 90% conf. level.

ATLAS analysis on full Run 1 statistics ongoing, more precise result expected soon.

A particular challenge in these analyses is a problem of separation of signals from B_s and B^0 decays, which have close masses and are not well resolved. A supplementary study in this direction is completed in ATLAS, the Determination of ratio of b-quark fragmentation functions f_s/f_d. Exclusive decays $B_s \to J/\psi\phi$ and $B^0 \to J/\psi K^{*0}(890)$ were used from data with integrated luminosity of 2.47 fb^{-1} at $\sqrt{s} = 7$ TeV. A theoretical calculation of Branching Fractions ratio $BR(B_s \to J/\psi\phi)/BR(B^0 \to J/\psi K^{*0}(890)$ from Ref. [11] was used. With $6640 \pm 100 \pm 220$ reconstructed $B_s \to J/\psi\phi$ and $36290 \pm 320 \pm 650$ $B^0 \to J/\psi K^{*0}$ decays, the following ratio of fragmentation functions in kinematical region $p_T > 8$ GeV was obtained:

$f_s/f_d = 0.240 \pm 0.004(stat.) \pm 0.013(syst.) \pm 0.017(branching)$.
Comparison of this result with other measurements presented at Fig.5(right).

Study of other semi-rare decay, $B^0 \to \mu^+\mu^- K^{*0}$ in ATLAS with full Run 1 statistics is ongoing.

Summary

ATLAS can provide precise measurements in B-decays, which are relevant for searches of effects beyond SM:

- CP-violating phase ϕ_s and decay width difference $\Delta\Gamma_s$ measured in 2012 data at 8 TeV;
- statistical combination performed for 2011+2012 data $(4.6 + 14.3 fb^{-1})$,
  $\phi_s = -0.094 \pm 0.083(stat.) \pm 0.033(syst.)\ rad$;
  $\Delta\Gamma_s = 0.082 \pm 0.011 \pm 0.007\ \mathrm{ps}^{-1}$;
- obtained results are consistent with SM predictions and other experiments.
- $B_s \to \mu^+\mu^-$ decay analyzed 2011 data, full Run 1 result expected soon;
- The ratio of b-quark fragmentation functions measured at $p_\mathrm{T} > 8$ GeV/c, $f_s/f_d = 0.240 \pm 0.004(stat.) \pm 0.013(syst.) \pm 0.017(branching)$;
- analysis of $B_d \to J/\psi K^{*0}$ decay on full Run 1 is ongoing;

Statistical errors dominate in measurements, we expect better precision from the future Run 2 data due to modifications in the ATLAS detector (most notably the IBL) and significantly more statistics.

ACKNOWLEDGMENTS

This work was supported in part by the Russian MES grant RFMEFI61014X0005 and Presidential Grant NSh-999.2014.2.

REFERENCES

[1] J.Charles et al., Predictions of selected flavor observables within the standard model Phys. Rev. D 84 (2011), 033005

[2] ATLAS collaboration, Flavor tagged time-dependent angular analysis of the $B_s \to J/\psi$ decay and extraction of $\Delta\Gamma_s$ and the weak phase ϕ_s in ATLAS, Phys. Rev. D90 (2015) 5, 052007, arXiv:1407.1796

[3] The Review of Particle Physics, K.A. Olive et al. (Particle Data Group), PDG Chinese Phys C V38 Number 9 September 2014

[4] LHCb collaboration, R Aaij et al., Precision measurement of CP violation in $B_s \to J/\psi K^+K^-$ decays, Phys.Rev. Lett. 114 (2015) 041801, arXiv:1411.3104

[5] CMS collaboration, Measurement of the CP-violating weak phase ϕ_s and the decay width difference $\Delta\Gamma_s$ using the $B_s \to J/\psi\phi(1020)$ decay channel, Tech.Rep. CMS-PAS-BPH-13-012, CERN, Geneva, 2014, arXiv:1507.07527, submited to PL B

[6] Y. Amhis et al. (Heavy Flavour Averaging Group), Averages of b-hadron, c-hadron, and τ-lepton properties of summer 2014, arXiv:1412.7515 [hep-ex] and online update at http://www.slac.stanford.edu/xorg/hfag [www.slac.stanford.edu]

[7] C.Bobeth et al., $B_{s,d} \to l^+l^-$ in the Standard Model with Reduced Theoretical Uncertainty, PRL 112,101801 (2014)

[8] CMS collaboration,LHCb collaboration, Observation of the rare $B_s^0 \to \mu^+\mu^-$ decay from combined analysis of CMS and LHCb data, Nature 522 (2015) 68, and ref. therein

[9] ATLAS collaboration, Limit on $B_s^0 \to \mu^+\mu^-$ branching fraction based on 4.9 fb^{-1} of integrated luminosity, ATLAS-CONF-2013-076, http://cds.cern.ch/record/1562934

[10] ATLAS collaboration, Search for the decay $B_s^0 \to \mu^+\mu^-$, Phys. Lett. B713 (2012) 387, arXiv:1204.0735

[11] Xin Lio et al., Penguin pollution $B \to J/\psi V$ decays and impact on the $B_s - \bar{B}_s$ mixing phase, Phys. Rev. 89, 094010 (2014).

Proceedings of the LHCP2015 Conference, St. Petersburg, Russia, August 31 - September 5, 2015

Editors: V.T. Kim and D.E. Sosnov

CP Violation and Rare B Decays with the CMS Detector

JACOPO PAZZINI

Padova University and INFN , CERN

On behalf of the CMS Collaboration

Abstract. The latest results involving rare decays and CP-violation of neutral B mesons, based on pp collisions collected during 2011 and 2012 at $\sqrt{s}$ = 7 TeV and 8 TeV respectively are presented. The first evidence for the rare decay $B_s^0 \to \mu^+\mu^-$ and the search for $B^0 \to \mu^+\mu^-$ at the CMS experiment is presented, with the complete dataset of LHC run 1. An excess over the background only hypothesis is found for the B_s^0, leading to measure $\mathcal{B}(B_s^0 \to \mu^+\mu^-) = (3.0^{+1.0}_{-0.9}) \times 10^{-9}$, while no significant excess is found for the B^0 and the upper limit $\mathcal{B}(B^0 \to \mu^+\mu^-) < 1.1 \times 10^{-9}$ at 95 % confidence level is set. The angular analysis and the differential branching fraction of the decay $B^0 \to K^*\mu^+\mu^-$ with the 2012 data is also presented. The forward-backward asymmetry of the muons, the K^* longitudinal polarization fraction, and the differential branching fraction are determined as a function of the dimuon invariant mass squared, and found to be in good agreement with the standard model expectations. Finally, the CP-violating weak phase ϕ_s and the decay width difference $\Delta\Gamma_s$ are measured in 2012 data using $B_s^0 \to J/\psi\phi$ decays. A flavor-tagged and time dependent angular analysis is performed, and the values of $\phi_s = -0.075 \pm 0.097(\text{stat}) \pm 0.031(\text{syst})$ rad and $\Delta\Gamma_s = 0.095 \pm 0.013(\text{stat}) \pm 0.007(\text{syst})$ ps^{-1} are measured, in agreement with the standard model predictions.

INTRODUCTION

The standard model of particle physics (SM) provides the most accurate and consistent description of the subatomic nature of the universe developed so far as it has withstood a multitude of experimental tests over the years. However, the SM is known not to be the ultimate description of the universe as for instance it does not include a formulation of gravity and it does not account for the existence of dark matter, confirmed by several cosmological data. The search for evidences of new physics can proceed through the study of loop-mediated processes where new particles could appear as virtual contributions in box and penguin diagrams leading to small but sizable effects compared to the theoretical predictions of the SM (for this reason often named *indirect* searches). Proceeding with the exchange of virtual particles, these processes can probe higher energy scales than those currently accessible with the *direct* searches for new resonant states. The flavor sector of the SM is an excellent framework to study the SM consistency as it provides a wide plethora of rare processes for which accurate theoretical predictions are now available. New physics phenomena can be inferred experimentally by the accurate measurement of branching fractions or phases related to CP-violation.

The results of three analyses with data collected by the CMS experiment [1] in pp collisions at a center of mass energies $\sqrt{s}$ of 7 and 8 TeV are presented. The measurement of the branching fraction of the $B_s^0 \to \mu^+\mu^-$ and the search for $B^0 \to \mu^+\mu^-$ decay performed with the data collected at 7 and 8 TeV [2] are described in Section 1. Section 2 presents the results of the angular analysis of the rare decay $B^0 \to K^*\mu^+\mu^-$ [3] with 8 TeV data. Finally, in Section 3 the flavor-tagged angular analysis of the $B_s^0 \to J/\psi\phi$ decay is described, along with the measurement of the CP-violating phase ϕ_s [4] also performed with the data collected at 8 TeV. Charge conjugation is implied throughout the text.

1 MEASUREMENT OF THE BRANCHING FRACTION $\mathcal{B}B_s^0 \to \mu^+\mu^-$ AND SEARCH FOR $B^0 \to \mu^+\mu^-$ DECAY

The flavor-changing neutral current (FCNC) leptonic decays $B_s^0 \to \mu^+\mu^-$ and $B^0 \to \mu^+\mu^-$ are predicted to have very small branching fractions in the SM due to several suppression factors. In the SM, the predicted decay-time integrated branching fractions are $\mathcal{B}(B_s^0 \to \mu^+\mu^-) = (3.66 \pm 0.23) \times 10^{-9}$, and $\mathcal{B}(B^0 \to \mu^+\mu^-) = (1.06 \pm 0.09) \times 10^{-10}$

respectively [5, 6]. The analysis performed by the CMS collaboration is based on the simultaneous search for the $B_s^0 \to \mu^+\mu^-$ and $B^0 \to \mu^+\mu^-$ in the dimuon invariant mass regions around the B_s^0 and B^0 masses, using a data sample of pp collisions collected in 2011 at $\sqrt{s} = 7$ TeV and in 2012 at $\sqrt{s} = 8$ TeV, corresponding to a total integrated luminosity of 25 fb^{-1}. The data reconstructed in signal region $5.20 < m_{\mu\mu} < 5.45$ GeV are kept blind until the full set of selections are completely established to avoid possible biases. The data collected in 2011, already analyzed in a previous result by CMS [7], are included and subject to re-blinding. The background for this analysis arise mainly from the combinatorial semileptonic decays of two separate B hadrons in the event. The yield of this background is estimated in data by the analysis of dimuon mass sidebands, and extrapolated into the signal region. Additional sources of backgrounds are the $B \to h\mu\nu$, $B \to h\mu\mu$, and $\Lambda_b \to h\mu\nu$ decays, where one hadron (h) is erroneously identified as a muon, and the rare "peaking" decays $B \to hh'$, where both the hadrons are mis-identified, leading to a reconstructed invariant mass close to the value of the B^0. These backgrounds are estimated from Monte Carlo (MC) simulations. Two additional samples of reconstructed B meson decays are used in this analysis. A sample of $B^+ \to J/\psi\, K^+$ decays, for which the knowledge of the branching fraction is already well established [8], is used as a normalization channel to reduce the uncertainties from the $b\bar{b}$ production cross section and the absolute luminosity. An additional sample of $B_s^0 \to J/\psi\phi$ decays is used to validate the features of the B_s^0 production in the MC simulation and to evaluate potential effects from differences in fragmentation between B^+ and B_s^0. Events are selected at trigger level by requiring two muon candidates in the muon detectors with compatible hits in the silicon tracker and invariant mass in the range of the B_s^0. The offline selection requires two well-identified muons consistent with the ones that triggered the event. The events are then reconstructed with a further set of stringent requirements to reduce the contribution of background events. Cuts are applied on the direction of the dimuon system with respect to the primary vertex of the events, on the flight length significance, and on the distance of closest approach of the two muons. A dedicated multivariate identification criterion is trained to enhance the separation from muons and mis-identified charged hadrons like pions, kaons and protons. Several variables are combined in a boosted decision tree (BDT) based on a set of different features: kinematic variables, tracker-based informations, muon detector track informations, and combined features of the fit of both tracker and muon spectrometer hits. The training is performed using the $B_s^0 \to \mu^+\mu^-$ MC signal sample, and simulated background samples of rare B mesons decays to pions and kaons. The mis-identification probability is found to be $(0.5-1.3)\times10^{-3}$, $(0.8-2.2)\times10^{-3}$, and $(0.4-1.5)\times10^{-3}$, for pions, kaons, and protons respectively, depending on pseudorapidity, running period, and particle momentum. A kinematic fit is applied to constrain the tracks of the muon candidates to a common vertex and the event is then retained if the dimuon mass is found to be in the range $4.9 < m_{\mu\mu} < 5.9$ GeV. Two categories have been defined based on the muon pseudorapidity, to account for the different mass resolution achieved in $|\eta|$: events are categorized as "barrel" if both the muons are found to be in the central region ($|\eta^\mu| < 1.4$), while if at least one muon is reconstructed at high pseudorapidity ($|\eta^\mu| > 1.4$) the event is categorized as "endcap". The mass resolution (estimated from MC) is found to be about 32 MeV for events where the dimuon is produced at $|\eta| \approx 0$, and 75 MeV if the candidate B_s^0 is reconstructed at $|\eta^{\mu\mu}| > 1.8$. The final event selection is performed using BDTs trained to separate the signal, described by $B_s^0 \to \mu^+\mu^-$ MC events, from background events, taken directly from data using the $m_{\mu\mu}$ sidebands. Separate BTDs are trained for data collected in 2011 and 2012, and for the barrel and endcap categories. A set of 12 input variables is used, including informations related to the primary vertex and to the dimuon vertex, the distance of closest approach of the muon pair, the B_s^0 vertex fit probability, $p_T^{\mu\mu}$ and $\eta^{\mu\mu}$, the flight length significance of the candidate B_s^0, and four different definition of isolation. The latter are defined to consider the isolation of each of the muons, and the isolation of the dimuon B_s^0 candidate from the rest of the event. For all the input variables a good agreement between data and simulation is observed, and the output of all the BTDs proved to be insensitive to the mass and independent to the number of simultaneous pp collisions per event (pileup). Analogous BDT selections are applied to normalization and control sample, with slight modifications of the vertex-related variables to take into account the different definition of the decay vertex. The output discriminant b of the BTDs is exploited using two different approaches. A first method has been set up to define the best upper limit on the $\mathcal{B}(B^0 \to \mu^+\mu^-)$ decay if no excess with respect to the SM expectations has been observed. In this method, referred as 1D-BDT, a single cut on b is defined separately for each channels and region by optimizing the signal sensitivity $S/\sqrt{S+B}$ (where S is the expected signal inferred from MC and B the background). The second method consists in the simultaneous fit to the invariant mass in categories defined by cuts on the discriminant b, with different levels of signal significances. This method gives the higher expected sensitivity and is thus chosen to extract $\mathcal{B}(B_s^0 \to \mu^+\mu^-)$. The set of cuts on b is chosen in order to have the same expected signal yield in each category. The branching ratios are measured relative to the B^+ normalization channels, for which $\mathcal{B}(B^+) = (6.0 \pm 0.2)\times10^{-5}$. The ratio of the B^+ and B_s^0 fragmentation fractions, $f_u/f_s = 0.256 \pm 0.020$, is taken from the LHCb measurement [9]. An unbinned maximum-likelihood fit to the $m_{\mu\mu}$ distribution is used to extract the signal and background yields taking into account the dimuon

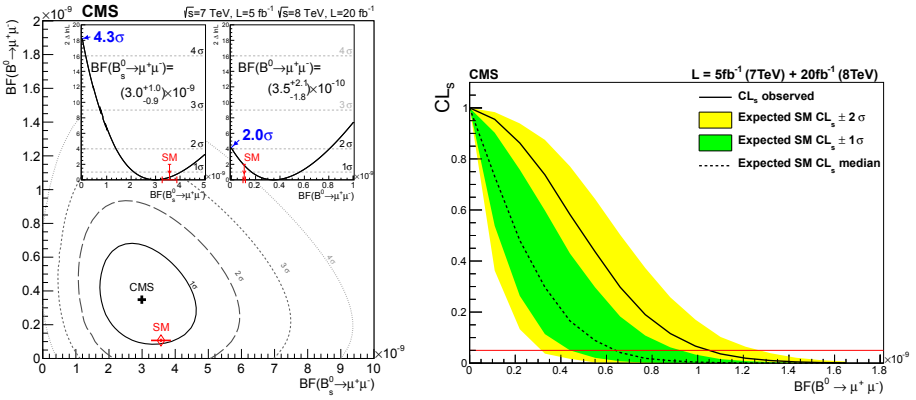

FIGURE 1. Scan of the likelihood ratio of the $\mathcal{B}(B_s^0 \to \mu^+\mu^-)\mathcal{B}(B^0 \to \mu^+\mu^-)$ plane (left). In the small box in the figure, the likelihood ratio scan for the two branching fractions when the other is considered a nuisance parameter to the fit. The observed and expected CL_s for the $\mathcal{B}(B^0 \to \mu^+\mu^-)$ decay (right) as a function of the assumed branching fraction.

mass resolution on event-by-event. An excess of $B_s^0 \to \mu^+\mu^-$ decays with respect to the background-only predictions is observed, allowing to measure a branching fraction of $\mathcal{B}(B_s^0 \to \mu^+\mu^-) = (3.0^{+1.0}_{-0.9}) \times 10^{-9}$, where the statistical and systematic uncertainties are combined, yet dominated by the statistical contribution. The $\mathcal{B}(B^0 \to \mu^+\mu^-)$ is treated as a nuisance parameter and left free to float in the fit to the $B_s^0 \to \mu^+\mu^-$, leading to a measure consistent with the expectations from the SM, as shown in Figure 1. No significant excess is observed for $B^0 \to \mu^+\mu^-$ and the 1D-BDT method is therefore used to estimate the upper limit $\mathcal{B}(B^0 \to \mu^+\mu^-) < 1.1 \times 10^{-9}$ at 95 % confidence level (C.L.) with the CL_s approach. This compares with the expected limits of 6.3×10^{-9} and 5.4×10^{-9} for the hypotheses of signal plus background and background only, respectively.

2 ANGULAR ANALYSIS OF THE $B^0 \to K^*\mu^+\mu^-$ DECAY

The $B^0 \to K^*\mu^+\mu^-$ decay (where K^* indicates the $K^*(892)^0$) is a FCNC process associated to the $b \to s\ell\ell$ transition, forbidden at tree level in the SM. Robust theoretical calculations are now available for most of the phase space of this decay, described in terms of the dimuon mass squared, q^2. Using the data collected in pp collisions at $\sqrt{s}$ = 8 TeV during 2012, the CMS collaboration performed a measurement of the $B^0 \to K^*\mu^+\mu^-$ branching fraction, the forward-backward asymmetry of the muons A_{FB}, and the longitudinal polarization fraction of the K^*, F_L. All these quantities have been measured as a function of q^2 in the range from 1 to 19 GeV^2. The $B^0 \to K^*\mu^+\mu^-$ decay is studied by reconstructing the K^* through the decay $K^* \to K^+\pi^-$. Background events mainly arise from B hadron decaying to J/ψ, and from the resonant channels $B^0 \to K^*J/\psi$ and $B^0 \to K^*\psi'$. These latter are separated from the non-resonant $B^0 \to K^*\mu^+\mu^-$ signal by specific cuts on the the dimuon invariant mass, and are used in the analysis as normalization and control channels, respectively. The events are selected from a trigger requiring two oppositely-charged muons forming a vertex displaced from the pp collision region (beamspot). The offline reconstruction is driven by the selection of muons well-identified by the combination of the informations from the silicon tracker and the muon detectors. Hadron candidates are reconstructed from all the tracks with $p_T^h > 0.8$ GeV that fail the muon identification and for which the extrapolation of their trajectories is significantly displaced from the beamspot in the transverse plane. To avoid contaminations from $\phi \to K^+K^-$ decays, the invariant mass of the track pair with the kaon mass hypothesis is required to be larger than 1.035 GeV. The two hadron candidates must have an invariant mass within 90 MeV from the world average K^* mass in either the $K^+\pi^-$ or $K^-\pi^+$ hypotheses. To obtain the B^0 candidate, a kinematic fit to the four selected tracks is applied by constraining all the tracks to a common vertex. The four-tracks candidates are then required to have $p_T > 8$ GeV, $|\eta| < 2.2$, and an invariant mass within 280 MeV from the accepted B^0 mass for either the $\mu^+\mu^-K^+\pi^-$ or $\mu^+\mu^-K^-\pi^+$ hypotheses. The common vertex is required to have a good fit probability, a large separation from the beamspot of the event in the transverse plane. The transverse momentum of the B^0 candidate is required to be aligned with its flight direction. To separate resonant $B^0 \to K^*J/\psi$ and $B^0 \to K^*\psi'$ events from the $B^0 \to K^*\mu^+\mu^-$ it is required $|q - m_{J/\psi(\psi')}| < 3\sigma_q$, where $\sigma_q \approx 26$ MeV on average. Residual background from charmonium production with the additional production of soft unreconstructed photons is removed

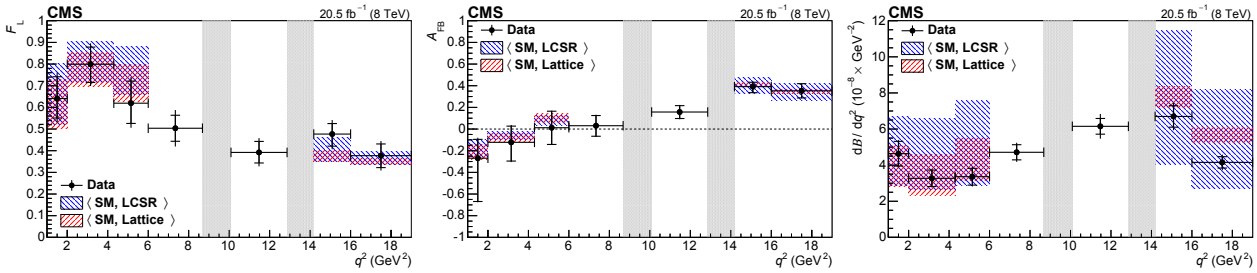

FIGURE 2. Measured values of F_L, A_{FB}, and $d\mathcal{B}/dq^2$ versus q^2 for $B^0 \to K^*\mu^+\mu^-$ showing the statistical (total) uncertainty with the inner (total) bars. The shaded rectangles show the two SM predictions after rate averaging across the q^2 bins to provide a direct comparison to the data. Two techniques for the evaluation of the form factors are compared: the light-cone sum rules (LCSR), made at low q^2 [12] and extrapolated to high q^2 [13]; and the lattice gauge (Lattice) calculation [14].

using a selection combining the informations of m_{B^0}, $m_{J/\psi(\psi')}$, and q. Neutral B mesons are identified as a $B^0(\bar{B}^0)$ if $K^+\pi^-(K^-\pi^+)$ is the mass hypothesis closest to the world average K^* mass. The fraction of B^0 candidates with wrong flavor assignment (mistag) is estimated in simulations to be 12 − 14 %, depending on the q^2. The four-body decay if fully described by three angles: the angle between the kaon momentum and the direction opposite to the B^0 in the K^* rest frame, θ_K; the angle between the positive (negative) muon momentum and the direction opposite to the $B^0(\bar{B}^0)$, θ_L; the angle between the plane containing the dimuon and the one containing the K^* decay, ϕ. The fraction of events from the spinless (S-wave) $K\pi$ contributions, and the amplitude of the interference term between the S-wave and the P-wave components are also included in the angular model. The differential branching fraction, $d\mathcal{B}/dq^2$, is measured relative to the $B^0 \to K^*J/\psi$ normalization channel. Seven q^2 bins have been used to fit the data, corresponding to a total number of 1430 signal events ($B^0 \to K^*\mu^+\mu^-$) events. For each q^2 bin, the three observables of interest are extracted from an unbinned extended maximum likelihood fit to the four-body invariant mass m, and the two angular variables θ_K and θ_L. The fit is performed in two steps: initially data is fit in the B^0 mass sidebands mass to obtain the angular background components; the latter are then fixed for the second step, which involve the fit to the data in the entire mass range, leaving A_{FB} and F_L free, as well as the S-wave parameters A_S, and F_S. The results of the three observables versus q^2 are shown in Figure 2 compared to the SM predictions from [10, 11], obtained by combining two different techniques: a quantum chromodynamic factorization approach in the low-q^2 region, and an operator product expansion in the inverse b quark mass and $1/\sqrt{q^2}$ combined with heavy-quark form-factor relations in the high-q^2 region. Good agreement between the results and the current SM predictions with the experimental results. The results described are combined with previous CMS measurements, obtained from a data sample collected during 2011 at $\sqrt{s}$ = 7TeV [15]. They are found to be competitive with previous measurements from other experiments.

3 FLAVOR-TAGGED ANGULAR ANALYSIS OF THE $B_s^0 \to J/\psi\phi$ DECAY

The CP-violating phase ϕ_s arise in the SM from the interference between direct B_s^0 meson b $\to$ c$\bar{c}$s decays into a CP eigenstate, and B_s^0 decays mediated by mixing to the same final state. Neglecting penguin diagram contributions, it can be expressed as $\phi_s \simeq -2\beta_s$, where $\beta_s = \arg(-V_{ts}V_{tb}^*/V_{cs}V_{cb}^*)$. A value of $\phi_s \simeq 2\beta_s = 0.0363^{+0.0016}_{-0.0015}$ rad is the current best estimate in the SM, determined via a global fit to experimental data [16]. The decay width difference $\Delta\Gamma_s$ is predicted to be non-zero in the SM, and the theoretical prediction, assuming no new physics in B_s^0 mixing, is $\Delta\Gamma_s = 0.087 \pm 0.021$ ps [17]. A time-dependent angular analysis is performed with the CMS detector in the $\mu^+\mu^-K^+K^-$ final state by measuring the decay angles of the final state particles, and the proper decay length of the B_s^0, using data collected in pp collisions at $\sqrt{s}$ = 8 TeV. In this measurement the transversity basis [18] is used to define the three angles of the four-body decay. The differential decay rate of the $B_s^0 \to J/\psi\phi$ in terms of proper decay length and angular variables is represented according to Ref. [19]. Events are selected with a trigger optimized for the detection of b-hadrons decaying to $J/\psi(\mu^+\mu^-)$, with a dimuon invariant mass $2.9 < m_{\mu\mu} < 3.3$ GeV, and $p_T^{\mu\mu} > 6.9$ GeV. The muons are fit to a common decay vertex required to have a good fit probability and to be significantly displaced from the primary vertex of the event in the transverse plane. Offline selection criteria requires the J/ψ to be reconstructed by well-identified muons with $p_T^{\mu} > 4$ GeV. The dimuon invariant mass is required to lie within 150 MeV from the world-average J/ψ mass value. Candidate ϕ are reconstructed from pairs of oppositely charged tracks with $p_T^h > 0.7$ GeV

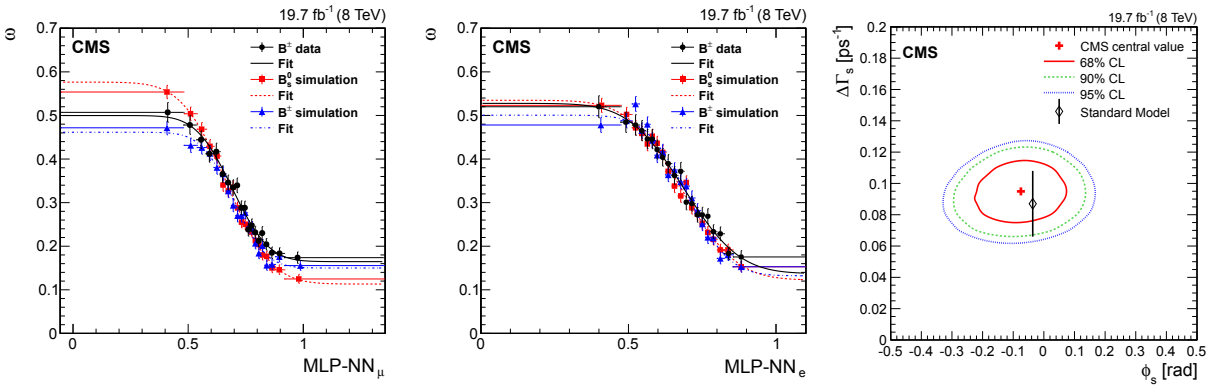

FIGURE 3. The mistag fraction ω as a function of the of the MLP-NN discriminators for muons (left) and electrons (center). The solid black line represents the parametrization curve extracted from the background-subtracted $B^{\pm}$ data; the dashed and dot-dashed lines refer to the parameterizations extracted from the simulated B_s^0 and $B^{\pm}$ samples, respectively. The CMS measured central value (right) and the 68 %, 90 %, and 95 % CL contours in the $\Delta\Gamma_s$ versus ϕ_s plane, together with the SM prediction. Uncertainties are statistical only.

if the hh′ invariant mass is found to be within 10 MeV from the world average ϕ mass. B_s^0 candidates are formed by combining a J/ψ with a ϕ candidate by performing a kinematic fit of the four tracks, by constraining the dimuon invariant mass to the nominal J/ψ mass. A B_s^0 candidate is retained if its invariant mass is found to be between 5.20 and 5.65 GeV. Simulated $B_s^0 \to J/\psi\phi$ samples, validated through comparison with the data, are used to determine the signal reconstruction efficiencies, and to estimate the background components in the signal mass window. The angular efficiency is obtained from simulations with a three-dimensional function of the angular variables in order to take into account the correlations. The proper decay length, ct, is required to be larger than 200 μm in order to avoid bias induced by the turn-on of the trigger efficiency. The flavor of each B_s^0 candidate at production time is determined with an opposite-side flavor tagging algorithm using information from the lepton (μ, e) produced in the decay of the other B hadron in the event, assuming the $b\bar{b}$ production process has occurred. For all the events in which a tag lepton is found the algorithm provides the tag decision, based on the charge of the lepton, and the expected mistag probability ω. The tagging algorithm is optimized by maximizing the tagging power $\mathcal{P}_{tag} = \varepsilon_{tag}\,(1-2\omega)^2$, figure of merit of the tagging performances, where ε_{tag} is the efficiency, defined as the fraction of events to which a tag decision is found by the tagging algorithm. The tag leptons are selected with a set of loose cuts optimized separately for muons and electrons using simulated signal samples of $B_s^0 \to J/\psi\phi$ decays. Two multilayer perceptron neural networks (MLP-NN), trained on $B_s^0 \to J/\psi\phi$ MC events, are used to provide variables (MLP $-$ $NN_{\mu(e)}$) used to separate the right- and wrong-tag leptons. Mistag probabilities are measured on data using the self-tagging channel $B^+ \to J/\psi\,K^+$ decays, where the charge of the reconstructed kaon determines the flavor of the $B^{\pm}$ and, in the absence of mixing, of the signal B_s^0. The parametrization of ω with analytic functions of the MLP-NN discriminators provide a per-event value of the predicted mistag probability, shown in Figure 3. The overall tagging power of the algorithm used in this analysis, as measured in a sample of $B^+ \to J/\psi\,K^+$ events, is $\mathcal{P}_{tag} = (1.307 \pm 0.031\,(\text{stat}) \pm 0.007\,(\text{syst}))$ %, corresponding to $\omega = (30.17 \pm 0.24\,(\text{stat}) \pm 0.05\,(\text{syst}))$ %. The results are extracted by an unbinned maximum likelihood fit to the data, performed including the flavor tagging informations. The proper decay length uncertainty (σ_{ct}) obtained propagating the uncertainties of the proper decay length measurement is included in the fit to model the per-event ct resolution. The fit is applied to the sample of 70 000 events (including 49 000 signal candidates), selected in the mass range $5.24 < m_{B_s^0} < 5.49$ GeV and proper decay length range $200 < ct < 3\,000$ μm. The Δm_s value is constrained in the fit to the current world average value $(17.69 \pm 0.08) \times 10^{12}$ $\hbar$/s. No direct CP violation is assumed in this measurement, and λ is set to one, as measured by the LHCb collaboration [20]. $\Delta\Gamma_s$ is constrained to be positive [21]. The weak phase and the decay width difference between the B_s^0 mass eigenstates are $\phi_s = -0.075 \pm 0.097(\text{stat}) \pm 0.031(\text{syst})$ rad and $\Delta\Gamma_s = 0.095 \pm 0.013(\text{stat}) \pm 0.007(\text{syst})$ ps^{-1}, respectively. The measured values are consistent with those obtained by the LHCb Collaboration using $B_s^0 \to J/\psi K^+K^-$ decays. The 68%, 90% and 95% C.L. likelihood contours of the fit for ϕ_s and $\Delta\Gamma_s$ are shown in Fig. 3. This measured value of ϕ_s agrees with the SM prediction, and $\Delta\Gamma_s$ is experimentally confirmed to be nonzero, with a value consistent with the theoretical predictions.

CONCLUSION

The most recent results of the CMS collaboration for the $\mathcal{B}(B_s^0 \to \mu^+\mu^-)$, the angular analysis of the $B^0 \to K^*\mu^+\mu^-$ decay, and the flavor-tagged angular analysis of the CP-violating phase ϕ_s are presented. The results are among the most precise currently available. The SM expectations for all the three analyses are in good agreement with the experimental results by CMS. The precision of all the presented measurements is currently dominated by the contribution of the statistical uncertainty.

REFERENCES

[1] The CMS Collaboration. The CMS experiment at the CERN LHC. *JINST*, 3:S08004, 2008.

[2] The CMS Collaboration. Measurement of the $B_s^0 \to \mu^+\mu^-$ branching fraction and search for $B^0 \to \mu^+\mu^-$ with the CMS Experiment. *Phys. Rev. Lett.*, 111:101804, 2013.

[3] The CMS Collaboration. Angular analysis of the decay $B^0 \to K^{*0}\mu^+\mu^-$ from pp collisions at $\sqrt{s} = 8$ TeV. 2015.

[4] The CMS Collaboration. Measurement of the CP-violating weak phase ϕ_s and the decay width difference $\Delta\Gamma_s$ using the $B_s^0 \to J/\psi\phi(1020)$ decay channel in pp collisions at $\sqrt{s} = 8$ TeV. 2015.

[5] A. J. Buras, J. Girrbach, D. Guadagnoli, and G. Isidori. On the Standard Model prediction for $\mathcal{B}(B_{s,d} \to \mu^+\mu^-)$. *Eur. Phys. J.*, C72:2172, 2012.

[6] K. De Bruyn, R. Fleischer, R. Knegjens, P. Koppenburg, M. Merk, A. Pellegrino, and N. Tuning. Probing New Physics via the $B_s^0 \to \mu^+\mu^-$ Effective Lifetime. *Phys. Rev. Lett.*, 109:041801, 2012.

[7] The CMS Collaboration. Search for $B_s^0 \to \mu^+\mu^-$ and $B^0 \to \mu^+\mu^-$ decays. *JHEP*, 04:033, 2012.

[8] K. A. Olive et al. Review of Particle Physics. *Chin. Phys.*, C38:090001, 2014.

[9] The LHCb Collaboration. Measurement of the fragmentation fraction ratio f_s/f_d and its dependence on B meson kinematics. *JHEP*, 04:001, 2013.

[10] C. Bobeth, G. Hiller, and D. van Dyk. The Benefits of $\bar{B} \to \bar{K}^*\ell^+\ell^-$ Decays at Low Recoil. *JHEP*, 07:098, 2010.

[11] C. Bobeth, G. Hiller, and D. van Dyk. General analysis of $\bar{B} \to \bar{K}^{(*)}\ell^+\ell^-$ decays at low recoil. *Phys. Rev.*, D87(3):034016, 2013.

[12] A. Khodjamirian, Th. Mannel, A. A. Pivovarov, and Y. M. Wang. Charm-loop effect in $B \to K^{(*)}\ell^+\ell^-$ and $B \to K^*\gamma$. *JHEP*, 09:089, 2010.

[13] A. Khodjamirian, Th. Mannel, and Y. M. Wang. $B \to K\ell^+\ell^-$ decay at large hadronic recoil. *JHEP*, 02:010, 2013.

[14] R. R. Horgan, Z. Liu, S. Meinel, and M. Wingate. Lattice QCD calculation of form factors describing the rare decays $B \to K^*\ell^+\ell^-$ and $B_s \to \phi\ell^+\ell^-$. *Phys. Rev.*, D89(9):094501, 2014.

[15] The CMS Collaboration. Angular analysis and branching fraction measurement of the decay $B^0 \to K^{*0}\mu^+\mu^-$. *Phys. Lett.*, B727:77–100, 2013.

[16] J. Charles et al. Predictions of selected flavour observables within the Standard Model. *Phys. Rev.*, D84:033005, 2011.

[17] A. Lenz and U. Nierste. Numerical Updates of Lifetimes and Mixing Parameters of B Mesons. In *CKM unitarity triangle. Proceedings, 6th International Workshop, CKM 2010, Warwick, UK, September 6-10, 2010*, 2011.

[18] A. S. Dighe, I. Dunietz, and R. Fleischer. Extracting CKM phases and $B_s^0 - \bar{B}_s^0$ mixing parameters from angular distributions of nonleptonic B decays. *Eur. Phys. J.*, C6:647–662, 1999.

[19] A. S. Dighe, I. Dunietz, H. J. Lipkin, and J. L. Rosner. Angular distributions and lifetime differences in $B_s^0 \to J/\psi\phi$ decays. *Phys. Lett.*, B369:144–150, 1996.

[20] The LHCb Collaboration. Measurement of the CP-violating phase ϕ_s in $\bar{B}_s^0 \to J/\psi\pi^+\pi^-$ decays. *Phys. Lett.*, B736:186, 2014.

[21] The LHCb Collaboration. Determination of the sign of the decay width difference in the B_s^0 system. *Phys. Rev. Lett.*, 108:241801, 2012.

Proceedings of the LHCP2015 Conference, St. Petersburg, Russia, August 31 - September 5, 2015

Editors: V.T. Kim and D.E. Sosnov

Higgs boson plus heavy flavour: searches and measurements from the LHC Run 1

LORENZO BIANCHINI

ETH Zürich, Institute for Particle Physics, Otto-Stern-Weg 5, 8093 Zürich (Switzerland)

lore.bianchini@gmail.com

On behalf of the ATLAS and CMS Collaborations

Abstract. This talk gives a review of the Run 1 ATLAS and CMS results on searches and measurements of Higgs bosons decaying to, or produced in association with heavy-flavour quarks (charm, bottom, and top quarks). The Standard Model of particle physics predicts that the Higgs boson interacts with the quarks through scalar, flavour-diagonal, Yukawa interactions, whose tree-level coupling strength is also fixed to be proportional to the quark mass. The detection of Higgs bosons decaying to a heavy flavour quark-antiquark pair (bottom and, to a smaller extent, charm quarks), or produced in association with heavy quarks (top and bottom quarks), is therefore the most favourable way to probe the quark Yukawa sector.

INTRODUCTION

The Standard Model (SM) of particle physics becomes a fully predictive theory once the mass of the Higgs boson is specified. In particular, the SM completely determines the Lorentz and the flavour structure of the interactions between the Higgs doublet, Φ, and the quark fields, Ψ, in the form of Yukawa interactions $\sim \lambda_{ij}\Psi_i\Psi_j\Phi$. More precisely, the only gauge-invariant, dimension-4 combinations are:

$$-\sum_{i,j}[\lambda^U_{ij}\bar{Q}_i i\sigma_2\Phi^* u^R_j + \lambda^D_{ij}\bar{Q}_i\Phi d^R_j] + h.c., \tag{1}$$

where λ's are arbitrary matrices in flavour space. After electroweak symmetry breaking, $\Phi \propto (0, \frac{1}{\sqrt{2}}(v+H))$, where v is the vacuum expectation value (*vev*) of the Higgs field, and upon diagonalisation of the quark mass, the Yukawa sector for the quarks becomes

$$\mathcal{L}_Y \supset \sum_{q=u,d,c,s,b,t} \lambda_q[\bar{q}_L q_R H + \bar{q}_R q_L H], \quad \text{with } \lambda_q = -\frac{\sqrt{2}m_q}{v}. \tag{2}$$

To summarise, the SM gives the following predictions on the quark Yukawa quark sector:

1. there is no tree-level CP violation, i.e. there are no tree-level interactions of the form $i\tilde{\lambda}_q\bar{q}\gamma_5 qH$;
2. there are no tree-level flavour changing neutral currents (FCNC), and the GIM mechanism further suppresses them to be totally negligible;
3. the coupling strength, λ_q, is proportional to the quark mass, m_q.

At the LHC, only production times decay rates of the form $\sigma_{ii\to H+X} \times \mathcal{B}(H \to ff)$ can be measured for $1 \to 2$ decays. These rates can be parametrised as $\kappa_i^2\kappa_f^2\cdot\kappa_H^{-2}$ times the corresponding SM prediction, where $\kappa_{i,f}$ are real-valued modifiers that shift the corresponding coupling strengths with respect to their SM expectation (*i.e.* $\lambda_q = \kappa_q\cdot\lambda_q^{\mathrm{SM}}$), while κ_H shifts the overall Higgs boson width, and thus depends on all the κ's as well as any unknown non-SM width. By measuring the signal rates for a large enough number of channels, it is possible to measure the individual κ's or, in

a more model-independent approach, their mutual ratios. In general, the production times decay rates are insensitive to the phase of the coupling (*i.e.* its sign, if the coupling is real). However, in a few cases the phase of the coupling matters due to the interference between different amplitudes, and a measurement of the sign (or, more generally, of the relative sign between different couplings) is possible. Finally, searches for events produced by flavour-changing currents, either in production (e.g $q \to Hq'$) or decay (e.g $H \to q\bar{q}'$) of the Higgs boson, can provide a direct evidence of discrepancy from the SM.

HEAVY FLAVOUR IN HIGGS DECAY: THE CHARM AND BOTTOM COUPLINGS

Both the ATLAS [1] and the CMS [2] Collaborations have made extensive searches for Higgs boson decays into a bottom quark-antiquark pair. Due to the large branching ratio and the relatively high experimental separation between jets arising from the hadronisation of bottom and light quarks, where a tag *vs* mistag ratio of about $\sim 0.70 : 0.02$ can be typically achieved, the $H \to b\bar{b}$ signature can be extracted from an otherwise overwhelming multi-jet background with a few tens of fb^{-1} of pp data. Due to the smaller branching ratio and the higher mistag rate, this is much less of the case for $H \to c\bar{c}$, and the whole LHC program will likely be not enough for a direct observation of this exclusive decay.

The charm Yukawa coupling

Given the experimental challenge posed by extracting the $H \to c\bar{c}$ decay at a hadron collider, different approaches have been proposed in the literature to probe the $c\bar{c}H$ coupling strength. In particular, it has been suggested to search for radiative decays of the form $H \to VM$, where $V = W^{\pm}, Z, \gamma$ and M is a vector meson [3, 4, 5]. The amplitude for the rare decay $H \to J/\Psi\gamma$ depends on the charm Yukawa coupling thanks to the (negative) interference between the direct $H \to c\bar{c} \to J/\Psi\gamma$ amplitude and the indirect amplitude $H \to \gamma\gamma \to J/\Psi\gamma$. The resulting branching ratio is however rather small, $\mathcal{B}(H \to J/\Psi\gamma) \approx 3 \cdot 10^{-6}$ [3], making this channel essentially a null test of the SM even with the full HL-LHC program. Searches for this process have been performed by both the ATLAS [6] and CMS [7] Collaborations. As an example, the ATLAS analysis [6] uses events with one high-p_T photon and a muon pair with $m_{\mu\mu}$ within 200 MeV of the J/Ψ mass. A simultaneous unbinned fit to the $m_{\mu\mu\gamma}$ and $p_T^{\mu\mu\gamma}$ distributions is performed to set limits on the branching ratio. The observed 95% CL upper limits on $\mathcal{B}(H \to J/\Psi\gamma)$ obtained by the ATLAS and CMS experiments are 1.2×10^{-3} and 1.5×10^{-3}, respectively, and are in agreement with the background only expectation.

The bottom quark Yukawa coupling

The measurement of $\sigma_{H+X} \times \mathcal{B}(H \to b\bar{b})$ provides the strongest constraint on κ_b, although model-dependent constraints can be obtained also from channels that do not include this decay mode because κ_H^2 strongly depends on κ_b. Three main production channels have been studied, namely associated production (VH), vector boson fusion (VBF), and associated top-Higgs production (ttH).

The VH analyses [8, 9] are performed in final states with 0, 1, or 2 leptons, targeting the decay $Z \to \nu\bar{\nu}$, $W^{\pm} \to \ell^{\pm}\nu$, and $Z \to \ell^+\ell^-$, respectively. The CMS analysis [9] further includes a channel where one jet is identified as a hadronically-decaying tau lepton. At least two jets tagged as b jets are required. Events are split into categories of increasingly larger transverse momentum of the reconstructed vector boson. The invariant mass of the di-jet system peaks around the true Higgs mass with an experimental resolutions of about 15% (Fig. 1, left). The dominant non-resonant background are V+jets and $t\bar{t}$, and are estimated using Monte Carlo (MC) simulation normalised in data control regions. Multivariate classifiers that use kinematic and b tagging information from the whole event are used to improve the signal/background separation. The observed (expected) signal p-values for a Higgs boson mass of 125 GeV are 1.4σ (2.6σ) and 2.1σ (2.1σ) for the ATLAS and CMS analyses, respectively. At the time of the publication, the CMS analysis [9] did not include the $gg \to ZH$ sub-process as part of the signal. After its inclusion, the expected p-value becomes 2.5σ [10].

A fully-hadronic analysis of four-jet final states with a VBF-like topology has been performed to search for $H \to b\bar{b}$ decays produced through vector boson fusion [10]. Several variables that exploit the properties of the VBF-jet system, the flavour tagging of the jets, and the overall event activity are used to select signal events with increasing purity. Simultaneous fits to the di-jet mass spectra in the various event categories are used to extract the signal yield (Fig. 1, centre). The observed (expected) significance is 2.5σ (0.8σ).

Searches for $t\bar{t}$ production in association with a Higgs boson that decays to bottom quarks have been performed in single and di-lepton final states [11, 12, 13]. The ttH signature is characterised by several jets, four of which are coming from the hadronisation of b quarks. The dominant background is the hadronic production of a top quark-antiquark pair with additional jets. The analysis is performed in mutually exclusive event categories based on the number of jets and b-tagged jets, which allows to account for the possibility that some of the b-jets have not been tagged. Multivariate discriminants based on the event kinematics and the b tagging properties of the jets are used to extract the signal yield. The observed (expected) exclusion limit at the 95% confidence level (CL) are 3.4 (2.2) and 4.1 (3.5) times the SM expectation, for the ATLAS and CMS experiments, respectively.

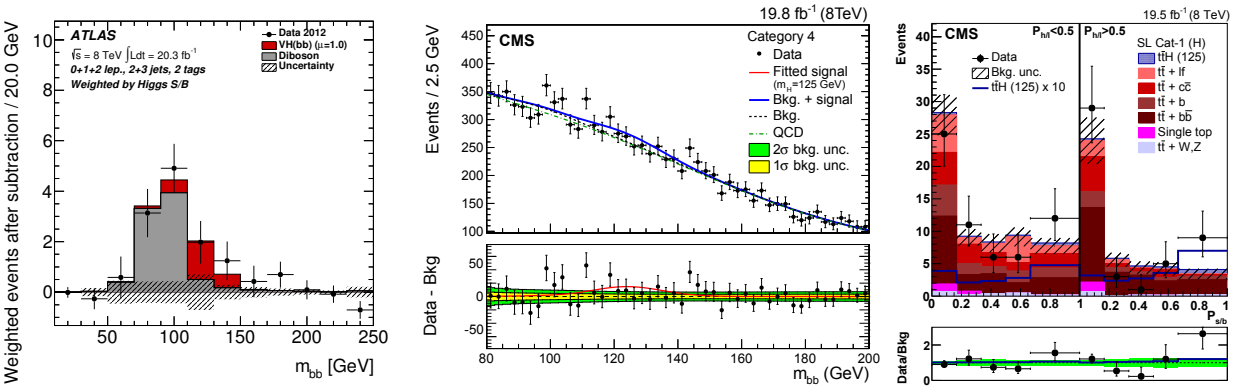

FIGURE 1. Left: invariant mass distribution of the di-jet system in VH-like events after subtracting the non-resonant backgrounds [8]. Centre: invariant mass distribution of the di-jet system for one of the VBF analysis category of Ref. [10]; the continuum background is fitted with an analytical function. Right: distribution of the matrix element ratio discriminant in the category with ≥ 6 jets and a large value of the $4b$-likelihood discriminant [13].

The combination of the ATLAS VH and ttH measurement yields a combined value of $\mu^{b\bar{b}} = 0.63^{+0.39}_{-0.37}$ [14], while the combination of the CMS VH, ttH, and VBF measurements gives $\mu^{b\bar{b}} = 1.03^{+0.44}_{-0.42}$, corresponding to a p-value of 2.6σ under the background-only hypothesis [10]. In terms of the signal strength modifier κ_b, a model-dependent fit that assumes no beyond the SM (BSM) particles in the loops or in decay yields a best-fit value $\kappa_b = 0.62^{+0.31}_{-0.27}$ [14] and $\kappa_b = 0.64^{+0.28}_{-0.29}$ [15], respectively (Fig. 2).

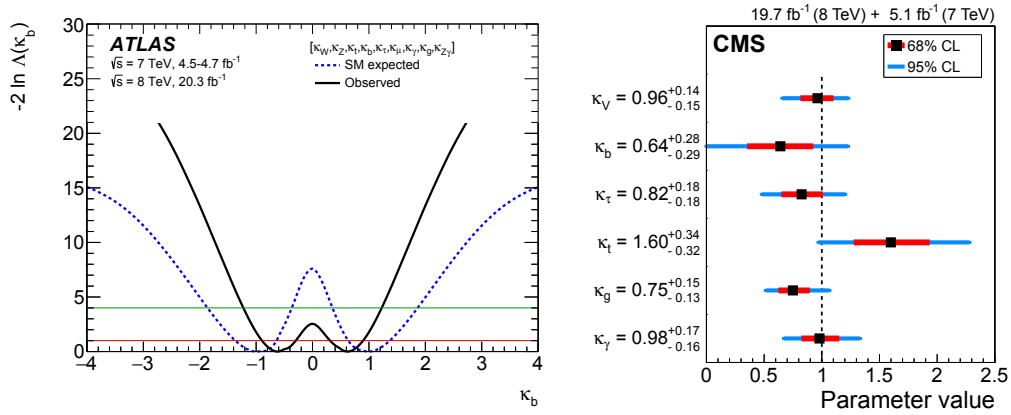

FIGURE 2. Left: the ATLAS likelihood scan as a function of κ_b when profiling all the other coupling modifiers in a model with no extra particles in the loops and no BSM decays [14]. Right: the 68% and 95% CL intervals on the κ modifiers for the same model, as obtained by the CMS experiment [15].

Although the SM $b\bar{b}H$ production cross section is almost a factor of two larger than $t\bar{t}H$, it is experimentally much more challenging. In the minimal supersymmetric extension of the SM (MSSM), the heavy CP-even (H) and

the CP-odd (A) Higgs bosons eigenstates (collectively denoted by Φ) are almost degenerate in mass in the so-called decoupling regime, and their production cross section via $b\bar{b}\Phi$ is enhanced for large value of $\tan\beta \equiv v_2/v_1$. The branching ratio is also increased for large value of $\tan\beta$, thus making the $b\bar{b}\Phi$, $\Phi \to b\bar{b}$ an appealing channel. However, the huge multi-jet background makes its less sensitive than the competing $\Phi \to \tau^+\tau^-$ search. On the positive side, radiative corrections involving high mass SUSY states (the so-called threshold parameter Δ_b) can affect the value of $\sigma(b\bar{b}\Phi) \times \mathcal{B}(\Phi \to b\bar{b})$ differently from $\sigma(b\bar{b}\Phi) \times \mathcal{B}(\Phi \to \tau^+\tau^-)$, in such a way that a higher sensitivity to the SUSY radiate corrections, hence on the SUSY parameters, is retained by the former [16].

A search for a narrow high-mass $\Phi \to b\bar{b}$ resonance in all-hadronic final states has been performed by the CMS Collaboration [17] using events with three jets and exactly two (control region) or exactly three b tagged jets (signal region). The control region is used to derive data-driven templates for the di-jet invariant mass spectrum corresponding to different jet flavour assignments. A fit to the invariant mass distribution is then used to set limits. No evidence of a signal is found, and the results are used to set limits for some MSSM benchmark scenarios [17].

HEAVY FLAVOUR IN HIGGS PRODUCTION: THE TOP COUPLING

Owing to its large mass, the top quark cannot be produced in the decay of an on-shell Higgs boson. Both the Higgs boson production cross section and the branching ratio for $H \to \gamma\gamma$ are sensitive to the top Yukawa coupling because these two amplitudes involve loops of top quarks that contain a $t\bar{t}H$ vertex. In order to perform model-independent measurements of the coupling, *i.e.* without assumptions on the loop structure, one would desire to make a direct measurement of the coupling strength through amplitudes that probe the $t\bar{t}H$ vertex at the tree-level.

Production of a top quark-antiquark pair in association with a Higgs boson

Searches for ttH production in the $H \to b\bar{b}$ channel have been already discussed in Section . These analyses have been complemented with measurements targeting other exclusive decay modes, namely $H \to \gamma\gamma$, $H \to W^+W^-$, $H \to ZZ*$, and $H \to \tau^+\tau^-$ [18, 19, 12]. The latter is searched in three distinctive signatures, corresponding to exactly two same-sign leptons, exactly three leptons, and exactly four leptons. Table 1 summarises the results for the various channels in terms of exclusion limits and best-fit value of the signal strength modifier μ_{ttH}. When combined together, the observed (expected) p-values for the background-only hypothesis are 2.5σ (1.5σ) and 3.6σ (1.2σ), as obtained by the ATLAS and CMS Collaborations, respectively.

TABLE 1. Exclusion limits and best-fit values for the signal strength modifier μ_{ttH} obtained by the ATLAS and CMS Collaborations.

	Observed (expected) 95% CL limit	**Best-fit value** $\pm 1\sigma$	**References**
$H \to b\bar{b}$	3.4 (2.2), 4.1 (3.5)	$1.5^{+1.1}_{-1.1}$, $0.7^{+1.9}_{-1.9}$	[11], [12]
$H \to \gamma\gamma$	6.7 (4.9), 7.4 (4.7)	$1.4^{+2.1}_{-1.4}$, $2.7^{+2.6}_{-1.8}$	[18], [12]
$H \to W^+W^-$	4.7 (2.4), 6.6 (2.4)	$2.1^{+1.4}_{-1.2}$, $3.7^{+1.6}_{-1.4}$	[19], [12]

The first (second) entry are the results reported by the ATLAS (CMS) Collaboration.

Production of a single-top quark in association with a Higgs boson

The single-top quark production in association with a Higgs boson (tH) has a rather small cross section ($\approx$ 18 fb at $\sqrt{s} = 8$ TeV). The dominant production mechanism through t-channel exchange of a W boson (tHq) is suppressed by the negative interference between amplitudes containing the $W_\mu W^\mu H$ and $t\bar{t}H$ vertices. The destructive interference is close to maximal for $\kappa_V = \kappa_t = 1$, implying that large deviations from the SM expectation can be obtained for non-SM values of κ_t, in particular for $\kappa_t/\kappa_V < 1$.

The ATLAS Collaboration has performed an inclusive search for top quark(s) plus Higgs bosons in the $H \to \gamma\gamma$ final states [18]. Figure 3 (left) shows the effect of including the tH production in the coupling fit combination. Owing to its non-trivial dependence on κ_t, this channel has the unique feature of lifting the sign degeneracy of the likelihood, if no further assumption is made on $\mathcal{B}(H \to \gamma\gamma)$. The corresponding best-fit value of κ_t obtained by the CMS Collaboration is reported in Fig. 2 (right).

The CMS Collaboration has carried out dedicated searches for tHq, targeting separately Higgs boson decays into two photons, two bottom quarks, and multi-lepton final states [20]. Differently from the analysis documented in Ref. [18], the CMS analyses are specifically optimised to separate the tHq signal from any other Higgs signal, in particular from the larger ttH production mechanism. The observed (expected) cross section exclusion limit at the 95% CL is shown in Figure 3 (right), and amounts to 2.8 (2.0) times the SM expectation for a flipped-sign hypothesis ($\kappa_t = -1$). These measurements were not included in the *grand combination* of Ref. [15].

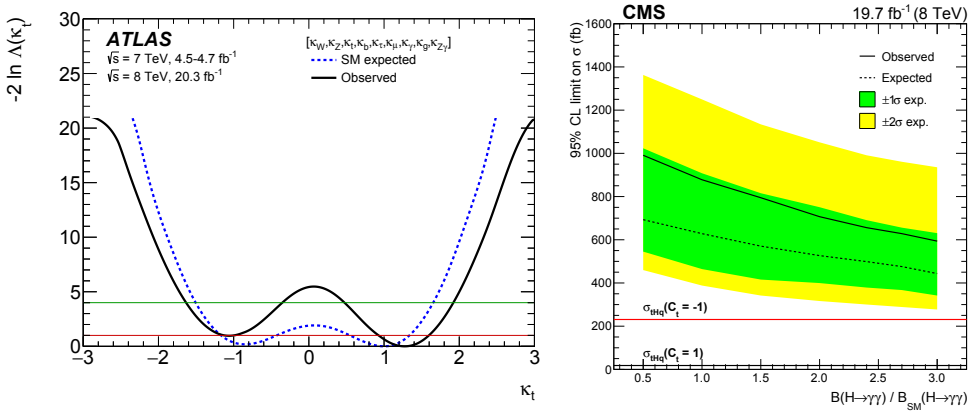

FIGURE 3. Left: the ATLAS likelihood scan as a function of κ_t as obtained from an analysis of di-photon events with additional jets [18]. Right: the 95% CL upper limits on σ_{tH} as a function of $\mu^{\gamma\gamma}$, as obtained from a combination of three independent searches for tHq production [20].

SEARCH FOR FLAVOUR CHANGING DECAYS

As introduced in Sec. , flavour changing neutral currents are suppressed in the SM. In the Yukawa sector, operators of the form $\bar{q}q'H$, where q and q' are quark with the same isospin number but of different families, are heavily suppressed. The transition $t \to Hc$ is experimentally appealing due to the large $t\bar{t}$ cross section, but in the SM the branching ratio is only of $O(10^{-15})$. However, FCNC naturally appear in almost all extensions of the SM, like two Higgs doublet models (2HDM), or quark singlet models (QS) [21]. As an heuristic example, imagine to introduce a higher dimensional operator in an EFT approach of the form $\epsilon_{ij}\Psi_i\Psi_j\Phi^3$, with $\epsilon_{ij} \propto \Lambda^{-2}$. Expanding Φ to first order around vev, the quark mass matrix becomes proportional to $(v\lambda_{ij} + v^3\epsilon_{ij})$, while the Yukawa matrix is proportional to $(\lambda_{ij} + 3v^2\epsilon_{ij})$, so unless a special flavour simmetry protects the higher-order operators, the diagonalisation of the mass matrix will not make, in general, the Yukawa matrix diagonal. By introducing an operator of the form $\mathcal{L}_{\mathrm{FCNC}} = -\lambda_{tuH}\bar{t}uH - \lambda_{tcH}\bar{t}cH + h.c.$, the flavour-changing branching ratio can be parametrised as:

$$\mathcal{B}(t \to (u,c)H) = \frac{\lambda_{tuH}^2 + \lambda_{tcH}^2}{g^2|V_{tb}|^2\chi^2}, \tag{3}$$

where g is the weak gauge coupling and χ is a kinematic function. Both the ATLAS and CMS Collaborations have performed a search for flavour-changing top quark transitions, followed by the decay $H \to \gamma\gamma$, using zero or one lepton events plus additional jets [22, 23]. Mass constraints on the jet and lepton system are used to suppress non-top backgrounds. The signal is extracted through a maximum likelihood fit to the di-photon mass spectrum, and the corresponding exclusion limits are translated into limits on the FCNC coupling by using Eq. 3. The observed (expected) exclusion limits on $\mathcal{B}(t \to (u,c)H)$ are 0.79% (0.51%), and 0.47% (0.71%), for the ATLAS and CMS experiments respectively. These results allow to exclude values of $\sqrt{\lambda_{tuH}^2 + \lambda_{tcH}^2}$ in excess of about 0.1. The CMS Collaboration has extended this search to multi-lepton final states, with sensitivity comparable to the di-photon channel [24, 25].

CONCLUSIONS

The Higgs physics program pursued in Run 1 at the LHC is already probing the Yukawa sector of the SM. Searches and measurements of Higgs bosons decaying to heavy quarks, or produced in association with heavy quarks, provide compatibility tests of the SM. Measurements sensitive to the charm quark Yukawa coupling are presently pursued by hunting the rare decay $H \to J/\Psi\gamma$. Sensitivity to the bottom quark coupling is provided by searches for the exclusive $H \to b\bar{b}$ decay, while the top Yukawa coupling can be probed, in the least model-dependent way, by measuring the ttH cross section. Dedicated tH measurements are important to rule out anomalous $t\bar{t}H$ couplings. Finally, the flavour structure of the Yukawa sector can be studied by searching for rare FCNC decays of the top quark.

All measurements performed to date show overall consistency with the SM prediction for the quark Yukawa sector. Most important, the larger data set that will be collected during the upcoming Run 2 of the LHC will allow to gather a conclusive evidence of the bottom and top Yukawa coupling.

REFERENCES

[1] ATLAS Collaboration, JINST **3**, p. S08003 (2008).
[2] CMS Collaboration, JINST **3**, p. S08004 (2008).
[3] G. T. Bodwin et al., Phys. Rev. D **88**, p. 053003 (2013).
[4] A. L. Kagan et al., Phys. Rev. Lett. **224**, p. 101802 (2015).
[5] G. Isidori et al., Phys. Lett. B **728**, 131–135 (2014).
[6] ATLAS Collaboration, Phys. Rev. Lett. **114**, p. 121801 (2015).
[7] CMS Collaboration, submitted to Phys. Lett. B (2015), arXiv:1507.03031 [hep-ex].
[8] ATLAS Collaboration, JHEP **01**, p. 069 (2015).
[9] CMS Collaboration, Phys. Rev. D **89**, p. 012003 (2014).
[10] CMS Collaboration, Phys. Rev. D **89**, p. 012003 (2014).
[11] ATLAS Collaboration, Eur. Phys. J. C **75**, p. 349 (2015).
[12] CMS Collaboration, JHEP **09**, p. 087 (2014).
[13] CMS Collaboration, Eur. Phys. J. C **75**, p. 251 (2015).
[14] ATLAS Collaboration, accepted by Eur. Phys. J. C (2015), arXiv:1507.04548 [hep-ex].
[15] CMS Collaboration, Eur. Phys. J. C **75**, p. 212 (2015).
[16] M. Carena et al., Eur. Phys. J. C **45**, p. 797 (2006).
[17] CMS Collaboration, accepted by JHEP (2015), arXiv:1506.08329 [hep-ex].
[18] ATLAS Collaboration, Phys. Lett. B **740**, 222–242 (2015).
[19] ATLAS Collaboration, Phys. Lett. B **749**, 519–541 (2015).
[20] CMS Collaboration, submitted to JHEP (2015), arXiv:1509.08159 [hep-ex].
[21] Aguilar-Saavedra, Acta Phys. Polon. **B35**, 2695–2710 (2004).
[22] ATLAS Collaboration, JHEP **06**, p. 008 (2014).
[23] CMS Collaboration, CMS Physics Analysis Summary **CMS-PAS-TOP-14-019** (2014).
[24] CMS Collaboration, CMS Physics Analysis Summary **CMS-PAS-TOP-13-017** (2013).
[25] CMS Collaboration, Phys. Rev. D **90**, p. 112013 (2013).

Proceedings of the LHCP2015 Conference, St. Petersburg, Russia, August 31 - September 5, 2015

Editors: V.T. Kim and D.E. Sosnov

ATLAS Heavy-Flavour Spectroscopy and Exotic States

SEMEN TURCHIKHIN[1,2]

[1]*D. V. Skobeltsyn Institute of Nuclear Physics, M. V. Lomonosov Moscow State University*
[2]*Faculty of Physics, M. V. Lomonosov Moscow State University*

Semen.Turchikhin@cern.ch

On behalf of the ATLAS Collaboration

Abstract. The paper presents a review of recent heavy-flavour spectroscopy studies performed with the ATLAS experiment using the data collected during the LHC Run 1. This includes the first observation of an excited state of the B_c^+ meson and a search for X_b and other hidden-beauty states in $\pi^+\pi^-\Upsilon(1S)$ channel.

INTRODUCTION

The LHC provides a good environment for studies of heavy-flavour spectroscopy. Both measurements of properties of the known states and searches for new ones are possible. In this paper, two recent results obtained by the ATLAS experiment [1] with the Run 1 data are presented: the first observation of an excited state of the B_c^+ meson [2] and a search for X_b and other hidden-beauty states in $\pi^+\pi^-\Upsilon(1S)$ channel [3].

OBSERVATION OF AN EXCITED B_c^+ MESON

Ground state of B_c^+ meson[1] was observed earlier in both semileptoic and hadronic decay modes; no excited state observations were reported before. However, their spectrum and properties are predicted by non-relativistic potential models, perturbative QCD, and lattice calculations (see reference 5 in Ref. [2]). Thus, observations and measurements of these states can provide a means to test those predictions and ultimately to extract information on the strong interaction potential. A good candidate for experimental search is a pseudo-scalar state of $B_c^+(2S)$ decaying into a ground state B_c^+ and a pair of pions.

The ATLAS analysis uses the full sample of pp collisions data collected at centre-of-mass energies $\sqrt{s}$ = 7 TeV and 8 TeV corresponding to integrated luminosities of 4.9 fb^{-1} and 19.2 fb^{-1}, respectively.

The ground state B_c^+ is reconstructed in $B_c^+ \to J/\psi(\mu^+\mu^-)\pi^+$ decay mode. The candidates are built by combining two tracks identified as muons with one additional track assigned a pion mass and fitting them to a common vertex. Requirements on the tracks and the candidate kinematics and the vertex fit quality are applied. The pion is also required to have high significance of the transverse impact parameter with respect to the primary vertex, which allows to substantially reduce the combinatoric backgrounds. Figure 1 shows the mass distribution of the reconstructed candidates in 7 TeV and 8 TeV data. They are fitted with a sum of a Gaussian shape to describe the signal peak and an exponential function for the background.

The $B_c^+(2S) \to B_c^+\pi^+\pi^-$ candidates are formed by combining a B_c^+ candidate with two oppositely charged hadronic tracks from the primary vertex. A cascade fit is performed, requiring the B_c^+ combined momentum to point back to the primary vertex. If more than one $B_c^+(2S)$ candidate is found in an event, the one with the best goodness of the cascade fit is kept.

The $B_c^+(2S)$ signal is searched for in the distribution of $Q = m(B_c^+\pi^+\pi^-) - m(B_c^+) - 2m(\pi^+)$, in order to reduce the effects of the ground state B_c^+ mass resolution. Figure 2 shows the distributions of this variable for the $B_c^+(2S)$

[1]Charge conjugate states are implied throughout the paper.

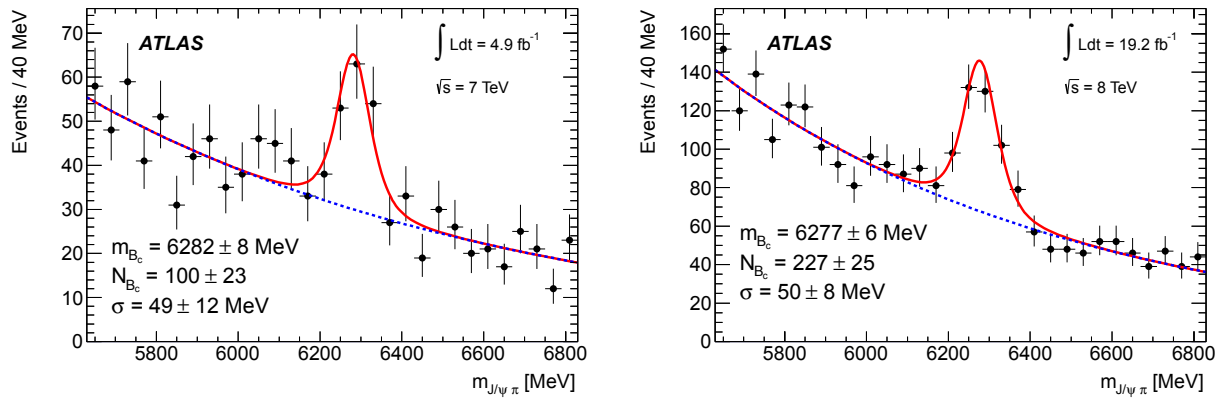

FIGURE 1. Invariant mass distributions of the reconstructed $B_c^+ \to J/\psi\pi^+$ candidates in (left) 7 TeV and (right) 8 TeV data. The solid line is the projection of the fit to all candidates in the mass range 5620–6820 MeV. The dashed line is the projection of the background component of the fit. Figures taken from Ref. [2].

candidates selected in 7 TeV and 8 TeV data. Clear peaking structure is seen in both datasets. To extract the signal yields, the Q distributions are fitted with a sum of a Gaussian function and a third order polynomial function to describe the observed peak and the background, respectively. The Q distributions for wrong charge combinations where the two pions from the primary vertex have the same sign are used to control the background behaviour and also shown in Figure 2. The peak positions, widths, and the yields obtained from the fit are quoted on the plots with only statistical uncertainty.

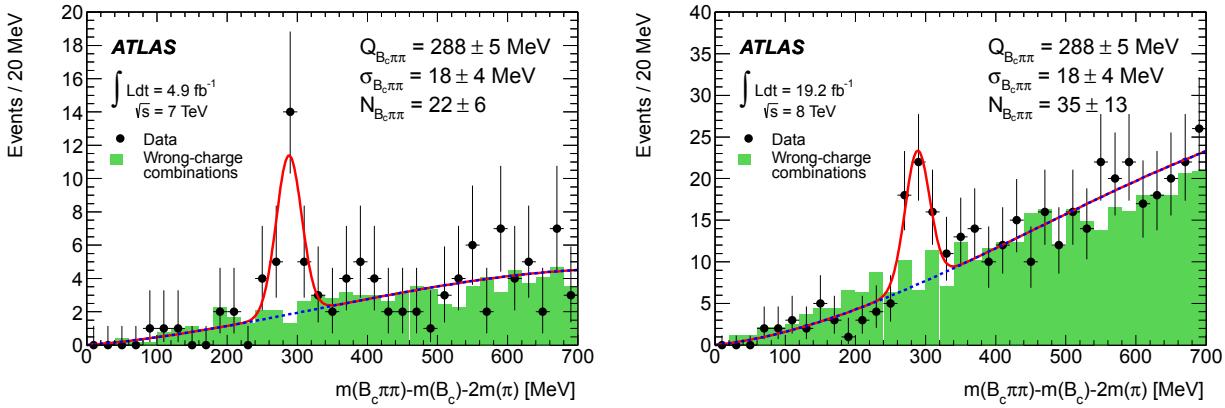

FIGURE 2. The Q distribution for the right-charge combinations (points with error bars) and for the same (wrong) pion charge combinations (shaded histogram) in (left) 7 TeV and (right) 8 TeV data. The wrong-charge combinations are normalized to the same yield as the right-charge background. The solid line is the projection of the results of the fit to all candidates in the range 0–700 MeV. The dashed line is the projection of the background component of the fit. Figures taken from Ref. [2].

The weighted average value of Q in the two datasets is $Q = 288.3 \pm 3.5$ (stat.) $\pm$ 4.1 (syst.) MeV, corresponding to the mass of a new state 6842 ± 4 (stat.) $\pm$ 5 (syst.) MeV. The statistical uncertainty is dominated by the uncertainty of the ground state B_c^+ mass and the Q distribution fitting procedure.

The statistical significance of the signal is evaluated with toy Monte Carlo studies and accounts for the "look-elsewhere effect" [4]. It is found to be 3.7σ and 4.5σ in 7 TeV and 8 TeV data, respectively, and the combined significance is 5.2σ.

Thus, a new state is observed in the $B_c^+\pi^+\pi^-$ channel. Its measured mass is consistent with the theoretical predictions for the $B_c^+(2S)$ excited state.

SEARCH FOR THE X_b AND OTHER HIDDEN-BEAUTY STATES

The $X(3872)$ is the best-studied of the new hidden-charm state seen in the last decade. Its mass, narrow width, quantum numbers and decay properties measured in several experiments make in unlikely to be a conventional quarkonium state, and various theoretical models are proposed in the literature to describe its structure. Heavy-quark symmetry suggests the existence of a hidden-beauty partner referred to as X_b which should be produced in pp collisions.

ATLAS experiment has performed a search for this particle in $\pi^+\pi^-\Upsilon(1S)$ channel with the pp collision data collected at $\sqrt{s} = 8$ TeV in 2012. The $\Upsilon(1S)$ candidates are built from two muon tracks. The candidates with the invariant mass within ±350 MeV window around the nominal $\Upsilon(1S)$ mass are retained. They are combined with two tracks assigned pion mass hypotheses and a 4-prong vertex fit is performed. The muon pair mass is constrained to the world average for the $\Upsilon(1S)$ to improve the $X_b \to \pi^+\pi^-\Upsilon(1S)$ mass resolution.

The whole data sample is separated into 8 kinematic bins with different signal sensitivity. First, based on the rapidity y of the X_b candidate, the barrel ($|y| < 1.2$) and endcap ($1.2 < |y| < 2.4$) regions having different invariant mass resolution are separated. Each of these sub-samples is then split into four bins with different signal-to-background ratio. This splitting is defined using the candidate transverse momentum p_{T} and $\cos\theta^*$, where θ^* is an angle between $\pi^+\pi^-$ combined momentum in the parent momentum rest frame and the parent momentum in the laboratory frame. Expected fractions of the signal in each bin are defined by splitting functions derived from the simulation.

Figure 3 shows the distribution of the $\pi^+\pi^-\Upsilon(1S)$ invariant mass. Only peaks at the masses corresponding to $\Upsilon(2S)$ and $\Upsilon(3S)$ signals are seen. These signals are used to validate correctness of the splitting functions and check agreement of the yields between data and simulation.

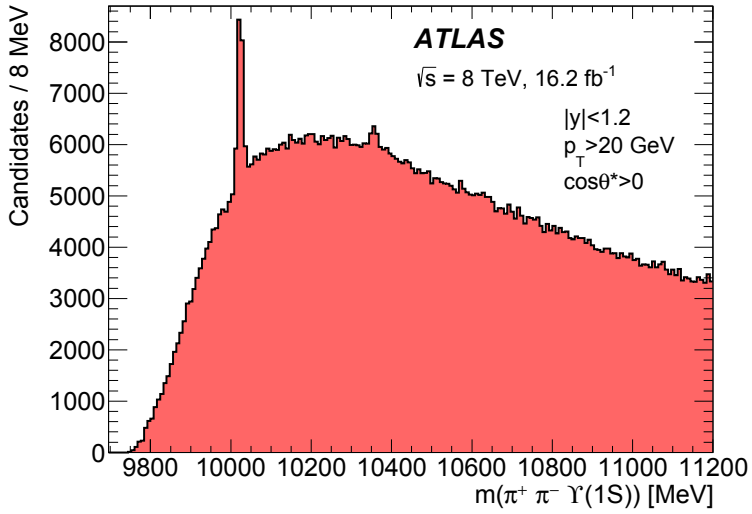

FIGURE 3. The $\pi^+\pi^-\Upsilon(1S)$ invariant mass distribution in the kinematic bin most sensitive to an X_b signal. The only apparent peaks are at the masses of the $\Upsilon(2S)$ (10023 MeV) and $\Upsilon(3S)$ (10355 MeV). Figure taken from Ref. [3].

To search for the X_b signal, a hypothesis test for the presence of a peak is performed every 10 MeV in the $\pi^+\pi^-\Upsilon(1S)$ mass range from 10 GeV to 11 GeV. At each mass, a simultaneous fit to all analysis bins is performed. A double Gaussian function is used in the fits for the expected signal shape thus assuming its width to be negligible with respect to the detector resolution. Other constraints used in the fit procedure assume the resolution dependence on y and p_{T} being the same as that for $\Upsilon(2,3S)$ states and the phase-space distribution of the di-pion invariant mass.

An upper limit on the value of $R = (\sigma\mathcal{B})/(\sigma\mathcal{B})_{2S}$ is set using the CL_S method by implementing asymptotic formulae for the $\tilde{q}_\mu$ statistic [5]. The $(\sigma\mathcal{B})$ is a product of the hypothetical state production cross-section and the branching fraction of its decay to $\pi^+\pi^-\Upsilon(1S)$ while $(\sigma\mathcal{B})_{2S}$ is the same quantity for the $\Upsilon(2S)$. Various systematic uncertainties were studied and included in the fit likelihood as nuisance parameters to be accounted in the limit setting. Figure 4 shows the 95% CL_S limit on R as a function of the X_b mass. The mass regions close to $\Upsilon(2S)$ and $\Upsilon(3S)$ resonances are excluded from the analysis due to poor sensitivity.

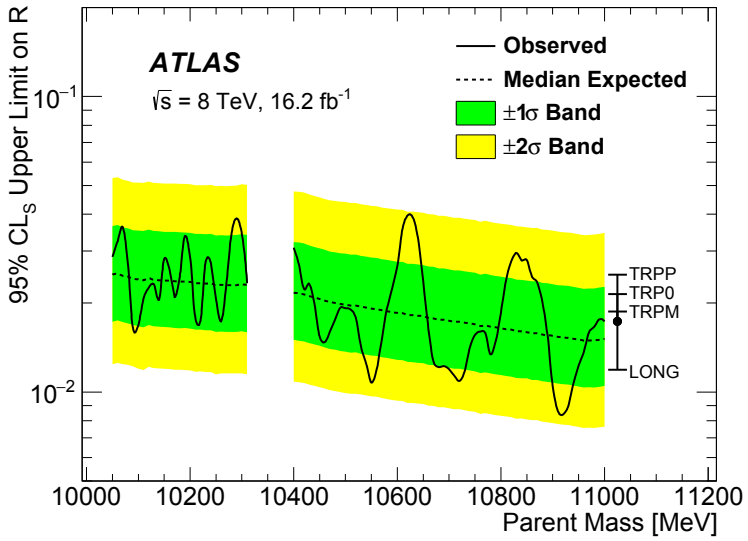

FIGURE 4. Observed 95% CL_S upper limits (solid line) on the relative production rate $R = (\sigma\mathcal{B})/(\sigma\mathcal{B})_{2S}$ of a hypothetical X_b parent state decaying isotropically to $\pi^+\pi^-\Upsilon(1S)$, as a function of mass. The median expectation (dashed) and the corresponding $\pm1\sigma$ and $\pm2\sigma$ bands (green and yellow respectively) are also shown. The bar on the right shows typical shifts under alternative X_b spin-alignment scenarios, relative to the isotropic ("FLAT") case shown with the solid point. Figure taken from Ref. [3].

The procedure assumes unpolarised production of the X_b state. However the X_b spin-alignment is unknown and can have a strong impact on the upper limit calculation. Rather than including this as a systematic uncertainty, upper limits are recalculated under longitudinal ("LONG") and three transverse ("TRPP", "TRP0", "TRPM") spin-alignment scenarios. Shifts in the upper limits (either up or down) depend only weakly on mass. Thus in Figure 4 the effect of each hypothesis is represented by a single number, chosen as a difference in the median expected CL_S from the unpolarised ('FLAT') case.

No evidence of X_b signal is found. An 95% CL_S upper limit on $(\sigma\mathcal{B})/(\sigma\mathcal{B})_{2S}$ is set at level of 0.8–4.0% depending on mass. The analogous ratio for the $X(3872)$ state is 6.56%: a value this large is excluded for all X_b masses considered.

Within the same analysis framework, searches for the $\Upsilon(1^3D_J)$ triplet as well as for wide resonances $\Upsilon(10860)$ and $\Upsilon(11020)$ states were performed. For these signals, the fit model was modified accordingly. None of these searches resulted in a signal evidence. For the triplet, an upper limit on the ratio of cross-sections $\sigma(\Upsilon(1^3D_J))/\sigma(\Upsilon(2S)) < 0.55$ was set.

ACKNOWLEDGMENTS

Participation in the conference was partly supported by the RFBR, grant No. 15-02-08133

REFERENCES

[1] ATLAS Collaboration, *The ATLAS Experiment at the CERN Large Hadron Collider*, JINST **3** (2008) S08003.

[2] ATLAS Collaboration, *Observation of an Excited $B_c^{\pm}$ Meson State with the ATLAS Detector*, Phys. Rev. Lett. **113** (2014) 212004, `arXiv:1407.1032 [hep-ex]`.

[3] ATLAS Collaboration, *Search for the X_b and other hidden-beauty states in the $\pi^+\pi^-\Upsilon(1S)$ channel at ATLAS*, Phys. Lett. B **740** (2015) 199–217, `arXiv:1410.4409 [hep-ex]`.

[4] E. Gross and O. Vitells, *Trial factors or the look elsewhere effect in high energy physics*, Eur. Phys. J. C **70** (2010) 525–530, `arXiv:1005.1891 [physics.data-an]`.

[5] G. Cowan, K. Cranmer, E. Gross, and O. Vitells, *Asymptotic formulae for likelihood-based tests of new physics*, Eur. Phys. J. C **71** (2011) 1554, `arXiv:1007.1727 [physics.data-an]`, [Erratum: Eur. Phys. J. C **73** (2013) 2501].

Proceedings of the LHCP2015 Conference, St. Petersburg, Russia, August 31 - September 5, 2015

Editors: V.T. Kim and D.E. Sosnov

Heavy Flavour Spectroscopy And Exotic States In CMS

LEONARDO CRISTELLA[1,2]

[1]*Dipartimento Interateneo di Fisica, Università di Bari - Bari, Italy*
[2]*INFN, Sezione di Bari - Bari, Italy*

leonardo.cristella@cern.ch

On behalf of the CMS Collaboration

Abstract. *The studies of the production of the X*(3872)*, either prompt or from B hadron decays, and of the $J/\psi\phi$ mass spectrum in B hadron decays have been carried out by using pp collisions at $\sqrt{s}$ = 7 TeV collected with the CMS detector at the LHC.*

The cross-section ratio of the $X(3872)$ with respect to the $\psi(2S)$ in the $J/\psi\pi^+\pi^-$ decay channel and the fraction of $X(3872)$ coming from B-hadron decays are measured as a function of transverse momentum (p_T), covering unprecedentedly high values of p_T. For the first time, the prompt $X(3872)$ cross section times branching fraction is extracted differentially in p_T and compared with NRQCD predictions. The dipion invariant-mass spectrum of the $J/\psi\pi^+\pi^-$ system in the $X(3872)$ decay is also investigated.

A peaking structure in the $J/\psi\phi$ mass spectrum near threshold is observed in $B^\pm \to J/\psi\phi K^\pm$ decays. The data sample, selected on the basis of the dimuon decay mode of the J/ψ, corresponds to an integrated luminosity of 5.2 fb^{-1}. Fitting the structure to an S-wave relativistic BreitWigner lineshape above a three-body phase-space nonresonant component gives a signal statistical significance exceeding five standard deviations. The fitted mass and width values are $m = 4148.0 \pm 2.4(stat.) \pm 6.3(syst.)$ MeV and $\Gamma = 28 + 1511(stat.) \pm 19(syst.)$ MeV, respectively. Evidence for an additional peaking structure at higher $J/\psi\phi$ mass is also reported.

INTRODUCTION

The observation of many new states, with masses above the open-charm threshold, that do not fit into the conventional quark model has renewed the interest in *exotic* quarkonium spectroscopy.

The X(3872) was discovered by the Belle experiment in 2003 [1] and, despite a series of detailed studies performed at B-factories and Tevatron, its nature still remains unknown. Some interpretations describe the X(3872) as a molecular state (loosely bound state of $D^{0*}\bar{D}^0$) or as a tetraquark state (bound state of diquark-antidiquark) [2]. At Large Hadron Collider (LHC) there is the opportunity to study this state with high statistics and the measurement of the prompt X(3872) production rate as a function of transverse momentum can provide a test of the NRQCD factorization approach to X(3872) production. In this note, the measurement of production of the X(3872) in pp collisions at a centre-of-mass energy ($\sqrt{s}$) of 7 TeV is presented in Section 2 while a study of the invariant-mass distribution of the dipion system in X(3872) decay is shown in Section 2.

The observation of $Y(3940)$ [3][4] near the $J/\psi\omega$ threshold motivates the search of other states close to the $J/\psi\phi$ threshold with similar characteristics (similar threshold enhancement? analogous rescattering effects?) or eventually partner states with a new quarks' aggregate (tetraquark?) or a molecular model ($D_s^*\bar{D}_s^*$ partner of a $D^*\bar{D}^*$ loosely bound molecule?). The CDF collaboration observed the $Y(4140)$ structure with a significance greater than 5σ [5][6], while LHCb collaboration did not confirm it and put an upper limit to its production [7].

Measurement of the X(3872) production cross section

The analysis is performed on the data recorded by the CMS experiment in 2011, corresponding to an integrated luminosity of 4.8 fb^{-1}. The X(3872) is observed using the decays into $J/\psi\pi^+\pi^-$, with the subsequent decay of the J/ψ into a pair of muons. This decay channel has a clean experimental signature in CMS thanks to the high granularity of the tracker and the high efficiency of J/ψ identification. A detailed description of the detector can be found elsewhere

[8]. The data are collected with requirements on the dimuon system imposed at the trigger level such as rapidity within 1.25 and a transverse momentum threshold of 9.9 GeV. The analysis is thus performed in the kinematic range of p_T of the $J/\psi\pi^+\pi^-$ system between 10 and 50 GeV and the rapidity within $|\ y\ | < 1.2$, collecting about 12000 X(3872) candidates. The event selection and the event simulations, used to determine acceptances and efficiencies, are described in detail in Ref.[9]. The X(3872) is assumed to be an unpolarized state and its J^{PC} is fixed at 1^{++} value, as favoured by existing data [2] and confirmed by latest LHCb study [10].

Measurement of the cross section ratio

The ratio of the X(3872) and $\psi(2S)$ cross sections times their branching fraction to $J/\psi\pi^+\pi^-$ is obtained from the measured numbers of signal events, $N_{X(3872)}$ and $N_{\psi(2S)}$, correcting for the efficiency (ϵ) and acceptance (A) estimated from simulations, according to

$$R = \frac{\sigma(pp \to X(3872) + anything) \cdot B(X(3872) \to J/\psi\pi^+\pi^-)}{\sigma(pp \to \psi(2S) + anything) \cdot B(\psi(2S) \to J/\psi\pi^+\pi^-)} = \frac{N_{X(3872)} \cdot A_{\psi(2S)} \cdot \epsilon_{\psi(2S)}}{N_{\psi(2S)} \cdot A_{X(3872)} \cdot \epsilon_{X(3872)}}. \quad (1)$$

The signal yields, $N_{X(3872)}$ and $N_{\psi(2S)}$, are determined from unbinned maximum-likelihood fits to the invariant-mass spectra of the $J/\psi\pi^+\pi^-$ system, separately for the X(3872) and $\psi(2S)$ in different mass windows. The $\psi(2S)$ is parametrized using two Gaussian functions with a common mean, while a single Gaussian is used for the X(3872) signal and the nonresonant background is fitted with a second-order Chebyshev polynomial. The acceptances and efficiencies of the X(3872) and $\psi(2S)$ final states are determined from the simulation. Studies on Monte Carlo are performed to determine the systematic uncertainties and a data-driven method is used to verify the efficiencies, as described in Ref.[9]. The main systematic uncertainty arises from the limited knowledge of the X(3872) transverse momentum. Both X(3872) and $\psi(2S)$ states are considered unpolarized and no systematic uncertainty is assigned to cover other cases. The total uncertainty for each p_T interval is typically 10% statistical and $5-13\%$ systematic. No significant dependence on p_T is observed.

Measurement of the nonprompt fraction

The fraction of X(3872) produced from decays of B hadrons is referred to as nonprompt fraction. The X(3872) candidates from B hadron decays are selected based on the pseudo-proper decay lenght (l_{xy}), defined in Ref.[9] and related to the distance between the primary vertex and the secondary one, formed by the $J/\psi\pi^+\pi^-$ system. A B-hadron-enriched sample is obtained requiring l_{xy} larger than 100 μm, with an estimated contribution from prompt X(3872) below 0.1%. The nonprompt fraction is then obtained from the ratio between the signal yields extracted from this B-hadron-enriched sample and the signal yields in the inclusive sample, after correction for the efficiencies of the decay-length-selection criteria determined from simulations. Detailed studies are performed to verify the stability of the results and to determine the systematic uncertainties leading to a total systematic uncertainty of $6-10\%$, as described in Ref.[9]. The measurement is dominated by its statistical uncertainty ($\sim$ 20%). The X(3872) nonprompt fraction reveals no significant dependence on transverse momentum. These results are obtained assuming null polarization for the X(3872) and no systematic uncertainty is assigned.

The prompt X(3872) production cross section

The cross section times branching fraction for prompt X(3872) production is determined from the measurement of the cross section ratio R and the nonprompt fraction, described above, combined with a previous result of the prompt $\psi(2S)$ cross section obtained in CMS [11]. The latter measurement was performed using the $\psi(2S) \to \mu^+\mu^-$ decay mode and provides results as a function of transverse momentum up to 30 GeV, in the same rapidity range of this analysis. By means of this combination, the differential cross section for prompt X(3872) production times the branching fraction is obtained as a function of p_T, in the rapidity region $|\ y\ | < 1.2$, as shown in Fig.1. The X(3872) and $\psi(2S)$ states are assumed to be unpolarized and no cancellation of systematic uncertainties is assumed in the combination. The main sources of systematic uncertainty are related to the measurement of R and of the prompt $\psi(2S)$ cross section [11]. The differential cross section for prompt X(3872) production in pp collisions at $\sqrt{s} = 7$ TeV has also been predicted with a calculation made within the NRQCD factorization formalism [12]. In this calculation the cross section is expressed as the sum of parton cross sections for creating $c\bar{c}$ pairs with vanishing relative momentum multiplied by phenomenological constants and results are normalized using Tevatron measurements with the statistical uncertainty obtained from the experimental input data. The predictions from Ref.[12] were modified by the authors to match the

phase-space of the measurement presented in this note. The comparison of this prediction with the data is shown in Fig.1 and demonstrates that, while the shape is reasonably well described, the predicted cross section is much larger than the measured one. The integrated prompt X(3872) cross section times branching fraction for the kinematic region $10 < p_T < 30$ GeV and $|y| < 1.2$ is also determined to be

$$\sigma^{prompt}(pp \to X(3872) + anything) \cdot B(X(3872) \to J/\psi\pi^+\pi^-) = 1.06 \pm 0.11(stat.) \pm 0.15(syst.)\, nb. \quad (2)$$

This measured value is significantly below the NRQCD prediction for the prompt X(3872) cross section times branching fraction in the same kinematic region, which is 4.01 ± 0.88 nb [12].

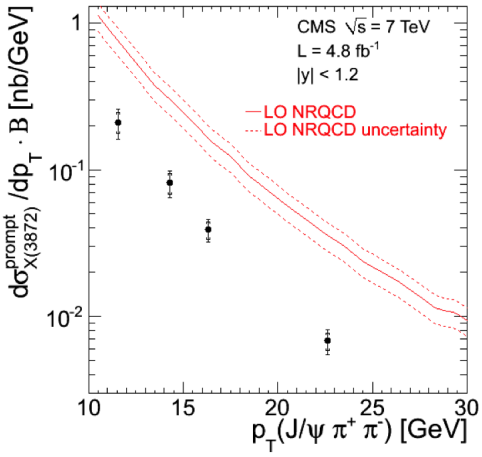

FIGURE 1. Measured differential cross section for prompt X(3872) production times branching fraction of $X(3872) \to J/\psi\pi^+\pi^-$ (B) as a function of p_T. The inner error bars indicate the statistical uncertainty while the outer error bars represent the total uncertainty. Prediction from a NRQCD model [12] are shown by the solid line. The data points are placed where the theoretical value is equal to its mean value over each bin.

Study of the X(3872) decay properties

The dipion invariant-mass distribution from X(3872) decays to $J/\psi\pi^+\pi^-$ is measured in order to investigate the decay properties of the X(3872) and evaluate the presence of an intermediate ρ^0 state in the decay, as suggested by previous studies [13]. The measurement is made within the kinematic region $10 < p_T < 50$ GeV and $|y| < 1.25$. To extract the dipion invariant-mass spectrum from X(3872) decays, the event sample is divided into intervals of $m(\pi^+\pi^-)$ in the range 0.5 – 0.78 GeV. In each interval, a maximum-likelihood fit to the $J/\psi\pi^+\pi^-$ invariant-mass distribution is performed with the signal modelled by a Gaussian. The position and width of the X(3872) signal are fixed to the values obtained in the fit to the full sample. The dipion invariant-mass distribution is extracted from the signal yields obtained from these fits to the data in each interval, after correction for detector acceptance and efficiency estimated from the simulation, as described in Ref.[9]. The main systematic uncertainties are related to the signal extraction (10 – 20%) and to corrections due to acceptance and efficiency (4 – 6%). The resulting dipion invariant-mass spectrum is normalized to the total cross section in the interval $0.5 < m(\pi^+\pi^-) < 0.78$ GeV. The data are compared to X(3872) signal simulations with and without an intermediate ρ^0 in the X(3872) decay. The assumption of an intermediate ρ^0 decay gives better agreement with the data.

Y(4140) decay reconstruction and signal extraction

The J/ψ candidates are reconstructed by couples of oppositely charged identified muons according to the selection implemented by the dimuon HLT, including muons' minimum p_T up to 4 GeV, $p_T > 7$ GeV and transverse flight length significance greater than 3. The $B^\pm \to J/\psi\phi K^\pm$ candidates are reconstructed by combining three additional good quality charged tracks, having $p_T > 1$ GeV, pointing to the displaced J/ψ vertex, with a total charge of ±1 and with kaon mass assigned (kaon track). The five tracks, with the $\mu^+\mu^-$ system kinematically constrained to the J/ψ mass nominal value, are required to form a good 3D vertex with χ^2 probability greater than 1%. The K^+K^- pair with

lower mass must have a reconstructed mass $1.008\ GeV < m(K^+K^-) < 1.035\ GeV$ to be considered as a ϕ candidate. The selection criteria, designed to maximize the B signal yield, were determined before examining the mass difference $\Delta m \equiv m(\mu^+\mu^-K^+K^-) - m(\mu^+\mu^-)$, that is the observable used to search for possibile structures in the $J/\psi\phi$ mass and investigated up to $1.568\ GeV$ in order to reject the reflection from $B_s^0 \to \psi(2S)\phi \to (J/\psi\pi^+\pi^-)\phi$.

Background-subtracted and fit of the Δm spectrum

Preliminarily signal Monte Carlo samples with specific values for $m(J/\psi\phi)$ (and thus for Δm) are produced to provide:

- B mass resolution as a function of $J/\psi\phi$ mass values;
- absolute B efficiency as a function of $J/\psi\phi$ mass values;
- $J/\psi\phi$ mass resolution as a function of $J/\psi\phi$ mass values.

The first information is needed by the used background subtraction method, the second by the relative efficiency correction and the third in the final Δm fit.

The background subtraction is obtained by a bin-wise fit method. After dividing the Δm spectrum in 20 MeV-sized 28 bins, the B yield for each bin is extracted by a binned maximum likelihood fit to the corresponding B candidates' mass spectrum. A second order Chebyshev polynomial is used for the background whereas the signal fit model consists of two gaussians with common mean (the nominal B^+ mass) and with widths and their relative ratio fixed to Δm-dependent values predicted by the signal Monte Carlo. The resulting yields as a function of the binned Δm provide the background-subtracted Δm spectrum. This result is found to be consistent with the distribution that can be extracted by applying the alternative technique of *sPlot* [14].

After performing the background subtraction and correcting for relative efficiency the resulting Δm distribution and its 1D-fit is shown in Fig. 2: the fit model includes the three-body phase-space profile for the background whereas each structure is modelled with an S-wave relativistic Breit-Wigner function convoluted with a Gaussian resolution function whose width is fixed to the value obtained from simulation. The mass resolution is about 1 MeV at the threshold and smoothly increases with increasing Δm: it is about 4 MeV for $\Delta m \simeq 1.25\ GeV$. A 4.5 MeV smearing is applied to the three-body phase-space profile to account for the width of the reconstructed ϕ signal. The signal yields associated to the two structures are 355 ± 46 and 445 ± 83 respectively. On the plot is also shown the result of a 2D simultaneous fit of both B^+ invariant mass and Δm distributions with implicit background subtraction and efficiency correction; the Δm continuum shape has been also investigated with an event-mixing technique. There are clearly enhancements, with respect to the phase-space continuum: at the kinematical threshold and around $\Delta m \approx 1.2\ GeV$. The three-body phase-space background lies above the event-mixed background in the region of these two structures.

Several checks have been done to validate the robustness of the two structures. Not only each selection requirement has been varied but the whole analysis has been repeated with tighter selection criteria that lowered the combinatorial background level by a factor of ten while retaining 40% of the B signal candidates.

CONCLUSIONS

X(3872)

The X(3872) production cross section is measured in pp collisions at $\sqrt{s} = 7$ TeV with data collected by the CMS experiment in 2011. The X(3872) and $\psi(2S)$ are observed using their decay into $J/\psi\pi^+\pi^-$. The ratio of their cross sections times branching fractions and the fraction of X(3872) from B-hadron decays are measured. Both do not show significant dependence on p_T. Using these measurements, for the first time the prompt X(3872) production cross section is obtained as a function of p_T. The available NRQCD predictions significantly overestimate it while the dependence on p_T is reasonably described by the theory. The study on the dipion mass spectrum for $X(3872) \to J/\psi\pi^+\pi^-$ favours the presence of an intermediate ρ^0 state in the X(3872) decay.

Y(4140)

Interpreting the two structures as $J/\psi\phi$ resonances with S-wave relativistic Breit-Wigner lineshapes laying over a residual three-body phase-space non-resonant component, the fitted mass of the first structure is $m = (4148.2 \pm 2.0(stat.) \pm 4.6(sys.))\ MeV$ whereas that of the second structure is $m = (4316.7 \pm 3.0(stat.) \pm 7.3(sys.))\ MeV$. Preliminary systematic uncertainties' evaluation has been obtained by changing signal and background fit models, Δm

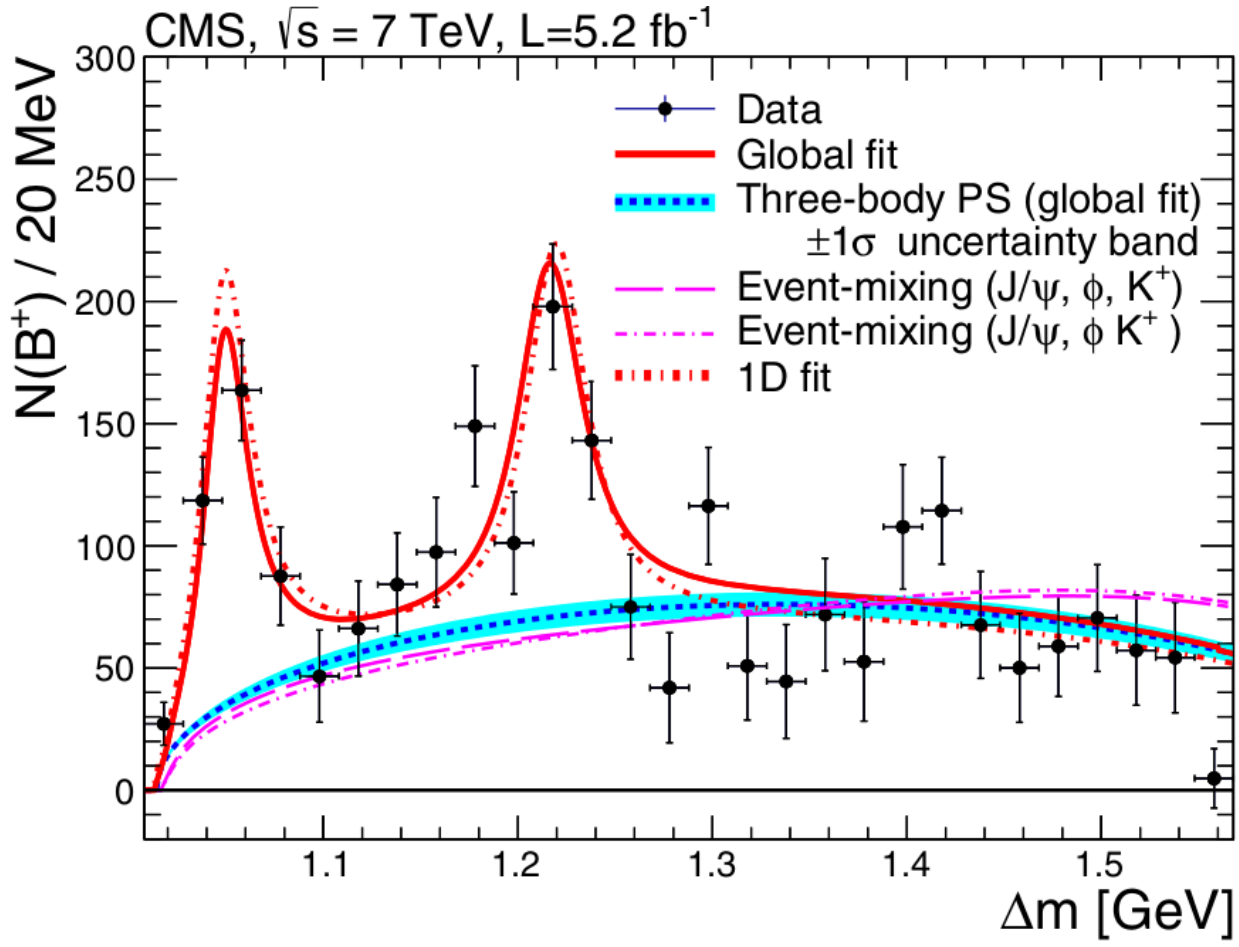

FIGURE 2. Number of $B^+ \to J/\psi\phi K^+$ candidates as a function of $\Delta m = m(\mu^+\mu^- K^+ K^-) - m(\mu^+\mu^-)$. The solid curve is the global UML fit of the data, and the dotted curve is the background contribution assuming three-body PS. The band is the $\pm 1\sigma$ uncertainty range for the background obtained from the global fit. The dashed and dash-dotted curves are background curves obtained from two different event-mixing procedures and normalized to the number of three-body PS background events. The short dashed curve is the 1D fit to the data.

binning, mass resolution, efficiency correction and selection criteria. The first structure is observed with a significance exceeding 5σ; this is evaluated either by performing a likelihood ratio test and applying Wilk's theorem, and by performing toy-MC simulation to calculate a *p-value* for the background fluctuations alone to give rise to a signal as significant as that seen in the data. This observation is consistent with a previous evidence for a narrow structure near $J/\psi\phi$ threshold by the CDF Collaboration [5][6].

The background-subtracted ϕK^+ invariant mass distribution shows an excess with respect to the pure phase-space profile in the $1.7 \div 1.8\ GeV$ region where large resonances, such as $K_2(1770)$ and $K_2(1820)$, may appear. The reflections studies subsequently carried out suggest that the first structure is not correlated to eventual ϕK^+ resonances.

The $J/\psi\phi$ system should be properly studied by performing an amplitude analysis of this five-body decay able to consider the helicity configurations of the decay products. However analyzed 2011 data do not provide an adequate and enough pure sample for this purpose.

REFERENCES

[1] B. Collaboration, Phys. Rev. Lett. **91** (2003).
[2] N. B. et al., Eur. Phys. J. C **71** (2011).

[3] B. Collaboration, Phys. Rev. Lett. **94** (2005).
[4] B. Collaboration, Phys. Rev. Lett. **101** (2008).
[5] C. Collaboration, Phys. Rev. Lett. **102** (2009).
[6] C. Collaboration, arXiv:1101.6058 (2011).
[7] L. Collaboration, Phys. Rev. B **85** (2012).
[8] C. Collaboration, JINST **3** (2008).
[9] C. Collaboration, JHEP **04** (2013).
[10] L. Collaboration, Phys. Rev. Lett. **91** (2013).
[11] C. Collaboration, JHEP **02** (2012).
[12] P. Artoisenet and E. Braaten, Phys. Rev. D **81** (2010).
[13] C. Collaboration, Phys. Rev. Lett. **96** (2006).
[14] M. Pivk and F. LeDiberder, Nucl. Instrum. Meth. A **555** (2005).
[15] M. P. Brown and K. Austin, Appl. Phys. Letters **85**, 2503–2504 (2004).
[16] R. T. Wang, "Title of chapter," in *Classic Physiques*, edited by R. B. Hamil (Publisher Name, Publisher City, 1999), pp. 212–213.
[17] C. D. Smith and E. F. Jones, "Load-cycling in cubic press," in *Shock Compression of Condensed Matter-2001*, AIP Conference Proceedings 620, edited by M. D. Furnish (American Institute of Physics, Melville, NY, 2002), pp. 651–654.
[18] B. R. Jackson and T. Pitman, U.S. Patent No. 6,345,224 (8 July 2004).
[19] D. L. Davids, "Recovery effects in binary aluminum alloys," Ph.D. thesis, Harvard University 1998.
[20] R. C. Mikkelson, (private communication).

Heavy Ion physics: parallel talks

Proceedings of the LHCP2015 Conference, St. Petersburg, Russia, August 31 - September 5, 2015

Editors: V.T. Kim and D.E. Sosnov

Ridges in p–A (and pp) collisions

ALICE OHLSON

CERN, Geneva, Switzerland

alice.ohlson@cern.ch

On behalf of the ALICE, ATLAS, CMS, and LHCb Collaborations

Abstract. Correlations between particles separated by several units of pseudorapidity were discovered in high-multiplicity pp and p–Pb collisions at the LHC. These long-range structures observed in two-particle correlation functions are reminiscent of features seen in Pb–Pb collisions, where they are often viewed as a signature of collective behavior and the formation of a quark-gluon plasma (QGP). Therefore, the discovery of these 'ridges' in small systems has implications for the study of collectivity in small systems as well as in heavy-ion collisions. The ridges in pp and p–Pb collisions have been studied in the ALICE, ATLAS, CMS, and LHCb experiments to characterize the p_{T}-, η-, and multiplicity-dependences of the ridge yield, as well as its particle composition.

INTRODUCTION

Two-particle angular correlations are used to study many aspects of the physics of heavy-ion collisions, in particular jet fragmentation and collective effects. The correlation function is defined as the distribution in relative azimuthal angle ($\Delta\varphi = \varphi_{assoc} - \varphi_{trig}$) and relative pseudorapidity ($\Delta\eta = \eta_{assoc} - \eta_{trig}$) between trigger and associated particles. In order to study various physical mechanisms, correlation functions can be constructed differentially as a function of, for example, the transverse momentum (p_{T}), species, and pseudorapidity of the trigger and associated particles, and the centrality or multiplicity of the collision.

Correlation functions in pp collisions show characteristic features attributed to jet production: a nearside peak localized around $(\Delta\varphi, \Delta\eta) = (0, 0)$, representing pairs of particles where the trigger and associated particles are fragments of the same jet, and the awayside peak localized around $\Delta\varphi = \pi$ but extended in $\Delta\eta$, representing pairs in which the trigger and associated particles are in back-to-back jets. In heavy-ion collisions, the same jet features are observed, on top of additional structures extended in $\Delta\eta$ around $\Delta\varphi = 0$ and $\Delta\varphi = \pi$. These 'ridges' are often viewed as a signature of collective behavior and the formation of a quark-gluon plasma, and are attributed to hydrodynamic flow in the QGP. The bulk features in the two-particle correlation function (excluding the jet components) can be described by a Fourier series,

$$\frac{dN}{d\Delta\varphi} \propto 1 + 2v_1^{trig}v_1^{assoc}\cos(\Delta\varphi) + 2v_2^{trig}v_2^{assoc}\cos(2\Delta\varphi) + 2v_3^{trig}v_3^{assoc}\cos(3\Delta\varphi) + ... \quad (1)$$

where the v_2 term is dominant in all but the most central collisions. Measuring v_2 and the other v_n components has been critical to determining the properties and dynamics of the medium created in heavy-ion collisions.

Causality arguments suggest that the origin of correlations between particles separated in η should be in the very early stages of the collisions, either in the initial state or in the initial energy distribution. In the latter case, collective behavior is needed to transform the spatial correlations into the observed momentum-space correlations. The discovery of long-range $\Delta\eta$ correlations (a ridge) on the nearside (around $\Delta\varphi = 0$) in high multiplicity collisions of small systems, pp [1] and p–Pb [2], therefore informs theories concerning the initial state of nuclear collisions and collective behavior in small and large systems.

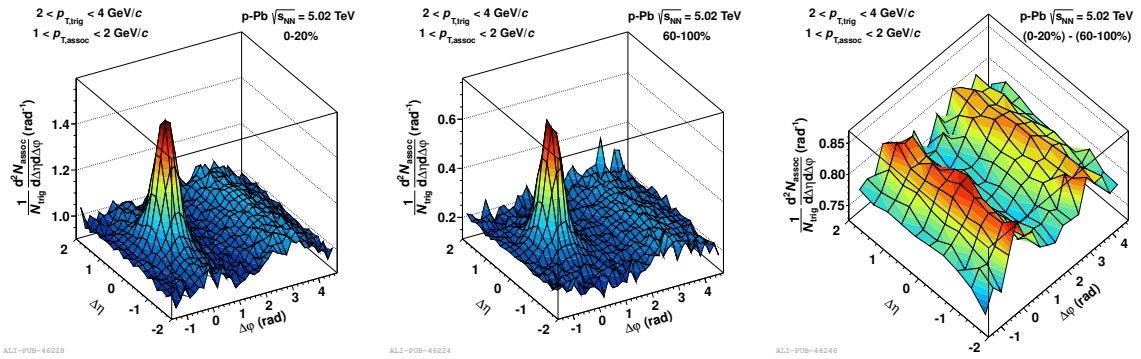

FIGURE 1. (left) The two-particle correlation function in high-multiplicity p–Pb collisions shows a ridge around $\Delta\varphi \sim 0$. (center) The correlation function in low-multiplicity collisions shows no visible ridge. (right) The subtracted distribution reveals the double ridge structure [3].

Ridges in p–Pb collisions

The nearside ridge has been observed in high-multiplicity p–Pb collisions by ALICE [3], ATLAS [4], CMS [2], and LHCb [5]. Furthermore, it was observed that the nearside peak yields are mostly independent of multiplicity [6], meaning that for the same trigger and associated p_{T} the same jet population is selected regardless of multiplicity. This served as justification to subtract the correlations in low-multiplicity events from the high-multiplicity correlation functions in order to remove correlations due to jet and minijet fragmentation. This subtraction procedure, shown in Fig. 1, showed the nearside ridge more clearly and also revealed a symmetric ridge on the awayside [3, 4], which is reminiscent of the ridges attributed to flow in heavy-ion collisions. This 'double ridge' structure was decomposed into Fourier coefficients (Eq. 1) in order to extract the parameter v_2. However, it is important to note that the physical mechanism leading to a non-zero v_2 is still under theoretical debate, and the presence of v_2 does *not* necessarily imply the existence of hydrodynamics or a QGP in small systems.

Further studies in p–Pb collisions measured v_2 as a function of p_{T} for various particle species: $\pi^{\pm}$, $K^{\pm}$, $p(\bar{p})$, K^0_S, and $\Lambda(\bar{\Lambda})$. The observed v_2, shown in Fig. 2, shows similar mass ordering as was observed in Pb–Pb collisions [7, 8]. Additionally, higher-order v_n coefficients were measured, and shown to be non-zero up to $n = 5$ [9]. Finally, v_2 was measured using the multiparticle cumulant method, which measures multiparticle correlations while subtracting all

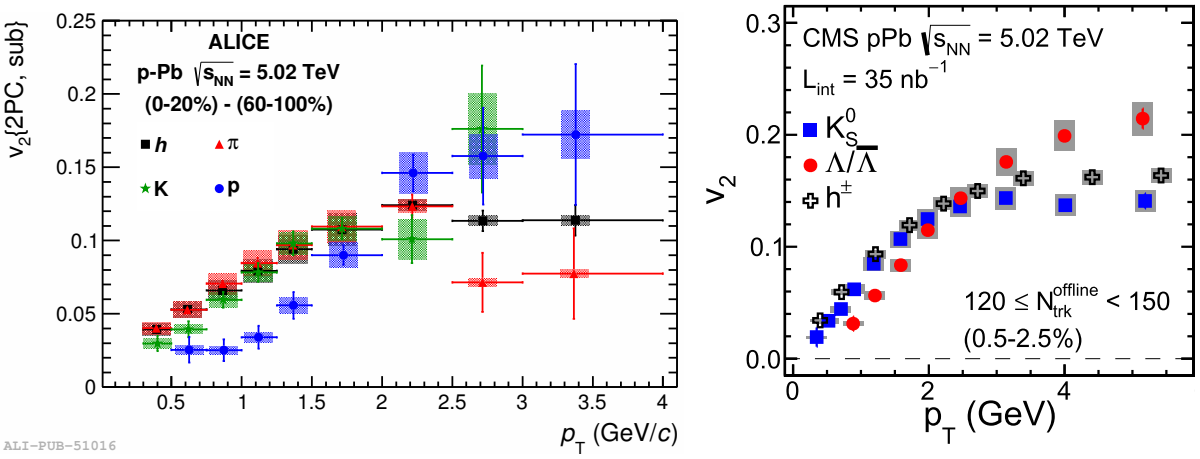

FIGURE 2. (left) The v_2 of π, K, and p as well as inclusive unidentified hadrons was measured as a function of p_{T} in p–Pb with the subtraction method [7]. (right) The v_2 of K^0_S and Λ as well as inclusive unidentified hadrons was measured with the harmonic decomposition technique [8].

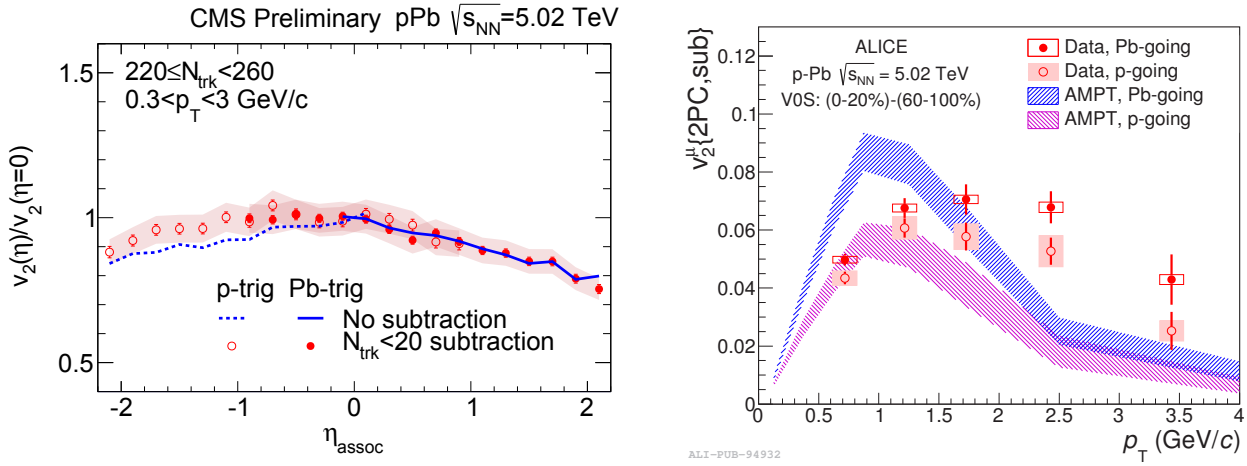

FIGURE 3. (left) The v_2 of particles at midrapidity was measured as a function of pseudorapidity relative to $v_2(\eta = 0)$ [13]. (right) The v_2 of forward muons was measured as a function of p_T [14]. Both results show that the v_2 is higher for particles traveling in the Pb-going direction than in the p-going direction.

lower-order correlations, as well as the Lee-Yang Zeros method [10]. The agreement of the $v_2\{4\}$, $v_2\{6\}$, $v_2\{8\}$, and $v_2\{\text{LYZ}\}$ measurements demonstrates that the double ridge structure is a global correlation amongst many particles in a given event.

Several theoretical explanations have been proposed to explain the ridge in pp and p–Pb collisions, such as higher-order glasma graphs within a Color Glass Condensate (CGC) picture, hydrodynamics in small systems, and others (see for example [11, 12]). Since some models make different predictions for the η-dependence of the ridge, making such a measurement may enable us to differentiate between theories for the physical mechanism responsible for the ridge phenomenon. To this end, several experiments have measured the η-dependence of the ridge. CMS measures $v_2(\eta)$ at midrapidity up to $|\eta| = 2.4$ while ALICE and LHCb measure v_2 and the ridge at forward rapidity up to $\eta \sim 4$ and $\eta \sim 5$, respectively. Because the LHC provided circulating proton and lead beams in both directions, the experiments were able to take data in both p–Pb and Pb–p configurations, and measure observables in both the p-going and Pb-going directions with the same experimental setup and under the same conditions.

Fig. 3 shows a measurement from two-particle correlations where the trigger particle is fixed in the range $2.0 < |\eta_{trig}| < 2.4$ and the pseudorapidity of the associated particle (η_{assoc}) is varied. In the ratio of $v_2^{trig} v_2^{assoc}$ measured at a given pseudorapidity to the $v_2^{trig} v_2^{assoc}$ at $\eta = 0$, the v_2 of the trigger particle cancels out, leaving only $v_2(\eta_{assoc})/v_2(0)$ as a function of η_{assoc} as shown in the figure. It is observed that the measured v_2 is larger for associated particles in the Pb-going direction than in the p-going direction.

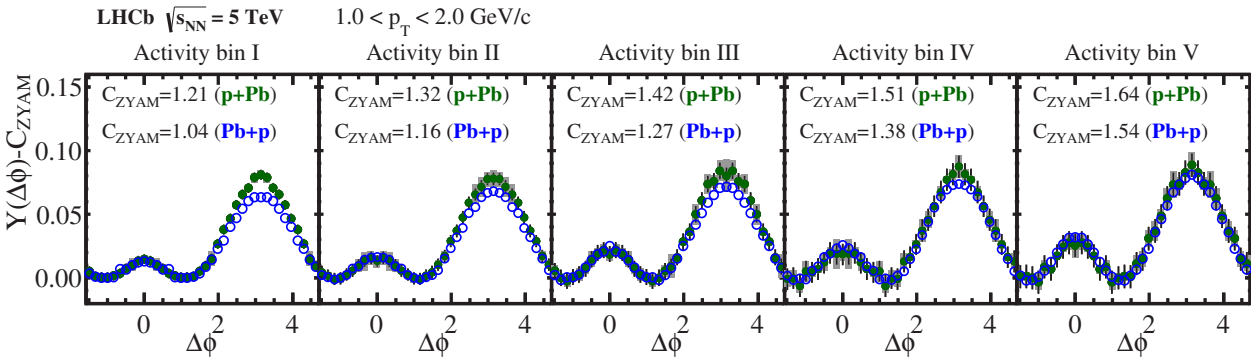

FIGURE 4. Correlation functions between trigger and associated particles in the range $2.0 < |\eta| < 4.9$ show that the ridge yield is identical in both directions when compared in the same *absolute* multiplicity bins [5].

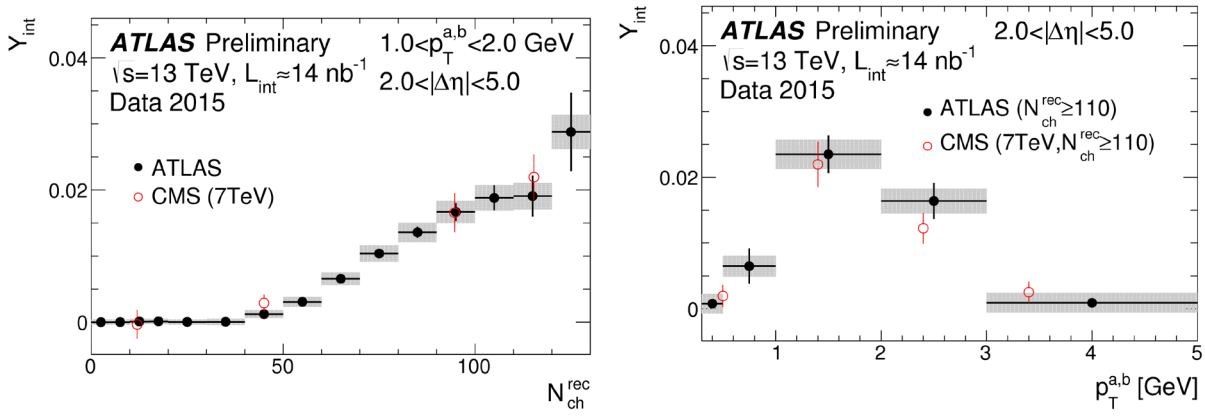

FIGURE 5. The ridge yield in $\sqrt{s} = 13$ TeV pp collisions is shown as a function of multiplicity (left) and p_{T} (right) [16]. No significant dependence on the center-of-mass energy is observed. (Note that these Preliminary results have been superseded by the results published in [17].)

The CMS finding was confirmed in the p_{T}-differential study of the v_2 of forward muons in ALICE. In this analysis, the correlations between mid-rapidity charged hadrons reconstructed as 'tracklets' in the Inner Tracking System (ITS, $|\eta| < 1$) and forward muons detected in the Forward Muon Spectrometer (FMS, $-4 < \eta < -2.5$) are constructed in the highest 20% multiplicity events and the lowest 40% multiplicity events. The correlation functions in low-multiplicity events are subtracted from those in high-multiplicity events, and then fit with a Fourier series to extract $v_2^{\mu}\{2\mathrm{PC,sub}\}$, which is shown as a function of p_{T} in Fig. 3. Furthermore, the ratio of $v_2^{\mu}\{2\mathrm{PC,sub}\}$ in the Pb-going direction to the $v_2^{\mu}\{2\mathrm{PC,sub}\}$ in the p-going direction is roughly independent of p_{T} within statistical and systematic uncertainties, and a constant fit to the ratio yields 1.16 ± 0.06. The data were compared to an AMPT [15] simulation, which qualitatively describes the p_{T}-dependence at low p_{T}, but shows significant quantitative differences in both the p_{T}- and η-dependences.

LHCb also confirms that for a given *relative* event activity (i.e. mutiplicity percentile), the ridge is stronger in the Pb-going direction than in the p-going direction. However, when comparing correlation functions in both beam configurations with the same *absolute* event activity (defined by particle production in $2.0 < \eta < 4.9$), as shown in Fig. 4, it is observed that the nearside ridge magnitude is the same in both hemispheres. This new observation will serve to constrain models of η-dependence of the ridge yield.

Ridges in pp collisions

The nearside ridge in pp was first observed by CMS in high multiplicity collisions at $\sqrt{s} = 7$ TeV, and further measurements showed that it was most prominent in the intermediate p_{T} region ($1 \lesssim p_{\mathrm{T}} \lesssim 3$ GeV/c) [1]. First results at a higher beam energy of $\sqrt{s} = 13$ TeV once again clearly showed the existence of the nearside ridge [16]. Measurements performed in ATLAS of the ridge yield as a function of multiplicity and p_{T} showed no significant differences between the two center-of-mass energies [16]. However, it should be noted that there are differences between the two analyses (for example, in the definition of the multiplicity N_{ch} and the $|\Delta\eta|$ integration range) which prevent a precise comparison between the ATLAS and CMS results. Despite significant challenges due to the influence of jets in pp collisions, later work by ATLAS produced a measurement of v_2 in pp collisions at $\sqrt{s} = 13$ TeV [17].

Conclusions

The nearside and awayside ridge structures observed in two-particle correlations have been studied and characterized in measurements from ALICE, ATLAS, CMS, and LHCb. The double ridge structure in p–Pb collisions has been quantified by the parameter v_2, which shows a similar p_{T}-dependence as in Pb–Pb, as well as mass splitting like that observed in heavy-ion collisions. Furthermore, it was observed that the v_2 is higher for particles in the Pb-going direction than in the p-going direction, when compared at the same relative multiplicity. However, the ridge yield is

identical in the positive- and negative-η directions for the same absolute multiplicity. These observations will serve to constrain future model calculations of collective dynamics in p–A collisions. The first measurements of the ridge in pp collisions at $\sqrt{s}$ = 13 TeV show no significant difference from the results at $\sqrt{s}$ = 7 TeV, and the first measurement of v_2 in pp collisions has been performed. The observation of long-range $\Delta\eta$ correlations in small collision systems at the LHC has significant implications for our understanding of the initial energy distribution of colliding protons (and larger nuclei) and the presence of collectivity over small length- and short time-scales.

REFERENCES

[1] CMS Collaboration, JHEP **09**, p. 091 (2010), arXiv:1009.4122 [hep-ex] .
[2] CMS Collaboration, Phys. Lett. **B718**, 795–814 (2013), arXiv:1210.5482 [nucl-ex] .
[3] ALICE Collaboration, Phys. Lett. **B719**, 29–41 (2013), arXiv:1212.2001 [nucl-ex] .
[4] ATLAS Collaboration, Phys. Rev. Lett. **110**, p. 182302 (2013), arXiv:1212.5198 [hep-ex] .
[5] LHCb Collaboration, submitted to Phys. Lett. B (2015), arXiv:1512.00439 [nucl-ex] .
[6] ALICE Collaboration, Phys. Lett. **B741**, 38–50 (2015), arXiv:1406.5463 [nucl-ex] .
[7] ALICE Collaboration, Phys. Lett. **B726**, 164–177 (2013), arXiv:1307.3237 [nucl-ex] .
[8] CMS Collaboration, Phys. Lett. **B742**, 200–224 (2015), arXiv:1409.3392 [nucl-ex] .
[9] ATLAS Collaboration, Phys. Rev. **C90**, p. 044906 (2014), arXiv:1409.1792 [hep-ex] .
[10] CMS Collaboration, Phys. Rev. Lett. **115**, p. 012301 (2015), arXiv:1502.05382 [nucl-ex] .
[11] A. Bzdak, B. Schenke, P. Tribedy, and R. Venugopalan, Phys. Rev. **C87**, p. 064906 (2013), arXiv:1304.3403 [nucl-th] .
[12] K. Dusling and R. Venugopalan, Phys. Rev. **D87**, p. 094034 (2013), arXiv:1302.7018 [hep-ph] .
[13] CMS Collaboration, CMS-PAS-HIN-14-008 (2014), https://cds.cern.ch/record/1703271 .
[14] ALICE Collaboration, Phys. Lett. **B753**, 126–139 (2016), arXiv:1506.08032 [nucl-ex] .
[15] Z.-W. Lin, C. M. Ko, B.-A. Li, B. Zhang, and S. Pal, Phys. Rev. **C72**, p. 064901 (2005), arXiv:nucl-th/0411110 .
[16] ATLAS Collaboration, ATLAS-CONF-2015-027 (2015), http://cds.cern.ch/record/2037663 .
[17] ATLAS Collaboration, submitted to Phys. Rev. Lett. (2015), arXiv:1509.04776 [hep-ex] .
[18] P. Bozek, A. Bzdak, and G.-L. Ma, Phys. Lett. **B748**, 301–305 (2015), arXiv:1503.03655 [hep-ph] .

Proceedings of the LHCP2015 Conference, St. Petersburg, Russia, August 31 - September 5, 2015

Editors: V.T. Kim and D.E. Sosnov

Nuclei and Anti-Nuclei Production in Heavy Ion Collisions

MAXIMILIANO PUCCIO[1,2]

[1]*Dipartimento di Fisica, Università degli Studi di Torino*
[2]*Istituto Nazionale di Fisica Nucleare, Sezione di Torino*

maximiliano.puccio@cern.ch

On behalf of the ALICE Collaboration

Abstract. The high integrated luminosity and the unprecedented collision energies provided by the Large Hadron Collider open the possibility to study extensively the production of light (anti-)nuclei, hypernuclei and exotic states in proton-proton (pp), proton-lead (p-Pb) and in particular in lead-lead (Pb-Pb) collisions. The transverse momentum spectra and the production yields of light nuclei and anti-nuclei are presented. Furthermore the study of the production of (anti-)hypertriton and searches for even lighter hyper-matter systems, i.e. Λ-Λ and Λ-n bound states are discussed. All results are compared with predictions from thermal (statistical) and coalescence models to inquire into the production mechanisms of nuclear, hyper-nuclear and exotic matter.

INTRODUCTION

Measuring nuclear matter and hyper-matter production at the LHC is a test of the theoretical models used to explain how such loosely bound composite objects could arise from pp, p-Pb and Pb-Pb collisions.

Nuclei production was measured with the ALICE experiment in all colliding systems available at the LHC. The results were compared with the two main groups of models that currently are able to describe the production of nuclear matter: the thermal models [1][2][3] and coalescence models such as [4].

The recent results on (anti-)nuclei production [5], as well as the results on the production of (anti-)hyper-triton [6] are presented here. Furthermore the results on the search for the ΛΛ and $\overline{\Lambda n}$ [7] exotic nuclear states – predicted by theory [8][9][10] but never found in the experiments – are shown here.

DETAILS ON THE ANALYSIS

Particle identification (PID) capabilities are required to study the nuclei production at collider experiments. For the time being, only the ALICE experiment has studied the light nuclei production at the LHC. Thanks to its Time Of Flight detector (TOF) and Time Projection Chamber (TPC), ALICE is able to identify particles over a large transverse momentum range. Using the information about the specific energy loss of particle traversing the TPC volume it is possible to identify deuteron and triton candidates in the range $0.7 < p_{\mathrm{T}} \leq 1.4$ GeV/c. With the same method it is possible to identify ^{3}He candidates over the full momentum range measured ($1.95 < p_{\mathrm{T}} \leq 6.95$ GeV/c). To complement the TPC information it is possible to use the time of flight information together with the information from the tracking to estimate the mass of the particles. A review of the Particle Identification capabilities of the ALICE experiment can be found in [11].

While the PID is the key aspect of the single track studies for light-(anti-)nuclei, the high granularity and pointing resolution of the Inner Tracking System (ITS) of ALICE were fundamental to study the production of hyper-nuclei and exotica states.

The data samples used for the analysis presented here were collected during the Run 1 of the LHC.

RESULTS

(Anti-)Nuclei production in different systems

Using the above-mentioned PID techniques, ALICE experiment measured the p_{T} differential production spectra for deuterons in pp and Pb-Pb collisions (figure 1) at $\sqrt{s}$ = 7 TeV and $\sqrt{s_{\mathrm{NN}}}$ = 2.76 TeV, respectively.

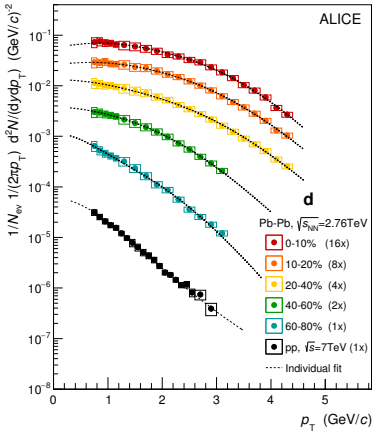

FIGURE 1: Deuteron p_{T} spectra in pp (black points) and Pb-Pb (colored points) collisions at $\sqrt{s}$ = 7 TeV and $\sqrt{s_{\mathrm{NN}}}$ = 2.76 TeV respectively. The Pb-Pb spectra have been fit individually with the Blast-Wave function [12] while the pp spectrum has been fitted with the Levy–Tsallis function [13].

The characteristic hardening of the spectra with the centrality in Pb-Pb collisions is interpreted in the framework of hydrodynamics as an effect of the increasing radial flow.

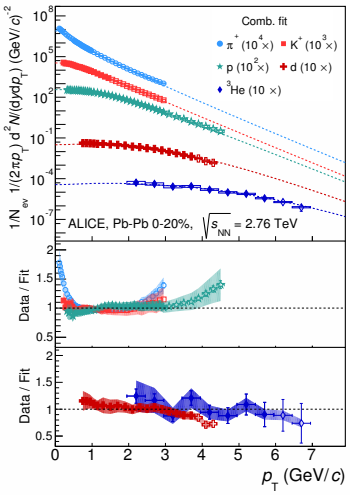

FIGURE 2: Combined Blast Wave fit [12] to the production spectra of different particle species. The two boxes on the bottom show the deviation of the fit from the data. The solid markers represent the fitted data points.

Based on the same data sample ALICE has been able to measure the production of ^{3}He nuclei and to perform a combined Blast Wave fit together with deuterons. The parameters obtained with this fit give some information about the kinetic freeze-out of nuclei. They are compatible with those obtained extending the fit to lighter particles

(figure 2), once the spectra are fitted in the p_T region where the production from hard processes is negligible. The fit describes well the thermal component and the radial flow of the production spectra using as kinetic freeze-out parameter: $\langle\beta\rangle = 0.632 \pm 0.01$, $T_{kin} = 113 \pm 12$ MeV, $n = 0.72 \pm 0.03$.

From the p_T differential production spectra, ALICE obtained the ratio between the production of matter and anti-matter in the nuclei sector [5]. From those ratios it is possible to conclude that in Pb-Pb collisions at the LHC energies the production rates of nuclei are compatible with those of anti-nuclei within uncertainties.

Moreover the ALICE experiment measured the production rates of deuteron and anti-deuteron in p-Pb collisions at $\sqrt{s_{NN}} = 5.02$ TeV. Figure 3 shows the p_T differential spectra for deuterons and anti-deuterons in different event multiplicity intervals. Similarly to what has been done for Pb-Pb collisions also in p-Pb collisions the Blast Wave fit is used to extrapolate the measured spectra to the unmeasured region in order to compute the integrated yield at mid rapidity. The transverse momentum distributions for deuterons and anti-deuterons show a hardening as a function of event multiplicity, similar to what has been observed for lighter particles in pp and Pb-Pb collisions at the LHC.

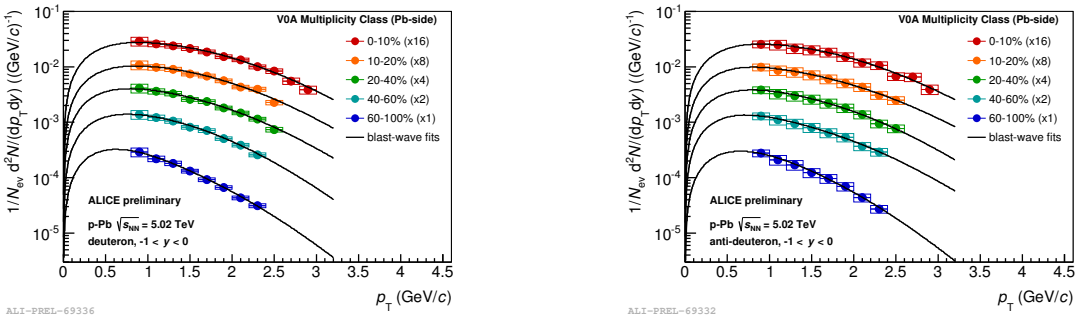

FIGURE 3: Deuteron (left) and anti-deuteron (right) spectra computed for different event activity bins in p-Pb collisions at $\sqrt{s_{NN}} = 5.02$ TeV. The Blast Wave function is used here to fit the distributions.

(Anti-)Hyper-nuclei production in Pb-Pb

The ALICE Collaboration has also measured the production rates of the hypertriton by exploring its decay into 2 charged particles. To reduce the combinatorial background and to improve the signal over background ratio, pions and ^{3}He were identified via energy loss (PID) and topological cuts were used.

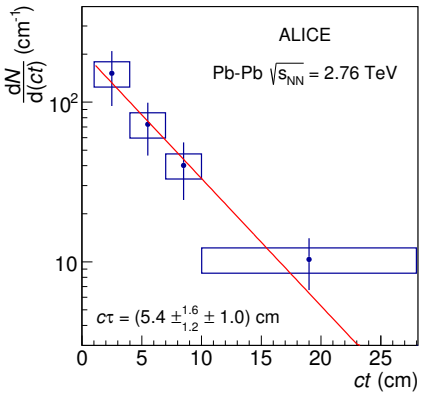

FIGURE 4: ct differential production spectrum of hypertriton. An exponential fit to the ct distribution is used to compute the $c\tau$ of the hypertriton.

As a result we obtain the invariant mass spectrum for the hyper-triton [6] and signal extraction can be performed

via a fit with a function that includes a signal and background contribution. The same procedure was applied for anti-hypertriton.

From the exponential fit to the extracted yields as a function of the decay length (*ct*) (figure 4) it is possible to evaluate the lifetime of the hypertriton. The value reported by ALICE of $\tau = 181^{+54}_{-39}(\text{stat.}) \pm 33(\text{syst.})$ ps is in agreement with the world average of 215 ps [6].

The fact that the lifetime of hyper-triton is lower than the lifetime of the free lambda still remains an open puzzle: being a loosely bound object one would expect the lifetime to be compatible with the lifetime of the lambda.

Search for exotic nuclear states

The ALICE collaboration looked for two particular exotic nuclear states in Pb-Pb collisions at $\sqrt{s_{\text{NN}}} = 2.76$ TeV: the H-dibaryon ($\Lambda\Lambda$) and the $\overline{\Lambda \text{n}}$ states. Both these states are predicted to exist according to theory and both should have a yield measurable by ALICE according to the thermal model expectations.

Nevertheless the observed invariant mass spectra for these two states do not show any evidence of the expected signal [7].

The upper limits set by the ALICE collaboration (figure 5) are well below the expected yield from the thermal model predictions. It is possible to conclude that the ALICE data do not support existence of the $\Lambda\Lambda$ and $\overline{\Lambda \text{n}}$ states.

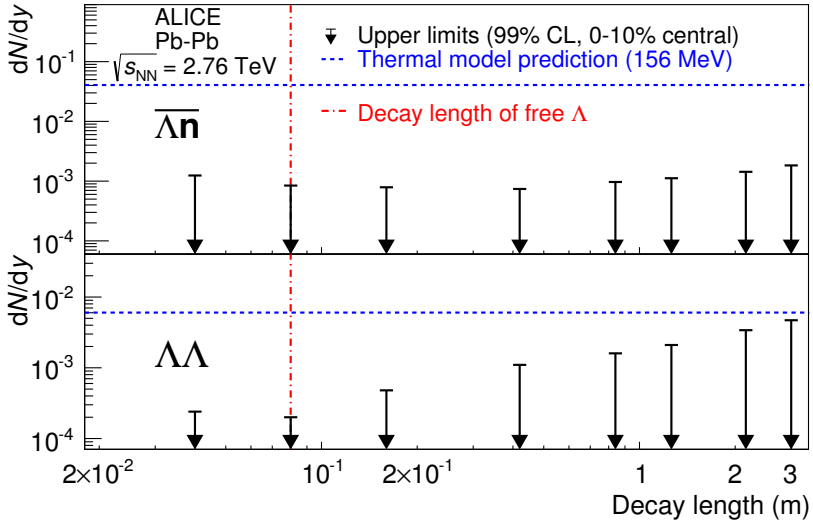

FIGURE 5: Upper limits for the yield of exotica states as a function of their decay length compared to the thermal model prediction at $T_{\text{chem}} = 156$ MeV.

Comparison with theoretical models

The results obtained by the ALICE experiment allow to test some of the theoretical models that predict how light nuclei and anti-nuclei are produced in high energy collisions between nuclei.

Studying how the ratio between the integrated yield of deuterons and the integrated yield of protons evolves as a function of the event multiplicity can help to test the validity of the coalescence model. The evolution of the ratio between the yields of deuterons and the yields of protons in different collision system (figure 6) is consistent with the coalescence model predictions. The flattening of the ratio in Pb-Pb collisions can be understood taking into account the fact that the size of the emitting source increases with the centrality.

Another probe of the coalescence model is the coalescence parameter B_2 [14]. In the simplest formulation of the coalescence model B_2 does not depend on the p_{T} of the nucleus. Conversely the results of ALICE for Pb-Pb collisions show that the coalescence parameter has a mild p_{T} dependence. These results are still in rough agreement with coalescence model if one considers the size of the emitting source computed using the Hanbury Brown and Twiss radii [5].

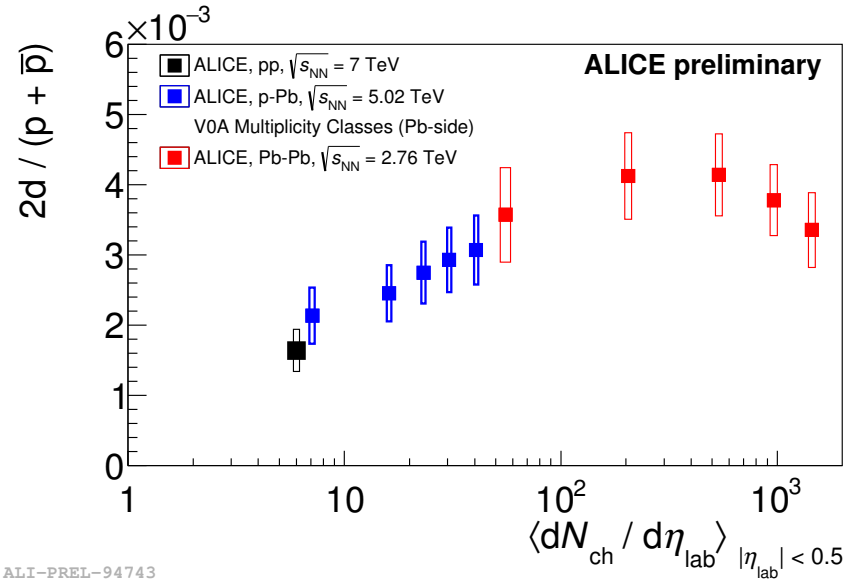

FIGURE 6: Deuteron over proton yields ratio as a function of event multiplicity in different collision systems. The ratio increases from pp collision up to p-Pb and stays constant for different multiplicities in Pb-Pb collisions.

Comparing the integrated yield of protons, deuterons, ^{3}He and $\overline{^4\text{He}}$ it is possible to probe one of the main predictions of the thermal models. The fit of production rates versus particle mass with an exponential function shows good agreement with the data and it tells us that adding one nucleon to a nucleus leads to a penalty in the integrated yield of a factor ~300. This kind of mass hierarchy is predicted by the grand-canonical statistical models.

Moreover the grand-canonical fits to the particles abundances show that the statistical-thermal models are able to reproduce the correct particle abundances of almost all the species measured by the ALICE experiment predicting a chemical freeze-out temperature of about 156 MeV (figure 7). It is possible to see that the three models [1][2][3] here reported describe well the nuclei production but fail to reproduce the correct abundances of protons and resonances like the $K^\star$.

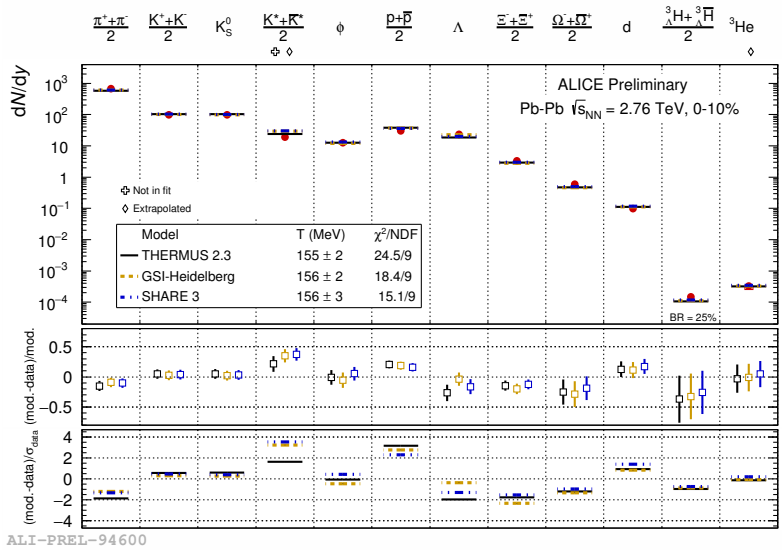

FIGURE 7: Grand-canonical fits to the particle abundances (red points) in heavy ion collisions at LHC.

CONCLUSIONS

The ALICE experiment, thanks to its unique PID and tracking capabilities, has been able to perform a wide set of different measurements on nuclei, anti-nuclei and hyper-nuclei production, allowing for systematic comparisons against theoretical models. The forthcoming data taking period of the LHC Run 2 will allow to study in more details collective effects in nuclei production in order to gain a deeper insight into their production mechanisms.

REFERENCES

[1] A. Andronic, P. Braun-Munzinger, J. Stachel, and H. Stocker, Phys. Lett. **B697**, 203–207 (2011), arXiv:1010.2995 [nucl-th] .
[2] J. Cleymans, S. Kabana, I. Kraus, H. Oeschler, K. Redlich, and N. Sharma, Phys. Rev. **C84**, p. 054916 (2011), arXiv:1105.3719 [hep-ph] .
[3] M. Petrn, J. Letessier, V. Petrek, and J. Rafelski, Phys. Rev. **C88**, p. 034907 (2013), arXiv:1303.2098 [hep-ph] .
[4] J. I. Kapusta, Phys. Rev. **C21**, 1301–1310 (1980).
[5] J. Adam *et al.* (ALICE), (2015), arXiv:1506.08951 [nucl-ex] .
[6] J. Adam *et al.* (ALICE), (2015), arXiv:1506.08453 [nucl-ex] .
[7] J. Adam *et al.* (ALICE), (2015), 10.1016/j.physletb.2015.11.048, arXiv:1506.07499 [nucl-ex] .
[8] R. L. Jaffe, Phys. Rev. Lett. **38**, 195–198Jan (1977).
[9] S. R. Beane *et al.* (NPLQCD), Phys. Rev. Lett. **106**, p. 162001 (2011), arXiv:1012.3812 [hep-lat] .
[10] T. Inoue, N. Ishii, S. Aoki, T. Doi, T. Hatsuda, Y. Ikeda, K. Murano, H. Nemura, and K. Sasaki (HAL QCD), Phys. Rev. Lett. **106**, p. 162002 (2011), arXiv:1012.5928 [hep-lat] .
[11] A. Kalweit (ALICE), *Quark matter. Proceedings, 22nd International Conference on Ultra-Relativistic Nucleus-Nucleus Collisions, Quark Matter 2011, Annecy, France, May 23-28, 2011*, J. Phys. **G38**, p. 124073 (2011), arXiv:1107.1514 [hep-ex] .
[12] E. Schnedermann, J. Sollfrank, and U. Heinz, Phys. Rev. C **48**, 2462–2475Nov (1993).
[13] C. Tsallis, J. Statist. Phys. **52**, 479–487 (1988).
[14] R. Scheibl and U. W. Heinz, Phys. Rev. **C59**, 1585–1602 (1999), arXiv:nucl-th/9809092 [nucl-th] .

Proceedings of the LHCP2015 Conference, St. Petersburg, Russia, August 31 - September 5, 2015

Editors: V.T. Kim and D.E. Sosnov

Jets, W and Z bosons in pA and AA collisions: ATLAS and CMS

ANTONIO SIDOTI

Istituto Nazione di Fisica Nucleare - Sezione di Bologna, Via Irnerio 46, 40126, Bologna, Italy
http://www.bo.infn.it

antonio.sidoti@bo.infn.it
URL: http://www.bo.infn.it

On behalf of the ATLAS and CMS Collaborations

Abstract. In these proceedings we will review the measurements related with jet physics, W and Z bosons performed by ATLAS and CMS during the heavy ion collisions program (Pb+Pb and p+Pb collisions) of LHC Run1 (2010-2013).

INTRODUCTION

Together with a very successful Run 1 physics program with p+p collisions at $\sqrt{s} = 7$ and 8 TeV, ATLAS (Ref.[1]) and CMS (Ref.[2]) performed very interesting measurements during the heavy ion collisions periods provided by the LHC. From 2010 to 2013 LHC provided Pb+Pb collisions at $\sqrt{s_{NN}} = 2.76$ TeV[1], p+Pb and Pb+p collisions at $\sqrt{s_{NN}} = 5.02$ TeV[2] and p+p collisions used as reference at $\sqrt{s} = 2.76$ TeV.[3] The center of mass energy increase of the heavy ion collisions with respect to the one reached by the previous generation machine (RHIC at BNL) enables jet measurements in a larger phase space and opens the possibility to study W and Z bosons production in heavy ion collisions.

Hadronic jets are produced in heavy ion collisions by hard scattering processes. Accurate predictions of rates of production are possible with perturbative QCD (pQCD) calculations. Once produced, hadronic jets evolve in the QCD medium produced by the collision of the two nuclei and therefore can be used as probes of the quark-gluon plasma (QGP). However, to disentangle specific effects due to the dense QCD medium from non collective effects like the impact of nuclear modification in parton distribution functions (nPDF) and other effects, it is important to study the jet evolution in p+p collisions and in p+Pb collisions as well. Also using different probes insensible to the dense QCD medium like electroweak bosons (W and Z) is fundamental to better understand the nature of the QGP.

These proceeding are organized as follows, jet measurements performed by ATLAS and CMS experiments are shown in the first section, while W and Z boson measurements are reported in the second section. A conclusion will briefly summarize results in view of the upcoming Run2.

JET MEASUREMENTS

A remarkable effect that occurs in high energy heavy ion collisions is the so-called *jet quenching*. This occurs when a di-jet event is produced in Pb+Pb collisions. In principle, without instrumental effects like jet energy miscalibration, inefficiency, *etc.*, in p+p collisions the transverse energy of the jets is balanced such that, roughly, the $E_{\mathrm{T},1}$ of one jet is counterbalanced by $E_{\mathrm{T},2}$, the energy of the second jet ($\vec{E}_{\mathrm{T},1} \simeq -\vec{E}_{\mathrm{T},2}$). At the contrary, in Pb+Pb collisions, jets loose

[1] In 2010 and 2011 LHC delivered respectively $9.6\mu b^{-1}$ and 166 μb^{-1}.
[2] in 2013 with a center of mass boost $y_{CM} = \pm 0.46$ and with a total delivered luminosity of 31 nb^{-1}.
[3] In 2013 a total of 5.5 pb^{-1} were delivered by LHC.

their energy when they interacts with the QCD medium produced in the collision. Hints of this effect were observed at RHIC heavy ion collider. Using the larger center of mass of the collisions produced by LHC, ATLAS and CMS were able to prove jet quenching and study its characteristics in a more quantitative way and with more statistics.

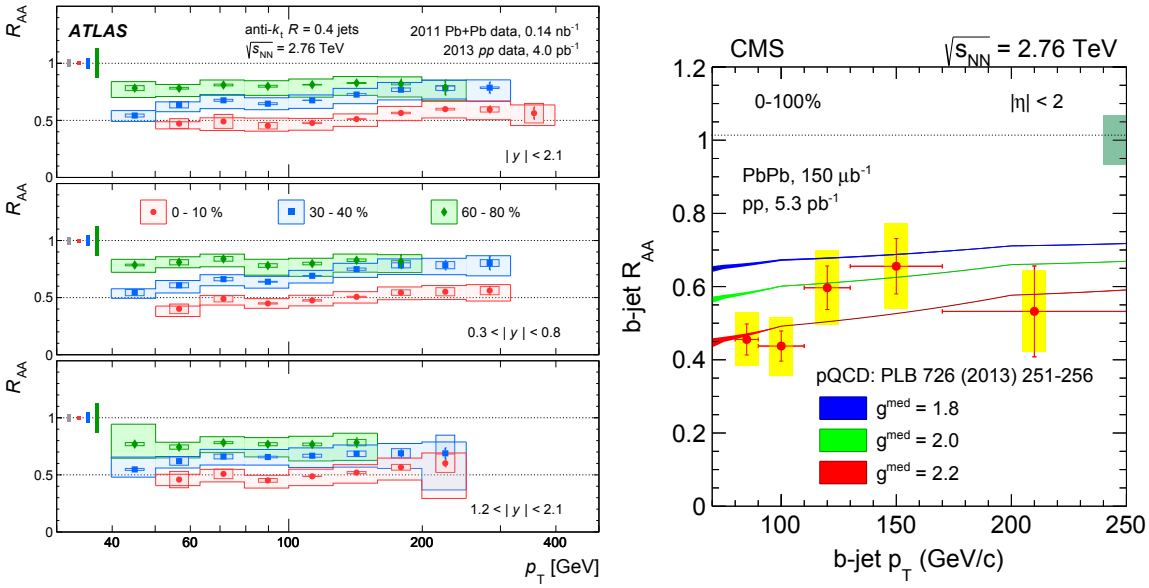

FIGURE 1. Left: $R_{\rm AA}$ ratio as a function of jet $E_{\rm T}$ and rapidity in different centrality bins (from Ref. [3]). Right: $R_{\rm AA}$ ratio for b-tagged jets as a function of jet $E_{\rm T}$. Data are compared to pQCD-based calculations Ref. [4] (from Ref. [5])

An important parameter to characterize Pb+Pb collisions is the *centrality* that is a quantitative measurement of how much the colliding nuclei overlap: small values of centrality indicate that nuclei collide head-on while large values indicate a large impact factor of the collisions. Experimentally centrality is measured with the energy deposited in forward region calorimeters[4] which is correlated to the centrality and the number of binary collisions $N_{\rm coll}$ through the Glauber model.

ATLAS and CMS have measured the nuclear modification form factor R_{AA} ratio (Ref. [3, 6]) defined as:

$$R_{AA} = \frac{\frac{1}{N_{\rm evt}} \frac{d^2 N_{\rm jet}}{dp_{\rm T} dy}\Big|_{\rm central}}{\langle T_{AA} \rangle \frac{d^2 \sigma^{pp}_{\rm jet}}{dp_{\rm T} dy}},$$

the ratio of the double differential jet production cross section measured in Pb+Pb collisions at a given *centrality* with respect to the one measured in p+p collisions with the same $\sqrt{S_{NN}}$ corrected by the nuclear overlap geometrical factor $< T_{AA} >$ obtained through the Glauber model. R_{AA} factor measured by ATLAS as a function of the jet $E_{\rm T}$ and rapidity for different centrality values is shown in Figure 1-left. For central events, the jet production is reduced in Pb+Pb collisions with respect to p+p collisions by $\approx$ 50%. A small logarithmic increase of R_{AA} with the jet $E_{\rm T}$ is observed indicating that the QCD medium formed tends to be more and more transparent with the increase of the probe momentum. The dependence on rapidity is interesting since the fraction of quark to gluon jets is modified by the jet rapidity (forward jets tend to be originated more by gluon than quarks).

Using secondary vertex tagging, CMS performed a measurement of $< R_{AA} >$ for jets coming from a b-quark Ref. [5] thus increasing the heavy flavor content of the probing jet. The measured $< R_{AA} >$ is shown in Figure 1-right and doesn't show any significant difference with respect to the $< R_{AA} >$ measured with inclusive jets. Additional investigations (Ref. [9]) to understand where the energy of the jets goes when it traverses the QGP have been reported in Ref. [10].

At the contrary the nuclear modification factor R_{p+Pb} is compatible with 1 for p+Pb collisions indicating no jet quenching (Ref.[8, 7]). A non negligible uncertainty in the measurement is given by the extrapolation procedure to get

[4] In ATLAS the forward calorimetry coverage in pseudorapidity goes from $3.2 < |\eta| < 4.9$ while in CMS it goes from $3.0 < |\eta| < 5.2$.

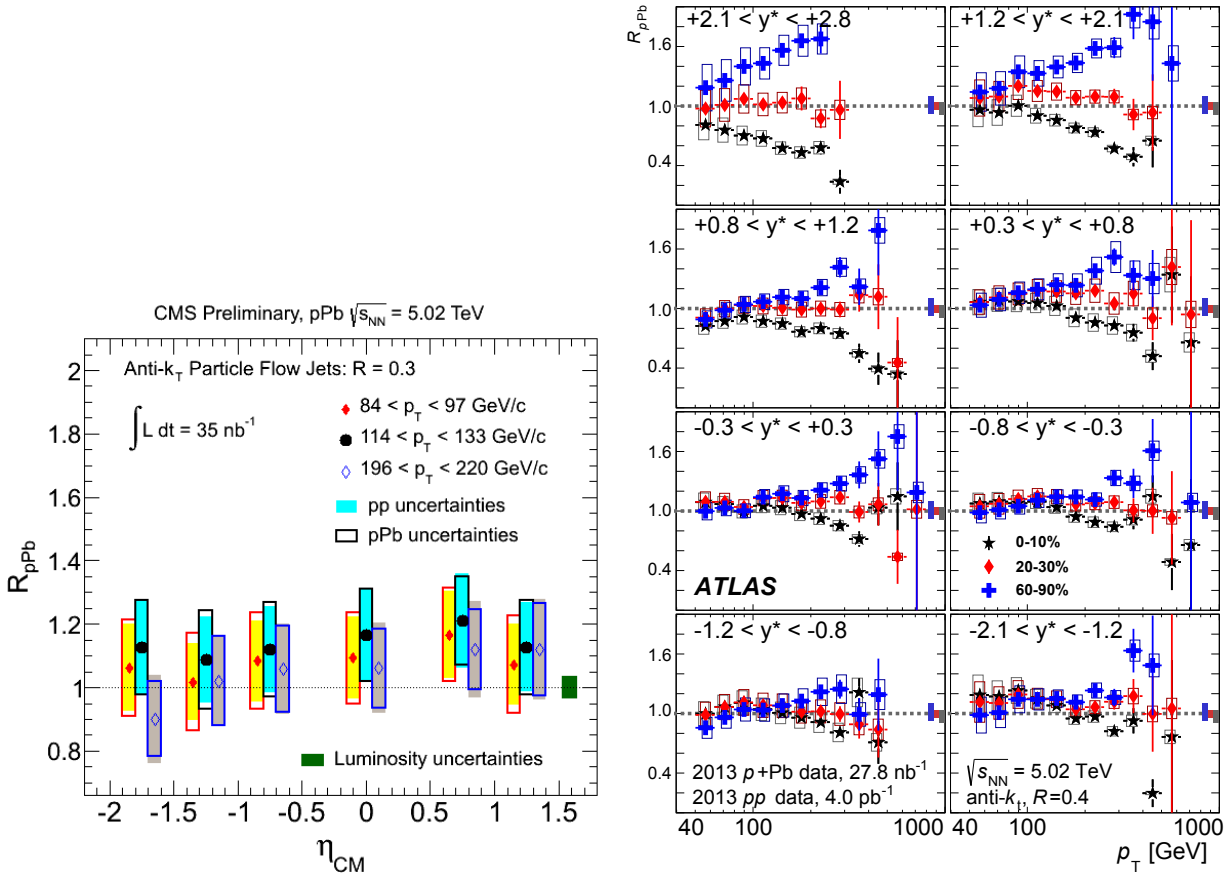

FIGURE 2. Left: R_{p+Pb} ratio as a function of the jet pseudorapidity using the extrapolated p+p reference for three selected P_{T} intervals (from Ref. [7]). Right: R_{p+Pb} as a function of E_{T} in different centrality bins (from Ref. [8]).

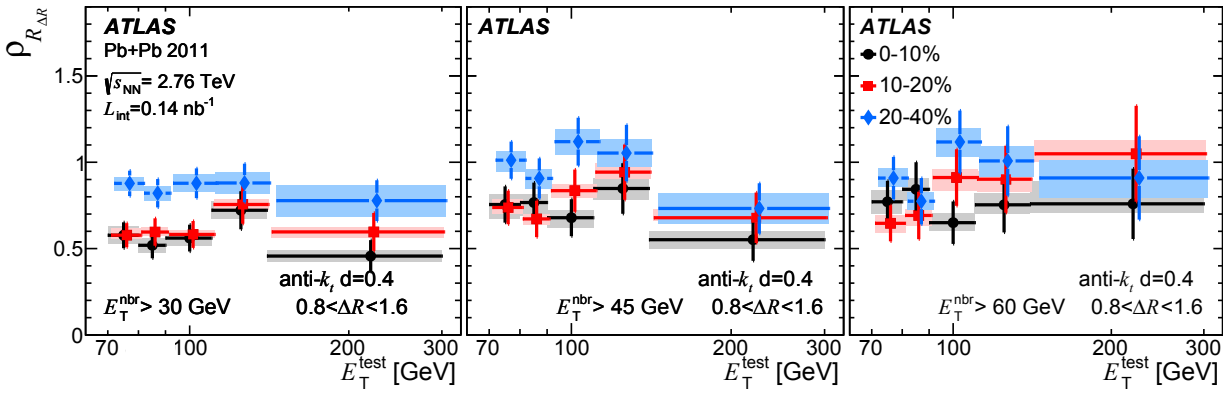

FIGURE 3. $\rho_{R_{\Delta R}}$ (see text) measured as a function of $E_{\mathrm{T}}^{\mathrm{test}}$ with increasing $E_{\mathrm{T,min}}^{\mathrm{nbr}}$ (from Ref. [11]).

the correct value for the reference p+p collisions at $\sqrt{s} = 5.02$ TeV that were realized only at the start of LHC Run2 (November 2015). The measured R_{p+Pb} value evaluated in intervals of centrality Figure 2-right shows deviation from unity in particular for large E_{T} jets. This could be caused by a slightly more problematic definition of the centrality in p+Pb collisions rather than in Pb+Pb collisions (*cf* Section) or some needed modification in the nPDF functions since

it is observed that R_{pPb} scales linearly with the jet total energy $E \approx P_{\mathrm{T}} \cosh(y^{\star})$ where $y^{\star}$ is the rapidity measured with respect of the centre of mass rapidity y_{CM} which is different from 0 in p+Pb collisions ($Y^{\star} = y - y_{CM}$).

Fluctuations in the energy loss of jets in the QCD medium are studied measuring the jets suppression for *neighboring* jets (nbr) with $E_{\mathrm{T}}^{\mathrm{nbr}} > E_{\mathrm{T,min}}^{\mathrm{nbr}}$ in ΔR [5] with respect of a *test* jet. On an inclusive two jets sample, the $R_{\Delta R}$ value defined as:

$$R_{\Delta R} = \frac{1}{dN_{\mathrm{jet}}^{\mathrm{test}}/dE_{\mathrm{T}}^{\mathrm{test}}} = \sum_{i=1}^{N_{\mathrm{jet}}^{\mathrm{test}}} \frac{dN_{\mathrm{jet},j}^{\mathrm{nbr}}}{dE_{\mathrm{T}}^{\mathrm{test}}(E_{\mathrm{T}}^{\mathrm{test}}, E_{\mathrm{T,min}}^{\mathrm{nbr}}, \Delta R)}$$

is measured as a function of the $E_{\mathrm{T}}^{\mathrm{test}}$ and for different ΔR intervals and $E_{\mathrm{T,min}}^{\mathrm{nbr}}$ values. The ratio $\rho_{R_{\Delta R}}$ is measured as the ratio of $R_{\Delta R}$ for central events normalized to peripheral collisions with centrality values 40 – 80% and is shown in Figure 3. The suppression factor of $\sim$ 50% is confirmed for all $E_{\mathrm{T}}^{\mathrm{test}}$ values while a weak increase is observed with $E_{\mathrm{T,min}}^{\mathrm{nbr}}$.

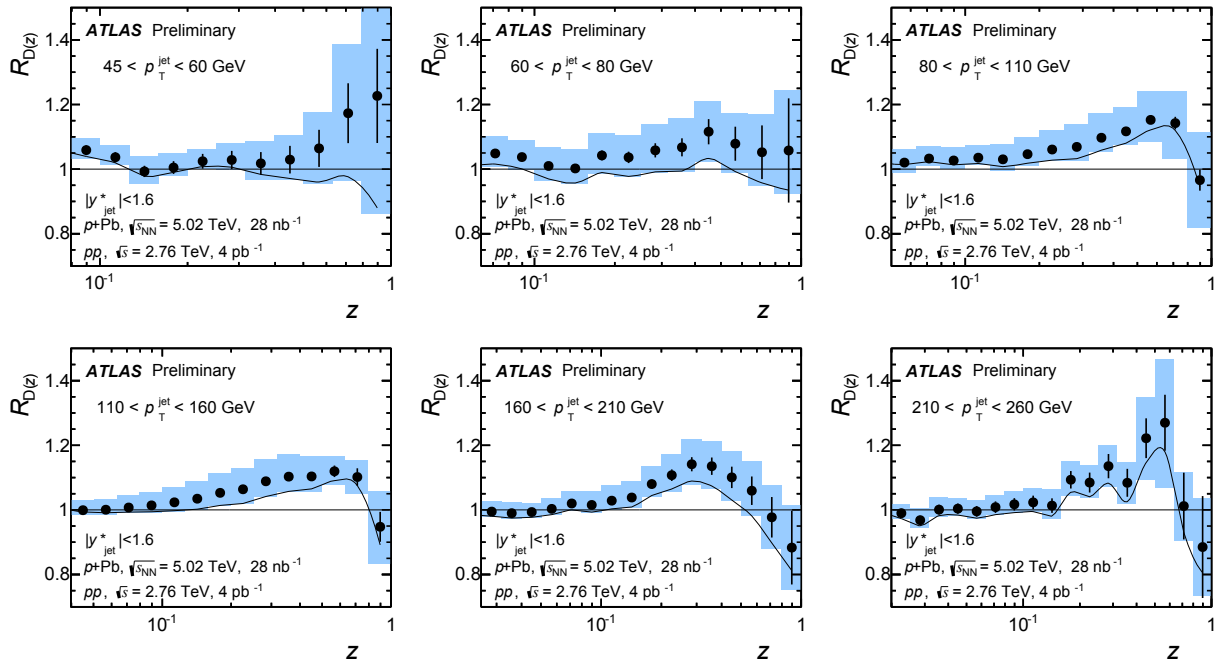

FIGURE 4. Ratios of fragmentation functions in p+Pb compared to those in p+p collisions for the six $E_{\mathrm{T}}^{\mathrm{jet}}$ intervals after subtraction from underlying event (from Ref. [12]).

Dense QCD matter also modifies the momentum of particles inside a jet. Fragmentation function have been measured by both ATLAS and CMS for Pb+Pb collisions Ref [13, 14] and p+Pb collisions Ref [12, 15]. The fragmentation function $D(z) = \frac{1}{N_{\mathrm{jet}}} \frac{dN_{\mathrm{ch}}}{dz}$ measured in p+Pb collisions normalized to p+p collisions is shown in Figures 4 and 5 as a function of $z = \frac{\vec{P}_{\mathrm{T,ch}} \vec{P}_{\mathrm{T,Jet}}}{|P_{\mathrm{T,Jet}}^2|}$ [6]. While CMS doesn't show a significant variation with respect to the p+p collisions, ATLAS shows an enhancement for values when charged-particles tracks bring more than 20% of the energy of the hadronic jets. However there are few differences that could explain the differences between the two measurements: the underlying event removal and the extrapolation method to get the reference for p+p collisions at $\sqrt{s} = 5.02$ TeV. For the latter, the data collected in November 2015 during p+p collisions at $\sqrt{s} = 5.02$ TeV will be of fundamental importance.

[5] Where $\Delta R = \sqrt{\Delta\phi(\mathrm{test,nbr})^2 + \Delta\eta(\mathrm{test,nbr})^2}$.
[6] Or an equivalent variable $\xi = \ln(1/z)$ for CMS.

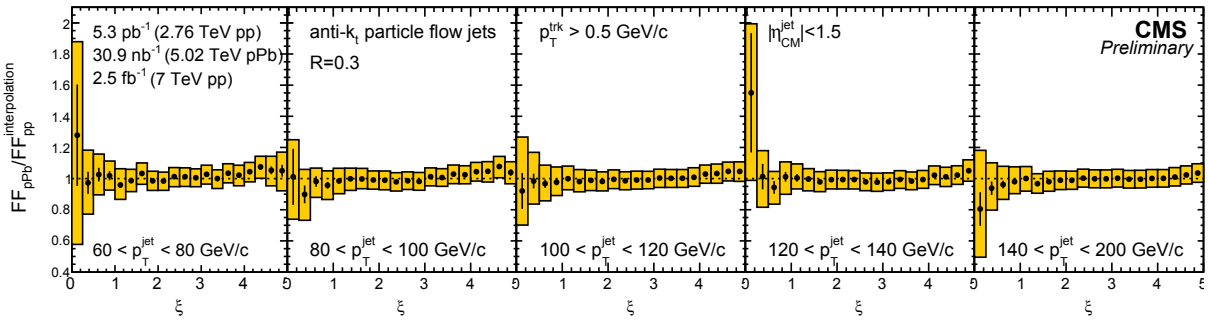

FIGURE 5. Ratio of fragmentation function for p+Pb using a p+p reference. Starting from the leftmost column, fragmentation functions for jets with increasing $E_{\mathrm{T}}^{\mathrm{jet}}$ are shown. Underlying event subtraction has been done using a 90 degree rotated cone in the ϕ direction. (from Ref. [15]).

W AND Z BOSONS

Electroweak bosons are produced with a significant rate in heavy ion collisions at LHC. They do not interact strongly with QCD matter and their properties have been measured in Pb+Pb, p+Pb and p+p collisions; therefore they complement the analysis of QGP. W and Z bosons are identified in heavy ion collisions with their leptonic decay channels. Background contamination for $W \to \ell\nu_\ell$ are smaller than $\lesssim 10\%$ (Figure 6-left) while $Z \to \ell\bar{\ell}$ are cleaner with less than $\lesssim 3\%$ of background contamination (Figure 6-right).

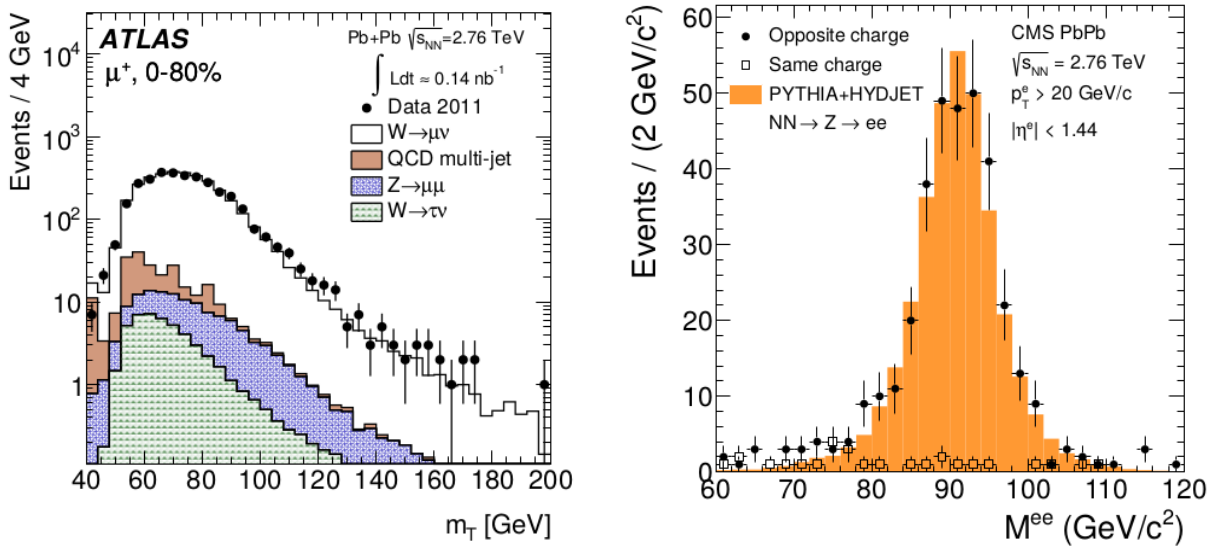

FIGURE 6. Left: Transverse mass distribution with the different background contribution for $W^+ \to \mu^+\bar{\nu_\mu}$ (from [16]). Right: Dielectron invariant mass spectra: full black circles represent opposite-charge electrons, open black squares show same charge electron pairs (from Ref [17]).

The Z boson yield is constant in Pb+Pb collisions Ref [18, 17] as a function of $< N_{\mathrm{coll}} >$ (Figure 7-left) confirming that electroweak bosons and their leptonic decay products (electrons and muons) are unaffected by the QCD matter. Also the ratio of production R_{AA} scaled by $< T_{AA} >$ is compatible with unity showing that Z boson remain unaffected when traversing the QCD hot medium (Figure 7-right).

In a way that is reminiscent of p+p collisions, W boson asymmetry measurement in Pb+Pb collisions give fundamental insight in the nPDF content since, at leading order, $W^+(W^-)$ are primarily produced by interactions between a $u(d)$ valence quark and a $\bar{d}(\bar{u})$ sea quark. The rapidity of the W boson is primarily determined by the

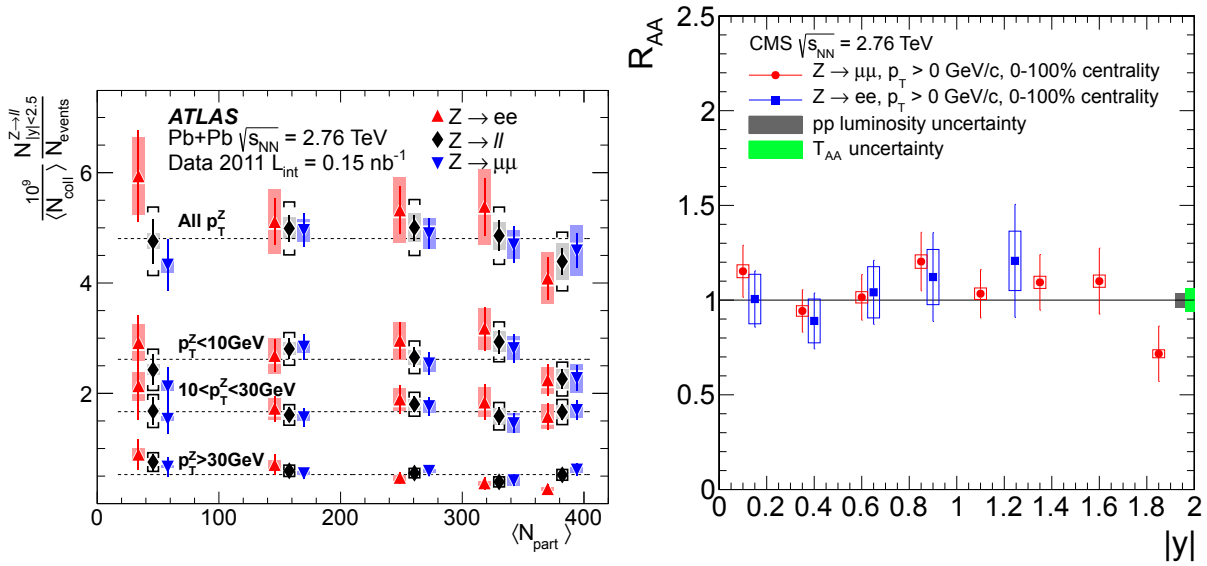

FIGURE 7. Left: Yields of Z boson as a function of $< N_{\rm coll} >$ measured in Pb+Pb collisions with $\sqrt{S_{NN}} = 2.76$ TeV for different $P_{\rm T}^{Z}$ intervals (from Ref [18]). Right: R_{AA} for Z bosons as a function of the rapidity of the Z (from Ref [17]).

momentum fractions x of the incoming partons. Information on the nPDF can be extracted by measuring the charge asymmetry as a function of the pseudorapidity of the charged lepton from W decays. Asymmetry measurements are more precise than just differential production ones since many uncertainties cance out in the ratio (in particular the luminosity uncertainty). The charge asymmetry is defined as:

$$A_\ell(\eta_\ell) = \frac{dN_{W^+\to\ell^+\nu_\ell} - dN_{W^-\to\ell^-\bar{\nu}_\ell}}{dN_{W^+\to\ell^+\nu_\ell} + dN_{W^-\to\ell^-\bar{\nu}_\ell}}$$

and is shown in Figure 8-left (Ref. [19]) where the impact of nuclear effects in the PDF is shown on the predictions. So far, more statistics and a better understanding of the uncertainties are needed to establish the existence of nuclear effects using W asymmetry measurements. Nuclear effects are expected to modify the Z production rapidity distribution asymmetrically (Ref. [16, 20]). Therefore nuclear effects in the PDF can be quantitatively evaluated with the forward-backward ratio defined as:

$$R_{FB} = \frac{d\sigma(+y)/dy}{d\sigma(-y)/dy}.$$

R_{FB} is shown in Figure 8-right and predictions using nuclear effects in PDF are clearly favoured.

W boson production studies have been performed also in p+Pb collisions (Ref. [21]). The forward-backward asymmetry defined as:

$$R_{W_{p+Pb}}(\eta_{\rm lab}) = \frac{N(+\eta_{\rm lab})}{N(-\eta_{\rm lab})}$$

is shown in Figure 9-left and is compared with predictions with PDF using nuclear modification factors that are favored by data. However, even pdf with EPS09 nuclear effect don't seem to predict well the data of the W boson charge asymmetry (Figure 9-right). A possible explanation of this discrepancy might be the fact that nuclear modiffication effects could be different for up and down quarks in heavy nuclei.

As anticipated in the previous section, some caution has to be given to centrality measurement in p+Pb collisions. In fact the presence of any hard process (including jets, Z and W boson production) is correlatred with a larger transverse energy in the underlying event. Consequently, more energy may be deposited in the Pb-going side of the forward calorimeters[7] in events containing a hard scattering process than in those that do not contain one causing a

[7] In p+Pb collisions the centrality value of an events is determined by the measurement of the forward calorimeter energy deposited in the Pb-going side.

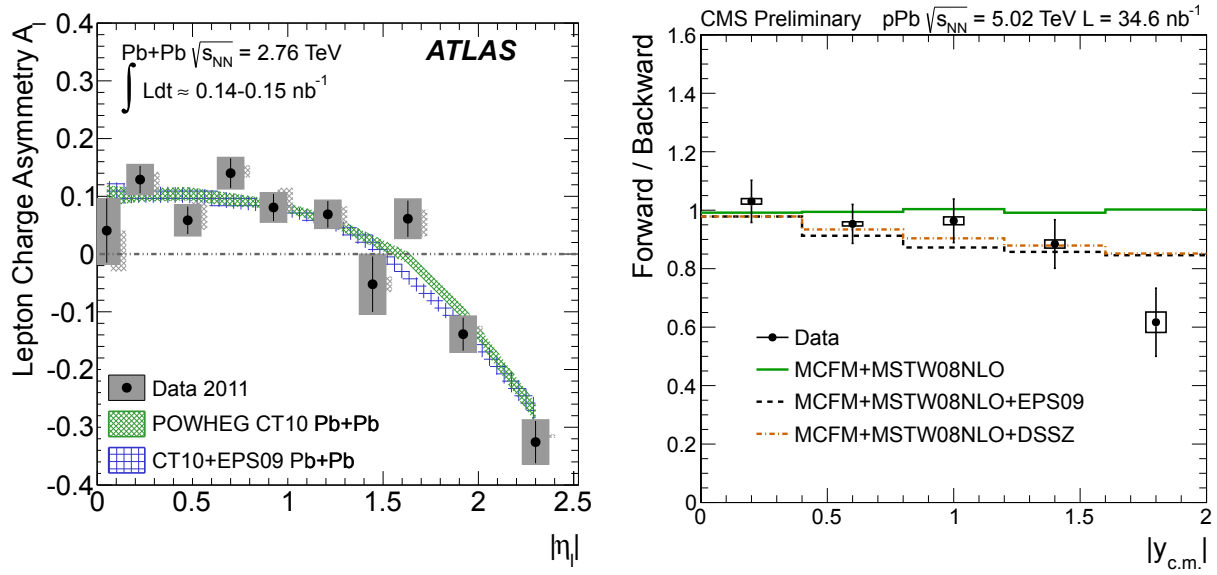

FIGURE 8. Left: W asymmetry measurements as a function of the lepton pseudorapidity compared with theoretical predictions using CT10 and CT10+EPS09 NLO sets where this latter include nuclear effects (from Ref. [19]). Right: $R_{\rm FB}$ distributions of Z bosons in p+Pb collisions corrected to full acceptance combining dielectron ad dimuon channels compared with predictions using different PDF (from Ref.[20]).

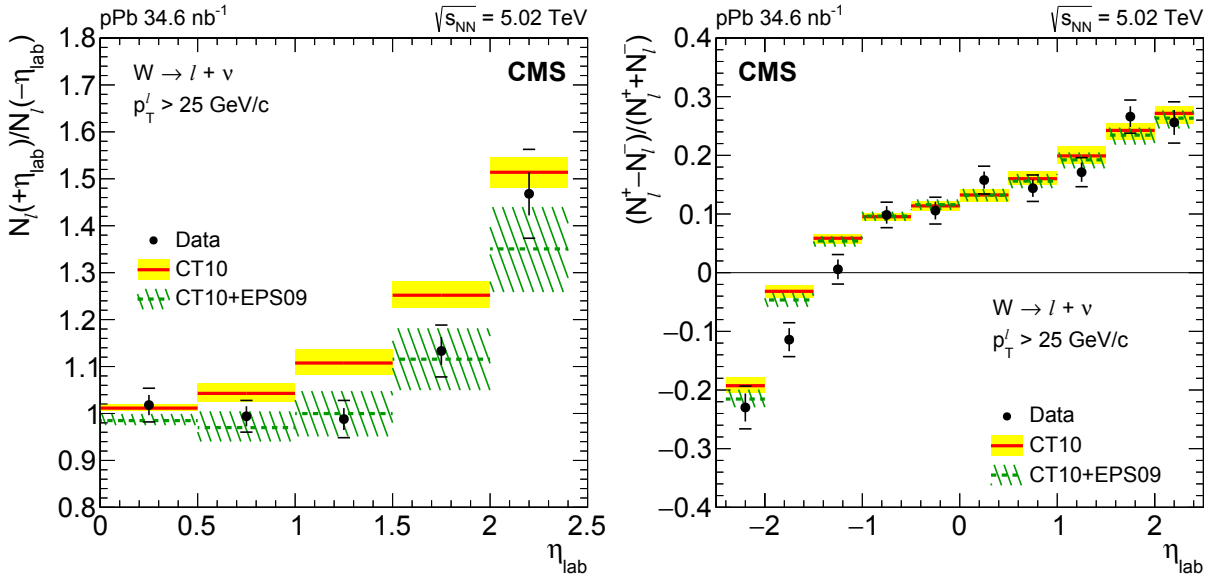

FIGURE 9. From Ref. [21]. Left: Forward-backward asymmetry of charge-summed W bosons, as a function of the lepton pseudorapidity. Right: Lepton charge asymmetry, $\frac{N^+-N^-}{N^++N^-}$, as a function of the lepton pseudorapidity. Theoretical predictions with (CT10+EPS09, dashed green line) and without (CT10, solid red line) PDF nuclear modifications are also shown, with their uncertainty bands.

centrality bias. This has been observed by PHENIX at RHIC in *d+Au* (Ref.[22]) and by ALICE in p+Pb collisions (Ref.[23]). The centrality bias is corrected with a data driven method (Ref.[16]), and the invariance of the yield of Z bosons as a function of $< N_{\rm part} >$ after the centrality bias correction is shown if Figure 10-left. The Z boson differential

yield is shown in Figure 10-right. The $< N_{\rm coll} >$-scaled ratio of central to peripheral events R_{CP} defined as:

$$R_{CP}(y_Z^\star) = \frac{< N_{\rm coll} >^{\rm peripheral}}{N_{\rm coll} >^{\rm central}} \times \frac{dN_Z^{\rm central}/dy_Z^\star}{dN_Z^{\rm peripheral}/dy_Z^\star}$$

shows changes in the rapidity distribution for different centrality bins. The slight slope difference of $R_{CP}(y_Z^\star)$ between central and peripheral events indicates that the Z boson asymmetry is slightly larger for central events than for peripheral ones.

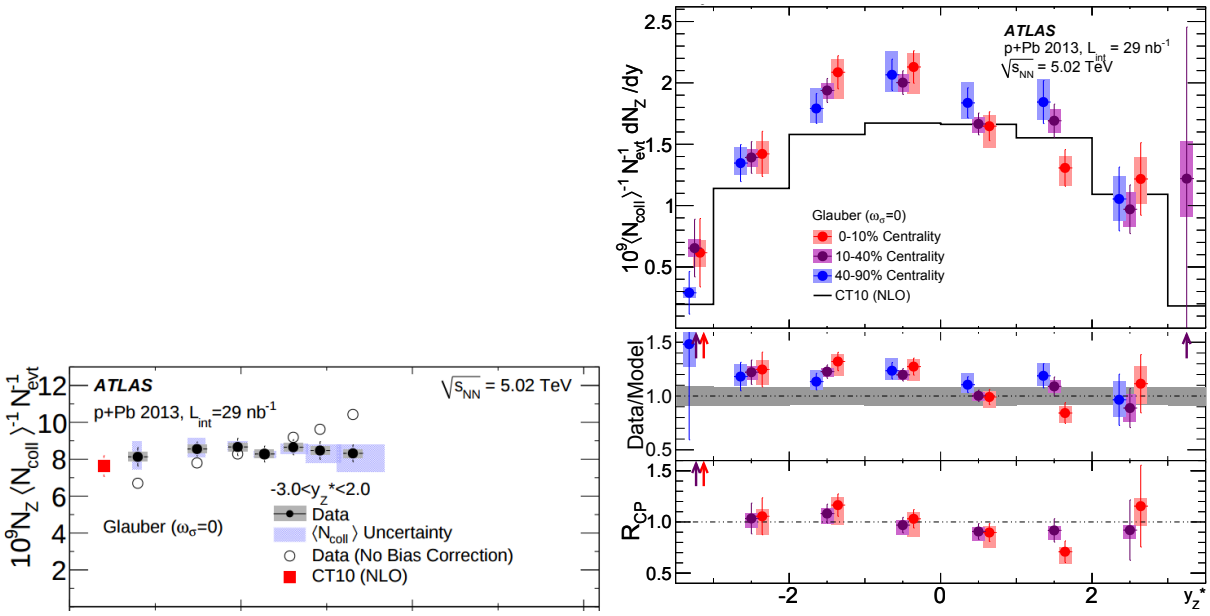

FIGURE 10. Left: Evidence for binary scaling of the Z boson yields after the *centrality bias* correction. Right: The Z differential yield as a function of the rapidity y_Z is reported for different centrality values (top). R_{CP} as a function of y_z is reported (bottom). (from Ref. [16])

SUMMARY

A new era of heavy ion collisions at the largest energies and integrated luminosity has started with LHC Run1. Hadronic jets and electroweak bosons are powerfool tools to understand the properties of quark-gluon plasma since the former are affected by the QCD matter while the latter are not. Measurements of processes involving jets and electroweak bosons performed in Pb+Pb, p+Pb and p+p collisions test characterize the impact of different aspects occurring in heavy ion collisions like nuclear effects in PDF, different fragmentation functions, *etc.*. We expect for the incumbent Run2 of LHC a larger wealth of data collected with larger energy in the centre of mass of collisions.

ACKNOWLEDGMENTS

It is a pleasure to thank here our colleagues R. Nania and P. Antonioli from the ALICE collabration group in Bologna for useful discussions and the LHCP2015 local organizing committee for the wonderful organization of the conference.

REFERENCES

[1] ATLAS Collaboration, JINST **3**, p. S08003 (2008).
[2] CMS Collaboration, JINST **3**, p. S08004 (2008).
[3] ATLAS Collaboration, Phys. Rev. Lett. **114**, p. 072302 (2015).
[4] J. Huang, Z.-B. Kang, and I. Itev, Phys. Lett. B **726**, p. 251 (2013).
[5] CMS Collaboration, Phys. Rev. Lett. **113**, p. 132301 (2014).
[6] CMS Collaboration, PAS-HIN-12-004 (2015).
[7] CMS Collaboration, PAS-HIN-14-001 (2014).
[8] ATLAS Collaboration, Phys. Lett. B **748**, p. 392 (2014).
[9] CMS Collaboration, Phys. Rev. C **84**, p. 024906 (2011).
[10] L. Cunqueiro, these proceedings (2015).
[11] ATLAS Collaboration, Phys. Lett. B **751**, p. 376 (2015).
[12] ATLAS Collaboration, ATLAS-CONF-2015-022 (2015).
[13] ATLAS Collaboration, Phys. Lett. B **739**, 320–342 (2014).
[14] CMS Collaboration, Phys. Rev. C **90**, p. 024908 (2014).
[15] CMS Collaboration, PAS-HIN-15-004 (2015).
[16] ATLAS Collaboration, Phys. Rev. C **92**, p. 044915 (2015).
[17] CMS Collaboration, JHEP **03**, p. 022 (2015).
[18] ATLAS Collaboration, Phys. Rev. Lett. **110**, p. 022301 (2013).
[19] ATLAS Collaboration, Eur. Phys. J. C **75**, p. 23 (2015).
[20] CMS Collaboration, PAS-HIN-15-002 (2015).
[21] CMS Collaboration, arXiv:1503.05825 submitted to Phys. Lett. B (2015).
[22] A. Adare et al. (PHENIX Collaboration), Phys. Rev. C **90**, p. 034902 (2014).
[23] J. Adams et al. (ALICE Collaboration), Phys. Rev. C **91**, p. 064905 (2014).
[24] ATLAS Collaboration, EPJC **75**, p. 23 (2015).

Proceedings of the LHCP2015 Conference, St. Petersburg, Russia, August 31 - September 5, 2015

Editors: V.T. Kim and D.E. Sosnov

Quarkonium Production in p-Pb and Pb-Pb Collisions

IGOR LAKOMOV

European Organization for Nuclear Research (CERN), CH-1211, Geneva 23, Switzerland.

igor.lakomov@cern.ch

On behalf of the ALICE, ATLAS, CMS and LHCb Collaborations

Abstract. Quarkonium production in heavy-ion collisions is one of the key tools to study the Quark-Gluon Plasma, the state of matter which is believed to be formed at the high energy density achieved in heavy-ion collisions. The Large Hadron Collider experiments studied quarkonium production in proton-proton, proton-lead and lead-lead collisions at center-of-mass energies of few TeV. Studying quarkonium production in pp, p–Pb and Pb–Pb collisions allows one to disentangle hot (related to the QGP formation) and cold nuclear matter effects. This article summarizes the recent measurements of quarkonium production by the LHC experiments in p–Pb and Pb–Pb collisions.

INTRODUCTION

Production of quarkonia, bound states of quark and anti-quark pairs, is intensively studied in last years. Its suppression in heavy-ion collisions compared to the production expected from pp collisions indicates the formation of a new state of matter, Quark-Gluon Plasma (QGP), which is believed to be formed at high energy densities. It was predicted that at sufficiently high energy densities the color screening of the heavy-quarks potential in deconfined QCD matter will lead to a sequential suppression of the production of different quarkonium states [1]. Contrary to Pb–Pb collisions the quarkonium production in p–Pb collisions is believed to be affected only by the Cold Nuclear Matter (CNM) effects. There are many different models of CNM effects. They all are usually classified into three groups depending on their nature: (a) pure initial-state effects, e.g. shadowing, saturation; (b) pure final-state effects, e.g. nuclear absorption, comover interaction; (c) other effects which cannot be assigned to pure initial-state or pure final-state effects, e.g. coherent parton energy loss.

The measurements in p–Pb collisions allows quantifying the CNM effects which need to be disentangled from the hot, QGP related effects, in Pb–Pb collisions. Usually hot and CNM effects are quantified with the nuclear modification factor, $R_{\rm AA}$, defined as the ratio of the quarkonium yield in Pb–Pb to that in pp collisions scaled with the average number of binary nucleon-nucleon collisions $\langle N_{\rm coll}\rangle$ in the corresponding centrality range. In the absence of any nuclear matter effects $R_{\rm AA}$ is equal to unity. For p–Pb collisions $R_{\rm pPb}$ is defined in the same way.

All the four Large Hadron Collider (LHC) experiments measure quarkonium production at the LHC for different collision systems (pp, p–Pb, Pb–Pb). In this review the latest results in p–Pb and Pb–Pb are presented and compared to theoretical models.

QUARKONIUM PRODUCTION IN Pb–Pb COLLISIONS

LHC experiments already produced many results on quarkonium production in Pb–Pb collisions from Run I of the LHC data-taking period. However there are still ongoing analyses which will produce more new results. Figure 1 shows one of the latest LHC results for Pb–Pb collisions performed by ALICE [2]. Left panel shows the ALICE measurement[1] of the J/ψ $R_{\rm AA}$ as a function of the average number of participants $\langle N_{\rm part}\rangle$, in three $p_{\rm T}$ intervals. For J/ψ with $0.3 \leq p_{\rm T} < 1$ GeV/c and with $1 \leq p_{\rm T} < 8$ GeV/c, the measured $R_{\rm AA}$ suggests a similar decreasing trend

[1] Here and later in the text the presented J/ψ production measured by ALICE is the inclusive J/ψ production.

with increasing centrality at $\langle N_{\rm part}\rangle < 110$, which represents the effect of the QGP. At central collisions ($\langle N_{\rm part}\rangle > 100$) lower-$p_{\rm T}$ J/ψ show no centrality dependence of the $R_{\rm AA}$. Such a behaviour of the J/ψ $R_{\rm AA}$ with similar $p_{\rm T}$ ranges was successfully explained in [3] by transport models [4, 5] including the J/ψ regeneration contribution and by the comover interaction model [6] which also includes a regeneration component. However an excess of the J/ψ production at very low $p_{\rm T}$ for the most peripheral collisions (small $\langle N_{\rm part}\rangle$) is not expected from these models. The nuclear modification factor $R_{\rm AA}$ reaches 7 in the centrality range 70–90% for $p_{\rm T} < 0.3$ GeV/c, which is significantly higher than for the other two $p_{\rm T}$ ranges where it is in the range of 0.7-0.8 in the same centrality interval. In the right panel the $p_{\rm T}$-distribution of opposite-sign dimuons in the J/ψ mass range ($2.8 < m_{\mu^+\mu^-} < 3.4$ GeV/c^2) for 70–90% centrality class is shown. The low-$p_{\rm T}$ excess is well pronounced for centrality interval 70–90%. The calculations of the STARLIGHT Monte Carlo generator [7] that is used to describe the J/ψ photoproduction in ultra-peripheral collisions, is able to reproduce the $p_{\rm T}$-shape of the low-$p_{\rm T}$ excess, which suggests that it could be dominated by the J/ψ coherent photoproduction mechanism. Such an observation might open new theoretical and experimental challenges and opportunities. In particular, coherent photoproduction accompanying hadronic collisions may provide insight into the dynamics of photoproduction and nuclear reactions.

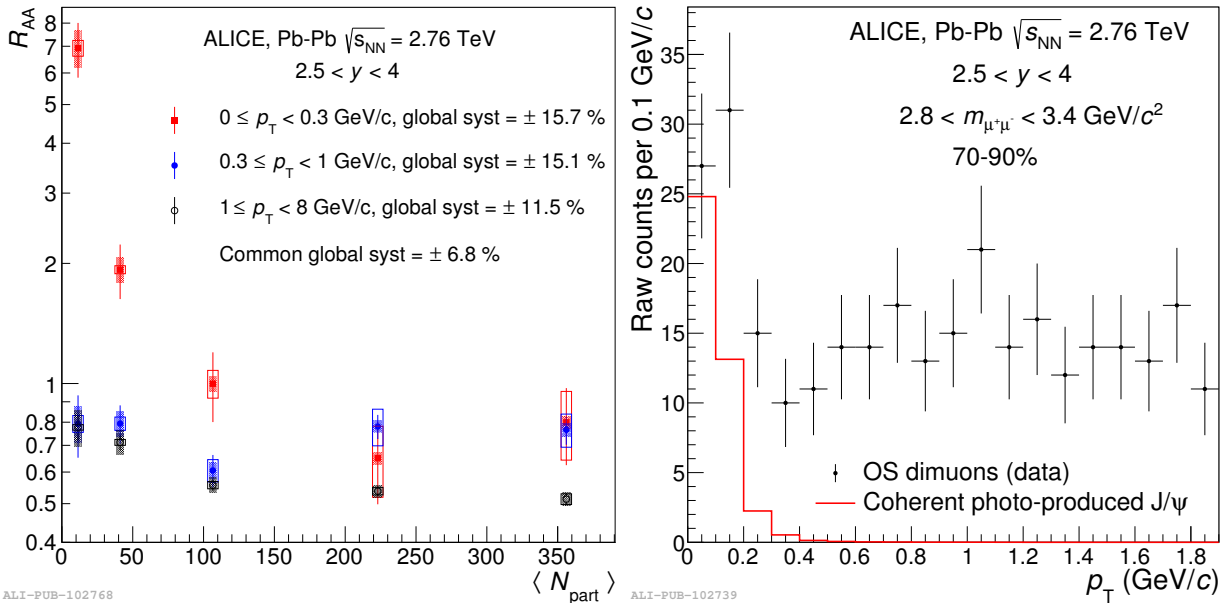

FIGURE 1: (Color online). Low-$p_{\rm T}$ excess of the J/ψ production in Pb–Pb collisions measured by ALICE. Left panel shows the nuclear modification factor $R_{\rm AA}$ as a function of centrality for three $p_{\rm T}$ ranges. Right panel shows the $p_{\rm T}$-distribution of the opposite-sign dimuons for the most peripheral collisions. Red line in the right panel represents the calculations from STARLIGHT Monte Carlo generator [7]. Both figures are taken from [2].

Another recent Pb–Pb measurement has been performed by CMS [8] and is shown in Fig. 2. These preliminary results represent differential measurements of $R_{\rm AA}$ of Υ(1S) and Υ(2S) as a function of $p_{\rm T}$ (left), y (center) and $N_{\rm part}$ (right). A strong Υ(1S) suppression is observed which is in agreement with the published measurement by ALICE at forward rapidity ($2.5 < y < 4$) [9]. The Υ(2S) is more suppressed than Υ(1S) in all the cases, which is in agreement with the expectations of sequential suppression of quarkonium states depending on their binding energy. There is no $p_{\rm T}$- nor y-dependence of such a suppression seen for both Υ(1S) and Υ(2S). However a clear trend for a stronger suppression of Υ(1S) with higher centrality is seen. For the Υ(2S) this trend is not so obvious due to larger statistical uncertainties. It is worth mentioning that, in pp collisions, a significant number of the measured Υ(1S) originates in the decay of heavier prompt bottomonium states, like $\chi_{\rm b}$ [10], Υ(2S) and Υ(3S) [11], and thus an important part (about 30% for $p_{\rm T} \lesssim 20$ GeV/c^2 [12]) of the Υ(1S) suppression in nuclear collisions is related to the smaller feed-down contribution.

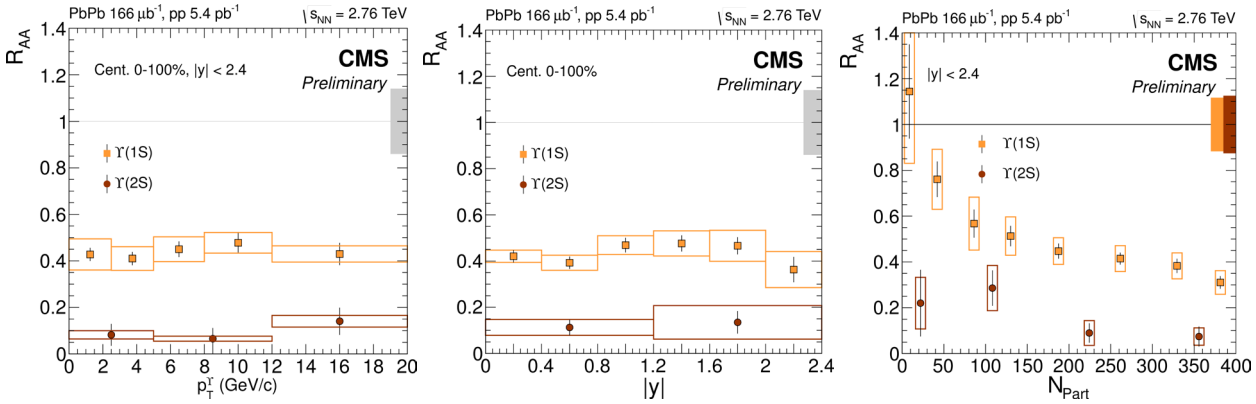

FIGURE 2: (Color online). Nuclear modification factor of ϒ(1S) and ϒ(2S) in Pb–Pb collisions as a function of p_{T} (left), y (center) and N_{part} (right), measured by CMS [8].

QUARKONIUM PRODUCTION IN p–Pb COLLISIONS

As mentioned above, one of the main motivations to study p–Pb collisions is to disentangle hot and CNM effects in Pb–Pb collisions. However the first measurements of the J/ψ production in p–Pb collisions at the LHC performed by ALICE [13] and LHCb [14] showed that quarkonium production in p–Pb collisions is an interesting topic by itself. Many theoretical efforts were done to explain the CNM effects seen in the data, e.g. [15, 16, 17, 18]. The ALICE Collaboration recently published its measurement of the centrality dependence of the J/ψ production in p–Pb collisions [19]. One of the main results presented in this paper is shown in Fig. 3. It is the J/ψ nuclear modification factor as a function of centrality[2] at backward (left), mid- (center) and forward (right) rapidity intervals. A strong dependence of the J/ψ suppression with centrality in p–Pb collisions is seen at backward and forward rapidities while at mid-y interval no strong conclusion could be made due to the large statistical uncertainties. While at forward rapidity the J/ψ seems to be suppressed more towards more central collisions, at backward rapidity there is hint for an enhancement of the J/ψ production in p–Pb collisions compared to the scaled pp collisions (i.e. $Q_{\mathrm{pPb}} > 1$). Theoretical models of the CNM effects based on shadowing with [17] or without [15, 16, 17] the comover contribution or on parton energy loss [18] fairly agree with the data. The latest preliminary results of the R_{pPb} measured by ATLAS at mid-y interval [21] shown in Fig. 4 show an excess of the prompt J/ψ production in p–Pb collisions while ALICE reports its suppression. Probably, this is due to the difference between prompt and inclusive J/ψ, and the effect of the higher p_{T} interval used in the ATLAS measurements.

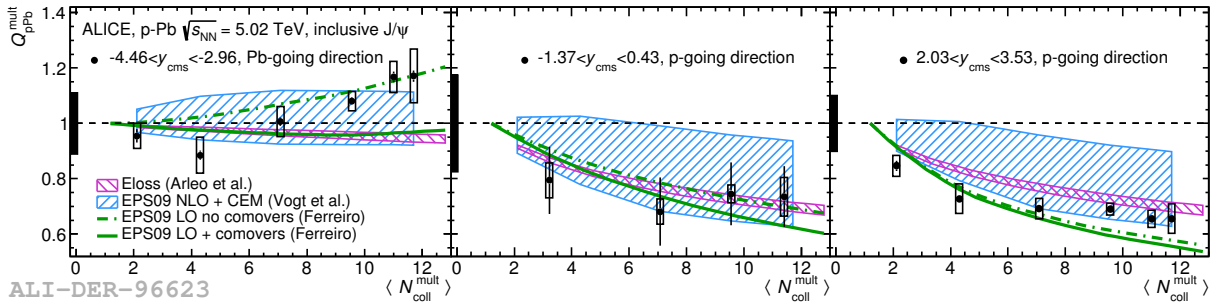

FIGURE 3: (Color online) Nuclear modification factor of J/ψ in p–Pb collisions as a function of centrality at backward (left), mid- (center) and forward (right) y intervals [19]. Bands are theoretical calculations from [15, 16, 17, 18].

[2]ALICE quotes the centrality-dependent nuclear modification factor in p–Pb collisions as Q_{pPb} and not R_{pPb} as it is done by the other LHC experiments. This is to emphasize that the centrality estimation in p–Pb collisions is not a well-defined procedure and all the centrality estimators might have some bias which is difficult to be quantified properly. There is a dedicated ALICE paper describing the ALICE centrality estimation procedure in p–Pb [20].

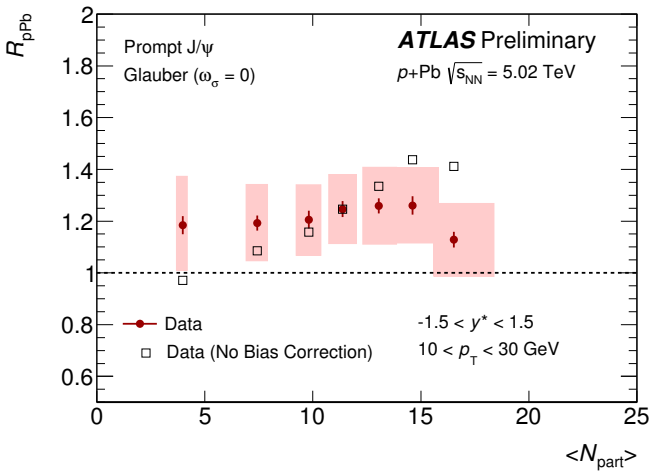

FIGURE 4: (Color online). ATLAS measurement of the nuclear modification factor for the standard Glauber configuration for the production of prompt J/ψ in p–Pb as a function of centrality [21]. Central solid points are corrected for centrality bias. The open points represent the data with no centrality bias correction and are shown as a reference.

Figure 5 shows the nuclear modification factor for inclusive (left) and prompt (right) ψ(2S) as a function of rapidity, measured by ALICE and ATLAS, respectively. Given huge uncertainties in ATLAS measurements, the ALICE and ATLAS measurements are compatible, despite different p_T range and the difference between prompt and inclusive ψ(2S) production. Only theoretical models including final state hadronic interactions [17, 22] are able to explain the ψ(2S) production in p–Pb collisions measured by ALICE. It is worth mentioning that the other models like pure shadowing [15, 16] or parton energy loss [18], which were successful in the description of the J/ψ production, are not able to describe the ψ(2S) production presented in Fig. 5. This indicates an importance of the final-state effects to describe the ψ(2S) suppression in p–Pb collisions.

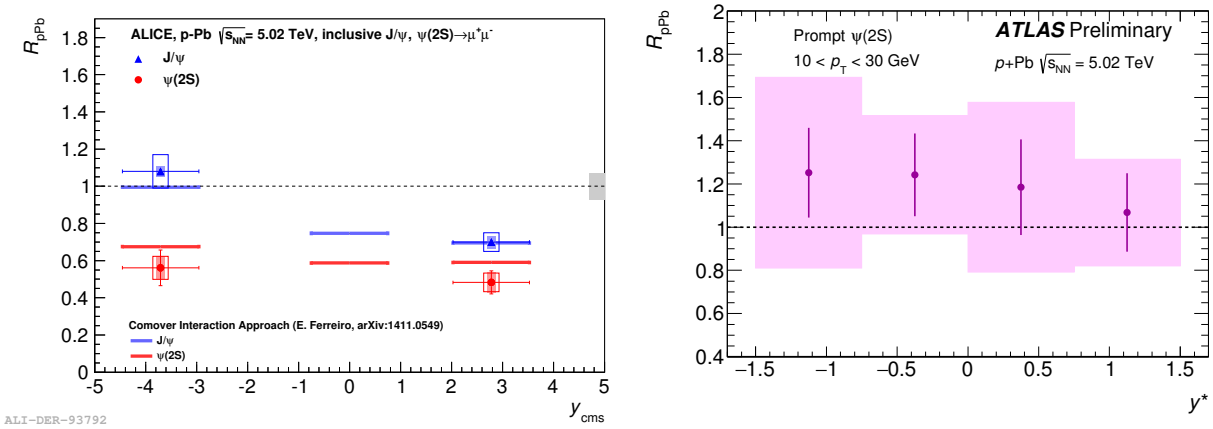

FIGURE 5: (Color online). Nuclear modification factor of inclusive (left) and prompt (right) ψ(2S) as a function of rapidity, measured by ALICE (left) and ATLAS (right). Left panel also contains J/ψ measurements from [13]. ALICE ψ(2S) data points are from [23], ATLAS points are preliminary results from [21]. Model calculations in the left panel are from [17].

In Fig. 6 the LHCb p–Pb results on the nuclear modification factor of inclusive Υ(1S) [24] are compared to its prompt and non-prompt J/ψ measurements [14]. The Υ(1S) state seems to be slightly less suppressed than prompt J/ψ. Shadowing model [16] fairly agrees with the data for both Υ(1S) and prompt J/ψ, however slightly underestimates the prompt J/ψ suppression at forward rapidity. These LHCb measurements agree within uncertainties with the ALICE

measurements of the Upsilon(1S) production in p–Pb collisions at similar rapidity ranges [25].

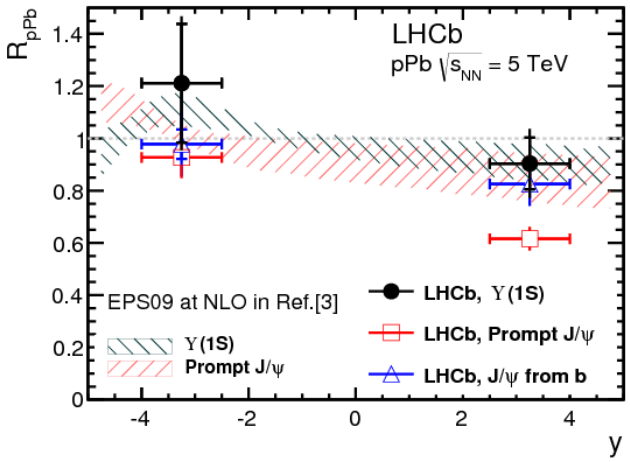

FIGURE 6: (Color online). Nuclear modification factor of inclusive $\Upsilon(1S)$, prompt J/ψ and J/ψ from b in p-Pb collisions as a function of rapidity, measured by LHCb and compared to theoretical calculations from [16]. Figure is taken from [24].

FROM p–Pb TO Pb–Pb

As mentioned above, one of the main motivations to study p–Pb collisions is to estimate the contribution from CNM effects to the quarkonium production in Pb–Pb collisions. ALICE performed this exercise for inclusive J/ψ production [26]. The following assumptions have been made assuming also that the shadowing is the dominant CNM effect:

- Similar Bjorken-x ranges in Pb-nucleus for both Pb–Pb collisions at 2.76 TeV and p–Pb collisions at 5.02 TeV.
- Factorization of shadowing effects in p–Pb and Pb–Pb collisions.

In that case the nuclear modification factor in Pb–Pb collisions estimated from shadowing, $R^{\rm Shad}_{\rm PbPb}$, can be found as a simple factor of nuclear modification factors in p–Pb collisions at forward and backward rapidities: $R_{\rm pPb}(y \geq 0) \cdot R_{\rm pPb}(y \leq 0)$. The result of this estimation is shown in Fig. 7 at forward (left) and mid- (right) rapidity intervals as magenta points. It is compared to the real measurements of the nuclear modification factor in Pb–Pb collisions (in green) performed by ALICE [27, 28]. As seen from this comparison, a huge J/ψ suppression seen in Pb–Pb at high $p_{\rm T}$ should be considered as a pure QGP-related effect since the estimated shadowing effect at high $p_{\rm T}$ is negligible: $R^{\rm Shad}_{\rm PbPb} \simeq 1$. In the low-$p_{\rm T}$ region the estimated J/ψ suppression is similar to the measured one which suggests that the J/ψ production scales with the number of binary collisions. However it does not necessarily mean that hot nuclear matter effects do not play a role. Indeed, at low $p_{\rm T}$ some other effects enter the game, for instance, regeneration of the J/ψ pairs. In that case the hot nuclear matter effects are compensated, yielding in a zero effect on the J/ψ suppression.

CONCLUSIONS

In this review we summarized the recent measurements of quarkonium production in p–Pb and Pb–Pb collisions performed by the four LHC experiments: ALICE, ATLAS, CMS and LHCb. All of them produced lots of exciting results using the data from the Run I data-taking period at the LHC. Now the heavy-ion community is preparing for the next bunch of the quarkonium production results from Run II. The following measurements are of particular interest:

- the relative suppression of different quarkonium states;
- low-pt J/ψ measurements;
- quarkonium production in pp collisions at 5.02 TeV expected to be used as a reference for both p–Pb collisions and Pb–Pb collisions at the same energy;
- and many others.

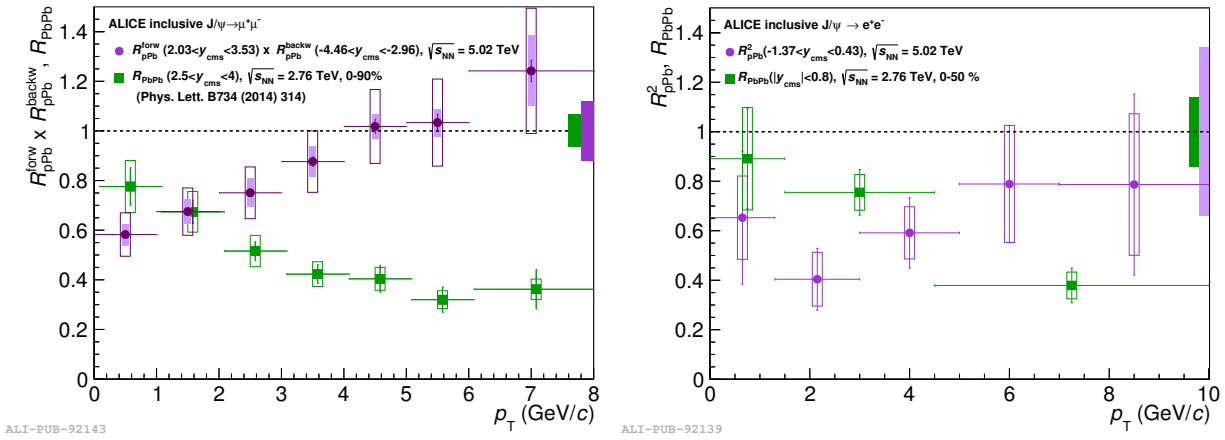

FIGURE 7: (Color online). Nuclear modification factor of J/ψ in Pb–Pb collisions at forward (left) and mid- (right) rapidity intervals. Green points are the measurements performed by ALICE [27, 28] while magenta points are the estimated results from shadowing (see text for details).

REFERENCES

[1] T. Matsui and H. Satz, Phys.Lett. **B178**, p. 416 (1986).
[2] J. Adam *et al.* (ALICE Collaboration), (2015), arXiv:1509.08802 [nucl-ex] .
[3] J. Adam *et al.* (ALICE Collaboration), (2015), arXiv:1506.08804 [nucl-ex] .
[4] X. Zhao and R. Rapp, Nucl. Phys. **A859**, 114–125 (2011), arXiv:1102.2194 [hep-ph] .
[5] K. Zhou, N. Xu, Z. Xu, and P. Zhuang, Phys. Rev. **C89**, p. 054911 (2014), arXiv:1401.5845 [nucl-th] .
[6] E. G. Ferreiro, Phys. Lett. **B731**, 57–63 (2014), arXiv:1210.3209 [hep-ph] .
[7] STARLIGHT website, http://starlight.hepforge.org/ (2013).
[8] CMS Collaboration, Nuclear modification of ϒ states in Pb–Pb, 2015, CMS-PAS-HIN-15-001.
[9] B. Abelev *et al.* (ALICE Collaboration), Phys. Lett. **B738**, 361–372 (2014), arXiv:1405.4493 [nucl-ex] .
[10] R. Aaij *et al.* (LHCb Collaboration), JHEP **11**, p. 031 (2012), arXiv:1209.0282 [hep-ex] .
[11] R. Aaij *et al.* (LHCb Collaboration), Eur. Phys. J. **C74**, p. 2835 (2014), arXiv:1402.2539 [hep-ex] .
[12] A. Andronic, F. Arleo, R. Arnaldi, A. Beraudo, E. Bruna, *et al.*, (2015), arXiv:1506.03981 [nucl-ex] .
[13] B. Abelev *et al.* (ALICE Collaboration), JHEP **1402**, p. 073 (2014), arXiv:1308.6726 [nucl-ex] .
[14] R. Aaij *et al.* (LHCb Collaboration), JHEP **1402**, p. 072 (2014), arXiv:1308.6729 [nucl-ex] .
[15] R. Vogt, Phys.Rev. **C81**, p. 044903 (2010), arXiv:1003.3497 [hep-ph] .
[16] J. Albacete *et al.*, Int.J.Mod.Phys. **E22**, p. 1330007 (2013), arXiv:1301.3395 [hep-ph] .
[17] E. G. Ferreiro, Phys. Lett. **B749**, 98–103 (2015), arXiv:1411.0549 [hep-ph] .
[18] F. Arleo *et al.*, JHEP **1305**, p. 155 (2013), arXiv:1304.0901 [hep-ph] .
[19] J. Adam *et al.* (ALICE Collaboration), JHEP **11**, p. 127 (2015), arXiv:1506.08808 [nucl-ex] .
[20] J. Adam *et al.* (ALICE Collaboration), Phys. Rev. **C91**, p. 064905 (2015), arXiv:1412.6828 [nucl-ex] .
[21] ATLAS Collaboration, Study of J/ψ and ψ(2S) production in $\sqrt{s_{\rm NN}}$ = 5.02 TeV p–Pb and $\sqrt{s}$ = 2.76 TeV pp collisions with the ATLAS detector, 2015, ATLAS-CONF-2015-023.
[22] X. Du and R. Rapp, Nucl. Phys. **A943**, 147–158 (2015), arXiv:1504.00670 [hep-ph] .
[23] B. Abelev *et al.* (ALICE Collaboration), JHEP **1412**, p. 073 (2014), arXiv:1405.3796 [nucl-ex] .
[24] R. Aaij *et al.* (LHCb Collaboration), JHEP **07**, p. 094 (2014), arXiv:1405.5152 [nucl-ex] .
[25] B. Abelev *et al.* (ALICE Collaboration), Phys. Lett. **B740**, 105–117 (2015), arXiv:1410.2234 [nucl-ex] .
[26] J. Adam *et al.* (ALICE Collaboration), JHEP **1506**, p. 055 (2015), arXiv:1503.07179 [nucl-ex] .
[27] B. Abelev *et al.* (ALICE Collaboration), Phys.Lett. **B734**, 314–327 (2014), arXiv:1311.0214 [nucl-ex] .
[28] J. Adam *et al.* (ALICE Collaboration), JHEP **07**, p. 051 (2015), arXiv:1504.07151 [nucl-ex] .

Proceedings of the LHCP2015 Conference, St. Petersburg, Russia, August 31 - September 5, 2015

Editors: V.T. Kim and D.E. Sosnov

Polarization signatures of local parity breaking in central heavy ion collisions

A.A. ANDRIANOV[1], V.A. ANDRIANOV[1], D. ESPRIU[2] and X. PLANELLS[2]

[1]*Physics Faculty, Saint-Petersburg State University, 198504 St. Petersburg, Russia*
[2]*ICCUB, University of Barcelona, Martí i Franquès, 1, 08928 Barcelona, Spain*

Abstract. In this talk we describe a possibility of local spatial parity breaking (LPB) emerging in a dense hot baryon medium (in a fireball) in heavy-ion collisions at high energies. The phenomenology of origin local spatial parity breaking in the fireball is based on introducing a topological (axial) charge and a topological (chiral) chemical potential. A signal (phase) with spatial parity breaking in heavy-ion collisions can be sought in experiments with an excess yield of dilepton pairs with different circular polarizations outside the resonance region of the ρ and ω- meson invariant masses. In these experiments, the asymmetry of longitudinal and transverse polarized states for different values of the invariant mass can serve as a characteristic indicating the possible existence of local spatial parity breaking.

Phenomenology of local spatial parity breaking (LPB) in strong interactions and chiral chemical potential

It is currently known that the spatial parity in QCD is a well established global symmetry of strong interactions [1]. But it was found some time ago that under different extreme conditions (high temperatures and baryon densities, strong electromagnetic fields) spatial domains in the QCD vacuum can arise with metastable non-zero topological density which leads to a spatial parity (P-parity) violation [2]. The formation of a parity-breaking phase can occur in a finite reaction volume (fireball) in heavy-ion collisions. This phase is manifested in the so-called chiral magnetic effect when strong electric and magnetic fields arise and result in chiral charge separation in the reactions for peripheral ion collisions [3]. On the contrary, an isosinglet pseudoscalar condensate can be formed as a result of creating large, "long-lived" topological fluctuations ($t \sim 5 - 10 fm/c$, where c is the speed of light) of gluon field configurations in the fireball in central collisions (see [4] for details). There are some experimental indications of an abnormal dilepton excess in the range of low invariant masses and rapidities and moderate values of the transverse momenta [5]–[9] (see the reviews in [10]), which can be thought of as a result of local spatial parity breaking in the medium (the details can be found in [11]). To describe various effects of hadron matter in a fireball with parity breaking, we must introduce the different chemical potentials and primarily the axial or chiral chemical potential [4].

The change of QCD vacuum properties in matter, and different vacuum transitions mediated by sphalerons can arise under the influence of external conditions [12]. In particular, in heavy-ion collisions at high energies, with raising temperatures and baryon densities, metastable domains can appear in the so-called fireball with a nontrivial topological charge T_5, which is related to the gluon gauge field G_i:

$$T_5(t) = \frac{1}{8\pi^2}\int_{\text{vol.}} d^3x\, \varepsilon_{jkl}\, \text{Tr}\Big(G^j\partial^k G^l - i\frac{2}{3}G^jG^kG^l\Big), \quad j,k,l = 1,2,3, \tag{1}$$

where the integration is over a finite part of the fireball volume. This is not a gauge-invariant object under global gauge transformations. Nevertheless, its jump ΔT_5 can be associated with the space-time integral of the gauge-invariant

Chern-Pontryagin density:

$$\Delta T_5 = T_5(t_f) - T_5(0) = \frac{1}{16\pi^2}\int_0^{t_f} dt \int_{\text{vol.}} d^3x\ \text{Tr}(G^{\mu\nu}\widetilde{G}_{\mu\nu}) == \frac{1}{4\pi^2}\int_0^{t_f} dt \int_{\text{vol.}} d^3x\, \partial^\mu K_\mu,$$
$$K_\mu = \frac{1}{2}\epsilon_{\mu\nu\rho\sigma}\,\text{Tr}\Big(G^\nu\partial^\rho G^\sigma - i\frac{2}{3}G^\nu G^\rho G^\sigma\Big). \tag{2}$$

We suppose a comparably long lifetime of domains and accordingly neglect a topological current flux through the fireball boundary during the corresponding thermodynamic phase.

It is known that the divergence of isosinglet axial quark current $J_{5,\mu} = \overline{q}\gamma_\mu\gamma_5 q$ is locally constrained via the relation of partial axial current conservation affected by the gluon anomaly:

$$\partial^\mu J_{5,\mu} - 2i\widehat{m}_q J_5 = \frac{N_f}{2\pi^2}\partial^\mu K_\mu; \quad J_5 = \overline{q}\gamma_5 q \tag{3}$$

This relation allows to find the connection of a nonzero topological charge with a non-trivial quark axial charge Q_5^q. Namely, integrating (4) over a finite volume of fireball we come to the equality

$$\frac{d}{dt}(Q_5^q - 2N_f T_5) \simeq 2i\int_{\text{vol.}} d^3x\,\widehat{m}_q\overline{q}\gamma_5 q,$$
$$Q_5^q = \int_{\text{vol.}} d^3x\, q^\dagger\gamma_5 q = \langle N_L - N_R\rangle, \tag{4}$$

where $\langle N_L - N_R\rangle$ stands for the vacuum averaged difference between left and right chiral densities of baryon number. Therefrom it follows that in the chiral limit (when the masses of light quarks are taken zero) and for a finite fireball volume the axial quark current is conserved in the presence of non-zero topological charge. If for the lifetime of fireball and the size of hadron fireball of order $L = 5 - 10$ fm , the created topological charge is non-zero, $\langle\Delta T_5\rangle \neq 0$, then it may be associated with a topological chemical potential μ_θ or an axial chemical potential μ_5 [4] for neglected light u, d quarks. Thus we have

$$\langle\Delta T_5\rangle \simeq \frac{1}{2N_f}\langle Q_5^q\rangle \iff \mu_5 \simeq \frac{1}{2N_f}\mu_\theta, \tag{5}$$

Thus adding to the QCD lagrangian the term $\Delta\mathcal{L}_{\text{top}} = \mu_\theta\Delta T_5$ or $\Delta\mathcal{L}_q = \mu_5 Q_5^q$, we get the possibility of accounting for non-trivial topological fluctuations (fluctons) in the nuclear (quark) fireball. In the Lorentz invariant form the field dual to fluctons is described by means of the classical pseudoscalar field $a(t)$, depending on time so that

$$\Delta\mathcal{L}_a = \frac{N_f}{2\pi^2}K_\mu\partial^\mu a(x) = \frac{1}{4\pi^2}\mu_\theta K_0 \iff \mu_5\overline{q}\gamma_0\gamma_5 q, \quad \mu_5 \simeq \dot{a}(t) \simeq \text{const.} \tag{6}$$

Thus in a quasi-equilibrium situation the appearance of a nearly conserved chiral charge can be incorporated with the help of a chiral chemical potential μ_5.

Effective meson theory in a medium with local spatial parity breaking

The model of vector dominance [13],[14] can serve as a basis for describing local parity breaking in the hadron fireball with electromagnetic interactions taken into account. Moreover, we assume that a time-dependent but approximately spatially homogeneous pseudoscalar field $a(t)$ induced at densities accessible in heavy-ion collisions arises in the fireball, and we define it as a four-vector$\zeta_\mu \simeq \partial_\mu a \simeq (\zeta, 0, 0, 0)$. The quark-meson interaction is described by

$$\mathcal{L}_{\text{int}} = \bar{q}\gamma_\mu V^\mu q; \quad V_\mu \equiv -eA_\mu Q + \frac{1}{2}g_\omega\omega_\mu\mathbf{I}_q + \frac{1}{2}g_\rho\rho_\mu^0\lambda_3 + \frac{1}{\sqrt{2}}g_\phi\phi_\mu\mathbf{I}_s, \tag{7}$$

while $Q = \frac{\lambda_3}{2} + \frac{1}{6}\mathbf{I}_q - \frac{1}{3}\mathbf{I}_s$, $g_\omega \simeq g_\rho \equiv g \simeq 6 < g_\phi \simeq 7.8$ and the values of the constants are extracted from the decays of the vector mesons. Here, $\mathbf{I}_q$ and $\mathbf{I}_s$ are the unit matrices in the non-strange and strange quark sectors, and λ_3 is a corresponding Gell-Mann matrix. The parity-odd contribution is given by the Chern-Simons term,

$$\mathcal{L}_{\text{CS}}(k) = -\frac{1}{4}\varepsilon^{\mu\nu\rho\sigma}\,\text{Tr}\Big[\hat{\zeta}_\mu V_\nu(x)\, V_{\rho\sigma}(x)\Big] = \frac{1}{2}\text{Tr}\Big[\hat{\zeta}\,\epsilon_{jkl}\,V_j\,\partial_k V_l\Big], \tag{8}$$

which describes the mixing of photons and vector mesons under the local spatial parity breaking. With our definitions we can obtain the relation $\zeta = N_c\, g^2\mu_5/8\pi^2$ where N_c is a number of colors, and numerically $\zeta \simeq 1.5\mu_5$. The analysis of the massive Chern-Simons electrodynamics [4] has shown that in the case of an isosinglet pseudoscalar background field, the spectrum of massless photons is not distorted when they are mixed with massive vector mesons, while the spectrum of massive vector mesons splits into three polarizations with the masses $m^2_{V,+} < m^2_{V,L} < m^2_{V,-}$. This splitting might be an indication of a possible parity breaking and also of a Lorentz-invariance breaking because the background field depends on time. Moreover, the position of resonance poles for transverse polarizations of ρ^0, ω - mesons is shifted with the wave vector $|\vec{k}|$ and also a resonance broadening occurs that leads to an increased contribution of the dilepton production compared with the situation with resonances in vacuum (for details, see [15]). A question hence arises. Could the splitting be measured in experiments with heavy-ion collisions?

Manifestation of local spacial parity breaking in heavy ion collisions

An effect of anomalous dilepton pair production in the range of low invariant masses and rapidities and moderate transverse momenta was established in a series of experiments with heavy-ion collisions in recent years [5]-[8]. Characteristically, this effect was observed only for central or nearly central collisions and is an effect of the nuclear medium [9].

Such an anomalous yield of dilepton pairs has not yet been satisfactorily explained from the standpoint of hadron phenomenology. A detailed consideration of the decay processes and their contributions to the dilepton yield can be found in [11], [15].

We present graphic results of calculating the anomalous yield of dilepton pairs in the vicinity of the polarized vector ρ- and ω -meson resonances. In Fig. 1, we show the excess of dilepton pairs for the ρ-meson spectral function (there is a similar effect for the ω meson too) and its corresponding contributions with different polarizations for the values of the parameter inducing the spatial parity breaking, $\zeta = 400$ MeV compared to $\zeta = 0$ MeV. Because of the mass dependence of polarizations on wave vector, the original Breit-Wigner resonance actually splits in three different peaks. This is shown in in Fig.1.

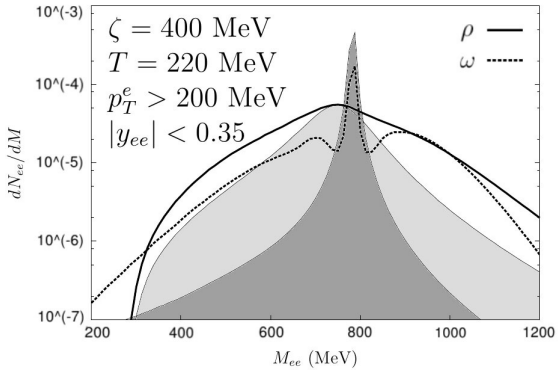

FIGURE 1. In-medium ρ and ω channels (solid and dashed line) and their vacuum contributions (light and dark shaded regions) for $\mu_5 = 290$ MeV.

It is well known that the angular distribution of leptons carries the information on the polarization. However, the current angular distribution studies based on full angular average do not seem to detect possible parity-odd effects.

Instead we define an angle as described in Fig. 2.

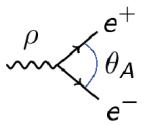

FIGURE 2. θ_A is the angle between the two outgoing leptons in the laboratory frame.

In order to isolate the transverse polarizations, we perform different cuts choosing the angle θ_A for the analysis and study the variations of the ρ (and ω) spectral functions. θ_A is the angle between the two outgoing leptons in the

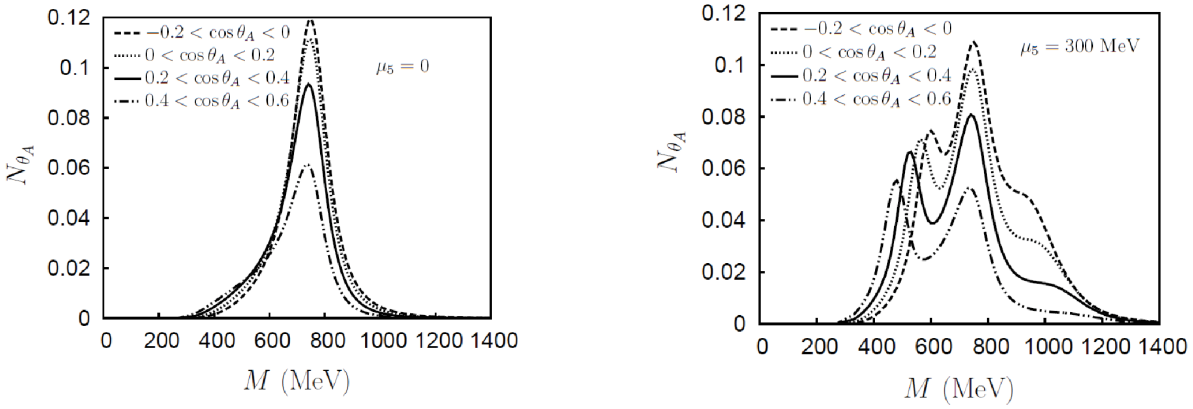

FIGURE 3. Angle θ_A between the two outgoing leptons in the laboratory frame. ρ spectral function depending on the dielectron invariant mass M in vacuum ($\mu_5 = 0$) and in a parity-breaking medium with $\mu_5 = 300$ MeV for different ranges of θ_A.

laboratory frame. A quite visible secondary peak appears in a P-odd medium! To isolate the transverse polarizations in the spectrum, we selected different angle sectors and studied the changes in the ρ-meson spectral function (analogously for ω -mesons). The results are shown in Fig.3. The appearance of the second peak in the parity-odd medium is quite obvious. Various experimental possibilities for its identification were discussed in [15] and also in the PhD theses [16].

It turns out that as this parameter increases the contributions of circular polarizations of the resonance become even more noticeable as compared with the vacuum situation. On this basis, we can assume that the magnitude of pseudoscalar condensate gradient in the fireball can serve as a measure of the anomalous yield of polarized dilepton pairs. The corresponding contributions for ρ- and ω -mesons in the medium and in the vacuum are shown in Fig.1, whence it follows that the excess of lepton pairs can occur aside the ρ -meson resonance peaks (analogously for ω-mesons) because of the momentum dependent mass shift in the circular polarizations of resonances in the phase of local spatial parity breaking.

Thus a signal (a phase) with spatial parity breaking in heavy-ion collisions (in a fireball) can be sought in experiments "event by event" using an excess yield of dilepton pairs and predominantly with different circular polarizations outside the resonance region of the ρ- and ω-meson invariant masses. The asymmetry of longitudinal and transverse polarized states for different values of the invariant mass can serve as a characteristic indication of the existence of local spatial parity breaking in these experiments. Of course, it should be kept in mind that there are also other possible contributions from processes occurring in the region under study and also in the thermal evolution of the medium in fireball, but we have here restricted ourself only to the dominant contributions from ρ- and ω -mesons and thus tried to quantitatively describe the mechanism for an anomalous excess yield of lepton pairs in the experiments CERES, PHENIX, STAR, NA60, and ALICE.

Conclusions and outlook

In this talk we described a possibility of local spatial parity breaking emerging in a dense hot baryon medium (fireball) in heavy-ion collisions at high energies. We stress that LPB is not forbidden by any physical principle in QCD at finite temperature/density. The phenomenology of local spatial parity breaking in a fireball is based on introducing a topological (axial) charge and a topological (chiral) chemical potential. Topological charge fluctuations transmit their influence to hadronic physics via an axial chemical potential. We suggested a generalized Lagrangian of the vector meson dominance model in the presence of the Chern-Simons interaction with a spatially homogeneous pseudoscalar field $a(t)$ for describing the electromagnetic interactions of hadrons in a fireball. An analysis showed that in the case of an isosinglet pseudoscalar background field $a(t)$, the spectrum of massless photons is not distorted when they are mixed with massive vector mesons. At the same time, the spectrum of massive vector mesons splits into three components with different polarizations and with different effective masses $m^2_{V,+} < m^2_{V,L} < m^2_{V,-}$. The positions of the

resonance poles for transverse polarizations of the corresponding ρ, ω -mesons are shifted depending on the wave vector $|\vec{k}|$, and a resonance broadening occurs that leads to an increase of the spectral contribution to the dilepton production as compared with the situation where the resonances are in the vacuum state. A signal (phase) with spatial parity breaking in heavy-ion collisions (in a fireball) can be sought in experiments with an excess yield of dilepton pairs with different circular polarizations outside the resonance region of the ρ and ω -meson invariant masses. In these experiments, the asymmetry of longitudinal and transverse polarized states for different values of the invariant mass can serve as a characteristic indication of possible existence of local spatial parity breaking. The proposed mechanism for generating local spatial parity breaking helps to explain qualitatively and quantitatively the anomalous yield of dilepton pairs in the CERES, PHENIX, STAR, NA60, and ALICE experiments, and the identification of its physical origin might serve as a base for a deeper understanding of QCD properties in a medium under extreme conditions. Experimental collaborations should definitely check this possibility.

Acknowledgements

It is a pleasure to thank the organizers of the Third Annual Large Hadron Collider Physics Conference for a fruitful meeting and an excellent atmosphere. This work has been supported through grants FPA2013-46570, 2014-SGR-104 and Consolider CPAN. Funding was also partially provided by the Spanish MINECO under project MDM-2014-0369 of ICCUB (Unidad de Excelencia 'Maria de Maeztu'). A.A. and V.A. were supported by Grant RFBR projects 13-02-00127 and 16-02-00348.

REFERENCES

[1] D. Weingarten, Phys. Rev. Lett. **51**, 1830 (1983); C. Vafa and E. Witten, Phys. Rev. Lett. **53** (1984) 535; S. Nussinov, Phys. Rev. Lett. **52**, 966 (1984); D. Espriu, M. Gross and J.F. Wheater, Phys. Lett. B **146**, 67 (1984);

[2] D. Kharzeev, R.D. Pisarski, Phys. Rev. D. **61** 111901(R)(2000); D. Kharzeev, Phys. Lett. B,**633** 260 (2006); D. Kharzeev, Ann. Phys. (NY), **325** 205(2010); D. Kharzeev, A. Zhitnitsky, Nucl. Phys. A, **797** 67(2007).

[3] D. Kharzeev, R. D. Pisarski and M. H. G. Tytgat, Phys. Rev. Lett. **81**, 512 (1998). D. E. Kharzeev, L. D. McLerran and H. J. Warringa, Nucl. Phys. A**803**, 227 (2008). K. Buckley, T. Fugleberg, A. Zhitnitsky, Phys. Rev. Lett., **84**,4814 (2000).

[4] A. A. Andrianov, V. A. Andrianov, D. Espriu and X. Planells, Phys. Lett. B **710** 230 (2012).A. A. Andrianov, V. A. Andrianov, D. Espriu, and X. Planells Proc.Sci., QFTHEP, 025 (2013).

[5] P. Wurn et al. (CERES Collab.), Nucl. Phys. A, **5901-2**, 103-116 (1995); CERES Collaboration (Agakichiev, G. et al.) Phys. Rev. Lett. **75** , 1272 (1995); Phys. Lett. B **422**, 405(1998); Eur. Phys. J. C **41**, 475(2005).

[6] R. Arnaldi et al. (NA60 Collab.), Phys. Rev. Lett., **96** , 162302 (2006).

[7] A. Adare et al. (PHENIX Collab.), Phys. Rev. C, **81**, 034911 (2010).

[8] G. Agakichiev et al. (HADES Collab.), Phys. Rev. Lett., **98**, 052302 (2007). Phys. Lett. B, **663**, 43-48 (2008).

[9] K. O. Lapidus, V. M. Emel'yanov, Phys. Part. Nucl., **40**, 29 (2009).

[10] I. Tserruya, Electromagnetic Probes, arXiv: 0903.0415; G. E. Brown, M. Rho, Phys. Rev. Lett., **66**,2720-2723 (1991).

[11] A. A. Andrianov, V. A. Andrianov, D. Espriu, X. Planells, Theor.Math.Phys., **170**, 17 (2012); A. A. Andrianov, V. A. Andrianov,Theor.Math.Phys., **185**, 1370 (2015).

[12] F.R. Klinkhamer, N.S. Manton, Phys. Rev. D,**30**, 2212-2220 (1984); V.A. Kuzmin, V.A. Rubakov, M.E. Shaposhnikov, Phys. Lett. B, **155**, 36-43 (1985); L.D. Maclerran, E. Mottola, M.E. Shaposhnikov, Phys. Rev. D, **43**, 2027 (1991); G.D. Moore, K. Rummukainen, Phys. Rev. D, **61**,105008 (2000); E. Shuryak, I. Zahed, Phys. Rev. D, **67**, 014006 (2003).

[13] R. Rapp, J. Wambach, Chiral Symmetry Restoration and Dileptons in Relativistic Heavy-Ion Collisions, Advances in Nuclear Physics, 25, Kluwer, New York, 2000; W. Liu, R. Rapp, Nucl. Phys. A, **796** , 101 (2007); arXiv: nucl-th/0604031; H. van Hees, R. Rapp, Nucl. Phys. A, **806**, 339 (2008).

[14] J. J. Sakurai, Ann. Phys., **11**, 1-48 (1960); Currents and Mesons, Univ. Chicago Press, Chicago, 1969.

[15] A. A. Andrianov, V. A. Andrianov, D. Espriu, and X. Planells, Phys. Rev. D, **90**,034024 (2014).

[16] X. Planells, Searching for P- and CP- odd effects in heavy ion collisions (PhD theses,2014), E-arXiv:1411.3283v1.

Performance: parallel talks

Proceedings of the LHCP2015 Conference, St. Petersburg, Russia, August 31 - September 5, 2015

Editors: V.T. Kim and D.E. Sosnov

The ALICE PID performance in Run 1 and perspectives in view of Run 2

FRANCESCO NOFERINI[1,2]

[1]*INFN, sez. Bologna and CNAF, Italy*
[2]*Museo Storico della Fisica e Centro Studi e Ricerche "Enrico Fermi", Rome, Italy*

fnoferin@cern.ch

On behalf of the ALICE Collaboration

Abstract. The extended capability in particle identification (PID) is one of the most characterizing features of the ALICE experiment. Several PID techniques are exploited in ALICE to cover a wide range of momenta based on specific energy loss (ITS, TPC), transition radiation (TRD), time of flight (TOF), Cherenkov radiation (HMPID), calorimetry (PHOS, EMCAL) measurements and topological PID. In Run 1 we explored extensively the combination of these techniques to improve particle separation in a statistical Bayesian approach or in a more traditional $N\sigma$ cut approach. The results of such developments will be presented together with the perspectives for Run 2. The completion of the installation of the central barrel detectors will allow us to further improve the performances.

INTRODUCTION

The main goal of the ALICE experiment [1] is the study of a state of matter ruled by partonic degree of freedom (deconfinement) produced in heavy ion collisions. Many observables needed to perform such a study require a very high capability in particle identification (PID) and therefore the ALICE detector was provided by many subsystems devoted to identify different particles in different momentum ranges. Many analyses during Run 1 benefitted of the PID performance achieved so far, both for the low p_T (soft physics, see also [2] and [3]) and high p_T (hard physics, see also [4]) observables. During the long shoutdown in preparaton of the Run 2 many subsytems were also upgradeted to improve the PID capability. The main upgrades concern the completion of the TRD installation [5], the addition of one PHOS module and the installation of the DCAL detector. The tools developed and tuned during Run 1 respresent a very solid baseline for the Run 2 era which is approaching. Moreover, the current understanding of each single PID detector will allow to use in Run 2 more refined techniques based on the combination of the information of many subsystems and then to reach higher performance than in the past.

PID detectors in the ALICE experiment

As mentioned one of the most advanced features of the ALICE detector is related to its high capability in particle identification. Many subsystems were deployed to do such a job in order to cover many particle species in a wide momentum range [6]. Starting from the inner radius of the detector the sub-detectors specialized to identify charged particles in the ALICE central barrel ($|\eta| < 0.8$) are:

- The Inner Tracking System (ITS) which is able to identify hadrons at low momenta ($p_{\mathrm{T}} < 0.6$ GeV/c) by measuring the specific energy loss ($\mathrm{d}E/\mathrm{d}x$).
- The Time Projection Chamber (TPC) which also provides the $\mathrm{d}E/\mathrm{d}x$ information and allows hadrons PID for momenta below 1 GeV/c and at very high momenta in the relativistic rise region of the Bethe-Bloch function. Moreover it provides a good electron/hadrons separation for p_{T} above 1 GeV/c.
- The Transition Radiation Detector (TRD) dedicated to the electron identification up to very high momenta.

- The Time Of Flight detector (TOF) which provides a measurement of the velocity of the particles up to several GeV/c with a time resolution better than 100 ps.
- The High Momentum PID detector (HMPID) based on the measurement of Cherenkov radiation.

In Run 1 all these subsytems covered the full azimuthal acceptance except the HMPID case, which covers a smaller $\eta - \phi$ region, and the TRD which was only partially installed (13 modules out of 18). The TRD installation was completed during the long shutdown and therefore during Run 2 ALICE will benefit of the full azhimuthal coverage also for it [5].

In Fig. 1 the separtion power expressed as numbers of the detectors' resolutions (σ) is reported for K/π and p/K separation as a function of p_{T}, averaging the momentum-dependent response over the range $|\eta| < 0.5$. In the bottom part of Fig. 1 the ranges for a separation better than 2σ are reported for all the detectors involved. It can be easily appreciated that a large p_{T} range is covered in a complementary way using the information of all systems.

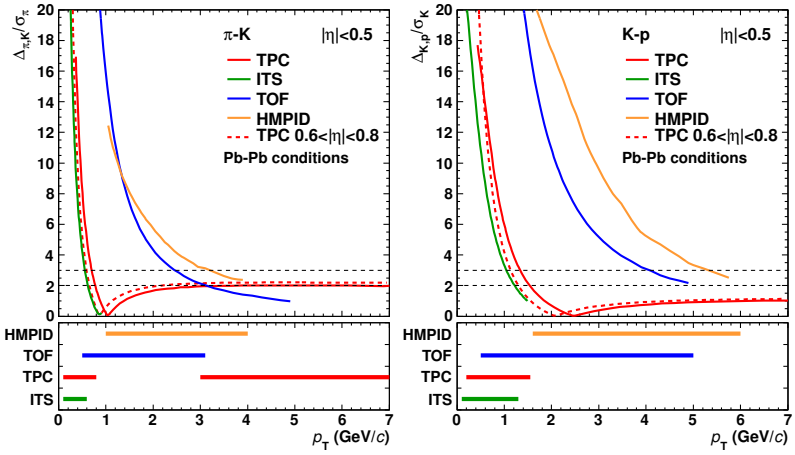

FIGURE 1. The separation power (in number of standard deviations) vs momentum for K/π and p/K. In the bottom pannels the ranges with a separation better 2σ than are reported as well.

The reconstruction of the secondary vertexes using the tracking dectors (ITS and TPC) of the weak decaying particles (K^0_s, Λ and cascades) allows also to perform PID using topological cuts. An example is reported in Fig.2 (left) for the K^0_s and Λ cases. Topological cuts were also used to select kaons looking at their decay in the TPC volume (Kink). The topology of the decay is well know and this allows to select a very pure sample of charged kaons up to very high momenta. In Fig. 2 (right) the very good separation of kaon and pion decay signals are reported in the full p_{T} range exploited.

Moreover neutral particles and electrons (like γ and π^0) are accessibile through the information collected in the electromagnetic calorimeters which are placed in the central barrel in dedicated $\eta - \phi$ regions. In fact ALICE is equipped by three calorimeters (the DCAL was installed recently during the long shutdown):

- PHOS and DCAL which cover a similar azimuthal region,
- and the EMCAL which is placed in front of the PHOS to allow the reconstruction of back-to-back events.

In Run 1 the PHOS detector contained 3 modules of 64×56 cells each ($|\eta| < 0.12$, $260^\circ < \phi < 320^\circ$), and the EMCal contains 10 supermodules of 48×24 cells and 2 supermodules of 48×8 cells ($|\eta| < 0.7$, $80^\circ < \phi < 187^\circ$).

In Fig. 3 the $\pi^0 \rightarrow \gamma\gamma$ peak as reconstructed by the PHOS and the electron/hadron separation reached by the EMCAL are reported.

PID perfromance achieved in Run 1

As mentioned PID techniques were extensively used in Run 1 analyses by ALICE. In this section only the most instructive scenarios can be reported although almost 55% of the ALICE publications involve PID. A very good example of a complementary usage of the information from many detectors is the measurement of particle p_{T} distributions.

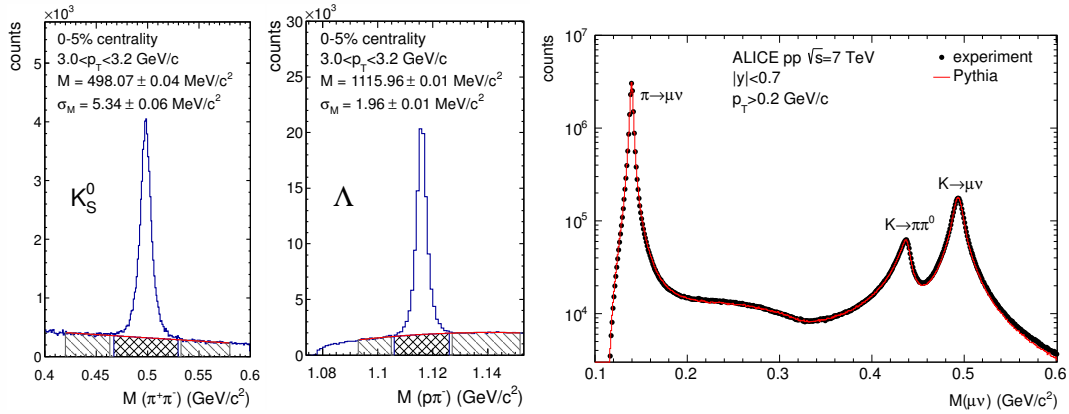

FIGURE 2. left: K^0_s and Λ peaks reconstructed after a selection on the secondary vertex. Right: Decay topology of pions and kaons in the TPC volume ($0.2 < p_{\mathrm{T}} < 6$ GeV/c)).

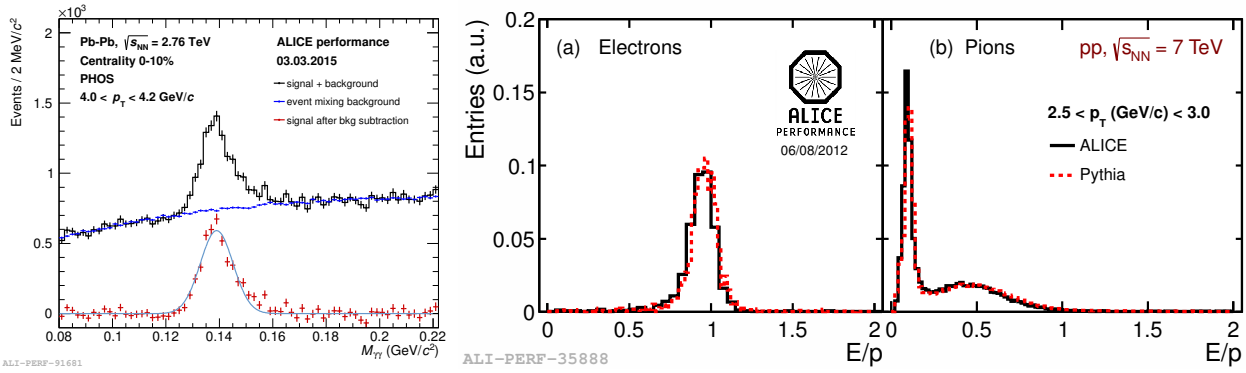

FIGURE 3. $\pi^0 \rightarrow \gamma\gamma$ peak as reconstructed by the PHOS and the electron/hadron separation reached by the EMCAL.

Such a measurement was performed in many collision systems (p-p, p-Pb and Pb-Pb) and at several center-of-mass energies, here we will focus on the work presented in [7] related to p-p collisions at $\sqrt{s} = 7$ TeV. An unfolding statistical approach was used to measure the particle spectra with different detectors in different momentum regions. Then the yields obtained were combined to construct the final p_{T} distributions:

- ITS covered a p_{T} range from 100 MeV/c to 600 MeV/c.
- TPC covered from few hundred MeV/c to about 1 GeV/c.
- TOF covered up to 2.4 GeV/c for pions and kaons and up to 4 GeV/c for protons.
- HMPID covered up to 3 GeV/c for pions and kaons and up to 6 GeV/c for protons.
- Kink technique allowed to select kaons from 200 MeV/c to 6 GeV/c.

In Fig. 4 the extraction of π, K and p yields with the unfolding procedure for the TOF case (left plot) and the final combined results (right plot) are reported.

A different PID approach was used for all the cases requiring a track-by-track identification. The method mostly exploited in ALICE is based on the definition of $N\sigma = (S - S(H_i))/\sigma$ variable which represents the distance of the measured signal (S) from the expected one for a given mass hypotesis H_i ($S(H_i)$) in number of the detector resolution (σ). Such a variable is expected to be distributed almost as a Gaussian centered at zero and with pull equal to one. Then a cut on this variable at a given threshold (2 or 3) guarantees a flat efficiency independently of the kinematics. The typical gain reached with such a technique is shown in Fig. 5 where the invariant mass distribution of $\phi \rightarrow$ KK is reported for the no PID case and with a cut on the TPC signal $N\sigma < 2$. In the PID case the background reduction in Pb-Pb 0-20% centrality class is at the level of a factor 40.

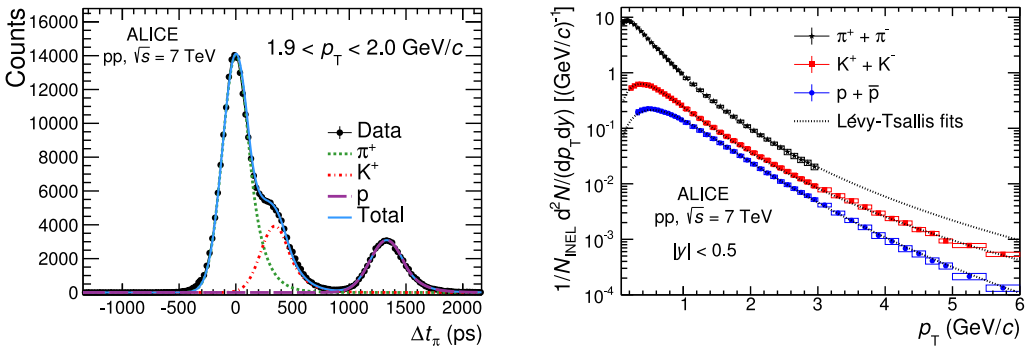

FIGURE 4. Left plot: unfolding procedure for the TOF case. Right plot: Final results obtained combining all the single detector analyses.

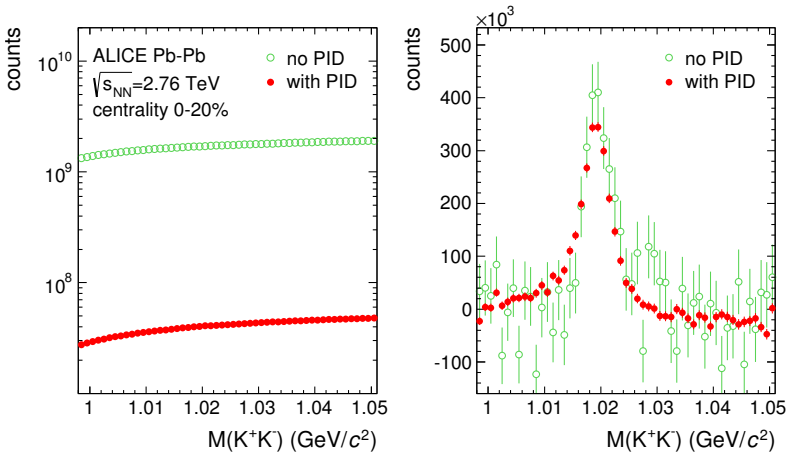

FIGURE 5. $\phi \rightarrow$ KK invariant mass distribution with and without PID cuts.

In the high p_{T} region one single detector may be not sufficient to provide a good PID. However the combination of the information from many detectors may still allow a good PID performance. An approach which was largely used to extend the identification up to 4 GeV/c in a track-by-track approach is based on the definition of a combined $N\sigma$ variable as the sum in quadrature of the single detector $N\sigma$. In Fig. 6 the PID signal distribution is reported in the TPC-TOF plane. The combined $N\sigma$ approach allows to perform one single cut (elliptic cut in the TPC-TOF plane) instead to cut on both the signals separately (rectangular cut in the TPC-TOF plane) reducing the contamination from other species at a fixed value of the efficiency.

Perspectives for Run 2: multi-detector PID

The progresses during Run 1 in the understanding of all the ALICE sub-detectors devoted to PID gave a strong indication of the big advantages behind the use of a multi-detector analyses. The optimization in combining detector information to identify particle is expected as the biggest improvement in Run 2. The use of a Bayesian approach, as also largely discussed in [1], is a quite attractive perspective because it provides a natural way to generalize PID to multi-detector cases. To illustrate it, let consider the single detector case. The probability, $P(H_i|S)$, that a certain detector signal, S, belongs to a particle species H_i can be expressed using Bayes' theorem as $P(H_i|S) = P(S|H_i)C(H_i)/(\sum_{\text{all species } k} P(S|H_k)C(H_k))$, where $P(S|H_i)$ is the probability that a given particle species releases the measured signal (response function) and $C(H_i)$ the corresponding abundance in the sample (priori proba-

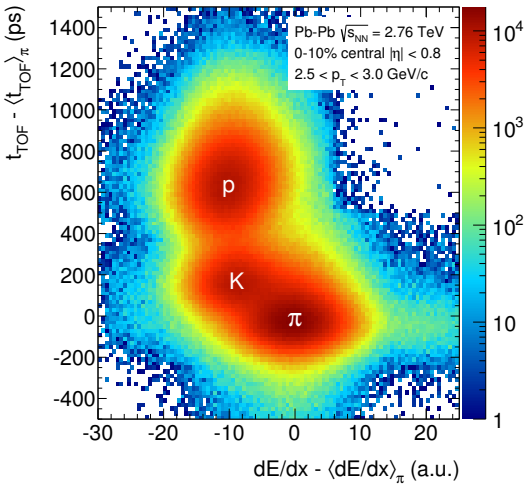

FIGURE 6. Distribution in the TPC and TOF signals plane. A cut on the combined information allows to benefit of the π/K TPC separation and of the p/K TOF separation simultaneously.

bility). The generalization to the multi-detecor case is very simple, just the replacement of S with $\vec{S} = (S_{det1}, S_{det2}, \ldots)$ is required with $P(\vec{S}|H_i) = \prod_{\alpha=ITS,TPC,\ldots} P(S_\alpha|H_i)$, i.e. the product of the single detector response functions. A cut on such a variable at a given threshold corresponds to the request of a given purity and then the efficiency, computed via Monte Carlo (MC) simulations, will depend on the particle p_T. Therefore in order to make use of the advantages provided by this approach the efficiency corrections via MC have to be validated. In order to do that high-purity samples of identified particles were selected via the study of specific decay channels. These samples served as a baseline for validating the Monte Carlo tools that are normally used to estimate the efficiencies and misidentification probabilities. The following decays were used to obtain high-purity samples of three different species: K^0_s to study charged pions, Λ (and respective charge conjugates) to study protons and ϕ to study charged kaons. For a given decay channel, a fit of the combinatorial invariant mass distribution allows the background to be subtracted and the yield of the decays to be extracted. The estimated yield is considered to be a pure sample of a given species (a precise measurement of the total number of particles of a given species in a given data set). This estimation was done without applying any PID selections. Then the exercise was repeated applying PID selections on each of the two prongs, selecting between pions, kaons and protons. Figure 7 shows examples of the fitting procedure for the K^0_s invariant masses in a given momentum bin of the daughter π^+. From left to right, the panels show the analysis without PID and then requiring the identification of a positive pion, kaon, or proton, respectively.

The comparison with the number of positively identified secondary prongs determines the efficiency and the misidentification with respect to the values estimated when not applying PID.

As can be seen from Fig. 8, the efficiencies and misidentification probabilities can be evaluated very precisely. The agreement between data and Monte Carlo is good, both in shape and absolute value using a high threshold maximises the purity.

CONCLUSIONS

Particle identification is one of the most characterizing features of ALICE as proved by the 55% ALICE publications involving PID. Different identification techniques are used to span a very wide range of momenta and several particle species and many PID approaches were successfully used during Run 1. After several years of data tacking and physics analyses the ALICE PID techniques are very well under control opening to more refined approaches in the close future and in particular for Run 2. The extension of the PID to the combination of multi-detector information, like the statistical Bayesian one, may represent a big improvement for future analyses and are now extensively studied.

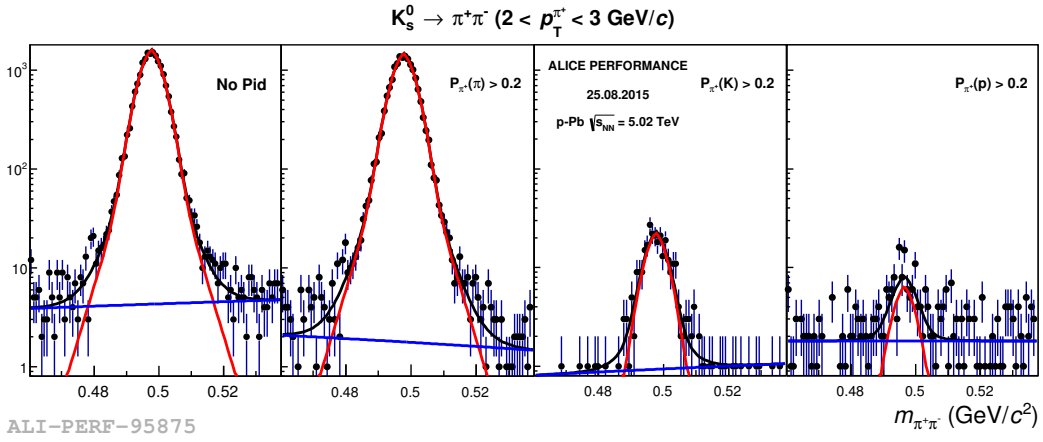

FIGURE 7. K^0_s peak used to select a pure sample of pions and then to test the effect of the PID cut on Bayesian probabilities.

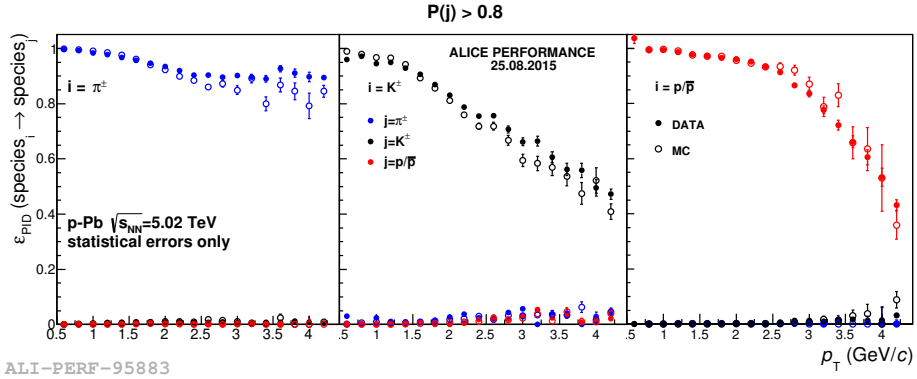

FIGURE 8. Efficiencies and misidentification probabilities: data and MC comparison for p-Pb MB collisions.

REFERENCES

[1] B. Alessandro *et al.*, Journal of Physics G: Nuclear and Particle Physics **32**, p. 1295 (2006).

[2] E. Kryshen, "ALICE: First look at 13 tev and highlights from the most recent analyses", talk presented at the LHCP2015 Conference, St.Petersburg, Aug.31-Sep.5, 2015.

[3] A. Ohlson, "Ridges in p–a (and pp) collisions", this LHCP2015 conference proceedings.

[4] Y. Kharlov, "SM and QCD results from ALICE", talk presented at the LHCP2015 Conference, St.Petersburg, Aug.31-Sep.5, 2015.

[5] J. Klein, "The ALICE Transition Radiation Detector: status and perspectives for Run II", this LHCP2015 conference proceedings.

[6] B. B. Abelev *et al.* (ALICE), Int. J. Mod. Phys. **A29**, p. 1430044 (2014), arXiv:1402.4476 [nucl-ex] .

[7] J. Adam *et al.* (ALICE), Eur. Phys. J. **C75**, p. 226 (2015), arXiv:1504.00024 [nucl-ex] .

Proceedings of the LHCP2015 Conference, St. Petersburg, Russia, August 31 - September 5, 2015

Editors: V.T. Kim and D.E. Sosnov

The ALICE Transition Radiation Detector: status and perspectives for Run II

JOCHEN KLEIN

CERN

jochen.klein@cern.ch

On behalf of the ALICE Collaboration

Abstract. The ALICE Transition Radiation Detector contributes to the tracking, particle identification, and triggering capabilities of the experiment. It is composed of six layers of multi-wire proportional chambers, each of which is preceded by a radiator and a Xe/CO_2-filled drift volume. The signal is sampled in timebins of 100 ns over the drift length which allows for the reconstruction of chamber-wise track segments, both online and offline. The particle identification is based on the specific energy loss of charged particles and additional transition radiation photons, the latter being a signature for electrons.

The detector is segmented into 18 sectors, of which 13 were installed in Run I. The TRD was included in data taking since the LHC start-up and was successfully used for electron identification and triggering. During the Long Shutdown 1, the detector was completed and now covers the full azimuthal acceptance. Furthermore, the readout and trigger components were upgraded. When data taking was started for Run II, their performance fulfilled the expectations.

INTRODUCTION

A Large Ion Collider Experiment (ALICE) is the experiment at the Large Hadron Collider (LHC) at CERN which was particularly optimized for the measurement of Pb–Pb collisions [1]. It consists of a central barrel and a forward muon spectrometer. The former is located in a warm magnet providing a solenoidal field of $B = 0.5$ T. A large cylindrical Time Projection Chamber (TPC) is used as the main tracking device. It is complemented by a silicon-based Inner Tracking System (ITS) close to the beam pipe and, towards larger radii, the Transition Radiation Detector (TRD) and the Time-Of-Flight (TOF) detectors. Part of the acceptance is covered by electromagnetic calorimetry, and further detectors are installed around the interaction point for triggering and event characterization.

Following the azimuthal segmentation of the ALICE central barrel, the TRD is organized in 18 sectors [2]. Each of them is filled with a supermodule consisting of 6 layers of Multi-Wire Proportional Chambers (MWPC). They are subdivided into five stacks to achieve manageable chamber sizes. The MWPCs are preceded by a drift volume and a fibre-foam radiator. The former allows for the detection of the ionization energy loss over a radial length of 3.7 cm. The detection includes the absorption of the transition radiation, which highly relativistic ($\gamma \gtrsim 800$) particles can emit while traversing the radiator. The transition radiation photons are predominantly in the X-ray regime, and Xenon is used as detection gas because of its high photon absorption cross section. For the central barrel, the TRD contributes tracking, triggering, and the identification of particles, in particular of electrons.

In the following, we will first discuss the setup and operation of the TRD in Run I. We will further summarize results showing the performance of the detector. Next, we will describe the consolidation and upgrade activities during the first long shutdown of the LHC, as well as the subsequent recommissioning. In the end, we will review the current situation and further plans for Run II.

RUN I

Since the beginning of Run I, the TRD was included in the data taking of ALICE with the supermodules already installed at that time [3]. By 2012, 13 out of 18 had been installed, resulting in the setup shown in Figure 1.

The central barrel tracking is based on a Kalman filtering approach [3]. Starting from seeding clusters at the outer radius of the TPC, tracks are found by inward propagation to the vertex, also attaching hits in the Inner Tracking System. In a second step, the track is propagated outwards through the TRD and TOF detectors, also attaching clusters there. In a final inward propagation, the track parameters are refitted, taking into account energy loss. The TRD clusters carry both position and charge information, the latter allowing for the particle identification.

The fundamental concept, i.e. the detection of specific energy loss and the onset of Transition Radiation (TR), could be verified using cosmic muons [4]. They can carry very large momenta and can traverse the TRD twice. In the outward direction, which corresponds to the normal scenario of particles coming from the interaction point, the radiator is traversed before the chamber and the transition radiation emitted into the drift volume. On the inward direction, however, the radiator is passed only after the chamber and the transitition radiation remains undetected. This allows for the separation of the measurements with and without transition radiation. Figure 1 shows a compilation of measurements in the experiments and from previous test beams. The cosmic muons bridge the gap between data points from test beam setups with electron and pion samples and confirm the expected onset of transition radiation around $\beta\gamma \simeq 800$.

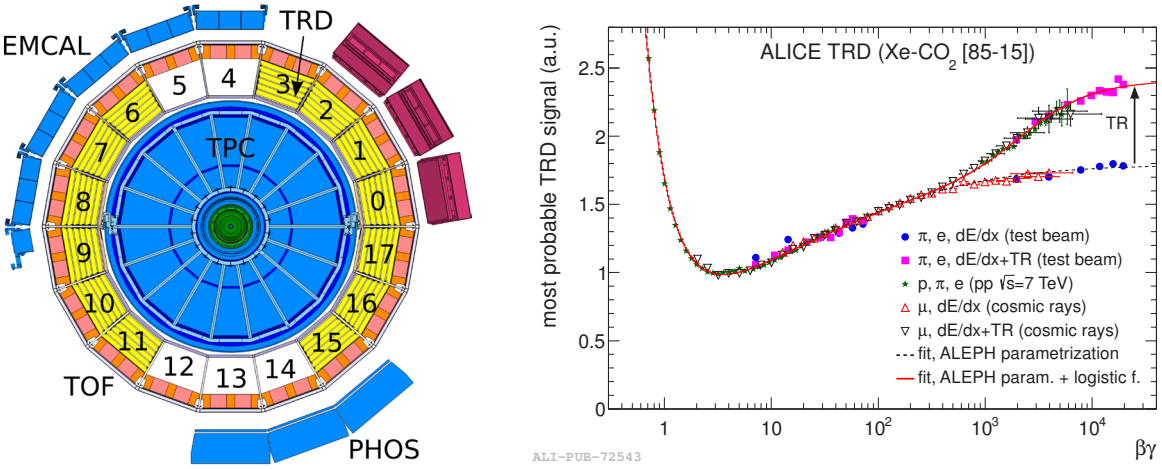

(a) ALICE central barrel (end of Run I)

(b) energy deposit in the TRD

FIGURE 1: TRD in the ALICE central barrel. Left: Cross-sectional view with the installation status of 2012/13. Right: Energy deposit in the TRD with and without transition radiation.

For electron identification, a likelihood can be calculated based on the total accumulated charge, which comprises the energy loss from ionization in the active volume and, if present, the absorption of transition radiation [5]. The transition radiation is most likely absorbed close to the entrance of the active volume. Thus, the sampling in time-bins along the radial drift allows for a more refined separation of electrons and pions by exploiting this information. The simplest extension is a two-dimensional likelihood, which uses the charges in two time windows as input. As generalization, the signal is subdivided into 7 slices, which can be used for higher dimensional methods or as input for a neural network which is trained for the identification of electrons. The performance of the methods can be judged by the fraction of pions which pass the electron cuts for a given electron efficiency. Figure 2 shows a comparison of the different methods. The performance improves with each TRD layer contributing to the measurement and deteriorates with increasing momenta since the separation in specific energy loss decreases and the production of transition radiation saturates.

Besides the usage for the offline reconstruction, the data are used for the derivation of several contributions to the level-1 trigger of the experiment, which is issued 6.5 μs after the level-0 trigger [6]. The low latency poses significant challenges on the calculations and requires highly parallelized front-end electronics for local processing. On 256 chamber-mounted multi-chip modules, each of which comprises an analog pre-amplifier and shaper and a digital chip with hardware units and four CPUs, the information is combined into chamber-wise track segments (tracklets). They are shipped to the Global Tracking Unit (GTU), which combines them to tracks using an algorithm specifically designed for linear scaling with multiplicity. For the found tracks, the transverse momentum p_{T} and position are calculated. The online tracks serve as input for a versatile trigger logic, which allows the implementation

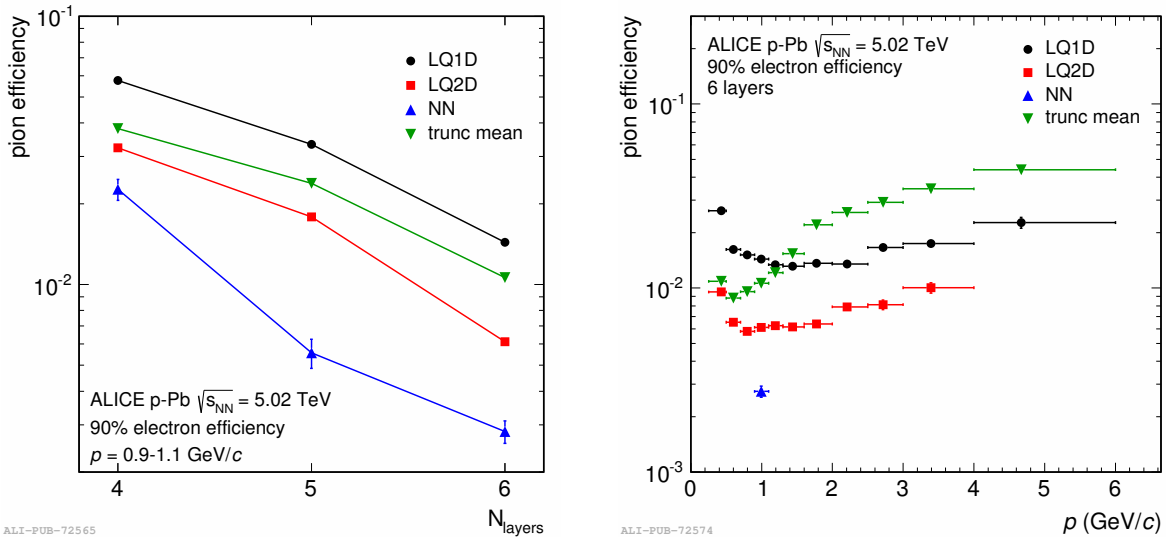

(a) layer dependence

(b) momentum dependence

FIGURE 2: Electron identification with the TRD [3]. The efficiency (inverse of rejection) for pions at a given electron efficiency of 90% is shown.

of various signatures. Noting that the η-φ coverage of a TRD stack is comparable to the area of a typical jet cone ($R = 0.2$), a jet trigger can be derived using the condition that at least three tracks with $p_{\mathrm{T}} > 3$ GeV/c are found in any TRD stack. Even though only charged particles enter the calculation, the trigger becomes fully efficient for charged jets with $p_{\mathrm{T}} \gtrsim 100$ GeV/c. The information on the deposited charge is also available online and was used for two electron triggers with p_{T} thresholds of 2 and 3 GeV/c, respectively. The identification was based on look-up tables translating the total charge to an electron likelihood. Figure 3 shows the enhancement by the TRD trigger for jets and electrons.

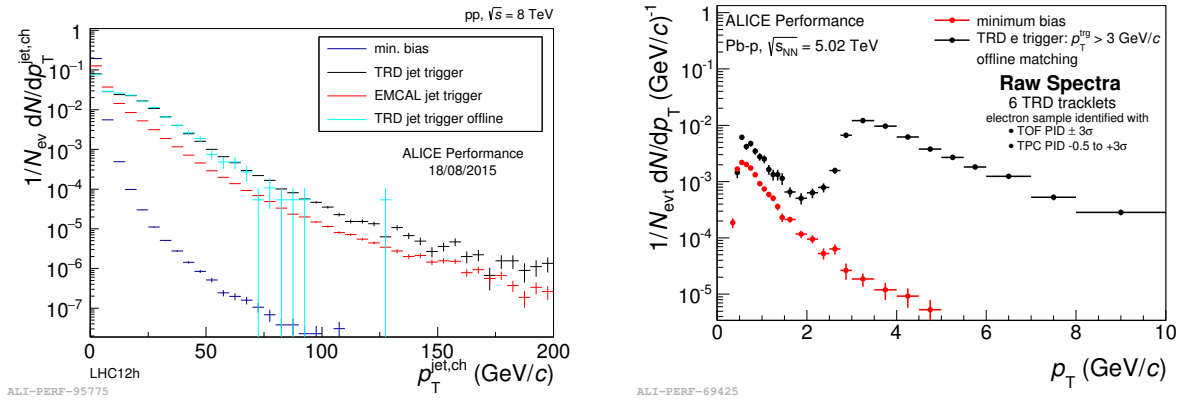

(a) jet trigger

(b) electron trigger

FIGURE 3: Transverse momentum spectra in TRD-triggered and minimum bias samples. Left: We compare the p_{T} spectra for charged jets in the triggered and minimum bias data samples. Right: We compare the p_{T} spectra for electrons in the triggered and minimum bias data samples.

In addition to extending the physics range by triggering, the TRD has been used for analyses requiring good and clean identification of electrons. A prime example is the dielectron decay channel of the $J/\psi \rightarrow e^{+}e^{-}$, for which the

TRD helps to improve the significance of the measurement [3]. Also for the measurement of heavy-flavour mesons through their semi-leptonic decay channel, the TRD electron identification is used [7].

LONG SHUTDOWN I

During the long shutdown of the LHC from 2013 to 2014, the production of the TRD electronics was completed. This allowed us to finish the assembly of the five remaining supermodules. They were installed at the end of 2014 before the experiment was prepared for the start of Run II. The completion of the TRD forms an important milestone in the project since it allows homogeneous usage of the TRD information in the full acceptance of the central barrel.

Besides the completion of the detector, consolidation and upgrade activities were carried out. Some low voltage connections at the supermodules had shown high resistance which resulted in increased temperatures and required short-term repairs. The affected supermodules were removed from the experiment one by one such that the connections could be reworked in the cavern before the supermodule was reinstalled. The rework resulted in stable operation of the low voltage connections for all supermodules.

Since Ethernet is used for the slow control of most detector components, failures of network components outside of the detector had resulted in the loss of control over parts of the detector during Run I. Therefore, special multiplexers were developed and manufactured to realize a redundant connection of the detector components to the upstream network. The installation for the most critical components in the supermodules had begun already in Run I. It was completed during the long shutdown such that now all connections can be remotely switched between two separate uplinks.

The front-end electronics of the TRD requires a wake-up signal prior to the experiment-wide level-0 trigger. In Run I, this signal was provided by a dedicated pretrigger system. To achieve the required low latency, it was installed inside the solenoid magnet and received direct copies of the signals from the trigger detectors. The system had some limitations in the interoperability with the central trigger processor, e.g. synchronized down-scaling was not possible. For Run II, the system has been merged with the central trigger processor to allow for a consistent trigger logic in one place.

To avoid a bottleneck in the readout, the Detector Data Links (DDL) to the data acquisition system were upgraded. The interface logic for the DDL was migrated from a dedicated mezzanine board to the fabric of the FPGAs in the GTU, using the in-FPGA multi-gigabit transceivers. This allowed for a doubling of the read-out bandwidth, resultin in a dead time similar to Run I despite the increased readout rates in Run II, see Figure 4.

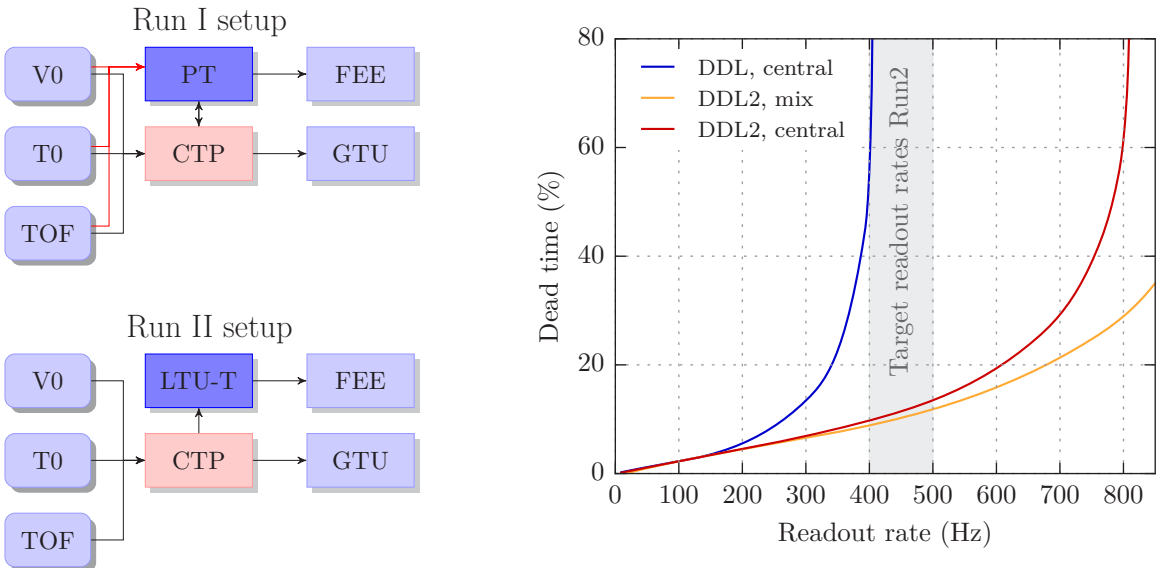

(a) wake-up generation

(b) read-out

FIGURE 4: Trigger and read-out upgrade. Left: We show the setup to derive the wake-up signal for the TRD front-end electronics in Run I and Run II. Right: We show the dead time corresponding to a given read-out rate [8].

RUN II

After the completion of the detector, the recommissioning started in the beginning of 2015. The upgraded read-out systems performed as expected. At first, the full detector was calibrated using Krypton injected to the gas system [9]. The detector was fully aligned using early data. After further tweaking of the detectors used for the wake-up trigger, the upgraded system was confirmed to fulfill the latency requirements.

With the full azimuthal coverage of the central barrel acceptance, the TRD information shall be used to update the track parametrization during the Kalman propagation. This leads to a significantly improved p_{T} resolution, see Figure 5.

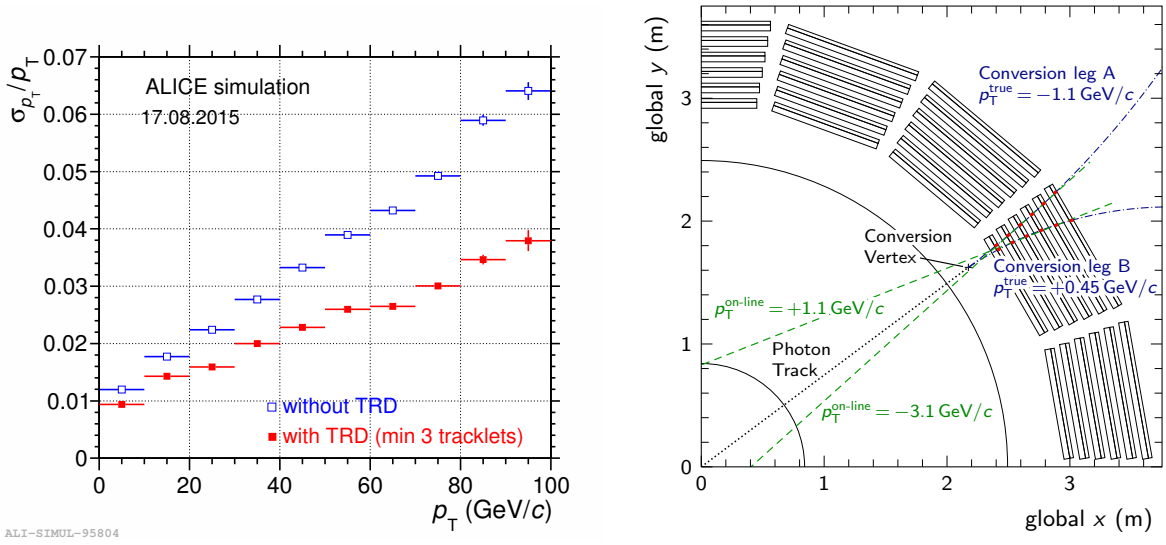

(a) p_{T} resolution (b) late conversions

FIGURE 5: TRD tracking. Left: Transverse momentum resolution without and with the TRD used for updating the global track parameters. Right: Event display of an exemplary late conversion which wrongly fires the trigger.

The dominant background for the single electron triggers was caused by photon conversions at large radii, close to or in the TRD, see Figure 5. For the online tracking, the resulting tracks resemble those with large transverse momenta. For Run II, a rejection of these late conversions has been included in the FPGA-based online tracking. It compares the p_{T}^{-1} estimated from the sagitta and from the global fit and rejects those with a large discrepancy.

In addition to the electron identification, the TRD can also be used for hadron identification. For this purpose, the truncated mean is calculated based on the TRD clusters attached to the track. For the identification, the deviation from the expectation for a given species is used after normalization to the resolution expected for the track under study.

SUMMARY AND OUTLOOK

The TRD has been completed in time for the start of Run II and performs well now. It shall contribute to the physics output of the experiment in various areas. The trigger helps to extend the p_{T} reach for jets and heavy-flavour electrons. The particle identification is used for analyses of heavy-flavour electrons with respect to their nuclear suppression factor and the second harmonic v_2.

REFERENCES

[1] K. Aamodt *et al.* (ALICE Collaboration), JINST **3**, p. S08002 (2008).

[2] P. Cortese *et al.* (ALICE Collaboration), *ALICE transition-radiation detector: Technical Design Report*, Technical Design Report ALICE No. CERN/LHCC 2001-021 (CERN, Geneva, 2001).

[3] B. B. Abelev *et al.* (ALICE), Int. J. Mod. Phys. **A29**, p. 1430044 (2014), arXiv:1402.4476 [nucl-ex] .
[4] X. Lu, "Exploring the performance limits of the ALICE time projection chamber and transition radiation detector for measuring identified hadron production at the LHC," Doctoral thesis, Universität Heidelberg 2013.
[5] D. Lohner, "Anisotropic flow of direct photons in Pb-Pb collisions at 2.76 TeV per nucleon," Doctoral thesis, Universität Heidelberg 2013.
[6] J. Klein (ALICE Collaboration), Nucl. Instrum. Meth. **A706**, 23–28 (2013), arXiv:1112.5110 [nucl-ex] .
[7] B. Abelev *et al.* (ALICE), Phys. Rev. **D86**, p. 112007 (2012), arXiv:1205.5423 [hep-ex] .
[8] S. Kirsch, "High-performance readout for the ALICE TRD," Doctoral thesis, Universität Frankfurt (in preparation).
[9] J. Stiller (ALICE), *Proceedings, TRDs for the 3rd Millenium: 4th Workshop on Advanced Transition Radiation Detectors for Accelerator and Space Applications (TRD2011)*, Nucl. Instrum. Meth. **A706**, 20–22 (2013).

Proceedings of the LHCP2015 Conference, St. Petersburg, Russia, August 31 - September 5, 2015

Editors: V.T. Kim and D.E. Sosnov

Performance of TOTEM in Run II

KENNETH ÖSTERBERG

Department of Physics and Helsinki Institute of Physics, P. O. Box 64, FI-0014 University of Helsinki, Finland.

kenneth.osterberg@helsinki.fi

On behalf of the TOTEM Collaboration

Abstract. The TOTEM experiment at the Large Hadron Collider is dedicated to diffractive and forward physics. Its consolidation and upgrade programme focuses on central diffractive processes. This article briefly describes the performance of the detectors in the 2015 run as well as the consolidation and upgrade work. Also a few highlights of the physics potential are discussed in detail.

Introduction

The TOTEM experiment [1] is dedicated to forward hadronic phenomena at the Large Hadron Collider (LHC). The three pillars of its physics programme are: an accurate determination of the total cross-section, a measurement of differential elastic scattering cross-section in a wide range of momentum transfer squared, t, and studies of diffractive and forward processes, mainly in cooperation with the CMS experiment [2]. The combination of the CMS and TOTEM experiments gives an exceptionally large pseudorapidity coverage for tracking and calorimetry that is especially well suited for studies of forward and diffractive processes. TOTEM comprises three subdetectors: the inelastic telescopes T1 and T2 and Roman Pots (RP) for leading proton detection, see Figure 1.

T1 and T2 are embedded in the forward regions of CMS on each side of the LHC interaction point IP5. T1 consists of Cathode Strip Chambers (CSC) and T2 of Gas Electron Multipliers (GEM). The pseudorapidity coverages of T1 and T2 are $3.1 \leq |\eta| \leq 4.7$ and $5.3 \leq |\eta| \leq 6.5$, respectively. T1 and T2 measure the charged particles produced in inelastic events and are, in addition to inelastic event counters and primary charged multiplicity measurers, excellent for defining "rapidity gaps", i.e. η-ranges without primary particle production, due to their low transverse momentum p_{T} thresholds, $\sim$ 100 MeV/c and $\sim$ 40 MeV/c for T1 and T2, respectively.

The RP system, that measures elastically and diffractively scattered protons very close to the outgoing beam, consists of two stations placed between z = 203 and 220 m on each side of IP5, named "RP210" and "RP220". Both of them are composed of two units (near and far with respect to IP5) separated by $\sim$ 5-10 m for reconstruction of the proton kinematics and background discrimination. Each unit includes two vertical (top and bottom) and one horizontal RP. The RPs are movable beam-pipe insertions that can bring sensitive detectors to sub-millimeter distance from the beam once it is stable. Each RP hosts 5 back-to-back mounted pairs of silicon-strip sensors with reduced ($\sim$ 50 μm) insensitive edge facing the beam, to accept protons scattered at very low angles.

The main purpose of the improvement of the experimental apparatus in view of Run II was to enhance the experiment's capability to measure Central Diffractive (CD) processes, $p+p \rightarrow p \oplus X \oplus p$. In CD reactions, the protons stay intact and rapidity gaps (indicated by $\oplus$) are formed between the protons and the state X. In CD reactions, the mass of X, M_X, can be reconstructed from the fractional momentum loss, ξ, of the scattered protons by $M_X = \sqrt{\xi_1 \xi_2 s}$. If the state X is a well-defined state, such as a particle or a fixed number of particles or jets, then the process is called Central Exclusive Production (CEP). In CEP reactions, to a very good approximation, the final state X obeys a $J_z = 0$, C-even, P-even, selection rule, where J_z is the projection of the total angular momentum along the beam axis.

The consolidation program of TOTEM [3] focuses on measurements of CD processes in special high-β^* optics runs with common data taking with CMS. The consolidation included the relocation of existing RPs to new RP210 near and far positions, see Figure 1, to improve the lever arm, to rotate the RP210 far by 8 degrees to improve the multitrack capability and upgrade the data acquisition system (DAQ) to sustain a significantly higher rate. By adding

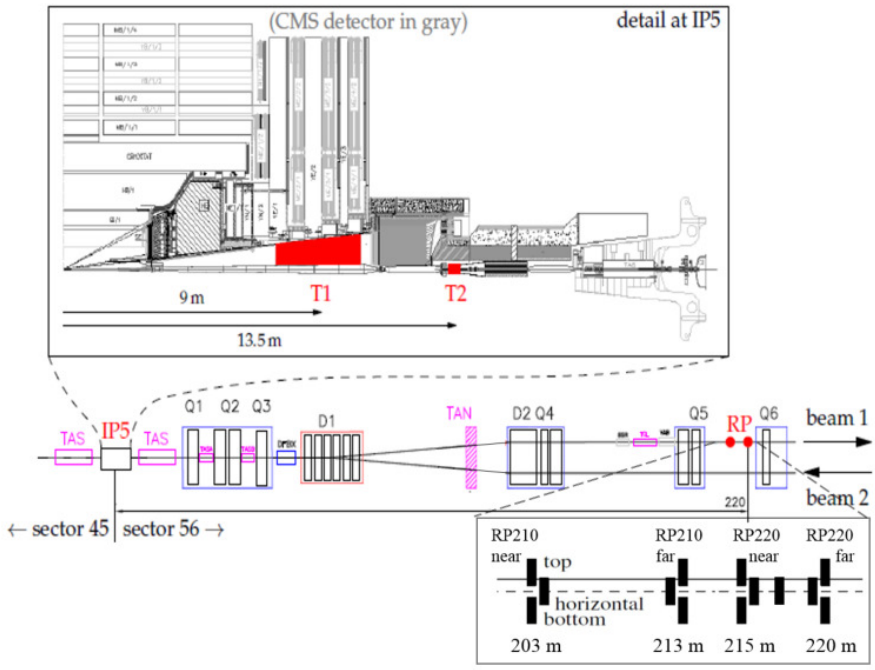

FIGURE 1. Top: the T1 and T2 telescopes embedded in the forward region of CMS. Bottom: the location of the Roman Pots (RP) along the LHC beam line with the 2015 RP setup as insert. All detectors are installed symmetrically with respect to IP5.

proton timing detectors with $\sim$ 50 ps timing resolution in the vertical RPs [4], can CD processes with O(pb) cross-sections be accessed in a $\beta^* = 90$ m run of about a week. With the $\beta^* = 90$ m optics, protons with any ξ can be detected in the vertical RPs and hence, in CEP reactions, any M_X, as long as the $|t|$ of both scattered protons is $\gtrsim 0.01$ GeV^2.

The reach with $\beta^* = 90$ m optics is complementary to the one of the other upgrade, CMS-TOTEM precision proton spectrometer (CT-PPS) [5] that aims to measure CEP processes with O(fb) cross-sections in normal high-luminosity running having access to $M_X \gtrsim 300$ GeV/c^2. The CT-PPS upgrade included adding RF-shields to all horizontal RPs to reduce the impedance seen by the LHC beams and adding a new additional cylindrical horizontal RP at 216 m for timing detector purposes, see Figure 1. With normal high-luminosity optics, the diffractive protons are measured in the horizontal RPs, whereas with high-β^* optics the diffractive protons are entering mainly the vertical RPs. The pile-up, multiple pp interactions per bunch crossing, is considerably smaller in high β^* runs with an average number of inelastic pp events per bunch crossing, $\mu \lesssim 1$, compared to $\mu = 20$-50 in normal high-luminosity LHC runs.

Performance in 2015 run

During long shutdown 1 (LS1), the inelastic telescopes T1 and T2 were extracted and reinstalled. Few months after re-installation, the DAQ loop of one of the T2 half arms started to be unreliable. It was decided to disconnect this half arm from the DAQ loop to ensure proper functionality of the other half arm connected to the same DAQ loop. The effect of the missing half arm on the trigger and veto efficiency as well as for the most important measurements involving T2 (inelastic cross-section, charged multiplicity measurement and the exclusive low mass resonances) was estimated to be acceptable, at most 1 %, and significantly smaller than the dominant uncertainty in any of the measurements.

With this exception, the indications from the 2015 data are that the performance of the inelastic telescopes T1 and T2 is similar to their performance in Run I in terms of efficiency, resolution and tracking. Their performance in Run I is described in detail in Reference [6]. Figure 2 shows examples of T1 and T2 distributions from the LHCf run with a very low pileup, $\mu \sim 0.003$, and the CMS solenoid off. This makes the LHCf run data attractive for the forward charged particle pseudorapidity density, $dN_{\rm ch}/d\eta$, measurement, especially for the T1 were the magnetic field effects are sizable. E.g. the transverse vertex resolution with the T1 is approximately a factor 2 better in the LHCf run data compared to data taken during run I with the CMS solenoid on, mainly due to magnetic field effects.

Figure 2 (left) shows the reconstructed η of T1 tracks with a good balance between left and right arm, indicating similar reconstruction efficiencies. Figure 2 (right) shows the distribution of the Z impact parameter [6] that is used for separating primary and secondary tracks for a pseudorapidity region in one half arm of T2.

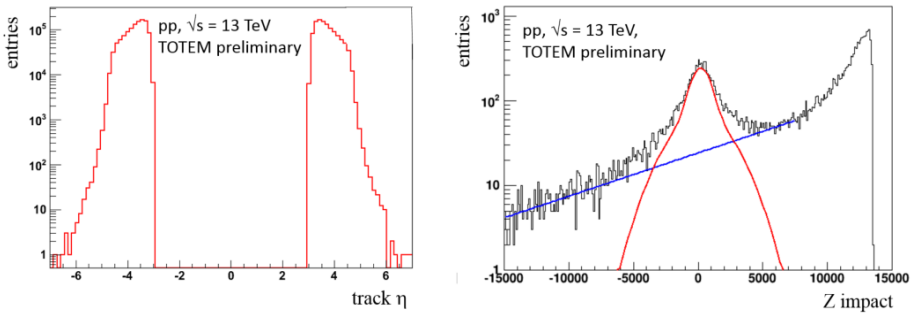

FIGURE 2. Performance plots from the LHCf run. Left: the pseudorapidity distribution of tracks in T1, right: the Z impact parameter distribution of tracks in a specific pseudorapidity region in one of the half arms of T2. The result of a global fit to the Z impact distribution is shown with the exponential (double-Gaussian) component due to secondary (mainly primary) particles.

During Run I, the data throughput on the VME bus was the bottleneck of the DAQ system translating into a maximum trigger rate of 1 kHz. A new DAQ architecture [7] was introduced to get rid of the bottleneck replacing the VME interface with Scalable Readout System components [8], which provided a faster and cost effective transmission. Also a zero suppression firmware was developed. As a result a trigger rate of about 20 (50) kHz could be sustained during raw data (zero suppressed) readout i.e. a factor 20 (50) improvement compared to the performance in Run I, allowing to increase the number of bunches in special runs to about 700 bunches without significant efficiency loss.

The existing RPs units at 147 m were successfully relocated to their new positions, RP210 near and far, with the latter one rotated by 8 degrees. Also all the RP silicon-strip sensors were removed and reinstalled during LS1. Furthermore, RF-shields for the horizontal RPs were added and a new ferrite material was introduced for all RPs followed by a bake-out at 1000 ^{o}C. These actions reduce the impedance and the outgassing, respectively. Finally, a new cylindrical horizontal RP was manufactured and installed at 216 m for the CT-PPS timing detector. This makes the TOTEM RP system, containing 26 RP units, the largest ever at any collider. Not all of them are to be used at the same time, the RP210 far, RP220 near and far are to be used for high β^* optics runs, whereas the RP210 near and far plus the cylindrical RP are to be used for normal high-luminosity running. It should also be noted that a new collimator, TCL6, was installed behind the RPs during LS1 to intercept showers from the RPs. This will allow the collimators between IP5 and RPs to be opened up even at highest luminosities and hence improve the high ξ acceptance.

At the time of the LHCP 2015 conference, the RP system had been commissioned and taken data during a $\beta^* = 19$ m run as an exercise for the main run, a one week $\beta^* = 90$ m run in October 2015. The indications from the first data taking were that everything was working as expected. From the successful data taking in October, it is known that the RP are working with the same efficiency, resolution and tracking performance as in Run I, for details see Reference [6], with the added redundancy of measuring each proton with three units instead of two as in Run I.

During normal high-luminosity running, insertions of the horizontal RPs were exercised. The experience from run I (2012) was that when the RPs were inserted, showers created by collision debris caused beam dumps due to large signals in the Beam Loss Monitors (BLMs), and that the beams caused impedance heating combined with outgassing in the RPs. The actions taken during LS1 (new ferrites, addition of RF-shields and TCL6) were done to solve these issues. During 2015, the RPs were inserted after 1-2 h of stable beam conditions in the second fill of each step of luminosity increase. The horizontal RPs were at $25\sigma_{\text{beam,trans}}$ and no beam instabilities due to RP insertions were observed up to a luminosity of about $5 \cdot 10^{33}$ cm^{-2}s^{-1}. Temperature and vacuum measurements in the RPs and BLM measurements were all OK. Extrapolation to a luminosity of 10^{34} cm^{-2}s^{-1} and closer distances (even to $15\sigma_{\text{beam,trans}}$) is well within the current BLM thresholds allowing regular insertions for physics in fills in 2016.

Physics Potential

As stated above, the motivation for the experimental apparatus improvements in Run II is the enhance the experiment's physics potential, especially in measuring CD processes that are t-channel exchange processes with either a system of

gluons g (with neutral color) or a photon γ. The leading order description of this color-singlet gluon system is called the Pomeron $\mathbb{P}$. For CEP processes in proton-proton collisions the dominant contribution comes from $\mathbb{P}\mathbb{P}$ scattering, with a small contribution from "photoproduction" i.e. $\mathbb{P}\gamma$ collisions and even smaller one from $\gamma\gamma$ fusion. The excellent CMS-TOTEM pseudorapidity coverage, allows, in addition to the comparison between the mass, M_{PF}, computed from the particle flow (PF) objects and M_X, to compare the summed transverse (p_T) and longitudinal (p_z) momentum of the PF objects with the two protons, as well as verify the rapidity gaps predicted by the proton ξ measurements.

Physics topics covered in $\beta^* = 90$ m runs include spectroscopy of exclusively produced low-mass resonances and glueball states, measurement of exclusive production of charmonia, studies of the rapidity gap survival probability as well as searches for new physics in CD reactions via missing mass or momentum signature. The physics topics covered by CT-PPS include searches for exclusively produced new particle states, measurement of exclusive dijet and divector boson production as well as searches for anomalous quartic gauge couplings. Below follows a description of two selected topics, more details and description of topics not covered here is found in References [4, 5].

Exclusive production of low mass resonances and glueballs

The CD process effectively turns LHC to a gluon-gluon collider and provides an excellent opportunity to study gluon systems with a longitudinal momentum fraction $x \sim 10^{-4}$ and, in particular, to search for glueball candidates. In the case of CMS-TOTEM, this is complemented with an excellent mass resolution ($\sim$ 20-30 MeV/c^2) with the tracker for charged-particle-only final states, in combination with a capability to measure and tag both outgoing protons as well as effectively select the exclusive events with high purity in the required very low ξ range, thus allowing clearly to identify the produced resonances without further steps like model- and parameter-dependent partial-wave analysis.

Glueballs are predicted by QCD as gluon bound states with no valence quark content. The absence of valence quarks, in combination with the $J_z^{PC} = 0^{++}$ selection rule, makes CD reactions an ideal place to search for them. QCD lattice calculation foresee a $J^{PC} = 0^{++}$ ground state and a 2^{++} state followed by a spectrum of excited states [9, 10]. The $f_0(1500)$ or the $f_0(1710)$ are generally regarded as potential glueball 0^{++} states since one of them is in excess to the meson SU(3) multiplet and both are compatible with a glueball in terms of mass, spin, parity, and decay channels (e.g. suppressed $\gamma\gamma$ mode). Recent unified lattice calculations [10, 11] predict the 0^{++} glueball at $\sim$ 1700 MeV/c^2 within $\sim$ 100 MeV/c^2 of overall uncertainty (statistical and systematic), thus favoring the $f_0(1710)$ as a glueball candidate. Whether a resonance is a glueball or not, can be studied by measuring its CD production cross-section, e.g in comparison with its production in $\gamma\gamma$-collisions, as well as its decay branching ratios [9]. The WA102 experiment [12] disfavored the $f_0(1710)$ to be the glueball by reporting that its branching ratio into K^+K^- exceeded its branching ratio to $\pi^+\pi^-$, contrary to the case of the $f_0(1500)$. This lead to the conclusion of a higher coupling to the s-quark compared the u,d-quarks unexpected for a glueball. Moreover the predicted decay mode into $\rho\rho$ has not been observed so far. An observation of the decay $f_0(1710) \to \rho\rho$ at the LHC would, in addition to be a first observation of this decay mode, change the branching ratio of its decay modes into K^+K^- vs "pionic" channels and therefore renormalize the expected couplings to u,d-quarks vs s-quark in the one expected for glueballs.

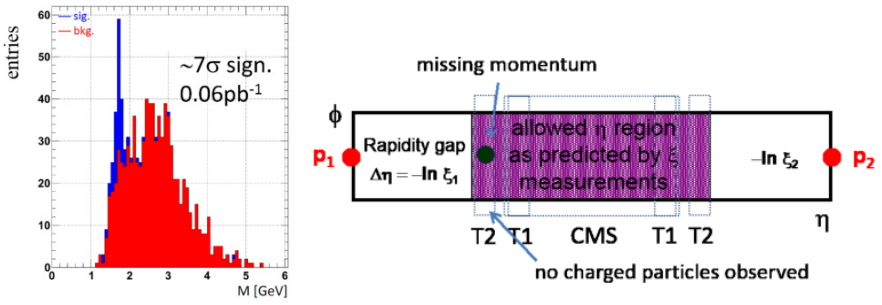

FIGURE 3. Left: Estimated signal and background mass distributions for exclusive $f_0(1710) \to \rho^0\rho^0 \to 2(\pi^+\pi^-)$ production in CMS-TOTEM. The background estimate from non-resonant exclusive $\rho^0\rho^0$ production is based on DIME [13]. Right: Schematical drawing of the the event topology used in the search for high missing momentum candidates.

Events with two RP protons and only two or four charged particles in the tracker with zero total charge are selected. Then, p_T compatibility (within $\sim$ 50 MeV/c) between the central and the pp systems as well as horizontal vertex compatibility for the two RP protons, under a $\xi \sim 0$ assumption, is required to remove incompletely reconstructed events and pileup. Preliminary analysis of a CMS-TOTEM Run I 1 nb^{-1} data sample reveals sensitivity to a

possible decay of $f_0(1710) \to \rho^0\rho^0 \to 2(\pi^+\pi^-)$. Figure 3 (left) shows $f_0(1710)$ simulated signal distributions together with background due to non-resonant exclusive $\rho^0\rho^0$ production for 0.06 pb^{-1} luminosity, which is estimated to be needed to observe the decay. As stated above, the precise measurement of f_0 branching ratios are essential in view of identifying the resonances as glueball candidates. As the branching ratios for low mass resonances may easily differ by an order of magnitude, a factor of ten of integrated luminosity, on top of the one estimated for observing $f_0(1710) \to \rho^0\rho^0 \to 2(\pi^+\pi^-)$, will be required to precisely measure the $\pi^+\pi^-$, K^+K^- and $\rho^0\rho^0$ decays modes. In reality slightly more, i.e. an integrated $\beta^* = 90$ m luminosity of $\sim 1\,\text{pb}^{-1}$, will be required for a detailed f_0 branching ratios measurement when backgrounds from exclusive $2(\pi^+\pi^-)$ production and adjacent f_2 states are taken into account.

A detailed angular momentum analysis is important to give full confidence that the measured branching ratios of the low mass glueball candidates are correct. Such a study has to be made as a function of the invariant mass in a wider interval than the resonance width itself to be able to deconvolute the overlapping contributions from adjacent resonances and background. The spin-parity analysis therefore has to be performed in mass steps ΔM with the minimal step size limited by the mass resolution $\sigma(M) \approx$ 20-30 MeV/c^2. Taking all into account, a full spin-parity analysis of the exclusive f_0 production should be made in mass bins with a size $\Delta M =$ 30-40 MeV/c^2 and if requiring sufficient statistics in each ΔM bin, it is strictly only fully feasible with an integrated $\beta^* = 90$ m luminosity of $\sim$ 4-5 pb^{-1}.

Search for missing mass and momentum candidates

CD provides simultaneous and precise measurement of the initial and final state kinematics, which can be used to search for events with missing mass or missing momentum signatures. This opens up ways for new physics searches that might have escaped the searches of the general purpose detectors, CMS and ATLAS. Only CD events with a $M_{PF+P_{miss}} \lesssim M_X$ are examined to avoid contamination from pileup events. The rapidity gaps, $\Delta\eta = -\ln \xi$, predicted by the proton ξ measurements are verified using the T2 detector with a rapidity coverage of $5.3 < |\eta| < 6.5$. To probe O(pb) cross-sections, a statistics corresponding to an integrated $\beta^* = 90$ m luminosity of $\sim 50\,\text{pb}^{-1}$ is needed.

The search signature is high missing momentum pointing towards a region with good CMS-TOTEM instrumentation ($|\eta| < 6.5$) and not observing charged particles or energy deposits in η regions close to where the missing momentum points, see Figure 3 (right). This happens if a particle is created in the CD reaction and escapes the detectors undetected. Events are rejected if more forward rapidity gaps than T2 would be allowed by the proton ξ measurements. For $\sqrt{s} = 13$ TeV, the search is confined to the 200-700 GeV/c^2 mass range, where the upper limit is due to the maximal central mass allowed by the T2 acceptance. Events with missing momentum up to 400 GeV/c were found in the Run I data set with background events expected from particles escaping detection in the forward region, due to "acceptance gaps" between detectors as well as from $p + p \to N^* \oplus X \oplus p$ or $p \oplus X \oplus N^*$ reactions. In the latter case, one of the observed protons comes from a decay of a nucleon resonance, N^*, and the other N^* decays products escape detection. With increased statistics, it is expected that these backgrounds will be modeled sufficiently well.

An example process is squark $\tilde{q}\tilde{\bar{q}}$ pair production with $\tilde{q} \to q + \tilde{\chi}_1^0$ decay for $\tilde{q}$ masses of just a few hundred GeV, where a central diffractive cross-section of 1-10 pb can be expected [4]. Since ~50 % are visible in the CMS-TOTEM acceptance, an integrated luminosity of ~50 pb^{-1} could yield ~25-250 events with the missing energy due to the two neutralinos ($\tilde{\chi}_1^0$) . Such a search could allow to check the current exclusion limits on the $m_{\tilde{q}} - m_{\tilde{\chi}_1^0}$ range without tight cuts on the centrally visible system, and especially explore the $m_{\tilde{q}} - m_{\tilde{\chi}_1^0} \leq$ 30-40 GeV/c^2 range in detail. The hypothesis of close $\tilde{q}$ and $\tilde{\chi}_1^0$ masses is particularly relevant for the supersymmetric top quark $\tilde{t}$ given the cosmological implications [14]. For $\tilde{t}$ masses above ~250 GeV, the decay $\tilde{t} \to c + \tilde{\chi}_1^0$ is currently not fully excluded [15, 16].

Status of upgrades

For 90 m optics and $\xi \lesssim 0.1$ %, the reconstructed proton transverse vertex has sufficient resolution to reduce pileup background in CD events [4]. For all other cases, pileup rejection can only be obtained by matching the proton vertex with the central detector vertex using the reconstructed longitudinal position of the proton vertex as depicted in Figure 4 (left). This requires precise timing measurement of the outgoing protons combined with an accurate timing reference system. For $\beta^* = 90$ m optics with $\mu \lesssim 1$, 50 ps precision is sufficient according to estimates from simulations and Run I data, whereas for the normal high-luminosity running with $\mu =$ 20-50, a precision of 10-30 ps is needed.

For the high β^* optics, 500 μm thick diamond sensors with variable pitch (0.7 - 4.2 mm) have been chosen due to the limited space in the vertical RPs [4]. The pitch has been adjusted to the expected track occupancy resulting in a double hit probability of $\lesssim 1$ %. Single sensors gave in test beams a time resolution better than 100 ps, see

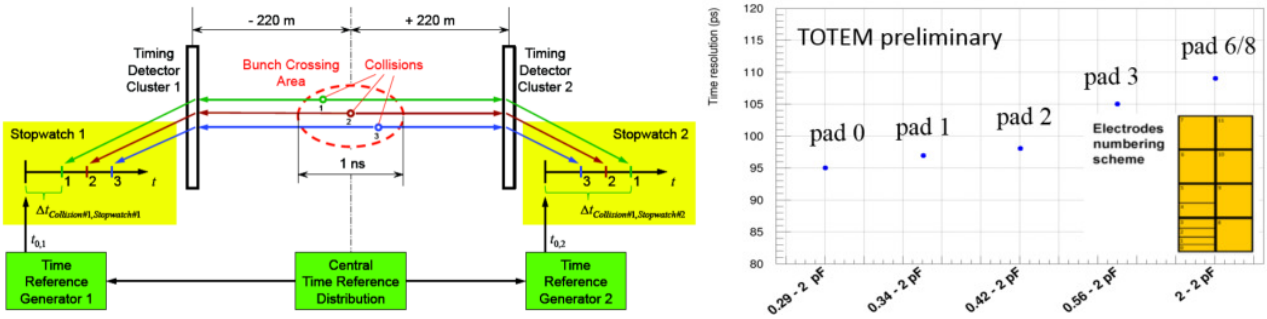

FIGURE 4. Left: The measurement principle of the longitudinal (z) position of the proton production point using timing detectors. The picture shows the arrival time of the protons inside the RPs, on each side of the IP. $z_{vertex} = c(\Delta t_{\text{collision\#1,left}} - \Delta t_{\text{collision\#1,right}})/2$. Right: The time resolution of a single diamond sensor as measured in test beams with the electrode numbering scheme as insert.

Figure 4 (right), indicating that a four-sensor package is able to provide the required resolution of 50 ps. The first sensor package will be installed in a RP in the LHC tunnel for the heavy ion run in November 2015 and the remaining three detector packages during the first half of 2016, being ready for a possible special run in the second half of 2016. The timing reference system is adopted from the "Universal Picosecond Timing System", developed for FAIR [17]. It is currently being built and tested in the laboratory and is planned to be installed during the end of year stop 2015-16.

For the high-luminosity runs, the baseline option is 3×3 mm^2 quartz bars with silicon photo multipliers for light detection in a 4×5 geometry. Single bars have shown resolutions of ~30 ps in early test beams and with two modules ~20 ps could be achievable. First modules are currently being tested inside RPs with minimum ionization particles. Four modules are planned to be ready for installation during the end of year stop 2015-16. In parallel solid state timing detector alternatives, diamond and ultra fast silicon sensors [18], are being developed to be able to vary the pitch and thus reduce the double hit probability that is expected to significant (up to 50 % at $\mu = 50$) for the pixels closest to the beam. These options are expected to be ready for a possible installation in the end of the year stop 2016-17. At high-luminosity, the number of tracks in the RPs are estimated to be several per event and thus the strip sensors are not capable to do the reconstruction. They are also not radiation hard enough. During 2016, strip modules in horizontal RPs will be replaced by 3D silicon modules with six sensor planes per RP. This should result in a ~ 10 μm position and a 1-2 μrad angular resolution. The 3D sensors will use the same readout as the Phase I CMS pixel upgrade.

REFERENCES

[1] G. Anelli *et al.* (TOTEM collaboration), JINST **3**, p. S08007 (2008).
[2] S. Chatrchyan *et al.* (CMS collaboration), JINST **3**, p. S08004 (2008).
[3] The TOTEM collaboration, TOTEM Upgrade Proposal, CERN-LHCC-2013-009; LHCC-P-007 (2013).
[4] The TOTEM collaboration, Timing Measurements in the Vertical Roman Pots of the TOTEM Experiment, CERN-LHCC-2014-020; TOTEM-TDR-002 (2014), addendum: CERN-LHCC-2014-024; TOTEM-TDR-002-ADD-1.
[5] The CMS and TOTEM collaborations, CMS-TOTEM Precision Proton Spectrometer (CT-PPS), CERN-LHCC-2014-021, CMS-TDR-13, TOTEM-TDR-003 (2014).
[6] G. Antchev *et al.* (TOTEM collaboration), Int. J. Mod. Phys. A **28**, p. 1330046 (2013).
[7] M. Quinto, F. Cafagna, A. Fiergolski and E. Radicioni, JINST **8**, p. C11006 (2013).
[8] J. Toledo *et al.*, JINST **6**, p. C11028 (2011).
[9] V. Matheiu, N. Kochelev and V. Vento, Int. J. Mod. Phys. E **18**, p. 1 (2009).
[10] Y. Chen *et al.*, Phys. Rev. D **73**, p. 014516 (2006).
[11] C. J. Morningstar and M. Peardon, Phys. Rev. D **60**, p. 034509 (1999).
[12] A. Kirk, Int. J. Mod. Phys. A **29**, p. 1446001 (2014), and references therein.
[13] L.A. Harland-Lang, V.A. Khoze and M.G. Ryskin, Eur. Phys. J. C **74**, p. 2848 (2014).
[14] K. Huitu, L. Leinonen and J. Laamanen, Phys. Rev. **D84**, p. 075021 (2011).
[15] G. Aad *et al.* (ATLAS collaboration), Eur. Phys. J. C **75**, p. 510 (2015).
[16] The CMS collabration, CMS Supersymmetry Physics Results/Summary plots for 8 TeV dataset, 11 September 2015, https://twiki.cern.ch/twiki/bin/view/CMSPublic/PhysicsResultsSUS.
[17] M. Bousonville and J. Rausch, Phys. Rev. ST Accel. Beams **12**, p. 042801 (2009).
[18] N. Cartiglia *et al.*, JINST **9**, p. C02001 (2014).

Upgrade: parallel talks

Proceedings of the LHCP2015 Conference, St. Petersburg, Russia, August 31 - September 5, 2015

Editors: V.T. Kim and D.E. Sosnov

Prospects for SUSY and BSM Physics at the High Luminosity LHC

JEFFREY D. RICHMAN

Department of Physics, University of California, Santa Barbara, CA 93106 USA

richman@hep.ucsb.edu

On behalf of the ATLAS and CMS Collaborations

Abstract. Prospects for the discovery of supersymmetry (SUSY) and other beyond-the-standard-model physics at the high-luminosity LHC are reviewed. Projections for the sensitivity for both strong and electroweak production of SUSY particles based on integrated luminosities up to 3000 fb^{-1} are presented, along with an analysis of several scenarios in which SUSY particles might be discovered. The potential complexity of the pattern of observed signals is highlighted, together with the importance of multi-signature "fingerprints," which can help to elucidate the origin of a signal. A brief discussion is also given for exotic particle searches, illustrating how high-luminosity data samples can provide key information on the properties of discovered particles.

MOTIVATIONS FOR NEW PHYSICS SEARCHES AT THE LHC

A central goal of the physics program of the Large Hadron Collider (LHC) is the exploration of particles and interactions at the TeV energy scale, which may hold answers to some of the most profound questions in particle physics. The mystery with the strongest empirical foundation is the nature of astrophysical dark matter. While there is no guarantee that the dark matter can be accounted for by weakly interacting massive particles (WIMPs) at the TeV scale, this explanation is well motivated, and the combined program of direct-detection experiments and further LHC searches are poised to make major progress in the next decade. A second, more theoretically motivated mystery, is the gauge hierarchy problem [1], which has become even more compelling with the discovery of the/a Higgs boson at a mass of approximately 125 GeV. Assuming that the Higgs is a fundamental scalar particle, its mass (and with it the entire electroweak scale) is subject to enormous short-distance quantum corrections which, on their own, would pull its value to some high cutoff scale, such as the Planck scale. This uncomfortable outcome can be avoided either by extreme fine tuning of the bare Higgs mass parameter, which is regarded as (extremely) unnatural, or by some new physics that cancels the effects of the quantum corrections. It is remarkable that this acute problem can be addressed by new physics scenarios ranging from supersymmetry (SUSY) to extra dimensions. Regardless of the physical mechanism, the new physics is expected to emerge somewhere around the TeV scale if fine tuning is to be avoided. A third mystery is whether the three standard model (SM) gauge coupling constants evolve with increasing energy such that they unify at some high scale, where a unified gauge group with this single gauge coupling constant would govern all non-gravitational interactions. The presence of SUSY at the TeV scale can lead to convergence of the running coupling constants at a high scale. Of course, a key element of the High Luminosity (HL) LHC program is the fullest possible study of the Higgs sector, which is covered in a separate talk by Aleandro Nisati at this conference. Thus, there are many indications, but no guarantees, that exploration of the TeV scale will lead to the discovery of new physics beyond the SM.

This talk considers the long-term discovery potential of the ATLAS [2] and CMS [3] experiments at LHC and High Luminosity (HL) LHC physics programs, which should help to resolve these mysteries and many others. Because of time constaints, I will focus on supersymmetry, but studies of other ("exotic") beyond-the-standard-model (BSM) scenarios are discussed briefly as well.

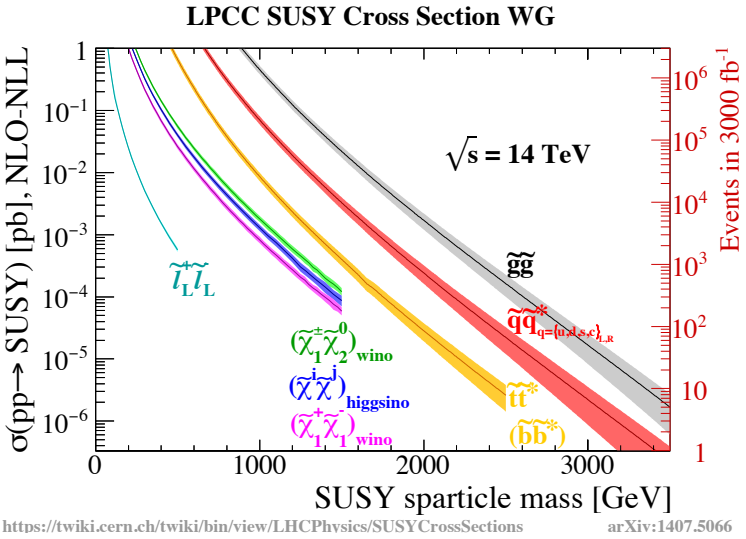

FIGURE 1. Cross sections for the pair production of supersymmetric particles at $\sqrt{s} = 14$ TeV, as a function of the SUSY particle mass [4]. The number of produced events in a sample of 3000 fb^{-1} is also given.

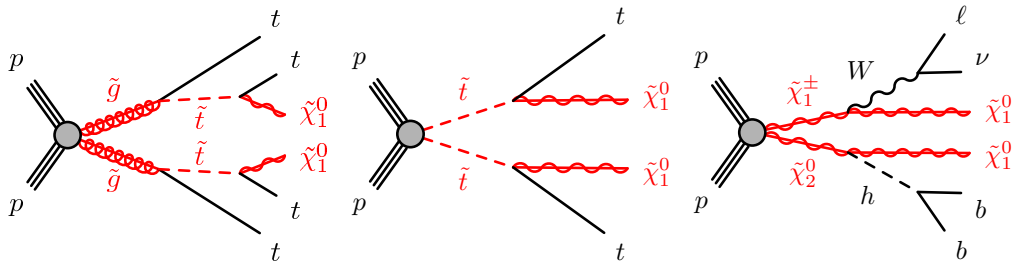

FIGURE 2. Diagrams for SUSY particle pair production and decay in the context of simplified models: (left) gluino pair production with decay into a top squark and an (anti-) top quark, (middle) top-squark + anti-top squark pair production, and (right) production of a chargino-neutralino pair.

SUSY SEARCHES: A SHORT PRIMER AND STATUS OF CURRENT SEARCHES

To understand the program of SUSY searches, it is useful to start from the cross sections for the most important processes. Figure 1 shows the dependence of key pair-production cross sections (left-hand axis) on the mass of the pair-produced SUSY particle in pp collisions at $\sqrt{s} = 14$ TeV [4]. The cross sections fall off rapidly with mass, as one would expect. At fixed particle mass, the largest cross section is for gluino pair production ($\tilde{g}\tilde{g}$). For example, for $m(\tilde{g}) = 2$ TeV, the cross section would be around 1 fb, yielding several thousands of produced events (right-hand axis) in the expected nominal HL-LHC sample of 3000 fb^{-1}. The pair production cross section for a specific scalar quark (squark) is much smaller, as shown for $\tilde{t}\tilde{t}^*$. (Here, an asterisk is used to denote an antiparticle rather than an off-shell particle.) Searches for top-squark pair production must therefore contend with a small cross section, as well as with a large SM background from $t\bar{t}$ production. As shown in Fig. 1, the combined cross section for squark-antisquark production, integrating over all squark degrees of freedom in the first two generations (two scalar partners, L and R, for each SM fermion, times four flavors), gives eight times this basic squark-antisquark cross section. Thus, under the assumption of degenerate squark masses, such searches generally have a much larger mass reach than a search for $\tilde{t}\tilde{t}^*$ alone. As we will see, however, a characteristic of natural SUSY scenarios is that, while both top squarks and one of the bottom squarks are typically constrained to be light, no such constraint applies to the first and second generation squarks. Figure 1 also shows that the cross sections for electroweak processes are much smaller at fixed mass than any of the strong production processes.

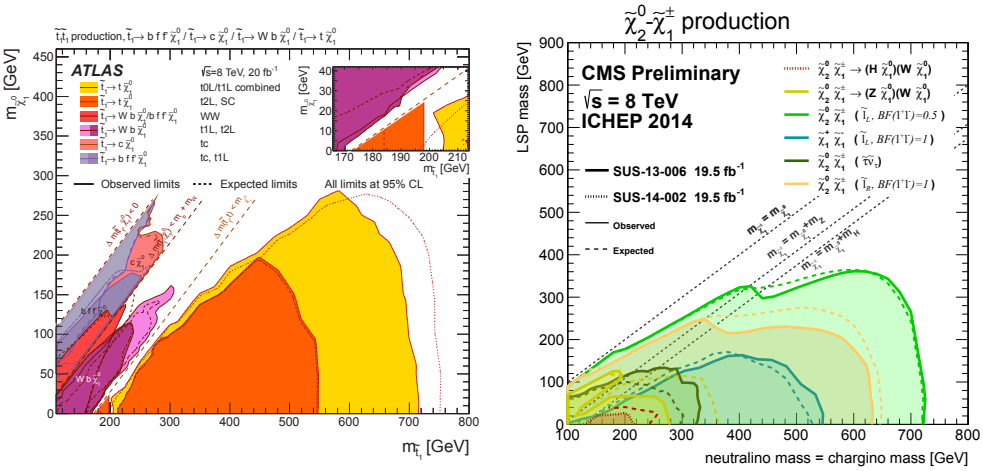

FIGURE 3. (Left) Summary of ATLAS searches for top-squark pair production: excluded regions in the $m(\tilde{t})$-$m(\tilde{\chi}_1^0)$ plane using Run 1 data [6]. (Right) Summary of CMS searches for EWKino pair production using Run 1 data [7].

To define a signal hypothesis, production processes such as those shown in Fig. 1 must be combined with a set of specified decay modes, which depend on the assumed mass spectrum of lighter SUSY particles, and potentially on mixing angles as well. Many of the exclusion plots are presented in the framework of simplified model spectra (SMS) [5], in which it is assumed that a very limited number of SUSY partners are involved in the decay chains of the produced particles. Under the assumption that the combined product branching fraction for the specified process is 100%, the excluded cross section is compared to a theoretical cross section, yielding an interpretation in terms of excluded SUSY particle masses. This approach greatly simplifies the interpretation, at the likely expense of some realism. Such models are used in many, but not all, ATLAS and CMS studies of sensitivity at the HL-LHC. Figure 2 shows a representative set of the many simplified models that have been defined for use in the design and interpretation of SUSY searches. In a full-spectrum SUSY model, the branching fraction for a given mode would typically be lower than the 100% value assumed in an simplified model, with a corresponding degradation in the mass reach of the search.

Figure 3 shows the exclusion regions resulting from the ATLAS Run 1 searches for top-squark pair production [6]. The regions are defined in the parameter space of a set of simplified models in which the only relevant SUSY particles are the lighter top squark ($\tilde{t}_1$) and the neutralino LSP ($\tilde{\chi}_1^0$). Depending on the masses of the $\tilde{t}_1$ and the χ_1^0, a variety of different two-, three-, and four-body decay scenarios can occur, and limits are placed on each one assuming a 100% branching fraction. The most basic two-body decay is $\tilde{t}_1 \to t\tilde{\chi}_1^0$; if there is not sufficient phase space for the top quark to be produced, the process becomes $\tilde{t}_1 \to bW^+\tilde{\chi}_1^0$, as long as the W-boson can be produced on mass shell. Roughly speaking, top squarks with masses up to $m(\tilde{t}) \approx 725$ GeV have been excluded for low values of $m(\tilde{\chi}_1^0)$. For $m(\tilde{\chi}_1^0) \geq 275$ GeV, however, there is no constraint on $m(\tilde{t}_1)$. In such exclusion plots, the mass of the produced particle is shown on the x-axis, so the decrease in cross section with increasing mass will always cut off the exluded region in this direction. The neutralino (LSP) mass is plotted on the y-axis; as its value approaches that of the top-squark mass, the amount of missing transverse energy, $E_{\mathrm{T}}^{\mathrm{miss}} = |\vec{p}_{\mathrm{T}}^{\mathrm{miss}}|$, in an event is reduced, and the detection efficiency falls off correspondingly. Figure 3 (right) shows the exclusion regions from CMS Run 1 searches for the pair production of neutralinos and/or charginos in a variety of simplified models [7]. Such particles are referred to generically as "electroweakinos" (EWKinos).

Naturalness considerations arising from the gauge hierachy problem constrain only a subset of the SUSY particles [8]. These are $\tilde{t}_L$ and $\tilde{t}_R$ (or the mass eigenstates $\tilde{t}_1$ and $\tilde{t}_2$), $\tilde{b}_L$, $\tilde{g}$, and the Higgsinos, denoted by $\tilde{H}$. Other SUSY particles are not generically constrained to be light and are typically assumed to be heavy and decoupled from the physics. As a consquence, the minimal natural SUSY spectrum has relatively few particles, and such models are typically handled reasonably well in simplified-model frameworks, in which there are only 2–3 particles. Although "natural SUSY endures" [8] is still the dominant fashion, this paradigm is under considerable stress from Run 1 results [9]. In any case, while natural SUSY is a key focus of investigations, CMS and ATLAS searches are not limited to these scenarios.

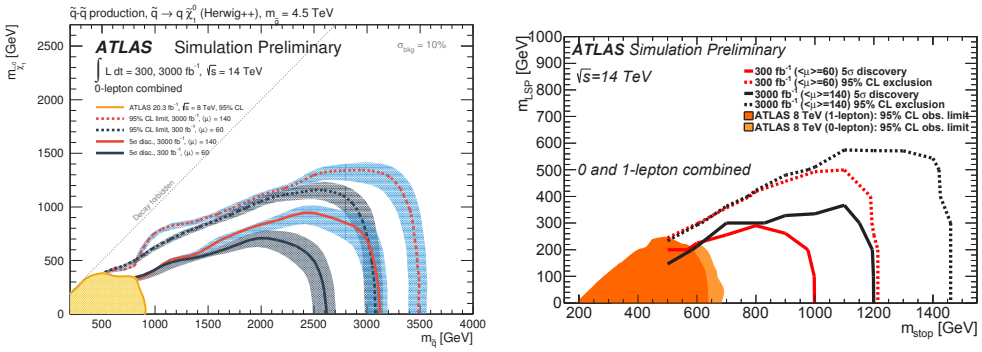

FIGURE 4. ATLAS estimates of the expected sensitivity to (left) squark-antisquark production (summed over eight states) [10] and (right) top squark + anti-top squark production [11] for samples with 300 fb^{-1} and 3000 fb^{-1}.

SUSY DISCOVERY REACH PROJECTIONS

In this section we consider ATLAS and CMS estimates of the sensitivity of future searches to SUSY particles with data samples from 300 fb^{-1} to 3000 fb^{-1}. Most of these studies use simulated event samples with parametrized detector performance descriptions and with background uncertainties that are either guessed (motivated by similar searches with 8 TeV data) or simply assumed. The searches usually employ very tight event selection criteria and operate on the extreme tails of the kinematic distributions of the SM backgrounds. In most but not all cases, the studies use simple, non-optimized methods, and it is best to regard the results as indicative and not to take them too literally.

We start with strong production processes. Figure 4 (left) shows the expected ATLAS sensitivity [10] from a search in the zero-lepton channel for squark pair production with the decay $\tilde{q} \to q\tilde{\chi}_1^0$, summing over cross sections for eight mass-degenerate squarks from the first and second generations. The event selection requires no leptons, 2–6 jets, large $E_{\mathrm{T}}^{\mathrm{miss}}$, and large m_{eff} (the sum of transverse momenta of the jets plus $E_{\mathrm{T}}^{\mathrm{miss}}$). With a sample of 3000 fb^{-1}, degenerate squarks with masses up to 3.1 TeV can be discovered at 5σ significance; squarks with masses up to 3.5 TeV can be excluded at 95% CL. Figure 4 (right) shows the estimated ATLAS sensitivity [11] from a simulated search for top-squark pair production. Here, two separate event selections are used, one requiring no leptons, ≥ 6 jets, ≥ 2 b-tagged jets, and large $E_{\mathrm{T}}^{\mathrm{miss}}$ and the other requiring 1 lepton, ≥ 4 jets, ≥ 1 b-tagged jet, and large $E_{\mathrm{T}}^{\mathrm{miss}}$. Top squarks with masses up to 1.2 TeV can be discovered at 5σ significance; the 95% CL exclusion curve excludes masses up to roughly 1.4 TeV. The results from the zero-lepton and one-lepton search channels have been combined.

Figure 5 shows the expected sensitivity of CMS and ATLAS to the pair production of EWKinos. The production of $\tilde{\chi}_1^{\pm}\tilde{\chi}_2^0$, with $\tilde{\chi}_1^{\pm} \to W^{\pm}\chi_1^0$ and $\tilde{\chi}_2^0 \to h\tilde{\chi}_1^0$, can be probed in a search for $Wh(bb) + E_{\mathrm{T}}^{\mathrm{miss}}$. Here, the signature includes a single lepton, a pair of b-tagged reconstructing to the Higgs-boson mass, and other kinematic variables such as $E_{\mathrm{T}}^{\mathrm{miss}}$. In a study based on full simulation, CMS [12] finds that, with 3000 fb^{-1}, the 5σ discovery sensitivity extends up to $m(\tilde{\chi}_1^{\pm}) = m(\tilde{\chi}_2^0) \approx 950$ GeV, where the masses of the produced chargino and neutralino are assumed to be equal for simplicity. The EWKino discovery reach is much larger than what would be obtained with only 300 fb^{-1}, where

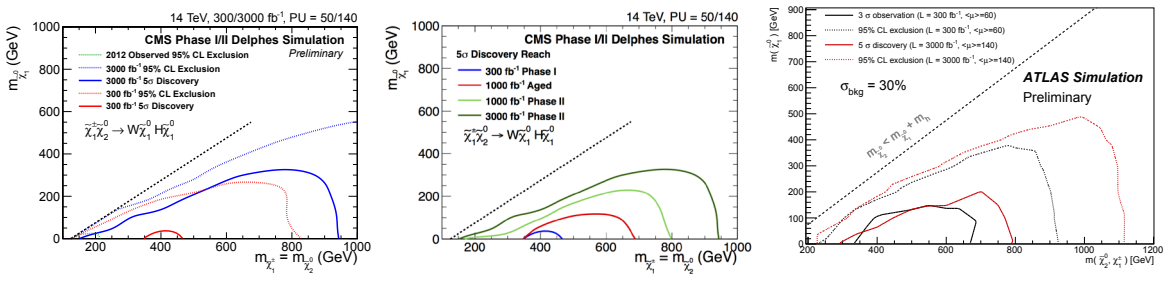

FIGURE 5. Estimated sensitivity to chargino-neutralino pair production from CMS [12] (left, middle) and ATLAS [13] (right).

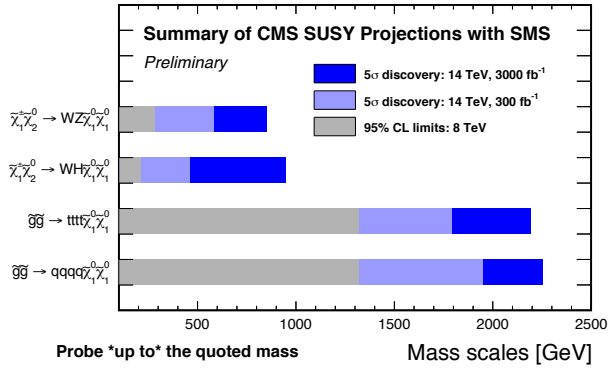

FIGURE 6. Summary of CMS SUSY mass reach projections [12] for integrated luminosities of 300 fb^{-1} and 3000 fb^{-1}. Results are given for simplified models involving EWKino pair production and gluino pair production.

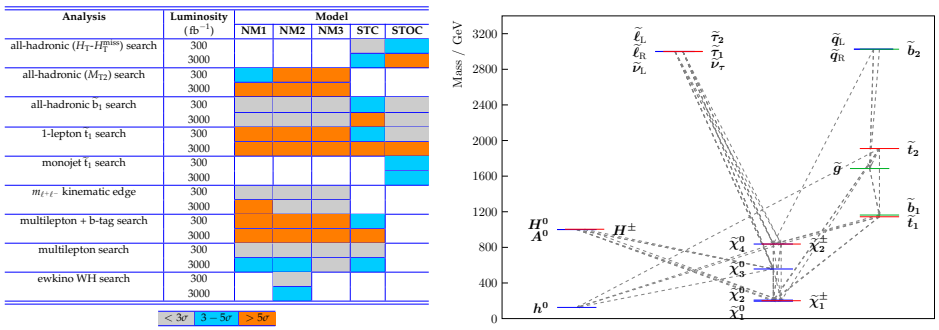

FIGURE 7. (Left) Summary of CMS study [12] of discovery scenarios in full-spectrum SUSY models. The color code indicates whether the observed significance would be $< 3\sigma$ (grey), $3 - 5\sigma$ (blue), or $> 5\sigma$ (orange) and is given for both 300 fb^{-1} and 3000 fb^{-1}. (Right) Mass spectrum for the NM3 model.

there is barely any reach at all. This situation is characteristic of electroweak (low cross section) production processes. Figure 5 (middle) shows the results of a related CMS study designed to assess the impact of using an aged detector through 1000^{-1} fb, as compared to an upgraded detector. It is clear that there are major gains in this search associated with the upgraded detector. Figure 5 (right) shows similar results from ATLAS [13]. The discovery reach of 800 GeV corresponds to a cut and count analysis; using a multivariate discriminator, the sensitivity is extended to 950 GeV. If $\tilde{\chi}_2^0 \rightarrow Z\tilde{\chi}_1^0$ instead of $h\tilde{\chi}_1^0$, the search is performed in the trilepton channel. ATLAS obtains [10] 5σ discovery sensitivity up to $m(\tilde{\chi}_1^{\pm}) = m(\tilde{\chi}_2^0) = 820$ GeV, assuming that the initial EWKinos are Winos.

Figure 6 summarizes the mass reach of CMS in several channels involving gluino pair production and EWKino pair production [12]. The discovery sensitivity for gluinos extends up to about 2.2 TeV with 3000 fb^{-1} and for neutralino/chargino pairs discovery sensitivity extends to about 1 TeV. The upper value of the mass shown corresponds to the reach achieved at low LSP mass. The largest relative increase in sensitivity with the 3000 fb^{-1} data sample is for the direct production of electroweak SUSY partners, because of their small production cross section. CMS finds that there is up to 500 GeV increase in discovery reach with the HL-LHC for chargino-neutralino production studied in the $Wh(bb) + p_{\mathrm{T}}^{\mathrm{miss}}$ final state. Thus, if strongly interacting SUSY partners are too heavy to be produced, EWKinos, which could be lighter, may still provide a window to SUSY at the HL-LHC.

DISCOVERY SCENARIOS WITH FULL-SPECTRUM SUSY MODELS

The observation of a significant excess event yield over the SM background contributions in a particular search channel would be tremendously exciting. The simplified model framework can be misleading, however, because the (very)

naive expectation is that an excess observed in a search for a particular process implies that the targeted process itself has been observed. This conlusion is, of course, not correct: an excess in a given search channel can arise from many different physics processes because typical SUSY search signatures are inclusive. To investigate the issue of how patterns of signals in different channels might be used to understand the origin of such excess event yields, CMS has studied [12] five full-spectrum SUSY models, performing analyses on nine separate signatures in parallel. The models are designated NM1, NM2, NM3 (natural models), STC (stau co-annihilation model), and STOC (stop co-annihilation model). For NM1-3, $m(\tilde{g}) = 1.7$ TeV and $m(\tilde{t}_1) = 1.1$ TeV. The branching fraction $B(\tilde{t} \to t\tilde{\chi}_1^0)$ is 0.6%, 1.5%, and 39%, respectively, in these models, due to differences in their electoweak sectors. In STC, $m(\tilde{\tau}_1) \approx m(\tilde{\chi}_1^0) \approx 190$ GeV, and in STOC, $m(\tilde{t}_1) \approx m(\tilde{\chi}_1^0) \approx 400$ GeV. A full description of each model is given in the references. NM1 includes the decay $\tilde{\chi}_2^0 \to \tilde{\ell}^{\pm}\ell^{\mp} \to \ell^+\ell^-\tilde{\chi}_1^0$, which generates the famous dilepton "edge" signature in the dilepton mass spectrum. In NM2, $\tilde{\chi}_1^{\pm}\tilde{\chi}_2^0$ production leads to a signature in the $Wh(bb) + E_{\mathrm{T}}^{\mathrm{miss}}$ final state. The STOC model is quite distinctive in that $\tilde{t}_1 \to c\tilde{\chi}_1^0$ proceeds with a branching fraction of nearly 100% because of the small mass splitting.

Figure 7 (left) shows, in color-coded form, the expected significance for each of the different experimental signatures investigated, while Fig. 7 (right) shows the mass spectrum for NM3. The patterns of significances show that very different amounts of data are required to obtain the full "fingerprint" of a given model. Furthermore, partly because there are no mass peaks in the SUSY signatures, the interpretation of even a full pattern of excess event yields is a complex matter. Thus, the discovery of a SUSY-related excess could well be very different from that for the Higgs boson, where the interpretation came very rapidly. Here, a discovery could involve multiple 3-4 σ excesses, rather than a single 5σ excess, and confirmation and interpretation could require many years of investigation at the HL-LHC.

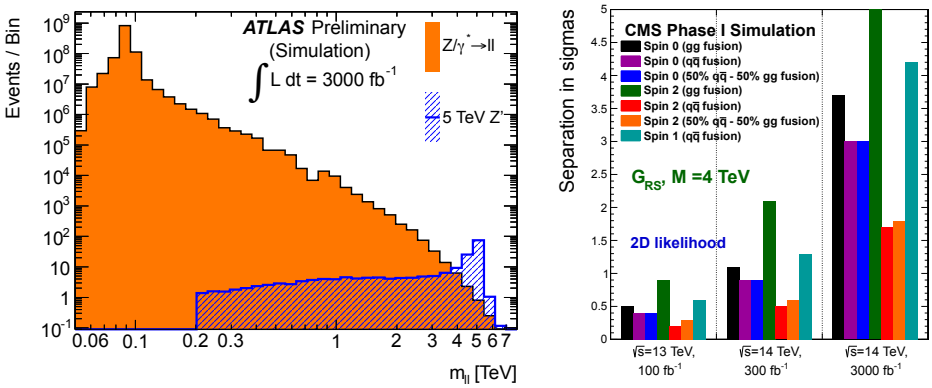

FIGURE 8. Studies of sensitivity to dilepton resonances in simulated event samples: (left) ATLAS study [16] of a sequential-standard-model (SSM) Z' boson and (right) CMS study [18] of spin determination for a Randall-Sundrum ($J = 2$) graviton.

EXOTIC PARTICLE SEARCHES

ATLAS and CMS have performed a broad range of studies to assess the discovery reach with high luminosity samples and to undertand the impact of detector performance on exotica searches. The areas investigated include dilepton and di-top resonances, dark matter, R-parity violating and stealth SUSY, degenerate Higgsinos, heavy stable charged particles, long-lived particles with displaced vertices, and more [14, 15, 16, 17]. Here we briefly consider dilepton resonance searches, which are sensitive to a variety of BSM scenarios. Figure 8 (left) shows the distribution of $m(\ell^+\ell^-)$ from ATLAS [16] for a simulated dilepton resonance search with 3000 fb^{-1}. One can exclude (95% CL) a sequential standard model Z boson (Z'_{SSM}), which has the same couplings at the SM Z boson, up to a mass of around 8 TeV. While this coupling scenario is not considered to be a highly motivated physics scenario, it is a standard physics benchmark. Figure 8 (right) shows the results of a CMS study [18] of how well one can determine the spin of such a resonance, assuming that its mass is 4 TeV. At this mass, one would obtain a few events with 100 fb^{-1} and 100-400 events with 3000 fb^{-1}. The figure shows the separation (in units of σ) between the true hypothesis, in this case a $J = 2$ Randall-Sundrum graviton, and a variety of other spin 0, 1, and 2 hypotheses. It is clear that the HL-LHC data sample provides extremely valuable information in this study.

CONCLUSIONS

Just as Columbus first "discovered" America by finding several islands in the Caribbean Sea, the observation of the top quark, and the W, Z, and Higgs bosons may just be the first sightings at the TeV scale. Full exploration of this scale will likely require a broad, multi-decade physics program.

ACKNOWLEDGMENTS

I would like to thank the organizers of LHCP2015 for a congenial and superbly organized conference. I would also like to thank experts from ATLAS and CMS who generously provided suggestions on many issues: from ATLAS, Jamie Boyd, Tommaso Lari, Tobias Golling, Koji Terashi, and Stephane Willocq; from CMS, Juan Alcaraz, Barbara Clerbaux, Daniele del Re, Kerstin Hoepfner, Filip Moortgat, Dominick Olivito, Laurent Thomas, and Keith Ulmer.

REFERENCES

[1] J. L. Feng, "Naturalness and the Status of Supersymmetry," Ann. Rev. Nucl. Part. Sci. **63**, 351 (2013) doi:10.1146/annurev-nucl-102010-130447.
[2] ATLAS Collaboration, "The ATLAS experiment at the CERN LHC", JINST 3:S08003, 2008.
[3] CMS Collaboration, "The CMS experiment at the CERN LHC", JINST 3:S08004, 2008.
[4] C. Borschensky, M. Krämer, A. Kulesza, M. Mangano, S. Padhi, T. Plehn and X. Portell, "Squark and gluino production cross sections in pp collisions at $\sqrt{s}$ = 13, 14, 33 and 100 TeV," Eur. Phys. J. C **74**, no. 12, 3174 (2014) doi:10.1140/epjc/s10052-014-3174-y.
[5] D. Alves *et al.* [LHC New Physics Working Group Collaboration], "Simplified Models for LHC New Physics Searches," J. Phys. G **39**, 105005 (2012) doi:10.1088/0954-3899/39/10/105005.
[6] ATLAS Collaboration, "ATLAS Run 1 searches for direct pair production of third-generation squarks at the Large Hadron Collider," Eur. Phys. J. C **75**, no. 10, 510 (2015) doi:10.1140/epjc/s10052-015-3726-9.
[7] CMS Collaboration, https://twiki.cern.ch/twiki/pub/CMSPublic/PhysicsResultsSUS/EWKino_ICHEP2014_2.pdf, based on CMS Collaboration, "Searches for electroweak production of charginos, neutralinos, and sleptons decaying to leptons and W, Z, and Higgs bosons in pp collisions at 8 TeV," Eur.P̃hys.J̃.C̃74 (2014) 9, 3036, DOI: 10.1140/epjc/s10052-014-3036-7 and CMS Collaboration, "Searches for electroweak neutralino and chargino production in channels with Higgs, Z, and W bosons in pp collisions at 8 TeV" Phys.Rev. D90 (2014) 9, 092007, DOI: 10.1103/PhysRevD.90.092007.
[8] M. Papucci, J. T. Ruderman and A. Weiler, "Natural SUSY Endures," JHEP **1209**, 035 (2012) doi:10.1007/JHEP09(2012)035.
[9] N. Craig, "The State of Supersymmetry after Run I of the LHC," Lectures delivered at the training week of the GGI workshop "Beyond the Standard Model after the first run of the LHC." arXiv:1309.0528 [hep-ph].
[10] ATLAS Collaboration, "Search for Supersymmetry at the high luminosity LHC with the ATLAS Detector," ATL-PHYS-PUB-2014-010, CDS 1735031.
[11] ATLAS Collaboration, "Prospects for benchmark Supersymmetry searches at the high luminosity LHC with the ATLAS Detector," ATL-PHYS-PUB-2013-011, CDS 1604505.
[12] CMS Collaboration, "Supersymmetry discovery potential in future LHC and HL-LHC running with the CMS detector," CMS-PAS-SUS-14-012, CDS 1981344.
[13] ATLAS Collaboration, "Prospect for a search for direct pair production of a chargino and a neutralino decaying via a W boson and the lightest Higgs boson in final states with one lepton, two b-jets and missing transverse momentum at the high luminosity LHC with the ATLAS Detector," ATL-PHYS-PUB-2015-032, CDS 2038565.
[14] CMS Collaboration, "Technical Proposal for the Phase-II Upgrade of the Compact Muon Solenoid," CERN-LHCC-2015-010, CDS 2020886.
[15] ATLAS Collaboration, "Sensitivity to WIMP Dark Matter in the Final States Containing Jets and Missing Transverse Momentum with the ATLAS Detector at 14 TeV LHC," ATL-PHYS-PUB-2014-007, CDS 1708859.
[16] ATLAS Collaboration, "Studies of Sensitivity to New Dilepton and Ditop Resonances with an Upgraded ATLAS Detector at a High-Luminosity LHC," ATL-PHYS-PUB-2013-003, CDS 1516108.
[17] ATLAS Collaboration, "Dijet resonance searches with the ATLAS detector at 14 TeV LHC," ATL-PHYS-PUB-2015-004, CDS 2002136.
[18] CMS Collaboration, Physics Performance for the 2nd ECFA Workshop, https://twiki.cern.ch/twiki/pub/CMSPublic/PhysicsResultsFP/ECFA-CMSPublicResults.pdf.

Proceedings of the LHCP2015 Conference, St. Petersburg, Russia, August 31 - September 5, 2015

Editors: V.T. Kim and D.E. Sosnov

Heavy Flavour prospects at the HL-LHC

DENIS DERKACH[1,2]

[1]*National Research University Higher School of Economics, 20 Myasnitskaya Ul., Moscow, 101000, Russia*
[2]*Yandex School of Data Analysis, 11/2, Timura Frunze St., Moscow 119021, Russia.*

Denis.Derkach@cern.ch

On behalf of the ATLAS, CMS and LHCb Collaborations

Abstract. The development of flavour physics has been impetuous in recent years: there have been discoveries of CP violation in different B-meson systems, detailed studies of mixing effects in neutral B and D mesons, and observation of rare decays with unprecedented sensitivities. New discoveries can be expected for larger samples available in the near future. In these proceedings, future upgrades in the LHC detectors will be discussed.

INTRODUCTION

Searches of the physics beyond the Standard Model of elementary particles (SM), commonly known as New Physics (NP) searches, can be performed either directly or indirectly. The direct searches, a domain of the general purpose detectors, aim at discovering particles not included into the SM spectrum by its direct observation. The indirect searches instead look for virtual effects of unknown particles which might influence measurable quantities and alter their values with respect to SM predictions. Depending on the NP model under consideration, indirect searches can probe energy scales much larger than those accessible by direct searches [1].

The last fifteen years have been a golden age for flavour physics. Hundreds of experimental analyses and theoretical articles lead to a tremendous success of the CKM picture [2, 3]. This is clearly apparent in an overall agreement of all experimental constraints shown in Fig. 1, taken from Ref. [4] and updates online.

UPGRADE

In the next years, the LHC detectors will pass through some major upgrades that would allow new and more precise results to be obtained. The first upgrade will happen already after run 2 for LHCb, while ATLAS and CMS will make a large upgrade after run 3. The expected luminosity is shown in Table 1. An important fact for flavour physics is that the $b-\bar{b}$ cross-section is roughly doubled passing from the center-of-mass energy of 7 TeV to 14 TeV. The extrapolation of the detector performances is done using the results available from run 1. The full description of the impact of the ATLAS and CMS upgrades is described in Refs. [5] and [6], respectively.

TABLE 1. Cumulative integrated luminosity that will be collected by the ATLAS, CMS, and LHCb experiment by the ends of the runs given.

		LHC era			HL-LHC era	
Experiment	Run period Center-of-mass energy Years	Run 1 7,8 TeV 2010-2012	Run 2 13 TeV 2015-2018	Run 3 14 TeV 2020-2022	Run 4 14 TeV 2025-2028	Run 5 14 TeV 2030+
ATLAS, CMS		25 fb^{-1}	100fb^{-1}	300fb^{-1}		3000fb^{-1}
LHCb		3fb^{-1}	8fb^{-1}	23fb^{-1}	46fb^{-1}	100fb^{-1}

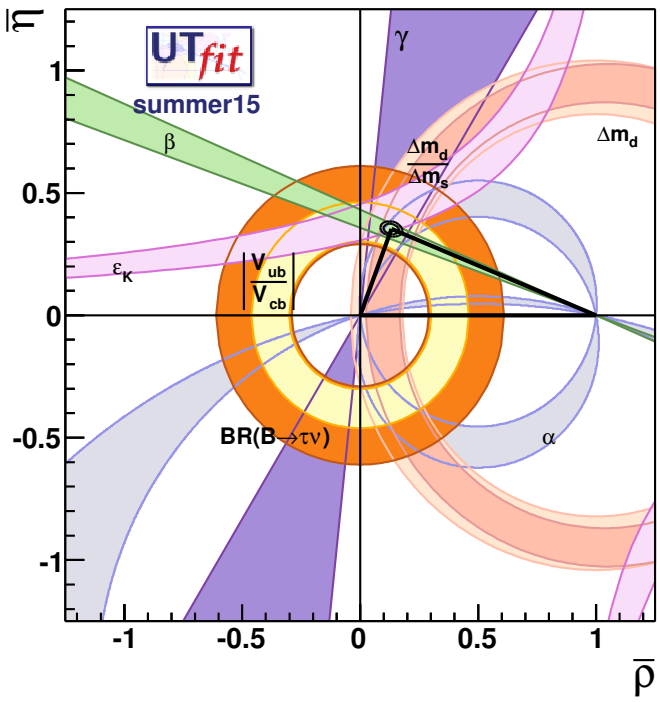

FIGURE 1. Determination of the Unitarity triangle apex within the SM. The two elliptical contours around the apex of the triangle correspond to 68% and 95% probability regions. The colored regions correspond to 95% probability for each single constraint. The analysis is performed using bayesian approach [4].

For the ATLAS experiment, in addition to the much higher number of events which will be available, a particularly important consideration should be done for the extensive upgrade programme to the inner tracking detector, which will have a very significant impact on flavour physics measurements. During run 2 ATLAS operates IBL, the inner tracker contains a fourth layer added to the present Pixel Detector between a new beam pipe and the current inner pixel layer (B-layer). The Phase-II upgrade of the ATLAS detector will allow operation at five times the nominal LHC luminosity. It is expected that these upgrades will affect B meson proper time resolution. The results of the simulations can be seen in Fig. 2.

The CMS experiment is expected to be completely refurbished with enhancements to the muon system and a new inner tracker, with improved granularity, to cope with average occupancy resulting from 140 interactions expected per bunch crossing. In particular, the new inner tracker system is expected to have L1 tracking capabilities, in order to reconstruct efficiently all tracks above 2 GeV p_T. The muon system will also have improved coverage in the forward direction and extended trigger capabilities. With the changes envisioned it is possible to maintain the same efficiency in triggering and analysis as we have achieved up until now.

The new tracker detector will feature 4 pixel barrel layers and 5 disks on either endcaps. The outer tracker material budget will diminish by roughly a factor of 2 in the central region ($|\eta| < 1$) and about a factor of 3 in the intermediate region around $1.2 < |\eta| < 1.5$. This, combined with a smaller silicon sensors pitch will improve the momentum resolution by about a factor of 1.5 in the barrel region ($|\eta| < 1.4$) and 1.2 elsewhere.

LHCb will undergo one major upgrade [7] between now and after run 2 running up to 2028 to allow the operation of the detector at a luminosity of up to $2 \times 10^{33} \mathrm{cm}^{-2}\mathrm{s}^{-1}$. The detector upgrade consists of a complete redesign of the readout system and the trigger in order to read out the full detector at the bunch crossing rate, and perform a full software trigger to select efficiently the relevant heavy-flavour decay chains. All silicon detectors will be upgraded. In addition the aerogel will be removed from RICH1 since it gives too few photons to actually allow reconstructing the rings in the higher multiplicities of the upgrade.

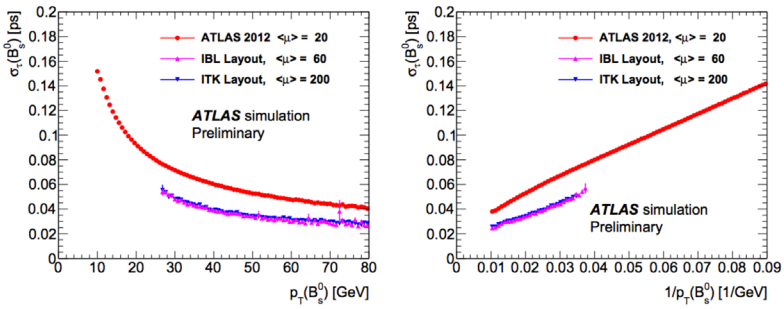

FIGURE 2. B_s^0 proper decay time resolution as a function of transverse momentum p_T of the B_s^0 meson, shown for three detector layouts: current ATLAS layout and pileup conditions of 2012 (red), IBL ATLAS layout with average number of pileup events, $< \mu >= 60$ (magenta) and ITK layout with, $< \mu >= 200$ (blue). The vertical axis gives an average value of per-candidate proper decay time errors for B_s^0 candidates within the p_T bin. Left and right plots are equivalent; the horizontal axis shows p_T in the left plot, and $1/p_T$ in the right plot.

BENCHMARK CHANNELS

In the following, I will briefly describe several important measurements that will be a benchmark of future upgrades: search for $B_{d,s} \to \mu\mu$, $B_d \to K^*\mu\mu$, mixing-induced CP violation in B_s, tree-level determination of the CKM angle γ.

The $B_{d,s} \to \mu\mu$ channel is one of the major players restricting the SUSY parameter space [8]. A joint observation of the $B_s \to \mu\mu$ decay has been published by LHCb and CMS [9] was published recently. The resulting branching fractions are:

$$\mathcal{B}(B_s \to \mu\mu) = \left(2.78\,^{+0.66}_{-0.60}(\text{stat})\,^{+0.27}_{-0.18}(\text{syst})\right) \times 10^{-9}, \quad (1)$$

$$\mathcal{B}(B_d \to \mu\mu) = \left(3.94\,^{+1.58}_{-1.41}(\text{stat})\,^{+0.31}_{-0.24}(\text{syst})\right) \times 10^{-10}, \quad (2)$$

with significances of 6.2 and 3.2 σ, respectively. An example of the expected sensitivities from CMS collaboration is shown in Table 2. The expected $B_{s,d} \to \mu\mu$ candidate invariant mass distribution can be seen in Fig. 3 corresponding to the end of run 3 and run 5.

TABLE 2. Number of expected events for $B_s \to \mu\mu$ and $B_d \to \mu\mu$ decays at CMS corresponding to different values of integrated luminosities. We also report the expected uncertainty in the branching fraction measurement for the $B_s \to \mu\mu$ and $B_d \to \mu\mu$, the range of significance of $B_d \to \mu\mu$ (the range indicates the $\pm 1\sigma$ of the distribution of significance), and the relative uncertainty on the B_d to B_s branching fractions.

$\mathcal{L}$, fb^1	No. of B_s	No. of B_d	$\delta\mathcal{B}/\mathcal{B}(B_s \to \mu\mu)$	$\delta\mathcal{B}/\mathcal{B}(B_d \to \mu\mu)$	B_d sign.	$\delta\left(\mathcal{B}(B_d \to \mu\mu)/\mathcal{B}(B_s \to \mu\mu)\right)$
20	16.5	2.0	35%	> 100%	0.01.5 σ	> 100%
100	144	18	15%	66%	0.52.4 σ	71%
300	433	54	12%	45%	1.33.3 σ	47%
3000	2096	256	12%	18%	5.47.6 σ	21%

An important decay that is expected to be sensitive to NP contributions is the decay $B_s \to J\psi\phi$. CP violation in the $B_s \to J\psi\varphi$ decay occurs due to interference between direct decays and decays proceeding through B_s-$\bar{B}_s$ mixing. The oscillation frequency of B_s meson mixing is characterized by the mass difference ΔM_s of the heavy and light mass eigenstates. The CP-violating phase ϕ_s is defined as the weak phase difference between the B_s-$\bar{B}_s$ mixing amplitude and the $b \to c\bar{c}s$ decay amplitude. In the SM the phase ϕ_s is small and can be related to CKM quark mixing matrix elements V_{ij} via the relation $\phi_s \approx 2\beta_s$, where $\beta_s = \arg\left(-(V_{ts}V_{tb}^*)/(V_{cs}V_{cb}^*)\right)$.

This analysis is very demanding to the detector and reconstruction performance as it requires not only good determination of the signal decay chain but also the high performance of the flavour tagging algorithm (i.e. the determination of initial b-flavour of the B_s meson). This is particular hard due to the high center-of-mass energy and pile up in the future runs.

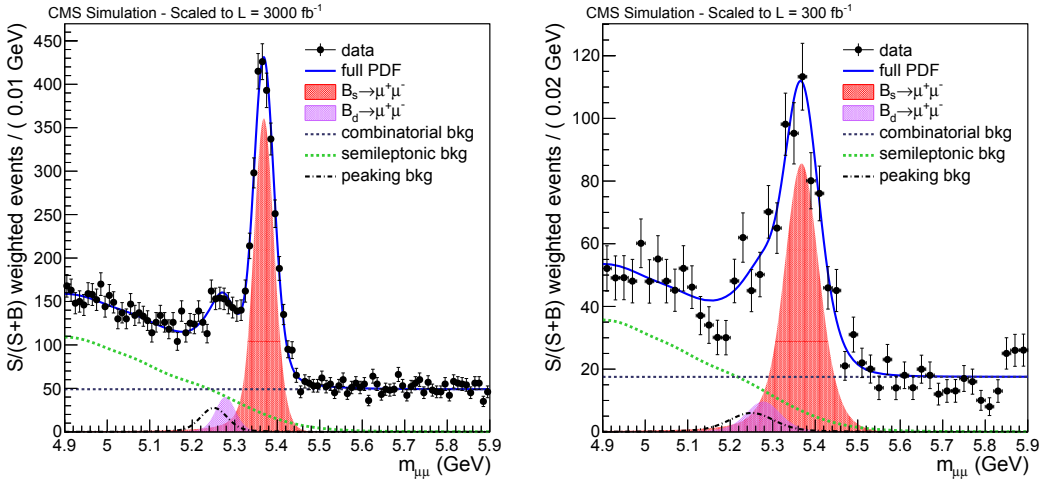

FIGURE 3. Fit results of the invariant mass distribution for 300 $^{-1}$ and 3000 fb^{-1} of the CMS simulated sample. The improvement in the mass resolution for the 3000 $^{-1}$ projection is expected from an improved inner tracker system and removing endcap candidates

ATLAS [10], CMS [11], and LHCb [12] carried out the analysis on the full data sets available for run 1. The realtive sensitivities of the various experiments can be seen in the HFAG compilation [13] shown in Fig. 4. The current experimental average is $\phi_s = -34 \pm 33$ mrad, compatible to the global fits prediction, $2\beta_s = 36.3^{+1.2}_{-1.4}$ mrad [14].

A dedicated study was performed by ATLAS to estimate sensitivity on the ϕ_s by the end of future runs. The study included the variation of the detector performance with the upgrade and the harsher conditions of the various runs. The results are reported in Table 3

TABLE 3. Estimated ATLAS statistical precision on ϕ_s for the considered LHC periods.

Year	2011	2012	2015-17		2019-21	2023-30+
Detector	current	current	IBL		IBL	ITK
Average interactions per BX $< \mu >$	6-12	21	60		60	200
Luminosity, fb^{-1}	4.9	20	100		250	3000
Signal events per fb^{-1}	4400	4320	3280	460	460	330
Signal events	22000	86400	327900	45500	114000	810 000
Total events in analysis	130000	550000	1874000	284000	758000	6461000
MC $\sigma(\phi_s)$ (stat.), rad	0.25	0.12	0.054	0.10	0.064	0.022

While channels with muons are generally considered as a mixed domain of ATLAS/CMS and LHCb, the fully hadronic channels are instead a prerogative of LHCb. Here the possibility to trigger on hadronic particles is particularly important. This is one of the main reasons for the forthcoming LHCb trigger upgrade [15].

Amongst other interesting measurement, the measurement of the CKM angle γ is attracting a lot of attention from the experimental community. This angle is one of the least known parameters of the unitarity triangle. The various measurements use B meson decays into $D^{(*)}_{(s)}K^{(*)}$ and $D^{(*)}\pi$ final states which have no penguin contribution. There is an important difference from most of other measurements of the unitarity triangle angles. These processes are theoretically clean provided that hadronic unknowns are determined from experiment. The LHCb experiment has already provided a number of analyses, which, combined with results from the B factories results, give the unprecedented precision of 7° [4], to be compared to the SM prediction of $(69 \pm 3)°$. The LHCb combination [16] gives $\gamma = (73^{+9}_{10})°$ and this will greatly improve owing to the next runs.

The LHCb experiment is expected to play a crucial role in the flavour physics programme of LHC. Expected sensitivities on several key flavour observables are reported in Table 4.

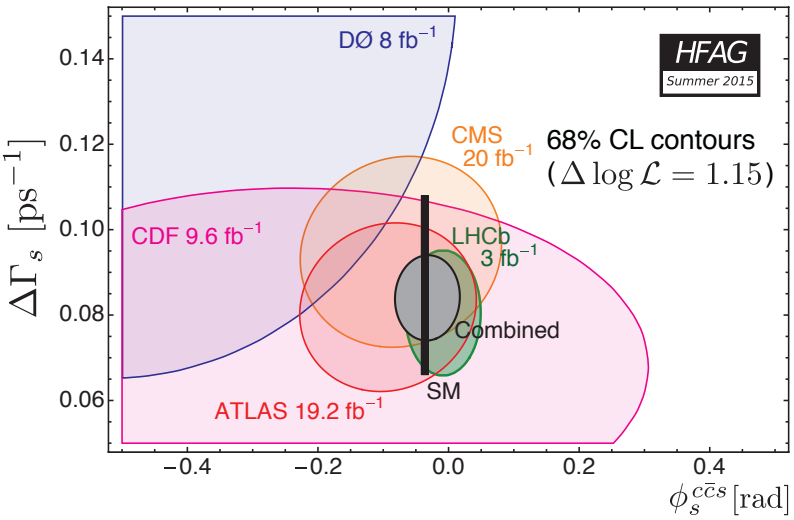

FIGURE 4. Individual contours of ATLAS, CMS, CDF, D0 and LHCb measurements, their combined contour (grey area) and the SM predictions (thin black rectangle). The prediction for ϕ_s is taken as the indirect determination of $2\beta_s$ via a global fit to experimental data within the SM.

TABLE 4. Statistical sensitivities of the LHCb upgrade to key observables. For each observable the current sensitivity is compared to that which will be achieved by LHCb before the upgrade, and that which will be achieved with 50fb^{1} by the upgraded experiment. Systematic uncertainties are expected to be non-negligible for the most precisely measured quantities.

Type	Observable	LHC Run 1	LHCb 2018	**LHCb upgrade**	Theory
B_s^0 mixing	$\phi_s(B_s^0 \to J/\psi\phi)$ (rad)	0.050	0.025	**0.009**	~ 0.003
	$\phi_s(B_s^0 \to J/\psi\, f_0(980))$ (rad)	0.068	0.035	**0.012**	~ 0.01
	$A_{\rm sl}(B_s^0)$ (10^{-3})	2.8	1.4	**0.5**	0.03
Gluonic	$\phi_s^{\rm eff}(B_s^0 \to \phi\phi)$ (rad)	0.15	0.10	**0.023**	0.02
penguin	$\phi_s^{\rm eff}(B_s^0 \to K^{*0}\bar{K}^{*0})$ (rad)	0.19	0.13	**0.029**	< 0.02
	$2\beta^{\rm eff}(B^0 \to \phi K_S^0)$ (rad)	0.30	0.20	**0.04**	0.02
Right-handed	$\phi_s^{\rm eff}(B_s^0 \to \phi\gamma)$	0.20	0.13	**0.030**	< 0.01
currents	$\tau^{\rm eff}(B_s^0 \to \phi\gamma)/\tau_{B_s^0}$	5%	3.2%	**0.8%**	0.2 %
Electroweak	$S_3(B^0 \to K^{*0}\mu^+\mu^-; 1 < q^2 < 6\,{\rm GeV}^2/c^4)$	0.04	0.020	**0.007**	0.02
penguin	$q_0^2\, A_{\rm FB}(B^0 \to K^{*0}\mu^+\mu^-)$	10%	5%	**1.9%**	$\sim 7\%$
	$A_{\rm I}(K\mu^+\mu^-; 1 < q^2 < 6\,{\rm GeV}^2/c^4)$	0.09	0.05	**0.017**	~ 0.02
	$\mathcal{B}(B^+ \to \pi^+\mu^+\mu^-)/\mathcal{B}(B^+ \to K^+\mu^+\mu^-)$	14%	7%	**2.4%**	$\sim 10\%$
Higgs	$\mathcal{B}(B_s^0 \to \mu^+\mu^-)$ (10^{-9})	1.0	0.5	**0.19**	0.3
penguin	$\mathcal{B}(B^0 \to \mu^+\mu^-)/\mathcal{B}(B_s^0 \to \mu^+\mu^-)$	220%	110%	**40%**	$\sim 5\,\%$
Unitarity	$\gamma(B \to D^{(*)}K^{(*)})$	7°	4°	**1.1°**	negligible
triangle	$\gamma(B_s^0 \to D_s^{\mp}K^{\pm})$	17°	11°	**2.4°**	negligible
angles	$\beta(B^0 \to J/\psi\, K_S^0)$	1.7°	0.8°	**0.31°**	negligible
Charm	$A_\Gamma(D^0 \to K^+K^-)$ (10^{-4})	3.4	2.2	**0.5**	–
CP violation	ΔA_{CP} (10^{-3})	0.8	0.5	**0.12**	–

CONCLUSIONS

The hunt for NP at the LHC is entering a new era with the great experience gained by the community from run 1. The CMS, ATLAS, and LHCb detectors have already given a lot of important results in the flavour physics sector. The present performances of the detectors and their planned upgrades lead to very promising estimations of the sensitivities for the HL-LHC phase.

REFERENCES

[1] M. Bona *et al.* (UTfit), JHEP **03**, p. 049 (2008), arXiv:0707.0636 [hep-ph] .

[2] N. Cabibbo, *Meeting of the Italian School of Physics and Weak Interactions Bologna, Italy, April 26-28, 1984*, Phys. Rev. Lett. **10**, 531–533 (1963), [,648(1963)].

[3] M. Kobayashi and T. Maskawa, Prog. Theor. Phys. **49**, 652–657 (1973).

[4] M. Ciuchini, G. D'Agostini, E. Franco, V. Lubicz, G. Martinelli, F. Parodi, P. Roudeau, and A. Stocchi, JHEP **07**, p. 013 (2001), arXiv:hep-ph/0012308 [hep-ph] .

[5] "ATLAS B-physics studies at increased LHC luminosity, potential for CP-violation measurement in the B0s J/ decay," Tech. Rep. ATL-PHYS-PUB-2013-010 (CERN, Geneva, 2013).

[6] "CMS reach in B[s] to dimuon and B to dimuon branching fractions for the new LHC runs," Tech. Rep. CMS-PAS-FTR-13-022 (CERN, Geneva, 2013).

[7] "Letter of Intent for the LHCb Upgrade," Tech. Rep. CERN-LHCC-2011-001. LHCC-I-018 (CERN, Geneva, 2011).

[8] S. R. Choudhury and N. Gaur, Phys. Lett. **B451**, 86–92 (1999), arXiv:hep-ph/9810307 [hep-ph] .

[9] V. Khachatryan *et al.* (LHCb, CMS), Nature **522**, 68–72 (2015), arXiv:1411.4413 [hep-ex] .

[10] J. Walder, "B-physics and quarkonium highlights and recent results from ATLAS," in *CERN seminar* (2015).

[11] V. Khachatryan *et al.* (CMS), (2015), arXiv:1507.07527 [hep-ex] .

[12] R. Aaij *et al.* (LHCb), Phys. Rev. Lett. **114**, p. 041801 (2015), arXiv:1411.3104 [hep-ex] .

[13] Y. Amhis *et al.* (Heavy Flavor Averaging Group (HFAG)), (2014), arXiv:1412.7515 [hep-ex] .

[14] J. Charles *et al.*, Phys. Rev. **D84**, p. 033005 (2011), arXiv:1106.4041 [hep-ph] .

[15] "LHCb Trigger and Online Upgrade Technical Design Report," Tech. Rep. CERN-LHCC-2014-016. LHCB-TDR-016 (CERN, Geneva, 2014).

[16] D. Derkach, T. M. Karbach, and M. Kenzie (LHCb), "Improved constraints on γ: CKM2014 update," in *8th International Workshop on the CKM Unitarity Triangle (CKM 2014) Vienna, Austria, September 8-12, 2014*, CERN (CERN, 2014. Geneva, 2014).

[17] "Flavour tagged time dependent angular analysis," Tech. Rep. ATLAS-CONF-2013-039 (CERN, Geneva, 2013).

[18] I. Bediaga *et al.* (LHCb), "Framework TDR for the LHCb Upgrade: Technical Design Report," Tech. Rep. CERN-LHCC-2012-007. LHCb-TDR-12 (CERN, Geneva, 2012).

Future Colliders: parallel talks

Proceedings of the LHCP2015 Conference, St. Petersburg, Russia, August 31 - September 5, 2015

Editors: V.T. Kim and D.E. Sosnov

Future Circular Collider Study (FCC)

TOBIAS GOLLING

Université de Genève, 24, Quai Ernest-Ansermet - CH-1211 Genève 4 - Switzerland

Tobias.Golling@unige.ch

Abstract. The status and plans for the Future Circular Collider (FCC) design study are presented. The ultimate goal, and the emphasis for the infrastructure, is a proton-proton machine operating at a center-of-mass energy of 100 TeV in a 100-km ring in the Geneva area, called FCC-hh. A stepping stone to this machine is a high-luminosity electron-positron collider (called FCC-ee) using the same ring with center-of-mass energies ranging from the Z pole to the $t\bar{t}$ threshold. The main goal is an extended search for physics beyond the Standard Model as well as a complete exploration of the Higgs boson and its dynamics.

INTRODUCTION

The LHC Run 1 gave us the Higgs bosons discovery [1], Run 2 is in full swing, and with the High Luminosity upgrade the LHC has a physics program until the year 2035. What is the next leap forward in collider physics? Are there physics opportunities beyond the LHC? The Future Circular Collider (FCC) design study explores the post-LHC particle accelerator options in a global context. It entails an in-depth analysis of infrastructure, operation concepts and technologies necessary to build such a future circular collider. The physics opportunities are evaluated for a proton-proton machine operating at a center-of-mass energy of 100 TeV (FCC-hh) and a high-luminosity electron-positron collider (FCC-ee) with center-of-mass energies ranging from the Z pole to the $t\bar{t}$ threshold. Both would use the same ring, with a circumference of about 100 km, to be built in the Geneva area at CERN. There is also an option for an electron-proton collider (FCC-he), which would in particular allow one to resolve the proton structure and associated parton distribution functions more than one order of magnitude deeper into matter than what HERA could do.

The FCC collaboration is currently composed of 68 institutes and 26 countries [2] (status of December 2015). A conceptual design report will be delivered before the end of 2018, in time for the next update of the European Strategy for Particle Physics.

The FCC study started officially in the beginning of 2014 with a Future Circular Collider Study Kick-Off Meeting at the University of Geneva [3]. Annual Meetings of the Future Circular Collider study (FCC Weeks) [4, 5] are planned once a year until the conceptual design report in 2018.

It appears early to start the FCC activities now with the collider community fully focused on LHC's Run 2 and the phase-2 detector research and development and construction activities ramping up. But history shows that large-scale projects like the LHC take about 20 years from the first design through construction up to the first physics results. If the goal is to have a first version of the FCC ready in 2035 then its preparation has to start now. In fact many workshops and meetings take place where FCC detector needs and physics benchmarks are discussed [6]. This ongoing activity can be followed on indico, see for instance Ref. [7] regarding the FCC-hh physics and detector activities. In this report a few selected and representative physics benchmarks studies will be given to illustrate the ongoing activities.

FCC-hh vs. LHC and FCC-ee vs. LEP

A collider's center-of-mass energy is proportional to the dipole magnetic field and the radius. In order to achieve a center-of-mass energy of 100 TeV, which is about one order of magnitude higher than the LHC's design energy of 14 TeV an increase in the radius by a factor of about 4 and an increase in the dipole magnetic field by a factor of about 2 are envisioned. The ultimate goal for the integrated luminosity of the FCC-hh is 10-20 ab^{-1}. More information is given in Tables 1 and 2, which show the currently considered design parameters for the FCC-hh and FCC-ee, respectively.

TABLE 1. Design parameters of the FCC-hh in comparison with LHC.

Parameter	FCC-hh	LHC
Center-of-mass energy [TeV]	100	14
Dipole field [T]	16	8.33
Number of interaction points (IP)	2 main, +2	4
Luminosity/IP$_{main}$ [10^{34}cm^{-2}s^{-1}]	5 - 25	1
Stored energy/beam [GJ]	8.4	0.39
Synchrotron radiation [W/m/aperture]	28.4	0.17
Bunch spacing [ns]	25 (5)	25

TABLE 2. Design parameters of the FCC-ee in comparison with LEP2.

Parameter	FCC-ee	FCC-ee	FCC-ee	LEP2
Center-of-mass energy [GeV]	90	240	350	210
Bunches/beam	13000 - 60000	500 - 1400	51 - 98	4
Beam current [mA]	1450	30	6.6	3
Luminosity/IP [10^{34}cm^{-2}s^{-1}]	21 - 280	5 -11	1.5 - 2.6	0.0012
Energy loss/turn [GeV]	0.03	1.67	7.55	3.34
Synchrotron power [MW]	100	100	100	22
RF voltage [GV]	0.3 - 2.5	3.6 - 5.5	11	3.5

FCC-ee physics program

The FCC-ee's core physics program [8] is composed of Standard-Model precision measurements at center-of-mass energies between 90 and 350 GeV:

- the Z pole scan at a center-of-mass energy from 88 to 95 GeV allows one to make precision measurements of the mass m_Z and width Γ_Z of the Z boson down to 100 keV, $\alpha_s(m_Z)$ down to 10^{-4}, $\alpha_{QCD}(m_Z)$ down to $2\ 10^{-5}$, as well as to study rare decays and flavor physics with up to 10^{13} Z bosons, including e.g. the search for right-handed neutrinos.
- the WW threshold scan at a center-of-mass energy from 160 to 165 GeV provides an unprecedented precision of the W boson mass measurement to a level of 300 keV and $\alpha_s(m_W)$ to 10^{-4}.
- the running scheme as a Higgs factory with a center-of-mass energy of 240 GeV and above is probably the centerpiece of the FCC-ee. It will considerably improve over the High Luminosity LHC precision on the Higgs couplings by an order of magnitude and allow for a measurement of the Higgs width to better than 1%, as well as the Higgs branching ratio to invisible particles down to 0.1%.
- the $t\bar{t}$ threshold scan at a center-of-mass energy from 340 to 350 GeV makes a measurement of the top quark mass possible with a precision of 10-20 MeV, as well as a $t\bar{t}Z$ coupling measurement in the sub-percent area.

FCC-ee Higgs physics program

The so-called recoil method is unique to lepton colliders and allows one to tag the Higgs event independent of the Higgs boson decay mode. Figure 1 shows the distribution of the mass recoiling against the lepton pair in the $e^+e^- \rightarrow HZ$ channel, in the $Z \rightarrow l^+l^-$ final state ($l = e, \mu$) corresponding to one year of data taking [9]. A fit is used to extract the number of Higgs boson events which allows one to measure the total $e^+e^- \rightarrow HZ$ production cross section with a precision of 0.4%.

Another unique measurement of FCC-ee is about the Higgs production in the s-channel which allows on measure directly the Higgs coupling to electrons, using various Higgs bosons decays modes. Preliminary studies predict sensitivity approaching the Standard Model Higgs-to-electron coupling with an integrated luminosity of order 10 ab^{-1} [10].

FCC-hh physics program

The FCC-hh physics program is essentially composed of three pillars:

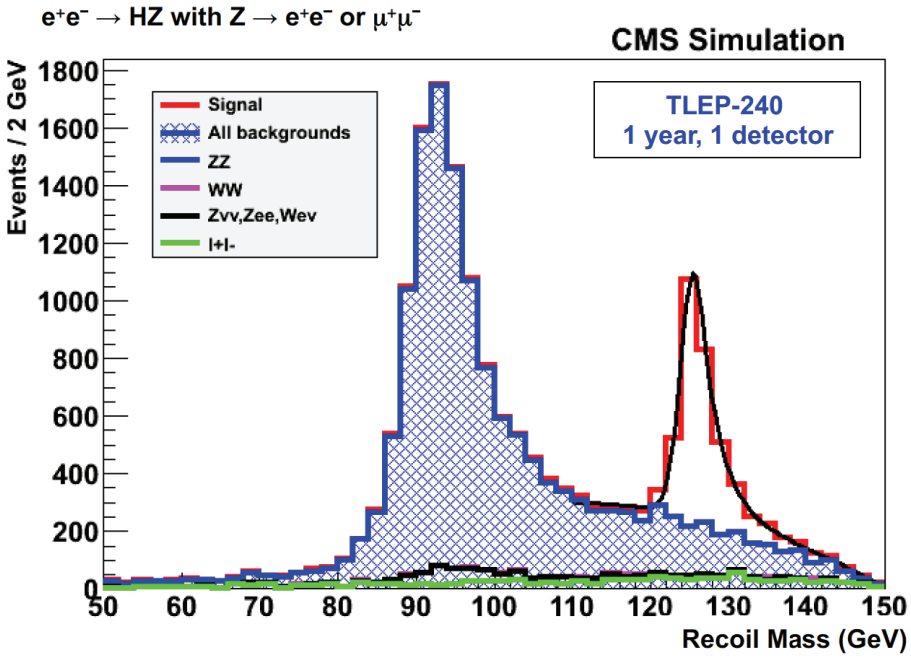

FIGURE 1. Distribution of the mass recoiling against the lepton pair in the $e^+e^- \to HZ$ channel, in the $Z \to l^+l^-$ final state ($l = e, \mu$), taken from Ref. [9], for an FCC-ee integrated luminosity equivalent to approximately one year of data taking at a center-of-mass energy of 240 GeV.

- direct searches for new high-mass physics objects as predicted by extensions of the Standard Model such as Supersymmetry or Composite Higgs models
- direct searches for rare new physics processes
- indirect probes of new physics by testing Standard Model predictions with high luminosity and rates

FCC-hh and naturalness

The so-called hierarchy problem, also known as the naturalness problem, has been the driving force over the past decades for the design of extensions of the Standard Model. The FCC-hh is a game changer regarding this pressing open question in the sense that the absence of new physics at the 100 TeV FCC-hh would correspond to a fine-tuning of the order of 10^{-4} - this is a level of tuning never seen in particle physics and according to N. Arkani-Hamed a "mortal blow to naturalness" [11].

FCC-hh - Supersymmetry and Dark Matter

Supersymmetry spectra with a pure wino LSP can be realized if anomaly mediation is the main mechanism through which the gaugino soft masses are generated. This scenario leads to small mass splittings between the chargino and neutralino of less than 1 GeV, which leads to the so-called disappearing-track signature. Extrapolations from corresponding ATLAS searches to the FCC-hh environment [12] show sensitivity to WIMPs well beyond 1 TeV in mass as can be seen in Figure 2.

In Ref. [13] a variety of Supersymmetry Simplified Models are studied with focus on strong production using final state signatures of jets + missing transverse energy, mono-jet signatures, or same-sign di-lepton approaches. In particular Table 21 of Ref. [13] compares the exclusion and discovery reach for the 14 TeV LHC and the 100 TeV FCC-hh, quantifying the extended reach. For instance assuming 3000 fb^{-1} of integrated luminosity, a gluino that decays to light flavor quarks can be discovered below 2.3 TeV at the 14 TeV LHC and below 11 TeV at a 100 TeV machine.

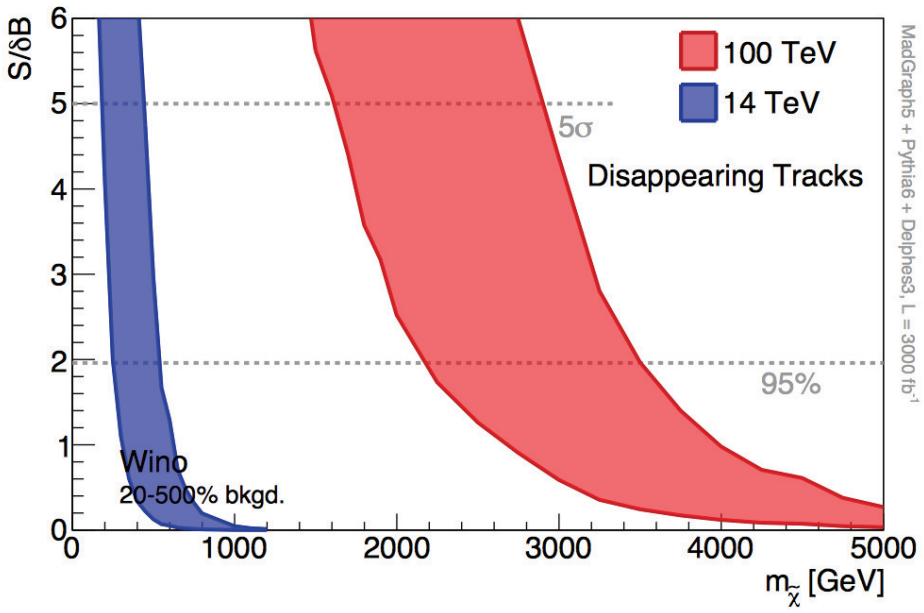

FIGURE 2. The mass reach in the pure wino scenario in the disappearing track channel with an integrated luminosity of 3000 fb^{-1} for the 14 TeV LHC and a 100 TeV proton-proton collider. The bands are generated by varying the background normalization between 20 - 500% [12].

FCC-hh and other Exotics Physics

The search for high-mass resonances is motivated by various new physics models, including models with Extra Dimension or a Composite Higgs boson. Here one example is given for the search of resonances decaying to dijets. Ongoing studies [14] quantify the discovery potential as a function of the mass of a color singlet vector resonance assuming a relative width of 1% and universal couplings to fermions. Figure 3 shows the dependence of the discovery reach on the detector energy resolution, assuming an integrated luminosity of 10 ab^{-1}. For an assumed jet energy detector resolution of 1% the discovery reach extends to resonance masses of about 35 TeV, while an assumed 10% detector resolution reduces this reach by about 10 TeV. As can be seen from this example, physics benchmarks represent a crucial input for the choice of the detector design.

Many hypothesized high-mass resonances are expected to decay to top quarks, W, Z or H bosons. The hadronic decays of these Standard Model particles have high branching fractions and the associated fully-hadronic final states are most promising to extend the discovery potential to the highest masses. The interesting p_T range of these so-called "superboosted" top quarks, W, Z or H bosons extends to the multi-TeV range which brings new challenges and opportunities [15].

FCC-hh precision physics program

The direct searches for new physics are complemented with a strong FCC-hh precision physics program. Compared to the LHC's center-of-mass energy of 14 TeV the Higgs production cross sections increase by at least a factor of 10 at 100 TeV, up to a factor of 42 for di-Higgs production and a factor of 61 for $t\bar{t}H$ production [10], resulting in FCC-hh Higgs data sets which are a factor of 10-400 larger than at the High Luminosity LHC. The FCC-hh Higgs physics program is largely complementary to the FCC-ee Higgs physics program and allows in particular to measure the top-Yukawa coupling with %-level precision.

The top quark offers another big opportunity for the FCC-hh to carry out precision measurements and probing rare decays with 10^{12} top quarks expected in 10 ab^{-1} at 100 TeV, and associated 10^{12} bottom hadrons and W bosons from the top quark decay. Furthermore searches for rare decays are made possible using a few times 10^{11} charm hadrons from the W boson decays from the top quark, as well as 10^{11} τ leptons from the W boson decays from the top quark, including e.g. searches for $\tau \to 3\mu$ or $\tau \to \mu\gamma$. This top quark physics program makes high demands on the

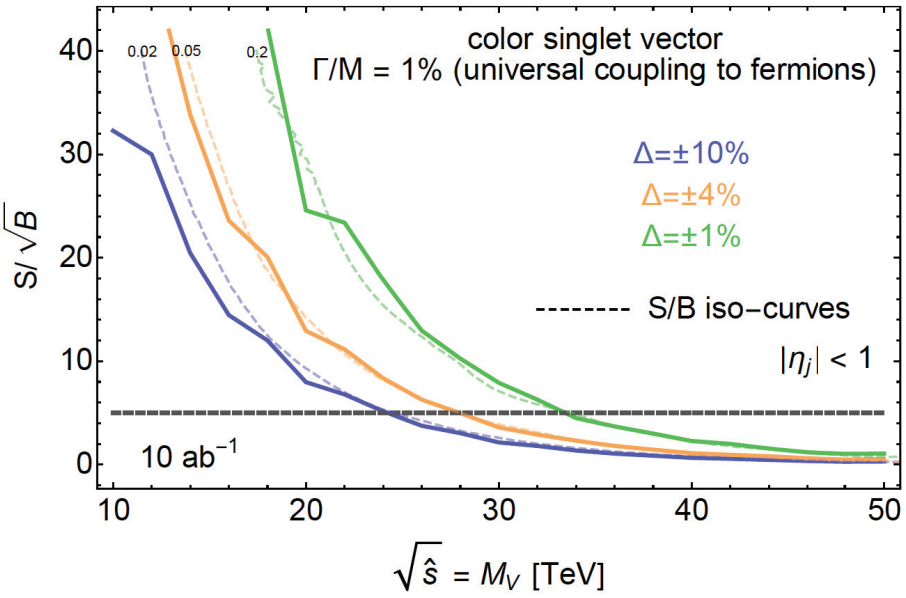

FIGURE 3. Discovery potential for a resonance assumed to decay to dijets, as a function of the resonance mass, assuming three different detector resolution scenarios, see text and Ref. [14] for more details.

detector capabilities regarding in particular reconstructed physics objects with a p_T in the range of 0.1-1 TeV.

Challenges for physics with 100 TeV proton-proton collisions

The exploration of physics beyond the Standard Model using proton-proton collisions with a center-of-mass energy of 100 TeV bears unprecedented challenges. In order to contain the highest p_T jets (of tens of TeV) fully in the hadronic calorimeter a depth of at least 12 λ is necessary. A calorimeter lateral segmentation in ηxϕ of 0.05x0.05 or 0.025x0.025 is currently considered. This resolution is mainly driven by the needs to mitigate pileup and to measure the jet substructure for superboosted top quarks, W, Z and H bosons with transverse momenta in the multi-TeV range. Another challenge is the momentum resolution for multi-TeV muons. The size of the ATLAS detector [16], for instance, is driven by the size of the muon system with the goal to measure the transverse momentum of muons with $p_T = 1$ TeV with a 10% uncertainty, resulting in a diameter of ATLAS of about 25 m. Scaling this up to muons of $p_T = 10$ TeV with a similar target uncertainty pushes the size of the detector and of the magnetic field beyond feasibility and alternative strategies are needed and are being developed. Not only the design of the calorimeter and the muon system manifest challenges for the reconstruction of multi-TeV objects, but also the tracking system. Identification of b-jets or tau leptons with a p_T well beyond the 1-TeV level has never been done before at a collider experiment. More generally, the high boost of Standard Model particles results in very collimated objects and makes high demands on tracking capabilities in very dense environments. The aforementioned physics benchmarks are used to specify the detector and identification needs. A fast simulation of different detector configurations and a close collaboration between physics analysis and detector design is crucial in this phase of the study.

Conclusion

This document just gives a glimpse of the ongoing activities to explore the physics opportunities for the FCC. A lot of work is still needed to complete a conceptual design report by the end of 2018. People interested in contributing are very welcome and are invited to contact the author or other organisers or conveners, see contacts e.g. in Ref. [6].

ACKNOWLEDGMENTS

The author wishes to thank Alain Blondel and Michelangelo Mangano for helpful input and discussions.

REFERENCES

[1] ATLAS Collaboration, "Observation of a new particle in the search for the Standard Model Higgs boson with the ATLAS detector at the LHC," Phys. Lett. B **716**, 1 (2012) doi:10.1016/j.physletb.2012.08.020 [arXiv:1207.7214 [hep-ex]]; CMS Collaboration, "Observation of a new boson at a mass of 125 GeV with the CMS experiment at the LHC," Phys. Lett. B **716**, 30 (2012) doi:10.1016/j.physletb.2012.08.021 [arXiv:1207.7235 [hep-ex]].

[2] https://fcc.web.cern.ch/Pages/default.aspx

[3] Future Circular Collider Study Kickoff Meeting, Geneva, 12-15 February 2014, https://indico.cern.ch/event/282344/

[4] First Annual Meeting of the Future Circular Collider study, Washington, DC, 23-29 March 2015, http://indico.cern.ch/event/340703/overview

[5] Second Annual Meeting of the Future Circular Collider study, Rome, 11-15 April 2016, http://fccw2016.web.cern.ch/fccw2016/

[6] https://twiki.cern.ch/twiki/bin/view/LHCPhysics/FutureHadroncollider (and hyperlinks on this twiki)

[7] https://indico.cern.ch/category/5258/

[8] M. Bicer et al., "First look at the physics case of TLEP", Journal of High Energy Physics 01 (2014) 164.

[9] P. Azzi, C. Bernet, C. Botta, P. Janot, M. Klute, P. Lenzi, L. Malgeri and M. Zanetti, "Prospective Studies for LEP3 with the CMS Detector," arXiv:1208.1662 [hep-ex].

[10] M. Klute, "Higgs physics at the FCC", talk presented at EPS-HEP2015, Vienna, 22-29 July 2015.

[11] N. Arkani-Hamed, "Energy frontier after the Higgs discovery", talk presented at the FCC kick-off meeting, Geneva, 12-15 February 2014.

[12] M. Low and L. T. Wang, "Neutralino dark matter at 14 TeV and 100 TeV," JHEP **1408**, 161 (2014) doi:10.1007/JHEP08(2014)161 [arXiv:1404.0682 [hep-ph]].

[13] T. Cohen, T. Golling, M. Hance, A. Henrichs, K. Howe, J. Loyal, S. Padhi and J. G. Wacker, "SUSY Simplified Models at 14, 33, and 100 TeV Proton Colliders," JHEP **1404**, 117 (2014) doi:10.1007/JHEP04(2014)117 [arXiv:1311.6480 [hep-ph]].

[14] R. Torre, "High mass resonances: reach and detector requirements," talk presented at Higgs & BSM at 100 TeV meeting, CERN, 12 March 2015, http://indico.cern.ch/event/352868/session/6/contribution/17/material/slides/

[15] S. Bressler, T. Flacke, Y. Kats, S. J. Lee and G. Perez, "Hadronic Calorimeter Shower Size: Challenges and Opportunities for Jet Substructure in the Superboosted Regime," arXiv:1506.02656 [hep-ph].

[16] ATLAS Collaboration, "The ATLAS Experiment at the CERN Large Hadron Collider," JINST **3**, S08003 (2008). doi:10.1088/1748-0221/3/08/S08003

Proceedings of the LHCP2015 Conference, St. Petersburg, Russia, August 31 - September 5, 2015

Editors: V.T. Kim and D.E. Sosnov

Three Stages of The NICA Accelerator Complex Nuclotron-based Ion Collider fAcility

V.D. KEKELIDZE[1], R. LEDNICKY[1], V.A. MATVEEV[1], I.N. MESHKOV[1,a)], A.S. SORIN[1] and G.V. TRUBNIKOV[1]

[1] *Joint Institute for Nuclear Resdearch, 141980 Dubna, Russia*

[a)] Corresponding author: meshkov@jinr.ru

Abstract. The project of Nuclotron-based Ion Collider fAcility (NICA) is under development at JINR (Dubna). The general goals of the project are providing of colliding beams for experimental studies of both hot and dense strongly interacting baryonic matter and spin physics (in collisions of polarized protons and deuterons). The first program requires running of heavy ion mode in the energy range of $\sqrt{s_{NN}} = 4 \div 11$ GeV at average luminosity of $L = 1 \cdot 10^{27}$ cm^{-2}·s^{-1} for $^{197}Au^{79+}$ nuclei. This stage of the project will be preceded with fixed target experiments on heavy ion beam extracted from *Nuclotron* at kinetic energy up to 4.5 GeV/u. The polarized beams mode is proposed to be used in energy range of $\sqrt{s_{NN}} = 12 \div 27$ GeV (protons) at luminosity up to $1 \cdot 10^{32}$ cm^{-2}·s^{-1}. The report contains a brief description of the facility scheme and characteristics in heavy ion operation mode, the description of the MultiPurpose Detector (*MPD*) and characteristics of the reactions of the colliding ions, which allow us to detect the mixed phase formation. Status and plans of the project development are presented.

INTRODUCTION: THE NICA PROJECT AT JINR

The NICA project is aimed to develop, construct and commission at Joint Institute for Nuclear Research (Dubna, Russia) a modern accelerator complex Nuclotron-based Ion Collider fAcility (NICA) equipped with two detectors MultiPurpose Detector (*MPD*) & Spin Physics Detector (*SPD*) and perform experiments on search of the mixed phase of baryonic matter state and nature of nucleon/particle spin.

A study of hot and dense baryonic matter should shed light on: in-medium properties of hadrons and nuclear matter equation of state; onset of deconfinement and/or chiral symmetry restoration; phase transition, mixed phase and critical end-point; possible local parity violation in strong interactions [1]. It is indicated in series of theoretical works, in particular, in [2] that heavy ion collisions at $\sqrt{s_{NN}} \leq 11$ GeV in the lab system allow to reach the highest possible baryon density.

A project NICA aimed to study hot and dense baryonic matter and spin physics is under development as a flagship project at JINR in high energy physics. In addition to the beams extracted from the *Nuclotron* the project foresees a construction of collider facility providing experiments in collider mode at the energy range of $\sqrt{s_{NN}} = 4 \div 11$ GeV for $^{197}Au^{79+}$ with the luminosity up to $L = 1 \cdot 10^{27}$ cm^{-2}·s^{-1}.

The NICA will also provide the polarized proton and deuteron beams up to the c.m.s. energy of 27 GeV for *pp* collisions with the luminosity higher than $L = 1 \cdot 10^{32}$ cm^{-2}·s^{-1}. The high intensity and high polarization (> 50%) of the colliding beams open up a unique possibility for spin physics research, which is of crucial importance for the solution of the nucleon spin problem ("spin puzzle") — one of the main tasks of the modern hadron physics.

The comparison of the parameters of the NICA accelerator complex with the existing and being developed machines of heavy ions and polarized beams shows that NICA does fit to the research goals formulated above.

NICA — STAGE I

Nuclotron facility consists today of the *"Old injector"* and the *Nuclotron*.

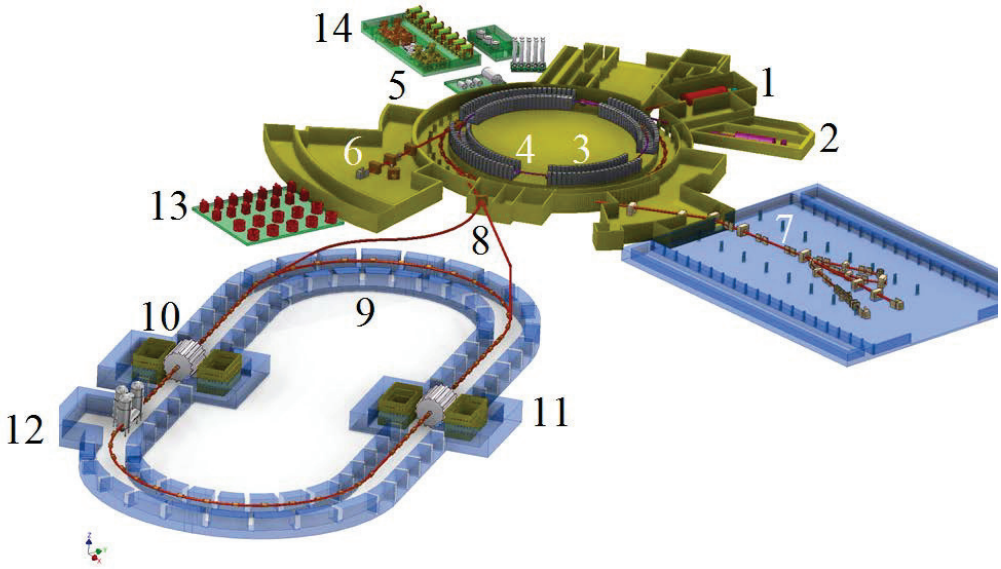

FIGURE 1. Scheme of NICA facility. Description on the text

The *"Old injector"* contains set of light ion sources including source of polarized protons and deuterons and Alvarez-type linac LU-20 (Fig. 1, pos. 1).

Nuclotron is SC proton synchrotron (Fig. 1, pos. 5) that has maximum magnetic rigidity of 45 T·m and the circumference of 251.52 m. It can provide the acceleration of completely stripped $^{197}Au^{79+}$ ions up to the experiment energy in the range of 1÷4.5 GeV/u and protons up to maximum energy of 12.6 GeV. It is used presently for fixed target experiments with extracted beams and experiments with internal target. The program includes experimental studies on relativistic nuclear physics, spin physics in few body nuclear systems (with polarized deuterons) and physics of flavours. The part of this program, *"The Baryonic Matter at Nuclotron"* (BM@N) is under development presently.

The development of the Stage I of the NICA project will be completed with construction of the *"New injector"* and the *Booster-synchrotron* and commissioning of the BM@N detector.

"New injector" (Fig. 1, pos. 2) is under construction. It contains ESIS-type ion source that provides $^{197}Au^{31+}$ ions of the intensity of $2 \cdot 10^9$ ions per pulse of about 7 μs duration at repetition rate of 10 Hz and heavy ioin linear accelerator (HILac) consisting of RFQ and RFQ Drift Tube Linac sections. The linac accelerates the ions at $A/Z \leq 8$ up to the energy of 3.2 MeV/u at efficiency not less than 80% (A, Z are ion mass and charge numbers). It has been delivered by BEVATECH Company (Germany) in 2014–2015 and is under commissioning presently. It will be complementary to that one to be performed at *Collider* in heavy ion beam mode.

Housed inside the Synchrophasotron yoke (Fig. 1, pos. 3), the *Booster-synchrotron* (Fig. 1, pos. 4) has superconducting (SC) magnetic system that provides maximum magnetic rigidity of 25 T·m at the ring circumference of 215 m. It is equipped with electron cooling system constructed by Budker INP. It allows us to provide cooling of the ion beam in the energy range from injection energy up to 100 MeV/u. The maximum energy of $^{197}Au^{31+}$ ions accelerated in the *Booster* is of 600 MeV/u. *Stripping foil* placed in the ion transfer line from the *Booster* to the *Nuclotron* provides the stripping efficiency at the maximum *Booster* energy not less than 80%. The *Booster* elements are under manufacturing and machine is planned to be commissioned in 2017.

Besides, the *Nuclotron* beams are used for research in radiobiology and applied research. Moreover, the *Nuclotron* is very good facility for testing of the *Collider* equipment and operational regimes, elements and prototypes for the *MPD* using extracted beams ($^{12}C^{6+}$ ions at 3.5 GeV/u and deuterons at 4 GeV/u presently). Particularly, in the run #45 (Feb. 2012) the circulation of 3.5 GeV/u deuteron beam during 1000 seconds was demonstrated. During 2011-2013 the first version of stochastic cooling system was designed, constructed and tested at *Nuclotron* at ion kinetic energy of 3.5 GeV/u with deuteron and carbon ($^{12}C^{6+}$) ion beams. This work was performed in close collaboration with the Forschungszentrum Julich. The results will be used also for design of the stochastic cooling system for the High-Energy Storage Ring (HESR, FAIR).

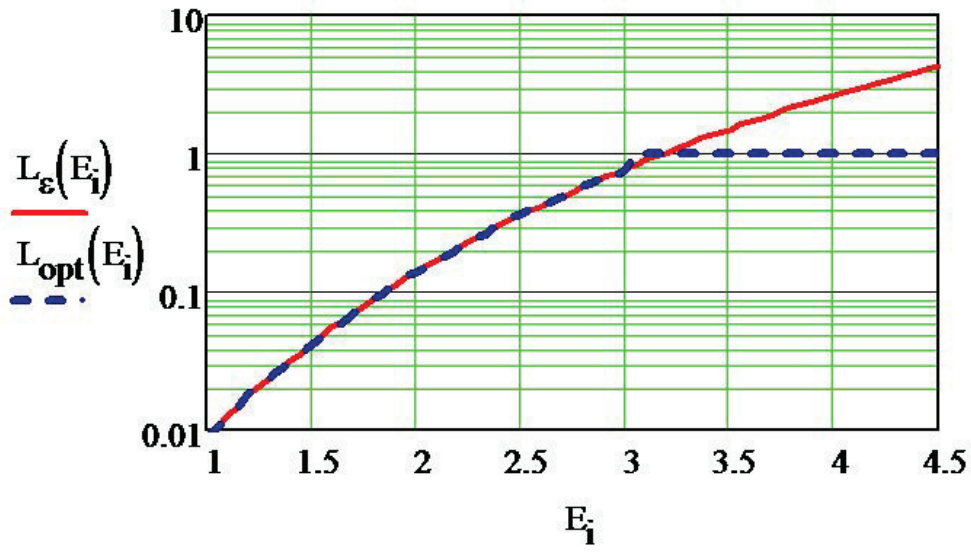

FIGURE 2. Project luminosity (10^{27} cm$^{-2}\cdot$s^{-1}) of the NICA *Collider* vs ion kinetic energy per nucleon (GeV/u); two modes: ion number per bunch is limited by the ion bunch space charge ($L_\epsilon(E_i)$, solid curve) and is optimized (dashed line, $L_{opt}(E_i)$)

Two transfer lines transport particle beams extracted from *Booster* (Fig. 1, pos. 6) and *Nuclotron* (Fig. 1, pos. 7) to research areas, where fixed target experiments both of basic and applied character will be set.

NICA — STAGE II

The Stage II of the NICA project includes construction of the *Collider*, the beam transfer line from *Nuclotron* to *Collider* and the MultiPurpose Detector (*MPD*). *The transfer line* (Fig. 1, pos. 8) will transports the particles from *Nuclotron* to *Collider* rings. The line is at the design stage presently.

Two SC Collider rings (Fig. 1, pos. 9) of racetrack shape have maximum magnetic rigidity of 45 T·m and the circumference of 503 m. The maximum field of SC dipole magnets is of 1.8 T. For luminosity preservation electron and stochastic cooling systems are constructed. The *Collider* design is in progress; the prototypes of its magnets have been fabricated and tested in 2013; the mass production is scheduled for 2016–2018.

Two detectors — the MultiPurpose Detector (*MPD*, Fig. 1, pos. 10) and the Spin Physics Detector (*SPD*, Fig. 1, pos. 11) are located in the opposite straight sections of the racetrack rings. The *MPD* is being designed presently; prototypes of the subdetectors are under construction and testing. The *SPD* is under conceptual design and is planned to be constructed at Stage III.

The electron cooler of electron energy of 0.5 ÷ 2.5 MeV will be placed in special building (Fig. 1, pos. 12).

Cryogenics and auxiliary equipment supply facility (Fig. 1, pos. 13, 14) provides LHe, LN2, electric power and cooling water to feed the accelerator complex and detectors.

The NICA parameters allow us to reach the project luminosity (Fig. 2).

THE *MPD*

The *MPD* [4] is a typical collider detector based on the solenoidal superconducting magnet (Fig. 3): with a magnetic field of 0.66 T (6.623 m in diameter and 9.010 m in length). The major sub-detectors of the *MPD* are the time projection chamber (TPC); inner tracker (IT); time-of-flight (TOF) system; electromagnetic calorimeter (ECal); end cap tracker (ECT), and two forward spectrometers based on toroidal magnets (optional). Three stages of putting *MPD* into operation are foreseen. The first stage of operation involves the magnet, TPC, TOF, ECal and IT (partially).

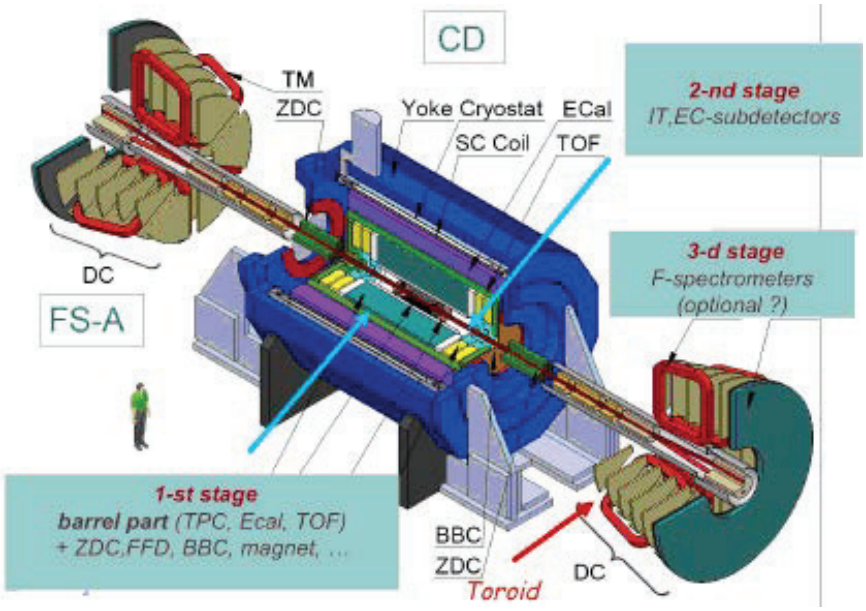

FIGURE 3. General view of the *MPD*, and sets of sub-detectors to be put in operation at different stages

The *MPD* experiment should be competitive and at the same time complementary to ones carried out at RHIC [5], and constructed in the frame work of FAIR [6] project.

There are several *MPD* detection tasks that should be fulfilled first [1]. Observation of the *elliptic flow of the secondary particles in the momentum space* does manifest a collective behavior of the *central fireball matter*.

A detailed measurement of the well-known "Horn effect" can give information about peculiarity of the heavy ion collisions. The effect was observed in experiments where energy dependence of the multiplicity ratio $R = \langle K^+/\pi^+ \rangle$ was measured at the pseudorapidity $y^* \approx 0$ (i.e. at the scattering angle $\theta \approx \pi/2$). Non-monotonic dependence of the $R(0)$ ratio on energy can be regarded as an indication of the *onset of deconfinement*.

A lot of information can be obtained from detection of leptons and photons. Leptons result from decays of mesons like π, ρ, ω, φ, J/ψ, and others, which give rise to e^+e, $\mu^+\mu^-$, ν_e, ν_μ (the latter are undetectable for the *MPD*). They provide the information about the QGP-phase structure. Detection of photons gives us the QGP temperature.

Very convincing are the fluctuations of the collision products parameters. They are "a sign" of the mixed phase formation. Indeed, the system becomes unstable at the two-phase stage (as in a classic process of boiling water — a flow of bubbles fluctuates tremendously). The idea is to locate the critical point using correlation/fluctuation of experimental data, e.g. dispersion and higher momenta of $R(0)$: $D = \langle (R - \langle R \rangle)^2 \rangle$, $M_{3R} = \langle (R - \langle R \rangle)^3 \rangle$ and higher, and fluctuations of other parameters of the collision reactions. None that the experiment at RHIC at a high ion energy $\sqrt{s_{NN}} = 200$ GeV/u gave zero result: $D_R = M_{3R} = \ldots = M_{6R} = 0$. An attempt to detect the fluctuations at low energy (Beam Energy Scan, BES) failed due to lack of statistics (low luminosity of the RHIC).

The measurement of the charge asymmetry WRT reaction plane characterizes *electric dipole moment of QCD matter* and is a possible signature of *strong parity violation*.

Processes studied with *MPD* were simulated using the dedicated software framework (MpdRoot). Evaluated rate in Au+Au collisions at $\sqrt{s_{NN}} = 7$ GeV (10% central interactions) at the luminosity of 10^{27} cm^{-2}·s^{-1} is of the order of 7 kHz. The *MPD* performance meets in general the required parameters for proposed experimental program.

THE STAGE III — POLARIZED IONS AND *SPD*

The polarized beam mode of NICA is being implemented in two steps. The first is acceleration of polarized deuterons at the *Nuclotron*, which has been performed since the 1990s. This beam is used in fixed target experiments, and the beam intensity will be increased with commissioning the new Source of Polarized Particles by the end of 2015. The second step is development of the *Collider* lattice for storing polarized beams and keeping them circulating in the

collider mode. This work is at the design stage.

The *SPD* will be constructed in the second IP. Its elaboration is also postponed to the second phase of the NICA project. Nevertheless, the *SPD* concept is formulated and creation of motivated collaboration has been started.

START-UP VERSION OF THE NICA PROJECT

Very important and hard task of the NICA project development is to begin its commissioning at the end of 2019. It is planned to be done in a reduced version of the facility and its elements parameters. Nevertheless, this will allow us to start experiments in colliding beams mode with the test and tuning of the *MPD* detector and the majority of the accelerators elements.

The start-up version of the NICA assumes the following.

1. An increased length of colliding beams bunches equal to $\sigma_{bunch} = 0.6$ m that provides the "concentration" of the luminosity at the inner tracker area of the *MPD*.
2. Maximum ion number per bunch is limited by the value of the betatron tune shift $\Delta Q \leq 0.05$.
3. Maximum emittance of the colliding bunches does not exceed 1.1 π mm·mrad; ratio of the horizontal emittance to the vertical one and the momentum spread of the ions is defined by the equilibrium state of the bunches in presence of the intrabeam scattering (IBS).
4. The bunch number per ring is limited by the requirement of avoiding of the parasitic collisions and is equal to $n_{bunch} = 22$.
5. RF systems consist of the barrier voltage system ("RF-1") and the RF system of the 3^{rd} harmonics of the revolution frequency ("RF-2"). RF-1 is used for storage in the *Collider* rings of the injected ions, RF-2 is used for formation of the bunched ion beams where each 3rd separatrix is filled with the ions. The square of the separatrix of the RF-2 is by 25 times larger of the longitudinal r.m.s. emittance of the bunch.
6. For suppression of the IBS one colling system will be constructed — namely, stochastic cooling system for longitudinal degree of freedom (the "filter method").

As result, maximum peak luminosity can be provided at the level of $5 \cdot 10^{25}$ cm^{-2}·s^{-1} at the energy of the $^{197}Au^{79+}$ ions in the range of $3 \div 4.5$ GeV/u.

CONCLUSION

The main characteristics of NICA project, its status and principle problems related to the NICA creation are considered in this report. The NICA project as a whole has passed the phase of design and is presently in stage of accelerator elements manufacturing and construction.

The project realization plan foresees a staged construction and commissioning of the accelerators which form the facility.

REFERENCES

[1] NICA White Paper: *http://theor.jinr.ru/twiki-cgi/view/NICA/WebHome*.
[2] J. Cleymans and J. Randrup, Phys. Rev. **C 74**, 2006, 047901.
[3] I. Meshkov, Phys. of At. Nucl., v. 75, N. 2, 2012, pp. 594-597.
[4] V.D. Kekelidze et al., in *Proceedings of the 36th International Conference on High Energy Physics*, Jule 4-11, 2012, Melbourne, Australia), Ed. by A. Limosani, Proceedings of Science, Trieste, PoS, p. 411.
[5] G.S. Stephans, J. Phys. **G 32**, S447 (2006), nucl-ex/0607030.
[6] P. Senger, J. Phys. **G 30**, S1087 (2004).

Closing plenary talks

Proceedings of the LHCP2015 Conference, St. Petersburg, Russia, August 31 - September 5, 2015

Editors: V.T. Kim and D.E. Sosnov

Landscape View at the Edge of a Mystery

D.I. KAZAKOV[1,2,3]

[1]*Bogoliubov Laboratory of Theoretical Physics, Joint Institute for Nuclear Research, Dubna*
[2]*Alikhanov Institute for Theoretical and Experimental Physics, Moscow*
[3]*Moscow Institute of Physics and Technology, Dolgoprudny*

kazakovd@threor.jinr.ru

Abstract. The situation in particle physics after the discovery of the Higgs boson is discussed. Is the Standard Model consistent quantum field theory? Does it describe all experimental data? Are there any indications of physics beyond the SM? Is there another scale except for the EW and the Planck ones? Is the SM of particles physics compatible with Cosmology? New challenges of hadron physics: exotic hadrons and dense hadronic matter. Search for new physics, from the Higgs sector to dark matter, supersymmetry, extra dimensions and compositeness. What do we expect? What are the main targets? We try to answer the main questions and describe the key issues of possible new physics beyond the SM.

INTRODUCTION: THE STANDARD THEORY

With the launch of the LHC we approached the mystery land that lies beyond the TeV border line. We do not know what is hidden there and our task is to be prepared and not to miss the new expected or unexpected phenomena. The guiding line here is our knowledge of physics at lower scales, first of all of the Standard Model of fundamental interactions which for our current understanding seems to be completed. Our search for possible new physics is based on the comparison of experimental data with the SM predictions. From this point of view it is useful to look back at the SM and remind its basic features.

The Standard Model (Theory) is the gauge quantum field theory based on the following main principles:

- Three gauged symmetries $SU_c(3) \times SU_L(2) \times U_Y(1)$ corresponding to the strong, weak and electromagnetic interactions, respectively;
- Three families of quarks and leptons belonging to the representations $(3 \times 2, 3 \times 1, 1 \times 2, 1 \times 1)$ of the gauge groups;
- The Brout-Englert-Higgs mechanism of spontaneous EW symmetry breaking accompanied with the Higgs boson;
- The CKM and PMNS mixing matrices of flavours;
- The CP violation via the phase factors in these matrices;
- Confinement of quarks and gluons inside hadrons;
- The Baryon and Lepton number conservation;
- The CPT invariance leading to the existence of antimatter.

The ST principles allow:

- Extra families of quarks and leptons — seems to be excluded experimentally already;
- Presence or absence of right-handed neutrino — still unclear;
- Majorana/Dirac nature of neutrino — the Majorana mass is slightly beyond the SM;
- Extra Higgs bosons — Already beyond but in the spirit of the SM.

The main questions to the Standard Theory (ST) can be formulated as:

- ► Is it self consistent?
- ► Does it describe all experimental data?

- Are there any indications of physics beyond the SM?
- Is there another scale except for the EW and the Planck ones?
- Is it compatible with Cosmology?

There are also many "why's" and "how's":

Why's	How's
why $SU(3) \times SU(2) \times U(1)$?	how does confinement actually work?
why 3 generations?	how does the quark-hadron phase transition happen?
why quark-lepton symmetry?	how do neutrinos get a mass?
why V-A weak interaction?	how does CP violation occur in the Universe?
why L-R asymmetry?	how to protect the SM from would be heavy
why B & L conservation?	scale physics?
etc	

In what follows we will try to answer the main questions and describe the key issues of possible physics beyond the SM.

IS THE SM CONSISTENT QUANTUM FIELD THEORY?

Ghosts

For a long time the known property of the SM is that the running couplings possess the Landau ghost poles at high energies. This is true for the U(1) coupling and for the Higgs coupling, but ... beyond the Planck scale, as shown in Fig.1. The Landau pole has a wrong sign residue that indicates the presence of unphysical ghost fields - intrinsic

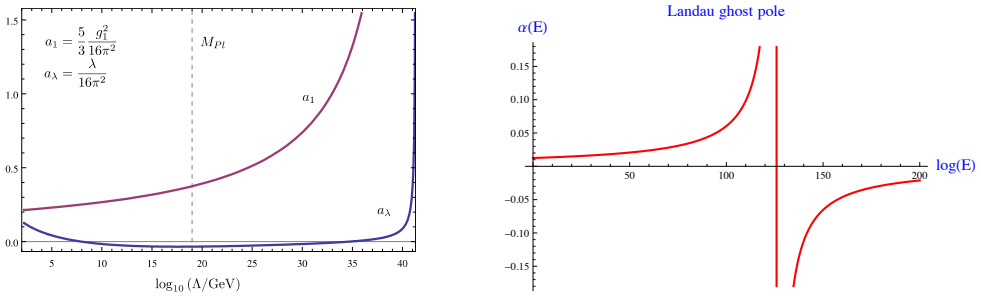

FIGURE 1. The running of the U(1) and the Higgs couplings (left) and the Landau ghost pole (right)

problem and inconsistency of a theory [1]. The one loop expression for the hyper charge coupling in the SM

$$\alpha_1(Q^2) = \frac{\alpha_{10}}{1 - \frac{41}{10}\frac{\alpha_{10}}{4\pi}\log(Q^2/M_Z^2)} \tag{1}$$

possesses the ghost pole at the scale $Q^* = M_Z e^{\frac{20\pi}{41\alpha_{10}}} \sim 10^{41}\ GeV$. It is far beyond the Planck scale and one may ignore it assuming that the Planck scale quantum gravity will change the situation. However, quantum gravity is still lacking and the presence of ghosts is intrinsically dangerous independently of the scale where they appear. The situation may change in GUTs due to new heavy fields at the GUT scale. In any case, this requires modification of the ST at VERY high energies.

Anomalies

As is well known, in quantum theories there may exist anomalies that can ruin the theory. In the SM there is a set of quantum anomalies. A famous example is the triangle chiral anomaly [2]. Its contribution to the electron-neutrino scattering amplitude is shown in Fig.2. It would destroy renormalizability if not cancelled among quarks and leptons.

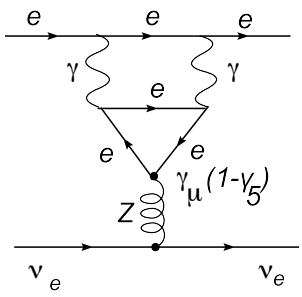

FIGURE 2. The chiral anomaly diagram in the electron-neutrino scattering amplitude

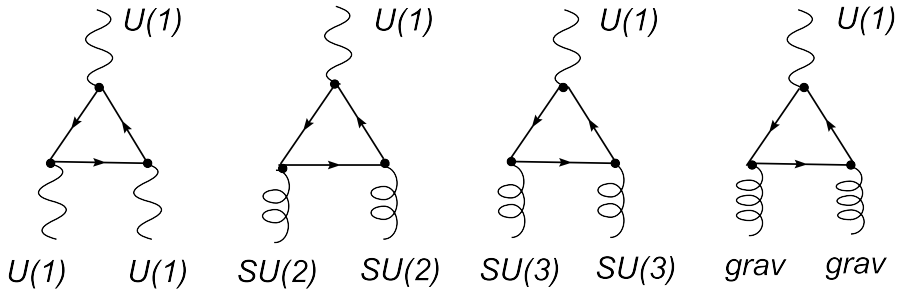

FIGURE 3. The gauge anomalies in the SM

The other anomalies existing in the SM are shown in Fig.3 [3]. Fortunately, they are all canceled in the SM for each generation of quarks and leptons, as can be seen from expressions below.

$$TrY^3 = 3\,(\underset{\uparrow}{\tfrac{1}{27}} + \tfrac{1}{27} - \tfrac{64}{27} + \tfrac{8}{27}) - 1 - 1 + 8 = 0,$$

$$color \quad u_L \quad d_L \quad u_R \quad d_R \qquad \nu_L \quad e_L \quad e_R$$

$$TrY_L = 3(\frac{1}{3} + \frac{1}{3}) - 1 - 1 = 0,$$

$$TrY_q = 3(\frac{1}{3} + \frac{1}{3} - \frac{4}{3} - (-\frac{2}{3})) = 0,$$

$$TrY = 3(\frac{1}{3} + \frac{1}{3} - \frac{4}{3} - (-\frac{2}{3})) - 1 - 1 - (-2) = 0.$$

Thus, the cancellation of anomalies requires the quark-lepton symmetry. Probably, this is a hint towards the Grand Unified Theories.

Vacuum Stability

Quantum corrections can make the vacuum unstable. Moreover, the whole construction of the SM may be in trouble being metastable or even unstable. This is related to the Higgs potential which at the tree level contains quadratic and quartic terms. The quartic coupling due to the radiative corrections depends on a scale and at some scale might change the sign, thus making the EW vacuum unstable. Indeed, it may happen at high energy scale, as shown in Fig.4 (left)[4]. The situation crucially depends on the top and Higgs mass values and requires severe fine-tuning and accuracy (see Fig.4 (right)). It seems that we are sitting just at the border line with the top quark and the Higgs boson masses specially adjusted. However, the account of the next-to-leading order corrections is essential and shifts the position towards the stability region, as can be seen in Fig.5[5].

In the case when the EW vacuum is indeed metastable the right question to ask would be: what is the life-time of the ground state? If it is bigger than the life-time of the Universe, it is still fine for the SM. Still the situation requires

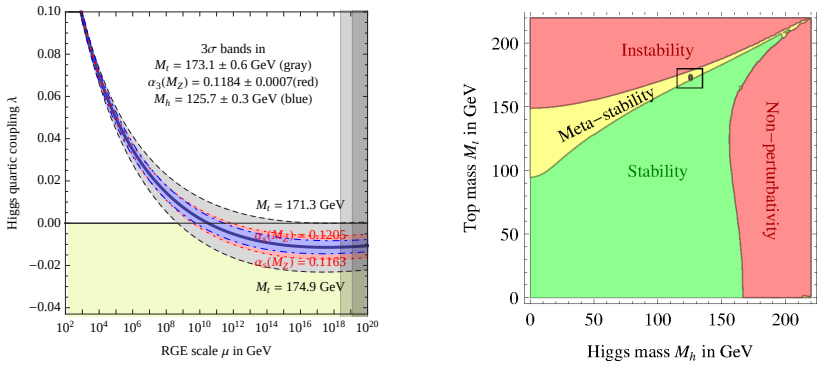

FIGURE 4. The running of the Higgs coupling (left) and the stability of the EW vacuum as a function of the Higgs and top masses

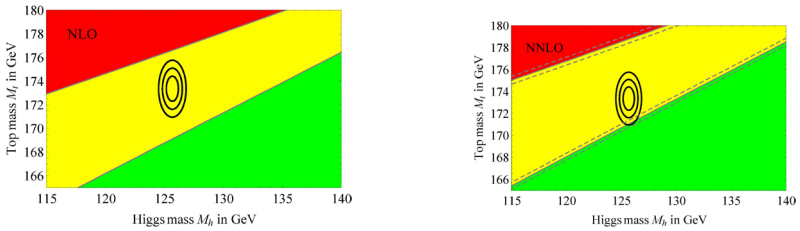

FIGURE 5. The vacuum stability point at the NLO and NNLO

some caution. The way out might be the new physics at higher scale. One example is supersymmetry: in this case the scalar potential is $V_{SUSY} = |F|^2 + |D|^2 \geq 0$ [6]. If SUSY is broken the potential can get negative corrections though the quartic scalar coupling remains to be positive. The second example is the extended Higgs sector. Several Higgs fields with several Higgs-like couplings push the smallest coupling up (might have also several minima). The third example is provided by GUTs. In a unified theory the Higgs coupling may be attracted by the gauge coupling, thus stabilizing the potential. Note that in all these cases one has an extension of the SM at high energies.

Scale Stability

New physics at high energy scale may destroy the EW scale of the SM. Indeed, the masses of quarks and leptons and the masses of gauge bosons in the SM are protected versus the radiative corrections originating from heavy new physics due to the gauge invariance. However, this is not true for the Higgs mass. The Higgs sector is not protected by any symmetry. Quantum corrections to the Higgs potential from to New physics (see Fig.6) are proportional to the heavy mass squared. These huge corrections would destroy the light Higgs potential and eventually the light EW scale of the SM. This creates a hierarchy problem: the coexistence of the light and heavy scales $\frac{m_H}{m_{GUT}} \sim 10^{-14}$ and requires modification of the SM.

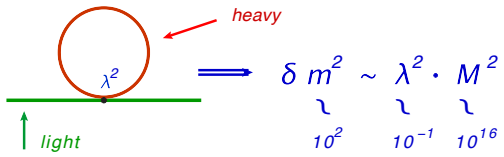

FIGURE 6. Radiative correction to the Higgs mass due to heavy particles

The way out again might be the new physics at higher scale. Two suggestions are popular. The first one is supersymmetry at TeV scale. In this case, the unwanted radiative corrections are canceled by super partners of the corresponding particles, as it is shown in Fig.7 [7]. This cancellation is true up to the SUSY breaking scale. If $m_{SUSY} \sim$ 1 TeV, the light Higgs mass is protected, which suggests an approximate scale of low energy supersymmetry. If, on

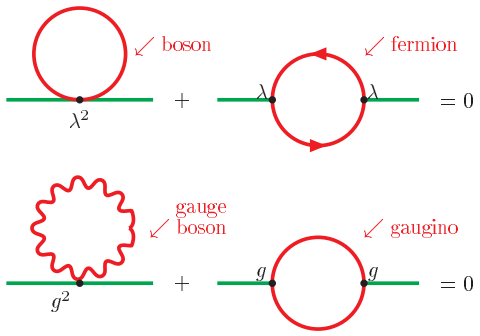

FIGURE 7. Cancellation of the radiative correction to the Higgs mass due to super partners

the contrary, $m_{SUSY} \geq 1$ TeV, one has the so-called little hierarchy problem that requires the fine tuning of the SUSY parameters [8].

The other proposal to solve the hierarchy problem is related to the extra dimensional theories. In this case the hierarchy is achieved due to the wrap factor which appears while going from the so-called Planck brane to the physical brane (Fig.8). In the Randall-Sundrum brane world construction [9] the gravity scale at the Planck brane and the TeV

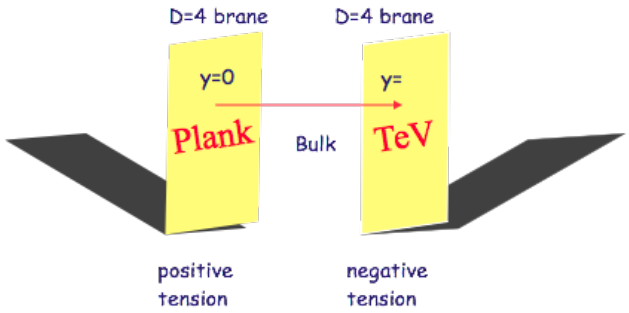

FIGURE 8. The Randall-Sundrum type brane world construction

brane are related by

$$M_{Pl}^2 = \frac{M^3}{k}(e^{2k\pi R} - 1). \tag{2}$$

As a result the gravity scale at the TeV brane, M, might be small enough not to create the hierarchy problem. Whether any of these scenarios are realized in Nature is unclear.

DOES THE ST DESCRIBE ALL EXPERIMENTAL DATA?

Remarkable success of the SM in describing practically all experimental data in particle physics manifests itself in a pool of EW observables (see Fig.9 left) [10]. Almost everywhere one has agreement within 1-2 standard deviations. The only exception is the forward-backward asymmetries in LEP data, the long ignored problem usually attributed to the analysis. The same is true for the flavor observables (see Fig.9 right) [11]. One has to admit very impressive progress achieved in the last decade in the EW and QCD perturbative calculations (see e.g. [12]). This became possible due to the development of new techniques and computer codes for multi-loop and multi-leg calculations. Today the accuracy of theoretical calculations competes with that of experimental data and further progress is on the way in both the cases.

For years the pain in the neck remains an almost 3 σ discrepancy in the anomalous magnetic moment of muon, the $a_\mu = (g-2)/2$, as illustrated in Fig.10 [13]. The attempts to fill the gap with the new physics contributions are not very successful due to the heaviness of the experimentally allowed new physics. The reason is that the new

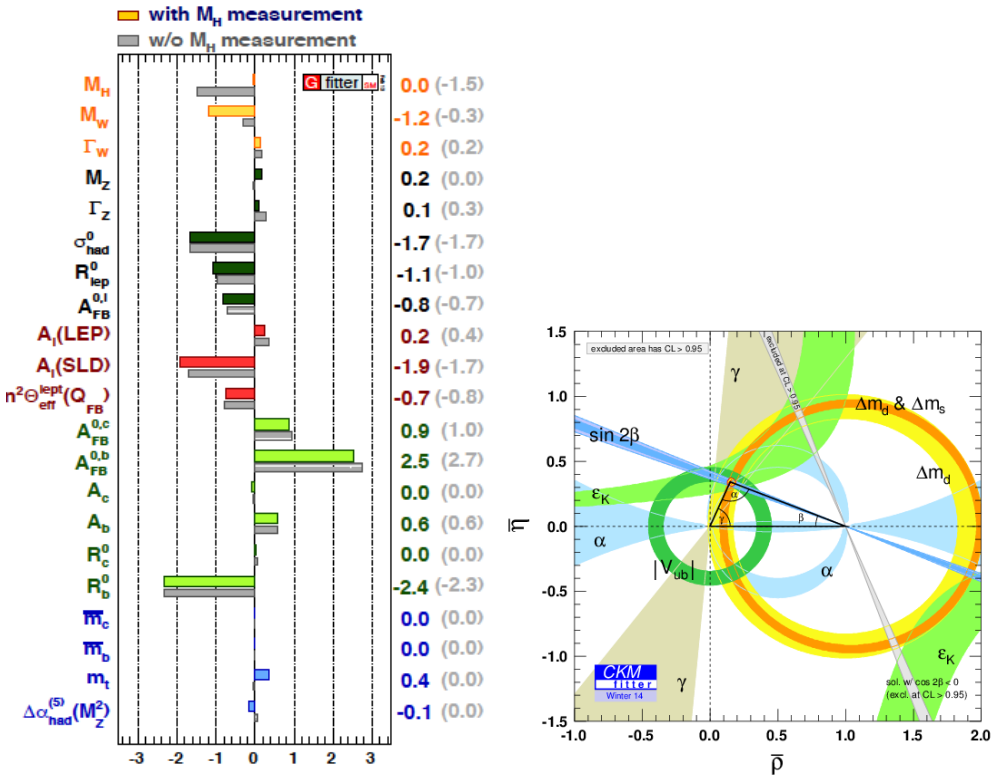

FIGURE 9. The pool of the EW data (left) and the flavour observables (right)

physics contributions come from the virtual particles in the loop and these diagrams are suppressed by the inverse mass squared of the intermediate particles. Though this explanation is still possible, the main hopes in resolving the a_μ puzzle are related with the still inaccurate strong interaction contribution or with the new experiment which is on the way.

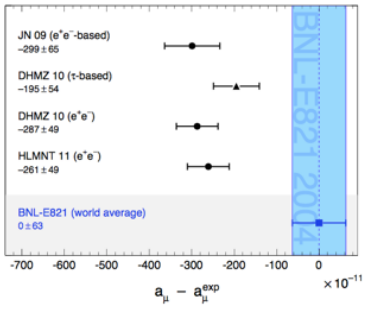

FIGURE 10. The difference between the experimental and theoretical values of a_μ

The other discrepancy which attracted attention is the value of the CKM mixing matrix element V_{ub} measured recently[14]. This quantity is slightly different when measured in inclusive and exclusive processes. The resolution of this puzzle presumably lies in the theoretical interpretation.

Looking at the other observables and unsolved problems one has to mention the strong CP problem which despite being known for several decades still has not found its solution. The elegant way of resolving it with the help of the axion field still lacks experimental confirmation. The existing models with the axion field allow almost invisible light particle leaving small chances for its detection [15]. Another field where the new physics might appear is the rare

decays. Here, despite some hopes connected in particular with the $B_s \to \mu\mu$ decay, everything looks fine for the SM so far [16]. QCD is another huge area of activity. It also looks fine, although the spin crisis related to the spin of the proton is still unresolved. Presumably, it is related to parton distributions. Relatively new activity with the generalized parton distributions depending on momentum transfer opens a new field for the check of the SM [17]. At last, the neutrino physics attracts much attention in recent and coming years. It seems that the neutrino masses and mixings look fine so far but still need to be clarified. The nature of neutrino (Dirac or Majorana) remains the major puzzle in this field.

In this situation one may wonder why do we talk about new physics at all. Everything seems to be described by the SM. It is useful to look back in history and find an analogy of the modern situation. For this purpose, let us go back to the middle of the 20th century. This was the world of a single generation of particles. Indeed, the world around us is made of the first generation. In the middle of the 20th century we had the following set of elementary particles: proton, neutron, electron and later neutrino. The structure of an atom was described in detail (see Fig.11 left). Who expected new physics to come? And at which scale?

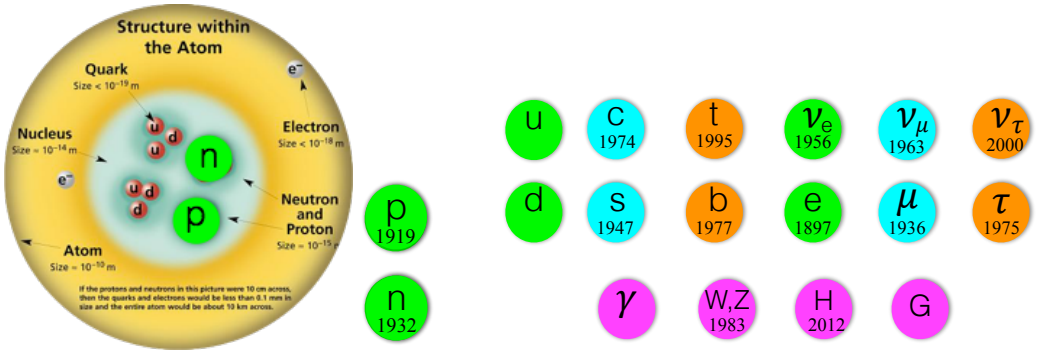

FIGURE 11. The structure of the atom (left) and the families of quarks and leptons and the force carriers (right)

We know what happened next: the muon was discovered in cosmic rays. It was first considered as a heavy electron and later was recognized as the beginning of the 2nd generation. Then the K-meson appeared, the strange particle. The following up discoveries of new hadrons at accelerators triggered the invention of the quark model and everything looked OK again. Then some problems with suppression of the flavour changing transitions appeared which were resolved with the help of the GIM mechanism [18]. The subsequent discovery of J/Psi completed the 2-nd generation with the charm quark. This second generation looked artificial and unexplained; however, something was missing since the CP-violation was discovered and called for the interpretation. The Kobayashi-Maskawa mixing matrix gave a hint for the 3rd generation and here we are. Discoveries of the force carriers and eventually of the Higgs boson already in the 21st century completed our picture, as shown in Fig.11 (right). Only the gravitational force with the graviton as a carrier still stands aside. Let me repeat, who expected this in the middle of the 20th century?

There were, however, unanswered questions. The challenge came from astrophysics and cosmology. Being at the earlier stage of the development they puzzled particle physics with the major problems of the baryon asymmetry of the Universe and the description of the Dark Matter known already at that time. Remarkably that these problems are still not resolved within the SM today.

IS THERE ANOTHER SCALE EXCEPT FOR THE EW AND PLANCK ONES?

The expectations of the new physics inevitably lead to the question of the scale. Is there any new scale between the EW and the Planck ones? Many new phenomena assume the existence of the proper scales. The forseeble panorama of high energy physics is shown in Fig.12 [19]. First of all there is the EW scale. All the masses (except for the top quark and the Higgs boson) lie below this scale and form a random pattern as of today. Then there is Λ_{QCD} which is not a fundamental scale but plays an essential role in strong interactions. Moving down from the Planck scale we have subsequently the hypothetical string scale, the GUT scale, the Majorana scale, the vacuum stability scale, probably some others like the Pechei-Queen scale, etc. Somewhere in between is the foreseen SUSY scale. There might also be the scale of extra dimensions positioned anywhere.

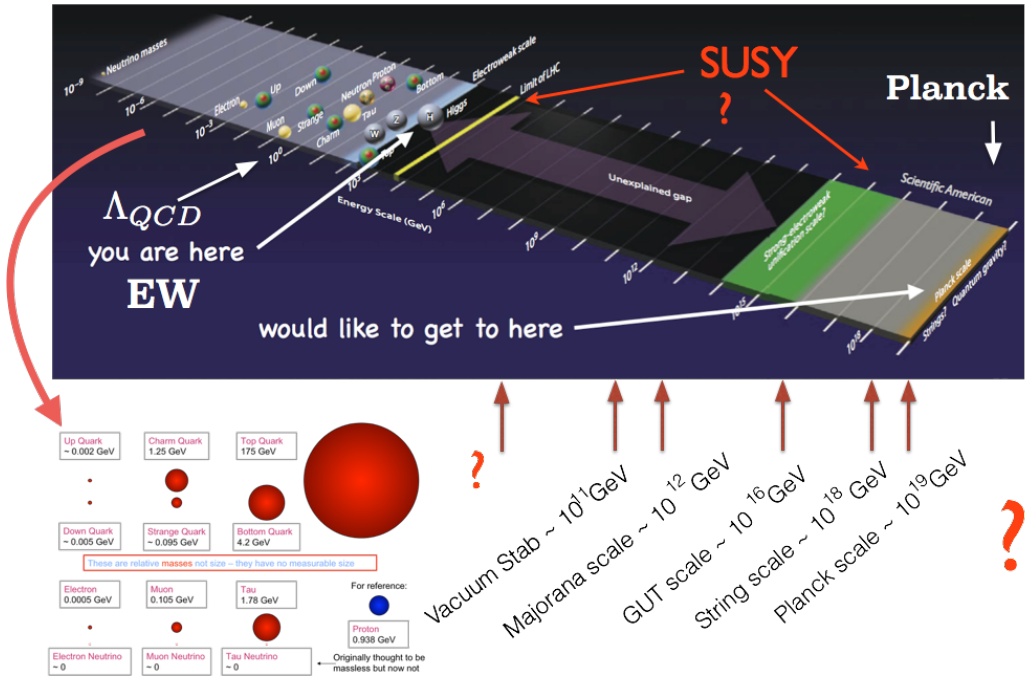

FIGURE 12. The high energy physics panorama and possible scales of the new physics

What is true of this picture? Is there anything that is revealing at the TeV scale? Future and presumably not so distant future will show us what is correct.

IS IT COMPATIBLE WITH COSMOLOGY?

The revolutionary development of cosmology in recent years and the appearance of the Standard model of cosmology called the ΛCDM model [20] allow one to compare the predictions of the Standard Model of particle physics with that of cosmology where they intersect. The main issues are:

- Baryon asymmetry of the Universe. The ratio of the number of baryons minus the number of anti-baryons in the Universe to the number of photons is given by an approximate formula [21]

$$\frac{N(B) - N(\bar{B})}{N_\gamma} \sim (6.19 \pm 0.14) \times 10^{-10}. \tag{3}$$

  This number is still not explained in the SM and may require modification of the SM in future. It requires larger CP-violation than in the strong sector of the SM giving some hints toward its lepton nature.
- Relic abundance of the Dark Matter. According to recent data from the Planck mission [22], the energy balance of the Universe has the following shape

$$\textit{Ordinary Matter} = 4.9\%,\ \textit{Dark Matter} = 26.8\%,\ \textit{Dark Energy} = 68.3\% \tag{4}$$

  The problem of the Dark matter content is the problem of particle physics and seems to be beyond the SM. We will come to this point later.
- Number of neutrinos. The recent combined data from the Cosmic Microwave Background (CMB), the baryon acoustic oscillations (BAO), the WMAP polarization data (WP), the Hubble Space Telescope (HST) and high-l temperature power spectrum (highL) give for the number of neutrinos the value [22]

$$N_{eff}(\nu) = 3.52 \pm 0.47 \ \ \textit{at } 95\%\ CL, \tag{5}$$

  that well suits the SM with 3 generations assuming the quark-lepton symmetry.

- Masses of neutrinos. From the same CMB, WP and HST data plus the gravitational lensing one gets the bound on the neutrino masses [23]

$$\sum m_\nu < 1.11(0.22)\ eV, \tag{6}$$

which is even stronger than in neutrino experiments. These extremely light neutrinos probably give us a hint towards new physics responsible for their smallness like the see-saw mechanism and the Majorana nature of the neutrino.

HADRON PHYSICS

Looking back at the SM as the highest achievement in the description of matter we find some problems that were put aside in our race for the highest energy and intensity, namely, the problem of confinement and the problem of hot dense hadronic matter.

Confinement and Exotic Hadrons

The understanding of confinement is the challenging problem in particle physics well inside the SM. Is it time to come back to it? We still do not understand how confinement actually works, why colorless states are the only observables, which bound states exist in Nature. Lattice calculations seem to shed some light on it: we know that in mesons quark and anti-quark pairs are linked by the gluon string which has a tension and thus provides a linearly growing potential leading to confinement. Trying to break this string one actually creates a new quark anti-quark pair thus again obtaining colorless mesons. For baryons the situation is more sophisticated, the strings form the Mercedes-Benz star with the same result as for mesons. However, it is still unclear how these strings are formed and why they are restricted to the colorless states. And even if so, what about other colorless states like the tetraquark, the pentaquark, the sextoquark, etc? Do they exist in Nature? (see Fig.13 [24]). According to recent data, the pentaquark hadrons are

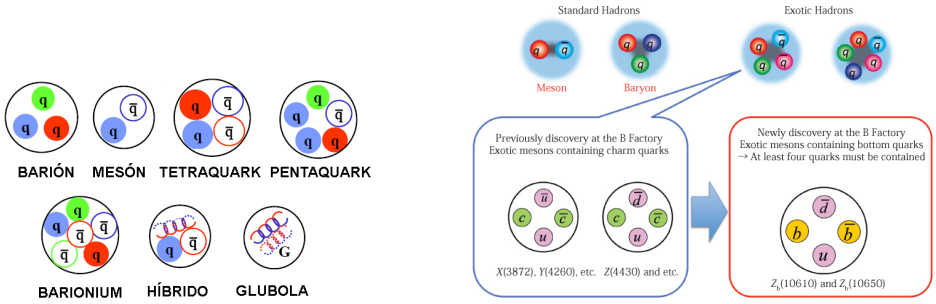

FIGURE 13. Possible exotic colorless hadrons and newly discovered tetraquarks

at last unequivocally discovered at the LHC by the LHCb collaboration [25].

These new states require an adequate description probably within the lattice gauge theories or within the holographic approach or dual gauge theories. Or maybe we are back to analyticity and unitarity?

Dense Hadron Matter

Dense hadron matter might well be a new phase of matter with yet unknown properties which has no name so far. It is known that at high density (high temperature) the usual description of hadron matter is not valid. Hadrons do not exist above the Hagedorn temperature [26]. What happens with a hadron gas at high pressure? How to get the new phase? What is the relevant description? The popular phase diagram of hadron matter is shown in Fig.14 [27]. Here T is the temperature and μ_B is the baryon chemical potential. Usually, it is assumed that the phase diagram contains several phases with the phase transitions and critical points. The high temperature phase is usually referred to as a deconfinement one. To check whether it is true, one uses various methods including statistical mechanics, nonequilibrium thermodynamics, hydrodynamics, and dual holographic models. There are several microscopic and macroscopic models [28]. As an example we show below (Fig.15) the nuclear phase diagram in different representations for different parameters [29]. It represents rich new phenomena which still have to be exploited.

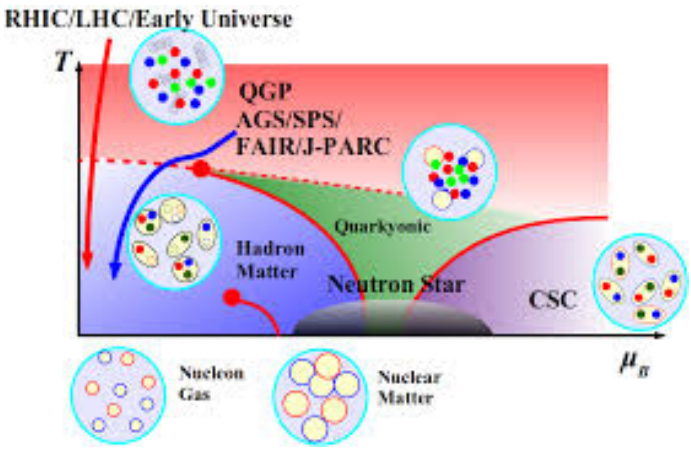

FIGURE 14. The phase diagram of hadron matter

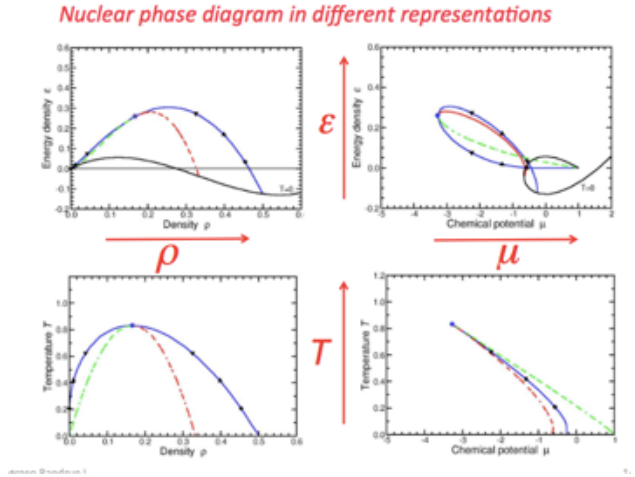

FIGURE 15. The nuclear phase diagram in different representations

SEARCH FOR NEW PHYSICS

The Higgs Boson

The Higgs boson still remains the target #1 in search for new physics. And though there is no doubt that the discovered particle is the CP-even scalar with all the properties of the Higgs boson, the main question remains: is it the SM Higgs boson or not? Are there alternatives to a single Higgs boson of the SM? The answer is positive. One may consider the singlet, doublet and triplet extensions of the SM, or their combinations [30]. The guiding principle for these extensions is the custodial symmetry. It indicates that an approximate global symmetry exists, broken by the vev to the diagonal custodial symmetry group $SU(2)_L \times SU(2)_R \to SU(2)_{L+R}$. The custodial symmetry of the SM is responsible for the ratio

$$\rho = \frac{M_W^2}{M_Z^2 \cos^2 \theta_W} = 1 \tag{7}$$

at the tree level. In the case of various extensions, when the Higgs field(s) transform under $SU(2)_L \times SU(2)_R$ as $\Phi \to L\Phi R$, the ρ-parameter can be constructed starting from the isospin and the hyper charge values of the Higgs

multiplets [30]

$$\rho = \frac{\sum_{i=0}^{n} [I_i(I_i+1) - \frac{1}{4}Y_i^2]v_i}{\sum_{i=0}^{n} \frac{1}{2}Y_i^2 v_i}. \tag{8}$$

For both $SU(2)$ singlet with $Y = 0$ and $SU(2)$ doublet with $Y = \pm 1$ one has $\rho = 1$. Moreover, any number of singlets and doublets respect custodial symmetry at the tree level. This is not so for an arbitrary number of triplets.

How can one probe that the Higgs boson is of the SM? There are two ways to do it. First of all, one has to probe the deviations from the SM Higgs couplings (see Fig.16 [31]).

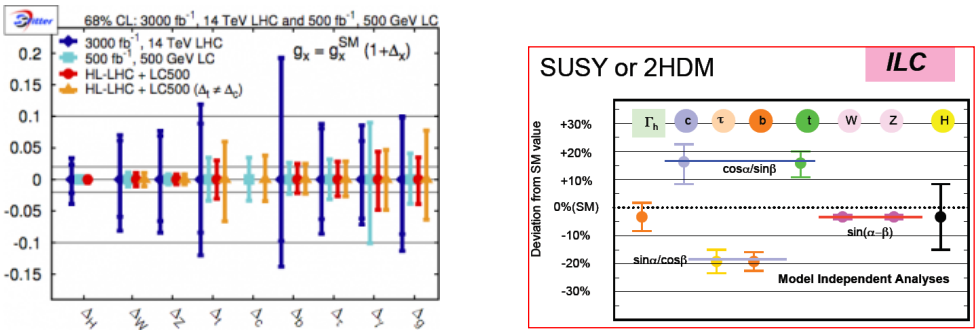

FIGURE 16. The accuracy of the measurement of the Higgs couplings at various accelerators (left) and the required precision to distinguish SUSY from the 2HDM (right)

The name of the game is precision. At the few percent level one can distinguish, for example, the two Higgs doublet model of the MSSM type from the SM [32].

The second way is the direct search for additional scalars. In various extensions one can have extra CP-even, CP-odd and charged Higgs bosons. As an example, we present in Fig.17 the spectrum of the Higgs bosons in supersymmetric models (the MSSM - two Higgs doublet model and the NMSSM - plus additional singlet). It may well be

Model	Particle content
SM	h CP-even
2HDM/MSSM	h,H CP-even A CP-odd H
NMSSM	H_1,H_2,H_3 CP-even A_1,A_2 CP-odd H
Composite	h CP-even + excited states

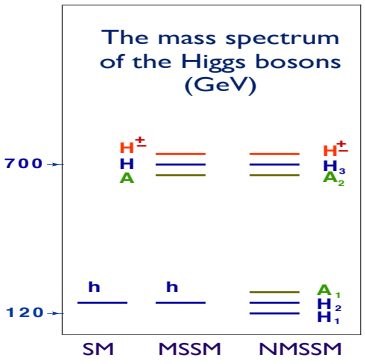

FIGURE 17. The field content and the spectrum in various models of the Higgs sector

that we have found one of the light states that may not even be the lightest one. The latter one may have very weak couplings and thus not being detectable [33].

The Higgs physics has already started. This is the task of vital importance to be fulfilled at the LHC but may require an electron-positron collider.

The Dark Matter

Target # 2 is the Dark matter. We know now that the amount of the Dark matter in the Universe exceeds that of the usual matter by a factor of 5 (see eq.(4), but we do not know what it is made of. Some possible candidates are:

- Macro objects – not seen in our Galaxy
- New particles

	– heavy right neutrino	not favorable but possible
Not the SM	– axion (axino)	might be invisible (?)
	– neutralino	detectable in three spheres
	– sneutrino	less theoretically favorable
	– gravitino	might be undetectable (?)
	– heavy photon	possible
	– heavy pseudo-goldstone	but not related
	– light sterile Higgs	to other models

Our best chance to detect the Dark matter particle would be via the weak interaction. The so-called WIMP (weakly interacting massive particle) can be simultaneously detected in three spheres: via annihilation in the halo of our Galaxy (irregularities in cosmic ray spectra), via scattering on a target in underground experiments (recoil of a nuclei) and via creation at accelerators (missing energy) (see Fig.18 [34]). This search is already on the way with a

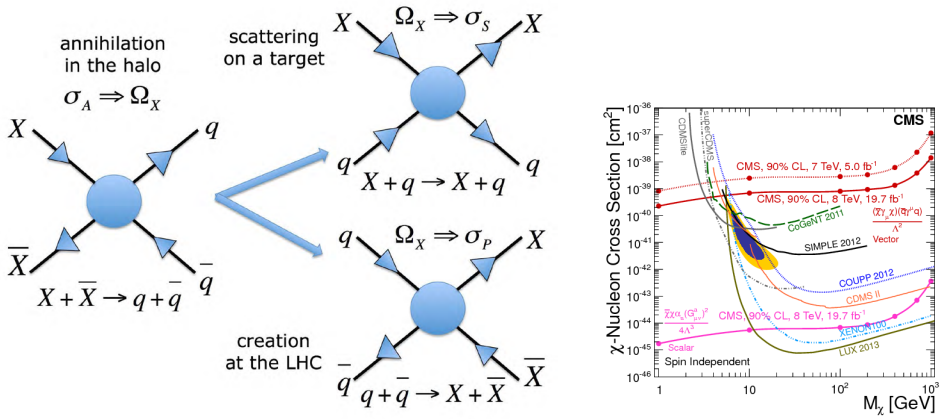

FIGURE 18. Detection of WIMPs in there different spheres (left) and experimental data for the underground experiments and accelerators (right)

negative result so far. The typical plot is shown in Fig.18 [35](right) where the results of the direct search and the collider experiments are presented. One can see the complimentary nature of these studies with the advantage of the accelerators at low masses and the advantage of the underground experiments at higher masses of WIMPs. The latter has already almost reached the neutrino floor where the background of neutrinos will be prevailing [36]. Apparently, WIMPs are our chance though we have to look elsewhere.

SUPERSYMMETRY

Supersymmetry is an obvious target #3. Supersymmetry is a dream of a unified theory of all particles and interactions [37]. Supersymmetry remains, to this date, a well-motivated, much anticipated extension to the Standard Model of particle physics [38].

With the advent of the LHC a huge new ground of SUSY masses is within reach. However, a search is defined by its signature and by its background estimation method. Still, if SUSY is the answer to the naturalness problem, then there must exist light colored particles. The typical spectrum of SUSY particles consistent with the naturalness paradigm in shown in Fig.20 [39]. At the left, it is shown how the scale of SUSY searches has shifted after the first run of the LHC.

Many available supersymmetric models differ mostly by the way of supersymmetry breaking. Since this problem has not found its obvious solution, one is left with the phenomenological set of parameters motivated by either the simplification of parameter space, like in the MSSM with universality requirement, or the restricted number of experimental signatures, like in the so-called simplified models.

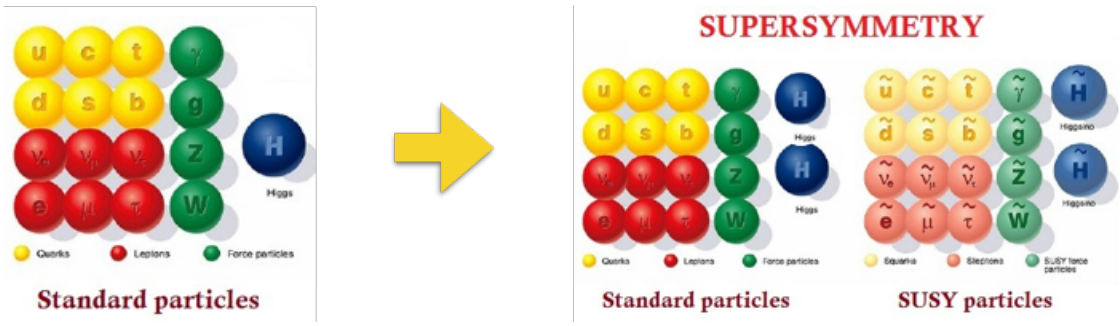

FIGURE 19. Particle content of Minimal SUSY model

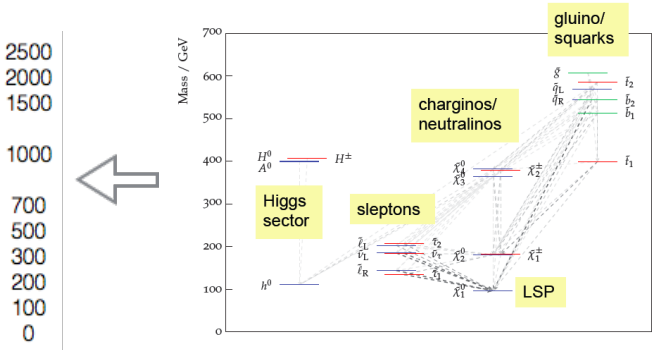

FIGURE 20. The typical SUSY mass spectrum

In both the cases the experimental data on direct SUSY searches and the indirect SUSY contributions to rare decays, relic dark matter abundance, the lightest Higgs mass, etc push the limits on SUSY masses to a few TeV scale [40], which makes the observation more problematic. Moreover, pushing the SUSY threshold even further, we start losing the main motivation for a low energy SUSY, namely the solution of the hierarchy problem and unification of the gauge couplings. Note, however, the conclusions crucially depend on the model applied, as one may see from Fig.21 below [33]. Going from the MSSM to the NMSSM, for example, allows one to incorporate the 125 GeV Higgs mass and still keep the light super partners.

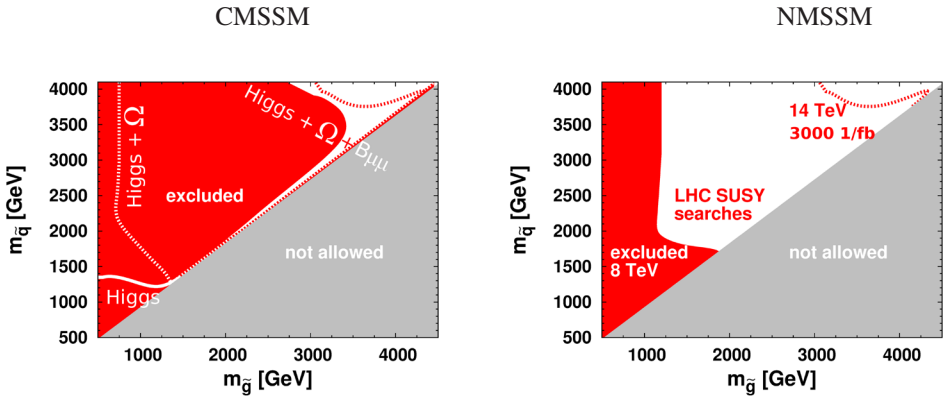

FIGURE 21. The SYSY reach of the LHC in the SUSY mass plane for the CMSSM (left) and NMSSM (right)

The absence of a model independent way of predictions and analysis makes it difficult to put strict limits on the

low energy supersymmetry. However, there is a crucial moment now: either we find SUSY at the LHC eventually or we might have no other chance. Then we have to solve the hierarchy problem some other way! (which way?).

Extra Dimensions/ Exotics

The extra dimensional approach might be an alternative to low energy supersymmetry or might also include SUSY within the brane world framework. Usually, the two main versions of extra dimensions are considered: the compact extra dimensions a la Kaluza-Klein picture (the ADD scenario [41]) or the large extra dimensions (the Randall-Sandrum scenarios [9]). Schematically, they are shown in Fig.22 [42].

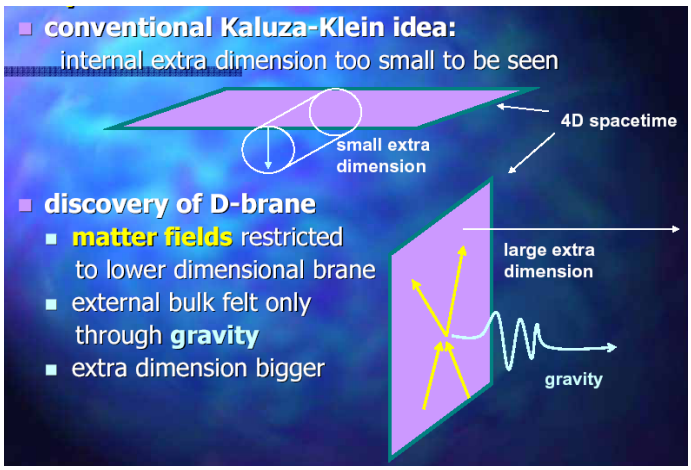

FIGURE 22. Compact or large extra dimensions scenarios

These kinds of models demonstrate a significant departure from the Standard Model since they not only contain the new fields and interactions but the whole framework of renormalizable quantum field theory is left behind. Apparently, this approach requires a new technique which is still to be developed. I would present my view on the extra dimensional brane world scenario in the form of a dialogue.

Q: Do we really live on a brane?
A: We have to check it.
Q: Do we have good reasons to believe in it?
A: No, but it is appealing.
Q: Why $D > 4$?
A: String theory loves it.
Q: Is it what we believe in?
A: We believe in BIG deal!

The phenomenology of extra dimensions is quite rich, though it is not linked to any particular scale. Possible experimental manifestations include: search for Z' (Di-muon events), search for W' (single muon/ jets), search for a resonance decaying into t-tbar, search for diboson resonances, search for monojets + invisible particles.

Besides extra dimension there are a lot of exotic possibilities. None of them have been found so far, though one cannot a priori say what is realized in Nature. Some common topics are listed below: Leptoquarks, long-lived particles, off-pointing photons, excited fermions, contact interactions, etc. The drawback of all these approaches is the lack of real motivation and hence the arbitrariness of the scale of new physics.

Compositeness

Compositeness is in a sense a natural continuation of the chain of particle physics starting from an atom and going down to quarks. The question is: moving to higher energies or smaller distances do we have to stay with the same fundamental particles or the new level appears. Answering this question we first of all look at the Higgs boson as an obvious analogy with the π-meson as a pseudo Nambu-Goldstone boson of the chiral symmetry. One has in mind the

construction when some global symmetry group G is broken down to the symmetry group of the Standard Model H (see Fig.23) [43].

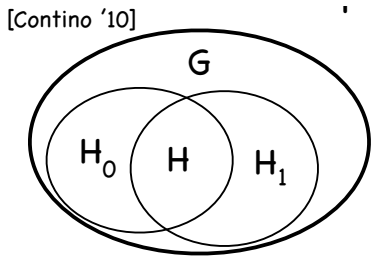

FIGURE 23. Breaking of the global group G down to the SM subgroup H

As a result, the Higgs boson becomes the pseudo Nambu-Goldstone particle like the π-meson, and the W and Z bosons have an analogy with the vector ρ-meson. There should also be exited states like $\pi', \pi'', \rho', \rho''$, etc.

The advantage of this approach is that there is no artificial scalar field, everything is dictated by the symmetry group. The masses of these states are protected from high energy physics contribution, thus eliminating the hierarchy problem.

One can go even further and consider quarks and leptons also as composite states made of some *preons* [44]. This would require new strong confining interactions. In earlier days, these types of models were referred to as technicolor, or walking technicolor, or extended technicolor. They have their own problems and got new development now [45]. The drawback of these models is the absence of excited states so far, the problems with the EW phenomenology and the absence of a viable simple scheme. Still this approach has the right to exist.

CONCLUDING REMARKS

The LHC experiments are at the front line of a mystery land. We make the first attempts to look beyond the horizon. We have to be persistent and have to be patient. The main goals are:

- Target #1: The Higgs sector;
- Target #2: The Dark Matter;
- Target #3: The New physics (supersymmetry);

In attempts to achieve these goals one should have in mind that

- The future development of HEP crucially depends on the LHC outcome;
- Complimentary searches for dark matter and insights in neutrino physics are of extreme importance;
- The areas that were left behind come to the front: confinement, exotic hadrons, dense hadron matter.

I bet that discoveries will come!

ACKNOWLEDGMENTS

I am grateful to the Organizing Committee of the LHCp-2015 Conference for a challenge to give this talk and for a warm hospitality at St.Petersburg.

REFERENCES

[1] L.D. Landau, On quantum field theory, in "Niels Bohr and the Development of Physics", London: Pergamon Press, 1955;

[2] S. Adler, Axial-Vector Vertex in Spinor Electrodynamics, *Phys. Rev.* **177** (1969) 2426 ; J.S. Bell and R. Jackiw, A PCAC puzzle: $\pi^0 \to \gamma\gamma$ in the σ-model, *Nuovo Cimento* **60A** (1969) 47; S. Adler and W.A. Bardeen, Corrections in the Anomalous Axial-Vector Divergence Equation, *Phys. Rev.* **182** (1969) 157.

[3] M.Peskin and D.Schreder, "An Introduction to Quantum Field Theory", Addison-Wesley Pub. Company, 1995.

[4] G. Degrassi et al, Higgs mass and vacuum stability in the Standard Model at NNLO, *JHEP* **1208** (2012) 098, e-Print: arXiv:1205.6497.

[5] J. R. Espinosa, Vacuum Stability and the Higgs Boson, PoS LATTICE2013 (2014) 010, e-Print: arXiv:1311.1970.

[6] J. Wess and J. Bagger, "Supersymmetry and Supergravity", Princeton Univ. Press, 1983.

[7] A.V. Gladyshev, D.I. Kazakov, Is (Low Energy) SUSY Still Alive?, Lectures at ESHEP-2012, CERN-2014-008.107, e-Print: arXiv:1212.2548.

[8] A. Birkedal, Z. Chacko, M. K. Gaillard, Little Supersymmetry and the Supersymmetric Little Hierarchy Problem, *JHEP* **0410** (2004) 036, e-Print: arXiv:hep-ph/0404197.

[9] L. Randall and R. Sundrum, Large Mass Hierarchy from a Small Extra Dimension, *Phys. Rev. Lett.* **83** (1999) 3370, e-print: hep-ph/9905221. L. Randall and R. Sundrum, An Alternative to Compactification, *Phys. Rev. Lett.* **83** (1999) 4690, e-print: hep-th/9906064.

[10] G-fitter, A Generic Fitter Project for HEP Model Testing, http://project-gfitter.web.cern.ch; PDG, *Chin.Phys.* **38** (2014) 090001.

[11] CKM-fitter, http://ckmfitter.in2p3.fr, PDG, *Chin.Phys.* **38** (2014) 090001.

[12] Talks at the LHCp2015 Conference: K. Melnikov, Calculating Higgs boson properties in SM; A. Vicini, General status and future prospects of HO corrections; S.Forte, Perturbative QCD at the LHC; S.A.Pozzorini, Electroweak theory at the LHC.

[13] A. Hoecker and W.J. Marciano, The muon anomalous magnetic moment, http://pdg.lbl.gov/2013/reviews/rpp2013-rev-g-2-muon-anom-mag-moment.pdf

[14] LHCb Collaboration, Determination of the quark coupling strength $|Vub|$ using baryonic decays, *Nature Physics* **11** (2015) 743, http://www.nature.com/nphys/journal/v11/n9/full/nphys3415.html

[15] J. E. Kim, Constraints on very light axions from cavity experiments, *Phys. Rev.* **D58** (1998) 055006.

[16] Talks at the LHCp2015 Conference: C. Bobeth (for CMS and LHCb Collaborations), Theoretical perspective on rare and semi-rare B decays.

[17] P. Mulders and R. Tangerman, The complete tree-level result up to order 1/Q for polarized deep-inelastic leptoproduction, *Nucl.Phys.* **B461** (1996) 197, e-print: hep-ph/9510301. R. Angeles-Martinez et al, Transverse momentum dependent (TMD) parton distribution functions: status and prospects, e-Print: arXiv:1507.05267

[18] S.L. Glashow, J. Iliopoulos, L. Maiani, Weak Interactions with LeptonHadron Symmetry, *Phys. Rev.* **D2 (7)** (1970) 1285.

[19] C. Quigg, The Coming Revolutions in Particle Physics, *Scientific American*, February, 2008; http://chemphys.armstrong.edu

[20] A. Linde, "An Introduction to Modern Cosmology" (2nd ed.). London: Wiley, 2003; S. Weinberg, "Cosmology", Oxford University Press, Oxford, (2008).

[21] E. W. Kolb and M. S. Turner, "The Early Universe", Addison-Wesley (1990).

[22] Planck 2013 results. XVI. Cosmological parameters, *Astronomy and Astrophysics* **571** (2014) A16, e-print: arXiv:1303.5076.

[23] Jian-Wei Hu, Rong-Gen Cai, Zong-Kuan Guo, Bin Hu, Cosmological parameter estimation from CMB and X-ray clusters after Planck, *JCAP* **1405** (2014) 020, e-print: arXiv:1401.0717.

[24] F.R.Villatoro, http://francis.naukas.com/2011/10/08/que-paso-con-los-pentaquarks http://phys.org/news/2012-01-belle-heavy-exotic-hadrons.html

[25] R. Aaij et al. (LHCb Collaboration), Observation of $J/\psi p$ resonances consistent with pentaquark states in $\Lambda_b^0 \to J/\psi K^- p$ decays, *Phys. Rev. Lett.* **115** (2015) 072001.

[26] J.Cleymans and D. Worku, The Hagedorn temperature Revisited, *Mod. Phys. Lett.* **A26** (2011) 1197; e-print: arXiv: 1103.1463.

[27] A. Ohnishi, Phase diagram and heavy-ion collisions: Overview, *Prog.Theor.Phys.Suppl.* **193** (2012) 1, e-Print: arXiv:1112.3210 [nucl-th].

[28] E. Bratkovskaya, Microscopic dynamical models for heavy ion collisions, Lectures at International Summer School "Dense Matter 2015", JINR, Dubna, July 2015, http://theor.jinr.ru/ diastp/dm15/

[29] J. Randrup, Spinodal instabilites at the deconfinement phase transition, Lectures at International Summer School "Dense Matter 2015", JINR, Dubna, July 2015, http://theor.jinr.ru/ diastp/dm15/

[30] M.Spannowsky, Higgs Phenomenology, Lectures at Helmholtz - DIAS International Summer School "Theory challenges for LHC physics," JINR, Dubna, July 2015, http://theor.jinr.ru/ calc2015/

[31] S-Fitter Collaboration, http://groups.lal.in2p3.fr/atlas/files/2013/01/HiggsComparisonLC500.png

[32] S. Yamashita, Physics at International Linear Collider, 7th ACFA WS, http://hep1.phys.ntu.edu.tw/.../P2-2-Yamashita.pdf

[33] C. Beskidt, W. de Boer, D.I. Kazakov, A comparison of the Higgs sectors of the CMSSM and NMSSM for a 126 GeV Higgs boson, *Phys. Lett.* **B726** (2013) 758, e-Print: arXiv:1308.1333 [hep-ph]

[34] E.W.Kolb, A Dark Universe: Dark Matter and Dark Energy , CERN Academic Lectures, www.infocobuild.com/.../cosmology-cern.htm

[35] J. Goodman, M. Ibe, A. Rajaraman, Wi. Shepherd, T. M.P. Tait, Hai-Bo Yu, Constraints on Dark Matter from Colliders, *Phys.Rev.* **D82** (2010) 116010, e-Print: arXiv:1008.1783;
D. d'Enterria, (CMS Collaboration), CMS physics highlights in the LHC Run 1, PoS Bormio2015 (2015) 027, e-Print: arXiv:1504.06519.

[36] P.Grothaus, M. Fairbairn, J. Monroe, Directional Dark Matter Detection Beyond the Neutrino Bound *Phys. Rev.* **D 90** (2014) 055018, e-print: arXiv:1406.5047 [hep-ph].

[37] P. Fayet and S. Ferrara, Supersymmetry, *Phys. Rep.* **32** (1977) 249;
M. F. Sohnius, Introducing Supersymmetry, *Phys. Rep.* **128** (1985) 41;
H. P. Nilles, Supersymmetry, supergravity and particle physics, *Phys. Rep.* **110** (1984) 1;
H. E. Haber and G. L. Kane, The search for supersymmetry: Probing physics beyond the standard model, *Phys. Rep.* **117** (1985) 75;
A. B. Lahanas and D. V. Nanopoulos, The road to no-scale supergravity, *Phys. Rep.* **145** (1987) 1.

[38] H. Baer and X. Tata, "Weak Scale Supersymmetry", Cambridge University Press, 2006.

[39] M.Monaco, M. Pierini, A. Romanino and M. Spinrath, Phenomenology of Minimal Unified Tree Level Gauge Mediation at the LHC, *JHEP* **1307** (2013) 078, arXiv:1302.1305 [hep-ph].

[40] C. Beskidt, W. de Boer, D.I. Kazakov, Where is SUSY? *JHEP* **1205** (2012) 094, e-Print: arXiv:1202.3366.

[41] N. Arkani-Hamed, S. Dimopoulos and G. Dvali, *Phys. Lett.* **B429** (1998) 263, e-print: hep- ph/9803315; N. Arkani-Hamed, S. Dimopoulos and G. Dvali, *Phys.Rev.* **D59** (1999) 086004, e-print: hep- ph/9807344.

[42] R.Maartens, Brane Cosmology, Rencontres de Moriond, Electro Weak Interactions and Unified Theories 2004, http:/moriond.in2p3.fr/J04/trans/maartens.pdf

[43] R.Contino, The Higgs as a Composite Nambu-Goldstone Boson, Theoretical Advanced Study Institute in Elementary Particle Physics : Physics of the Large and the Small. (TASI 2009), e-Print: arXiv:1005.4269.

[44] I.A. D'Souza, C.S. Kalman, "Preons: Models of Leptons, Quarks and Gauge Bosons as Composite Objects", World Scientific, 1992

[45] A. Belyaev, M.S. Brown, R. Foadi, M.T. Frandsen, The Technicolor Higgs in the Light of LHC Data *Phys.Rev.* **D90** (2014) 035012 , e-Print: arXiv:1309.2097 [hep-ph]; M. Antola, S. Di Chiara, K. Tuominen, Ultraviolet Complete Technicolor and Higgs Physics at LHC, *Nucl.Phys.* **B899** (2015) 55, e-Print: arXiv:1307.4755 [hep-ph].

Poster presentations

Proceedings of the LHCP2015 Conference, St. Petersburg, Russia, August 31 - September 5, 2015

Editors: V.T. Kim and D.E. Sosnov

A new read-out architecture for the ATLAS Tile Calorimeter Phase-II Upgrade

ALBERTO VALERO

Instituto de Física Corpuscular (Universidad de Valencia - CSIC)

alberto.valero@cern.ch

On behalf of the Tile Calorimeter System of the ATLAS Collaboration

Abstract. The Large Hadron Collider will undergo a series of upgrades culminating in the High Luminosity Large Hadron Collider which will have an average luminosity 5-7 times larger than the nominal Run-2 value. The read-out electronics of the hadronic Tile calorimeter of the ATLAS experiment at the LHC will be redesigned introducing a new read-out strategy. The new TileCal read-out architecture is presented including a description of the main electronics modules and some preliminary results obtained with the first demonstrator system.

INTRODUCTION

TileCal is the hadronic calorimeter of the ATLAS experiment at the Large Hadron Collider (LHC) [1]. TileCal is an iron-scintillator sampling detector which is read-out by 9852 photomultiplier tubes (PMTs). The PMT signals are digitized with a 40 MHz clock which is synchronous with the beam crossing. The digital samples are stored in pipeline memories during the Level 1 (L1) trigger latency (2.5 μs). Simultaneously, the PMT analog signals are grouped and transmitted to the Level 1 Calorimeter system. The digital samples of the events selected by the Level 1 trigger system are transmitted to the Read-Out Drivers (RODs) located in the back-end system at a maximum average rate of 100 kHz (Figure 1).

The LHC has planned a series of upgrades culminating in the High Luminosity LHC (HL-LHC) which will have an average luminosity 5-7 times larger than the nominal Run-2 value. TileCal will undergo an upgrade to accommodate to the HL-LHC parameters. The TileCal read-out electronics will be redesigned introducing a new read-out strategy [2]. The data generated in the detector will be transferred to the PreProcessors (TilePPr) located in off-detector (up link) for every bunch crossing before any event selection is applied (Figure 2). Furthermore, the TilePPr will be responsible of providing preprocessed digital trigger information to the ATLAS Level 0 trigger. In addition, the TilePPr system will implement pipeline memories to cope with the latencies and rates specified in the new trigger schema and in overall it will represent the interface between the data acquisition, trigger and control systems and the on-detector electronics.

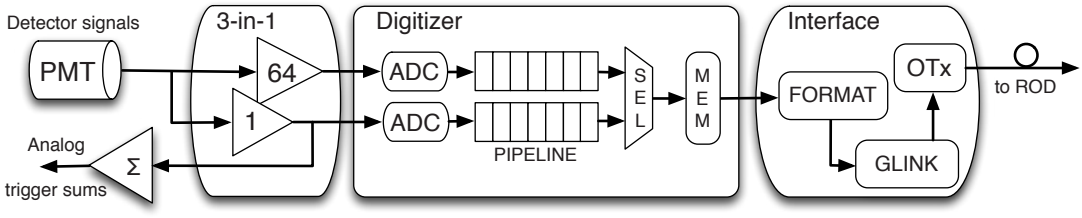

FIGURE 1. Sketch of the TileCal front-end read-out electronics in the current system.

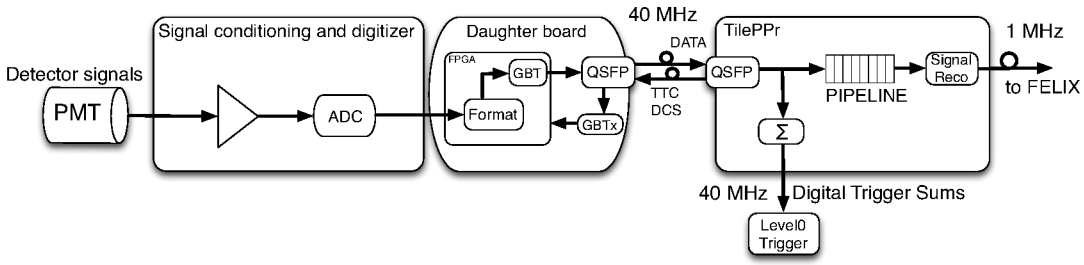

FIGURE 2. Sketch of the TileCal Phase-II upgrade read-out electronics.

TILECAL UPGRADE READ-OUT AND TRIGGER STRATEGY

The HL-LHC will imply an increase in the average luminosity 5-7 times the nominal Run-2 value. In order to cope with this high luminosity levels, a new trigger strategy will be adopted (Figure 3). The first level trigger system, namely Level 0 in Phase-II, will receive digital trigger information from the calorimeters with improved granularity and longitudinal segmentation. The PMT signals will be digitized and transmitted to the TilePPr for every bunch crossing at 40 MHz. The PMT data will be processed to provide calibrated energy associated to correct bunch crossing [3]. Dedicated optical links to each calorimeter trigger feature extractor subsystem will allow the transmission of different information depending on their requirements. For instance, it will be possible to use different energy precision, granularity and longitudinal segmentation for each subsystem. In addition, the TilePPr will provide processed trigger data to the muon trigger system similar to the present analog trigger read-out [4].

In parallel to the trigger data processing, the TilePPr will store the data samples in pipeline memories awaiting for the Level 0 acceptance signal. Then, two different approaches are being evaluated; first, upon the reception of the Level 0 acceptance signal, the samples corresponding to the selected event would be transferred to the Front-End Link eXchange (FELIX) module within the general ATLAS data acquisition (DAQ) system, which would provide trigger information to the Level 1 trigger system. The second option is to transmit the data to the Level 1 trigger system from the TilePPr which will send then the data to the general DAQ for events selected by the Level 1 trigger system. In the baseline the maximum trigger rate for the Level 0 trigger will be 1 MHz and 500 kHz for the Level 1.

The FELIX is the interface between the TilePPr and the ATLAS global DAQ system [5]. The TilePPr will transmit detector-data, monitoring, detector control and calibration data to the FELIX which forwards the data to a network. In the other direction the FELIX will send the Trigger, Timing and Control (TTC) information and detector control commands to the TilePPr.

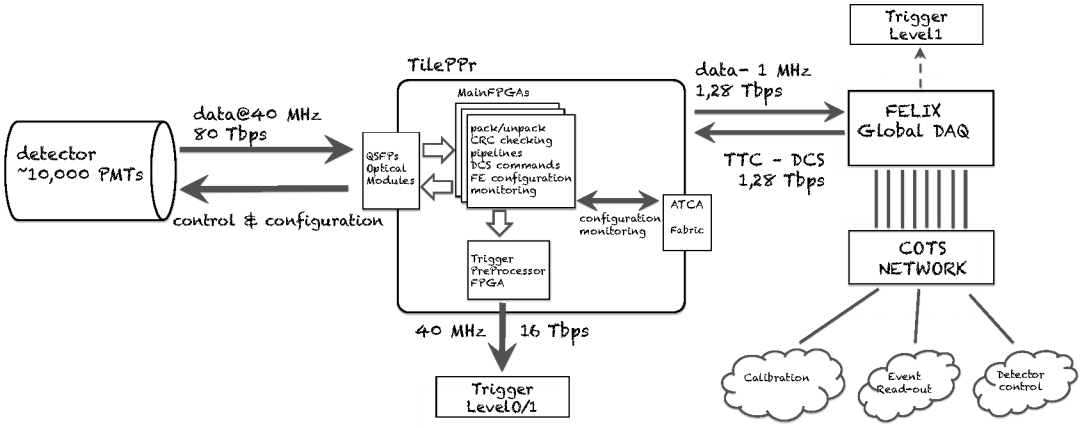

FIGURE 3. Diagram of the TileCal read-out architecture for ATLAS Upgrade Phase-II.

TABLE 1. The TileCal read-out system in the present and Phase-II upgrade architectures.

Up Link only	Present	Upgrade
Total Bandwidth	200 Gbps	80 Tbps
Number of fibers	256	8192
Fiber bandwidth	800 Mbps	9,6 Gbps
Number of modules	32	32
Number of crates	4 (VME)	4 (ATCA)
Input bandwidth per board	6,4 Gbps	2,5 Tbps
Out bandwidth to DAQ per module	3,2 Gbps	40 Gbps
Out bandwidth to trigger per module	Analog front-end	500 Gbps

The PreProcessor demonstrator board

TileCal has built a demonstrator prototype to evaluate the new electronics and the proposed read-out architecture for Phase-II upgrade [6]. The demonstrator will be evaluated in various test-beam campaigns during 2015-2016 and it will be inserted in the ATLAS detector for data taking at the end of 2016. A PPr prototype has been designed to operate one TileCal demonstrator module which represents 1/8 of the final PPr module (Figure 4). Four QSFP optical modules provide the interface with the front-end electronics. The links data are managed from a Virtex7 MainFPGA which implements the communication protocol (GBT) with the front-end, packs and unpacks the data and commands, stores the detector in pipelines memories, receives and decodes legacy TTC information and provides communication with the old ROD system. A second Kintex7 PPrFPGA pre-process and transmits the data to the trigger system through a Parallel Optical Device (POD). The board has a standard double-mid size AMC format and can be operated in an ATCA/uATCA framework which provides power and ethernet communication with both FPGAs for control and monitoring purposes. Power and RJ45 ethernet connectors are included to operate the module in standalone mode. The first three modules have been produced and are fully operative.

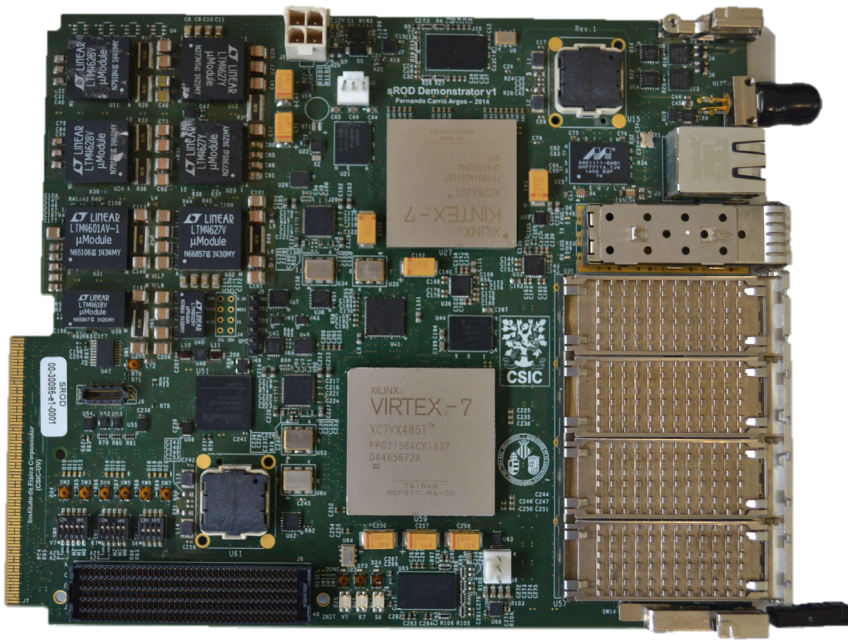

FIGURE 4. Picture of the TilePPr prototype for the TileCal demonstrator project.

The TileCal PreProcessor module

The final TilePPr board must be compliant with the ATCA standard which has been selected by ATLAS as the modular electronics standard for Phase-II upgrade (Figure 5). A total of 32 PPr modules will be needed to operate the complete TileCal detector. They will be installed in four ATCA chassis thus maintaining the current back-end structure (Table 1).

Each TilePPR module has to process the data of up to 8 consecutive TileCal modules (432 PMT channels) thus keeping the (1:8) ROD to module ratio as in the legacy system. The bi-directional communication with the on-detector electronics will use high speed parallel optics devices. The MainFPGAs will implement the communication protocols with the detector electronics and with the FELIX Global DAQ system. In addition, they will store the data samples in pipeline memories as described in the previous sections.

A second FPGA, located in the Trigger and DAQ interface (TDAQi) rear transition board, will process and transmit the data to the Level 0 calorimeter and muon trigger systems through dedicated parallel optics connections.

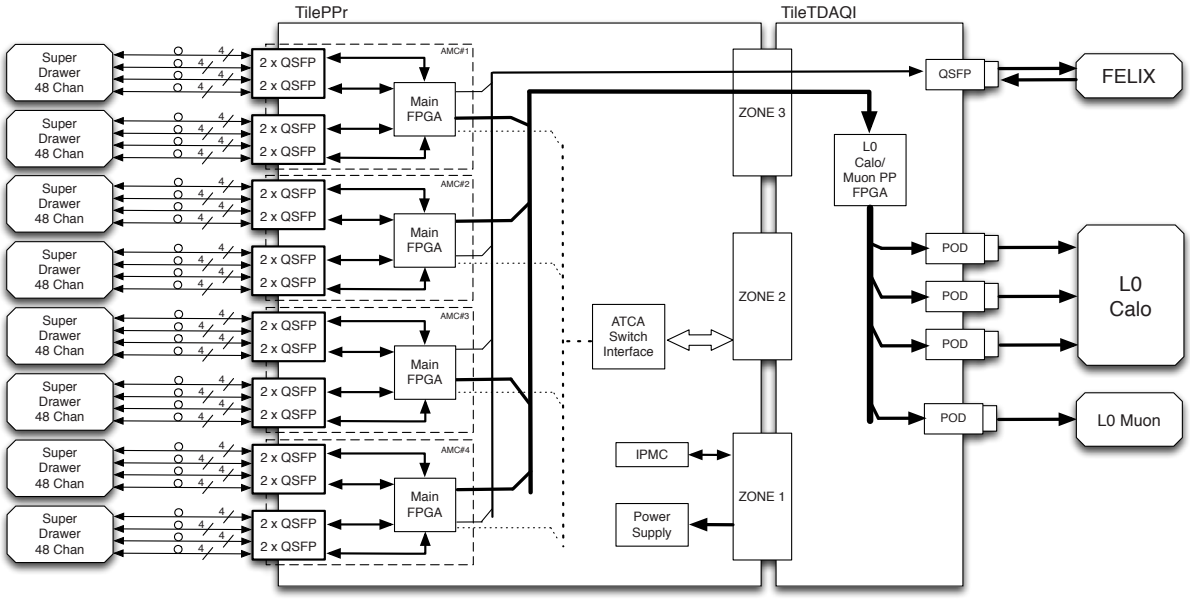

FIGURE 5. Block diagram of the TileCal PPr module for the Phase-II upgrade.

REFERENCES

[1] ATLAS Collaboration, Journal for Instrumentation **3**, p. S08003 (2008).

[2] D. Eriksson et al., *Proceedings, Topical Workshop, TWEPP-11, Vienna, Austria, September 26-30, 2011*, JINST **7**, p. C02006 (2012).

[3] ATLAS Collaboration, Letter of Intent for the Phase-II Upgrade of the ATLAS Experiment, Dec 2012.

[4] J. Souza, "Upgrading the ATLAS Tile Calorimeter electronics," Tech. Rep. ATL-TILECAL-PROC-2014-017 (CERN, Geneva, 2014).

[5] J. T. Anderson et al., "FELIX: a High-Throughput Network Approach for Interfacing to Front End Electronics for ATLAS Upgrades," Tech. Rep. ATL-DAQ-PROC-2015-014 (CERN, Geneva, 2015).

[6] F. Carrio Argos and A. Valero, "Performance of the Tile PreProcessor Demonstrator for the ATLAS Tile Calorimeter Phase II Upgrade," Tech. Rep. ATL-TILECAL-PROC-2015-018 (CERN, Geneva, 2015).

Proceedings of the LHCP2015 Conference, St. Petersburg, Russia, August 31 - September 5, 2015

Editors: V.T. Kim and D.E. Sosnov

Jet Vertex Charge Reconstruction

SNEŽANA NEKTARIJEVIĆ[1,2,a)]

[1]*Radboud Universiteit Nijmegen, The Netherlands*
[2]*Nikhef, The Netherlands*

[a)]snezana.nektarijevic@cern.ch

On behalf of the ATLAS Collaboration

Abstract. A newly developed algorithm called the jet vertex charge tagger, aimed at discriminating between jets initiated by a b-quark from those initiated by a $\bar{b}$-quark, is presented. This algorithm relies on the well established track-based jet charge determination, extended by introducing the so-called *jet vertex charge* reconstruction, which exploits the charge information associated to the displaced vertices within the jet. Furthermore, the charge of a soft muon contained in the jet is taken into account when available. All available information is combined into a multivariate discriminator. The algorithm has been developed on jets matched to generator level b-hadrons, referred to as b-jets, provided by $t\bar{t}$ events simulated at $\sqrt{s}$=13 TeV using the full ATLAS detector simulation and reconstruction.

INTRODUCTION

Final states with multiple jets containing generator level b-hadrons, called b-jets, such as those involving top quarks, Higgs bosons decaying into a $b\bar{b}$ pair, or new heavy states like supersymmetric or vector-like quarks, often suffer from large combinatorial backgrounds. The possibility of distinguishing between jets originating from b-quarks and $\bar{b}$-quarks provides information potentially useful for reducing this background. However, b-quarks (as well as other quarks except the top quark, and gluons) hadronise before their electric charge can be measured, so that the charge information of the initial quark is diluted. A method of indirectly inferring the sign of the electric charge of a hadronised object was first proposed by Field and Feynman [1]. In this method, the charge of a jet is reconstructed as a sum of the charges of all charged-particle tracks associated to it, weighted by their transverse momenta to maximise the sensitivity to the leading particles, which tend to carry most of the information of the fragmenting parton, while suppressing the impact of fluctuations. Jet charge observables motivated by this method have already been investigated extensively within the ATLAS Collaboration. A study of jet charge performance was carried out with dijet, $t\bar{t}$ and W+jets events [2], while a measurement of jet charge was performed in dijet events [3], both using pp-collision data at 8 TeV. Reconstruction of b-jet charge was used in the context of CP violation studies in the B_s system [4] and for the measurement of the top quark charge in pp-collision data at $\sqrt{s} = 7$ TeV [5].

A novel method described in this writing and published in [6], is mainly based on the vertex charge reconstruction algorithm [7], which represents an evolution of these ideas aimed at improving the discrimination between b-jets initiated by a b-quark from those initiated by a $\bar{b}$-quark. In addition to the established jet charge information, called Q_{j} in the following, this method exploits the topology and kinematics of b-hadron decays more extensively. With a mean lifetime of $\sim 10^{-12}$s, b-hadrons make a characteristic secondary vertex (SV) displaced from the primary vertex (PV) by O(mm), often followed by a tertiary vertex (TV) resulting from the subsequent decay of the resulting charmed hadron.[1] In addition, both b- and c-hadrons have substantial branching ratios for decays involving leptons (11% and 10%, respectively, for semimuonic decays [8]). The method presented in this note, called the jet vertex charge (JVC) tagger, makes use of the reconstructed displaced vertices by computing further charge variables, the so called secondary vertex charge Q_{SV}, and tertiary vertex charges Q_{TV}, using the tracks associated to the respective vertices. Displaced vertices are reconstructed using the JetFitter algorithm [9]. The charge of a soft muon present within the

[1]The mean $c\tau$ for B mesons is ≈ 492 μm, while for $D^0/D^{\pm}$ mesons it is only $\approx 123/312$ μm, respectively [8].

jet, Q_μ, is also taken into account. A final discriminant is formed by combining the aforementioned information using a multi-variate analysis (MVA). The final discriminant is then interpreted as the ratio of likelihoods for a b-jet to be positively and negatively charged.

THE ATLAS DETECTOR AND MONTE CARLO SAMPLES

The ATLAS detector [10], one of four particle detectors along the LHC circular accelerator [11], has a near cylindrical geometry[2] and consists of an inner tracking detector (ID) surrounded by a 2 T superconducting solenoid, electromagnetic and hadronic calorimeters, and a muon spectrometer (MS) with a toroidal magnetic field. The ID provides tracking of charged particles for $|\eta| < 2.5$. It consists of silicon strip (SCT) and pixel detectors surrounded by a straw tube tracker (TRT) which also provides transition radiation measurements for electron identification. A new detector, the Insertable B-Layer (IBL), has been installed closer to the beam pipe [12] before the start of Run 2 of the LHC, increasing the precision in the reconstruction of displaced vertices. The electromagnetic and hadronic calorimeter system covers the pseudorapidity range $|\eta| < 4.9$. The MS covers the range $|\eta| < 2.7$.

The optimisation and the performance evaluation of this algorithm are carried out using a sample of $t\bar{t}$ events corresponding to 13 TeV pp collisions simulated with Powheg+Pythia [13, 14], considering only single- and dilepton final states. EvtGen [15] is used to model the decays of b- and c-hadrons. Minimum bias interactions consistent with the expected 2015 run conditions are generated with Pythia8 [16] and are overlaid on the $t\bar{t}$ events. The propagation of particles through the detector and the detector response are simulated fully using a GEANT4 [17] based framework [18].

OBJECT DEFINITION, SELECTION AND FLAVOUR LABELLING

The algorithm described in this report is based on jets reconstructed from energy deposits in the calorimeter, ID tracks and muons reconstructed by combining ID and MS tracks. More details regarding the selection of objects can be found in Section 3 of [6].

The flavour of the simulated jet is assigned with a cone-labelling scheme: if a weakly decaying b-hadron with $p_{\mathrm{T}} > 5$ GeV at the generator level is found within the jet in a cone of $\Delta R < 0.3$, the jet is labelled as a *truth b-jet*. This association is done in an exclusive way: the b-hadron is matched only to the closest jet in ΔR.

The charge of the b-jet is then assigned according to the quark composition of the b-hadron matched to the jet: if the hadron contains a b-quark the jet is considered negative, i.e. it is assigned a negative *truth charge*. The opposite happens for $\bar{b}$-quarks. If more than one b-hadron is found inside a jet, the one with highest p_{T} is chosen to tag the truth charge of the jet. It should be noted that the use of the weakly decaying b-hadron ignores the effects of B-meson mixing [8]. These effects are studied in the performance evaluation by considering the parentage of the weakly decaying b-hadron: if any of its parents contains a b ($\bar{b}$) quark while the b-hadron contains a $\bar{b}$ (b) quark, B-meson mixing is considered to have occurred.

ALGORITHM

The central role in the algorithm has the formula for estimating the charge of a jet as a sum of the p_{T}-weighted charges of the associated tracks:

$$Q_{\mathrm{jet}} = \frac{\sum_{i \in \mathrm{Trk}} q_i \cdot {p_{\mathrm{T}}}_i^{\kappa}}{\sum_{j \in \mathrm{Trk}} {p_{\mathrm{T}}}_j^{\kappa}} \tag{1}$$

where Trk stand for the set of tracks used in the computation, while q_i and ${p_{\mathrm{T}}}_i$ stand for the charge and the transverse momentum of the track i. κ is a parameter tuned to maximise the separation power between the distributions of positive and negative b-jets.

This formula is used to compute four different charge variables, using different sets of tracks and numerical values of the κ parameter. The jet charge Q_{j} variable is calculated using the tracks selected as explained in Section 3 of [6],

[2] ATLAS uses a right-handed coordinate system with its origin at the nominal interaction point (IP) in the centre of the detector and the z-axis along the beam line. The x-axis points from the IP to the centre of the LHC ring and the y-axis points upwards. Cylindrical coordinates (r, ϕ) are used in the transverse plane, ϕ being the azimuthal angle around the beam line. The pseudorapidity is defined in terms of the polar angle θ as $\eta = -\ln(\tan(\theta/2))$, while $\Delta R = \sqrt{\Delta\eta^2 + \Delta\phi^2}$. Observables labelled as "transverse" are projected onto the x–y plane.

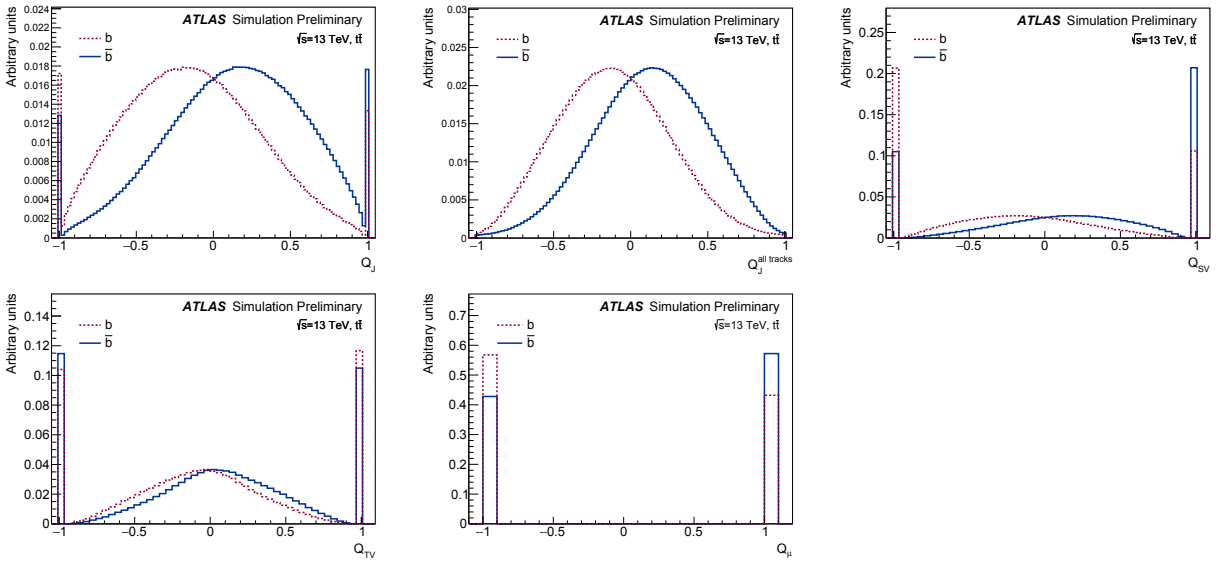

FIGURE 1. Distributions of the basic charge variables, for positive (full line) and negative (dashed line) truth b-jets, normalised to unity. From top to bottom and from left to right: Q_{j}, $Q_{\text{j}}^{\text{all tracks}}$, Q_{SV}, Q_{TV} and Q_μ. The peaks at values of ± 1 arise when the charge computation relies on a single track or when all particles considered have the same charge. Taken from [6].

and the optimal value $\kappa = 1.1$. The same value of the κ parameter is used for the computation of the $Q_{\text{j}}^{\text{all tracks}}$ variable, for which all tracks matched to the jet are taken into account. This variable is used only in few cases when no other charge information is available. Secondary and tertiary vertex charges, Q_{SV} and Q_{TV} respectively, are reconstructed using the tracks refitted by JetFitter and passing the fake track cleaning explained in Section 3 of [6]. as well as the values $\kappa = 0.7$. The numerical values of the κ parameter are optimised for the best separation between positive and negative b-jets for each variable separately.

In Figure 1 the distributions of the basic charge variables are shown, for truth b-jets with $p_{\text{T}} > 20$ GeV and $|\eta| < 2.5$, which pass the pileup cleaning [19]. The aforementioned jet (vertex) charge variables show regular distributions in the interval $(-1, +1)$ with a broad peak around 0. These smooth shapes are accompanied by spikes at the values of ± 1, populated by the jets in which the charge in question is computed using a single track, or a number of tracks with the same charge.

Semi-leptonic b-hadron decays are a source of valuable information; the charge of a muon originating from a b-hadron decay carries the same sign as the charge of the b-quark contained in the hadron, while the sign is opposite for muons originating from the subsequent c-hadron decay. Muons selected as described in Section 3 of [6] are used in this algorithm. If more than one muon is associated to the jet, only the muon with the highest p_{T} is considered. The charge of the considered muon, Q_μ, is shown in Figure 1.The information of the muon origin vertex is inferred from its kinematics. Muons originating from b-hadron decays tend to have a harder spectrum and a wider opening angle with respect to the jet axis than those originating from c-hadron decays. These properties are exploited by including the muon transverse momentum components perpendicular to and along the jet plus muon axis, as well as the muon-jet opening angle in the MVA training.

MULTIVARIATE ANALYSIS

The basic charge variables described above are sensitive to the charge of the quark that triggered the jet formation, but do not provide optimal discrimination individually. Jets initiated by b and $\bar{b}$ quarks populate different regions in the phase-space of these variables. To best recognise these regions and separate them from one another, an MVA is employed. To keep the analogy of the jet charge sign and the numerical values of the MVA discriminators, $\bar{b}(b)$-initiated jets are considered signal (background) in the MVA trainings.

To best exploit the available information, b-jets are grouped into eight exclusive categories according to the

availability of the basic charge variables. The definitions of categories and their relative abundances in the sample at hand are summarised in Table 1. The available charges are indicated by the subscript of the category names. For the categories $C_{j,\mu}$, $C_{j,SV}$, $C_{j,SV,\mu}$, $C_{j,SV,TV}$, and $C_{j,SV,TV,\mu}$, available information is combined in the corresponding MVA discriminator trained using the Multi-layer Perceptron (MLP) method implemented in the TMVA toolkit [20]. For the categories C_j, C_{SV} and $C_{\text{all tracks}}$, the discrimination between the positive and negative b-jets relies on the only charge information available in this category, i.e. the Q_j, Q_{SV} and $Q_j^{\text{all tracks}}$ variables respectively.

TABLE 1. Relative abundance per category measured on the sample of simulated $t\bar{t}$ events at $\sqrt{s} = 13$ TeV as a function of the MV2c20 working points. Only truth b-jets with $p_T > 20$ GeV and $|\eta| < 2.5$ and passing the JVT requirement are considered.

Category	C_j	$C_{j,\mu}$	C_{SV}	$C_{j,SV}$	$C_{j,SV,\mu}$	$C_{j,SV,TV}$	$C_{j,SV,TV,\mu}$	$C_{\text{all tracks}}$
Untagged	11%	2.0%	3.0%	53%	10%	15%	3.5%	1.3%

To improve the performance of the MVA, further variables are included in the machine learning procedure. Variables describing the vertex reconstruction quality and the corresponding track multiplicity help the MVA to distinguish well reconstructed vertices from those that are poorly reconstructed, and thus give them a higher importance. Variables describing kinematics of the assigned muon help the MVA differentiate between same-sign and opposite-sign muon charge cases. Description of all accompanying variables as well as details regarding the MVA training configuration are documented in Section 4.3.1. of [6]. The effects of B-meson mixing discussed above are ignored in the training procedure, but are properly accounted for in the final performance evaluation.

Finally, the best available JVC discriminator, referred to as the *JVC weight w*, is constructed for each category, relying on a single variable in three categories and the corresponding MLP response in the other five categories. The JVC weight distributions normalised to unity are shown in Figure 2 for all eight categories. The plots show the overlaid distributions for the positive (solid line) and negative (dashed line) b-jets. Different ranges of the JVC discriminator across the categories reflect different MLP settings.

Given the different shapes of the JVC discriminators across the categories, a given JVC weight value w corresponds to different positive b-jet efficiency and negative b-jet rejection depending on the category to which the jet in question belongs. Thus, a more general discriminator with a unique interpretation across the full spectrum of its values is constructed. For each separate given category, the JVC weight distributions for positive b-jets, $\bar{b}(w)$, and for negative b-jets, $b(w)$, are normalised to unity. For a given jet with a jet vertex charge w, the logarithm of the likelihood ratio $\lambda_{JVC}(w) \equiv \ln\left(\bar{b}(w)/b(w)\right)$ is used, as the variable offering the best discrimination between positive and negative b-jets. The λ_{JVC} distribution for all categories combined is presented in Figure 2 (bottm right plot).

PERFORMANCE

The performance of the final λ_{JVC} discriminant is evaluated in terms of the negative b-jet (background) rejection as a function of the positive b-jet (signal) efficiency for the sample containing all categories combined. The background rejection is defined as (1− background efficiency); if a negative (positive) b-jet is identified to be the result of B-meson mixing, in the following it is considered as a positive (negative) b-jet. Discrimination power curves based on the final λ_{JVC} discriminant for all individual categories are compared to each other in Figure 3 (top left). The overall improvement of the b-jet charge reconstruction is illustrated in Figure 3 (top right), where the separation power of the final JVC discriminant is compared to that of the Q_j variable. This figure shows that for a given signal efficiency in the range 50–80%, the background rejection improves by ∼ 6–8%.

Since the inputs used in the construction of the final JVC discriminant rely on quantities that have a substantial dependence on the jet kinematics, it is to be expected that this dependence is also reflected in the JVC performance. Furthermore, the information exploited in the JVC reconstruction overlaps to some extent with that used in the b-tagging algorithms, so that the JVC performance is expected to depend upon the b-tagging requirement too.

Variables such as multiplicities and momenta of tracks and muons produced within a jet are rather correlated to the transverse momentum of the jet. The track momentum then affects the track charge reconstruction efficiency, which significantly drops at high transverse momentum. Furthermore, jets with a direction close to the edge of the angular acceptance of the inner detector are likely to lose some tracks due to the acceptance loss, which also affects the JVC performance. These effects are demonstrated in the plots in Figure 3 (bottom left and right), which show the JVC separation power curves split in intervals of p_T and $|\eta|$ of the jet. The figures show that the JVC algorithm has

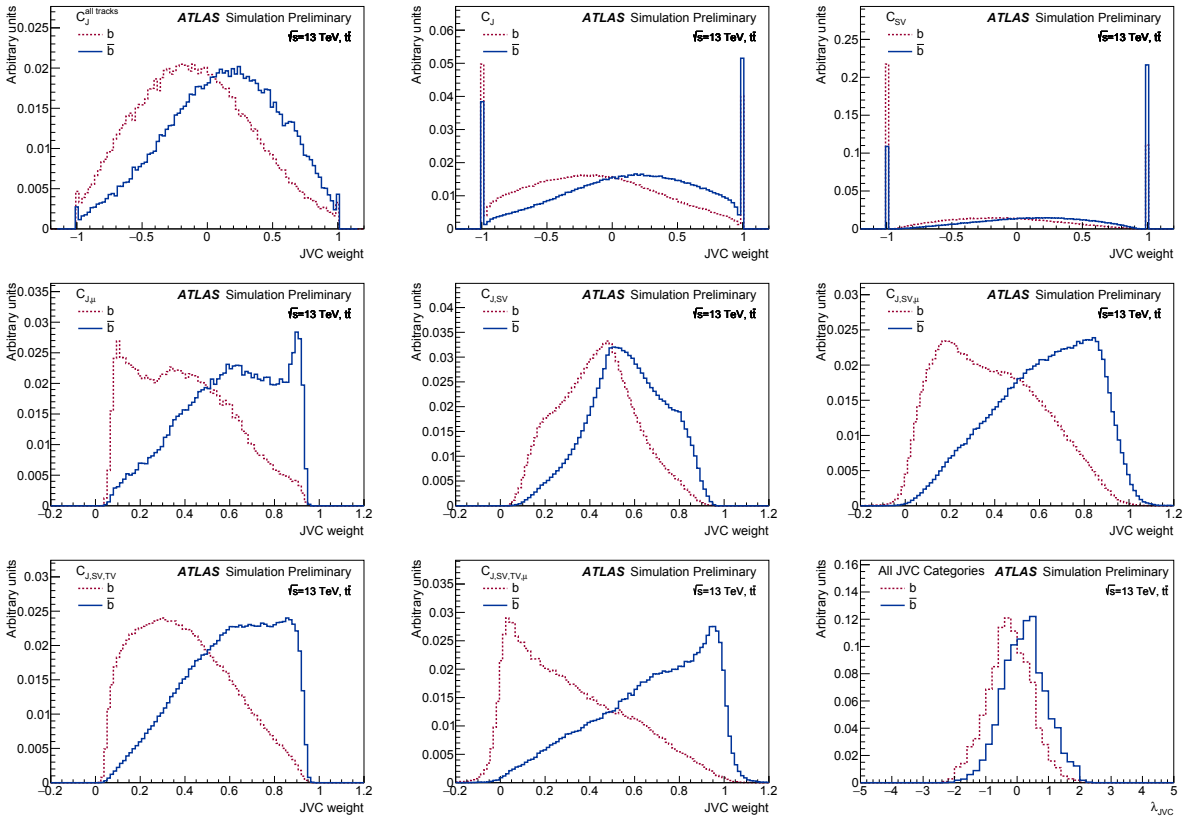

FIGURE 2. JVC weight distributions in all categories, as well as the λ_{JVC} distribution for all categories combined. All distributions are normalised to unity. Dashed (solid) lines correspond to distributions composed of $b(\bar{b})$-jets. Taken from [6].

a rather stable performs for lower jet p_{T} (up to 250 GeV). Above 250 GeV however, the separation power weakens significantly. As a function of $|\eta|$, the performance is rather stable up to $|\eta| < 2.1$, above which it slowly deteriorates, following the degradation of the track reconstruction performance in the forward region.

The interplay of the JVC algorithm and b-tagging has been studied by evaluating the JVC performance with and without requirements on the b-tagging weight provided by the MV2c20 algorithm [21]. Notably, b-tagging affects the relative abundance of the b-jet categories, as shown in Table 1. The fraction of b-jets not containing displaced vertices decreases noticeably as the b-tagging requirement is tightened. However, the overall performance is rather independent from b-tagging, improving by only $\sim 1\%$ for a tagged sample.

CONCLUSIONS

A new algorithm for inferring the charge of b-jets called the jet vertex charge tagger has been developed. The algorithm relies on the reconstructed jets, inner detector tracks assigned to the jet and to the displaced vertices found within it, as well as the associated combined muons. Using these objects, five basic charges are reconstructed: two jet charges computed using selected or non-selected tracks, a secondary and a tertiary vertex charge computed using the tracks associated to the respective vertices, and the charge of the muon. Jets are categorised according to the availability of these basic charges, resulting in three categories relying on single variables for the discrimination between positively and negatively charged b-jets, as well as five further categories based on MLP discriminants. All categories are combined by providing a likelihood ratio based discriminant, with a universal interpretation for all categories. The final discriminant can be calibrated with the early LHC Run-2 data at 13 TeV, exploiting a kinematic reconstruction of $t\bar{t}$ candidate events. This variable can be particularly useful to reduce the combinatorial background in analyses with a high b-jet multiplicity.

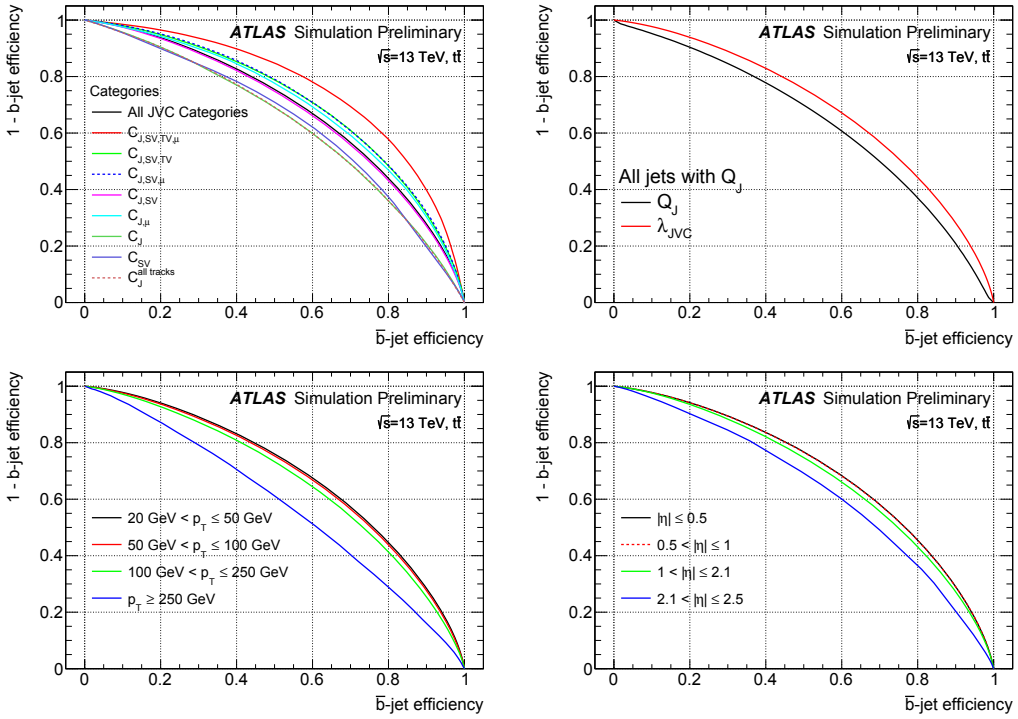

FIGURE 3. Performance comparison between different categories (top left), and a comparison of the separation power based on the Q_j variable and the λ_{JVC} discriminant for all categories with a reconstructed Q_j (top right). In the latter figure, the kinks in the Q_j curve are due to jets with a reconstructed $Q_j = \pm 1$. Background rejection curves for all categories combined decomposed in intervals of jet p_T (bottom left) and $|\eta|$ (bottom right). Taken from [6].

REFERENCES

[1] R.D. Field and R.P. Feynman, Nucl. Phys. B **136**, 1–76 (1978).
[2] ATLAS Collaboration, ATLAS-CONF-2013-086 (2013).
[3] A. Collaboration, (2015), arXiv:1509.05190 [hep-ex] .
[4] ATLAS Collaboration, Phys. Rev. **D90**, p. 052007 (2014), arXiv:1407.1796 [hep-ex] .
[5] ATLAS Collaboration, JHEP **1311**, p. 031 (2013), arXiv:1307.4568 [hep-ex] .
[6] ATLAS Collaboration, ATL-PHYS-PUB-2015-040 (2015).
[7] K. Abe *et al.* (SLD), Phys. Rev. Lett. **94**, p. 091801 (2005), arXiv:hep-ex/0410042 [hep-ex] .
[8] K.A. Olive et al. (Particle Data Group), Chin.Phys. **C38**, p. 090001 (2014).
[9] G. Piacquadio and C. Weiser, J.Phys.Conf.Ser. **119**, p. 032032 (2008).
[10] ATLAS Collaboration, JINST **3**, p. S08003 (2008).
[11] L. Evans and P. Bryant, JINST **3**, p. S08001 (2008).
[12] A. Collaboration, CERN-LHCC-2010-013 (Sep 2010).
[13] P. Nason, JHEP **11**, p. 040 (2004), arXiv:hep-ph/0409146 [hep-ph] .
[14] T. Sjöstrand, S. Mrenna, and P. Skands, JHEP **05**, p. 026 (2006), arXiv:hep-ph/0603175 .
[15] D. Lange, Nucl. Instrum. Meth. **A462**, 152–155 (2001).
[16] T. Sjöstrand, S. Mrenna, and P.Z. Skands, Comput. Phys. Commun. **178**, 852–867 (2008), arXiv:0710.3820 [hep-ph] .
[17] S. Agostinelli *et al.* (GEANT4), Nucl. Instrum. Meth. **A506**, 250–303 (2003).
[18] ATLAS Collaboration, Eur. Phys. J. **C70**, 823–874 (2010), arXiv:1005.4568 [physics.ins-det] .
[19] ATLAS Collaboration, ATLAS-CONF-2014-018 (2014).
[20] A. Hoecker *et al.*, PoS **ACAT**, p. 040 (2007), arXiv:physics/0703039 .
[21] ATLAS Collaboration, ATL-PHYS-PUB-2015-022 (2015).
[22] M. Cacciari, G.P. Salam, and G. Soyez, JHEP **0804**, p. 063 (2008), arXiv:0802.1189 [hep-ph] .
[23] ATLAS Collaboration, ATL-PHYS-PUB-2015-015 (2015).

Proceedings of the LHCP2015 Conference, St. Petersburg, Russia, August 31 - September 5, 2015

Editors: V.T. Kim and D.E. Sosnov

The ATLAS Liquid Argon Calorimeters At The Dawn Of LHC Run-2

CLÉMENT CAMINCHER

LPSC, Université Grenoble-Alpes, CNRS/IN2P3, 53 Avenue des Martyrs 38026 Grenoble Cedex

camincher@lpsc.in2p3.fr

On behalf of the ATLAS LAr Calorimeter Group

Abstract. The Liquid Argon Calorimeters are key sub-detectors of ATLAS. They are essential to detect and measure the properties of electrons, photons and are also crucial for jets and missing transverse momentum measurements. During the LHC shutdown in 2013-2014, the hardware and the software have been optimized to improve their reliability. The first collisions allow an assessment of the performance of the detector in the LHC Run-2 conditions. In view of the next LHC Run in 2020, an upgrade of the level-1 trigger system is also under test. The status at the restart of the LHC Run-2 is presented in this document.

The Liquid Argon (LAr) Calorimeters

The LAr Calorimeters [1] are sampling calorimeters, using liquid argon as active medium. The general layout is visible in Fig. 1a.

The primary aim of the electromagnetic calorimeters is the detection of electrons and photons and the measurement of their energy and momentum direction. An electromagnetic barrel (EMB) and two electromagnetic end-caps (EMEC) cover the pseudorapidity regions of respectively $|\eta| < 1.475$ and $1.375 < |\eta| < 3.2$. Their passive material is lead and they have an innovative accordion shape, enabling a full azimuthal coverage and a fast readout while avoiding dead regions.

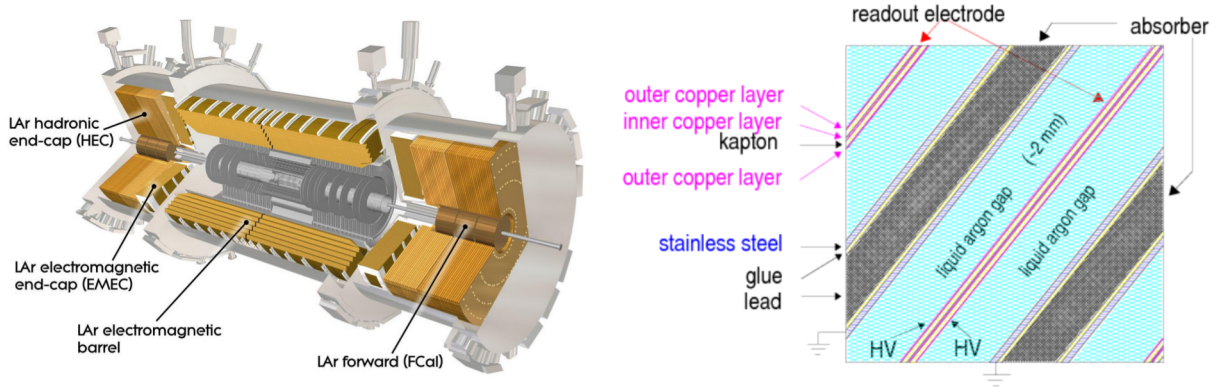

(a) (b)

FIGURE 1. (a) General layout of the LAr Calorimeters. (b) Internal structure of the electromagnetic partitions[2].

The hadronic end-caps (HEC) are also part of the LAr Calorimeters. They detect jets in the pseudorapidity range $1.5 < |\eta| < 3.2$ and use copper plates as passive material. Those plates allow to easily extract the heat deposited in those regions.

The forward calorimeters (FCal) cover the large pseudorapidity ($3.1 < |\eta| < 4.9$) region. They use a specific design of either copper or tungsten matrix with argon gaps of $150 - 400\ \mu m$ to have a fast readout and avoid ion build-up effects up to the LHC design luminosity.

The internal electromagnetic structure may be seen in Fig. 1b. When particles ionize the argon, the ionization products are collected by the outer layers of the copper electrodes, powered by two independent high voltage (HV) lines. By capacitive coupling, this induces a current pulse in the inner electrodes layers, which is proportional to the energy deposit of the initial particle. The LAr Calorimeters are divided into 182 468 independent cells. The cell pattern, in three layers, allows the reconstruction of the longitudinal development of the electromagnetic shower. Radiation lengths larger than 22 X_0 (EMB) and 24 X_0 (EMEC) enable to contain most of the shower for an electron energy up to 5 TeV. The typical size of a cell in EMB layer where most of the shower is contained is $\Delta\eta \times \Delta\phi = 0.025 \times 0.025$.

The LAr Calorimeters are also an input to the level-1 trigger (L1Calo). An energy summation is performed over the layers and on regions of typical size: $\Delta\eta \times \Delta\phi = 0.1 \times 0.1$ to form trigger towers (TT). The level-1 trigger decision is taken based on this coarse information.

The LAr Calorimeters were essential to the Higgs boson discovery. The most sensitive decay channels were the ones with electromagnetic objects : $H \to \gamma\gamma$ and $H \to 4l$. In the design of the calorimeters, these processes constrained the requirements for an excellent energy resolution on a range from 10 to 300 GeV [3]. The typical energy resolution in the barrel was measured during the Run-1 to be [4]:

$$\frac{\sigma_E}{E} = \frac{10\%}{\sqrt{E}} \oplus \frac{250\ \text{MeV}}{E} \oplus 1\% \tag{1}$$

Novelties for the Run-2

The ionization pulse has a triangular shape, as can be seen in Fig. 2. The typical drift time of $450 - 600\ ns$[1], in the electromagnetic partitions, is much longer than the bunch crossing period ($25\ ns$). After pre-amplification, a $CR - (RC)^2$ filter shapes the signal in the bipolar form visible in Fig. 2. The signal pulse is digitized at a frequency of 40 MHz. During the Run-1, five digitized samples were used to compute physical values as the energy and the peak time, making such measurements more resilient to the out of time pile-up (energy deposits due to the previous collisions).

In order to run at a higher instantaneous luminosity in the years to come, the current L1 trigger rate of around 70 kHz would need to be raised up to 100 kHz. To enable such an increase, the number of digitized samples was reduced from five to four, at the start of Run-2 due to the limited size of the online data buffers. Studies have shown that the impact on the energy resolution is negligible.

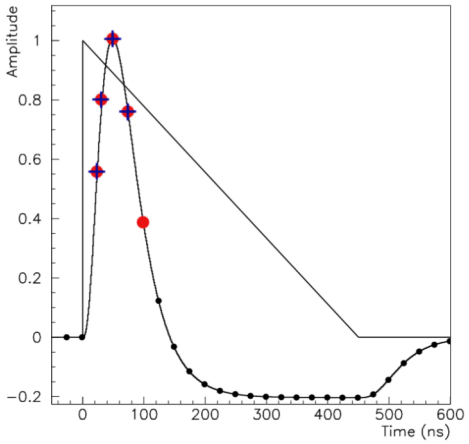

FIGURE 2. Typical pulse shape within the liquid argon before and after its shaping. The large dots (resp. crosses) show the typical position of the five (resp. four) digitized samples.

[1] In the FCal, the drift time is shorter due to the smaller gaps of liquid argon and the position of the used samples is different.

Besides this, a majority of high voltage (HV) power supplies were replaced. During the Run-1 they were subject to intensity spikes, leading to a voltage trip. This induced the main source of data rejection namely 0.46% out of a total of 0.88% in 2012 for the LAr Calorimeters [5]. A new generation of HV generators was successfully tested during Run-1 and proved to be more resilient to such spikes. They could sustain high intensity for a longer period, allowing to reduce the data losses. Therefore they were largely deployed before the LHC Run-2.

Global synchronization

In April 2015, single circulating beams were dumped in the ATLAS upstream collimators. They created huge particle showers flowing through the detector. Such events are called "beam splashes" and induce energy deposition in most of the detector.

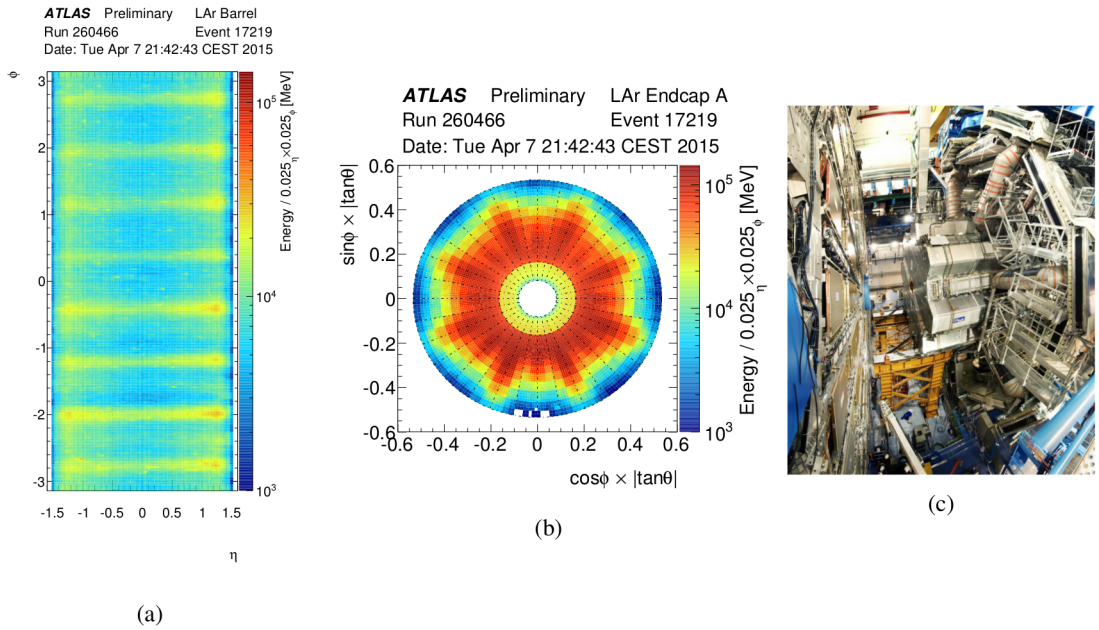

FIGURE 3. Energy deposits during a beam splash event: (a) in the barrel and (b) in the end-cap [6]. (c) End-cap toroid during the installation in the ATLAS cavern.

The energy deposition during a beam splash is presented in Fig. 3a in the barrel and Fig. 3b in an end-cap. The various equipments, subdetectors, services, etc, installed between the collimators and ATLAS act as a mask for the flowing particles. The eight visible structures with lower energy deposits are mainly due to the end-cap toroid magnet. This component of ATLAS is visible in Fig. 3c during its installation. Beam splashes allow to highlight the inactive channels. Their number was found to be around 0.06% and stable compared to the 2012 data taking.

Another use of such events is the synchronization of the LAr Calorimeters which is crucial for a precise energy measurement. A correction is applied to take into account that the particles are not coming from the interaction point. Then it is possible to evaluate the shift in time with a very good accuracy. Figure 4 shows the typical time offset distribution in the electromagnetic barrel. Each Front End Board (FEB) reads out 128 channels and the peak time position is averaged over them. The dispersion (RMS) of the time offset distribution is of the order of 1 ns. Such offset makes negligible the impact on the energy reconstruction accuracy.

Early energy measurements

A dataset of a typical size of a few pb^{-1} allows to the reconstruction of well known Standard Model processes ("standard candles"). Figure5 shows the dielectron invariant mass focused on the $Z \rightarrow ee$ and $J/\Psi \rightarrow ee$ regions [7]. Both peaks are clearly visible around respectively 91 GeV and 3 GeV with a very low background. The simulation is in a satisfactory agreement with the data. This shows that the behaviour of the LAr Calorimeters is well under control and that the modelling of the background is understood.

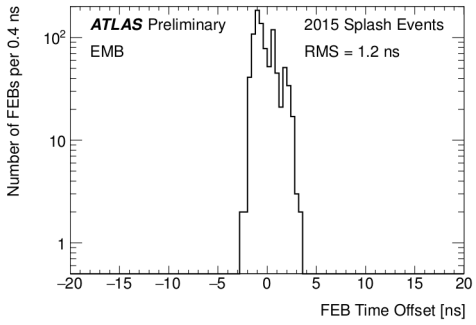

FIGURE 4. Time offset, averaged per FEB, in the electromagnetic barrel (EMB)[6].

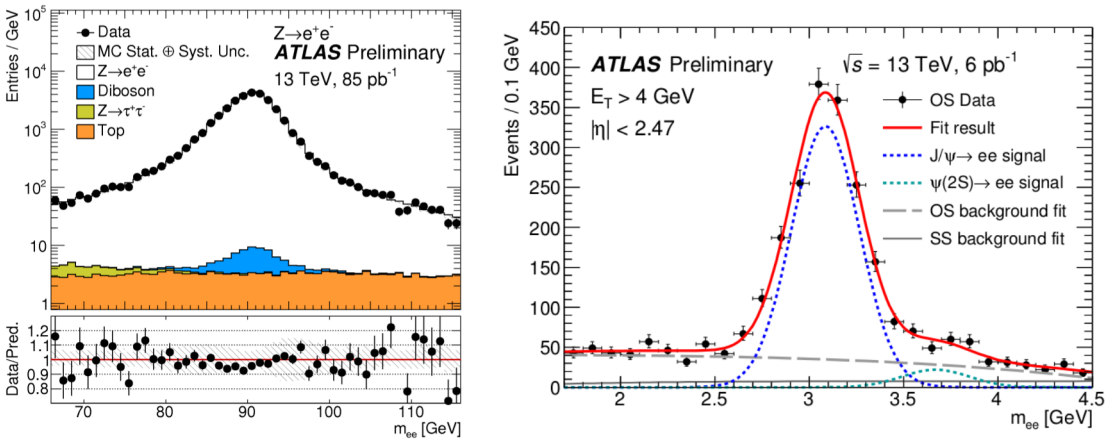

(a) (b)

FIGURE 5. Dielectron invariant mass distribution (a) around 91 GeV and (b) around 3 GeV[7].

Trigger upgrade for higher luminosity

The design instantaneous luminosity of the LHC for ATLAS is $10^{34}\ cm^{-2}s^{-1}$. It could be largely exceeded in 2020 (LHC Phase-1 upgrade) to reach up to $3 \times 10^{34}\ cm^{-2}s^{-1}$. The mean number of interactions per bunch crossing could also raise up to $\mu = 80$. This would lead to an increase of the detector occupancy and of the triggered event rate. To cope with such conditions an upgrade of the L1Calo trigger system has been designed [8].

The allowed bandwidth is hardware limited of 100 kHz. In order to have a balanced trigger menu, the single electromagnetic objects bandwidth is limited to around 20 kHz. At $\mu = 80$ and in the Run-2 trigger conditions, it would lead to a transverse energy (E_T) threshold around 30 GeV, as shown in Fig. 6a. Such a threshold would reduce significantly the physics potential of ATLAS.

The upgrade is based on the use of a finer granularity and on a preserved availability of layer information at the first trigger level. Such new subdivisions are called Super Cells (SC) and are visible in Fig. 6c. They are compared to the original trigger towers used so far in Fig. 6b). The information of the longitudinal shower development and a finer granularity at the first trigger level, allow deriving shower shape variables which improve the electron and photon versus jet discrimination. Figure 6a (triangle distributions) shows that a 20 kHz L1Calo rate is compatible with an E_T threshold of 20 GeV preserving ATLAS physics potential.

The increase of information available at the level-1 of the trigger forced to re-design parts of the calorimeter readout. To assess and validate the performance on running conditions, a parasitic SC readout was installed on 0.8% of the barrel channels. The full installation is foreseen in 2018, at the end of the LHC Run-2.

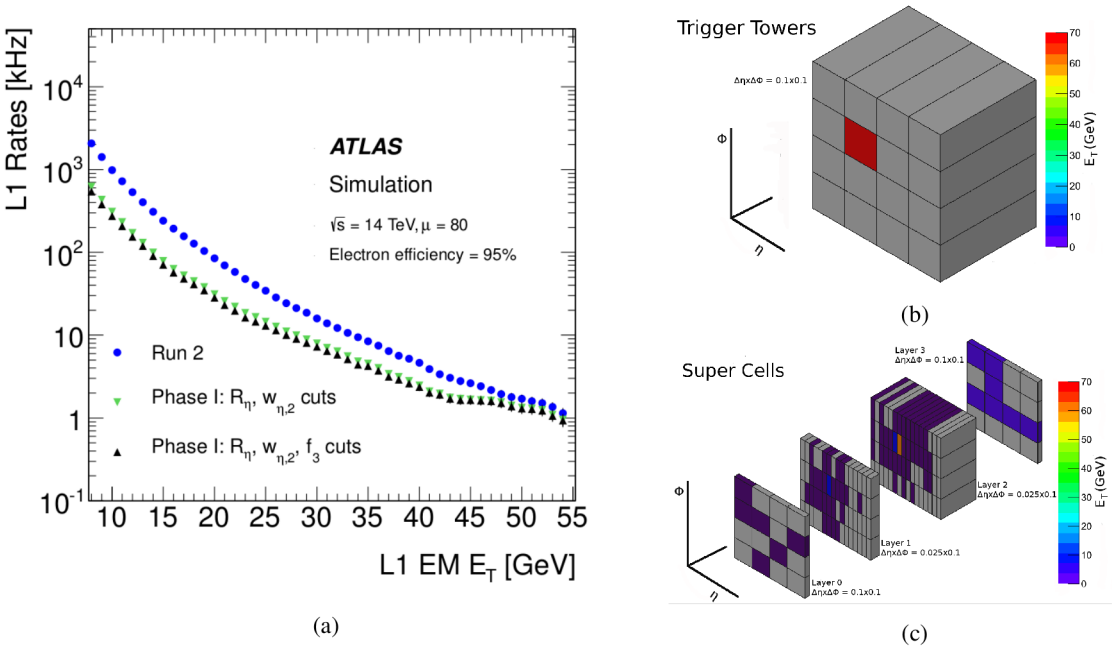

FIGURE 6. (a) Simulation of the L1-Calo rate versus the electromagnetic E_T threshold with and without the information produced by Super Cells. R_η, $w_{\eta,2}$ and f_3 are typical shower shape variables derived from SC information. (b) Trigger tower layout. (c) Super Cells layout[8].

Conclusion

In 2015, the LAr Calorimeters have successfully resumed data taking. Using the Run-1 experience, two main modifications have been implemented: the reduction of the number of samples used to digitize the signal and the replacement of the HV generators. This should increase the level-1 trigger rate and reduce the amount of data losses. The first collisions were used to assess the performance of the LAr Calorimeters. They show that the system is well understood. The overall time synchronization over the cells is acceptable given that the calorimeters are not yet optimally calibrated. The energy measurement is in a very good agreement with the simulation, proving a good understanding of the detector behaviour. Finally, studies for the next upgrade are also ongoing and prototypes are under test. The LAr Calorimeters are ready to take more data and to play their central role within ATLAS.

REFERENCES

[1] ATLAS Collaboration, *The ATLAS experiment at the CERN Large Hadron Collider*, JINST 3 (2008) S08003
[2] ATLAS Collaboration, *Liquid-Argon Calorimeter Plots on Detector Status* https://twiki.cern.ch/twiki/bin/view/AtlasPublic/LArCaloPublicResultsDetStatus
[3] ATLAS Collaboration, *ATLAS calorimeter performance*, CERN/LHCC-96-40
[4] ATLAS Collaboration, *Electron and photon energy calibration with the ATLAS detector using LHC Run 1 data*, Eur.Phys.J. C74 (2014) 3071
[5] ATLAS Collaboration, *Monitoring and data quality assessment of the ATLAS liquid argon calorimeter*, JINST 9 (2014) P07024
[6] ATLAS Collaboration, *LArCaloPublicResults2015* https://twiki.cern.ch/twiki/bin/view/AtlasPublic/LArCaloPublicResults2015
[7] ATLAS Collaboration, *Measurement of W and Z boson Production Cross Section in pp Collisisions at* $\sqrt{s} = 13TeV$ *in the ATLAS detector*, ATLAS-CONF-2015-039 https://atlas.web.cern.ch/Atlas/GROUPS/PHYSICS/CONFNOTES/ATLAS-CONF-2015-039/
[8] ATLAS Collaboration, *ATLAS Liquid Argon Calorimeter Phase-I Upgrade Technical Design Report*, CERN/LHCC-2013-017, ATLAS-TDR-022.

Proceedings of the LHCP2015 Conference, St. Petersburg, Russia, August 31 - September 5, 2015

Editors: V.T. Kim and D.E. Sosnov

Alignment of the ATLAS Inner Detector in the LHC Run 2

LAURA BARRANCO NAVARRO

Instituto de Físca Corpuscular, Universitat de València and CSIC, Valencia, Spain

laura.barranco.navarro@cern.ch

On behalf of the ATLAS Collaboration

Abstract. ATLAS physics goals require excellent resolution and unbiased measurement of all charged particle kinematic parameters. These critically depend on the layout and performance of the tracking system and on the quality of its offline alignment. ATLAS is equipped with a tracking system built using different technologies, silicon planar sensors (pixel and micro-strip) and gaseous drift- tubes, all embedded in a 2 T solenoidal magnetic field. For the Run 2 of the LHC, the system was upgraded with the installation of a new pixel layer, the Insertable B-layer (IBL). An outline of the track based alignment approach and its implementation within the ATLAS software will be presented. Special attention will be paid to integration of the IBL into the alignment framework, techniques allowing to identify and eliminate tracking systematics as well as strategies to deal with time-dependent alignment. Performance from the commissioning of cosmic data and potentially early LHC Run 2 proton-proton collisions will be discussed.

INTRODUCTION

Between the Run 1 and the Run 2 of the LHC a long technical stop, known as the Long Shutdown I (LS1), took place. During this LS1 several maintenance works were performed in the ATLAS [1] Inner Detector (ID) [2], together with the installation of new detectors such as the new Insertable B-Layer (IBL) [3]. To deal with these new features, the ID software has been updated.

In order to get the detector ready for the stable beams, alignment has become a major task during the cosmic ray data taking and first 13 TeV collisions, since there were expected large inicial misalignments due the maintenance works performed in the ID and the instalation of the IBL, a new pixel layer attached to the beam pipe.

ATLAS Inner Detector

The ATLAS Inner Detector consists of three subdetectors, the Pixel detector which includes the IBL, the Semiconductor Tracker (SCT), and the Transition Radiation Tracker (TRT), all embedded in a superconducting solenoid which produces a 2 T axial magnetic field. Figure 1 shows a schematic representation of the barrel region. The ID has been designed to reconstruct the trajectories of the charged particles within a pseudorapidity range of $|\eta| < 2.5$. The Pixel detector consists of 1744 silicon pixel modules arranged in three barrel layers and two end caps with three disks each. The expected hit resolution is 10 μm in $r-\phi$ coordinates and 115 μm in z coordinate. During LS1, the IBL was added as an additional layer to the Pixel detector, reducing the distance from the interaction point to the first tracking layer. The IBL is composed of 280 modules, mixing planar and 3D technology, arranged in 14 azimuthal carbon fiber staves and it is placed at 3.3 cm radius. The expected hit resolution is 8 μm in $r-\phi$ and 40 μm in z. In order to simplify the notation throughout the remainder of the text, the term Pixel will be used to refer only to the three outer Pixel layers and the end cap Pixel disks and IBL to the new layer. The SCT consists of 4088 silicon strip modules, arranged in four barrel layers and two end caps with nine wheels each. The intrinsic resolution is 17 μm and 580 μm in $r-\phi$ and z, respectively. The TRT is the outermost detector of the ID subdetectors and is made of 350848 Argon-filled straw tubes with a single hit resolution of 130 μm along $r-\phi$.

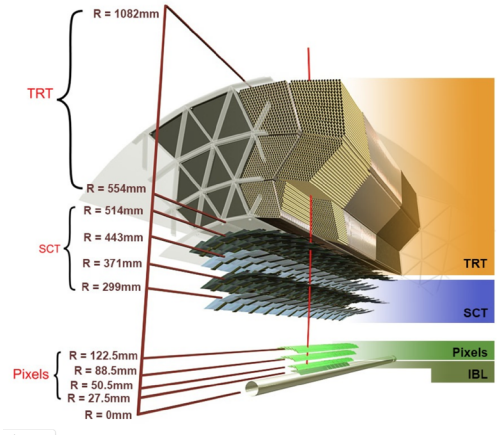

FIGURE 1. A 3D visualisation of the structure of the barrel of the ID. The beam pipe, the IBL, the three Pixel layers, the four cylindrical layers of the SCT and the 72 straw layers of the TRT are shown. System span from 27.5 mm to 1082 mm

Alignment Procedure

The alignment of the ATLAS Inner Detector is performed using a track-based technique [4][5], which minimises the track-to-hit residuals via the following χ^2:

$$\chi^2 = \sum_{tracks} [\mathbf{r}(\mathbf{a}, \boldsymbol{\tau})]^T \, \mathbf{V}^{-1} \, [\mathbf{r}(\mathbf{a}, \boldsymbol{\tau})] \,, \tag{1}$$

where $\mathbf{r}(\mathbf{a}, \boldsymbol{\tau})$ are the track-to-hit residuals, $\boldsymbol{\tau}$ the track parameters, $\mathbf{a}$ the alignment parameters (degrees of freedom, DOF) and $\mathbf{V}$ the covariance matrix of the detector measurements. Each module or sub-detector can be treated as an alignable structure. Each structure has six DOF corresponding to thethree translations (T_x, T_y and T_z) ant three rotations rotations (R_x, R_y and R_z) that define its position and orientation in space. The translations are measured with respect to the origin of the reference frame while the rotations are defined around the cartesian axes. Two types of reference frame are defined. The ATLAS reference frame is a right-handed Cartesian coordinate system, where the origin is at the nominal proton-proton interaction point, corresponding to the centre of the detector. The reference frame describing the position and orientation of individual detector modules of the ID is a right-handed reference frame with the origin in the geometrical centre of each device. Figure 2 shows a schematic view of how the position of misaligned module is updated by minimizing the χ^2 function.

The alignment procedure is split into three levels, in order to cope with the large number of alignable DoFs and to mimic the detector assembly structures. In this way, at level 1 the detector subsystems are aligned separating into endcaps and barrel regions in order to correct for collective movements. Level 2 treats individual barrel layers and end-cap disks as physical structures (barrel modules and end-cap wheels in case of the TRT). Level 3 corresponds to a silicon module and TRT wire level alignment. The levels are addressed consecutively during the alignment procedure. Table 1 shows the number of DOFs for each detector and level of alignment. A new L11 has been defined to align IBL indepently from the old pixel.

TABLE 1. Number of DOFs by detector and level of alignment

Levels	IBL	Pixel	SCT	TRT
L1 (structure)	6	6	18	17
L2 (layer/disk)	6	54	132	960
L3 (module)	1680	10464	25528	701696

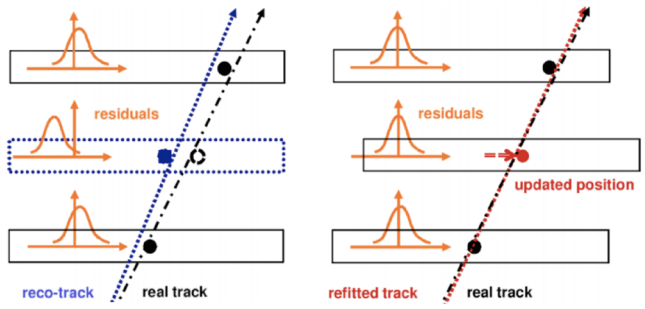

FIGURE 2. Alignment procedure based on residuals χ^2 function minimization. On the left, the central module position is wrongly determined, thus biasing the reconstructed track parameters. On the right, the misalignment is detected by minimizing the residual distributions and the position of the detector is updated.

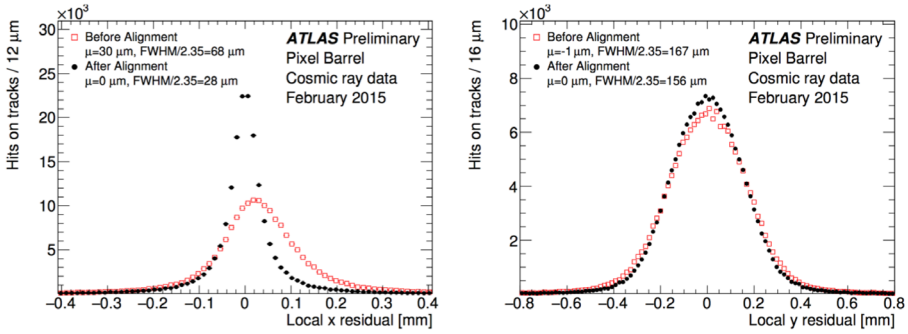

FIGURE 3. The Pixel local x (left) and local y (right) residual distribution for the cosmic-ray data sample reconstructed before (red) and after (black) alignment. The distributions are integrated over all hits associated to tracks (hits-on-tracks) in the barrel modules of Pixel layers one, two and three. Taken from Ref. [6]

Cosmic Ray Data Campaign

Data recorded by ATLAS during the 2014 and 2015 cosmic-ray campaigns were used to perform a first alignment of the ID after the LS1 and to test the performance of the new IBL detector. Results shown here were obtained using 1.1 M events recorded during February 2015. These data include $3x10^5$ ID tracks, which are used for alignment. The data were taken in a configuration with the toroid field off and solenoid field on. After the track selection requirements, 50000 tracks were used in alignment. More details about the track selection and the obtained results can be found elsewhere [6].

During LS1, the Pixel detector was removed from ATLAS for the performance of maintenance and put back in place with a precision from the survey of $100\,\mu$m. The IBL was installed during LS1 for the first time, so there was no previous experience from Run 1. The SCT and TRT barrels were not moved during LS1, so they were expected to occupy the same position as at the end of Run 1. Thus, the alignment was focused on the Pixel and the IBL. They were both aligned up to module level alignment (level 3). The SCT barrel was aligned up to level 2 and the TRT was fixed as a reference point. Figure 3 shows the improvement achieved by the alignment on local x (left) and local y (right) residual distributions for the Pixel. A bias of $30(-1)\,\mu$m in the Pixel barrel local x (local y) direction has been corrected while the width of the distribution has been reduced from $68(167)\,\mu$m to $28(156)\,\mu$m in x (y).

To test the goodness of the alignment the half-track method is used. Since cosmic tracks traverse the whole detector, they are divided into upper and lower parts, and each part is reconstructed independently as shown in Fig. 4 (left). The perigee parameters τ_{up} and τ_{down} of each half track pair are compared to each other and their difference, $\Delta(\tau_{up} - \tau_{down})$, is compared before and after the alignment. The resolution of a track parameter is obtained by the width of the distribution of $\Delta(\tau_{up} - \tau_{down})$ divided by $\sqrt{2}$.

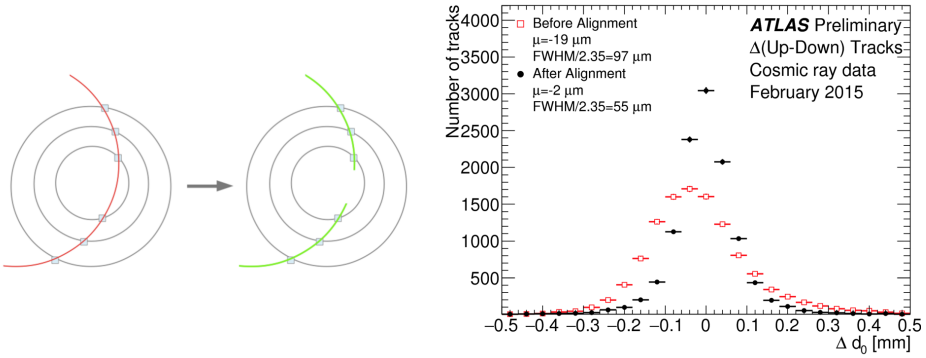

FIGURE 4. (left) Diagram illustrating the half-track parameter study. In red is shown a full track reconstructed in the inner detector, while in green are shown the two half-tracks reconstructed in the top and bottom parts. (right) Distribution of the difference of the reconstructed track transverse impact parameter Δd_0 using tracks reconstructed in the top part of the inner detector with respect to track reconstructed in the bottom part. Taken from Ref. [6]

Using this technique, biases of 19 μm in Δd_0 and of 9.4 TeV^{-1} in $\Delta(q/p_T)$ have been corrected, with the traverse impact parameter resolution being reduced from 69 to 39 μm and 3.5 to 1.4 TeV^{-1}, respectively. In the same way, the longitudinal impact parameter resolution was reduced from 160 to 134 μm. An example of the transverse impact parameter (d_0) distribution is shown in Fig. 4 (right).

First 13 TeV Collision Data

The data used for this alignment were collected by the ATLAS detector during the first 13 TeV collision run, in June 2015. The integrated luminosity is 7.9 pb^{-1} and after applying the selection criteria the final sample used for performance validation consisted of about 1.4 million tracks. More details about the track selection and the obtained results can be found elsewhere [8].

Two passes of the alignment chain were performed. During Run 1 it was observed that when the system conditions changed, for instance due to magnet power cycling, detector cooling system or high voltage being switched on/off, some relative movements of the big structures were introduced. A first pass was thus performed in order to correct for such relative movements. After this first chain, a second pass alignment was performed with the aim of improving the resolution on the transverse impact parameter of the tracks.

Figure 5 shows the improvement achieved by the alignment in the residual distributions of the TRT barrel (left) and the SCT barrel (right), where the alignment results are compared to the perfect aligned simulation (red) and results from the cosmic campaign (March Alignment, in green). A bias of 1(1) μm in the SCT(TRT) barrel has been corrected while the width of the distribution has been reduced from 123(33) μm to 123(27) μm in SCT and TRT, respectively.

June 2015 data have also been used to study the stability of the alignment between runs. For this study, the Pixel detector was fixed as a reference, while the rest of the subdetectors were aligned at Level 1 with respect to it using the June alignment constants. Figure 6 shows the run by run corrections (T_X) found for IBL, SCT and TRT with respect to the baseline constants (June alignment).

Temperature Distortion of the IBL

During the Cosmic Campaign it was discovered that the IBL shows an in-plane deformation (stave bowing) in the negative local x direction, with respect to the nominal geometry, that can be seen clearly in the local x-residuals. This observed distortion turned out to depend on the operation temperature of the IBL. Detailed investigations of the characteristic of this distortion are reported in [7].

Using cosmic ray data collected in March 2015 the dependance of the size of the IBL distortion on the operation temperature has been quantified. For this purpose, the mean of the track-to-hit residual distributions has been determined as a function of the module position in global z and integrated over the 14 staves. The cosmic ray data

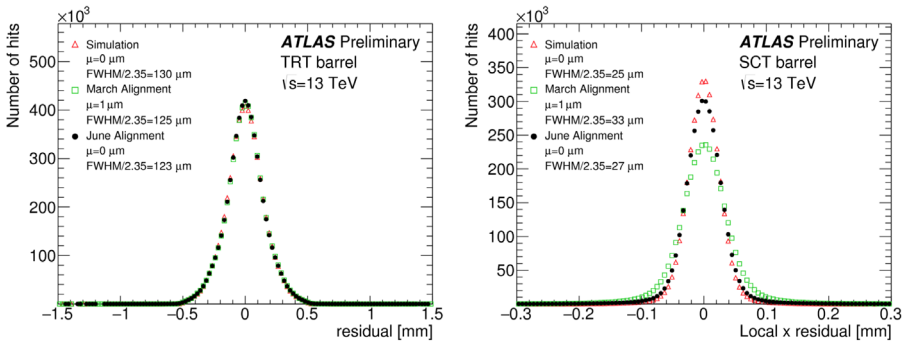

FIGURE 5. The TRT Barrel (left) and SCT Barrel (right) residual distribution for the 13 TeV collision data sample reconstructed with the June alignment (black) and March alignment (green) as well as observed in the perfectly aligned simulation (red). The distributions are integrated over all hits assigned to tracks in the respective TRT regions. Taken from Ref.[8]

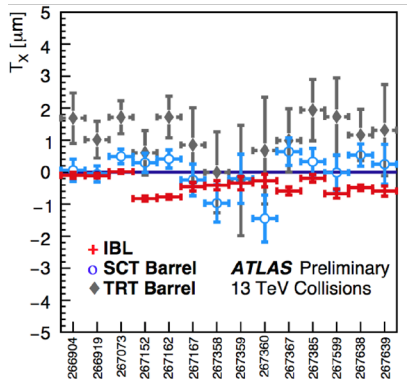

FIGURE 6. The T_X global alignment corrections of all IBL, SCT Barrel and TRT Barrel sub-detectors (with respect to the Pixel detector) as a function of the 2015 13 TeV run. Errors shown are statistical uncertainties on the determined alignment parameters and vary according to the duration of the run. Taken from Ref.[8]

have been collected at different IBL operating points and the resulting distributions are shown in Fig. 7 (left). The track-to-hit residual distributions have been fit using a parabolic formula

$$\Delta_{x_L}(z) = B - \frac{M}{z_0^2}(z^2 - z_0^2), \tag{2}$$

where Δ_{x_L} is the in-plane module displacement as a function of the global z position, B is the fit baseline, M is a free parameter that represent the bowing magnitude and $z_0 = 366.5$ mm is the fixing point of the stave at both ends. The magnitude of the distortion as function of the operating temperature is shown in Fig. 7 (right).

Alignment in the Calibration Loop

Data collected by the ATLAS experiment are promptly processed to provide fast access to high quality data for physics analysis. The high quality of the data is achieved by a so-called ”calibration loop” that relies on the detector calibrations becoming available within 48 hours based on a selected subset of the data designed to allow detailed data investigations of the detector response.

Inner detector alignment was one of the tasks included in the calibration loop during the Run 1. The implementation of the alignment in the calibration loop allows the detection of ”on the fly” movements or deformations of the different subdetectors so that these can be corrected as soon as possible. The calibration loop alignment procedure has

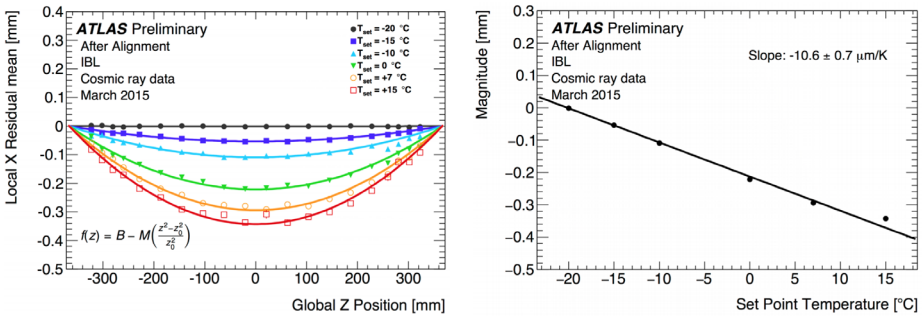

FIGURE 7. (left) The track-to-hit residual mean in the local x direction. The residual mean is averaged over all hits of modules at the same global-z position. Each data set is fitted to a parabola which is constrained to match to the baseline $B = 0$ at $z = \pm z_0 = \pm 366.5$ mm. (right) The magnitude of the distortion as a function of the temperature set point. Each data point is a best fit of a parabola to the local x residual mean as function of the global-z of the module position. Taken from Ref.[7]

been updated to include the latest changes introduced in the alignment procedure and has been extended to perform a more detailed alignment. It has been successfully tested during the Cosmic Campaign and first collisions. In order to allow for a fast reaction, a web display has been developed to monitor online the results of the alignment.

Conclusions

During the LS1 a number of upgrades have been performed on the ATLAS ID, including the addition of the IBL. In order to determine the positions of all ID systems, a first trackbased alignment was performed using cosmic-ray events recorded with the ATLAS detector. The initial 7.9 pb^{-1} of the 13 TeV proton-proton collisions from LHC have been used to align the ID. A special focus on the new IBL detector was necessary as this was the first time this system operated in real LHC conditions. An important part of the alignment work consists on knowing in real time if there is a movement or deformation of the ID in order to correct it as soon as possible. For this reason, a first alignment has been implemented in the Calibration Loop.

REFERENCES

[1] ATLAS Collaboration, *The ATLAS Experiment at the CERN Large Hadron Collider*, JINST **3**, p. S08003 (2008).

[2] ATLAS Collaboration, *ATLAS inner detector: Technical Design Report, 1*, CERN (1997). `https://cds.cern.ch/record/331063`.

[3] ATLAS Collaboration, *ATLAS Insertable B-Layer Technical Design Report*, CERN (2010). `https://cds.cern.ch/record/1291633`.

[4] ATLAS Collaboration, *Alignment of the ATLAS Inner Detector and its Performance in 2012*, ATLAS-CONF-2014-047. `http://cdsweb.cern.ch/record/1741021`.

[5] ATLAS Collaboration, *Common Framework Implementation for the Track-Based Alignment of the ATLAS Detector*, ATL-SOFT-PUB-2014-003. `https://cds.cern.ch/record/1670354`.

[6] ATLAS Collaboration, *ATLAS Inner Detector Alignment Performance with February 2015 Cosmic Ray Data*, ATL-PHYS-PUB-2015-009. `http://cdsweb.cern.ch/record/2008724`.

[7] ATLAS Collaboration, *Study of the mechanical stability of the ATLAS Insertable B-Layer*, ATL-INDET-PUB-2015-001. `http://cds.cern.ch/record/2015222`.

[8] ATLAS Collaboration, *Alignment of the ATLAS Inner Detector with the initial LHC data at* $\sqrt{s} = 13$ *TeV*, ATL-PHYS-PUB-2015-031. `http://cdsweb.cern.ch/record/2038139`.

Proceedings of the LHCP2015 Conference, St. Petersburg, Russia, August 31 - September 5, 2015

Editors: V.T. Kim and D.E. Sosnov

Flavour Tagged Time Dependent Angular Analysis of the $B_s^0 \to J/\psi\phi$ Decay on Run 1 Data in ATLAS

ARTEM MAEVSKIY[1,2]

[1] *Skobeltsyn Institute of Nuclear Physics (SINP MSU), 1(2), Leninskie gory, GSP-1, Moscow 119991, Russia*
[2] *Lomonosov Moscow State University (MSU), Faculty of Physics, Leninskie Gory, Moscow 119991, Russia*

artem.maevskiy@cern.ch

On behalf of the ATLAS Collaboration

Abstract. The paper presents the measurement of the B_s^0 decay CP-violation parameters in the $B_s^0 \to J/\psi\phi$ channel using 14.3 fb^{-1} integrated luminosity collected by the ATLAS detector in pp collisions at $\sqrt{s} = 8$ TeV at the LHC. The measured values are statistically combined with those from 4.9 fb^{-1} of $\sqrt{s} = 7$ TeV data.

INTRODUCTION

The New Physics (NP) contributions may alter CP-violation parameters in the b-hadron decays with respect to their Standard Model (SM) predictions. $B_s^0 \to J/\psi\phi$ decay is of particular interest in this regard since SM prediction of its CP-violating weak phase ϕ_s is small ($-0.0363^{+0.0016}_{-0.0015}$, [1]) and thus may be significantly affected by the NP contributions (Fig. 1).

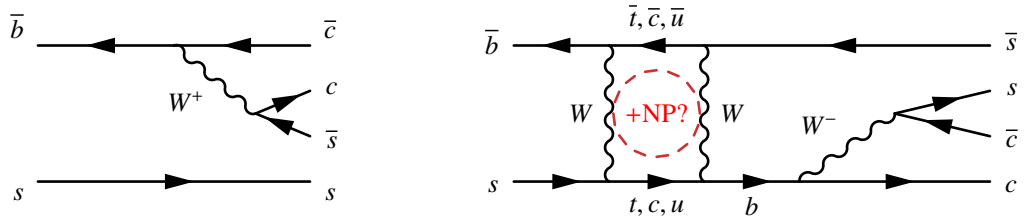

FIGURE 1. Feynman diagrams of direct $B_s^0 \to J/\psi\phi$ decay (left) and such decay via an oscillation (right).

The ϕ_s parameter is defined as the weak phase difference between the $B_s^0 - \overline{B_s^0}$ mixing amplitude and $b \to c\overline{c}s$ decay amplitude and is related to the Cabibbo-Kobayashi-Maskawa (CKM) quark mixing matrix elements via the relation $\phi_s \simeq -2\beta_s$, with $\beta_s = \arg\left[-(V_{ts}V_{tb}^*)/(V_{cs}V_{cb}^*)\right]$. The vector-vector $J/\psi\ \phi$ final state results in an admixture of CP-even and CP-odd states with angular momentum $L = 0, 2$ (CP-even) or $L = 1$ (CP-odd), thus requiring statistical angular analysis for disentanglement.

Along with ϕ_s, the time evolution of $B_s^0 - \overline{B_s^0}$ mixing is defined by the mass difference Δm_s of the heavy and light mass eigenstates and their decay width difference $\Delta\Gamma = \Gamma_L - \Gamma_H$. The latter quantity is predicted to be 0.087 ± 0.021 ps^{-1} within the SM [2] and is not expected to be significantly affected by the NP.

ANALYSIS STRATEGY

The analysis is performed using the 14.3 fb^{-1} data sample of pp collisions collected by the ATLAS detector [3] during the $\sqrt{s} = 8$ TeV LHC run.

$B_s^0 \to J/\psi(\mu^+\mu^-)\phi(K^+K^-)$ event candidates are selected by searching for a pair of oppositely charged muon tracks and also a pair of oppositely charged tracks not identified as muons. Muon tracks are refitted to a common vertex and cut on their invariant mass within a defined J/ψ mass region. The fit is further constrained by fixing the invariant mass of the muon pair to the J/ψ mass value, all four tracks being refitted to a common vertex and requirement being imposed on the KK invariant mass to fall into a defined ϕ mass region.

An unbinned maximum likelihood fit is then performed on the $B_s^0 \to J/\psi(\mu^+\mu^-)\phi(K^+K^-)$ event candidates to extract the parameter values. The fit uses information about the reconstructed mass, the measured proper decay time along with its uncertainty, B_s^0 flavour tagging probability (see "Flavour Tagging" section) and the three transversity angles θ_T, ϕ_T and ψ_T of each $B_s^0 \to J/\psi\phi$ candidate.

The angles $(\theta_T, \psi_T, \phi_T)$ are defined in the rest frames of the final-state particles. The x-axis is determined by the direction of the ϕ meson in the J/ψ rest frame, and the K^+K^- system defines the $x-y$ plane, where the y component of the K^+ is taken to be greater than zero. The three angles are defined as:

- θ_t, the angle between the μ^+ momentum and the normal to the $x-y$ plane, in the J/ψ rest frame,
- ϕ_T, the angle between the x-axis and the $x-y$ component of the μ^+ momentum, in the J/ψ rest frame,
- ψ_T, the angle between the K^+ momentum and the direction opposite to the J/ψ momentum, in the ϕ meson rest frame.

The likelihood function is defined as a combination of the signal and background probability density functions (PDF). The signal PDF is described as the product of the following components:

- mass shape modelled by a sum of three Gaussian distributions,
- decay time error and p_{T} probability terms described by gamma functions (unchanged from the analysis described in [4]),
- joint PDF for the decay time and the transversity angles for the $B_s^0 \to J/\psi(\mu^+\mu^-)\phi(K^+K^-)$ decay according to [5],
- the angular sculpting term to account for the effect of the detector and kinematic cuts on the angular distributions, and
- signal tagging probability PDF (see "Flavour Tagging" section).

There are two background components in the fit: the mis-reconstructed $B_d^0 \to J/\psi K^*$ events and combinatorial background. The combinatorial background PDF is constructed of the mass term, proper decay time function, the PDF of the background tagging probability, angular PDF and probability terms for the decay time error and p_{T}. The mass term is an exponential function with a constant term added. The proper decay time PDF is combined from a prompt Gaussian peak to account for combinatorial background events with lifetimes distributed around zero, two positive exponential functions representing a fraction of longer-lived backgrounds with non-prompt J/ψ, and a negative exponential function to account for events with poor vertex resolution. The probability terms for the decay time error and p_{T} are modelled by gamma functions as described in [4]. The background tagging probability PDF is described in the "Flavour Tagging" section. The shape of the background angular distribution arises primarily from detector and kinematic sculpting effects and is described by Legendre polynomial functions.

Contamination from $B_d^0 \to J/\psi K^*$ events mis-reconstructed as $B_s^0 \to J/\psi\phi$ is described by its mass, transversity angle and lifetime distributions. The mass shape, transversity angle distributions and the fraction of this contribution are evaluated from MC simulation and are fixed in the main fit, transversity angle distribution being again described by Legendre polynomial functions. The B_d^0 lifetime is accounted for by adding an additional exponential term, scaled by the ratio of B_d^0 and B_s^0 masses.

Flavour Tagging

The use of information about the initial flavour of the decaying B_s^0 meson, although not absolutely necessary for the ϕ_s parameter extraction, significantly reduces the uncertainty of its measured value [6]. This information can be obtained from the opposite-side B meson that contains the other pair-produced b-quark in the event. This is referred

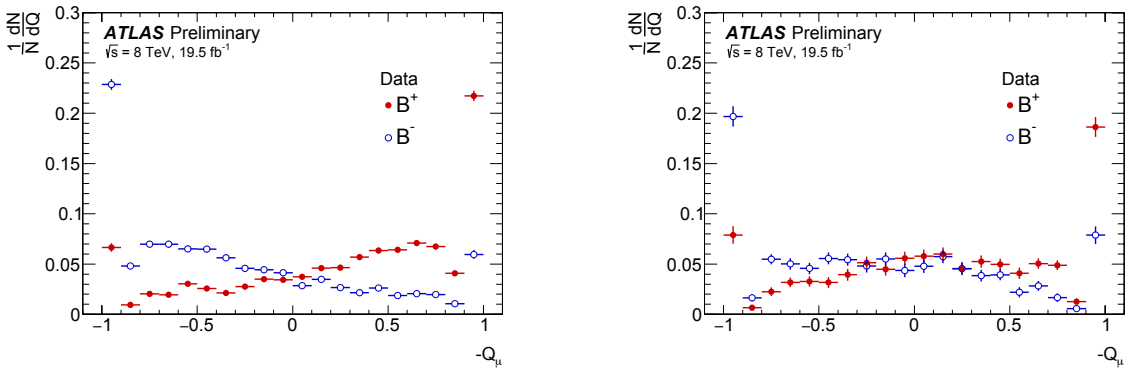

FIGURE 2. Charge variable distribution for the combined muon (left) and segment-tagged muon tagging methods.

to as opposite-side tagging (OST). To study and calibrate the OST methods, events containing $B^{\pm} \to J/\psi K^{\pm}$ decays can be used, where the flavour of the $B^{\pm}$ meson is provided by the kaon charge.

Several methods are available to determine the opposite side b-quark flavour. The measured charge of a lepton from a semileptonic decay of the B meson provides strong separation power; however there is dilution from neutral B meson oscillations as well as cascade $b \to c \to \ell$ decays. The separation power may be enhanced by measuring the weighted sum of the track charges around the lepton, weighting function being optimized for different tagging methods:

$$Q_{\mu,e,\mathrm{jet}} = \frac{\sum_i^{N\mathrm{tracks}} q^i \cdot \left(p_{\mathrm{T}}^i\right)^{\kappa_{\mu,e,\mathrm{jet}}}}{\sum_i^{N\mathrm{tracks}} \left(p_{\mathrm{T}}^i\right)^{\kappa_{\mu,e,\mathrm{jet}}}}$$

In case of absence of leptons, the weighted sum of the charge of tracks in a jet associated with the opposite-side B meson decay is used.

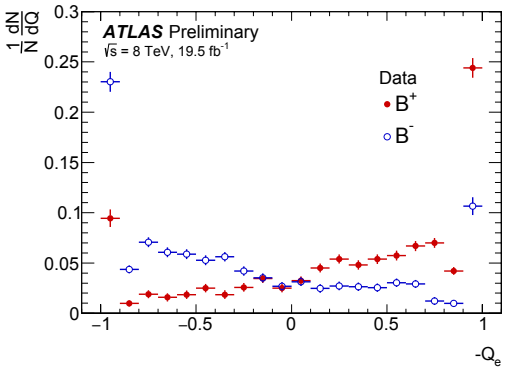

FIGURE 3. Charge variable distribution for the electron tagging method.

Muons are classified according to their reconstruction class as follows. *Combined* muons are the ones identified using a combination of the muon spectrometer (MS) and the inner detector (ID) track parameters, *segment-tagged* muons are the ones having a MS track segment that is not associated with a MS track but is matched to an ID track extrapolated to the MS. The muon tagging method is therefore divided into two separate methods basing on the opposite-side muon type. The charge variable distributions for the $B^{\pm} \to J/\psi K^{\pm}$ opposite side muons are shown in Fig. 2. Similar charge distributions for the electron and jet tagging methods can be seen in Fig. 3 and 4, respectively.

These distributions define the probabilities of having a value of Q of the charge variable for the given B flavour, i.e. $P(Q|B^+)$ and $P(Q|B^-)$. The probability of having the B flavour given the charge Q is therefore $P(B|Q) = P(Q|B^+)/(P(Q|B^+) + P(Q|B^-))$ and $P(\overline{B}|Q) = 1 - P(B|Q)$. The $P(B|Q)$ distributions are fitted firstly for the sideband

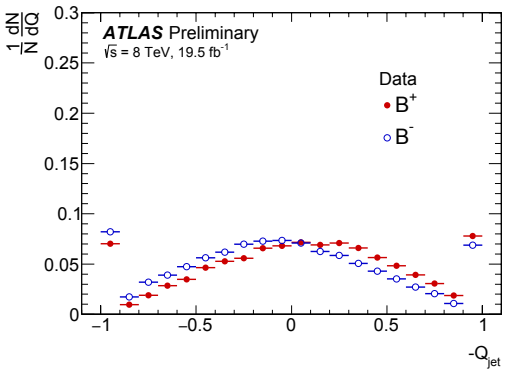

FIGURE 4. Charge variable distribution for the jet tagging method.

data, thus obtaining the PDF of the background tagging probability. Then, the B_s^0 signal region is fitted fixing the background component parameters as well as the background fraction to obtain the signal tagging probability PDF. These PDFs are used in the main fit as described in the previous section.

RESULTS

The mass and lifetime projections of the fit are shown in Fig. 5. Such projections for the transversity angles can be seen in Fig. 6. The fitted values for ϕ_s and $\Delta\Gamma_s$ are $-0.119 \pm 0.088(\text{stat.}) \pm 0.036(\text{syst.})$ rad and $0.096 \pm 0.013(\text{stat.}) \pm 0.007(\text{syst.})\,\text{ps}^{-1}$, respectively.

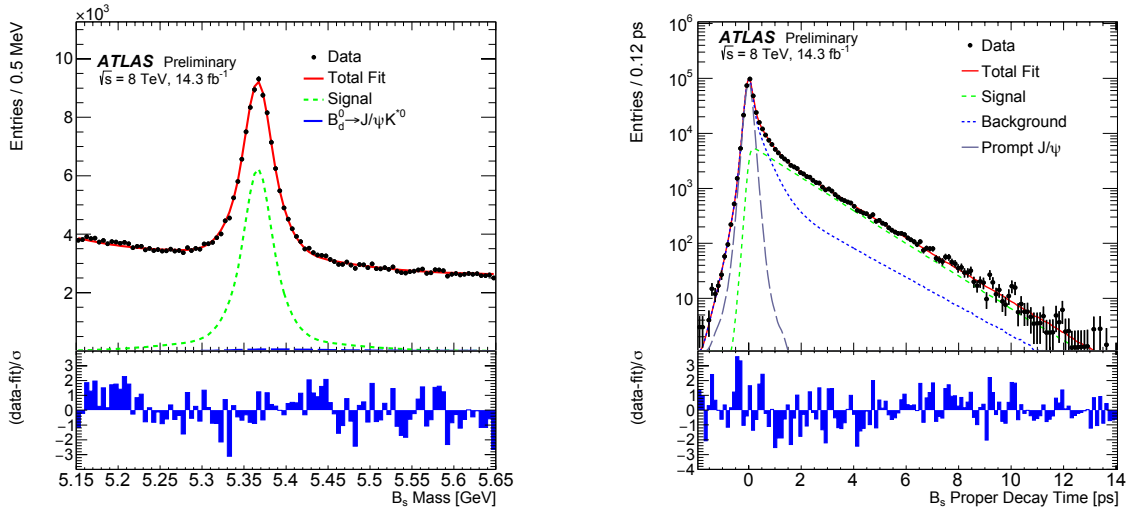

FIGURE 5. Mass (left) and lifetime (right) projections of the final fit.

The measured values are consistent with those obtained in the previous analysis [6], using $\sqrt{s} = 7\,\text{TeV}$ data collected by ATLAS in 2011. This consistency is clear from the comparison of likelihood contours in the $\phi_s - \Delta\Gamma_s$ plane shown in Fig. 7 (left). A Best Linear Unbiased Estimate (BLUE) combination [7] is used to combine the 7 and 8 TeV measurements to give an overall Run 1 result (Fig. 7, right): $\phi_s = -0.094 \pm 0.083(\text{stat.}) \pm 0.033(\text{syst.})$ rad and $\Delta\Gamma_s = 0.082 \pm 0.011(\text{stat.}) \pm 0.007(\text{syst.})\,\text{ps}^{-1}$. This result is consistent with the Standard Model predictions.

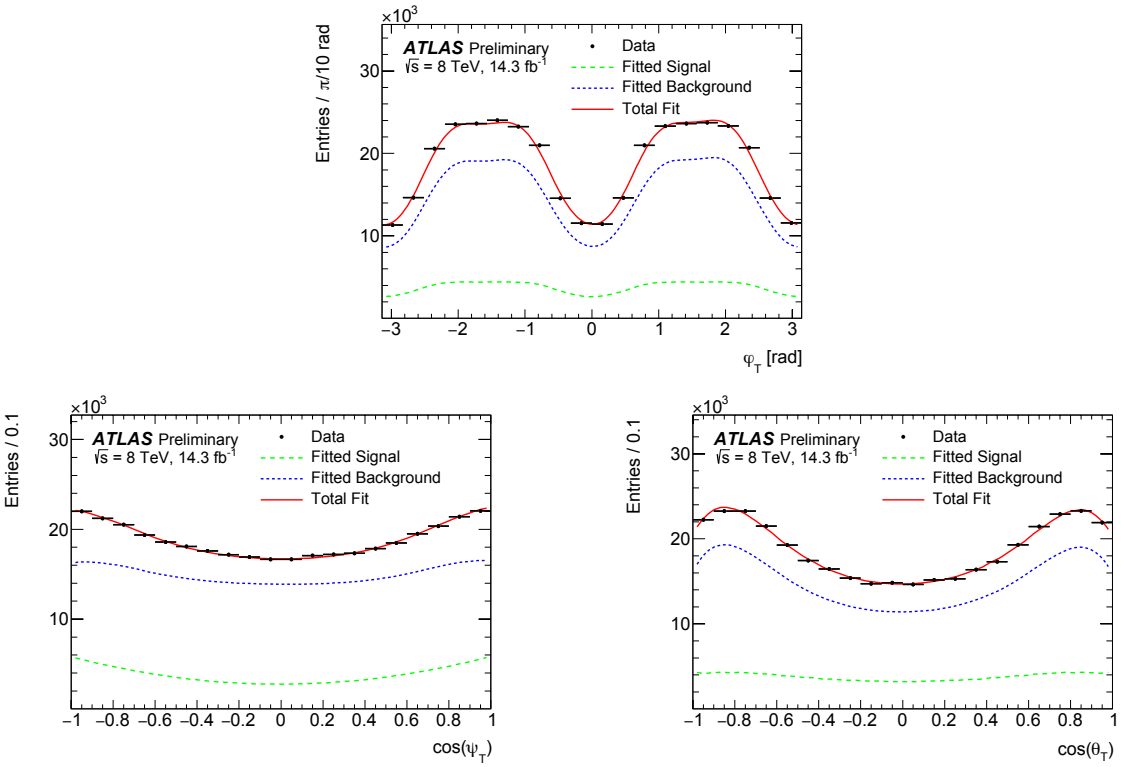

FIGURE 6. Transversity angles projections of the final fit.

SUMMARY

A time-dependent angular analysis of the CP asymmetry parameters in $B_s^0 \to J/\psi\phi$ decay is presented. This analysis was performed using the 14.3 fb^{-1} data sample of pp collisions collected by the ATLAS detector during the $\sqrt{s}$ = 8 TeV LHC run. The measurement results from the 8 TeV analysis are consistent with those obtained in the 7 TeV ATLAS data analysis [6]. These two measurements are statistically combined, leading to the following overall Run 1 result:

$$\phi_s = -0.094 \pm 0.083(\text{stat.}) \pm 0.033(\text{syst.})\,\text{rad}$$

$$\Delta\Gamma_s = 0.082 \pm 0.011(\text{stat.}) \pm 0.007(\text{syst.})\,\text{ps}^{-1}$$

This result agrees very well with the Standard Model.

ACKNOWLEDGMENTS

This work was partially supported by RFBR, research project No. 15-02-08133.

REFERENCES

[1] J. Charles et al., *Predictions of selected flavour observables within the Standard Model*, Phys. Rev. **D84** (2011) 033005, arXiv:1106.4041 [hep-ph].

[2] A. Lenz and U. Nierste, *Numerical Updates of Lifetimes and Mixing Parameters of B Mesons*, in *CKM unitarity triangle. Proceedings, 6th International Workshop, CKM 2010, Warwick, UK, September 6-10, 2010*. 2011. arXiv:1102.4274 [hep-ph].

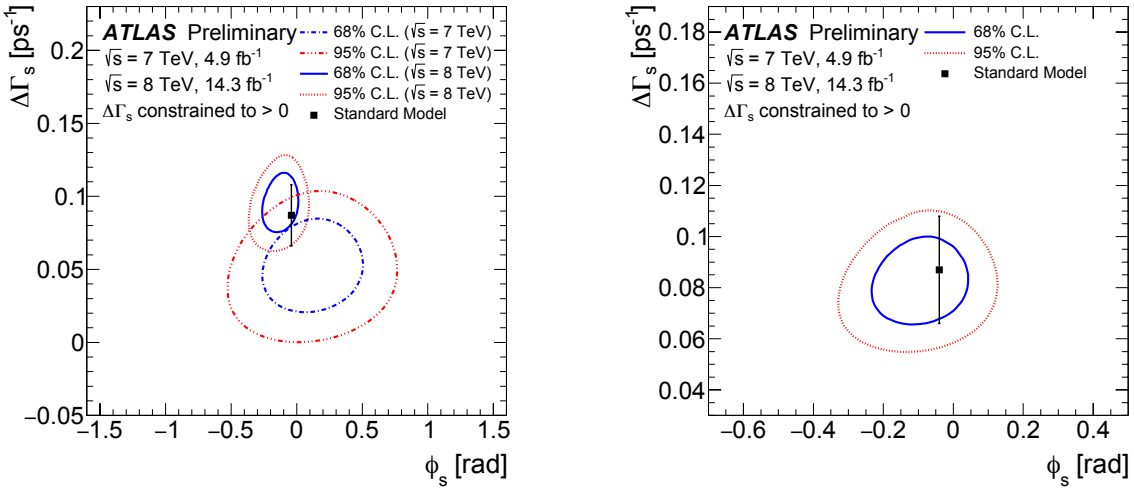

FIGURE 7. Likelihood contours in the $\phi_s - \Delta\Gamma_s$ plane for the individual results from 7 TeV and 8 TeV data (left) and a final statistical combination of the results from 7 TeV and 8 TeV data (right).

[3] ATLAS Collaboration, *The ATLAS Experiment at the CERN Large Hadron Collider*, JINST **3** (2008) S08003.

[4] ATLAS Collaboration, *Time-dependent angular analysis of the decay $B_s^0 \to J/\psi\phi$ and extraction of $\Delta\Gamma_s$ and the CP-violating weak phase ϕ_s by ATLAS*, JHEP **12** (2012) 072, arXiv:1208.0572 [hep-ex].

[5] A. S. Dighe, I. Dunietz, and R. Fleischer, *Extracting CKM phases and $B_s - \bar{B}_s$ mixing parameters from angular distributions of nonleptonic B decays*, Eur. Phys. J. **C6** (1999) 647–662, arXiv:hep-ph/9804253 [hep-ph].

[6] ATLAS Collaboration, *Flavor tagged time-dependent angular analysis of the $B_s \to J/\psi\phi$ decay and extraction of $\Delta\Gamma$s and the weak phase ϕ_s in ATLAS*, Phys. Rev. **D90** no. 5, (2014) 052007, arXiv:1407.1796 [hep-ex].

[7] R. Nisius, *On the combination of correlated estimates of a physics observable*, Eur. Phys. J. **C74** no. 8, (2014) 3004, arXiv:1402.4016 [physics.data-an].

Proceedings of the LHCP2015 Conference, St. Petersburg, Russia, August 31 - September 5, 2015

Editors: V.T. Kim and D.E. Sosnov

ATLAS Muon Reconstruction Performance in LHC Run 2

NICOLAS KÖHLER

Max-Planck-Institut für Physik (Werner-Heisenberg-Institut), Munich, Germany

nicolas.koehler@cern.ch

On behalf of the ATLAS Collaboration

Abstract. The performance measurements of the new muon reconstruction algorithm during the early pp-collision data taking of the LHC in 2015 at a centre-of-mass energy of $\sqrt{s} = 13\,\text{TeV}$ are discussed. The muon reconstruction efficiency, transverse momentum resolution and scale has been measured in the different detector regions and for muon transverse momenta between 4 and 110 GeV using datasets containing $J/\psi \to \mu^+\mu^-$ and $Z \to \mu^+\mu^-$ decays.

INTRODUCTION

The ATLAS muon spectrometer efficiently identifies muons and precisely reconstructs their momenta over a wide energy range and within a pseudorapidity interval up to $|\eta| < 2.7$. Precise knowledge of the muon momentum resolution and reconstruction efficiency is crucial for all measurements performed at the ATLAS detector that use muons, e.g. $H \to 4\ell$.

This contribution discusses the new muon reconstruction and selection as well as measurements of the muon momentum scale, resolution and reconstruction efficiencies. The results presented are based on a pp-collision dataset containing $J/\psi \to \mu^+\mu^-$ and $Z \to \mu^+\mu^-$ decays corresponding to an integrated luminosity of $85\,\text{pb}^{-1}$ recorded in 2015 at $\sqrt{s} = 13\,\text{TeV}$ with the ATLAS detector.

MUON RECONSTRUCTION AND SELECTION

The ATLAS muon reconstruction uses information from the Inner Detector (ID) and Muon Spectrometer (MS) (cf. Figure 1) and to a lesser extent from the calorimeters. A detailed description of these detector components can be found in Ref. [1].

The ID's task is to track charged particles and determine their charge and momentum using a 2 T solenoid magnetic field and to identify vertices.

The MS [2, 3] is designed to detect muons in the pseudorapidity range of $|\eta| < 2.7$ and to provide momentum measurements with a relative resolution better than 3% over a wide range of transverse momenta and up to 10% at transverse momenta of $p_\text{T} \approx 1\,\text{TeV}$.

The new muon reconstruction algorithm for ATLAS Run 2 combines several techniques [4] based on the information provided by ID, MS and calorimeters (cf. Figure 2).

The primary muon type used in ATLAS are the so-called *Combined* muons which are formed by the successful combination of ID and MS tracks. Other approaches complement the *Combined* muons in order to further enhance the reconstruction efficiency.

- In the region $|\eta| > 2.5$ which is not covered by the ID, *Standalone* muons, independent MS tracks, are used.
- For muons with low transverse momenta that do not traverse the whole MS, *Segment-Tagged* muons consisting of ID tracks and at least one track segment of the MS are used.
- *Calorimeter-Tagged* muons consisting of an ID track with a characteristic energy deposit in the calorimeter compatible with a minimum ionizing particle provide sensitivity in the region $|\eta| < 0.1$, where the MS is only partially instrumented.

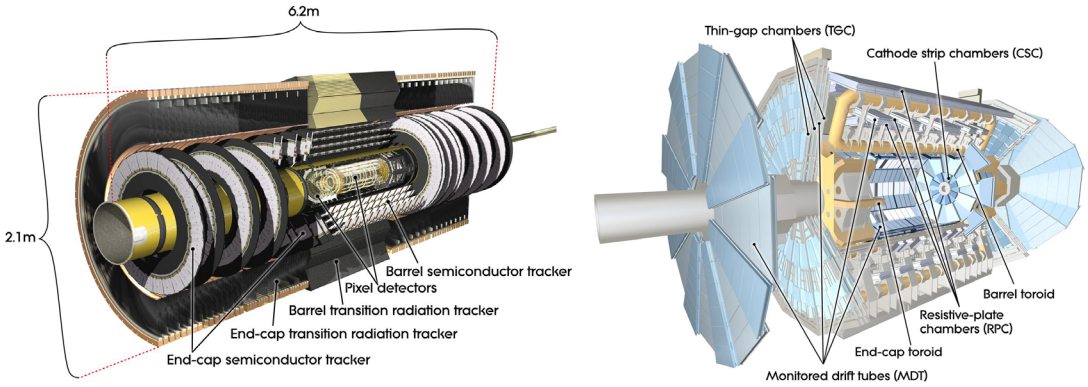

FIGURE 1. Cut-away view of the ATLAS inner detector (left) and ATLAS muon system (right) [1].

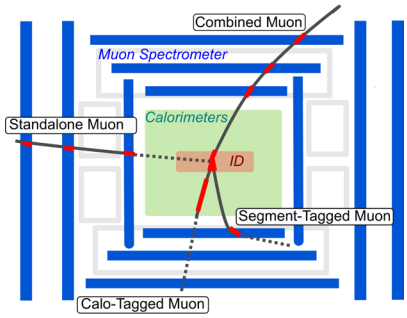

FIGURE 2. Schematic drawing of the detector parts used for muon reconstruction. Dependent on the detector parts used for the recontruction, several muon *types* are defined: *Combined* muons use the information of both inner detector and muon spectrometer, *Standalone* muons are reconstructed in the muon spectrometer only, *Segment-Tagged* muons are reconstructed in the inner detector and a single segment of the muon spectrometer and *Calorimeter-Tagged* muons get reconstructed in the inner detector and additionally leave a characteristic energy deposit in the calorimeter.

For use in physics analysis, four sets of muon identification criteria are defined, optimized for different use cases: The *Loose*, *Medium*, *Tight* and *High-*p_{T} selection.

The *Medium* identification criteria are the default muon selection in ATLAS and only use *Combined* and *Standalone* muons in order to minimize systematic uncertainties but still allow for good angular acceptance throughout the detector. The *Combined* muons are required to have at least 3 hits on at least 2 layers of precision chambers (MDT or CSC), except for the $|\eta| < 0.1$ region, where tracks with at least 3 hits in one single precision layer are allowed. The *Standalone* muons are required to have at least 3 hits in each of the 3 layers of MDT or CSC and to have a pseudorapidity of $2.5 < |\eta| < 2.7$.

The *Loose* identification criteria are used to maximize the reconstruction efficiency. Thereby, *Calorimeter-Tagged* muons and *Segment-Tagged* muons are restricted to $|\eta| < 0.1$ where *Combined* muons are less efficient due to acceptance holes of the MS which allow for cabling and services for the ID and the calorimeters. For pseudorapidities of $2.5 < |\eta| < 2.7$, *Standalone* muons are used in order to extend the acceptance outside the ID coverage.

The *Tight* identification criteria reduce fake muons. Only *Combined* muons with additional cuts on the normalized chi-squared of the combined track fit and on the compatibility between the momenta measured in the ID and MS are used.

The *High-*p_{T} selection is optimized to provide a maximum momentum resolution for muons with transverse momenta $p_{\mathrm{T}} > 100\,\mathrm{GeV}$. This is achieved by using *Combined* muons, but additionally requiring the muons to have at least hits in 3 different precision layers and vetoing specific regions of the MS with poor alignment due to a lack of statistics for determining the alignment constants.

More information on the different muon identification types can be found in Ref. [3].

LHC RUN 2 DATA

The LHC has commenced data-taking at a centre-of-mass energy of $\sqrt{s} = 13$ TeV in 2015. At the end of July 2015, the ATLAS dataset comprised an integrated luminosity of around $100\,\text{pb}^{-1}$ (cf. Figure 3) of which $85\,\text{pb}^{-1}$ were suitable for physics analyses.

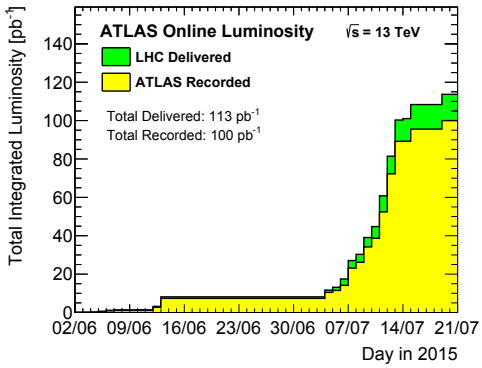

FIGURE 3. Cumulative luminosity versus time delivered to (green) and recorded by ATLAS (yellow) during stable beams for pp collisions at $\sqrt{s} = 13$ TeV centre-of-mass energy in 2015. The delivered luminosity accounts for luminosity delivered from the start of stable beams until the LHC requests ATLAS to put the detector in a safe standby mode to allow for a beam dump or beam studies. The recorded luminosity reflects the DAQ inefficiency, as well as the inefficiency of the so-called warm start: when the stable beam flag is raised, the tracking detectors undergo a ramp of the high-voltage and, for the pixel system, turning on the preamplifiers. Shown is the luminosity as determined from counting rates measured by the luminosity detectors. These detectors have been calibrated with the use of the van-der-Meer beam-separation method, where the two beams are scanned against each other in the horizontal and vertical planes to measure their overlap function. The luminosity shown represents the preliminary 13 TeV luminosity calibration present at July, 30th 2015 [5].

Figure 4 shows the dimuon invariant mass spectrum measured with this dataset. It was obtained by requiring exactly two oppositely charged *Combined* muons with transverse momentum above 4 GeV and pseudorapidity $|\eta| < 2.5$ with one of them triggering the ATLAS event readout. The dimuon invariant mass spectrum clearly resolves the J/ψ, ψ', Υ, Υ' and Z-resonances with about 750000 $J/\psi \to \mu^+\mu^-$ and 50000 $Z \to \mu^+\mu^-$ events which already allow for precise performance measurements.

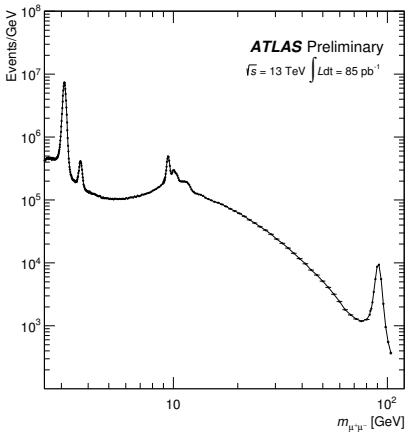

FIGURE 4. Dimuon invariant mass distribution showing oppositely charged, combined muon pairs with transverse momentum above 4 GeV and pseudorapidity $|\eta| < 2.5$. No specific ATLAS trigger is required [3].

MUON RECONSTRUCTION EFFICIENCY

In order to measure the muon reconstruction efficiency using $J/\psi \rightarrow \mu^+\mu^-$ or $Z \rightarrow \mu^+\mu^-$ events, a tag-and-probe method [4] is applied. Thereby, the *tag* muon has to fullfil the *Medium* identification criteria, to be a isolated and to have triggered the event readout. It has to have a transverse momentum of $p_{\mathrm{T}} > 4$ (28) GeV for $J/\psi \rightarrow \mu^+\mu^-$ ($Z \rightarrow \mu^+\mu^-$) events.

The *probe* muon has to be of opposite charge compared to the *tag* muon and to be an ID track (*Calorimeter-Tagged* muon) with $p_{\mathrm{T}} > 2.5$ (10) GeV.

Both *tag* and *probe* muon are restricted to pseudorapidities of $|\eta| < 2.5$ and an dimuon invariant mass between 2.7 and 3.4 GeV (within 10 GeV of the Z boson mass). For $Z \rightarrow \mu^+\mu^-$ events, the muons are additionally requested to be emitted back-to-back ($\Delta\phi > 2.0$).

If a muon fullfilling a certain set of identification criteria is found within a cone of $\Delta R = \sqrt{\Delta\eta^2 + \Delta\phi^2} < 0.05$ around the *probe* muon track, the *probe* muon is successfully reconstructed. The efficiency for this set of identification criteria is defined as the ratio between the successfully reconstructed *probe* muons and all *probe* muons. The efficiencies get corrected for the ID track reconstruction efficiency by using MS tracks as *probe* muons.

For $Z \rightarrow \mu^+\mu^-$ events, the residual background contributions are estimated by using a data-driven method (Monte Carlo simulation) for the reducible (irreducible) backgrounds while for $J/\psi \rightarrow \mu^+\mu^-$ events, the number of signal and background events are extracted using a fit to the dimuon invariant mass distribution.

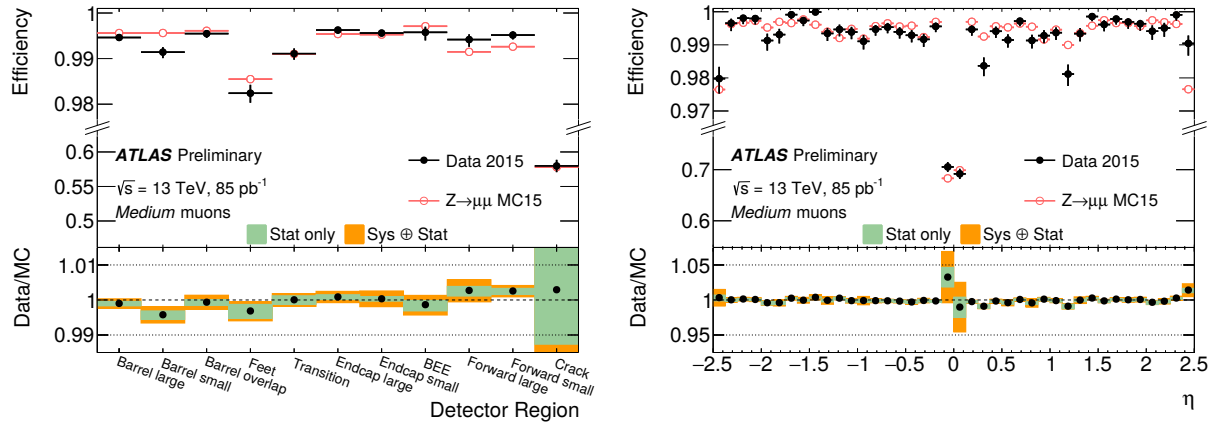

FIGURE 5. Muon reconstruction efficiency for the *Medium* identification criteria measured in $Z \rightarrow \mu^+\mu^-$ decays for various regions of the ATLAS muon spectrometer (left) and the pseudorapidity of the probe muon (right). The black dots indicate the measured data points and the red circles show the simulated distribution. The bottom panel shows the ratio between observed and expected efficiency, the efficiency scale factor, where the green area indicates the statistical uncertainty and the orange area the quadratic sum of the statistical and systematic uncerterainty [3].

The upper panel of Figure 5 (left) shows both measured and simulated muon reconstruction efficiencies for various regions of the ATLAS muon spectrometer for the *Medium* identification criteria. The efficiencies are found to be close to 99% except from the *Crack* region which is defined by the pseudorapidity interval $|\eta| < 0.1$. The bottom panel shows the ratio between observed and expected efficiency, the efficiency scale factor, including statistical and systematic errors. Figure 5 (right) shows the efficiencies and efficiency scale factors as a function of the pseudorapidity of the probe muon. Again, the efficiency drop for $|\eta| < 0.1$ can be observed.

Muon reconstruction efficiencies and efficiency scale factors measured in both $J/\psi \rightarrow \mu^+\mu^-$ and $Z \rightarrow \mu^+\mu^-$ decays are shown in Figure 6 as a function of the transverse momentum of the probe muon. The combination of the measurements using both decays allows for well defined efficiency scale factors for transverse muon momenta from 4 GeV up to several 100 GeV. Both measurements are in good agreement and together provide a precise determination of the muon reconstruction efficiencies and scale factors.

Overall, the measured muon reconstruction efficiencies exceed 99% for pseudorapidities of $0.1 < |\eta| < 2.5$ and transverse momenta of $p_{\mathrm{T}} > 10$ GeV. Systematic uncertainties are small and dominated by the data-driven background normalization [4] and by the possible dependence on the charge of the *probe* muon.

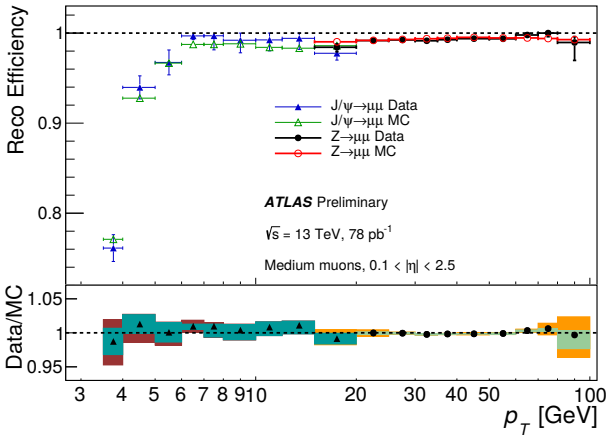

FIGURE 6. Muon reconstruction efficiency for the *Medium* identification algorithm measured in $J/\psi \to \mu^+\mu^-$ and $Z \to \mu^+\mu^-$ decays as a function of the transverse momentum of the probe muon. The filled blue triangles (black dots) indicate the measured data points and the open green triangles (red circles) show the simulated distribution for $J/\psi \to \mu^+\mu^-$ ($Z \to \mu^+\mu^-$) events. The bottom panel shows the ratio between observed and expected efficiency, the efficiency scale factor, where the cyan (green) area indicates the statistical uncertainty and the red (orange) area the quadratic sum of the statistical and systematic uncterainty [3].

MUON MOMENTUM SCALE AND RESOLUTION

In order to correctly predict the muon momentum resolution in the reconstructed collision data, the simulation has to be corrected to account for imperfect alignment of the muon spectrometer. Parameters accounting for the energy losses in material, radial distortions or mismodelling of the magnetic field integral, multiple scattering, intrinsic resolution effects and detector misalignment enter the smearing of the original muon momentum [3]. Corrections are derived seperately for ID and MS muon momentum measurements allowing for a better understanding of the sources of mismodelling in simulation. They are extracted by a template-based likelihood fit using $J/\psi \to \mu^+\mu^-$ and $Z \to \mu^+\mu^-$ decays following the procedure described in Ref. [4].

The muon momentum scale and resolution measurement requires events with exactly 2 oppositely charged *Medium* muons with pseudorapidity $|\eta| < 2.5$ and transverse momentum of $5\,\text{GeV} < p_\text{T} < 20\,\text{GeV}$ ($p_\text{T} > 20\,\text{GeV}$) for $J/\psi \to \mu^+\mu^-$ ($Z \to \mu^+\mu^-$) decays. The dimuon invariant mass has to be in the range of $2.4\,\text{GeV} < p_\text{T} < 3.6\,\text{GeV}$ and $75\,\text{GeV} < p_\text{T} < 105\,\text{GeV}$, respectively.

The dimuon mass spectrum is modeled by a Crystal-Ball PDF [6, 7], of which the Gaussian component estimates the detector resolution and the exponential component approximates the residual energy loss of the muon from traversing the material. The Crystal-Ball PDF is convoluted with a Breit-Wigner PDF of the same mean and with the width fixed to the natural width of the Z boson [8]. The mean and resolution paramenters of the maximum likelihood estimate are proportional to the muon momentum scale and resolution, respectively. More detailed information can be found in Ref. [3].

Due to the limited size of the $\sqrt{s} = 13\,\text{TeV}$ dataset taken in 2015, the bulk of the muon momentum scale and resolution corrections is determined from a $5\,\text{fb}^{-1}$ dataset of pp-collisions taken in 2012 at $\sqrt{s} = 8\,\text{TeV}$ which was reprocessed using the same reconstruction as designed for 2015. The residual data-to-simulation mismodelling is then corrected using the $85\,\text{pb}^{-1}$ dataset taken at $\sqrt{s} = 13\,\text{TeV}$.

Figure 7 shows those residual mismodelling effects on muon momentum scale (left) and resolution (right) obtained by fitting the dimuon invariant mass resonance for $J/\psi \to \mu^+\mu^-$ decays. A good agreement between data and simulation withing the systematic uncertainties is observed. Figure 8 shows the same measurement using $Z \to \mu^+\mu^-$ decays.

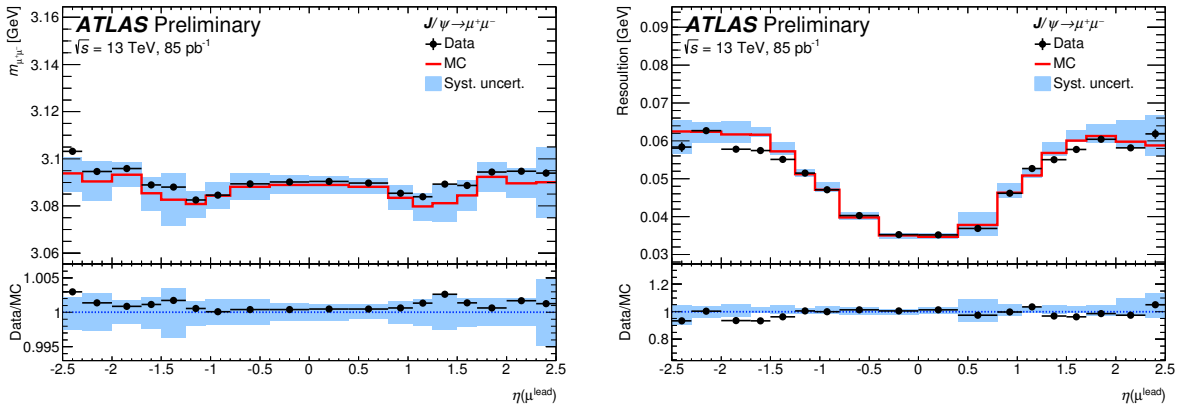

FIGURE 7. Mean value (left) and energy resolution (right) of the dimuon invariant mass resonance for $J/\psi \to \mu^+\mu^-$ decays as a function of the pseudorapidity of the muon with higher transverse momentum. The black dots indicate the measured data points, the red line shows the simulated distribution and the blue area is the quadratic sum of the systematic uncertainties [3].

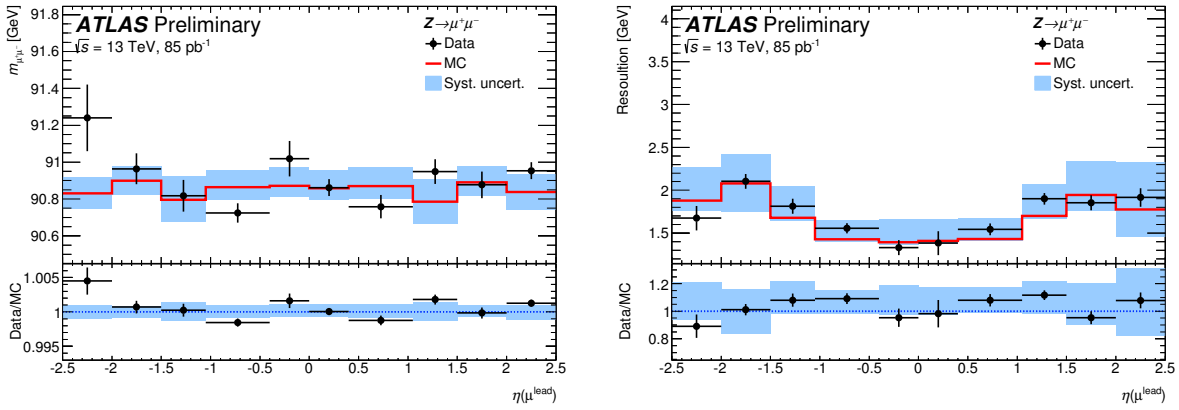

FIGURE 8. Mean value (left) and energy resolution (right) of the dimuon invariant mass resonance for $Z \to \mu^+\mu^-$ decays as a function of the pseudorapidity of the muon with higher transverse momentum. The black dots indicate the measured data points, the red line shows the simulated distribution and the blue area is the quadratic sum of the systematic uncertainties [3].

SUMMARY

The ATLAS muon reconstruction and identification criteria for LHC Run 2 have been introduced and discussed. The 85 pb^{-1} dataset at $\sqrt{s} = 13\,\text{TeV}$ already allows for a precise determination of muon reconstruction efficiencies, momentum scale and resolution. A first measurement has been performed using $J/\psi \to \mu^+\mu^-$ and $Z \to \mu^+\mu^-$ decays.

The measured muon reconstruction efficiencies exceed 99% for pseudorapidities of $0.1 < |\eta| < 2.5$ and transverse momenta of $p_\text{T} > 10\,\text{GeV}$. Applying the muon momentum calibration to simulation correctly describes the reconstructed muon momentum scale and resolution within the systematic uncertainties.

REFERENCES

[1] ATLAS Collaboration, The ATLAS Experiment at the CERN Large Hadron Collider, JINST **3**, p. S08003 (2008).

[2] ATLAS Collaboration, ATLAS muon spectrometer: Technical design report, CERN-LHCC-97-22, ATLAS-TDR-10 (1997).

[3] ATLAS Collaboration, Muon reconstruction performance in early 13 TeV data, ATL-PHYS-PUB-2015-037 Aug (2015).
[4] ATLAS Collaboration, Measurement of the muon reconstruction performance of the ATLAS detector using 2011 and 2012 LHC protonproton collision data, Eur.Phys.J. **C74**, p. 3130 (2014).
[5] ATLAS Collaboration, https://atlas.web.cern.ch/Atlas/GROUPS/DATAPREPARATION/PublicPlots/ /2015/DataSummary/ (July 2015).
[6] M. Oreglia, A Study of the Reactions $\psi' \to \gamma\gamma\psi$ (1980), appendix D., SLAC.
[7] J. Gaiser, Charmonium Spectroscopy From Radiative Decays of the J/ψ and ψ' (1982), appendix F., SLAC.
[8] K. Olive *et al.* (Particle Data Group), Review of Particle Physics, Chin. Phys. **C38**, p. 090001 (2014).
[9] T. Kawamoto *et al.*, New Small Wheel Technical Design Report, CERN-LHCC-2013-006. ATLAS-TDR-020 Jun (2013).
[10] J. Illingworth and J. Kittler, A survey of the Hough transform **44**, 87 – 116 (1988).

Proceedings of the LHCP2015 Conference, St. Petersburg, Russia, August 31 - September 5, 2015

Editors: V.T. Kim and D.E. Sosnov

Photons in ATLAS: from Run1 to Run2

MIKHAIL LEVCHENKO

National Research Centre "Kurchatov Institute" B.P.Konstantinov Petersburg Nuclear Physics Institute, St. Petersburg, Russia

Mikhail.Levchenko@cern.ch

On behalf of the ATLAS Collaboration

Abstract. The performance of the reconstruction and identification of photons with the ATLAS detector at the LHC is a key component to realize the ATLAS full physics potential, both in the searches for new physics and in precision measurements. For instance, photons played a critical role in the discovery of a Higgs boson, announced by the ATLAS Collaboration in 2012, and in the measurement of its properties. These proceedings present a description of the algorithms used for the reconstruction and identification of photons with the ATLAS detector, as well as results from the measurements of their efficiencies in pp collisions.

INTRODUCTION

Several physics processes occurring in the proton-proton collisions at the Large Hadron Collider (LHC) produce final states with prompt photons. The main contributions originate from non-resonant production of photons in association with jets or of photon pairs, with cross sections of the order of tens of nanobarns or picobarns, respectively. The study of such final states, and the measurement of their production cross sections, are of the great interest as a probe of the perturbative QCD and can provide useful information on the parton distribution functions of the proton. Prompt photons are also produced in rarer events that are key to the ATLAS [1] physics programme, such as di-photon decays of the Higgs boson with a mass near 125 GeV, occurring with a cross section of around 20 fb at $\sqrt{s} = 8$ TeV. Finally, some of the typical expected signatures of physics beyond the Standard Model (SM) are characterized by the presence of prompt photons in the final state. They include for instance resonant photon pairs from graviton decays in models with extra spatial dimensions, pairs of photons accompanied by large missing transverse momentum produced in the decays of pairs of supersymmetric particles, and events with highly energetic photons and jets from decays of excited quarks or more exotic scenarios.

ATLAS DETECTOR

ATLAS is a multipurpose particle physics detector with a forward-backward symmetric cylindrical geometry and near 4π solid angle coverage. A detailed description of the instrument can be found in ref. [1]. The inner tracking detector (ID) is composed of a silicon pixel detector, a silicon strip detector and a transition radiation tracker. The ID is surrounded by a thin super-conducting solenoid that provides a 2 T magnetic field. It allows an accurate reconstruction of tracks from the primary proton-proton collision and also identifies tracks from secondary vertices, permitting the efficient identification of photon conversions. A high-granularity liquid-argon (LAr) sampling electromagnetic calorimeter (ECAL) surrounds the ID system. It is divided into a barrel section, covering the pseudorapidity region $|\eta| < 1.475$, and two endcap sections, covering the pseudorapidity regions $1.375 < |\eta| < 3.2$. It consists of three longitudinal layers for $|\eta| < 2.5$ and two for $2.5 < |\eta| < 3.2$. Up to $|\eta| < 2.4$, the first ECAL layer uses highly granular strips segmented in the η direction. The second layer of the ECAL collects most of the energy deposited by electromagnetic showers. Significant energy deposits in the third layer are an indication for leakage beyond the ECAL from a high energy shower. The measurements from the third layer are used to correct for this effect. A thin presampler layer in front of the accordion calorimeter, covering the pseudorapidity interval $|\eta| < 1.8$, is used to correct for energy loss

upstream of the calorimeter. The hadronic calorimeter (HCAL), surrounding the ECAL, includes a central ($|\eta| < 1.7$) iron/scintillator tile calorimeter, two endcap ($1.5 < |\eta| < 3.2$) copper/LAr calorimeters and two forward calorimeters that extend the coverage to $|\eta| < 4.9$, using copper and tungsten as absorber. The muon spectrometer, located beyond the calorimeters, completes the detector.

RECONSTRUCTION OF PHOTONS

Photon reconstruction [2] begins with the creation of a preliminary set of clusters in the ECAL whose size corresponds to 3×5 cells in $\eta \times \varphi$ in the middle layer. After that reconstruction is seeded from such clusters with transverse energy $E_{\mathrm{T}} > 2.5$ GeV, using a sliding window algorithm over the full acceptance of the ECAL. The final cluster size is dependent on the particle hypothesis and the region of the detector (3×7 for unconverted photons in the barrel, 3×7 for converted photons and electrons in the barrel, 5×5 in all other cases). These clusters are matched with tracks that are reconstructed in the ID and extrapolated to the calorimeter.

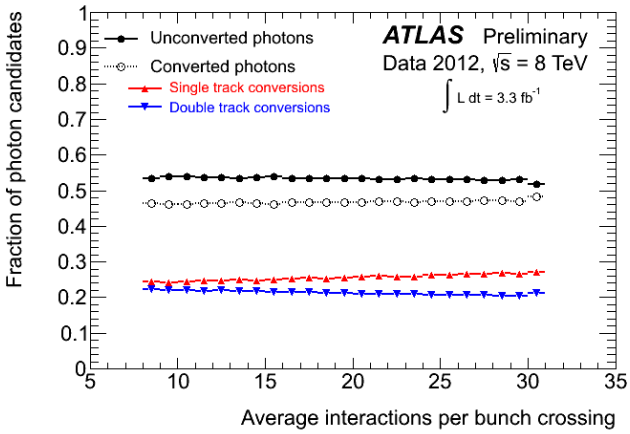

FIGURE 1. Fraction of the different categories of photon candidates as a function of the average number of interactions per bunch crossing [3].

If the matching cannot be performed, the clusters are classified as unconverted photon candidates. For clusters with matched tracks, those tracks are matched to a reconstructed secondary vertex. If the matching is successful, the clusters are classified as converted photon candidates, otherwise they are classified as electron candidates. Figure 1 shows the fraction of the different categories of photon candidates as a function of the average number of interactions per bunch crossing. The stability of this fraction illustrates the robustness of the classification procedure with respect to the pileup effect. In addition to identifying efficiently electromagnetic showers, the ATLAS ECAL measures their energies with high accuracy and with a linearity better than 0.5% over a large energy range, from 10 GeV to a few TeV. The cluster energy is determined precisely by computing and summing four different contributions:

- the energy deposited in the material in front of the EM calorimeter,
- the energy deposited in the calorimeter inside the cluster,
- the energy deposited outside the cluster (lateral leakage),
- and the energy deposited beyond the EM calorimeter (longitudinal leakage).

The four terms are parametrised as a function of the cluster measured energies in the presampler (where it is present) and in the three accordion longitudinal layers.

The final energy measurement of the photon candidates is performed using a cluster size depending on the classification of the candidate and on its pseudorapidity.

IDENTIFICATION OF PHOTONS

The photon identification aims to provide a good separation between isolated photons and background objects (non-isolated electrons, hadron jets, etc.). The requirements include a veto on the amount of energy deposited in the hadronic calorimeter and criteria on the lateral an longitudinal shower shape. The granularity of the first layer allows an efficient discrimination between single photon showers and two overlapping showers originating from a neutral hadron decay (π^0, η, ω, etc.). Different sets of criteria with increasing background rejection are developed. These sets are optimized in bins of pseudorapidity and several optimizations have been performed to cope with the increase in pileup. A dedicated "multilepton" set of requirements is implemented to achieve the high signal efficiency which is crucial for the search of the Higgs boson in the four lepton decay channel. Figure 2 illustrates the distribution of the R_η variable for unconverted photons selected from $Z \to ll\gamma$ events and fake candidates from hadronic jets in $Z(\to ll)$+jets events. Comparison of data with corresponding simulated events is shown. This figure exhibits a clear difference between isolated prompt photons and hadronic jets. This difference, however, is mainly observed in the tails of the distribution and therefore illustrates the need to use multiple variables to get a powerful rejection of the fake candidates.

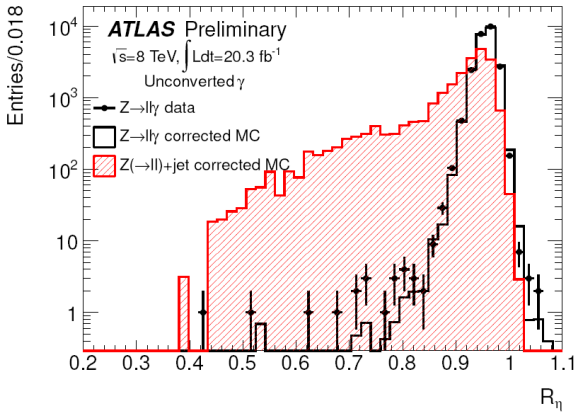

FIGURE 2. Distribution of the calorimetric discriminating variable R_η for unconverted photon candidates with $E_T > 20$ GeV and $|\eta| < 2.37$ (excluding $1.37 < |\eta| < 1.52$) selected from $Z \to ll\gamma$ events obtained from the 2012 data sample (dots). The distributions for photons from simulated $Z \to ll\gamma$ events (black hollow histogram) and for fake photons from hadronic jets in $Z(\to ll)$+ jets (red hatched histogram) are also shown, after reweighting their 2D E_T versus η distributions to match that of the data candidates, and correcting their R_η value by the average shift between data and simulation distributions determined from the inclusive sample of isolated photon candidates passing the identification criteria [3].

PHOTON IDENTIFICATION EFFICIENCY MEASUREMENTS

The photon identification efficiency can be estimated with simulation but, as illustrated on Fig. 2, the description of the shower shape in simulation is not perfect. Therefore a direct measurement of the efficiency in data improves its precision. This measurement, described in ref. [4], uses three complementary methods to cover a large range of E_T:

- in the low E_T region, the measurement can be performed using a sample of pure photons from $Z \to ll\gamma$ decays. Using the proton-proton collision dataset collected in 2012, the measurement is performed up to $E_T = 80$ GeV.
- in the intermediate E_T region, the measurement can be performed with electrons from Z decays. The shower shape variables are corrected on an event-by-event basis to account for the difference between electron and photon shower shape using simulation. The "transformed" electrons are then used to measure the photon identification efficiency.
- at large E_T, an inclusive sample of photon candidates is selected to perform the measurement. The method, called "matrix method", allows to measure the identification efficiency by determining the composition of the

selected sample before and after applying the identification criteria, by using an additional discriminating variable.

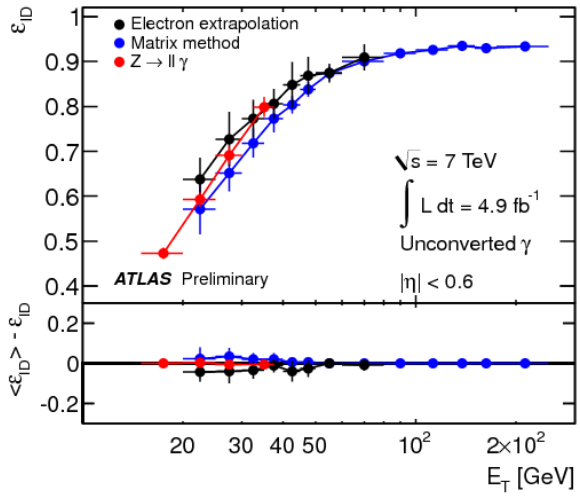

FIGURE 3. Photon identification efficiency as a function of E_{T} for unconverted photons in the pseudorapidity region $0 < |\eta| < 0.6$ [4].

The measurements are performed in bins of pseudorapidity separately for converted and unconverted photons. A good agreement is found between the three methods in the overlapping regions. Figure 3 shows the efficiency obtained by the three methods as a function of E_{T} for unconverted photons in the pseudorapidity region $0 < |\eta| < 0.6$.

The results of the three methods are combined, and the uncertainties on the measurement range from $\sim 5\%$ to $\sim 1.2\%$ decreasing with E_{T}. A dedicated treatment of correlations among photons has been developed to reduce the uncertainty on the event efficiency for multi-photon events. This treatment allows to reduce significantly the effect of the corresponding uncertainty on the $H \to \gamma\gamma$ signal strength.

CONCLUSION

The performances of ATLAS to detect and measure the properties of the photons have been presented. Powerful tools to separate photons from background processes are developed and their efficiencies are measured from data with the great precision. The detection strategy is revisited for the second run of the LHC in order to cope with the harsher pileup conditions.

Important improvements have been made, mostly based on a new track algorithm and track-cluster matching, enhancing the reconstruction efficiency by $\sim 7\%$ at low E_{T} , as well as a identification discriminant, improving the background rejection by 30 to 50% for a fixed efficiency. This is helps to get a high selection efficiency of Higgs decaying to ZZ keeping the background rejection as high as possible. The calorimeter energy measurement has now reached a stability over time and pile-up at $\sim 0.05\%$. This new procedure is leading to a resolution improvement of the Higgs boson mass (decaying to two photons) by 10%. and a reduction of the total mass systematic uncertainty from this and other improvements by a factor of 2.5 with respect to the previous measurement [4].

REFERENCES

[1] ATLAS collaboration, JINST **3**, p. S08003 (2008).
[2] ATLAS collaboration, ATLAS-CONF-2010-005 (2010).
[3] ATLAS collaboration, https://twiki.cern.ch/twiki/bin/view/AtlasPublic/ElectronGammaPublicCollisionResults .
[4] ATLAS collaboration, ATLAS-CONF-2012-123 (2012).

Proceedings of the LHCP2015 Conference, St. Petersburg, Russia, August 31 - September 5, 2015

Editors: V.T. Kim and D.E. Sosnov

Research and Development for the ATLAS Forward Calorimetry at the Phase-II LHC

ALEXANDER CHEPLAKOV

Joint Institute for Nuclear Research, 6 Joliot-Curie, 141980 Dubna, Moscow region, Russia

Alexander.Cheplakov AT cern.ch

On behalf of the Liquid Argon Calorimeter Group of the ATLAS Collaboration

Abstract. During the LHC Run-1 data taking period the ATLAS calorimeter system demonstrated an excellent performance of electron and photon reconstruction as well as hadronic jets and missing transverse energy measurements. These precision measurements played a major role in the discovery of the Higgs boson. Further studies of the Higgs properties and SUSY searches should be performed at the High Luminosity LHC (HL-LHC) which will run at 5-7 times the original design luminosity to provide 3000 fb^{-1} of data by 2037. Total irradiation doses will be more than doubled compared to the original design, taking into account a reduced safety factor of 2 representing our confidence in radiation background simulations. Moreover, the increased instantaneous luminosity will result in much higher detector occupancy. The ATLAS Forward Calorimeters (FCal) will be affected by these factors. A rich R&D program is ongoing to evaluate the consequences of the LHC modernization and to investigate different scenarios proposed for the Phase-II detector upgrade.

Introduction

The ATLAS Detector [1] is a general-purpose apparatus at the LHC designed for studying *pp*-collisions at the centre-of-mass energy of 14 TeV and an instantaneous luminosity of 10^{34} $cm^{-2}s^{-1}$.

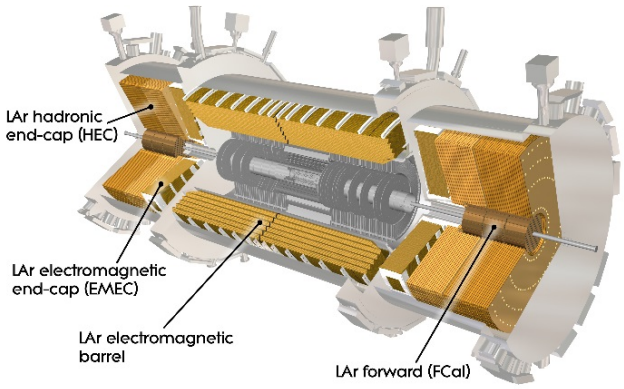

FIGURE 1. A general layout of the ATLAS liquid argon calorimeter system [1].

A general view of the ATLAS liquid argon calorimeter system is presented in Fig.1. The current very good performance of the calorimeter system which comprises the liquid-argon electromagnetic, hadronic (HEC) and forward (FCal) sub-systems, should be maintained also at HL-LHC instantaneous luminosities of $5 \cdot 10^{34}$ $cm^{-2}s^{-1}$. This corresponds to about 140 inelastic *pp*-collisions per beam-crossing. Although a number of studies have confirmed that the intrinsically radiation hard LAr technology will operate at the HL-LHC, the calorimeter upgrade program is proposed [2-3] to deal with the expected challenges and to maximize the physics performance and discovery potential of the experiment.

In contrast to the liquid argon electromagnetic and hadronic end-cap calorimeters, the performance of the forward (FCal) calorimeter will be degraded by high energy particle density at HL-LHC conditions. The upgrade program includes a new Liquid Argon Forward Calorimeter (sFCal), with higher granularity and smaller electrode gaps, with improved cooling to reduce the impact of the very high instantaneous luminosity at HL-LHC. It can lead to space-charge effects from ion-buildup in the LAr gap, as well as large reductions in the voltage on the electrodes, and finally to potential over-heating (possibly even local boiling) in the LAr. The scenario may also include a finely segmented Si - based preshower layer (HGTD) with precision time resolution covering approximately the pseudo-rapidity[1] range $2.4 < |\eta| < 4.0$, in order to assign charged particles to different collision vertices to mitigate pile-up effects in energy reconstruction . The readout electronics need to be upgraded because of radiation tolerance limits, lifetime, and because the on-detector front-end electronics cannot operate with the Level-0 and Level-1 trigger rates and latencies required for the HL-LHC luminosities.

Upgrade options for the ATLAS forward calorimeters

The effect of space charge on the pulse shape which affect the detector performance is under study in the HiLum experiment at Protvino. Heat flow measurements with a mock-up are also performed to study the possibility for argon over-heating and bubble formation in the cryostat. If it cannot be established that the liquid argon will not boil in the harsh HL-LHC environment, the upgrade of the forward region will be required. Upgrade options under investigation are:

- a new sFCal replacing existing FCal and employing smaller LAr gaps (100μm), with better cooling and higher transverse granularity;
- a miniFCal in front of the high-η part of the existing FCal, which would be based on either LAr/Cu technology ("cold" miniFCal option) or on Si/W or single-crystal diamond/Cu technology (the "warm" option).

Different detector technologies will be tested for HGTD, including:

- multi-channel plate-based detectors;
- single-crystal or poly-crystalline diamond sensors;
- various silicon-based detectors.

Detailed simulation studies and R&D's are needed for optimization of the upgrade scenario.

Test-beam experiment at U-70 accelerator at Protvino

Optimization of detector parameters in the HiLum experiment at the Protvino U-70 beam-test forms a basis for the detector upgrades required for HL-LHC. Several prototype modules of the ATLAS forward calorimeters have been tested in high-intensity proton beams addressing, in particular, the effect of space charge on the pulse shape which affects the detector performance.

Beam-test results for two modules, one with a narrow LAr gap (119 μm) and another with nominal (269 μm) electrodes are compared in Fig. 2. Whereas the latter (shown in the inset) shows the fall of response at a critical beam intensity corresponding (within uncertainties [4]) to the nominal LHC luminosity, 10^{34} $cm^{-2}s^{-1}$, the narrow-gap electrodes demonstrate a stable response up to ten times higher intensities.

---

1 The ATLAS reference system is a Cartesian right-handed co-ordinate system, with the nominal collision point at the origin. The anti-clockwise beam direction defines the positive z-axis, while the positive x-axis is defined as pointing from the collision point to the centre of the LHC ring and the positive y-axis points upwards. The azimuthal angle φ is measured around the beam axis, and the polar angle θ is measured with respect to the z-axis. The pseudorapidity is defined as $\eta = -\ln \tan(\theta/2)$.

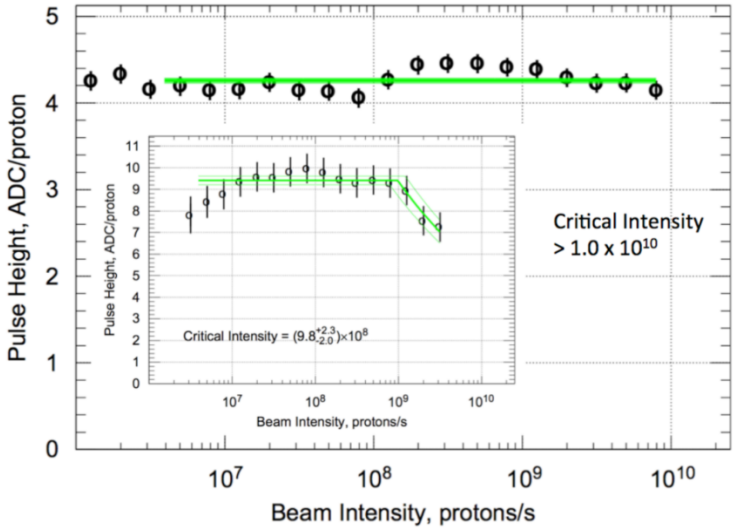

FIGURE 2. Response from the test cells of the forward calorimeter (signal pulse height) with two different gaps - small (119 μm) and nominal one (269 μm, shown in the inset) - to the increase of proton beam intensity [4].

Simulation results for the high-granularity sFCal

The expected improvements of the forward calorimeter performance will come from an increase of the readout granularity by a factor 4 in the range $3.2<|\eta|<4.3$ in the first FCal section. This will result in better η and ϕ resolutions for the calorimeter clusters, an increased sensitivity to the jet substructure and a reduced pile-up contribution per calorimeter cell.

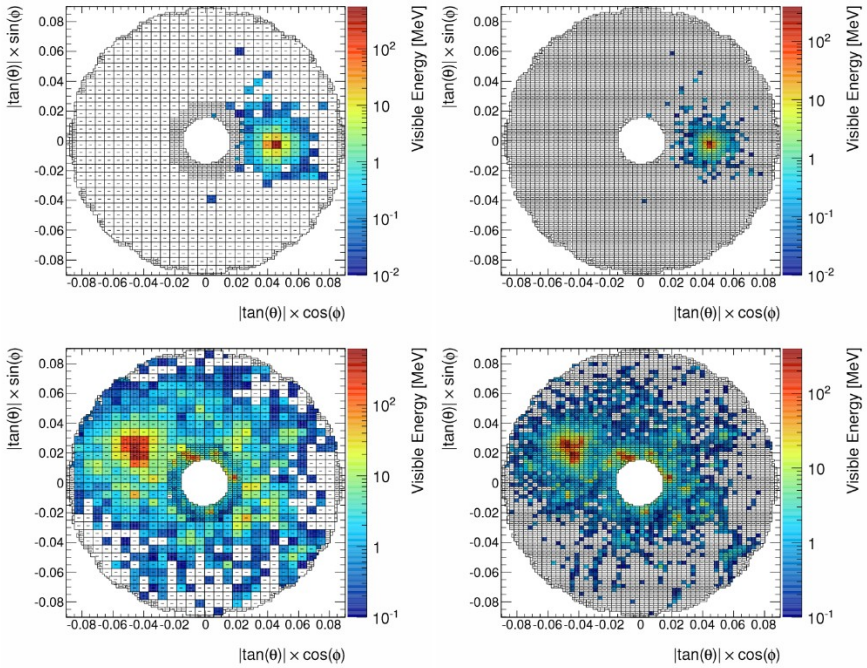

FIGURE 3. Event for the same electron (upper plot) and the same single jet (lower plot) in the FCal (left) and the high-granularity sFCal (right).

The effect of improvements in the readout granularity is evident from the simulation results presented in Fig.3. The plots show the energy deposited in the calorimeter cells for one electron and for one hadronic jet simulated for both the present FCal detector and for the geometry of the high-granularity sFCal implemented in the full chain of the ATLAS simulation infrastructure.

LAr calorimeter readout electronics

The current LAr calorimeter readout electronics is incompatible with the future L0 and L1 trigger rates of 1 MHz and 400 kHz. It will be improved in two steps. In the Phase-I upgrade the trigger readout will be equipped with additional electronics to provide better granularity signals to the L1 trigger system. The Phase-II L0 trigger will be based on calorimeter and muon spectrometer signals. Full replacement of the front-end and back-end readout system is foreseen for the Phase-II upgrade. Only the HEC pre-amplifier system, which is designed to withstand HL-LHC radiation doses and is located inside the cryostat, and LAr trigger digitizer board (LTDB) installed during the Phase-I upgrade [5] will not be replaced.

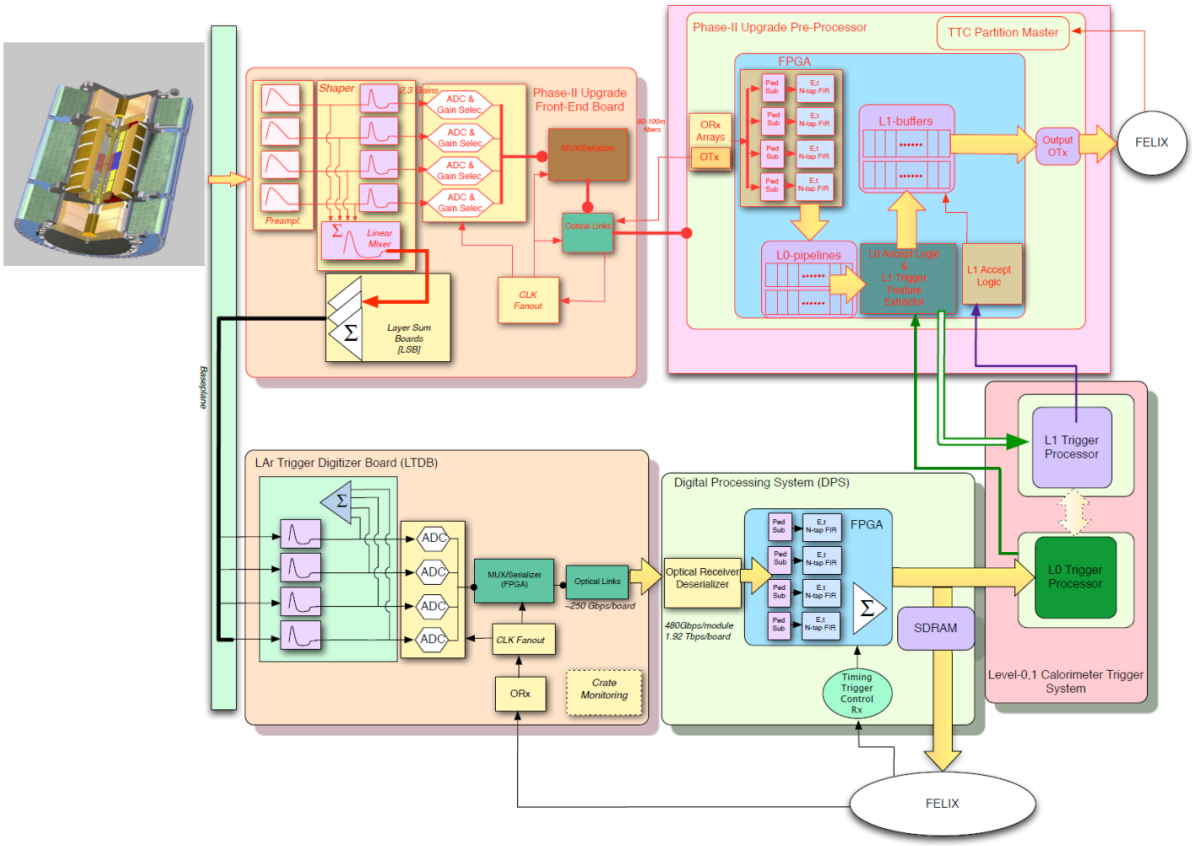

FIGURE 4. Architecture of the Phase-II readout system of the ATLAS LAr calorimeters.

The layout of the Phase-II LAr readout is presented in Fig. 4. Pre-amplification, shaping and digitization of signals from all 183000 LAr detector channels will be performed on the new Front-end Boards (FEB2) at the rate of 40 or 80 MHz. The data will be received by the back-end pre-processor system for energy calibration and pile-up suppression. The FEB2 will also produce input signals to the LTDBs which will feed L0 trigger system with inputs for the so-called Super-Cell readout.

Several alternatives are under study in various groups of the LAr community for the analog, ADC and optical link parts of the front-end. The R&D program includes development of a new radiation-tolerant calibration board,

the radiation and performance tests of commercial analog and digital components for the low-voltage power system of the HEC. Efforts continue on development of the back-end system relying on commercial components.

Irradiation facility at the IBR-2m reactor at JINR Dubna

The detector materials and electronic components must satisfy the future trigger and radiation tolerance requirements. An intensive program of irradiation tests has been carried out at the pulsed neutron IBR-2 reactor at JINR Dubna during the period of the ATLAS detector construction. To provide adequate conditions for radiation hardness tests aimed at the HL-LHC conditions the irradiation facility has been modernized [6]. The general view is shown in Fig. 5a. The plot in Fig. 5b represents the measured neutron flux as a function of the neutron energy.

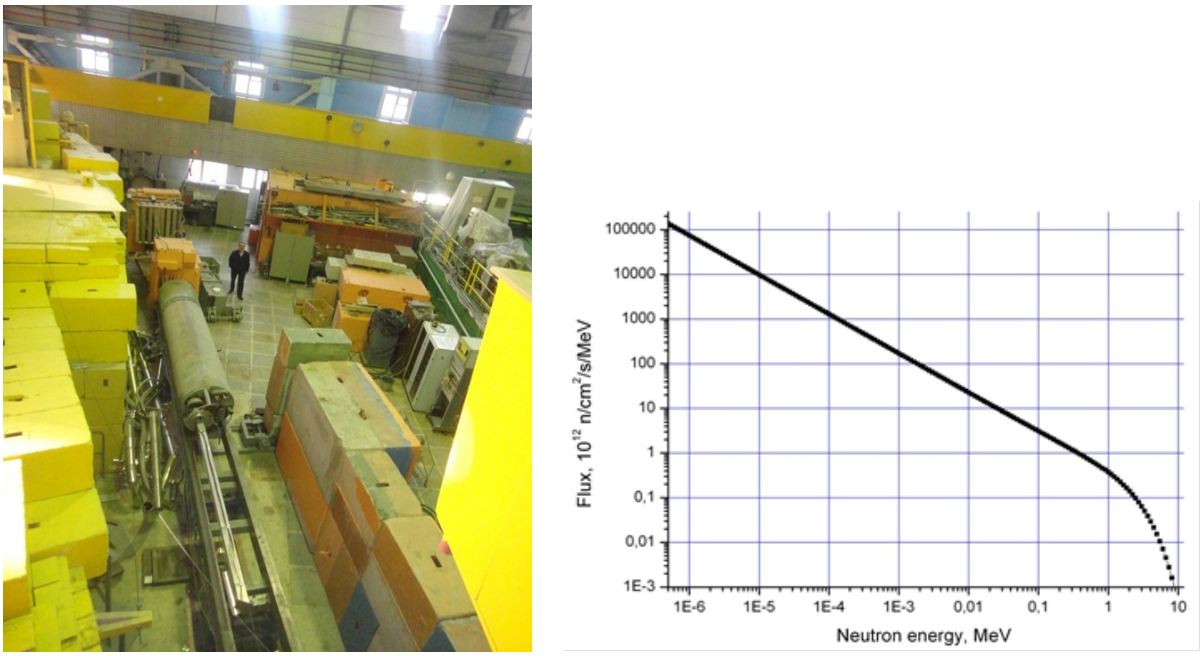

a) b)

FIGURE 5. General view of the Dubna irradiation facility (a) and the fast neutron flux (b).

Samples for the irradiation tests are located in a container with lateral dimensions of 16cm×16cm at the edge of an extension arm which is mounted at the head of a movable platform. To control the neutron fluence, activation foils are placed near irradiated materials and the induced activity is subsequently measured. The maximum fluence of neutrons with energies above 1 MeV for the sample placed at a distance of 30 mm from the reactor moderator is 10^{18} n cm^{-2}. High flux of fast neutrons and a large beam aperture makes the facility very suitable for testing detectors and electronics which are supposed to be used in the Phase-II upgrade program.

Some examples of the tests performed recently at the Dubna facility are presented in Fig. 6. The plot on the left (6a) shows a "standard" PCB sample made of FR4 and irradiated to the neutron fluence about 3×10^{17} n cm^{-2}. The radiation damages resulted in outgassing from the plastic material which caused destruction of the PCB. Similar results were observed for another popular material – G10. In the same tests (doses) the PCB samples made of Rogers 4450B and Arlon 85N survived [7], but more tests are required for the final conclusion.

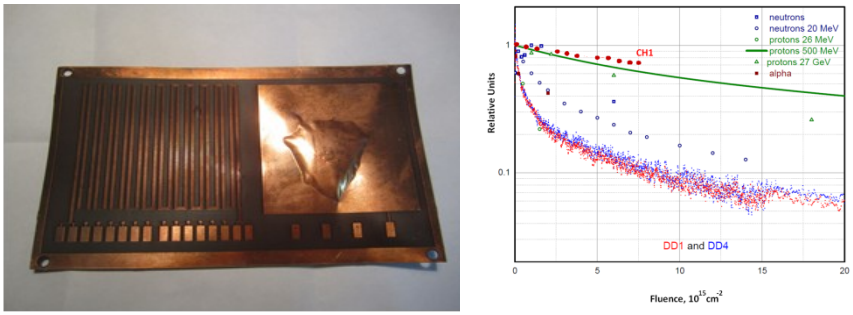

a) b)

FIGURE 6. Irradiation tests examples: (a) PCB sample made of FR4 and irradiated to fluence about 3×10^{17}n cm^{-2}; (b) signal degradation of the diamond sensors in various beams (see legend), DD1 and DD4 are two poly-crystalline sensors irradiated in Dubna in 2012 and CH1 denotes recent irradiation results for a single-crystal diamond sensor from Nanjing University (China).

The plot on the right (6b) shows compilation of the irradiation tests performed on diamond sensors in various beams (see legend) [8]. The bottom curve made of small red and blue dots represents data for two poly-crystalline sensors (DD1 and DD4) irradiated in Dubna in 2012: only 2% of the initial response remained after the fluence of 10^{17} n cm^{-2}. The very recent tests performed at the IBR-2m on a single-crystal sensors from the Nanjing University (China) and labelled as CH1 [9] show much better resistance to neutron irradiation. These sensors are therefore promising candidates for a future application in high energy physics experiments.

Conclusions

A rich R&D program is proposed for ATLAS calorimetry, including modernization of the design and development of new detectors. The final selection of the upgrade options and technologies will be driven by performance considerations and results of risk analyses. Intensive simulation studies and comprehensive tests, including mock-up, test-beam and irradiation tests are ongoing in order to prepare the ATLAS LAr calorimeters for the HL-LHC running.

ACKNOWLEDGMENTS

The author acknowledges support from the Ministry of Education and Science of the Russian Federation (grant RFMEFI61014X0005) for modernization of the irradiation facility at the JINR in Dubna.

REFERENCES

1. ATLAS Collaboration, JINST, 3 (2008), p. S08003
2. ATLAS Collaboration, Letter of Intent for the Phase-II Upgrade of the ATLAS Experiment, CERN-LHCC-2012-022 ; LHCC-I-023
3. ATLAS Collaboration, ATLAS Phase-II Upgrade Scoping Document, CERN-LHCC-2015-020 ; LHCC-G-166
4. A. Glatte et al., Liquid argon calorimeter performance at high rates, NIM A 669 (2012) 47–65
5. ATLAS Collaboration, ATLAS Liquid Argon Calorimeter Phase-I Upgrade Technical Design Report, CERN-LHCC-2013-017 ; ATLAS-TDR-022
6. M. V. Bulavin et al., Irradiation Facility at the IBR-2 Reactor for Investigating Material Radiation Hardness, in *Physics of Particles and Nuclei Letters*, 2015, Vol. 12, No. 2, pp. 344–348. © Pleiades Publishing, Ltd., 2015.
7. A. Snesarev (private communication)
8. D. Axen et al., Diamond detector irradiation tests at TRIUMF, JINST 6 (2011) no. 05, P05011.
9. Ming Qi (private communication)

Proceedings of the LHCP2015 Conference, St. Petersburg, Russia, August 31 - September 5, 2015

Editors: V.T. Kim and D.E. Sosnov

Search for Direct Pair Production of Top Squark in the Final State of Two Tau Leptons at ATLAS

AHMED HASIB

Homer L. Dodge Department of Physics and Astronomy, University of Oklahoma, Norman, Oklahoma, USA

On behalf of the ATLAS Collaboration

Abstract. The first hadron collider search for direct pair production of the supersymmetric partner of the top quark, decaying via a scalar tau to a nearly massless gravitino is performed using data from proton–proton collisions at the Large Hadron Collider. The collision data collected by the ATLAS detector corresponding to an integrated luminosity of 20 fb^{-1} at the center-of-mass energy of 8 TeV are used for these results. Top squark candidates are searched for in events with either two hadronically decaying tau leptons, one hadronically decaying tau and one light lepton, or two light leptons. No significant excess over the Standard Model expectation is observed. Exclusion limits at 95% confidence level are set as a function of the top squark and scalar tau masses. Depending on the scalar tau mass, ranging from the 87 GeV LEP limit to the top squark mass, lower limits between 490 GeV and 650 GeV are placed on the top squark mass within the model considered.

1 INTRODUCTION

Supersymmetry (SUSY), a possible extension of the SM, can naturally resolve the hierarchy problem of the Standard Model (SM) by introducing a supersymmetric partner of the top quark [1]. The supersymmetric top quark partner with a mass close to the electroweak symmetry breaking energy, would stabilize the Higgs boson mass against the quadratically divergent quantum corrections and can be discovered at the Large Hadron Collider (LHC) [2]. In a minimal supersymmetric extension of the SM, the scalar partners of the left-handed and right-handed quarks and leptons mix, to form two top squark and two slepton mass eigenstates, respectively. The lighter of the two squark and stau particles is referred to as scalar top ($\tilde{t}_1$) and scalar tau ($\tilde{\tau}_1$), respectively. The decay processes of the SUSY particles are largely dependent on the SUSY symmetry breaking scenario under consideration. In the case of gauge mediated supersymmetry breaking, the lightest supersymmetric particle is a gravitino ($\tilde{G}$). In such a scenario, a complex three-body decay of $\tilde{t}_1$ to $b\nu_\tau\tilde{\tau}_1$ can be dominant, where ν_τ is the tau neutrino, followed by the scalar tau decay into tau lepton and a gravitino.

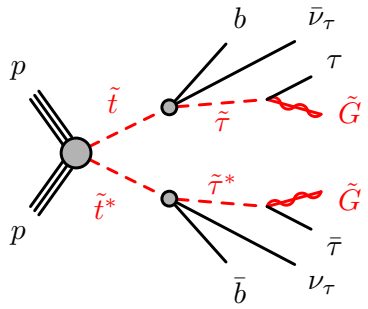

FIGURE 1. Diagram showing the decay topology of the signal process. Taken from Reference [3].

This paper presents a dedicated search for pair production of scalar tops in a final state with two tau leptons, two

jets initiated from b-quarks (b-jets), and two very light gravitationally interacting particles. The decay topology of the signal process is shown in Figure 1. The model considered is a simplified model in which all the supersymmetric particles other than the scalar top and the ones entering its decay chain are decoupled. In order to maximize the sensitivity, two distinct analyses are performed based on the decay mode of the tau leptons in the final state: one analysis requires two hadronically decaying tau leptons (the hadron–hadron channel) and the other requires one hadronically decaying tau lepton and one tau decaying into an electron or muon, plus neutrinos (the lepton–hadron channel). In addition, the results of the search reported in Reference [4], sensitive to events where both tau leptons decay leptonically (lepton–lepton channel), are reinterpreted and limits are set on the scalar top and scalar tau masses.

2 THE ATLAS DETECTOR

The ATLAS detector [5] is the largest particle detector at the LHC measuring 45m in length and 25m in diameter. It is a multipurpose detector with forward-backward cylindrical symmetry and divided into four main subsystems. The inner detector (ID) covers the pseudorapidity [1] range, $|\eta| < 2.5$ and consists of a silicon pixel detector, a semiconductor microstrip detector, and a transition radiation tracker. The ID is surrounded by a 2T solenoidal superconducting magnet which allows for precision tracking of charged particles and vertex reconstruction. The electromagnetic sampling calorimeter uses liquid-argon as the sampling material covering $|\eta| < 3.2$. A scintillator-tile calorimeter provides energy measurements for the hadrons within $|\eta| < 1.7$. The muon spectrometer is the outermost subsystem, consisting of three air-core superconducting toroidal magnets, each with eight superconducting coils, tracking chambers (covering $|\eta| < 2.7$) and trigger chambers (covering $|\eta| < 2.4$).

3 SIGNAL SELECTION AND BACKGROUND ESTIMATION

The data sample used in this paper was recorded in 2012, with the LHC operating at the center of mass energy $\sqrt{s} = 8$ TeV. The data are collected based on the decisions of a three-level trigger system [6]. Events are selected for the electron–hadron (muon–hadron) channel if they are accepted by a single-electron (single-muon) trigger. For the hadron–hadron channel, a missing transverse momentum ($\mathbf{p}_{\mathrm{T}}^{\mathrm{miss}}$) trigger is used. After beam, detector and data-quality requirements, the integrated luminosity of the data samples in the hadron–hadron and lepton–hadron channels are 20.1 fb^{-1}and 20.3 fb^{-1}, respectively. A number of simulated event samples are also used to model the signal and describe the background processes.

The analysis is based on cut and count method to estimate the signal and background contributions and relies on the following discriminating variables to differentiate the signal from the SM backgrounds:

- The transverse mass associated with two final-state objects a and b, defined as,

$$m_{\mathrm{T}}(\mathrm{a},\mathrm{b}) = \sqrt{m_{\mathrm{a}}^2 + m_{\mathrm{b}}^2 + 2\left(E_{\mathrm{T}}^{\mathrm{a}} E_{\mathrm{T}}^{\mathrm{b}} - \mathbf{p}_{\mathrm{T}}^{\mathrm{a}} \cdot \mathbf{p}_{\mathrm{T}}^{\mathrm{b}}\right)}, \tag{1}$$

  where m, E_T and $\mathbf{p}_T$ are the object mass, transverse energy and transverse momentum vector, respectively.
- The *stransverse mass* (m_{T2}) [7, 8] computed as,

$$m_{\mathrm{T2}}(\mathrm{a},\mathrm{b}) = \sqrt{\min_{\mathbf{q}_{\mathrm{T}}^{\mathrm{a}}+\mathbf{q}_{\mathrm{T}}^{\mathrm{b}}=\mathbf{p}_{\mathrm{T}}^{\mathrm{miss}}} \left(\max\left[m_{\mathrm{T}}^2\left(\mathbf{p}_{\mathrm{T}}^{\mathrm{a}}, \mathbf{q}_{\mathrm{T}}^{\mathrm{a}}\right), m_{\mathrm{T}}^2\left(\mathbf{p}_{\mathrm{T}}^{\mathrm{b}}, \mathbf{q}_{\mathrm{T}}^{\mathrm{b}}\right)\right]\right)}, \tag{2}$$

  where $\mathbf{q}_{\mathrm{T}}^{\mathrm{a}}$ and $\mathbf{q}_{\mathrm{T}}^{\mathrm{b}}$ are vectors satisfying $\mathbf{q}_{\mathrm{T}}^{\mathrm{a}} + \mathbf{q}_{\mathrm{T}}^{\mathrm{b}} = \mathbf{p}_{\mathrm{T}}^{\mathrm{miss}}$, and the minimum is taken over all possible choices of $\mathbf{q}_{\mathrm{T}}^{\mathrm{a}}$ and $\mathbf{q}_{\mathrm{T}}^{\mathrm{b}}$.

The selection criteria on these variables are different for the hadron–hadron and the lepton–hadron channels.

[1] ATLAS uses a right-handed coordinate system with its origin at the nominal interaction point (IP) in the centre of the detector and the z-axis along the beam pipe. The x-axis points from the IP to the centre of the LHC ring, and the y-axis points upward. Cylindrical coordinates (r, ϕ) are used in the transverse plane, ϕ being the azimuthal angle around the z-axis. The pseudorapidity is defined in terms of the polar angle θ as $\eta = -\ln\tan(\theta/2)$.

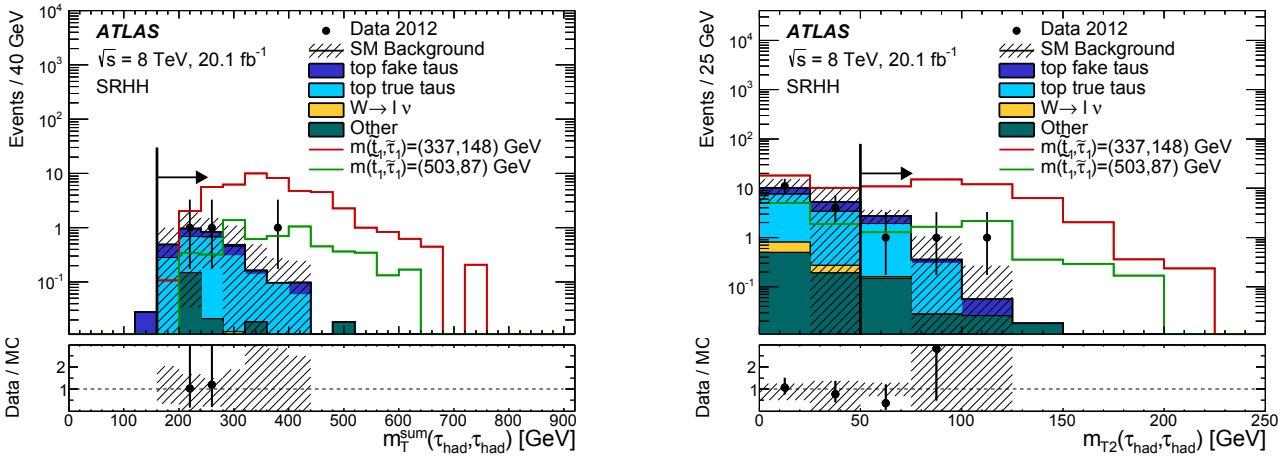

FIGURE 2. Left: distribution of $m_{\mathrm{T}}^{\mathrm{sum}}(\tau_{\mathrm{had}}, \tau_{\mathrm{had}})$ for the events passing all the hadron–hadron signal region requirements, except that on $m_{\mathrm{T}}^{\mathrm{sum}}(\tau_{\mathrm{had}}, \tau_{\mathrm{had}})$. Right: distribution of $m_{\mathrm{T2}}(\tau_{\mathrm{had}}, \tau_{\mathrm{had}})$ for the events passing all the hadron–hadron signal region requirements, except that on $m_{\mathrm{T2}}(\tau_{\mathrm{had}}, \tau_{\mathrm{had}})$. The contributions from all SM backgrounds are shown as a histogram stack; the bands represent the total uncertainty. The background yields have been rescaled by the post-fit normalisation factors. The arrows mark the cut values used to define the SRs. The distributions expected for two signal models are also shown. Taken from Reference [3].

3.1 Hadron–hadron channel

The events in the hadron–hadron channel are required to have exactly two opposite-charged hadronically decaying tau leptons (τ_{had}), no electrons or muons, and at least two jets, and at least one of which is initiated by a b-quark. In addition, the following discriminating variables are used to define the signal region:

- m_{T2} $(\tau_{\mathrm{had}}, \tau_{\mathrm{had}})$ of the hadronically decaying taus and the missing transverse momentum as defined in Equation 2. This variable is bounded from above by the W boson mass and differentiates the dominant $t\bar{t}$ background, where the taus originate from W bosons, from the signal processes.
- $m_{\mathrm{T}}^{\mathrm{sum}}$ $(\tau_{\mathrm{had}}, \tau_{\mathrm{had}})$, the sum of the transverse mass of each τ_{had} candidate and missing transverse momentum as defined in Equation 1.

Figure 2 shows distributions of these two variables and the requirement applied to construct the signal region (SR) of the hadron–hadron channel along with the expected backgrounds. The signal efficiency, defined as the total number of signal events that pass the full selection over the total number of generated events, is weakly dependent on the scalar tau mass and increases from 0.02% to 0.7% as the scalar top mass increases from 150 GeV to 700 GeV, for a scalar tau mass of 87 GeV.

The background contributions in this SR can be grouped into three categories. In the first category of backgrounds, both the final state hadronically decaying tau leptons are real. It consists of mainly $t\bar{t}$ events, with smaller contributions from single-top quark, Z+jets, diboson (WW, WZ, ZZ) and $t\bar{t}$ + $V(=W, Z)$ production. These type of backgrounds are estimated directly in the simulation. Events where an electron or a jet is misidentified as a τ_{had} (*fake*-τ_{had}) is the second category of backgrounds. Backgrounds of this type are composed of $t\bar{t}$, single-top and W+jets events. The single-fake τ_{had} backgrounds are estimated in dedicated regions of phase space, called control region (CR), where the signal events do not contribute. A simultaneous likelihood fit is performed to determine the normalization factors of these backgrounds constrained to the number of data events in each CR, with the systematic uncertainties discussed in Section 4 as nuisance parameters. The last category of backgrounds with contributions smaller than 4.5%, are composed of two-fake τ_{had} and they are estimated using simulation without normalizing to data in a CR.

3.2 Lepton–hadron channel

The lepton–hadron search channel targets both low-mass and high-mass scalar top quarks. This selection requires exactly one hadronically decaying tau, exactly one electron or muon, where the hadronically decaying tau and the

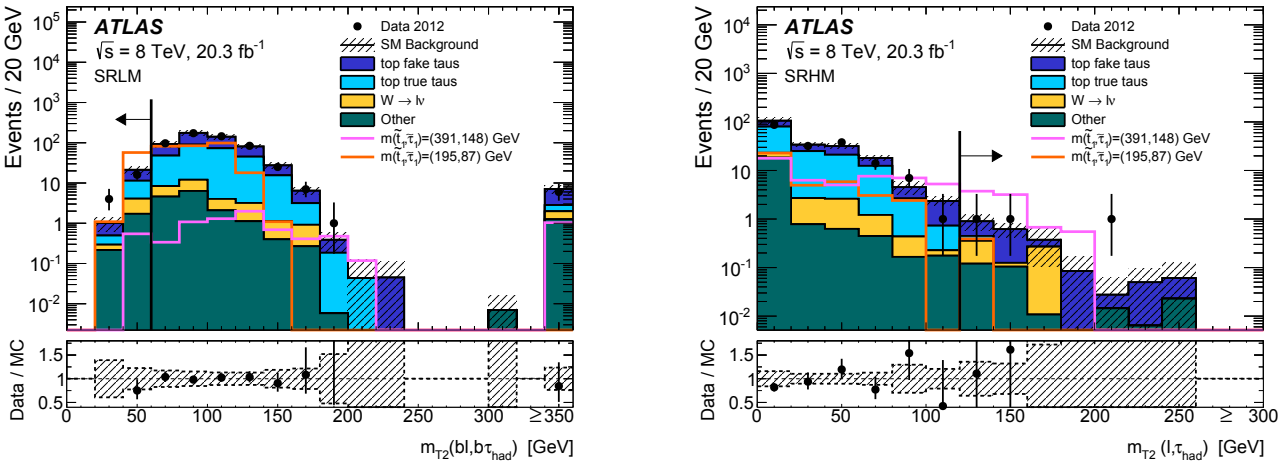

FIGURE 3. Left: distribution of $m_{\mathrm{T2}}(b\ell, b\tau_{\mathrm{had}})$ for events passing all the lepton–hadron LM signal region requirements, except that on $m_{\mathrm{T2}}(b\ell, b\tau_{\mathrm{had}})$. Right: distribution of $m_{\mathrm{T2}}(\ell, \tau_{\mathrm{had}})$ for events passing all the lepton–hadron HM signal region requirements, except that on $m_{\mathrm{T2}}(\ell, \tau_{\mathrm{had}})$. The contributions from all SM backgrounds are shown as a histogram stack; the bands represent the total uncertainty. The background yields have been rescaled by the post-fit normalisation factors. The arrows mark the cut values used to define the SRs. The overflow bin in the $m_{\mathrm{T2}}(b\ell, b\tau_{\mathrm{had}})$ plot is filled with the events that have for both pairings of $m(b\ell)$ and $m(b\tau_{\mathrm{had}})$ at least one invariant mass larger than m_t. The distributions expected for two signal models are also shown. Taken from Reference [3].

lepton have opposite electric charge. Each event is also required to contain at least two jets, where at least one (high-mass) or two (low-mass) of the jets are originated from a b-quark. In addition, the following discriminating variables are used:

- $m_{\mathrm{T2}}(\ell, \tau_{\mathrm{had}})$, calculated using the momenta of the light lepton and the τ_{had}. This variable is bounded from above by the W boson mass. The $t\bar{t}$ and Wt processes where the light lepton, τ_{had} and missing transverse momentum originate from a W boson can be distinguished with this variable. The high-mass selection requires this variable to be large, because its distribution for signal models with heavy scalar taus and scalar top, peaks at higher values than for the top-quark-dominated SM background.
- $m_{\mathrm{T2}}(b\ell, b\tau_{\mathrm{had}})$, calculated using two jets originated from a b-quark. For $t\bar{t}$ events where the jet and the lepton belong to the decay of the same top quark, this variable is bounded from above by the top-quark mass. Whereas, for the signal events, the upper bound on this variable is the scalar top mass. A maximum cut value is therefore used for the low-mass selection.

The distributions for these variables for the low mass and the high mass points are shown in Figure 3 along with the expected background contributions. The signal selection efficiency of the low mass selection is between 0.008% and 0.01% for the models with scalar top mass between 150 GeVand 200 GeV, while for high mass selection it varies between 0.0007% and 1% for a scalar top mass between 200 GeVand 700 GeV.

The background contribution in the lepton–hadron signal region can be grouped into two categories. The first type of background is dominated by W+jets processes where the light lepton is always a real lepton from W decay, while the τ_{had} is faked by a recoiling hadronic object. The second category is contributed by $t\bar{t}$ and Wt processes where the light lepton is originated from the W boson and the τ_{had} can be either real or fake. Dedicated CRs are used to estimate these backgrounds. A simultaneous likelihood fit is performed to obtain the normalization factors for each background, using the observed number of data events as a constraint, along with the systematic uncertainties as nuisance parameters.

4 SYSTEMATIC UNCERTAINTIES

Various sources of systematic uncertainties originated from detector simulation and modeling of the major SM backgrounds, affecting the predicted background yields in the SRs, are taken into account. The uncertainties are either

computed directly in the SR where are the backgrounds are estimated from simulation, or propagated through the fit for backgrounds that are normalized in CRs. The impact of systematic uncertainties on the total background estimated in the different SRs is shown in Table 1, quoting the relative background uncertainty attributed to each source.

TABLE 1. Summary of background estimates and the associated total uncertainties.The size of each systematic uncertainty is quoted as a relative uncertainty on the total background. A dash indicates a negligible contribution to the uncertainty. The individual uncertainties can be correlated, and thus do not necessarily sum in quadrature to the total relative uncertainty. The observed number of events in each signal region is also shown. Taken from Reference [3].

	hadron–hadron	lepton–hadron (low-mass)	lepton–hadron (high-mass)
Observed events	3	20	3
Background events	3.1 ± 1.2	22.1 ± 4.7	2.1 ± 1.5
Uncertainty Breakdown [%]:			
Jet energy scale and resolution	17	13	2
Tau energy scale	9	4	3
Cluster energy scale and resolution	1	2	4
b-tagging	2	4	2
Top-quark theory uncertainty	37	11	64
W+jets theory and normalisation	-	1	19
Simulation statistics	20	6	21
Top normalisation	18	6	20

5 RESULTS AND INTERPRETATION

Good agreement is seen between the observed yields and the background estimates. Upper limits at 95% confidence level (CL) on the number of beyond-the-SM (BSM) events for each signal region are derived with the CL_s likelihood ratio prescription as described in Reference [9]. The limits are calculated for each signal region separately, with the observed number of events, the expected background and the background uncertainty as input to the calculation. Dividing the limits on the number of BSM events by the integrated luminosity of the data sample, these can be interpreted as upper limits on the visible BSM cross section, $\sigma_{\text{vis}} = \sigma \times \mathcal{A} \times \epsilon$, where σ is the production cross section for the BSM signal, $\mathcal{A}$ is the acceptance defined as the fraction of events passing the geometric and kinematic selections at particle level, and ϵ is the detector reconstruction, identification and trigger efficiency. These quantities are summarized in Table 2.

TABLE 2. Left to right: Total constrained background yields, number of observed events, 95% CL observed (expected) upper limits on the number of BSM events, $S^{95}_{\text{obs.(exp.)}}$, and the visible cross section, $\langle \mathcal{A}\epsilon\sigma \rangle^{95}_{\text{obs.(exp.)}}$. Taken from Reference [3].

Signal Region	Background	Observation	$S^{95}_{\text{obs.(exp.)}}$	$\langle \mathcal{A}\epsilon\sigma \rangle^{95}_{\text{obs.(exp.)}}$ [fb]
hadron–hadron	3.1 ± 1.2	3	$5.5\left(5.5^{+2.1}_{-1.3}\right)$	$0.27\left(0.27^{+0.11}_{-0.06}\right)$
lepton–hadron (low-mass)	22.1 ± 4.7	20	$12.4\left(13.2^{+4.9}_{-3.5}\right)$	$0.61\left(0.65^{+0.24}_{-0.17}\right)$
lepton–hadron (high-mass)	2.1 ± 1.5	3	$6.4\left(5.2^{+2.6}_{-0.9}\right)$	$0.31\left(0.26^{+0.13}_{-0.04}\right)$

Exclusion limits are derived for the scalar top pair production, assuming $\tilde{t}_1$ decays with 100% branching ratio into $b\nu_\tau\tilde{\tau}_1$. The likelihood fit is performed with the expected signal and overall signal-strength parameter constraint to be positive. The control and signal region are fitted simultaneously, taking into account the experimental and theoretical systematic uncertainties as nuisance parameters. For each mass hypothesis, the expected limits are calculated for the hadron–hadron selection, the two lepton–hadron selections, and the statistical combination of the lepton–lepton selections described in Reference [4]. The selection giving the best expected sensitivity is used to compute the expected and observed CL_s value. The resulting exclusion contour is shown in Figure 4 demonstrating scalar top mass below

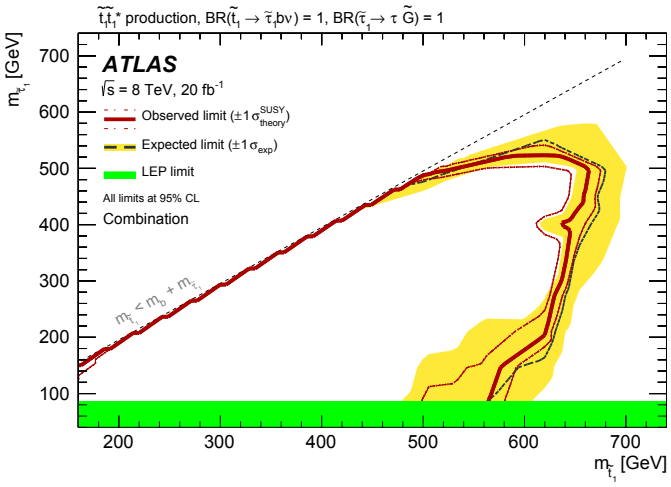

FIGURE 4. Observed and expected exclusion contours at 95% CL in the $(\tilde{t}_1, \tilde{\tau}_1)$ mass plane from the combination of all selections. The dashed and solid lines show the 95% CL expected and observed limits, respectively, including all uncertainties except for the theoretical signal cross-section uncertainty (PDF and scale). The band around the expected limit shows the $\pm 1\sigma$ expectation. The dotted $\pm 1\sigma$ lines around the observed limit represent the results obtained when varying the nominal signal cross section up or down by the theoretical uncertainty. The LEP limit on the mass of the scalar tau is also shown. Taken from Reference [3].

490 GeV to be excluded. Depending on the scalar tau mass, some models with scalar top masses up to 650 GeV are also excluded.

6 SUMMARY

A search for the direct pair production of supersymmetric partners of the top quark decaying via a scalar tau to lightest supersymmetric particle – nearly massless gravitino is performed. The data used in this analysis is collected in proton–proton collisions at center-of-mass energy, $\sqrt{s} = 8$ TeV, by the ATLAS detector during the 2012 operation of the LHC and corresponds to an integrated luminosity of 20 fb^{-1}. The scalar top candidates are searched for in events with either two hadronically decaying tau leptons, one hadronically decaying tau and one light lepton, or two light leptons. This is the first result from a hadron collider search for the three-body decay mode to scalar tau. Good agreement is observed between Standard Model background and the data, and lower limits on the scalar top mass are set at 95% confidence level. The lower limit on the scalar top mass is found to be between 490 GeV and 650 GeV for the scalar tau masses ranging from the LEP limit to scalar top mass.

7 ACKNOWLEDGMENTS

I would like to thank the ATLAS Collaboration for the opportunity to give this presentation. I would also like to thank Dr. Phillip Gutierrez, University of Oklahoma and acknowledge the support of the Department of Energy (USA).

REFERENCES

[1] R. Barbieri and G. F. Giudice, Nucl. Phys. **B306**, p. 63 (1988).
[2] L. Evans and P. Bryant, JINST **3**, p. S08001 (2008).
[3] ATLAS Collaboration, (2015), arXiv:1509.04976 [hep-ex] .
[4] ATLAS Collaboration, JHEP **06**, p. 124 (2014), arXiv:1403.4853 [hep-ex] .
[5] ATLAS Collaboration, Journal of Instrumentation **3**, p. S08003 (2008).
[6] ATLAS Collaboration, Eur. Phys. J. **C72**, p. 1849 (2012), arXiv:1110.1530 [hep-ex] .
[7] C. G. Lester and D. J. Summers, Phys. Lett. **B463**, 99–103 (1999), arXiv:hep-ph/9906349 [hep-ph] .
[8] A. Barr, C. Lester, and P. Stephens, J. Phys. **G29**, 2343–2363 (2003), arXiv:hep-ph/0304226 [hep-ph] .
[9] A. L. Read, Journal of Physics G: Nuclear and Particle Physics **28**, p. 2693 (2002).

Proceedings of the LHCP2015 Conference, St. Petersburg, Russia, August 31 - September 5, 2015

Editors: V.T. Kim and D.E. Sosnov

Search for Heavy Charged Vector Bosons Decaying to a Charged Lepton and a Neutrino with the ATLAS Experiment

VICTOR SOLOVYEV

National Research Centre "Kurchatov Institute" B.P.Konstantinov Petersburg Nuclear Physics Institute, St. Petersburg, Russia.

victor.solovyev@cern.ch

On behalf of the ATLAS Collaboration

Abstract. These proceedings present a search for high-mass states, such as heavy charged vector bosons (W' and W^*), decaying to a charged lepton (electron or muon) and a neutrino. Results are based on 20.3 fb^{-1} of proton-proton collision data at $\sqrt{s}$ = 8 TeV recorded by the ATLAS experiment at the Large Hadron Collider. No significant excess beyond Standard Model expectations is observed. A W' with Sequential Standard Model couplings is excluded at the 95% confidence level for masses up to 3.24 TeV. A W^* with equivalent coupling strengths is excluded for masses up to 3.21 TeV.

INTRODUCTION

High-energy collisions at CERN's Large Hadron Collider (LHC) provide new opportunities to search for physics beyond the Standard Model (SM) of strong and electroweak interactions. One extension common to many models is the existence of additional heavy gauge bosons, the charged ones commonly denoted W'. Such particles are most easily searched for in their decay to a charged lepton (electron or muon) and a neutrino.

These proceedings describe such a search performed using 8 TeV pp collision data collected with the ATLAS detector [1] during 2012, corresponding to a total integrated luminosity of 20.3 fb^{-1} [2]. The search is performed in the context of the Sequential Standard Model (SSM), i.e. the extended gauge model of ref. [3]. The W' has the same couplings to fermions as the SM W boson and a width that increases linearly with the W' mass. The coupling of the W' to WZ is set to zero.

A search is also performed for the charged partners, denoted W^*, of the chiral boson excitations described in ref. [4] with theoretical motivation in ref. [5]. The anomalous (magnetic-moment type) coupling of the W^* leads to kinematic distributions significantly different from those of the W'.

This analysis is also sensitive to the direct production of weakly interacting candidate dark matter particles. This new-physics scenario is discussed in ref. [2] but not considered here since it goes beyond the subject of these proceedings.

SEARCH STRATEGY

Candidate events in this search contain one high-transverse-momentum lepton (electron or muon) and substantial missing transverse momentum due to undetected neutrino. The kinematic variable used to identify the signal is the transverse mass

$$m_{\mathrm{T}} = \sqrt{2p_{\mathrm{T}}E_{\mathrm{T}}^{\mathrm{miss}}(1-\cos\varphi_{\ell\nu})}, \tag{1}$$

where p_{T} is the lepton transverse momentum, $E_{\mathrm{T}}^{\mathrm{miss}}$ is the magnitude of the missing transverse momentum vector and $\varphi_{\ell\nu}$ is the angle between the p_{T} and $E_{\mathrm{T}}^{\mathrm{miss}}$ vectors. Throughout these proceedings, transverse refers to the plane

perpendicular to the colliding beams, longitudinal means parallel to the beams, θ and φ are the polar and azimuthal angles with respect to the longitudinal direction, and pseudorapidity is defined as $\eta = -\ln(\tan(\theta/2))$.

The m_{T} distribution in data is examined for a significant excess above the SM expectations. If no excess is found then limits are set on the cross-section times branching fraction (σB) separately in the electron and muon channels. These limits are then combined assuming a common branching fraction for the two final states.

SIGNALS AND BACKGROUNDS

Signal processes considered in this search are W' and W^* bosons decaying to a charged lepton (electron or muon) and a neutrino, i.e. $W' \to \ell\nu$ and $W^* \to \ell\nu$ where $\ell = e$ or μ.

The main background to the W' and W^* signals comes from the tail of the m_{T} distribution from SM W boson production with decays to the same final state. Other relevant backgrounds are Z boson production with decays into two leptons where one lepton is not reconstructed, W or Z production with decays to τ leptons where a τ subsequently decays to either an electron or a muon, and diboson production. There is also a contribution to the background from $t\bar{t}$ and single-top production, collectively referred to as the top background, which is most important for the lowest W'/W^* masses considered in this search, where it constitutes about 10% of the background after event selection in the electron channel and 15% in the muon channel. Other relevant strong-interaction background sources occur when a light or heavy hadron decays semileptonically or when a jet is misidentified as an electron or muon. These are referred to as the multi-jet background in these proceedings.

With the exception of the multi-jet background, which is estimated from data, expected signals and backgrounds are evaluated using simulated Monte Carlo samples and normalized using the calculated cross-sections and the integrated luminosity of the data.

EVENT SELECTION

The analysis makes use of all of the $\sqrt{s} = 8$ TeV data collected in 2012 for which the relevant detector systems were operating properly and all data quality requirements were satisfied. Candidate events are selected using single-electron and single-muon triggers in the electron and muon channels respectively.

Events are required to have exactly one electron with $p_{\mathrm{T}} > 124$ GeV or one muon with $p_{\mathrm{T}} > 45$ GeV. The difference in these requirements originates from the difference in thresholds used in the electron and muon triggers. Electrons are required to have $|\eta| < 1.37$ or $1.52 < |\eta| < 2.47$, while muons are restricted to the ranges $|\eta| < 1.0$ and $1.3 < |\eta| < 2.0$. Events having additional electrons (muons) with $p_{\mathrm{T}} > 20$ GeV are discarded in the electron (muon) channel.

To suppress the multi-jet background, the lepton is required to be isolated. In the electron channel, the isolation energy is measured with the calorimeter in a cone $\Delta R = \sqrt{(\Delta\eta)^2 + (\Delta\varphi)^2} = 0.2$ around the electron track, and the requirement is $\Sigma E_{\mathrm{T}}^{\mathrm{calo}} < 0.007 \times p_{\mathrm{T}} + 5$ GeV, where the sum includes all calorimeter energy clusters in the cone excluding those that are attributed to the electron. The scaling of the isolation requirement with the electron p_{T} reduces the efficiency loss due to radiation from the electron at high p_{T}. In the muon channel, the isolation energy is measured using inner detector tracks with $p_{\mathrm{T}}^{\mathrm{trk}} > 1$ GeV in a cone $\Delta R = 0.3$ around the muon track. The isolation requirement is $\sum p_{\mathrm{T}}^{\mathrm{trk}} < 0.05 \times p_{\mathrm{T}}$, where the muon track is excluded from the sum. As in the electron channel, the scaling of the isolation requirement with the muon p_{T} reduces the efficiency loss due to radiation from the muon at high p_{T}.

An $E_{\mathrm{T}}^{\mathrm{miss}}$ requirement is imposed to select signal events and to further suppress the contributions from the multi-jet and SM W backgrounds. In both channels, the requirement placed on the charged lepton p_{T} is also applied to the $E_{\mathrm{T}}^{\mathrm{miss}}$: $E_{\mathrm{T}}^{\mathrm{miss}} > 125$ GeV for the electron channel and $E_{\mathrm{T}}^{\mathrm{miss}} > 45$ GeV for the muon channel.

The same event selection is applied to both the data and simulated samples. Figure 1 shows the m_{T} spectra for each channel after event selection for the data, the expected background and three examples of W' signals at different masses. Table 1 shows an example of how different sources contribute to the background for $m_{\mathrm{T}} > 1500$ GeV, the region used to search for a W' with a mass of 2000 GeV. No significant excess above SM expectations is observed in the data.

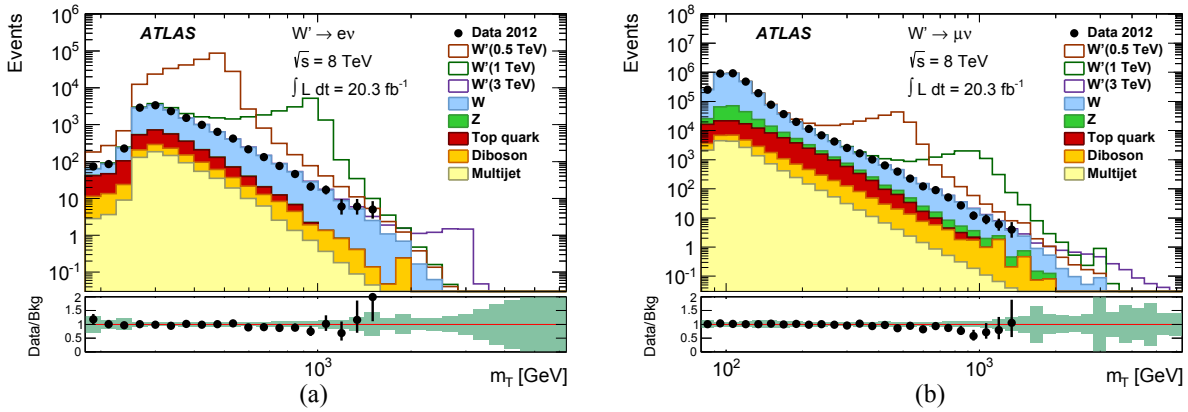

FIGURE 1. Spectra of m_{T} for the electron (a) and muon (b) channels after the event selection. The points represent data and the filled, stacked histograms show the predicted backgrounds. Open histograms are $W' \to \ell\nu$ signals added to the background with their masses in GeV indicated in parentheses in the legend. The error bars on the data points are statistical. The ratio of the data to the total background prediction is shown below each of the distributions. The bands include systematic uncertainties on the background including the ones arising from the statistical uncertainty of the simulated samples [2].

TABLE 1. Expected numbers of events from the various background sources in each decay channel for $m_{\mathrm{T}} > 1500$ GeV, the region used to search for a W' with a mass of 2000 GeV. The $W \to \ell\nu$ and $Z \to \ell\ell$ rows include the expected contributions from the τ-lepton. The listed uncertainties are statistical only [2].

	$e\nu$		$\mu\nu$	
$W \to \ell\nu$	2.65	± 0.10	2.28	± 0.21
$Z \to \ell\ell$	0.00163	± 0.00022	0.232	± 0.005
Diboson	0.27	± 0.23	0.46	± 0.23
Top	0.0056	± 0.0009	0.0017	± 0.0001
Multi-jet	0.066	± 0.020	0.046	± 0.039
Total	2.99	± 0.25	3.01	± 0.31

STATISTICAL ANALYSIS AND SYSTEMATIC UNCERTAINTIES

In the absence of a signal, a Bayesian analysis is performed to set limits on the studied processes. For each candidate mass and decay channel, events above an m_{Tmin} threshold are counted. The optimization of m_{Tmin} is done separately for $W' \to \ell\nu$ and $W^* \to \ell\nu$. For each candidate mass, the m_{Tmin} values that minimize the expected cross-section limits are obtained in the electron and muon channels separately, but for simplicity the lower value is used in both channels since this has a negligible impact on the final results. The expected number of events in each channel is

$$N_{\mathrm{exp}} = \varepsilon_{\mathrm{sig}} L_{\mathrm{int}} \sigma B + N_{\mathrm{bg}}, \tag{2}$$

where L_{int} is the integrated luminosity of the data sample, $\varepsilon_{\mathrm{sig}}$ is the signal selection efficiency defined as the fraction of signal events that satisfy the event selection criteria as well as $m_{\mathrm{T}} > m_{\mathrm{Tmin}}$, N_{bg} is the expected number of background events, and σB is the cross-section times branching fraction. Using Poisson statistics, the likelihood to observe N_{obs} events is

$$\mathcal{L}(N_{\mathrm{obs}}|\sigma B) = \frac{(L_{\mathrm{int}}\varepsilon_{\mathrm{sig}}\sigma B + N_{\mathrm{bg}})^{N_{\mathrm{obs}}} \mathrm{e}^{-(L_{\mathrm{int}}\varepsilon_{\mathrm{sig}}\sigma B + N_{\mathrm{bg}})}}{N_{\mathrm{obs}}!}. \tag{3}$$

Uncertainties are included by introducing nuisance parameters θ_i, each with a probability density function $g_i(\theta_i)$, and integrating the product of the Poisson likelihood with the probability density function. The integrated likelihood is

$$\mathcal{L}_B(N_{\mathrm{obs}}|\sigma B) = \int \mathcal{L}(N_{\mathrm{obs}}|\sigma B) \prod g_i(\theta_i) d\theta_i, \tag{4}$$

where a log-normal distribution is used for the $g_i(\theta_i)$. The nuisance parameters are taken to be: $L_{\rm int}$, $\varepsilon_{\rm sig}$ and $N_{\rm bg}$, with the appropriate correlation accounted for between the first and the third parameters.

The measurements in the two decay channels are combined assuming the same branching fraction for each. Equation (4) remains valid with the Poisson likelihood replaced by the product of the Poisson likelihoods for the two channels. Correlations of nuisance parameters between the two channels are taken into account.

Bayes' theorem gives the posterior probability that the signal has signal strength σB:

$$P_{\rm post}(\sigma B|N_{\rm obs}) = N\mathcal{L}_B(N_{\rm obs}|\sigma B)\, P_{\rm prior}(\sigma B) \tag{5}$$

where $P_{\rm prior}(\sigma B)$ is the assumed prior probability, here chosen to be flat in σB, for $\sigma B > 0$. The constant factor N normalizes the total probability to one. The posterior probability is evaluated for each mass and decay channel as well as for their combination, and then used to set a limit on σB.

The inputs for the evaluation of $\mathcal{L}_B$ (and hence $P_{\rm post}$) are $L_{\rm int}$, $\varepsilon_{\rm sig}$, $N_{\rm bg}$, $N_{\rm obs}$ and the uncertainties on the first three. The uncertainties on $\varepsilon_{\rm sig}$ and $N_{\rm bg}$ account for experimental and theoretical systematic effects as well as the statistics of the simulated samples. The experimental systematic uncertainties include those on the efficiencies of the electron or muon trigger, reconstruction and event/object selection. Uncertainties in the lepton energy/momentum and $E_{\rm T}^{\rm miss}$, characterized by scale and resolution uncertainties, are also included. Table 2 summarizes the uncertainties on the event selection efficiencies and the expected number of background events for the $W' \to \ell\nu$ signal with $m_{W'} =$ 2000 GeV using $m_{\rm T} > 1500$ GeV. The uncertainty on $L_{\rm int}$ is 2.8%.

TABLE 2. Relative uncertainties on the selection efficiency $\varepsilon_{\rm sig}$ and expected number of background events $N_{\rm bg}$ for a W' with a mass of 2000 GeV. The efficiency uncertainties include contributions from the trigger, reconstruction and event selection. The last row gives the total relative uncertainties [2].

	$\varepsilon_{\rm sig}$		$N_{\rm bg}$	
Source	$e\nu$	$\mu\nu$	$e\nu$	$\mu\nu$
Reconstruction and trigger efficiency	2.5%	4.1%	2.7%	4.1%
Lepton energy/momentum resolution	0.2%	1.4%	1.9%	18%
Lepton energy/momentum scale	1.2%	1.8%	3.5%	1.5%
$E_{\rm T}^{\rm miss}$ scale and resolution	0.1%	0.1%	1.2%	0.5%
Beam energy	0.5%	0.5%	2.8%	2.1%
Multi-jet background	-	-	2.2%	3.4%
Monte Carlo statistics	0.9%	1.3%	8.5%	10%
Cross-section (shape/level)	2.9%	2.8%	18%	15%
Total	4.2%	5.6%	21%	27%

RESULTS

The number of observed events is generally in good agreement with the expected number of background events for all mass bins. None of the observations for any mass point in either channel or their combination show an excess above background, so there is no evidence for the observation of either $W' \to \ell\nu$ or $W^* \to \ell\nu$. Therefore, 95% confidence level (CL) limits on σB were set in the electron channel, the muon channel and their combination.

Figure 2 presents the 95% CL observed limits on σB for both $W' \to \ell\nu$ and $W^* \to \ell\nu$ for combination of the electron channel and muon channels. The expected limits and the theoretical σB for a W' and for a W^* are also shown.

In Fig. 2 the intersection between the central theoretical prediction and the observed limits provides the 95% CL lower limits on the mass. The expected and observed W' and W^* mass limits for the electron and muon decay channels as well as their combination are listed in Table 3. The mass limits presented here are a significant improvement over those reported in previous ATLAS searches [6, 7, 8].

CONCLUSIONS

A search for new high-mass states decaying to a lepton (electron or muon) plus missing transverse momentum using 20.3 fb^{-1} of proton-proton collision data at $\sqrt{s} = 8$ TeV recorded with the ATLAS experiment at the Large Hadron

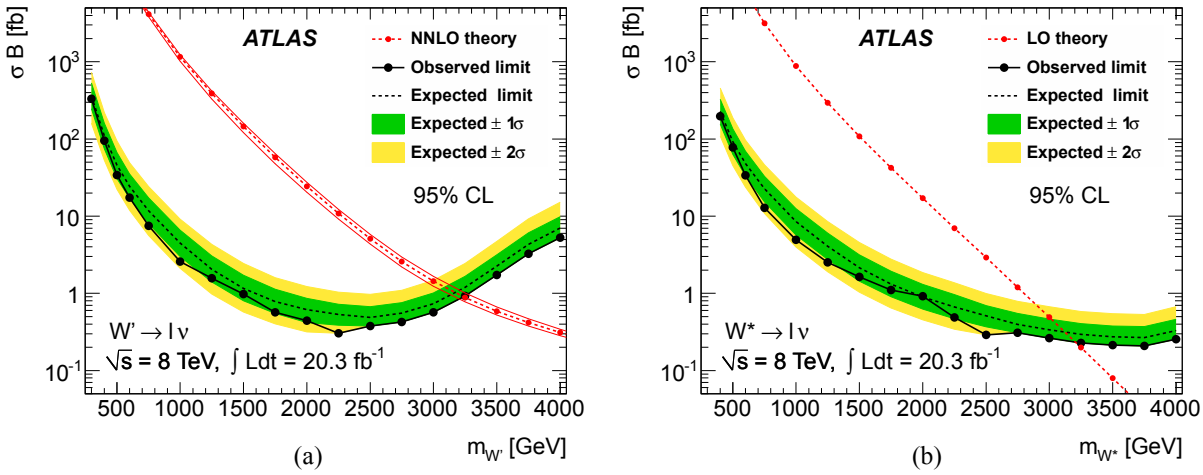

FIGURE 2. Observed and expected limits on σB for W' (a) and W^* (b) at 95% CL in the combination of the electron and muon channels. The predicted values for σB and their uncertainties (except for W^*) are also shown [2].

TABLE 3. Lower limits on the W' and W^* masses. The first column is the decay channel ($e\nu$, $\mu\nu$ or both combined) and the following give the expected (Exp.) and observed (Obs.) mass limits [2].

	$m_{W'}$ [TeV]		m_{W^*} [TeV]	
Decay	**Exp.**	**Obs.**	**Exp.**	**Obs.**
$e\nu$	3.13	3.13	3.08	3.08
$\mu\nu$	2.97	2.97	2.83	2.83
Both	3.17	3.24	3.12	3.21

Collider is presented. No significant excess above SM expectations is observed. Limits on σB are presented. A W' with SSM couplings is excluded for masses below 3.24 TeV at 95% CL. The exclusion for W^* with equivalent couplings is 3.21 TeV.

ACKNOWLEDGMENTS

I thank the organizers of the conference, particularly National Research Centre "Kurchatov Institute" B.P.Konstantinov Petersburg Nuclear Physics Institute, and acknowledge the support of Ministry of Education and Science of the Russian Federation.

REFERENCES

[1] ATLAS Collaboration, JINST **3**, p. S08003 (2008).
[2] ATLAS Collaboration, JHEP **09**, p. 037 (2014), arXiv:1407.7494 [hep-ex] .
[3] G. Altarelli, B. Mele, and M. Ruiz-Altaba, Z. Phys. C **45**, p. 109 (1989).
[4] M. V. Chizhov, V. A. Bednyakov, and J. A. Budagov, Phys. Atom. Nucl. **71**, 2096–2100 (2008), arXiv:0801.4235 [hep-ph] .
[5] M. V. Chizhov and G. Dvali, Phys. Lett. B **703**, 593–598 (2011), arXiv:0908.0924 [hep-ph] .
[6] ATLAS Collaboration, Phys. Lett. B **701**, 50–69 (2011), arXiv:1103.1391 [hep-ex] .
[7] ATLAS Collaboration, Phys. Lett. B **705**, 28–46 (2011), arXiv:1108.1316 [hep-ex] .
[8] ATLAS Collaboration, Eur. Phys. J. C **72**, p. 2241 (2012), arXiv:1209.4446 [hep-ex] .

Proceedings of the LHCP2015 Conference, St. Petersburg, Russia, August 31 - September 5, 2015

Editors: V.T. Kim and D.E. Sosnov

New Physics search in mono-jet final states with the ATLAS experiment at the LHC

GIULIANO GUSTAVINO

Universita e INFN, Roma-1, Piazzale Aldo Moro 5, 00185 Roma, Italy.

giuliano.gustavino@cern.ch

On behalf of the ATLAS Collaboration

Abstract. The search for New Physics in final states with an energetic jet and large missing transverse momentum plays a major role in the physics program of the LHC experiments. This experimental signature is sensitive to different New Physics models including different scenarios of supersymmetry, models that predict the existence of extra dimensions and the production of weakly interacting Dark Matter candidates. Results based on the LHC Run-1 dataset corresponding to 20.3 fb^{-1} and firsts performance plots based on the data collected at the center of mass energy of 13 TeV with the ATLAS experiment at the LHC are presented.

Motivations

The existence of Dark Matter (DM) particles [1] is a well-established hypothesis to explain a range of astrophysical and cosmological measurements. Since none of the known Standard Model (SM) particles provides suitable candidates for this kind of matter, several theories postulate the existence of new particles that are stable (or at least long-lived) and neutral, thus fulfilling two important requirements for being the DM in the universe. One class of particle candidates of interest for searches at the LHC consists of weakly interacting massive particles (WIMPs) [2]. These are expected to couple to Standard Model particles through a generic weak interaction, which could be the known weak interaction of the SM or a new type of interaction.

Since that WIMPs do not interact with the detector material, their production leads to signatures with missing transverse momentum ($p_{\mathrm{T}}^{\mathrm{miss}}$), the magnitude of which is called $E_{\mathrm{T}}^{\mathrm{miss}}$, and one can be tagged by the identification of a high energy jet in the final state. This event topology is particular interesting in a hadronic machine as LHC because can count on a higher expected rate and a higher sensitivity in most of the theoretical interpretations with respect to the other mono-X final states.

Mono-jet final states have been studied also in the context of searches for supersymmetric compressed scenarios, large extra spatial dimensions (LED) and invisible decays of the Higgs boson.

Run-1 Analysis

The final states in the mono-jet analysis [3] in the ATLAS experiment [4] consist of a limited number of jets with the leading one with very high p_{T} plus a large energy imbalance in the plane transverse to the colliding proton beams. The data are selected during the data taking using a trigger logic that selects events with high $E_{\mathrm{T}}^{\mathrm{miss}}$ as computed at the final stage of the three-level trigger system [5]. The event selection used in the analysis is summarized in Table 1.

The strategy adopted is based on the building of nine Signal Regions (SR), defined applying the lepton veto and lower $E_{\mathrm{T}}^{\mathrm{miss}}$ cut from 150 GeV to 700 GeV. Four Control Regions (CR) are defined kinematically close with the SR and requiring the presence of one or two isolated leptons in the final state. They are used in a simultaneous fit to evaluate the normalization factors associated to the dominant electroweak background V + jets (where $V = W/Z$) in the SR. The top and di-boson processes are estimated by MC simulations while the multi-jet background is based on the data.

TABLE 1. Event selection criteria applied for the selection of mono-jet like SRs. Taken from Ref. [3].

Selection criteria
Primary vertex
$E_{\mathrm{T}}^{\mathrm{miss}} > 150, ..., 700$ GeV
Jet quality requirements
At least one jet with $p_{\mathrm{T}} > 30$ GeV and $\|\eta\| < 4.5$
Lepton and isolated track vetoes
The leading jet with $p_{\mathrm{T}} > 120$ GeV and $\|\eta\| < 2.0$
Leading jet $p_{\mathrm{T}}/E_{\mathrm{T}}^{\mathrm{miss}} > 0.5$
$\Delta\phi(\mathrm{jet}, E_{\mathrm{T}}^{\mathrm{miss}}) > 1.0$

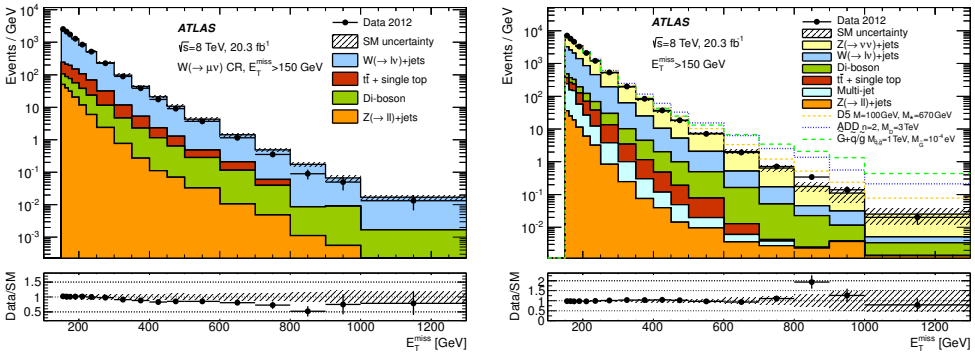

FIGURE 1. Data/MC comparison in the one muon CR (left) and in the SR with $E_{\mathrm{T}}^{\mathrm{miss}} > 150$ GeV (right) after the fit using the entire data sample of 20.3 fb^{-1} at $\sqrt{s} = 8$ TeV. The error bands in the ratios include the statistical and experimental uncertainties on the background expectations. Signal hypotheses in the DM, SUSY and LED scenarios are also plotted. Taken from Ref. [3].

In Figure 1 the SR and one muon CR are shown. This CR has a major role in the analysis because it is used to evaluate the main irreducible background $Z(\nu\nu)$ + jets through the $W(\mu\nu)$ + jets control sample, using the entire data sample at $\sqrt{s} = 8$ TeV corresponding to 20.3 fb^{-1}, thus allowing to reduce the systematical uncertainty on the $Z(\nu\nu)$ + jets background.

In general, a good agreement is observed between the data and the SM expectations (see Table 2). The largest difference between the number of events in data and the SM expectations is observed in the SR with $E_{\mathrm{T}}^{\mathrm{miss}} > 700$ GeV, corresponding to a 1.7σ deviation from the background-only hypothesis. The agreement between the data and the SM expectations for the total number of events in the different signal regions is translated into model-independent 95% confidence level (CL) upper limits on the visible cross section varying between 726 fb and 3.4 fb in several SRs.

TABLE 2. Data and SM background expectation in several SRs. For the SM expectations both the statistical and systematic uncertainties are included. Taken from Ref. [3].

SR (lower $E_{\mathrm{T}}^{\mathrm{miss}}$cut)	150 GeV	300 GeV	500 GeV	700 GeV
Observed events	364378	18020	1028	126
SM expectation	372100 ± 9900	18000 ± 500	1030 ± 60	97 ± 14
$Z \to \nu\nu$	217800 ± 3900	12800 ± 410	740 ± 60	71 ± 13
$W \to \tau\nu$	79300 ± 3300	2800 ± 200	130 ± 20	11 ± 3
$W \to e\nu$	23500 ± 1700	880 ± 80	43 ± 7	3 ± 1
$W \to \mu\nu$	28300 ± 1600	850 ± 80	35 ± 6	2 ± 1
$Z \to \mu\mu$	530 ± 220	7 ± 3	2 ± 1	1 ± 1
$Z \to \tau\tau$	780 ± 320	14 ± 6	0 ± 0	0 ± 0
$t\bar{t}$, single top	6900 ± 1400	200 ± 70	7 ± 7	0 ± 0
di-bosons	8000 ± 1700	690 ± 200	65 ± 35	8 ± 7
multi-jets	6500 ± 6500	44 ± 44	1 ± 1	0 ± 0

Interpretations

As just mentioned before, the mono-jet analysis is sensitive to a wide spectrum of theoretical interpretations so it is possible to intepret the model independent limits in the several scenarios to allow a comparison of the results with the other analyses and experiments.

Dark Matter scenarios

The interaction of WIMPs with Standard Model particles can be investigated in two different approaches: in the Effective Field Theory (EFT) and in the so called Simplified Models.

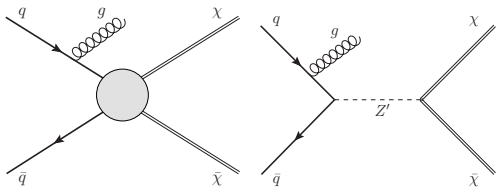

FIGURE 2. Feynman diagrams for the production of WIMP pairs $\chi\bar{\chi}$ associated with a jet from initial-state radiation of a gluon: a contact interaction described with effective operators (on the left) and a simplified model with a Z' boson (on the right). Taken from Ref. [3].

In the EFT context the processes are studied in a contact interaction scenario, and the DM production processes are mediated by a single new heavy particle with a mass M_{med} too large to be produced directly at the LHC and bigger than the DM mass m_χ ($M_{\text{med}} >> \sqrt{s} >> m_\chi$). In these hypotheses it is possible to integrate out the mediator in the process and probing the different scenarios choosing a particular operator that describes the kind of interaction (vectorial, axial, scalar, pseudo-scalar, tensorial etc.). Considering that no evidences and excesses are seen in the SRs it is possible to set the limits in several EFT scenarios. The limits on the signal strength are translated to bounds on the WIMP-nucleon scattering cross sections to compare the results with the direct search experiment ones.

Figure 3 demonstrates that the detection of DM candidates in a collider can give complementary results with respect to the direct (DAMA, LUX etc.) and indirect (AMS, Ice-Cube etc.) detection experiments and in particular in the low DM mass region where these detectors loose their sensitivity (currently the direct detection cannot reach the spectrum area below $\sim$ 3 GeV).

Besides the EFT operators, in the collider experiments the pair production of WIMPs is also investigated within the Simplified Models, where a pair of WIMPs couples to a pair of quarks explicitly via a new mediator particle (for example a Z'). The free parameters to constrain in this context are the mass and spin property of the mediator and of the DM particles, the width of the mediator and the vertex couplings $\sqrt{g_q\, g_\chi}$.

Figure 4 shows how, for a given mediator mass (in this specific case a Z' like mediator) and two values of the width Γ, the real value of the mass suppression scale would compare to the suppression scale $M_* = M_{\text{med}}/\sqrt{g_q\, g_\chi}$ value derived assuming a contact interaction (shown as dashed lines). In this case the contact interaction regime is reached for M_{med} values larger than 5 TeV. In the intermediate range the contact interaction approach would't be the proper choice. In fact, the bounds would be underestimated in the middle region (in 700 GeV $< M_{\text{med}} <$ 5 TeV) with respect to the actual values because the mediator would be produced resonantly and the actual M_* value is higher than in the contact interaction regime. Instead, in the small mediator mass regime below 700 GeV, the M_* limits would be optimistic and overestimated because the WIMP would be heavier than the mediator, and WIMP pair production via this mediator would thus be kinematically suppressed.

It is also possible to constrain the couplings $\sqrt{g_q\, g_\chi}$ of the simplified model vertex in the plane of mediator and WIMP mass (M_{med} versus m_χ) as shown in left plot in Figure 4. Within this model, the regions above the relic density (as measured by the WMAP satellite, assuming annihilation in the early universe in the absence of any interaction other than the one considered) line lead to values of the relic density larger than measured and are excluded.

Other interpretations

The mono-jet final states have been studied also in the other theoretical contexts getting stringent constrains to the models investigated.

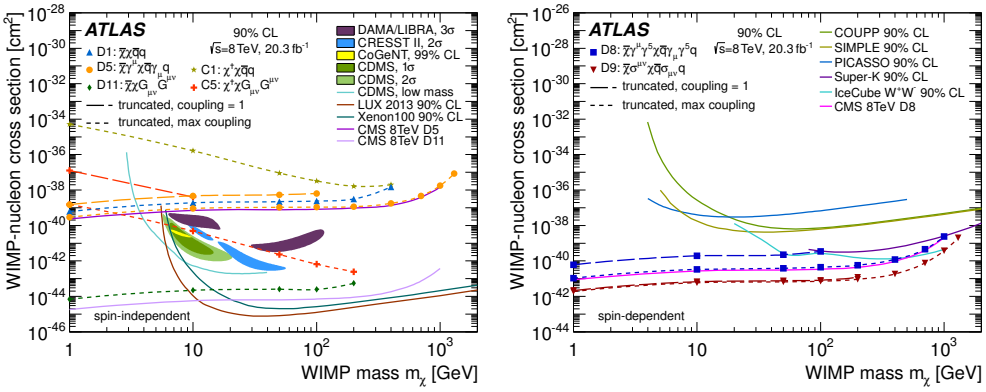

FIGURE 3. Inferred 90% CL limits on the spin-independent (left) and spin-dependent (right) WIMP-nucleon scattering cross section as a function of DM mass m_χ for different operators. Results from direct-detection experiments for the spin-independent cross section, and the CMS (untruncated) are shown for comparison. Taken from Ref. [3].

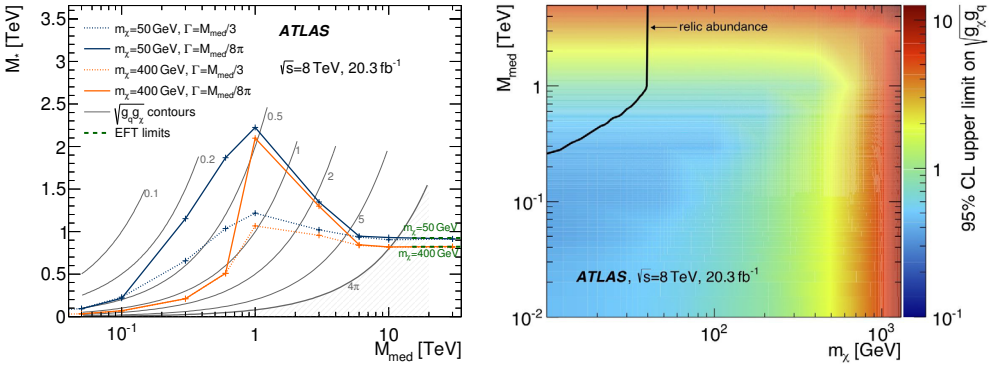

FIGURE 4. Left: comparison between the limits in the plane (M_{med}, M_*) in the EFT and simplified model approach choosing two m_χ and Γ hypotheses. Right: upper limit on the couplings $\sqrt{g_q\, g_\chi}$ in the plane (M_{med}, m_χ). In both the figure is it used a Z' like mediator model. More informations in the text. Taken from Ref. [3].

Several SUSY compressed scenarios can lead to a mono-jet like topology. The Run-1 results are expressed in limits on the cross-section for the dominant associated production of a Gravitino and a gluino (or a squark) , $pp \to \tilde{G}\tilde{g}(\tilde{q}) + X$, decaying into a quark (gluon) in association with a Gravitino, $\tilde{g}(\tilde{q}) \to \tilde{G}g(q)$ [6]. The limits on the Gravitino mass $m_{\tilde{G}}$ in the cases of degenerate and non-degenerate squarks and gluinos scenarios are also computed. In Figure 5 the cross-section times efficiency as a function of the squark/gluino mass for different $m_{\tilde{G}}$ in the degenerate squarks and gluinos scenario and different gravitino masses for the SR with $E_{\text{T}}^{\text{miss}} > 500$ GeV are shown and compared with the corresponding model-independent limits.

The large extra dimensions theory would aim to provide a solution to the mass hierarchy problem by postulating the presence of n extra spatial dimensions of size R, and defining a fundamental Planck scale in $4 + n$ dimensions, M_D, given by ${M_{\text{Pl}}}^2 \sim {M_D}^{2+n} R^n$ [7]. In this scenario the graviton modes may escape detection and its production in association with a jet taking to a mono-jet signature. In this context the scenarios with several number of extra dimensions are investigated. The predicted product of cross section, acceptance and efficiency, for the SR with $E_{\text{T}}^{\text{miss}} >$ 500 GeV as a function of M_D, for n = 2, n = 4, and n = 6 is shown in Figure 5 (the bands represent the theory uncertainty). For comparison, the model-independent observed (solid line) and expected (dashed line) 95% CL limits on the cross section are also plotted.

Finally, the mono-jet analysis can give competitive and important results in the invisible Higgs decays interpretation since that the study of the Higgs boson properties does not exclude a sizeable branching ratio [8]. The Higgs scalar field could also play an important role in describing the interaction between dark and ordinary matter in the

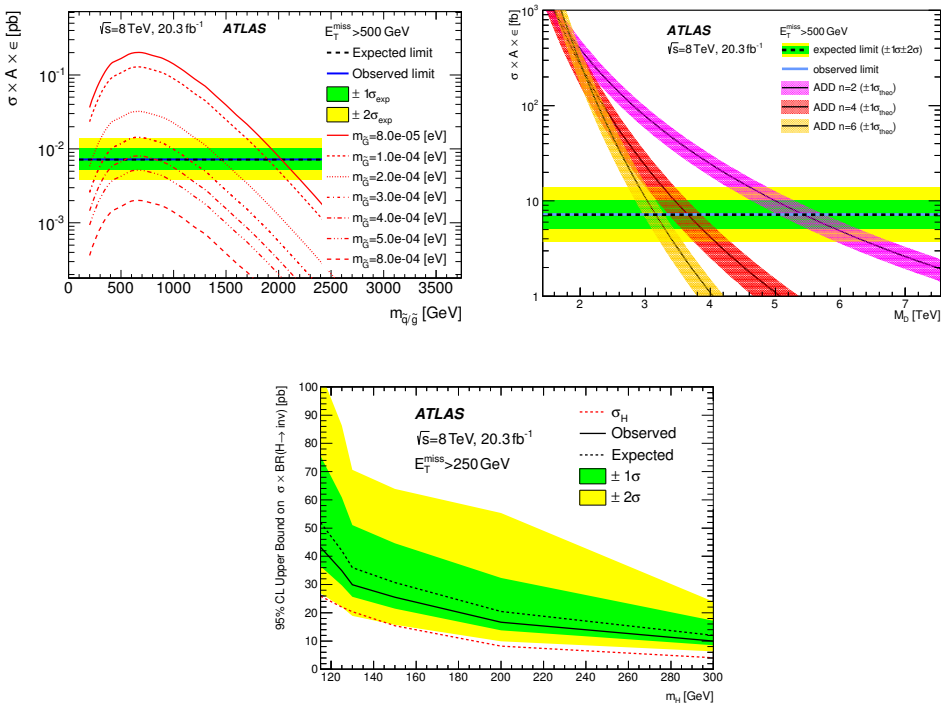

FIGURE 5. Top: comparison between the model independent results and the supersymmetric degenerate squarks and gluinos scenarios in which $pp \to \tilde{G}\tilde{g}(\tilde{q}) + X \to \tilde{G}\tilde{G}g(q)$ (top-left) and LED interpretation varying the number of dimensions n (top-right). Bottom: cross section times branching ratio limit in the Higgs invisible decay scenario as a function of the Higgs mass m_H. The expectation for a Higgs boson with BR($H \to$ inv) = 1 is also plotted. More informations in the text. Taken from Ref. [3].

universe and a considerable fraction of the branching ratio to invisible particles could be interpreted in terms of the DM production. In Figure 5 the results are translated into 95% CL limits on the production cross section times the branching ratio for a Higgs boson decaying into invisible particles as a function of the boson mass. The expectation for a Higgs boson decaying completely in the invisible sector is also plotted.

First analysis of $\sqrt{s} = 13$ TeV data

The Run-2 analysis follows a similar strategy of the one already performed with the Run-1 statistics adapting the criteria selection on the data at the new center of mass energy and bunch crossing frequency. For these reason a new object selection is applied and a new definition of the Signal and Control regions are performed.

In Figure 6 are shown the firsts results based on 68-78 pb^{-1} of collision data at $\sqrt{s} = 13$ TeV [10]. The left plot shows the muon CR defined using "relaxed" $E_{\mathrm{T}}^{\mathrm{miss}}$ and jet p_{T} cuts with respect to the Run-2 selection and this tests the analysis control on the background estimation. The picture on the right is a single-jet sample SR-like distribution where the jet cleaning requirements are removed to point out the importance of the good quality jet requirements. In fact the mono-jet final states would be dominated by the non-collision background (NCB) and an azimuthal structure characteristic of fake jets due to beam-induced backgrounds is visible. In order to suppress the NCB below the 1% level, an efficient jet cleaning is required with a suppression power of at least three orders of magnitude [11].

Preliminary expected results are just done at an energy collision of $\sqrt{s} = 14$ TeV showing promising prospectives for the Run-2 results. In particular the Run-2 projections in the WIMP search sector [12] in the EFT context show that it is possible to gain in sensitivity already with a few fb^{-1} of data collected, compared to the 8 TeV results. In the case where no excesses are observed, it is possible just using the Run-1 mono-jet analysis to improve the limits on the suppression scale M_* of a factor two (Figure 7).

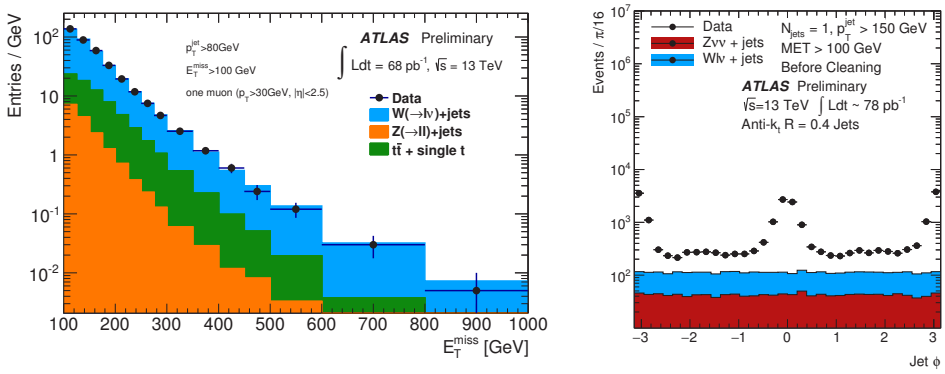

FIGURE 6. On the left: $E_{\mathrm{T}}^{\mathrm{miss}}$ distribution in the one muon Control Region of the mono-jet analysis with $E_{\mathrm{T}}^{\mathrm{miss}} > 100$ GeV and jet $p_{\mathrm{T}} > 80$ GeV cuts, showing 68 pb^{-1} of data at $\sqrt{s} = 13$ TeV. The MC predictions for SM backgrounds are normalised to data. On the right: The jet phi distribution for a single-jet sample selected with $E_{\mathrm{T}}^{\mathrm{miss}} > 100$ GeV and jet $p_{\mathrm{T}} > 150$ GeV The MC prediction corresponds to $Z(\nu\nu)$ + jets and $W(\ell\nu)$ + jets processes, normalised to the luminosity of the sample, which is measured to be 78 pb^{-1}. Additional collision processes, contributing at the 10% level or lower, are neglected. Taken from Ref. [10].

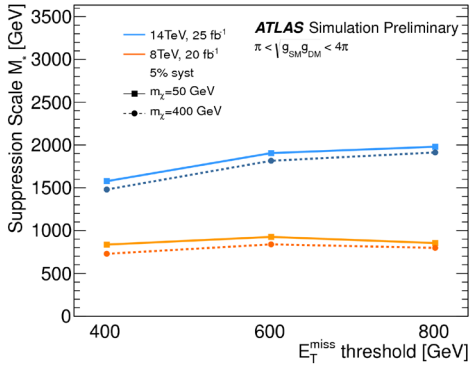

FIGURE 7. The 95% CL lower limits on the suppression scale M_* from 20 fb^{-1} at $\sqrt{s} = 8$ TeV, and 25 fb^{-1} at $\sqrt{s} = 14$ TeV. The limits for the vector operators with $m_\chi = 50$ and 400 GeV are shown for three signal regions defined by $E_{\mathrm{T}}^{\mathrm{miss}} > 400$, 600 and 800 GeV, considering 5% systematic uncertainty on Standard Model background. The 8 TeV limits presented are based on simulation only. These results assume that the EFT is a valid approach. Taken from Ref. [12].

Conclusions

The mono-jet topology constitutes a clean and distinctive signature in search of new phenomena that escape from the direct detection at colliders. Promising prospects at the new energy are estimated in all the theoretical scenarios in this analysis. As shown in the firsts Run-2 mono-jet results, the analysis is ready to use the new data thanks also to the excellent detector performance and it is ready to intepret its results in all the theoretical scenarios previoulsy cited in particular increasing the commitment in the dark sector probing a wide spectrum of possible signal hypotheses in the simplified model approach [9].

To conclude, the last results at $\sqrt{s} = 8$ TeV are in agreement with the SM predictions but with the start of Run-2 at LHC, working at the never reached centre of mass energy proton-proton collision of 13 TeV, a wide spectrum of New Physics beyond the Standard Model scenarios could be opened and the mono-jet analysis is ready to give its crucial contribution with the hope of finding a solution to the questions still open in the cosmological and particle physics fields.

REFERENCES

[1] G. Bertone, D. Hooper, and J. Silk, Phys.Rept.405:279-390,2005.
[2] G. Steigman and M. S. Turner, Nucl. Phys. **B253** (1985) 375.
[3] ATLAS Collaboration, Eur. Phys. J. C **75** (2015) 7, 299
[4] ATLAS Collaboration, JINST **3**, S08003 (2008).
[5] ATLAS Collaboration, Eur. Phys. J. **C 72** (2012) 1849.
[6] M. Klasen and G. Pignol, Phys. Rev. **D 75** (2007) 115003.
[7] N. Arkani-Hamed, S. Dimopoulos, and G. Dvali, Phys. Lett. **B 429** (1998) 263.
[8] ATLAS Collaboration, Phys. Rev. Lett. **112** (2014) 201802.
[9] D. Abercrombie *et al.*, arXiv:1507.00966 [hep-ex].
[10] ATLAS Collaboration, EXOT-2015-005, https://atlas.web.cern.ch/Atlas/GROUPS/PHYSICS/PLOTS/EXOT-2015-005/.
[11] ATLAS Collaboration, ATLAS-CONF-2015-029, https://cds.cern.ch/record/2037702
[12] ATLAS Collaboration, ATL-PHYS-PUB-2014-007, https://atlas.web.cern.ch/Atlas/GROUPS/PHYSICS/PUBNOTES/ATL-PHYS-PUB-2014-007/.

Proceedings of the LHCP2015 Conference, St. Petersburg, Russia, August 31 - September 5, 2015

Editors: V.T. Kim and D.E. Sosnov

Search for Quantum Black Holes in Lepton+Jet Final State Using pp-Collisions at $\sqrt{s}$ = 8 TeV with the ATLAS

Z.M. KARPOVA[1,a)] S.N. KARPOV[1,b)]

[1] *Joint Institute for Nuclear Research, Dubna*

[a)]Corresponding author: zkarpova@cern.ch
[b)]skarpov@cern.ch

On behalf of the ATLAS Collaboration

Abstract. Search for quantum black holes (QBHs) was performed with proton-proton collision data collected by the ATLAS detector at the LHC in 2012 at a center-of-mass energy $\sqrt{s}$ = 8 TeV with the integrated luminosity of 20.3 fb^{-1}. The QBH production is modeled with the ADD-model with the number of large extra dimensions n = 6. The QBH is assumed to decay into a final state with a lepton (electron or muon) and a jet. This final state is preferred in the above model and it is assumed to be sensitive to the TeV scale gravity. There are no events with a lepton-jet invariant mass of 3.5 TeV or more in both electron and muon channel. The measurement is consistent with the expected background. The combined 95% confidence level upper limit on product of the QBH production cross sections and the branching fractions of decay into the lepton+jet is equal to 0.18 fb. The upper limit constrains the threshold quantum black-hole mass to be above 5.3 TeV in the model considered.

INTRODUCTION

This paper presents a search for Quantum Black Hole (QBH) production in pp collisions at the ATLAS detector. Analysis was done for Run 1 (2012) at a center-of-mass energy $\sqrt{s}$ = 8 TeV with the integrated luminosity of 20.3 ± 0.6 fb^{-1}. This model offers an interesting search channel to be performed at the Large Hadron Collider (LHC) because quantum black holes are predicted in low-scale quantum gravity theories which offer solutions to the mass hierarchy problem of the Standard Model (SM) by lowering the scale of quantum gravity (M_{D}) from the Planck scale ~10^{16} TeV to ~1 TeV. That is why a search region for invariant masses of QBH is studied near 1-10 TeV. Here M_{D} is a multidimensional mass of QBH.

The Large Extra Spatial Dimension Model with n compact extra dimensions with a gravitational radius R was suggested by Arkani-Hamed, Dimopoulos and Dvali (ADD-model) [1, 2, 3]. The analysis utilizes the feature of the model that the QBHs with masses near M_{D}, postulated to conserve total angular momentum, color, and electric charge, may decay to two particles [4]. The behavior of QBHs is different from semi-classical black holes that decay via Hawking radiation to a large number of objects [5]. The two-particle decay of QBH into a lepton (electron or muon) and a light quark (u or d) violates conservation of both lepton and baryon number and provides a distinctive signal for physics beyond the SM. Therefore, it is assumed in this analysis that QBHs decay mode is with one lepton (electron or muon) and a jet in final state with a high invariant mass. This mode also has the highest branching fraction and ratio of signal to background in comparison with other possible decay modes [4].

A brief description of the ADD Model

To solve the hierarchy problem the multi-dimensional Planck scale is assumed to be equal to the electroweak scale $M_{\mathrm{D}} = M_{\mathrm{EWK}}$, where the electroweak scale is M_{EWK} ~1 TeV and the true Planck scale is equal $M_{\mathrm{Pl}} \sim 10^{16}$ TeV. Therefore the gravity becomes strong, and quantum effects are important. The true Planck scale (M_{Pl}) is related to multi-dimensional one (M_{D}) as:

$$M_{\mathrm{Pl}}^2 \sim M_{\mathrm{D}}^{2+n} \cdot R^n. \quad (1)$$

Extra spatial dimensions are large, i.e. their gravitational radius R could be about 1μm or even up to ~1 mm. According to the ADD scenario it is expected, if collisions energy will exceed a certain threshold mass M_{th}, the microscopic black holes should form. The threshold mass can be above M_{D}, but far below M_{Pl}. This phenomenology of QBHs production should be significantly different from production of semi-classical black holes: if the black hole was produced far above threshold M_{th}, then it can decay into large quantity of objects via the Hawking radiation. In case of Quantum Black Hole: the QBH could form near threshold M_{th} and later it can decay into the two-body final states. The production of QBH close to M_{th} dictates a possible quasi-resonant final state with an observable enhancement for a certain invariant mass.

The largest cross section of QBH production for a final state with a lepton and a jet depends on the initial state. For the initial state with two u-quarks the QBH is produced with an electric charge of +4/3 and the branching fraction is $BF = 11\%$. For the ud-quarks collision the QBH will have charge of +1/3 and the Branching Fraction will be $BF = 5.7\%$. For the initial dd-quarks and QBH with charge of -2/3 the branching fraction is $BF = 6.7\%$. Processes with initial states of anti-quarks and heavier sea-quarks are suppressed by a factor of ~100.

THE ATLAS DETECTOR

The ATLAS detector [6] is a multipurpose detector with a forward-backward symmetric cylindrical geometry and it covers about 4π of solid angle. The dimensions of the detector are 25 m in height and 44 m in length. The overall weight of the detector is approximately 7000 tons.

Identification of vertex, electrons, muons and jets and measurement of energy and momentum are achieved by a combination of different detectors and systems. They are Magnetic system, Inner Detector, Liquid-Argon electromagnetic calorimeter, Hadronic calorimeters and Muon System. Inner Detector (tracker) covers a pseudo-rapidity range of $|\eta| < 2.5$. The pseudo-rapidity, η, is defined by equation:

$$\eta = -\log\left(\tan\frac{\theta}{2}\right). \quad (2)$$

The Inner Detector is surrounded by a superconducting solenoid providing a 2 T magnetic field in the central tracking volume with a peak field of 2.6 T. A liquid-Argon (LAr) electromagnetic (EM) sampling calorimeter provides the energy measurements in range $|\eta| < 3.2$. A scintillator-tile hadronic calorimeter (TileCal) covers range $|\eta| < 1.7$. A LAr hadronic calorimeter covers $1.4 < |\eta| < 3.2$, and a LAr forward calorimeter covers $3.1 < |\eta| < 4.9$. The Muon Spectrometer (MS) consists of tracking chambers covering $|\eta| < 2.7$ and trigger chambers covering $|\eta| < 2.4$ in a magnetic field produced by a system of air-core toroids. Magnetic field is ~0.5 T and ~1 T for the central and end-cap regions of the muon detector, respectively.

EVENT SELECTION

Six criteria of the object selection are used in the analysis [7]:

1. In the electron (muon) channel events are required to have exactly 1 electron (muon).
2. Electron candidates are identified as localized depositions of energy in the EM calorimeter with $p_{\mathrm{T}} > 130$ GeV and $|\eta| < 2.47$, excluding the barrel-endcap transition region, $1.37 < |\eta| < 1.52$, and matched to a track reconstructed in the tracking detectors.
3. Isolated electrons are selected by requiring the transverse energy deposited in a cone of radius $\Delta R = \sqrt{(\Delta\eta)^2 + (\Delta\phi)^2} = 0.3$ centered on the electron cluster, excluding the energy of the electron cluster itself, to be less than $(0.0055 \cdot p_{\mathrm{T}} + 3.5)$ GeV after corrections for energy due to pileup and energy leakage from the electron cluster into the cone.
4. Muon candidates are required to be detected in at least three layers of the muon spectrometer and to have $p_{\mathrm{T}} > 130$ GeV and $|\eta| < 2.4$.
5. Signal muons are required to be isolated such, that $\sum p_{\mathrm{T}} < 0.05 \cdot p_{\mathrm{T}\mu}$, where $\sum p_{\mathrm{T}}$ is the sum of the p_{T} of the other tracks in a cone of radius $\Delta R = 0.3$ around the direction of the muon.
6. Jets are constructed from three-dimensional noise-suppressed clusters of calorimeter cells using the anti-kt algorithm with a radius parameter of 0.4. All jets are required to have $p_{\mathrm{T}} > 50$ GeV and $|\eta| < 2.5$. In addition, the most energetic jet is required to have $p_{\mathrm{T}} > 130$ GeV.

SOURCES OF BACKGROUND FOR QUANTUM BLACK HOLES

Events with a high p_T of lepton and one or more jets can arise from electroweak processes. They include a vector-boson production with additional jets and di-bosons (WW, WZ, ZZ). Strong processes include top-quark pairs ($t\bar{t}$), a single top-quark (t or $\bar{t}$) and multi-jets (QCD) production. The multi-jets background can include non-prompt leptons from the semi-leptonic hadrons decays and also include jets, which were identified as leptons by mistake.

Multi-jets background was estimated with a data-driven method. The electroweak background and strong production of top-quarks were estimated in Signal Region using Monte Carlo samples, normalized to data in Control Regions. Simulation was based on GEANT4 [8] with the corresponding model of the ATLAS detector geometry. List of dominant backgrounds in decreasing order of importance is below:

- W+jets;
- Z+jets;
- Di-bosons: WW, WZ, ZZ;
- Production of $t\bar{t}$ pairs;
- Single top-quarks;
- Multi-jets (QCD).

Additional inelastic proton-proton's interactions, termed pileup, were included into the event simulation in order to agree with the data distribution of the number of interactions per bunch crossing. The average number of interactions per bunch crossing was about 21.

RESULTS OF THE SEARCH FOR QBH IN RUN 1

The invariant mass (m_{inv}) is calculated with two 4-vectors of the lepton and highest-p_T jet. The Signal Region (SR) is defined by a lower bound, m_{min}, of invariant mass, that accounts for experimental resolution. In the electron channel $m_{min} = 0.9 \cdot M_{th}$ is used. In the muon channel, the requirement is loosened at high invariant mass, as muon resolution has a term quadratic in p_T, resulting in $m_{min} = (0.95 - 0.05 \cdot M_{th}/1\ \text{TeV}) \cdot M_{th}$. A low invariant-mass Control Region (CR) is defined with m_{inv} between 400 and 900 GeV, which has a negligible contamination from a potential signal ($< 2\%$) for the lowest M_{th} considered.

In Figure 1 you can see the distribution of events over the invariant mass of the lepton and highest-p_T jet for data (points with error bars) and for SM backgrounds (solid histograms) [7]. Panel (a) corresponds to the electron channel and panel (b) – muon channel. The hatched area shows the total uncertainty in the background estimate, in which the systematic uncertainties dominate. Dashed lines represent two examples of QBH signals.

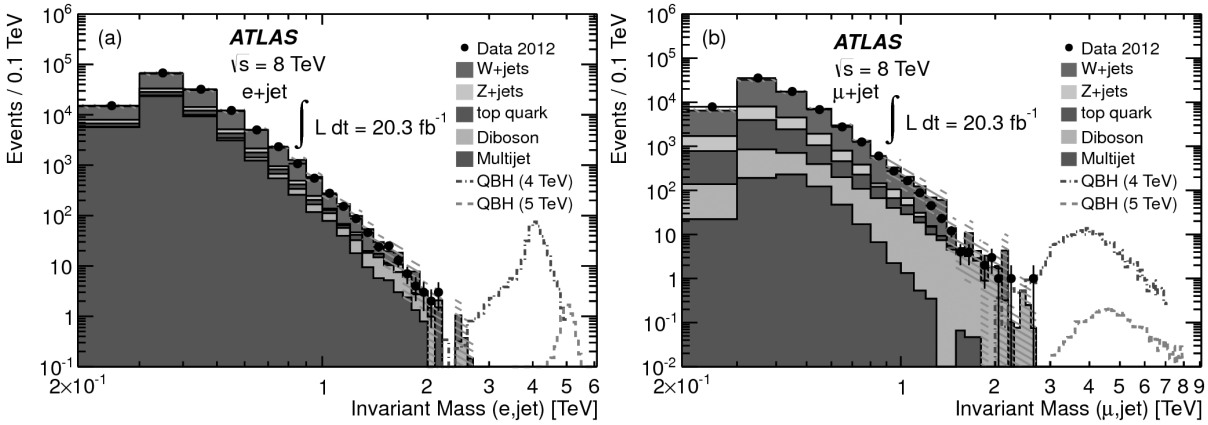

FIGURE 1. The distribution of events over the invariant mass of the lepton and highest-p_T jet for data (points with error bars) and for SM backgrounds (solid histograms). Two examples of QBH signals are overlaid here too. The sum of the uncertainties due to the finite MC sample size and from various sources of systematic uncertainty is shown by the hatched area. (a) – the electron+jet channel, (b) – the muon+jet channel. Taken from Ref. [7].

In Table 1 the numbers of expected background (Exp.), observed (Obs.) events and cumulative signal efficiencies (Eff.) are shown [7]. The observed numbers of events and expected total background are in agreement within the total uncertainty. There is no evidence for any excess.

TABLE 1. Numbers of expected background (Exp.) and observed (Obs.) events, along with the cumulative signal efficiencies (Eff.), with uncertainties including both the statistical and systematic components for various values of $M_{\rm th}$. Taken from Ref. [7].

$M_{\rm th}$		Electron+jet			Muon+jet	
TeV	**Obs.**	**Exp.**	**Eff. [%]**	**Obs.**	**Exp.**	**Eff. [%]**
1.0	1200	1210^{+230}_{-220}	57 ± 4	620	550 ± 280	38 ± 4
1.5	100	110 ± 40	57 ± 4	49	65^{+45}_{-40}	36 ± 4
2.0	12	19^{+13}_{-12}	56 ± 4	8	14^{+16}_{-14}	36 ± 4
2.5	0	$5.3^{+4.5}_{-3.9}$	55 ± 4	3	5^{+6}_{-5}	34 ± 4
3.0	0	$1.8^{+1.8}_{-1.6}$	54 ± 4	1	$2.1^{+2.9}_{-2.1}$	34 ± 4
3.5	0	$0.76^{+0.79}_{-0.67}$	54 ± 4	0	$1.0^{+1.6}_{-1.0}$	33 ± 4
4.0	0	$0.35^{+0.38}_{-0.34}$	53 ± 4	0	$0.57^{+0.94}_{-0.57}$	33 ± 5
5.0	0	$0.09^{+0.10}_{-0.09}$	52 ± 4	0	$0.24^{+0.39}_{-0.24}$	32 ± 5
6.0	0	$0.03^{+0.04}_{-0.03}$	52 ± 4	0	$0.13^{+0.22}_{-0.13}$	32 ± 6

The uncertainties of the signal efficiency are associated with the selection cuts on $\Delta\eta$, $\Delta\phi$, $<\eta>$, $m_{\rm inv}$ and isolation. The uncertainties of the background, the detector simulation and luminosity were taken into account as well. The combined uncertainty on the signal efficiency from these sources spans the values from 3.5% at 1 TeV up to 3.9% at 6 TeV for the electron channel and from 3.6% at 1TeV to 5.6% at 6 TeV for the muon channel.

The cumulative efficiency in Table 1 is taken from the signal MC simulation for QBHs with charge of +4/3. The differences in efficiency between the +4/3 charge state and other charged states are substantially smaller than the above uncertainties.

In Figure 2 you can see the combined 95% Confidence Level upper limits on $\sum \sigma_{\rm qq} \times BF_{\rm qq}$ for QBHs decaying to a lepton and jet, as a function of threshold mass [7].

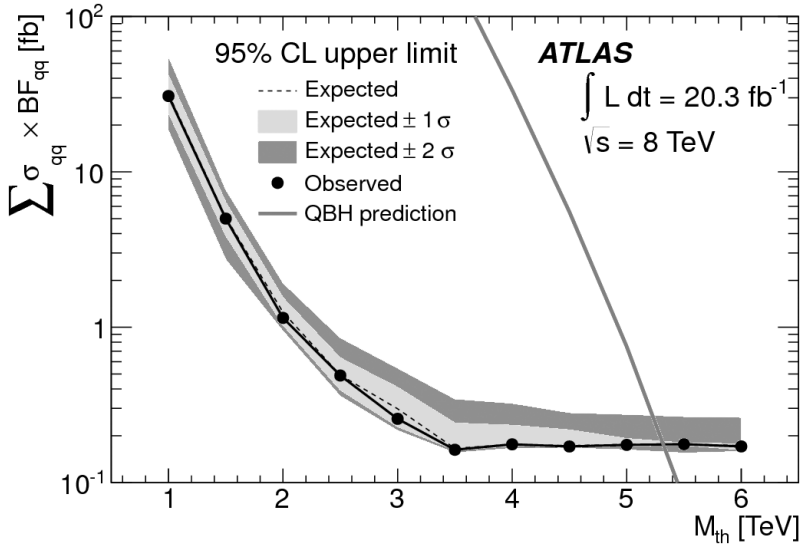

FIGURE 2. The combined 95% CL upper limits on $\sum \sigma_{\rm qq} \times BF_{\rm qq}$ for QBHs decaying to a lepton and jet, as a function of $M_{\rm th}$, assuming $M_{\rm D} = M_{\rm th}$ and $n = 6$ ADD extra dimensions. The limits take into account statistical and systematic uncertainties. Points along the solid black line indicate the mass of the signal where the limit is computed. The $\pm 1\sigma$ and $\pm 2\sigma$ bands indicating the underlying distribution of possible limit outcomes under the background-only hypothesis are also shown. The predicted cross section for QBHs is shown as the solid curve. Taken from Ref. [7].

In this case the multidimensional mass is equal to threshold mass and the number of extra dimensions in the ADD-model is equal $n = 6$. To extract the upper limit on the lepton+jet cross section, a fit to the invariant-mass distribution is performed, replacing the uncertainties due to MC sample size by the statistical uncertainties on the fit parameters. The used CLs method is designed to give conservative limits in cases, where the observed background fluctuates below the expected values. Upper limits on $\sum \sigma_{qq} \times BF_{qq}$ for the production of QBH above M_{th} are determined in the interval 1-6 TeV.

The statistical combination of the channels uses a likelihood function constructed as the product of terms of the Poisson probability, which are describing the total number of events observed in each channel. The systematic uncertainties are included as noise parameters into the likelihood through their effect on the average of the Poisson function. Furthermore, they are also included by convolutions with the Gaussian distributions.

The observed and expected upper limit values are equal to 0.18 fb above 3.5 TeV due to insufficient statistics. The 95% C.L. lower limit on M_{th} is 5.3 TeV.

CONCLUSIONS

In conclusion, a first search for two body lepton+jet final states with a large invariant mass has been performed using 20.3 ± 0.6 fb^{-1} of pp collisions recorded at $\sqrt{s} = 8$ TeV with the ATLAS detector at the LHC. In the invariant mass region above 1 TeV the observed events are consistent with extrapolated background from the low-invariant-mass control region. Above 3.5 TeV the expected background drops below one event and the 95% C.L. upper limit on the electron (muon)+jet $\sum \sigma_{qq} \times BF_{qq}$ is 0.27 (0.49) fb, and the lower limit on M_{th} is 5.2 (5.1) TeV. Assuming lepton universality, the 95% C.L. upper limit on the sum of the product of the QBH production cross sections and branching fractions of decay to lepton+jet is 0.18 fb. The 95% C.L. lower limit on M_{th} is 5.3 TeV.

ACKNOWLEDGMENTS

We thank CERN for the very successful operation of the LHC, as well as the support staff from our institutions without whom ATLAS could not be operated efficiently and members of the Exotics working group for careful analysis and fruitful discussions.

REFERENCES

[1] N. Arkani-Hamed, S. Dimopoulos, and G. R. Dvali, Phys. Lett. B **429**, p. 263 (1998).
[2] I. Antoniadis, N. Arkani-Hamed, S. Dimopoulos, and G. R. Dvali, Phys. Lett. B **436**, p. 257 (1998).
[3] N. Arkani-Hamed, S. Dimopoulos, and G. R. Dvali, Phys. Rev. D **59**, p. 086004 (1999).
[4] D. M. Gingrich, J. Phys. G **37**, p. 105008 (2010).
[5] L. A. Anchordoqui, J. L. Feng, H. Goldberg, and A. D. Shapere, Phys. Rev. D **65**, p. 124027 (2002).
[6] The ATLAS Collaboration, JINST **3**, p. S08003 (2008).
[7] The ATLAS Collaboration, Phys. Rev. Lett. **112**, p. 091804 (2014).
[8] The GEANT4 Collaboration, Nucl. Instrum. Methods Phys. Res. **Sect. A 506**, p. 250 (2003).

Proceedings of the LHCP2015 Conference, St. Petersburg, Russia, August 31 - September 5, 2015

Editors: V.T. Kim and D.E. Sosnov

Search for Scalar Leptoquarks in pp Collisions at $\sqrt{s} = 8$ TeV with ATLAS Detector

ANDREY KAMENSHCHIKOV

State Research Center of Russian Federation - Institute for High Energy Physics of National Research Center "Kurchatov Institute", 1, Nauki square, 142281, Protvino, Moscow region, Russian Federation

On behalf of the ATLAS Collaboration

Abstract. The work is dedicated to a search for pair-produced scalar leptoquarks using 20.3 fb^{-1} of data recorded by the ATLAS detector at the LHC in proton-proton collisions at $\sqrt{s} = 8$ TeV. Leptoquarks are hypothetical particles with non-zero lepton and baryon numbers, predicted by many extensions of the Standard Model, and can provide an explanation for the similarity between the quark and lepton sectors. Searches for pair-produced scalar leptoquarks have been performed with final states including leptons. Thereby the new limits on the leptoquarks mass were set at 95% Confidence Level.

INTRODUCTION

Several theories beyond Standard Model (SM) predict an existence of leptoquarks (LQs), e.g. Grand Unification Theories (SU(5) [1], constrained SU(5) [2], SU(15) [3], etc.), Pati Salam SU(4) model [4], Superstring model [5], Composite model [6], Technicolor model [7], etc. In accordance with analyses' benchmark model (constrained SU(5)) LQs carry both leptonic and baryonic charges, a fractional electric charge, grouped into three generations as SM leptons and quarks and appear as mediators of quark-leptons transitions. LQs and their decay products are required to be of the same generation (diagonal coupling) in order to prevent the proton decay. Scalar LQs pair production cross-section in pp collisions depends on strong coupling constant α_s and does not depend on unknown Yukawa coupling constant $\lambda_{\mathrm{LQ}\to\ell q}$. The dominating processes of scalar LQs pair production in pp collisions at a center-of-mass energy of $\sqrt{s} = 8$ TeV are gluon-gluon fusion and quark-antiquark annihilation [8, 9].

The search for pair production of first (LQ1) and second (LQ2) generations scalar LQs with ATLAS detector [10] has been performed in pp collisions at $\sqrt{s} = 8$ TeV in $eejj$ channel and in $\mu\mu jj$ channel respectively. The corresponding search for pair production of third (LQ3) generation scalar LQs has been completed in $b\nu_\tau\bar{b}\bar{\nu}_\tau$ and $t\nu_\tau\bar{t}\bar{\nu}_\tau$ channels as reinterpretation of analyses which are optimized for SUSY signatures searches. Since no evidence of a new physics is observed in any of the considered channels the new limits on scalar LQs mass, mass-dependent pair production cross-section and β (for LQ1 and LQ2 only) are set.

SEARCH FOR PAIR-PRODUCED SCALAR LEPTOQUARKS

These results are based on data, collected by the ATLAS detector at the LHC during 2012 in proton-proton collisions at $\sqrt{s} = 8$ TeV, corresponding to an integrated luminosity of 20.3 fb^{-1}. LQ3 ($b\nu_\tau\bar{b}\bar{\nu}_\tau$) analysis uses 20.1 fb^{-1} because of the trigger requirements.

Both LQ1 and LQ2 analyses require exactly 2 charged leptons and at least 2 jets in final state. The leading (sub-leading) electron of the LQ1 search is requested to have transverse momentum p_{T} above 40 (30) GeV, according to the trigger requirements [11], and both electrons are restricted to have $|\eta| < 2.47$, excluding transition region between barrel and endcap calorimeters $1.37 < |\eta| < 1.52$. Both muons of the LQ2 search are required to have p_{T} above 40 GeV and $|\eta| < 2.4$. The jets treatment is the same for LQ1 and LQ2 searches: jets are asked to have p_{T} above 30 GeV, $|\eta| < 2.8$ and not to be overlapped with the selected charged leptons within the cone of $\Delta R = \sqrt{(\Delta\eta)^2 + (\Delta\phi)^2} = 0.4$. Only two leading jets are finally considered.

The LQ3 ($b\nu_\tau\bar{b}\bar{\nu_\tau}$) search requires the absence of a lepton by vetoing an event with one or more electrons (muons) with p_{T} above 7 (6) GeV. Exactly 2 b-tagged jets with p_{T} above 20 GeV and $|\eta| < 2.5$ are requested to be present in the event. Furthermore, an additional event's missing transverse energy requirement of $E_{\mathrm{T}}^{\mathrm{miss}} > 150$ GeV is applied. LQ3 ($t\nu_\tau\bar{t}\bar{\nu_\tau}$) search select the events with exactly 1 electron (muon) with p_{T} above 25 GeV and $|\eta| < 2.47$ (2.4). At least 4 jets with p_{T} above 25 GeV and $|\eta| < 2.5$ have to be present in an event, given at least 1 of them has to pass b-tagging condition. The additional selection of $E_{\mathrm{T}}^{\mathrm{miss}} > 100$ GeV is applied to an event.

TABLE 1: The minimum values of $m_{\ell\ell}$, S_{T}, and $m_{\mathrm{LQ}}^{\mathrm{min}}$ used to define each of the signal regions targeting different LQ masses in the *eejj* and $\mu\mu jj$ channels. Each signal region is valid for one or more mass hypotheses, as shown in the second column. The table is taken from Ref. [11].

	LQ masses [GeV]	$m_{\ell\ell}$ [GeV]	S_{T} [GeV]	$m_{\mathrm{LQ}}^{\mathrm{min}}$ [GeV]
SR1	300	130	460	210
SR2	350	160	550	250
SR3	400	160	590	280
SR4	450	160	670	370
SR5	500–550	180	760	410
SR6	600–650	180	850	490
SR7	700–750	180	950	580
SR8	800–1300	180	1190	610

The background compositions of LQ1 and LQ2 searches are similar. The major background processes for both channels are Z/γ^* +jets and $t\bar{t}$ production. The control regions (CRs) are defined for each of these backgrounds in order to validate the modeling accuracy and estimate the background normalisation scale factors in the following way:

- Z/γ^* +jets CR: dilepton invariant mass ($m_{\ell\ell}$) is restricted to pass the requirement of $60 < m_{\ell\ell} < 120$ for LQ1 search and $70 < m_{\ell\ell} < 110$ for LQ2 search;
- $t\bar{t}$ CR: exactly one electron and exactly one muon have to be selected.

Such a strategy allows to use samples which are strongly dominated by the corresponding backgrounds and hence provides an opportunity to supply these backgrounds with data-driven normalization factors, eliminating a theoretical systematic uncertainty of cross-sections. The remaining (minor) backgrounds are estimated either purely via Monte Carlo modeled samples, e.g. $Z/\gamma^* \to \tau\tau$ production, dibosons, single top $+W$ associated production, or via data-driven techniques, like fake lepton backgrounds (where one or more leptons are misidentified jets) from QCD background, W+jets production, single top production through both $s-$ and $t-$ channels.

The major backgrounds in LQ3 ($b\nu_\tau\bar{b}\bar{\nu_\tau}$) search are $Z/\gamma^*(\to \nu\nu) + b\bar{b}$ (dominant one) production, $t\bar{t}$ production, W boson + heavy flavor quarks associated production. The dominant backgrounds in LQ3 ($t\nu_\tau\bar{t}\bar{\nu_\tau}$) channel search are $t\bar{t}$ production and $W(\to l\nu)$+jets production. All these major backgrounds are treated with corresponding CRs to increase the quality and reliability of analyses' background estimation.

The main sources of analyses' systematic uncertainties are either of theoretical or of experimental category. The dominating sources of experimental uncertainties are: trigger efficiency estimate uncertainty, lepton-related (identification, reconstruction and isolation), jet-related (Jets Energy Scale, Jets Energy Resolution and b-tagging procedure). The fake leptons background estimation technique also brings its own experimental systematics. The leading considered theoretical uncertainties are: Parton Density Function (PDF) uncertainty impact on the processes' cross-section and acceptance, strong coupling constant's normalization and factorization scales variation impacts on the processes' cross-section and acceptance, background modeling systematic uncertainty.

Statistical analysis is provided using Signal Regions (SRs), optimized in order to maximize an expected significance of signal. In both LQ1 and LQ2 analyses those SRs are defined in terms of three discriminative variables: $m_{\ell\ell}$, smallest reconstructed leptoquark's mass ($m_{\mathrm{LQ}}^{\mathrm{min}}$) and sum of transverse momenta of two leptons and two leading jets

(S_{T}). The final set of SRs of LQ1 and LQ2 searches is presented in Table 1. The distributions of $m_{\ell\ell}$, S_{T} and $m_{\mathrm{LQ}}^{\mathrm{min}}$ quantities after pre-selections for both searches are on Figures 1, 2 and 3 respectively. Both LQ3 ($b\nu_\tau\bar{b}\bar{\nu_\tau}$) and LQ3 ($t\nu_\tau\bar{t}\bar{\nu_\tau}$) analyses are provided using signal regions, optimized for SUSY searches [11].

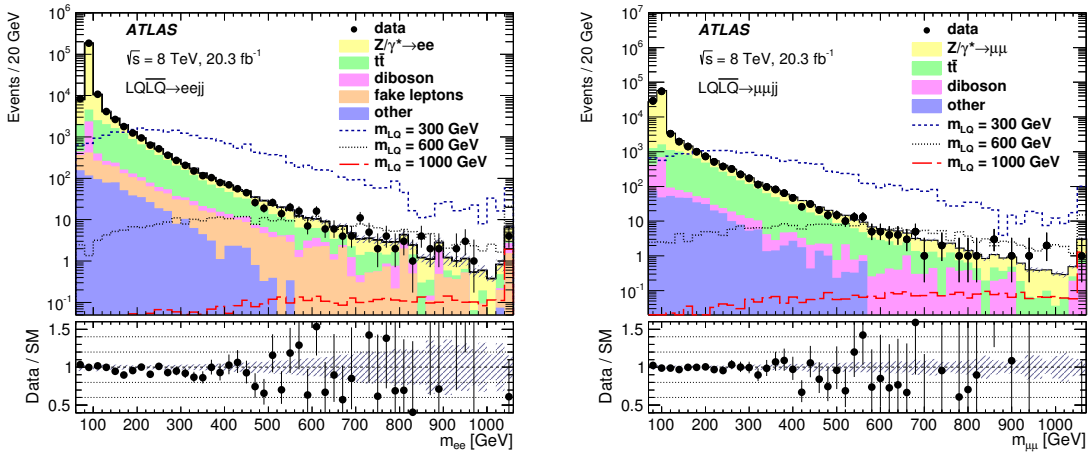

(a) *eejj* channel (b) *μμjj* channel

FIGURE 1: Distributions of the dilepton invariant mass ($m_{\ell\ell}$) in the *eejj* (left) and *μμjj* (right) channels after applying the pre-selection cuts. The signal model assumes $\beta = 1.0$. The last bin includes overflows. The ratio of the number of data events to the number of background events (and its statistical uncertainty) is also shown. The hashed bands represent all sources of statistical and systematic uncertainty on the background prediction. The figures are taken from Ref. [11].

Joint likelihood model which involves CRs and SR is built in order to process the hypotheses testing and the limits setting procedures. Frequentist approach and simple counting experiment technique are applied in LQ1 and LQ2 searches. CLs method [12] is used to set mass-dependent limits in all LQs searches at 95% Confidence Level (CL). The cross-section limits as a function of leptoquark's mass are presented in Figure 4 for LQ1 and LQ2 searches and in Figure 5 for LQ3 ($b\nu_\tau\bar{b}\bar{\nu_\tau}$) and LQ3 ($t\nu_\tau\bar{t}\bar{\nu_\tau}$) searches.

The limits on the excluded leptoquark's mass as a function of β are also provided by LQ1 (LQ2) analysis and presented in Figure 6, where the previous ATLAS results from pp collisions at $\sqrt{s} = 7$ TeV searches from *eejj* +*evjj* (*μμjj* +*μνjj*) are also shown. Limits as a function of β are not being estimated by LQ3 analyses since in that case the kinematic suppression factors which favor LQs decays to $b-$quarks over $t-$quarks and relative strengths of the Yukawa couplings would have to be considered, given they are model-dependent.

CONCLUSION

ATLAS has completed the search of pair-produced scalar leptoquarks using 20 fb^{-1} of proton-proton collisions data provided by the LHC during 2012 at $\sqrt{s} = 8$ TeV. The current results extend the sensitivity compared to previous searches of LQ1 [13], LQ2 [14] and LQ3 [15], provided by ATLAS collaboration in pp collisions at $\sqrt{s} = 7$ TeV with integrated luminosity of 1.03 fb^{-1}. First (second)-generation scalar LQs are excluded for $\beta = 1$ at 95% CL for $m_{\mathrm{LQ1}} < 1050$ GeV ($m_{\mathrm{LQ2}} < 1000$ GeV). The expected exclusion ranges are the same as the observed ones. Pair-produced third-generation scalar LQs decaying to $b\nu_\tau\bar{b}\bar{\nu_\tau}$ are excluded at 95% CL for $m_{\mathrm{LQ3}} < 625$ GeV. The expected excluded range is $m_{\mathrm{LQ3}} < 640$ GeV. Third-generation scalar LQs decaying to $t\nu_\tau\bar{t}\bar{\nu_\tau}$ are excluded at 95% CL in the mass range $210 < m_{\mathrm{LQ3}} < 640$ GeV. The expected exclusion range is $200 < m_{\mathrm{LQ3}} < 685$ GeV. The limit worsens at low mass, due to the effect of greater contamination from top backgrounds.

Searches in the low mass regions are important to evaluate the limits on low values of β parameter for LQ1 and LQ2 searches, since β is not constrained by theory. First (second)-generation scalar LQs are excluded for $m_{\mathrm{LQ1}} < 650$ GeV ($m_{\mathrm{LQ2}} < 650$ GeV) at $\beta = 0.2$ and $m_{\mathrm{LQ1}} < 900$ GeV ($m_{\mathrm{LQ2}} < 850$ GeV) at $\beta = 0.5$.

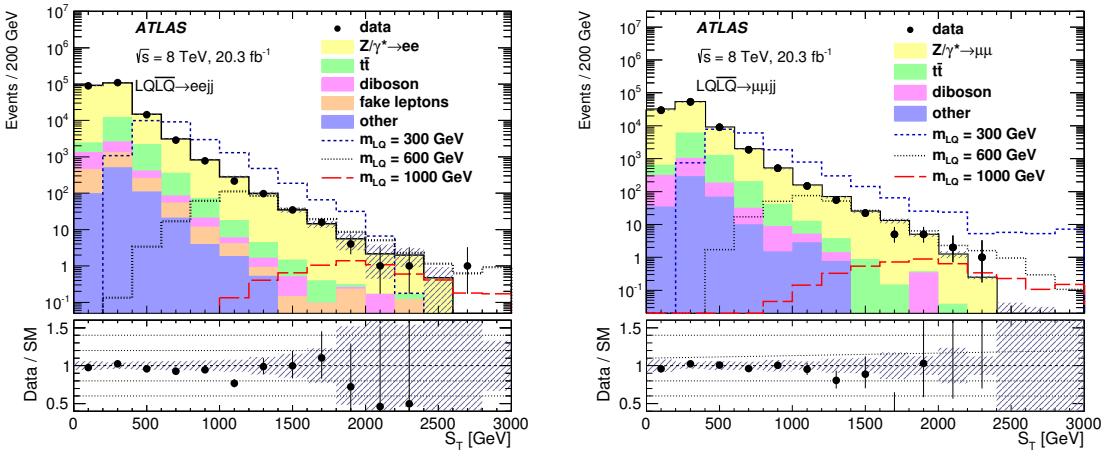

(a) *eejj* channel (b) *μμjj* channel

FIGURE 2: Distributions of the total scalar energy (S_{T}) in the *eejj* (left) and *μμjj* (right) channels after applying the pre-selection cuts. The signal model assumes $\beta = 1.0$. The last bin includes overflows. The ratio of the number of data events to the number of background events (and its statistical uncertainty) is also shown. The hashed bands represent all sources of statistical and systematic uncertainty on the background prediction. The figures are taken from Ref. [11].

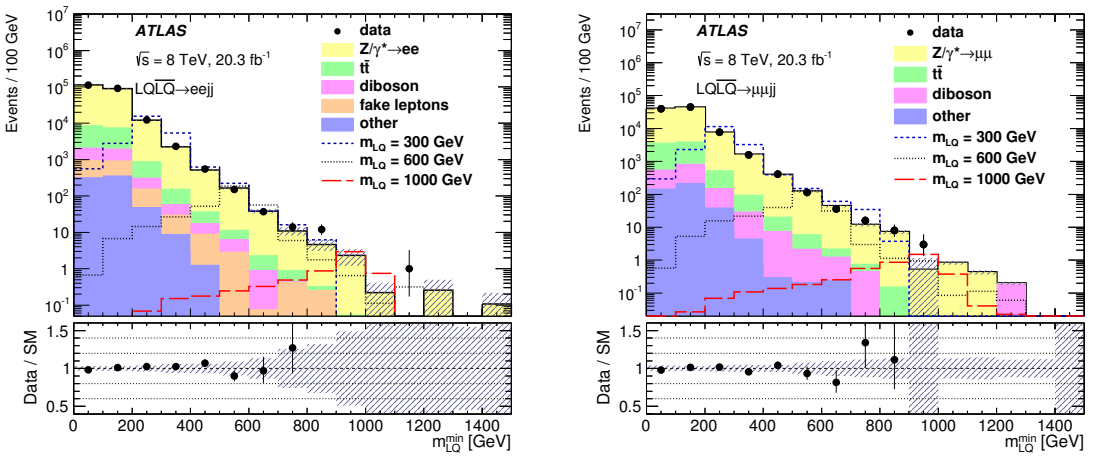

(a) *eejj* channel (b) *μμjj* channel

FIGURE 3: Distributions of the lowest reconstructed LQ mass ($m_{\mathrm{LQ}}^{\mathrm{min}}$) in the *eejj* (left) and *μμjj* (right) channels after applying the pre-selection cuts. The signal model assumes $\beta = 1.0$. The last bin includes overflows. The ratio of the number of data events to the number of background events (and its statistical uncertainty) is also shown. The hashed bands represent all sources of statistical and systematic uncertainty on the background prediction. The figures are taken from Ref. [11].

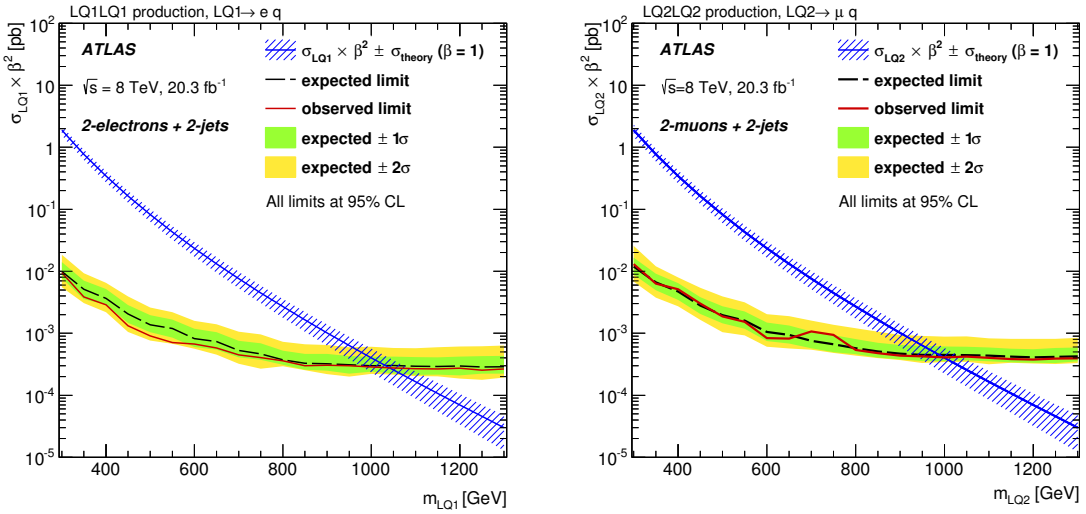

(a) *eejj* channel (b) *μμjj* channel

FIGURE 4: The cross-section limits on scalar LQ pair-production times the square of the branching ratio as a function of mass for the *eejj* channel (left) and for the *μμjj* channel (left). The $\pm 1(2)\sigma$ uncertainty bands on the expected limit represent all sources of systematic and statistical uncertainty. The expected NLO production cross-section ($\beta = 1.0$) for scalar LQ pair-production and its corresponding theoretical uncertainty due to the choice of PDF set and renormalisation/factorisation scale are also included. The figures are taken from Ref. [11].

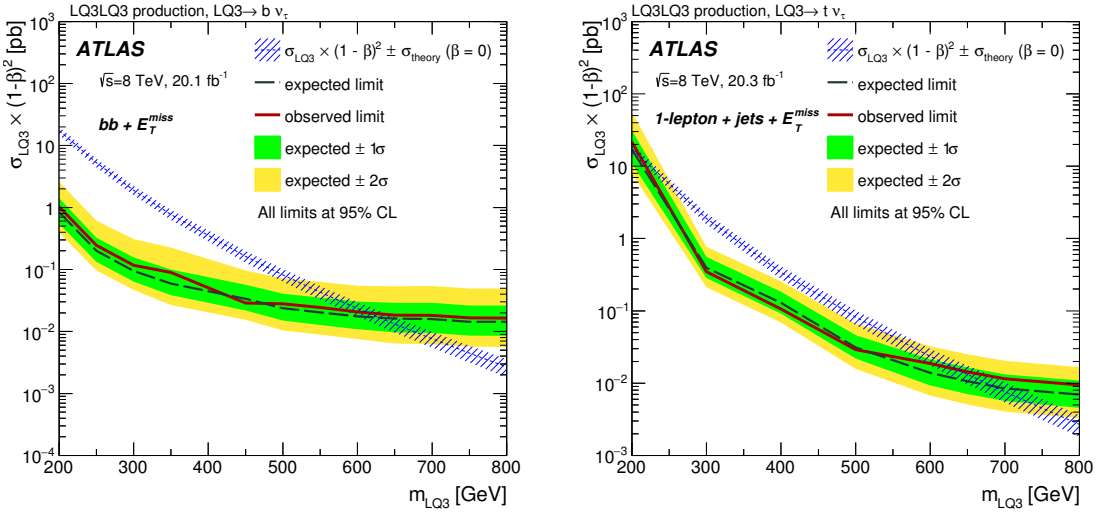

(a) *eejj* channel (b) *μμjj* channel

FIGURE 5: The expected (dashed) and observed (solid) 95% CL upper limits on the third-generation scalar LQ pair-production cross-section times the square of the branching ratio to $b\nu_\tau$ as a function of LQ mass, for the $b\nu_\tau\bar{b}\bar{\nu_\tau}$ channel (left), and to $t\nu_\tau$ as a function of LQ mass, for the $t\nu_\tau\bar{t}\bar{\nu_\tau}$ channel (right). The $\pm 1(2)\sigma$ uncertainty bands on the expected limit represent all sources of systematic and statistical uncertainty. The expected NLO production cross-section ($\beta = 0.0$) for third-generation scalar LQ pair-production and its corresponding theoretical uncertainty due to the choice of PDF set and renormalisation/factorisation scale are also included. The figures are taken from Ref. [11].

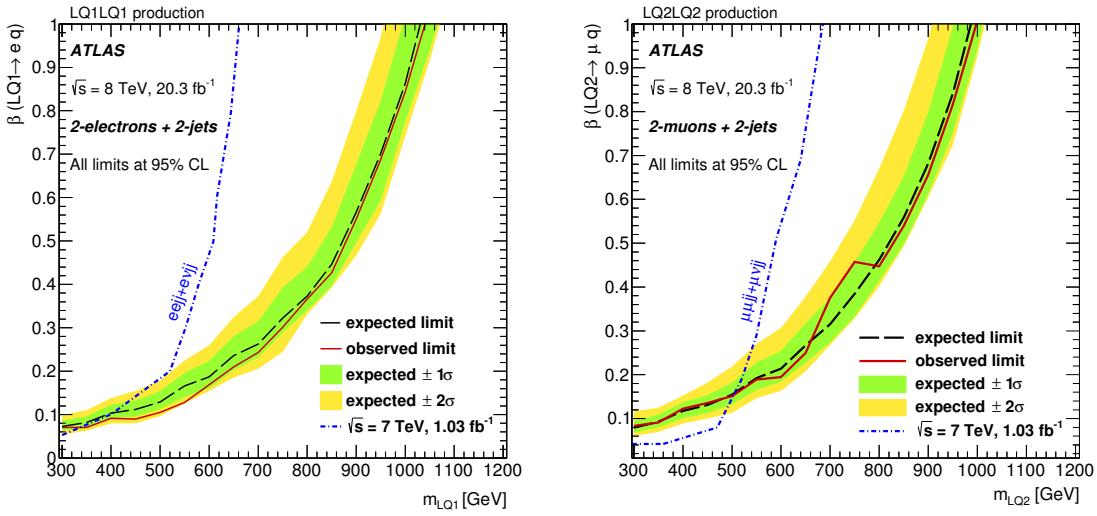

(a) $eejj$ channel (b) $\mu\mu jj$ channel

FIGURE 6: The cross-section limits on the excluded branching ratio as a function of the LQ mass (right) to eq for the $eejj$ channel (left) and to μq for the $\mu\mu jj$ channel (right). The $\pm 1(2)\sigma$ uncertainty bands on the expected limit represent all sources of systematic and statistical uncertainty. The exclusion limits on LQ1 [13] and LQ2 [14] set by ATLAS in the $eejj$ +$e\nu jj$ and $\mu\mu jj$ +$\mu\nu jj$ search channels using 1.03 fb^{-1} of data collected at $\sqrt{s}$ = 7 TeV are also shown. The figures are taken from Ref. [11].

ACKNOWLEDGMENTS

This work is supported by the Russian MES grant RFMEFI61014X0005 and Presidential Grant NSh-999.2014.2 (Russia). The particular great thanks are to IHEP (Protvino) Central Linux Cluster [16] and IHEP (Protvino) IT Department for their extensive computing support of the presented studies during whole period of the work.

REFERENCES

[1] H. Georgi and S. Glashow, Phys.Rev.Lett. **32**, 438–441 (1974).
[2] W. Buchmüller, R. Rückl, and D. Wyler, Phys.Lett. **B191**, 442–448 (1986), *Erratum ibid.* B448:320, 1999.
[3] P. H. Frampton, Mod.Phys.Lett. **A07**, 559–562 (1992).
[4] J. C. Pati and A. Salam, Phys.Rev. **D10**, 275–289 (1974), *Erratum ibid.* D11.703, 1975.
[5] V. D. Angelopoulos, J. R. Ellis, H. Kowalski, *et al.*, Nucl.Phys. **B292**, 59–92 (1986).
[6] A. Barr, B. Gripaios, and C. Lester, JHEP **02**, p. 045 (2010), arXiv:0910.1789 [hep-ph] .
[7] E. J. Eichten and K. Lane, Phys.Lett. **B90**, 125–130 (1980).
[8] M. Kramer, T. Plehn, M. Spira, and P. Zerwas, Phys.Rev. **D71**, p. 057503 (2005), hep-ph/0411038 [hep-ph] .
[9] J. Blümlein, E. Boos, and A. Kryukov, Z.Phys. **A76**, 136–153 (1997), 9811271 [hep-ph] .
[10] ATLAS Collaboration, JINST **3**, p. S08003 (2008).
[11] ATLAS Collaboration, arXiv:1508.04735 [hep-ex] .
[12] A. L. Read, Journal of Physics G: Nuclear and Particle Physics **28**, p. 2693 (2002).
[13] ATLAS Collaboration, Phys.Lett. **B709**, 158–176 (2012), *Erratum ibid.* B711:442-455, 2012, 1112.4828 [hep-ex] .
[14] ATLAS Collaboration, Eur.Phys.J. **C72**, p. 2151 (2012), 1203.3172 [hep-ex] .
[15] ATLAS Collaboration, JHEP **06**, p. 033 (2013), 1303.0526 [hep-ex] .
[16] V. Gusev, V. Kotlyar, V. Kukhtenkov, E. Popova, N. Savin, A. Soldatov, "WLCG Tier-2 computing infrastructure at IHEP," in *Proceedings of the Fifth International Conference "Distributed computing and grid-technologies in science and education"* (Joint Institute for Nuclear Researches, Dubna, 2012), pp. 150–157.

Proceedings of the LHCP2015 Conference, St. Petersburg, Russia, August 31 - September 5, 2015

Editors: V.T. Kim and D.E. Sosnov

Semileptonic (lepton, neutrino and jets) WW/WZ resonances search at $\sqrt{s} = 8$ TeV with the ATLAS detector at the LHC

EVGENIYA CHEREMUSHKINA

State Research Center of Russian Federation — Institute for High Energy Physics of National Research Center "Kurchatov Institute", 1, Nauki square, 142281, Protvino, Moscow region, Russian Federation

evgenia.cheremushkina@cern.ch

On behalf of the ATLAS Collaboration

Abstract. This poster presents the analysis results of the diboson (WW or WZ) resonances production search in pp collisions at $\sqrt{s} = 8$ TeV with the ATLAS detector at the LHC in 2012, using a total integrated luminosity of 20.3 fb^{-1}. The analysis is optimized for two benchmark signal models: Randall-Sundrum model (Spin-2 RS G^*) for WW and Extended Gauge Model (Spin-1 EGM W') for WZ resonances. The search is performed for semileptonic final state, i.e. one W boson decays to lepton (electron or muon) and neutrino and other W or Z — hadronically. No significant excess for diboson resonances production is observed and upper limits on the production cross section times branching fraction of G^* and W' are determined at 95% CL. Resonance masses below 760 GeV for G^* and 1490 GeV for W' are excluded, that gives a significant improvement to the results over previously reported limits in the same final state.

INTRODUCTION

There are several physics models, such as Supersymmetry, Technicolor, Extra Dimensions, which predict new particles, that can decay to gauge bosons pairs. This poster presents the results of the analysis, that strategy is optimized by using Randall-Sundrum (RS) model [1] and Extended Gauge Model (EGM) [2] and based on the diboson (WW for Spin-2 RS G^* or WZ for Spin-1 EGM W') resonances production search. Figure 1 shows s-channel leading-order Feynman diagrams for $G^* \to WW$ (a) and $W' \to WZ$ (b) production. The search is performed for semileptonic final state, i.e. one W boson is decayed to lepton (electron or muon) and neutrino and other W or Z — hadronically.

This analysis is made on data, collected in pp collisions at $\sqrt{s} = 8$ TeV by the ATLAS detector [3] at the LHC in 2012, using a total integrated luminosity of 20.3 fb^{-1} [4].

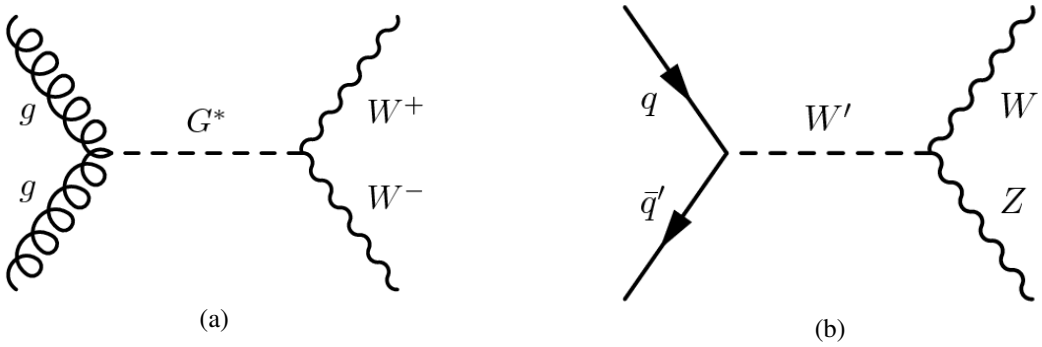

FIGURE 1. s-channel leading-order Feynman diagrams for $G^* \to WW$ (a) and $W' \to WZ$ (b) production [4].

EVENT SELECTION

In accordance with the analysis final state, interesting objects within an event are leptons (electrons or muons), jets and missing transverse momentum ($E_{\mathrm{T}}^{\mathrm{miss}}$). Each event should have at least 1 primary vertex with at least 3 associated tracks. The primary vertex is chosen with the largest sum of the tracks transverse momenta $\sum p_{\mathrm{T}}^2$. Also events are required to pass single lepton trigger.

Two different lepton categories are used for the selection procedure: "signal" — for the final analysis and "veto" — for the orthogonalization of this analysis with other final state topologies, such as *lvll*, *llqq*. Lepton candidates both electrons and muons are required to have transverse momentum $p_{\mathrm{T}} > 25$ GeV (20 GeV) and $|z_0 \sin\theta| < 0.5$ mm (2 mm) for "signal" ("veto"), where z_0 is the longitudinal impact parameter of the lepton with respect to the reconstructed primary vertex and θ — polar angle, track isolation $p_{\mathrm{T}}^{\mathrm{cone20}}/E_{\mathrm{T}} < 0.15$ for both "signal" and "veto", calorimeter isolation $E_{\mathrm{T}}^{\mathrm{cone20}}/E_{\mathrm{T}} < 0.14$ only for "signal" leptons, where $p_{\mathrm{T}}^{\mathrm{cone20}}$ ($E_{\mathrm{T}}^{\mathrm{cone20}}$) is a scalar sum of p_{T} of charged particle tracks (E_{T} in calorimeters) within a cone in η-ϕ plane (η — pseudorapidity and ϕ —azimuthal angle) of a radius $R = \sqrt{\eta^2 + \phi^2} = 0.2$ around the candidate excluding its own track (cluster). Also both "signal" and "veto" leptons should satisfy $|\eta| < 2.47$ excluding crack region $1.37 < |\eta| < 1.52$ ($|\eta| < 2.5$) and $|d_0/\sigma(d_0)| < 6$ (3.5) for electrons (muons), where d_0 is the transverse impact parameter and $\sigma(d_0)$ is the uncertainty on the measured d_0.

Tree different jet selections with three corresponding signal regions, depending on p_{T} of the leptonically (W) and hadronically (W or Z) decayed bosons, are used in the analysis. For the low-p_{T} hadronically decayed W/Z bosons, two leading jets, reconstructed by anti-k_t algorithm with $R = 0.4$ (small-R jets) are selected. This region is called Low-p_{T} Resolve Region (LLR). The small-R jets are required to pass next criteria: $p_{\mathrm{T},j} > 30$ GeV, $|\eta| < 2.8$, $p_{\mathrm{T},jj} > 100$ GeV, $p_{\mathrm{T},W\to lv} > 100$ GeV. For the high-p_{T} hadronically decayed W/Z bosons, one boosted leading jet, reconstructed by Cambridge–Aachen algorithm with $R = 1.2$ (large-R jet) is selected. This is called Merged Region (MR). The large-R jet has to be with $p_{\mathrm{T},J} > 400$ GeV, $|\eta| < 2.8$, as well as for leptonically decayed W $p_{\mathrm{T},W\to lv} > 400$ GeV. To optimize the selection in the transition area between LRR and MR High-p_{T} Resolve Region (HRR) is included with the selection: $p_{\mathrm{T},j} > 80$ GeV, $|\eta| < 2.8$, $p_{\mathrm{T},jj} > 300$ GeV, $p_{\mathrm{T},W\to lv} > 300$ GeV. Furthermore, for all three signal regions b-jet veto and invariant jet mass cut $65 < m_{jj/J} < 105$ GeV are applied. Prioritization for signal regions is done by applying firstly MR selection, events which are not passed MR then run through HRR cuts and then LRR requirements.

The missing transverse momentum is calculated as the negative of the vectorial sum of the transverse momenta of all electrons, muons, and jets, that are not associated with any other objects.

The analysis includes two channels, according to the lepton flavor. The criteria applied to select signal events are: exactly one "signal" lepton (muon or electron) and no additional "veto" leptons both flavors, $E_{\mathrm{T}}^{\mathrm{miss}} > 30$ GeV, exactly 2 small-R jets or 1 large-R jet. Figure 2 shows the signal efficiency for G^* (a) and W' (b) in both muon and electron channels and three signal regions [4].

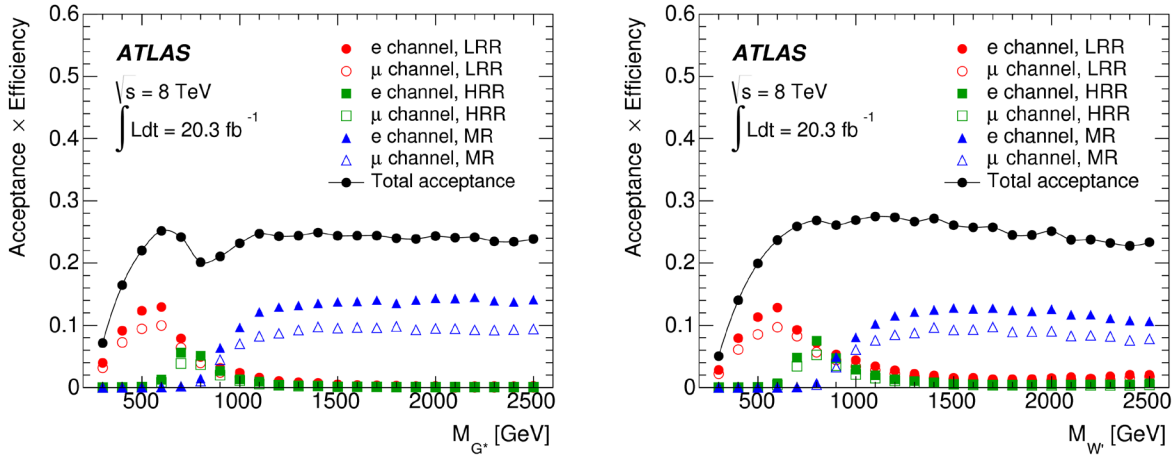

FIGURE 2. G^* (a) and W' (b) signal efficiencies in both channels and three signal regions. The efficiency is expressed with respect to the total number of $WW \to lvqq$ for G^* and $WZ \to lvqq$ for W' events with $l = e, \mu, \tau$ [4].

BACKGROUND ESTIMATION

The dominant background for this analysis arises from Standard Model (SM) production of the W/Z+jets, where one lepton from W or Z can be selected as a "signal" lepton and jets mimic hadronically decayed W or Z bosons. The backgrounds from SM production of single t and $t\bar{t}$ (top) are predominant, as a t quark decays to b quark and W boson. The next significant background appears from multijet production, that can mimic the analysis final state due to misidentification leptons. And finally, the small contribution from SM diboson production (WW, WZ, ZZ, $W\gamma$, $Z\gamma$) increases the total background.

The shapes of the W/Z+jets, top and diboson backgrounds are taken from the Monte Carlo (MC) simulation in the signal, control and validation regions. The shape of the multijet background is obtained by data driven method by creating enriched multijet data sample. The top and diboson backgrounds are normalized to the number of events from MC background samples. The normalizations of the W/Z+jets and multijet backgrounds are estimated by data driven method using the events in a control region, where the inverted cut on invariant mass is required: $45 < m_{jj/J} < 65$ GeV and $105 < m_{jj/J} < 200$ GeV. They are determined from binned minimum χ^2 fits to the $E_{\mathrm{T}}^{\mathrm{miss}}$ distributions in the control data samples corresponding to each signal region and channel separately. The fitted parameters are the normalizations of the W/Z+jets and multijet processes. Figure 3 shows an example for the low-p_{T} resolved region [4]. Multijet background is validated by the enriched multijet sample, that is obtained by inverting $E_{\mathrm{T}}^{\mathrm{miss}}$ cut: $E_{\mathrm{T}}^{\mathrm{miss}} < 30$ GeV for electron channel and $50 < E_{\mathrm{T}}^{\mathrm{miss}} < 80$ GeV for muon channel. $t\bar{t}$ background is also validated by the enriched top pairs sample by requiring at least 1 b-jet in the event.

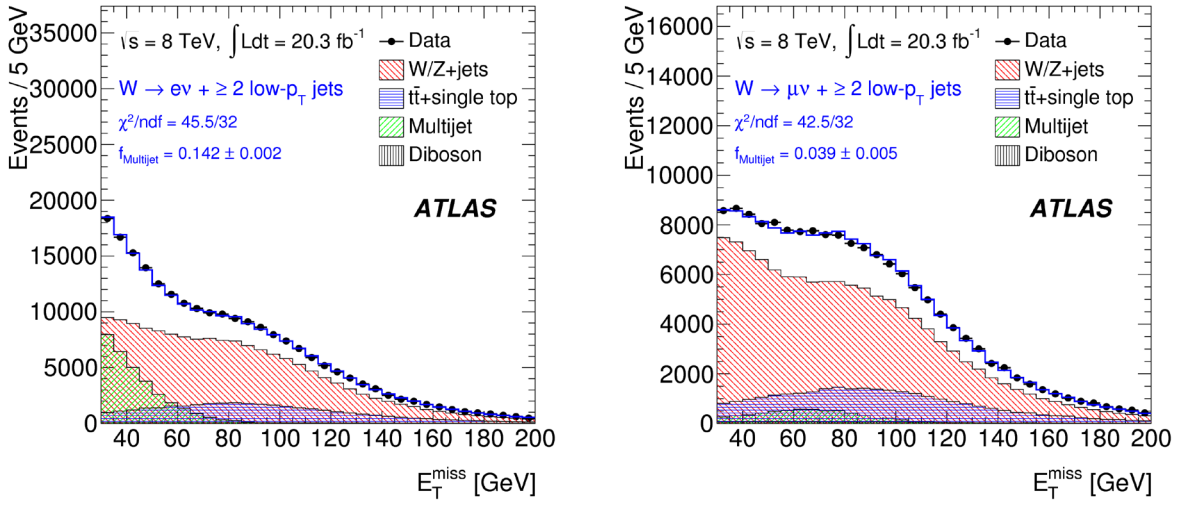

FIGURE 3. χ^2 fit to the E_T^{miss} spectrum in the electron (a) and muon (b) channels for the selected events of the W/Z+jets control sample in the low-p_T resolved regime. For reference, the fraction of the multijet background contribution ($f_{Multijet}$) is also calculated. The errors shown here are statistical only [4].

SYSTEMATIC UNCERTAINTIES

The systematic uncertainties on the background estimation, such as uncertainties on scale and shape of the W/Z+jets, multijet, $t\bar{t}$ and diboson backgrounds are included in the analysis. Also uncertainties due to single top production, parton distribution functions (PDF), initial- and final-state radiation modeling (ISR and FSR) uncertainties of the $t\bar{t}$ background are estimated. For the objects reconstruction the following sources of uncertainties are considered: for the leptons — electron and muon reconstruction, electron energy scale and resolution, muon momentum scale and resolution, for the missing transverse momentum — missing transverse momentum soft terms, for jets reconstruction — jet energy scale and resolution, jet mass scale and resolution, jet vertex fraction, momentum balance scale and resolution and b-tagging uncertainties. The dominant uncertainties on the signal come from ISR/FSR and PDF uncertainties. The uncertainty associated to the measurement of the integrated luminosity is also considered [4].

RESULTS AND INTERPRETATION

On Figure 4 (a) the table shows the total number of observed and predicted events for three signal regions and on Figure 4 (b) the histogram shows the reconstructed invariant mass m_{lvJ} distributions for data and backgrounds and also signal models in the merged signal region for the combined electron and muon channels [4]. There is a good agreement between data and background. 95% CL upper limits on the production cross section times branching fraction of RS G^* and EGM W' are determined for the interpretation of the result. These limits are calculated by performed fit of the likelihood to $m_{lvjj/J}$ by RooStats [5]. Upper limits are obtained using the CLs method [6] applied to binned histograms (templates) derived from MC. The fit is performed simultaneously to the electron and muon channels. In each channel five components are included in the fit for the $lvjj/J$ final state: signal (G^* or W'), W/Z+jets, multijet, top and diboson backgrounds. Systematic uncertainties are included as nuisance parameters. All tree signal regions and two lepton channels are combined. In order to stabilize the combined fit, not all tree signal regions are used in each mass point. A region is only used if it contributes more than 10% of the total signal sensitivity. The likelihood is performed for LRR from 300 to 800 GeV, for HRR from 600 to 1000 GeV and for MR from 800 to 2000 GeV. Figure 5 shows observed and expected 95% CL upper limits on the cross section times branching fraction as a function of the resonance pole mass for the G^* (a) and W' (b). The LO theoretical cross sections for G^* (a) and NNLO theoretical cross sections for W' (b) production are also shown. Resonance masses below 760 GeV and 1490 GeV are excluded for G^* and W' accordingly [4]. The shoulder, observed around 800 GeV, is a result of the transition between the high-p_{T} resolved and merged region.

Sample	LRR	HRR	MR
$W/Z+$jets	104800 ± 1600	415 ± 10	180 ± 20
$t\bar{t}+$single top	37700 ± 1600	271 ± 13	42 ± 7
Multijet	13500 ± 500	84 ± 9	29.3 ± 2.9
Diboson	5500 ± 270	96 ± 6	43 ± 7
Total	161500 ± 2300	870 ± 40	295 ± 22
Data	157837	801	323
G^* signal	7000 ± 500	36 ± 6	5.5 ± 2.3
W' signal	6800 ± 600	318 ± 21	70 ± 4

(a)

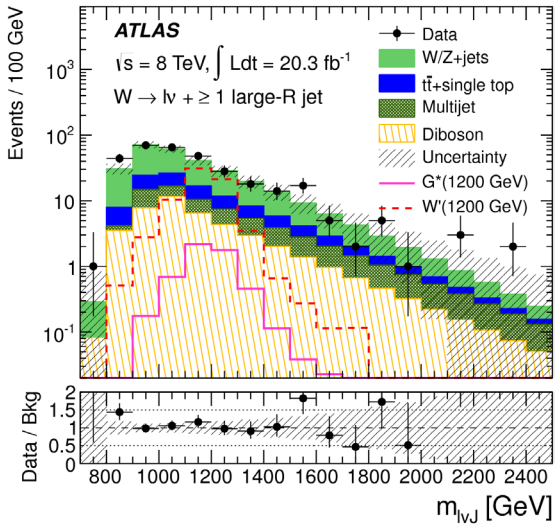

(b)

FIGURE 4. (a) the total number of observed and predicted events for tree signal regions, (b) the reconstructed m_{lvJ} distributions for data and backgrounds and also signal models in the merged signal region for the combined electron and muon channels [4].

CONCLUSION

As a result of the analysis no evidence for resonant diboson production is observed. 95% CL upper limits on the production cross section times branching fraction of G^* and W' are determined. Also resonance masses below 760 GeV and 1490 GeV are excluded for G^* and W' respectively [4], that is stricter as compared with the previous 7 TeV analysis results with lower limits on resonance masses 710 GeV for G^* and 950 GeV for W' [7]. Comparative results of other parallel 8 TeV analyses with different final states for ATLAS and CMS experiments are shown in Table 1. This analysis sets the most stringent limit for G^* resonance mass. Observed limit for the W' resonance mass is competitive with the ones obtained in parallel analyses.

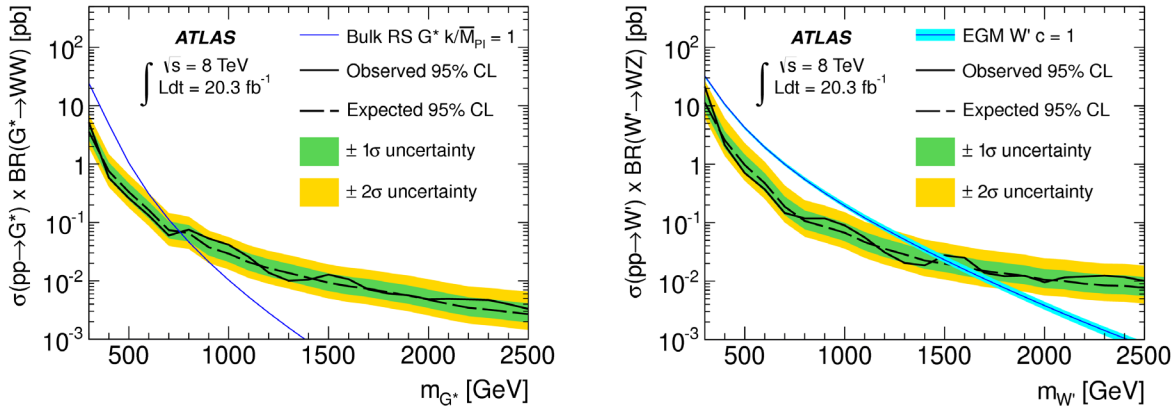

(a) (b)

FIGURE 5. Observed and expected 95% CL upper limits on the cross section times branching fraction as a function of the resonance pole mass for the G^* (a) and W' (b). The LO theoretical cross sections for the G^* (a) and NNLO theoretical cross sections for the W' (b) production are also shown. The inner and outer bands around the expected limits represent $\pm 1\sigma$ and $\pm 2\sigma$ variations respectively [4].

TABLE 1. Lower limits on resonance masses for 8 TeV analyses with semileptonic *lvqq* [4], semileptonic *llqq* [8], fully leptonic *lvll* [9] and fully hadronic *qqqq* [10] final states for ATLAS and semileptonic *lvqq* [11], fully leptonic *lvll* [12] and fully hadronic *qqqq* [13] for CMS experiments.

Experiments	**Channels**	$M(G^*)$	$M(W')$
ATLAS	$WW/WZ \to lvqq$	760 GeV	1490 GeV
	$WZ/ZZ \to llqq$	740 GeV	1590 GeV
	$WZ \to lvll$	—	1520 GeV
	$WW/WZ/ZZ \to qqqq$	2 TeV 2.6σ (WW)	1500 GeV
		2 TeV 2.9σ (ZZ)	2 TeV 2.5σ
CMS	$WW/WZ \to lvjj$	No limit set	—
	$WZ \to lvll$	—	1470 GeV
	$WW/WZ \to qqqq$	No limit set	1700 GeV

ACKNOWLEDGMENTS

This work is supported by the Russian MES grant RFMEFI61014X0005 and Presidential Grant NSh-999.2014.2 (Russia).

REFERENCES

[1] L. Randall and R. Sundrum, Phys. Rev. Lett. **83**, 3370–3373 (1999).
[2] G. Altarelli, B. Mele, and M. Ruiz-Altaba, Z. Phys. C **45**, p. 109 (1989).
[3] ATLAS Collaboration, JINST **3**, p. S08003 (2008).
[4] ATLAS Collaboration, Eur. Phys. J. C **75**, p. 370 (2015).
[5] L. Moneta and K. Belasco, PoS **ACAT2010**, p. 057 (2010).
[6] A. L. Read, J. Phys. G **28**, p. 2693 (2002).
[7] ATLAS Collaboration, Phys. Rev. D **87**, p. 112006 (2013).
[8] ATLAS Collaboration, Eur. Phys. J. C **75**, p. 69 (2015).
[9] ATLAS Collaboration, Phys. Let. B **737**, 223–243 (2014).
[10] ATLAS Collaboration, arXiv:1506.00962 [hep-ex] (2015).
[11] CMS Collaboration, JHEP **08**, p. 174 (2014).
[12] CMS Collaboration, Phys. Let. B **740**, 83–104 (2015).
[13] CMS Collaboration, JHEP **08**, p. 173 (2014).

Proceedings of the LHCP2015 Conference, St. Petersburg, Russia, August 31 - September 5, 2015

Editors: V.T. Kim and D.E. Sosnov

Study of $B_c^+ \to J/\psi D_s^+$ and $B_c^+ \to J/\psi D_s^{*+}$ decays with the ATLAS detector

SEMEN TURCHIKHIN[1,2]

[1]*D. V. Skobeltsyn Institute of Nuclear Physics, M. V. Lomonosov Moscow State University*
[2]*Faculty of Physics, M. V. Lomonosov Moscow State University*

Semen.Turchikhin@cern.ch

On behalf of the ATLAS Collaboration

Abstract. The results of the measurement of the $B_c^+ \to J/\psi D_s^+$ and $B_c^+ \to J/\psi D_s^{*+}$ decay properties with the ATLAS experiment are presented. The analysis uses pp collision data collected by ATLAS at $\sqrt{s} = 7$ and 8 TeV. The ratios of the branching fractions of the two decays and that of a reference mode $B_c^+ \to J/\psi\pi^+$ are measured. The transverse polarisation fraction in the $B_c^+ \to J/\psi D_s^{*+}$ decay is determined. The results are found to be in agreement with the earlier LHCb measurement. Available theoretical predictions for the measured properties are generally consistent with the data.

INTRODUCTION

The B_c^+ meson[1] is the only known weakly decaying particle consisting of two heavy quarks, thus providing a good probe for heavy quark dynamics. In the B_c^+ decays, both b and c quark decays compete; the $\bar{b}c$ annihilation process can also contribute substantially.

Properties of the $B_c^+ \to J/\psi D_s^+$ and $B_c^+ \to J/\psi D_s^{*+}$ decays are addressed in various theoretical calculations [1–7] and can also be compared to the analogous properties in the lighter B meson decays such as $B_d^0 \to D^{*-} D_s^{(*)+}$ or $B^+ \to \bar{D}^{*0} D_s^{(*)+}$ to test the factorisation approximation. These B_c^+ decays were recently observed by the LHCb experiment [8].

In this work, the measurement of their properties in the ATLAS experiment at LHC is presented [9]. The measured observables are the ratios of the branching fractions $\mathcal{R}_{D_s^+/\pi^+} = \mathcal{B}_{B_c^+ \to J/\psi D_s^+}/\mathcal{B}_{B_c^+ \to J/\psi\pi^+}$, $\mathcal{R}_{D_s^{*+}/\pi^+} = \mathcal{B}_{B_c^+ \to J/\psi D_s^{*+}}/\mathcal{B}_{B_c^+ \to J/\psi\pi^+}$, and $\mathcal{R}_{D_s^{*+}/D_s^+} = \mathcal{B}_{B_c^+ \to J/\psi D_s^{*+}}/\mathcal{B}_{B_c^+ \to J/\psi D_s^+}$, where $\mathcal{B}_{B_c^+ \to X}$ denotes the branching fraction of the $B_c^+ \to X$ decay. Also the fraction of transverse polarisation of the daughter particles in $B_c^+ \to J/\psi D_s^{*+}$ decay is determined.

RECONSTRUCTION AND EVENT SELECTION

The analysis uses the combined sample of pp collisions data collected by ATLAS at centre-of-mass energies $\sqrt{s} = 7$ TeV and 8 TeV corresponding to integrated luminosities of 4.9 fb^{-1} and 20.6 fb^{-1}, respectively. The detailed description of the ATLAS experimental setup can be found elsewhere [10].

The D_s^+ meson is reconstructed via the $D_s^+ \to \phi\pi^+$ decay with the ϕ meson decaying into a pair of charged kaons. The D_s^{*+} meson decays into a D_s^+ meson and a soft photon or π^0 not reconstructed in the analysis. The J/ψ meson is reconstructed via its decay into a muon pair.

Online event selection for the analysis is based on search for single-muon, dimuon, and three-muon signatures. Two muons are produced in the J/ψ decay and the third one can appear in semileptonic decays of the two other b and c hadrons present in a B_c^+ event.

[1]Charge conjugate states are implied throughout the paper.

The Monte Carlo (MC) samples used in the analysis were generated with Pythia 6.4 [11] along with a dedicated extension for B_c^+ production modelling [12–15]. Signal decays were simulated with EvtGen [16].

The $J/\psi \to \mu^+\mu^-$ candidates are built by combining two oppositely charged particle tracks identified as muons. For the $D_s^+ \to \phi(K^+K^-)\pi^+$ reconstruction, tracks of particles with opposite charges are assigned kaon mass hypotheses and combined in pairs to form ϕ candidates. An additional track is assigned a pion mass and combined with the ϕ candidate to form a D_s^+ candidate.

The $B_c^+ \to J/\psi D_s^+$ candidates are built by combining the five tracks of the J/ψ and D_s^+ candidates. The J/ψ meson decays instantly at the same point as the B_c^+ does (secondary vertex) while the D_s^+ lives long enough to form a displaced tertiary vertex. Therefore the five-track combinations are refitted assuming this cascade topology. The invariant mass of the muon pair is constrained to the nominal J/ψ mass [17]. The three D_s^+ daughter tracks are constrained to a tertiary vertex and their invariant mass is fixed to the mass of D_s^+ [17]. The combined momentum of the refitted D_s^+ decay tracks is constrained to point to the dimuon vertex.

The B_c^+ meson is reconstructed within the kinematic range $p_{\mathrm{T}}(B_c^+) > 15\,\mathrm{GeV}$ and $|\eta(B_c^+)| < 2.0$, where the detector acceptance is high and depends weakly on $p_{\mathrm{T}}(B_c^+)$ and $\eta(B_c^+)$.

Signal event selection is aimed mostly at suppression of the combinatorial background. The selection requirements use the following properties of the signal candidates to separate them from the background:

- kinematic properties of the reconstructed candidate tracks and intermediate resonances;
- cascade fit quality;
- displacement of the secondary and tertiary vertices;
- narrow invariant mass windows for the intermediate resonances (ϕ, D_s^+, J/ψ);
- angular distributions of the decay particle momenta.

Various possible exclusive background contributions were also studied. The only significant exclusive background contribution was found from the $B_s^0 \to J/\psi\phi$ decay process. This arises when the combination of the tracks from a true $B_s^0 \to J/\psi(\mu^+\mu^-)\phi(K^+K^-)$ decay with a fifth random track results in a fake $B_c^+ \to J/\psi(\mu^+\mu^-)D_s^+(K^+K^-\pi^+)$ candidate. This contribution is suppressed by rejecting the B_c^+ candidates with the invariant mass of $\mu^+\mu^-K^+K^-$ system close to the B_s^0 mass.

The mass distribution of the selected $B_c^+ \to J/\psi D_s^{(*)+}$ candidates is shown in Figure 1. The peak near the B_c^+ mass, $m_{B_c^+} = 6275.6$ MeV [17], is attributed to the signal of $B_c^+ \to J/\psi D_s^+$ decay while a wider structure between 5900 MeV and 6200 MeV corresponds to $B_c^+ \to J/\psi D_s^{*+}$ with subsequent $D_s^{*+} \to D_s^+\gamma$ or $D_s^{*+} \to D_s^+\pi^0$ decays where the neutral particle is not reconstructed.

SIGNAL FIT

An extended unbinned maximum likelihood fit is performed to evaluate the signal yields and the polarisation in the $B_c^+ \to J/\psi D_s^{*+}$ decay. The fit uses the information about the reconstructed $J/\psi D_s^+$ candidate mass and absolute cosine of the helicity angle, $\theta'(\mu^+)$, which is defined in the rest frame of the muon pair as the angle between the μ^+ and the D_s^+ candidate momenta.

The decay $B_c^+ \to J/\psi D_s^{*+}$ is a transition of a pseudoscalar meson into a pair of vector states and is thus described by the three helicity amplitudes, A_{++}, A_{--}, and A_{00}, where the subscripts correspond to the helicities of J/ψ and D_s^{*+} mesons. The contribution of the A_{++} and A_{--} amplitudes, referred to as the $A_{\pm\pm}$ component, corresponds to the J/ψ and D_s^{*+} transverse polarisation. The information about the polarisation is encoded both in the $J/\psi D_s^+$ mass distribution and in the distribution of the helicity angle. A simultaneous fit to the mass and angular distributions significantly improves the sensitivity to the polarisation in the $B_c^+ \to J/\psi D_s^{*+}$ decay with respect to a one-dimensional mass fit.

Four two-dimensional probability density functions (PDFs) are defined to describe the $B_c^+ \to J/\psi D_s^+$ signal, the $A_{\pm\pm}$ and A_{00} components of the $B_c^+ \to J/\psi D_s^{*+}$ signal, and the background.

The signal PDFs are factorised into mass and angular components. The mass distribution of the $B_c^+ \to J/\psi D_s^+$ signal is described by a modified Gaussian function [18]. For the mass description of the $B_c^+ \to J/\psi D_s^{*+}$ signal helicity components, templates produced from the MC samples are used. Angular shapes of all signals are also described with templates obtained from the MC simulation.

The background mass shape is described with a two-parameter exponential function. An angular PDF for the background is based on the templates extracted from the $|\cos\theta'(\mu^+)|$ distribution of the sidebands of the $J/\psi D_s^+$ mass spectrum.

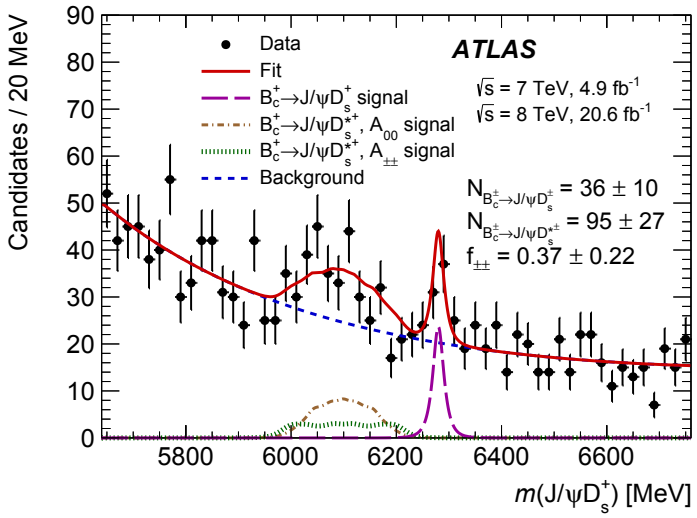

FIGURE 1. The mass distribution of the selected $J/\psi D_s^+$ candidates. The red solid line represents the projection of the fit model. The contribution of the $B_c^+ \to J/\psi D_s^+$ decay is shown with the magenta long-dashed line; the brown dash-dot and green dotted lines show the $B_c^+ \to J/\psi D_s^{*+}$ A_{00} and $A_{\pm\pm}$ component contributions, respectively; the blue dashed line shows the background model. The uncertainties of the listed fit result values are statistical only. Figure taken from Ref. [9].

The mass and angular projections of the fit on the selected $J/\psi D_s^+$ candidate dataset are also shown in Figures 1 and 2 (left), respectively. The signal yields, $N_{B_c^+ \to J/\psi D_s^+}$ and $N_{B_c^+ \to J/\psi D_s^{*+}}$, and the relative contribution of the $A_{\pm\pm}$ component to the $B_c^+ \to J/\psi D_s^{*+}$ decay rate in the selected sample, $f_{\pm\pm}$, are shown on the plot. In order to illustrate the effect of the angular part of the fit in separating the helicity components, the $|\cos\theta'(\mu^+)|$ fit projection for the subset of candidates with the masses 5950 MeV $< m(J/\psi D_s^+) <$ 6250 MeV corresponding to the region of the observed $B_c^+ \to J/\psi D_s^{*+}$ signal is shown in Figure 2 (right).

The statistical significance for the observed B_c^+ signal estimated from toy MC studies is 4.9 standard deviations.

NORMALISATION TO THE REFERENCE DECAY MODE

$B_c^+ \to J/\psi\pi^+$ decay is used as a normalisation mode for the branching fractions measurement. The decay candidates are reconstructed by fitting a common vertex of a pion candidate track and the two muons. Reconstruction and selection of the candidates is done in a very close manner to that of $B_c^+ \to J/\psi D_s^{(*)+}$ decays in order to reduce systematic uncertainties in the measured ratios of the branching fractions. Thus, the same selection requirements as used for the signal decay candidates are chosen for the normalisation mode where it is possible. Additionally, a veto on pion candidate tracks identified as muons is applied in order to suppress the substantial background from $B_c^+ \to J/\psi\mu^+\nu_\mu X$ decays.

Figure 3 shows the mass distribution of the selected candidates. It is fitted with a sum of a modified Gaussian function describing the $B_c^+ \to J/\psi\pi^+$ peak and an exponential function for the background. The extracted yield, $N_{B_c^+ \to J/\psi\pi^+}$, is shown on the plot.

The ratios of the branching fractions $\mathcal{R}_{D_s^+/\pi^+}$, $\mathcal{R}_{D_s^{*+}/\pi^+}$, and $\mathcal{R}_{D_s^{*+}/D_s^+}$ are calculated as

$$\mathcal{R}_{D_s^{(*)+}/\pi^+} = \frac{\mathcal{B}_{B_c^+ \to J/\psi D_s^{(*)+}}}{\mathcal{B}_{B_c^+ \to J/\psi\pi^+}} = \frac{1}{\mathcal{B}_{D_s^+ \to \phi(K^+K^-)\pi^+}} \times \frac{\mathcal{A}_{B_c^+ \to J/\psi\pi^+}}{\mathcal{A}_{B_c^+ \to J/\psi D_s^{(*)+}}} \times \frac{N_{B_c^+ \to J/\psi D_s^{(*)+}}}{N_{B_c^+ \to J/\psi\pi^+}},$$

$$\mathcal{R}_{D_s^{*+}/D_s^+} = \frac{\mathcal{B}_{B_c^+ \to J/\psi D_s^{*+}}}{\mathcal{B}_{B_c^+ \to J/\psi D_s^+}} = \frac{N_{B_c^+ \to J/\psi D_s^{*+}}}{N_{B_c^+ \to J/\psi D_s^+}} \times \frac{\mathcal{A}_{B_c^+ \to J/\psi D_s^+}}{\mathcal{A}_{B_c^+ \to J/\psi D_s^{*+}}},$$

where $\mathcal{A}_{B_c^+ \to X}$ is the total acceptance of the corresponding mode and $\mathcal{B}_{D_s^+ \to \phi(K^+K^-)\pi^+}$ is a partial branching fraction of the $D_s^+ \to \phi(K^+K^-)\pi^+$ decay with a kaon-pair mass within the ±7 MeV window around the nominal ϕ meson mass

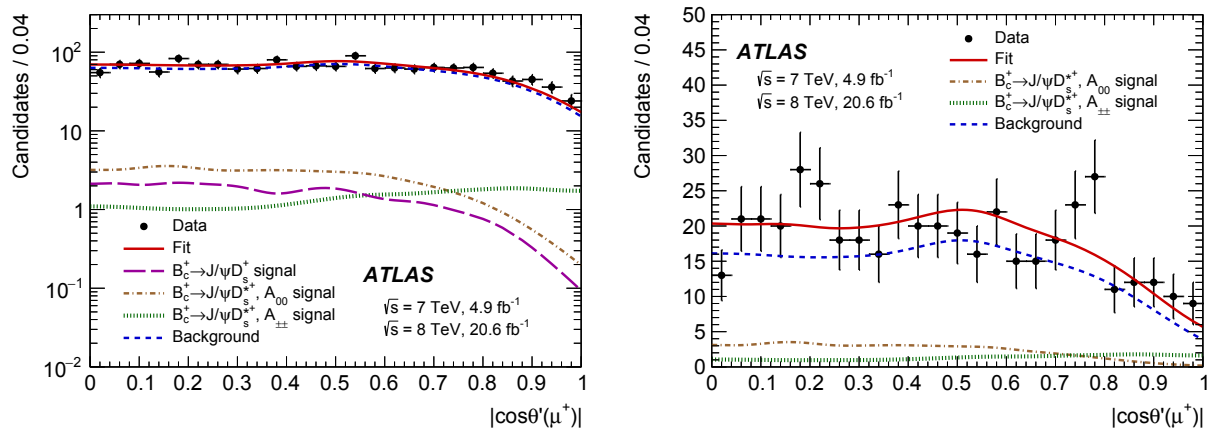

FIGURE 2. The projection of the likelihood fit on the variable $|\cos\theta'(\mu^+)|$ for (left) the full selected $J/\psi D_s^+$ candidate dataset and (right) a subset of the candidates in a mass range 5950 MeV $< m(J/\psi D_s^+) <$ 6250 MeV corresponding to the observed signal of $B_c^+ \to J/\psi D_s^{*+}$ decay. The red solid line represents the full fit projection. The contribution of the $B_c^+ \to J/\psi D_s^+$ decay is shown with the magenta long-dashed line; the brown dash-dot and green dotted lines show the $B_c^+ \to J/\psi D_s^{*+}$ A_{00} and $A_{\pm\pm}$ component contributions, respectively; the blue dashed line shows the background model. Figures taken from Ref. [9].

used in the analysis. This is interpolated from the measurement [19]. The acceptances are obtained from the MC simulation.

The transverse polarisation fraction, $\Gamma_{\pm\pm}/\Gamma$, is calculated from the $f_{\pm\pm}$ value by applying a correction to account for the slightly different acceptances for the two helicity component contributions.

Various sources of systematic uncertainties of the measured values were studied. Although some of them can have rather large effects on the individual decay rate measurements, they largely cancel in the ratios of the branching fractions due to correlation between the effects on the different decay modes.

The dominant systematic uncertainty originates from the signal extraction procedure, both for $B_c^+ \to J/\psi D_s^{(*)+}$ and $B_c^+ \to J/\psi\pi^+$ decays. Thus, the ratios of branching fractions measurement is mostly affected by variation of the signal and background mass shape parametrisations, while the major contribution to the uncertainty of the polarisation measurement is produced by varying the background angular modelling.

The statistical uncertainty of all measured observables prevails over the systematic one.

RESULTS AND CONCLUSION

The following ratios of the branching fractions are measured:

$$\mathcal{R}_{D_s^+/\pi^+} = 3.77 \pm 1.13\ (\text{stat.}) \pm 0.39\ (\text{syst.}) \pm 0.22\ (\text{BF}),$$
$$\mathcal{R}_{D_s^{*+}/\pi^+} = 10.36 \pm 3.13\ (\text{stat.}) \pm 1.47\ (\text{syst.}) \pm 0.61\ (\text{BF}),$$
$$\mathcal{R}_{D_s^{*+}/D_s^+} = 2.75\ ^{+1.19}_{-0.89}\ (\text{stat.}) \pm 0.30\ (\text{syst.}).$$

In the former two, the (BF) uncertainty corresponds to the limited knowledge of $\mathcal{B}(D_s^+ \to \phi(K^+K^-)\pi^+)$ and is counted separately from the systematic uncertainty. The transverse polarisation fraction in the $B_c^+ \to J/\psi D_s^{*+}$ decay is measured to be

$$\Gamma_{\pm\pm}/\Gamma = 0.38 \pm 0.23\ (\text{stat.}) \pm 0.07\ (\text{syst.}).$$

Figure 4 shows the comparison of the ATLAS results to those of the LHCb measurement [8] and to the expectations from various theoretical calculations. The polarisation is found to be well described by the available theoretical approaches. The measured ratios of the branching fraction are generally described by perturbative QCD, sum rules, and relativistic quark models. There is an indication of underestimate of the decay rates for the $B_c^+ \to J/\psi D_s^{(*)+}$ decays by some models, although the discrepancies do not exceed two standard deviations when taking into account only the experimental uncertainty. The measurement results agree with those published by the LHCb experiment.

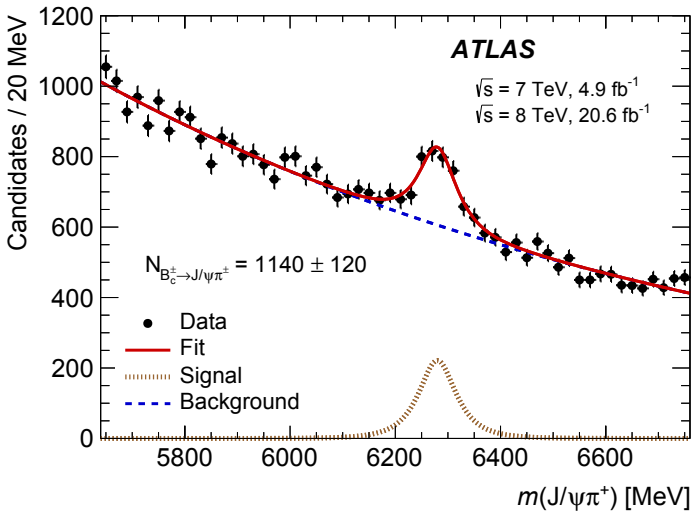

FIGURE 3. The mass distribution of the selected $B_c^+ \to J/\psi\pi^+$ candidates. The red solid line represents the result of the fit to the model described in the text. The brown dotted and blue dashed lines show the signal and background component projections, respectively. The uncertainty of the shown signal yield is statistical only. Figure taken from Ref. [9].

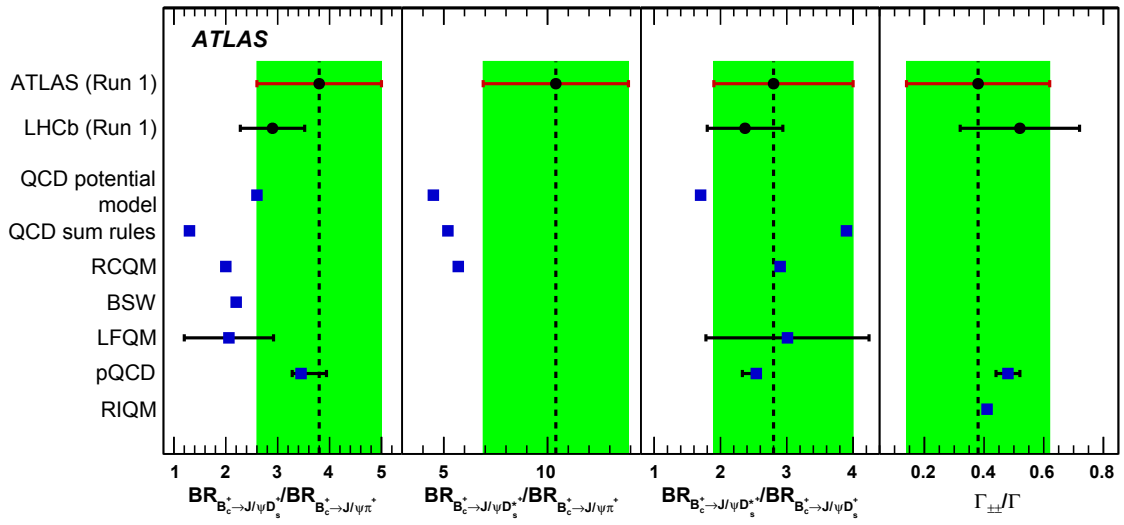

FIGURE 4. Comparison of the results of this measurement with those of LHCb [8] and theoretical predictions based on a QCD relativistic potential model [1], QCD sum rules [2], relativistic constituent quark model (RCQM) [3], BSW relativistic quark model (with fixed average transverse quark momentum $\omega = 0.40$ GeV) [4], light-front quark model (LFQM) [5], perturbative QCD (pQCD) [6], and relativistic independent quark model (RIQM) [7]. The uncertainties of the theoretical predictions are shown if they are explicitly quoted in the corresponding papers. Statistical and systematic uncertainties added in quadrature are quoted for the results of ATLAS and LHCb. Figure taken from Ref. [9].

ACKNOWLEDGMENTS

This work was partially supported by RFBR, research project No. 15-02-08133.

REFERENCES

[1] P. Colangelo and F. De Fazio, *Using heavy quark spin symmetry in semileptonic B_c decays*, Phys. Rev. D **61** (2000) 034012, arXiv:hep-ph/9909423 [hep-ph].

[2] V. Kiselev, *Exclusive decays and lifetime of B_c meson in QCD sum rules*, 2002, arXiv:hep-ph/0211021 [hep-ph].

[3] M. Ivanov, J. Korner, and P. Santorelli, *Exclusive semileptonic and nonleptonic decays of the B_c meson*, Phys. Rev. D **73** (2006) 054024, arXiv:hep-ph/0602050 [hep-ph].

[4] R. Dhir and R. Verma, *B_c Meson Form-factors and $B_c \to PV$ Decays Involving Flavor Dependence of Transverse Quark Momentum*, Phys. Rev. D **79** (2009) 034004, arXiv:0810.4284 [hep-ph].

[5] H.-W. Ke, T. Liu, and X.-Q. Li, *Transitions of $B_c \to \psi(1S, 2S)$ and the modified harmonic oscillator wave function in LFQM*, Phys. Rev. D **89** (2014) 017501, arXiv:1307.5925 [hep-ph].

[6] Z. Rui and Z.-T. Zou, *S-wave ground state charmonium decays of B_c mesons in the perturbative QCD approach*, Phys. Rev. D **90** (2014) 114030, arXiv:1407.5550 [hep-ph].

[7] S. Kar, P. Dash, M. Priyadarsini, S. Naimuddin, and N. Barik, *Nonleptonic $B_c \to VV$ decays*, Phys. Rev. D **88** (2013) 094014.

[8] LHCb Collaboration, R. Aaij, et al., *Observation of $B_c^+ \to J/\psi D_s^+$ and $B_c^+ \to J/\psi D_s^{*+}$ decays*, Phys. Rev. D **87** (2013) 112012, arXiv:1304.4530 [hep-ex].

[9] ATLAS Collaboration, *Study of the $B_c^+ \to J/\psi D_s^+$ and $B_c^+ \to J/\psi D_s^{*+}$ decays with the ATLAS detector*, arXiv:1507.07099 [hep-ex].

[10] ATLAS Collaboration, *The ATLAS Experiment at the CERN Large Hadron Collider*, JINST **3** (2008) S08003.

[11] T. Sjostrand, S. Mrenna, and P. Skands, *PYTHIA 6.4 Physics and Manual*, JHEP **0605** (2006) 026, arXiv:hep-ph/0603175 [hep-ph].

[12] A. Berezhnoy, A. Likhoded, and O. Yushchenko, *Some features of the hadronic $B_c^{(*)}$ meson production at large p_T*, Phys. Atom. Nucl. **59** (1996) 709–713, arXiv:hep-ph/9504302 [hep-ph].

[13] A. Berezhnoy, V. Kiselev, and A. Likhoded, *Hadronic production of S - and P-wave states of $\bar{b}c$-quarkonium*, Z. Phys. A **356** (1996) 79–87, arXiv:hep-ph/9602347 [hep-ph].

[14] A. Berezhnoy, V. Kiselev, A. Likhoded, and A. Onishchenko, *B_c meson at LHC*, Phys. Atom. Nucl. **60** (1997) 1729–1740, arXiv:hep-ph/9703341 [hep-ph].

[15] A. Berezhnoy, *Color flows for the process $gg \to B_c + c + \bar{b}$*, Phys. Atom. Nucl. **68** (2005) 1866–1872, arXiv:hep-ph/0407315 [hep-ph].

[16] D. Lange, *The EvtGen particle decay simulation package*, Nucl. Instrum. Meth. A **462** (2001) 152–155.

[17] K. A. Olive et al. (Particle Data Group), *Review of Particle Physics*, Chin. Phys. C **38** (2014) 090001.

[18] ZEUS Collaboration, S. Chekanov, et al., *Measurement of inelastic J/ψ production in deep inelastic scattering at HERA*, Eur. Phys. J. C **44** (2005) 13–25, arXiv:hep-ex/0505008 [hep-ex].

[19] CLEO Collaboration, J. Alexander, et al., *Absolute Measurement of Hadronic Branching Fractions of the D_s^+ Meson*, Phys. Rev. Lett. **100** (2008) 161804, arXiv:0801.0680 [hep-ex].

Proceedings of the LHCP2015 Conference, St. Petersburg, Russia, August 31 - September 5, 2015

Editors: V.T. Kim and D.E. Sosnov

The ATLAS Data Flow System for LHC Run 2

ANDREI KAZAROV[1,2]

[1]*CERN, CH1211 Geneva 23, Switzerland*
[2]*on leave from: Petersburg NPI Kurchatov NRC, Gatchina, Russian Federation*

Andrei.Kazarov@cern.ch

On behalf of the ATLAS Collaboration

Abstract. After its first shutdown, the LHC will provide pp collisions with increased luminosity and energy. In the ATLAS experiment, the Trigger and Data Acquisition system has been upgraded to deal with the increased event rates. The Data Flow element of the TDAQ is a distributed hardware and software system responsible for buffering and transporting event data from the readout system to the High Level Trigger and to the event storage. The DF has been reshaped in order to profit from the technological progress and to maximize the flexibility and efficiency of the data selection process. The updated DF is radically different from the previous implementation both in terms of architecture and expected performance. The pre-existing two level software filtering, known as Level 2 and the Event Filter, and the Event Building are now merged into a single process, performing incremental data collection and analysis. This design has many advantages, among which are: the radical simplification of the architecture, the flexible and automatically balanced distribution of the computing resources, the sharing of code and services on nodes. In addition, logical HLT computing cluster slicing, with each slice managed by a dedicated supervisor, has been dropped in favour of global management by a single master operating at 100 kHz. The Data Collection network that connects the HLT processing nodes to the Readout and the storage systems has evolved to provide network connectivity as required by the new Data Flow architecture. The old Data Collection and Back-End networks have been merged into a single Ethernet network and the Readout PCs have been directly connected to the network cores. The aggregate throughput and port density have been increased by an order of magnitude and the introduction of Multi Chassis Trunking significantly enhanced fault tolerance and redundancy. We will discuss the design choices, the strategies employed to minimize the data-collection latency, architecture and implementation aspects of DF components.

INTRODUCTION

The ATLAS experiment [1] is one of the major experiments of the Large Hadron Collider (LHC). It is a general purpose experiment, aiming at studying the Standard Model Higgs Boson, and looking for physics beyond the Standard Model of particle physics. It consists of various charged particle tracking detectors (the Inner Detector), a liquid-argon based electromagnetic and a hadronic calorimeter and a muon spectrometer. The detector provides many millions of read-out channels, able to capture data every 25 ns. This volume of data can not be recorded and kept for further data analysis. The ATLAS Trigger & Data Acquisition (TDAQ) system is responsible for the readout, selection and delivering to the permanent storage of the physics events and also for central infrastructure services like Controls, Configuration and Monitoring. TDAQ plays a fundamental role in the ATLAS experiment operation.

The TDAQ system performed very well during LHC Run 1 (2009-2012) [2], in many aspects well beyond its design values. It allowed ATLAS to collect events relevant for physics analyses with a high efficiency and desired event recording rates.

This paper focuses on the evolution of the Data Flow (DF) system. DF is the TDAQ component responsible for reading out and buffering ATLAS detector event fragments at Level 1 trigger rate, providing necessary fragments and events to the High-Level Trigger (HLT) system, building the selected events and finally sending them to the permanent storage as shown in Fig. 1.

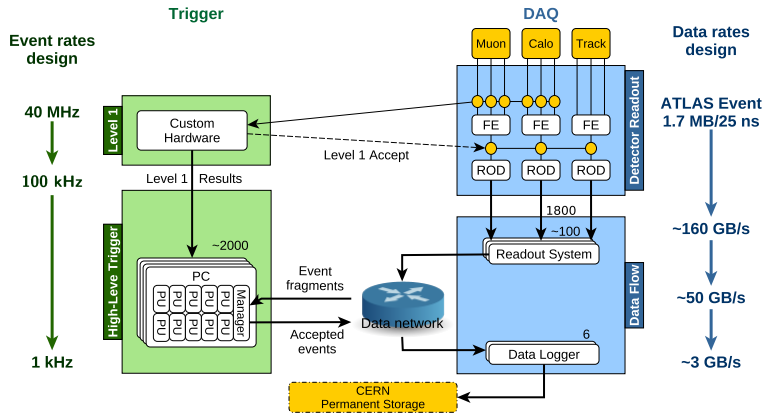

FIGURE 1: TDAQ architecture for Run 2.

New requirements for Data Flow system for Run 2

LHC Run 2 started in June 2015, bringing higher collision energy, luminosity and Level-1 trigger rate limitations as summarized in Table 1.

TABLE 1: Characteristic properties of LHC Run 1 and expected values for Run 2.

	Bunch spacing [ns]	Inst. luminocity $[cm^{-2}s^{-1}]$	L1 accept rate [kHz]	Readout fraction [%]	Event building bandwidth [GBps]	Peak recording rate [kHz/GBps]	N of readout channels	Event size (max) [MB]
Run 1	50	$8x10^{33}$	70	15	10	1/1.6	1600	1.6
Run 2	25	$1.7x10^{34}$	100	50	50	2/3	1800	2.0

In order to meet the updated requirements, the DF system was redesigned and reimplemented in the course of LHC long shutdown 1 (LS1). This process resulted in a simpler and streamlined design taking advantage of new hardware and software technologies.

New Data Flow architecture

The updated DF architecture (Fig. 2) is radically different from the previous implementation. The Region of Interest (RoI) concept has been kept, and processing and data collection proceeds in stages, beginning with fast algorithms based on RoIs. The decision when to build the full event is flexible, and afterwards more off-line style algorithms have access to the full event. Two levels of software filtering, known as Level 2 and the Event Filter are now merged into a single level, performing incremental data collection and analysis on the nodes of the flat HLT computing cluster. This design has many advantages, in particular:

- the radical simplification of the architecture, reducing number of components, dependencies and communication patterns;
- flexible and implicitly balanced utilization of the computing resources over the cluster, based on the active HLT algorithms;
- sharing of HLT code and services on the cluster nodes among all processing units, reducing the memory and resources utilization and allowing to run more HLT processing unit instances per node.

In addition, logical cluster slicing, with each slice managed by a dedicated supervisor, has been dropped in favour of global management by a single master (HLTSV) operating at 100 kHz. This simplifies management of the cluster utilization at the cost of higher reliability requirements for the central node. These were addressed by adding an idle backup element to the system.

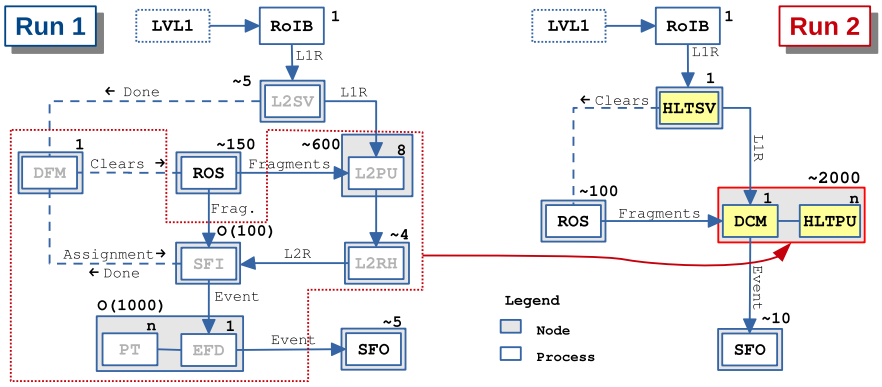

FIGURE 2: Evolution of DF architecture from Run 1 (provided as reference. A detailed description can be found in Ref. [2]) to Run 2.

As shown in Fig. 2, the system is composed of the following elements:

- the Readout System (ROS) buffers front-end data from the detectors and provides a standard interface to the DF;
- the Region of Interest Builder (RoIB) receives L1 trigger information and RoIs and combines the information for the HLT Supervisor;
- the HLT supervisor (HLTSV) schedules events to the HLT cluster, clears ROS buffers and handles possible time-outs;
- the Data Collection Manager (DCM) handles all I/O on the HLT nodes, including RoI requests from the HLT and full event building;
- the HLTPU processing tasks are forked from a single mother process to maximize memory sharing and run the ATLAS Athena/Gaudi framework performing event selection;
- the Data Loggers (SFO) are responsible for saving accepted events to disk, and for sending the files to permanent data storage.

All elements in the system are communicating via high-performance data and control Ethernet networks.

Data and Control networks

The Data network experienced a significant technological upgrade and simplification. With Multi-Chassis Trunking, a Brocade proprietary technology, the core routers provide load balancing and link redundancy to the network (Fig. 3). This is achieved by creating aggregated links on the devices connected to the routers. The latter are perceived as a single virtual network device. A proprietary protocol running between the two routers ensures the Routing and Forwarding table synchronization between the two network cores.

The internal architecture of the routers incorporates a major improvement in the packet forwarding capacity by introducing the Virtual Output Queuing (VOQ) technique which, already at the input stage, assigns different packet queues to each output port. Thanks to the VOQ technique, the packets addressed to a given output port can be forwarded independently of the traffic going to the other output ports, removing the head-of-line blocking phenomenon.

The Control network is a parallel network to the Data network in which the traffic for the control, configuration and monitoring of the TDAQ infrastructure flows. There are not strong performance requirements for the control network so the main upgrade activities concerned the redundancy and fail-over techniques. As part of the redundancy improvements, an Active-Backup setup has been installed for all important nodes in the system.

Figure 4 shows the achieved Data Collection bandwidth (which is a data flow from the ROS to the HLT cluster) during a test run (comparing to Run 1 capacity) and bandwidth utilization during a p-p run in 2015.

The following sections give more details on the DF components.

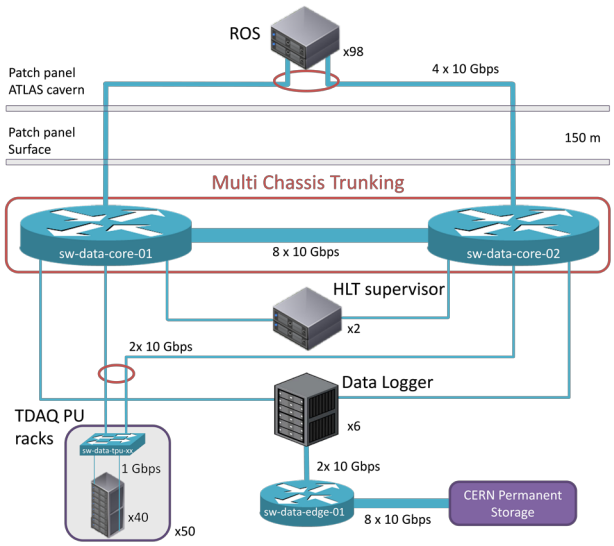

FIGURE 3: TDAQ Data network topology.

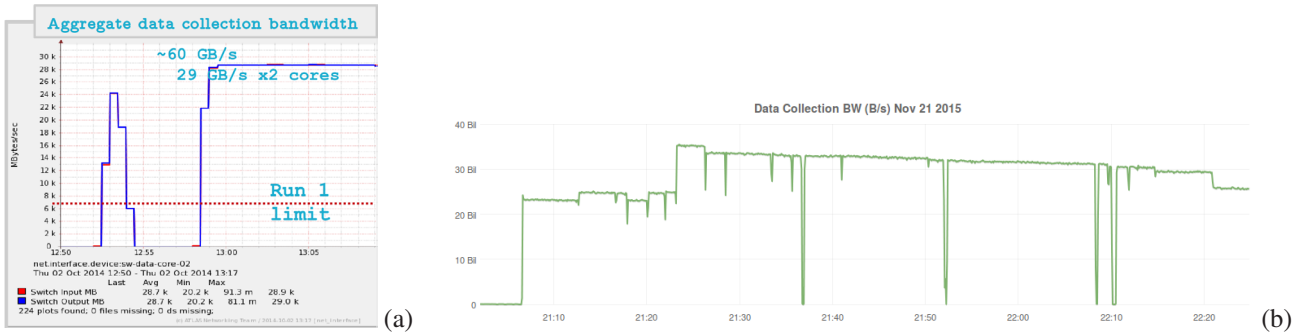

(a) (b)

FIGURE 4: Data Collection bandwidth utilization in a test run (a) and in one of p-p runs in Nov 2015 (b).

Region of Interest Builder

The RoIB is a 9U VME based custom hardware solution, consisting of multiple cards. The original hardware from Run 1 is the current baseline. Larger input fragments for the Run 2 upgrade show that the hardware is close to its limits. A replacement based on a custom board is being developed, using common hardware between ROS and RoIB [3].

A single PCI Express board integrated directly into the HLT supervisor will suffice for all 11 inputs, and combining of the input fragments will be done in software. First test results in the lab are very promising, far exceeding the requirements.

Read-Out System

Addition of new detectors to ATLAS, higher luminosity and L1 trigger rates requires a more dense and a more performant readout system. Therefore the ROS system went through a full overhaul. Fully new ROS PCs feature: 2U form factor instead of 4U; 4x10GbE per ROS PC (was 2x GbE); higher density of optical links per server: 12 per input card, 2 cards per PC [4].

ROS PC hosts a new powerful input card (S-Link input and buffer hardware) which is based on ALICE C-RORC card [5] with ATLAS firmware and software. It includes: 8x PCI Express lanes Xilinx Virtex-6 @ 125MHz FPGA; DDR3-1600 SO-DIMM RAM 2x4GB Buffer memory; 12 input optical channels.

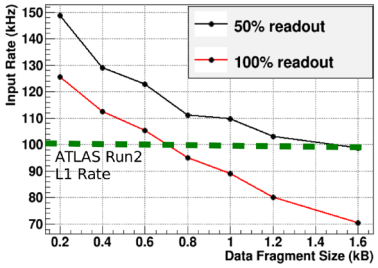

FIGURE 5: Sustained input rate of ROS as a function of readout fraction and fragment size. Taken from Ref. [4].

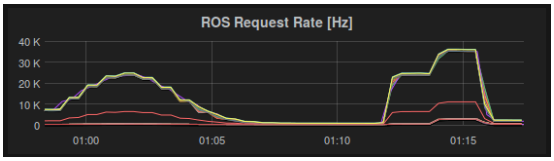

FIGURE 6: A screenshot of the online monitoring tool showing request rate to all ATLAS ROSes during a special run.

The connectivity of the ROS PCs to the HLT computing cluster is provided by four 10 GbE ports on two dual-port network interface cards.

A fully connected (24 links) ROS can sustain up to 50% readout for a wide set of request patterns (e.g. 35kHz of L1 during a scan run in 2015 as shown in Fig. 6). A ROS with fewer input links and/or small enough fragments can provide fragments at 100 kHz.

Software components

The following subsections describe the features of the main DF software components, running on more then 2400 commodity PCs in the HLT computing cluster.

Data Collection Manager

The DCM is a single application per HLT node. It deals with all data requests from multiple HLT processing tasks on the same node. It handles all requests to the ROS and communicates to the tasks via sockets and shared memory. Its design is essentially single-threaded based on non-blocking I/O using the Boost ASIO [6] library. A credit based traffic shaping mechanism [7] is used to prevent overloading the incoming network link on switches. For the selected events, DCM compresses the event payload before sending it to the data logger.

HLT Supervisor

A single HLT supervisor replaces the set of L2 supervisors used in Run 1. It uses a heavily multi-threaded, asynchronous design using the Boost ASIO library for communication and Intel Thread Building Blocks [8] for concurrent data structures. It reads RoIB fragments from 2x optical inputs links and sends assigned events to the HLT cluster via 2x10GbE links. A single HLTSV application can handle the input from the RoIB and manage the HLT cluster of 2000 machines at 115 kHz under realistic ATLAS conditions. In the future it is foreseen to merge the RoIB and HLTSV functionalities into a single PC equipped with C-RORC cards.

HLT Processing Unit

The HLT processing unit encapsulates the Athena framework [9] that executes the actual HLT algorithms. It communicates with the DCM for I/O requests and provides the trigger decision for each event. On each node a mother process is started first and goes through all the configuration process. A set of child processes is forked when a run starts. Thanks to the Linux kernel copy-on-write feature the memory sharing across the child process is maximized, hence the memory usage per node is minimized. Crashed HLT applications can be quickly replaced by forking another child instance. Tests with the full 2012 trigger menu show a memory consumption on a node of 1.8 GByte for the mother process plus 700 MB per child process. On a 12 core server this corresponds to 50% memory saving.

Transient Data Storage

In Run 1 the transient data storage [10] was implemented with storage server equipped with internal raid card. For Run 2 external SAS units with multiple front-ends and redundant data paths for fault tolerance and resilience are used (Fig. 7). Total capacity of the system is 340 TB, allowing ATLAS to record data being disconnected from offline storage

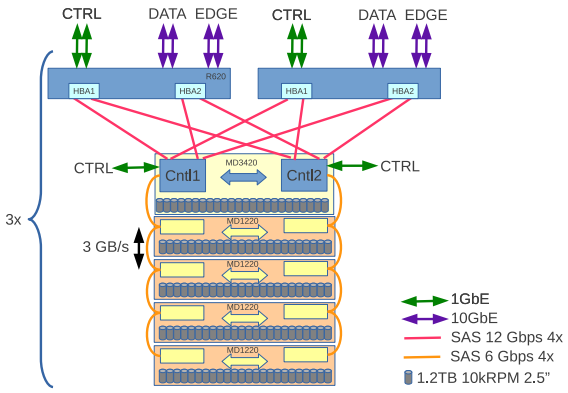

FIGURE 7: Internal architecture of a SFO unit.

for at least 24hrs. Performance depends on the trigger menu, number of streams, etc. In typical configurations, 4 GB/s of peak recording bandwidth is available.

Background jobs copy the files to permanent storage, deleting them on the local disk only when they are safely stored on tape.

Conclusions

The smooth operation of the TDAQ system has a direct impact on the efficiency of the ATLAS experiment and on the achievement of its Physics goals. In this paper we have shown how the Data Flow architecture has been reshaped during the LS1 in order to profit from the technological progress and to maximize the flexibility and efficiency of the data selection process.

REFERENCES

[1] The ATLAS Collaboration, JINST **3**, p. S08003 (2008).

[2] G. Avolio, S. Ballestrero, and W. Vandelli, Physics Procedia **37**, 1819 – 1826 (2012), proceedings of the 2nd International Conference on Technology and Instrumentation in Particle Physics (TIPP 2011).

[3] R. Blair, G. J. Crone, B. Green, J. Love, J. Proudfoot, O. Rifki, W. Panduro Vazquez, W. Vandelli, J. Zhang, and B. Abbott, "The Evolution of the Region of Interest Builder for the ATLAS Experiment at CERN," Tech. Rep. ATL-DAQ-PROC-2015-052 (CERN, Geneva, 2015).

[4] A. Borga, "Evolution of the ReadOut System of the ATLAS experiment," Tech. Rep. ATL-DAQ-PROC-2014-012 (CERN, Geneva, 2014).

[5] A. Borga, F. Costa, G. Crone, H. Engel, D. Eschweiler, D. Francis, B. Green, M. Joos, U. Kebschull, T. Kiss, A. Kugel, J. P. Vazquez, C. Soos, P. Teixeira-Dias, L. Tremblet, P. V. Vyvre, W. Vandelli, J. Vermeulen, P. Werner, and F. Wickens, Journal of Instrumentation **10**, p. C02022 (2015).

[6] Boost asio library, https://think-async.com, .

[7] T. Colombo and ATLAS Collaboration, Journal of Physics: Conference Series **608**, p. 012005 (2015).

[8] Intel Corporation, Intel threading building blocks library, https://www.threadingbuildingblocks.org, .

[9] The ATLAS Collaboration, *ATLAS Computing: technical design report*, Technical Design Report ATLAS (CERN, Geneva, 2005).

[10] A. Battaglia, H. Beck, M. Dobson, S. Gadomski, K. Kordas, and W. Vandelli, "Performance of the final data-logging system of the trigger and data acquisition for the ATLAS experiment at CERN," in *Nuclear Science Symposium Conference Record, 2008. NSS '08. IEEE* (2008), pp. 2173–2179.

Proceedings of the LHCP2015 Conference, St. Petersburg, Russia, August 31 - September 5, 2015

Editors: V.T. Kim and D.E. Sosnov

Performance of the ATLAS Tile Calorimeter

ALEXANDER SOLODKOV

State Research Center of Russian Federation - Institute for High Energy Physics of National Research Center "Kurchatov Institute", 1, Nauki square, 142281, Protvino, Moscow region, Russian Federation

On behalf of the ATLAS Collaboration

Abstract. The Tile Calorimeter (TileCal), the central section of the hadronic calorimeter of the ATLAS experiment, is a key detector component to detect hadrons, jets and taus and to measure the missing transverse energy. Due to the very good muon signal to noise ratio it assists the spectrometer in the identification and reconstruction of muons. The calorimeter consists of thin steel plates and 460,000 scintillating tiles configured into 5182 cells, each viewed by two photomultipliers. The calorimeter response and its readout electronics is monitored to better than 1% using radioactive source, laser and charge injection systems. The performance of the calorimeter has been measured and monitored using calibration data, cosmic ray muons and the large sample of proton-proton collisions acquired in 2011 and 2012. The results demonstrate a very good understanding of the performance of the Tile Calorimeter that is well within the design expectations.

INTRODUCTION

The ATLAS Tile Calorimeter [2] (TileCal) is the central hadronic calorimeter section of the ATLAS experiment [3] at the CERN Large Hadron Collider [4]. TileCal is a sampling calorimeter made of scintillating tiles as active medium and steel plates as absorbers. It is divided into long barrel (LB), and two extended barrel (EB) cylinders (Fig. 1.left), covering in total a pseudorapidity range of $|\eta| < 1.7$ and is segmented into 64 modules along the azimuth angle ϕ. The length of the LB is 5.56 m and the length of each EB is 2.91 m. Wavelength shifting fibers collect the light generated in the tiles and carry it to photomultipliers (PMT) (Fig. 1.right). Two fibers, attached to every tile from different sides in ϕ, go to different PMTs, providing redundant double readout of a signal. Each PMT receives signal from multiple tiles which are grouped into cells of different size depending on their pseudorapidity and depth. Three longitudinal layers A, BC, D are defined inside the modules and the dimensions of the cells are optimized to obtain a structure of projective towers with granularity of $\Delta\eta \times \Delta\phi = 0.1 \times 0.1$ in the first two layers (A,BC) and $\Delta\eta \times \Delta\phi = 0.2 \times 0.1$ in the outer layer (D) (see cell layout in Fig. 3). Cells of an additional special layer E, attached to extended barrel modules, are read out by a single PMT each. In total, TileCal has 5182 cells and 9852 channels.

ENERGY RECONSTRUCTION AND CALIBRATION PROCEDURE

The signal from the PMTs is shaped and amplified using two gains (1:64) with 10-bits ADCs every 25 ns. The digitized signals are reconstructed with the Optimal Filtering algorithm [5], which computes for each channel the signal amplitude, time and quality factor. A series of calibration constants, C_i are used to convert the reconstructed channel amplitude in ADC-counts (A) to energy (E)

$$E = A \times C_{ADC \to pC,CIS} \times C_{pC \to GeV,TB} \times C_{Cs} \times C_{Laser} \quad (1)$$

The constant $C_{pC \to GeV,TB} = 1.05$ pC/GeV, is the global electromagnetic scale of the TileCal, obtained during beam tests of 11% of the modules using electrons [6]. The other three calibration constants are derived using dedicated calibration systems. Different calibration systems control different parts of the readout chain (Fig. 2.left) and three systems together allow to maintain the electromagnetic scale across the calorimeter with precision of about 1% [1].

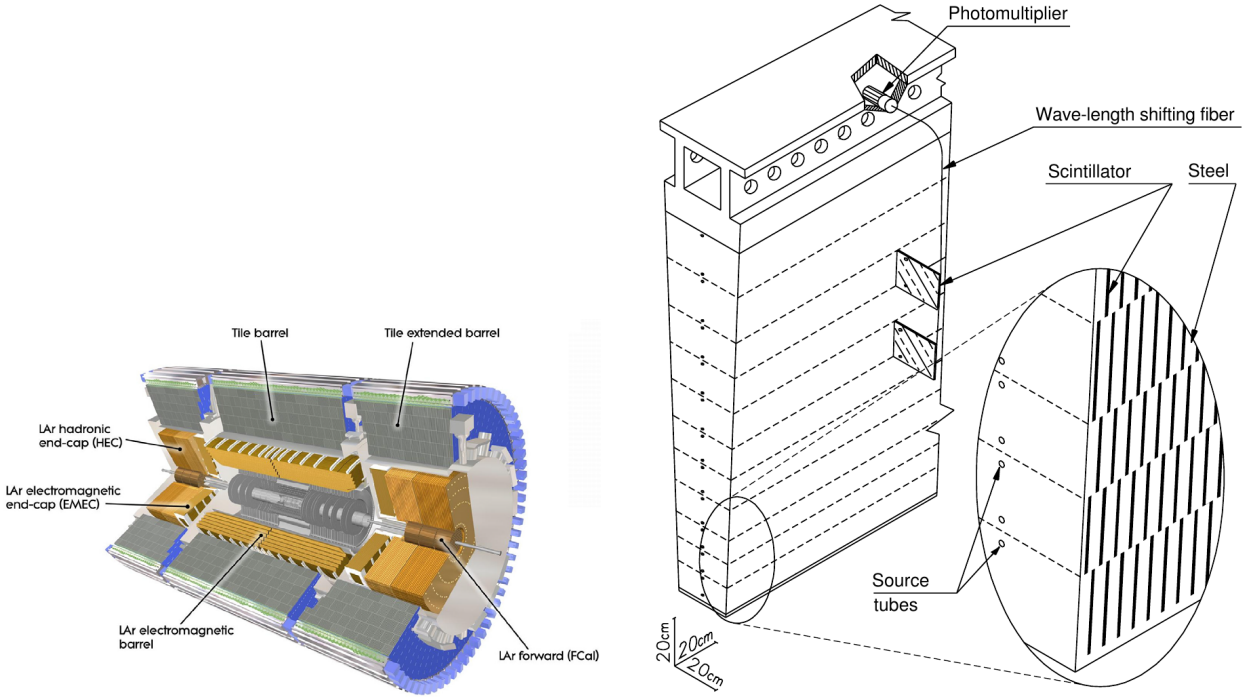

FIGURE 1. Left: A cut-away drawing of the ATLAS inner detector and calorimeters. The Tile Calorimeter consists of one barrel and two extended barrel sections and surrounds the Liquid Argon barrel electromagnetic and endcap hadronic calorimeters. Right: Schematic of one TileCal module showing the system of signal collection. The trapezoidal scintillating tiles are oriented radially and normal to the beam line and are read out by fibres coupled to their non-parallel sides. Figures are taken from Ref. [1].

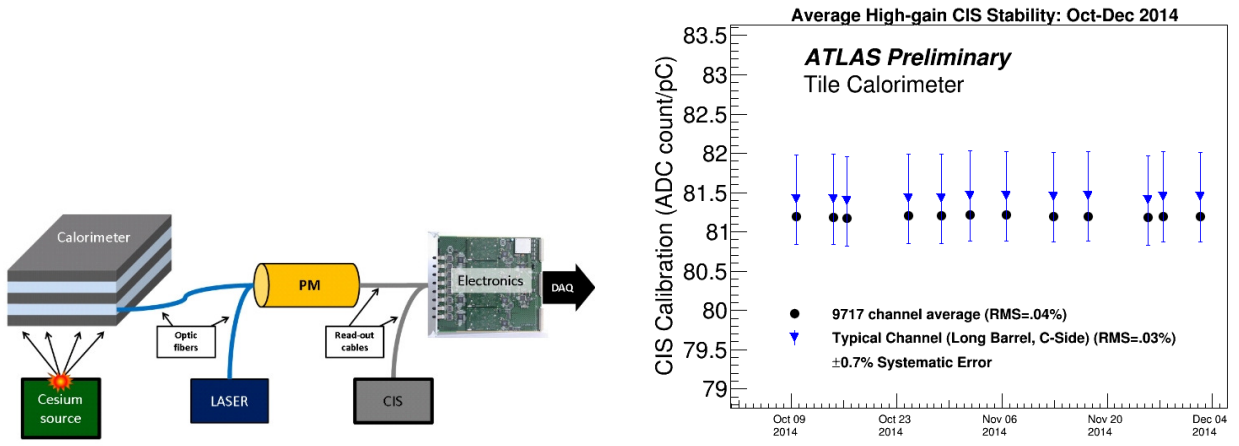

FIGURE 2. Left: The ATLAS Tile Calorimeter calibration chain. Right: TileCal-wide CIS calibration constant averages of all the high-gain channels for each CIS calibration run from 01 Oct 2014 to 04 Dec 2014. Figures are taken from Ref. [7].

The Charge Injection System

The Charge Injection system (CIS) is used to calibrate the readout electronics by injecting a known charge and measuring the resulting response of the electronics. This allows to determine the conversion factor from pC to ADC counts $C_{ADC \to pC}$. The injected charge spanned a range of values scanning both the high gain and the low gain range. This system is also used to monitor the front-end electronics and correct for non-linearities. During data taking CIS calibration runs are performed twice per week. The overall stability of the calibration factor is at the level of 0.02%

(Fig. 2.right). Less than 1% of channels exhibits large fluctuations and their calibration constants are updated if the deviation from previous measured value is above 0.7% - CIS systematic error.

The Laser System

In the Laser System the light of adjustable intensity is sent directly to the PMTs via clear fibers and by reconstructing the signal it is possible to extract the PMT gain. Laser calibrations are typically taken together with CIS calibrations twice per week and the main purpose of the system is to monitor and to measure the individual PMT gain variations between the monthly cesium scans. It can also measure the variation over longer time period and one example of such a measurement over the period of six months, from April to October 2012 is shown in Fig. 3. Here PMT drift is averaged over cells of the same type in 64 modules. In 2012 the maximum drift was observed in the E cells (-2.6%) and A cells (-1.3%) which are the cells with the highest energy deposit. The stability of the calibration system itself is better than 0.5% over the period of one month.

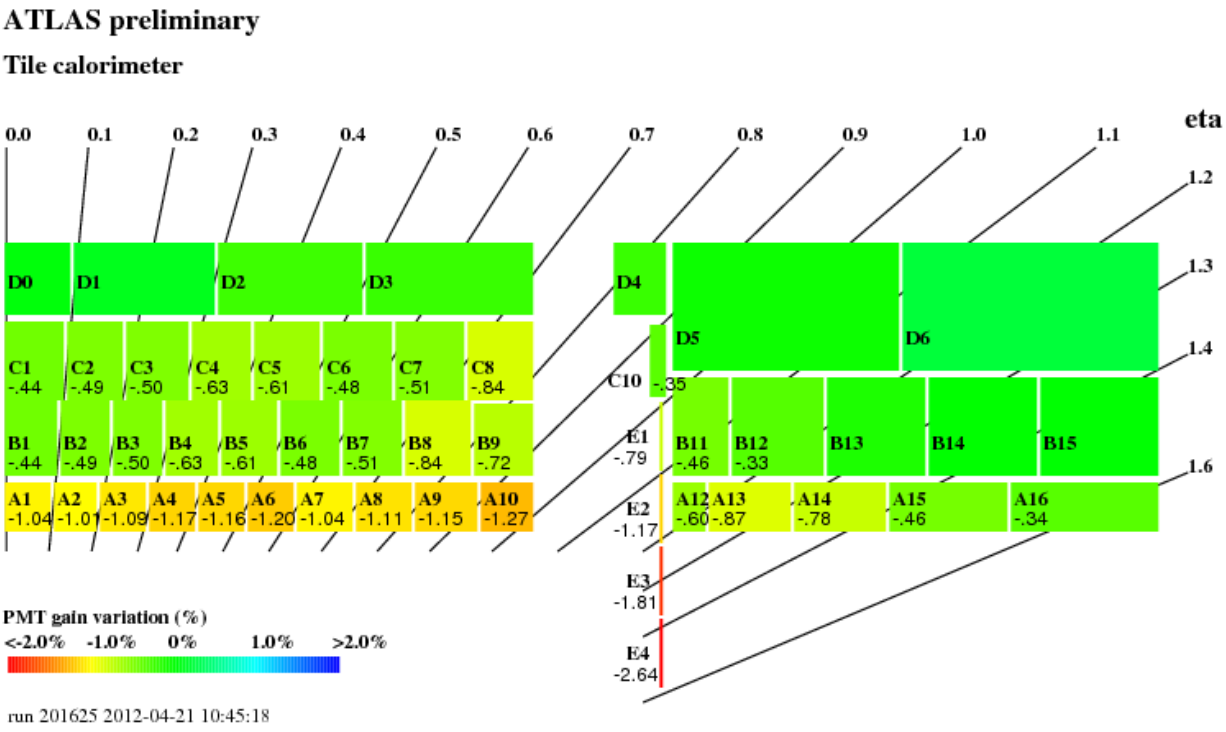

FIGURE 3. Difference in PMT response in % (averaged over 64 modules) measured in two laser calibration runs in April and October 2012. Figure is taken from Ref. [7].

The Cesium System

The Cesium calibration system uses movable ^{137}Cs γ-source, emitting 0.662 MeV photons to illuminate every single scintillator. The signal generated by the Cs source is read out through a special integrator readout that integrates the analog PMT signals with time constant $\tau = 90$ ms. This system and associated constant are used to calibrate the scintillators, PMTs, and to correct for residual cell differences. Cesium calibrations are taken approximately every month and precision of the measurements is at the level of 0.3%. The deviation of C_{Cs} calibration constant from 1 for A cells (in %) over the period of 6 years (2009-2015) is shown in Fig. 4.left. All the cells were equalized in June 2009 by adjusting PMT HV voltage and the next equalization was done in February 2015. The big gap between February 2013 and July 2014 corresponds to the electronics maintenance campaign during long shutdown.

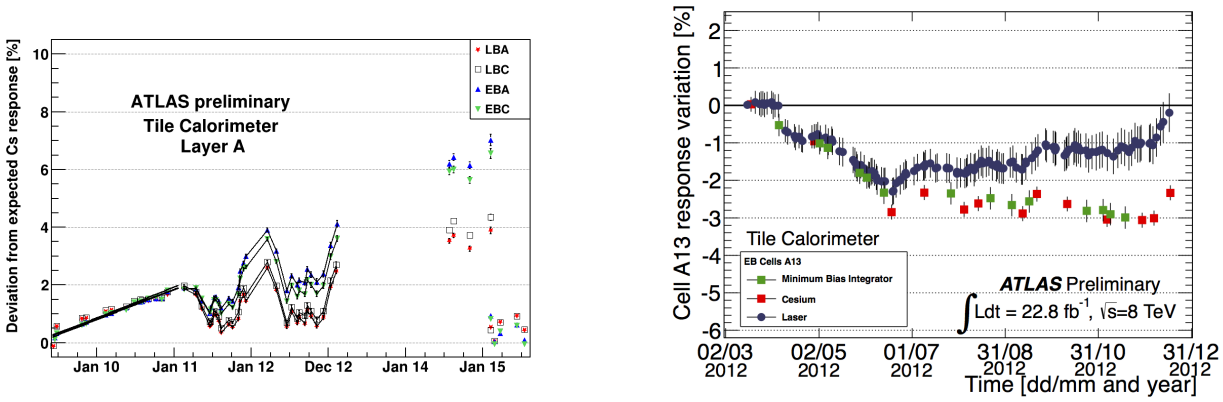

FIGURE 4. Left: Variation of Tile Calorimeter response in barrel (LBA, LBC) and extended barrel (EBA, EBC) over period of 6 years measured in Cesium calibration runs averaged over all cells in layer A. Right: Variation of the response in cell A13 ($1.2 < |\eta| < 1.3$) during 2012 measured by 3 calibration systems: Minimum Bias (red squares), Cesium (green squares), Laser (blue circles). Figures are taken from Ref. [7].

Combination of the Calibration Systems

In addition to three calibration systems mentioned above, TileCal has the Minimum Bias System. The system uses the integrator readout and measures the detector response to the minimum-bias events. It is used for the monitoring of the instantaneous luminosity in ATLAS. Both the Minimum Bias and the Cesium systems measure the signal coming from scintillators and variation in PMT response over time is expected to be the same. The difference between Laser and Minimum Bias (or Cesium) response allows to estimate the effect of the scintillators irradiation, which found to be at the level of 2% for the most irradiated cell A13 in 2012 (Fig. 4.right)

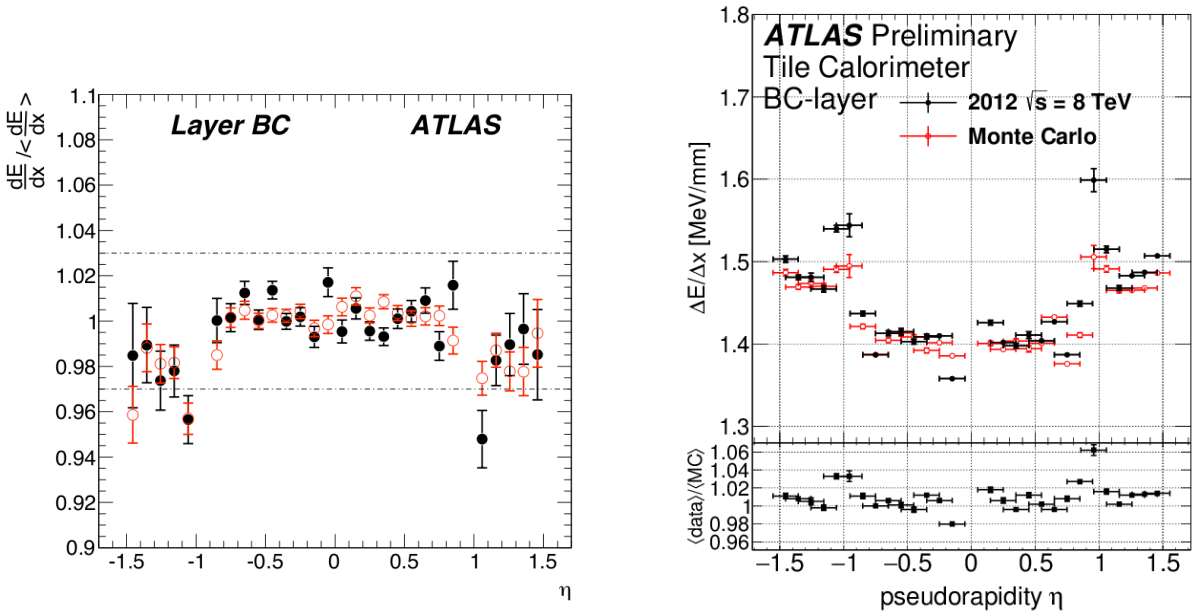

FIGURE 5. Left: Uniformity of the cell response to cosmic muons, expressed in terms of normalized truncated mean of dE/dx, as a function of η for radial layer BC. Figure is taken from Ref. [1]. Right: Uniformity of the cell response to muons from $W \to \mu\nu$ decays in 2012 collision data, expressed in terms of truncated mean of dE/dx in MeV/mm, as a function of η for radial layer BC. Figure is taken from Ref. [8].

PERFORMANCE WITH SINGLE PARTICLES

The performance of the TileCal, and hence the methods used to reconstruct, calibrate, and correct for problematic regions of the detector, was evaluated with single isolated particles.

Single isolated muons were used to check the electromagnetic scale across the detector, using the ratio of the energy deposited to the path length traveled by the muon in a cell, dE/dx. For muon energies below 100 GeV this ratio is approximately constant. The muons can either come from cosmic rays or from heavy gauge boson decays in proton-proton collisions. Uniformity between cells in the same calorimeter layer and uniformity between layers as well as stability over time were checked. Mean dE/dx, as a function of η for radial layer BC in shown in Fig. 5.left. The response is integrated over all cells in each η bin and results for data and Monte Carlo (MC) are normalized to their averages. Similar results for muons from $W \to \mu\nu$ decays in 2012 collision data are shown in Fig. 5.right. For all cells in any single layer RMS of the data/MC ratio was found to be below 2%. Most of data and MC agrees within 4%, except gap regions between LB and EB around $|\eta| = 1$. In these regions agreement is a bit worse and it is changing from one year to another mostly because of bigger effect of pileup noise contribution, which is also changing.

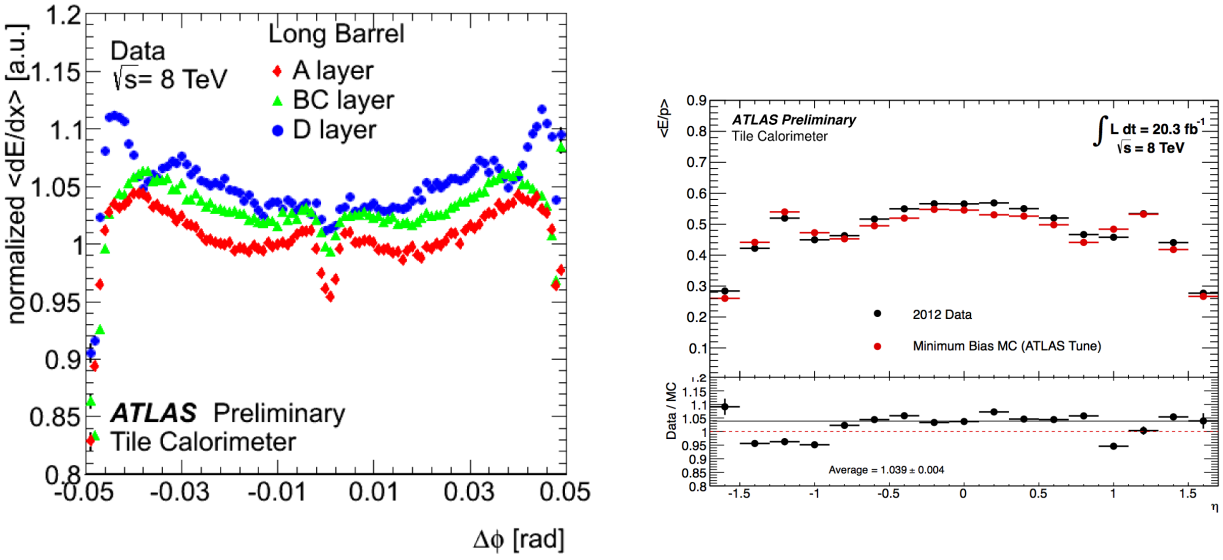

FIGURE 6. Left: Normalized truncated mean of dE/dx for muons from $W \to \mu\nu$ decays as a function of distance between track ϕ and ϕ of the center of the corresponding cell for 3 radial layers. Right: Energy over momentum E/p as a function of η for isolated hadron tracks. Figures are taken from Ref. [8].

Due to non-uniformities in the individual tiles and due to exponential attenuation of the light in the scintillators, measured deposited energy in a cell (calculated as a sum of two PMT energies) depends on the exact position of local energy deposit. Transverse size of hadronic shower is much bigger than size of single tile and therefore the effect is not visible, but for single muon track it is possible to obtain energy profile as a function of ϕ of the track. In Fig. 6.left the values of dE/dx obtained from collision events with muons produced in $W \to \mu\nu$ decays as a function of $\Delta\phi$ - difference between ϕ value of muon impact point and ϕ of the cell center in a module are shown. Variations up to 10% were observed with Run 1 data and this profile is used now in Run 2 MC. In addition to non-uniformities at the cell edges, one can clearly see the effect of the hole in the cell center through which Cesium source in passed (see holes in Fig. 1.right).

The performance of the TileCal was also studied with single isolated charged hadrons, using the ratio of the energy measured by the TileCal, E, to the momentum as measured by the inner detector, p, for a single track. A signal compatible with a minimum ionizing particle in the EM calorimeter in front of the TileCal was required, to avoid any bias of the TileCal response due to interactions in upstream material. The E/p distributions are shown in Fig. 6.right for data taken in 2012 and MC simulations as a function of η. The data and MC agree within 5%, except one point at $|\eta| = -1.5$ where the disagreement is 9%.

CONCLUSIONS

The ATLAS TileCal performed very well in the LHC Run 1, both in operation, calibration, performance and stability. The TileCal calibration and monitoring systems guarantee stability in time of the calorimeter response within 1%. The energy scale uncertainty, which was successfully extrapolated from the beam tests to ATLAS, is conservatively considered to be 4%. Correct modeling of the calorimeter in MC is essential as many searches use MC for background estimation techniques. Measurements done during Run 1 contributed to the improvement of the detector description for Run 2 MC. Overall, TileCal performs within expectations and together with other ATLAS subdetectors it contributes to the measurement of jets, taus and missing energy.

ACKNOWLEDGMENTS

This work is supported by Russian MES grant RFMEFI61014X0005.

REFERENCES

[1] ATLAS/TileCal Collaboration, Eur. Phys. J. C **70.4**, 1193–1236 (2010).
[2] ATLAS Collaboration, CERN-LHCC-96-42 (1996).
[3] ATLAS Collaboration, JINST **3**, S08003 (2008).
[4] L. Evans and P. Bryant (editors), JINST **3**, S08001 (2008).
[5] W. E. Cleland and E. G. Stern, NIM **A338**, 467–97 (1994).
[6] ATLAS/TileCal Collaboration, NIM **A606**, 362–94 (2009).
[7] TileCal Calibration Plots, https://twiki.cern.ch/twiki/bin/view/AtlasPublic/ApprovedPlotsTileCalibration .
[8] TileCal Public Results, https://twiki.cern.ch/twiki/bin/view/AtlasPublic/TileCaloPublicResults .

Proceedings of the LHCP2015 Conference, St. Petersburg, Russia, August 31 - September 5, 2015

Editors: V.T. Kim and D.E. Sosnov

The ATLAS Trigger System: Ready for Run-2

JUNPEI MAEDA

Graduate School of Science, Kobe University, Kobe, Japan

junpei.maeda@cern.ch

On behalf of the ATLAS Collaboration

Abstract. The ATLAS trigger system was operated very successfully during the LHC Run-1 (2009-2013) at a centre-of-mass energy between 900 GeV and 8 TeV, and has undergone a major upgrade in the long shutdown (2013-2014) to cope with the tightened requirements and the increased rates for the LHC Run-2. After a successful commissioning phase, the ATLAS trigger system was running smoothly and highly reliably, with the Level-1 trigger rate of 75 kHz and the HLT rate of 2 kHz at a peak luminosity of 5×10^{33} cm^{-2}s^{-1}. This proceedings present a brief review of the ATLAS trigger system upgrade implemented during the shutdown, allowing us to cope with the increased trigger rates while maintaining or even improving our efficiency to select relevant physics objects. This includes changes to the Level-1 calorimeter and muon trigger system, the introduction of a new Level-1 topological trigger module and the merging of the previously two-level higher-level trigger system into one system. The commissioning of the trigger system and its initial performance from the 2015 run is also presented.

INTRODUCTION

The ATLAS trigger system [1] operated successfully in Run-1 data-taking period of the Large Hadron Collider (LHC) [2] at centre-of-mass energies up to 8 TeV between 2009 and 2013. It achieved high efficiencies for a wide range of Run-1 ATLAS physics program. In Run-2 data-taking period, the centre-of-mass energy increases from 8 to 13 TeV, namely more high-p_{T} physics objects, such as leptons and jets, generated. Moreover, the peak luminosity is expected to rise from approximately 8×10^{33} cm^{-2}s^{-1} to 1.5×10^{34} cm^{-2}s^{-1} with half bunch-spacing of 25 ns. Thus the trigger rates of the Run-1 trigger selections are expected to increase by a factor of 5 in Run-2, although the pile-up will decrease at the same instantaneous luminosity due to the half bunch-spacing with respect to Run-1.

To deal with such a challenging data-taking conditions of the increased trigger rates while maintaining efficiency in selecting physics processes of interest, upgrades to the ATLAS trigger system were mandatory and implemented during LHC shutdown. In these proceedings, the new features of the ATLAS trigger system are reviewed and the initial performance results from the first 13 TeV proton-proton collision data are presented.

ATLAS Trigger system and Upgrades for Run-2

Figure 1 shows a schematic overview of the Run-2 ATLAS trigger and data acquisition system. The trigger system in Run-2 consists of two trigger levels, a hardware-based first level trigger (Level-1) and a software-based high-level trigger (HLT). The Level-1 trigger is implemented in custom electronics to determine Regions-of-Interest (RoIs) in the detector based on coarse calorimeter or muon detector information. The Level-1 trigger reduces the event rate from the LHC bunch crossing rate which is approximately 30 MHz expected in Run-2, to 100 kHz. The decision time for an Level-1 accept is 2.5 μs, without any delay due to the pipelines. The RoIs are then passed to the HLT farm which the sophisticated algorithms are running using full granularity detector information in either the RoI or the whole detector after certain steps in the HLT, in order to reduce the rate from 100 kHz to 2 kHz on average within an average processing time of 0.2 s.

As shown in Figure 1, the Level-1 trigger consists of several sub-systems: the Level-1 calorimeter, the Level-1 muon, and the Level-1 central trigger systems.

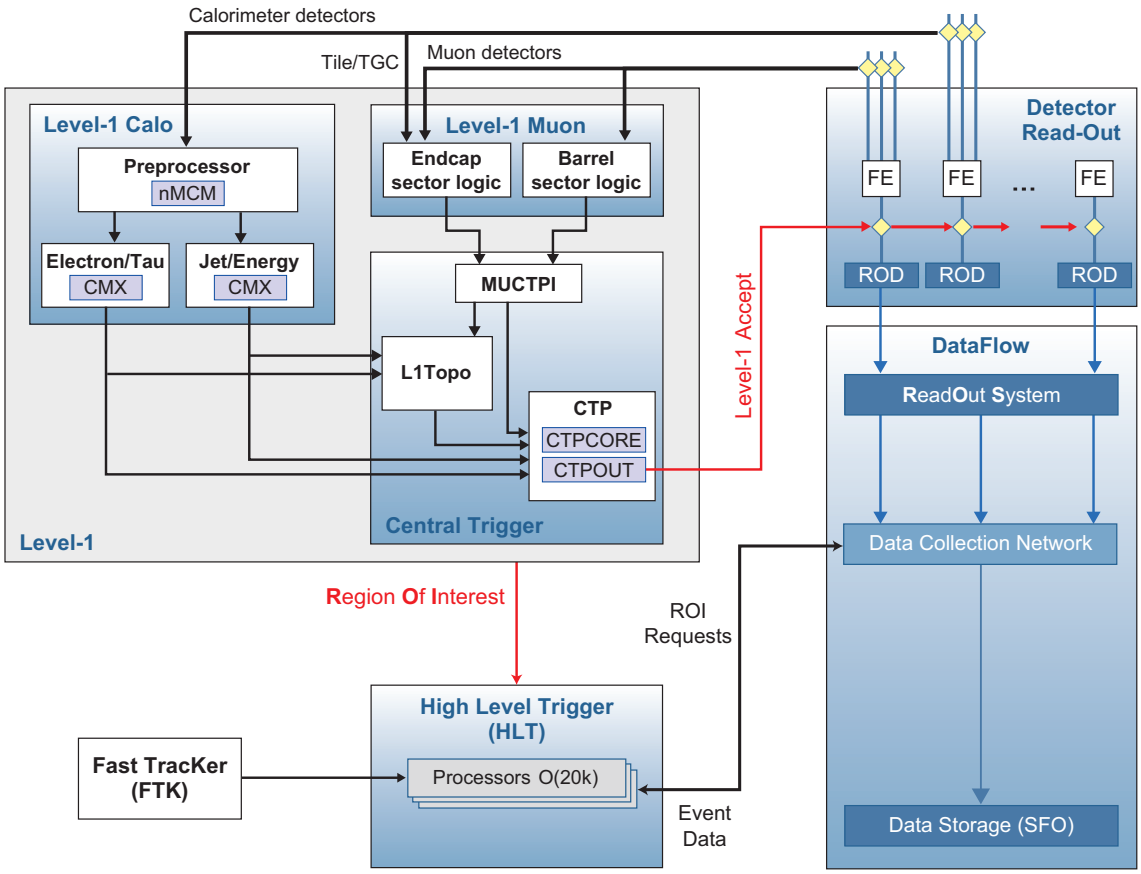

FIGURE 1: Schematic overview of the Run-2 ATLAS trigger and data acquisition system.

The Level-1 calorimeter sub-system processes signals from the electromagnetic and hadronic calorimeter detectors and provides trigger signals to the central trigger processor (CTP). One of new feature of the Level-1 calorimeter trigger for Run-2 is the use of new Multi-Chip Modules (nMCM) which are based on the field-programmable gate array (FPGA) technology replaced from the corresponding modules using application-specific integrated circuits (ASICs). The nMCMs enable the use of auto-correlation filters for improved energy resolution and a more flexible processing of the calorimeter signals with dynamic pedestal subtraction based on the global cell occupancy and timed with respect to the position of colliding bunches inside the proton bunch trains. These new features result in a significant reduction of the missing transverse[1] momentum trigger rates at Level-1, with keeping the physics efficiency, which were major limitation in Run-1. In addition, the number of definable Level-1 calorimeter trigger thresholds has been doubled with respect to Run-1 and provides flexibilities for the trigger selections.

In Run-1, many Level-1 muon triggers in the end-cap region ($1.05 < |\eta| < 1.9$) were caused by low-p_{T} out-of-time protons generated in endcap toroid magnets and shieldings. This effect increases in 25 ns bunch spacing, hence the Level-1 trigger rates increases in Run-2 if there is no upgrade. In order to reduce such out-of-time protons, the new coincidence scheme which uses information from the inner end-cap muon chambers placed in front of the end-cap toroid magnets and from the extended Tile calorimeter is introduced. Using both detectors, approximately 50 % rate reduction for Level-1 muon rate of $p_{\mathrm{T}} > 20$ GeV is expected with tiny efficiency loss. In addition, new trigger chambers in the feet of the barrel region are installed in the shutdown period, and are expected to bring a gain of approximately 4 % in acceptance for Level-1 muon at $|\eta| < 1.05$.

[1] ATLAS uses a right-handed coordinate system with its origin at the nominal interaction point (IP) in the centre of the detector and the z-axis along the beam pipe. The x-axis points from the IP to the centre of the LHC ring, and the y-axis points upward. Cylindrical coordinates (r, ϕ) are used in the transverse plane, ϕ being the azimuthal angle around the beam pipe. The pseudorapidity is defined in terms of the polar angle θ as $\eta = -\ln\tan(\theta/2)$. The distance in $\eta - \phi$ plane is defined as $R = \sqrt{\Delta\eta^2 + \Delta\phi^2}$

In addition, we are being to introduce a conceptually new Level-1 topological trigger systems (L1Topo) [3] for Run-2. It performs topological selections on Level-1 physics objects at the LHC bunch crossing rate. The L1Topo algorithms are implemented in FPGAs and provide a decision within short latency (~200 ns). There are several possibilities of algorithms in L1Topo, for example, angular requirements, invariant mass calculation, and global event quantities such as the sum of the transverse momenta of all Level-1 jet objects. The L1Topo system are crucial for the Run-2 physics program as it allows the energy and momentum thresholds for multi-object final states to be kept low, while significantly decreasing the trigger rates. For the higher luminosity, we need much more rate reduction on Level-1 in the current trigger menu, otherwise the triggers would be highly prescaled. Therefore, a sophisticated trigger using topological information of calorimeter and muons is needed. The commissioning of L1Topo has started during the 2015 data taking in situ.

The information of all Level-1 sub-systems are combined in the CTP which forms the final Level-1 trigger accepts. The CTP has undergone a major upgrade for Run-2 and is able to accommodate the twice number of Level-1 trigger algorithms due to the need of L1Topo. Moreover, the CTP can now handle trigger rates of up to 100 kHz which is significantly improved from the limit of 70 kHz in Run-1.

The HLT system has been also significantly upgraded for Run-2. The main change is that higher-level trigger farms[2] and event building farms are merged into a unique HLT farm. It reduces the overall complexity of the system, and allows for dynamic resource sharing between algorithms that were previously separated to one of the two higher trigger levels. The advantage of this unification is to achieve an efficient coupling of the HLT selection steps, which reduces the duplication of CPU usage and network transfer of detector data, and allows flexible combination of fast and detailed processing in several steps. In addition, the trigger reconstruction algorithms has been redesigned to be closer to offline reconstruction algorithms. It makes a large reduction of codes and commissioning duplications, an easier calibration of triggers along with offline selections, and a capability to use of real-time pile-up information to correct for effects of multiple interactions per bunch crossing.

Initial Performance of main physics triggers in the first 13 TeV collision data

The ATLAS trigger system has been successfully commissioned in the start-up phase of Run-2 and is now running highly reliable and efficient. In this section, the initial performance of some physics triggers of single physics object using the first 13 TeV collision data with 50 ns proton bunch spacing is discussed.

Figure 2 (top left) shows the trigger efficiency, combined by Level-1 and HLT, of a single electron trigger as a function of electron transverse energy (E_{T}) reconstructed in the offline data processing. The efficiency is measured with respect to fully reconstructed electrons required to pass likelihood-based identification of medium quality. The HLT trigger is seeded by a level-1 trigger L1_EM18VH that applies an E_{T} dependent veto against energy deposited in the hadronic calorimeter behind the electron candidate's electromagnetic cluster. The trigger also requires an electron candidate with $E_{\mathrm{T}} > 24$ GeV satisfying the likelihood-based identification of medium quality and a requirement of $p_{\mathrm{T,iso}}/E_{\mathrm{T}} < 0.1$ on the relative track isolation calculated within a cone of $R = \sqrt{(\Delta\eta)^2 + (\Delta\phi)^2} = 0.2$. The efficiency is measured with a tag-and-probe method using $Z \to ee$ decays with no background subtraction applied. It is also compared to an expectation from $Z \to ee$ simulation. Figure 2 (top right) shows the output rate of single electron triggers as a function of the instantaneous luminosity. These triggers comprise of hardware-based first-level and software-based high-level trigger selections [4]. Medium-quality identification criteria will move to tight selections for higher luminosities.

The efficiency of single photon triggers requiring a transverse energy (E_{T}) greater than 25 and 35 GeV and medium photon identification criteria with respect to photon candidates is also shown in Figure 2 (middle left). The efficiency is measured using events taken by a Level-1 trigger requiring an electromagnetic cluster with $E_{\mathrm{T}} > 7$ GeV and reconstructed offline passing the tight identification selection for $|\eta| < 2.37$ excluding the transition region between the barrel and end-cap electromagnetic calorimeters at $1.37 < |\eta| < 1.52$. No background subtraction is applied.

Figure 2 (middle right) shows missing transverse momentum trigger efficiency turn-on curves for a threshold of 50 GeV as a function of offline reconstructed $E_{\mathrm{T,miss}}$ reference for different algorithms: a 2-sided 2-sigma noise suppression cell-based algorithm (denoted cell), a topological cluster-based algorithm [5] with no further corrections (denoted topocl), an eta-ring pile-up subtraction (denoted topoclPS), or a pile-up fit procedure (denoted topoclPUC), and an algorithm based on the sum of jet momenta (denoted mht). All algorithms reach the plateau efficiency around 150 GeV, and studies are currently in progress to determine the choice for future data-taking, since the missing

[2] In Run-1, there were Level-2 and Event Filter independently.

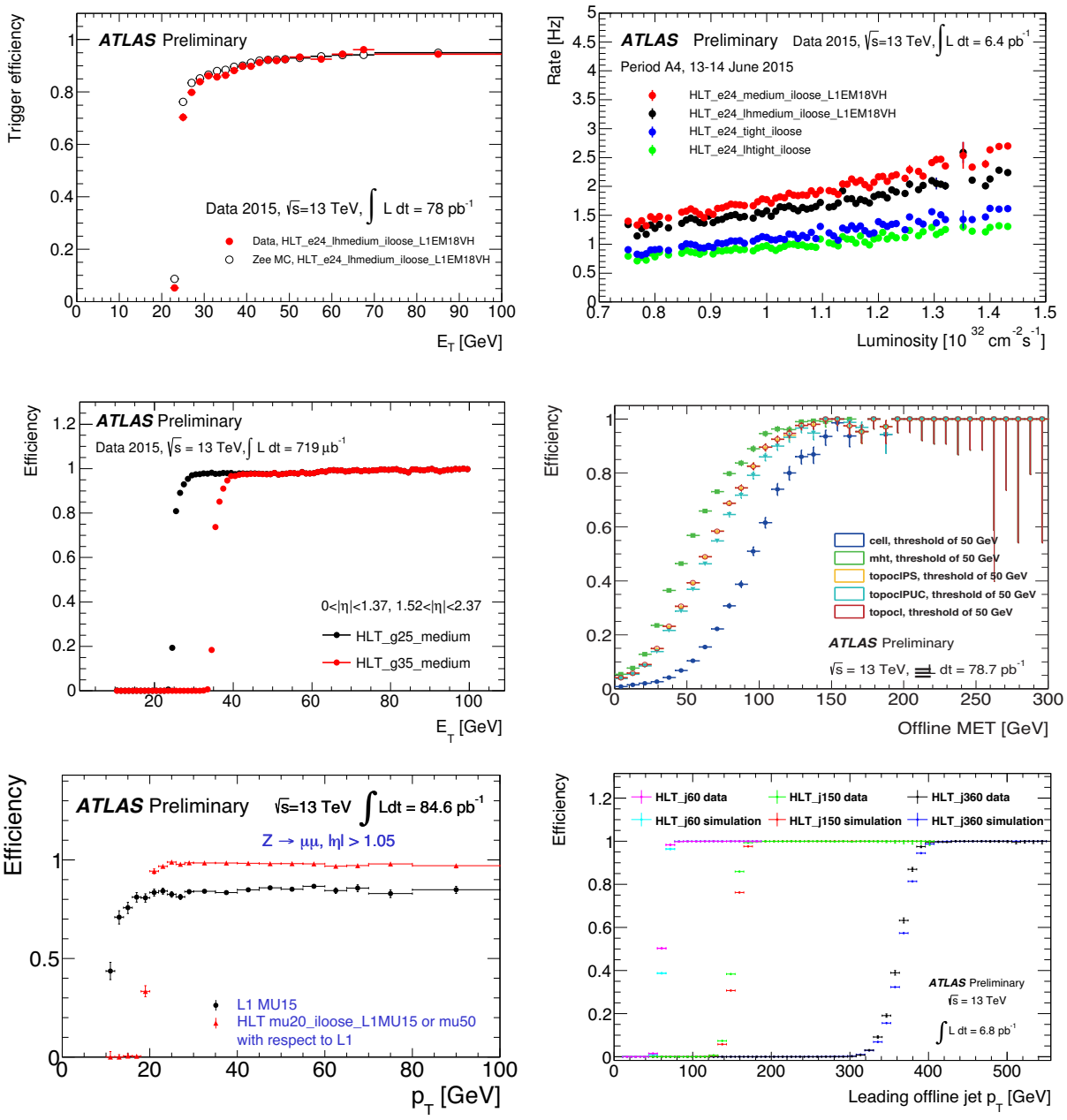

FIGURE 2: The performance of main physics triggers in the first 13 TeV collision data is shown: The efficiency of one of single electron triggers as a function of the transverse energy and their output trigger rates as a function of instantaneous luminosity (top) [6], the efficiency of single photon triggers (middle left) [6], missing transverse energy triggers (middle right) [7], single muon triggers (bottom left) [8], and single jet triggers (bottom right) [9]. Details are given in the text.

transverse momentum distribution are event topology dependent, but this figure allows a qualitative comparison of the different algorithms.

Figure 2 (bottom left) shows the efficiency of Level 1 single muon trigger (denoted L1_MU15) and the OR of the HLT_mu20_iloose_L1MU15 and HLT_mu50 high-level trigger as a function of the transverse momentum of offline muon candidates in the end-cap detector region. The L1_MU15 trigger requires that a candidate passed the 15 GeV threshold requirement of the Level-1 muon trigger system. The HLT_mu20_iloose_L1MU15 trigger is seeded by the L1_MU15 trigger and is required to satisfy a 20 GeV HLT threshold and to pass a loose isolation selection computed using inner detector tracks reconstructed online by the HLT. The HLT_mu50 trigger is seeded by the L1_MU20 trigger and is required to satisfy a 50 GeV HLT threshold without any isolation requirements. The efficiency is computed with respect to offline muon candidates which are reconstructed using standard ATLAS software. The HLT efficiency for the OR of two chains is presented with respect to the OR of the two Level-1 chains. The efficiency is measured using a tag-and-probe method with $Z \to \mu\mu$ candidates in 13 TeV data with 50 ns bunch spacing, with no background subtraction applied. Only statistical data uncertainties are shown in Figure 2.

Figure 2 (bottom right) shows a comparison of trigger efficiency of data and MC simulation for three typical jet trigger thresholds, as a function of the jet transverse momentum. The HLT jets are formed from topo-clusters calibrated to the electromagnetic energy scale. The jets are then calibrated to the hadronic scale by first applying a jet-by-jet area subtraction procedure followed by a jet energy scale weighting that is dependent on the HLT jet transverse momentum and pseudorapidity. Each efficiency is determined using events retained with a lower threshold trigger that is found to be fully efficient in the phase space of interest.

In Figure 2, the thresholds are presented in each physics object, and MC simulation describes data well. Hence the Run-2 trigger system satisfies the performance required from physics analyses.

SUMMARY

Many upgrades have been implemented in the ATLAS trigger system during the LHC shutdown period to cope with the increased trigger rates due to the expected larger centre-of-mass energy and higher luminosity. There are several new features of Level-1 calorimeter and muon systems, the Level-1 central trigger processor, and a conceptually new Level-1 topological-trigger system. For the HLT, the main upgrade is the merging of the previously two-level systems into a single event processing farm, and a major redesign of the trigger reconstruction algorithm. Trigger commissioning with 13 TeV collisions has been done and the system is running in the 25 ns data-taking campaign in a reliable production mode. Reliable and sophisticated diagnostic tools on the online and offline side are fundamental for a successful commissioning of the trigger. Comprehensive trigger strategies are in place to make use of the new resources and to exploit the full physics potential of ATLAS in Run-2.

REFERENCES

[1] ATLAS Collaboration, "The ATLAS Experiment at the CERN Large Hadron Collider", JINST **3** S08003 (2008).
[2] L. Evans and P. Bryant, "LHC Machine", JINST **3** S08001 (2008).
[3] ATLAS Collaboration, "Technical Design Report for the Phase-I Upgrade of the ATLAS TDAQ System", CERN-LHCC-2013-018, ATLAS-TDR-023 (2013). https://cdsweb.cern.ch/record/1602235
[4] ATLAS Collaboration, "Performance of the ATLAS Electron and Photon Trigger in p-p Collisions at $\sqrt{s}$ = 7 TeV in 2011", ATLAS-CONF-2012-048 (2012). https://cdsweb.cern.ch/record/1450089
[5] W. Lampl *et al.*, "Calorimeter clustering algorithms: Description and performance", ATL-LARG-PUB-2008-002 (2008). https://cdsweb.cern.ch/record/1099735
[6] ATLAS Collaboration, Public Egamma Trigger Plots. https://twiki.cern.ch/twiki/bin/view/AtlasPublic/EgammaTriggerPublicResults
[7] ATLAS Collaboration, Missing Energy Trigger Public Plots. https://twiki.cern.ch/twiki/bin/view/AtlasPublic/MissingEtTriggerPublicResults
[8] ATLAS Collaboration, Muon Trigger Public Results. https://twiki.cern.ch/twiki/bin/view/AtlasPublic/MuonTriggerPublicResults
[9] ATLAS Collaboration, Public Jet Trigger Plots. https://twiki.cern.ch/twiki/bin/view/AtlasPublic/JetTriggerPublicResults

Proceedings of the LHCP2015 Conference, St. Petersburg, Russia, August 31 - September 5, 2015

Editors: V.T. Kim and D.E. Sosnov

The Challenge of Building Large Area, High Precision Small-Strip Thin Gap Trigger Chambers for the Upgrade of the ATLAS Experiment

VICTOR MALEEV

National Research Centre "Kurchatov Institute" B.P.KONSTANTINOV Petersburg Nuclear Physics Institute, Gatchina, Russia

Victor.Maleev@cern.ch

On behalf of the Muon System of the ATLAS Collaboration

Abstract. The current innermost stations of the ATLAS muon end-cap system must be upgraded in 2019 and 2020 to retain the good precision tracking and trigger capabilities in the high background environment expected with the upcoming luminosity increase of the LHC. Large area small-strip Thin Gap Chambers up to 2 m^2 in size and totaling an active area of 1200 m^2 will be employed for fast and precise triggering. The precision reconstruction of tracks requires a spatial resolution of about 100 μm while the Level-1 trigger track segments need to be reconstructed with an angular resolution of 1 mrad. The upgraded detector will consist of eight layers each of Micromegas and small-strip Thin Gap Chamber detectors together forming the ATLAS New Small Wheels. The position of each strip must be known with an accuracy of 30 μm along the precision coordinate and 80 μm along the beam. On such large area detectors, the mechanical precision is a key point and then must be controlled and monitored all along the process of construction and integration. The precision cathode plane has strips with a 3.2 mm pitch for precision readout and the cathode plane on the other side has pads to produce a 3-out-of-4 coincidence to identify the passage of a track in an sTGC quadruplet.

INTRODUCTION

ATLAS is a multi-purpose detector at the Large Hadron Collider (LHC) at CERN [1] with almost full solid angle coverage. The outermost layer of the detector is formed by the muon system [2], that consists of separate tracking and triggering chambers in toroidal magnetic fields, enabling a stand-alone muon momentum measurement. The common view of the ATLAS Muon Spectrometer (MS) is shown in Fig. 1. Four different types of detectors are used in the ATLAS muon spectrometer depending on the task and region where they are located. Monitored Drift Tube Chambers (MDT) are used for precision tracking in the barrel and the end-cap regions. Only in the central region of the end-cap station, in the so called Small Wheel, that is closest to the interaction point, Cathode Strip Chambers (CSC) are used for precision tracking also. Resistive Plate Chambers (RPC) provide the trigger in the barrel and Thin Gap Chambers (TGC) in the end-cap region of the muon spectrometer.

The motivation for the luminosity upgrade of the Large Hadron Collider (LHC) is to precisely study the Higgs sector and to extend the sensitivity to new physics to the multi-TeV range. The LHC will deliver beams to the ATLAS detector with a center of mass energy of 13-14 TeV and instantaneous luminosities up to $7 \times 10^{34} cm^{-1} s^{-1}$. In order to achieve these goals the ATLAS experiment has to maintain its capability to trigger on moderate momentum leptons under more challenging background conditions than those present at the LHC during Run-1 and Run-2. Figure 2(b) shows the rate of the L1 muon trigger measured in data during Run-1. As shown, the background rate is about 90%. That can be explained by tracks originating from the material activation in the end-cap toroid (tracks types B and C in Fig. 2(a)). To solve this problem the end-cap detectors in the small wheel will be replaced during the Phase-1 upgrade (2019-2020). The New Small Wheels (NSWs) [3] will give tracking resolution better than 100 μm and an angular resolution of 1 mrad at the trigger level for the expected rate of 15 kHz/cm^2.

The implications of the NSW for muon reconstruction and triggering are:

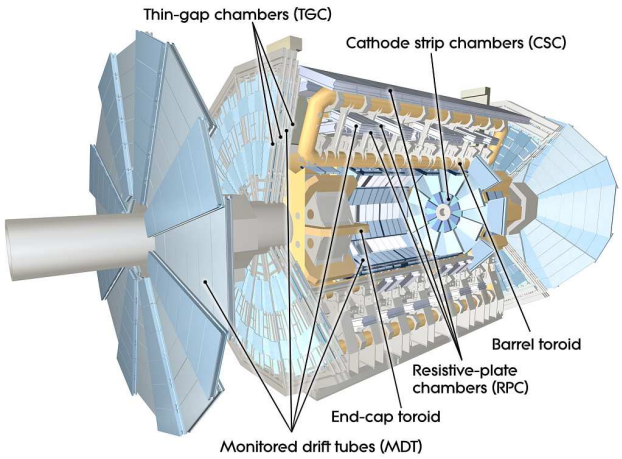

FIGURE 1. Overview of the ATLAS muon spectrometer.

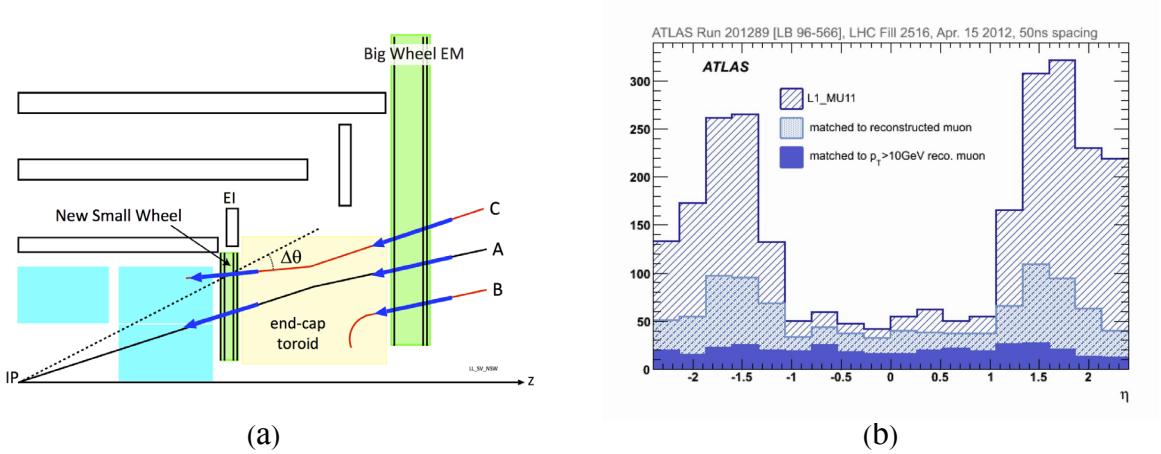

(a) (b)

FIGURE 2. A z-y view of 1/4 of the ATLAS detector. The detector regions of the Small Wheel and Big Wheel are outlined in green, and the black lines indicate the location of a triggering plane. A type A track is good track from interaction point. Tracks of the types B and C are fakes originating from the activation of material in the end-cap toroid.

- Momentum resolution better than 10% for muons with $p_T \sim 1\ TeV$. The performance will not degrade for higher background rates.
- Significant rejection of the background tracks originating from the activation of material in the end-cap toroid and misidentified as muons . The NSWs will allow similar p_T trigger thresholds to Run 2 to be maintain while having higher background rates.

NEW SMALL WHEEL

The two detector technologies chosen for the NSW, Micromegas (MM) and small-strip Thin Gap Chambers (sTGC), are complementary. The sTGC is required to reconstruct track segments online with an angular resolution of better than 1 mrad for triggering purposes, as well as a spatial resolution of about 100 μm for tracks reconstructed offline. Figure 3(a) shows a schematic diagram of the NSW. The NSW consists of two types of sectors (small and large sectors), and each sector includes eight sTGC detector planes (layers) arranged in two quadruplets (chambers) sandwiching two MM chambers. This layout maximizes the distance between the two main triggering planes and therefore the angular resolution of the track segment measurement.

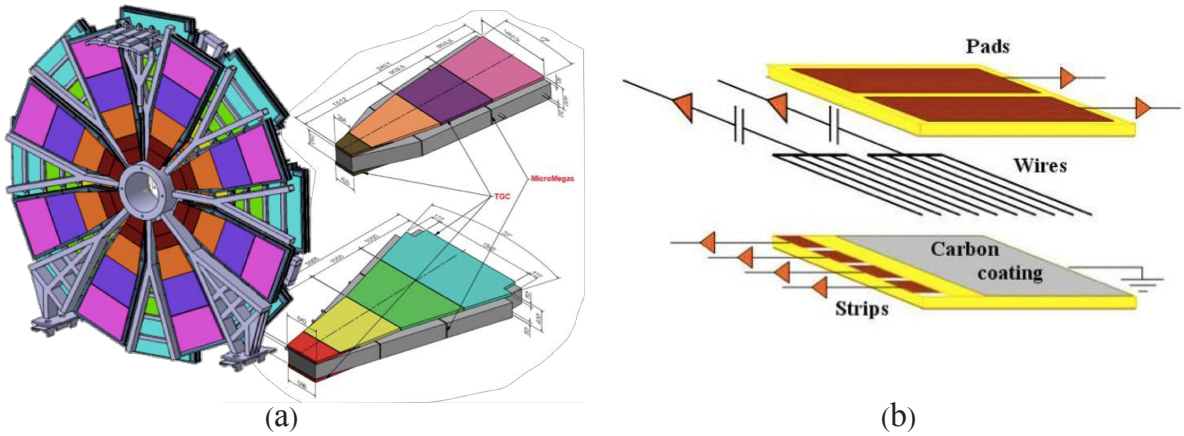

FIGURE 3. (a) schematic diagram of the NSW and (b) sketch of the sTGC structure.

Each sTGC quadruplet consists of four pad-wire-strip planes schematically shown in Figure 3(b). The sTGC consists of a grid of 50 μm gold plated tungsten wires at a potential of 2.9 kV, with a 1.8 mm pitch, sandwiched between two cathode planes at a distance of 1.4 mm from the wire plane. The cathode planes are made of a graphite-epoxy mixture with a typical surface resistivity of 100(200) $k\Omega/\square$ sprayed on a 100(200) μm thick G-10 plane for inner(outer) chambers. Behind the cathode plane there are precision strips (that run perpendicular to the wires) on one side and on the other side there are pads (covering large rectangular surfaces 8 cm in R-direction, and from 5 cm to 50 cm in ϕ-direction depending on R), on a 1.6 mm thick printed circuit board (PCB) with the shielding ground on the opposite side. The strips have a 3.2 mm pitch. The pads are used through a 3-out-of-4 coincidence to identify muon tracks roughly pointing to the interaction point. They are also used to define which strips need to be readout to obtain a precise measurement in the bending coordinate (region of interest), for the online event selection. The azimuthal coordinate is obtained from the wires. The operational gas is a mixture of 55% CO2 and 45% n-pentane.

sTGC PRODUCTION

To meet the requirements for robust single-muon triggering, in particular, achieve 1 mrad angular resolution to select muons from IP, sTGC itself has to be precisely constructed:

- Strip relative transverse alignment within quadruplet to be better than 30 μm
- Strip board relative parallelism within quadruplet to be better than 80 μm
- Allow for assembly of stiff wedges with less than 80 μm deformation

It necessitates careful assembly procedure. This procedure should be focused at:

- Producing a precise strip board to be referenced externally
- Careful alignment of stiff structures (strips + pads boards and wires)
- Robust alignment QC at every step of the quad assembly
- Robust QA at the single detector level
- Use x-ray source to measure gain uniformity
- Robust QA at the quadruplet level
- Measure pad efficiency, strip position using cosmic rays
- Assess full quadruplet performance at high irradiation -source at GIF++

There are six types of sTGC quadruplets - three for the large and small sectors, respectively. As shown in Fig. 3(a) all of them have trapezoidal shapes with dimensions between 1 and 2 m^2. A large collaboration has been established to construct these devices and is composed of members from Canada, Chile, China, Israel and Russia institutions. A key step in the preparation for full sTGC production is assembling module-0 at each production site to verify technological readiness of equipment and personnel.

TEST BEAM RESULTS

An important step in the sTGC development and proving of production procedure was the construction of the full size quadruplet, with dimensions $1.2 \times 1\ m^2$. This prototype consists of four sTGC strip and pad layers and is constructed using the full specification of one of the quadruplets to be used in the NSW upgrade (the middle quadruplet of the small sector). Beam tests of the full size sTGC prototype have been performed at the Fermilab and at CERN. The Fermilab test was devoted to the spatial resolution measurement. The test utilized a pixel telescope to precisely track the incident point of 32 *GeV* pions on the sTGC quadruplet and compare it to the measured position in each of the four sTGC detection planes. A moveable x-y table is used to expose different regions of the sTGC detector to the particle beam. At perpendicular incidence and with all corrections in the details explained in ref. [4] , a resolution of about 45 μm has been found to be uniform (within 3 μm of RMS) across the tested area of $65 \times 11\ cm^2$ for the runs where the measurement was not influenced by the presence of mechanical supports in the considered layers. In Figure 4(a)

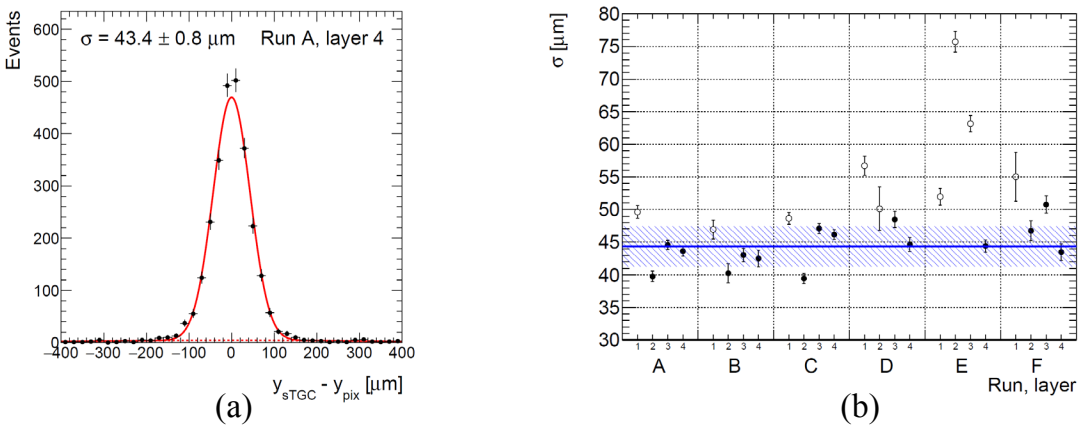

FIGURE 4. (a) The residual distribution after all corrections are applied together with the result for the intrinsic resolution parameter σ for Run A, strip-layer 4 [4]. (b) Summary of the measured intrinsic sTGC resolution using the pixel telescope analysis for different data taking runs.

the residual distribution after all corrections are applied together with the result for the intrinsic resolution is shown. While Figure 4(b) presents the summary of the measured intrinsic sTGC resolution using the pixel telescope analysis for different data taking runs. Results for runs with no expected degradation due to sTGC detector support structure or calibration are shown as black filled circles. The horizontal line represents the average resolution for these runs whereas the hashed band represents the RMS spread. Results for the remaining runs are shown as open circles.

At the CERN test beam, the charge sharing between pads was measured by centering the beam (130 *GeV* muons) in the transition region between two pads. The charge fraction (F) is defined using the analog peak values (P) of two neighboring pads

$$F = \frac{(P_n - P_{n+1})}{(P_n + P_{n+1})},$$

where n is pad number. Figure 5 demonstrates the principle of charge sharing measurements on the left panel and the result of the measurement on the right panel as a function of the position with respect to the center of the transition region between the pads. It shows that the transition region, where the two pads share more than 70% of the induced charge, spans about 4 *mm* (5% of the pad width).

Earlier measured time spectrum (see Fig. 6) demonstrates that 95% of the total events are contained within a 25 *ns* time window [3].

CONCLUSION

The sTGC detectors will provide the Muon NSW with excellent triggering and tracking capabilities. The construction protocol has been validated by test beam measurements on a full-size prototype showing the performance requirements

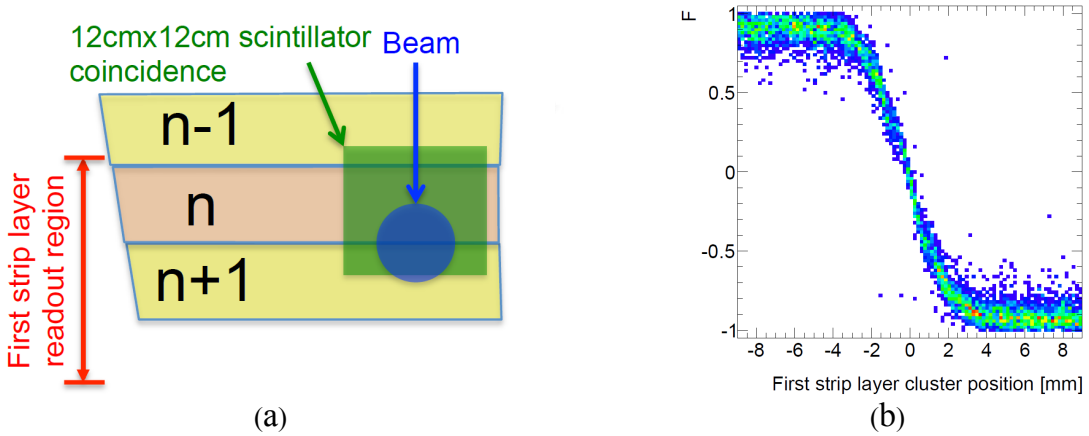

(a) (b)

FIGURE 5. Schematics of the experimental setup for charge sharing measurements (a) and a fraction of the charge collected by pad n as a function of the position with respect to the center of the transition region (b).

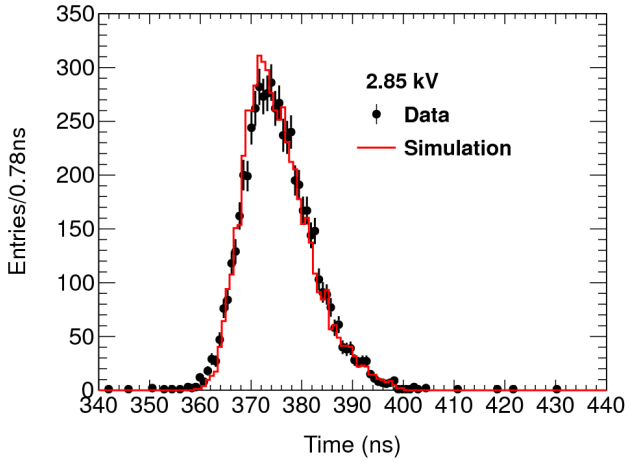

FIGURE 6. Comparison of a simulated time spectrum with experimental data for muons traversing normally an sTGC detector (95%of the events are contained within a 25 *ns* time window).

are met.

REFERENCES

[1] ATLAS Collaboration, *The ATLAS Experiment at the CERN Large Hadron Collider*, JINST 3 S08003 (2008).
[2] ATLAS Collaboration, ATLAS Muon Spectrometer Technical Design Report, CERN/LHCC 97-22 (1997).
[3] ATLAS Collaboration, New Small Wheel Technical Design Report, CERN-LHCC-2013-006.
[4] A. Abusleme et al., *Performance of a Full-Size Small-Strip Thin Gap Chamber Prototype for the ALTAS New Small Wheel Muon Upgrade*, (2015) arXiv:1509.06329

Proceedings of the LHCP2015 Conference, St. Petersburg, Russia, August 31 - September 5, 2015

Editors: V.T. Kim and D.E. Sosnov

ATLAS b-tagging performance during LHC Run-2 with the new Insertable B-layer

Yulia Rodina[1,2]

[1]*Centre de Physique des Particules de Marseille, Aix-Marseille Université & CNRS/IN2P3*
[2]*Institut de Física d'Altes Energies, The Barcelona Institute of Science and Technology, Universitat Autònoma de Barcelona*

rodina@cppm.in2p3.fr

On behalf of the ATLAS Collaboration

Abstract. Expected b-tagging performance in ATLAS during LHC Run-2 is presented together with results of commissioning studies with early Run-2 data. The performance of b-tagging is expected to be significantly improved in Run-2 thanks to the addition of a new pixel detector layer and to updates in the tracking and b-tagging algorithms. First commissioning studies show a promising agreement of Monte Carlo simulation with the new 2015 data recorded at 13 TeV.

INTRODUCTION

Identifying jets containing b-hadrons, a capability known as b-tagging, is useful in various analysis domains with b-jets in final state performed by the ATLAS experiment, like Standard Model measurements (top quark physics and Higgs physics) and beyond the Standard Model searches.

For b-tagging various algorithms are used, which rely on special properties of b-hadrons, such as their high mass ($\approx$ 5 GeV) and relatively long lifetime ($\approx$ 1.5 ps). For the Run 2 of LHC with higher center of mass energy (13 TeV) of the proton-proton collisions, the b-tagging algorithms were revisited. The b-tagging performance during Run-2 is expected to be improved thanks to the insertion of a new innermost layer of pixel detector and algorithmic enhancements in both tracking and b-tagging algorithms.

THE INSERTABLE B-LAYER (IBL)

The major ATLAS inner detector upgrade for Run-2 is the addition of the Insertable B-Layer (IBL), a fourth pixel layer in order to have better track and vertex reconstruction performance at the higher luminosities [1].

The pixel detector used during Run-1 was designed for a peak luminosity of $\mathcal{L} \approx 10^{34}\text{cm}^{-2}\text{s}^{-1}$, while during Run-2 peak luminosity is expected to be $\mathcal{L} \approx 1.7 \times 10^{34}\text{cm}^{-2}\text{s}^{-1}$. Because of that the addition of the new pixel layer was necessary to maintain tracking and b-tagging performance despite the increased pile-up.

The IBL was inserted inside the existing pixel detector at a radius of $\approx$ 3.3 cm from the beamline, while the next to innermost layer (which was innermost pixel layer in Run-1) is located at a radius of $\approx$ 5 cm. Another advantage of the IBL is its higher granularity, with pixels of size 50 μm $\times$ 250 μm instead of 50 μm $\times$ 400 μm for the former innermost pixel layer. Finally, the average number of pixel measurements on a single track became 4 instead of 3. This improves the tracking robustness with respect to pile-up and possible pixel module failures.

The Run-2 to Run-1 data comparison showed already that IBL significantly improves track impact parameter resolution: by up to a factor of 2 for both transverse and longitudinal components for low-p_T tracks. For a typical 2 GeV track, the transverse impact parameter resolution is now $\approx$ 30 μm and the longitudinal one $\approx$ 80 μm [2].

RUN-2 B-TAGGING ALGORITHMS

In the ATLAS Run-2 b-tagging scheme there are three basic algorithms:

- Impact parameter-based (IP2D, IP3D), making use of the fact that tracks from the b-hadron decay are not pointing to the primary vertex.
- Secondary vertex finding (SV), reconstructing an inclusive displaced secondary vertex within the jet.
- Decay chain multi-vertex fit (JetFitter), attempting to reconstruct the full b-hadron decay chain.

Several observables from these algorithms are combined with a multivariate algorithm (MV2), that provides the final discriminant between the different jet flavours.

Impact parameter-based (IP2D, IP3D)

IP2D and IP3D algorithms use the signed impact parameter significance of tracks associated to a jet. The impact parameter is the distance of closest approach of a track to the primary vertex (PV). Its sign is defined positive (negative) if the point of closest approach of the track to the primary vertex is in front (behind) the primary vertex with respect to the jet direction.

IP2D algorithm is using as input only the transverse impact parameter, while IP3D uses both transverse and longitudinal components and their correlation. Probability density functions (PDFs) of the track's impact parameter are built from simulation for the b- and light-flavour jet hypotheses and are then combined using a log-likelihood ratio method to define a tagging weight for a jet:

$$w_{track} = \frac{p_b}{p_{light}}, \quad w_{jet} = \sum_{tracks} \log w_{track}. \tag{1}$$

In the IP2D and IP3D algorithms different PDF sets are used for different track categories, depending on the quality of the tracks, which is defined using information on hits in the different silicon layers of the inner detector.

Run-2 track categorisation is different from the one used in Run-1, making use of new tracking variables related to the presence of the IBL. Table 1 shows 14 exclusive track categories used at Run-2 and indicates percentage of tracks from b-, c- and light flavour jets in each category for simulated $t\bar{t}$ events.

The number of hits in the innermost (L0) and the next to innermost (L1) layers of pixel detector, as well as information on whether the hit in a layer is expected or not (based on the detector coverage and dead module maps) are important variables for defining the track quality. Also the information on the presence of shared hits (clusters which are shared among more than one track) and split hits (clusters which have been identified as coming from different particles and have therefore been split into sub-clusters) is used when dividing tracks into categories.

TABLE 1. Run-2 IP2D and IP3D track categories and fraction of tracks from b-, c- and light flavour jets in each category for the $t\bar{t}$ sample [3].

#	Category	light jets	b-jets	c-jets
0	No hits in first two layers; expected hit in both L0 and L1	1.6%	1.5%	1.6%
1	No hits in first two layers; exp. hit in L0 and no exp. hit in L1	0.1%	0.1%	0.1%
2	No hits in first two layers; no exp. hit in L0 and exp. hit in L1	0.03%	0.03%	0.03%
3	No hits in first two layers; no exp. hit in L0 and L1	0.02%	0.03%	0.03%
4	No hit in L0; exp. hit in L0	2.1%	2.4%	2.3%
5	No hit in L0; no exp. hit in L0	0.9%	0.9%	0.9%
6	No hit in L1; exp. hit in L1	0.5%	0.5%	0.5%
7	No hit in L1; no exp. hit in L1	2.3%	2.4%	2.4%
8	Shared hit in both L0 and L1	0.04%	0.01%	0.01%
9	Shared hits in other pixel layers	1.8%	2.1%	1.6%
10	Two or more shared SCT hits	2.2%	2.4%	2.2%
11	Split hits in both L0 and L1	0.8%	1.2%	1.1%
12	Split hits in other pixel layers	1.1%	2.1%	1.6%
13	Good: a track not in any of the above categories	86.6%	84.3%	85.5%

Secondary Vertex Finding Algorithm (SV)

The secondary vertex algorithm attempts to reconstruct the inclusive vertex formed by the decay products of the b-hadron, including those from the subsequent c-hadron decay. Firstly it searches for all two-track pairs that form a good vertex, using tracks displaced from the primary vertex. Then the algorithm removes those tracks that are compatible with decays of long lived particles (K_s, Λ etc) or interaction with the detector material. After this selection the algorithm fits an inclusive secondary vertex. Several properties of this vertex are useful to tag b-jets, such as its mass, number of tracks, distance to primary vertex, energy fraction of tracks at vertex with respect to all tracks in the jet.

Multi-vertex fit (JetFitter)

Another algorithm, called JetFitter, attempts to reconstruct the full PV to b- to c-hadron decay chain. A Kalman filter is used to find a common line on which the primary vertex and all secondary vertices are placed, approximating the b-hadron path. This approach allows to separate b- and c-hadron vertices even if only one track is attached to each of them.

Multivariate algorithm (MV2)

Discriminant observables from the above algorithms are combined together into a boosted decision tree (BDT) based algorithm. The default algorithm for Run-2, MV2c20, is a BDT which is trained using b-jets as signal and a mixture of light-flavour jets and c-jets as background (the amount of c-jets in the background is equal to 20% of the amount of light-jets). The kinematic properties (p_T and η) of the jets are included in the training to take advantage of correlations with the other input variables.

MV2c20 is an upgrade of Run-1 main b-tagging algorithm MV1, which was combining the outputs of the various b-tagging algorithms using neural network approach.

The MV2c20 algorithm provides better performance and easier retraining and software maintenance.

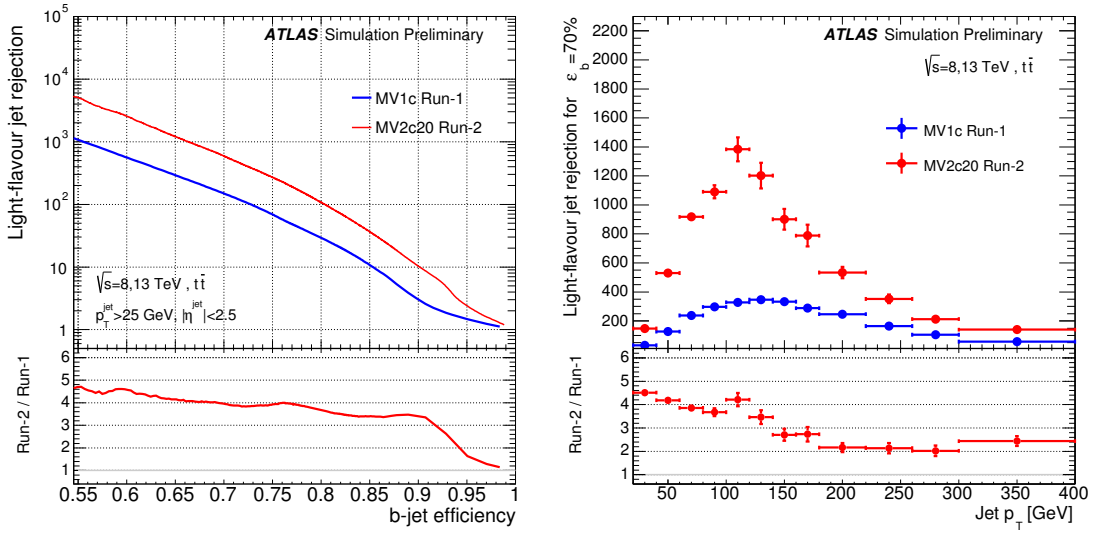

(a) (b)

FIGURE 1. Performance of default Run-2 b-tagging algorithm MV2c20 and the equivalent Run-1 b-tagging algorithm MV1c in simulated $t\bar{t}$ events: light jet rejection vs b-jet efficiency (a) and light jet rejection as a function of jet p_T for a fixed b-jet efficiency of 70% in each bin (b) [3].

EXPECTED B-TAGGING PERFORMANCE ENHANCEMENT

A b-tagging performance improvement is expected to be achieved in Run-2 due to addition of the IBL and many algorithmic updates in track reconstruction [4] and b-tagging, both in the basic taggers and final multivariate algorithm.

Figure 1 show a comparison of the default Run-2 b-tagging algorithm MV2c20 and the equivalent Run-1 b-tagging algorithm MV1c: light jet rejection vs b-jet efficiency (a) and light jet rejection as a function of jet p_T given a fixed b-jet efficiency of 70% in each bin (b). Light jet rejection is the number of light jets over the number of light jets tagged as b-jets. Improvement at low and medium p_T is mostly due to the addition of the IBL, while the improvement at high p_T is due to algorithm improvements. At 70% efficiency the light-flavour jet rejection in Run-2 is improved inclusively by a factor of 4 compared to Run-1. This corresponds to a 10% gain in efficiency at a constant light-jet rejection.

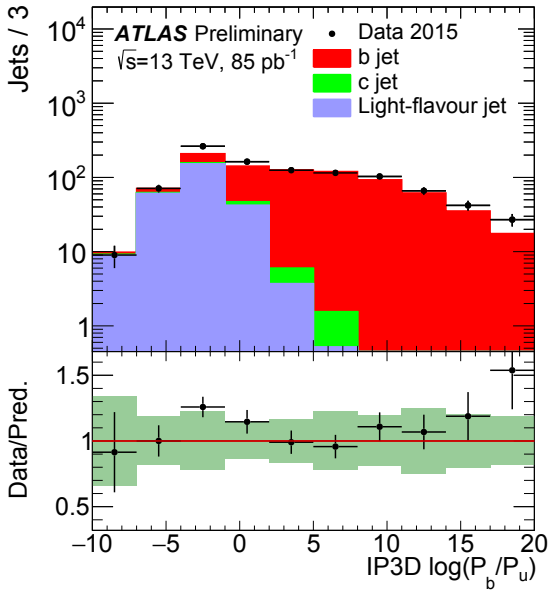

FIGURE 2. IP3D impact parameter-based algorithm output for jets selected from the $t\bar{t}$ dominated $e + \mu$ sample [5].

RUN-2 DATA TO MONTE CARLO COMPARISON

To confirm the Monte Carlo performance, simulation needs to be compared with data and the early Run-2 data commissioning studies are a first step in this direction. A first study of the b-tagging modeling was performed using pp collision data collected by ATLAS at the centre-of-mass energy of 13 TeV with 50 ns bunch-spacing on a high purity b-jet sample of $e + \mu$ di-leptonic $t\bar{t}$ candidate events. Only jets with $p_T > 20$ GeV and $|\eta| < 2.5$ are considered [5].

Input observables from the basic b-tagging algorithms and the output of the multivariate algorithm MV2c20 have been studied. Figure 2 shows the log-likelihood ratio of the IP3D algorithm. Figure 3 represents properties of the secondary vertices reconstructed by the SV algorithm: the invariant mass of the tracks from the vertex (a) and the energy fraction, defined as the energy from the tracks in the displaced vertex relative to all tracks reconstructed within the jet (b). Figure 4 illustrates vertex decay chain fit properties provided by the JetFitter algorithm: the number of vertices with no less than two tracks (a) and the number of tracks at vertices with no less than two tracks (b). Finally, Figure 5 shows the output distribution of the MV2c20 algorithm. On all plots the data are shown by the points and the simulation by the filled area, divided into b (red), c (light green) and light-flavour (blue) components. The dark green shaded area represents the total systematic and statistical uncertainty on the simulation and the error on the points corresponds to the statistical uncertainty on the data.

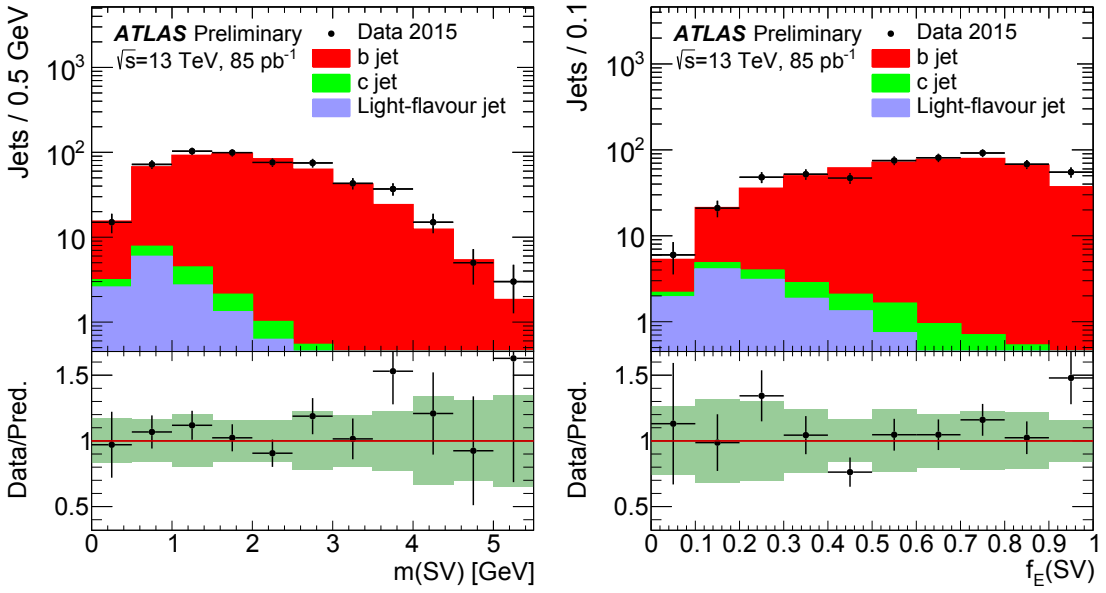

(a) (b)

FIGURE 3. Two properties of the secondary vertices reconstructed by the SV algorithm: the invariant mass (a) and the energy fraction of tracks at vertex with respect to all tracks in the jet (b) [5].

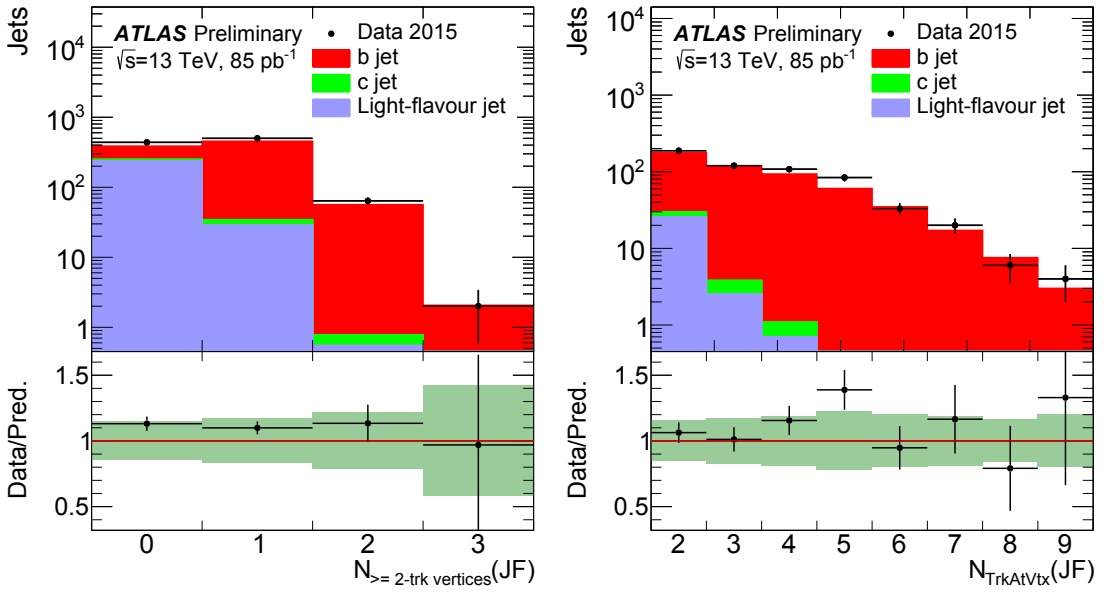

(a) (b)

FIGURE 4. Vertex decay chain fit properties reconstructed by the JetFitter algorithm: the number of vertices with at least two tracks (a) and the number of tracks at vertices with at least two tracks (b) [5].

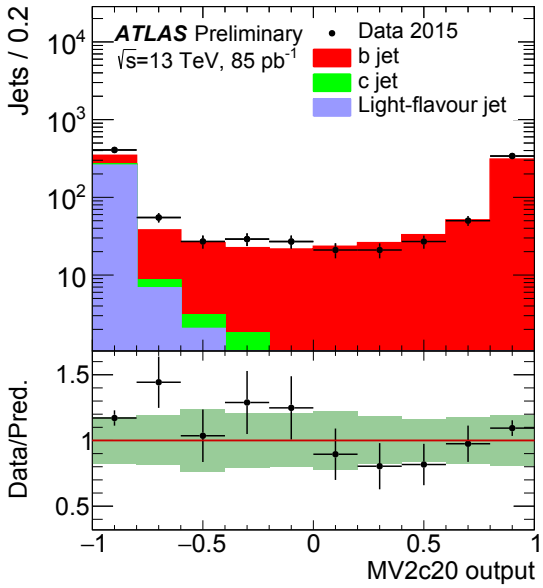

FIGURE 5. Output distribution of the MV2c20 algorithm [5].

CONCLUSIONS

The b-tagging performance in ATLAS is expected to be significantly improved in Run-2 thanks to the addition of a new pixel detector layer and to various updates in the tracking and b-tagging algorithms.

The Monte Carlo studies of the b-tagging performance showed significant enhancement in light-flavour jet rejection in Run-2 compared to Run-1: by a factor of 4 at 70% efficiency, which corresponds to an improvement of $\approx 10\%$ in efficiency at a constant light-jet rejection. Thanks to this improvement, the final signal acceptance for different type of analysis with b-jets in final state is increased (for example, for the search for the Higgs boson decaying to b-quarks and produced in association with top quarks signal acceptance could be increased by up to $\approx 46\%$).

First commissioning studies of basic b-tagging algorithms as well as the multivariate algorithm on Run-2 data showed promising agreement with simulation within the present statistical and systematic uncertainties.

REFERENCES

[1] ATLAS Collaboration, *ATLAS Insertable B-Layer Technical Design Report,* CERN-LHCC-2010-013, ATLAS-TDR-19. https://cds.cern.ch/record/129163

[2] https://atlas.web.cern.ch/Atlas/GROUPS/PHYSICS/PLOTS/IDTR-2015-007/

[3] ATLAS Collaboration, *Expected performance of the ATLAS b-tagging algorithms in Run-2,* ATL-PHYS-PUB-2015-022. https://cds.cern.ch/record/2037697

[4] ATLAS Collaboration, *The Optimization of ATLAS Track Reconstruction in Dense Environments,* ATL-PHYS-PUB-2015-006. https://cds.cern.ch/record/2002609

[5] ATLAS Collaboration, *Commissioning of the ATLAS b-tagging algorithms using $t\bar{t}$ events in early Run-2 data,* ATL-PHYS-PUB-2015-039. http://cds.cern.ch/record/2047871

Proceedings of the LHCP2015 Conference, St. Petersburg, Russia, August 31 - September 5, 2015

Editors: V.T. Kim and D.E. Sosnov

Angular analysis of the decay $B_0 \to K^*\mu\mu$ with the CMS detector

ALESSIO BOLETTI[1,2]

[1] *Università degli Studi di Padova, Italy*
[2] *INFN Padova, Italy*

boletti@pd.infn.it

On behalf of the CMS Collaboration

Abstract. The Flavour Changing Neutral Current decay, $B_0 \to K^*_0\mu^+\mu^-$ is very sensitive to New Physics contributions through its observables like the muon forward-backward asymmetry, the fraction of K^* longitudinal polarization, and the differential branching fraction. These parameters, as reported from previous experiments, remain so far consistent with SM prediction. We will report the recent results from CMS on these parameters using the 20 fb^{-1} data collected during 2012.

Introduction

Rare decays are those processes that are highly suppressed according to the Standard Model (SM) predictions. These decays are an excellent laboratory to probe SM, since an eventual new physics contribution would have an amplitude comparable with the expected one and it would considerably modify the features of the process. The CMS Collaboration gave its significant contribution to the study of two rare decays within the heavy flavour physics: the $B^0_{d(s)} \to \mu\mu$ decays [1] and the $B^0 \to K^*(892)^0\mu\mu$ decay [2]. Here only the latter decay analysis is reported.

The flavour changing neutral current decay $B^0 \to K^*(892)^0\mu^+\mu^-$ is particularly fertile for new phenomena searches thanks to the modest theoretical uncertainties, due to the semileptonic final state. Furthermore, this decay is forbidden at tree level and the leading order diagrams that mediate this process are the box and penguin ones. This fact makes this decay channel very sensitive to virtual contributions of new particles.

In this three body decay, there are two angular parameters that have small theoretical uncertainties: the forward-backward asymmetry of the muons, A_{FB}, and the K^{*0} longitudinal polarization fraction, F_L. These parameters, along with the differential branching fraction dB/dq^2, can be determined as a function of the dimuon invariant mass squared, q^2, and compared with the SM expectations.

Analysis

The CMS collaboration performed this analysis [2] using data collected from proton-proton collisions at the Large Hadron Collider (LHC) with the Compact Muon Solenoid (CMS) experiment in 2012 at a center-of-mass energy of 8 TeV. The analyzed dataset corresponds to an integrated luminosity of 20.5 ± 0.5 fb^{-1}.

Angular parametrization

The considered final state contains two opposite charged muons and a kaon and a pion as the decay products of the K^{*0}. Three angular variables are defined to describe completely the decay: the angle between the kaon momentum and the direction opposite to the B^0 in the K^{*0} rest frame, θ_K, the angle between the positive (negative) muon momentum and the direction opposite to the B^0 ($\bar{B}^0$) in the dimuon rest frame, θ_l, and the angle between the plane containing the two muons and the plane containing the kaon and the pion, ϕ.

Contribution from spinless $K\pi$ combination is present, although the $K\pi$ invariant mass is imposed to be consistent with the K^{*0} one. The fraction of S-wave contribution is parametrized as F_S and the interference contribution between S-wave and P-wave is A_S.

The angular distribution of the decay is then:

$$\begin{aligned}\frac{1}{\Gamma}\frac{d^3\Gamma}{d\cos\theta_K d\cos\theta_l dq^2} &= \frac{9}{16}\Bigg\{\left[\frac{2}{3}F_S + \frac{4}{3}A_S\cos\theta_K\right](1-\cos^2\theta_l) \\ &+(1-F_S)\Bigg[2F_L\cos^2\theta_K(1-\cos^2\theta_l) \\ &+\frac{1}{2}(1-F_L)(1-\cos^2\theta_K)(1+\cos^2\theta_l) \\ &+\frac{4}{3}A_{FB}(1-\cos^2\theta_K)\cos\theta_l\Bigg]\Bigg\}\end{aligned} \quad (1)$$

where the dependence on ϕ is integrated out, since the A_{FB} and F_L parameters do not depend on it.

Control samples and background events

The range of q^2 considered goes from 1 GeV^2 to 19 GeV^2 and it is divided in nine bins of different width. The fifth and the seventh bins correspond to the mass resonances of J/ψ and ψ'. The former one contains mass square values in the range $8.68 < q^2 < 10.09$ GeV^2 and the events here contained are used as normalization sample, to normalize the branching fraction measurement. The latter resonance bin covers a range with $12.86 < q^2 < 14.18$ GeV^2 and its events are used as control sample.

After the selection cuts and the K^{*0} mass requirement, a further cut is applied to reduce the contribution of resonant events with q^2 out of the resonance bin, due to a photon radiation from one of the muons. The background in the final sample is then mostly the combinatorial one. The small contribution from the remaining resonant-event background is taken into account as a systematic uncertainty.

Fit algorithm

In order to extract the values of the angular parameters and the signal and background yield, a simultaneous unbinned maximum likelihood fit to the B^0 recontructed mass, to the $\cos\theta_K$ and to the $\cos\theta_l$ distributions is performed for each q^2 bin.

The $p.d.f.$ used to fit the data is

$$\begin{aligned}\mathrm{PDF}(m,\theta_K,\theta_l) &= \Upsilon_S^C\Big[S^C(m)S^a(\theta_K,\theta_l)\epsilon^C(\theta_K,\theta_l) \\ &+\frac{f^M}{1-f^M}S^M(m)S^a(-\theta_K,-\theta_l)\epsilon^M(\theta_K,\theta_l)\Big] \\ &+\Upsilon_B B(m)B^{\theta_K}(\theta_K)B^{\theta_l}(\theta_l),\end{aligned} \quad (2)$$

where the first contribution corresponds to the correctly-tagged signal events, the second one to the wrongly-tagged signal events, where the pion track and the kaon track are misidentified, and the third contribution correspond to background events.

The parameters Υ_S^C and Υ_B are the yields of correctly tagged signal events and background events, respectively, and are free parameters in the fit. The parameter f^M is the fraction of signal events that are mistagged and is determined from MC simulation. The signal mass probability functions $S^C(m)$ and $S^M(m)$ are each the sum of two Gaussian functions and describe the mass distribution for correctly tagged and mistagged signal events, respectively. In the fit, there is one free parameter for the mass value in both signal functions, while the other parameters (four Gaussian σ parameters and two fractions relating the contribution of each Gaussian) are obtained from MC simulation. The function $S^a(\theta_K,\theta_l)$ describes the signal in the two-dimensional space of the angular observables and corresponds to Eq. 1. The combination $\Upsilon_B B(m)B^{\theta_K}(\theta_K)B^{\theta_l}(\theta_l)$ is obtained from B^0 sideband data and describes the background in the space of (m,θ_K,θ_l), where the mass distribution is an exponential function and the angular distributions are polynomials ranging from second to fourth degree, depending on the q^2 bin and the angular variable. The functions

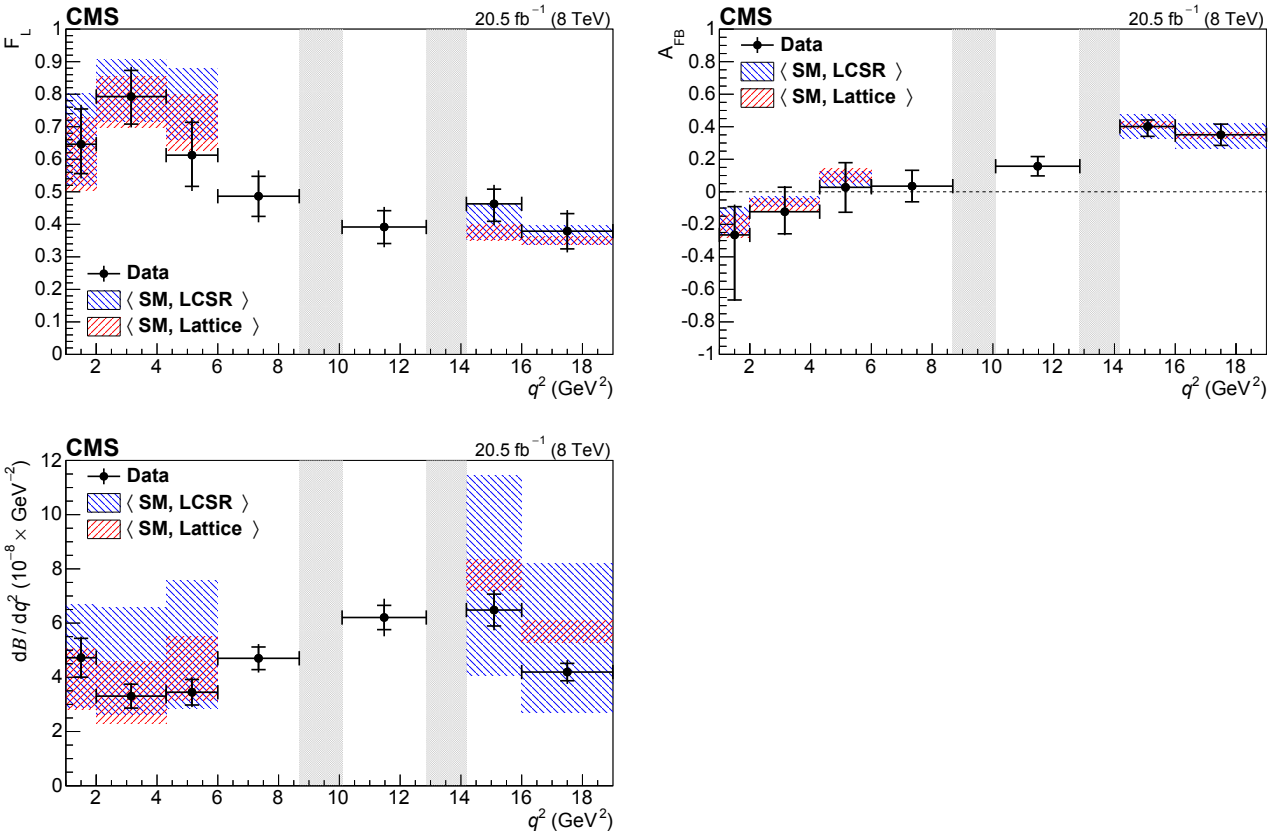

FIGURE 1. Results of the measurement of F_L (top left), A_{FB} (top right) and dB/dq^2 (bottom) versus q^2. The statistical uncertainty is shown by inner error bars, while the outer error bars give the total uncertainty. The vertical shaded regions correspond to the J/ψ and ψ' resonances. The other shaded regions show the SM prediction as a continuous distribution and after rate-averaging across the q^2 bins (SM) to allow direct comparison to the data points.

$\epsilon^C(\theta_K, \theta_l)$ and $\epsilon^M(\theta_K, \theta_l)$ are the efficiencies in the 2D space of the angular observables for correctly tagged and mistagged signal events, respectively.

Results

The fit results are plotted in figure 1 and compared with the SM expectations [3, 4]. Controlled theoretical predictions are not available near the resonance regions.

The results are also combined with those obtained from the analysis on the data collected at $\sqrt{s} = 7$ TeV [5]. This combination is compared with the results from previous measurements [6, 7, 8, 9, 10] in figure 2.

Conclusions

The angular analysis of the $B^0 \to K^{*0}\mu^+\mu^-$ decay has been presented. The measured values of A_{FB}, F_L and of the differential branching fraction dB/dq^2 are compatible with the SM predictions. Since the experimental uncertainty is dominated by the statistical error, a great precision improvement is expected repeating this analysis with more statistics. A recent LHCb mesurement [11] shows a discrepancy whith the expectations and this raises great interest in this analysis.

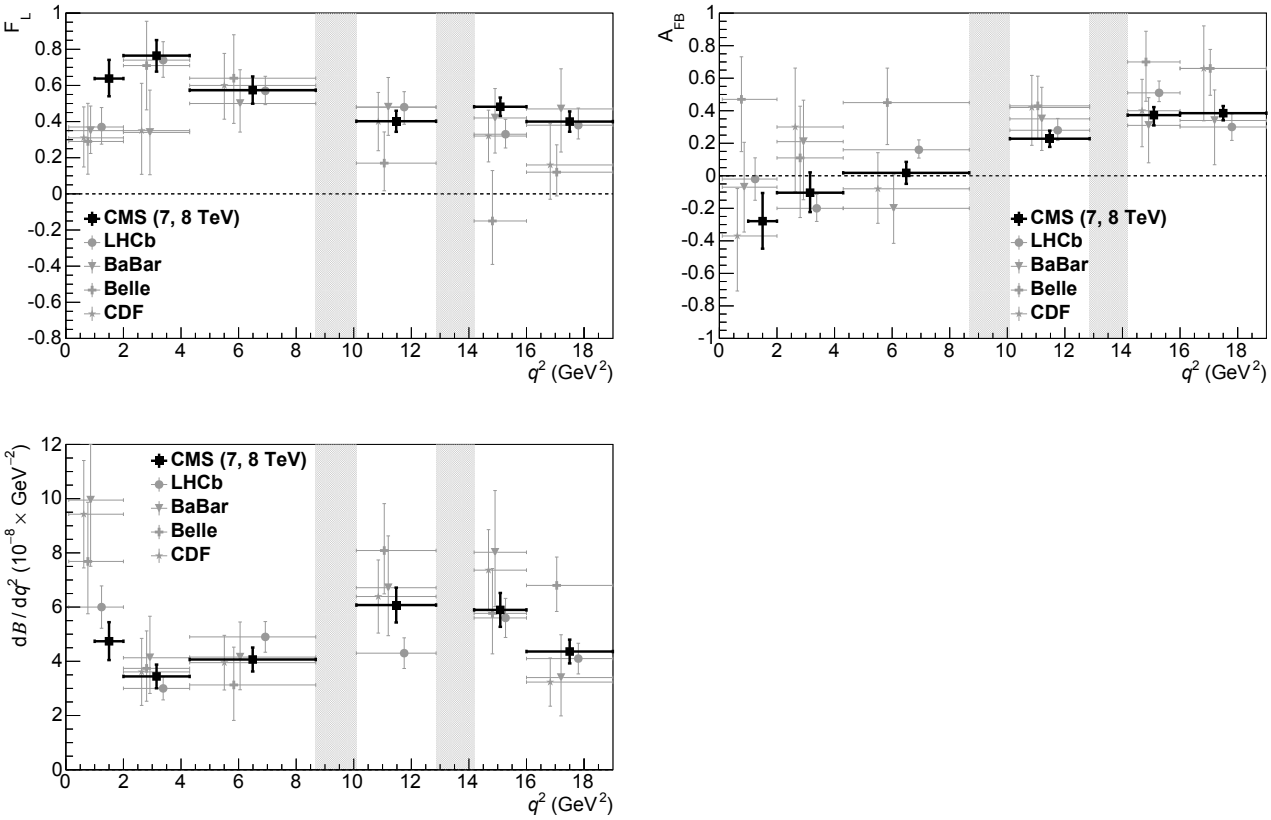

FIGURE 2. Results of the measurement of F_L (top left), A_{FB} (top right) and dB/dq^2 (bottom) versus q^2. Only the total uncertainty is shown. The vertical shaded regions correspond to the J/ψ and ψ' resonances.

REFERENCES

[1] CMS Collaboration, *Phys. Rev. Lett.* **111** (2013) 101804.
[2] CMS Collaboration, CMS-BPH-13-010, CERN-PH-EP-2015-178
[3] C. Bobeth, G. Hiller, and D. van Dyk, *JHEP* **07** (2010) 098
[4] C. Bobeth, G. Hiller, and D. van Dyk, *Phys. Rev. D* **87** (2012) 034016
[5] CMS Collaboration, *Phys. Lett. B* **727** (2013) 77
[6] LHCb Collaboration, *JHEP* **08** (2013) 131
[7] BaBar Collaboration, *Phys. Rev. D* **86** (2012) 032012
[8] CDF Collaboration, *Phys. Rev. Lett.* **108** (2012) 081807
[9] CDF Collaboration, *Phys. Rev. Lett.* **106** (2011) 161801
[10] Belle Collaboration, *Phys. Rev. Lett.* **103** (2009) 171801
[11] LHCb Collaboration, LHCb-TALK-2015-040.

Proceedings of the LHCP2015 Conference, St. Petersburg, Russia, August 31 - September 5, 2015

Editors: V.T. Kim and D.E. Sosnov

CMS Drift Tubes status

DANIEL TEYSSIER

RWTH Aachen University, III Phys. Inst. A

teyssier@cern.ch

On behalf of the CMS Collaboration

Abstract. The CMS muon barrel system includes 250 Drift Tubes (DT) stations that require 172,000 readout channels for triggering and measurement of the muon transverse momentum. After the first Long Shutdown (LS1) of CMS, the fraction of active channels remains higher than 99%. The spatial resolution ranges between 200 and 250 μm in the phi direction, and the intrinsic time resolution is about 2ns. In addition the DT system showed excellent performance during Run 1, with very low associated down time and only a small fraction of data not qualified by the data certification procedure. However, the conditions anticipated for the High Lumi (HL)-LHC will require an upgrade of the on-board electronics to deal with the higher radiation environment and the higher trigger rate. Replacement of the so-called mini-crates installed alongside the chambers is scheduled for LS3.

Introduction

The CMS detector [1] has a large coverage for muon detection, combining endcap and barrel chambers, and also redundancy using different technologies. Standard Model physics as well as new phenomena searches, as supersymmetry or exotica searches, are relying on the ability of the detector to trigger and measure the muon momentum up to the TeV scale.

CMS Drift Tubes chambers

The CMS muon barrel Drift Tubes (DT) system [2] consists of 250 DT chambers organized in five wheels. From the interacting point, a central muon crosses four chambers Fig.1. Each chamber MB1, MB2 and MB3 is made of three superlayers (2-ϕ and 1-θ) except the MB4 made of two ϕ superlayers. Each superlayer contains four single layers. For a central muon, there is a maximum of 32 ϕ hits and 12 θ hits. Finally the DT system covers the region up to $\eta = 1.2$

The individual cell has a section of $42 \cdot 13$ mm and is equipped with anode wire, strip and cathode. There is a total of 172,000 such tubes in the muon barrel system. The gas mixture is made of Ar/CO2 with relative fractions 85/15.

DT performance

DT chambers showed an excellent performance in overall during run 1, causing very small down time for CMS as well as very tiny amount of data not qualified "good" for physics. The different performances [3] are described below. First of all, the DT local trigger efficiency is very high independently of the muon transverse momentum (p_T) Fig.2. This efficiency is computed assuming a reconstructed track passing through the chamber and thus considering the relative ratio of detected hits in the same chamber. All four types of chambers are reaching the same level of efficiency as shown on Fig.2.

The observed level of background is shown to be linear with the increase of the instantaneous luminosity during run 1 (Fig.3). There is a dependency as a function of the wheel, from central to external wheels. As this background in the DT system is mainly induced by the neutron gas filling the experimental cavern, the most affected parts are the outermost chambers (MB4) in the top sectors.

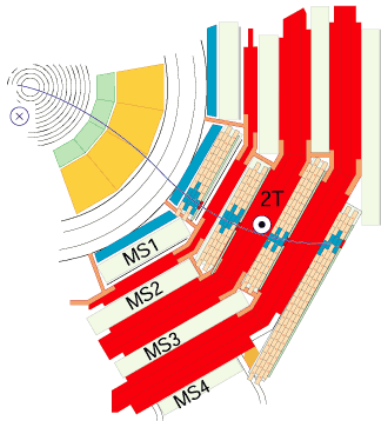

FIGURE 1. Overview of the CMS DT muon barrel system.

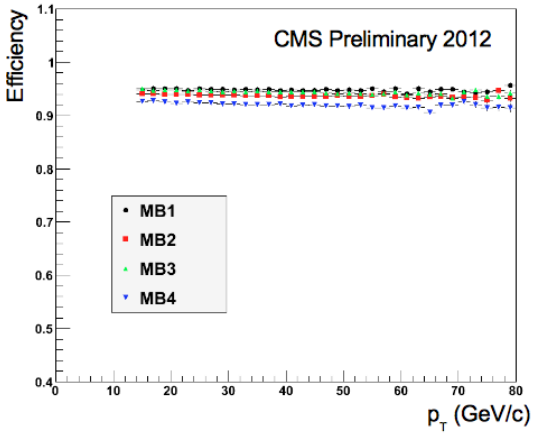

FIGURE 2. The DT local trigger efficiency is presented as a function of the muon η value.

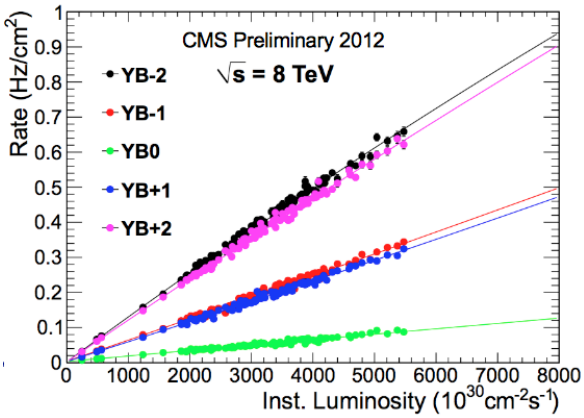

FIGURE 3. The background in the DT system is measured for all luminosities during run 1.

Two key parameters are the spatial and time resolution of the DT system. Figure 4 shows the ϕ and θ view resolutions. In the ϕ view the typical resolution ranges between 200 μm and 250 μm. The observed "hat" shape is explained for both ϕ and θ views by some geometrical differences: a longer path in the external wheels in the ϕ direction leads to a better resolution and the contrary in the θ view. An additional slight geometrical effect is giving a hierarchy from the MB1 to the MB3 in the θ view. Finally the worse resolution, in the MB4, is due to the absence of the θ superlayer.

Figure 5 shows the time resolution obtained compiling run 1 data. Considering the in-time tracks and fitting the central peak, the DT time resolution is assumed to be about 2ns.

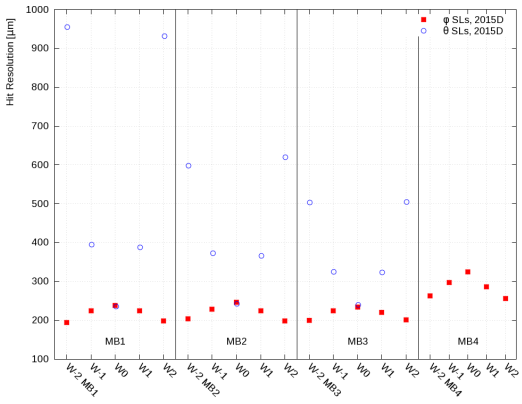

FIGURE 4. The hit resolution is presented for both ϕ and θ directions, per wheel and per chamber.

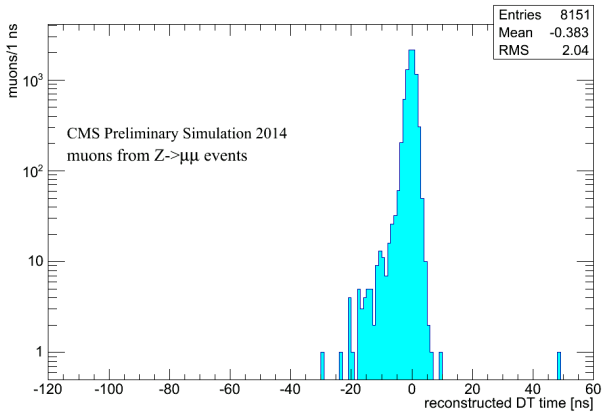

FIGURE 5. The time resolution is computed from the fit to the central peak.

Long Shutdown 1 work

During the Long Shutdown 1 (LS1), a lot of repairs and maintenance work was performed for two years in the DT system [4]. The fraction of active channels was again higher than 99% at the beginning of run 2. In addition some new hardware was installed during LS1 in order to get a more robust system: the Trigger Sector Collectors (TSC) and the Read Out Servers (ROS) were extracted from the experimental cavern to be placed in the service cavern (Fig.6). The main advantage is the accessibility of those critical components. Some copper to optical fiber (CuOF) signal converters were deployed as well as well the optical fibers going up to some OFCu located in service cavern (Fig.7). The commissioning tests performed during LS1 showed the comparable performance of the new electronics by comparison with previous electronics chain.

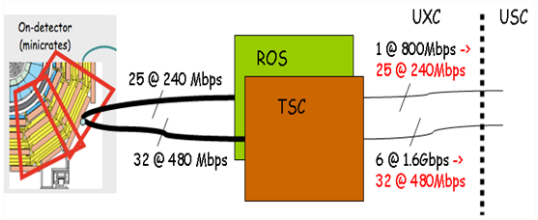

FIGURE 6. Schematic view of the DT electronics before LS1.

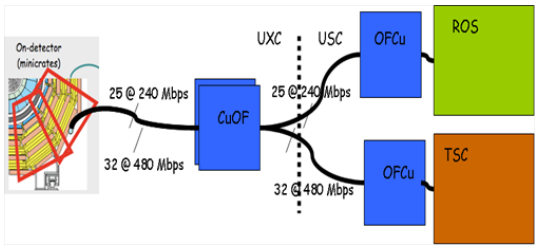

FIGURE 7. The DT electronics was already improved during LS1, putting TSC and ROS in the service cavern.

Electronics upgrade

Some longevity tests and several failure rate estimations showed that there is no need to upgrade the detector itself in the gas volume. On the contrary, several arguments came in favour to upgrade the electronics for phase 2 High Luminosity (HL) program: the radiation issues due to the increased luminosity, the intrinsic Level 1 trigger limitations in the current electronics called MiniCrate (MC), and also the need to get a more robust system by transferring some functionalities in the service cavern.

The first step of the trigger chain upgrade will be performed during phase 1 (run 2): a TwinMux system will be completed, allowing to combine the informations of the DT chambers and two others sub-systems, Resistive Plate Chambers (RPC) and Hadron Outer (HO), to get the trigger primitives. The redundancy will improve the resolution for instance in the gaps between the wheels and should avoid the repetition by the trigger processors. The TwinMux system is expected to be completed in 2016.

The second step of the electronics upgrade for phase 2 [5] will consist in replacing all the readout and trigger boards currently in the MC. The new board, called On Board Electronics for DT (OBEDT), will contain the digitization of the signals as well as the slow control Fig.8. The trigger primitive functionality will be transferred outside the experimental cavern. The design of the new boards is still on-going and the replacement should occur during LS3, that should begin possibly after 2023.

Conclusion

The DT system showed an excellent stability and performance during run 1 as well as the beginning of run 2. The data quality reached indeed the maximum possible level and the DT chambers delivered a very high trigger efficiency. The detector benefited from the improvements performed during LS1 and restarted in run 2 with a renewed and better efficiency. Finally, the long-term upgrade phase 2 program will be dedicated to the electronics replacement, to deal with HL-LHC environment and higher trigger rate.

ACKNOWLEDGMENTS

This work was supported by the BMBF (Bundesministerium für Bildung und Forschung).

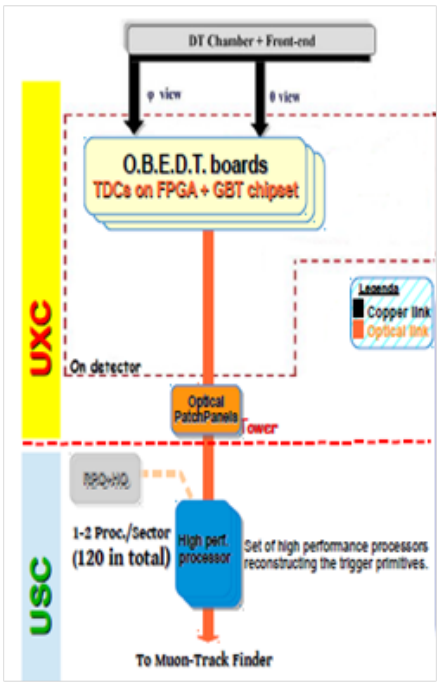

FIGURE 8. The upgraded electronics will consist of new mini-crates and the transfer of the Level 1 functionality to the service cavern. It will be replaced during LS3.

REFERENCES

[1] CMS Collaboration, *The CMS experiment at the CERN LHC*, JINST 3:S08004 (2008).

[2] The CMS Collaboration, *The Muon Project, Technical Design Report*, CERN/LHCC 97-31, CMS TDR2 (1997).

[3] https://twiki.cern.ch/twiki/bin/view/CMSPublic/MuonDPGResults

[4] The CMS Collaboration, *CMS Drift Tubes Sector Collector Relocation Phase 1 Upgrade*, CMS DN-2015/011.

[5] The CMS Collaboration, *Technical Proposal for the Phase-II Upgrade of the CMS Detector*, CERN/LHCC 2015-010, LHCC-P-008 (2015).

Proceedings of the LHCP2015 Conference, St. Petersburg, Russia, August 31 - September 5, 2015

Editors: V.T. Kim and D.E. Sosnov

First Search for the Associated Production of a Higgs Boson with a Single Top Quark

BENEDIKT MAIER

Karlsruhe Institute of Technology (KIT) – D-76131 Karlsruhe, Germany

benedikt.maier@kit.edu

On behalf of the CMS Collaboration

Abstract. The production of the Higgs boson in association with a single top quark is sensitive to the relative sign of the coupling parameters describing its interaction with fermions and gauge bosons. The tHq production mode therefore provides an good handle on the Yukawa coupling Y_t. The first searches for single-top + Higgs in the $H \to b\bar{b}$, $\gamma\gamma$, $\tau^+\tau^-$ and W^+W^- decay channels are presented, using the full 8 TeV dataset recorded with the CMS detector. Special emphasis is put on the analyses' peculiarities and their dominating systematic uncertainties, and a combination of all individual channels is performed. The analyses are optimized for a scenario of $Y_t = -1$, which is enhanced by a factor of ~ 13 with respect to the Standard Model production rate. The observed combined upper exclusion limit is $2.8 \times \sigma_{Y_t=-1}$ (2.0 expected).

INTRODUCTION

In 2012 [1, 2], the ATLAS and CMS collaborations announced the discovery of a new boson that is consistent with the Higgs boson as postulated in the 1960's [3, 4]. Since then it is the goal to measure its characteristics as precisely as possible in order to pin down possible deviations from the Standard Model (SM) predictions. The Yukawa coupling mechanism to fermions is an important feature and subject to such tests. In the theory coupling strengths are proportional to the fermion masses. In particular, since the top quark is the heaviest elementary particle known to exist, the coupling Y_t is a significant parameter for verification of the electroweak sector of the SM. According to $Y_f = \sqrt{2}\frac{m_f}{v}$, where the vacuum expectation value of the Higgs field is $v \sim 246\,\text{GeV}$, this gives an absolute value of $Y_t \simeq 1$. This is in accordance with recent measurements [5, 6]. Most channels however are insensitive to the sign of Y_t or, more precisely, to its relative sign with respect to the parameter describing the coupling of the Higgs boson to gauge bosons.

Figure 1 shows two leading-order Feynman diagrams for the associated production of a Higgs boson with a single top quark in the t-channel.[1] For the SM, there exists a destructive interference between the two diagrams, which results in a tiny production cross section of $\sigma_{tHq} = 18.3\,\text{fb}$ [7]. The scenario of $C_t = -1$ has a cross section enhanced by a factor ~ 13. This brings it into reach for searches with the integrated luminosity collected at $\sqrt{s} = 8\,\text{TeV}$. First and most recent phenomenological studies on tHq production can be found in [8, 9].

CHANNEL TOPOLOGY

For a single top t-channel-like process, the most characteristic feature is the upper outgoing quark line in Figure 1, which represents a light quark that has recoiled against the exchanged virtual W boson. It produces a typically very forward light jet with a substantial p_T. The other resonance besides the Higgs boson, the top quark, is required to decay leptonically for all decay channels considered here. The presence of a prompt lepton can help in rejecting multi-jet background processes. Moreover, the sign of the lepton will be used for constructing same-sign final states together with leptons stemming from the Higgs boson for the relevant decay modes. The top decay also features a b quark

[1] Diagrams where the Higgs boson is attached to b quark lines can be neglected because their contribution is suppressed by $(m_b/m_t)^2$.

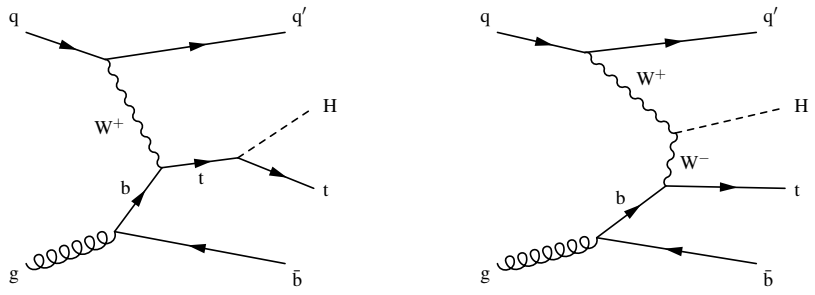

FIGURE 1. Leading order tHq Feynman diagrams.

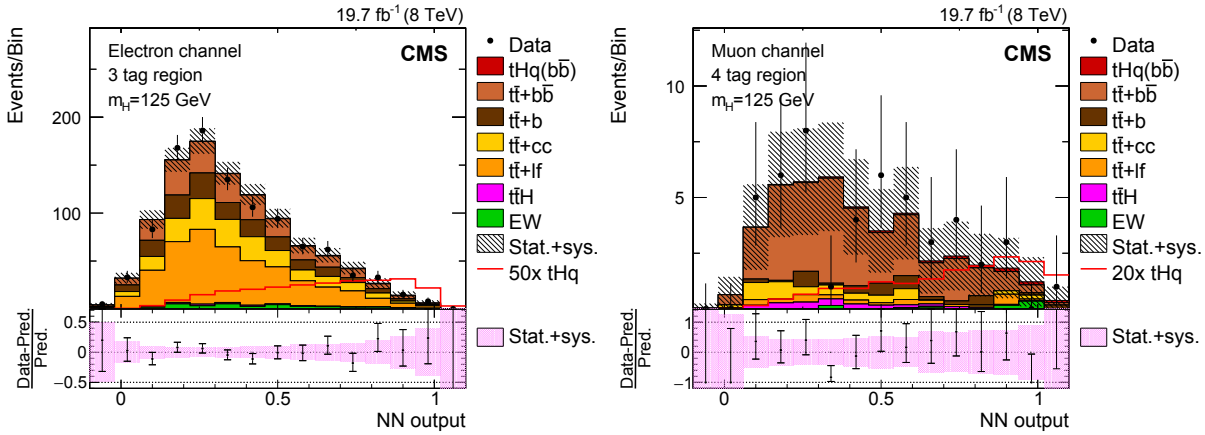

FIGURE 2. Post-fit NN output for the 3 tag region in the μ channel (left) and the 4 tag region in the electron channel (right). The red hollow line gives the pre-fit expectation for tHq ($C_t = -1$), scaled by a factor 50 (20).

giving rise to a central b jet. The initial gluon splitting creates a second, additional b quark. The corresponding b jet however lies out of the tracker acceptance most of the time and thus cannot be tagged. All considered final states have to fight a large $t\bar{t} + X$ background ($X = W, Z, H$, or jets).

HIGGS BOSON FINAL STATES

A pair of b quarks

Given the small production rates, the decay $H \to b\bar{b}$ with a branching fraction of 58% is a promising channel, as it retains most of the anyways sparse signal events. The electron (muon) from the leptonic top decay is required to have a transverse momentum larger than 30 GeV (26 GeV) and to lie in a central detector region with $|\eta| < 2.4$ (2.1). Additional leptons with a relaxed selection are vetoed in each event, leading to the rejection of Drell-Yan + jets processes. The analysis uses a jet $p_T$threshold of $p_T > 20$ GeV for central jets and 40 GeV for forward jets. E_T^{miss}, which is identified with the escaping neutrino, is required to be $> 45/35$ GeV (e/μ). At least one untagged jet is required in the event selection. Two categories are introduced, differing in the number of b tagged jets. The 3 tag category expects b jets stemming from the decays of the two reconances. A 4 tag category is introduced to be sensitive to the fraction of events where the additional b quark is produced centrally. The expected signal-over-background (S/B) ratios are 13/1900 in the 3 tag region and 1.4/66 in the 4 tag region.

This means that even after a dedicated event selection as described above, there is a dominating background contribution mainly from $t\bar{t}$+ jets production. A classification Neural Network (NN) is therefore employed to further separate the signal process from backgrounds, using as inputs observables that are genuine to tHq or $t\bar{t}$ events. Prior to this, a correspondence between the observed jets and the final state objects must be constructed in order to define

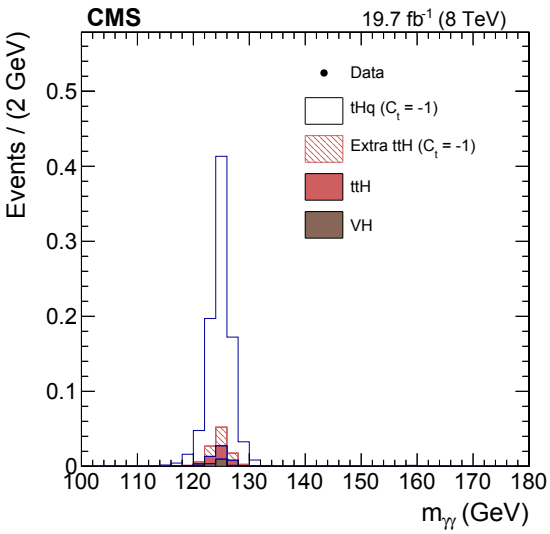

FIGURE 3. Invariant mass of the reconstructed diphoton system. Zero evets are observed.

the input variables to the classification NN in the most efficient way. Because of the large jet multiplicity, a correct jet assignment is a complex problem and is addressed by another Neural Network. It is trained with correct versus wrong jet assignments, where "correct" refers to the event interpretation where each parton (the three b quarks from the resonances, and the light quark) can be matched uniquely to a reconstructed jets, and a "wrong" interpretation is any other random jet assignment. When applying this reconstruction NN to unknown events, the event interpretation is picked that results in the largest response value of the discriminator. The same is done under the assumption the jets come from semi-leptonic $t\bar{t}$ production, matching the two b quarks from the tops and the two light quarks from the hadronically decaying W boson. Based upon these interpretations, the final classification NN is fed with input variables such as the p_T of the reconstructed Higgs boson, the mass of the reconstructed hadronically decaying W, and the lepton charge. The latter is an example for a variable that is independent from any type of reconstruction, but still provides a significant discrimination power between the symmetric case of $t\bar{t}$, and the t-channel-like tHq, which is more likely to be induced by quarks than by antiquarks, and consequently the charge of the lepton is ~ twice more often positive than negative in proton-proton collisions.[2]

Templates in the NN discriminator are then used to extract the signal and to set upper limits on σ_{tHq}. Figure 2 shows the NN output distributions in two of the four analysis bins. The $t\bar{t}$+ jets background has been split into categories varying in their additional heavy flavor content. The uncertainties on their rates and on higher order effects are the main sources of systematic uncertainty. An upper limit of $5.4 \times \sigma_{C_t=-1}$ at 95% confidence level (C.L.) is found. The observed limit is slightly higher (7.6).

Two photons

The decay of the Higgs boson to two photons happens via a virtual loop of either top quarks or W bosons. Just like for the production there is a constructive interference for $C_t = -1$, leading to a further enhancement on the expected rates by a factor 2.8. The event selection foresees two photons with $p_{T,\gamma_1} > 50 m_{\gamma\gamma}/120\,\text{GeV}$ and $p_{T,\gamma_2} > 25\,\text{GeV}$, where $m_{\gamma\gamma}$ denotes the invariant mass of the reconstructed diphoton system. Further required are a b tagged jet ($p_T > 20\,\text{GeV}$), an untagged forward jet ($p_T > 20\,\text{GeV}$ and $|\eta| > 1$) and an isolated muon or electron with $p_T > 10\,\text{GeV}$. The signal region is defined in the window $122 < m_{\gamma\gamma} < 128\,\text{GeV}$, i.e. ±3 GeV around the expected Higgs mass.

With several variables discriminating against $t\bar{t}H$, like the jet multiplicity in the event, the pseudorapidity of the light quark candidate jet or again the lepton charge, a simple likelihood classifier is constructed and cut on in order to reduce the resonant background. The resulting expected yields are 0.67 for tHq, and 0.03 + 0.05 for $t\bar{t}H$ and

[2] In fact, the t-channel's high sensitivity to the quark/antiquark density in protons makes it an ideal place to constrain PDFs. This is being done for the case without the Higgs, where cross sections are much higher and almost pure signal samples can be obtained.

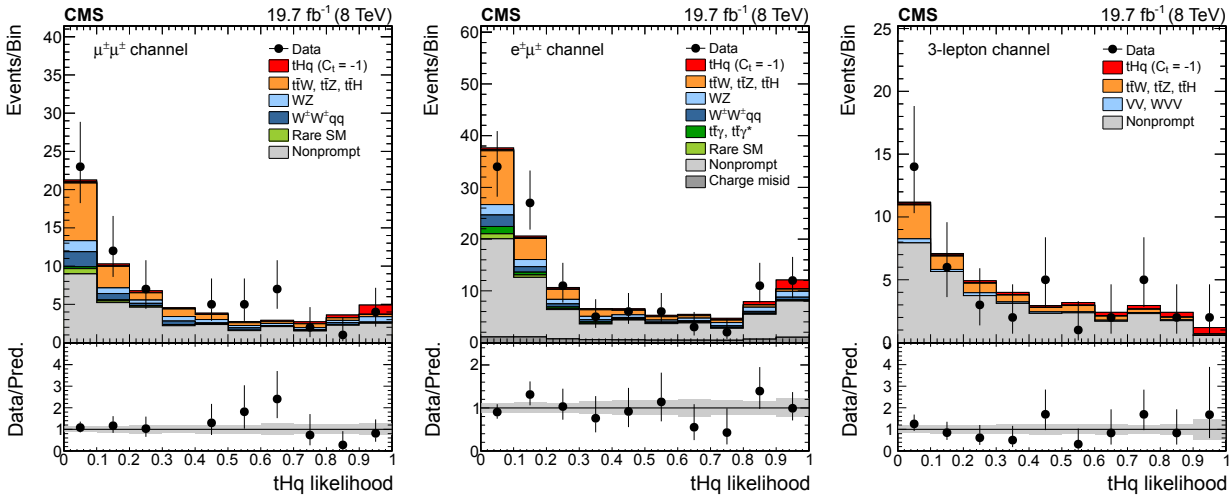

FIGURE 4. Post-fit likelihood disciminator for the μμ (left), the eμ (center) and the trilepton channel (right). The gray bands represent the combined statistical and systematic uncertainties as determined in the maximum-likelihood fit to data.

0.01 + 0.01 for VH. The latter numbers describe the aforementioned effect of enhanced rates in the Higgs boson decay. Predictions for all the Higgs related processes are taken from simulation. Other background contributions would stem from $t\bar{t}$ + γγ or γγ + jets production. These have a non-resonant shape in the invariant diphoton mass $m_{\gamma\gamma}$ and are best determined with a data-driven technique from the sidebands (100, 122) GeV and (128, 180) GeV. In order to have enough data in these regions, b tagging criteria are relaxed. A falling exponential is the assumed fuction[3]; its parameters are determined from the sidebands, and it is extrapolated into the signal region to estimate the contribution of the non-resonant backgrounds.

In Figure 3 the resulting distribution for $m_{\gamma\gamma}$ is shown. Zero events are observed in both signal and sideband regions. In such a case the observed and expected limits coincide; the analysis is able to exclude $4.1 \times \sigma_{C_t=-1}$ at 95% C.L.

Multi-leptons

In the trilepton channel contributions are expected from events where the Higgs boson decayed into a pair of W bosons or taus which then have an entirely leptonic decay chain. This leads to the allowed lepton combinations (eee), (μμμ), (eeμ) and (eμμ) with $p_T > 20/10/10$ GeV. A cut on $E_T^{miss} > 30$ GeV accounts for the presence of three neutrinos. The reconstructed dilepton mass closest to m_Z must lie outside ($m_Z \pm 15$ GeV) to suppress the Drell-Yan background. Exactly one central jet must be tagged as b jet, and at least one forward jet is required with $|\eta| > 1.5$. The dilepton channel asks for exactly two leptons with same electric charge, allowing the combinations (eμ), (μμ) with $p_{T,\ell} > 25$ GeV and $m_{\ell\ell} > 20$ GeV. There has to be at least one central tagged b jet and one or more forward jets ($|\eta| > 1.0$). Since for this channel one of the W bosons is assumed to decay hadronically, one additional central jet is required. Hadronically decaying τ's are vetoed explicitly. The jet p_T threshold for both channels is 25 GeV.

The most significant background comes from $t\bar{t}$ events, where leptons can be produced in the decay of B hadrons, or when light jets are misidentified as leptons. A "tight-to-loose" method employs the p_T- and η-dependent probabilities that a non-prompt lepton which passes looser isolation and impact parameter criteria also fulfills the tight lepton ID criteria used in the analysis. It estimates the probabilities in data using a control sample enriched in background leptons. With the determined fake rates the event yields in sideband regions differing only in the lepton isolation can be weighted into the signal region to obtain an estimate for the non-prompt backgrounds. Contamination due to misidentified lepton charge is estimated from $Z \to \ell\ell$ events. The misidentification rate for electrons amounts to $< 0.08\%$ in the barrell and $\sim 0.28\%$ in the endcap. For muons it is negligible. A likelihood discriminator is built from information on lepton charge and kinematics, forward jet activity and b jet multiplicity. It discriminates between 3.3

[3]The uncertainty on the knowledge of the background shape is estimated using another control region with inverted isolation requirements on one of the two photons.

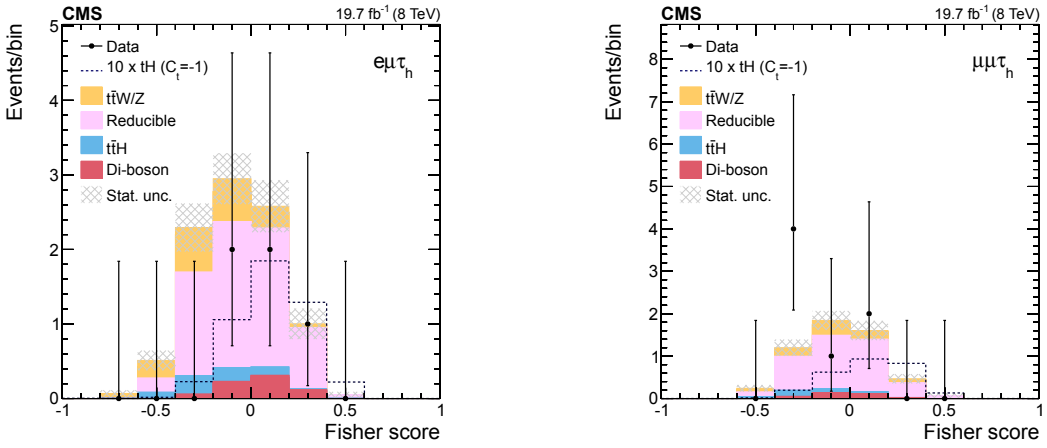

FIGURE 5. Post fit Fisher discriminant distributions for the eμ (left) and μμ (right) channel. The dotted line gives the expected contribution from tHq; for making it visible it is scaled up by a factor 10.

(2.6) signal events and 106 (53) background events for the eμ (μμ) channel. The S/B ratio for the trilepton channel is 1.5/42. The post-fit classifier output in all channels can be seen in Figure 4. Upper exclusion limits at 95% C.L. on tHq production are derived from these distributions and is found to be $5.0 \times \sigma_{C_t=-1}$ (expected) and $6.7 \times \sigma_{C_t=-1}$ (observed), respectively.

$\tau_{lep}\,\tau_{had}$

While there is a substantial leakage of events with two leptonically decaying taus into the previously described selection of the multi-lepton search, this complementary analysis is looking for final states where a hadronically decaying τ could be reconstructed and two other same-sign leptons (eμ,μμ) are identified, one of which is expected to stem from the top quark decay. The same-sign requirement strongly suppresses backgrounds with a prompt dilepton pair of opposite charge, like in $Z/\gamma^* \to \mu\mu$, that has been produced in association with a faked hadronically decaying τ. The two leading leptons (electrons or muons) must fulfill $p_T > 20/10$ GeV. For electrons (muons), the η requirement is $|\eta| < 2.5$ (2.4). A boosted decision tree trained with variables affecting lepton isolation is used to further reject events with secondary leptons such as from B hadron decays. The third lepton – the hadronically decaying tau, τ_{had} – must have a transverse momentum larger than 20 GeV and must be reconstructed in a central detector region with $|\eta| < 2.3$. It must have opposite charge compared to the other two leptons. All three of them need be separated by $\Delta R_{\ell\ell} > 0.5$. At least one b tagged jet is required with $p_T > 25$ GeV. This does not only reflect the expected signal topology with the top quark decay, but also significantly reduces the $Z \to \tau\tau$ + jets background, which lacks a genuine b jet.

Akin to the situation in the multi-lepton analysis, background contributions due to misidentified non-prompt leptons are estimated using a data-driven technique via fake rates in control samples and applying them to a signal sideband region. Irreducible backgrounds such as diboson production or $t\bar{t}$ +W/Z are modelled using Monte-Carlo simulations. One expects 0.48 (0.30) signal events and 9.5 (5.4) background events in the $e\mu\tau_{had}$ ($\mu\mu\tau_{had}$) channel. A Fisher discriminant shall separate between tHq and the backgrounds. It is formed from variables describing e.g. the forward jet kinematics and the b jet multiplicity. The training is performed in a control region with inverted isolation criteria on the reconstructed τ_{had} because of statistics.

The expected upper limit is derived from the two Fisher discriminators in Figure 5 and is (at 95% C.L.) $11 \times \sigma_{C_t=-1}$, while the data allows to exclude scenarios with cross sections larger than $9 \times \sigma_{C_t=-1}$.

COMBINATION

All of the distributions that have been shown so far can be used to derive common observed and expected upper limits on the $C_t = -1$ scenario. The predictions of all channels are simultaneously fit to data; the underlying statistical model involves all the nuisance parameters of the single analyses. Two results are presented: the first approach fully takes

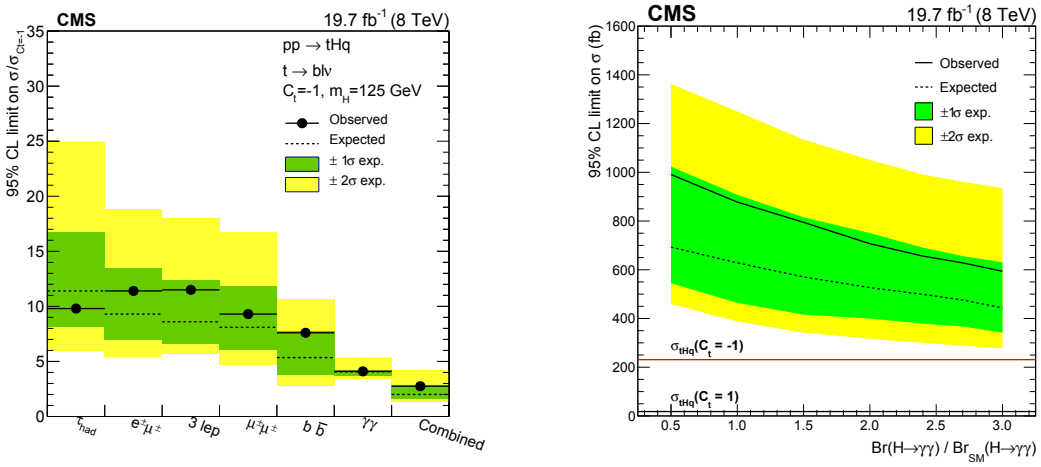

FIGURE 6. Left: observed and expected exclusion limits for $C_t = -1$ for the single analyses as well as for their combination. Here the additional expected contributions from $C_t = -1$ in the decay $H \to \gamma\gamma$ are explicitly taken into account as signal. Right: the search sensitivity is quoted as a function of $\mathcal{B}(H \to \gamma\gamma)$.

the enhancement effects also in the decay to two photons into account. The expected search sensitivity turns out to be $2.0 \times \sigma_{C_t=-1}$ at 95% C.L., the observed limit is $2.8 \times \sigma_{C_t=-1}$. Another approach provides the limits as a function of the branching fraction $\mathcal{B}(H \to \gamma\gamma)$, which depends on C_t. Figure 6 summarizes the limits of the single analyses and shows the combined results.

REFERENCES

[1] ATLAS collaboration, *Phys. Lett.* B **716**, 1-29 (2012)
[2] CMS collaboration, *J. High Energy Phys.* **06**, 081 (2013)
[3] F. Englert and R. Brout, *Phys.Rev.Lett.* **13** (1964)
[4] P. W. Higgs, *Phys.Rev.Lett.* **13** (1964)
[5] ATLAS collaboration, ATLAS-CONF-2014-009 (2014)
[6] CMS collaboration, CMS-PAS-HIG-14-009 (2014)
[7] M. Farina et al., *J. High Energy Phys.* **06**, 103 (2013)
[8] F. Maltoni et al., *Phys. Rev.* **D64** (2014)
[9] F. Demartin et al., *Eur. Phys. J.* **C75** (2015)

Proceedings of the LHCP2015 Conference, St. Petersburg, Russia, August 31 - September 5, 2015

Editors: V.T. Kim and D.E. Sosnov

Search for the Standard Model Higgs boson produced by vector boson fusion and decaying to bottom quarks

GIORGIA RAUCO

Physik-Institut, Universität Zürich, CH-8057 Zürich, Switzerland

giorgia.rauco@cern.ch

On behalf of the CMS Collaboration

Abstract. The search for the Standard Model (SM) Higgs boson (H) produced through the Vector Boson Fusion (VBF) mechanism and decaying to a pair of bottom quarks is reported. The used data have been collected with the CMS detector and correspond to an integrated luminosity of 19.8 fb^{-1} of proton-proton collisions at $\sqrt{s}$ = 8 TeV at the CERN LHC. Parked data have been exploited as well. This search resulted in an observed (expected) significance in these data samples for a $H \to b\bar{b}$ signal at a mass of 125 GeV of 2.2 (0.8) standard deviations. The cited signal strength, $\mu = \sigma/\sigma_{SM}$, was measured to be $2.8^{+1.6}_{-1.4}$. This result has been combined with other CMS searches for the SM Higgs boson decaying in a pair of bottom quarks exploiting other Higgs production mechanisms. The obtained combined signal strength is 1.0 ± 0.4, corresponding to an observed signal significance of 2.6 standard deviations for a Higgs boson mass of 125 GeV.

INTRODUCTION

In the Standard Model theory [1, 2, 3] the electroweak symmetry breaking is explained by the Brout-Englert-Higgs mechanism [4, 5, 6] which is responsible for the electroweak gauge bosons to acquire mass. This mechanism predicts the existence of a Higgs scalar boson. The observation of a new particle in the mass region around 125 GeV, consistent with the Higgs boson, was announced by the ATLAS [7] and CMS [8] experiments at CERN's Large Hadron Collider (LHC) on 4 July 2012.

After the Higgs boson discovery, the main goal is now to precisely measure and study the properties of the recently discovered particle and to compare them with the ones expected for the predicted boson. One of the most interesting aspects to analyze is the coupling between the particle and the fermions and, in the SM theory, the most probable decay of the Higgs boson of m_H = 125 GeV is in a pair of b-quarks. This process is particularly difficult to be observed at the LHC in the inclusive production (dominated by Gluon Fusion) since the QCD background is overwhelming. It is therefore searched in other production channels: Vector Boson Fusion (VBF), Associated Vector Boson Production (VH) and Associated Top-Pair Production (ttH), where the Higgs boson is produced in association with other particles, resulting in a more distinguishing signal topology. The VBF production channel is the one exploited in the analysis here presented.

In the VBF process a quark of each one of the colliding protons radiates a W or Z boson that subsequently interact or fuse. The two valence quarks are typically scattered away from the beam line and inside the detector acceptance, where they can be revealed as hadronic jets. The prominent signature of VBF is therefore the presence of two energetic hadronic jets, roughly in the forward and backward direction with respect to the proton beam line. As a result, the signal final state features are a central b-quark pair (from the Higgs decay) and a light- quark pair (u,d-type) from each of the colliding protons, in the forward and backward regions.

The overwhelmingly most relevant and irreducible background to the signal search comes from the QCD production of four jets events with true or mistagged b-jets. Other backgrounds arise from: (i) hadronic decays of Z or W bosons produced in association with additional jets, (ii) hadronic decays of top quark pairs, and (iii) hadronic decays of singly produced top quarks. The final expected signal yield includes also the contribution of the Higgs bosons produced in Gluon Fusion processes with at least two associated jets.

TRIGGER

The data used for this analysis were collected with two different trigger strategies:

1. **Dedicated VBF qqH → qqb$\bar{\text{b}}$ trigger**. A set of dedicated trigger paths was specifically designed and deployed for the VBF qqH → qqbb signal search, both for the L1 and HLT levels, and operated during the full 2012 data-taking period. This set of triggers, called nominal, collected the largest fraction of the signal event.
   The L1 paths require the presence of three jets with p_T above optimized thresholds X, Y, Z (X = 64 - 68 GeV, Y = 44 - 48 GeV, Z = 24 - 32 GeV) according to instantaneous luminosity. Among the three jets, at most one among the two p_T leading jets can be in the forward pseudorapidity region, while the remaining two have to be central. The HLT paths are seeded by the L1 paths described above, and require the presence of four jets with p_T above thresholds that are again adjusted to the data-taking luminosity, p_T > 75 - 82, 55 - 65, 35 - 48, and 20 - 35 GeV, respectively. At least one of the selected four jets must further fulfill minimum b-tagging requirements. To identify the two VBF-tagging jets two criteria have been exploited: (i) the pair with the smallest HLT b-tagging values; (ii) the pair with the maximum pseudorapidity opening. Both pairs are required to exceed variable minimum thresholds on $|\Delta\eta_{jj}|$ of 2.2-2.5, and of 200-240 GeV on the dijet invariant mass m_{jj}, depending on the instantaneous luminosity.
2. **General-purpose VBF trigger.**
   The L1 paths for the general-purpose VBF trigger require minimum hadronic activity in the event with a scalar p_T sum of 175 or 200 GeV, depending on the instantaneous luminosity. The HLT path is seeded by the L1 path described above, and requires the presence of at least two CaloJets with p_T > 35 GeV. Out of all the possible jet pairs in the event the pair with the highest invariant mass is selected as the most probable VBF tagging pair. The corresponding invariant mass m_{jj} and absolute pseudorapidity difference $|\Delta\eta_{jj}|$ are required to be larger than 700 GeV and 3.5.

The integrated luminosity collected with the first set of triggers was 19.8 fb^{-1} , while for the second trigger it was 18.2 fb^{-1} .

EVENT RECONSTRUCTION AND SELECTION

The offline analysis uses reconstructed charged-particle tracks and candidates of the Particle-Flow (PF) algorithm [9, 10, 11]. Jets are reconstructed by clustering the PF candidates with the anti-k_T algorithm with distance parameter 0.5 and jets that are likely to be originated from the hadronization of b quarks are identified with the CSV b-tagger [12].

The events used in the offline analysis are required to have at least four reconstructed jets and the four p_T-leading ones are considered as the most probable b-jet and VBF jet candidates. A multivariate discriminant taking into account the b-tag value, the b-tag ordering, the η value, and the η ordering is exploited to distinguish between the two jet types. The offline event selection is based upon the kinematic properties of the b-jet and VBF jets. Selected events are divided into two sets: set A and set B, whereof the selection requirements are shown in Table 1.

After all the selection requirements, 2.3% of the VBF simulated signal events end up in set A and 0.8% end up in set B. In set B 39% of the signal events would also satisfy the requirements to enter set A. Such events are taken into set A and vetoed from set B, as noted in the last line of Table 1.

SIGNAL PROPERTIES

Jet transverse-momentum regression

In order to improve the b$\bar{\text{b}}$ mass resolution a regression technique is applied. It is essentially a refined calibration for individual b-jets which takes into account the jet composition properties beyond the default jet-energy corrections. This regression technique mainly targets the b decays in a neutrino that lead to a substantial mismeasurement of the jet p_T.

For this purpose a regression Boost Decision Tree (BDT), trained on simulated signal events, is applied. Its inputs include: (i) the jet p_T, η and mass; (ii) the jet-energy fractions carried by neutral hadrons and photons; (iii) the mass and the uncertainty on the decay length of the secondary vertex, when present; (iv) the event missing transverse energy

TABLE 1. Summary of selection requirements for the two analysis sets. Reprinted from [13].

	set A	**set B**
trigger	**dedicated VBF qqH → qqbb̄**	**general-purpose VBF trigger**
jets p_T	$p_{T,1,2,3,4} > 80, 70, 50, 40$GeV	$p_{T,1,2,3,4} > 30$GeV $p_{T,1} + p_{T,2} > 160$GeV
jets $\|\eta\|$	< 4.5	< 4.5
b-tag	at least 2 CSVL jets	at least 1 CSVM and 1 CSVL jets
$\Delta\phi_{bb}$	< 2.0	< 2.0
VBF topology	$m_{jj} > 250$GeV $\|\Delta\eta_{jj}\| > 2.5$	m_{jj}, $m_{jj}^{trig} > 700$GeV $\|\Delta\eta_{jj}\|$, $\|\Delta\eta_{jj}^{trig}\| > 3.5$
veto	none	events that belong to set A

and its azimuthal direction relative to the jet; (v) the total number of jet constituents; (vi) the p_T of the soft-lepton candidate inside the jet, when present, and its p_T component perpendicular to the jet axis; (vii) the p_T of the leading track in the jet; (viii) the event's average p_T density in the $y - \phi$ space.

The improvement on the jet p_T leads to an improvement on the dijet invariant mass resolution by approximately 17%.

Discrimination between quark-and gluon-originated jets

The VBF-tagging jets originate from the hadronization of a light (u,d-type) quark, while the jets produced in QCD processes are more likely to come from gluons. As a consequence, in order to further identify if the jet pair with the smallest b-tagging values among the four selected jets is a signal event or a background event, a quark-gluon discriminator [14, 15, 16] is applied to the b-tag sorted jj candidate jets.
The discriminator exploits the differences in the showering and the fragmentation of gluons and quarks and it uses, as an input to a likelihood trained on gluon and quark jets from simulated QCD events, the following variables: (i) the jet constituents' major quadratic mean (RMS) in the $\eta - \phi$ plane; (ii) the jet constituents' minor quadratic mean (RMS) in the $\eta - \phi$ plane; (iii) the jet asymmetry pull (essentially a p_T-weighted vector); (iv) the jet particle multiplicity; (v) the maximum energy fraction carried by a jet constituent.

Soft QCD activity

In the region between the two VBF-tagging jets (with the exception of the more centrally produced Higgs decay products), the QCD color flow is suppressed. In order to measure the additional hadronic activity associated with the main primary vertex, only charged tracks are used.

A collection of *additional tracks* is built, selecting reconstructed tracks that: (i) have a *high purity* quality flag; (ii) have p_T >300 MeV; (iii) are not associated to any of the four leading jets; (iv) have a minimum longitudinal impact parameter, $|d_z(PV)|$ with respect to the event's main primary vertex; (v) satisfy $|d_z(PV)| < 2$ mm and $|d_z(PV)| < 3\sigma_z(PV)$ where $\sigma_z(PV)$ is the uncertainty on $d_z(PV)$; (vi) are not in the region between the most b-tagged jets. This region is defined as an ellipse in the $\eta - \phi$ plane around the b-jets with axis $(a, b) = (\Delta R(bb) + 1, 1)$ where $\Delta R = \sqrt{(\Delta\eta_{bb})^2 + (\Delta\phi_{bb})^2}$.

The additional tracks are then clustered in *soft TrackJets* within the anti-k_T algorithm [17] (with R = 0.5).

In order to discriminate between the signal and the QCD background, a discriminating variable H_T^{soft} is used and it is defined as the scalar p_T sum of the soft TrackJets with p_T >1 GeV.

SEARCH FOR A HIGGS BOSON

In order to separate the overwhelmingly large QCD background from the Higgs boson signal, all the discriminating features have to be used in an optimal way. This is achieved by using a BDT multivariate discriminant, which exploits as input, variables very weakly correlated to the dynamics of the $b\bar{b}$ system, in particular to $m_{b\bar{b}}$. These variables are conceptually grouped into five groups: (i) the dynamics of the VBF jet system, expressed by $\Delta\eta_{jj}$, $\Delta\phi_{jj}$, and m_{jj}; (ii) the b jet content of the event, expressed by the CSV output for the two most b-tagged jets; (iii) the jet flavor of the event: quark-gluon likelihood (QGL) for all four jets; (iv) the soft activity, quantified by the scalar p_T sum H_T^{soft} of the additional "soft" TrackJets with $p_T > 1$ GeV, and the number N^{soft} of "soft" TrackJets with $p_T > 2$ GeV; (v) the angular dynamics of the production mechanism, expressed by the cosine of the angle between the jj and $b\bar{b}$ vectors in the center-of-mass frame of the four leading jets $\cos\theta_{jj,bb}$.

Since the properties of the selected events are significantly different between the two selections (set A and set B) and two BDT's are trained.

According to the BDT outputs, seven categories are defined: four for set A and three for set B. The QCD $m_{b\bar{b}}$ spectrum shape is assumed to be the same in all BDT categories of the same set of events. In reality small differences between the categories are present and to take into account this effect transfer functions are exploited (linear function in set A and quadratic in set B). With the introduction of the transfer functions, the fit model for the Higgs boson signal is

$$f_i(m_{b\bar{b}}) = \mu_H \cdot N_{i,H} \cdot H_i(m_{b\bar{b}}; k_{JES}, k_{JER}) + N_{i,Z} \cdot Z_i(m_{b\bar{b}}; k_{JES}, k_{JER}) + N_{i,Top} \cdot T_i(m_{b\bar{b}}; k_{JES}, k_{JER}) + N_{i,QCD} \cdot K_i(m_{b\bar{b}}) \cdot B(m_{b\bar{b}}; \vec{p}_{set}), \quad (1)$$

where the subscript i denotes the category and μ_H, $N_{i,QCD}$ are free parameters for the signal strength and the QCD event yield. $N_{i,H}$, $N_{i,Z}$, and $N_{i,Top}$ are the expected yields for the Higgs boson signal, the Z+jets, and the top background respectively. The shape of the top background $T_i(m_{b\bar{b}}; k_{JES}, k_{JER})$ is taken from the simulation (sum of the $t\bar{t}$ and single-top contributions) and is described by a broad gaussian. The Z/W+jets background $Z_i(m_{b\bar{b}}; k_{JES}, k_{JER})$ and the Higgs boson signal $H_i(m_{b\bar{b}}; k_{JES}, k_{JER})$ shapes are taken from the simulation and are parameterized as a crystal-ball function on top of a polynomial background. The position and the width of the gaussian core of the MC templates (signal and background) are allowed to vary by the free factors k_{JES} and k_{JER}, respectively, which quantify any mismatch of the jet energy scale and resolution between data and simulation. Finally, the QCD shape is described by a Bernstein polynomial $B(m_{b\bar{b}}; \vec{p}_{set})$, common within the categories of each set, and whose parameters $\vec{p}_{set}$ are determined by the fit, and a multiplicative transfer function $K_i(m_{b\bar{b}})$ that accounts for the shape differences between the categories. For set A, the Bernstein polynomial is of 5th order, while for set B it is of 4th order. Figure 1 show the simultaneously fitted $m_{b\bar{b}}$ distributions in the signal enriched categories for set A and set B, respectively.

RESULTS

The models representing the two hypotheses, of background only, and of background+signal are fitted to the data, simultaneously in all the categories. The limits on the signal strength are computed with the Asymptotic CLs method [18]. Figure 2 shows the observed (expected) 95% C.L. limit on the signal strength, as a function of the Higgs boson mass, which ranges from 5.1 (2.2) at $m_H = 115$ GeV to 5.9 (3.8) at $m_H = 135$ GeV, together with the expected limits in the presence of a SM Higgs boson with mass 125 GeV. For a 125 GeV Higgs boson signal the observed (expected) significance is 2.2 (0.8) standard deviations, and the fitted signal strength is $\mu = \sigma/\sigma_{SM} = 2.8^{+1.6}_{-1.4}$. The measured signal strength is compatible with the SM Higgs boson prediction $\mu = 1$ at the 8% level.

The search for the Standard Model Higgs boson decaying in a pair of bottom quarks, as described in the previous Sections, is performed by the CMS Collaboration in the VH [19], VBF and ttH [20] production channels. The results of these searches are summarized in Table 2, along with the resulting combined results.

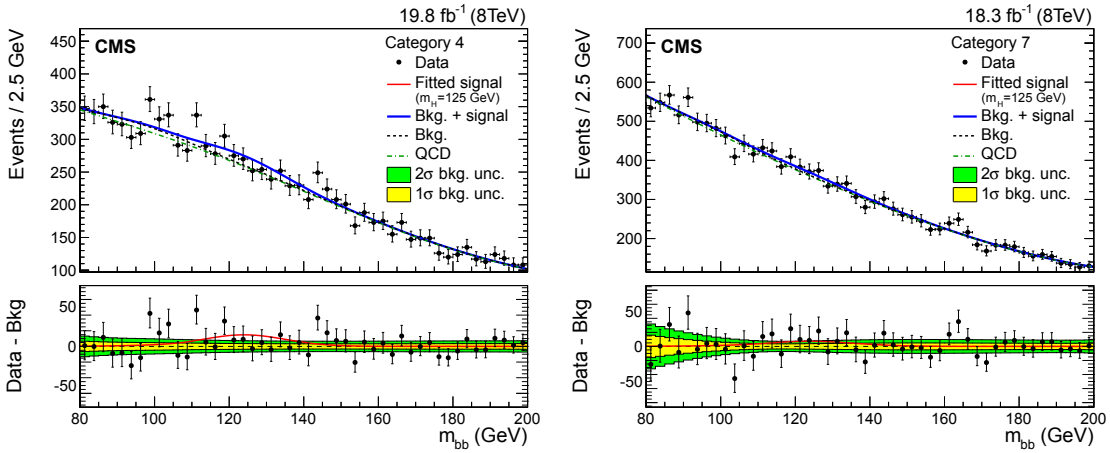

FIGURE 1. Fit for the Higgs boson signal (m_H = 125 GeV) on the invariant mass of the two b-jet candidates in the signal enriched event category of set A (left) and set B (right). Data is shown with markers. The solid line is the sum of the post-fit background and signal shapes, the dashed line is the background component, and the dashed-dotted line is the QCD component alone. The bottom panel shows the background-subtracted distribution, overlaid with the fitted signal, and with the 1-σ and 2-σ background uncertainty bands. Reprinted from [13].

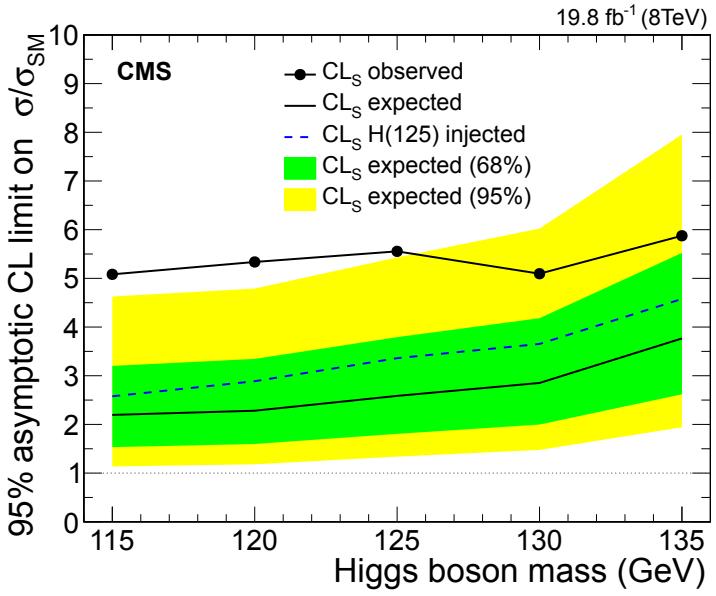

FIGURE 2. Expected and observed 95% confidence level limits on the signal cross section in units of the SM expected cross section, as a function of the Higgs boson mass, including all event categories. The limits expected in the presence of a SM Higgs boson with mass 125 GeV are indicated by the dotted curve. Reprinted from [13].

TABLE 2. Observed and expected 95%CL limits, best fit values and significance on the signal strength parameter $\mu = \sigma/\sigma_{SM}$ at m_H = 125 GeV, for each $H \to b\bar{b}$ channel and combined. Reprinted from [13].

$H \to b\bar{b}$ channel	Best-fit (68% CL)	Upper Limits (95% CL)		Signal significance	
	Observed	Observed	Expected	Observed	Expected
VH	0.89 ± 0.43	1.68	0.85	2.08	2.52
ttH	0.7 ± 1.8	4.1	3.5	0.37	0.58
VBF	$2.8^{+1.6}_{-1.4}$	5.5	2.5	2.20	0.83
combined	$1.03^{+0.44}_{-0.42}$	1.77	0.78	2.56	2.70

REFERENCES

[1] S. Glashow, Nuclear Physics **22**, 579–588 (1961).
[2] A. Salam and J. Ward, Nuovo Cimento **19**, 165–170 (1961).
[3] S. Weinberg, Physical Review Letters **19**, 1264–1266 (1967).
[4] F. Englert and R. Brout, Phys.Rev.Lett. **13**, 321–323 (1964).
[5] P. Higgs, Physical Review Letters **13**, 508–509 (1964).
[6] G. S. Guralnik, C. R. Hagen, and T. W. B. Kibble, Phys. Rev. Lett. **13**, 585–587 (1964).
[7] ATLAS Collaboration, Physics Letters B **716**, 1–29 (2012).
[8] CMS Collaboration, Physics Letters B **716**, 30–61 (2012).
[9] CMS Collaboration, Commissioning of the Particle-Flow Event Reconstruction with the first LHC collisions recorded in the CMS detector, 2010, CMS-PAS-PFT-10-001.
[10] CMS Collaboration, Commissioning of the Particle-Flow reconstruction in minimum-bias and jet events from pp collisions at 7 TeV, 2010, CMS-PAS-PFT-10-002.
[11] CMS Collaboration, Particle-Flow Event Reconstruction in CMS and Performance for Jets, Taus, and MET, 2009, CMS-PAS-PFT-09-001.
[12] CMS Collaboration, JINST **8**, p. P04013 (2013).
[13] CMS Collaboration, Phys. Rev. D **92**, p. 032008Aug (2015).
[14] CMS Collaboration, JHEP **10**, p. 101 (2013).
[15] CMS Collaboration, The European Physical Journal C **75** (2015).
[16] CMS Collaboration, Performance of quark/gluon discrimination in 8 TeV pp data, 2013, CMS-PAS-JME-13-002.
[17] M. Cacciari, G. P. Salam, and G. Soyez, JHEP **0804**, p. 063 (2008), arXiv:0802.1189 [hep-ph] .
[18] G. Cowan, K. Cranmer, E. Gross, and O. Vitells, The European Physical Journal C **71** (2011).
[19] CMS Collaboration, Phys. Rev. D **89**, p. 012003Jan (2014).
[20] CMS Collaboration, Journal of High Energy Physics **2013** (2013).

Proceedings of the LHCP2015 Conference, St. Petersburg, Russia, August 31 - September 5, 2015

Editors: V.T. Kim and D.E. Sosnov

LHCb's Real-Time Alignment in Run II

VARVARA BATOZSKAYA

National Centre for Nuclear Research (NCBJ), Warsaw, Poland

varvara.batozskaya@cern.ch

On behalf of the LHCb Collaboration

Abstract. The LHCb collaboration has introduced a novel real-time detector alignment and calibration strategy for LHC Run II. The data collected at the start of the fill will be processed in a few minutes and used to update the alignment, while the calibration constants will be evaluated for each run. This procedure will improve the quality of the online alignment. Critically, this new real-time alignment and calibration procedure allows identical constants to be used in the online and offline reconstruction, thus improving the correlation between triggered and offline selected events. This offers the opportunity to optimise the event selection in the trigger by applying stronger constraints. The required computing time constraints are met thanks to a new dedicated framework using the multi-core farm infrastructure for the trigger. The motivation for a real-time alignment and calibration of the LHCb detector is discussed from both the operational and physics performance points of view. Specific challenges of this novel configuration are discussed, as well as the working procedures of the framework and its performance.

INTRODUCTION

The LHCb detector [1] is a single-arm forward spectrometer that covers the pseudorapidity range $2< \eta <5$, designed for the study of particles containing b or c quarks. The detector includes a high-precision tracking system consisting of a silicon-strip vertex detector (VELO) surrounding the pp interaction region [2], a large area silicon-strip detector (TT) located upstream of a dipole magnet with a bending power of about 4 Tm, and three stations of silicon-strip detectors (IT) and straw drift tubes (OT) [3] placed downstream. The combined tracking system has momentum resolution $\Delta p/p$ that varies from 0.4% at 5 GeV/c to 0.6% at 100 GeV/c and an impact parameter resolution of 20 μm for tracks with high transverse momentum. Charged hadrons are identified using two ring-imaging Cherenkov detectors (RICH) [4]. Photons, electrons and hadrons are identified by a calorimeter system consisting of scintillating-pad and preshower detectors, an electromagnetic calorimeter and a hadronic calorimeter. Muons are identified by a system composed of alternating layers of iron and multiwire proportional chambers [5]. The online event selection is performed by a trigger [6], which consists of a hardware stage (L0), based on information from the calorimeter and muon systems, followed by software stages (HLT1 and HLT2), which apply a full event reconstruction.

The spatial alignment of a detector and the accurate calibration of its subcomponents are important elements of achieving the best physics performance [7]. The correct alignment of the VELO is needed to identify secondary vertices from the decay of particles with b or c quarks while a misalignment of the all tracking system would degrade the mass resolution. The improvement of alignment significantly increases the Υ mass resolution from 86 MeV/c^2 with the first to 44.3 MeV/c^2 with the improved alignment as is shown in Figure 1. It is clear that a more effective selection and a higher signal purity of studied channels can be achieved by a real-time alignment and calibration.

Trigger strategies

In Run I the rate of collisions was 15 MHz and it will double in Run II while the output rate of events saved on disk will change from 5 kHz in Run I to 12.5kHz in Run II (Fig. 2). The online event reconstruction in Run I was simpler and faster than the one used offline on triggered events and did not use the latest alignment and calibration constants. In Run II, the selected events after L0 and HLT1 triggers are buffered on local disks and an automatic calibration and

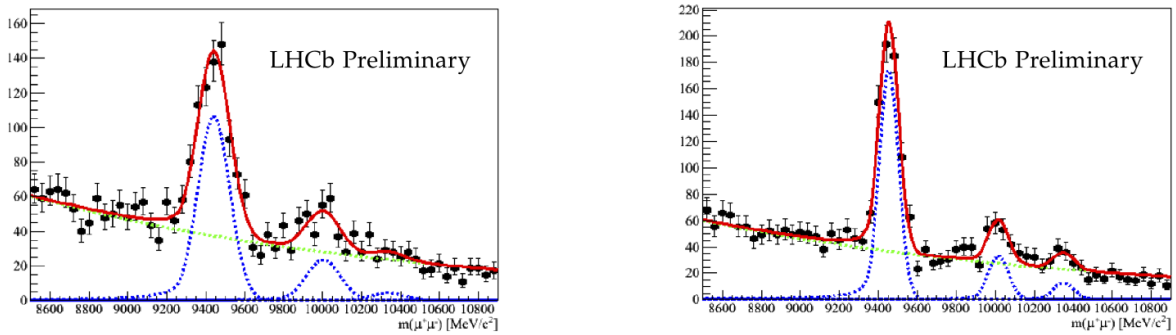

FIGURE 1. Invariant mass distribution of $\Upsilon \to \mu\mu$ decay. The mass resolution is 86 MeV/c^2 with the first alignment (left) and is 44.3 MeV/c^2 with an improved alignment (right).

alignment are performed in the trigger farm within a few minutes. This online procedure enables the best possible calibration and alignment information to be used at the trigger level and provide better reconstruction performance in the trigger. It also minimises the differences between online and offline reconstruction performance, and allows some physics analyses to be run directly on the trigger output [8].

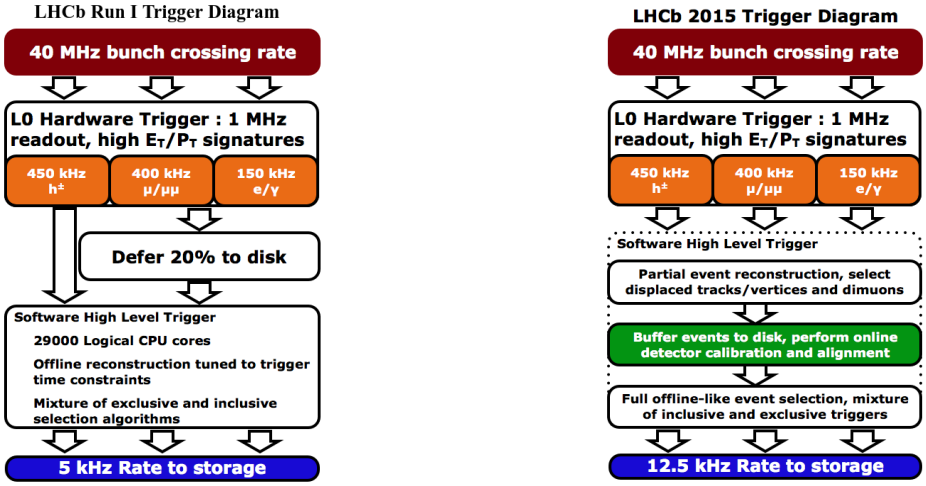

FIGURE 2. Schematic diagram of the LHCb trigger data-flow in Run I data taking (left) compared to the trigger data-flow in Run II (right).

The real-time alignment

The real-time evaluation is performed at the beginning of run or a fill. A change of run is implemented in a few minutes when the new alignment and calibration constants are available if the difference from the previous values is significant. The constants are updated for the next run and are used online by the two software trigger stages and offline for further reconstruction and selection of events.

Tracking alignment method

The tracking alignment is based on an iterative procedure where the residuals of a Kalman filter fit are minimised [9, 10]. Multiple scattering and energy loss in the material together with magnetic field information are taken into account. The Kalman filter also allows particle mass and vertex constraints to be included. It is possible to align

many subdetectors at once. Detector elements can be constrained to their nominal, surveyed or previously aligned position.

Given an initial alignment parameter value α_0, the solution for $\alpha = \alpha_0 + \Delta\alpha$ is obtained by solving the set of linear equations

$$\left.\frac{d^2\chi^2}{d\alpha^2}\right|_{\alpha_0} \Delta\alpha = -\left.\frac{d\chi^2}{d\alpha}\right|_{\alpha_0}. \tag{1}$$

The first and second derivatives of the total χ^2 with respect to the alignment parameters are obtained by summing the contributions from all the tracks:

$$\begin{aligned} \frac{d\chi^2}{d\alpha} &= 2 \sum_{tracks\ i} \frac{dr_i^T}{d\alpha} V_i^{-1} r_i, \\ \frac{d^2\chi^2}{d\alpha^2} &= 2 \sum_{tracks\ i} \frac{dr_i^T}{d\alpha} V_i^{-1} R_i V_i^{-1} \frac{dr_i}{d\alpha}, \end{aligned} \tag{2}$$

where r_i is the hit residuals of reconstructed particle tracks, V_i is the covariance matrix of the measurement coordinates and R_i is the covariance matrix of the residuals after the track fit. It is assumed that the χ^2 for each track has been minimised with respect to the track parameters for the initial alignment parameter value α_0.

The χ^2 derivatives calculation can be parallelised by computing part of the sum over different events on different nodes and reconstructing the tracks. The partial sums can then be added together and Equation 1 can be minimised on a single node. For this reason two different alignment tasks are defined:

- The analyser performs the track reconstruction based on the alignment constants and evaluates the partial of the sums from Equation 2. Many samples run in parallel within the ∼1700 nodes of the HLT farm. Only one sample is run per node in order not to compete with the HLT1 processes.
- The iterator collects the output of the analysers and minimises the χ^2 (Eq. 1) computing the alignment constants for the next iteration.

The behaviour of both the analyser and the iterator are determined by the finite state diagram in Figure 3. After the initial configuration, a run controller issues the start transition to the analysers which read the initial alignment constants and run on the events assigned to them and then go the paused state. When all the analysers are paused the run controller issues them the stop transitions during which the analysers write on a fixed location of a shared file system the partial sums that they computed and go back to the ready state. The run controller then starts the iterator which reads the output of the analysers, combines them and computes a new set of alignment constants. The run controller then issues another start command to the analysers for a new iteration of the alignment procedure. The iterations continue until the difference of the χ^2 between two successive iterations falls below a threshold. The reason for this is that the change in the total χ^2 is equivalent to the significance of the alignment correction [11]:

$$\Delta\chi^2 = -(\alpha - \alpha_0)^T \left.\frac{d\chi^2}{d\alpha}\right|_{\alpha_0} = -(\alpha - \alpha_0)^T Cov(\alpha)^{-1} (\alpha - \alpha_0) \tag{3}$$

where $Cov(\alpha_0) = \left.\left(\frac{d^2\chi^2}{d\alpha^2}\right)^{-1}\right|_{\alpha_0}$ is a covariance matrix for the alignment parameters.

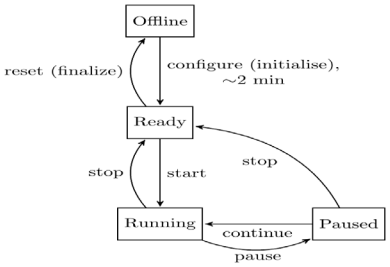

FIGURE 3. A finite state diagram defining the behaviour of the alignment tasks.

Alignment of the LHCb detector

VELO and tracker alignment

The VELO is made of two halves that open during LHC filling and close at the beginning of each fill when the beams are declared stable.

The VELO halves are moved using stepper motors. The position is read from resolvers mounted on the motor axes with an accuracy better than 10 μm. An automated closure procedure has been developed to position the VELO halves around the beams using the hardware failures or corruption and the measured positions of the beams. By considering the two independent beam profiles compiled by each half, the VELO is observed to close symmetrically around the beam to an accuracy of better than 4 μm. As the VELO is closed for each fill, its alignment may change with the same frequency.

The VELO alignment is evaluated first and, since the alignment of the VELO can change for each fill, in case a significant variation of alignment parameters is found, a change of run is performed and the new alignment constants are used for the following run. An update of the alignment parameters of the VELO is expected often but not for each fill.

Figure 4 shows the stability of the VELO halves alignment during the first fills of Run II. Each point is obtained running the online alignment procedure and presents the difference between the initial alignment constants and the new ones computed by the alignment. It is normal that the alignment constants evaluated for two different fills may vary due to statistical fluctuations even without real movement as different input data samples are used. A maximum variation is a comparable with the $O(2\ \mu\text{m})$ precision of the alignment procedure.

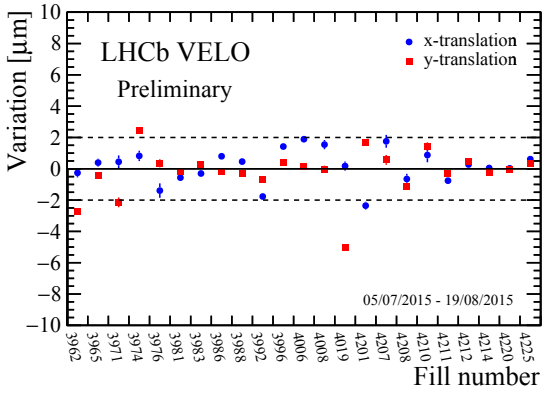

FIGURE 4. Misalignment between the two VELO halves in each fill, evaluated by fitting primary vertices separately with tracks in the two halves of the VELO. The fill numbers span the period from July 5 to August 19 in 2015.

The tracker alignment is performed at the beginning of each fill after the alignment of the VELO. The sub-detectors aligned are the TT, the IT and the OT. The alignment constants are updated at every change of the magnet polarity or after the technical stops to account for any change in detectors condition during the time. These alignment constants are expected to change every few weeks and, if a significant variation is found, the new alignment parameters are applied to the following fill.

The left Figure 5 shows the stability of the IT boxes alignment during the first fills of Run II. Each point is obtained running the online alignment procedure and presents the difference between the initial alignment constants and the new ones computed by the alignment. The alignment constants evaluated for two different fills may vary due to statistical fluctuations even without real movement as different input data samples are used. A Δx variation of about $O(50\ \mu\text{m})$ is smaller than the $O(75\ \mu\text{m})$ precision of the alignment procedure. The right Figure 5 presents the convergence of alignment of the IT boxes obtained on fill 3835 starting from 2012 tracker alignment. Each point shows the x variation of the each IT boxes with respect to the previous iteration. The alignment of each IT boxes is converged after 10 iterations.

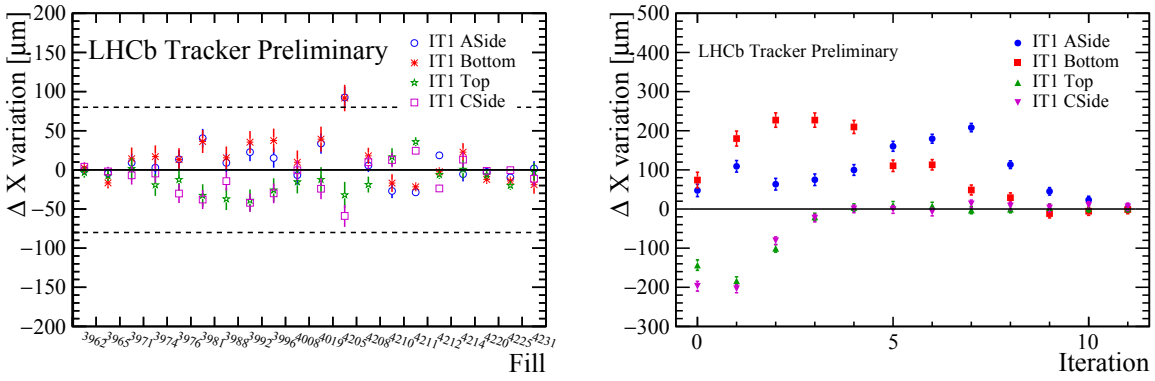

FIGURE 5. The variation of x position of the IT boxes with respect to the alignment during the Run II data taking as a function of a fill number (left) and as a function of an iteration number (right).

RICH mirror alignment

Both RICH detectors have two sets of mirrors: photons are reflected off a primary mirror onto a secondary mirror, from where they are deflected out of the LHCb acceptance onto the photon detection plane.

The RICH mirror alignment has the same general procedure of the tracking alignment: there is a task performed in parallel by the analysers while the calculation of alignment constants is performed by the iterator on a single node. The alignment of the RICH mirror relies on the fact that a misalignment of the mirrors causes the Cherenkov ring on the Hybrid Photon Detector (HPD) plane to be shifted with respect to the position expected from the momentum of the incoming track. The misalignments are extracted by fitting the variation of the Cherenkov angle (θ) given by:

$$\Delta\theta = \theta_x \cos(\phi) + \theta_y \sin(\phi) \tag{4}$$

where the extracted θ_x and θ_y are the misalignment on the HPD plane and ϕ is the polar angle measured from the vector that defines the distance of the point where the track hit the detector and the reconstructed centre of the Cherenkov ring [4].

The analysers perform the photon reconstruction and fill $\Delta\theta(\phi)$ distribution histograms for each pair of mirrors on different events. The iterator collects all the histograms and combines them. Then the iterator fits the combined histogram by Equation 4 and extracts the alignment constants. The procedure is performed until the variations are below a threshold. The alignment constants are determined at the beginning of each fill. Figure 6 shows the distribution of $\Delta\theta$ as a function of ϕ before and after the mirror alignment for one mirror.

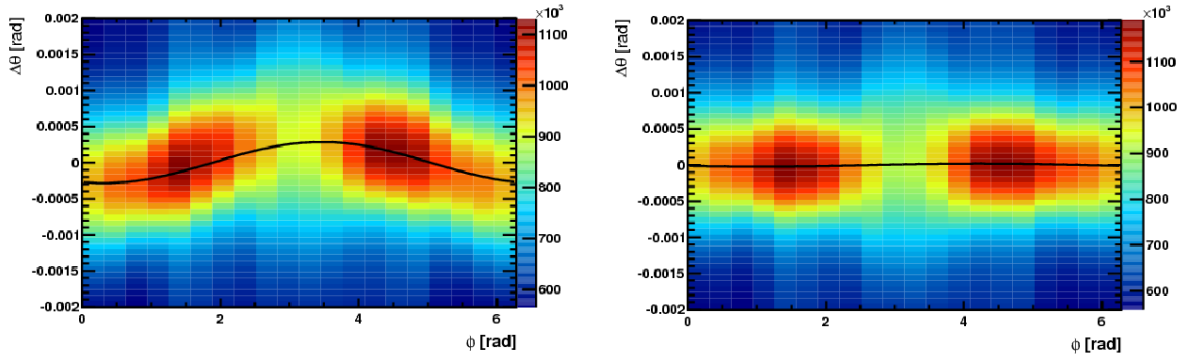

FIGURE 6. Difference between the measured and expected Cherenkov angle $\Delta\theta$ as a function of the polar angle ϕ before (left) and after (right) the mirror alignment for one mirror.

Conclusion

An automatic real-time alignment and calibration strategy is introduced by LHCb in Run II. Data collected at the start of the fill are processed in a few minutes and the output is used to update the alignment. The same framework is used to perform finer calibration less frequently and to monitor the alignment quality of various sub-detectors. This procedure allows a more stable quality of the alignment, more effective trigger selections and offline-online consistency. A dedicated framework has been put in place to parallelise the alignment and calibration tasks on the multi-core farm infrastructure used for the trigger in order to meet the computing time constraints. Physics analyses can be performed directly on the trigger output with the same offline-online performance.

REFERENCES

[1] Alves Jr A A *et al.* (LHCb collaboration), *The LHCb detector at the LHC*, 2008 *JINST* **3** S08005.
[2] Aaij R *et al.* (LHCb collaboration), *Performance of the LHCb Vertex Locator*, 2014 *JINST* **9** P09007.
[3] Arink R *et al.*, *Performance of the LHCb Outer Tracker*, 2014 *JINST* **9** P01002.
[4] Adinolfi M *et al.*, *Performance of the LHCb RICH detector at the LHC*, 2013 *Eur.Phys.J.* **C73** 2431.
[5] Alves Jr A A *et al.*, *Performance of the LHCb muon system*, 2013 *JINST* **8** P02022.
[6] Aaij R *et al.*, *The LHCb trigger and its performance in 2011*, 2013 *JINST* **8** P04022.
[7] Aaij R *et al.*, *LHCb Detector Performance*, 2015 *Int.J.Mod.Phys.* **A30** 1530022.
[8] Benson S *et al.*, *The LHCb Turbo Stream*, in proceedings of *CHEP2015*, (2015).
[9] Amoraal J *et al.*, *Application of vertex and mass constraints in track-based alignment*, 2013 *Nucl.Instrum.Meth.* **A712** 48-55.
[10] Hulsbergen W D, *The global covariance matrix of tracks fitted with a Kalman filter and an application in detector alignment*, 2009 *Nucl.Instrum.Meth.* **A600** 471-477.
[11] Dujany G, *Novel real-time alignment and calibration of the LHCb detector in Run II*, in proceedings of *VERTEX2015*, (2015).

Proceedings of the LHCP2015 Conference, St. Petersburg, Russia, August 31 - September 5, 2015

Editors: V.T. Kim and D.E. Sosnov

Discovering New Physics with Voronoi Tessellations

DIPSIKHA DEBNATH[1,a)], JAMES S. GAINER[2], DOOJIN KIM[1] and KONSTANTIN T. MATCHEV[1]

[1]*Physics Department, University of Florida, Gainesville, FL 32611, USA*
[2]*Dept. of Physics and Astronomy, University of Hawaii, Honolulu, HI 96822, USA*

[a)]Corresponding author: dipsikha.debnath@gmail.com

Abstract. High energy experimental data can be viewed as a sampling of the relevant phase space. We point out that one can apply Voronoi tessellations in order to understand the underlying probability distributions in this phase space. Interesting features in the data can then be discovered by studying the properties of the ensemble of Voronoi cells. For illustration, we demonstrate the detection of kinematic "edges" in two dimensions, which may signal physics beyond the standard model. We motivate the algorithm with some analytical results derived for perfect lattices, and show that the method is further improved with the addition of a few Voronoi relaxation steps via Lloyd's method.

INTRODUCTION

In high energy physics, the data is a collection of "events", which are distributed in phase space, $\mathcal{P}$, according to the differential cross-section

$$\frac{d\sigma}{d\vec{\mathbf{x}}} \equiv f(\vec{\mathbf{x}}, \{\alpha\}). \tag{1}$$

Here $\vec{\mathbf{x}} \in \mathcal{P}$ is a phase space point, which is often parameterized in terms of the momentum components of the final state particles. The set $\{\alpha\}$ is a set of model parameters, e.g., particle masses, widths, couplings, etc. The function (1) consists of two contributions:

$$f(\vec{\mathbf{x}}, \{\alpha\}) \equiv f_{SM}(\vec{\mathbf{x}}, \{\alpha_{SM}\}) + f_{NP}(\vec{\mathbf{x}}, \{\alpha_{NP}\}), \tag{2}$$

where f_{SM} represents the distribution expected from Standard Model (SM) processes, a.k.a. "the background", while f_{NP} is the contribution due to new physics, i.e., "the signal". A promising way to look for new physics is to identify structural features in the differential distributions of the observed events, which might be present in f_{NP}, but not in f_{SM}. This idea is similar to the bump-hunting technique in resonance searches, where we look for the Breit-Wigner peak in f_{NP} over the smooth background described by f_{SM}. Even when some of the decay products (e.g., neutrinos or dark matter particles) are invisible in the detector, one may still look for discontinuities or singularities [1] in the invariant mass distributions of the visible particles observed in the detector. Examples of such special features in f_{NP} include: kinematic endpoints [2, 3, 4, 5], kinematic boundaries [6, 7, 8, 9, 10], kinks [11, 12, 13, 14, 15] and cusps [16, 17, 18, 19] These features are *not present* in the background distribution f_{SM}.

Here we concentrate on two-dimensional high energy particle physics data, but our study can be easily generalized to higher dimensions [20]. We assume that the signal distribution, f_{NP}, changes dramatically or has a discontinuity in phase space. Such a kinematic boundary or "edge" can reveal the existence of new particles. Edge detection has been studied in the experimental and observational sciences [21]. However, in particle physics, the standard methods of edge detection face several challenges, namely

1. *The data may be sparse.* Traditional edge detection methods focus on images, where each pixel contains a data point for a continuous variable (intensity). In contrast, in particle physics we look for an edge, which is a possible signature of new physics, with a comparatively small number of signal events.

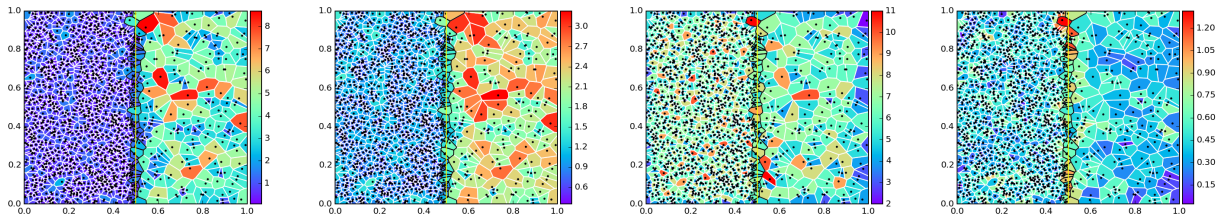

FIGURE 1. Voronoi tessellations for 1400 data points selected from the probability density (3) with $\rho = 6$. The Voronoi polygons are color-coded by their area (left), perimeter (middle left), number of neighboring polygons (middle right) or scaled variance (4) (right).

2. *The analytic form of the distributions f_{SM} and f_{NP} describing the data may be unknown.* If the parametric form of the distribution (2) is known, we can promptly apply likelihood methods to determine edges. However, it is usually difficult to get an exact analytical form for f_{SM}, especially in the case of reducible backgrounds, where detector effects play a major role. Moreover, we cannot be sure, *á priori*, that we have correctly assumed the specific new physics model [22]. Even if we have some idea of where the new physics edges may show up, a general procedure is always of greater practical value.
3. *The data may be in more than two dimensions.* As we mentioned above, edge detection is generally applied to two-dimensional images. However, in particle physics, multivariate analyses [23] are present everywhere. Therefore, in general we will be facing the problem of finding an $(n-1)$-dimensional kinematic boundary in an n-dimensional parameter space.

Our proposed method for edge detection can handle all three of these challenges, and may become a useful tool for the experimental analyses in Run 2 of the CERN Large Hadron Collider (LHC).

A Voronoi Method for Edge Detection

We start our analysis by making the Voronoi tessellation of some two-dimensional data, where each "event", i, represents the corresponding generator point for the i^{th} Voronoi polygon [24, 25, 26]. This particular method of tessellation divides a given volume containing data points $\{d_i\}$ into several regions, $\mathcal{R}_i$, such that each $\mathcal{R}_i$ contains exactly one data point, d_i, and for any point $p \in \mathcal{R}_i$, d_i is the nearest data point.

We focus to identify edge features such as discontinuities [27] without assuming the exact knowledge of the f_{NP} distribution. There exist several edge detection algorithms for binned data [28]. Our Voronoi method of edge detection avoids binning and includes the following steps:

1. Construct the Voronoi tessellation for the data set.
2. Compute relevant attributes of the Voronoi cells.
3. (Optionally) use the information from the previous step to further process the data in some way.
4. Use some criterion to flag "candidate" edge cells.
5. Identify an edge from the collection of edge cell candidates.

Some useful intuition can be gained from the following toy example. We generate 1400 points according to the probability distribution

$$f(x, y) = \frac{2}{1+\rho}\left[\rho\, H(0.5 - x) + H(x - 0.5)\right]. \tag{3}$$

within the unit square. In eq. (3), $H(x)$ is the Heaviside step function and ρ is a constant density ratio. The resulting Voronoi tessellation is shown in Figure 1, where the color-code for each Voronoi polygon represents some standard property, such as area, perimeter, or number of immediate neighbors. The square is divided into left (L) and right (R) regions of constant, but unequal densities. Our goal is to spot the the vertical edge at $x = 0.5$ (yellow solid line) where the density sharply changes from one region to other. For convenience, we outline the boundaries of the Voronoi cells, crossing the edge at $x = 0.5$ as black and the remaining Voronoi cells away from the edge as white.

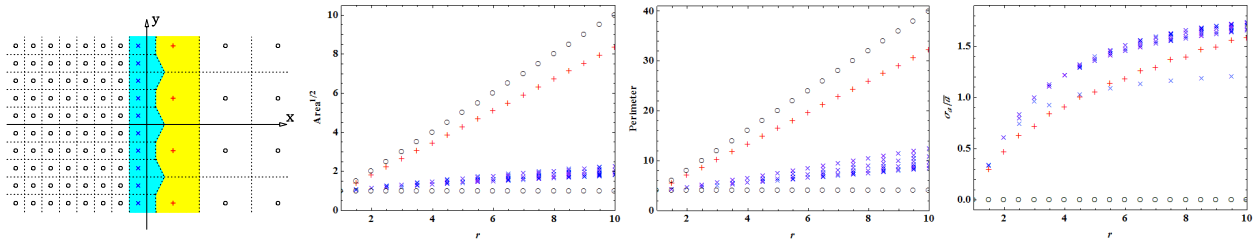

FIGURE 2. A regular lattice (5) generated for linear density ratio $r = 3$ (left), and the dependence on r of several parameters of interest, namely cell area (middle left), cell perimeter (middle right) and scaled variance (right). Black circles indicate bulk cells, while blue × (red +) symbols denotes edge cells in the L (R) region.

The two leftmost panels of Figure 1 show that the area and perimeter of the Voronoi polygons are somewhat correlated, while the middle right panel reveals that the typical number of nearest neighbors is similar in the two bulk regions. Therefore, these properties or aspects of Voronoi polygons cannot help in finding the edge cells (outlined in black). This is why we introduce a new variable, the scaled standard deviation of the areas of the neighboring cells,

$$\frac{\sigma_a}{\bar{a}} \equiv \frac{1}{\bar{a}} \sqrt{\sum_{n \in N_i} \frac{(a_n - \bar{a})^2}{|N_i| - 1}}, \tag{4}$$

where N_i is the set of neighbors of the i-th Voronoi polygon, and $\bar{a}(N_i)$ is their mean area. The scaled standard deviation is quite successful in picking out edge cells and this can be visualized in the rightmost panel in Figure 1. Thus we choose (4) as our main selection variable[1].

In order to understand the above results analytically, we consider a perfect grid of points which follows the probability distribution (3). The grid is generated by two integers n and m as

$$\vec{R} = [(n + 0.5)\,\hat{x} + (m + 0.5)\,\hat{y}]\,[H(-n) + rH(n)]\,, \tag{5}$$

where the vectors $\hat{x}$ and $\hat{y}$ form an orthonormal basis and $r \equiv \sqrt{\rho}$ is the corresponding linear density ratio. The left panel of Figure 2 shows an example grid for $r = 3$. We highlight the two columns of edge cells: in the L region (blue × symbols) and the R region (red + symbols). The other three panels in Figure 2 show the behavior of some of their properties as a function of r. For the case of area and perimeter we notice that the values for edge cells are intermediate between the two bulk values. However, the scaled standard deviation is exactly zero for both bulk regions, and nonzero for the edge region, thus offering the possibility for good discrimination.

Voronoi relaxation via Lloyd's algorithm

As we are dealing with a stochastic process, statistical fluctuations are unavoidable in the data. In particular, in Figure 1 we can easily spot a few bulk cells having relatively high values of $\sigma_a/\bar{a}$. This is why we introduce the idea of "smoothing" the data by applying a few iterations of Lloyd's algorithm [29], where at each iteration, the generator point is replaced by the centroid of the corresponding Voronoi cell.[2] Figure 3 shows the Voronoi tessellation after one (left panel) and five (right panel) Lloyd iterations. We find that the Voronoi polygons become more regularly shaped after relaxation and the fluctuations on each side of the boundary are washed out. Most importantly, the values of the scaled standard deviation (4) for the edge cells are enhanced relative to the rest.

Figure 3 also shows that as a result of the Voronoi relaxation, the data points from the dense L region flow towards the relatively sparse R region. Consequently, the edge cells with high $\sigma_a/\bar{a}$ are displaced from their original locations (near the vertical yellow line). For this reason, once we select edge cell candidates after a certain number of Lloyd iterations, we need to trace them back to their original locations before doing any further quantitative data analysis.

[1] This is not the only option, however — we have investigated a number of other promising variables which will be discussed in a longer publication [20].

[2] An alternative approach, illustrated below in Figure 6, would be to leave the original Voronoi tessellation intact, but extend the calculation of (4) to include next-to-nearest neighbors, next-to-next-to-nearest neighbors, etc.

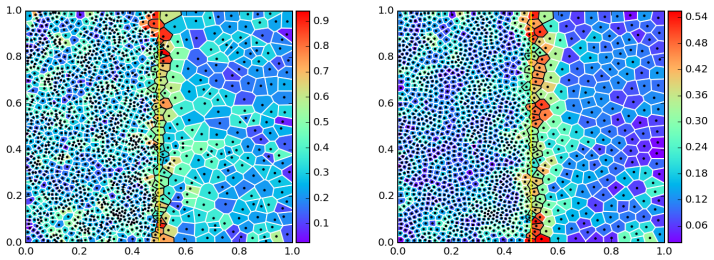

FIGURE 3. The evolution of the Voronoi tessellation shown in Figure 1 after one (left panel) and five (right panel) applications of Lloyd's algorithm. The cells are color-coded by the scaled variance (4).

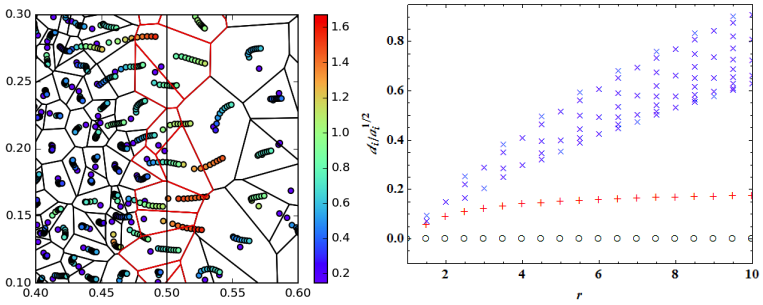

FIGURE 4. Left: a zoomed-in region near the vertical edge, which shows the originally generated points and their subsequent locations after repeated application of Lloyd's algorithm. The points are color-coded by scaled displacement, $d_i/\sqrt{a_i}$. Right: Predictions for $d_i/\sqrt{a_i}$ after applying Lloyd's algorithm once, as a function of r, for the case of a regular lattice (5).

By comparing the displacements d_i of the generator points, we notice that the edge points tend to be displaced the farthest. We can use this as an alternative tagging method. To quantify this criterion, we define a dimensionless variable, the scaled displacement, $d_i/\sqrt{a_i}$, where we normalize by the square root of the cell area, a_i. The left panel in Figure 4 gives a closer view of one representative area near the edge and shows the result of several successive Lloyd iterations. The color code indicates that the scaled displacement is indeed a useful quantity, just like the scaled standard deviation (4). We confirm this by showing in the right panel of Figure 4 the exact result for the perfect grid (5).

We study the efficiency of our edge detection algorithm by analyzing ROC curves [30]. We generate a large dataset for (3), where we consider the edge cells as "signal" and the bulk cells as "background". We plot the signal selection efficiency, ε_S, versus the background efficiency, ε_B, for different values of the minimum cut on the variable (4). Several $\varepsilon_S(\varepsilon_B)$ curves, for different values of the density ratio ρ, and either with (solid) or without (dashed) Lloyd relaxation are shown in Figure 5. The ROC curves reveal that the algorithm is more efficient for higher density contrasts between the two regions. In addition, the Voronoi relaxation leads to a significant improvement of the result.

The accuracy of our selection criteria is quantified by using the standard area under the curve [31] (AUROC) as represented by the Gini coefficient

$$G_1 \equiv 2\,\mathrm{AUROC} - 1 = 2\int_0^1 d\varepsilon_B \times \varepsilon_S(\varepsilon_B) - 1, \tag{6}$$

where a value of 1 is obtained from the ROC curve of a perfectly discriminating variable, while a value of 0 corresponds to a totally random selection of events. The right panel of Figure 5 shows the dependence of G_1 on the number of Lloyd steps. We see that the sensitivity improves dramatically within the first few iterations, and reaches an optimum plateau, after which the power of the test is degraded as the Voronoi grid begins to asymptote to the centroidal tessellation.

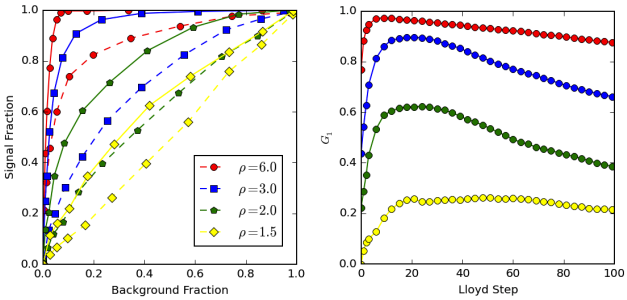

FIGURE 5. Left: ROC curves $\varepsilon_S(\varepsilon_B)$ obtained using (4) as the discriminating variable. Right: The Gini index (6) found from the ROC curve obatined after the given number of Lloyd iterations.

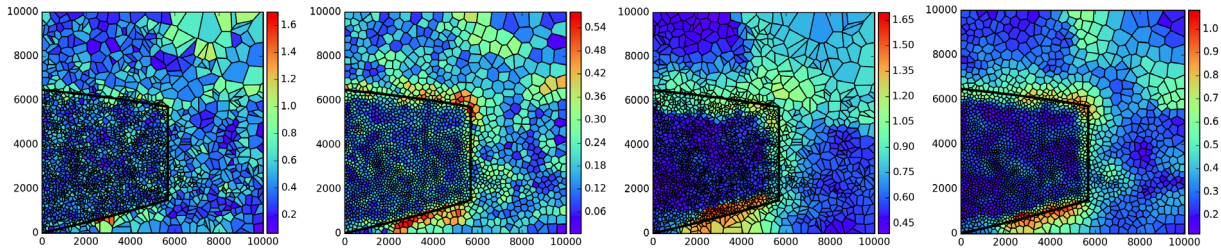

FIGURE 6. Voronoi tessellations for the supersymmetry example described in the text.

An example from supersymmetry

We apply our proposed edge detection method to a standard benchmark example from supersymmetry; squark pair production at the 13 TeV LHC. We consider events where one squark undergoes a long cascade decay through a heavy neutralino, $\tilde{\chi}_2^0$; a slepton, $\tilde{\ell}$; and a light neutralino, $\tilde{\chi}_1^0$; while the other decays directly to $\tilde{\chi}_1^0$. The mass spectrum is chosen to be $m_{\tilde{q}} = 400$ GeV, $m_{\tilde{\chi}_2^0} = 300$ GeV, $m_{\tilde{\ell}} = 280$ GeV, and $m_{\tilde{\chi}_1^0} = 200$ GeV. The invariant mass distributions of the final state particles, the two jets and the two leptons, exhibit kinematic edges.

In particular, here we consider the dilepton invariant mass, $m_{\ell\ell}$, and the three-body jet-lepton-lepton invariant mass, $m_{j\ell\ell}$. In Figure 6 we use the $(m_{\ell\ell}^2, (m_{j\ell\ell}^2 - m_{\ell\ell}^2)/6)$ plane for plotting convenience. The solid black line in Figure 6 [8, 32] marks the location of the kinematic endpoint for signal events with the correct jet assignment. (The lack of knowledge of the charge of the jet creates a two-fold combinatorial ambiguity. Thus, for each event there are two entries in the plot.) The main SM background from $t\bar{t}$ dilepton events is also included here.

In Figure 6, the Voronoi cells are color coded by their scaled standard deviation (4). In the left panel we exhibit the original data, while in the middle left panel we show the data after 5 Lloyd iterations. We reconsider the original data and extend the calculation of (4) including up to 5 tiers of nearest neighbors, showing the resulting plot in the middle right panel. We observe that either Voronoi relaxation or the addition of more tiers of neighboring cells reduces the fluctuation and sharpens the edge. Finally, in the rightmost panel of Figure 6 we show the result after 3 Lloyd iterations *and* also including 3 tiers of neighbors in the calculation of (4).

Summary

We argue that the discovery of new kinematic features is an essential step in the discovery of physics beyond the standard model at the LHC and advocate the use of Voronoi methods for this purpose. The great flexibility of Voronoi methods is a blessing for the experimentalist; many useful properties of the Voronoi cells can be used to construct powerful variables tailored to specific new physics scenarios. A voluminous, quantitative study of the many options available to the experimenter will be presented in a companion paper [20].

Acknowledgements

We thank S. Das, C. Kilic, Z. Liu, R. Lu, P. Ramond, X. Tata, J. Thaler, B. Tweedie, and D. Yaylali for useful discussions. Work supported in part by U.S. Department of Energy, in part by Grant DE-SC0010296. DK acknowledges support by LHC-TI postdoctoral fellowship under grant NSF-PHY-0969510.

REFERENCES

[1] I. W. Kim, Phys. Rev. Lett. **104**, 081601 (2010) [arXiv:0910.1149 [hep-ph]].
[2] I. Hinchliffe, F. E. Paige, M. D. Shapiro, J. Soderqvist and W. Yao, Phys. Rev. D **55**, 5520 (1997) [hep-ph/9610544].
[3] W. S. Cho, J. E. Kim and J. H. Kim, Phys. Rev. D **81**, 095010 (2010) [arXiv:0912.2354 [hep-ph]].
[4] A. J. Barr and C. G. Lester, J. Phys. G **37**, 123001 (2010) [arXiv:1004.2732 [hep-ph]].
[5] A. J. Barr, T. J. Khoo, P. Konar, K. Kong, C. G. Lester, K. T. Matchev and M. Park, Phys. Rev. D **84**, 095031 (2011) [arXiv:1105.2977 [hep-ph]].
[6] D. Costanzo and D. R. Tovey, JHEP **0904**, 084 (2009) [arXiv:0902.2331 [hep-ph]].
[7] M. Burns, K. T. Matchev and M. Park, JHEP **0905**, 094 (2009) [arXiv:0903.4371 [hep-ph]].
[8] K. T. Matchev, F. Moortgat, L. Pape and M. Park, JHEP **0908**, 104 (2009) [arXiv:0906.2417 [hep-ph]].
[9] K. T. Matchev and M. Park, Phys. Rev. Lett. **107**, 061801 (2011) [arXiv:0910.1584 [hep-ph]].
[10] P. Agrawal, C. Kilic, C. White and J. H. Yu, Phys. Rev. D **89**, no. 1, 015021 (2014) [arXiv:1308.6560 [hep-ph]].
[11] W. S. Cho, K. Choi, Y. G. Kim and C. B. Park, Phys. Rev. Lett. **100**, 171801 (2008) [arXiv:0709.0288 [hep-ph]].
[12] B. Gripaios, JHEP **0802**, 053 (2008) [arXiv:0709.2740 [hep-ph]].
[13] A. J. Barr, B. Gripaios and C. G. Lester, JHEP **0802**, 014 (2008) [arXiv:0711.4008 [hep-ph]].
[14] W. S. Cho, K. Choi, Y. G. Kim and C. B. Park, JHEP **0802**, 035 (2008) [arXiv:0711.4526 [hep-ph]].
[15] M. Burns, K. Kong, K. T. Matchev and M. Park, JHEP **0903**, 143 (2009) [arXiv:0810.5576 [hep-ph]].
[16] T. Han, I. W. Kim and J. Song, Phys. Lett. B **693**, 575 (2010) [arXiv:0906.5009 [hep-ph]].
[17] K. Agashe, D. Kim, M. Toharia and D. G. E. Walker, Phys. Rev. D **82**, 015007 (2010) [arXiv:1003.0899 [hep-ph]].
[18] T. Han, I. W. Kim and J. Song, Phys. Rev. D **87**, no. 3, 035003 (2013) [arXiv:1206.5633 [hep-ph]].
[19] T. Han, I. W. Kim and J. Song, Phys. Rev. D **87**, no. 3, 035004 (2013) [arXiv:1206.5641 [hep-ph]].
[20] D. Debnath, J. S. Gainer, D. Kim and K. T. Matchev, (work in progress).
[21] See, e.g., Davies, E. R., "Computer & Machine Vision: Theory, Algorithms, Practicalities", Academic Press; 4 edition (March 19, 2012).
[22] D. Debnath, J. S. Gainer and K. T. Matchev, Phys. Lett. B **743**, 1 (2015) [arXiv:1405.5879 [hep-ph]].
[23] P. C. Bhat, Ann. Rev. Nucl. Part. Sci. **61**, 281 (2011).
[24] G. Voronoi, Journal für die Reine und Angewandte Mathematik, **133**, 97 (1908).
[25] G. L. Dirichlet, Journal für die Reine und Angewandte Mathematik, **40**, 209 (1850).
[26] See, e.g., S. Okabe, B. Boots and K. Sugihara, "Spatial Tessellations: Concepts and Applications of Voronoi Diagrams," John Wiley & Sons, 1992.
[27] For a study in one dimension, see D. Curtin, Phys. Rev. D **85**, 075004 (2012) [arXiv:1112.1095 [hep-ph]].
[28] See, e.g., J. Canny, IEEE Trans. Pattern Analysis and Machine Intelligence, 8(6):679-698, (1986).
[29] S. P. Lloyd, IEEE Trans. on Information Theory, 28 (2): 129-137, (1982).
[30] T. Fawcett, "An introduction to ROC analysis,"
[31] J. Hanley and B. McNeil, Radiology, **143** (1), 29-36 (1982).
[32] C. G. Lester, M. A. Parker and M. J. White, JHEP **0710**, 051 (2007) [hep-ph/0609298].

Proceedings of the LHCP2015 Conference, St. Petersburg, Russia, August 31 - September 5, 2015

Editors: V.T. Kim and D.E. Sosnov

Naturalness, renormalization group and the scale of new physics

GRIGORII PIVOVAROV

Theoretical Physics Department, Institute for Nuclear Research, Russian Academy of Sciences, Moscow, Russia.

gbpivo@ms2.inr.ac.ru

Abstract. The two existing and opposite theoretical points of view on the scale of new physics are exhibited. An alternative point of view is advocated, by which this scale is a subject of an involved and still unfinished computation within the Standard model.

Introduction

The presence of UV divergences in Feynman amplitudes is still a source of controversies among theoreticians. Here is a recent example: in [1] it is maintained that the divergence in the Higgs mass is unnatural, and that "the multiverse offers the most plausible answer at our disposal." In contrast, in [2] it is claimed that the Standard model is self-consistent up to the Plank scale.

The scale up to which the Standard model is self-consistent is a subject of a nontrivial computation. The different approaches to this computation yield different outcomes, two of which are mentioned above. Below I point out an alternative approach to this computation [3]. This third approach still has to give its outcome for the Standard model. But a consideration withing ϕ^4 suggests that the new approach may lead to a conclusion which is a compromise between the above two points of view. On the one hand, the problem of naturalness is real, and in this I agree with [1]. On the other hand, the energy scale at which the problem appears may be much larger than 1 TeV, and in this I agree with [2].

Naturalness

Generally, if some particular symmetry is not preventing it, there are large quantum corrections to scalar mass squared [4]. The corrections are proportional to UV cut-off squared, or some large mass squared of the model replacing the cut-off. This fact does not depend on the regularization used in the computation [1].

The Higgs mass is known. So, the presence of the large quantum corrections implies a fine-tuning between the parameters appearing in the corrections. This conclusion can be questioned. The quantum corrections are divergent, which means that the Higgs mass is not a calculable quantity but an input parameter taken from experiment.

Still, the computation of the quantum corrections to masses is not completely meaningless. One can take the physical masses as input parameters, but it is not an obligatory choice, and even not the most convenient one. A particular choice of input parameters of a theory defines a particular renormalization scheme. The most popular choice at the moment is the MS-scheme. I conclude that quantum corrections to masses appear when one computes relationships between different sets of input parameters used in different renormalization schemes.

Next I consider requirements on the sets of input parameters. There should be a one-to-one correspondence between the parameters of two different sets. Because of this, a relative accuracy with which the parameters of one set are measured are translated unambiguously to the knowledge of relative accuracy for another set. It may be considered unnatural if the relation between the two sets is such that a modest accuracy for one set is translated to a high accuracy for another set.

Now I specify the pair of input parameter sets under comparison. For this I point out that input parameters in high-energy physics always go with an energy scale. The meaning of this scale is the energy at which the input

parameters are to be measured. The most convenient particular case of two input parameter sets to compare are the sets related to one and the same renormalization scheme, but at different energy scales.

For such a choice, consider the mass squared of a scalar particle measured at the energy scale Q^2, $m^2(Q^2, m^2_{ph})$, where m^2_{ph} is the physical mass squared. By definition, $m^2(m^2_{ph}, m^2_{ph}) = m^2_{ph}$. With function $m^2(Q^2, m^2_{ph})$ I define another function:

$$\frac{\delta m^2(Q^2, m^2_{ph})}{m^2(Q^2, m^2_{ph})} = r\Big(\frac{m^2_{ph}}{Q^2}\Big)\frac{\delta m^2_{ph}}{m^2_{ph}}, \tag{1}$$

where

$$r\Big(\frac{m^2_{ph}}{Q^2}\Big) = \frac{m^2_{ph}}{Q^2}\frac{\partial \log(m^2(Q^2, m^2_{ph})/Q^2)}{\partial(m^2_{ph}/Q^2)}. \tag{2}$$

The value $r\Big(\frac{m^2_{ph}}{Q^2}\Big)$ gives the factor transforming the relative error in the physical mass squared to the relative error in the mass squared measured at the energy scale Q^2.

A theory is natural if it satisfies the condition

$$\lim_{x\to 0} r(x) \neq 0.$$

Otherwise, if

$$\lim_{x\to 0} r(x) = 0,$$

a theory is unnatural, because in this case one is able to improve infinitely the relative accuracy of the mass squared simply by increasing the energy scale Q^2 of the measurement.

The case of ϕ^4

To determine the r-function one has to determine the running mass squared of the scalar particle, $m^2(Q^2, m_{ph})$. Different answers for this running are available in the literature. Below I give it for the ϕ^4 model.

Within the MS-scheme,

$$m^2_{ms}(Q^2, m^2_{ph}) = Q^2\Big(\frac{m^2_{ph}}{Q^2}\Big)^{1-\gamma_\phi}, \tag{3}$$

where γ_ϕ is the so-called anomalous dimension [5, 6]:

$$\gamma_\Phi = \frac{g^2}{12(16\pi^2)^2}. \tag{4}$$

Using the definition (2), one obtains

$$r_{ms}(x) = 1 - \gamma_\phi, \tag{5}$$

which means that the r-function calculated within MS-scheme is constant. I conclude that ϕ^4 is natural within MS-scheme.

Next I consider the momentum subtraction scheme using subtraction at momentum Q. First I give the result disregarding the logarithms of Q^2 appearing in the running mass:

$$m^2_S(Q^2, m^2_{ph}) = m^2_{ph} + \gamma_\phi Q^2, \tag{6}$$

and for the r-function

$$r_S(x) = \frac{x}{x + \gamma_\phi}. \tag{7}$$

Here the subscripts on m^2_S and r_S mean Susskind's running mass squared and r-function, because it corresponds to considerations in [4]. I conclude that within this treatment there is a naturalness problem.

There is a third treatment in the literature of the mass squared evolution in ϕ^4 [3]. It is obtained by applying a version of the Gell-Mann–Low scheme to the ϕ^4 theory. As a result, a nonlinear equation for the renormalized propagator is obtained. It implies a running of the scalar mass squared at large Q^2:

$$m^2_{GML}(Q^2, m^2_{ph}) = \frac{\gamma_\phi Q^2}{1 + 4\gamma_\phi \log \frac{m^2_{ph}}{Q^2}} + o\Big(\frac{Q^2}{1 + 4\gamma_\phi \log \frac{m^2_{ph}}{Q^2}}\Big). \tag{8}$$

Here the subscript means "Gell-Mann–Low running." The r-function corresponding to the Gell-Mann–Low running of the mass squared is

$$r_{GML}(x) = \frac{-4\gamma_\phi}{1 + 4\gamma_\phi \log\, x}. \tag{9}$$

I conclude that there is a naturalness problem within this treatment, but much less severe than in the previous treatment, because $r(x)$ vanishes as $x \to 0$ only as inverse logarithm.

Conclusion

I conclude from the above that it is desirable to develop an analog of the Gell-Mann–Low scheme for the Standard model. Computing r-function for the Standard Model within Gell-Mann–Low scheme may shed new light on the naturalness problem. It is plausible that resummatinon of the energy scale logarithms in the quantum corrections to scalar mass will push the expectations of new physics to higher energies.

ACKNOWLEDGMENTS

I thank the organizers for the useful and productive conference. I also thank Dmitry Gorbunov, Nikolai Krasnikov, and Sergei Trunov for helpful discussions.

REFERENCES

[1] G. F. Giudice, *Proceedings, 2013 European Physical Society Conference on High Energy Physics (EPS-HEP 2013)*, PoS **EPS-HEP2013**, p. 163 (2013), arXiv:1307.7879 [hep-ph] .
[2] A. Boyarsky, O. Ruchayskiy, and M. Shaposhnikov, Ann. Rev. Nucl. Part. Sci. **59**, 191–214 (2009), arXiv:0901.0011 [hep-ph] .
[3] G. Pivovarov, Phys. Rev. **D81**, p. 076007 (2010), arXiv:0912.1521 [hep-ph] .
[4] L. Susskind, Phys. Rev. **D20**, 2619–2625 (1979).
[5] J. C. Collins and A. J. Macfarlane, Phys. Rev. **D10**, 1201–1212 (1974).
[6] J. C. Collins, Phys. Rev. **D10**, 1213–1218 (1974).

Proceedings of the LHCP2015 Conference, St. Petersburg, Russia, August 31 - September 5, 2015

Editors: V.T. Kim and D.E. Sosnov

The Main Results of the Borexino Experiment

A DERBIN[6] and V MURATOVA[6] on behalf of the Borexino collaboration:
M AGOSTINI[13,14], S APPEL[14], G BELLINI[8], J BENZIGER[11], D BICK[19], G BONFINI[5], D BRAVO[17], B CACCIANIGA[8], F CALAPRICE[12], A CAMINATA[3], P CAVALCANTE[5], A CHEPURNOV[18], D D'ANGELO[8], S DAVINI[13], A DERBIN[13], L DI NOTO[3], I DRACHNEV[6,13], A ETENKO[7], K FOMENKO[2], D FRANCO[1], F GABRIELE[5], C GALBIATI[11,8], C GHIANO[3], M GIAMMARCHI[8], M GOEGER-NEFF[14], A GORETTI[5,11], M GROMOV[18], C HAGNER[19], E HUNGERFORD[20], ALDO IANNI[5], ANDREA IANNI[11,5], K JEDRZEJCZAK[4], M KAISER[19], V KOBYCHEV[15], D KORABLEV[2], G KORGA[5], D KRYN[1], M LAUBENSTEIN[5], B LEHNERT[22], E LITVINOVICH[7], F LOMBARDI[5], P LOMBARDI[8], L LUDHOVA[8], G LUKYANCHENKO[7], I MACHULIN[7], S MANECKI[17], W MANESCHG[9], S MARCOCCI[13], E MERONI[8], M MEYER[19], L MIRAMONTI[8], M MISIASZEK[4], M MONTUSCHI[23], P MOSTEIRO[11], V MURATOVA[13], B NEUMAIR[14], L OBERAUER[14], M OBOLENSKY[1], F ORTICA[10], M PALLAVICINI[3], L PAPP[14], L PERASSO[3], A POCAR[16,24], G RANUCCI[8], A RAZETO[5], A RE[8], A ROMANI[10], R RONCIN[8,1], N ROSSI[8], S SCHÖNERT[14], D SEMENOV[6], H SIMGEN, M SKOROKHVATOV[7], O SMIRNOV[2], A SOTNIKOV[2], S SUKHOTIN[7], Y SUVOROV[21], R TARTAGLIA[5], G TESTERA[3], J THURN[22], M TOROPOVA[7], E UNZHAKOV[6], A VISHNEVA[2], R B VOGELAAR[17], F VON FEILITZSCH[14], H WANG[21], S WEINZ[8], J WINTER[25], M WOJCIK[4], M WURM[25], Z YOKLEY[17], O ZAIMIDOROGA[2], S ZAVATARELLI[3], K ZUBER[22], and G ZUZEL[4]

[1]*APC, Univ. Paris Diderot, CNRS/IN2P3, CEA/Irfu, Obs. de Paris, Sorbonne Paris Cité, France*
[2]*Joint Institute for Nuclear Research, Dubna 141980, Russia*
[3]*Dipartimento di Fisica, Università e INFN, Genova 16146, Italy*
[4]*M. Smoluchowski Institute of Physics, Jagiellonian University, Crakow, 30059, Poland*
[5]*INFN Laboratori Nazionali del Gran Sasso, Assergi 67010, Italy*
[6]*St. Petersburg Nuclear Physics Institute NRC Kurchatov Institute, Gatchina 188350, Russia*
[7]*NRC Kurchatov Institute, Moscow 123182, Russia*
[8]*Dipartimento di Fisica, Università degli Studi e INFN, Milano 20133, Italy*
[9]*Max-Plank-Institut für Kernphysik, Heidelberg 69029, Germany*
[10]*Dipartimento di Chimica, Università e INFN, Perugia 06123, Italy*
[11]*Chemical Engineering Department, Princeton University, Princeton, NJ 08544, USA*
[12]*Physics Department, Princeton University,Princeton, NJ 08544, USA*
[13]*Gran Sasso Science Institute (INFN), 67100 £'Aquila, Italy*

[14]*Physik Department, Technische Universität München, Garching 85747, Germany*
[15]*Institute for Nuclear Research, Kiev 03680, Ukraine*
[16]*Physics Department, University of Massachusetts, Amherst MA 01003, USA*
[17]*Physics Department, Virginia Polytechnic Institute and State University, Blacksburg, VA 24061, USA*
[18]*Lomonosov Moscow State University Skobeltsyn Institute of Nuclear Physics, Moscow 119234, Russia*
[19]*Institut für Experimentalphysik, Universität Hamburg, Germany*
[20]*Department of Physics, University of Houston, Houston, TX 77204, USA*
[21]*Physics and Astronomy Department, University of California Los Angeles (UCLA), Los Angeles, CA 90095, USA*
[22]*Department of Physics, Technische Universitat Dresden, 01062 Dresden, Germany*
[23]*Dipartimento di Fisica e Scienze della Terra Universit degli Studi di Ferrara e INFN, 44122 Ferrara, Italy*
[24]*Amherst Center for Fundamental Interactions and Physics Department, University of Massachusetts, Amherst, Massachusetts 01003, USA*
[25]*Institute of Physics and Excellence Cluster PRISMA, Johannes Gutenberg-Universität Mainz, 55099 Mainz, Germany*

Abstract. The main physical results on the registration of solar neutrinos and the search for rare processes obtained by the Borexino collaboration to date are presented.

INTRODUCTION

The study of solar neutrinos is at the intersection of elementary particle physics and astrophysics. On one hand these neutrinos allow for the study of neutrino oscillations, and on the other they provide key information for accurate solar modeling. The Borexino first detected and then precisely measured the flux of the ^{7}Be solar neutrinos, ruled out any significant day-night asymmetry of their interaction rate, performed the measurement of ^{8}B-neutrino with 3 MeV threshold, made the first direct observation of the pep neutrinos, and set the tightest upper limit on the flux of solar neutrinos produced in the CNO cycle.

The uniquely low background level of the Borexino detector made it possible to set new limits on the effective magnetic moment of the neutrino, on the stability of the electron for decay into a neutrino and a photon, on the heavy sterile neutrino mixing in ^{8}B-decay, on the possible violation of the Pauli exclusion principle, on the flux of high energy solar axions and on some other rare processes.

The Borexino detector

Borexino is a real-time liquid scintillator detector for solar neutrino spectroscopy located at the Gran Sasso Underground Laboratory [1]. Its main goal is to measure low-energy solar neutrinos via (ν, e)-scattering in an ultrapure liquid scintillator. At the same time, the extremely high radiopurity of the detector and its large mass allow it to be used for the study other fundamental questions in particle physics and astrophysics.

The detector energy and spatial resolution were studied with radioactive sources placed at different positions inside the inner vessel. For high energies the calibration was performed with a AmBe neutron source [2]. The energy resolution scales approximately as $\sigma_E/E = 5\%E^{-1/2}$. The position of an event is determined using a photon time of flight reconstruction algorithm. The resolution of the event reconstruction, as measured using the ^{214}Bi - ^{214}Po decay sequence, is 13.2 cm.

The fluxes and the energy spectra of solar neutrinos from pp-chain and CNO-cycle are predicted by solar models. Thanks to the unprecedented low background level achieved in the scintillator, Borexino already measured the fluxes and electron recoil spectra of neutrinos coming from the $pp-$, $pep-$, ^{7}Be -and ^{8}B- nuclear reactions which take place inside the Sun.

^{7}Be-neutrinos

Borexino was designed to measure the spectrum of recoil electrons from 862 keV neutrino due to EC-process: $^{7}\mathrm{Be} + \mathrm{e}^{-} \rightarrow ^{7}\mathrm{Li} + \nu_{\mathrm{e}}$. The measured count rate of ^{7}Be-neutrino is [3]: R(^{7}Be) = 46.0 ± 1.5(stat) ± 1.6(syst)

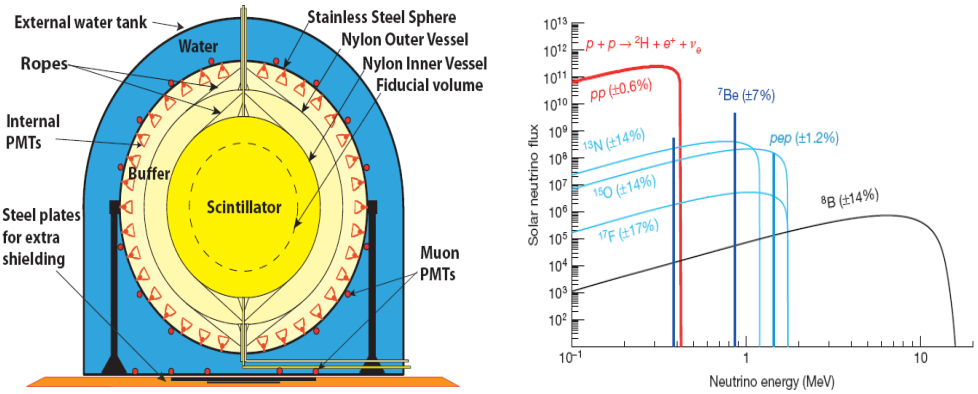

FIGURE 1. Left: the schematic view of the Borexino detector. Right: solar neutrino energy spectrum predicted by standard solar model.

counts/(d 100 t). Study on a possible asymmetry between day and night ^{7}Be-neutrino interaction rate gives [4]: $A_{dn} = 0.001 \pm 0.012(stat) \pm 0.07(syst)$. Borexino excluded the LOW region of the MSW parameter space for neutrino without the use of reactor anti-neutrino data and therefore without the assumption of CPT symmetry.

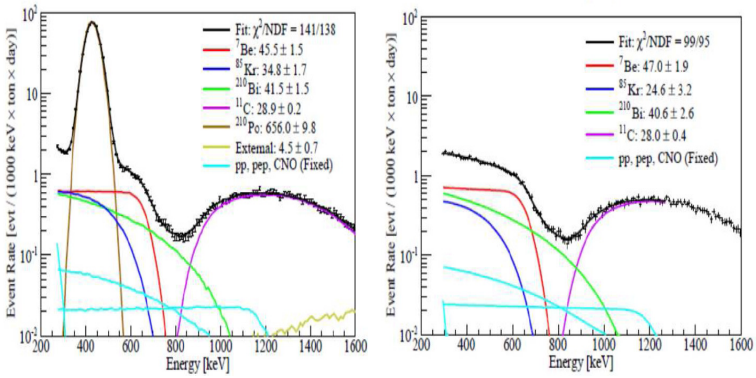

FIGURE 2. Two example fitted spectra. Left: A Monte Carlo based fit over the energy region 270–1600 keV to a spectrum from which some, but not all, of the α events have been removed. Right: An analytic fit over the 290–1270 keV energy region to a spectrum obtained with α subtraction.

^{8}B-neutrinos

Borexino reported the first measurement of ^{8}B solar neutrino rate with 3 MeV threshold [5] $R(^8B) = 0.22 \pm 0.04(stat) \pm 0.01(syst)$ counts/(d 100 t) in good agreement with measurements from SNO and SuperKamiokaNDE.

pep- and CNO-neutrino

Standard Solar Model provides an very accurate (1.2%) flux prediction for 1.44 MeV neutrinos emitted in $p+p+e^- \rightarrow d + \nu_e$ reaction. Borexino performed the first measurement of the *pep*-neutrino interaction rate and set the strongest limit on the CNO neutrino interaction rate (at present, it is not sufficient to solve the High/Low metallicity problem) [6]: R(pep) = 3.1 ± 0.6(stat) ± 0.3(syst) counts/(d 100 t) and R(CNO) ≤ 7.9 counts/(d 100 t) at 95% C.L..

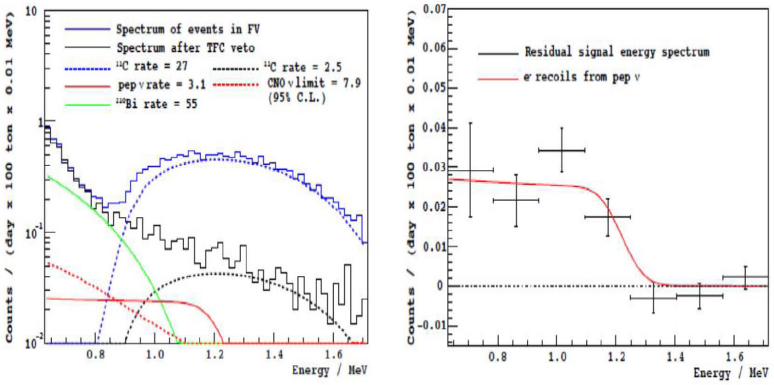

FIGURE 3. Left: energy spectra of the events in the fiducial volume before and after the the threefold coincidence veto ($\mu, n,^{11}$C is applied. Right: residual energy spectrum after best-fit rates of all considered backgrounds are subtracted. The e–recoil spectrum from pep-ν at the best-fit rate is shown for comparison.

pp-neutrino

Neutrino produced from the fusion of two protons for the first time has been detected in a real time detector. The unique properties of the Borexino provided an opportunity to extract pp-neutrino spectrum from the background components [7]: R(pp) = *44* ± *13*(*stat*) ± *10*(*syst*) counts/(d 100 t). Assuming LMA-MSW solution this value corresponds to solar pp-neutrino flux $\Phi(pp) = (6.6 \pm 0.7) \times 10^{10}\text{cm}^{-2}\text{s}^{-1}$ which is in good agreement with the prediction of the standard solar model.

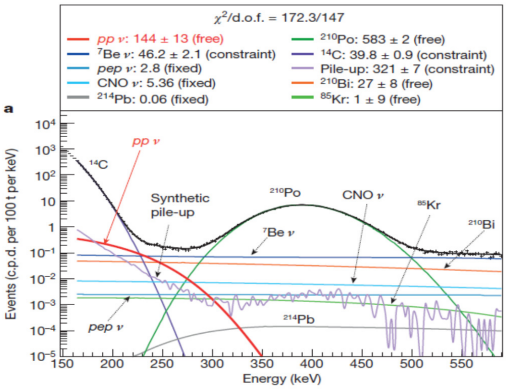

FIGURE 4. Fit of the energy spectrum between 165 and 590 keV. a, The bestfit pp neutrino component is shown in red, the ^{14}C background in dark purple and the synthetic pile-up in light purple. The large green peak is 210Po a-decays. ^{7}Be (dark blue), *pep*- and CNO (light blue) solar neutrinos, and ^{210}Bi (orange) are almost flat in this energy region. The values of the parameters (in c.p.d. per 100 t) are in the inset above the figure.

Electron neutrino survival probability

Survival probability of electron-neutrinos produced by the different nuclear reactions in the Sun. All the numbers are from the Borexino. Because pp- and ^{8}B-neutrino are emitted with a continuum of energy the reported P_{ee} value refers to the energy range contributing to the measurement. The violet band corresponds to the $\pm 1\sigma$ prediction of the MSW-LMA solution.

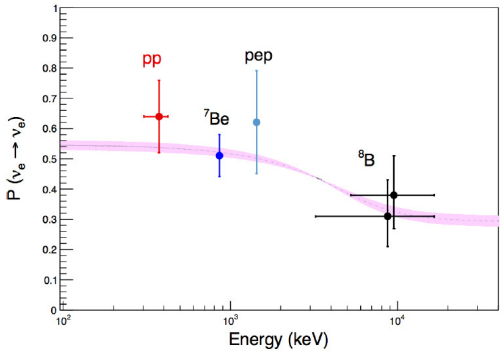

FIGURE 5. Electron neutrino survival probability obtained by Borexino as a function of energy.

Neutrino magnetic moment

The shape of the electron recoil spectrum is sensitive to the possible presence of a non-null magnetic moment, and the sensitivity is enhanced at low energy since E_e^{-1}. For solar neutrinos we detect the effective magnetic moment, which is composition of magnetic moments for mass or flavor eigenstates. Borexino obtained the upper limit [8]: $\mu_{eff} \leq 5.4 \times 10^{-10} \mu_B$ (90% C.L.).

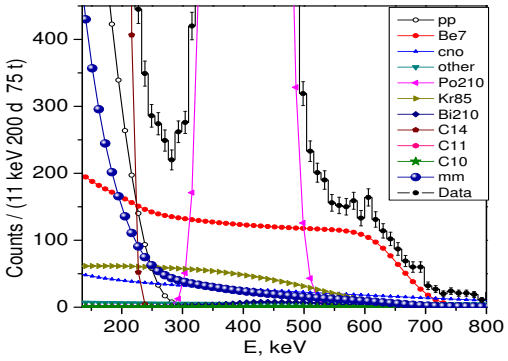

FIGURE 6. The e-recoil spectrum due to magnetic moment equals $5.4 \times 10^{-11} \mu_B$ (blue cycles) in comparison with others components of the Borexino data.

Detection of geo- and reactor neutrinos

Geo-neutrinos are electron anti-neutrinos produced by decays of long-lived isotopes, which are naturally present in the interior of the Earth, such as decays in the ^{238}U and ^{232}Th chains, and ^{40}K. Results from 2056 days of data taking correspond to exposure of $(5.5 \pm 0.3) \times 10^{31}$ proton×yr. Assuming a chondritic Th/U mass ratio of 3.9, Borexino detected $(23.7^{+6.5}_{-5.7})$ geo-neutrino events and $(52.7^{+8.5}_{-7.7})$ reactor (anti)neutrinos [9]. The Borexino reported on the search for anti-neutrinos of yet unknown origin and, in particular, set a new upper limit for a hypothetical solar $\tilde{\nu}$ flux of 760 cm^{-2}s^{-1}, obtained assuming an undistorted solar ^{8}B energy spectrum [10].

Heavy sterile neutrino

The Borexino constrains the mixing of a heavy neutrino with mass 1.5 MeV $\leq m_H \leq$ 14 MeV appearing in ^{8}B-decay to be $|U_{eH}|^2 \leq (10^{-3} - 4 \times 10^{-6})$, respectively [13]. These limits are 10 to 1000-fold stronger than those obtained by

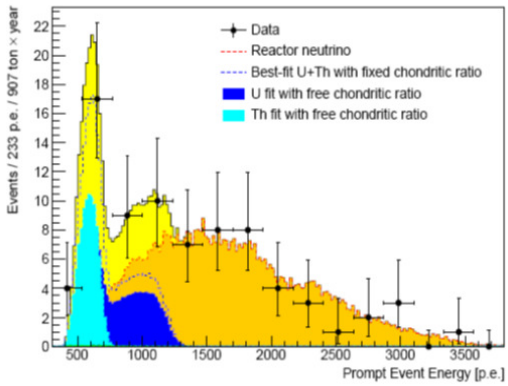

FIGURE 7. Prompt light yield spectrum, in units of photoelectrons (p.e.), of $\tilde{\nu}_e$ candidates and the best-fit. The best-fit shows the geo-neutrino and reactor neutrino spectra (dotted lines) assuming the chondritic ratio. Colored areas show the result of a separate fit with U (blue) and Th (light blue) set as free and independent parameters.

experiments searching for $\nu_H \to \nu_L + e^+ + e^-$ decays at nuclear reactors and 1.5-4 times stronger than those inferred from $\pi \to e + \nu$ decay.

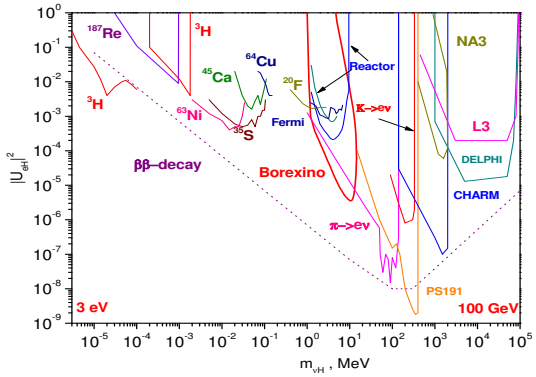

FIGURE 8. The Borexino constraints (red) and limits on $|U_{eH}|^2$ versus m_H in the mass range (3 eV – 100 GeV) from different experiments.

Test of Pauli Exclusion Principle

Using the unique features of the Borexino detector the following new limits on non-paulian transitions of nucleons from the $1P_{3/2}$-shell to the filled $1S_{1/2}$-shell in ^{12}C with the emission of γ, n, p and $\beta^{\pm}$ particles have been obtained [11]: $\tau(^{12}\mathrm{C} \to {}^{12}\widetilde{\mathrm{C}} + \gamma) \geq 5.0 \times 10^{31}$ y, $\tau(^{12}\mathrm{C} \to {}^{11}\widetilde{\mathrm{B}} + p) \geq 8.9 \times 10^{29}$ y, $\tau(^{12}\mathrm{C} \to {}^{11}\widetilde{\mathrm{C}} + n) \geq 3.4 \times 10^{30}$ y, $\tau(^{12}\mathrm{C} \to {}^{12}\widetilde{\mathrm{N}} + e^- + \nu) \geq 3.1 \times 10^{30}$ y and $\tau(^{12}\mathrm{C} \to {}^{12}\widetilde{\mathrm{B}} + \mathrm{e}^+ + \overline{\nu}) \geq 2.1 \times 10^{30}$ y, all with 90% C.L. These limits are the best to date.

High energy solar axions

A search for 5.5-MeV solar axions produced in $p + d \to {}^3$ He + A (5.5 MeV) reaction was performed [12]. The Compton conversion of axions to photons - $\mathrm{A} + \mathrm{e}^- \to \mathrm{e}^- + \gamma$; the axio-electric effect - $\mathrm{A} + \mathrm{e}^- + \mathrm{Z} \to \mathrm{e}^- + \mathrm{Z}$; the decay of axions into two photons - $\mathrm{A} \to 2\gamma$; and inverse Primakoff conversion on nuclei - $\mathrm{A} + \mathrm{Z} \to \mathrm{Z} + \gamma$, are considered.

Model independent limits on axion-electron (g_{Ae}), axion-photon ($g_{A\gamma}$), and isovector axion-nucleon (g^3_{AN}) couplings are obtained: $|g_{Ae} \times g^3_{AN}| \leq 5.5 \times 10^{13}$ and $|g_{A\gamma} \times g^3_{AN}| \leq 4.6 \times 10^{11}\text{GeV}^{-1}$ at $m_A \leq 1$ MeV (90% c.l.).

Test of electron stability

A new limit on the stability of the electron for decay into a neutrino and a single monoenergetic photon $e \rightarrow \nu + \gamma$ was obtained [14]. This new bound, $\tau \geq 6.6 \times 10^{28}$ yr at 90% C.L., is two orders of magnitude better than the previous limit obtained with Borexino prototype CTF.

ACKNOWLEDGMENTS

The Borexino program is made possible by funding from INFN (Italy), NSF (USA), BMBF, DFG, and MPG (Germany), RFBR: Grants 15-02- 02117 and 14-22-03031, RFBR-ASPERA-13-02-92440 (Russia), RSF: Grant 16-12-10369 (Russia), and NCN Poland (UMO-2012/06/M/ST2/00426). We acknowledge the generous support and hospitality of the Laboratori Nazionali del Gran Sasso (LNGS).

REFERENCES

[1] G. Bellini et al. (Borexino Collaboration), Final results of Borexino phase-I on low-energy solar neutrino spectroscopy, Phys. Rev. D 89, 112007 (2014)
[2] H. Back et al . (Borexino Collaboration), Borexino calibrations: hardware, methods, and results. JINST 7 P10018 (2012)
[3] G. Bellini et al. (Borexino Collaboration), Precision measurement of the 7Be solar neutrino interaction rate in Borexino, Phys. Rev. Lett. 107, 141302 (2011)
[4] G. Bellini et al. (Borexino Collaboration), Absence of day-night asymmetry of 862 keV Be-7 solar neutrino rate in Borexino and MSW oscillation parameters, Phys. Lett. B 707, 22 (2012)
[5] G. Bellini et al. (Borexino Collaboration), Measurement of the solar 8B neutrino rate with a LS target and 3 MeV energy threshold in the Borexino detector, Phys. Rev. D82:033006 (2010)
[6] G. Bellini et al. (Borexino Collaboration), First evidence of pep solar neutrinos by direct detection in Borexino, Phys. Rev. Lett. 108, 051302 (2012)
[7] G. Bellini et al. (Borexino Collaboration), Neutrinos from the primary proton-proton fusion process in the Sun. Nature, 512:383386, (2014)
[8] C. Arpesella et al. (Borexino Collaboration), New results on solar neutrino fluxes from 192 days of Borexino data, Phys. Rev. Lett. 101:091302, (2008)
[9] M. Agostini et al. (Borexino Collaboration), Spectroscopy of geo-neutrinos from 2056 days of Borexino data, Phys. Rev. D 92, 031101 (2015)
[10] G. Bellini et al. (Borexino Collaboration), Study of solar and other unknown anti-neutrino fluxes with Borexino at LNGS, Phys. Lett. B 696, 191 (2011)
[11] G. Bellini et al. (Borexino Collaboration), New experimental limits on the Pauli forbidden transitions in 12C nuclei obtained with 485 days Borexino data, Phys. Rev. C81:034317 (2010)
[12] G. Bellini et al. (Borexino Collaboration), Search for Solar Axions Produced in p(d,3He)A Reaction with Borexino Detector, Phys. Rev. D 85, 092003 (2012)
[13] G. Bellini et al. (Borexino Collaboration), New limits on heavy sterile neutrino mixing in 8B-decay obtained with the Borexino detector, Phys. Rev. D 88, 072010 (2013)
[14] M. Agostini et al. (Borexino Collaboration), Test of Electric Charge Conservation with Borexino, Phys. Rev. Lett. 115, 231802 (2015)

Proceedings of the LHCP2015 Conference, St. Petersburg, Russia, August 31 - September 5, 2015

Editors: V.T. Kim and D.E. Sosnov

Experiment NEUTRINO-4 Search for Sterile Neutrino

A.P. SEREBROV[1]

[1]*B. P. Konstantinov Petersburg Nuclear Physics Institute of National Research Centre "Kurchatov Institute," 188300 Gatchina, Leningrad region, Russia*
[2]*Natonal Research Centre "Kurchatov Institute", 123182 Moscow, Russia*
[3] *Scientific Centre - Research Institute of Atomic Reactors, 433510 Dimitrovgrad, Russia*

serebrov@pnpi,spb.ru.

On behalf of the PNPI[1]-KI[2]-RIAR[3] Collaboration

Abstract. In connection with the question of possible existence of sterile neutrino the laboratory on the basis of SM-3 reactor was created to search for oscillations of reactor antineutrino. A prototype of a neutrino detector with scintillator volume of 400 l can be moved at the distance of 6-11m from the reactor core. The measurements of background conditions have been made. It is shown that the main experimental problem is associated with cosmic radiation background. Test measurements of dependence of a reactor antineutrino flux on the distance from a reactor core have been made. The prospects of search for oscillations of reactor antineutrino at short distances are discussed.

At present there is a widely spread discussion of possible existence of a sterile neutrino having much less cross-section of interaction with matter than, for example, reactor electron antineutrino. It is assumed that owing to reactor antineutrino transition to sterile condition, oscillation effect at a short reactor distance and deficiency of a reactor antineutrino beam at a long range are likely to be observed [1,2]. Moreover, sterile neutrino can be regarded as being a candidate for the dark matter.

We have studied possibility of making new experiments at research reactors in Russia. Due to some peculiar characteristics of its construction, reactor SM-3 provides the most favorable conditions for conducting an experiment on search for neutrino oscillations at short distances. Advantages of SM-3 reactor are a compact reactor core center (35×42×42 cm^3) with high reactor power being equal to 100 MW, as well as a sufficiently short distance (5 m) from the center of a reactor core to the walls of an experimental hall. Besides, of special significance is the fact that an antineutrino beam can be measured within a sufficiently wide range from 6 to 13 meters [3, 4].

Passive shielding from the outside and inside is created from elements based on steel plates 1 x 2 m^2, 10mm thick, to which are attached 6 sheets of lead as thick as 10 mm. The cabin volume is 2x2x8 m^3. From the inside the cabin is covered with plates of borated polyethylene 16 cm thick. The total weight of passive shielding are 60 tons, the volume of borated polyethylene is 10 m^3. Inside passive shielding there is a platform with the antineutrino detector which can be moved with a step motor along the rails within the range of 6 to 12 meters from the reactor core center [5].

The detector volume 0.9x0.9x0.5 m^3 is filled with liquid scintillator with addition of Gd. The detector makes use of 16 photoelectron multipliers PMT-49b located on the upper surface of the detector.

The scintillation type detector is based on using the reaction $\tilde{\nu}_e + p \rightarrow e^+ + n$. At the first moment the detector registers positron, whose energy is determined by antineutrino energy and also registers 2 annihilation gamma quanta with energy 511 keV each. At the second moment neutrons emerging in reaction are absorbed by Gd to form a cascade of gamma quanta with total energy about 8 MeV [6]. The detector keeps records of two subsequent signals from positron and neutron - so named correlated events.

The neutrino detector model involved can be used for cosmic ray registration and gamma quanta from radioactive contaminations.

Investigation of Cosmic Ray Background

In the course of long-term measurements temporary variations of cosmic radiation intensity were found. They are caused by fluctuations of atmospheric pressure and temperature drift during season changes. It is a well known barometric and temperature effect of cosmic rays [7-9]. Muons are formed in the upper layers of atmosphere. Higher pressure gives rise to a larger amount of substance over the detector and to intensity attenuation of cosmic rays. Fig. 1 shows anti-correlation effect between atmospheric pressure and total intensity of rigid and soft components of cosmic radiation, i.e. within energy range from 10 to 120 MeV [5]. This effect is barometric.

As a result of studying background conditions for performing an experiment on search for neutrino oscillations at short distances, it became clear that background conditions were extremely unfavorable. Cosmic background depends on the distance from the reactor core center because of distribution of concrete structure of the building. Moreover, cosmic background is changing with time due to atmospheric pressure and temperature fluctuations in lower atmosphere layers.

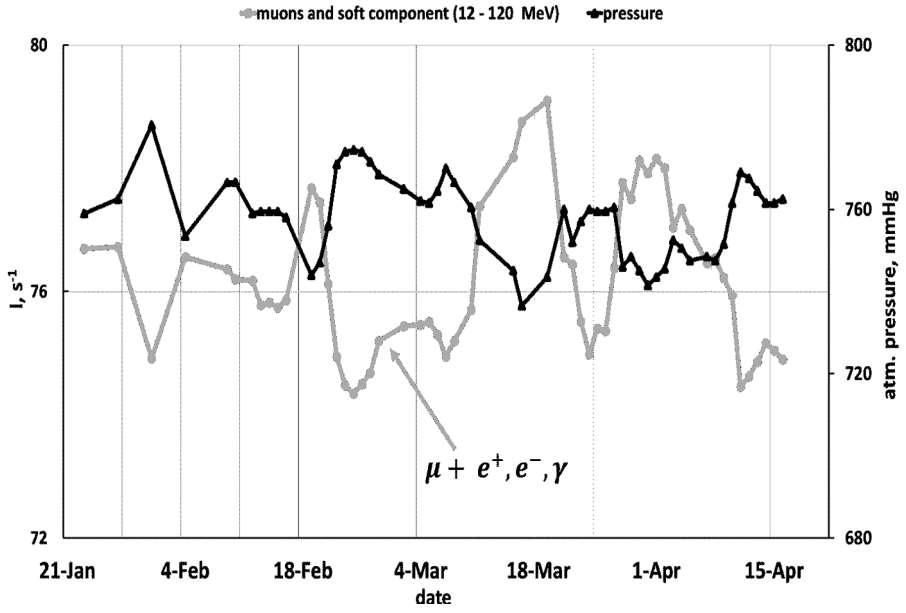

FIGURE 1. Barometric effect of cosmic rays: the left axis shows summary detector count rate, the right axis shows atmospheric pressure, horizontal axis gives the measurement time since 23d of January to 15th April 2014.

Energy and Time Spectra of Correlated Events

As it was noted earlier, in measuring antineutrino flux from the reactor the technique of correlated coincidences is employed for distinguishing the registration process of antineutrino - $\tilde{\nu}_e + p \to e^+ + n$. Fig. 2 gives the spectrum of delayed coincidences. The background of random coincidences is subtracted. One can see two exponents (straight lines in logarithmic scale), which correspond to a muon decay and a neutron capture by Gd. Without employing an active shielding, the integral under the first exponent corresponds to the muon stop rate 1.54 μ/s, and the exponent (2.2 μs) corresponds to a muon lifetime. The integral under the second exponent is relevant to

the neutron capture rate in the detector – 0.15 n/s, and the exponent (31.3 μs) corresponds to neutron lifetime in the scintillator at 0.1% Gd concentration.

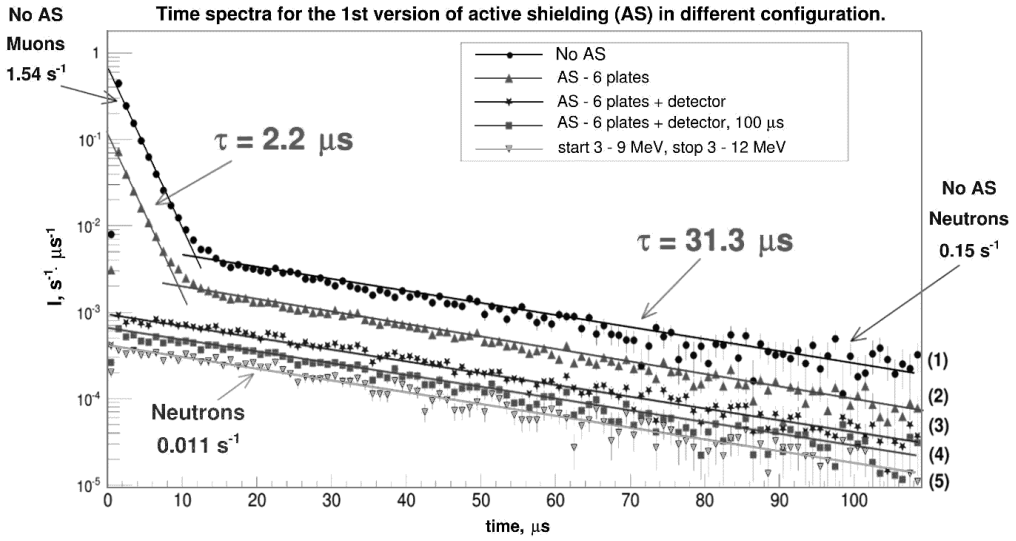

FIGURE 2. Time spectra at different configurations of the active shielding: 1 - no active shielding, 2 – plates of the active shielding are on, 3 – the same + ban from the detector at signals higher than 12 MeV, 4 – the same + ban on 100 μs after the detector signal, at energy higher than 12 MeV, or after the signal in the active shielding, 5 – the same + limit on start and stop signals in ranges 3 – 9 MeV and 3 – 12 MeV respectively.

The number of muon stops per second corresponds to estimation on the muon flux and scintillator mass calculation, while the number of captured neutrons per second corresponds to the calculated rate of neutron formation in the detector itself, caused by a muon flux passing through it. It points out that, in general, one succeeded in solving the task under consideration by means of the passive shielding in combination with lead placed outside with 16 cm of borated polyethylene inside. Indeed, addition of 10 cm borated polyethylene upon the detector cover did not alter the neutron capture rate in the detector. Use of a ban from active shielding and the detector, which gives evidence for muon passing, allows to suppress the capture rate by the detector to level $1.8 \cdot 10^{-2}$ n/s. Fig.2 presents the first version of the active shielding. Detailed studies of the active shielding are quoted in the next section

Active Shielding of the Detector

The next stage of research was concerned with the active shielding of the detector. The first part of measurements was made with the first version of the active shielding, with scintillator plates being 3 cm thick.

The second version of the active shielding was made of plates 12 cm thick. In this case one succeeded in obtaining the effect-background ratio equal to 0.23 rather than 0.12 for the point nearest to the reactor (Fig. 3) [10]. As earlier this ratio 0.23 remains unsatisfactory to measure within a few percent accuracy dependence $1/R^2$, i.e. for search for neutrino oscillation. It is necessary to obtain the ratio equal to unit for the furthest point from the reactor. We assume the remaining background of correlated events to be mainly related to fast neutrons of cosmic background. Fast neutron produces a start signal via a recoil proton and gives a stop signal at absorbing the same neutron. Now we are undertaking investigation on separating signals according to an impulse shape, as a signal shape in recording a recoil proton or a positron must be different. We do hope to improve the signal-background ratio by increasing the detector efficiency due to enlarging the detector volume. The full scale detector volume is expected to be increased by 4 times.

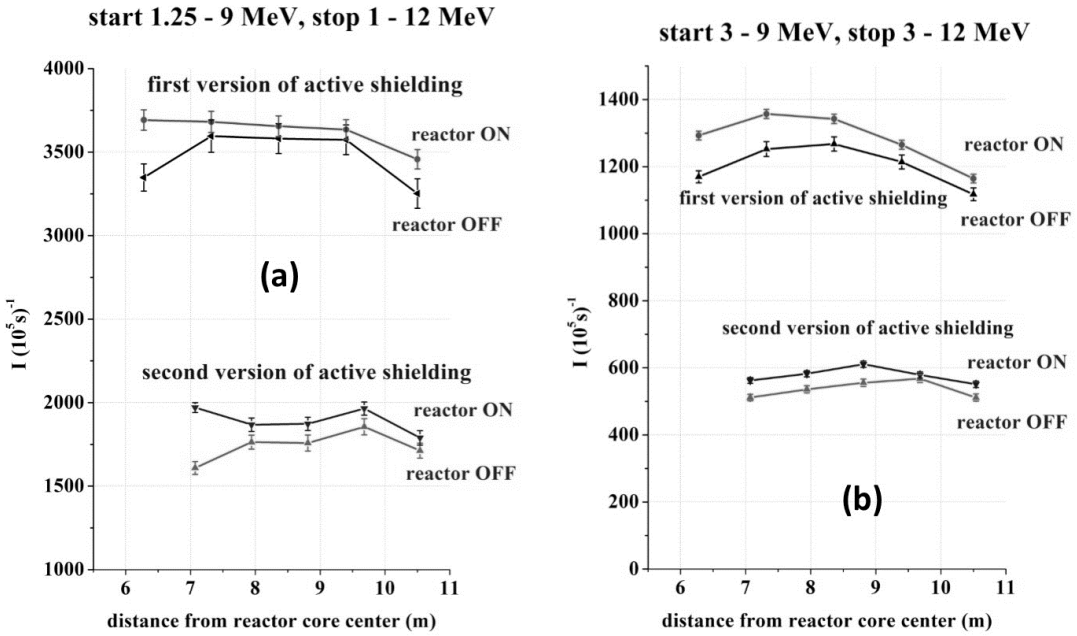

FIGURE 3. (a) measuring results on count rate of correlated events for start signals within the energy range of 1.25 – 9 MeV and stop signals 1 – 12 MeV at the reactor on and off, as well as for two versions of the active shielding, (b) results of the same measurements for start signals within the energy range of 3 – 9 MeV and for stop signals 3 – 12 MeV.

To conclude, investigations with the external active shielding were carried on (external one with respect to the passive shielding). On the roof of the passive shielding over the detector was installed the active shielding («umbrella») made of scintillator plates 12 cm thick and the total area 2 x 3 m^2. Taking into account the fact that the detector area is 0.9 x 0.9 m^2, such an «umbrella» must capture the main muon flux flying into the neutrino detector area. As a result, it improved the effect-background ratio by 15% only and the ratio increased up to the level of 0.32. The remaining correlated background is likely to be related to fast neutrons which are only partly blocked by the active shielding. Thus, we mainly hope on employing the technique of signal separation according to the impulse shape.

Measuring the Dependence of Reactor Antineutrino Flux on the Distance from the Reactor Core

At the next stage measurements were made of antineutrino flux from SM-3 reactor and its distance dependence. Measuring results of correlated signals depending on distance with the reactor on and off were presented in Fig.3. From the difference of these results was derived the dependence of the reactor antineutrino flux on the distance from the reactor core center (Fig. 4) [10]. Unfortunately, attempt to increase statistics for the sake of a wider energy interval does not improve the situation, since in a small energy area the contribution of correlated events from cosmic background is growing.

In order to verify that the difference effect is mainly relevant to antineutrino of reactor SM-3, additional measurements were made, when another lining of borated polyethylene of 0.3 m was installed near the reactor wall. It could attenuate the flux of fast neutrons from the reactor 3-4 times. Measuring results with an additional wall show that difference decrease (reactor on – reactor off) was not found within the statistical measuring accuracy of 20%.

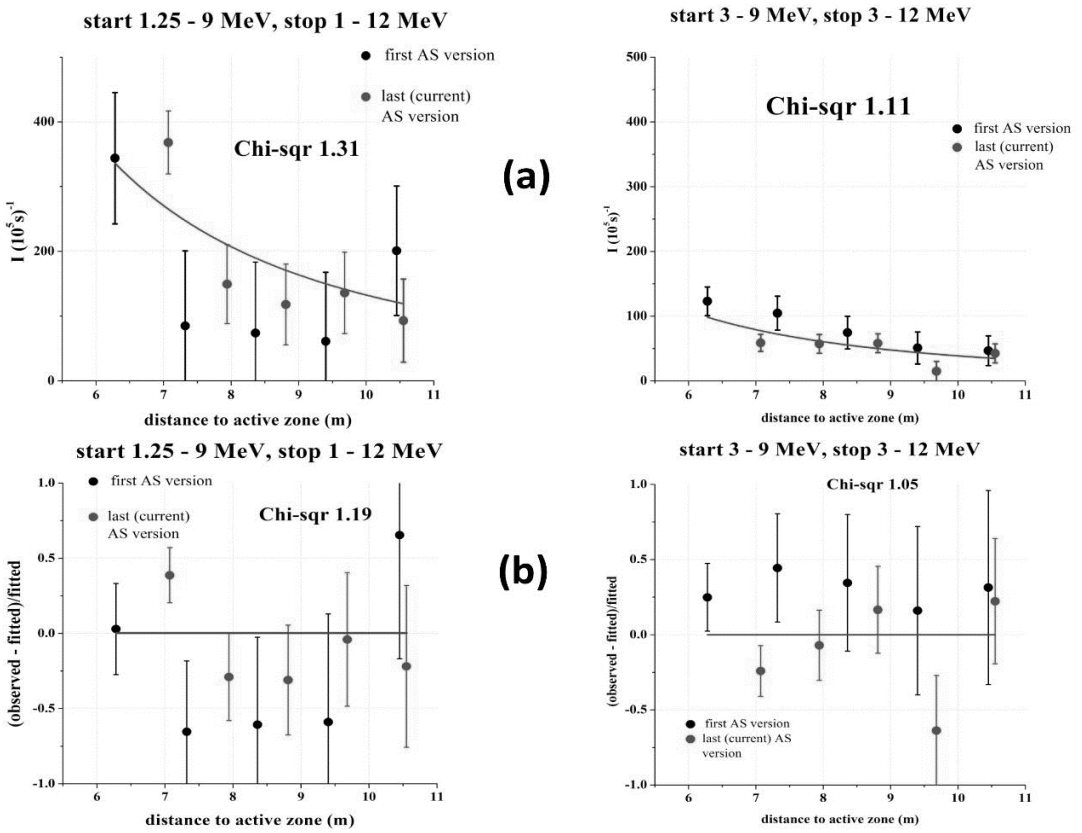

FIGURE 4. (a) On the left - dependence of count rate difference of correlated events (reactor on – reactor off) on distance from the reactor core center within the range of 1.25 – 9 MeV and for stop signals 1 – 12 MeV, on the right – the same for the energy range of 3 – 9 MeV and 3 – 12 MeV; (b) – treatment of the same data on deviation from the law $1/R^2$.

CONCLUSIONS

Summarizing, the following conclusions can be done.

- For the first time, an attempt was realized to measure the reactor antineutrino flux dependence at short distances (6 – 11 m) from the reactor core center. Undoubtedly, the accuracy is not sufficient for making conclusions concerning the statement of the task on search for a sterile neutrino. The task was only aimed at studying the possibility of performing such an experiment at the cosmic background level on the Earth surface and at the reactor operation background level. This experiment made use of a prototype of a small volume detector.
- The main problem of this experiment is concerned with correlated background related to cosmic radiation. Cosmic background depends on the distance from the reactor core center due to the distribution structure of concrete mass of the building.
- Employment of the active shielding allows suppressing correlated background of cosmic radiation only by 66%. This cosmic background component seems to be related to muons. It can be controlled by the active shielding. But fast neutron cosmic background component is the main problem.

The carried out work gave enough information for development of the full-scale detector. At the moment the project of the full-scale detector with a full volume of 3 m^3 is developed.

This work was supported by the Russian Foundation for Basic Research, grant No. 14-22-03055-ofi_m.

REFERENCES

1. G. Mention, M. Fechner, Th. Lasserre, Th. A. Mueller, D. Lhuillier, M. Cribier, and A. Letourneau, Phys. Rev. D **83**, 073006 (2011).
2. Th. A. Mueller, D. Lhuillier, M. Fallot, A. Letourneau, S. Cormon, M. Fechner, L. Giot, T. Lasserre, J. Martino, G. Mention, A. Porta, and F. Yermia, Phys. Rev. C **83**, 054615 (2011).
3. A. P. Serebrov, A. K.Fomin, V. G. Zinov'ev, Yu. E. Loginov, M. S. Onegin, A. M. Gagarskiy, G. A. Petrov, V. A. Solovei, A. V. Chernyi, O. M. Zherebtsov, V. P. Martem'yanov, V. G. Tsinoev, V. G. Tarasenkov, V. I. Aleshin, A. L. Petelin, S. V. Pavlov, M. N. Svyatkin, A. L. Izhutov, S. A. Sazontov, D. K. Ryazanov, M. O. Gromov, N. S. Khramkov, and V. I. Rykalin, Pis'ma Zh. Tekh. Fiz. **39**, no. 14, 25 (2013) [Tech. Phys. Lett. **39**, 636 (2013)].
4. A. P. Serebrov, A. K. Fomin, V. G. Zinoviev, V. G. Ivochkin, Yu. E. Loginov, G. A. Petrov, V. A. Solovey, A. V. Chernyi, O. M. Zherebtsov, R. M. Samoylov, V. P. Martemyanov, V. G. Tsinoev, V. G. Tarasenkov, V. I. Aleshin, A. L. Petelin, S. V. Pavlov, M. N. Svyatkin, A. L. Izhutov, S. A. Sazontov, D. K. Ryazanov, M. O. Gromov, V. V. Afanasiev, and V. I. Rykalin, Pis'ma Zh. Tekh. Fiz. **40** no. 11, 8 (2014) [Tech. Phys. Lett. **40**, 456 (2014)].
5. A. P. Serebrov, V. G. Ivochkin, R. M. Samoilov, A. K. Fomin, V. G. Zinov'ev, P. V. Neustroev, V. L. Golovtsov, N. V. Gruzinskii, V. A. Solovei, A. V. Chernyi, O. M. Zherebtsov, V. P. Martem'yanov, V. G. Tsinoev, V. G. Tarasenkov, V. I. Aleshin, A. L. Petelin, S. V. Pavlov, A. L. Izhutov, S. A. Sazontov, D. K. Ryazanov, M. O. Gromov, V. V. Afanas'ev, L. N. Matrosov, and M. Yu. Matrosova, Zh. Tekh. Fiz. **60**, no. 12, 128 (2015) [Tech. Phys. **60**, 1863 (2015)].
6. A. P. Serebrov, A. K.Fomin, M. S. Onegin, V. G. Ivochkin, and L. N. Matrosov, Yad. Fiz. Inzh. **5**, 789 (2014).
7. L. Myssowsky and L. Tuwim, Zeits. für Phys. **39**, 146 (1926).
8. P. M. S Blackett, Phys. Rev. **54**, 973 (1938).
9. L .I. Dorman and E. L. Feinberg, Usp. Fiz. Nauk **59**, 189 (1956).
10. A. P. Serebrov, V. G. Ivochkin, R. M. Samoylov, A. K. Fomin, V. G. Zinoviev, P. V. Neustroev, V. L. Golovtsov, N. V. Gruzinsky, V. A. Solovey, A. V. Chernyi, O. M. Zherebtsov, V. P. Martemyanov, V. G. Tsinoev, V. G. Tarasenkov, V. I. Aleshin, A. L. Petelin, S. V. Pavlov, A. L. Izhutov, S. A. Sazontov, D. K. Ryazanov, M. O. Gromov, V. V. Afanasiev, L. N. Matrosov, and M. Yu. Matrosova, Zh. Eksp. Teor. Fiz. **148**, 665 (2015) [JETP **121**, 578 (2015)].

Proceedings of the LHCP2015 Conference, St. Petersburg, Russia, August 31 - September 5, 2015

Editors: V.T. Kim and D.E. Sosnov

High precision measurement of the muon capture rate on the proton and determination of the pseudoscalar coupling G_p

J. EGGER[1], D. FAHRNI[1], M. HILDEBRANDT[1], A. HOFER[1], L. MEIER[1], C. PETITJEAN[1], V.A. ANDREEV[2], T.I. BANKS[3], S.M. CLAYTON[4], V.A. GANZHA[2], F.E. GRAY[5,6,3], K.A. IVSHIN[2], P. KAMMEL[6,4], B. KIBURG[6,4], P.A. KRAVTSOV[2], A.G. KRIVSHICH[2], B. LAUSS[1,3], E.M. MAEV[2], O.E. MAEV[2], G. PETROV[2], G.G. SEMENCHUK[2], V.A. TROFIMOV[2], A.A. VASILYEV[2], A.A. VOROBYOV[2], M.E. VZNUZDAEV[2] and P. WINTER[6,4]

[1]*Paul Scherrer Institute, CH-5232 Villigen PSI, Switzerland*
[2]*Petersburg Nuclear Physics Institute, Gatchina 188350, Russia*
[3]*Department of Physics, University of California, Berkeley, California 94720, USA*
[4]*Department of Physics, University of Illinois at Urbana-Champaign, Urbana, Illinois 61801, USA*
[5]*Department of Physics and Computational Science, Regis University, Denver, Colorado 80221, USA*
[6]*Department of Physics, University of Washington, Seattle, Washington 98195, USA*

Abstract. The goal of the MuCap experiment was a high precision measurement of the ordinary capture (OMC) rate Λ_S from the ground state of $p\mu$-atoms:

$$(\mu^- p)_{1S} \to n + \nu_\mu, BR = 0.16\% \quad (1)$$

The experiment was designed for 1% precision measurement, thus improving the existing world data of Λ_S by an order of magnitude. This gives a possibility to determine the unknown nucleon pseudoscalar form factor G_P. The experiment was carried out by international collaboration of scientists from Russia, Switzerland, USA, and Belgium. The MuCap experiment was performed in the high intensity muon beam of the "meson factory" of Paul Scherrer Institute (PSI, Switzerland) using the experimental method developed at PNPI NRC "Kurchatov institute.

INTRODUCTION

In the limit of isospin symmetry, the V-A structure of the electroweak interaction on the nucleon level can be described by introducing four form factors: G_V, G_M, G_A, and G_P.

$$V_\alpha = G_V(q^2)\gamma_\alpha + \frac{iG_M(q^2)}{2M_N}\sigma_{\alpha\beta}q^\beta \quad (2)$$

$$A_\alpha = G_A(q^2)\gamma_\alpha\gamma_5 + \frac{G_P(q^2)}{m_\mu}q_\alpha\gamma_5 \quad (3)$$

Three of them, G_V, G_M and G_A, were determined by available experimental data, while the pseudoscalar form factor G_P remained practically unknown in spite of the efforts of experimentalists during the five previous decades. On the other hand, the value of g_P is predicted by the Chiral Perturbation Theory. Therefore, a precision measurement of g_P has an additional motivation as a crucial test of this theory. Measurement of the muon capture rate on the proton is a unique way to determine the value of G_P. The relatively large transfer momentum makes muon capture, contrary to neutron beta decay, sensitive to G_P. However, this sensitivity is rather limited: 1% precision measurement of the muon capture rate determines G_P with only 6% precision. Therefore, to be scientifically valuable, the muon capture

rate should be measured with at least 1% precision. There is also a strict requirement to the experimental conditions: the observed muon capture should occur in a well defined μp atomic state to avoid controversial interpretation of the experimental data. All previous studies of the μp capture rate were unable to satisfy these requirements. That is why the results of previous experiments allowed G_P values ranging from 2 to 14.

Strategy and experimental set-up of the MuCap experiment

New experimental method developed by the MuCap collaboration made it possible to measure with high precision the muon capture rate Λ_S from the $1S$ singlet state of the μp atom. The strategy of the experiment was to measure with 10^{-5} precision the disappearance rate of μ^- stopped in ultra-pure 10-bar pressure hydrogen (protium) and to compare it with the decay rate of free positive muons μ^+ known at present with 10^{-6} precision. The disappearance rate is determined by measuring the time distribution of muon decay electrons. The relatively low hydrogen gas pressure guaranties that the muon capture occurs predominantly from the 1S state of the $p\mu$ atom. The ultra-high chemical and isotopic purity of the protium gas ($1{\cdot}10^{-8}$ content for overall chemical impurities and $6{\cdot}10^{-9}$ content for HD molecules) prevents from other muon disappearance channels (muon capture on impurities, diffusion of $d\mu$ atoms). The apparatus consisted of an active hydrogen gas target (a Time Projection Chamber (TPC)) which registered every single muon stop, and a surrounding electron detector (two sets of cylindrical wire chambers (ePC1, ePC2) and a plastic counter hodoscope eSC) which registered the electrons from muon decay (Fig. 1).

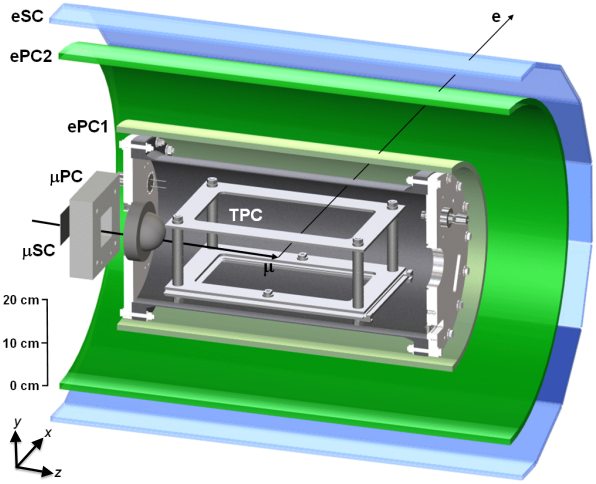

FIGURE 1. MuCup setup.

Measurements and results

The experiment was carried out in the PSI high flux muon beam. The measurement procedure started with selection of the muon stops within the 10.4×8.0×20.4 cm^3 fiducial volume inside the TPC accompanied by outgoing electrons reconstructed in the wire chambers ePC1 and ePC2. Special care was taken to select clean muon stops inside the TPC fiducial volume isolated by at least 15 mm from any material in the TPC. The muon pile-ups were eliminated also. $1.2{\cdot}10^{10}$ μ stops with fully reconstructed $\mu^- e$ pairs were registered, and the muon life time distribution was measured (Fig. 2). From this distribution, the disappearance rate of the negative muons stopped in the TPC has been obtained [1]:

$$\lambda_{\mu^-} = 455855.2{\pm}5.4(stat){\pm}4.2(syst)s^{-1}. \quad (4)$$

Two small corrections have been added to this value: $\Delta\lambda_{p\mu} = 12.3{\pm}0.0s^{-1}$ (the $p\mu$ bound state correction) and $\Delta\lambda_{pp\mu} = 17.72{\pm}1.87s^{-1}$ (a correction for the small, about 3% muon capture probability from the molecular states).

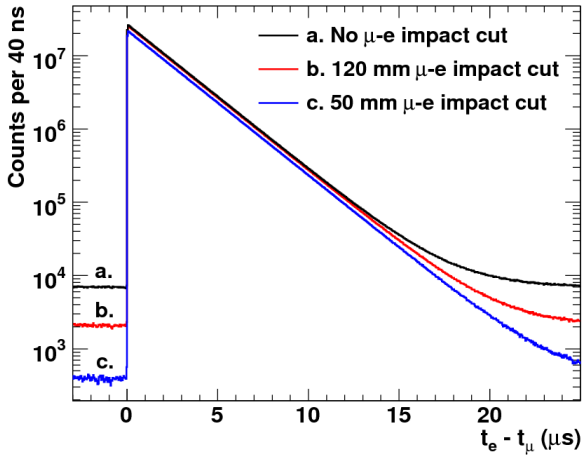

FIGURE 2. μ^- life time distribution.

Then, the muon capture rate from the atomic singlet state Λ_S has been determined according to the expression:

$$\Lambda_S = \lambda_{\mu^-} - \lambda_{\mu^+} + \Delta\lambda_{p\mu} + \Delta\lambda_{pp\mu}, \tag{5}$$

where

$$\lambda_{\mu^+} = 455170.05 \pm 0.46 s^{-1} \tag{6}$$

is the decay rate of free μ^+ muons [2]. The result is:

$$\Lambda_S = 714.9 \pm 5.4(stat) \pm 5.1(syst) s^{-1} \tag{7}$$

Within the existing formalism for calculations of Λ_S, this result corresponds to the following value of the nucleon pseudoscalar form factor:

$$G_P^{MuCap}(q^2 = -0.88 m_\mu^2) = 8.06 \pm 0.48(stat) \pm 0.28(syst). \tag{8}$$

With this measurement, the last of the four nucleon form factors G_P became well determined. Moreover, the measured value of G_P proved to be in close agreement with the prediction [3] of the Chiral Perturbation Theory,

$$G_P^{ChPT}(q^2 = -0.88 m_\mu^2) = 8.26 \pm 0.23, \tag{9}$$

thus supporting the basic principles of this theory.

ACKNOWLEDGMENTS

This work was supported by the Russian Science Foundation (Project 14-12-01056) and by the RF President Foundation Grant SS-393.2012.2.

REFERENCES

[1] V.A. Andreev et al. (MuCap collaboration) *Phys. Rev. Lett.* **110**, 022504 (2013).
[2] D. Webber et al. (MuLan experiment) *Phys. Rev. Lett.* **106**, 041803 (2011).
[3] V. Bernard, L. Elouadrhiri, and U.-G. Meissner *J. Phys.* **G28**, R1 (2002).

Proceedings of the LHCP2015 Conference, St. Petersburg, Russia, August 31 - September 5, 2015

Editors: V.T. Kim and D.E. Sosnov

Study of Fundamental Interactions with Use of Ultra Cold Neutrons at PNPI and ILL

A.P. SEREBROV[1]

[1]*B. P. Konstantinov Petersburg Nuclear Physics Institute of National Research Centre "Kurchatov Institute," 188300 Gatchina, Leningrad region, Russia*
[2]*Institut Max von Laue – Paul Langevin, BP 156, 38042 Grenoble Cedex 9, France*
[3]*Ioffe Physical Technical Institute RAS, 194021 St. Petersburg, Russia*

serebrov@pnpi,spb.ru

On behalf of the PNPI[1]-IIL[2]-PTI[3] Collaboration

Abstract. Neutrons of very low energy (~10^{-7} eV), which are called ultracold, have a unique property: they can be stored in material and magnetic traps. This phenomenon gives new methodical opportunities for carrying out precision experiments and studying of fundamental questions of physics. One of the most important problems of physics is violation of time invariance which is directly connected with emergence of the Universe. Experiments on search of the electric dipole moment of a neutron, other than zero, are the test for violation of time invariance, and a method of ultracold neutrons provides very high precision of measurements. Precision measurements of neutron lifetime by means of ultracold neutrons are extremely important for test of model of formation of the Universe at its early stage. This article is devoted to experimental investigations with ultracold neutrons at PNPI and ILL. Results and research perspectives are under discussion.

Standard model (SM) in physics of elementary particles is a theory successfully describing their interactions. However, Standard model fails to account for symmetry violation between matter and antimatter. In the Universe, everything is made up of matter and there is almost no antimatter at all. At now the theory of supersymmetry is the most used, within the framework of which the so-called CP-symmetry or time invariance is violated in such a way, that it can interpret baryon asymmetry of the Universe. Experiments on search of the electric dipole moment, other than zero, are the test of time invariance violation, with the ultracold neutron method providing a very high precision of measurements. One and the same mechanism of CP-symmetry violation is responsible for creation of neutron EDM and baryon asymmetry of the Universe, thus, neutron research makes it possible to study, how the asymmetry arose during baryogenesis at the stage of Universe emergence. Moreover, precision measurements of the neutron lifetime with ultracold neutrons (UCN) are extremely important for testing the theory of Universe formation at its early stage.

It is to these two particular tasks that investigations carried out at PNPI are devoted. They were started in the 70-s. Here were elaborated UCN intensive sources with liquid hydrogen moderators in the reactor core [1, 2] with a magnetic resonance spectrometer designed for search of the neutron EDM [3]. In recent years these investigations have been continued at ILL.

Neutron EDM

Ultra cold neutrons can be stored in traps made, for the tens and hundreds of seconds, of substance with a high boundary velocity. In view of this effect, one can sufficiently increase energetic resolution of a magnetic resonance spectrometer for search of the neutron EDM.

The first results of experiments on search of neutron EDM by UCN method were obtained in 1980 at PNPI (Gatchina, Russia) [3, 4], and then at ILL (Grenoble, France) [5, 6]. The first limit on the neutron EDM, obtained with UCN in Gatchina, was $|d_n|<1.6\cdot10^{-24}\,e\cdot cm$ (90% C.L.). By 1981 the result obtained in Gatchina was improved: $|d_n|<6\cdot10^{-25}\,e\cdot cm$ (90% C.L.) [4]. In the 1990-s both groups succeeded in reaching the EDM limit of $\sim1\cdot10^{-25}\,e\cdot cm$ (90% C.L.) [6-9]. At this stage the measurements, which carried out in Gatchina, were stopped, because of exploitation of the UCN source was finished. While in Grenoble the collaboration of RAL/Sussex/ILL continued measurements and after about 10 years the limit on the neutron EDM was been lowered to 3 times [10]. In this work the best constraint on the value of the electric dipole moment of neutron for present time was obtained $|d_n|<2.9\cdot10^{-26}\,e\cdot cm$ (90% C.L.).

In 2008, the PNPI EDM spectrometer was installed on the beam of UCN PF2 MAM of the reactor of ILL. The work was performed by collaboration of PNPI-ILL-PTI. In 2013 the collaboration could reach limit on neutron EDM $|d_n|<5.5\cdot10^{-26}\,e\cdot cm$ at 90% confidence level [11, 12]. The result of this work is, to some extent, weaker that achieved in the work [10], however, it was obtained at the methodically different experimental installation. We make use of a magnetic resonance spectrometer with two UCN storage chambers, with a common constant magnetic field and oppositely directed electric fields into the volumes of neutron storage. This experimental scheme provides a principally new possibility to control systematic errors. In the course of conducting measurements at the attained precision level, we did not find any systematic effects.

Accuracy of the result, recently obtained by collaboration of PNPI- ILL- PTI $|d_n|<5.5\cdot10^{-26}\,e\cdot cm$, is expected to be approximately 3 times higher owing to utilize the more intensive beam of UCN PF2 EDM and a new scheme of the spectrometer. The main opportunity for increasing precision up to the level of $|d_n|<5\cdot10^{-28}\,e\cdot cm$ is concerned with application of the UCN source elaborated at the WWR-M reactor.

At present, employing UCN for the EDM experiment remains the most promising direction. At considerable enhancement of intensity of the UCN source, sensitivity of the installation will be also increased, thus perspectives of developing EDM experiment are associated with designing a new generation of UCN sources. Tasks solved in the EDM experiment have given a decisive impetus to elaborating a new technology for producing ultracold neutrons. The existing UCN sources do not allow to hope for significant improvement of the already achieved result. Now work on creating new sources of ultracold neutrons is under way in several foreign scientific centers: ILL (France), LANL (USA), PSI (Switzerland), TUM (Germany). The aim of PNPI project is to elaborate UCN sources of high intensity on superfluid helium (Gatchina, Russia) at the operating WWR-M reactor [13]. Moreover, UCN sources are supposed to be built at the reactor PIK under construction [14]. The calculated density of UCN for these sources is by 2-3 orders of magnitude higher than that in the existing ILL source. The creation of such sources will enable to achieve precision of EDM neutron estimations at the level better than $10^{-27}\,e\cdot cm$, as shown in Fig. 1.

Fig. 1 illustrates chronology of decreasing the upper limit by the neutron EDM value in the experiments carried out in Gatchina and Grenoble and shows further projects for development at the reactor WWR-M in Gatchina.

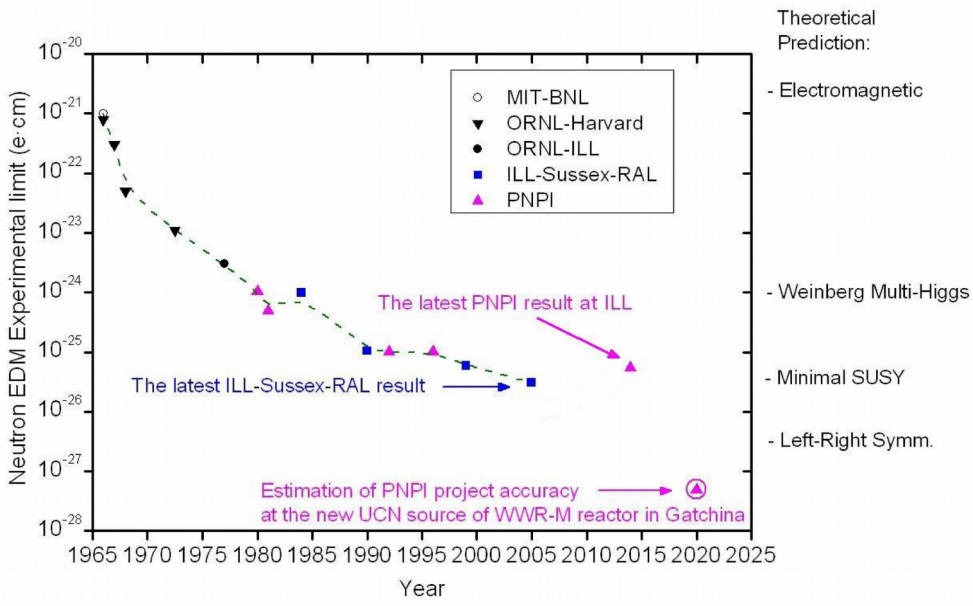

FIGURE 1. History of lowering the experimental limit on the neutron EDM and perspectives of the accuracy increase

Neutron Life Time

In the Standard Model of elementary particles, quark mixing described by the matrix of Cabibbo-Kobayashi-Maskawa (CKM), which should be unitary, indicating completeness of our understanding the number of quark and lepton generations. A module of the matrix element V_{ud} can be derived from the decay of neutron. Precision measurements of the neutron lifetime are also extremely important to test the model of formation of the universe in its early stages, determining the number of neutrino types.

There are two methods of measuring the neutron lifetime: method of UCN storage in the trap and method of products registration of the neutron decay on the beam of cold neutrons.

Analysis of the two techniques has shown discrepancy to be 3.3 standard deviations [15]; after publishing the paper [16] discrepancy increased up to 3.9 standard deviations [17]. The difference between techniques lies in the fact that in a beam experiment, only one neutron decay mode with emitting protons is estimated, while at UCN storage all possible channels resulting in disappearance of a neutron are taken into account. At the present, neutron lifetime measured with the UCN storage is approximately by 4 standard errors less [16] than that estimated in the beam experiment. Though, the most probable interpretation of this fact is systematic error being made in a beam experiment, one cannot guarantee a systematic error to be avoided in an experiment with UCN. Thus, an experiment with UCN storage is supposed to be upgraded.

At present at PNPI a new more precise experiment has been elaborated to measure the neutron lifetime in a material trap. In this setup the principle of gravitational valve is used to hold UCN in a material trap. The UCN storage volume in a new trap is approximately 4 times bigger than that in the previous one. In addition to this, the setup is equipped with an insert which lifted and putted into trap without opening up the installation. This enables not only to eliminate systematic errors but also to raise essentially statistical accuracy of experiment. Accuracy enhancement will make it possible to resolve the discrepancy between different techniques, aimed at measuring the neutron lifetime, i.e. the neutron beam method and the UCN storage one.

Projects of Construction of High Intensity UCN Sources at PNPI

As already mentioned, at PNPI various sources of UCN were developed. In Fig. 2 a general layout of the development of UCN sources, the contribution of PNPI in this process are shown, as well as a new project of the UCN source at the WWR-M reactor based on utilize of superfluid helium as converter of cold neutrons in UCN is presented.

The project of UCN source for the WWR-M reactor was proposed in 2006 [13, 18-20]. The WWR-M reactor at PNPI provides quite suitable conditions for solving a task of compromise between the level of thermal flux and the flux of neutron, as it has a thermal column. The thermal column is a channel of a large diameter (1 m), which abuts to the reactor core. Such diameter of the channel enables to locate a powerful lead shielding protecting from a reactor core ɣ-radiation and to place a graphite moderator with a liquid deuterium pre-moderator at temperature 20 K for producing cold neutrons, as well as the UCN source itself based on superfluid helium at temperature 1,2 K.

At present PNPI has elaborated a project of UCN source for the WWR-M reactor. There have been made detailed calculations with the MCNP program, which show that the source with a lead shielding will release 15 kW which is easily removed by a circulating flow of water. A liquid deuterium moderator will be cooled by passing gaseous helium at temperature 20 K. Finally, the most essential point is that the source with superfluid helium is to release 19 W. Such a power at the level of 1,2 K can be removed using accessible cryogenic devices. The Monte-Carlo calculations of UCN density show that in an experimental installation (for instance, in the EDM spectrometer trap) UCN density $\sim 1 \cdot 10^4 n/см^3$ [13,18-20] is to be obtained. It means that the gain factor with respect to the UCN density in Grenoble will be 1000 times. In view of this, we will be able to make considerable progress in fundamental research with UCN. Fig. 2 illustrates development of sources of ultracold neutrons in the world.

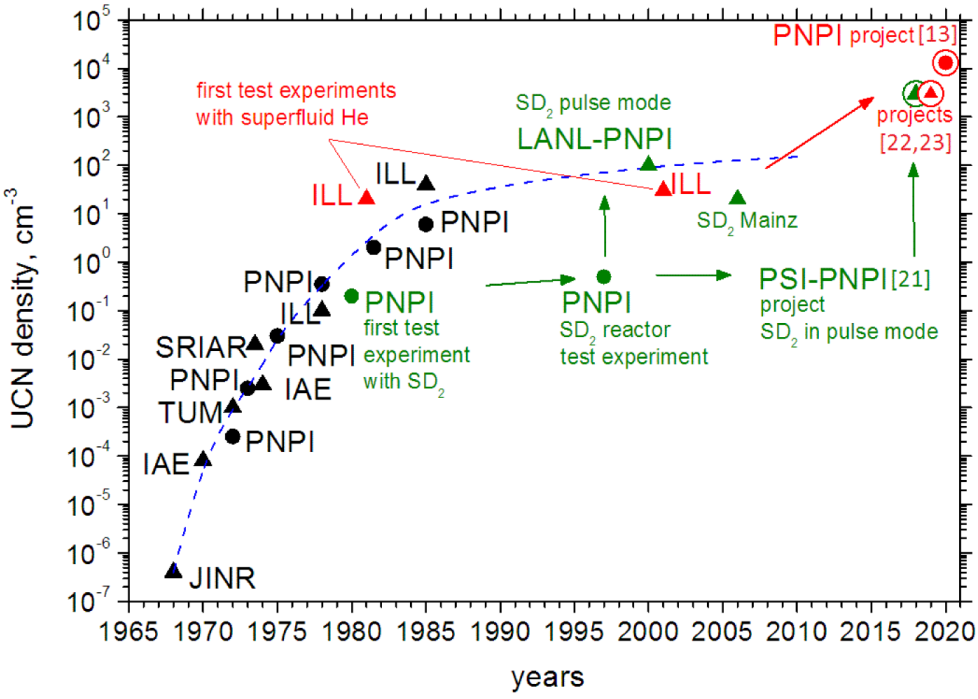

Figure 2. Progress in development of UCN sources is shown. The final point of this diagram is related to the project parameters of a new source, based on use of superfluid helium, at the WWR-M reactor of PNPI, where possible density of UCN in the EDM spectrometer trap is shown

Concluding this article, it is worth emphasizing that methods of precision measurements and those for search of small deviations from the Standard laws of physics make it possible to obtain information on fundamental interactions and successfully compete with investigations performed with the colliders. Examples of such research are given in the present paper. Realization of experiments on search for the neutron EDM with accuracy of $1 \cdot 10^{-27} e \cdot cm$ is of principle significance for physics of fundamental interactions.

The research has been performed at the Petersburg Nuclear Physics Institute of NRC "KI" with support of the grant of the Russian Science Foundation (project №14-22-00105).

REFERENCES

1. I. S. Altarev, Yu. V. Borisov, A. B. Brandin, V. F. Ezhov, S. N. Ivanov, G .K. Kunstman, V. M. Lobashev, V. A. Nazarenko, V. L. Ryabov, A. P. Serebrov, and R. R. Taldaev, Phys. Lett. A **80**, 413 (1980).
2. I. S. Altarev, N. V. Borovikova, A. P. Bulkin, V. A. Vesna, E. A. Garusov, L. A. Grigor'eva, A. I. Egorov, B. G. Erozolimskii, A. N. Erykalov, A. A. Zakharov, S. N. Ivanov, V. Ya. Kezerashvili, S. G. Kirsanov, E. A. Kolomenskii, K. A. Konoplev, I. A. Kuznetsov, V. M. Lobashev, N. F. Maslov, V. A. Mityukhlyaev, I. S. Okunev, B. G. Peskov, Yu. V. Petrov, R. G. Pikulik, A. N. Pirozhkov, G. D. Porsev, A. P. Serebrov, Yu. V. Sobolev, R. R. Tal'daev, V. A. Shustov, and A. F. Shchebetov, JETP Lett. **44**, 344 (1986).
3. I. S. Altarev, Yu. V. Borisov, A. B. Brandin, A. I. Egorov, V. F. Ezhov, S. N. Ivanov, V. M. Lobashov, V. A. Nazarenko, G. D. Porsev, V. L. Ryabov, A. P. Serebrov, and R. R. Taldaev, Nucl. Phys. A **341**, 269 (1980).
4. I. S. Altarev, Yu. V. Borisov, N. V. Borovikova, A. B. Brandin, A. I. Egorov, V. F. Ezhov, S. N. Ivanov, V. M. Lobashev, V. A. Nazarenko, V. L. Ryabov, A. P. Serebrov, and R. R. Taldaev, Phys. Lett. B **102**, 13 (1981).
5. J. M. Pendlebury, K. F. Smith, R. Golub, J. Byrne, T.J. L. McComb, T. J. Sumner, S. M. Burnett, A. R. Taylor, B. Heckel, N. F. Ramsey, K. Green, J. Morse, A. I. Kilvington, C. A. Baker, S. A. Clark, W. Mampe, P. Ageron, and P. C. Miranda, Phys. Lett. B **136**, 327 (1984).
6. K. F. Smith, N. Crampin, J. M. Pendlebury, D. J. Richardson, D. Shiers, K. Green, A. I. Kilvington, J. Moir, H. B. Prosper, D. Thompson, N. F. Ramsey, B. R. Heckel, S. K. Lamoreaux, P. Ageron, W. Mampe, and A. Steyerl, Phys. Lett. B **234**, 191 (1990).
7. I. S. Altarev, Yu. V. Borisov, N. V. Borovikova, S. N. Ivanov, E. A. Kolomensky, M. S. Lasakov, V. M. Lobashev, V. A. Nazarenko, A. N. Pirozhkov, A. P. Serebrov, Yu. V. Sobolev, E. V. Shulgina, and A. I. Yegorov, Phys. Lett. B **276**, 242 (1992).
8. I. . S. Altarev, Yu. V. Borisov, N. V. Borovikova, S. N. Ivanov, E. A. Kolomensky, M. S. Lasakov, V. M. Lobashev, V. A. Nazarenko, A. N. Pirozhkov, A. P. Serebrov, Yu. V. Sobolev, E. V. Shulgina, and A. I. Yegorov, Phys. At. Nucl. **59**, 1152 (1996).
9. P. G. Harris, C. A. Baker, K. Green, P. Iaydjiev, S. Ivanov, D. J. R. May, J. M. Pendlebury, D. Shiers, K. F. Smith, M. van der Grinten, and P. Geltenbort, Phys. Rev. Lett. **82**, 904 (1999).
10. C. A. Baker, D. D. Doyle, P. Geltenbort, K. Green, M. G. D. van der Grinten, P. G. Harris, P. Iaydjiev, S. N. Ivanov, D. J. R. May, J. M. Pendlebury, J. D. Richardson, D. Shiers, and K. F. Smith , Phys. Rev. Lett. **97**, 131801 (2006).
11. A. P. Serebrov, E. A. Kolomenskiy, A. N. Pirozhkov, I. A. Krasnoschekova, A. V. Vassiljev, A. O. Polushkin, M. S. Lasakov, A. K. Fomin, I. V. Shoka, V. A. Solovey, O. M. Zherebtsov, P. Geltenbort, S. N. Ivanov, O. Zimmer, E. B. Alexandrov, S. P. Dmitriev, and N. A. Dovator, JETP Lett. **99**, 4 (2014).
12. A. P. Serebrov, E. A. Kolomenskiy, A. N. Pirozhkov, I. A. Krasnoschekova, A. V. Vassiljev, A. O. Polushkin, M. S. Lasakov, A. K. Fomin, I. V. Shoka, V. A. Solovey, O. M. Zherebtsov, P. Geltenbort, S. N. Ivanov, O. Zimmer, E. B. Alexandrov, S. P. Dmitriev, and N. A. Dovator, Phys. Rev. C **92**, 055501 (2015).
13. A. P. Serebrov, V. A. Mityuklyaev, A. A. Zakharov, A. N. Erykalov, M. S. Onegin, A. K. Fomin, V. A. Ilatovskiy, S. P. Orlov, K. A. Konoplev, A. G. Krivshitch, V. M. Samsonov, V. F. Ezhov, V. V. Fedorov, K. O. Keshyshev, S. T. Boldarev, and V. I. Marchenko, , Nucl. Instr. Meth. A **611**, 276 (2009).
14. A. P. Serebrov, A. K. Fomin, M. S. Onegin, A. G. Kharitonov, D. V. Prudnikov, V. A. Lyamkin, and S. A. Ivanov, Tech. Phys. Lett. **40**, 10 (2014).
15. A. P. Serebrov, A. K. Fomin, Phys. Procedia **17**, 199 (2011).
16. A. T. Yue, M. S. Dewey, D. M. Gilliam, G. L. Greene, A. B. Laptev, J. S. Nico, W. M. Snow, and F. E. Wietfeldt, Phys. Rev. Lett. **111**, 222501 (2013).
17. F. E. Wietfeldt, preprint arXiv:1411.3687v1 [nucl-ex] (2014).
18. A. P. Serebrov, V. A. Mityukhlyaev, A. A. Zakharov, A. N. Erykalov, M. S. Onegin, A. K. Fomin, V. A. Ilatovskiy, S. P. Orlov, K. A. Konoplev, A. G. Krivshich, V. M. Samsonov, V. F. Ezhov, V. V. Fedorov, K. O. Keshishev, S. T. Boldarev, and V. I. Marchenko, Phys.Solid State **52**, 1034 (2010).
19. A. P. Serebrov, Crystallogr. Rep. **56**, 1230 (2011).
20. A. P. Serebrov, S. T. Boldarev, A. N. Erykalov, V. F. Ezhov, V. V. Fedorov, A. K. Fomin, V. A. Ilatovskiy, K. O. Keshyshev, K. A. Konoplev, A. G. Krivshitch, V. I. Marchenko, V. A. Mityuklyaev, M. S. Onegin, S. P. Orlov, V. M. Samsonov, and A. A. Zakharov, Phys. Procedia **17**, 251 (2011).

21. A. Fomin, S. Kalcheva, A. Kharitonov, M. Lasakov, V. Mityukhlyaev, I. Potapov, M. Sazhin, A. Serebrov, G. Shmelev, V. Shustov, R. Taldaev, D. Tytz, V. Varlamov, A. Vasiliev, A. Zakharov, F. Atchison, B. Van den Brandt, M. Daum, W. Gloor, G. Heidenreich, R. Henneck, P. Hautle, St. Joray, K. Kirch, K. Kohlik, J. A. Konter, S. Mango, H. Obermeier, Ch. Perret, U. Rohrer, H. J. Temnitzer, K. Bodek, P. Geltenbort, S. Kistryn, A. Magiera, D. Pocanič, and E. Frlež, PSI Report TM-14-01-01 (2000).
22. O. Zimmer, K. Baumann, M. Fertl, B. Franke, S. Mironov, C. Plonka, D. Rich, P. Schmidt-Wellenburg, H.-F. Wirth, and B. van den Brand, Phys. Rev. Lett. **99**, 104801 (2007).
23. Y. Masuda, T. Kitagaki, K. Hatanaka, M. Higuchi, S. Ishimoto, Y. Kiyanagi, K. Morimoto, S. Muto, and M. Yoshimura, Phys. Rev. Lett. **89**, 284801 (2002).

LHCP2015 PHOTOS


© ИННО-МИР inno-mir.ru


© ИННО-МИР inno-mir.ru


© ИННО-МИР inno-mir.ru


© ИННО-МИР inno-mir.ru


© ИННО-МИР inno-mir.ru


© ИННО-МИР inno-mir.ru


© ИННО-МИР inno-mir.ru


© ИННО-МИР inno-mir.ru

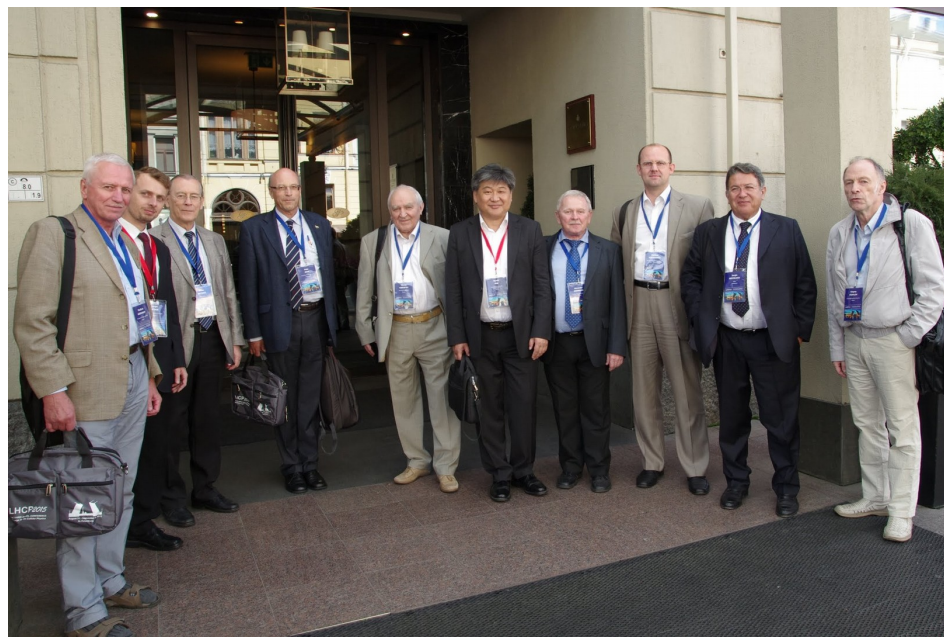


© ИННО-МИР inno-mir.ru


LHCP2015
August 31 – September 5, 2015
St. Petersburg
© ИННО-МИР inno-mir.ru


COLLIDER
2015


THE THIRD ANNUAL CONFERENCE ON
LARGE
HADRON COLLIDER
PHYSICS
LHCP2015
August 31 – September 5, 2015
St. Petersburg, Russia
© ИННО-МИР inno-mir.ru


© ИННО-МИР inno-mir.ru


THE THIRD ANNUAL CONFERENCE ON
LARGE
HADRON COLLIDER
PHYSICS
LHCP2015
August 31 – September 5, 2015
St. Petersburg, Russia
© ИННО-МИР inno-mir.ru


ПРЕСС-КОНФЕРЕНЦИЯ,
ПОСВЯЩЕННАЯ ФИЗИКЕ БОЛЬШОГО
АДРОННОГО КОЛЛАЙДЕРА
LHCP 2015
THE THIRD ANNUAL CONFERENCE
on Large Hadron Collider Physics
LHCP2015


Санкт-Петербургский
государственный
университет
Saint Petersburg
State University
www.spbu.ru
Виктор Анатольевич
Матвеев
Владимир Игоревич
Шевченко


on Large Hadron Collider Physics
LHCP2015
Yandex
Data Factory
Saint Petersburg
State University
www.spbu.ru
Виктор Анатольевич
Матвеев


Saint Petersburg State University
www.spbu.ru
Санкт-Петербургский государственный университет
Виктор Анатольевич Матвеев
Владимир Игоревич Шевченко
Григорий Александрович Феофилов


THE THIRD ANNUAL
on Large Hadron Collid
HCP

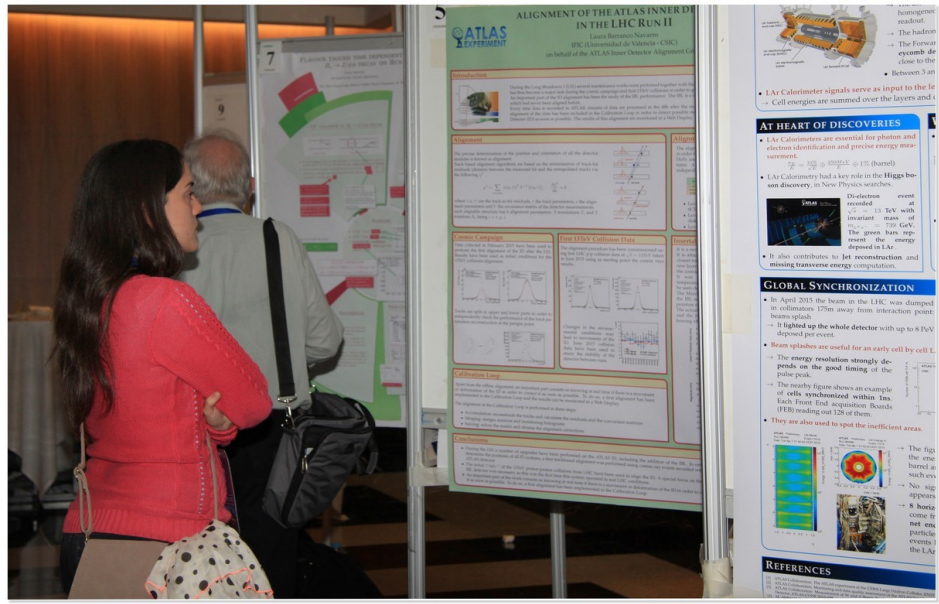
ATLAS EXPERIMENT
ALIGNMENT OF THE ATLAS INNER D
IN THE LHC RUN II
Laura Barranco Navarro
IFIC (Universidad de Valencia - CSIC)
on behalf of the ATLAS Inner Detector Alignment
Alignment
Cosmic Campaign
First 13TeV Collision Data
Calibration Loop
AT HEART OF DISCOVERIES
Global Synchronization
References


Alignment
Cosmic Campaign
Calibration Loop


C.BECHSTEIN


THE THIRD ANNUAL CONFERENCE
on Large Hadron Collider Physics
LHCP2015
August 31 – September 5, 2015
St. Petersburg, Russia

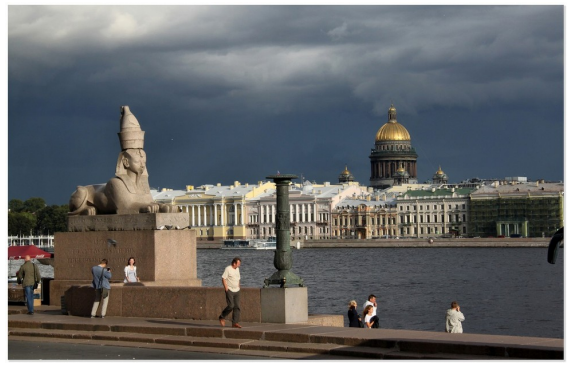


© ИННО-МИР inno-mir.ru


© ИННО-МИР inno-mir.ru


© ИННО-МИР inno-mir.ru


© ИННО-МИР inno-mir.ru


© ИННО-МИР inno-mir.ru


© ИННО-МИР inno-mir.ru


© ИННО-МИР inno-mir.ru


© ИННО-МИР inno-mir.ru


CCCP


NATIONAL
RESEARCH CENTRE
«KURCHATOV INSTITUTE»


PNPI - NRC KI


IHEP


ITEP NRC KI


CERN


JINR
DUBNA


Saint Petersburg
State University


POLYTECH
Peter the Great
St.Petersburg Polytechnic
University


Saint Petersburg Scientific Center RAS


RFBR
RUSSIAN
FOUNDATION
FOR BASIC
RESEARCH


INNO-MIR


Yandex